LEVEL II

Sixth Symposium
(International)

on

DETONATION

Naval Surface Weapons Center
White Oak
August 24-27, 1976

AD-75143

REPORT DOCUMENTATION PAGE

READ INSTRUCTIONS
BEFORE COMPLETING FORM

1. REPORT NUMBER	2. GOVT ACCESSION NO.	3. RECIPIENT'S CATALOG NUMBER
ACR-221		

4. TITLE *(and Subtitle)*	5. TYPE OF REPORT & PERIOD COVERED
SIXTH SYMPOSIUM (INTERNATIONAL) ON DETONATION	
	6. PERFORMING ORG. REPORT NUMBER

7. AUTHOR(s)	8. CONTRACT OR GRANT NUMBER(s)
D. J. Edwards and S. J. Jacobs, Editors	

9. PERFORMING ORGANIZATION NAME AND ADDRESS	10. PROGRAM ELEMENT, PROJECT, TASK AREA & WORK UNIT NUMBERS
Naval Surface Weapons Center White Oak Laboratory Silver Spring, Maryland 20910	0

11. CONTROLLING OFFICE NAME AND ADDRESS	12. REPORT DATE
Office of Naval Research Department of the Navy Arlington, Virginia	24-27 August 1976
	13. NUMBER OF PAGES
	806

14. MONITORING AGENCY NAME & ADDRESS*(if different from Controlling Office)*	15. SECURITY CLASS. *(of this report)*
	UNCLASSIFIED
	15a. DECLASSIFICATION/DOWNGRADING SCHEDULE

16. DISTRIBUTION STATEMENT *(of this Report)*

APPROVED FOR PUBLIC RELEASE: DISTRIBUTION UNLIMITED

17. DISTRIBUTION STATEMENT *(of the abstract entered in Block 20, if different from Report)*

18. SUPPLEMENTARY NOTES

Available from:
Superintendent of Documents   Stock Number:
U. S. Government Printing Office   S/N 008-051-00067-4
Washington, D. C. 20402

19. KEY WORDS *(Continue on reverse side if necessary and identify by block number)*

DETONATION	PROPELLANTS	DEFLAGRATION
EXPLOSIVES	EQUATION OF STATE	
EXPLOSIONS	REACTIVE FLOWS	
SHOCK WAVES	DEFLAGRATION TO DETONATION TRANSITION	

20. ABSTRACT *(Continue on reverse side if necessary and identify by block number)*

This is the Proceedings of the Sixth Symposium on Detonation sponsored by the Lawrence Livermore Laboratory, Los Alamos Scientific Laboratory, Naval Surface Weapons Center, and the Office of Naval Research. Contents include texts of 62 presented papers and 19 poster display presentation on the subject of detonation in condensed media, deflagration, and shock waves related thereto.

DD $_{1\ JAN\ 73}^{FORM}$ 1473   EDITION OF 1 NOV 65 IS OBSOLETE
S/N 0102-LF-014-6601

DEPARTMENT OF THE NAVY
NAVAL SURFACE WEAPONS CENTER
DAHLGREN, VIRGINIA 22448

WHITE OAK LABORATORY
SILVER SPRING, MD. 20910
(202) 394—

DAHLGREN LABORATORY
DAHLGREN, VA. 22448
(703) 663—

IN REPLY REFER TO·
R13:CSC:1vm

Notice of Publication

SIXTH SYMPOSIUM (INTERNATIONAL) ON DETONATION

A limited number of copies of the Proceedings of the Sixth Symposium (International) on Detonation are now available from the U. S. Government Printing Office.

The symposium which took place 24-27 August 1976 at Coronado, California, was sponsored by the Lawrence Livermore Laboratory, the Los Alamos Scientific Laboratory, the Naval Surface Weapons Center, and the Office of Naval Research.

The proceedings give the texts of 62 presented papers plus 19 additional papers which made up a poster display presentation.

Topics which are treated include:

* Shock to Detonation Transition and Detonation Studies

* Deflagration to Detonation Studies

* Detonation and Initiation

* New Explosives Properties

* Explosively Driven Shocks in Inert Media

In addition, critical discussions are presented on the $P^2\tau$ shock initiation threshold criteria and on the decomposition kinetics of nitromethane.

The book is clothbound, 806 pages. Current price (1978, U.S.A.) is $12.25.

Order from:

Superintendent of Documents
U. S. Government Printing Office
Washington, D. C. 20402

Sixth Symposium (International) on Detonation
Stock Number: S/N 008-051-00067-4

(6)

PROCEEDINGS

Sixth Symposium

(International)

on

DETONATION (6th)

Held at Coronado, California
on 24-27 August 1976,

Sponsored by

LEVEL

LOS ALAMOS SCIENTIFIC LABORATORY

LAWRENCE LIVERMORE LABORATORY

NAVAL SURFACE WEAPONS CENTER

OFFICE OF NAVAL RESEARCH

(11) Aug 76

(12) 818 p.

(10) David J. Edwards
Sigmund J. Jacobs

August 24-27, 1976
Coronado, California

(14) ONR - ACR-221

D D C
RECEIVED
SEP 27 1978
A

OFFICE OF NAVAL RESEARCH-DEPARTMENT OF THE NAVY
Arlington, Virginia

78 09 26 310

265250   LB

PREVIOUS PUBLICATIONS IN THIS DETONATION SERIES

"Proceedings—Conference on the Chemistry and Physics of Detonation," January 11, 12, 1951, sponsored by the Office of Naval Research, Unclassified, 110 pp.; AD 127020, printed copy—$6.00.

"Preprints—Second ONR Symposium on Detonation," February 9, 10, 11, 1955, sponsored by the Office of Naval Research.

> Unclassified Volume, 502, pp.; PB 128369, photocopy—$81.90; microfilm—$11.10; available from Labrary of Congress, Washington, D.C. 20540.

> Volume (Declassified Dec. 1974), 157 pp.; AD 52145.

"Preprints—Third Symposium on Detonation," September 26, 27, 28, 1960, cosponsored by Naval Ordnance Laboratory at White Oak and the Office of Naval Research, ONR Symposium Report ACR-52.

> Volume 1—Unclassified, 325 pp.; PB 181172, paper copy $6.00.
> Volume 2—Unclassified, 333 pp.; PB 181173, paper copy $6.00.
> Volume 3—(Declassified Dec. 1974), 187 pp.; AD 322061.

Note: AD numbered reports available from the Defense Documentation to qualified persons and organizations. PB numbered reports (except PB 128369) available from the National Technical Information Service, Department of Commerce, Springfield, VA 22150.

The following are available from

> Superintendent of Documents
> U.S. Government Printing Office
> Washington, D.C. 20402.

"Proceedings—Fourth Symposium (International) on Detonation," October 12-15, 1965, Office of Naval Research, Department of the Navy. Clothbound, 658 pages, illustrated, Cat. No. D210.15:ACR-126, (1976 price, $11.15).

"Proceedings—Fifth Symposium (International) on Detonation," August 18-21, 1970, Office of Naval Research, Department of the Navy. Clothbound, 612 pages, illustrated, Cat. No. D210.15:ACR-184, (1976 price, $10.70).

PREFACE

The Sixth Symposium (International) on Detonation was held at the Hotel del Coronado in Coronado, California (a suburb of San Diego) in the four day period August 24 to 27, 1976.

The sponsoring organizations were:

> Lawrence Livermore Laboratory, Livermore, CA (LLL)
> Los Alamos Scientific Laboratory, Los Alamos, NM (LASL)
> Naval Surface Weapons Center, White Oak, Silver Spring, MD (NSWC)
> Office of Naval Research, Arlington, VA (ONR)

The following committees were responsible for the operational details:

ORGANIZING COMMITTEE

William E. Deal, LASL
David J. Edwards, NSWC
Lee H. Hicks, LLL
John W. Kury, LLL
Richard Miller, ONR
D. John Pastine, NSWC

GENERAL ARRANGEMENTS

Lee H. Hicks, Secretary
  Treasurer. LLL
Alita Roach, LASL
Wanda Dowling, NSWC
Diana L. Vargas, Systems, Science,
  and Software

TECHNICAL PAPERS REVIEW

William E. Deal, LASL
John W. Kury, LLL
D. John Pastine, NSWC
Donna Price, NSWC
Sigmund J. Jacobs, NSWC

WOMEN'S ACTIVITIES

Mary Kury, LLL

LOCAL ARRANGEMENTS

John L. Deuble. Systems, Science,
  and Software

POSTER SESSION

John W. Kury, LLL
Donald Ornellas, LLL

PREPRINTS/PROCEEDINGS

David J. Edwards, NSWC
Minge Frye, NSWC

The meeting was divided into sessions for the floor presentations. We were honored to have Dr. Harold M. Agnew, Director, Los Alamos Scientific Laboratory as the Guest Speaker for the Symposium's Banquet. His topic was, "Advanced Energy Technologies". It dealt with the broad problems facing the world in its need for development of new sources of energy to meet the growing demand.
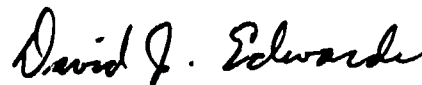
A unique addition to the presentations at the symposium was the inclusion of a "Poster Session", an exhibit form of presentation in which the authors employed posters and displays of hardware to illustrate the subject matter. The experiment was so successful that it is very likely to be repeated in future meetings of this series.

This volume contains the complete set of papers and discussions for both the formal sessions and the poster sessions of the Sixth Symposium (International) on Detonation. To assist in identifying contributors an index has been appended at the end of this volume. A list of attendees to the symposium is also appended.
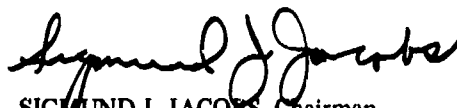
This series of symposia began in 1951 when a "Conference on the Chemistry and Physics of Detonation" was held at the old Navy Building under the sponsorship of the Office of Naval Research. The meetings became international with the Fourth Symposium on Detonation jointly sponsored by ONR and NOL at the Naval Ordnance Laboratory in 1965. Information regarding availability of the documentation of previous symposia is included here for the reader's information.

The chairman is grateful to the above organizations and to the many contributors.

The chairman is grateful to the sponsoring organizations, to the members of the above mentioned committees, and to the contributors of papers and poster displays for their cooperation.

David J. Edwards

DAVID J. EDWARDS, Editor

Sigmund J Jacobs

SIGMUND J. JACOBS, Chairman
Naval Surface Weapons Center
White Oak Laboratory

iv

CONTENTS

SESSION I. SHOCK-TO-DETONATION TRANSITION AND DETONATION STUDIES

SESSION II. SHOCK-TO-DETONATION TRANSITION AND DETONATION STUDIES

SESSION III. DEFLAGRATION-TO-DETONATION TRANSITION STUDIES

SESSION IV. DEFLAGRATION-TO-DETONATION TRANSITION STUDIES

SESSION V. MOSTLY THEORETICAL STUDIES

*Abstract only

POSTER SESSION

Session I
SHOCK-TO-DETONATION TRANSITION AND DETONATION STUDIES

Chairmen: Joseph Hershkowitz
               Picatinny Arsenal
           Paul A. Urtiew
               Lawrence Livermore Laboratory

SEPARATION OF IGNITION AND BUILDUP TO DETONATION IN PRESSED TNT

B. C. Taylor and L. W. Ervin
Detonation & Deflagration Dynamics Laboratory
Ballistic Research Laboratories
Aberdeen Proving Ground, Maryland 21005

A 4-inch light gas gun is used to impact pressed TNT and a streak camera is used to measure the velocity of the resulting disturbance generated at the rear surface. At one extreme, one can measure the minimum shock pressure required to generate an immediately visible reaction and at the other extreme the conditions required to produce detonation. These two different tests allow one to separate the sensitivity to ignition by shock from the sensitivity to detonation by shock. Measurements were made on TNT charges pressed to three different conditions: (1) large grain TNT pressed to 1.30 grams/cc density, (2) large grain TNT pressed to 1.55 grams/cc, and (3) small grain TNT pressed to 1.55 grams/cc. The sensitivity to ignition followed the order (1), (2), (3) with (1) being ignited at the lowest pressure, and the sensitivity to detonation followed the order (3), (2), (1) with (3) requiring the least critical energy.

INTRODUCTION

There is a long-standing need to understand the process by which shock waves initiate reaction and buildup to detonation in high explosives, both from the standpoint of fundamental interest and from the need to know the parameters controlling the sensitivity of explosives. The majority of high explosives used are too sensitive—they don't have to be this sensitive to be detonated when detonation is desired. The excess sensitivity represents an unnecessary hazard. If the sensitivity of the high explosive is to be decreased, it will be done by raising the pressure at which reaction starts, and that is why we are concerned with measuring this parameter.

The recent addition of the 4-inch diameter Light Gas Gun Facility to the Ballistic Research Laboratories, coupled with existing high speed optical recording equipment has made it possible to generate precisely controlled shocks in explosive samples and to study the resulting reaction. The net result is that the shock pressure region where explosive reaction is just beginning can be accurately delineated. With these techniques this parameter now can be measured as a function of explosive density and grain size for a variety of explosives.

The technique for detecting the start of reaction in the explosive consists of using the 4-inch diameter Light Gas Gun to generate a precisely controlled shock of large planar area in the explosive sample and measuring the velocity of the rear surface of the explosive. When the shock pressure is too low to cause reaction, the velocity of the rear surface can be calculated from the porous equation of state for the explosive with the explosive considered to be inert. The streak camera measurements in the low pressure range are in agreement with these calculations. When the shock pressure becomes high enough to cause reaction, there is a divergence of the measured velocity from the calculated (inert) velocity, and the break point defines the start of reaction.

The energy per unit area just necessary to cause detonation which is transferred to the explosive by the flyer plate will be referred to hereafter simply as critical energy. This critical energy can be determined using a modification of the above technique. A thin plate of aluminum is projected against the explosive sample and the velocity of the reaction products emerging from the rear surface of the explosive is measured. Since the velocity of these products is known for full detonation, the velocity of the donor aluminum plate can be varied in small steps until full detonation occurs, and the critical energy can be calculated (1).

These two different tests allow one to separate the sensitivity of the explosive to ignition by shock from the sensitivity to detonation by shock.

EXPERIMENTAL SET-UP

A schematic drawing of the experimental arrangement is shown in Fig. 1. The light gas gun fires a nominal 4-inch diameter projectile which impacts the explosive sample in an evacuated target chamber (approximately 50 torr pressure.) Both the exploding wire light source and the ever-ready rotating mirror streak camera are external to the target chamber and view the event through glass ports. The streak camera is located alongside the gun barrel due to space limita-

tions; hence the turning mirror is required to deflect the image as shown.

For the experiments designed to detect the minimum pressure at which visible reaction occurred, the projectile impacted the explosive sample directly, as indicated in Fig. 1. However, for the experiments designed to measure the critical energy required to cause detonation, the projectile had a brass face plate 0.318 cm (0.125 in.) thick attached to the normal 1.27 cm (0.50 in.) thick aluminum front. The projectile did not impact the explosive sample directly, but instead struck an aluminum plate of either 0.10 cm (0.040 in.) or 0.32 cm (0.125 in.) nominal thickness which was spaced 1.27 cm (0.50 in.) from the explosive sample. When impacted by the brass faced projectile, this aluminum plate, having a smaller shock impedance than the brass, acquired a higher velocity and separated from the brass. Over the 1.27 cm (0.50 in.) of travel before striking the explosive sample, the aluminum ran ahead of the brass faced projectile an appreciable distance. When the aluminim flyer plate then struck the explosive, one had sufficient time to observe the resultant reaction before the slower moving brass faced projectile struck the explosive and caused additional reaction. The low density (1.3 gram/cc) explosive was 0.95 cm (0.375 in.) thick and the higher density (1.55 gram/cc) explosive was 1.59 cm (0.625 in.) thick.
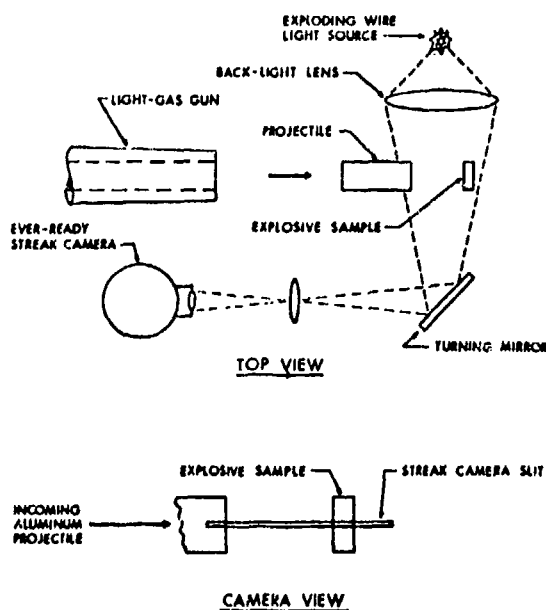
POROUS EQUATION OF STATE

The Hugoniot for the shocked porous TNT can be developed in the following manner (2). Figure 2 shows the situation where both a solid material (s subscript) and a porous material or foam (f subscript) are shocked to the same specific volume V from different initial states (o subscript). The pressure in the foam material will be higher than that in the solid due to the additional internal energy deposited in the foam material by the collapse of the pores. The Gruneisen equation of state assumes that the independent variables are specific volume and internal energy, that the pressure is proportional to the internal energy or $P = F(V)E$, and that $F(V)$ is of the form $F(V) = \Gamma(V)/V$. In the pressure range of interest here, one can assume that the Gruneisen parameter $\Gamma(V)$ is not a function of V but is a constant, and can be evaluated at the initial specific volume to give,

$$\Gamma(V) = \Gamma_o = V_o (\partial P/\partial E)_{V_o} = \alpha C_o^2/C_p,$$

Fig. 1. Experimental arrangement.

where α is the coefficient of thermal expansion, C_o is the bulk sound velocity, and C_p is specific heat at constant pressure. Thus $P = \Gamma_o E/V$, and it follows that $P_f - P_s = \Gamma_o (E_f - E_s)/V$. One can use the Hugoniot jump conditions to evaluate E_f and E_s:

Since $\quad E_f - E_{of} = P_f(V_{of} - V)/2$

and $\quad E_s - E_{os} = P_s(V_{os} - V)/2$

and $\quad\quad\quad E_{of} \cong E_{os}$

Then subtracting gives

$$E_f - E_s = P_f(V_{of} - V)/2 - P_s(V_{os} - V)/2$$

Thus

$$P_f - P_s = \Gamma[P_f(V_{of} - V)/2 - P_s(V_{os} - V)/2]/V$$

which simplifies to

$$P_f = P_s \frac{V_{os} - V - 2V/\Gamma}{V_{of} - V - 2V/\Gamma} \qquad (1)$$

Thus the shock in the porous explosive is expressed in terms of the pressure produced in the solid (P_s) by compression to the same specific volume V multiplied by a function of the various specific volumes, all of which are known or can be calculated.

Using the shock jump condition relating pressure, shock velocity U and particle velocity u,

Fig. 2. Shock compression of solid and porous explosives.

$$P = \rho_{of} uU; \quad \text{then } U^2 = PV_{of}^2/(V_{of} - V) \qquad (2)$$

$$u = U(V_{of} - V)/V_{of} \qquad (3)$$

For the shock pressures and porosities employed in these studies, it is assumed that the voids in the explosive are completely collapsed by the passage of the shock wave and that the subsequent expansion that occurs when the pressure is reduced to zero is that of the solid explosive.

RESULTS

Measurements were made on TNT of two different grain sizes and of two different densities to determine the minimum shock pressure at which immediately visible reaction begins and to measure the critical energy necessary to detonate these samples. The minimum shock pressure which causes reaction is a measure of the ease of ignition of the samples, while the critical energy required for detonation is a measure of the ease of detonation of the samples. The shock buildup to detonation process can be viewed as one in which ignition is caused by shock collapse of the voids within the explosive, and the subsequent reaction which leads to detonation as a grain burning process. If the density and the grain size of the samples are varied separately, this will be equivalent to varying the void size and the surface area of the explosive grains separately, and should affect the ignition process and the buildup to detonation process independently.

The TNT pressings which were used in these experiments were made from fractions sifted from TNT powder prepared by solvent precipitation. The coarse-grained samples represented that fraction which passed a #50 U.S. Standard Sieve and was retained on a #70 sieve. The fine-grained ones represented that fraction which passed a #200 sieve and was retained on a #230 sieve. Surface area measurements were made on the resulting pressings by V. Boyle of BRL (3) and are given in Table 1.

In Fig. 3, the reaction products velocity is shown for the coarse grain TNT pressed to two different densities ($\rho = 1.3$ gm/cc and $\rho = 1.55$ gm/cc). The velocity which the sample would have if no reaction had occurred was computed from the porous equation of state for TNT and is plotted on the

5
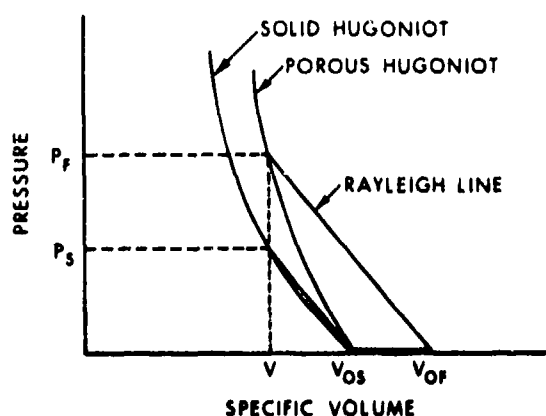
figure. It can be seen that the low density sample indicates reaction at 4.5 kilobars, while the high density sample with its smaller voids starts to react at about 14 kilobars. It was found that jetting from the pores of the sample could cause a false reading, and a layer of plastic 0.5 mil thick was used to retard this jetting without interfering with the expansion of the reaction products.

The results for fine grain and coarse grain TNT pressed to a density of 1.55 gm/cc are shown in Fig. 4. Since only density (or specific volume) is involved in calculating the shock response of the porous explosive (Eqs. 1, 2, and 3), both grain sizes have the same inert shock response.

Although both samples have the same total void volume, the coarse grain pressings have larger individual voids than the fine-grain pressings and show reaction at the slightly lower pressure of 14 kilobars compared to 15 kilobars required for the fine grain. Although the fine grain pressings required a higher pressure to cause initial reaction, once reaction started, it went to detonation more rapidly. The fine grain pressings were unreacted at 15 kilobars and at full detonation at 16.1 kilobars. The two experimental points at 12.9 kilobars and 13.9 kilobars are considerably above the calculated inert curve for the coarse grain 1.55 density TNT. This may be experimental error or it may represent a small amount of immediately visible reaction, as examination of Fig. 5

TABLE 1

Physical Characteristics of TNT Pressings

Sieve Size Range	Sieve Opening Range (μm)	Density (gm/cc)	Surface Area (cm^2/gm)
50–70	210–297	loose powder 1.30 1.55	1.14×10^3 1.23×10^3 1.66×10^3
200–230	62–74	loose powder 1.30 1.55	2.25×10^3 3.22×10^3 2.45×10^3
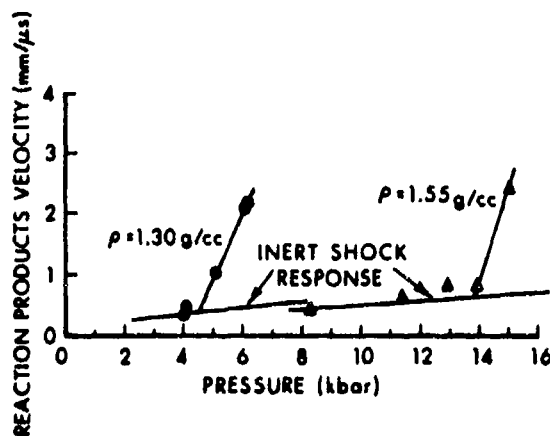
Fig. 3. Reaction of coarse grain TNT at two densities.
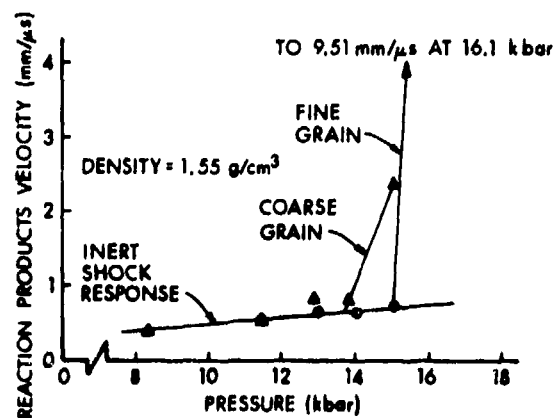
Fig. 4. Reaction of TNT of different grain sizes at same density.

6

will show. Here, the reaction products velocity is plotted versus time after shock emergence for the three shots at 11.4, 12.9, and 13.9 kilobars. For the 11.4 kilobar shot, the velocity of the reaction was constant for approximately 10 μsec after which the velocity jumped to a higher value. The shot at 12.9 kilobars had a constant velocity for approximately 1.5 μsec after which delayed reaction gradually increased the velocity of the products to 2 mm/μsec. The shot at 13.9 kilobars had the same initial velocity as the 12.9 shot but delayed reaction started sooner at 1.0 μsec, the velocity then increased more rapidly than the 12.9 shot, and a jump occurred at 7.7 μsec to a higher velocity.

Flyer plate measurements and calculations are in Tables 2, 3, and 4 and Figs. 6 and 7. The measurements tabulated in Table 2 are also plotted in Figs. 6
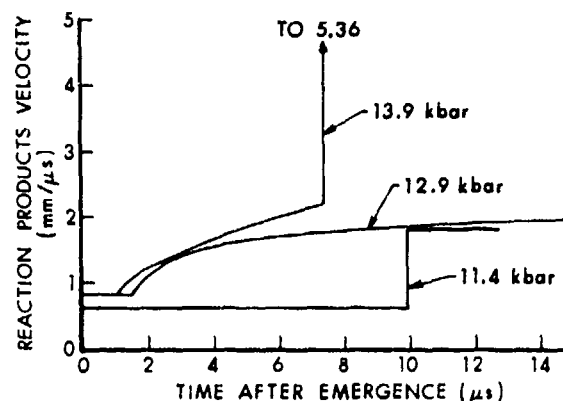
Fig. 5. Reaction products velocity versus time.

TABLE 2

Energy Versus Reaction Response

0.040 In. Thick Aluminum Flyer Plate

TNT: Coarse Grain—Thru #50 Sieve onto #70, Density = 1.55 gm/cm^3

Gun Breech Pressure (psi)			1250	1300	1350	1400	1450	1500
Flyer Plate Energy (cal/cm^2)			21.0	22.0	22.7	23.3	24.1	25.0
Reaction Products Velocity (mm/μsec)			0.75	1.77	5.60	10.2	9.19	9.39

TNT: Fine Grain—Thru #200 Sieve onto #230, Density = 1.55 gm/cm^3

Gun Breech Pressure (psi)			1150	1225	1300	1400		
Flyer Plate Energy (cal/cm^2)			19.2	20.6	22.0	23.3		
Reaction Products Velocity (mm/μsec)			0.27	0.35	9.32	9.73		

TNT: Coarse Grain—Thru #50 onto #70, Density = 1.3 gm/cm^3

Gun Breech Pressure (psi)	1200	1250	1300	1400	1600	2000	2500	3000
Flyer Plate Energy (cal/cm^2)	20.2	20.9	21.9	23.6	26.6	32.4	39.6	45.3
Reaction Products Velocity (mm/μsec)	2.2	2.92	3.96	4.55	5.55	7.30	9.22	10.2

0.125 In. Thick Aluminum Flyer Plate

TNT: Coarse Grain—Thru #50 onto #70, Density = 1.3 gm/cm^3

Gun Breech Pressure (psi)			980	1030	1080	1130	1200	1275
Flyer Plate Energy (cal/cm^2)			45.29	51.25	54.16	56.74	60.08	63.36
Reaction Products Velocity (mm/μsec)			6.28	7.60	8.17	8.87	9.42	9.57

7

and 7. The critical energy criterion can be formulated as:

$$Pu(\Delta t) = \text{constant}.$$

An alternative criterion is:

$$p^2(\Delta t) = \text{constant},$$

where (Δt) is the time of application of the shock pressure P against the explosive, and u is the particle velocity of the explosive at this pressure. These values are tabulated in Table 3 for the estimated detonation point in the four series of tests. Only the two tests made with coarse grain TNT of 1.30 gm/cc density allow a comparison to be made of the criteria. In Table 4, the estimated detonation point obtained with the 0.040 in. aluminum flyer plate has been chosen as a reference. The values of $Pu(\Delta t)$ and $p^2(\Delta t)$ at each of the shot points of the 0.125 in. aluminum flyer plate have been calculated. Here detonation first occurs at a flyer plate energy of 60.1 cal/cm^2. The $P^2(\Delta t)$ values of 378 kilobar^2-μsec agree exactly, while the $Pu(\Delta t)$ value for the 0.125 in. aluminum is 31.1 cal/cm^2 versus 24.6 cal/cm^2 for the 0.040 in. aluminum. Thus, in this limited test, using a

TABLE 3

Critical Energy for Detonation

Flyer Plate Thickness (in. nominal)	0.040	0.040	0.040	0.125
Flyer Plate Kinetic Energy (cal/cm^2)	22.0	23.2	43.	60.1
Explosive Density (gm/cc)	1.55	1.55	1.3	1.3
Grain Size	Fine	Coarse	Coarse	Coarse
Explosive Pressure (Kbar)	29.5	30.5	32.0	18.2
Explosive Particle Velocity (mm/μsec)	0.578	0.592	0.871	0.627
Pulse Time (μsec)	0.372	0.371	0.370	1.142
Pu (Δt) (cal/cm^2)	15.2	16.0	24.6	31.1
P^2 (Δt) (Kbar^2-μsec)	324.	346.	378.	378.

TABLE 4

Aluminum Flyer Plate Against Coarse Grain TNT
($\rho = 1.30$ gm/cc)

Flyer Plate Thickness (in. nominal)	0.040	0.125	0.125	0.125	0.125	0.125	0.125
Flyer Plate Kinetic Energy (cal/cm^2)	43.0	45.3	51.3	54.2	56.2	60.1	63.4
Reaction Products Velocity (mm/μsec)	9.75	6.28	7.60	8.17	8.87	9.42	9.57
Explosive Pressure (Kbar)	32.0	14.7	16.1	16.8	17.4	18.2	19.0
Explosive Particle Velocity (mm/μsec)	0.871	0.553	0.584	0.598	0.611	0.627	0.643
Pulse Time (μsec)	0.370	1.149	1.145	1.145	1.142	1.142	1.138
Pu (Δt) (cal/cm^2)	24.6	22.2	25.8	27.5	29.0	31.1	33.2
P^2 (Δt)(Kbar^2-μsec)	378	247	298	323	346	378	411

fairly low density (ρ = 1.30 gm/cc) pressing, the $P^2(\Delta t)$ criterion holds but the Pu(Δt) criterion does not.

It should be recalled that the explosive sample is 0.375 in. thick, or only 3 times as thick as the 0.125 in. impacting flyer plate. No experiments have been performed yet to determine whether a thicker explosive sample would detonate when impacted by a 0.125 in. thick aluminum flyer plate with less than 60.1 cal/cm^2 kinetic energy. If so, this would shift the Pu(Δt) value closer to that obtained with the 0.040 in. thick flyer.

The results of the experiments to measure the minimum shock pressure required to produce visible reaction and the experiments to measure the critical energy required to cause detonation are summarized in Table 5.

CONCLUSIONS

The ignition process and the buildup to detonation process are independent. The ignition process depends primarily on total void volume, the larger the total void volume, the lower the shock pressure required for ignition. While for buildup to detonation, the process depends upon the specific surface area of the explosive grains. For a large surface area, or small grain size, the buildup takes place more rapidly than for a small specific surface area (or large grain size).

Table 5 summarizes the results of these experiments. The ignition process depends primarily on total void volume. The larger the total void volume, then the lower is the shock pressure required for ignition. This can be seen by comparing the shock pressure of 4.5 kilobars required to ignite the large
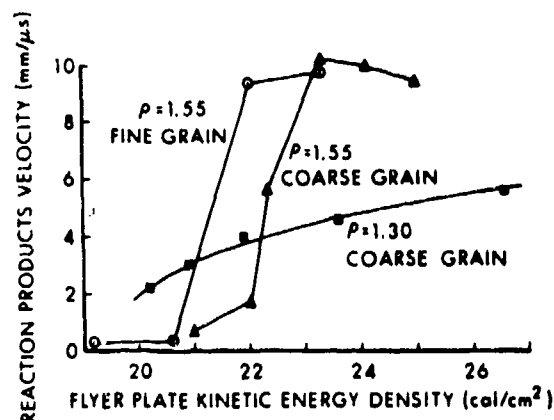
Fig. 6. *Energy versus reaction response for 0.040 in. aluminum flyer.*
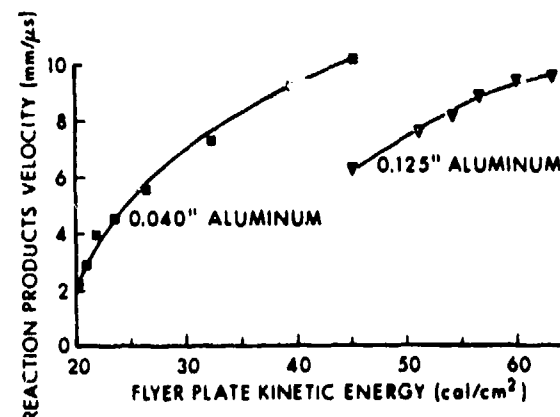
Fig. 7. *Energy versus reaction response for 1.30 gm/cc TNT.*

TABLE 5

Ignition Pressure and Energy for Detonation

Spec. Surface Area (cm^2/gm)	Density (gm/cm^3)	Grain Size	Min. Shock Pressure for Ignition (Kbar)	Critical Energy for Detonation (cal/cm^2) for 0.040 In. Aluminum
1.23 $\times$ 10^3	1.30	Coarse	4.5	24.6
1.66 $\times$ 10^3	1.55	Coarse	14.	16.0
2.45 $\times$ 10^3	1.55	Fine	15	15.2

grain 1.30 density samples compared to the 14 kilo-bars required to ignite the 1.55 density. Furthermore, on the basis of these limited tests, there seems to be a lower pressure required to ignite large individual voids compared to small individual voids when the total void volume of both large and small voids are identical. This is seen by comparing the shock pressure of 14 kilobars required to ignite the large grain 1.55 density pressings to the 15 kilobars required for the small grain 1.55 density.

From examination of the energy required to pro-duce detonation for coarse grain and fine grain TNT, both at 1.55 gm/cc, it can be seen that while the coarse grain TNT requires a shock pressure slightly less than the fine grain to cause ignition, (14 kbar vs. 15 kbar) the critical energy required to cause detona-tion is actually larger (16.0 cal/cm^2 vs. 15.2 cal/cm^2). The reversal in response is even more marked when the coarse grain pressings are compared at low and high densities. Here the shock pressures to ignite low and high density pressings are 4.5 kbar vs. 14 kbar, while the critical energies required to det-onate low and high densities are 24.6 cal/cm^2 vs. 16.0 cal/cm^2.

These results illustrate that when explosives are tested for sensitivity, one explosive can appear more sensitive than another in one type of test, but in another type of test the order can reverse and it will appear less sensitive.

Finally, on the basis of limited tests on TNT of 1.30 gm/cc density, it appears that the $P^2(\Delta t)$ criterion for detonation applies to these tests rather than the $Pu(\Delta t)$ criterion.

REFERENCES

1. F. E. Walker and R. J. Wasley, *Critical Energy for Shock Initiation of Heterogeneous Explosives*, Explosivestoffe, 17, No. 9, 1969.

2. J. O. Erkman and D. J. Edwards, *Computed and Experimental Hugoniots for Unreacted Porous High Explosives*, this symposium.

3. V. Boyle, *Papers presented at the DEAAF-F/G-7304, Technical Meeting: Physics of Ex-plosives, at Naval Ordnance Laboratory*, Silver Springs, MD., April-May 1974, Air Force Armament Laboratory, Eglin Air Force Base, Florida, pp. 104-11.

DISCUSSION

JULIUS ROTH
Portola Valley, California

Table 3 "Critical Energy for Detonation" gives the "Explosive Pressure" in 1.3 g/cc coarse TNT as 32.0 kbar. In the same table, the explosive pressure for coarse TNT at 1.55 g/cc, and the same flyer plate thickness as above, is given as 30.5 kbar. My under-standing is that these are "threshold" pressures. If so, is it not most surprising that the threshold pressure for 1.55 g/cc TNT is less than for 1.3 g/cc TNT? Moreover, what effect does this apparent incon-sistency have on your contention about the constancy of $P^2\Delta t$?

REPLY BY B. C. TAYLOR

One of the main points of this paper is that the sensitivity to detonation varies independently to the sensitivity to ignition. In our case, the coarse grain 1.3 g/cc TNT requires an appreciably higher critical energy (and a slightly higher pressure) to cause deton-ation than does the coarse grain 1.55 g/cc TNT.

I did not use the term "threshold pressure" and am not certain what is your definition of this term. The values to which you refer are the calculated shock pressures induced in the explosive (considered as inert) by the specified flyer plate which has just sufficient energy to detonate the explosive. These pressures are considerably higher than the pressures required to cause immediately visible reaction, which are 4.5 kbar for coarse grain 1.3 g/cc TNT and 14 kbar for coarse grain 1.55 g/cc TNT (see Fig. 3). If these latter pressures were maintained for a sufficient time, then the reactive shock would build up to det-onation. If this is what you mean by "threshold pressure", then this would satisfy your expectation that the "threshold pressure" for 1.3 g/cc TNT should be less than that for 1.55 g/cc TNT.

As for the $P^2\Delta t$ criterion, there is no incon-sistency since the constancy of this value applies only when comparing identical samples having the same density and grain size.

SHOCK INITIATION AND THE CRITICAL ENERGY CONCEPT

P. Howe, R. Frey, B. Taylor and V. Boyle
Detonation & Deflagration Dynamics Laboratory
Ballistic Research Laboratories
Aberdeen Proving Ground, Maryland 21005

Analysis and a series of experiments have been performed on the shock initiation of secondary explosives. The experiments demonstrate clearly that the initiation process consists of two parts, an ignition and a buildup process. The ignition phase appears to be consistent with the assumption of a thermal explosion occurring at hot spots. The buildup is controlled by the intergranular surface area, and the data are consistent with the assumption of a heat transfer controlled grain burning mechanism.

INTRODUCTION

The concepts of "hot spots" in explosive initiation and "grain burning" in the propagation of detonation were originally proposed by Bowden (1) and Eyring (2). The necessity of the "hot spot" concept arises from the fact that under shock initiation conditions the bulk temperature of the explosive is much too low to initiate decomposition. Therefore, it is assumed that there are localized "hot spots" which are hotter than the bulk material, and that these "hot spots" are responsible for initiation. The "hot spot" concept seems to be generally accepted, and numerous explanations, most of them quite reasonable, have been offered to explain the occurrence of hot spots. For instance Bowden (1) has suggested adiabatic compression of gas; Mader (3) has studied the direct heating of the explosive by void closure, and Seeley (4) has suggested that jetting in collapsing voids may be important. Unfortunately, due to the large number of possible hot spot types, the relation of hot spot size and temperature to such parameters as void size, particle size, and porosity is unknown. While there is general acceptance of the hot spot concept, the exact function of the hot spots is not well understood. Frequently, it has been proposed that the energy released in hot spots is transmitted to the shock front, where it strengthens the shock and

leads to more energetic hot spots at points downstream in the charge, and that this process eventually leads to detonation (5,6). We believe that this is an incorrect interpretation and shall present our reasons for so believing.

Eyring's (2) grain burning concept seems to enjoy less acceptance. It was proposed by Eyring to explain the dependence of failure diameter on particle size, but it has not been generally exploited in discussions of initiation. The concept states that during the detonation process explosive grains burn inwards from the outside and that the net reaction rate is determined by the burning surface area or grain size. The relation between grain burning and hot spot decomposition has not been discussed. It has not been clear which process is dominant under various conditions or which is most responsible for the sensitivity of the explosive. Many discussions in the literature suggest that there is a fast energy release at the shock front and a slower release behind the front, and it is tempting to attribute this to hot spot decomposition and grain burning (7,8). Apparently, this association has not been made. Some investigators have attributed the slow heat release to delayed thermal explosions at hot spots (6). Many theories of initiation treat the burning of the explosive using kinetic parameters derived from thermal explosion experi-

ments. This ignores the implicit assumption of the grain burning model, namely that heat transfer must play a role in the energy release and that the dependence of the net reaction rate on temperature and pressure must be quite different from the dependence of fundamental chemical processes on these parameters.

Several years ago, Walker and Wasley (9) proposed a "critical energy" criterion for initiation of detonation. This criterion states that there is a critical energy per unit area which must be delivered to the explosive to obtain detonation. The criterion may also be stated in the form:

$$\frac{P^2 t}{\rho_0 U} = \text{constant or Put} = \text{constant, where}$$

P is the shock pressure in the explosive, t is the duration of the shock pressure (it should be noted that t is *not* the time to detonation), ρ_0 is the initial explosive density, and U is the shock velocity in the explosive. An alternate form of the criterion is $P^2 t$ = constant. In the region where initiation occurs prior to first shock transit of the sample, and for explosives of moderately low void volume fraction, these two criteria and nearly identical, as is shown in Fig. 1 for PBX 9404. In general, however, they are quite different. (We note that the term "critical energy" can be misleading when one is considering projectile impacts or other multidimensional experiments. In some such

cases the Put or $P^2 t$ criterion will work, but initiation is not related to projectile energy per unit area.) Even in the regime of single shock initiation there are conflicting data and numerous hypotheses have been advanced to develop critical conditions (see for example Price (10), Roth (6), and Lindstrom (11)).

PRELIMINARY ANALYSIS

We performed some preliminary analysis to determine if energy release by thermal explosion in hot spots is consistent with the critical energy criterion. We assumed that a certain amount of energy must be released in the duration of the initiating shock in order for buildup to detonation to occur. To perform these calculations, we first assumed that the hot spot temperature was related to the bulk thermodynamic temperature by the relation

$$T_H = T_0 + n(T_b - T_0),$$

where T_H is the hot spot temperature, T_0 is the initial temperature, T_b is the bulk thermodynamic temperature determined by the technique of Walsh and Christian (12), and n is an arbitrary parameter. There is no sound theoretical justification for this equation, it simply provides an appropriate temperature dependence. One should note that it assumes all hot spots reach the same temperature. This would be true if hot spot formation took place by the hydrodynamic closure of spherical voids, but if frictional processes are involved or if void shapes are more complicated, it will not be true. Using this equation, coupled with thermal explosion theory, as described by Frank-Kamenetskii (13), we compared the thermal explosion time, at a particular shock pressure, with the shock duration necessary to initiate detonation. The results are shown in Fig. 2 where we have plotted the thermal explosion time versus pressure on the same graph as a plot of minimum shock duration for initiation versus pressure. The thermal explosion times were computed for several activation energies as shown in the figure, and the frequency factor was chosen arbitrarily so that all of the curves would coincide at one pressure. The dependence of thermal explosion time on pressure is obviously very different from the dependence of minimum shock duration on pressure. Calculations were performed which considered the effect of a hot spot distribution as a function of temperature, and the effect of hot spot size. These calculations will not be described further here.
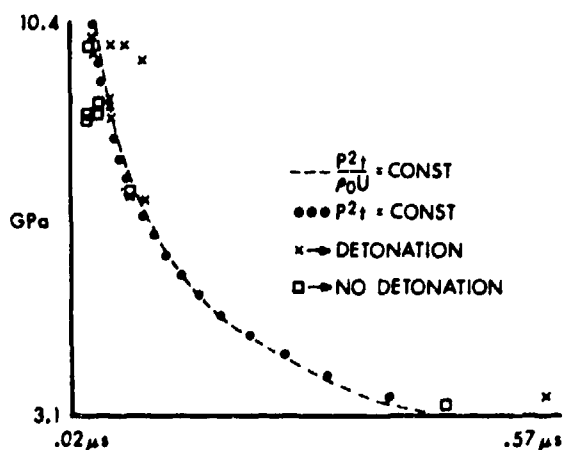
Fig. 1. *Critical energy and $P^2 t$ criteria for shock initiation of PBX 9404.*

However, the results had a negligible effect on the earlier analysis.

Comparison of the calculated curves in Fig. 2 with the critical energy curve permits one to conclude that, if thermal decomposition at hot spots is the dominant method of heat release during initiation of detonation, the critical energy criterion could not exist. In fact, any form of energy release dominated by Arrhenius kinetics is incom tible with the critical energy criterion. The reason fo 'his is simply that small changes in pressure are expected to cause small changes in hot spot temperature. which in turn cause very large changes in reaction rate. This dilemma can be avoided if the dominant method of heat release occurs by a grain burning mechanism. In this case, the temperature dependence of the chemical kinetics is moderated because it is coupled with heat transport. This point of view does not preclude the existence of hot spots. Indeed, they are extremely important for getting reaction started, but they are not the dominant contributors to the energy release.

EXPERIMENTAL RESULTS

With these considerations in mind, we performed a number of different experiments designed to determine the relationship between hot spots, grain burning, and the buildup to detonation. The experiments and their impact are described below.

A. Wedge Experiments with Nitromethane

Inclusions of controlled number and sizes were added to the homogeneous explosive, nitromethane, in order to simulate a heterogeneous explosive of known defect structure. The inclusion size, material, and amount were varied in order to study their effects on shock sensitivity. A gelling agent, Cab-O-Sil* was added to stabilize the mixtures. (Additional experiments showed that Cab-O-Sil had no effect in the behavior of the nitromethane to shock loading.) Mixtures were emplaced in a transparent, wedge shaped container. A 10 cm diameter explosive plane wave generator and buffer plate were used to generate a 6.0 GPa shock wave flat within forty nanoseconds over the area of the experiment. Shock arrival at the slant face of the wedge was observed with a rotating mirror camera writing at 8.8 mm/μsec. The experimental setup and results are shown in Figs. 3 through 7. The results clearly show that the initiation of detonation, at least for this system, is controlled by the surface area of the inclusions. The results will be discussed further in the general discussion.

---

*Cab-O-Sil is a fire dried, fumed silica of submicron particle size manufactured by Cabot Corporation.

Fig. 2. Comparision of critical energy criterion with thermal explosion predictions.
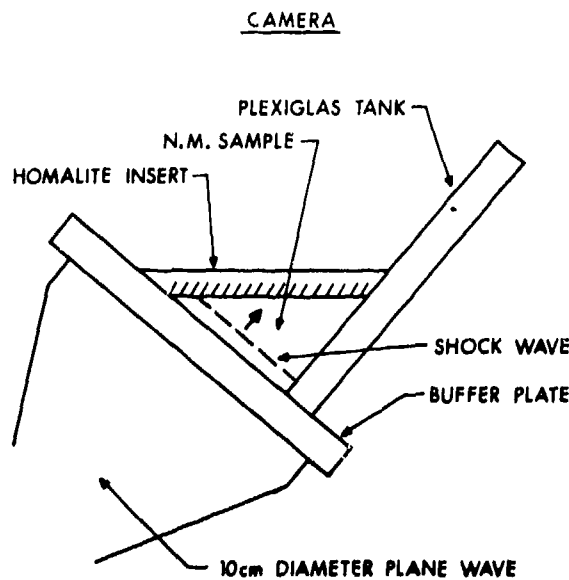
Fig. 3. Schematic of experimental setup for nitromethane with glass beads.

13

B. Wedge Experiments with TNT

In this set of experiments, the shock initiation of detonation in pressed TNT samples of known particle size and known density was observed. Two particle sizes (68 and 254 microns) and two densities (1.55 g/cm^3 and 1.30 g/cm^3) were used. Surface areas were determined in the pressed samples using nitrogen absorption techniques. Measurements of the buildup to detonation were made using the wedge technique, identical to that described in Section A. The results are presented in Figs. 8 through 10 and will be described in the general discussion.

5% VOLUME GLASS BEADS
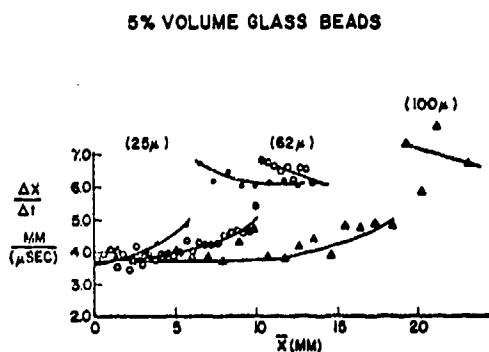
Fig. 4. Shock velocity versus distance for nitromethane with glass beads.

C. Light Gas Gun Experiments in Pressed TNT

A 10 cm diameter light gas gun was used to generate precisely controlled shocks of large planar area within the explosive samples. An every-ready rotating mirror streak camera was used to monitor the velocity of the explosive rear surface as a function of time, shock strength, and explosive parameters. Explosive samples were prepared in exactly the same manner as described in the previous section permitting good conditions for comparison of results. Two sets of experiments were conducted. One set used massive projectiles in order to generate long duration shocks, the other used thin flyer plates to generate short duration shocks. The experimental setup is shown in Fig. 11 and the results are shown in Figs. 12-16. (For additional details, see the paper "Separation of Ignition and Buildup to Detonation in Pressed TNT," by Boyd Taylor, presented elsewhere in this symposium.)

GENERAL DISCUSSION

A. Evidence for Grain Burning

Figure 4 shows the buildup to detonation in the nitromethane glass system for three sizes of glass beads. The beads serve as hot spot generators by providing for shock reflection and focussing effects

Fig. 5. Distance to detonation versus volume % inclusions for a 6 GPa shock input.
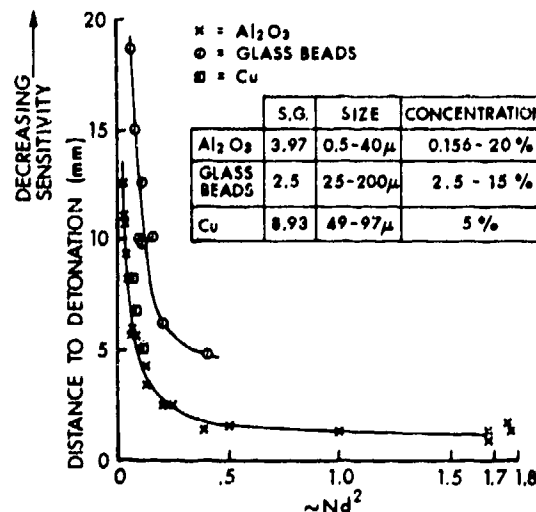
Fig. 6. Distance to detonation versus total specific surface area of inclusions.

14

which lead to localized high temperatures. Shock velocity is plotted against the distance the shock has propagated into the mixture. The initial pressure is ~6.0 GPa. As can be seen from the figure, for constant inclusion volume, the smaller sizes promote more rapid buildup. In Fig. 5, it can be seen that the distance to detonation does not correlate well with total inclusion volume. Neither did it correlate with the summed linear dimension. As can be seen in Fig. 6, a good correlation obtains for distance to detonation versus total surface area, for all three types of inclusions, and over the range 0.5-200 micron particle sizes. At a constant surface area, the variation of buildup time with the composition of the inclusion correlated with the shock impedance of the inclusion, see Fig. 7.

Our explanation for these results is as follows. We presume that the inclusions create hot spots by shock reflection. The hot spots do not coincide with the original inclusion, but their surface area and volume are proportional to the surface area and volume of the inclusions. Decomposition of the hot spots leads to energy release which is proportional to the volume of the original inclusions. This process can not be the dominant form of heat release, because the results do not correlate with inclusion volume. It is consistent with the data to believe that after the initial decomposition, the cool nitromethane adjacent to the hot spots is in contact with hot products and begins to burn in a heterogeneous process. The net energy release rate is thus controlled by the surface area of the original hot spots and is proportional to the surface area of the inclusions. This is apparently the dominant mechanism for energy release.

The experiments performed with the pressed TNT samples corroborate these ideas. In Fig. 8, buildup curves are shown for the two different densities and

	S.G.	SIZE (μ)	CONC.(%v)
○ Al₂O₃	3.47	0.5-40	0.156-20
△ GLASS	2.5	25-200	2.5-15

Fig. 7. Reduced time to detonation versus total specific surface area of inclusions.
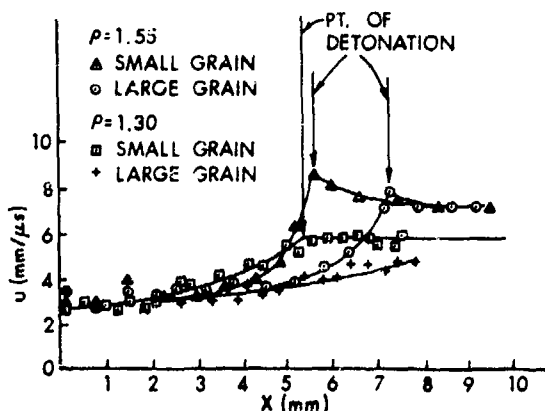
Fig. 8. Shock velocity versus distance for pressed TNT samples.

U_S (MM / μSEC)

TNT ($P=1.55$ G/CM^3)

△ SMALL GRAIN

⊙ LARGE GRAIN

TIME (μSEC)
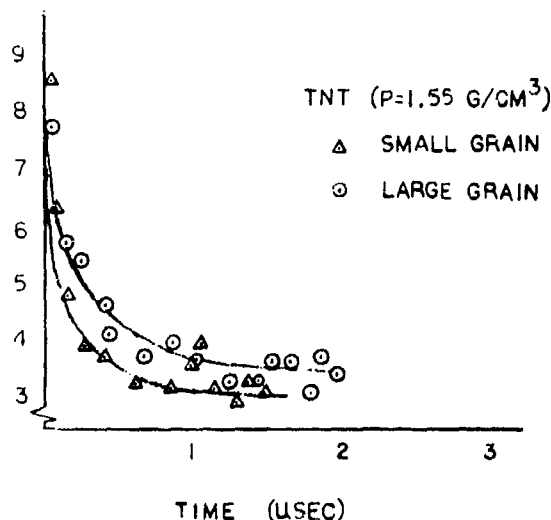
Fig. 9. Shock velocity versus time to detonation for pressed TNT.

15

surface areas considered. At each density, the larger surface area sample detonated sooner. The data are replotted in Fig. 9 using the detonation point as origin. In Fig. 10, the abscissa is corrected to account for the total surface area. (The details of the analysis are presented in (14).) When this is done, the data for the 1.55 gm/cm³ samples collapse to a single curve. (This surface area correction could not be made for the 1.30 g/cm³ samples, as only one detonated.) These results show rather conclusively that the buildup process is controlled by a grain burning mechanism which is surface area controlled.

B. The Ignition and Buildup Processes

The gas gun experiments shed additional light on both the ignition and buildup processes. Presentation of the results is somewhat complicated by the fact that the free surface velocity may increase with time after shock emergence, when reaction occurs. In Fig. 12, we have plotted the free surface velocity at the instant of shock emergence as a function of shock pressure for two particle sizes at the 1.55 g/cm³ density. The shock pressure refers to the pressure at impact, on the upstream surface and is determined from Hugoniot calculations. Reaction is indicated when the downstream free surface velocity rises above the value for an inert sample. The divergence of the reactive and inert free s . ace velocities provides a sensitive measure of the onset of reaction. Figure 12 shows the effect of density. Figure 13 shows that, at

a given density, the sample with large particles begins to react at slightly lower pressures than the sample with small particles. However, detonation occurred at lower pressures in the samples with smaller particle size. In terms of the immediate free surface velocity, the difference between the large and small grain samples is not great. The large grain sample shows evidence of some reaction at about 12.5 kilobars as opposed to about 15.5 kilobars for the small grain. Figure 14 shows that in the large grain samples the velocity increased markedly with time after shock emergence. Even the point at 11.5 kilobars showed evidence of reaction after 10 μsec. On the other hand, the samples with small particle size showed very little increase in velocity with time even for pressures just below the detonation limit. Figure 15 shows the free surface velocity versus time for the small particle size sample at 15.5 kilobars.

An increase in the immediate free surface velocity above the inert value indicates that reaction is causing the shock to accelerate. An increase in free surface velocity with time after shock emergence indicates that delayed reaction is occurring well behind the shock front and that the pressure is higher at some distance behind the front than it is at the front.

Fig. 10. Shock velocity versus product of specific surface area and time for pressed TNT.
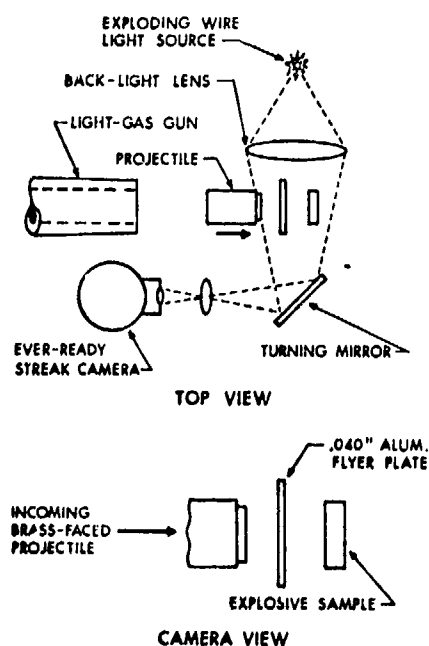
Fig. 11. Schematic of experimental setup for gas gun experiments.

15

Delayed reaction may or may not affect the shock initiation process depending on whether the reaction is felt at the front before or after lateral rarefactions reach the center of the charge. Reaction which is delayed by as much as 10 μsec probably would not affect shock initiation in most situations, but might be crucial in the occurrence of nondetonative violent reactions which can be very important in certain practical applications.

All of the experiments described above used shock generators which produced long duration loading (for purposes of this discussion, the pulses can be considered planar, semiinfinite). Because of this, one cannot expect a critical energy criterion to apply (and it doesn't). A critical specific energy or a critical pressure might be applicable, however. Neither the nitromethane experiments nor the TNT wedge experiments are useful in this regard, as only one input shock strength was used. The light gas gun experiments are more helpful. From Fig. 12 a marked dependence of the pressure for incipient reaction upon density is noted. Similarly, Figs. 13, 14, 15 show that the pressure for incipient reaction depends also upon particle size. The particle velocities corresponding to incipient reaction are almost independent of particle size and density, indicating that it is reasonable to apply a critical specific energy as an ignition criterion. This result is consistent with the work of Roth (6) and Howe and Boyle (14) and can be identified with a critical hot spot temperature.

It is noteworthy that the pressure for incipient reactions depends slightly on particle size. This is in contradiction with all previous calculations, but can be explained in the following way. The temperature of hot spots formed by void closure as a result of plastic flow would be independent of void size. This follows from the fact that there are no dimensional inputs to the problem other than the size of the void. If the void size is scaled up or down, the size of the resulting hot spot must scale in the same manner, and its temperature must not change. However, if void closure occurs as the result of brittle fracture and/or slippage between grains, the resulting hot spots will be heated by friction and will consist of hot surfaces. Their dimension perpendicular to the sliding surface will be determined by the rate of heat conductivity.
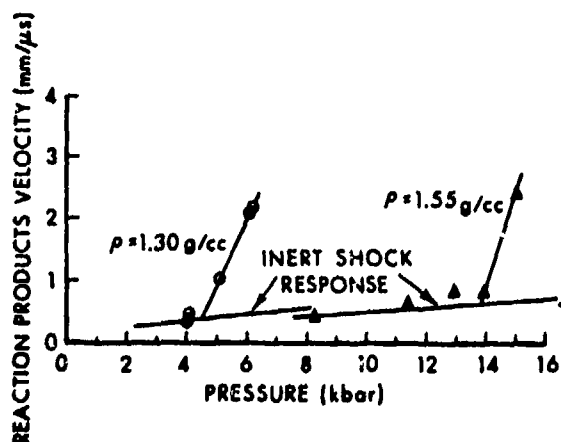
Fig. 12. Free surface velocity versus input pressure for pressed TNT.
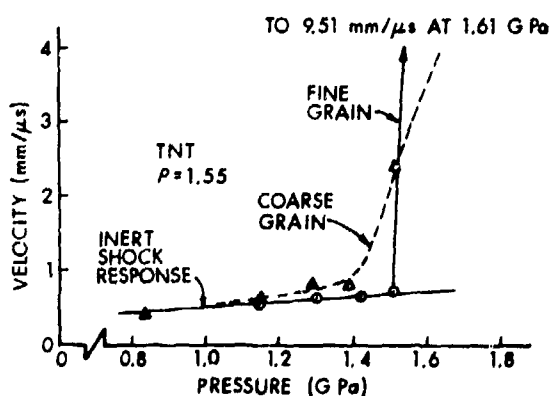
Fig. 13. Free surface velocity versus input pressure for high density TNT.
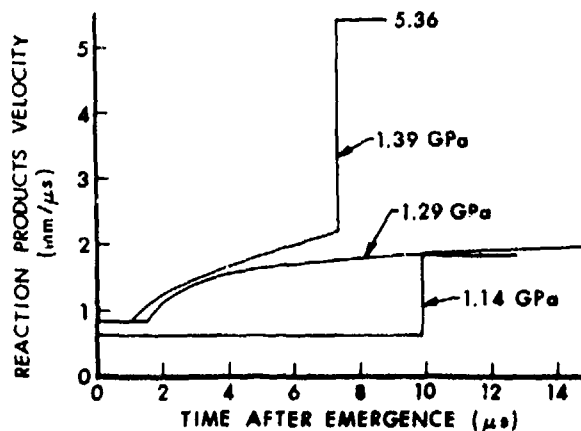
Fig. 14. Temporal behavior of reaction products velocity for coarse grain TNT.

17

This is a second dimensional input to the problem and allows the temperature attained to vary with void size. The thermal energy per unit area in a hot spot formed by frictional processes should be proportional to the pressure times the distance moved along the slip plane. If slippage is occurring as the result of void closure, this distance should be proportional to a void dimension, and peak temperature attained will be a function of the product of void diameter and pressure.

C. Dependence of P^2t on Particle Size and Density

Experiments with thin flyer plates were used to obtain critical energy data shown in Fig. 16. The results and experimental details are discussed by Taylor. The important features of his work are that (1) for the low density coarse grain TNT, the $Put = $ constant criterion is inoperative, but the data are consistent with $P^2t = $ constant (this is shown in Fig.

17); (2) for constant duration pulses, a particle size effect is observed, with small particle size samples requiring lower values of P^2t and; (3) a very strong density effect is observed, with low density samples requiring much larger values of P^2t for initiation of detonation. Note the dependence of P^2t on particle size and density is exactly the opposite of the dependence of ignition on particle size and density.

It appears that P^2t correlates with the buildup to detonation, but not with ignition, and is useful for predicting the effect of peak pressure on required pulse length *provided* that grain size and density are held constant.[*] Neither the critical energy criterion ($Put = $ constant) nor the P^2t criterion is useful for predicting effects of particle size or density changes.

SUMMARY AND CONCLUSIONS

A series of experiments have been conducted on the shock initiation of secondary explosives. The experiments demonstrate clearly that the shock initiation process consists of two parts, an ignition and a buildup process. It is consistent with the data to assume ignition occurs by thermal explosion at hot

---

[*]Even this conclusion is mitigated by the fact that only two data points, fairly close together, are available.

Fig. 15. Temporal behavior of reaction products velocity for fine grain TNT.
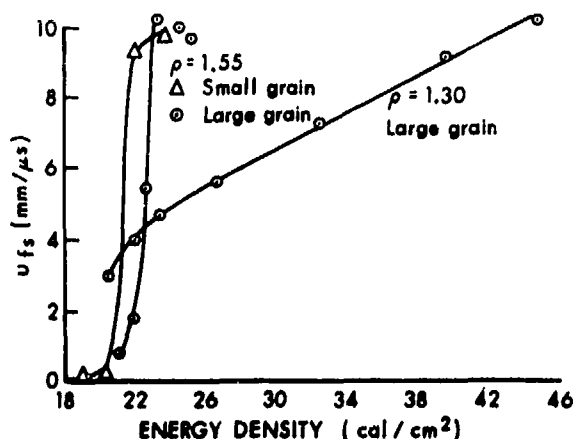
Fig. 16. Energy input/area to achieve a given reaction products velocity.
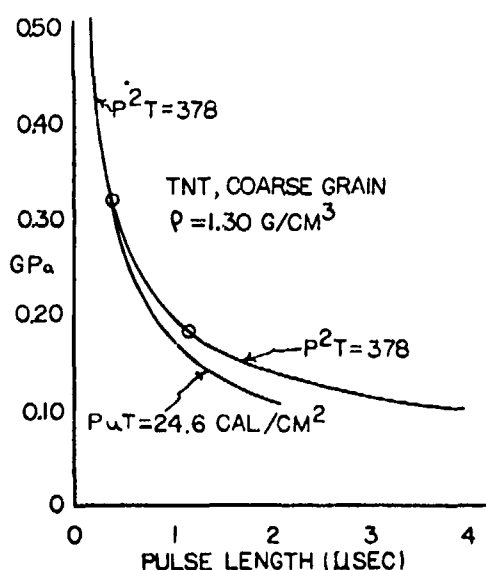
Fig. 17. A comparison of the critical energy and the P^2t criteria for low density TNT.

spots. However, the total energy release must be small and is not the controlling factor in the buildup to detonation. The buildup process correlates with the surface area of the hot spots which, for heterogeneous explosives, is related to the intergranular surface area. The evidence is very strong that the buildup to detonation is controlled by a heat transfer dominated grain burning process. Both the initial density and the particle size have an effect on sensitivity. Using pressure as a criterion, low densities and large particle sizes increase sensitivity to ignition. However the specific energy (equivalent to a temperature) required for ignition is approximately independent of density and particle size. The slight dependence of the energy density required for ignition upon particle size can be explained by assuming hot spots are formed by frictional processes at void closure. The critical energy criterion (Put = constant— was inconsistent with all the data. The P^2t criterion appears useful for predicting the effect of peak pressure upon pulse length required for detonation, provided particle size and density are held constant. The data base must be extended, however.

REFERENCES

1. F. P. Bowden and A. D. Yoffe, *Initiation and Growth of Explosions in Liquids and Solids*, Cambridge University Press (1952).

2. H. Eyring, R. E. Powell, G. H. Duffrey, and R. B. Darlin, Chemical Review 45, 69 (1949).

3. Charles L. Mader, Physics of Fluids 8, 10 (1965).

4. L. B. Seeley, "A Proposed Mechanism for Shock Initiation of Low Density Granular Explosives,"

Proceedings of the Fourth Electric Initiator Symposium (1963).

5. Charles L. Mader, LA-4475, An Empirical Model of Heterogeneous Shock Initiation of the Explosive 9404.

6. Julius Roth, "Shock Sensitivity and Shock Hugoniots of High Density Granular Explosives," Fifth Detonation Symposium.

7. D. Stirpe, J. O. Johnson, and J. Wackerle, Journal of applied Physics 41, 9 (1970).

8. C. Fauquignon and R. Cheret, "Generation of Detonations in Solid Explosives," Twelfth Symposium on Combustion (1969).

9. F. E. Walker and R. J. Wasley, Explosivstoffe 17, 9 (1969).

10. Price, Donna "Shock Sensitivity, A Property of Many Aspects," Fifth Detonation Symposium.

11. Lindstrom, I., Journal of Applied Physics 41, 337, (1970).

12. J. M. Walsh and R. H. Christian, Physical Review 97, 6 (1955).

13. Frank-Kamenetskii, D., "Diffusion and Heat Transfer in Chemical Kinetics," Plenum Press, New York, 1969.

14. Howe, P., Boyle, V., Minutes of the 14th Explosive Safety Seminar, New Orleans (1972).

SHOCK INITIATION OF HIGH-DENSITY PETN

Jerry Wackerle, J. O. Johnson, and P. M. Halleck*
Los Alamos Scientific Laboratory
University of California
Los Alamos, New Mexico 87545

The prompt (1- to 3-µs), planar shock initiation of 1.75-g/cm³ (98.4% crystal density) pentaerythritol tetranitrate (PETN) has been studied with impact-generated shocks and observations with the explosive wedge technique and quartz and embedded-Manganin pressure-gauge measurements. Dynamic compression properties, shock buildup to detonation, and pressure-field histories during initiation were determined. An analysis of the latter data show that shock-induced decomposition begins near the impact surface, forming a pressure pulse that in turn produces a compression wave that overtakes the shock front and effects the shock to detonation transition. Maxima in the pressure are interpreted to be due to sudden and spontaneous decreases in reaction rate when only partial decomposition has occured. Implications of this interpretation and possible errors that could invalidate it are discussed.

INTRODUCTION

A detailed understanding of the shock initiation of heterogeneous explosives remains unattained by explosives researchers. It is generally recognized that local high temperature regions, or hotspots, play a major role in inducing decomposition, pressure increases, and the buildup to detonation [1]. Although the mechanisms of hotspot development must be related to the inhomogeneity of the explosive, both quantitative experiments on the shock initiation process and their theoretical modeling with numerical hydrocodes necessarily assume local homogeneity. For computer simulations, relations between reaction rates and gross thermodynamic states (rate laws) are developed from proposed hotspot models [2], or "calibrated" to certain observations [3-5], or are almost purely empirical [6]. While yielding agreement with a limited number of observations—most notably those of short-duration shock sensitivity [2,3,5]—such

calculations have not been tested against details of the reactive flow.

In this work we have performed a comprehensive set of planar shock initiation experiments on 1.75-g/cm³ (98.4%-crystal-density) pentaerythritol tetranitrate (PETN), observing the shock compression properties, shock front buildup, and pressure-field histories during the initiation. Input shock strengths were chosen which produce buildup to detonation in 2 to 9 mm of run. The data obtained are sufficient to estimate density and energy fields during the buildup, and, with an assumed reactant-product equation of state, to calculate decomposition fields and reaction rates. While this analysis also assumes local homogeneity, it is hoped that the results—along with the more stringent tests of computer simulations that the data provide—will lead to a better selection of hotspot mechanisms, and to their more realistic modeling in theoretical treatments of shock initiation.

Our previous studies of the planewave initiation of high-density PETN began with explosive wedge experiments on 1.72-g/cm³ explosive [7]. Uniform shock

20

velocities observed during the buildup to detonation and other features of the streak-camera records led to the conjecture that pressure waves were formed near the input shock surface, and moved forward to overtake the front at the onset of detonation. This description of the initiation was supported by gas gun experiments with quartz gauges on 1.7-g/cm^3 PETN (8), where impact-face pressure excursions and transmitted wave profiles indicated significant, if not complete, reaction near the impact face prior to detonation at the front. The present work fully confirms and extends the previous description.

EXPERIMENTS

The PETN samples were machined from 1.75 ± 0.01 g/cm^3 pressings, of 99.95% pure material similar to that used in the previous studies (7,8). The experiments were all performed on a 70-mm gas gun, under vacuum, and included measurements of pressure histories with quartz and Manganin gauges and observations of shock-front trajectories with the streak camera explosive wedge technique. Planar shock waves were produced by the impact of projectiles faced with either x-cut quartz or 2024 aluminum alloy. Projectile velocities in the range of 0.1 to 0.6 mm/μs were used, where velocities could be predicted to ±0.005 mm/μs and measured to ±0.001 mm/μs; tilts at impact were usually less than one milliradian. The tilt and velocity determinations were made with electrical pin contactors. This measurement method, and the techniques for the pressure-gauge measurements are detailed elsewhere (9).

The arrangement for our "quartz-gauge front-back" experiments is shown in Fig. 1. A projectile-mounted quartz gauge strikes the sample, and its electrical response is transmitted via the signal pins and pickup ring for recording on an oscilloscope. Analysis provided an impact-face stress history for the 1.6-μs useful recording time of the gauge. The back or target gauge provides a record of the reflected-wave pressure at the gauge-sample interface. The target-gauge elements were usually too large to allow for side rarefactions, and observations with them were used for qualitative studies of the transmitted wave and shock transit-time determinations. Accuracy in both projectile-gauge pressures and transit times is ±2%.

Manganin gauges were used mainly in the multiple-embedded gauge arrangement shown in Fig. 2. Usu-
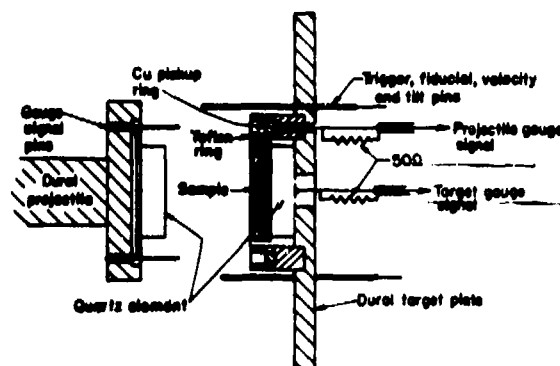
Fig. 1. Quartz-gauge front-back experimental arrangement.
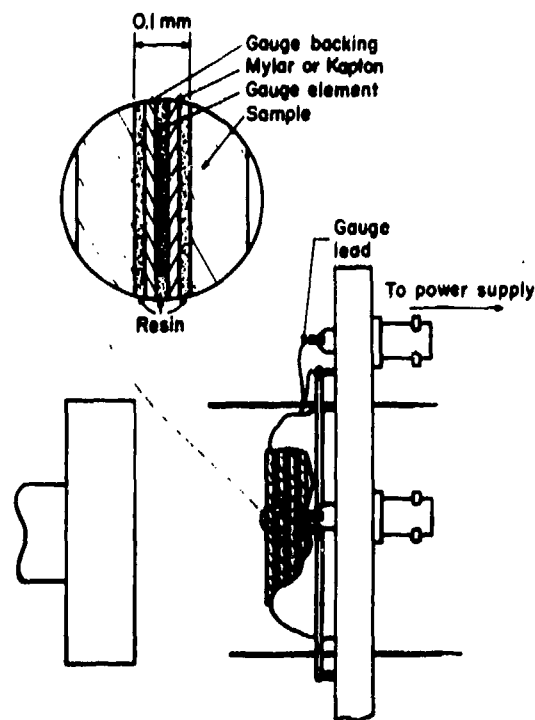
Fig. 2. Multiple-embedded Manganin-gauge experiment. Resin and gauge thicknesses are exaggerated.

ally four gauge assemblies were interleaved between 1- to 3-mm thick, 40-mm diameter disks of PETN, often with the last gauge at about the expected distance to detonation. The etched-grid, 50-Ω gauge elements used were 3- or 6-mm square and, respectively, 5- or 12-μm thick. The plastic layers had shock properties similar to high-density PETN.

21

Pulsed bridge power supplies with about 1 V/GPa response were employed. The gauges were specifically calibrated for use in high-density PETN, using an independent set of shock-wave and gauge-pressure measurements in Kel-F plastic—an excellent shock impedance match for 1.75 g/cm^3 PETN (10). Scatter in the calibration tests indicated that our Manganin-gauge measurements are accurate to no better than ±5%.

The explosive wedge technique was adapted to the gas gun as shown in Fig. 3. The illumination source shown was adequate to give film records as displayed in Fig. 4. Analysis was done by least squares fitting of the film readings and preshot measurements of the marker coordinates to determine magnification, effec-
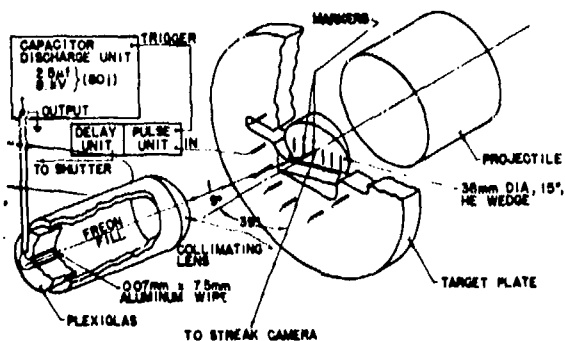
Fig. 3. Explosive wedge experiment.
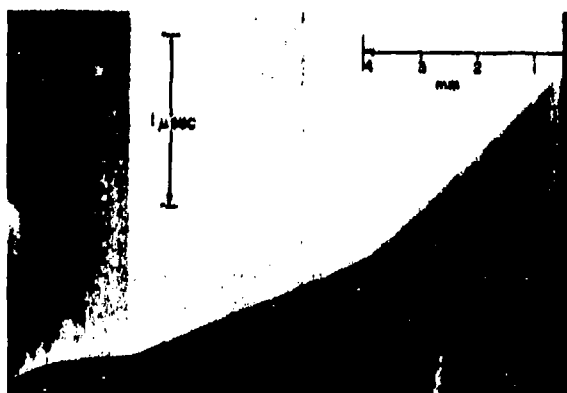
Fig. 4. Typical streak-camera record from an explosive wedge experiment. Time increases downward and the upper scale shows the distance of the shock from the impact face. The slope of the trace at right is proportional to the shock velocity during buildup to detonation.

tive wedge angle and shock position. The analysis program also provided for fitting the distance-time history to various empirical forms and correction for tilt at impact. Distances to detonation were measured to about ±0.1 mm. Other determinations were complicated by the wedge toes, lack of impact time indication on the streak-camera film, and inaccuracy in the impact tilt measurements. Estimated errors are 5% in times to detonation, 3% in average shock velocities and 8 to 10% in detonation velocities.

SHOCK COMPRESSION PROPERTIES

Quartz-gauge front-back experiments were the principal means of studying the shock compression properties of 1.75-g/cm^3 PETN. Target-gauge measurements at low impact velocities showed that ~0.25-GPa elastic precursors were produced in the explosive (10). At input shock strengths for the initiation studies (>1 GPa), the plastic wave velocity exceeded the precursor velocities, and elastic waves need not further concern us here. Two interesting features are seen in the projectile-gauge records in Fig. 5. In experiments with shock strengths between 1 and 2.5 GPa, a stress relaxation occurs after impact. This could be due to viscoelastic behavior, but more likely stems from a noninstantaneous void collapse. This explanation is consistent with the observed ~0.2-GPa pressure reductions, the 1.6% void fractions and ~15-GPa bulk modulus of the explosive. The second feature is the pressure excursions that follow the stress relaxation. These arise from decomposition
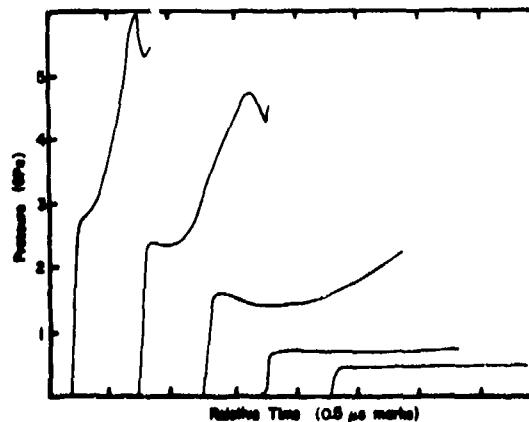
Fig. 5. Typical impact-face pressure histories measured with quartz gauges.

22

near the impact face, and as expected, become stronger and more rapid as the input shock strength is increased.

The shock Hugoniot for 1.75-g/cm^3 was calculated with the standard impedance-match method, using the initial impact-face pressures, the accurately measured projectile velocities, and the known Hugoniot for x-cut quartz. The results are plotted in pressure-particle velocity space in Fig. 6. These data were least-squares fitted to the usual linear shock velocity-particle velocity form, with the shock velocity at zero particle velocity held equal to the bulk sound speed. The resulting solid curve is seen to lie appropriately below and close to a Hugoniot for fully-dense PETN (dashed curve) derived from high-pressure static experiments (11).

SHOCK BUILDUP TO DETONATION

Explosive wedge experiments were performed on 1.75-g/cm^3 PETN with input shock strengths ranging from 1.5 to 2.6 GPa. The streak-camera record

shown earlier in Fig. 4 is typical of those obtained. The linear cutoff trace indicates a nearly constant shock-front velocity and shock strength during buildup, characteristic of high-density PETN (7). Fitting of the distance-time data showed that shock velocities during buildup were found to increase slightly at input shock strengths above 1.8 GPa and to decrease slightly with lower initial pressures. This behavior has no semblance of the "single-curve buildup" (12) observed of most heterogeneous explosives, including more porous PETN (13).

Input shock pressures for the wedge experiments were calculated by an impedance-match solution, using the Hugoniot for 1.75-g/cm^3 PETN given in Fig. 6, the known Hugoniot for the aluminum alloy projectiles, and the projectile velocities. The relationship of distance to detonation to input shock strength $D = 20.4 \, P^{-2.2}$ (D in mm, P in GPa) was fitted to the data plotted in Fig. 7. Reasonable agreement is seen with the previous such determinations on pressed PETN (7,8). The arrows on the upper two data points indicate that the distance to detonation was greater than the effective wedge thickness, and not observed. The fitted curve should lie above these points, but this would have required a more complicated form, which was unjustified with the scattered data.

Fig. 6. Shock Hugoniots for 1.75-g/cm^3 (solid curve) and fully dense PETN.
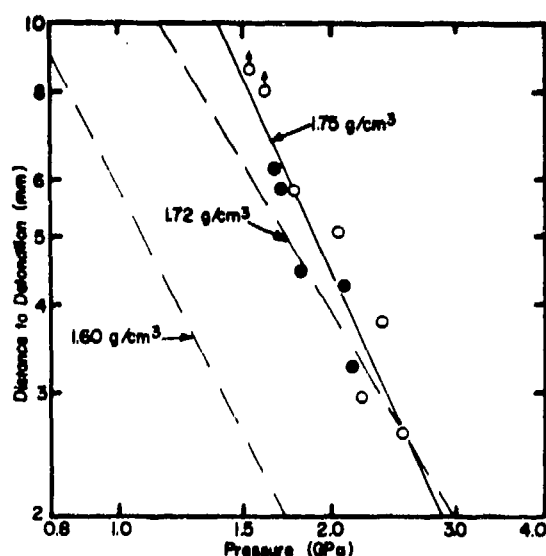
Fig. 7. Dependence of the distance to detonation on input shock strength for 1.75-g/cm^3 PETN. Dark symbols indicate shots in which the illumination failed.

23

The ~20% scatter in the distances to detonation is almost as severe as in the previous investigation (7), where input shock strengths were not so accurately determined. In this work, our method of calculating shock strengths, while perhaps not absolutely accurate, does not admit to significant scatter in that parameter. The variations in distance to detonation, and corresponding times to detonation, much exceed experimental error, and must be actual irreproducibility in the initiation buildup. In high-density explosives, buildup distances are well known to increase strongly with decreasing void fraction (1,7,8,12). Variations in initial pressing densities, particularly within a given sample, are the most likely explanation of the scatter.

DECOMPOSITION DYNAMICS DURING INITIATION

The embedded-Manganin-gauge data, supplemented with impact-face pressure histories obtained with both quartz and Manganin gauges, provide the principal information for assessing the thermodynamic states and extent of the reaction during the buildup to detonation. Such data have been collected at 1.5-, 1.9-, and 2.3-GPa input shock strengths, but for brevity our further discussion will be limited to results with the intermediate pressure. Both observations and interpretations in the other two cases are quite similar to those presented.

Pressure histories typical of those obtained in embedded Manganin gauge experiments are shown in Fig. 8. The profiles consistently have a step increase, representing the shock arrival, followed by a rise to a maximum pressure, and a subsequent decay. In most cases the gauges were lost shortly after peak pressure was attained, but in those instances in which they survived longer, a second pressure increase was recorded. Little increase is seen in the shock amplitudes as expected from the explosive wedge experiments. In a given experiment the pressure maxima were consistently observed to increase with increasing gauge distance into the sample. The risetimes between shock arrivals and the pressure maxima decrease as the gauge depth is increased.

Despite good reproducibility of the observed shock strengths, considerable shot-to-shot variation was seen in the later portions of the pressure profiles.

In experiments where gauge locations were duplicated, pressure maxima could vary by 20% and the risetimes differ by 0.3 μs. This data scatter is comparable to that in the explosive wedge data, and is believed due to the same cause. Some selection and averaging of the data were necessary in defining pressure-field histories for the analysis described below.

The "direct analysis" to complete the state history during initiation involves alternate evaluations of gradients of state variables and time integrations of the conservation relations (8,14). Given the pressure field p(h,t), in Lagrangian distance, h, and time, the pressure gradients, $\partial p/\partial h$, are first evaluated and the momentum equation integrated in time to determine the particle velocity, u. This can be written:

$$u(h,t) = u_s(h) - \frac{1}{\rho_0} \int_{t_s}^{t} \frac{\partial p}{\partial h} dt' \qquad (1)$$

where ρ_0 is the initial density, the subscript s denotes evaluation at the shock front, and the integration is along a particle path. Similar treatment of the mass conservation gives the compression, $\xi = (1-\rho_0/\rho)$, as

$$\xi(h,t) = \xi_s(h) - \int_{t_s}^{t} \frac{\partial u}{\partial h} dt' \qquad (2)$$
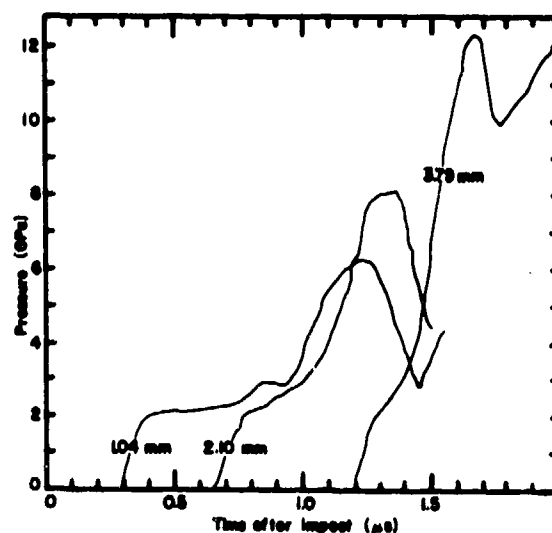
Fig. 8. Typical pressure-time profiles from multiple embedded Manganin-gauge experiments. Labels indicate gauge distances from the impact face.

24

and the specific internal energy is

$$e(h,t) = e_s(h) + \frac{1}{\rho_o} \int_{t_s}^{t} p \, \frac{\partial \xi}{\partial t} \, dt' \quad . \qquad (3)$$

With the pressure, compression, and energy determined, the degree of reaction, λ, can be obtained from a complete $p(\xi,e,\lambda)$ equation of state.

In the analysis presented, we treated fifteen pressure records at six locations, ranging from h = 0 to h - 4.2 mm, during the period from 0 to 1.5 μs. (With 0.3 mm allowed for gauge thickness, buildup to detonation is expected in 5.2 mm of run and 1.67 μs.) "Average" pressure histories at each location were idealized by assuming a step shock rise and fitting the data with polynomials; neither impact-face stress relaxation nor the second pressure increases were considered. Shock-front positions and state parameters were calculated using the Hugoniot given earlier and the slight increase in velocity indicated by the wedge experiments. Equations (1) through (3) were numerically integrated, using mathematical cubic splines to connect the pressure at the gauge sites and the shock front and to evaluate gradients at each time cycle. At h = 0 the pressure gradient was specified to give the correct particle velocity, known from continuity conditions, the pressure history, and the aluminum alloy isentrope.

The calculated pressure and compression profiles are shown in Fig. 9. The pressure-distance curves indicates reaction starting about 1 mm from the impact face, forming a pressure pulse which grows and moves toward the shock front. The front of this pulse steepends with run, and should become a strong shock by the time it reaches the 5.2-mm expected distance to detonation. This is in accordance with our earlier picture of the initiation buildup (7,8). The compression profiles show that the decomposition causes an expansion near the impact face, and that the front of the pressure pulse propagates as a compressive wave. Both features result from the pressure excursion occurring near the impact face.

Estimates of decomposition were made by interpolating the calculated p, ξ, and e values into a tabulation of Mader's HOM-SG equation of state (15). This formulation represents both the unreacted explosive and fully reacted products with Mie-Grüneisen

forms; we used the Hugoniot of Ref. 11, and a calculated BKW isentrope (16), respectively, as the reference curves for high-density PETN. Partially reacted states are calculated in HOM-SG with a "mix rule" that partitions the energies in the solid and gas phases in proportion to the offset of the mixture energy from those on the Hugoniot and isentrope.

The decomposition profiles obtained are sketched in Fig. 10, covering the time period from 0.75 to 1.5 μs. Reaction in the first 1.5 mm occurs after an $\sim$0.7-μs induction time. Comparison with Fig. 9 shows that a reaction front propagates with about shock velocity, and lags about 1 mm behind the shock. Unless this picture changes drastically in the 0.17 μs remaining to detonation, it is the overtaking compressive wave, and not a reaction wave, that is responsible for the onset of detonation at the front. Concentrating on a specific position, it is seen that decomposition proceeds until partially complete, and

Fig. 9. Calculated pressure-distance and compression-distance profiles for a 1.9-GPa shock into 1.75-g/cm^3 PETN. Labels on the pressure curves denote the time after impact. The 1.5-μs curves are cut off at 2.1 mm because of the loss of late-time data near the impact face.

Fig. 10. Calculated reaction profiles.

then slows down or ceases. This is seen better in Fig.
11, where reaction rates (dashed curves) are com-
pared with the pressure histories at the impact face
and two millimeters into the sample. If our observa-
tions and calculations are to be believed, a spontane-
ous and abrupt reduction in reaction rate occurs
while the pressure is still increasing, and is responsible
for the pressure maxima recorded.

DISCUSSION

We at first believed that the observed pressure
maxima might not represent such unusual reaction
kinetics, but rather that a reasonable reaction rate
was sustained, and the pressure decrease occurred
because the material became highly expanded. How-
ever, if the thermodynamic states are assumed to vary
uniformly between gauge locations (see below), the
fluid dynamics of the experimental configuration will
not allow the expansions required. The direct analy-
sis was rather sensitive to the selection and fitting of
data, but alterations in these parameters only
modestly change the decomposition attained when
reaction is interrupted. Similarly, different choices of
mix rules for the assumed equation of state can alter
the decomposition attained, but the unreacted and
fully reacted state configurations are well defined,
and the interpretation does not change. If the sur-
mised reaction behavior is invalid, the observations,
and not the calculations, are at fault.

Possible experimental artifacts include electrical
conductivity at the gauges, side rarefactions, and

*Fig. 11. Pressure histories and calculated reaction
rates at the impact face and at 2-mm depth.*

increased reaction at explosive-inert interfaces. Argu-
ing against the first explanation are the consistent
occurrence of the pressure maxima, their recording
with better insulated Manganin gauges (10) and
quartz gauges (Fig. 7, Ref. 8), and the second increase
in pressure sometimes observed. Sound speeds ex-
ceeding 12 mm/μs would be necessary for side rare-
factions to reach the gauges in their usual central
locations, and tests with off-center gauges gave no
indication of such unrealistic conditions. The most
likely experimental defect is greatly enhanced de-
composition at explosive-gauge interfaces. This viola-
tion of our assumed-uniform variations of state condi-
tions would allow complete reaction in localized
regions to produce the pressure maxima. This conjec-
ture will receive further experimental study.

Should our measurements prove correct, they
imply that more complex reaction rate dependencies
are needed for computer simulation of the initiation
of high-density PETN. The previously cited theories
(2-6) all explicitly or implicitly incorporate reaction
rates that increase monotonically with pressure.
While these rate laws can be adjusted to match the
pressure increases we observe, the pressure maxima
under partially reacted conditions cannot be
simulated.

26

In two cases where the pressure maxima were either ignored or above the practical gauge range, records from our quartz-gauge front-back experiments have been modeled with numerical hydrocodes. Pressure excursions derived from observations on 1.7-g/cm^3 PETN were matched using an Arrehnius rate law with arbitrarily chosen constants (6,8), and a more recent treatment with the "Forest Fire" rate dependency (3,4) reproduced target-gauge records on 1.75-g/cm^3 PETN (17). As well as not predicting pressure maxima under partially reacted conditions, both simulations had other limitations. The first calculation gave too much pressure increase (too fast a decomposition) for the actual reflected-wave conditions at the target gauge, while the second matched a target-gauge pressure history but failed to give the observed pressure excursion at the impact face. This inconsistent treatment of single- and double-shock initiation is a common failing of computer simulations.

The gross partial reaction implied by our measurements could be due either to completion of an intermediate stage in the decomposition throughout the explosive, or to the full reaction of localized portions of the explosive—hotspots whose growth is suppressed. We are unaware of chemical kinetic evidence for the first picture, and find it difficult to reconcile with the very prompt initiation of high-density PETN with relatively strong shocks and partial reaction at our maxima. We believe a hotspot model can be found to explain this disparity.

Presently, our candidate mechanism involves a "shell model" for dynamic void collapse (18) and the notion that hotspots result from plastic work at void peripheries (13,19). This approach has provided one rationale for the $p^2\tau$ criterion for short-duration shock initiation (20). An extension of the model gives a reaction rate depending primarily on the void collapse rate, which in turn is determined by the pressure and the rate at which it is applied, the void fraction, and the degree of reaction. The model can explain the large differences in decomposition rates induced by shocks and more gradual compressive waves. If one assumes that decomposition gases at partial reaction stop the void collapse, then our unusual decomposition dynamics are justified.

Further experiments may eliminate concern with the reaction-rate behavior we have described, but such shock-initiation phenomena as desensitization by preshock remain inadequately treated by theory. The property of heterogeneity dominates the initiation of solid explosives, and we believe that some parameter representing this property, such as the porosity, must be added to the usual thermodynamic state variables now employed in theory. The model outlined above is but one such alternative to the current, essentially empirical, treatments.

ACKNOWLEDGMENTS

REFERENCES

1. A. W. Campbell, W. C. Davis, J. B. Ramsay, and J. R. Travis, "Shock Initiation of Solid Explosives," Phys. Fluids 4, 511 (1961).

2. B. D. Trott and R. G. Jung, "Effect of Pulse Duration on the Impact Sensitivity of Solid Explosives," in Fifth Symposium (International) on Detonation, Office of Naval Research report ACR-184, p. 191.

3. C. L. Mader and C. A. Forest, "Two Dimensional Homogeneous and Heterogeneous Detonation Wave Propagation," Los Alamos Scientific Laboratory report LA-6259 (1976).

4. C. L. Mader, "Two Dimensional Homogeneous and Heterogeneous Detonation Wave Propagation," this Symposium.

5. D. B. Hayes, "A $p^n t$ Detonation Criterion from Thermal Explosion Theory," this Symposium.

6. Jack Jacobson and Wildon Fickett, "Plane Shock Initiation of Detonation: Computer Simulation of a Gas Gun Experiment," Los Alamos Scientific Laboratory report LA-5915-MS (1975).

7. Dante Stirpe, James O. Johnson, and Jerry Wackerle, "Shock Initiation of XTX-8003 and Pressed PETN," J. Appl. Phys. 41, 3884 (1970).

8. Jerry Wackerle and J. O. Johnson, "Pressure Measurements on the Shock-Induced Decomposition of High-Density PETN," Los Alamos Scientific Laboratory report LA-5131 (1973).

9. Jerry Wackerle, J. O. Johnson, and P. M. Halleck, "Projectile-Velocity Measurements and Quartz- and Manganin-Gauge Pressure Determinations in Gas-Gun Experiments," Los Alamos Scientific Laboratory report LA-5844 (1975).

10. Jerry Wackerle and J. O. Johnson, "Pressure Observations on the Shock-Induced Decomposition of 1.75-g/cm^3 PETN," Bull. APS Series II, 17, 1105 (1972).

11. B. Olinger, P. M. Halleck, and H. H. Cady, "The Isothermal Compression of Pentaerythritol Tetranitrate (PETN) to 10 GPa (100 kbar) and the Calculated Shock Compression," J. Chem. Phys. 62, 4480 (1975).

12. I. E. Lindstrom, "Planar Shock Initiation of Porous Tetryl," J. Appl. Phys. 41, 337 (1970).

13. Jerry Wackerle, J. O. Johnson, and P. M. Halleck, "Shock Compression and Initiation of Porous PETN," Bull. APS Series II, 20, 20 (1975).

14. M. Cowperthwaite, "Determination of Energy Release Rate with the Hydrodynamic Properties of Detonation Waves," in *14th Symposium (International) on Combustion*, (The Combustion Institute, Pittsburgh, 1973), p. 1259.

15. James D. Kershner and Charles L. Mader, "2DE: A Two-Dimensional Continuous Eulerian Hydrodynamic Code for Computing Multicomponent Reactive Hydrodynamic Problems," Los Alamos Scientific Laboratory report LA-4846 (1972).

16. Charles L. Mader, Los Alamos Scientific Laboratory, private communication (1973). The BKW calculations are described by Mader in "Detonation Properties of Condensed Explosives Using the Becker-Kistiakowsky-Wilson Equation of State," Los Alamos Scientific Laboratory report LA-2900 (1973).

17. Charles W. Forest and Charles L. Mader, Los Alamos Scientific Laboratory, private communication (1976).

18. B. M. Butcher, M. M. Carroll, and A. C. Holt, "Shock-wave Compaction of Porous Aluminum," J. Appl. Phys. 45, 3865 (1974).

19. John W. Taylor, Los Alamos Scientific Laboratory, private communication (1971).

20. F. E. Walker and R. J. Wasley, "Critical Energy for the Shock Initiation of Heterogeneous Explosives," Explosivestoffe, Issue 1, p. 9 (1969).

NOTE ADDED IN PROOF

The "interrupted decomposition" at partially reacted states was shown above to result from the relatively low pressure maxima observed with the embedded-Manganin gauges, and the possibility that these maxima were an artifact of a highly consistent gauge failure was recognized. Since the Symposium, evidence has accumulated that such an anomaly and misinterpretation occurs. In similar studies on PBX-9404, both Cochran and coworkers at Lawrence Livermore Laboratory and we have found that increased plastic electrical insulation on the embedded gauges gave higher pressures and longer gauge life. The direct analysis of our newer PBX-9404 data gave no indication of interrupted decomposition.

Recently, we have repeated the experiment on 1.75-g/cm^3 PETN depicted in Fig. 8, using thicker plastic sheathing, and again found that higher pressure maxima were recorded. We expect that further tests will eliminate the notion of interrupted decomposition in high-density PETN, but that such features as an induction time for appreciable decomposition and a transition to detonation by an unreactive, compressive wave should remain valid. These aspects of the initiation of heterogeneous explosive still present currently unmet demands on its computer simulations and the physical characterization of hot-spots, but elimination of the interrupted decomposition should simplify the task of finding realistic models.   4 April 1977

ON SHOCK WAVE EXPLOSIVE DECOMPOSITION

A. N. Dremin, K. K. Shvedov
Institute of Chemical Physics Academy
of Sciences USSR, Chernogolovka, Moscow
Region, 142432, USSR

The registration of the inert material-explosive interface under various shock waves of rectangular profile has been proposed as the observation method of the character of shock wave condense explosive decomposition. Liquid and cast charges of TNT as well as TNT and hexogen charges of loose density filled with different gases or liquids have been investigated. It has been shown that the gases' nature and their initial pressure (from 0.1 to 10 atm) do not affect the loose density charges decomposition character. There are two regions of the shock pressure for all charges investigated. The explosives' decomposition character in these two regions is different. A homogeneous thermal explosion seems to occur at higher pressures but the reaction processes in individual "hot spots" are responsible for the decomposition at low pressures. An alteration of the decomposition character takes place in a narrow range of pressures. It depends on the explosive state (liquid or solid) and the explosive particles structure.

For further progress of the explosive detonation theory it is necessary to investigate shock wave condense explosive decomposition. There are few quantitative data on the subject involved at present, in essence they are concerned with the registration of the chemical spike of normal detonation. Some information on condense explosives decomposition under shock waves of low intensity has been obtained at the investigation of the shock initiation of detonation mechanism. The information was qualitative. It has been found that liquid explosives decomposition follows the pattern of a homogeneous thermal explosion, but solid heterogeneous explosives decomposition is due to reaction processes in individual "hot spots" (1,2). The investigation of the shock wave solid explosive decomposition mechanism involves considerable difficulties. Because of the explosives being opaque, it is difficult to observe the decomposition process. The decomposition process itself is extremely complicated due to initial physical heterogeneity of charges. The information for solid explosives has been obtained at the investigation of shock to detonation transition process; shock front velocities and partical velocity profiles have been measured during the investigation. It has been observed that the change of the shock wave parameters is different for various charges (liquid, cast, bulk) in the transition process. The difference is caused by the charges' decomposition mechanism characteristics. The mechanism depends on many factors. The elucidation of some of their effects is the subject matter of the paper. The registration of the inert material-explosive interface motion has been proposed (3) to investigate the effect of the factors on the decomposition character. However, the use of shock to detonation transition process registration would be a very labour-consuming procedure in the investigation involved. The main investigations have been carried out with TNT and hexogen charges.

The test set-up measurement of the inert material-explosive interface velocity u(t) with the electro-

magnetic probe is shown in Fig. 1. Rectangular profiles different shock waves of $3 \div 6$ μs duration have been applied, the observation time being $2 \div 3$ μs.

The u(t) depends on explosives decomposition character. If the decomposition does not take place, the u(t) profile will be rectangular similar to that for inert material. The decomposition causes pressure increase and decelerates the inert-explosive interface. The degree of the u deceleration provides a qualitative information on explosives decomposition intensity. To calculate the pressure in the explosives the initial values of the interface velocities and the explosives shock adiabats have been used. The shock adiabats we have used are the following:

$$D = (2.0 + 1.68 \, u) \, km/s$$

(4) for liquid TNT at $85 \div 90°C$ (here D is shock velocity and u—particle velocity).

$$D = (2.16 + 2.24 \, u) \, km/s$$

(5) for cast TNT at initial charge density of 1.62 g/cm^3.

$$D = (1.5 + 2.36 \, u) \, km/s$$

(6) for TNT filled with water at initial charge density of 1.31 g/cm^3.

$$D = (0.3 + 1.75 \, u) \, km/s$$

(7) for powder TNT of loose charge density 0.9 g/cm^3.

$$D = (0.4 + 2.0 \, u) \, km/s$$
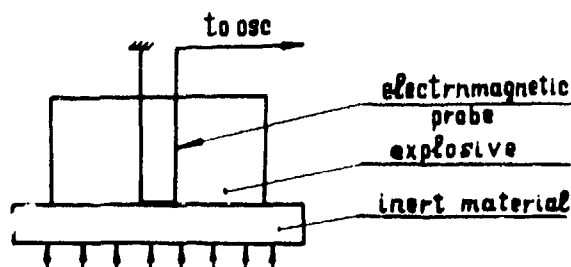
(8) for powder hexogen of loose charge density 1.0 g/cm^3.

$$D = (1.5 + 2.3 \, u) \, km/s$$

(obtained at the investigation) for powder hexogen filled with water at initial charge density 1.43 g/cm^3.

Some oscillograms of the u(t) are shown in Fig. 2 to demonstrate the method's potentiality. The oscillogram (a) corresponds to the experiments when explosive has been substituted by acetone and the shock pressure equals 8 kbar. Once can see that the shock wave profile is in fact rectangular for inert material. The oscillogram (b) is for liquid TNT; the shock pressure equals 100 kbar. The shock wave rectangular profile indicates that liquid TNT behavior at the pressure is similar to that of inert substance. The oscillogram (c) is for powder hexogen charge (particle size equals approximately 0.25 mm) with the density of 1.0 g/cm^3; the shock pressure is 9 kbar. The gradual decrease of the u shows that powder hexogen even at this low shock pressure starts to decompose at the moment of shock entrance. The oscillogram (d) is for liquid TNT at 155 kbar shock pressure. The rapid decrease of the interface velocity indicates that liquid TNT explodes at the moment of the shock entrance. It should be noted that for all the charges investigated, one of the oscillograms presented has been registered at various shock pressures.

Fig. 1.
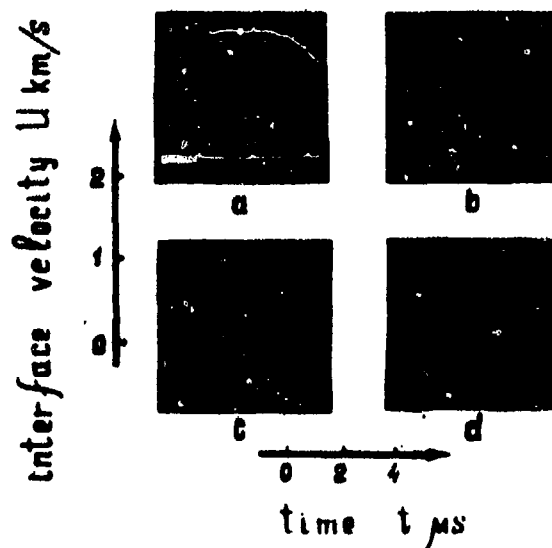
Fig. 2.

Liquid and cast TNT. Textolite has been used as an inert material in the liquid TNT (85 ÷ 90°C) experiments whereas paraffin has been used in the cast TNT experiments. The diagrams of the u(t) for various shock pressures in liquid (a) and cast (b) TNT are shown in Fig. 3. Figures in the diagrams represent the shock pressure values at the interface. One can see that liquid TNT at 120 kbar does not start to decompose in one μs and at 155 kbar, it explodes without any time delay.

The gradual practically linear decrease of the u for the registration time is observed in the cast TNT experiments up to 120 kbar. This character of the cast TNT interface velocity dependence differs from that of liquid TNT. In the cast TNT experiments at pressures more than 120 kbar and in the liquid TNT
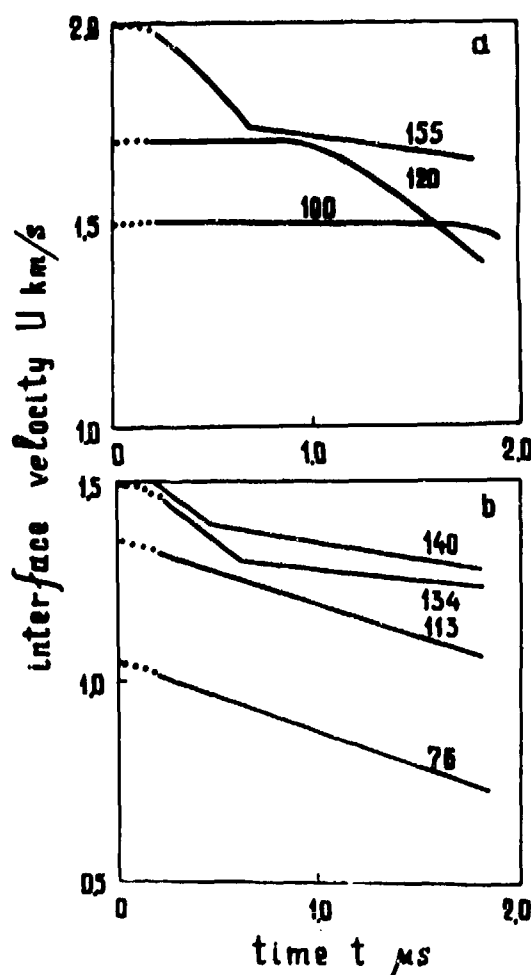
experiments at 155 kbar, the u(t) dependences of similar character are observed. A slight decrease of the u(t) initial part width has been observed at the shock pressure increase. It must be noted that the change of the u(t) dependence character occurs in a narrow interval of pressures. The oscillograms without an abrupt initial decrease of the u have been perfectly reproduced at the pressures below 110 kbar or equal to. The oscillograms with the abrupt initial decrease have been perfectly registered either at the pressures equal to or more than 130 kbar. Both types of oscillograms have been observed at the intermediate pressures.

Filled TNT and hexogen charges. Paraffin has been used as inert material in the experiments with the TNT and hexogen charges filled with water.

Figure 4 shows the data (a) for TNT, (b) for hexogen. The TNT charge density was approximately 1.31 g/cm^3. Figures in circles mark the u(t) dependences for the TNT charges of different size and density particles: 1,3,5—the particles of 1.54 ÷ 1.57 g/cm^3 density and 2 ÷ 3 mm size; 2—1.0 mm size and of the same particles density; 4—the particles of 1.64-1.65 g/cm^3 density and 2 ÷ 3 mm size. The hexogen charges filled with water have 1.43 g/cm^3 density and the particle size of 0.3 ÷ 0.5 mm.

The oscillogram with the abrupt initial decrease of the u for the TNT charges with the particles of 1.54 ÷ 1.57 g/cm^3 density has been obtained at 110 kbar, the initial abrupt decrease of the u being registered in 0.6 μs time interval. It must be emphasized that the initial abrupt decrease of the u has not been observed for the TNT charges with the particles of 1.64 ÷ 1.65 g/cm^3 density at 110 kbar.

The minimal pressure when the initial abrupt decrease occurs has not depended upon the filler nature in the TNT charges the same kind of particles. To illustrate this fact the TNT particles of 1.54 ÷ 1.57 g/cm^3 have been chosen for the experiments. The charges have been filled with water, paraffin, and carbon tetrachlorate. Approximately 110 kbar minimal pressure has been registered for all the fillers used. But for all the charges the initial abrupt decrease of the u has not been registered at the shock pressure lower than 100 kbar in time of registration. In this pressure region the change of the particles sizes by 2 ÷ 3 times does not affect the u(t) dependences incline (see Fig. 4a: 1,2).

Fig. 3.

The u(t) dependence for the hexogen charges filled with water were qualitatively similar to those of the TNT charges. The initial abrupt decrease of the u appears at the shock pressure some 200 kbar for the charges filled with water and at some 220 kbar for the charges filled with carbon tetrachlorate. These pressures are considerably more than those of the TNT charges (~110 kbar).

TNT and hexogen charges of loose density. The TNT charges of 0.9 g/cm^3 density were prepared from the spherical particles of $1.54 \div 1.57$ g/cm^3 density and $2 \div 3$ mm diameter. The hexogen particles of 1.8 g/cm^3 density had irregular shape and 1.0, 0.25, 0.06 mm characteristic sizes, respectively. The density of hexogen charges prepared of 0.06 mm

particle size was 0.87 g/cm^3 and the other hexogen charges had 1.0 g/cm^3 density. Figure 5 shows the paraffin-explosives interface velocity dependences on time for TNT (a) and hexogen (b) at different shock pressures. The hexogen particles of 0.25 mm size was for all the data presented in Fig. 5.

The figure shows that the u(t) dependences for TNT are the direct lines slightly inclined, a tendency to some incline increase being observed as the pressure increases. The abrupt decrease of the u has been registered at 68 kbar for 0.5-μs time interval.

The initial parts of the breaking curves (t_c time) have a convex shape for the hexogen charges at $10 \div 31$ kbar. The convex shape obviously indicates the
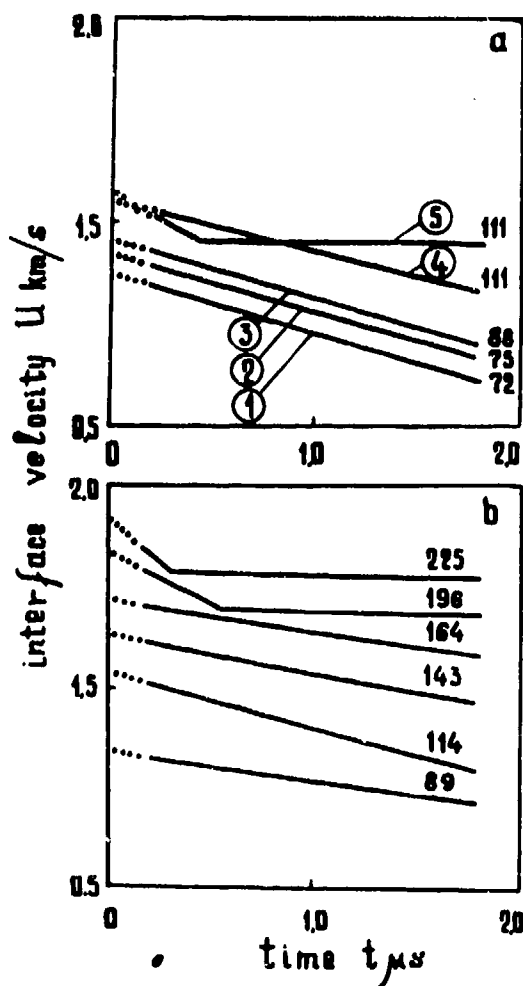
Fig. 4.
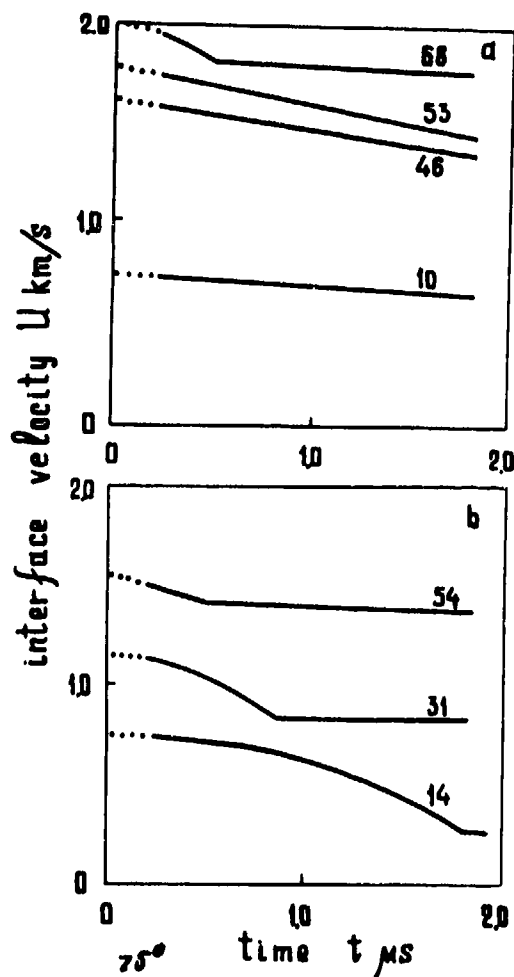
Fig. 5.

decomposition acceleration. It must be mentioned that the u(t) of the convex shape transforms to the u(ᵗ) of the triangular shape at the pressure increase. The transition pressure was about 40 kbar and did not depend on the particles size, but the characteristic time t_c did. Figure 6 shows that the dependence extent changes at the different pressures. The particle size considerably affects the t_c value in the region of low pressures (~10 kbar) but it does not affect pressures as high as 50 kbar. It is interesting to note that the normal detonation reaction time values (the points at 190 kbar) coincide with the t_c value obtained by the data extrapolation to the detonation pressure.

The strong hexogen particle size influence on the t_c value at low pressures could be accounted for by the action of hot gases in pores. Special experiments to verify the assumption have been carried out. The decomposition of the TNT, hexogen, and tetryl charges filled with different gases (air, argon, and carbon dioxide) have been investigated. The breaking curves within the experimental accuracy limits turned out to be similar for all the gases used. The change of the gases' initial pressure in pores did not give rise to a marked alteration of the breaking curves (9). Figure 7 shows the relative interface velocity $u(t)/u_o$ for the hexogen charges (the hexogen particles size—0.25 mm and the shock pressure—9 kbar), where u_o is the initial interface velocity value. The black circle points correspond to the experiments with air in pores at 1 atm pressure; light circle points to air at 0.05 mm Hg; triangular black points to carbon

dioxide at $10 \div 12$ atm; triangular light points to carbon dioxide at 1 atm. The fact that all the points fall on one curve means that the decomposition character does not actually depend on the nature and initial pressure of the gases in pores. The data on shock initiation of detonation confirm the conclusion. It has been found that the critical shock pressure to initiate detonation also does not depend on the gases nature (3).

The data obtained in the present paper enable one to make some consideration on condense explosives decomposition mechanism in shock and detonation waves. Two shock pressure regions of the different kind of the breaking curves have been revealed for all the charges investigated. The various factors' influence on the breaking curves in these regions differs either. The regions are divided by an interval of shock pressure. The interval is different for the various charges. For most of the charges studied the interval is small in comparison with the pressure values and therefore the two pressure regions can be conditionally divided by some pressure P^*. The P^* pressure is the average in the interval.

In the shock pressure region below P^* the interface velocity is characterized by a gradual decrease with time for the heterogeneous solid explosives. The decrease depends upon many factors. Shock explosives heating in the region is obviously insufficient to cause a homogeneous explosives decomposition reaction in the registration time. However, as the interface breaking starts at the moment the shock enters the explosives, one can conclude that the explosives decomposition process begins also at this very

Fig. 6.

Fig. 7.

33
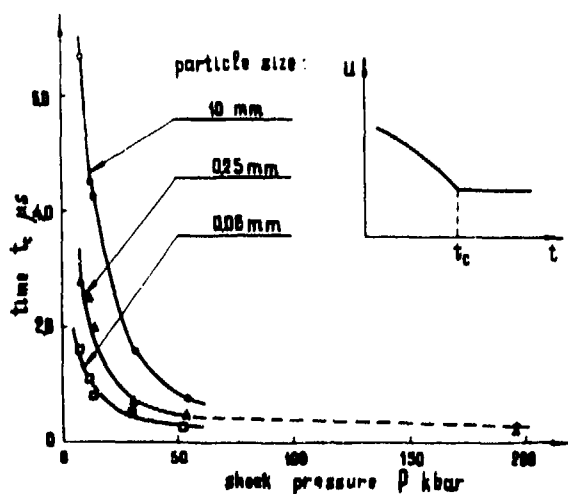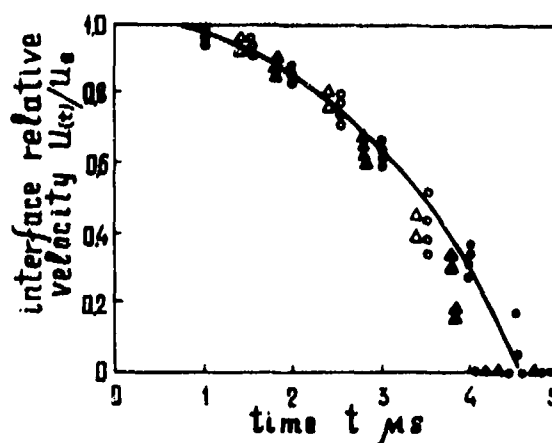
moment and is due to the reaction in individual "hot spots." Some reasonable assumptions on the "hot spots" origin have been offered in literature. They can be divided in two groups: (1) It is the heating of explosives particles by a hot medium among the particles that is considered the main cause of initiating the decomposition. (2) It is nonhomogeneous shock heating of the very explosives that is thought to be the main cause of initiating the reaction. From our standpoint, the former is not correct. The breaking curves independence on the gases nature and their initial pressure in pores as well as the independence of P^* on the nature of fillers mean that the shock heating of the media among the particles is, in fact, not the principal cause of the initiation and the decomposition reaction process under the shock waves investigated. As to the latter, we consider it to be correct; the data confirm that. From our data follows that the $u(t)$ is the function of the explosives particle size and their structure in a large scale.

The breaking curves character depends on the "hot spots" quantity, on the reaction progress in the "hot spots" as well as on the reaction spreading over the explosive matter. Therefore, the interface breaking registration can be applied as a method of determining relative sensitivity of various kinds of charges to reaction shock initiation. For all the charges concerned the experiments should be performed under the same conditions; that is, the same amplitude and shock wave profile, as well as the same material of inert barrier, should be observed. For our experiments the amonium nitrate, TNT, tetryl, hexogen, and PETN charges have been chosen. The shock wave amplitude was $10 \div 12$ kbar and the barrier was made of paraffin. The ratio of the u to the u_o value has been determined in 2 μs after the shock wave front enters the charges. The less the value, the more sensitive explosive to which the value corresponds. As a result the following sensitivity succession has been obtained: ammonium nitrate—0.99, TNT—0.94; tetryl—0.79, hexogen—0.76, PETN—0.39. It must be noted that the sensitivity succession coincides with the mechanical impact sensitivity succession for these explosives [9]. The coincidence obviously indicates that similar processes in the explosives are involved in weak shock and mechanical impacts action.

The breaking curves are similar for all the charges investigated at the pressures more than the P^* value. It has been found that a gradual decrease followed an

abrupt initial $(0.5 \div 0.7\ \mu s)$ decrease of the u. The explosives particles size, the fillers nature, and shock wave amplitude slightly affect the interface breaking curves and the time of an abrupt decrease of the u. Slight influence of these factors on the charges detonation wave reaction time has been noted earlier [1]. From the data obtained it follows that the various factors slight influence on the explosives decomposition time is observed at the shock pressures markedly less than that of the shock front of the detonation waves P_f at the charges diameters near the critical ones; that is, P^* is always less than P_f. So for liquid TNT P^* is 135 kbar and P_f is 250 kbar; for cast TNT P^* is 120 kbar and P_f is 190 kbar; for the filled TNT charges P^* is 110 kbar and P_f is 120 kbar; for the TNT charges of loose density P^* is 70 kbar and P_f is 80 kbar; for the filled hexogen charges P^* is 210 kbar and P_f is 240 kbar.

The strong initial interface breaking indicates a rapid explosives decomposition into the products characteristic of detonation. This conclusion is confirmed by the coincidence of the states corresponding to the point of an abrupt change of the breaking curve with the states on the detonation products isoentropy curve. The calculation of the transition process of the shock waves from the inert barrier directly into the detonation products provides the detonation products states.

The explosives solid charges decomposition presumably follows the adiabatic explosion mechanism at pressures more than P^*. It is the similarity of the breaking curves for heterogeneous solid charges to those of homogeneous liquid explosives that is the background for this conclusion.

The difference of the decomposition character at high and low shock pressures is probably due to the peculiarity of the hot spots shock generation process. It is not improbable that the number of the hot spots increases in such a manner that at the pressures more than P^* their concentration becomes so high that the temperature nonuniformities caused by them disappear earlier than the marked explosive fraction has reacted. However, it is not excluded that similar behavior of heterogeneous solid explosives and homogeneous liquid explosives at pressures more than P^* does not indicate that the temperature nonuniformities in solid explosives disappear. On the contrary, it indicates that temperature nonuniformities originate in liquid explosives. On the other hand,

as the decomposition time depends little on the shock pressure at the pressures more than P*, the decomposition process is, presumably, of non-temperature nature. The non-temperature nature can be due to the shock compression features' influence on the explosive decomposition kinetics (high pressure, tremendous rates of loading, etc.).

Thus, from the data in question, it follows that the solid explosives decomposition mechanisms at the shock pressures more than P* and less than P* are of a qualitatively different nature and, therefore, one can not advance a unified theory for the full scale of shock pressures.

The data on shock explosives decomposition formal kinetics are of interest for some problems. In spite of some difficulties, such data can probably be obtained by applying mathematical treatment to the results measured by the method suggested in the investigation.

REFERENCES

1. A. N. Dremin, S. D. Savrov, V. S. Trofimov, K. K. Shvedov, "Detonation Waves in Condensed Media," Moscow, Nauka, 1970.

2. A. W. Campbell, W. C. Davis and J. R. Travis, "Shock Initiation of Detonation in Liquid Explosives," Phys. Fluids, Vol. 4, No. 2, pp. 498-510, 1960.

A. W. Campbell, W. C. Davis, J. B. Ramsay and J. R. Travis, Phys. Fluids, Vol. 4, No. 2, 511, 1961.

3. S. A. Koldunov, K. K. Shvedov, A. N. Dremin, "Shock Wave Decomposition of Porous Explosives," Fiz. Gor. i Vzr., No. 2, pp. 295-304, 1973.

4. W. B. Garn, "Determination of the Unreacted Hugoniot for Liquid TNT," J. Chem. Phys., Vol. 30, No. 3, pp. 819-826.

5. A. N. Dremin, S. A. Koldunov, "Shock Initiation of Detonation in Cast and Pressed TNT," Vzrivnoe Delo, No. 63/20, 37-50, Moscow, Nedra, 1967.

6. K. K. Shvedov, A. N. Dremin, A. L. Krivchenko, N. A. Murashova, V. S. Kozlov, "Shock Initiation of Detonation in Granular TNT Filled with Water," Fiz. Gor. i Vzr., No. 4, pp. 561-568, 1974.

7. K. K. Shvedov, S. A. Koldunov, Fiz. Gor. i Vzr., No. 4, 1976.

8. A. N. Dremin, K. K. Shvedov, O. S. Avdonin, "Shock Wave Compressibility and Temperature of Some Porous Explosives," Fiz. Gor. i Vzr., No. 4, pp. 520-529, 1970.

INVESTIGATION OF SOME CAST TNT PROPERTIES AT
LOW TEMPERATURES

V. M. Titov, V. V. Sil'vestrov, V. V. Kravtsov, I. A. Stadnitshenko
Institute of Hydrodynamics
Siberian Division of the USSR Academy of Sciences
Novosibirsk 630090, USSR

Critical diameter and shock initiation threshold are determined for cast TNT at initial explosive temperatures of 291, 77.4, and 20.4°K. The data on the initiation threshold are obtained in divergent shock geometry (gap test). Trotyl is found to be less shock sensitive at reduced initial temperatures. However, the critical diameter decreases from 15 mm at 291°K to 11 mm at 20.4°K. It is shown that this is connected with the considerable irreversible change in physical-mechanical structure of cast TNT at a decrease in temperature. The chemical reaction zone length calculated from the detonation velocity dependence on the charge diameter according to the curved front theory increases by a factor of 1.5. In this case the ideal detonation velocity increases not more than by 1% while the explosive density increases by about 5% with initial temperature decrease. It is shown that the simple kinetic representations developed for homogeneous explosives are not suitable to describe the changes in the reaction zone length and in the critical diameter. The notion of critical initiation energy proposed for heterogeneous explosives is made more accurate. Effect of initial temperature on the initiation threshold is analysed using the introduced notion of critical initiation power for explosives.

INTRODUCTION

The influence of a low initial temperature (T_0) on detonation limits of cast TNT is studied in this paper, relative to the fact that in a series of experiments some explosives are used at the boiling temperature of liquid nitrogen and liquid hydrogen (1). It makes sense for the proper design of explosive devices as well as for the development of theoretical models of the initiation process and the detonation propagation. The effect of variation in initial temperature for homogeneous explosives can be described by different models based on the thermal explosion theory (TET). In these models the typical reaction time and related values depend upon T_0 (2-4). However, the predictions of these theories for heterogeneous explosives do not agree with experimental results (5-7).

Therefore, a systematic study of the influence of different factors including also T_0 on the critical conditions of ignition and propagation of detonation are likely to make a certain contribution to an understanding of these phenomena.

There are only some papers dealing with the characteristics of heterogeneous explosives at low initial temperatures. In paper (5) it was observed that the critical diameter (d_c) of powdered TNT with initial density $\rho_0 = 1$ g/cc increased to 10 mm with decreasing T_0 to -193°C (at $T_0 = 75$°C, $d_c = 5.5$ mm). Authors associated these results with the fact that the reaction rate decreases at reduced T_0 of matter. In (6,7) the increase in the chemical reaction time was observed by the electromagnetic technique: for cast RDX/TNT 50/50 the reaction time increased by a

factor of 1.5 at T_o = 77 - 20.4°K; for powdered (1 g/cc) and cast (1.62 g/cc) TNT it increased, approximately, by a factor of 2 at T_o = 140°K. But in this case the steady state detonation parameters changed only slightly. Calculation of the induction time change of the adiabatic thermal explosion with the "low"-temperature kinetic parameters for TNT (4) showed that the decrease in temperature T_s by 150-250° at a level of 1100-1300°K must result in the reaction time increase at least by an order of magnitude (here T_s is the shock initial temperature behind the front of the shock preceding the reaction zone).

If the value of a critical diameter is proportional to the reaction time (τ_c) at a charge diameter d = d_c and the ideal detonation reaction time (τ_r) is a good approximation for τ_c one should expect the increase in d_c for both powdered and cast TNT. According to (5,7) a satisfactory agreement between the change in d_c and experimentally determined τ_r occurs for powdered TNT. As will be shown below, for cast TNT even a qualitative agreement does not take place: the reaction time increases, but the critical diameter decreases.

The influence of the initial temperature on the initiation threshold (P_i) was studied in a series of works, however, the quantitative data are few in number. The main conclusion of these papers is that shock sensitivity of explosive increases at elevated T_o. Qualitatively, this conclusion is clear as under preheating the bulk shock heating temperature of the test explosive increases at the shock pressure of the same magnitude, and the induction time in TET occurs to be the extremely sensitive function of temperature. For heterogeneous explosives the shock heating is small, and therefore it should be supposed that T_o would influence sufficiently on the initiation threshold. However, the presence of hot spots, i.e., localized regions of high temperature, reduces this effect. In (8) an attempt was made to relate the hot spot temperature to dynamical properties of the input shock and T_o. This made it possible to calculate the chemical induction time from measured shock pressure. However, a quantitative explanation of P_i vs T_o was absent.

In this paper on the basis of the notion of critical initiation energy introduced in (9) for heterogeneous explosives and analysed for some explosives in (10,11) the attempt has been made to describe quantitatively the effect of initial temperature on the initiation threshold. The internal thermal energy of an explosive sample in the initial state which is determined by its specific heat and initial temperature has been included into consideration, additionally. The data (8) at elevated T_o and the data of this work at reduced T_o have been analysed on the basis of this hypothesis. Calculated data are in satisfactory agreement with measured values of P_i.

EXPERIMENTAL TECHNIQUE

Cast TNT was chosen for the present work because it has received the most study. Moreover, it is castable material and hence can provide charges which are approximate in the degree of physical homogeneity to homogeneous explosives, i.e. it should be expected that the conclusions of the thermal explosion theory are more widely applicable to cast TNT than to other heterogeneous explosives (pressed, powdered, mixed). Charges were made of creamed TNT with 10% powder addition and with rapid cooling and continuous mixing. Castings had a uniform fine-crystalline structure at a density of 1.615 g/cm³. At low initial temperatures a density was determined by the precision weighing of the explosive samples in liquid nitrogen or liquid hydrogen. The densities of liquid gases under 1 atm and at the boiling point were assumed to be equal to 0.808 g/cm³ for nitrogen and to 0.071 g/cm³ for hydrogen (12).

The detonation velocity (D) as a function of charge diameter was measured by means of pins placed in five positions down a cylindrical charge in a 0.2 mm paper confinement. The charge diameter varied from 8 mm to 56 mm. In all the experiments a powerful hexolite booster was used, the parameters being determined in the steady state detonation regime. The charge length with diameter close to the critical one was equal to (10 ÷ 12)d. Time intervals were measured by four 100-MHz digital chronographs. The detonation velocity was determined with an accuracy better than 0.5%. In the low temperature experiments the charge was placed inside a styrofoam case. Immediately before the firing liquid gas was poured off.

The scheme of the test used to determine the shock sensitivity is shown in Fig. 1. It is a conventional gap test with a 1.61 g/cm³ cast trotyl donor (5 cm in diameter, 5 cm long) and a plane wave lens.

FAILURE

$T_0 = 77.4°K$
$H = 34$ mm
$U_s = 3.8$ km/sec

IGNITION

$T_0 = 20.4°K$
$H = 32$ mm
$X_{run} = 24$ mm
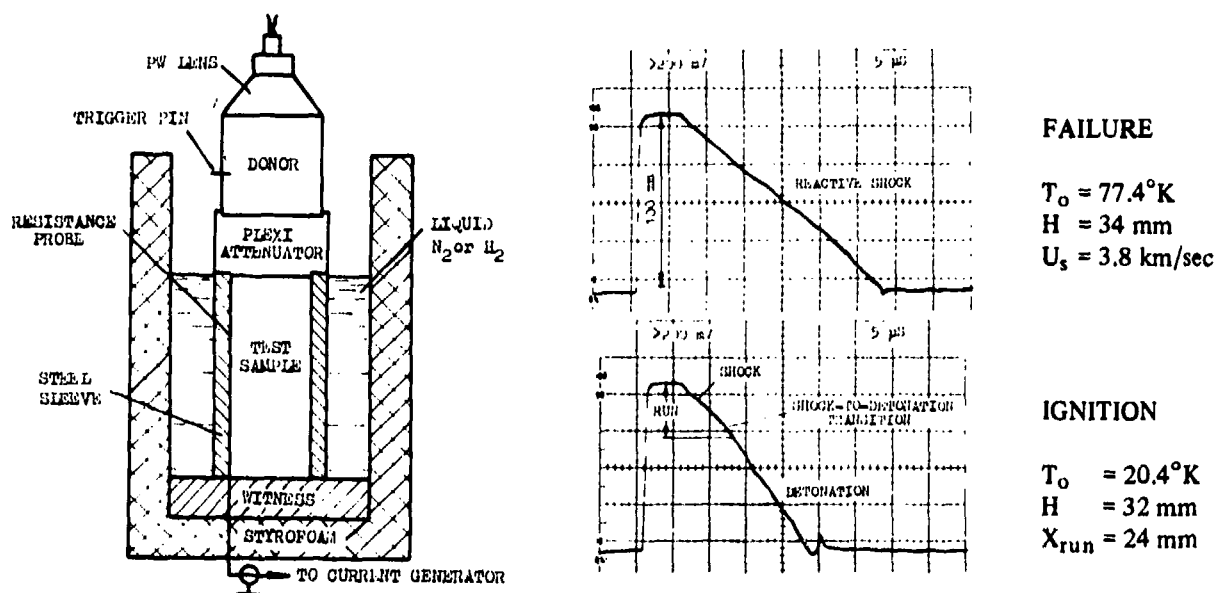
Fig. 1. Schematic diagram of the gap test and typical resistance probe oscillograms.

A 5.4-cm-diameter polymethyl methacrylate attenuator separates a donor from the test charge. The acceptor explosive (3.8 cm diameter, 10 cm long) has a confinement of a steel sleeve (3.8 cm ID, 5.4 cm OD), thus an equivalent diameter of the acceptor is approximately equal to 9.6 cm. A mild steel witness plate and a resistance probe are used in every shot to determine ignition and failure. The usage of the resistance probe is explained by the fact that at low initial temperatures a toughness of the witness material sufficiently decreases and therefore the degree of witness destruction can't serve as a reliable indicator of high-velocity detonation. The use of the resistance probe analogous to that described in (13) with impulsive constant current supply, visualizing the initiating shock trajectory on the screen of a storage oscilloscope allows easily to distinguish initiation or failure, and to obtain additionally the initiation distance, character of the shock-to-detonation transition, mean velocity of the reactive wave (Fig. 1). The input shock amplitude is varied by varying the gap length. Data for obtaining the 50% initiation threshold were gathered in the "up-down" procedure. In the low temperature experiments an assembly was placed in a styrofoam case filled with liquid gas. Immediately before the firing the donor was put on the attenuator, and a level of liquid was situated near the gap/acceptor interface.

Gap pressure (P_g) at the 50% gap length is measured using a shock polarization effect of plexiglas

(14). For this purpose a 10 mu aluminum layer was sprayed on the attenuator bottom, and this layer served as a grounded electrode. A measuring plexiglas plate (1 cm diameter, 1.2 mm thickness) was put against it, and the run time of shock through the plate was measured. These experiments were carried out at 291°K, and it was assumed that P_g, at the fixed cap length, didn't depend on the initial temperature. Then the 50% pressure at the end of the gap was converted to the initiating pressure transmitted to the explosive by use of the Hugoniots of the plexiglas and cast TNT which were determined at normal temperature (15):

plexiglas, $\rho_0 = 1.18$ g/cc, $U = 2.56 + 1.69$ u
for $0.54 < u < 1.42$

cast TNT, $\rho_0 = 1.614$ g/cc, $U = 2.39 + 2.05$ u
for $0.32 < u < 1.48$

where U is the shock velocity in mm/μsec, u is the particle velocity in mm/μsec. Hugoniot data were not corrected for the changes in T_0, because for trotyl it does not make sense: at reduced T_0 and at the same shock amplitude the explosive occurs to be more inert matter than at normal T_0. The use of uncorrected explosive Hugoniot results in the increase in the calculated value of P_i at the reduced T_0. Using the calculated Hugoniot for the unreacted TNT presented in paper (16, Fig. 3), one can estimate this effect: the resulting error at the highest pressure (~60 kbar) is not in excess of $3 \div 5$ kbar.

38

RESULTS

The detonation velocity as a function of charge diameter, initial density and a series of other calculated values at different T_o are presented in Fig. 2 and Table 1. Ideal detonation velocity (D_i) and re-
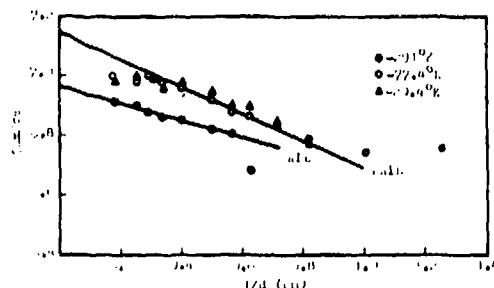
Fig. 2. Detonation velocity vs inverse diameter for cast TNT at various initial temperatures. The values of D at 77.4°K and 20.4°K are not corrected for the change of the measurement base. Solid lines represent D against 1/d at 291°K and 20.4°K according to the curved front theory.

action zone length (a_o) are computed from Eyring's curved front theory. Reaction time is assumed to be approximately equal to $4 a_o/3D_i$. According to (2) the polytropic exponent n_c of detonation products for cast TNT was assumed to be equal to 4.5 near the limit of steady state detonation. Therefore, the detonation pressure at d_c was calculated from the relationship

$$P_c = \frac{\rho_o D_c^2}{n_c + 1} \simeq 0.182 \, \rho_o \, D_c^2$$

The discrepancy between the data obtained at normal temperature and those presented in (10,17) is explained by the difference in the production technique of cast TNT: the solidification and addition of the fine TNT powder to the melt results in the formation of many crystallization centers, and, respectively, to the decrease in the reaction zone length and in the initiation threshold (Table 1 and Table 2).

The change in ρ_o at the temperature decrease accounts for 5% what is in agreement with the calculated value (7) and allows to estimate the change in the measurement base (x_o) assuming that the thermal contraction of explosive is isotropic:

$$\Delta x_o/x_o = \frac{1}{3}(\Delta \rho_o/\rho_o) = 1.7 \cdot 10^{-2}$$

This estimate permits to make correction of the measured detonation velocities. The data of Table 1 show that the detonation velocity and detonation pressure for both ideal and non-ideal regimes differ only slightly from the analogous parameters at 291°K what is in good agreement with the results of papers (6,7). Measured change in D_i is sufficiently less than it could be supposed from the increase of the initial explosive density from the linear dependence $D(\rho_o)$ with the proportionality factor of 3230 m · cc/g · sec determined at normal conditions. Instead of the supposed increase in D_i approximately by 300 m/sec, the increase only by 50 m/sec was measured. This is obviously connected with the chemical equilibrium shift of explosive decomposition resulting in the change in a quantitative composition of detonation products and chemical energy of the detonation reaction.

The increase in the reaction zone length approximately by a factor of 1.5, and, respectively, in reaction time vs T_o is in agreement with (6,7), but, in the same time, it is much less than we could expect from the thermal explosion theory. Probably, it is explained by the weak dependence of reaction time on detonation pressure, and, consequently, on T_s for TNT (2). This can be explained by the following (7):

1. Kinetic constants change under detonation pressures. It is noted, however, that according to (18) kinetic constants for TNT do not change at static pressures up to 50 kbar in the temperature range of 500 ÷ 700°K, and the reaction of low TNT decomposition is of the zeroth order.

2. Reaction time in solid TNT detonation wave is defined by not T_s, but by the final decomposition stages weakly dependent on initial temperature.

3. Dynamical loads influence specifically on decomposition kinetic of solid explosives. From our point of view, however, the usage of the dependence of induction time on T_s according to TET is not a correct way in estimating τ_r vs T_s for heterogeneous explosives. It is connected with the statistical character of the formation of hot spots and with their interaction one another, what makes this process more complicated, and, besides, makes impossible the usage of simple relations of TET which are suitable only for

39

TABLE 1

Summarized Data for TNT on Propagation of Detonation at Various Initial Temperatures

T_o °K	ρ_o g/cc	D_i mm/μsec	a_o mm	τ_r μsec	d_c mm	D_c mm/μsec	$(D/D_i)_c$	P_c kbar
291	1.615	6.97	0.42	0.08	15	6.68	0.96	131
77.4*	1.70	6.99	0.55	0.105	<8	–	–	–
20.4	1.71	7.00	0.62	0.12	11	6.64	0.95	137

*In calculating D_i and a_o at 77.4°K the values of detonation velocity at only $d \geqslant 12$ mm were used, because at $d = 8$ mm and 10 mm the large departures of the data from calculated line were observed.

TABLE 2

Gap Test Shock Sensitivity Data for Cast TNT at Various Initial Temperatures

T_o °K	$H_{50} \pm 95\% \Delta H$ mm	P_g kbar	$P_{i,exp}^*$ kbar	$P_{i,calc}$ kbar	E_o j/g	E''** j/cm^2 μsec	E'/τ** j/cm^2 μsec
291	47.8 ± 0.9	24	28	28	265	217	70
77.4	33 ± 0.6	47	57	52	22	248	233
20.4	33.3 ± 0.6	47	57	55	0.2	235	233
				average $E'' = 233 \pm 15$			

*Determination accuracy of the experimental P_i accounts for ± 10%.
**Values of E'/τ and E'' are calculated for experimental values of P_i.

describing the development process of a single hot spot. It will be shown below how one can estimate the maximum change in τ_r vs T_o without using the notions of TET.

As stated in the introduction, the existing theories of a critical diameter for homogeneous explosives predict its increase as T_o decreases. But in the experiments with cast TNT the decrease in the critical diameter was observed though the reaction zone length increased (Table 1). Critical diameter is determined as being midway between the nearest diameters of detonation and failure, the data are accurate to ± 1 mm. The cause of such abnormal behaviour of d_c vs T_o is not cleared up. It is probably connected with the change in physical-mechanical structure of cast TNT as T_o decreases because of appearing local spatial temperature gradients. To test this hypothesis, the

experiments were carried out at 291°K with the cast fine-crystalline TNT, pre-cooled up to 77.4°K the charge diameters being 12 and 10 mm. The steady state detonation was registered with the velocities of 6.87 and 6.84 km/sec, respectively. As far as these diameters are less than the critical one for TNT not subjected to low temperatures, it means that the irreversible change occurs in physical-mechanical structure of cast TNT as T_o decreases. Additional experiments were made with cast large-crystalline TNT ($\rho_o = 1.60$ g/cc) having $d_c = 27.5$ mm at normal temperatures (2). The charges, 18 and 14 mm in diameter, were fired at 77.4°K. As in the case of the fine-crystalline trotyl, a significant decrease in d_c was observed: at the indicated diameters the charges detonated with constant velocities of 6.85 and 6.70 km/sec, respectively. Thus we were not able to reveal purely temperature effect on d_c as T_o decreases

40

for cast TNT, because of the change in its physical-mechanical structure. In experiments of paper (5) with 1 g/cc powdered TNT already at normal temperature a degree of physical-mechanical heterogeneity was significant. As T_o decreased to -193°C, it didn't change significantly and therefore it has been possible in paper (5) to reveal the influence of reduced T_o on d_c. Apparently, the influence of T_o on d_c for heterogeneous explosives can be properly explained only by two-dimensional gas dynamical calculations taking into account real kinetic of chemical decomposition and real physical-mechanical properties of explosives as it was done by Dremin for homogeneous explosives (2,3).

Listed in Table 2 are the shock sensitivity data for cast TNT at different T_o. It is seen that the explosive becomes less shock sensitive at reduced T_o than at room temperature. Qualitatively, it is connected with the change in temperature of shocked explosive and characteristics of hot spots appearing in the shock passage through a heterogeneous explosive. The possible change of a degree of physical homogeneity connected with the increase in ρ_o makes a certain contribution as well. However, if to characterize physical homogeneity by the value of $(D/D_j)_c$ (17) than, as seen from Table 1, it changes only slightly. Initiation distance and time to detonation decrease due to the increase in initiating pressure. The shock-to-detonation transition is characterized by the gradual increase in the initiating shock velocity. In this respect the results are in qualitative agreement with the existing idea of the shock initiation character of heterogeneous explosives.

In the cases when high-velocity detonation was absent at both normal and reduced initial temperatures the sustained wave propagation with an average velocity of 3.3 km/sec at 291°K and that of 3.9 km/sec at 77 ÷ 20°K was registered. In this case the witness plate proved to be partly destroyed. This regime is a known regime of low-velocity detonation of explosives in the moderate confinement which are initiated by a weak shock. It is interesting that as T_o decreases the limits of the existence of this regime somewhat extend, i.e. its limiting velocity and pressure in the leading compression wave increase. Probably, it is connected with the decrease in shock temperature behind the front of the leading compression wave and, respectively, with the slower reaction rate of the partial decomposition of explosive.

PHENOMENOLOGICAL THEORY OF P_i DEPENDENCE ON T_o

Since detonation depends on many parameters of explosive and initiating pulse characteristics, detonation limits should be thought as a hypersurface in a many-dimensional space of these variables (17). Then different two-dimensional sections of this surface would give the dependence of detonation limits on one parameter, for example, critical diameter vs initial density or initiation threshold vs initiating pulse duration. Further we will consider this effect without taking into account the lateral rarefaction and for the rectangular initiating pulse with the amplitude P_i and duration τ. For the purposes of this work it is enough to consider the three-dimensional section (P, τ, T_o) of the initiation hypersurface under the assumption that all other parameters of explosive are little changed, though it might be not quiet so.

The section of hypersurface (P, τ, T_o) by the plane $T_o = const$ gives the functional relationship $E' = E'(P_i, \tau)$ which represents a curve on the plane (P, τ) dividing the initiation region and the failure one. In the general case E' is a function of T_o (Table 2). The existence of a similar relationship is shown in (9), and the retaining value is called the critical energy for shock initiation and used to describe the observed dependence of P_i on τ. As an analytical expression for E' the following one is used

$$E_1 = P_i u \tau \qquad (1)$$

It is not difficult to understand the physical sense of E_1 if to rewrite Eq. 1 as follows

$$E_1 = \rho_o U \tau \cdot u^2 \qquad (2)$$

Here $\rho_o U \tau$ is the mass of shocked matter per unit area, u^2 is the total energy per unit mass, including kinetic energy of matter and both thermal and potential components of internal energy. Thus, E_1 represents the total energy per unit area which is stored in the shock wave in explosive.

Such a determination of E' seems to be not quiet correct. It is associated with the fact that the action of high statical pressures in the order of 50 ÷ 100 kbar does not result by itself in explosive initiation.

Therefore it is logical to eliminate the potential component of internal energy from consideration, because it does not effect immediately on the formation of the initiation centers. Then in Eq. 2 only a portion of energy of unit mass of explosive, conditioned by the dynamical nature of shock compression, should be used instead of u^2

$$E'(T_o) = \rho_o U\tau \cdot \frac{k}{2} u^2, \qquad (3)$$

where

$$k = 1 + 2E_{th}/u^2$$

Similar re-determination of the critical energy for shock initiation does not contradict to the conclusions based on the previous determination (9-11) if E_1 is interpreted to be $2E'/k$. Just the value of E' from Eq. 3, however, should be considered as constant at given T_o, characterizing the shock sensitivity of explosive. Exactly this magnitude depends only on T_o, while E_1 from Eq. 2 must in principle depend on initiation pressure. This is connected with the fact that the shock wave in explosive represents the reactive wave. Therefore, the thermal component E_{th} used in determining k (Eq. 3) must incorporate the energy formed at the partial decomposition of explosive. This process is conditioned by the explosive sensitivity and the initiating pressure magnitude. In so doing, in the general case k is a function of P_i. The correct calculation of k (P_i) is possible when considering the shock propagation through the reactive medium with the given equation of state and the given law of energy output behind the shock front. In the general case it is difficult to make such a calculation.

But one can consider two limiting cases the difference between which is connected with the character of the shock-to-detonation transition at shock initiation of explosives (19). The first one is peculiar to homogeneous and little sensitivity explosives, for example, liquid or cast clear explosives, and also to P_i much less than the detonation pressure. In this case the steady shock velocity changes abruptly into the steady detonation velocity, and the shock is only slightly reacting one, that is, in the limit unreactive wave. Therefore,

$$E_{th} \ll u^2/2 \text{ and } k \simeq 1 \qquad (4)$$

The second case is realized when initiating more sensitivity explosives, for example, pressed explosives, and

at a great amplitude of initiating pulse. In this case the shock-to-detonation transition occurs to be smooth, and the shock is strong reactive wave. In so doing

$$E_{th} \simeq u^2/2 \text{ and } k \simeq 2 \qquad (5)$$

So the exact k (P_i) function can be substituted by its estimate according to Eqs. 4 and 5.

The proposed improvement of the determination of critical energy for shock initiation explains the experimental fact of the decrease in E_1 approximately by a factor of 2 as P_i increases which was discovered for liquid and cast explosives (11). The author of paper (11) also explained the decrease in E_1 by partial decomposition of explosive behind the front of the strong shock, but there was no explanation of the quantitative change. In our interpretation there occurs the transition from $k \simeq 1$ to $k \simeq 2$ with increasing the initiating pulse amplitude. As $E' = \text{const}$, then $E_1 = 2E'/k$ must decrease approximately by a factor of 2. The character of the decrease in E_1 which is sharp for liquid explosive and more smooth for cast one is simply explained by the physical sense of k (P_i) function.

Now let us consider the section of hypersurface (P, τ, T_o) by the plane $\tau = \text{const}$. The resulted relationship $E'' = E''$ (P_i, T_o) describes the change in the initiation threshold with the initial temperature of explosive at the fixed initiating pulse duration. Within the framework of the developing energetic approach to a problem of explosive initiation the following expression can be used as an analytical one for E''

$$E''(\tau) = \rho_o U(ku^2/2 + E_o) \qquad (6)$$

The notion introduced by Eq. 6 has a sense of critical power (per unit area) for shock initiation of explosive. Here E_o is the initial thermal energy of the explosive sample determined by its specific heat and initial temperature. E'' (τ) allows to predict P_i vs T_o if the pulse duration remains constant. In this case it is necessary to know the initial densities and Hugoniots of explosive at T_{o1} and T_{o2}, as well as the initiation threshold at one of the temperatures, for example, at T_{o1} (reference point). Having written the explosive Hugoniot in the form of $U = A + Bu$ it is not difficult to show that the critical particle velocity u_2 at T_{o2} is determined from the cubic equation

42

$$u_2^3 + \frac{A_2}{B_2} u_2^2 + \frac{2E_{o2}}{k_2} u - \frac{2A_2}{k_2 B_2}\left[\frac{\rho_{o1}U_1}{\rho_{o2}A_2}\left(E_{o1} + \frac{k_1}{2}u_1^2\right) - E_{o2}\right] = 0 \qquad (7)$$

For the positive solution of this equation to exist it is necessary that the absolute term is negative. It leads to the presence of the maximum initial temperature T_m at which the absolute term of Eq. 7 vanishes and $u_2 = 0$ provides the unique physical solution. Thus, there exists $T_m(\tau)$ at which explosive is exploded at no action of the shock. This temperature can be considered as an analog of temperature in the thermal explosion theory, and the value of τ as the induction time. In this case in the expression for T_m by the coefficient A_2 should be meant the sound velocity c_o in the explosive at $T_o = T_m$

$$T_m(\tau) \simeq \frac{\rho_{o1}U_1}{\rho_{o2}A_2} \cdot \frac{k_1 u_1^2/2 + E_{o1}}{\overline{c}_v} \simeq \frac{E''(\tau)}{\rho_{o2}\, c_o \overline{c}_v}$$

Here $\overline{c}_v$ is the average specific heat of explosive in the temperature range from zero to T_m. To estimate T_m let us use the data for TNT at $291^\circ K$ listed in Table 2. In so doing it is necessary to assume $k_1 = 2$, that is, to take into account the total energy per unit mass in Eq. 3. It is connected with the fact that in the final stage the matter is not compressed and potential component of internal energy equals zero. Therefore, the total energy of the shock in state 1 converts to the thermal energy in state 2. Assuming $\rho_{o2} = 1.47$ g/cc, $c_o = 1.37$ km/sec, what corresponds to the similar parameters for liquid TNT (15), we'll obtain $T_m = 1065^\circ K$. The corresponding induction time calculated from TET using kinetic and thermal constants from paper (4) is about $1 \div 2 \, \mu$sec. This value is close to the equivalent pulse duration of the test used which is analogous to the known NOL large scale gap test for which the estimate $\tau \simeq 1.6 \, \mu$sec is available (9,10). Thus in this case the interpretation of the value of τ as an induction time of the thermal explosion really is made possible. This is likely to be consequence of the fact that there is a connection between the presented approach to a problem of explosive initiation and the thermal explosion theory.

The values of P_i at different T_o for some explosives, for which the experimental data exist, obtained on gap tests at elevated temperatures (8) and reduced T_o in this paper were calculated by Eq. 7. The values

of P_i at normal T_o are taken to be the reference points. It was assumed that at the change in T_o the equivalent pulse duration remained constant, and the equivalent amplitude of the initiating shock was equal to P_i. If the Hugoniot was not known at the required T_o it was considered to coincide with the determined one at normal T_o. The dependence of specific heat $c_v(T)$ on temperature for solid explosives was expressed with the help of one of the simplest modifications of Debay theory, in which one Debay temperature dependent only upon volume was used (20). In this case the required constants were determined from the condition that the calculated c_v would coincide with the experimental one at room temperature and zero pressure. For all explosives $c_v(291^\circ K) = 1.28$ j/g $\cdot$ deg was assumed.

The calculated and experimental values for P_i are summarized in Table 2 for cast TNT and in Table 3 for some pressed explosives (3). In spite of the fact that the equivalent $\sqrt{\tau}$ changes a little as the barrier lenght varies, an agreement occurs to be good. The approximation $k_1 = k_2 = 2$ was used for pressed preheated explosives, and the approximation $k_1 = k_2 = 1$ was used for cast cooled TNT according to a physical sense of the k function. The change in c_v weakly affects the calculated results for P_i, for example, at $c_v(291^\circ K) = 1.47$ j/g $\cdot$ deg the calculated P_i for pressed RDX and NONA are equal to 7.9 kbar and 9.0 kbar, respectively. The calculated values for PBX-9404 do not agree with the experimental ones in the gap test as well as in the plane wedge test. As was noted in (3), in this case the lateral rarefaction leads to the decrease in τ and to the increase in P_i compared to the calculated data.

The obtaining of correct experimental data from the P_i dependence on T_o at different τ, for example, by the foil test, is of interest. Then it would allow to determine the E'' dependence on τ and to make the correction of the calculated values of P_i on the change in τ. Though the presented theory, strictly speaking, is applicable to rectangular initiating pulses, the comparison made for the extended pressure pulse tests (gap test, wedge test) shows good results. It means that E'' weakly changes with small change in τ.

Above the restrictions were not imposed on the magnitudes of P_i and τ. Therefore one can use the presented notions to estimate the change in critical reaction time (τ_c) at d_c. In this case Zeldovich-Newmann's model is suitable according to which the

TABLE 3

Comparison of Experimental and Calculated Initiation Thresholds for Some Explosives at Elevated T_o

Explosive parameters at $T_{o1} = 298°K$*				T_{o2} °K	$P_{i,exp.}$ kbar	$P_{i,calc.}$ kbar
Type	ρ_o g/cc	P_i kbar	E''† j/cm² µsec			
PETN	1.59	9.1	110	383	6.7	6.3
RDX	1.64	15.2	165	453	7.8	8.4
NONA	1.60	19.5	205	523	8.8	9.9
HNS	1.57	23.2	243	533	13.2	12.1
HNS**	1.57	19.0	200	533	9.0	9.0
PBX-9404	1.84	64.5	734	423	64.5	55.3
PBX-9404**	1.84	15	196	423	15	7.1

*Gap test (8)

**Plane-wedge shots (8)

†E'' is calculated from experimental data at $298°K$.

one-dimensional steady detonation wave is characterized as a shock wave in the unreacted explosive followed by a reaction zone. In so doing one can treat τ_c and P_c as proper estimates of equivalent duration and amplitude of initiating pulse, respectively (10). Then, using the notion of $E''(\tau)$, the detonation velocity (D_c') will be estimated at other initial temperature T_{o2} but at constant $\tau = \tau_{c1}$, ($k_1 = k_2 = 2$):

$$E''(\tau_{c1}) \simeq \rho_{o1} D_{c1}\left[\frac{D_{c1}^2}{(n_{c1} + 1)^2} + E_{o1}\right] = \rho_{o2} D_c' \cdot$$
$$\cdot \left[\frac{D_c'^2}{(n_c' + 1)^2} + E_{o2}\right].$$
$$(8)$$

Further, using the notion of $E'(T_o)$ at T_{o2} we will obtain

$$E'(T_{o2}) \simeq \rho_{o2} D_c' \tau_{c1}\frac{D_c'^2}{(n_c' + 1)^2} = \rho_{o2} D_{c2} \cdot$$
$$\cdot \tau_{c2} \cdot \frac{D_{c2}^2}{(n_{c2} + 1)^2}$$
$$(9)$$

At low T_{o2} about $20°K$ the value of E_{o2} can be neglected (Table 2). Then, from Eqs. 8 and 9 it follows that

$$\tau_{c2} \simeq \frac{\rho_{o1}}{\rho_{o2}}\left(\frac{n_{c2} + 1}{n_{c1} + 1}\right)^2\left(\frac{D_{c1}}{D_{c2}}\right)^3 \left[1 + \frac{(n_{c1} + 1)^2 E_{o1}}{D_{c1}^2}\right]\tau_{c1}$$

Assuming $n_{c1} = n_{c2} = 4.5$ and using the data of Tables 1 and 2 we will obtain the maximum estimate ($T_{o2} \simeq 0$) of the increase in τ_c:

$$\tau_{c2} \simeq 1.13\ \tau_{c1}$$

Measured in paper (7) and calculated in this work, reaction times are similar to the ideal reaction time. Therefore, the comparison of the above estimated and measured change in reaction time is difficult because the accurate relationship between τ_c and τ_r is unknown. However, the estimate shows that within the bounds of the hypotheses used we should not expect considerable change in τ_{r2} as distinct from predictions of the thermal explosion theory.

44

It is noted that there is one more interesting consequence. As is shown in (10), within the boundaries of the determination accuracy of the critical initiation energy it is constant for the critical detonation pulse for pressed TNT at various initial densities from 0.8 to 1.62 g/cc. It allows to determine the reaction time vs the detonation pressure (P). From the presentation of E' in the form of Eq. 9 it follows that

$$\tau_c \simeq E'(T_o)\sqrt{\rho_o(n_c + 1)}\, P_c^{-1.5} \sim \sqrt{\rho_o}\, P_c^{-1.5}$$

Generalizing the relation to the values of τ_r and P at $d > d_c$ and taking into account the fact that the detonation pressure is proportional to the square of ρ_o it is easy to show that

$$\tau_r \sim P^{-1.25}$$

must be valid. This $\tau_r(P)$ dependence is in good agreement with the experimental data for TNT with various forms and initial densities (2,7), and explains in a way the weak τ_r dependence on P, and, consequently, on the shock temperature.

In conclusion it should be noted that the presented theory is a phenomenological one. At present we can not explain the existence of such values as E' and E'' and to calculate them in independent manner. Probably, their existence is associated with the statistical character of the accurate theory of shock initiation of explosive. Homogeneous explosives may be considered as the limiting case of this theory: that is, the case when temperatures of all hot spots are the same and equal to the temperature of bulk shock heating, what governs the applicability of the thermal explosion theory to them.

REFERENCES

1. S. A. Bordzilovski, V. V. Sil'vestrov, V. M. Titov, "Shock Compression of Liquid Hydrogen at Various Experimental Geometries," Paper presented at The Fifth International Colloquium on Gasdynamics of Explosions and Reactive Systems, Bourges, France, 1975.

2. A. N. Dremin, S. D. Savrov, V. S. Trofimov, K. K. Shvedov, Detonation Waves in Condensed Materials, Nauka, Moskow, 1970.

3. J. W. Enig, F. J. Petrone, "The Failure Diameter Theory of Dremin," Fifth Symposium on Detonation, NOL-ONR, ACR-184, pp. 99-104 (1970).

4. M. W. Evans, "Detonation Sensitivity and Failure Diameter in Homogeneous Condensed Materials," J. Chem. Phys., Vol. 36, No. 1, pp. 193-200 (1962).

5. A. F. Belyaev, R. Kh. Kurbangalina, "The Effect of the Initial Temperature on the Value of the Critical Diameter of Nitroglycerine and Trotyl," Russ. J. Phys. Chem., Vol. 34, No. 3, pp. 603-610 (1960).

6. V. F. Nesterenko, "Study of Detonation Parameters of TG 50/50 at the Low Temperatures," Fizika Goreniya i Vzryva, Vol. 11, No. 2, pp. 324-325 (1975).

7. K. K. Shvedov, S. A. Koldunov, "The Influence of Physical State and Structure of Trotyl Charge on Decomposition Time in Detonation Wave." Sbornik "Gorenie i Vzryv," pp. 439-443, Nauka, Moskow (1972).

8. J. Roth, "Shock Sensitivity and Shock Hugoniot of High-Density Granular Explosives," ibid. 3, pp. 219-230 (1970).

9. F. E. Walker, R. J. Wasley, "Critical Energy for Shock Initiation of Heterogeneous Explosives," Explosivstoffe, Vol. 1, pp. 9-13 (1969).

10. D. Price, "Shock Sensitivity, a Property of Many Aspects," ibid. 3, pp. 207-217 (1970).

11. Y. de Longueville, "Comportement de Divers Explosifs Condenses Soumis a des Ondes de Choc Calibrées en Intensité et Durée," ibid. 1 (1975).

12. R. B. Scott, Cryogenic Engineering, Princeton, 1959.

13. J. Ribovich, W. Watson, F. C. Gibson, "Instrumented Card-Gap Test," AIAA Journal, Vol. 6, No. 7, pp. 1260-1263 (1968).

14. G. E. Hauver, "Shock-Induced Polarization in Plastics. II. Experimental Study of Plexiglas and

Polystyrene," J. Appl. Phys., Vol. 30, No. 7, pp. 2113-2118 (1965).

15. "Compendium of Shock Wave Data," UCRL-50108, Vol. II, Section C, General Editor, M. van Thiel, LRL, June 1966. Equation 23-2-1(5-8-2)-12 for PMMA, Equation 23-18-2-1(7-3-5-6)-1 for TNT and Equation 23-18-2-1(7-3-5-6)-2 for Liquid TNT.

16. J. B. Ramsay, A. Popolato, "Analysis of Shock Wave and Initiation Data for Solid Explosives," Fourth Symposium on Detonation, NOL-ONR, ACR-126, pp. 233-238 (1965).

17. W. E. Gordon, "Detonation Limits in Condensed Explosives," ibid. 16, pp. 179-197 (1965).

18. E. L. Lee, R. H. Sanborn, H. D. Stromberg, "Thermal Decomposition of High Explosives at Static Pressures 10-50 kilobars," ibid. 3, pp. 331-337 (1970).

19. A. N. Dremin, S. A. Koldunov, "Initiation of Detonation by Shock Waves in Cast and Pelletized TNT," UCRL-Translation-10408 from Vzryvnoye Delo, Vol. 63, pp. 37-50 (1967).

20. A. Isihara. Statistical Physics, Academic Press, New York—London, 1971.

MODES OF SHOCK WAVE GROWTH IN THE INITIATION OF EXPLOSIVES

J. W. Nunziato and J. E. Kennedy
Sandia Laboratories, Albuquerque, New Mexico

and

D. R. Hardesty
Sandia Laboratories, Livermore, California

The literature on shock initiation has carefully distinguished between the behavior of homogeneous and heterogeneous explosives with regard to reaction ignition, reaction growth, and the modes of wave growth. In this paper we illustrate the differences in shock growth modes in explosives representative of these two classes, nitromethane and PBX-9404, through the use of numerical calculations and previously reported experimental data. We then correlate the observed phenomena with some basic properties of the recently introduced concept of critical acceleration λ for shock front growth, which is proportional to the reaction rate, and a new concept called the reaction communication distance, which is defined as the ratio of the sound speed to the reaction rate. This distance, which varies inversely with λ, determines whether the energy released during the decomposition reaction becomes distributed throughout the shocked material or remains concentrated near the point of ignition. As a result, we are able to provide an explanation for such distinctly different growth phenomena as superdetonation in homogeneous explosives and the strong pressure disturbance and growth at the front in heterogeneous explosives.

1. INTRODUCTION

Recent experimental developments have contributed significantly to the understanding of wave evolution during the shock initiation of explosives in planar geometry. Lagrangian measurement methods such as electromagnetic, manganin, and quartz gauges and laser velocity interferometry have provided information on the entire shape of the shock pulse as well as the shock trajectory and amplitude. Consequently, the data obtained are more complete and more suitable for correlation with analytical predictions.

At the present time there is considerable interest in the application of wave front (or singular surface) analysis to extract from experimental data quantitative information concerning the initiation process. Using this type of analysis, it has been shown by several authors that the particle acceleration $(\partial_t u)^-$ behind the shock front at a given time determines whether the front will tend to grow or to decay in amplitude. In general, there exists a *critical acceleration* λ at which the shock amplitude will remain steady; if $(\partial_t u)^- > \lambda$ the shock front will grow and if $(\partial_t u)^- < \lambda$ the shock will decay. The quantity λ is determined by the physical properties of the material and by the reaction kinetics immediately behind the shock front. Thus, kinetic information pertaining to the shocked material can be derived from data indicating the critical acceleration and, conversely, critical acceleration information can be derived from reaction rate laws. Both the kinetics and the critical acceleration are functions of the shock amplitude and, for

47

example, for elastic materials undergoing exothermic chemical reaction, $\lambda < 0$.

Another important factor in the initiation of explosives is the acoustic communication within the shocked material which controls the distribution within the wave profile of the pressure generated by the reaction as the wave evolves. This effect can be made precise by defining the *reaction communication distance* as the ratio of the sound speed to the reaction rate in the explosive. It is interesting to note that at the shock front this parameter is inversely proportional to the critical acceleration λ.

Our objective in this paper is to discuss the various modes of one-dimensional shock growth during initiation in homogeneous and heterogeneous explosives and to correlate the observed phenomena with some basic features of the curves representing the critical acceleration and the reaction communication distance as functions of pressure. The literature on shock initiation has distinguished clearly between the behavior of homogeneous and heterogeneous explosives with regard to reaction ignition, reaction growth, and the modes of wave development. The differences are caused by the fact that homogeneous explosives react due to bulk shock-heating while heterogeneous explosives react due to the formation of hot spots.

Here we confine our discussion to input pulses of infinite duration and illustrate the effects of these differences with the use of numerical calculations and previously reported experimental data for two materials representative of these two classes of explosives, nitromethane and PBX-9404, respectively. We then consider the critical acceleration curve for each material and show how the differences in ignition and initiation are related to the differences in the shapes of the curves. Furthermore, by comparing the reaction communication distance in these explosives with the propagation distance for a given input shock, we are able to provide an explanation for such distinctly different growth phenomena as superdetonation in homogeneous explosives and the strong pressure disturbance and growth at the front in heterogeneous explosives.

2. THE CRITERION FOR SHOCK FRONT GROWTH

In a one dimensional context, it suffices to characterize explosive materials as chemically reacting,

elastic fluids which do not conduct heat. Such fluids can be characterized by constitutive equations for the Helmholtz free energy ψ and the reaction rate ω (1):

$$\psi = \hat{\psi}(v, \theta, \xi), \qquad \omega = \dot{\xi} = \hat{\omega}(v, \theta, \xi), \qquad (1)$$

where ν is the specific volume, $\theta > 0$ is the absolute temperature, and ξ, $0 \leq \xi \leq 1$, is the reaction coordinate of the products. Thus,

$$\psi_f(v, \theta) = \hat{\psi}(v, \theta, 0), \qquad \omega_f(v, \theta) = \hat{\omega}(v, \theta, 0) \qquad (2)$$

specifies the *frozen* response of the unreacted fluid and

$$\psi_p(v, \theta) = \hat{\psi}(v, \theta, 1),$$
$$\omega_p(v, \theta) = \hat{\omega}(v, \theta, 1) = 0, \qquad (3)$$

specifies the response of the reaction products.

The second law of thermodynamics requires that the pressure p be given by

$$p = - \partial_v \hat{\psi} \qquad (4)$$

and that the inequality

$$(\partial_\xi \hat{\psi})\omega \leq 0 \qquad (5)$$

be satisfied for all (v, θ, ξ). We further define the internal energy e by

$$e = \hat{e}(v, \theta, \xi) = \hat{\psi} - \theta(\partial_\theta \hat{\psi}) \qquad (6)$$

and the thermodynamic derivatives

$$E = - (\partial_v \hat{p}), \qquad G = \partial_\theta \hat{p}, \qquad c_v = \partial_\theta \hat{e}, \qquad (7)$$

E being the isothermal pressure-volume modulus, G the pressure-temperature modulus, and c_v the specific heat at constant volume. It is natural to assume

$$E > 0, \qquad G > 0, \qquad c_v > 0. \qquad (8)$$

In view of eqs. $(7)_2$ and $(8)_2$, we see that $\hat{p}(v, \theta, \xi)$ is invertible and thus the internal energy can be written as

$$e = \tilde{e}(v, p, \xi). \qquad (9)$$

The quantity Q, defined by

(17). To carry this out, we first consider the frozen response and make use of the results obtained previously by Lysne and Hardesty (7) using impact-loading techniques. They determined the frozen equation of state up to 10 GPa and subsequently extrapolated it to over 20 GPa (the spike point at detonation $\approx$ 19.5 GPa). In this study, the resulting thermodynamic surfaces were fit with analytic functions subject to thermodynamic requirements and the requirement that they match the calculated frozen Hugoniot pressure-temperature and volume-temperature curves, $p_H(\theta)$ and $v_H(\theta)$, respectively. Thus, the frozen pressure and energy surfaces were expressed as

$$p_f(v, \theta) = \frac{WR_1 v(v + \chi_2)}{(R_2 + v)(v + \chi_1)} \left(\frac{\theta}{v} - \frac{\theta_o}{v_o} \right), \quad (18)$$

$$e_f(v, \theta) = -\frac{1}{2} p_H(\theta)[v_H(\theta) - v_o]$$

$$+ \frac{R_1 \theta_o W}{v_o} \left\{ [v - v_H(\theta)] \right.$$

$$+ \frac{R_2(R_2 - \chi_2)}{R_2 - \chi_1} \ell n \left[\frac{(R_2 + v_H(\theta))}{(R_2 + v)} \right] \quad (19)$$

$$\left. + \frac{\chi_1(\chi_1 - \chi_2)}{R_2 - \chi_1} \ell n \left[\frac{(\chi_1 + v)}{(\chi_1 + v_H(\theta))} \right] \right\},$$

where R_1, R_2, W, χ_1, and χ_2 are all constants given by

$$R_1 = \gamma(\theta_o + \beta)v_o/\theta_c, \quad R_2 = a + (\beta v_o/\theta_o), \quad (20)$$

$$W = 1 - \delta\beta, \quad (21)$$

$$\chi_1 = a - v_o, \quad \chi_2 = (\delta R_2 \theta_o + \chi_1)/W, \quad (22)$$

and γ, δ, a, and β are the constants appearing in the Hugoniot fits (8):

$$p_H(\theta) = \gamma(1 + \delta\theta)(\theta - \theta_o), \quad (23)$$

$$v_H(\theta) = v_o - \frac{a(\theta - \theta_o)}{\theta + \beta}. \quad (24)$$

The experimental kinetic data reported for nitromethane has been typically expressed in terms of the ignition time τ deduced in shock wave experiments and the estimated shock temperature θ^-. In Fig. 1, we show the results obtained by Hardesty (9) from interferometric observation of plate deceleration behind reacting nitromethane and the results obtained by Walker and Wasley (10) from streak camera and photographic records. In particular, the data points shown indicate the actual reported values of the ignition time and the error bars show the range of values which could be deduced from the experimental observations. There are several ways that this data can be represented. However, recognizing that streak camera and photographic data tend to be late in time, we choose to fit the data with a straight line biased in favor of Hardesty's data (the solid line in Fig. 1). Since, during the time of ignition there is little change in volume and essentially no formation of products ($\xi \doteq 0$), this linear fit implies that thermal ignition theory holds and the frozen kinetics are of the Arrhenius type; i.e.,

$$\omega_f(v, \theta) = A \exp \left(-\frac{\theta_a}{\theta} \right), \quad (25)$$

where the frequency factor A and the activation temperature θ_a are related to the ignition time τ by
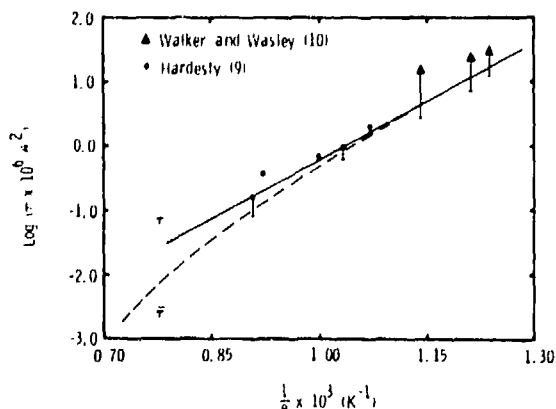
Fig. 1. Thermal ignition times τ and $\bar{\tau}$ for a single reaction and two parallel reactions, respectively, as a function of shock temperature. The error bars indicate the uncertainty in individual data points.

49

$$\tau = \frac{c_{vf}\theta^2}{\theta_a A|Q_{vf}|} \exp\left(\frac{\theta_a}{\theta}\right). \tag{26}$$

The heat of reaction at constant volume Q_v is defined by

$$Q_v = \partial_\xi \hat{e} \tag{27}$$

and, by eq. (10), is also related to the heat of reaction Q of the shock process through

$$Q = - \frac{v_o c_v}{G} (\partial_\xi \hat{p}) + Q_v. \tag{28}$$

It should be evident at this point that we need only evaluate the heats of reaction Q and Q_v in order to evaluate the kinetic parameters θ_a and A and to compute λ as a function of shock compression.

The quantities Q and Q_v can be determined by prescribing the mixing rule by which the unreacted nitromethane goes over to products and the constitutive equations for the products. Here we shall employ a linear mixing rule such that the free energy ψ and the reaction kinetics ω are of the form

$$\hat{\psi}(v, \theta, \xi) = \psi_f(v, \theta)(1 - \xi) + \psi_p(v, \theta)\xi,$$
$$\hat{\omega}(v, \theta, \xi) = \omega_f(v, \theta)(1 - \xi) + \omega_p(v, \theta)\xi. \tag{29}$$

Note that these are first-order kinetics. Then it is not difficult to show from eq. (4) and eq. (6) that

$$\hat{p}(v, \theta, \xi) = p_f(v, \theta)(1 - \xi) + p_p(v, \theta)\xi,$$
$$\hat{e}(v, \theta, \xi) = e_f(v, \theta)(1 - \xi) + e_p(v, \theta)\xi. \tag{30}$$

The products will be assumed to be in thermochemical equilibrium and to satisfy Abel's equation of state in which case

$$\omega_p(v, \theta) \equiv 0,$$

$$p_p(v, \theta) = \frac{R_g \theta}{v - b}, \tag{31}$$

$$e_p(v, \theta) = c_g(\theta - \varphi),$$

R_g being the product gas constant, b being the product covolume, c_g the gas specific heat, and φ the temperature at which the product gases have zero internal energy. These constants were chosen to match the C-J conditions of pressure, temperature, volume, and specific heat calculated using the thermochemical equilibrium code TIGER (11). With these results we can now calculate Q and Q_v. In particular, using eqs. (27), (28), and (30), we have

$$Q_v = \{e_p(v, \theta) - e_f(v, \theta)\},$$

$$Q = \left\{- \frac{c_v}{G} (p_p(v, \theta) - p_f(v, \theta)) \right. \tag{32}$$
$$\left. + (e_p(v, \theta) - e_f(v, \theta))\right\}.$$

Then eq. $(32)_1$, along with eq. (26) and Fig. 1, yields a frequency factor A of $6.9 \times 10^4/\mu s$ and an activation temperature θ_a of 14400 K. We now have all the data required. It is interesting to note that over the range of Hugoniot temperatures shown in Fig. 1, the magnitude of Q_v is nearly constant and equal to 1.4 kcal/g which agrees favorably with previously reported values (12). The activation temperature θ_a of 14400 K corresponds to an activation energy of ≈ 29 kcal/mole which agrees well with the value of 31 kcal/mole deduced by Hardesty (9) from the data of Berke, *et al.* (13).

The critical acceleration λ was computed as a function of particle velocity amplitude u^- using these values and the results are shown in Fig. 2 as the solid curve. Also shown in Fig. 2 is the maximum value of λ at detonation, as estimated from the detonation properties and some experimental information due to Hayes (14). At detonation, the shock is steady and by eq. (13), $\lambda = (\partial_t u)^-$. Thus, the maximum value of λ can be estimated by

$$\lambda_{det} = - \frac{u_s^- - u_{CJ}}{t_r} \tag{33}$$

where u_s^- is the spike amplitude, u_{CJ} is the particle velocity at the C-J point, and t_r is the time duration of the reaction. For $u_s^- = 2.78$ km/s, $u_{CJ} = 1.74$ km/s, $t_r \leqslant 0.0015\,\mu s$, eq. (33) yields $\lambda \leqslant -690 \times 10^6$ km/s^2. The large discrepancy between this estimated value of λ and the solid curve strongly suggests that a
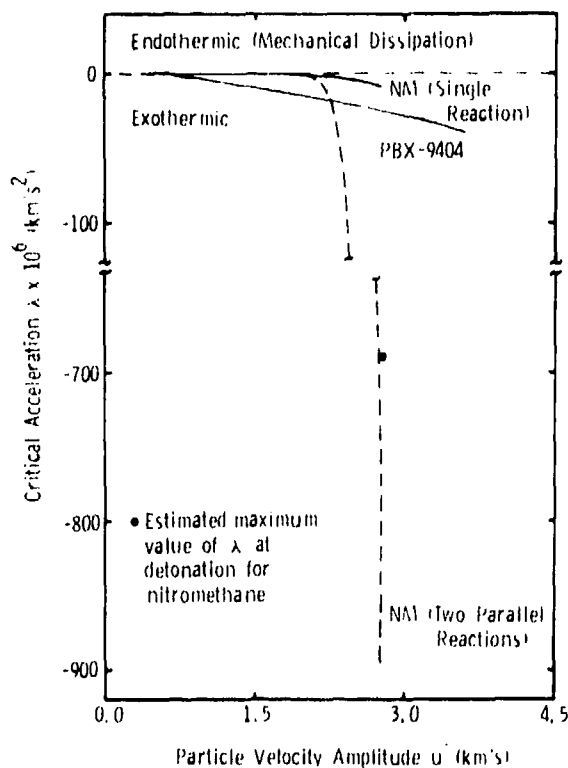
Fig. 2. Critical acceleration for steady wave propagation as a function of shock amplitude u^- for nitromethane and PBX-9404. The right end of each curve represents the detonation spike point. At the left end of the PBX-9404 curve, λ slightly exceeds zero.

reaction with a higher activation temperature dominates the kinetics near detonation. In complex reactions occurring by a free-radical mechanism involving several elementary reactions, the overall reaction rate may be controlled principally by one reaction step at low temperatures and by another step, with a higher activation temperature, at higher temperatures. We suggest that the decomposition of nitromethane is such a reaction. Accordingly, we replaced eq. (25) by a kinetic expression for two parallel Arrhenius reactions,

$$\omega_f(v, \theta) = A \exp(-\theta_a/\theta) + A^* \exp(-\theta_a^*/\theta). \quad (34)$$

Nitromethane decomposition kinetics with a high activation temperature have been suggested by Benson and O'Neal (15), and we have used their

value of the activation temperature in the second term of eq. (34), i.e., $\theta_a^* = 29700$ K. Their estimate for A^* was $3.98 \times 10^9/\mu s$. The dashed line shown in Figs. 1 and 2 was calculated using $A^* = 1 \times 10^{10}/\mu s$.

This choice for A^* was not entirely arbitrary. It provided a value of λ_{det} which was consistent with Hayes' datum point and gave us good agreement with the apparent time of reaction completion from Hardesty's data (see Section 4). We also found that the addition of the parallel reaction did not greatly reduce the values of ignition time predicted by thermal explosion theory in the range of the experimental data. The dashed curve in Fig. 1 was calculated using ignition times, $\bar{\tau}$, for the two parallel reactions of eq. (34) obtained from the relation (cf. ref. (16))

$$\bar{\tau} = \frac{\tau\tau^*}{\tau + a\tau^*} \ F\left(1, 1; \ \frac{2a-1}{a-1} \ ; \ \frac{a\tau^*}{\tau + a\tau^*}\right), \quad (35)$$

where τ is given by eq. (26),

$$\tau^* = \frac{c_{vf}\theta^2}{\theta_a^* A^* |Q_{vf}|} \ \exp\left(\frac{\theta_a^*}{\theta}\right), \quad (36)$$

$$a = \theta_a^*/\theta_a, \quad (37)$$

and $F(\cdot, \cdot; \cdot; \cdot)$ is the hypergeometric function. This function is evaluated in terms of a convergent infinite series of its fourth argument.

PBX-9404

Kennedy and Nunziato (6) have previously determined the critical acceleration λ for PBX-9404 by using eq. (13) along with data from experimental measurements of shock wave evolution. Typical transmitted wave profiles observed using laser velocity interferometry are shown in Fig. 3 and from these data du^-/dt and $(\partial_t u)^-$ were determined for each amplitude u^-. Combining this information with the known frozen properties of PBX-9404 resulted in the curve also shown in Fig. 2. Notice that λ is slightly greater than zero ($Q^-\omega^- > 0$, endothermic behavior) when 0.5 km/s $< u^- <$ 0.6 km/s, which was the lower amplitude range of the experiments reported. This is interpreted to mean that mechanical dissipation, which yields behavior similar to an endothermic

51

$$Q = \partial_\xi \tilde{e} = -\left[\frac{c_v}{G}\ (\partial_\xi \hat{p}) - (\partial_\xi \hat{e})\right], \qquad (10)$$

is called the heat of reaction; the reaction is said to be exothermic if the net heat release $Q\omega < 0$, endothermic if $Q\omega > 0$ (2,3).

Here, a shock front is considered to be a propagating singular surface (4) across which the motion and the reaction coordinate ξ are continuous but the particle velocity u, the specific volume v and the temperature θ and their derivatives suffer jump discontinuities. Assuming that the shock is compressive and propagating into fluid material essentially at thermochemical equilibrium at the frozen state ($\xi \doteq 0$) with specific volume v_o, we can use eq. (9) and the familiar Hugoniot relation to define the frozen Hugoniot pressure-volume curve

$$p^- = p_H(v^-) \qquad (11)$$

where ( )$^-$ denotes evaluation immediately behind the front. Then the material shock velocity is given by

$$U^2 = -v_o^2 \left\{\frac{p_H(v^-) - p_H(v_o)}{v^- - v_o}\right\} \qquad (12)$$

and the evolution of the particle velocity amplitude u$^-$ is governed by the differential equation (5,6)

$$\frac{du^-}{dt} = (1 - \mu)\left[1 + \frac{2\mu}{1 + \kappa}\right]^{-1}\left\{(\partial_t u)^- - \lambda\right\} \quad (13)$$

where $(\partial_t u)^-$ is the particle acceleration immediately behind the front,

$$\mu = \frac{U^2}{(C^-)^2}, \qquad (14)$$

$$C^- = v_o\left[E^- + \frac{\theta^-(G^-)^2}{c_v^-}\right]^{1/2} \qquad (15)$$

is the sound speed immediately behind the shock front,

$$\kappa = -\frac{U^2}{v_o^2 p_H'(v^-)}, \qquad (16)$$

and

$$\lambda = \frac{v_o UG^-Q^-\omega^-}{c_v^-(1 - \mu)(C^-)^2} \qquad (17)$$

is called the *critical acceleration*. Since the shock velocity is always subsonic with respect to the fluid behind the front (2,3), $\mu < 1$, and thus it is evident from eq. (13) that the shock front can grow only if $(\partial_t u)^- > \lambda$. Notice from eq. (17) that λ is directly proportional to the net heat release rate $Q^-\omega^-$ at the shock front.

The fact that the critical acceleration λ governs growth of the shock front indicates that it is an important quantity to evaluate in order to understand and quantify initiation behavior of explosives. Furthermore, it is evident from eqs. (13) and (17) that there are two methods by which we can evaluate λ as a function of the particle velocity amplitude. On one hand, we can make observations of a growing (or decaying) shock front, corresponding to a given initial condition, to determine du^-/dt and $(\partial_t u)^-$ for various values of u$^-$. This data, along with the known frozen properties of the material, can then be used with eq. (13) to determine $\lambda(u^-)$. Since λ is proportional to ω^- through eq. (17), this approach is particularly useful in that it provides a means of evaluating the frozen kinetic, i.e., $\omega^- = \hat{\omega}_f(v^-, \theta^-)$, of the explosive from shock wave experiments. Alternatively, if the frozen properties and the reaction kinetics are known, then $\lambda(u^-)$ can be computed directly from eq. (17).

3. THE CRITICAL ACCELERATION FOR NITROMETHANE AND PBX-9404

We consider nitromethane (NM) and PBX-9404 to be typical examples of homogeneous and heterogeneous explosives, respectively, and thus we shall consider them in some detail in order to illustrate our ideas with regard to shock growth modes.

Nitromethane

In the case of nitromethane, there exists sufficient data to characterize the frozen response and the reaction kinetics of the material and thus we shall evaluate the critical acceleration λ directly from eq.
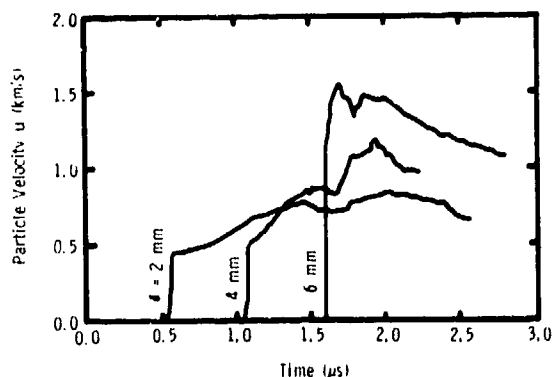
Fig. 3. Particle velocity histories observed in a window material behind a shock-loaded PBX-9404 sample of thickness δ. The input pulse duration was 1.1 μs (6).

reaction, is the dominant effect at low shock amplitudes. It is important to remember that the critical acceleration λ only reflects the net effect (6), that is,

$$\lambda = \lambda_{chem} + \lambda_{mech}.$$

Thus, since the individual contribution of λ_{chem} to λ cannot be determined, it would be inappropriate at this time to advance a kinetic model describing the chemical reaction of shocked PBX-9404.

4. SHOCK GROWTH MODES

The critical acceleration curves shown in Fig. 2 for nitromethane (NM) and PBX-9404 are quite different in shape. We believe that these differences are representative of the observed differences in reaction ignition, reaction growth, and shock wave growth during initiation in homogeneous and heterogeneous explosives, respectively. To correlate these ideas, we will confine our discussion to the problem of shock growth when the boundary has constant support and the boundary pressure is less than, or equal to, the C-J pressure of the explosive. This amounts to a square input pulse, infinite in duration. In this case, $(\partial_t u)^- = 0$ at least initially and thus it follows from eq. (13) that

$$\frac{du^-}{dt} = -(1 - \mu)\left[1 + \frac{2\mu}{1 + \kappa}\right]^{-1}\lambda. \qquad (38)$$

Clearly, then, the initial growth of the wave will be proportional to the critical acceleration, λ.

Nitromethane

The critical acceleration curve for nitromethane corresponding to two parallel reactions shows two distinct regions; for $u^- < 2.1$ km/s ($p^- < 12$ GPa), λ is very small in magnitude and changes only slightly with the shock amplitude u^-, and for $u^- > 2.1$ km/s ($p^- > 12$ GPa) λ becomes large in magnitude and changes rapidly with the shock amplitude u^-. Since the C-J pressure for nitromethane is approximately 12.2 GPa, it is expected that long-duration shock pulses with input pressures less than the C-J pressure will grow very slowly at the front. This is precisely what is observed experimentally until the particle acceleration $(\partial_t u)^-$ behind the front is altered due to the occurrence of thermal ignition at some point in the flow field. Just where this thermal ignition occurs, however, has been the subject of considerable discussion. Walker and Wasley (10) and Hardesty (9) have observed thermal ignition at pressures in this low-amplitude range and their observations appear to differ from one another. Walker and Wasley performed experiments with an initial pressure of ≈ 6 GPa and concluded that the thermal ignition occurred at some distance from the boundary. It was difficult to tell from their observations whether superdetonation occurred, although their streak camera results suggest it did. In Hardesty's study, plate-impact experiments were performed in the pressure range of 7.5-9.5 GPa. By observing the deceleration of a copper plate behind the reaction and measuring the wave velocity in the nitromethane, he concluded that there was thermal ignition at the boundary which subsequently led to superdetonation. To see whether these various observations are consistent with the model for nitromethane developed in the previous sections, we have carried out numerical calculations using the one-dimensional Lagrangian wave-propagation code WONDY IV (17).

This code solves the finite-difference analogs of the one-dimensional field equations of mass and momentum and employs an artificial viscosity method to treat shock discontinuities. The model, i.e., eqs. (18), (19), (29)$_2$, (30) and (31), was introduced into the code as a special subroutine and an Adams method, differential equation integrator was coupled to WONDY to integrate the kinetic law (e.g., eqs.

53

$(29)_2$, $(31)_1$, and $(34))$ and the energy equation during each WONDY time step (18). This time step Δt was taken to be

$$\Delta t = \min \left\{ \frac{\Delta X}{C} , \frac{\Delta \xi}{\omega} \right\}$$

where ΔX is the mesh size and $\Delta \xi$ is the maximum change in the reaction coordinate permitted during each time cycle (19).

The numerical results we shall report here concern waves generated in a plate-impact configuration similar to that employed in Hardesty's experiments. This configuration is shown in Fig. 4 and involves the symmetric impact of copper on copper with the wave subsequently transmitted into the nitromethane. The copper flyer was sufficiently thick to ensure that the input pulse could be considered infinite in duration. It is appropriate at this point to first show some comparison of code results with Hardesty's observations. Recall that in his experiments, he monitored the motion of the Cu/NM interface (cf. Fig. 4). In Figs. 5 and 6 we show his experimental traces of the particle velocity history at the Cu/NM interface for shots N4 ($p^- = 7.5$ GPa, $\theta^- = 934$ K) and N8 ($p^- = 9.2$ GPa, $\theta^- = 1101$ K). Hardesty attributed the observed deceleration to thermal ignition at the Cu/NM interface and the lower level of particle velocity to the boundary condition corresponding to superdetonation. At some later time, after the superdetonation wave overtook the shock front, the particle velocity should increase slightly to match the boundary condition for steady detonation. The ignition time $\bar{\tau}$ was taken as the time after arrival at which deceleration began.

Also shown in Figs. 5 and 6 are the results obtained using WONDY IV. While the comparison of the numerical results with the experimental observations would not appear to be as good as one might
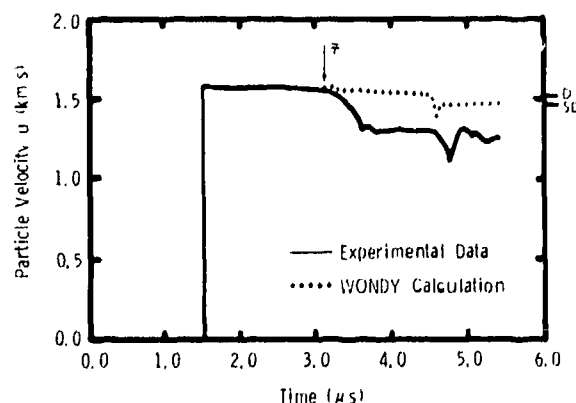
Fig. 5. Comparison of computed particle velocity history at the Cu/NM interface with Hardesty's experimental observation (9) in shot N4, where $p^- = 7.5$ GPa and $\theta^- = 934$ K. Velocity levels SD and D refer to boundary conditions behind superdetonation and detonation, respectively, independently calculated using TIGER (11).
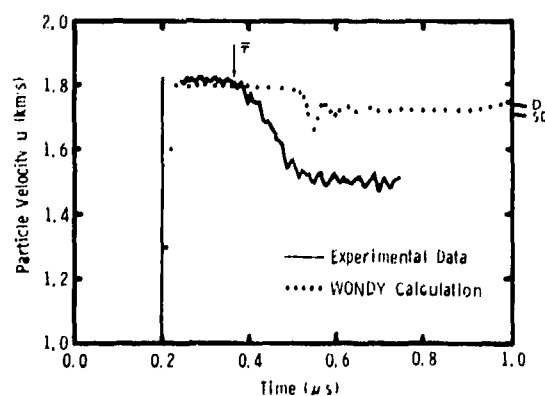
Fig. 6. Comparison of computed particle velocity history at the Cu/NM interface with Hardesty's experimental observation (9) in shot N8, where $p^- = 9.2$ GPa and $\theta^- = 1101$ K. Velocity levels SD and D refer to boundary conditions behind superdetonation and detonation, respectively, independently calculated, using TIGER (11).

Fig. 4. Schematic of the experimental configuration employed by Hardesty (9) to study shock initiation of nitromethane (NM).

54

like, the comparison must be considered carefully. There is some interesting agreement in timing. In particular, the time $\bar\tau$ at which the initial deceleration occurs and the time at which the minimum particle velocity is achieved (i.e., the time at which the reaction goes to completion at the interface) agree well with the observations. In addition, the levels of interface velocity achieved behind the superdetonation and steady detonation waves in WONDY calculations are in excellent agreement with the levels we have calculated with the use of the TIGER code (11). These levels are identified as SD and D, respectively, in Figs. 4 and 5. We believe that the apparent discrepancies in the magnitude of the deceleration between the calculated wave profiles and those which are observed are the result of distortion due to index-of-refraction and velocity dispersion effects (20). It should be recalled that the laser beam of the interferometer passes through the reaction products as well as the nitromethane as the wave propagates and initiates the reaction. Thus any reflectivity of the products or changes in the index of refraction of the reactant-product mixture must be taken into account in reducing the data. Hardesty presumed that the products were gases which exhibited Gladstone-Dale behavior; however, the calculations suggest they did not.

The numerical results shown in Figs. 5 and 6 give some indication of the principal growth mode in nitromethane, that is, they show the effect of super-detonation on the motion of the loaded interface. To explore this phenomenon in more detail, we carried out numerical calculations for input pulses of $\approx 6, 9,$ and 12 GPa. The results shown in Fig. 7 for 6 GPa were fairly typical. Here we see the particle velocity histories one would observe in nitromethane at propagation distances δ ranging from $\delta = 0$ to $6U_0\bar\tau$, where U_0 is the initial value of the shock velocity. Consistent with our earlier remarks, we see very little growth at the front until thermal ignition and, in fact, the growth is slow even until the time when the thermal explosion is complete. In all our calculations involving constant support at the boundary, we found that the thermal explosion occurs at the loaded interface ($\delta = 0$) at $3.25\,\bar\tau \pm 0.1\,\bar\tau$. We note a related point in Hardesty's data (9), i.e. his earliest indication of light emission occurs at $\approx 2.5\,\bar\tau$.

When thermal explosion has occurred, super-detonation begins to build up and overtake the front. The buildup appears to continue until the super-

detonation reaches the shock front. It is to be expected that the superdetonation will be unsteady because it is propagating into a region which is non-uniform with respect to reactant depletion, compression and compressibility, and this unsteadiness is evident in the calculations (cf. Fig. 7). After the superdetonation breaks through the front, the shock amplitude u^- relaxes back to the spike point of 2.78 km/s. This relaxation process is again governed by the shock amplitude eq. (13) and the critical acceleration λ. Unfortunately, we cannot check the consistency of this type of analysis with the relaxation observed in the code results since our computations tended to step over the spike and thus the spike amplitude is not determined in these calculations. This overstepping is due to the thinness of the spike and the lack of sufficient resolution (small enough meshing) in our computations.

The results in Fig. 7 for a 6 GPa input pulse differ somewhat from Walker and Wasley's observations (10) in that we see thermal explosion at the wall. We have concluded that this location of thermal explosion is due to the fact that in the calculations we maintained constant support at the loaded interface. Clearly, in the case of unsupported waves, such as triangular pulses, we could expect thermal explosion to occur at positions removed from the interface. Since the input wave in Walker and Wasley's experiments was not completely supported, this may provide the explanation for their observations.

Having exhibited the growth modes in nitromethane, let us now return to the critical acceleration
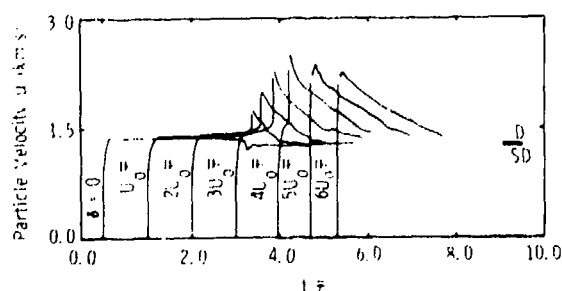
Fig. 7. Computed particle velocity histories during shock wave growth in NM following a 6-GPa input shock. Both the time scale and the observation stations are normalized in terms of the thermal ignition time $\bar\tau$.

55

curve (Fig. 2) and draw some conclusions. As we have already seen, the λ-curve tells us about the growth at the shock front when $(\partial_t u)^- = 0$ through eq. (38). When the input shock amplitude is low so that it corresponds to the flat portion of the λ-curve, then the shock develops nearly as a growing square wave (cf. Fig. 7). In this region, the reaction proceeds so slowly behind the shock front that the implicit assumption of thermal ignition theory (i.e., essentially no reaction until the ignition time $\bar{\tau}$ is reached) is nearly satisfied. In fact, our calculations show that the extent of reaction at the loaded interface is 2-4% by the time $\bar{\tau}$ and perhaps 15% at $3.25\,\bar{\tau}$, shortly before the thermal explosion is completed and superdetonation occurs.

However, it is equally important to point out that there is another way to look at the λ-curve which provides some information about the flow field behind the front and indicates the presence of superdetonation. To do this, we must keep in mind two facts: (i) that, by eq. (17), the critical acceleration λ is directly proportional to the frozen kinetic law $\omega_f(v, \theta)$, and (ii) that the values of the particle velocity amplitude u^- have a one-to-one correspondence with values of temperature. These observations enable us to conclude that, neglecting the effects of reactant depletion (which appears reasonable for NM), the shape of the λ-curve is a portrait of the kinetic process in a given wave profile. That is, we can track along the λ-curve in terms of the temperature and obtain a qualitative picture of how the reaction rate changes in the wave profile. Thus, the fact that $|\lambda|$ is small at lower temperatures indicates that at the lower temperatures in a wave profile we can expect a very slow reaction. However, the fact that at some point on the λ-curve the shape changes abruptly and λ becomes large in magnitude indicates that at some point in the flow field the reaction rate ω will change abruptly and become very high. It is this character of the λ-curve which suggests the presence of superdetonation in the initiation process.

This shape of the critical acceleration curve, however, does not guarantee the existence of superdetonation. For superdetonation to occur, it is also necessary that the time of reaction completion at the ignition point be extremely short in comparison to the time it takes for the resulting pressure disturbance to communicate with the rest of the wave profile (cf. Enig (21)). Since the sound speed C governs this communication, it is useful to compute the ratio C/ω,

which represents the distance over which a weak pressure disturbance can propagate during the time required for the reaction to go to completion. We then compare C/ω with the thickness of the shocked region, i.e., the shock propagation distance. By assuming that the frozen response of nitromethane dominates the structure of the wave profile until the thermal explosion occurs, we can use eq. (17) to obtain a reasonable estimate of

$$\frac{C}{\omega} = \frac{v_0 G Q \sqrt{\mu}}{c_v \lambda (1 - \mu)} \tag{39}$$

for every point in the wave profile. This expression allows us to determine C/ω as a function of pressure and the results are shown in Fig. 8. Also shown in Fig. 8 are two curves representing the propagation distance δ as a function of the shock front pressure p^- and as a function of the pressure at the loaded interface p_I, both of which were obtained from our numerical results for the 6-GPa input pulse.

In comparing the reaction communication distance C/ω with the propagation distance δ in terms of the shock front pressure, we see that there is good communication ($C/\omega > \delta$) until the superdetonation has overtaken the front. This implies that the pressure disturbances generated in the neighborhood of the front communicate well with that portion of the
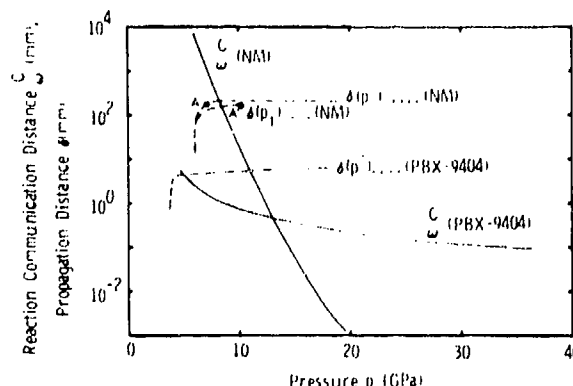
Fig. 8. Reaction communication distance C/ω and shock propagation distance δ as functions of pressure. The argument p^- denotes the shock front pressure and p_I the loaded interface pressure. Points A and A' correspond to the same propagation distance (and time) during shock growth in NM.

wave which is ahead of the superdetonation. However, after superdetonation has broken through the front, we see that communication becomes very limited ($C/\omega \ll \delta$). This corresponds to the fact that in detonation the reaction effects are localized immediately behind the shock front, and consequently as the shock passes over each material plane the reaction accelerates itself to a prompt completion. Thus, poor communication suggests a small reaction zone.

Comparison of the communication distance C/ω with the propagation distance δ in terms of the loaded interface pressure leads to some additional conclusions. First, disturbances generated at the loaded interface are well communicated to the rest of the wave until the shock has propagated a distance $\approx 3.25\ U_o\bar{\tau}$. This good communication is evident in Fig. 7 by the small value of the particle acceleration behind the front as the wave propagates. However, after the shock front has traveled $\approx 3.25\ U_o\bar{\tau}$, the communication becomes poor (cf. Fig. 8). It is of interest at this point to consider the pts. A and A' on the two curves of the propagation distance. These points correspond to the same distance, slightly greater than $3.25\ U_o\bar{\tau}$, and they show the difference in the pressure between the shock front (pt. A) and the loaded interface (pt. A'). The important thing to notice here is that the communication ranges from good at the shock front to poor at the loaded interfaces. This implies that the loaded interface cannot communicate with the rest of the wave. This effect, along with an accelerating reaction rate, results in a highly localized pressure excursion at the loaded interface. The result is superdetonation, initiated essentially at the loaded interface.

It is important to note that Fig. 8 is fairly representative of nitromethane over the pressure range of 6-12 GPa and we would have arrived at the same type of conclusions had we used the numerical results for the 9- or 12-GPa input pulses.

PBX-9404

Now let us consider the shock growth modes in PBX-9404. Kennedy and Nunziato (6) have observed the growth process using velocity interferometry for an input pulse of 3.7 GPa and the measured wave profiles at propagation distances δ of 2, 4, and 6 mm were shown previously in Fig. 3. There are several features of these wave profiles which should be noted.

First of all, the particle acceleration behind the front at $\delta = 2$ mm is small and positive and there is slight growth of the front by 4 mm. Secondly, there is a strong pressure disturbance which develops at some point behind the front and nearly overtakes the front by 6 mm propagation distance. From the point of overtake to detonation at ≈ 7 mm, the shock grows at the front (22).

This type of shock growth behavior can be inferred from the critical acceleration curve for PBX-9404 shown in Fig. 2. In the case of an infinite-duration input pulse, the initial growth of the shock front amplitude is governed by eq. (38) since $(\partial_t u)^- = 0$. Thus, the growth is proportional to λ and, since λ is small in magnitude at low amplitudes, we would expect low amplitude waves to grow slowly at first. This initially slow growth is borne out in the experimental observations (Fig. 3) and closely resembles the growing square-wave hypothesis considered by Kennedy (23). By also recognizing that the overall shape of the λ-curve is related to a combination of the frozen kinetics and the mechanical dissipation of the material, we can see the reason for the development of the strong pressure disturbance behind the wave. That is, since $|\lambda|$ increases slowly with the amplitude, and hence with pressure, we can expect that in a given wave profile the reaction will be relatively gradual and spread out. Thus, any "thermal explosion" in PBX-9404 will not be very vigorous. The fact that the resulting pressure disturbance remains spread out over a large time and that it overtakes the front and does *not* immediately result in detonation is a consequence of communication effects.

The effect of reaction communication upon shock wave growth in PBX-9404 is well illustrated in Fig. 8. Here the communication distance, C/ω, is evaluated for conditions immediately behind the shock front, using the frozen Hugoniot (6), a value of the heat reaction Q of -1.37 kcal/g (24), and the critical acceleration curve in conjunction with eq. (39). The right end of the C/ω curve represents the detonation spike point. Using experimental data (6), we have also shown in Fig. 8 the growth in shock front pressure with propagation distance δ for the case of the supported 3.7-GPa input shock. The right end of the δ curve represents the overtake of the shock front by the strong pressure pulse from behind.

The significant point to recognize in Fig. 8 is that rapid growth in the shock front pressure is nearly

coincident with the onset of limited communication, i.e., as the shock propagates and grows, we enter a region where $C/\omega < \delta$. In this region, pressure disturbances generated by the reaction in the neighborhood of the front do not have the opportunity to communicate with the rest of the wave profile. If, for the moment, we neglect depletion, then we can also apply the communication curve to other parts of the wave profile and conclude that there is limited communication within much of the wave profile once rapid growth at the front has begun. This effect, along with the slow acceleration of the reaction, gives rise to the slowly growing disturbance which develops at some point in the body of the wave separated from the loaded interface. Notice, however, that the communication is not so limited as to result in superdetonation, as in the case of nitromethane. Rather, there is still sufficient communication to permit regions close to the pressure disturbance to be influenced and thus the disturbance remains spread out in time until it overtakes the front. The fact that the reaction-generated pressure disturbance migrated toward the front and that the loaded interface pressure is always lower than the peak pressure in the disturbance is believed to be due to the effect of depletion on communication. That is, communication will tend to be better in partially reacted solid material than in the gaseous products. Thus, the disturbance will tend to propagate toward the shock front where the material is less depleted and to lose communication with the loaded interface. Finally, it should be observed that although the communication is limited, it is still sufficient to permit the disturbance to overtake the front before its peak achieves pressures of the order of the detonation spike pressure. Thus, after overtake, growth at the front occurs.

5. CONCLUSIONS

In this paper we have attempted to correlate various types of shock growth modes observed in the initiation of homogeneous and heterogeneous explosives with the behavior of certain physical and chemical properties, namely, the critical acceleration λ and the reaction communication distance C/ω. Throughout our discussion, we have confined our attention to input pulse which were infinite in duration and square in shape.

In the case of the homogeneous explosive nitromethane, we found that at low amplitudes, $|\lambda|$ was

small and communication was good. This results in low amplitude waves growing slowly as square waves. The fact that the reaction rate, and hence λ, changed abruptly at higher pressures (temperatures) and the evidence of very limited communication in this pressure range provides an explanation for the occurrence of superdetonation. In the case of the heterogeneous explosive PBX-9404, we found that at low amplitudes, λ was less than that of nitromethane. This correctly suggests that at lower pressures PBX-9404 is more reactive and is more easily initiated due to hot spots. Nevertheless, $|\lambda|$ is still small enough that the communication is good; thus, square wave-type growth again occurs initially. At higher pressures, λ decreases relatively slowly indicating the presence of slower reaction kinetics than in NM. This, coupled with better communication than in high-temperature NM, resulted in the generation of a pressure disturbance which was spread out in time and overtook the front before the detonation pressure was achieved. It is only in cases of this nature, when the shock front becomes unsupported, that one can expect to observe growth at the front. Growth at the front has also been observed in the case of initially unsupported shocks by Dremin, *et al.* (25).

ACKNOWLEDGEMENTS

FOOTNOTES AND REFERENCES

1. The theory of chemically reacting, elastic materials has been considered by many authors. See, for example, J. von Neumann, Office of Scientific Research Dev. Rept. No. 549 (1942); B. D. Coleman and M. E. Gurtin, J. Chem Phys. 49, 1625 (1968).

2. Cf. R. Courant and K. O. Friedrichs, *Supersonic Flow and Shock Waves*, Interscience, New York (1948); and H. D. Grushka and F. Wecken, *Gasdynamic Theory of Detonation*, Gordon and Breach, New York (1971).

3. J. W. Nunziato, J. Chem. Phys. **58**, 961 (1973).

4. C. Truesdell and R. A. Toupin, "The Classical Field Theories," in Handbuch der Physik, Band III/1, Sect. C, Springer, Berlin (1960).

5. The shock amplitude eq. (13) has been derived using either particle velocity or specific volume as a measure of the amplitude. See, for example, M. Cowperthwaite, Stanford Research Institute Rept. GHU-5265 (1967); P. J. Chen and M. E. Gurtin, Phys. Fluids **14**, 1091 (1971); and Ref. (3).

6. J. E. Kennedy and J. W. Nunziato, J. Mech. Phys. Solids **24**, 107 (1976).

7. P. C. Lysne and D. R. Hardesty, J. Chem. Phys. **59**, 6512 (1973).

8. The value of the Hugoniot constants were: $\gamma = 0.01275$ GPa/K, $\delta = -0.00008$/K, $a = 0.4342$ cm^3/g, $\beta = -119.2$ K.

9. D. R. Hardesty, Comb. and Flame **27**, 229 (1976).

10. F. E. Walker and R. J. Wasley, Comb. and Flame **15**, 233 (1970).

11. M. Cowperthwaite and W. H. Zwisler, "TIGER Computer Program Documentation," Stanford Research Institute Rept. PYU-1281, 1974. The values of the constants used were: $R_g = 0.001376$ GPa-cm^3/K-g, b = 0.2467 cm^3/g, $\varphi = 2729$ K, $c_g = 0.002794$ GPa-cm^3/K-g.

12. D. R. Hardesty and P. C. Lysne, "Shock Initiation and Detonation Properties of Homogeneous Explosives," Sandia Laboratories Rept. SLA 74-0165, 1974, p. 71.

13. J. G. Berke, R. Shaw, D. Tegg, and L. B. Seely, *Proceedings of the Fifth Symposium (International) on Detonation*, Office of Naval Research, 1970, p. 237.

14. B. Hayes, *Proceedings of the Fourth Symposium (International) on Detonation*, Office of Naval Research, 1965, p. 595.

15. S. W. Benson and H. E. O'Neal, "Kinetic Data on Gas Phase Unimolecular Reactions," NSRDS-NBS 21, U. S. Govt. Printing Office (1970).

16. J. W. Nunziato, J. E. Kennedy, and D. E. Amos, Comb. and Flame (1977), forthcoming.

17. R. J. Lawrence and D. S. Mason, "WONDY IV ... A Computer Program for One-Dimensional Wave Propagation with Rezoning," Sandia Laboratories Rept. SC-RR-71-0284, 1971.

18. M. E. Kipp and A. L. Stevens, "Numerical Integration of a Spall-Damage, Viscoplastic Constitutive Model in a One-Dimensional Wave Propagation Code," Sandia Laboratories Rept. SAND 76-0061, 1976.

19. D. B. Hayes, private communication, 1974.

20. The method for treating these effects, especially those due to velocity dispersion, is discussed in J. R. Asay and L. M. Barker, J. Appl. Phys. **45**, 2540 (1974).

21. J. W. Enig, *Proceedings of the Third Symposium (International) on Detonation*, Office of Naval Research, 1960, p. 534.

22. B. G. Craig and E. F. Marshall, *Proceedings of the Fifth Symposium (International) on Detonation*, Office of Naval Research, 1970, p. 321.

23. J. E. Kennedy, *Proceedings of the Fourteenth Symposium (International) on Combustion*, The Combustion Institute, 1973, p. 1251.

24. B. M. Dobratz, "Properties of Chemical Explosives and Explosive Simulants," Lawrence Livermore Laboratory Rept. UCRL-51319, 1974.

25. A. N. Dremin, S. A. Koldunov, and K. K. Shvedov, Fizika Goreniya i Vzryva **1**, 103 (1971).

DISCUSSION

A. N. DREMIN
Institute of Chem. Physics
USSR Academy of Sciences
Chernogolovka, Moscow Region, USSR

The research of the kinetics of relaxation processes in shock waves is also being done at our Laboratory.[1] The investigation on the determination of TNT decomposition kinetics behind the shock wave front has been completed recently.[2] The technique of our investigation can be described as follows. TNT samples are subjected to a one-dimensional shock wave and a series of pressure profiles is then obtained by means of manganin gages located at different places within these samples. Based on these data, the dependence of the specific volume change on time for various coordinates of the sample is determined. This method, proposed earlier by our Laboratory in 1967,[3] as well as the method of two phase velocities,[4] uses the additivity principle. As shock compressibilities of TNT and its explosion products become known, one can take into account the time dependences of pressure and specific volume of an arbitrary sample and find the time rate of change of the explosion products concentration for that sample.

Figure 1 shows the pressure profiles for three experimental series. The shock waves with various pressures and times have been used during these experiments. Numbers along the lines represent the gage coordinates in mm. Figure 2 shows the kinetic curves obtained as the result of the experimental data reduction. The curves represent the mass change of the explosion products with time. The curves are labeled in accordance with Figure 1 indicating the series and gage location.

Some common characteristics about the kinetic curves are as follows: immediately behind the shock fronts, the decomposition rates are almost equal to zero; the rates increase with the extent of decomposition and when the pressure change is not too large, it reaches a maximum value in the neighborhood of 0.2-0.3. A sharp pressure decrease is responsible for the decomposition rate decrease.

The following formula represents the dependence of the decomposition rate on pressure:

$$\frac{d\alpha}{dt} = 3.9 \, (\alpha + 0.01)(1 - \alpha)^3 \, p_1 \left(1 - \frac{v_1}{v_0}\right) p \cdot 10^3 \, \text{sec}^{-1}$$

Here p is the pressure, p_1 and v_1/v_0 is the pressure and compressibility at the shock front, with the extent of decomposition up to $\alpha \approx 0.6$. The rates, calculated by the above formula, differ from the experimental data by not more than 30%.
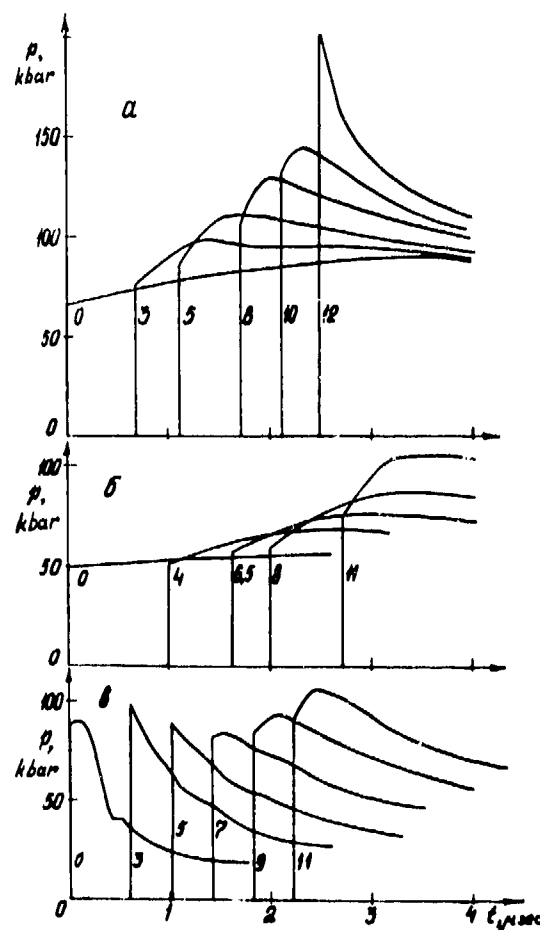
Fig. 1
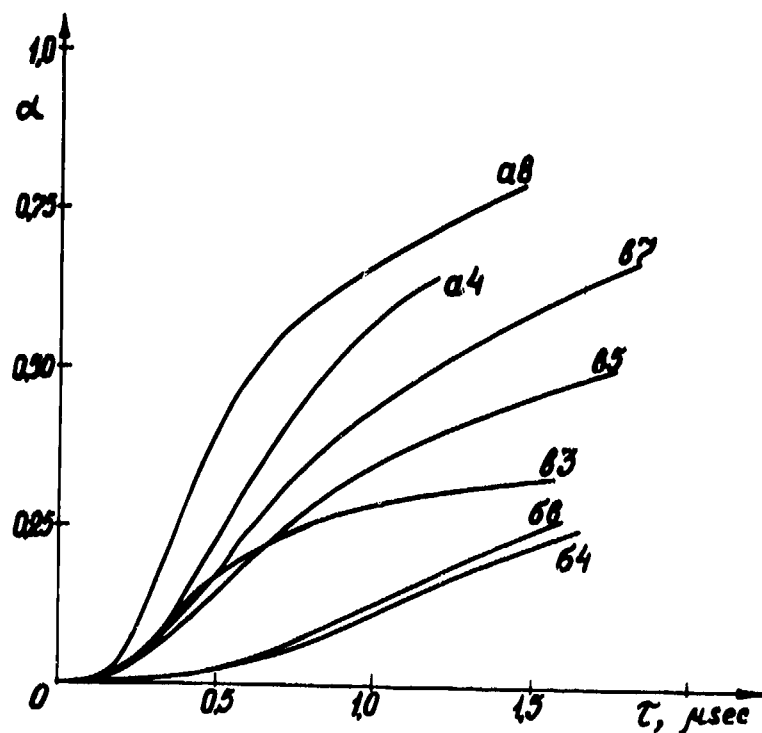
Fig. 2

REFERENCES

1. A. B. Ananin, A. N. Dremin, G. I. Kanel, Fizika Goreniya i Vzryva, 1973, N3, 437.

2. G. I. Kanel, A. N. Dremin, "Shock Wave Decomposition in Cast TNT" Fizika Goreniya i Vzryva. (to be published)

3. G. A. Adadurov, V. S. Trofimov, V. A. Yakovleva, Fizika Goremya i Vzryva, 1968, N3, 397.

4. M. Cowperthwaite, R. J. Williams, *J. Appl. Phys.*, 1971, **42**, N1, 456

GEOMETRICAL SHOCK FOCUSING AND FLYING PLATE
INITIATION OF SOLID EXPLOSIVES

J. Q. Searcy and A. C. Schwarz
Sandia Laboratories
Albuquerque, New Mexico 87115

Two dimensional hydrodynamic computer calculations suggest substantial en-hancement of shock temperature and pressure in a hexanitrostilbene (HNS) core if a flying plate overlaps a metal containment cylinder at impact. Experimental results on a similar geometry indicate a substantial reduction in flyer kinetic energy at the initiation threshold velocity for the overlap case. Shock interac-tions for this geometry are discussed, and guidelines are suggested for utilizing this effect.

In recent years, the desire for inherently safe initi-ators has led to experimentation with so-called "flying plate" or "slapper" detonators. In such de-vices the flyer is accelerated by hot gases generated from the reaction of a pyrotechnic material or the high pressure gases generated by vaporizing a metal foil with an electrical discharge. The explosive de-tonates if the flyer impinges with sufficient velocity. It has been previously suggested that "pressure aug-mentation" results if a metal flyer overlaps the ex-plosive column and housing (1). Recent experiments indicated a reduction in initiation stimulus when a small diameter detonating fuse was compared with large diameter detonating fuse. A shock focusing effect was postulated to explain these results. This effect, if understood and utilized, might lead to more reliable initiation in actual devices. This paper reports an experimental and computer investigation of this phenomenon. A more complete description of the computer study has been previously reported (2).

The computer results were obtained with a two dimensional wave propagation computer code CSQ (3) developed by S. L. Thompson. This code solves Lagrangian equations of motion, but continuously rezones the problem to the original mesh. Since the code was limited to two materials in any one prob-lem, the results presented here use the same metal

for the flyer plate and the containment cylinder. A porous material option was used to simulate the HE, and an elastic plastic option was used to simulate the metal. Known material properties for low density HNS and the metal containment cylinder were taken from several sources (4). Reasonable estimates were used for those parameters not in the referenced source. The results are strictly for hydrodynamic flow and chemical reaction and detonation were not allowed. All calculations were similar in that a per-fectly aligned, perfectly flat flyer impacted the end of a metal containment cylinder with an HE core with perfect contact between the HE core and con-tainment cylinder assumed.

The experimental technique used in this work has been explained in an earlier report (5), and only a cursory explanation will be given here. Figure 1 pre-sents the basic elements of this approach. A capaci-tor discharge exploded a foil bridge driving the Kapton flyer forward. The Kapton flyer was sheared by the barrel to the desired diameter, and the flyer continued down the barrel to impact the acceptor explosive. For a given geometry, the velocity of the flyer was controlled by the capacitor voltage. Streak camera records of the flyer were used to determine a velocity versus voltage curve. This experimental apparatus was carefully characterized and the error
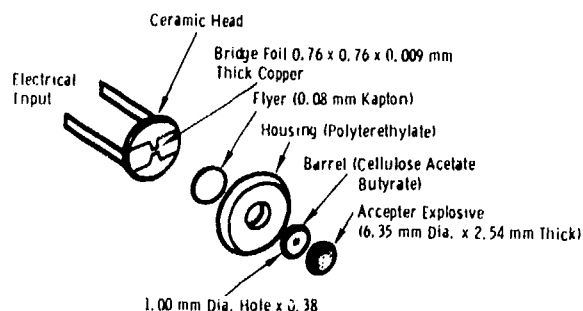
Fig. 1. Exploded view of the test device.

Fig. 2. Geometries investigated. Each grid dash represents 0.042 cm.

in flyer velocity for a capacitor voltage greater than 1000 volts was ±8 percent.

The computer calculations and the experimental results were not for identical situations. The computer calculations were limited to two materials, therefore the flyer had to be composed of either the explosive or the same metal as the confinement cylinder. The experiments used three materials. In the computer code the explosive was allowed no reactivity. The real case involved chemical reactivity during growth to detonation from impact.

The maximum shock enhancement should occur when the dimensions of the flyer and containment cylinder are so large that no rarefaction from any free surface can interfere. With that in mind, the geometry in Fig. 2a was chosen for calculations. For comparison, the calculation was also performed with a flyer that can not give shock enhancement as illustrated in Fig. 2b. The HNS diameter is 0.78 mm and the flyer velocity in both calculations was the same. The outer diameter of the metal sleeve is 4.0 mm.

Figures 3 and 4 give two dimensional displays of pressure and temperature as a function of time for a flyer velocity of 0.1 mm/μsec. These calculated results are for the same geometry as 2a but with appropriate changes in scale so that only the portion of the problem shown in the unnumbered frame is displayed. The scale factors relating dots per unit area to temperature, or dots per unit area to pressure are held constant throughout this report. Darkest areas on the numbered frames (i.e., most dots per unit area) indicate greatest intensity. The frames on each figure throughout this paper are given at the same time increments of 3×10^{-8} seconds with the first frame taken at 2×10^{-8} seconds after the collision. The approximate position of the HE-metal
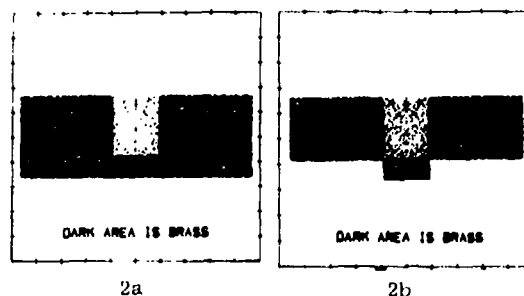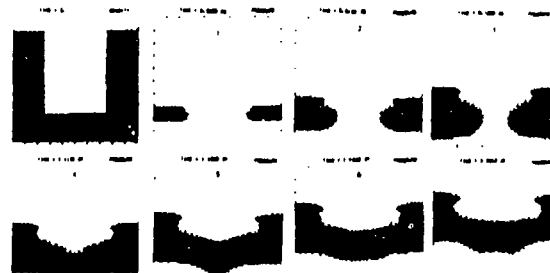
Fig. 3. Pressure dot plots for geometry 2.A. Each grid dash represents 0.0156 cm.
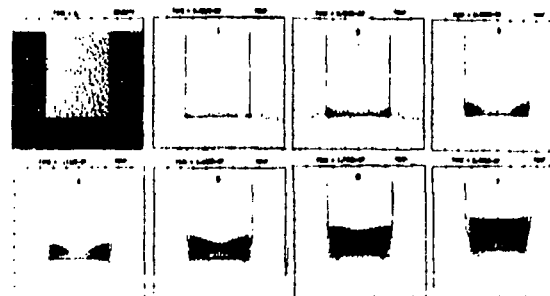
Fig. 4. Temperature dot plots for geometry 2.A. Each grid dash represents 0.0156 cm.

interface is outlined on all frames as a continuous dark line.

An examination of Figures 3 and 4 suggests substantial temperature and pressure enhancement. A shock moves radially into the HNS from the surrounding brass and coalesces to form a strong planar shock. On the other hand, the shock structure calculated for geometry 2. B (not illustrated here) is basically

a straight-forward one-dimensional flow with small perturbations and with a magnitude that is the same as the lighter center area in Fig. 3 and 4. The absolute magnitude of this shock pressure enhancement is illustrated on Fig. 5. This figure gives pressure as a function of position along a cylindrical surface illustrated on the geometry frame as two straight vertical lines in the HE. The bottom of the geometry frame corresponds to zero on the abscissa of the other frames.

The shock interactions for the large flyer can be explained qualitatively if certain fundamental principles of shock wave behavior are considered. At the instant of impact, pressures are generated at the interface that can easily be determined by crossing right-going and left-going Hugoniots on a pressure-particle velocity graph. There is one pressure for the metal-metal impact, and another considerably smaller pressure for the metal-HE impact. A plane shock wave begins propagating away from the impact surface in both directions. A second pressure discontinuity is simultaneously created along the

circle formed by the HE-brass cylinder interface on the impact plane, and a disturbance is propagated away from the circle. But this time it is not planar.

If for the purpose of illustration we consider the shock velocity in the HE and brass as identical and constant, and if we consider a plane through the axis of the cylinder, the disturbance propagates in that plane as illustrated in Fig. 6. In addition to the plane waves propagating away from the impact plane, a second radial disturbance is propagated away from the points of intersection of the different materials on the impact plane. In the brass containment cylinder this disturbance is a rarefaction, but in the HE it is a compression wave. In the flyer it is a rarefaction for that part of the flyer overlapping the container, and it is a shock wave in that part of the flyer that impacts the HE. Figure 6 suggests geometrical attenuation of the radial disturbance. However, the real system is not planar, but cylindrically symmetrical. The three dimensional disturbance is in fact propagated as a toroid (doughnut shape) with a constant major radius and an ever
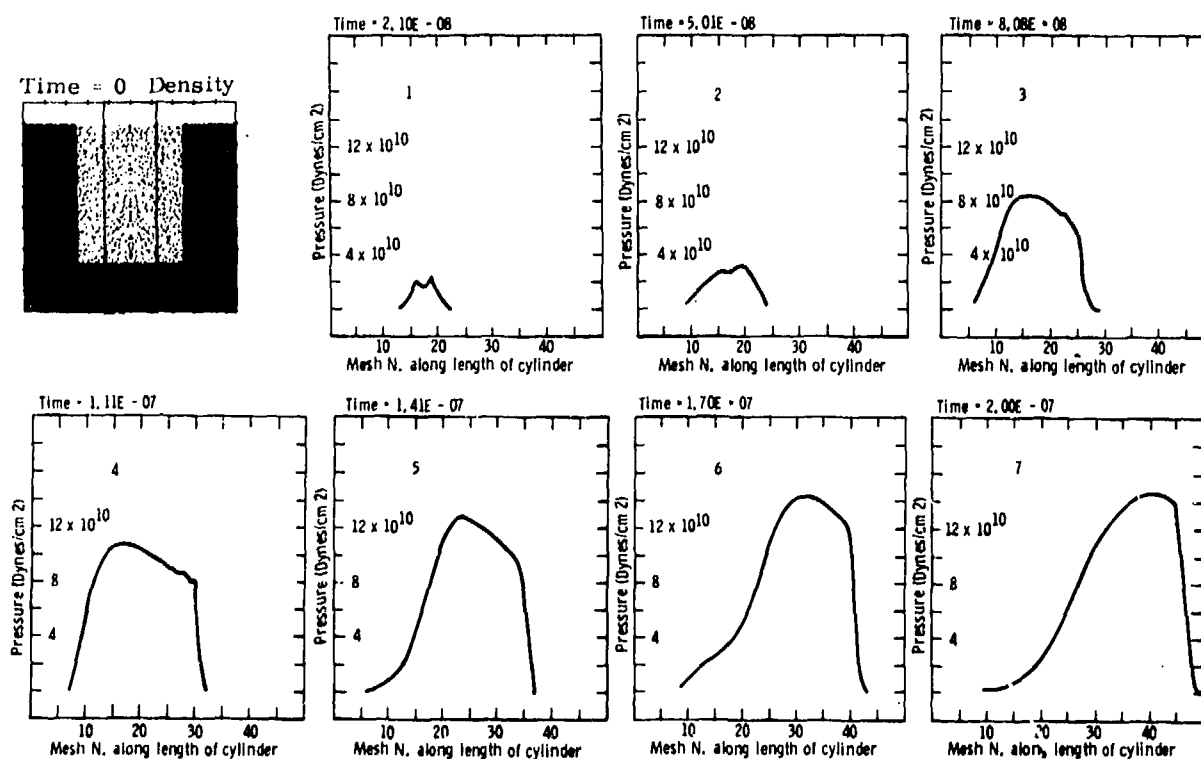
Fig. 5. Pressure versus mesh number for geometry 1.A. The position of the cylindrical surface for these plots is indicated on the unnumbered frame as two straight lines. Each vertical dash represents 0.010 cm.
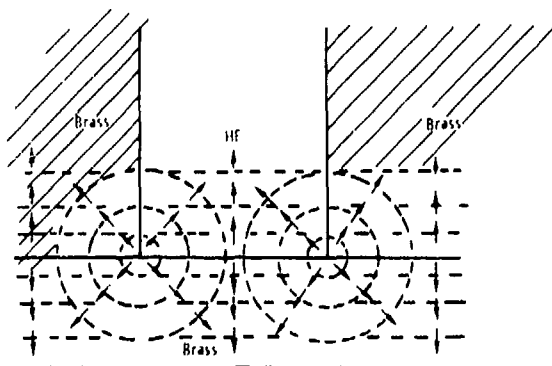
Fig. 6. Idealized shock structure.

increasing minor radius. A second geometrical relationship for the magnitude of the torous is suggested by this symmetry, and geometric convergence occurs in some region near the axis of cylindrical symmetry. Even if we could shift Hugoniots around on a pressure vs. particle velocity graph and determine the initial magnitude of the disturbance, and even if the grossly simplified picture on Fig. 6 were correct, the magnitude of the disturbance would be some as yet undetermined function of geometrical parameters.

This simple approach has been discussed for explanatory purposes only. The real system has several complications. In most real systems the disturbance moves faster in the surrounding metal than in the HE. With each increment that the metal disturbance moves ahead of the HE disturbance, a new discontinuity is formed at the interface of the two materials along the length of the cylinder. Each new discontinuity is relieved by sending rarefactions into the metal and shocks into the HE. The circular front as shown in Fig. 6 is elongated in the HE near the HE-brass interface, and truncated in the brass interface, and truncated in the brass. There is some flow from the plane wave in the metal back toward the HE that tends to increase the pressure in the brass near the HE, but this is a small effect in the overall picture. Except for the elongation of the toroidal front along the metal interface, there is no evidence from these calculations that the faster shock velocity in the metal increases the pressure in the HE significantly. This elongation does add some to the toroidal pressure disturbance in the HE, but the total added does not seem to be very substantial since the toroidal

disturbance is rapidly attenuated by the porous HE. Based on these observations there does not seem to be a good reason for necessarily choosing a metal with a very high shock velocity as the containment cylinder.

The high velocities for the larger amplitude shocks also distort the circle in Fig. 6. The circular disturbance is a larger amplitude shock in the HE than is the plane shock, and it moves ahead of the plane wave. It also adds to the plane wave giving a larger amplitude shock. A shock in an already crushed material (pre-shocked material) moves faster than the same amplitude shock would move in a distended material. All these effects combine to produce further, not easily predicted, distortions in the pressure front.

An unusual effect is caused by the porous nature of the HE. The highest temperature does not necessarily correspond to the highest pressure. The disturbance propagating horizontally inwards in Fig. 6 is moving through already crushed HE, and does not raise the temperature as much as if the same disturbance were moving through distended material. The highest pressure occurs along the axis of cylindrical symmetry, but the highest temperature occurs in front of the position where the plane wave would normally be. The maximum temperature is achieved at the point where the intersection of the converging circular disturbance overtakes the plane wave along the axis of symmetry in the HE. A comparison of Figs. 3 and 4 illustrates this. Because probably it is temperature that initiates chemical reaction, the most likely position for detonation is along the toroidal disturbance after its intersection overtakes the plane wave. Detonation would most likely be initiated where the darkest areas of Fig. 4 are maintained for the longest time period.

If the flyer is too thin, its diameter too small, or if the diameter of the confinement cylinder is too small, rarefactions from a free surface can get back to the HE quickly and seriously attenuate the focusing effect. Because rarefactions move considerably faster in crushed HE than do shocks in distended HE, rarefactions can completely attenuate the toroidal disturbance before it coalesces. Different geometries have been investigated in this study that clearly illustrate this, although the results are not presented here. On the other hand, any overlap at all adds something to the planar shock.

Experimental data consisted of the threshold velocity for initiation for two geometry series: Geometrical variation was accomplished by changing the receptor geometry and always using a Kapton flyer 1 mm in diameter and 0.076 mm thick. One geometry series used receptors consisting of aluminum cylinders with an outside diameter of 6.3 mm and containing a core of superfine hexanitrostilbene (HNS-SF) at several diameters. The second geometry series was aluminum sheathed mild detonating fuse containing HNS-II. All HNS was held at a density of 1.60 Mg/M^3. For reference free standing pellets of HNS-SF and HNS-II were tested. Data for each geometry is presented on Tables 1 and 2. Following the Walker-Wasley approach (5) a $P_0^2 \tau_0$ threshold was determined for the free standing pellets. Pressure and time are indicated by P and τ, respectively. An apparent $P^2 \tau$ for each geometry was calculated using only the one-dimensional shock parameters obtained by crossing pressure vs. particle-velocity Hugoniots at the threshold velocity. The ratio of the apparent $P^2 \tau$ divided by $P_0^2 \tau_0$ is also given on the two tables. Fig. 7 gives a plot of $P^2 \tau / P_0^2 \tau_0$ versus (flyer diameter)/ (explosive diameter).

If the experimental configuration could be computer modeled, a general trend similar to that shown in Fig. 7 as a dotted line would result. The computer code would predict no change in $P^2 \tau$ until the flyer overlapped the metal confinement cylinder. For larger and larger overlap, the apparent $P^2 \tau$ would decrease sharply until the overlap exceeded twice the thickness of the flyer. For this 0.076 mm thick by 1 mm diameter flyer this would occur at a ratio of

TABLE 1

Data for HNS-SF Core Pressed into an Aluminum Cylinder

OD, ED, FD, and FV represent aluminum cylinder diameter, explosive diameter, flyer diameter, and flyer velocity, respectively.

OD/ED	FD/ED	FV cm/μs	$P^2 \tau / P_0^2 \tau$
-/0.63	0.16	0.246	1.0
0.63/0.31	0.32	0.252	1.05
0.63/0.16	0.64	0.274	0.87
0.63/0.08	1.28	0.221	0.76

TABLE 2

Data for HNS-II Mild Detonating Fuse

Symbolism is identical to Table 1

OD/ED	FD/ED	FV cm/μs	$P^2 \tau / P_0^2 \tau$
-/0.63	0.16	0.274	1.0
0.28/0.12	0.68	0.236	0.68
0.20/0.089	1.14	0.238	0.70
0.12/0.056	1.90	0.218	0.57
0.881/0.036	3.08	0.198	0.44
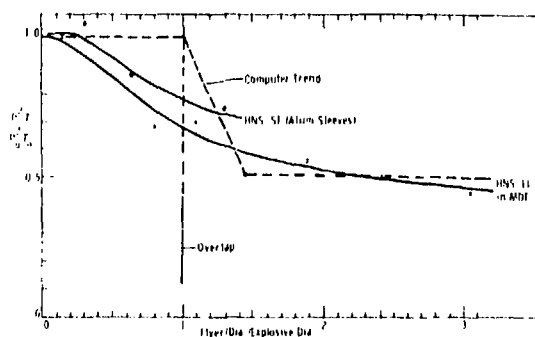
Fig. 7. Reduction in flyer energy fluence required at threshold vs overlap (flyer dia./explosive dia.).

about 1.44 in Fig. 7. At overlap ratios greater than this, rarefactions moving in from the back side of the flyer substantially attenuate the shock in the HE before rarefactions from the flyer perimeter get to the explosive. At smaller ratios, rarefactions from the perimeter are the primary attenuation mechanisms. The apparent discrepancy between the computer suggested trend and the experimental observations is no doubt real. The computer ignores effects such as minimum critical diameter and any enhanced reactivity due to extra confinement.

It should be pointed out that the computer code predicts a substantially greater shock focusing effect if the flyer is metallic. Calculations have been done using the explosive material as a flyer in order to approximate the experimental arrangement. These calculations predict a pressure and temperature enhancement, but much less than that shown in Fig. 2, 3, and 4. If our experiments had been conducted

using an aluminum flyer, we would expect a much more dramatic effect than shown in Fig. 7 or the Kapton flyer.

Figure 7 clearly indicates that the flyer has a lower kinetic energy at the initiation threshold for the overlap cases. Since the same flyer is used throughout, a lower value of $P^2\tau/P_0^2\tau_0$ indicates less kinetic energy. This suggests that the over-all reliability of a flying plate device can be improved by utilizing shock focusing. The degree of improvement depends on the materials.

Calculations were made with a number of materials including a high shock impedance flyer (gold), a low shock impedance flyer (the aluminum). While the calculations were too expensive and time consuming to do complete parameter studies, certain guidelines can be suggested for making good use of the shock amplitude in the HE and the containment cylinder at the instant of impact. This simple guideline requires consideration of the flyer velocity and subsequently the flyer mass. In most cases the best choice for the flyer material would be a low density metal such as aluminum or beryllium. The containment cylinder usually would be a high shock impedance material. The maximum possible shock focusing effect would occur in an infinitely large flyer and containment cylinder. On the other hand, most of the possible shock enhancement can be utilized if the following geometrical restrictions are observed. The minimum flyer thickness should be chosen so that twice the shock transit time through the flyer is at least as great as the shock transit time through a length of explosive equal to the radius of the HE column. The radius of the flyer should exceed the radius of the HE column by twice the minimum flyer thickness, and the diameter of the containment cylinder should not be less than the diameter of the flyer. Any dimension can be greater than that suggested by these guidelines, but additional shock focusing is not very substantial with increased dimensions.

REFERENCES

1. R. H. Stresau and D. H. Chamberlain; private communication, 1972.

2. J. O. Searcy, "Geometrical Shock Focusing in the Flying Plate Detonator Configuration, SAND76-0151, March 1976.

3. S. L. Thompson, "CSQ–A Two Dimensional Hydrodynamic Program With Energy Flow and Material Strength," SAND74-0122, August 1975.

4. a. B. M. Dobratz, "Properties of Chemical Explosives and Explosives and Explosive Simulants." revised edition *UCRL-51319 (1974).

   b. Selected Hugniots by Group GMX-6, Los Alamos Scientific Laboratory, 1969.

   c. S. L. Thompson and H. S. Lauson, "Improvements in Chart D Radiation-Hydrodynamic Dode III: Revised Analytic Equations of State," SC-RR-71 0714 (1974).

5. A. C. Schwarz, "A New Technique for Characterizing an Explosive for Shock Initiation Sensitivity, SAND75-0314, December 1975.

CRITICAL CONDITIONS FOR SHOCK INITIATION OF DETONATION IN REAL SYSTEMS

R. H. Stresau
R. Stresau Laboratory
Spooner, Wisconsin

and

J. E. Kennedy
Sandia Laboratories
Albuquerque, New Mexico

An heuristic model of the shock initiation of heterogeneous explosives is described. To initiate detonation, we hypothesize that a shock must exceed some minimum intensity required to obtain thermal ignition at hot spots and to offset heat transfer losses. Thus, shock strength is the parameter controlling initiation when the pulse duration is long, but shock energy fluence, or a related quantity, controls when the pulse duration is short. From this approach we develop alternative forms of initiation criteria which are hyperbolic in shock energy-shock power coordinates. This model is compared with existing criteria for the one explosive, PBX-9404, for which an adequate data base exists.

INTRODUCTION

The shock initiation process in granular explosive charges of limited dimensions is considered here in terms of reaction kinetics, hydrodynamics, thermodynamics, and heat transfer. It is assumed that the threshold conditions for initiation in such systems are those for equilibrium between energy liberated by the reaction and that lost from the "reaction nucleus," the region so affected by an external stimulus as to react at a significant rate. The following heuristic model of the reaction nucleus seems to apply to a wide range of situations of practical as well as theoretical interest.

From a macroscopic viewpoint, the reaction nucleus may be considered to be that region bounded at the front by the shock jump induced by the initiating stimulus, at the rear by a surface of the following rarefaction wave and at the edges by the peripheral boundaries of the shock wave or the explosive charges. Energy is lost through all boundaries except the shock front. Considered microscopically, the reaction nucleus is only that part (the "hot spots") of this region in which the temperature has been raised sufficiently to result in self-sustaining reaction before the pressure drops due to the encroaching rarefaction waves or the hot-spot temperature is reduced by conductive redistribution of the heat.

As has been pointed out by many investigators (1-3), the concentration of energy in hot spots is essential to initiation of detonation of porous explosives under threshold conditions. The total shock energy density under threshold conditions for initiation of many explosives, if uniformly distributed in the form of heat, would be sufficient to raise the temperature only a few degrees. A number

of mechanisms, including compression of interstitial gases, friction between grains and at shear surface, impact between particles, and viscous friction within deforming grains, contribute to a greater or lesser extent to the nonuniformity of temperature in a shocked porous medium.

It does not appear to be possible at present to construct a rigorous and detailed model of the distribution of hot spots and their individual responses to shock loading. The initiation criteria which are currently most useful in a quantitative sense are macroscopic in nature. We believe that a major advance in the understanding of initiation of heterogeneous explosives will require a reasonable treatment of the propagation of reaction from the hot spots into the surrounding heterogeneous explosive, such that the reaction may be shown to decay or to accelerate to detonation. Our objective in this paper is less ambitious; it is to examine the macroscopic consequences of certain types of microscopic behavior.

In this paper we discuss certain mechanisms of hot spot formation in solid explosives and relate them to the shock parameters of pressure and particle velocity. We then propose several alternative initiation criteria based on the idea that some minimum stimulus is necessary to begin the processes that eventually lead to detonation. A comparison of one of these proposed relations with experimental data and with existing initiation criteria provides encouragement for further study of minimum-stimulus initiation criteria.

MECHANISMS OF HOT SPOT FORMATION

Shock pressure was viewed as the controlling parameter in the shock initiation of detonation some years ago. However, Gittings (4), Trott and Jung (5), and recently de Longueville (6) have clearly shown the shock initiation threshold for solid explosives to be dependent on both the shock pressure, P, and duration, τ. Data from a variety of sources suggest that the threshold conditions for shock initiation can be expressed by the equation (7, 8)

$$P^2\tau = \text{constant} . \qquad (1)$$

Walker and Wasley (7) used such information in 1969 to develop their concept of a critical energy fluence,

$$E_c = \frac{P^2\tau}{\rho_0 U} = Pu\tau = \text{constant} , \qquad (2)$$

where U is the shock velocity and ρ_0 is the initial density, as an initiation criterion.

Macroscopic models, such as Walker and Wasley's concept of critical energy fluence and Pastine, Bernecker and Bauer's (9) concept of critical thermal energy, do not explicitly address the point that the concentration of the energy in hot spots is essential to initiation, nor its consequence, that the temperature of the hot spot plays a significant role in the initiation process. It seems that the distribution, rather than the density, of the thermal energy should be expected to be decisive in the initiation process. To relate the temperature of the hot spots to the shock-wave parameters, it is necessary to consider the mechanisms of hot-spot formation.

Seely (3) has postulated the following mechanism of hot-spot formation:

As a shock wave propagates through a granular explosive, ". . . the shocks are randomly oriented within the grains. On leaving the grain surfaces, the shocks cause material to move off, and because the surfaces are randomly oriented to each other, this material interacts in various ways, producing jets in some cases. The projected material, which apparently must be broken up and must act hydrodynamically rather than as particles, collides with the surface directly ahead. ... the jetted material stagnates ..."

Although, as Seely points out, "the actual conditions are difficult to calculate," stagnation temperature, in general, is proportional to the square of the velocity of the flow which is stagnating. The mean effective jet velocity should be proportional to the particle velocity change at the shock front, thus the hot-spot temperature rise, T_s, can be expected to be proportional to the square of the particle velocity u immediately behind the shock front:

$$T_s = Zu^2 . \qquad (3)$$

Other suggested mechanisms of hot spot formation, such as collision of the walls of implosively collapsing pores, also result in the relationship expressed in Eq. (3). The notion that the particle velocity plays a decisive role in the determination of critical conditions for shock initiation is supported by data given by Roth (10). He showed that the critical particle velocity u_c immediately behind the shock

front was nearly independent of loading density for each of four high explosives. Examination of the small-scale gap-test data given by Bauer (11) in support of the concept of a critical thermal energy, E_T, reveals that u_c varies as little as E_T for a given explosive pressed to various densities.

Another mechanism for the concentration of energy in hot spots, proposed by Taylor (12), is the plastic work done upon the explosive surrounding the pores as the pores implosively collapse behind the shock front. Taylor derived Eq. (1) by using this assumption together with established elastic, rheological thermodynamic, and reaction kinetic relationships.

MINIMUM STIMULUS INTENSITY FOR INITIATION

A number of workers in explosive initiation believe, on the basis of intuition or empirical evidence, that some minimum shock amplitude must be exceeded before reaction can be ignited with sufficient vigor to grow to detonation. Napadensky (13) conducted probably the largest well-characterized experiments in which shock initiation occurred at minimum shock inputs. In experiments in which a large steel plate impacted a 76-mm diameter cylinder of unconfined PBX-9404, she found that the minimum impact velocity for attainment of shock initiation during the first pass of the wave was independent of the impactor thickness. That minimum impact velocity was 0.18 km/s, which drove a wave with $P \cong 0.94$ GPa, $u = 0.16$ km/s into the PBX-9404, and detonation was observed after 10-26 μs in three separate experiments.

In the same sense that $Pu\tau$ is an expression of energy, Pu is an expression of power. If it is accepted that a minimum shock pressure, P_m, is necessary for initiation, the power, $P_m u_m = \pi_m$, associated with this minimum can be assumed to be that necessary to replace the losses which make this minimum shock strength necessary. The rate at which energy accumulates in the reaction nucleus is thus given by

$$\frac{dE}{dt} = Pu - \pi_m ,$$ (4)

which, for a square input pulse of duration τ, integrates to

$$E'_c = (Pu - \pi_m)\tau .$$ (5)

By analogy, Eq. (1) becomes:

$$(P^2 - P_m^2)\tau = \text{constant} .$$ (6)

Each of the mechanisms we have discussed for the concentration of energy at hot spots involves relative movement with respect to the macrostructure of material adjacent to interstitial pores. That relative movement is probably related to the excess of stress (or strain) beyond the failure or yield point. For pressed powders this point must be related to the pressure used in consolidation, which may be several kilobars. The equation derived by Taylor (12) for the thermal energy, W_p, deposited as a result of plastic deformation of the explosive surrounding a pore is

$$W_p = \frac{9}{32\eta} (P - Y)^2 \tau , P > Y ,$$ (7)

where η is an effective coefficient of viscosity and Y is the pressure at which pore collapse begins. Taylor suggested that the sensitivity of such explosives can be characterized in terms of a critical value of W_p. In Eq. (2), this yield point can be taken into account in an equation of the form

$$E''_c = \frac{(P-Y)^2 \tau}{\rho_0 U} .$$ (8)

In terms of the heuristic model which has been described herein, the shock initiation process requires the formation of hot spots and subsequent reaction at a rate sufficient to maintain them. The formation of hot spots requires stresses beyond the yield point and their maintenance requires a minimum rate of energy input. Thus, Eqs. (5) and (8) should be combined as

$$E'''_c = \left(\frac{(P-Y)^2}{\rho_0 U} - \pi_m\right) \tau .$$ (9)

While discussing effects of the mechanical strength of an explosive charge on initiation processes, we should point out that the hot-spot temperature is also affected. If we denote by u_y the particle velocity associated with elastic deformation of the explosive matrix, only the velocity difference $(u - u_y)$ contributes significantly to the movement into the pores, so Eq. (3) becomes

70

$$T_s = Z(u - u_y)^2 , \qquad (10)$$

where

$$u_y = Y/\rho_o c \qquad (11)$$

and c is the longitudinal sound speed of the explosive.

INITIATION CRITERIA BASED ON PARTICLE VELOCITY

The only difference between the $P^2\tau$ criterion and critical energy fluence, $P^2\tau/\rho_o U$, is the shock impedance terms in the denominator of the energy fluence expression. Shock impedance varies rather slowly, and initiation threshold data usually are not sufficiently extensive or accurate to distinguish which of these forms more closely describes the data in the regions where both provide good correlations with observations. We would like to consider a criterion of the basic form $u^2\tau$, which corresponds to $P^2\tau/\rho_0^2 U^2$ and also to $T_s\tau/Z$.

One may postulate forms corresponding to the pressure criteria which are written instead in terms of particle velocity, and which fit the data equally well. By analogy to Eq. (6) we may write

$$(u^2 - u_m^2)\tau = \text{constant} , u > u_m , \qquad (12)$$

where u_m refers to the minimum value of the particle velocity *jump* behind which the reaction can grow with sufficient vigor to lead to detonation. Alternatively, by analogy to the Taylor argument (12), but in the context of pore closo as mentioned in connection with Eq. (10), we may postulate

$$(u - u_y)^2\tau = \text{constant} , u > u_y , \qquad (13)$$

where u_y represents the yield point value of the particle velocity as given by Eq. (11). Probably $u_m > u_y$.

Both of the expressions above have the following desirable characteristics:

(1) At relatively high shock strengths such that $u \gg u_m$ and $u \gg u_y$, the criteria reduce to $u^2\tau \approx$ constant.

(2) The presence of the u_m and u_y terms provide that the shock must exceed a certain amplitude before initiation will occur, as discussed above.

(3) u^2 terms represent specific kinetic energies which can become concentrated in pores and create hot spots upon flow stagnation.

(4) Based on Roth's (10) and Bauer's (11) observations discussed previously, a particle-velocity jump criterion has a chance to describe the initiation threshold of a given explosive over a range of loading densities, which pressure criteria cannot do.

Indeed, it might be necessary for the shock pulse to exceed both the yield condition and the minimum power level discussed in connection with Eq. (4). If the quantity u_y were subtracted from both u and u_m in Eq. (12) to account for the yield or failure condition, the criterion would become

$$[(u - u_y)^2 - (u_m - u_y)^2]\tau = \text{constant}, \\ u > u_m > u_y . \qquad (14)$$

Further, if we assume, following de Longueville, *et al.* (14), that the hot-spot temperature T_s determines the time required for a thermal explosion, which will develop into detonation, to occur, the expression for the critical pulse duration τ_c (15) can be written as

$$\tau_c = \frac{c_v T_s^2}{AQT_a} \exp\!\left(\frac{T_a}{T_s}\right), \qquad (15)$$

where A and $T_a = E_a/R$ are the Arrhenius frequency factor and activation temperature, respectively (E_a is the activation energy), c_v is specific heat at constant volume and Q is the energy of reaction. With T_s expressed according to Eq. (10), Eq. (15) becomes

$$\tau_v = \frac{c_v Z^2}{AQT_a} (u - u_y)^4 \exp[T_a/Z(u - u_y)^2] . \quad (16)$$

Application of this relation requires kinetic data on the explosive material as well as knowledge of the coupling factor Z which relates kinetic energy to hot-spot temperature. Thus, while we are not ready to test Eq (16) as an initiation criterion, some data are available which permit examination of Eqs. (5), (6), (9), (12), (13) and (14).

With algebraic manipulation, Eq. (5) can be shown to be that of an hyperbola in coordinates of energy fluence E (where E = Puτ) and power flux π (where π

71

= Pu), with asymptotes of E'_c and π_m. The hyperbola can be readily recognized when Eq. (5), is rewritten as

$$(E - E'_c)(\pi - \pi_m) = E'_c\pi_m \ . \tag{17}$$

Similarly, Eq. (6) is an hyperbola in coordinates of $P^2\tau$ and P^2, Eqs. (7), (8), (10), and (12) are also hyperbolas in appropriate coordinate systems and Eq. (9) and (14) are those of generally hyperbolic curves (although proof that they are hyperbolas as strictly defined is not immediately obvious). This hyperbolic relationship between the magnitude of a critical stimulus for initiation, defined as the time integral of a rate, and that of the rate is a consequence of the assumption that the threshold conditions for initiation are those for equilibrium between energy liberated by the reaction and that lost by dissipative processes. Observations which have been made of the wide applicability of such relationships to explosive initiation phenomena (16-19) may be taken as empirical justification for this view.

COMPARISON OF INITIATION CRITERIA WITH DATA

The minimum-stimulus criteria proposed above exhibit asymptotic behavior. As the pulse duration is extended indefinitely, the required value of pressure,

power or particle velocity approaches its minimum value Y, π_m, u_m or u_y, respectively. As the shock pressure is increased, the effect of the minimum stimulus is reduced and the criteria more closely approach the critical energy fluence form, in the case of Eqs. (5) and (9), and $P^2\tau$ and $u^2\tau$ forms in the other cases. Thus, the critical energy would be expected to be least at high shock pressures and to increase as the pressure is decreased. Such behavior has been observed by de Longueville *et al.* (14) for homogeneous and some heterogeneous explosives.

In the preceding discussion, the shock parameters u and P have been treated as single-valued quantities rather than as functions of time, as they might be in real systems. The criteria may be adapted to more general input pulses, but this is not done here in the interest of brevity. In seeking to compare the behavior of various existing and proposed criteria with that of data defining the initiation threshold, we found that the only data with well-characterized loading histories are for step input pulses. Close examination of available data revealed that the widest range of useful information on initiation of detonation existed for the heterogeneous explosive PBX-9404 (20).

Table 1 contains the PBX-9404 data base which we considered for purposes of comparing the various ini-

TABLE 1

Initiation Parameters Near Detonation Threshold for 1.84 Mg/m^3 PBX-9404

(Y = 0.1 GPa, I_m = 0.7 GPa)

F (GPa)	τ (μs)	$P^2\tau$ (GPa^2 - μs)	Puτ (kPa-m)	$[(u-u_y)^2-(u_m-u_y)^2]\tau$ (10^{-6}km^2/s)	Response	Ref.
12.2	0.035	5.21	569.	598.	Threshold	(4)
10.8	0.048	5.60	635.	690.	Threshold	(4)
10.2	0.042	4.37	504.	556.	Threshold	(4)
9.0	0.065	5.26	630.	718.	Threshold	(4)
8.1	0.075	4.79	596.	695.	Go	(22)
8.0	0.090	5.76	713.	836.	Threshold	(5)
7.4	0.088	4.82	609.	727.	Threshold	(4)
4.5	0.139	2.81	404.	526.	Go	(22)
3.7	0.28	3.83	572.	760.	Go	(23)
0.61	10.	3.72	700.	< 0.	No Go	(13)

tiation criteria. The data marked "threshold" are conditions intermediate between a closely spaced pair of "go" and "no go" experiments. The other conditions are considered to be marginal "go" or "no go" results. Certain data have not been used because the sample thickness was too small to determine threshold conditions, e.g., in Liddiard's underwater tests (21) which led to a burning reaction, the samples were not thick enough to run to detonation. Trott and Jung's data (5) below 8 GPa were also rejected. Their values of the threshold pulse duration were much larger than those of Green et al. (22) and Kennedy and Nunziato (23) in the region of 3-5 GPa, apparently for the same reason.

We were unable to use long-duration loading information in any way which would permit consistent estimates of the pulse duration required for threshold initiation. Thus a datum point by Napadensky (13) indicating shock initiation of detonation with a sustained input of 0.94 GPa was used, together with her 0.61 GPa result (which we called a "no go" because detonation occurred only after wave reflections and crushup of the explosive) only to estimate that the minimum pressure P_m for shock initiation of PBX-9404 is ~ 0.7 GPa. We estimated that the yield strength is equal to the pressure used in compacting the pressing, 0.1 GPa.

In Table 1, we have included two existing criteria, $P^2\tau$ and $Pu\tau$ (7) and one of the minimum-stimulus criteria. We chose to use the form in Eq. (14), $[(u - u_y)^2 - (u_m - u_y)^2]\tau$, because it is the most general particle-velocity criterion we have proposed. In comparing the representation of threshold data by the criteria, we note that the relative spread between maximum and minimum values is slightly less for $[(u - u_y)^2 - (u_m - u_y)^2]\tau$ than for $P^2\tau$ of $Pu\tau$. But the most interesting point is that use of the minimum stimulus of $P_m = 0.7$ GPa causes a well-defined prediction of failure for the 0.61 GPa experiment, while failure cannot be predicted from the $P^2\tau$ or $Pu\tau$ values for that experiment.

We do not claim that this comparison shows that $[(u - u_y)^2 - (u_m - u_y)^2]\tau$ is a better initiation criterion than critical energy fluence or $P^2\tau$ for PBX-9404 or other explosives. It appears that $[(u - u_y)^2 - (u_m - u_y)^2]\tau$ and the other forms of minimum-stimulus criteria can do essentially as well as the existing criteria, and thus are worthy of further study. The minimum stimulus criteria, even if physically well well-founded, will be of practical value only if a rather general method can be found for evaluation of the yield parameters and minimum power for initiation.

CONCLUDING REMARKS

The real value of minimum-stimulus initiation criteria may lie in their close ties with physical models of the processes which control reaction development. The work of Howe et al. (24) points to ignition at hot spots followed by grain burning as the dominant energy-releasing mechanism in the shock buildup to detonation. Analysis of ignition might be done by balancing heat transfer losses against reaction energy, and buildup can be considered as an interplay between cooling due to the release wave and heat conduction into grains and adiabatic self-heating due to surface burning. These processes involve certain physical properties—the porosity, particle size (specific surface), and the explosive's mechanical strength, which is related to the compaction pressure—and chemical properties, e.g. the burning rate law and amount of gas generation per unit of reaction.

Some comprehensible reversals in behavior patterns results from these interactions. It is well known that fine-particle powders are often harder to ignite than coarse powders, but reactions in fine powders grow to detonation more rapidly once ignited. The fine powders thus may have a higher value of P_m because of their high compaction pressure, which must be exceeded, and high energy losses into the particle surfaces. But they can have a lower value of E_c. TNT pressed to 1.55 Mg/m^3 showed such behavior in work by Taylor and Ervin (25). This behavior is also exhibited in Fig. 1 using data from gap tests of various charge diameters, hence various pulse duration, generated by the Stresau Laboratory (26, 27) for PBXN-5 of both fine and coarse granulations. These interchanges are directly related to the parameters of the minimum-stimulus criteria.

We are presently developing a data base on initiation of pressed explosives by arbitrary shock pulses through computer studies of gap tests of various types, and plan to use these data to test the applicability of the various forms of these criteria.

73

Fig. 1. Crossover in sensitivity to gap-test peak shock pressure P_o for 1.80 Mg/m^3 PBXN-5 (HMX/Viton A, 95/5 by weight) of two particle size distributions. Here τ denotes the computed time for pressure to decay to P_o/e. The curves suggest that P_m is smaller for coarse than for fine powder (at large τ), but E_c is smaller for fine than for coarse powder (at small τ).
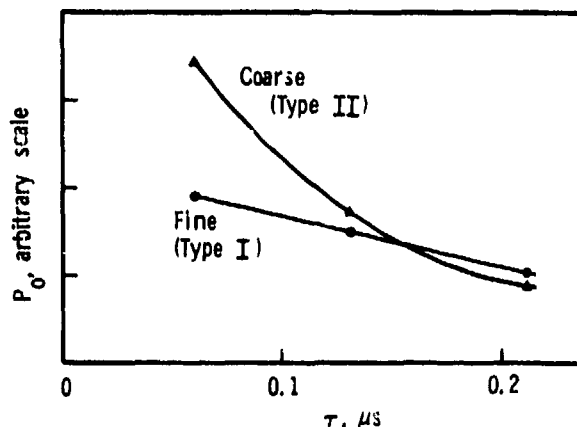
ACKNOWLEDGMENTS

REFERENCES

1. G. Gamow and R. V. Finkelstein, "Theory of the Detonation Process," Navord Rept. 90-46, 20 April 1947.

2. F. P. Bowden and A. Yoffe, *Initiation and Growth of Explosion*, Cambridge Univ. Press, 1952.

3. L. B. Seely, "A Proposed Mechanism for Shock Initiation of Low-Density Granular Explosives," Paper 27, *Fourth Electric Initiator Symposium*, Franklin Inst., Philadelphia, 1963.

4. E. F. Gittings, "Initiation of a Solid Explosive by a Short-Duration Shock," *Proceedings of the Fourth Symposium (International) on Detonation*, Office of Naval Research, 1970, p. 191.

6. Y. de Longueville, "Comportement de Divers Explosifs Condenses Soumis à des Ondes de Choc Calibrées en Intensité et Durée," presented at Fifth International Colloquium on Gasdynamics of Explosions and Reactive Systems, Bourges, 1975.

7. F. E. Walker and R. J. Wasley, "Critical Energy for Shock Initiation of Heterogeneous Explosives," Explosivstoffe No. 1, 9, 1969.

8. H. Cheung, A. Weston, L. Green and E. James, "Explosive Initiation," Preprint UCRL-756578, June 18, 1975.

9. D. J. Pastine, R. R. Bernecker and R. J. Bauer, "A Theoretical Relation Between Initiating Shock Pressure and Porosity in Secondary Explosives," *Proceedings of the Fourth International Conference on High Pressure*, Kyoto, 1974, p. 460.

10. J. Roth, "Shock Sensitivity and Shock Hugoniots of High-Density Granular Explosives," *Proceedings of the Fifth Symposium (International) on Detonation*, Office of Naval Research, 1970, p. 219.

11. R. J. Bauer, "An Analysis of Small Scale Gap Test Sensitivity Data Using Porosity Theory and Nonreactive Shock Hugoniots," NSWC/WOL/TR 75-67, 20 June 1975.

12. J. W. Taylor, Los Alamos Scientific Laboratory, private communication, 1974.

13. H. S. Napadensky, private communication, 1960-76. Also "Initiation of Explosives by Low Velocity Impact," *Proceedings of the Fourth Symposium (International) on Detonation*, Office of Naval Research, 1965, p. 473.

14. Y. de Longueville, C. Fauquignon and H. M Moulard, "Initiation of Several Condensed Explosives by a Given Duration Shock Wave," *Preprints of the Sixth Symposium (International) on Detonation,* Office of Naval Research, 1976, p. 16.

15. D. A. Frank-Kamenetskii, *Diffusion and Heat Transfer in Chemical Kinetics,* Plenum Press, New York, 1969.

16. NOLR 1111, Fuze Explosive Train Designers Handbook, Naval Ordnance Laboratory (White Oak), Apr. 1952.

17. NOLM 10771, "Firing Characteristics of Electric Initiators Made by the Spray Metal Process," Mar. 30, 1950.

18. Stresau, R. H., "The Sensitivity of Explosive Initiators," from the JANAF Fuze Committee Journal Articles, Volume 1, JANAF Journal Article #13, published by Picatinny Arsenal, Aug. 1960.

19. Kabik, I. B., L. A. Rosenthal and A. D. Solem, "The Response of Electro-explosive Devices to Transient Electrical Pulses," Paper No. 18, Proceedings, Electrical Initiator Symposium, Franklin Institute, Philadelphia, 29-30 Nov. 1960.

20. PBX-9404 is 94% by wt. HMX, 3% tris-2-chloroethylphosphate and 3% nitrocellulose.

21. T. P. Liddiard, Jr., "The Initiation of Burning in High Explosives by Shock Waves," *Proceedings of the Fourth Symposium (International) on Detonation,* Office of Naval Research, p. 487.

22. L. G. Green, E. J. Nidick, Jr., and F. E. Walker, "Critical Shock Initiation Energy of PBX-9404, a New Approach," UCRL-51522, Jan. 25, 1974.

23. J. E. Kennedy and J. W. Nunziato, "Shock Wave Evolution in a Chemically Reacting Solid," J. Mech. Phys. Solids 24, 107, 1976.

24. P. Howe, R. Frey, B. Taylor and V. Boyle, "Shock Initiation and the Critical Energy Concept," *Preprints of the Sixth Symposium (International) on Detonation,* Office of Naval Research, 1976, p. 8.

25. B. C. Taylor and L. H. Ervin, "Separation of ignition and Buildup to Detonation in Pressed TNT," *Preprints of the Sixth Symposium (International) on Detonation,* Office of Naval Research, 1976. p. 1.

26. R. Stresau Laboratory, Inc., "Development of the Varicomp Method, Expansion of Applicability," Rept. RSLR 72-7, 1972 and RSLR 74-4, 1974, for Naval Weapons Center, China Lake, CA, under Contract N00123-73-C-0247.

27. Means, J. E., "An Expanded Varicomp Method for Determining Detonation Transfer Probabilities," NWC TP 5789, Naval Weapons Center, China Lake, CA, Dec. 1975.

A $P^n t$ DETONATION CRITERION FROM THERMAL
EXPLOSION THEORY*

D. B. Hayes
Sandia Laboratories
Albuquerque, New Mexico 87115

Existing data on the growth of shocks in the explosive PBX-9404 are combined with thermodynamically complete equations of state for the unreacted high explosive and for the completely reacted high explosive to deduce the chemical reaction rate behind the shock. Such rate information allows wave propagation calculations on shock initiation of that high explosive; these calculations lead to a detonation criterion based on shock heating and subsequent thermal explosion at the impact interface. A separate analytical calculation of the thermal explosion time as a function of initial shock pressure leads to a criterion of the well-known form, $P^n t =$ const., with n about equal to 2. The effect that accounting for the actual heterogeneous shock heating would have on these results is discussed.

INTRODUCTION

For the explosive PBX-9404, introduction of a plane shock wave of pressure amplitude P and pulse duration t will lead to a detonation whenever the product $P^2 t$ exceeds some critical value (1). In the approximation that shock impedance of the explosive is constant, the product $P^2 t$ has been shown to be proportional to the energy fluence transmitted to the explosive. Hence, critical energy fluence has been proposed as a detonation criterion.

We have examined an alternate hypothesis, namely, that shock initiation has its origin in shock heating and and subsequent thermal explosion at or near the boundary where the plane shock is introduced by thin flyer impact. The results of this study indicate that, for the explosive PBX-9404, n must be chosen about equal to 2 in a shock initiation criterion of the form $P^n t =$ const. Thus, our result is essentially in agreement with the previous model on shock initiation by short duration, square pressure pulses. However, by

using this model, substantially different results will be achieved when calculating an initiation criterion for a pressure pulse which is not square.

This study has three important parts:

1. Development of a constitutive relation for chemically reacting materials. To develop such a constitutive relation, we must have thermodynamically complete equations of state for the solid unreacted high explosive and for the reacted products. In addition, it is necessary to make an assumption which allows definition of the rules describing the thermodynamic properties of a mixture of unreacted solid and reacted gas for those instances when the high explosive is partially reacted.

2. Information on the kinetic rate governing the chemical reaction. Kennedy has measured the spontaneous growth of pressure at the impact interface in the explosive PBX-9404 (2). We have used those results in conjunction with both our constitutive relation for chemically reacting materials and with the theory of shock propagating in Maxwellian materials to determine the chemical reaction rate

immediately behind the shock. This experimentally based chemical reaction rate is the one which is used in subsequent calculations.

3. Development of an analytical model for shock initiation. In essence, it is assumed that the shock passage heats the high explosive which subsequently thermally explodes. The criterion is that this heated region must thermally explode before the arrival of a release wave which would cool it and hence quench the reaction. Certain approximations are used to show that, for a criterion of the form $P^n t = \text{const.}$, n should be chosen about equal to 2. That is in agreement with what has been previously observed in initiation of the explosive PBX-9404 by square pressu ᵥ pulses.

CONSTITUTIVE RELATION

We have developed a semiempirical, analytical, free-energy function to describe unreacted PBX-9404. The analytical form that we have chosen for the Helmholtz free energy as a function of temperature and volume is shown in Eq. 1.

$$F(T, V) = C_V \left[(T - T_0)(1 + \frac{\gamma}{V}(V_0 - V) \right.$$

$$\left. + T \log (T_0/T) \right] + \frac{K_{T_0} V_0}{N(N-1)} \quad (1)$$

$$\left[\left(\frac{V_0}{V} \right)^{N-1} - \left(1 - \frac{V}{V_0} \right) \left(N - 1 \right) - 1 \right].$$

This analytical form was actually arrived at by assuming specific functional forms for three second-derivatives of the Helmholtz free energy, and obtaining Eq. 1 through integration. The analytical forms given in Eq. 2 completely define those three second-derivatives:

$$C_V = C_{V_0} = \text{const.}; \frac{\gamma}{V} = \left(\frac{\gamma}{V} \right)_0 = \text{const.}$$

$$(2)$$

$$K_T = K_{T_0} \left(\frac{V_0}{V} \right)^N.$$

The first assumption is that the specific heat at constant volume remains constant. The second assumption is that Grüneisen's ratio divided by specific volume is constant. Thermodynamic compatibility of second derivatives in conjunction with these first two assumptions requires that the isothermal bulk modulus, K_T, be a function of volume only. We have chosen the function of volume, as shown in Eq. 2, so that the reference isotherm would have the form of a Murnaghan solid. Hence, specifying five parameters, C_{V_0}, $(\gamma/V)_0$, V_0, K_{T_0}, and N, uniquely defines the Helmholtz free energy. Unfortunately, available thermodynamic properties are in a form which is not directly usable. For instance, what is available is information on the thermal-expansion coefficient at zero pressure and the specific heat at constant pressure, C_P (3). In addition, the experimentally determined shock Hugoniot for unreacted PBX-9404 is available (4). We obtained our five parameters from the above information in the following way: Consider the two thermodynamic identities

$$\frac{\gamma}{V} C_P = \alpha K_S \quad (3a)$$

and

$$C_P = C_V (1 + \alpha \gamma T). \quad (3b)$$

At reference conditions, K_S can be determined from the intercept of the shock Hugoniot at zero pressure in the shock-velocity/particle-velocity plane. Thus at reference conditions all quantities in Eq. 3a required for calculating (γ/V) are known. From this value of (γ/V), Eq. 3b can be used to evaluate C_V at reference conditions. The procedure thus far is sufficient to determine four of the parameters. However, we need to specify the value of the fifth parameter, N. That was done by calculating the shock Hugoniot for various values of N and finding that value of N which most closely reproduced the known shock Hugoniot of the form (4):

$$U = 0.269 + 1.72 \, u \, (\text{cm}/\mu s). \quad (4)$$

This procedure gives us the following five parameters:

$$V_0 = 0.5435 \, \text{cm}^3/\text{g}$$

$$K_{T_0} = 0.126 \, \text{Mb}$$

77

$$C_{V_0} = 1.11 \times 10^{-5}\,\text{cm}^2/\mu\text{s}^2/\text{K}$$

$$\frac{\gamma}{V} = 1.976\,\text{g/cm}^3$$

$$N = 5.6$$

The well-known JWL equation of state is available for the gaseous products of the explosive PBX-9404 (3). Its shortcoming for this study is that it is a (P, V, E) equation of state, hence thermodynamically incomplete. We have extended it to thermodynamic completeness by assuming constant specific heat, C_V. When this is done, the following expressions for thermodynamic quantities result:

$$C_V = \text{const.}$$

$$W = \text{const. } (\gamma - \text{Grüneisen's ratio in our notation})$$

$$K_S = (1 + W)P - \sum_{i=1}^{2} A_i(1 - R_i V + W) \tag{5}$$

$$\exp(-R_i V).$$

In these equations, standard JWL notation has been retained (3).

The process of shock initiation of high explosives is known to be closely related to the production of hot spots or hot regions within the shocked solid. Hence, initiation depends strongly upon the heterogeneous nature of the temperature distribution. In the analysis which follows, an assumption of homogeneity of the shocked state must be made since we have no information about the nature of that temperature distribution. The procedure here will be to make an incorrect assumption, that is, one of temperature uniformity in the shocked solid, and then discuss the kinds of errors which are thereby introduced in the analysis.

Kirkwood and Wood (5) have developed a constitutive relation for a mixture of unreacted and reacted high explosive under the condition that the constituents of this mixture are at equal temperature and equal pressure. The mixture is not assumed to be in thermodynamic equilibrium. That constitutive relation is given as Eq. 6.

$$\dot{P} = a_{S,x}^2\dot{\rho} + \frac{K_{S,x}}{VC_{P,x}}$$

$$\left[\Delta V\left(\frac{\partial E}{\partial T}\right)_{P,x} - \Delta E\left(\frac{\partial V}{\partial T}\right)_{P,x}\right]\dot{x}. \tag{6}$$

All of the symbols in Eq. 6 have their usual thermodynamic meaning. The symbol x denotes the mass fraction of chemically reacted material. Thus, when $x = 0$, the material is in the unreacted state. The quantity ΔV is the difference between the specific volume of the gaseous products and the specific volume of the solid while $a_{S,x}$ denotes the isentropic sound speed for the frozen mixture.

KINETICS OF THE CHEMICAL REACTION

Kennedy (2) has used the front and back quartz-gauge technique to study pressures at the impact and downstream surfaces in the explosive PBX-9404. Of particular interest are the measurements which he reported on the pressure variation after impact at the impact interface. Kennedy's experimental results are used here to evaluate the time rate of change of pressure at the impact time and the impact interface. The equation.

$$\left(\frac{\partial P}{\partial t}\right)_h = 192\,P^3\left(\text{Mb},\mu\text{s}\right) \tag{7}$$

fits the initial pressure variation over nearly four decades in the pressure/time derivative.

It is a well-known approximation (6) that, neglecting hydrodynamic attenuation because of nonzero pressure gradients behind shock fronts, shocks grow or decay in Maxwellian solids according to

$$\frac{DP}{Dt} \simeq \left.\frac{F\dot{x}}{2}\right|_{x=0}, \tag{8}$$

where the operator $D/..$, is the time derivative along the shock front which is assumed to lie along a C^+ characteristic and $F\dot{x}$ is the last term on the righthand side of Eq. 6. Assuming that the pressure wave grows along a single growth curve (i.e., as a growing square wave), an assumption which was used by Kennedy and later expounded by Cowperthwaite (7), it is

obvious that the pressure growth rate along the shock front must equal the pressure growth rate at the impact interface. We only need to apply this result at early times to get an estimate of the initial chemical reaction rate at impact time. Eq. 9 shows the way in which the chemical reaction rate was deduced using this analysis.

$$\dot{x} = \frac{384}{F} P^3 \qquad (g, cm, \mu s) \qquad (9)$$

where F is calculated from the constitutive equation. It should be emphasized that the values of $\dot{x}$ obtained from Eq. 9 are inferred from experiment. Fig. 1 shows those values of chemical reaction rate, $\dot{x}$, versus the reciprocal of the average shock temperature. Since experiments were conducted at pressures below 5 GPa, the chemical reaction rates for shock temperatures in excess of about 425 K must be obtained by extrapolation of Eq. 9. That extrapolation is also shown in Fig. 1.

ANALYTICAL MODEL FOR SHOCK INITIATION

Using the techniuqes outlined in the previous section, we are able to calculate the chemical reaction
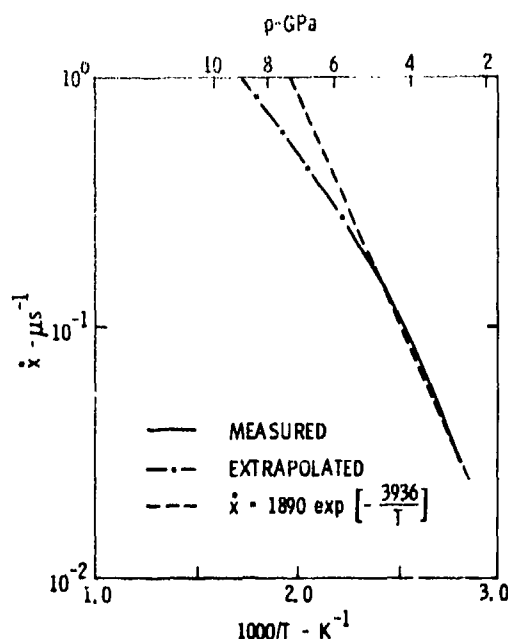
Fig. 1. The measured chemical reaction rate behind the shock front. Also shown is an Arrhenius fit in the region where data were taken.

rate along the shock Hugoniot for the unreacted explosive (i.e., for x = 0). For these results to be useful, it is necessary to know the chemical reaction rate at all possible states, including those different from x = 0, so we arbitrarily extend the measured chemical reaction rate information to all degrees of reaction by assuming that the reaction rate is zeroth order and is a function of temperature only as shown in Eq. 10.

$$\dot{x}(x, T) \equiv \dot{x}(0, T). \qquad (10)$$

The constitutive equation, Eq. 6, and the kinetic equation, Eq. 10, are sufficient to allow calculation of shock initiation of PBX-9404. That has been accomplished by means of finite-difference, wave-propagation calculations using established techniques (8). Numerous calculations on the shock initiation of PBX-9404 have been performed during the course of this study but will not be reported in detail here. What was seen in the calculations was that for low-impact stress, in order to achieve a detonation, the flyer plate producing the shock had to be of sufficient thickness to prevent a rarefaction from reaching the impact interface before the completion of reaction at that interface (9). If the flyer plate was thin enough, rarefactions arrived before that time and cooled — hence quenched—the reaction. Of course, reaction completion did not constitute immediate detonation in the calculations, since the pressure produced at the instant of completion lies approximately at the point on the Hugoniot for the reacted products, where the impactor Hugoniot crosses in the pressure/particle-velocity plane. Nonetheless, reaction completion was always seen as the first step in a complicated sequence of building and overtaking waves culminating in a steady detonation.

In summary, we have a detonation criterion in which the explosive is shock heated. The reaction proceeds in the heated region, liberating additional heat and hence increasing the temperature. The process proceeds in an accelerated manner. At a time approximately equal to the thermal explosion time, reaction completion is achieved. If the pressure is released before reaction completion, in this simple model we will fail to achieve initiation of detonation.

We can be quantitative with the above model since all the necessary ingredients to perform such a calculation are at hand. The well-known Todes formula relates the thermal-explosion time, t, to the initial temperature, T_0, to the total temperature rise

79

associated with the chemical reaction, ΔT, and to the coefficients which appear in the Arrhenius kinetic law, the frequency factor, A, and, the activation temperature, E°/k. Todes formula is shown in Eq. 11.

$$t = \frac{T_0^2}{A\Delta T(E^\circ/k)}\exp\left[E^\circ/kT_0\right]. \qquad (11)$$

In order to apply Eq. 11, the chemical reaction rate must have the Arrhenius form. However, the chemical reaction rate, $\dot{x}$, is not described well by the Arrhenius form over a large temperature range. In the region covered by experiments, however, one can fit a straight line on the data and that is shown in Fig. 1.

From Eq. 11 we can estimate the value of P^2t necessary to initiate PBX-9404 using our model and the following data: at 5 GPa, the shock temperature is 421 K according to our calculations. The adiabatic, constant-volume burn temperature, as calculated from our complete equation of state, is 2280 K.leading to a value for ΔT of 1980 K. In the vicinity of 5 GPA, the reciprocal of the slope of the straight line fit in Fig. 1 is 3940 K, hence the time to thermal explosion as calculated by Eq. 11 is 0.14 μs. Accordingly, the critical value of P^2t is calculated to be 3.4 GPa^2 μs. This is in surprisingly close agreement with the observed value of 5.5 GPa^2 μs. Values of thermal explosion time versus shock pressure are plotted in Fig. 2.

Although the Arrhenius equation fits the reaction rate data fairly well in the same region as Kennedy's
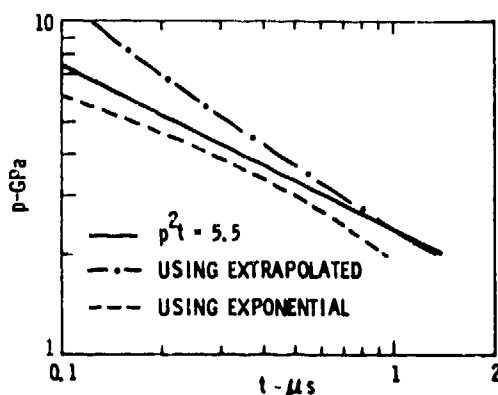
Fig. 2. Calculated and measured values of P^2t for the explosive PBX-9404.

experiments, the discrepancy is fairly large for higher temperatures. Fig. 2 shows the thermal-explosion time calculated using the measured and the extrapolation of the measured chemical reaction rate. Note that the two calculations bracket the observed result (1) that $P^2t = 5.5$ GPa^2 μs.

It is of interest to carry the approximation of Eq. 11 one step further. Since the shock temperature and shock pressure are nearly linearly related, we can estimate n in a criterion of the form $P^nt =$ const.

$$n = \frac{-d\log t}{d\log P} \simeq \left[1 - \frac{T_{00}}{T_0}\right]\left[\frac{E^\circ}{kT_0} - 2\right] \quad (12)$$

The quantity T_{00} is room temperature. As is obvious from Fig. 2, n is nearly equal to 2 for a large range of shock pressure in agreement with what is calculated by using Eq. 12. However, Eq. 12 predicts that for a material with a larger apparent activation temperature, E°/k (i.e., a stronger variation of $\dot{x}$ with T_0), the value of n in a criterion of the form $P^nt =$ const. will be larger than 2.

DISCUSSION

It is widely recognized that shock heating of solids does not produce homogeneous heating. Rather, because of heterogeneous plastic flow associated with, for instance, shear banding, certain regions of a shocked solid are preferentially heated.

We can examine the nature of the constitutive equation for a mixture of two components of the same material at different temperatures in the following way. Let the subscript 1 denote regions which are cold and let the subscript 2 denote regions which are hot. Then the following relations must hold:

$$\dot{P}_1 = K_1\dot{\epsilon}_1 + F_1\dot{x}_1$$
$$\dot{P}_2 = K_2\dot{\epsilon}_2 + F_2\dot{x}_2. \qquad (13)$$

We have changed the density variable, ρ, in Eq. (6) to strain, ϵ, in an attempt to condense the notation in the following analysis. Eq. (14) shows how the total strain, ϵ, is related to the strain in each region, while Eq. (15) shows the way that the average chemical reaction rate is related to the reaction rates in those regions.

$$\epsilon = w_1 \epsilon_1 + w_2 \epsilon_2 \qquad (14)$$

$$x = w_1 x_1 + w_2 x_2 \qquad (15)$$

The variable w denotes mass function. Assume that $\dot{x}_1 = 0$; that is, in the cold regions the chemical reaction is not proceeding. We can develop the constitutive relation for the entire mixture. Combining Eqs. 13, 14, and 15 with the assumption $P_1 = P_2$, we obtain the following result.

$$\dot{P} = K\dot{\epsilon} + F\dot{x}$$

$$\frac{1}{K} = \frac{w_1}{K_1} + \frac{w_2}{K_2} \qquad (16)$$

$$F = \frac{K_2}{K} F_2$$

Equation 16 shows that a two-temperature mixture of constituents, with one component reacting, is describable as a Maxwell solid. That result is useful in interpreting the previous calculation of the chemical reaction rate. The values of chemical reaction rate deduced previously depended upon the functions K and especially on F. We have evaluated the functions F and K for a variety of temperatures and volumes, and they are relatively insensitive to temperature variation. In fact, varying the temperature by an order of magnitude causes variations in the functions of K and F of much less than a factor of 2. Hence, if temperature differences in region 1 and 2 are less than an order of magnitude, the chemical reaction rate deduced from the functions K and F evaluated using the average temperature rise will certainly be within a factor of 2 those which would be calculated based upon the correct temperature distribution.

We conclude that the calculation of the chemical reaction rate, $\dot{x}$, in this study, is probably correct in an absolute sense although, strictly speaking, it results from a small fraction of the material, w_2, which is reacting at a much higher rate, $\dot{x}_2$ with the product of w_2 and $\dot{x}_2$ equalling $\dot{x}$. If we had information on w_2,

treatment of preferential shock heating would lead to a much larger variation of shock temperature with pressure in the hot regions than is calculated by the homogeneous calculation. Such a variation would lead to proportionately larger values of T_0, A, and $E°/k$ in Eq. 11. These larger values could, when used in Eq. 11, lead to similar values for the thermal explosion time, t. At the same time a larger value of $E°/k$ would explain the large discrepancy between activation temperatures observed in shock loading and observed in zero-pressure thermal-explosion experiments.

REFERENCES

1. F. E. Walker and R. J. Wasley, Explosivstoffe, No. 1, 9 (1969).

2. J. E. Kennedy, "Pressure Field in a Shock-Compressed High Explosive," 14th Symposium on Combustion, The Combustion Institute, Pittsburgh 1973.

3. B. M. Dobratz, "Properties of Chemical Explosives and Explosive Simulants," UCRL-51319, Lawrence Livermore Laboratory, 1972.

4. J. E. Kennedy and J. W. Nunziato, J. Mech. Phys. Solids 24, 107 (1976).

5. J. G. Kirkwood and W. W. Wood, J. Chem. Phys. 22, 1915 (1954).

6. See, for instance, L. E. Malvern, Q. Appl. Math. 8, 405 (1951), or G. E. Duvall in Stress Waves in Anelastic Solids, Springer-Verlag, Berlin (1964).

7. M. Cowperthwaite, "Theoretical Studies of Detonation Waves," SRI-PYU-1322, Final Report, Stanford Research Institute, Menlo Park (1974).

8. D. B. Hayes, J. Appl. Phys. 46, 3438 (1975).

9. A. W. Campbell, W. C. Davis, and J. R. Travis, Phys. of Fluids 4, 498 (1961).

DISCUSSION ON SHOCK INITIATION AND $P^2\tau$

(SESSION I)

1. COMMENTS BY F. E. WALKER, LAWRENCE LIVERMORE LABORATORY

Several misconceptions regarding the critical energy concept and shock initiation have appeared in the writing and the discussions on this topic. It may be appropriate at this time to review the development of this concept and the assumptions and factors which affect its application.

As shown in the original publication (1), the critical energy criterion was shown to provide a very good correlation of several sets of data on the shock initiation of solid explosives. It was observed that initiation or non-initiation in PBX-9404, LX-04, and TNT correlated very well with the kinetic energy of a flying foil or plate that impacted the test explosive. The data could be plotted as a hyperbolic function as shown in Figure 1a or, analogously, as a function of shock wave pressure P and duration t, as shown in Figure 1b. (These are representative plots to illustrate the analogy.) Algebraically and physically P and V are directly related, as are m and t.

The critical energy equation was derived from the kinetic energy expression $E_c = mV^2/2$ where E_c was the critical plate kinetic energy for initiation in the original data sets discussed (1). Substitution of the following relationships — $m = A\rho w$, $t = 2w/U_s$, $P - Po = \rho U_s U_p$, and $V = 2U_p$ — gave $E_c = AtP^2/\rho U_s$ and, for a unit area, $E_c = tP^2/\rho U_s$. Since for each specific explosive ρ is a constant and U_s changes slowly with P, the equation can be written as $E_c \cong \alpha P^2 t$, where α is a constant. In fact, this P^2t relationship was pointed out by the author in early discussions of the critical energy concept. It was also pointed out very soon that unless the explosive was well characterized the confidence limits were fairly wide, and even with very well characterized HEs the usual initiation probabilities as seen in gap tests, drop hammer tests, etc. must be considered.

There were several assumptions that seem obvious in the application of the critical energy concept, but these have all been abused by critics. The criterion applies most ideally to the pure chemical explosive compound. Each specific explosive has a specific critical energy over a large range of initiating shock pressures and times. (It was stated clearly in early discussions that it probably would not be a constant value at very low or very high initiating pressures.) The critical energy in the equation represents only that energy that is transmitted to the explosive by the flying plate. (A discussion was given in the original paper (1) on this point. Also, it was presented as a correlation.)

Relative to these assumptions, the following factors can affect the critical initiation energy: 1) binders and other inert additives generally reduce the energy that gets into the explosive, particularly at the lower pressures; 2) when the physical and mechanical properties of the test explosive are changed, the critical energy is likely to change; 3) additives with chemical effects may change the critical energy of the pure explosive; and 4) other energy inputs or energy sinks will influence the critical energy. Any factor that reduces the energy that acts on the pure explosive will cause an apparent increase in critical energy and vice versa.

The author proposed several years ago that the shock initiation process could be discussed helpfully by reference to the graph given as Figure 2. The sigmoid curve shows a probable relationship between percent decomposition and the reaction time in a thermal decomposition. The points on the curve described by P_1 and P_2 separate the initiation process into three regimes. Shocks with pressures between P_1 and P_2 will probably
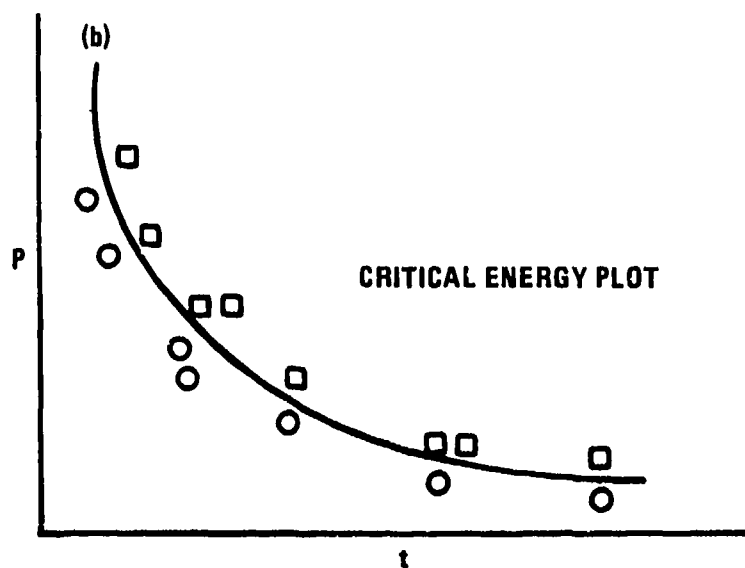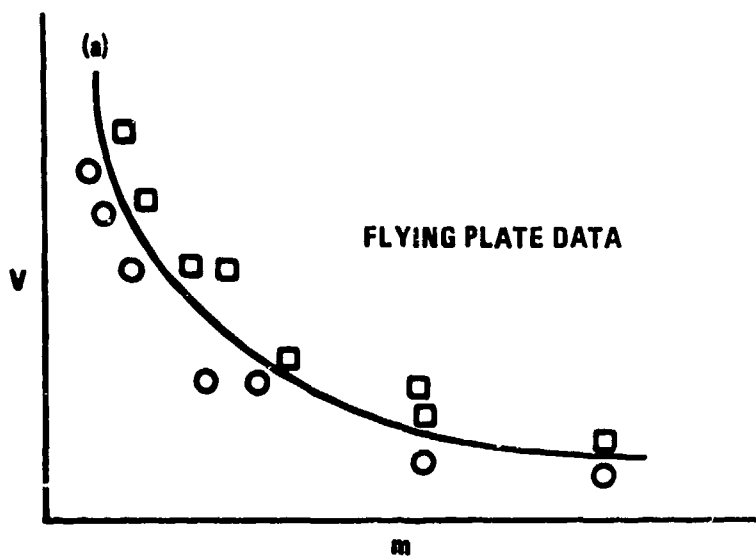
Fig. 1. Development of the critical energy concept

initiate with a nearly constant critical energy, for the process is primarily thermal. ($E_c = \rho U_p^2 \Delta \chi$ is another form of the equation which shows a relationship to the internal energy increase.) When $P \leqslant P_1$, there is a very low level of initiation reaction (few radicals), and the long delay times and poor "communication" between reacting molecules allow energy losses. The apparent critical energy will then be higher than normal. When $P \geqslant P_2$, there is a very high level of initiating reaction with almost instantaneous "communication" between reacting molecules and initiation sites (many radicals). In this regime there is probably very little "equilibrium thermal" character to the initiation process and greatly reduced delay times. Here there could be an apparent decrease in critical energy.
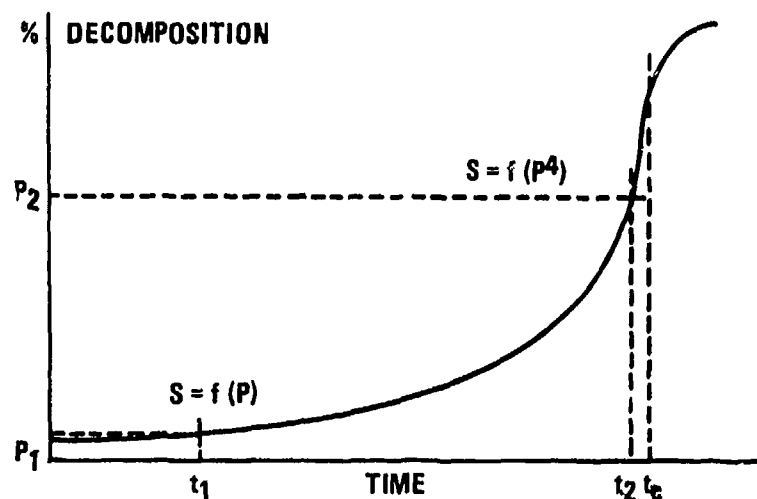
Fig. 2. Explosive decomposition as a function of time

It is important to note that these changes in critical energy in the three regimes do not invalidate the critical energy concepts, but this understanding can extend its utility into regions of very high and very low initiating pressures, since curves such as those given in Figure 3 can be determined rather easily.

Experience in the application of this concept has shown that the natural initiation probability factors can not be ignored. The spread of initiating pressures in a gap test for the 50% initiation values warns us to expect fairly wide confidence limits on specific critical energies, and since it has been suggested (2) that the critical energy holds relatively constant over two to four orders of magnitude in very unrelated tests on several explosives, it would seem prudent to maintain some suspicion of data that seem to select the P^2t criteria as superior to the energy fluence concept or to show radical changes in critical energy values for a well-characterized explosive.

84
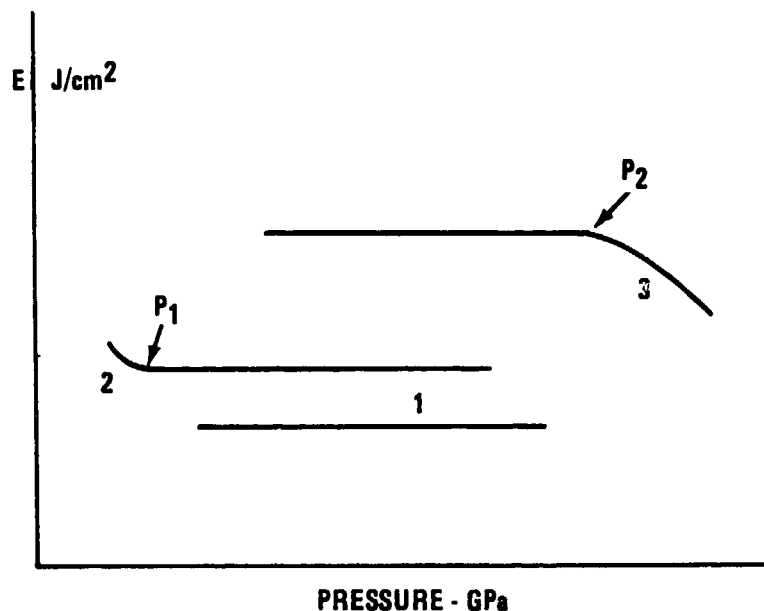
Fig. 3. Critical energy and initiation regimes

REFERENCES

1. Walker, F. E. and R. J. Wasley, *Explosivstoffe* 17, No. 1, 9 (1969).

2. Weston, A., private communication, Brobeck Company, Berkeley, California.

2. COMMENTS BY M. COWPERTHWAITE, STANFORD RESEARCH INSTITUTE

The empirical p^2t criterion for the initiation of detonation formulated by Walker and Wasley is an important relationship for assessing the behavior of condensed explosives in many engineering applications. The acceptance of this criterion for all shock initiation problems is not realistic however until conditions for its validity have been identified and established. A consideration of the shock initiation process in an explosive by the impact of a flying plate is presented here to establish conditions imposed by the validity of the p^2t criterion and give some understanding of its significance.

The $p_i^2 t_c(i)$ criterion specifies for each initial shock pressure p_i produced by a flying plate in an explosive of a given length a critical time $t_c(i)$ for the onset of detonation. The time $t_c(i)$ is the time taken after impact for the rarefaction from the free surface of the plate to reach the explosive-flier interface. It can therefore be regarded as the time the shock-induced reaction initiated at pressure p_i must proceed to ensure detonation. In other words, a criticality condition is established at the explosive-flier interface in a time $t_c(i)$ such that the initiating shock is not appreciably influenced by the energy liberated in the vicinity of the explosive-flier interface after the time

85

$t_c(i)$. Moreover, since $t_c(i)$ is in principle a function of charge length, it should be remembered that the $p_i t_c(i)$ criterion represents a sufficient but not a necessary condition for the onset of detonation.

In the event that the $p_i^2 t_c(i)$ criterion is a fundamental relationship for explosives it must be possible to identify the criticality condition at the explosive-flier interface, and express the critical time in terms of explosive parameters, such as the equation of state and the energy release rate. A theoretical study along these lines is required to validate the $p_i^2 t_c(i)$ criterion and put it on a firm foundation. A criticality condition for the different types of buildup to detonation must be considered because the $p_i^2 t_i(c)$ relationship takes no account of the mechanism of initiation.

It is my conjecture that the different modes of initiation that proceed without the formation of a second shock will exhibit the same criticality condition. Such a criticality condition is the formation of a reactive rarefaction fan centered on the explosive-filter interface that contains the characteristic that eventually becomes the Chapman-Jouguet (CJ) characteristic and the line of complete reaction in the self-sustaining wave. The critical time $t_c(i)$ is thus the time the reaction at the interface must proceed in order to ensure the formation of the CJ characteristic in the detonation wave. The family of characteristics emitted from the explosive-flier interface before $t_i(c)$ influence the shock, but the family emitted after $t_i(c)$ do not.

Further investigation of the $p^2 t$ criterion is, in my opinion, necessary before its full significance can be established. More experimental evidence is required to support the criterion, and theoretical evidence is required to place the criterion on a firm foundation by establishing conditions under which it is valid or approximately valid.

3. COMMENTS BY R. FREY AND P. HOWE, USA BALLISTIC RESEARCH LABORATORIES

The papers by Hayes, de Longueville et al, and Howe et al all discuss the $p^2 t$ criterion for the initiation of detonation. The three papers agree on one point: If thermal explosion theory is used to explain the $p^2 t$ criterion, and if the shock temperature is computed on the basis of equilibrium thermodynamics, a very low value for the activation energy is required. Hayes and de Longueville, et al, suggest that a more reasonable activation energy will result if the hot spot temperature is much higher than the bulk temperature. This is true, but we do not think this approach is adequate to explain the $p^2 t$ criterion. In this regard, we would like to add the following comments to those already made in our paper.

In our paper we introduced the following relation to account for hot spot temperature:

$$T = n(T_{wc} - T_o) + T_o, \tag{1}$$

where T is the hot spot temperature, T_{wc} is the bulk temperature computed by the Walsh-Christian technique, and T_o is the initial temperature. In Figure 1, we show the effective activation energy which gives the best least square fit to the $P^2 t$ criterion as a function of the parameter n. The calculation assumes that t is the thermal explosion time as computed by the standard formula (see Frank-Kamenetskii, "*Diffusion and Heat Transfer in Chemical Kinetics,*" Plenum Press, New York, 1969). This equation has the form

$$t = (\text{constant}) \frac{T^2}{E} \exp\left(\frac{E}{RT}\right)$$

where: T is the temperature; t is the thermal explosion time; and E is the activation energy.

Even for n = 20 (shock heating at hot spots is twenty times as great as predicted by the Walsh-Christian technique), the activation energy which best fits the criterion is only 17 Kcal/mole, which is considerably lower than the values of 30 to 50 Kcal/mole which were determined by Lee, et al (Fifth Detonation Symposium) or Rideal (Proceedings of the Royal Society A-195, 135 (1948). The best fit frequency factor is also low by many orders of magnitude, and the fit of theory to experiment is not very good. With n = 20, the temperature of PBX 9404 at 5 GPa is already about 3300°K. In the light of Mader's calculations on nitromethane hot spots [Physics of Fluids 8, 1811 (1965)], a temperature of 3300° at 5 GPa seems to be a reasonable estimate of an upper limit. It is probable that the effective activation energy is a function of temperature and that the values determined from thermal explosion experiments at 500 to 1000K do not apply at higher temperatures. However, the expected direction of change would be for activation energy to increase with increasing temperature, thus causing a greater difficulty for this approach.

We have also considered the possibility that a distribution of hot spot temperatures might explain the result. Let us assume that the hot spots are distributed with respect to temperature with a density distribution function which has the form

$$\frac{1}{aP^\alpha} \, \rho \left[\frac{T}{aP^\alpha} \right]$$

where T is temperature, P is shock pressure, a and α are arbitrary constants, and ρ is an arbitrary function having the properties of a distribution function.

Thus, the nature of the temperature dependence can be quite general. Let us also assume that the criterion for detonation is that some critical number of hot spots must react in order for buildup to detonation to occur. Then the following equation must hold:

$$N(P, t) = \int_{T_i(t)}^{\infty} \rho \left[\frac{T}{aP^\alpha} \right] \left(\frac{dT}{aP^\alpha} \right) = \text{constant}$$

where N is the number of hot spots which react in time t, t is the duration of the shock pulse, ρ is the density distribution function, and T_i is the temperature which gives a thermal explosion in time t. If we evaluate the derivative dP/dt defined by this relation and the equation for thermal explosion, we find

$$\frac{dP}{dt} = \frac{P}{\alpha t} \cdot \frac{1}{\left[2 - \frac{E}{RT_i} \right]}$$

where E is the activation energy. On the curve $p^2 t$ = constant, this derivative has the value $- P/2t$. For $\alpha = 1$, these derivatives cannot be equivalent unless $T_i = 0.25 \, E/R$. On the basis of existing kinetic data (see earlier reference to Lee or Rideal) $T_i(t)$ will not be this large. If it is this large, it presumably will be so only for a narrow range of shock durations, so we are forced to reject the thermal explosion model.

An additional problem with the thermal explosion model is that only a small fraction of material can attain the necessary high temperature. The fraction of material involved cannot be greater than 1/n, where n is the parameter in equation 1. After this reacts, one must still account for the reaction of the remainder of the material. For these reasons and for the reasons presented in our paper, we concluded that the dominant mode of heat release must occur in a grain burning fashion.

$T = T_{wc} + n(T_{wc} - T_0)$
$T_0 = $ INITIAL TEMPERATURE
$T_{wc} = $ WALSH - CHRISTIAN TEMPERATURE

ACTIVATION ENERGY, kcal/mole

n
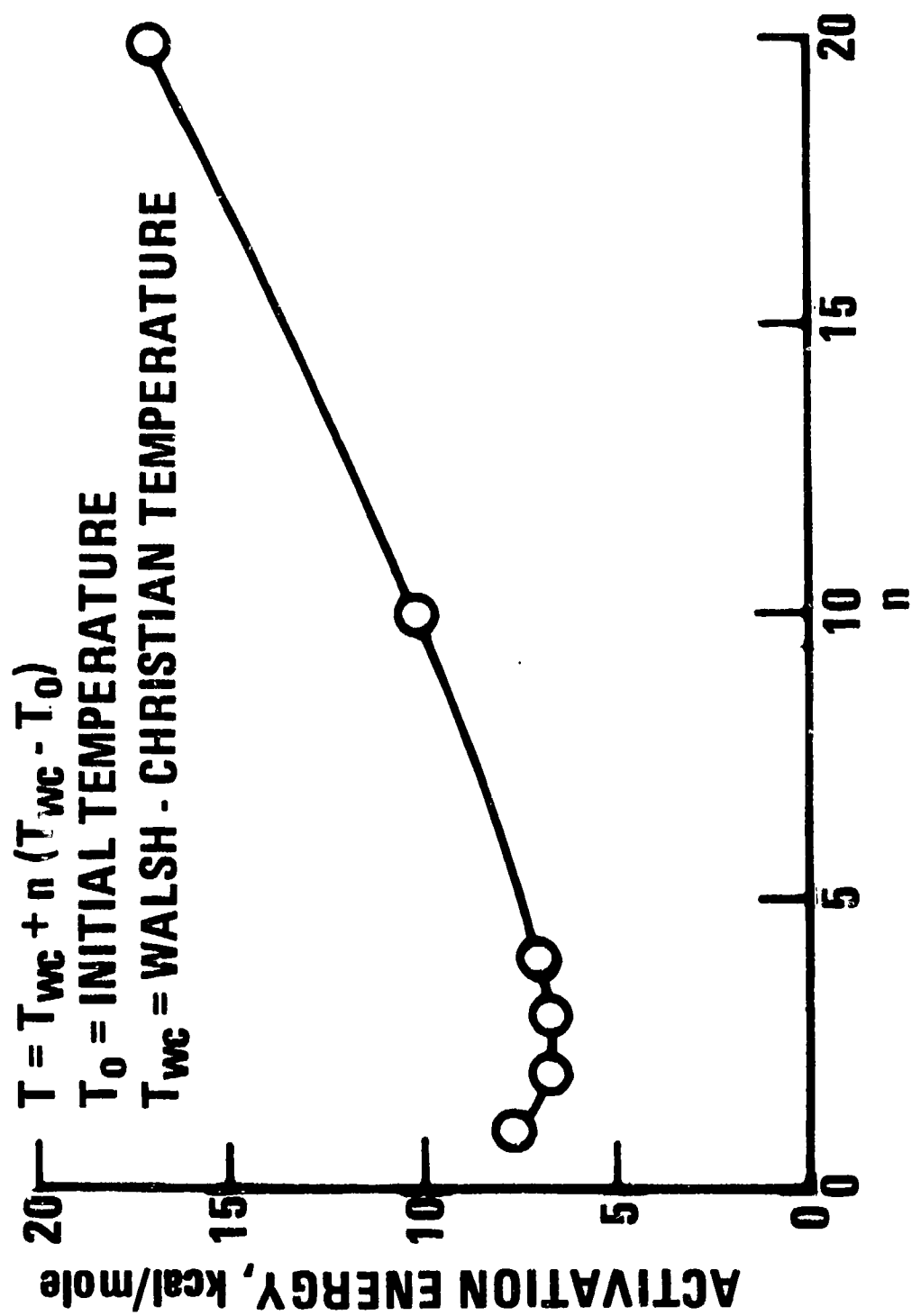
4. INVITED DISCUSSION OF SHOCK INITIATION MECHANISM
BY C. MADER, LOS ALAMOS SCIENTIFIC LABORATORY

The papers we have heard contribute very useful data to help us describe the explosive sensitivity to shock. Perhaps the experimental studies of Titov will be extended to furnish us Pop plot data for TNT at different initial temperatures in addition to the gap data. Pop plot data (distance of run as a function of plane wave initiation pressure) is the most useful type of data for shock initiation as it is essential for engineering or modeling studies.

The embedded Manganin gauge measurements of Wackerle exhibit curious maxima in the pressure histories which, if real for PETN or 9404, are poorly understood. We need to know more about this experimental technique under these conditions.

The mechanism of shock initiation of heterogeneous explosives is one of debate as evidenced by Howe's assumption of grain burning with heat conduction, Wackerle's assumption of the plastic work model, and by Titov and Nunziato/Kennedy's hydrodynamic flow modeling.

How important are transport mechanisms such as heat conduction, viscosity, elastic-plastic flow compared to the hydrodynamic flow? Are there pressure ranges where one transport mechanism may dominate and others where it is not important? Can the mechanism of adiabatic compression of the air in holes be important?

When heat conduction has been included into hydrodynamic calculations of hot spot propagation (1) or hot spot formation and propagation (2), it has been found to be negligible. The energy transfer accomplished by shocks and rarefactions is several orders of magnitude faster than energy transfer accomplished by heat conduction. If shocks are present and the time scale of interest is of the order of microseconds then heat conduction is not an important energy transfer mechanism. A grain burning model using heat conduction for its energy transfer mechanism is therefore of little interest for describing shock initiation phenomenon.

The adiabatic compression of gas bubbles to high temperatures and the transfer of the heat to the explosive by heat conduction has been investigated both experimentally and theoretically as a mechanism of explosive shock initiation. The classical experimental studies of Seely and Seay[3] showed that changing the gas in the voids of PETN from one that would give low temperatures to one that would give an order of magnitude higher temperatures had no effect on the shock initiation properties. Several other experimental studies have confirmed this observation. Since the last Detonation Symposium the Joint Services Explosive Program sponsored some useful studies of this problem. Experimental studies of Craig[4] of the shock compression of various layers of gases in contact with explosives showed that the nature of the gas did not matter. Detailed numerical modeling[5] of the experiment showed that plane surface heat conduction across the compressed gas-explosive interface could not give a high enough temperature for a sufficient amount of time to result in any significant amount of explosive decomposition for systems experimentally observed to decompose. The gap initiation problem is still unsolved and apparently some other source of initiation energy is required such as shock interactions with surface irregularities or with internal voids to explain the experimental observations. It is surprising that the mechanism of initiation that is probably important in the accidental premature initiation of explosives in shells in unknown. We do know that some phenomenon other than plane surface heat conduction and adiabatic gas compression is dominating the initiation process.

The heating that results from viscous and elastic-plastic flow has been suggested (6) as a source of energy for initiating explosives at low shock pressures (~ 1 kbar) and long times (~ milliseconds). If realistic viscous or yield coefficients are used, the amount of heating has been found to be insufficient to produce initiation. However, the notion that hotspots result from plastic work at void peripheries is being studied by groups led by John Taylor and by Jerry Wackerle at LASL. While it is a great hand waving model, it has so far required what are probably unrealistic material properties to result in sufficient heating to be of interest in explosive initiation.

89

However at this stage of our understanding of very low pressure shock initiation mechanisms it is unwise to ignore the possibility that viscous and elastic-plastic heating may be important for some applications.

For higher pressure ($\sim$ 10 kbar) shock initiation of heterogeneous explosives we have found the heating from shock interactions at density discontinuities to be more than sufficient to result in initiation. The "Hydrodynamic Hot Spot" concept includes all the effects that can occur when shocks interact with discontinuities or with each other such as jetting, void collapse, shock separation and collision, mach and regular shock reflection and anything else one might observe in a reactive fluid dynamical numerical simulation of the flow. The development of this concept may be followed by studing the papers in previous Detonation Symposiums. Perhaps the most convincing experimental and theoretical demonstration of the hydrodynamic flow mechanism was the observed agreement between the computed (8) and experimental induction times (9) resulting from the shock interactions formed in nitromethane by corners of Plexiglas, gold and aluminum. An important consequence (2) of the hydrodynamic hot spot model is that the hot spot continues to decompose after the initial shock wave passage thus reproducing the experimentally observed decomposition behind the shock wave such as Dremin burn in addition to the shock front build-up.

The major mechanism of hot spot formation and energy transport in the shock initiation of heterogeneous explosives is hydrodynamic flow. The correlation of initiation properties with surface area, particle size, density and other physical properties can be interpreted as the necessary consequence of a hydrodynamic mechanism and one does not need to invoke transport mechanisms.

As we have previously mentioned, the details of the hydrodynamic flow for many problems of practical interest are still unknown. Those attempting to investigate a shock initiation problem should concentrate first on the hydrodynamics of the problem and then add transport or material properties as needed.

LITERATURE CITED

1. C. L. Mader, International Conference on Sensitivity and Hazards of Explosives, Waltham Abbey (1963).

2. C. L. Mader, Fifth Symposium on Detonation, pp 177 (1970).

3. G. E. Seay and L. B. Seely, *J. App. Phys.*, 32, 1092 (1961).

4. A. Popolato, Editor, JSEP Program, Los Alamos Scientific Laboratory report LA-5521-PR, pp 9-18 (1973).

5. A. Popolato, Editor, JSEP Program, Los Alamos Scientific Laboratory report LA-5616-PR, pp 16-17 (1974).

6. A. Popolato, Editor, JSEP Program, Los Alamos Scientific Laboratory report LS-5402-PR, pp 9-11 (1973).

7. J. Wackerle, J. O. Johnson and P. M. Halleck, Sixth Symposium on Detonation, pp 25 (1976).

8. C. L. Mader, Los Alamos Scientific Laboratory report LA-3450 (1966).

9. J. R. Travis, Fourth Symposium on Detonation, pp 386 (1965).

5. RESPONSE TO C. MADER BY R. FREY AND P. HOWE, USA BALLISTIC RESEARCH LABORATORIES

Mader's objection to a grain burning mechanism is that the process can not be fast enough to release significant energy in the few microseconds available during shock initiation. In considering the reaction rate which may be achieved in a grain burning reaction one must consider the rate per unit surface area and the total

ignited surface area per unit volume of explosive. In the examples Mader cites, hot spots are formed as the result of void collapse by hydrodynamic processes. The resulting hot spots have a size and shape similar to the original void. In this case the surface area available for grain burning is small, and significant heat release by a grain burning mechanism is unlikely. However, the total ignited area available for grain burning may be much greater if hot spots arise from frictional processes associated with void collapse. Friction could occur as a result of grains sliding past one another or as a result of grains cracking and sliding along the cracked surface. The former would be more likely in low percent theoretical maximum density materials, such as our TNT, the latter in high percent theoretical maximum density materials. In either case the surface to volume ratio of the heated and ignited area would be very great. At the high strain rates which exist under shock loading, we feel that such processes are more likely than viscous and/or plastic flow. In fact, it is commonly recognized that many materials, including most explosives, fracture extensively under shock loading. (Incidentally, we certainly agree with Mader that adiabatic compression of gas in voids cannot be responsible for shock initiation.)

For our TNT samples, the intergranular surface area was of the order of 2×10^3 cm^2/gr. It is not unreasonable to take this as the ignited area. Burning rates for explosives are not known above a pressure of about 1 GPa. However, burning rates for many explosives seem to vary in an approximately linear fashion with pressure up to the maximum pressures which have been employed. By extrapolating data reported by Wachtel [1], we infer that a burning rate of 120 cm/sec is not unreasonable for TNT at 2 GPa. Combining this burning rate with the surface area of our samples, we conclude that about 37% of our explosive at 1.55 gr/cm^3 could react in one microsecond. This is clearly sufficient to cause shock acceleration.

In this regard, it is interesting to consider the reaction rates reported by Mader and Forest in LA-6259 [2] and employed in the calculations reported by Mader in this Symposium. The calculations are a very impressive demonstration of hydrocode techniques. The rates were obtained by an analysis of "Pop plots" and partially reactive Hugoniot relations with an additional assumption. The derived reaction rate for PBX 9404 varies approximately as P^n, where P is pressure and n is between 2.6 and 2.8. If this is translated into a temperature dependence using the temperatures calculated in LA-6259, an extremely weak dependence on temperature is observed. This is consistent with our observations. This weak temperature dependence, as well as the surface area and porosity dependencies discussed in our paper, are consistent with a grain burning model and are inconsistent with homogeneous kinetics.

Hydrodynamics is obviously very important in the initiation of detonation. However, hydrodynamics is closely coupled with kinetics, and to say that one must be completely understood before considering the other seems unrealistic. In some cases, consideration of the kinetics may lead one to an improved understanding of the hydrodynamic processes which are involved. We believe that the evidence presented in our paper and in our other comment in this session can be explained more easily in terms of grain burning than in terms of homogeneous kinetics. If this is so, hydrodynamic descriptions of void collapse must be altered to include fracture or some other process which increases the surface to volume ratio of the hot spot.

REFERENCES

1. S. Wachtell and C. McKnight, "A Method for Determination of the Detonability of Explosives and Propellants," Third Symposium on Detonation (1960).

2. C. Mader and C. Forest, "Two-Dimensional Homogeneous and Heterogeneous Detonation Wave Propagation," LA-6259 (1976).

6. COMMENTS BY C. FAUQUIGNON, FRANCO-GERMAN RESEARCH INSTITUTE OF SAINT LOUIS

I would like to point out that we made no attempt to explain the so-called p^2t criterion because our experiments have shown that it can only apply in a limited range of pressure and only in the case of heterogeneous explosives.

Concerning the thermal explosion model, it has been found that it fits correctly the experiment when applied to homogeneous explosives and it supports the decrease of the energy threshold when pressure increases.

I agree that one might suspect the p^2t applicable to heterogeneous explosives; the earlier the energy is released the better it fits. I think that the fact that the $(T' - T_s)/T_s$ function (see Fig. 12 of our paper) tends to zero, is in favor of this applicability; but the higher the pressure the more particles which will be initiated early, therefore, the more homogeneous the behavior.

COMMENTS ON "INITIATION OF SEVERAL CONDENSED EXPLOSIVES BY A GIVEN DURATION SHOCK WAVE," Y. de LONGUEVILLE, C. FAUQUIGNON, AND H. MOULARD BY JOHN B. RAMSAY, LOS ALAMOS SCIENTIFIC LABORATORY, LOS ALAMOS, NM, USA

One facet of the initiation of heterogeneous explosives by short-duration shock waves which needs more discussion is the interaction of the rarefaction wave with the shocked zone and the leading shock. The approach presented by de Longueville, Fauquignon, and Moulard considers this problem and provides an excellent starting point for the problem. I would like to present a brief and elementary consideration based on an extremely simplified model (Note: after the session C. Fauquignon commented that he has published a paper using the same simplified model but with a somewhat different emphasis). (1)

In the model used it is assumed that a shock wave enters the explosive and travels to the point (X^*, t^*) where it transforms to a detonation wave. This point is a function of the initial shock pressure and is experimentally determined using shock waves of long duration. The experimental data can be represented by either of two equations:

$$P^\beta X^* = \Phi, \text{ or}$$

$$P^\alpha t^* = \Psi,$$

where P is the initial pressure, X^* and t^* are the distance and time to detonation and β, Φ, α, and Ψ are adjustable parameters determined from the experimental data. It will be assumed that a detonation occurs if the rarefaction wave does not catch the shock front before the transformation occurs and that it will fail to transform if the rarefaction wave catches the front before (X^*, t^*). The time in the case where the rarefaction enters the back surface and just catches the shock front at (X^*, t^*) is defined as τ and is given implicitly by

$$X^* = \int_0^{t^*} U_s(t)dt = \int_0^\tau u_p dt + \int_\tau^{t^*} (c + u)_r dt,$$

where U_s is the shock velocity as a function time, u_p is the piston velocity which is considered constant over the time of interest, and $(c + u)$ is the sum of the local sound and particle velocities at the head of the rarefaction wave.

This equation cannot be solved explicitly for τ because we do not have a complete understanding of the wave structure. By making extremely simplifying assumptions, it is possible to obtain solutions which provide some insight into the behavior of τ with P.

Consider a wave in which the state behind the shock wave is constant and the wave velocity remains constant. Then τ is given explicitly as

$$\tau = t^* \left(\frac{c + u - U_s}{c} \right).$$

Assuming the material follows a Walsh equation of state (the adiabat is a reflection of the Hugoniot) then

$$c = V/V_0(a + 2bu),$$

where a and b are the coefficients of the linear relationship between shock and particle velocities. Since only the lead characteristic is considered, V/V_0 is determined from the shock relationship and

$$\tau = t^* \left(\frac{bu}{a + 2bu} \right).$$

Now multiplying by P^n and substituting for t^* we get

$$P^n \tau = P^{n-\alpha} \Psi \left(\frac{bu}{a + 2bu} \right).$$

A comparison of this relationship with the experimental data for PBX-9404 is shown in Fig. 1. Also shown is the relationship

$$P^2 \tau = 5.5 \times 10^{-4} \text{ (Mbar}^2 \text{ } \mu\text{sec)}$$

Fig. 1. Critical pulse duration vs. pressure calculated for PBX-9404 using the constant pressure flow model. Experimental data as referenced by Christiansen and Taylor for PBX-9404 are shown for comparison.
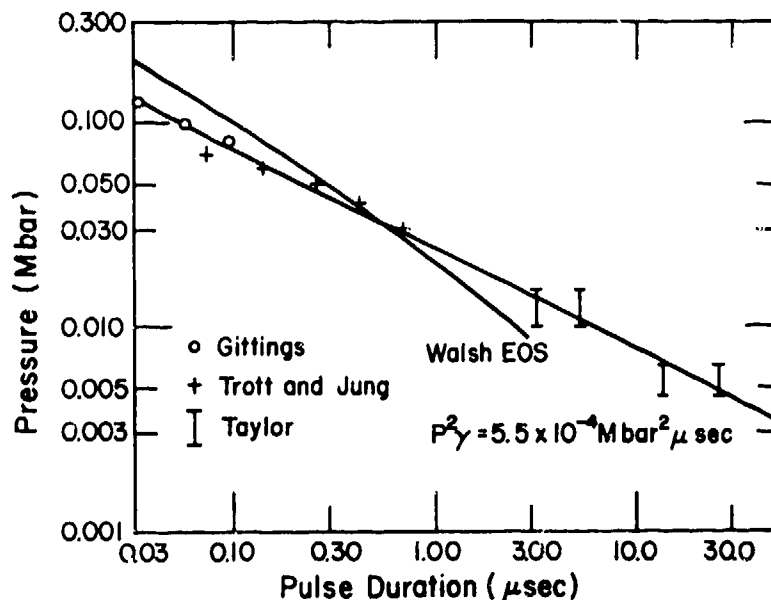
as reported by Taylor (2). Variation in the parameters of the $U_s - u_p$ relation do not appear to affect the shape or position appreciably, while α and Ψ have a stronger effect. Using a Grüneisen equation of state for the material and a more complex model as proposed by Kennedy (3) does not make significant changes in the comparison of the experimental data and the models.

However, in trying to make this comparison I became acutely aware that the proper data for modeling "thin shock wave" initiation does not exist. Most of the previously available data were obtained on this pellets with excess transit time as a function of initial pressure. What are needed are shock histories before and after the rarefaction has caught the front and data indicating whether longer runs will still lead to detonation.

REFERENCES

1. C. Fauquignon, "Correlation Between Sensitivity and Initiation Parameters of a Detonation," Acta Astronautica **3**, 313-316 (1976).

2. D. E. Christiansen and J. W. Taylor, "HE Sensitivity Study," Los Alamos Scientific Laboratory Report LA-5440-MS (December 1973).

3. J. E. Kennedy, "Pressure Field in a Shock Compressed High Explosive," in *Fourteenth Symposium (International) on Combustion,* (The Combustion Institute, Pittsburg, PA, 1973) pp. 1251-1258.

DISCUSSION ON NITROMETHANE DECOMPOSITION KINETICS

(SESSION I)

1. COMMENTS BY R. F. CHAIKEN, BUREAU OF MINES

There is a seriou problem in attempting to match model reaction rate calculations, or results inferred from such calculations, to detonation data (such as induction times) obtained from actual experiments. The problem lies with our ability to predict (or measure) reaction temperature, and the fact that reaction rates can be extremely sensitive to temperature. This is easily recognized when the rate of reaction, S, is expressed by some Arrhenius type function, e.g.,

$$S \simeq Ae^{-E_a/RT} \quad \frac{moles}{cm^3\text{-sec}}$$

By differentiation with respect to temperature, T we obtain the following error relationship:

$$(\delta S/S) \simeq \frac{E_a}{RT} (\delta T/T),$$

where δS and δT are the errors in the respective parameters.

For detonation reaction mechanisms involving bond scission as a rate controlling step (e.g. the C-N bond in nitromethane), $E_a \sim 50$ kcal/mole. At a reaction temperature of $\sim 1500°K$, E_a/RT is about 17. Thus, a 10% error in temperature will lead to a 170% error in S. Under these circumstances, the significance of the agreement (or lack of agreement) between computed and measured reaction rates, or those parameters inferred from reaction rates, may be questionable.

On the other hand, one might effectively utilize the temperature sensitivity of S in the other direction, i.e., to determine temperature accurately from experimental Arrhenius rate constants. The problem here is that reliable experimental kinetic constants are generally unavailable for the high pressure and temperature conditions encountered in detonation. Extrapolation of low pressure and low temperature data could be misleading due to changes in the rate controlling step or even the possible effects of pressure on reaction rate. This latter point is referred to in the paper by D. J. Pastine, M. J. Kamlet and S. J. Jacobs (this conference).

In this same connection, I would like to refer to the work that I carried out a number of years ago on the shock initiation of nitromethane (NM) (1,2). Utilizing activated complex theory (3), the rate constant for NM decomposition can be expressed as

$$k_r = \frac{kT}{h} e^{-\Delta F^+/RT} = \frac{kT}{h} e^{-(\Delta E^+ + P\Delta V^+ - T\Delta S^+)/RT}$$

where ΔF^+ is the standard free energy of formation of the activated complex (see references for further definition of terms). Comparing this to the more frequently used Arrhenius rate constant, i.e.,

$$K_r = A^{-E_a/RT},$$

we have

$$A = \frac{kT}{h} e^{\Delta S^+/R},$$

and

$$E_a = \Delta E^+ + P\Delta V^+$$

The quantity $e^{\Delta S^+/R}$, which is sometimes referred to as the steric factor, is usually of the order of unity for small molecules. For bond scission (e.g., the C-N bond), ΔV^+ corresponds to $\sim 10\%$ extension of the bond (or approx. +2.8 cm^3/mole for NM). At 1 atm, where most isothermal decomposition kinetic studies have been carried out, $P\Delta V^+$ is negligible compared to ΔE^+. However, at 10^5 atm, the $P\Delta V^+$ term can account for ~ 20 fold decrease in the nitromethane reaction rate. It is interesting to note that for an equation of state which results in shock conditions where P/T = constant, the $P\Delta V^+$ term will not lead to an effective increase in E_a but rather an effective decrease in the Arrhenius preexponential factor, A.

It should be further noted that biomolecular decomposition reactions would be expected to have $\Delta V^+ < 0$, which will lead to a high pressure enhancement of the reaction rate. Whether or not this is significant in the sensitization of NM by amine catalyst can be speculated upon. It is known that a tautomeric aci-form of NM can exist, i.e.,

$$CH_3 - NO_2 = CH_2 = NO - OH,$$
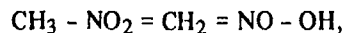
and a strong organic base such as an amine would tend to stabilize the aci-form. If the rate controlling step of the catalyzed NM decomposition in detonation is the formation of the aci-form, the reaction could be bimolecular with respect to the concentration of amine and NM, and the ΔV^+ for the formation of the activated complex would in this case probably be negative.

REFERENCES

1. Chaiken, R. F., "The Kinetic Theory of Detonation of High Explosives," MS Thesis, Polytechnic Institute of Brooklyn, Brooklyn, N.Y. (June 1958).

2. Chaiken, R. F., "A Kinetic Approach to Detonation of Homogeneous High Explosives," Eighth Symposium (International) on Combustion, Williams and Wilkins Co., Baltimore (1962), pp. 759-767.

3. Glasstone, S., H. Eyring and L. J. Laidler, "The Theory of Rate Processes," McGraw-Hill Book Co., N.Y. (1941).

2. COMMENTS BY L. C. SMITH, LOS ALAMOS SCIENTIFIC LABORATORY

Kamlet has suggested that the decomposition of nitromethane (NM) behind a shock wave proceeds through the aci form implies, among other things, that the isomerization reaction is rapid on a microsecond time scale. That seems unlikely to me, since it is generally agreed that the isomerization involves a two-step, base-catalyzed proton transfer:

$$CH_3NO_2 + B \underset{k_{-1}}{\overset{k_1}{\rightleftharpoons}} CH_2NO_2^- + BH^+ \underset{k_{-2}}{\overset{k_2}{\rightleftharpoons}} CH_2 = NO_2H + B.$$
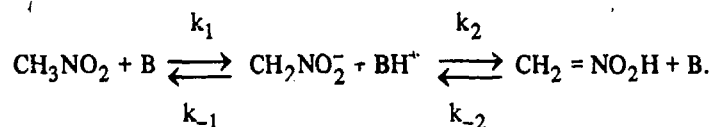
Indeed, Maron and La Mer (1) found that even under favorable conditions (aqueous solution, strong bases), k_1, the rate-determining step, is only 200 to 300 ℓ/mole-min. In "pure" NM B is another NM molecule. Presumably the reaction is subject to the Brønsted general catalysis law, and since NM is an extremely weak base, the reaction as written would, I believe, be much too slow in spite of the favorable effects of the high temperature and pressure behind the shock wave (2).

In partial support of Kamlet's thesis we may note that Eyster, Smith, and Walton (3) did find a weak correlation between the gap sensitivities of NM solutions of various amines and the base constants of the amines determined in water (values determined in NM were unavailable). This could imply that the shock sensitivity of NM depends in part on either the concentration of the $CH_2NO_2^-$ ion or, as Kamlet suggests, the rate of formation of the aci form.

REFERENCES

1. S. H. Maron and V. K. La Mer, *J. Amer. Chem. Soc.* **60**, 2588 (1938); **61**, 692 (1939).

2. E. L. Lee, R. H. Sanborn, and H. D. Stromberg, Proc Fifth Symp (Int'l) on Det'n, p 331.

3. E. H. Eyster, L. C. Smith, and S. R. Walton, U.S. Naval Ordnance Lab Report No. NOLM 10336.

3. COMMENTS BY R. FREY AND P. HOWE, USA BALLISTIC RESEARCH LABORATORIES

Kamlet has suggested (on several occasions) that the dependence of the time to detonation upon inclusion surface area in the nitromethane experiments is a result of a wall catalyzed conversion of the nitromethane to the aci form. Kamlet's suggested mechanism is qualitatively consistent with the data. However, we are unable to use the wall catalyzed isomerization reaction to explain the quantitative differences in efficiency demonstrated by the glass, copper, and aluminum oxide inclusions. In another paper (1) we had developed an equation of the form:

$$st = be^{-aE}$$

where

t is the time to detonation;
s is the inclusion surface area per unit volume of mixture;
E is the internal energy density behind the reflected shock;
a, b are constants;

which we used to reduce the data for all the nitromethane experiments onto a single curve, as shown in Figure 7 of our paper, this Symposium. The physical properties of this inclusion material we assumed to be manifested through E, the internal energy density, behind the reflected shock. The magnitude of E, of course, depends very strongly upon the shock impedance of the inclusions. Relevant values are shown below (2).

Material	Density	ρC
Cu	8.93	35.18
glass	2.5	11.17
Al_2O_3	3.97	31.42

The copper and aluminum oxide have very similar shock impedances and lead to very similar values of E. These data are therefore already scaled with respect to each other (see Figure 6) and the copper data were not replotted in Figure 7. The fact that we are able to scale all the data by considering shock impedance effects is, we believe, a strong argument in favor of the mechanism we proposed. The fact that the particle size effects observed here were also observed in the TNT studies lends additional support to this mechanism.

REFERENCES

1. Howe, P. and Boyle, V., "Effect of Heterogeneity on the Sensitivity of High Explosives to Shock Loading," Minutes of 14th Explosive Safety Seminar, New Orleans (1974).

2. Compendium of Shock Wave Data, M van Thiel, ed. UCRL 50108 (June 1966).

4. COMMENTS BY R. SHAW, CONSULTANT

The activation energy for reaction Eq. (1) in the homogeneous gas phase

$$CH_3NO_2 \rightarrow CH_3 + NO_2 \tag{1}$$

has been calculated to be 59.8 kcal/mol by Seely, Tegg, Shaw, and Berks (1), 59.0 kcal/mol by Benson and O'Neal (2), and measured to be 58.5 kcal/mol by Glanzer and Troe (3). The activation energy for the shock initiation of liquid nitromethane from 60 to 105 kbar measured by various workers and plotted on a single graph by Walker and Wasley (4) has an activation energy of 13.5 kcal/mol (5) using shock temperatures calculated (4) assuming C_v (nitromethane) = C_p (nitromethane). If a C_v (T) equation of state is used (6) the activation energy becomes 21.6 kcal/mol which is still in very poor agreement with the gas phase value.

Chaiken (7) has drawn attention to the effect of pressure on the activation energy predicted by transition state theory. The activation energy for reaction (1) at high pressures is equal to or greater than that in the first order region of the ideal gas state unless the volume of activation is negative. Reaction (1) is very unlikely to have a negative volume of activation because the volume of transition state is probably between that of the initial and final states.

It has been observed that nitromethane is made more sensitive to shock initiation by the addition of some acids and bases (8). For bases, the sensitizing effect is approximately linear with the pKa of the base (see Figure 1). The most likely explanation of this effect is that nitromethane undergoes an acid-or base-catalysed decomposition (9). Nitromethane is itself a weak acid (10). Therefore it is reasonable to expect nitromethane to undergo autocatalytic decomposition by an ionic mechanism. For example I have estimated that reaction Eq. (2) is 36.9 kcal/mol exothermic.

$$\overset{HO}{\underset{O}{\diagup}}N = CH_2 + CH_3NO_2 \rightarrow HON = CHCH_2NO_2 + H_2O \tag{2}$$

acid form
nitromethane
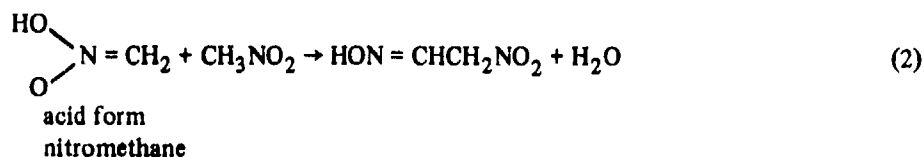
Some results on transient detonation phenomena in the two isomers, 1,1-dinitropropane (1,1-DNP) and 2,2-dinitropropane (2,2-DNP) at 60°C are relevant. The physical properties of the two liquids and their Arrhenius parameters for decomposition in the gas phase are very similar (see Table 1). However, 1,1-DNP has a smaller failure diameter, lower pressure for shock initiation, and slower failure wave velocity than 2,2-DNP. These differences in transient detonation phenomena indicate that under shock initiation or reinitiation during detonation failure 1,1-DNP decomposes significantly faster than 2,2-DNP. 1,1-DNP has an alpha hydrogen atom and so can decompose in the liquid phase by an ionic intermediate $[RC(NO_2)_2]^-$. 2,2-DNP has no alpha hydrogen atom and can not decompose via the same ionic intermediate.

I conclude that the chemical mechanical mechanism of decomposition of pure nitromethane during shock initiation contains an ionic component in addition to the free radical component.
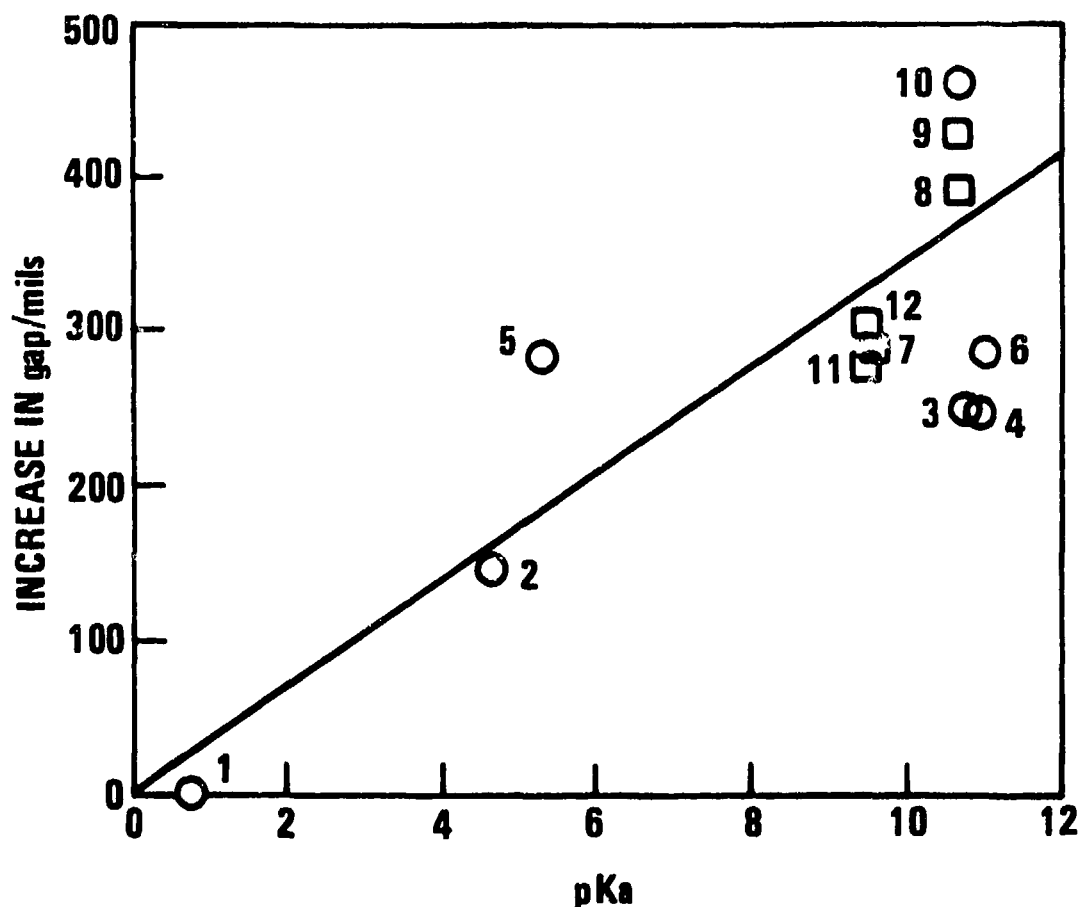
Fig. 1. The sensitizing effect of various based on the card gap value of nitromethane (8). (The gap determined by this test is the thickness of cellulose acetate by which the test sample, contained in 1-inch diameter schedule 40 aluminum pipe, must be separated from a 50 gram tetryl booster to reduce probability of detonation of the sample to 50%) (8). The circles represent bases whose pKa's have been measured (11). The squares represent bases whose pKa's have been estimated (9). The key is: 1. Diphenylamine, 2. Aniline, 3. Butylamine, 4. Dibutylamine, 5. Pyridine, 6. Triethylamine, 7. Furfurylamine, 8. Triethylenetetramine, 9. Diethylaminetriamine, 10. Ethylenediamine, 11. 2-Dimenthylamino-2-methyl-1-propanol, 12. 2-Amino-2-methyl-1-propanol.

TABLE 1

*Physical, Thermochemical, Kinetic, and Transient Detonation Properties
of 1,1-Dinitropropane and 2,2-Dinitropropane[12,13]*

Chemical Name	1,1-Dinitropropane	2,2-Dinitropropane
Chemical structure	$HC(NO_2)_2CH_2CH_3$	$CH_3C(NO_2)_2CH_3$
Molecular weight	134.1	134.1
Specific volume/(cc/g) at 60°C	0.833	0.819
Sound speed/(km/s) at 60°C	1.33	1.24
Heat of formation/(kacl/mol) of liquid (nominally 25°C)	−39.9	−42.3
Arrhenius A factor/(s^{-1}) for C-N fission (gas phase)	17.5	17.5
Activation energy/(kcal/mol) for C-N fission (gas phase)	49	49
Arrhenius A factor/(s^{-1}) for HONO elimination (gas phase)	11.5	11.5
Activation energy/(kcal/mol) for HONO elimination (gas phase)	43	39
Lead block failure diameter/(mm) at 60°C	7	27
Peak initial shock pressure/(kbar) for initiation in 1 μsec	93	116
Failure wave velocity/(km/s) at 60°C	2.966	5.022

REFERENCES

1. L. B. Seely, D. Tegg, R. Shaw, and J. G. Berke, Tech. Prog. Rept 67-2, Semiannual 16 Mar 1966 to 15 Sep 1967 Contract Nonr 3760(00).

2. S. W. Benson and H. E. O'Neal, "Kinetic Data on Gas Phase Unimolecular Reactions," NSRDS-NBS 21, U.S. Department of Commerce, 1970.

3. K. Glanzer and J. Troe, *Helv. Chim. Acta* 55, 2884 (1972).

4. F. E. Walker and R. J. Wasley, *Comb. and Flame* 15, 223 (1970).

5. R. Shaw, unpublished results.

6. M. Cowperthwaite and R. Shaw, *J. Chem. Phys.,* 53, 555 (1970).

7. R. F. Chaiken, Fourth Symposium (International) on Detonation, ACR-126 Office of Naval Research, Department of the Navy, 1965, p. 398.

8. J. L. Trocino and Associated "Techniques for Sensitizing and Detonating Nitromethane-Based Explosive Systems" Bulletin JLTN-2 April 1972.

9. Private communication from J. R. Keeffe, San Francisco State College, to R. Shaw, May 1976.

10. M. Breant, G. Demange-Guerin, *Bull. Soc. Chim. Fr. 1975*, (1-2 Part 1), 163.

11. Handbook of Chemistry and Physics, 55th Ed. 1974-1975, p. D-126.

12. R. Shaw, *Int. J. Chem. Kin.* 5, 261 (1973).

13. C. M. Tarver, R. Shaw, and M. Cowperthwaite, *J. Chem. Phys.* 64 2665 (1976).

COMMENT ON CHAIKEN'S CONTRIBUTION BY ROBERT SHAW

Suppose that there is a single rate-determining step in the decomposition of nitromethane under static high pressure (1). Chaiken's remarks and the observed (1) increase in rate of decomposition with increase in pressure at constant temperature strongly suggest that the rate-determining step is second order in nitromethane.

REFERENCE

1. E. L. Lee, R. H. Sanborn, and H. D. Stromberg, Fifth Symposium (International) on Detonation, Pasadena, California, 1970 ACR-184, ONR-Department of the Navy, Arlington, Virginia, p. 331.

5. COMMENTS BY J. E. KENNEDY AND J. W. NUNZIATO, SANDIA LABORATORIES

Our paper made the point that the nitromethane (NM) detonation profile (which determines the critical particle acceleration behind the shock front) cannot be described by the simple Arrhenius kinetics which appear to be appropriate for shock initiation of NM. We should emphasize that this conclusion is based on the assumption that the particle velocity profile is concave upward in the reaction zone, i.e., that there is no "plateau" immediately behind the shock front.

The chemical reaction mechanism is undoubtedly quite complex, probably involving a free-radical chain reaction as described in Shaw's comments above, and highly reactive intermediates such as the aci- form of nitromethane. We wanted to choose reaction kinetics with minimum complexity beyond the single-step Arrhenius model, and which would be compatible with the above mechanisms. Our choice of two parallel first-order reactions from NM to products seems to fit these requirements. It is simpler than any scheme involving reactions in series.

To be more specific about the chemistry, the high-activation-energy step in our calculations is Shaw's reaction (1) in his comments above. If we accept Kamlet's suggestion that aci-NM is formed in the shocked NM and the aci-NM quickly decomposes to products, our second parallel reaction could then be taken as

normal NM → aci-NM (low activation energy).
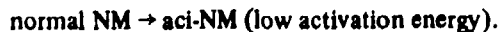
This pair of reactions is consistent with our mathematics.

On the other hand, let us consider Smith's argument above that any aci-NM reacting within a few microseconds in the shocked NM must have been present before shock loading, in a small concentration relative to that of the normal NM. Shaw's reaction (2) might then be taken as the low-activation-energy step, and thus the controlling initial reaction in shock initiation. This appeals to us because of the partial heat release (about half) in reaction (2), for the following reason. The shape of the deceleration profiles measured in Hardesty's NM initiation experiments suggested to us that a reaction liberating a significant fraction of the energy might be going essentially to completion soon after thermal ignition, with total reaction completion controlled by reaction (1) occurring at a later time. However, since depletion of the aci-NM would occur earlier than depletion of normal NM, we should point out that these kinetics would differ somewhat from the parallel reaction scheme we adopted.

The additional point made by Kamlet (paper by Pastine *et al.* in these proceedings) and Chaiken (above) concerning the volume of activation, and hence a pressure-dependent activation energy, is well-taken and further complicates the matter. However, since this effect tends to reduce the reaction rate as the shock pressure is increased, it cannot by itself reconcile our finding that detonation kinetics must be faster than the simple Arrhenius kinetics which describe shock initiation observations.

Session II

SHOCK-TO-DETONATION TRANSITION AND DETONATION STUDIES

Chairmen: Prof. N. Manson
                University of Poitiers
           William C. Davis
                Los Alamos Scientific Laboratory

INITIATION OF SEVERAL CONDENSED EXPLOSIVES BY A
GIVEN DURATION SHOCK WAVE*

Y. de Longueville,† C. Fauquignon, H. Moulard
French-German Research Institute of Saint-Louis
68300—Saint Louis—France

The response of granular, pressed, cast, and liquid explosives to shock waves of given intensity and duration has been experimentally investigated by use of flyer plates. The sensitivity is quantitatively given by a "critical" curve in the pressure-time plane. The kinetic energy transferred to the explosive is calculated for each point of this curve; this permits examination of the validity of the "energy-threshold" concept.

A possible interpretation of the critical shock duration as related to the reaction kinetics of the explosive is given. The application of this model to heterogeneous explosives leads to an "efficient temperature" essentially higher than that which the equation of state gives for the same shock pressure.

1. INTRODUCTION

The sensitivity of an explosive under shock load is usually investigated either by the gap test or by the impact of a flyer plate, the velocity and thickness of which determine shock pressure and duration, respectively. It has already been pointed out (1) that this second method can determine the sensitivity of two quantities: the sensitivity is described by the curve separating the detonation from the nondetonation region. It has been proposed (2) to characterize the sensitivity by the minimum amount of mechanical energy transferred from the projectile into the explosive. We will show how this concept of energy holds for different homogeneous and heterogeneous explosive compositions we have studied. Finally, we propose an interpretation of the critical shock duration as the minimum time required for the exothermic chemical reactions to lead to an immediate or delayed transition to detonation. The application of this crude model to heterogeneous explosives needs the

use of a temperature, which has been called "efficient temperature," higher than that given by the equation of state at the same shock pressure.

2. EXPERIMENTAL METHOD

The response (detonation or not) of a cylindrical explosive is investigated under the action of a plane shock wave with a rectangular pressure profile characterized by its pressure p and time duration t produced by the impact of a metal plate on the front plane.

2.1. Choice of the Impacting Plate

The shock intensity p is dependent on the impact velocity and the Hugoniots of plate and explosive material. t is the time needed for the shock to be reflected from one face to the other in the flyer plate.

Figure 1 shows the space-time diagram associated with the pressure-velocity curves of both materials as well as the derived pressure-time profile at the entrance side of the explosive. The plate material must satisfy the following conditions:
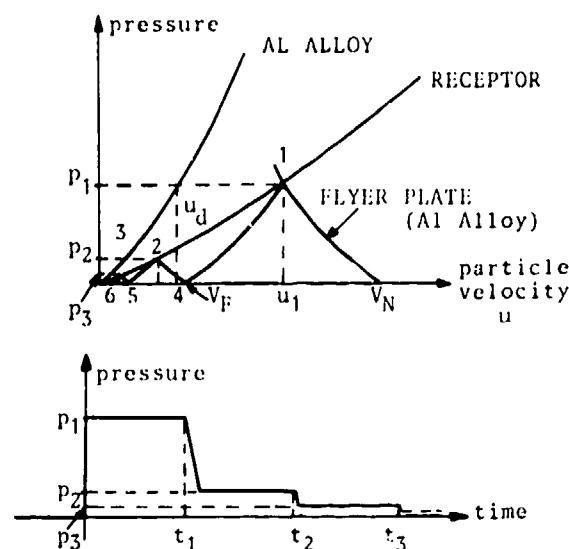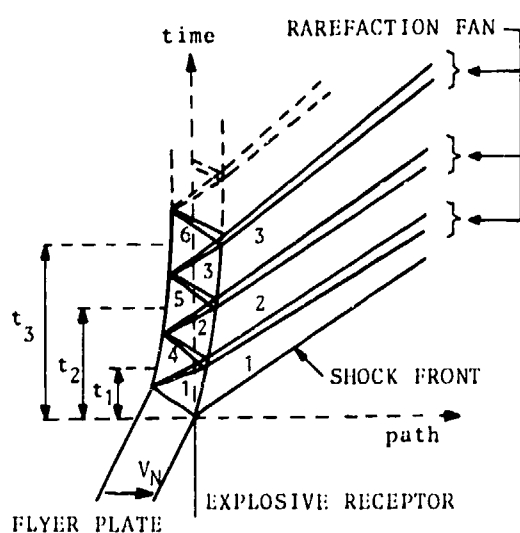
Fig. 1. Principle of generation of rectangular pressure pulses.

- High sound velocity in order to obtain very short shock durations (t_1).

- Weak Hugoniot slopes so that pressures p_2, p_3, ... are negligible with respect to p_1.

- Sound velocity, which is only a little dependent on pressure in order to obtain a rarefaction fan as narrow as possible.

For the present investigations, ST-aluminum was chosen because it meets the above conditions.

2.2. Experimental Setup

On the basis of their physical properties, the explosives under study can be classed into three groups with increasing sensitivities:

a. Liquid explosives (melted TNT and nitromethane)

b. Cast or pressed explosives (Comp B, plastic-bonded RDX and HMX)

c. Granular explosives (RDX).

Flyer plates are accelerated by a plane explosive layer detonating along the plate (3).

Figure 2 illustrates the experimental setup for rather insensitive explosives [groups (a) and (b)]. It should be recalled here that the plate after the deflection by an angle ϕ is in an expanded state, is plane, and travels at a velocity v, the normal component v_N, given by:

$$v_N = D \sin \phi$$

and given by the Richter formula

$$\frac{1}{\phi} = b + c \frac{\rho_m \cdot e}{\rho_{ex} \cdot \epsilon},$$

where D = detonation velocity,
  b, c = parameters of the explosive,
  ρ_m, ρ_{ex} = density of metal and explosive, respectively,
  e, ϵ = thickness of metal and explosive.

The velocity, which the generator of Fig. 2 is able to cover, has a lower limit at about 600 m/s, due to the fact that the plate tends to spall when the explosive layer is too thin. The upper limit is given by the energy efficiency of the system, which decreases for $\phi > 20°$ and corresponds to a velocity of about 2500 m/s.

For sensitive explosives (like granular RDX), impact velocities lower than 600 m/s are needed. To
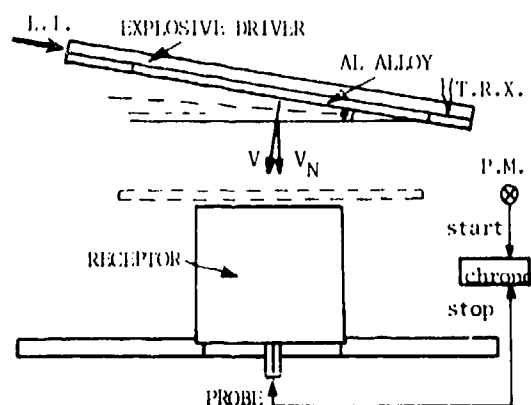
Fig. 2. Experimental (one stage) setup.

LI = Linear initiation
TRX = Probe for triggering, with delay, the x-ray flash
PM = Photomultiplier for control of the instant of the x-ray flash.

obtain these, the experimental arrangement of Fig. 3 was used.

The explosively accelerated plate is made of a high impedance (brass) metal impacting a barrier of the same material. The rear side of this barrier is covered with a ST-aluminum plate. Because of the impedance mismatch, the aluminum plate separates from the barrier and, after a sufficient path of flight, impinges on the explosive. Figure 4 shows that the impact velocity of the duraluminum can be reduced from 600 m/s to 425 m/s because the high-density brass can be explosively accelerated to velocities as low as 300 m/s without risking spallation. The usefulness of this method is limited at low impact velocities by the constraints imposed by the thicknesses of the barrier, brass, and ST-aluminum plates. Moreover, the angle ϕ must be determined with high accuracy in order to obtain acceptable conditions of flight for the aluminum plate.

The measurements and checks performed are based on a flash radiograph taken a few microseconds prior to impact (Fig. 2). This x-ray flash record allows us to:

● verify the flatness of the flying plate,

● check the accuracy of the assumed projection angle ϕ (simultaneity of impact),
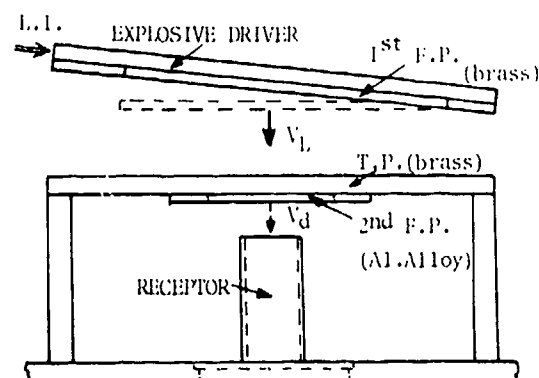
Fig. 3. Two-stage setup for the study of granular explosive.

FP = Flyer plate
TP = Momentum transfer plate.
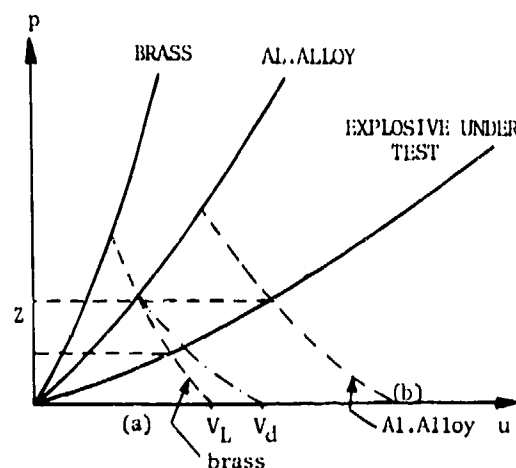
Fig. 4. Principle of the two-stage setup.

Z = Zone of pressures to be explored
(a) and (b) = minimum velocities reached by one stage setup, respectively, with brass and Al-alloy flyer plates.

● derive from the preceding observation the exact value of impact velocity V_N using the formula $V_N = D \sin \phi$,

● calculate the time of flight remaining, knowing V_N and the actual position at the time of the flash x-ray picture, and

107

• discriminate between initiation and failure. The latter is possible since the transit time necessary for the wave to run through the cartridge is known.

To this end, the time interval between the instant when the radiograph is taken and when the wave exits from the cartridge end is measured.

Depending on the length of the cartridge, the transit times vary at a ratio of 1 to 2, whether initiation takes place or not.

As far as the accuracy of the shock generator is concerned, densitometric measurements performed on the flash x-ray records show that the flatness error does not exceed 0.3 mm in a rectangular area of 90 × 60 mm. Besides, the error in the evaluation of angle ϕ remains below 2%, which is negligible. Thus, impact velocity V_N is known to less than 3% error. This is compatible with the accuracy with which the Hugoniots of non-reacting explosives are evaluated.

2.3. Diagnostics of Homogeneous Liquid Explosives

We see from a streak camera record (slit along a diameter of the setup) that:

• initiation originates from the plane part of the induced shock and not from the walls, and

• induction time could be measured for nitromethane and corresponds approximately to the critical shock duration for a given pressure.

3. RESULTS

3.1. Explosives Tested—Presentation of the Results

The experimental method described above has been applied to the following compositions:

• granular explosive = RDX at a density of 1.55 g/cm^3 with two grain sizes (40/80 μ and 200/400 μ),

• cast explosives = Comp. B3 and RDX/polybutadiene (86% RDX),

• pressed explosive = HMX/nylon (89.5% HMX),

• liquid explosive = TNT at 81°C and nitromethane.

The results are stated as follows: Velocity of impact-thickness of plate diagram (characteristic of the shock generator) or shock pressure-shock duration diagram (characteristic of the receptor explosive). As far as the latter is concerned, the Hugoniot of the receptor must be known. Although the possible reaction of the medium limits the reliability of the experimental results achieved, the various sensitivity curves are, nevertheless, plotted in a pressure-duration diagram, because this property is characteristic to the explosive. It allows us to define the kinetic energy transferred into the explosive by the plate during the impact process. Linear relationships between the velocity of the wave and that of the material are adopted and shown in the following table. These relations have been taken from published papers or established by computation according to A. K. Hopkins' method (4).

	U = c + s u (mm/µs)	Origin	Density (g/cm^3)
Granular RDX	U = 1.1 + 2.4 u	Ref. 5 and computed	1.54
Composition B3	U = 2.71 + 1.86 u	Ref. 6	1.73
RDX-polybutadiene	U = 2.3 + 1.8 u	Computed	1.60
HMX-nylon	U = 2.4 + 2.4 u	Computed	1.77
TNT (molten)	U = 2.14 + 1.57 u	Ref. 7	1.47
Nitromethane	U = 1.54 + 1.68 u	Ref. 15	1.12

Each rectangular pressure profile corresponding to the impact of a thin plate can be associated to a value of the kinetic energy transferred into the explosive. Computation of this value is derived from the diagrams shown in Fig. 1. If the residual pressures (too low for initiation of the explosive) are neglected, the loss in kinetic energy of the plate during time interval t can be written as follows:

$$\Delta \epsilon = \frac{1}{2} \rho_{p1} \cdot eS(v_N^2 - v_F^2),$$

where ρ_{p1} is the density of the plate, e = thickness of the plate, S = entrance area of the shock in the explosive, and v_N, v_F = impact and residual velocities of the plate. Since

$$v_N + v_F = 2 u_1 \quad \text{and} \quad v_N - v_F = 2 u_d,$$

the loss in the kinetic energy per surface unit becomes

$$\frac{\Delta \epsilon}{S} = 2 \rho_{p1} e u_1 u_d.$$

As the shock duration is written in the form $2e = t_1 \cdot U$, where U is the velocity of the shock in the plate at pressure p_1, we have

$$\frac{\Delta \epsilon}{S} = (\rho_{p1} U u_d) u_1 t_1.$$

Writing $\rho_{p1} U u_d = p_1$, representing the pressure value, we get

$$\frac{\Delta \epsilon}{S} = p_1 u_1 t_1.$$

And, u_1 being a function of p_1, a value of the kinetic energy transferred per surface unit of the plate into the explosive, is simply associated with each pair (p_1, t_1). Since the value $\Delta \epsilon/S$ is established, the foregoing relation defines in the (p,t) diagram an iso-energetic curve. Thus it is possible to relate and compare the experimental results to a network of iso-energetic curves.

3.2. Results

The explosives investigated are granular, homogeneous, or contained binder. The representation given below considers this classification and illus-trates the increasing homogeneity of the compositions used.

(a) **Granular Explosive**: pressed RDX ($\rho = 1.55$ g/cm^3)

For this sensitive explosive, critical impact velocities are of the order of 400 m/s, and the mode of operation described in Sec. 2 is applied. Furthermore, due to the compression necessary to reach the density of 1.55 g/cm^3, the critical grain-size distribution is changed. The grain-size ranges 200/400 μm and 100/200 μm are obtained by seeving and show, after compression, two maxima corresponding to an asymmetric rupture of the grains. The grain-size range 40/80 is obtained by pulverizing and undergoes only a reduction of its mean grain size. The distribution curves plotted after compression are obviously the only representative ones for the RDX investigated.

The sensitivity of the ranges 40/80 μm and 200/400 μm is shown in Fig. 5. We observe essentially an inversion of the sensitivity as a function of the shock duration. None of the curves confirm the criterion of a constant energy threshold. It is seen, however, that the two curves pass through an identical maximum energy value (18 kbar and 750 ns). The energy transferred per surface unit is then 68 J/cm^2.

(b) **Explosives with Binder**

In this class of explosives, we have to mention the composition B3 and the two inert binder compositions that are, therefore, more homogeneous than RDX.

- For Comp B3 the criterion of the energy threshold holds remarkably well. Over the whole range of shock duration, the threshold curve lies between 125 and 148 J/cm^2. The curve corresponding to an ignition energy of 140 J/cm^2 divides the two regions of ignition and non-ignition (see Fig. 6).

- RDX-polybutadiene shows a quite different behavior. For shock durations ranging from 600 to 2100 ns, it is initiated by a constant minimum energy supply of 325 J/cm^2. It appears to be more sensitive for short shocks. For a duration of 160 ns, a shock of 85 kbar (i.e., approximately 175 J/cm^2) suffices to provoke initiation (see Fig. 7).
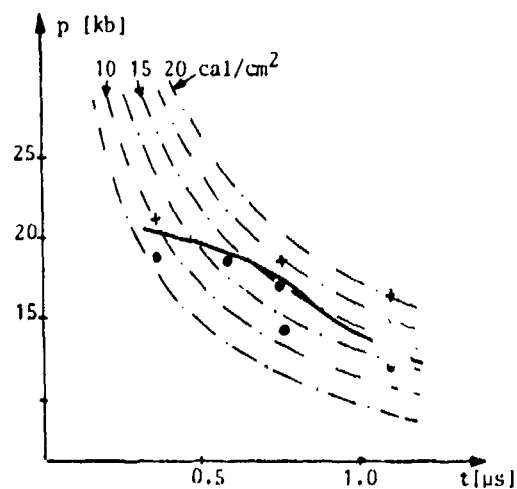
(a) - grain size : 40/80 μ
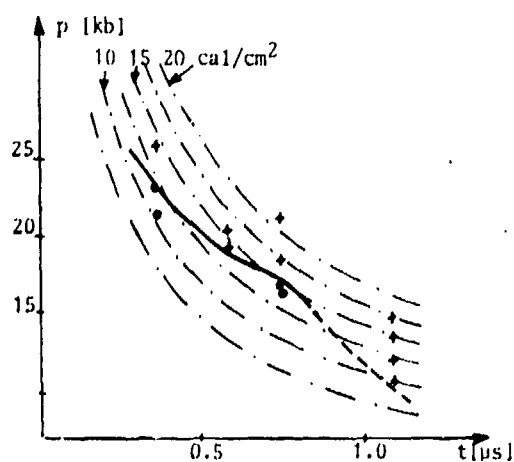
(b) - grain size : 200/400 μ

Fig. 5. Sensitivity of granular RDX.

+ detonation   *● no detonation*

● The HMX-nylon composition has a sensitivity, which is analogous to that of the composition B3. The energy threshold of initiation, which is constant and equal to 150 J/cm^2 for shock duration between 160 and 1200 ns, increases thereafter, and exceeds 180 J/cm^2 if the induced wave has a duration of 2100 ns (see Fig. 8).

(c) Homogeneous Explosives

Nitromethane and liquid TNT (T_o = 354°K) were investigated over a relatively limited pressure range
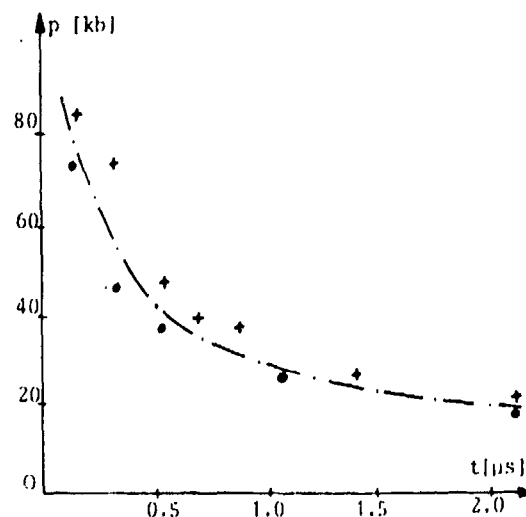
Fig. 6. Sensitivity of Composition B3 (60/40).

+ detonation   *● no detonation*

· · ― iso-energy curve E = 33 cal/cm^2
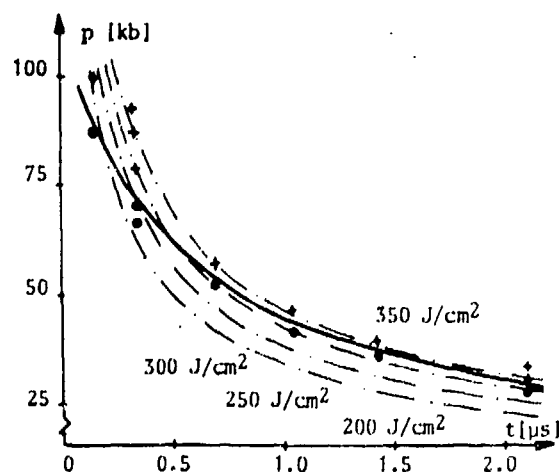
Fig. 7. Sensitivity of RDX-polybutadiene.

+ detonation   *● no detonation*

corresponding to a shock duration varying from 300 to 1700 ns. The streak camera was used (Sec. 2) to observe the points located in the vicinity of the sensitivity curve in order to ascertain that the detonation achieved was actually due to the plane part of the wave.

110
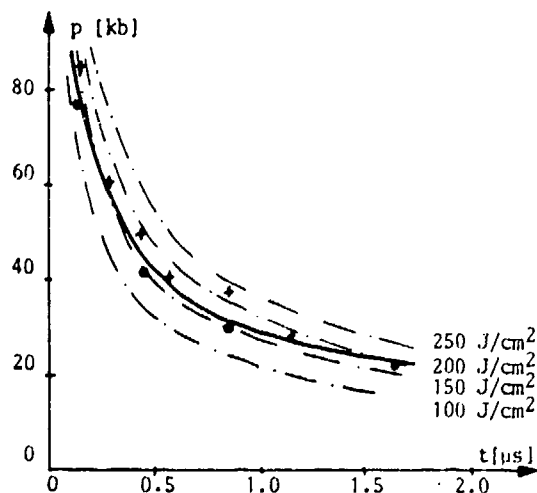
Fig. 8. Sensitivity of HMX-nylon.

+ detonation   *● no detonation*

The energy threshold for both explosives varies along the sensitivity curve (Fig. 9).

3.3. Validity of the Concept of the Energy Threshold

Except for granular RDX and liquid explosives, all of the other compositions show a certain pressure range in which the sensitivity curve coincides with an iso-transfer curve.

Figure 10 illustrates the energy threshold as a function of shock pressure.

Except for the composition B3, the energy required for initiation is seen to be lower for intense shocks.

It is presently impossible to answer the question of whether the phenomena observed are of a physical nature or can be related to an erroneous extrapolation of the Hugoniot data determined at lower pressures.

4. INTERPRETATION BY USE OF REACTION KINETICS

It has just been shown that the sensitivity can be interpreted as the minimum energy to be transferred to the explosive. This energy is, in general, a function of the shock pressure.
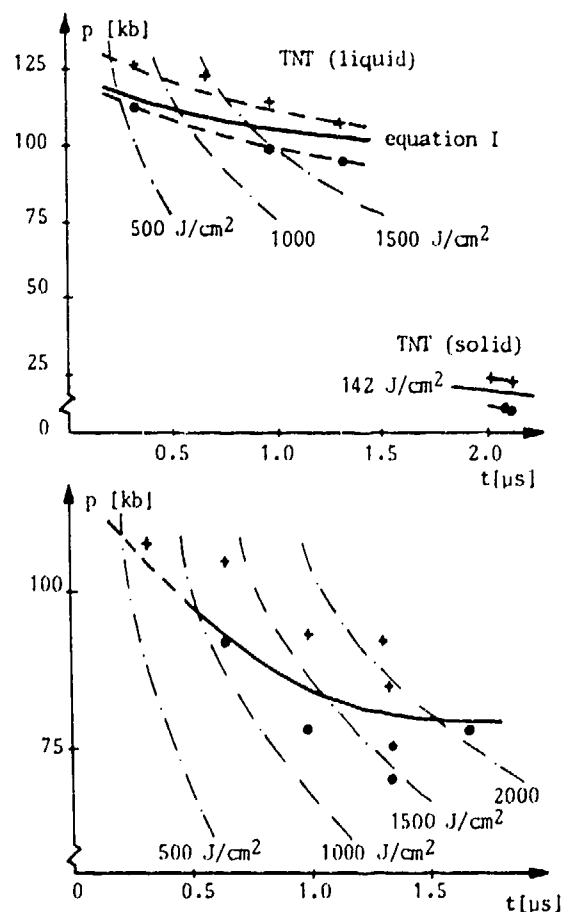
Fig. 9. Sensitivity of liquid and solid TNT (a), and nitromethane (b).

+ detonation   *● no detonation*

Another viewpoint related to an assumed role of the critical shock duration is now presented. It is supported by the following assumptions:

● Chemical reactions are initiated at the shock front, and the corresponding critical shock duration is the shortest time needed to establish a self-sustaining process: the reactions can no longer be quenched by cooling due to release waves arriving from the rear face.

● More precisely, it is assumed that a sufficient number of particles are initiated so that a subsequent transition to detonation is only governed by the energy they release.

111
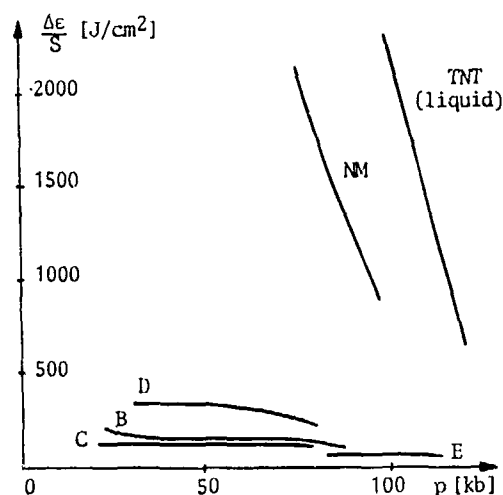
Fig. 10. Energy threshold vs shock pressure.

B = HMX-nylon
C = RDX-TNT (60/40)
D = RDX-polybutadiene
E = PBX 9404

- This condition is always fulfilled by homogeneous explosives (8); it may be a reasonable approximation for heterogeneous high explosives that are heated by a volume process rather than at a surface as occurs for granular explosives, which will not be considered for this reason.

- A comparison at a given initiation pressure between build-up times both experimental (9) and computed (10,11) and the critical shock duration would give interesting information on the possibility of quenching reactions before grain burning or any energy transfer process has occurred.

- The initiated particles are assumed to behave according to the thermal explosion model which is used for the first time with the critical shock duration assumed to be the build-up time (5,8).

Main Features of the Thermal Explosion Model Based upon the Arrhénius Law (12)

(a) The shock of pressure p heats the explosive at a temperature T_s.

(b) The instantaneous temperature is equal to $T_s + \Delta T$ where ΔT corresponds to the self heating by the chemical reactions.

(c) The numerical application of the Arrhénius law shows that a significant fraction of the explosive has reacted only during the very late stage of the total process.

Correspondingly, without knowing the minimum reaction rate for a self-sustaining regime a negligible error occurs when we assume that the critical shock duration τ is equal to the induction time t, which corresponds to a complete reaction.

Let us write

$$\tau = t_i = \nu^{-1} T_s^2 (T_q \cdot T_a)^{-1} \exp (T_a/T_s) \qquad (1)$$

where

ν = collision frequency,

$$T_a = \frac{E_a}{R} \ldots E_a = \text{activation energy,}$$

$$T_q = \frac{Q}{C_v} \ldots C_v = \text{specific heat, assumed constant.}$$

Equation (1) expresses the sensitivity (p,τ) of an explosive as a function of its chemical composition (E_a, ν, Q) and of properties $(T_s = f[p])$.

It is important to note that the following results and remarks are restricted to the case where the Arrhénius law is used.

RESULTS

Homogeneous Explosive = Liquid TNT

The numerical values of ν, E_a, Q, C_v are given by (13) =

$$\nu = 10^{12 \cdot 2} \text{ sec}^{-1}$$

$$E_a = 1.82 \cdot 10^5 \text{ J/mole}$$

$$Q = 3.87 \cdot 10^6 \text{ J/kg}$$

$$C_v = 1.37 \cdot 10^3 \text{ J/kg.}$$

$$T_s = T_0 + \frac{u^2(p)}{2 C_v}$$

112

where

$$T_o = 354°K,$$

u(p) is deduced of the momentum equation $p = \rho_o U_u$ and of the linear relationship

$$U = C + Su$$

where

$$\rho_o = 1.47 \text{ g/cm}^3$$

and

$$C_s = 2.14 \text{ mm/}\mu s$$

$$S = 1.57.$$

Figure 9a shows that the relationship $\tau(p)$ given by Eq. (1) is well within the domain (limited by dotted lines) where the experimental sensitivity curve is present.

An interesting conclusion is that the thermal explosion model supports a decrease of the energy threshold as the pressure increases.

Heterogeneous Explosives

On Fig. 9a are also reported experimental points relative to the sensitivity of solid TNT (2).

Equation (1) cannot match this region simply by changing the temperature T_o, the density ρ_o, and the values of the parameters C and S.

It is possible to get a good fit between Eq. (1) and experiment by using an activation energy about ten times lower than the one given in the literature. This has been checked for TNT and several compositions containing RDX and HMX.

It seems better to consider that the chemical constants must be kept but that the temperature previously calculated by assuming a uniform energy distribution is no longer correct. Due to the large dependence of Arrhénius law on temperature, the temperature of the hot spots or, more generally, the highest local temperature responsible for the initiation of the chemical reactions must be considered.

Later on this temperature will be called "efficient temperature" and noted T'_s. The prior calculation of T'_s as a function of p is quite impossible and it will be determined by using Eq. (1), in which τ is a known experimental quantity.

The calculations have been performed on composition B3 (where it is assumed that only the RDX is responsible for the initiation), RDX-polybutandiene, HMX-nylon, PBX 9404 (the sensitivity curve is given by Refs. 2 and 14).

In all cases, the reaction energy per unit mass is multiplied by the mass fraction of the explosive in the composition.

Figure 11 represents the "efficient energy" $C_v T'_s$ vs the pressure. It can be seen that the "efficient energy" is a slowly increasing function of the pressure.

More interesting observations can be drawn from Fig. 12 which represents the relative degree of heterogeneity of the explosive expressed by the ratio $(T'_s - T_s)/T_s$:
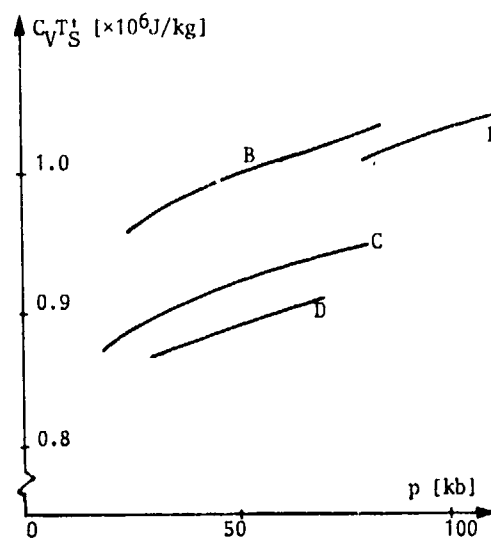
Fig. 11. Efficient energy vs shock pressure.

B = HMX-nylon

C = RDX-TNT (60/40)

D = RDX-polybutadiene

E = PBX 9404-03
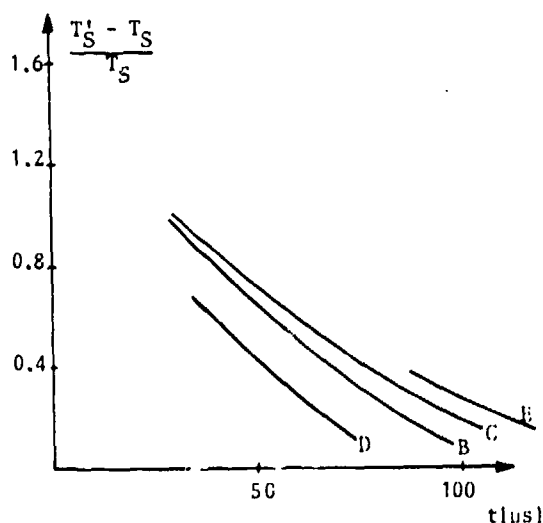
Fig. 12. Relative degree of heterogeneity =
$(T'_s - T_s)/T_s$

(See legend on Fig. 11)

- The degree of heterogeneity is at the most equal to one which corresponds to an efficient temperature equal to twice the bulk temperature.

- The higher the shock pressure, the more homogeneous is the explosive behavior.

REFERENCES

1. Y. de Longueville, "Compartment de Divers Explosifs Condensés Soumis à des Ondes de Choc Calibrées en Intensité et Durée," 5ème Coll. Intern. sur "La Dynamique des gaz en Explosion et des Systèmes Reactifs," Poitiers, September 1975. to be published in Acta Astronautica.

2. F. E. Walker, R. J. Wasley, "Critical Energy óf Shock Initiation of Heterogeneous Explosives," UCRL Report 70891, 1968.

3. H. Richter, "Sur la Théorie des Charges Creuses. Movement de Revêtements Minces en Matériau Plastique à la Surface d'un Explosif Plan," ISL Report 42/46, December 1946.

4. A. K. Hopkins, "On the Response of Mixed Material to One-Dimensional Shock Wave," Wright-Patterson AFB, Ohio, Technical Report AFML-TR-70-158.

5. J. Roth, "Shock Sensitivity and Shock Hugoniots of High-Density Granular Explosives," Fifth Symposium (International) on Detonation, pp. 219-230, ACR-184, U. S. Gov. Print. Office, Washington, DC, 1971.

6. T. P. Liddiard, "The Unreacted Shock Hugoniots for TNT and Composition B3." Proceedings of the International Conference on Sensitivity and Hazards of Explosives, ERDE Waltham Abbey, Essex, England, 1-3 Oct. 1963. Session 1.

7. UCRL-50108, Vol. 2, "Compendium of Shock Wave Data."

8. A. W. Campbell, W. C. Davis, J. R. Travis, "Shock Initiation of Detonation in Liquid Explosives," Phys. Fluids, Vol. 4, p. 498, 1961.

9. J. E. Kennedy, "Pressure Field in a Shock-Compressed High Explosive," 14th Symposium (International) on Combustion, p. 1251, The Combustion Institute, Pittsburgh, 1973.

10. M. Cowperthwaite, "Theoretical Studies of Detonation Waves," Stanford Research Institute, Final Report Project PYU-1322, March 1974.

11. C. L. Mader, "An Empirical Temperature Dependent Dremin Burn Model," Los Alamos Scientific Laboratory Report to be published.

12. R. F. Chaiken, "Thesis, Brooklyn Polytechnic Institute, Brooklyn, NY, June 1958.

13. M. A. Cook, M. T. Abbegg, Ind. Eng. Chem., 48, pp. 1090-1095, 1956.

14. B. O. Trott, R. G. Jung, "Effect of Pulse Duration on the Impact Sensitivity of Solid Explosives," Fifth Symposium (International) on Detonation, pp. 191-205, ACR-184, U. S. Gov. Printing Office, Washington, DC, 1971.

15. D. R. Hardesty, P. C. Lysne, "Shock Initiation and Detonation Properties of Homogeneous Explosives," SCA Report 74-0165, 1974.

INITIATION OF DETONATION IN INSENSITIVE LIQUID EXPLOSIVES
BY LOW-AMPLITUDE COMPRESSION WAVES

J. E. Hay and R. W. Watson
Pittsburgh Mining and Safety Research Center
Bureau of Mines
Department of the Interior
Pittsburgh, Pennsylvania 15213

An experiment devised to simulate the development of explosive reaction in a large mass of cavitated liquid is described in which a massive steel piston is propelled into a container (diameter 10 cm) filled with a liquid explosive into which bubbles have been introduced. In this experiment, transition to "detonation" has resulted using nitromethane and other marginally detonable liquids at initial piston velocities of 24 to 90 meters per second. With further increase in scale size, abrupt accelerations of the order of those occurring in transport may suffice to produce explosion.

A mathematical model is described by which the hazard potential of deflagration-to-detonation transition in large masses of a reactive liquid subjected to cavitating conditions and pressure surges can be assessed from burning rate data or from small-scale experiments such as that described.

INTRODUCTION

The accidental explosion of marginally explosive materials has been of concern for many years. "Marginally explosive materials" is here taken to mean substances not intended to be used as explosives and which are insensitive to detonation by a No. 8 blasting cap. Such substances include, for example, nitromethane (NM). Most of these substances are also assessed as "nondetonable" in the card-gap test since they have a critical diameter greater than the diameter in which the card-gap test is normally performed, usually 2.5 cm. (1) (In this paper, the discussion will be limited to those materials that are liquids as normally handled and used.) Even those substances that are known to be detonable, however, have been involved in accidental explosions in which no stimulus that would be considered adequate by the standards of normal sensitivity tests appears to have been present.

This situation is analogous to the problem encountered with nitroglycerine (NG) and related materials, which although acknowledged to be detonable, to have a small critical diameter, and to be "sensitive" by the standards of experience, and handled accordingly, nevertheless have been involved in numerous accidental explosions resulting presumably from very weak stimuli. The nature of this problem was clarified by the elucidation of the mechanisms of low-velocity detonation (LVD) as a quasi-steady-state process in which the fluid is cavitated by a precursor shock. The cavities are subsequently collapsed by the reaction pressure field, causing local heating sufficient to ignite the liquid at the cavities; the resultant burning of the liquid releases sufficient energy to sustain both the precursor and reaction wave. (2, 3, 4, 5, 6, 7) A theoretical description of LVD has been given by Chaiken. (8) In this treatment, theoretical calculations of the LVD parameters for various liquid

explosives, including nitromethane (NM), were performed; the results obtained tend to indicate that the possibility of LVD in NM is marginal. This result, however, is attributed to the large value of the calculated cavitation rate constant, which results in low values of liquid volume fraction and detonation pressure and consequent decoupling of the cavitation and reaction processes. However, interest in explosive reactions of this type is not limited to "stable" LVD, in which the cavitation is itself maintained indefinitely by the propagating reaction. It is, for instance, valid to stipulate that a significant portion is already cavitated as a result of a variety of processes that can occur in a mass of liquid in transit. In the following discussion, no attempt will be made to distinguish between gas-filled bubbles and vapor-filled cavities, although the former are more sensitive to initiation by compression, since it will be assumed that a compression wave adequate to initiate either type is present. It is then reasonable to suppose that the reaction rate is dominated by the time constant for the burning of the bubbles, given by Chaiken as

$$T_6 = \frac{K}{2N_b^{1/3}} \left[\frac{2\pi W}{RT_f}\right]^{1/2} e^{\Delta H_v/RT_f},$$

where K is the evaporation accommodation coefficient, N_b the bubble concentration, W the molecular weight, R the universal gas constant, T_f the flame temperature, and ΔH_v the heat of vaporization. This equation presupposes a pressure sufficiently high that the deflagration reaction zone is of essentially negligible thickness so that the liquid surface temperature can be considered approximately equal to the flame temperature. For the constants given by Chaiken for NM—viz K = 1, W = 61 g/mole, T_f = 2700°K, and ΔH_v = 8 kcal/mole—this results in a linear burning rate of ca 5.5×10^3 cm/sec. Elementary calculations show that such a burning rate is adequate to support a bubble growth rate of about 10^4 cm/sec at a pressure of a few Kbar; these values are "typical" at least for the system in which they have been measured (the nitroglycerine/ethylene glycol dinitrate system). (4) However, the assumption that the liquid surface temperature is equal to the flame temperature is questionable at lower pressures and may not apply to the early stages of development. Moreover, the kinetic parameters for many substances of interest are unknown. If burning rate-vs-pressure data over the entire range of pressure

were known, it should be possible to couple such a relationship to the overall hydrodynamic constraints and to predict the susceptibility of a given system to LVD, given the charge size, confinement, etc.; an attempt to do this is sketched in a later section of this paper.

Unfortunately, burning rate data for liquid explosives and monopropellants at pressures beyond a few hundred bars do not exist to the best of the authors' knowledge, nor can they be obtained by extrapolating data obtained at lower pressures, since, as is well known, (9,10) for many liquid explosives and propellants there occurs an abrupt increase in the slope of the effective burning rate-vs-pressure curve due to hydrodynamic enhancement of the burning surface; neither the pressure at which this occurs nor the magnitude of the increase in the slope can be predicted from low-pressure data.

The continued introduction of new materials in industry makes it desirable to have some kind of test that can be used to predict the possibility of the development of explosions from weak stimuli which might occur in the handling of large masses of material. That this cannot be done on the basis of tests presently considered standard is shown dramatically by the explosion of a tank car of aqueous monomethylamine nitrate solution at Wenatchee, Wash., in 1974, (11) and by the explosions of two tank cars of NM at Mt. Pulaski, Ill., and Niagara Falls, N.Y., in 1958. (12)

The purpose of this paper is to describe a test devised for the study of the development of explosive reactions from weak stimuli in large masses of marginally explosive liquids. It is not pertinent to the purpose of this paper to differentiate precisely between high-velocity detonations, low-velocity detonations, non-ideal detonations, etc. An "explosion" will be considered to be any chemical reaction that releases gases and energy rapidly enough to cause rupture of the confinement and displacement of surrounding objects. A marginal explosive is any material not intended to be used as an explosive and that cannot be detonated by a No. 8 blasting cap, but that is at least theoretically capable of reacting in the way just described. A weak stimulus is arbitrarily defined as one that produces pressures less than 1 kilobar.

DESCRIPTION OF THE EXPERIMENT

A schematic drawing of the experiment is given in figure 1. The marginally explosive liquid (MEL) is contained in a steel cylinder of 10.2-cm inside diameter, 15.2-cm length, and 1.27-cm wall thickness, with a 20.3-cm-square, 5.1-cm-thick steel plate welded to one end and a 0.0076-cm-thick polyethylene diaphragm fastened across the other end. Air bubbles are introduced into the liquid by means of a 15-cm length of polyvinyl chloride tubing (0.24-cm outside diameter, 0.04 cm wall thickness) which is closed at the end but which has two rows of pinholes (.023-cm diameter) spaced 0.3 cm apart along the entire length. Air is supplied to the bubbler tube at a gage pressure of 0.55 to 1.4 bars, depending on the properties of the liquid, to maintain a bubble field as nearly uniform as possible from one liquid to another.

The initiating stimulus is provided by the impact of a steel projectile 9.84 cm in diameter, and 13.3 cm long, weighing 8.1 kg. The projectile is provided with two bands of rubber tape 1.9 cm wide; one of the bands is at the rear of the projectile, and the other is slightly forward of the middle of the projectile. The bands are just thick enough to produce a snug fit in the projector barrel. The projectile is propelled down a steel barrel (10.2-cm ID, 3.3-m length) by compressed air from a 72-liter reservior. A quick-opening "valve" used to admit the air to the barrel, consists of a multilayer diaphragm made from cellulose acetate sheets 0.025-cm thick across a pipe flange at the breech end of the barrel. The number of layers

needed depends on the pressure used: approximately one layer for each three bars is typical. The diaphragm is burst by a No. 8 electric blasting cap. The projectile velocity is measured electronically by the contact of the projectile with two pairs of fine copper wires stretched across the diameter of the barrel spaced 50 cm apart. As would be expected, the velocity attained varies roughly as the square root of the pressure: at 21 bars, approximately 90 m/sec is attained. The sample (acceptor) is approximately 4 cm from the end of the barrel and is aligned co-axially with it to a precision of about ±0.04 cm. It should be noted that the projectile diameter is less than that of the sample container by 0.32 cm; this is to allow some margin for misalignment so that the projectile does not touch the walls, and also to provide some relief for the internal pressure, since the experiment is intended to simulate realistic situations in which there is some possibility of venting and in which the confinement is provided primarily by the mass (inertia) of the material itself. In this experiment the inertia is provided by the projectile, which must be deccelerated and repulsed in order to relieve the pressure in the sample.

The occurrence of explosion is based on the rupture of the sample cylinder, the blast produced, and the consumption of the liquid. Although the materials tested vary greatly in their explosive output and the impact pressures are occassionally sufficient to crack the weld joint, the minimum criterion for assessing the occurrence of explosion is that the cylinder be essentially completely unfolded into a strip or broken to pieces, that significant blast be produced, and that the material be completely consumed. Only one material, liquid dinitrotoluene, was found to be consumed without container damage or blast, and one other, 52/48 nitromethane/1-nitropropane, was consumed and produced blast without container damage; these were assessed as "deflagrations."

It was found to be quite difficult to either control or characterize the bubble field in the sample. Photographic observation suggests that the diameters of the bubbles are in the range of 0.05 to 0.2 cm, and the density of the bubbles appears to be in the range of 0.5 to 10 cm^{-3}, depending on the viscosity and surface tension of the liquid. The importance of bubble size and density was established in the earliest experiments with nitromethane, wherein it was found that initiations could not be obtained at the highest
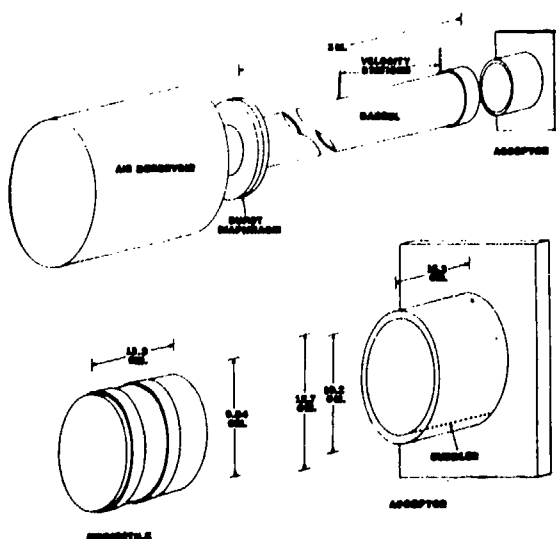

Fig. 1. Experimental arrangement

117

velocity available when only one or a few large bubbles were present. This observation also lends weight to the supposition that the compression of the bubbles is the initiation mechanism, rather than friction due to possible contact of the projectile with the acceptor walls, or viscous heating of the liquid flowing between the projectile and the acceptor walls.

The pressures produced by reaction cannot be stated with certainty. Several experiments using NM were instrumented with piezoresistive pressure gages, (13) and the response of these suggests pressures in the range 1-10 kilobars, but it is not certain whether the calibration of the gages for normal shock waves should be applied in a situation where th gage is subjected to non-uniform pressure fields that increase over a time scale of about 10^{-4} seconds. Since the impact of the projectile at the highest velocity produces about 2.5 kilobars and this normally only slightly bulges the acceptor and/or cracks the weld, the pressures involved in those cases assessed as "explosions," which completely unfold or shatter the acceptor, would seem to be much greater. However, since deliberate initiation of high-velocity detonation in NM in these acceptors by means of a tetryl booster produces smaller fragments than the reaction induced in this experiment, the latter probably cannot be considered a fully developed Chapman-Jouguet detonation.

RESULTS AND DISCUSSION

To date, most of the materials tested have been those that are, or have been, transported in large bulk quantities (e.g., 38,000-liter railroad tank cars). The results are given in table 1. The "threshold velocities" given in this table are the mean between the highest velocity at which no explosion resulted, and the lowest velocity at which explosion resulted. The error interval given is the difference between these values. No inversions (negative result at a higher velocity than a positive result) were observed in this experiment. In one case (52/48 nitromethane/1-nitropropane) a negative and positive result were obtained at the same velocity.

Referring to this table, it will be noted that the two materials that have "detonated" without obviously sufficient stimulus in tank cars, namely NM and the amine nitrate solution, are those that have

the lowest threshold velocities for explosion in this experiment, namely 24 m/sec. Because of differences in scale size, confinement, etc., it is of course not possible to state that the velocities in the table can be identified with impact velocities that are likely to cause explosion in realistic situations; it does, however, seem reasonable to believe that the velocities reported give relative rankings of the safety of a particular formulation in a large-scale bulk transport operation. Since the LVD model assumes that the reaction at the walls of the bubbles is a monopropellant burning, it would be tempting to attempt to correlate the results obtained with burning rates. Only limited success would be expected with such a correlation, since the dependence of burning rate on pressure is in general not known, and the pressures in the bubbles are probably much higher than that attainable in a strand-burning apparatus. Nevertheless, such a comparison is set out in table 1, from which it can be seen that rough correlation exists; namely, that those systems that have burning rates less than about 0.13 cm/sec at 11 Mpa do not seem to explode at the highest velocity attainable in this experiment, and those that have burning rates substantially greater than 0.13 cm/sec at the same pressure exploded at lower impact velocities.

THEORETICAL DISCUSSION

A detailed description of the dynamics of a field of bubbles that are burning at their surfaces requires a twofold, three-dimensional hydrodynamic treatment (the neighborhood of any bubble is a three-dimensional problem, and the motion of the whole liquid in response to the collective motions of the bubbles is another such problem); such a treatment is quite beyond the scope of this paper. What is presented here is an extremely simplified model; it is believed, however, that the assumptions made do not invalidate the predictions of the model, but only limit their accuracy.

The first such assumption is that the liquid may be considered as essentially incompressible. This obviously limits the applicability of the model to pressures less than the order of a few kilobars, that is, to the early stages of deflagration-to-detonation transition. With this assumption, the radial velocity u of the liquid at a distance r from the center of a bubble of radius r_b is

118

$$u = \frac{r_b^2 U_b}{r^2}, \qquad (1)$$

$$\frac{dr_b}{dt} = U_b + U_B. \qquad (2)$$

where U_b is the radial velocity of the liquid at the boundary of the bubble.

One notes that the growth of the bubble is due to the flame eroding the liquid at an effective velocity U_B, as well as to the outward motion of the liquid, U_B, i.e.,

Equation (1) can be differentiated with respect to time, and substituting equation (2), one has

$$\frac{du}{dt} = \frac{r_b^2 \dfrac{dU_b}{dt} + 2r_b U_b(U_b + U_B)}{r^2}. \qquad (3)$$

TABLE 1

*Comparison of Experimental Results with Liquid
Strand Burning Rates*

Material	Threshold velocity, m/sec	Burning rate at 11 MPa[1] cm/sec
NM	24 ± 2	.27
Amine nitrate aqueous* solution 88%	24 ± 6	1.5[2]
Amine nitrate aqueous* solution 69%	59 ± 6	.605
Nitrate ester aqueous* solution 75%	53.5 ± 7.5	.28
Nitrate ester aqueous* solution 50%	61 ± 2	.31
n-Propyl nitrate	91.5 ± 1.5	.21 – 12[3]
Dinitrotoluene	52.5 ± 4.5[4]	.29[2]
NM/1-NP 52/48	∿90[4]	.026[5]
Nitrate ester aqueous* solution 38%	>113	[6]
NM/Toluene 70/30	>122	.10
NM/Benzene 70/30	>114	.12
NM/2-NP 53/47	>119	.028
NM/Cyclohexanone 75/25	>92	.04
NM/Dioxane 65/35	>91	.03
NM/Methanol 55/45	>91	.031
NM/Methylchloroform 70/30	>92	.08
NM/Butylene Oxide 60/40	>74	.015[5]

*Proprietary compositions.
1/Data reference.
2/Measured at 7 MPa.
3/Unstable burning.
4/Deflagrations.
5/Measured at 9.5 KPa.
6/Cannot be ignited at this pressure.

One then defines a "vicinal pressure," P_v, as the pressure at a large distance, r_v, from the bubble under consideration ($r_v \gg r_b$); it should be remembered that, for the bubble field as a whole, P_v is still a local pressure, not to be confused with the pressure external to the entire system. The hydrodynamic form of Newton's second law may then be integrated from r_b to r_v, using equation (3) and neglecting terms in $1/r_v$ (since $1/r_v \ll 1/r_b$), obtaining

$$P_b = P_v + \rho \left[r_b \frac{dU_b}{dt} + 2U_b(U_b + U_B) \right], \quad (4)$$

where P_b is the pressure in the bubble and ρ is the density of the liquid. Setting the volume of the bubble equal to the volume of the combustion products, using the Abel equation-of-state, and assuming isothermal expansion for the sake of simplicity, one obtains

$$\frac{4\pi}{3} r_b^3 = n \left(\frac{RT}{P_b} + b \right), \quad (5)$$

where n is the number of moles of gas contained in the bubble, R is the gas constant, T is the absolute temperature, and b is the average covolume. Differentiating equation (5) with respect to time and using equation (2), one obtains

$$4\pi r_b^2 (U_b + U_B) = \left(\frac{RT}{P_b} + b \right) \frac{dn}{dt} - \frac{nRT}{P_b^2} \frac{dP_b}{dt} \quad (6)$$

but

$$\frac{dn}{dt} = 4\pi n_o \rho r_b^2 U_B, \quad (7)$$

where n_o is the number of moles of product gases produced per gram of liquid consumed Inserting this into equation (6) and rearranging, one has

$$U_b = \left[\left(\frac{RT}{P_b} + b \right) n_o \rho - 1 \right] U_B \frac{nRT}{4\pi r_b^2 P_b^2} \frac{dP_b}{dt} . \quad (8)$$

Before proceeding further, other simplifying assumptions will be made. First, the quantity $(bn_o\rho - 1)$

may be neglected in comparison with RT/P_b; this is a good assumption for values of P_b less than the order of tens of kilobars. Second, the effective burning rate U_B will be considered a linear function of the pressure P_b, i.e.,

$$U_B = \beta P_b \quad (9)$$

where β is a constant. Inserting equation (9) into equation (8), dropping the term $(bn_o\rho - 1)$, and rearranging, one has

$$\frac{dP_b}{dt} = \frac{4\pi r_b^2 P_b^2}{nRT} (RTn_o\rho\beta - U_b). \quad (10)$$

Inserting equation (9) into equation (4) and rearranging yields

$$\frac{dU_b}{dt} = \frac{1}{r_b} \left\{ \left(\frac{1}{\rho} - 2\beta U_b \right) P_b - 2U_b^2 \frac{P_v}{\rho} \right\} \quad (11)$$

(In the solution of equations (2), (10), and (11), r, P, and U_b are found to be slowly damped oscillating functions of time.)

It remains now to consider the vicinal pressure and the system as a whole. Consider a spherical mass of reactive liquid of radius r_x and a spherical shell of radius r within the liquid, enclosing a constant mass. Due to the expansion of the bubbles contained within it, this shell will expand with a velocity given by

$$U = \frac{1}{4\pi r^2} \frac{dV}{dt}, \quad (12)$$

where dV/dt is the rate of expansion of the volume enclosed.

If the liquid is incompressible, then dV/dt is just the rate of increase in the volume of the gas minus the volume rate of consumption of the liquid and by the arguments used in developing equation (10) it is just

$$\frac{dV}{dt} = 16\pi^2 \nu \int_0^r r^2 r_b^2 U_b \, dr, \quad (13)$$

where ν is the number of bubbles per unit volume of liquid. Thus

$$U = 4\pi\nu \, \frac{\displaystyle\int_0^r r^2 r_b^2 U_b \, dr}{r^2} \, . \qquad (14)$$

For simplicity it will be assumed that the spherical mass of liquid consists of an inner region of radius r_1, containing uniformly reacting bubbles, and an outer shell of radius r_0, in which the bubbles, if present, are nonreactive. Then equation (14) may be rewritten

$$U = \frac{4\pi}{3} \, \nu r_1^3 \, \frac{r_b^2 U_b}{r^2} \, . \qquad (15)$$

Differentiating equation (15) again with time and noting that νr_1^3 is invariant (creation of new cavities is not a feature of this model), and using equation (2), one has

$$\frac{dU}{dt} = \frac{4\pi}{3} \, \nu r_1^3 \, \frac{r_b^2 \, \dfrac{dU_b}{dt} + 2r_b U_b(U_b + U_B)}{r^2} \, . \qquad (16)$$

Using equation (9) for U_B, the resulting expression for dU/dt may be substituted into the hydrodynamic form of Newton's second law and integrated to give

$$P_v = P_o + \frac{4\pi}{3} \, \rho\nu r_1^2 r_b \left\{ r_b \, \frac{dU_b}{dt} + 2U_b(U_b + U_B) \right\} \left(1 - \frac{r_1}{r_o} \right) , \qquad (17)$$

where P_o is the pressure external to the entire mass of liquid. Noting that ρ times the quantity in brackets is just $P_b - P_v$ by equation (4), one can write

$$P_v = P_o + \frac{4\pi}{3} \, \nu r_1^2 r_b (P_b - P_v) \left(1 - \frac{r_1}{r_o} \right) . \qquad (18)$$

This can be rearranged to yield

$$P_v = \frac{P_o + \dfrac{4\pi}{3} \, \nu r_1^2 r_b P_b \left(1 - \dfrac{r_1}{r_o} \right)}{1 + \dfrac{4\pi}{3} \, \nu r_1^2 r_b \left(1 - \dfrac{r_1}{r_o} \right)} \, . \qquad (19)$$

This shows that, as the quantity $4\pi/3 \, \nu r_1^2 r_b (1 - r_1/r_o)$ increases, the value of P_v approaches that or P_b. The effect is to reduce the outward acceleration of the bubbles, given by equation (11), which is precisely what would be expected. The bubble volume thus cannot increase as rapidly as product gases are formed, and the internal pressure increases much more rapidly than in the case of a single bubble. Equations (2), (10), and (11) may be integrated numerically using equation (19). Results for various values of the parameters are illustrated in figure 2.

These curves show, as expected, that the development of explosive reaction is very sensitive to the burning rate parameter β (compare curves A and B, which show an order of magnitude increase in the pressure at any time with a factor of 2 increase in β), somewhat sensitive to the radius r_1 of the cavitated portion (compare B and C), slightly sensitive to the radius r_0 of the entire mass (compare curves C and D), and somewhat sensitive to the bubble density ν (compare curves D and E). These calculations were started with atmospheric pressure in the bubbles, with initial bubble radius 0.1 cm, and with initial value of $U_b = 1$ cm/sec. The value of the quantity $RTn_o\rho$ was taken as 10^{10} dyn/cm^2. The "hook" at the end of some of the curves is due to the fact that the outer boundary of the liquid is now expanding so rapidly that the reaction can no longer sustain the pressure.
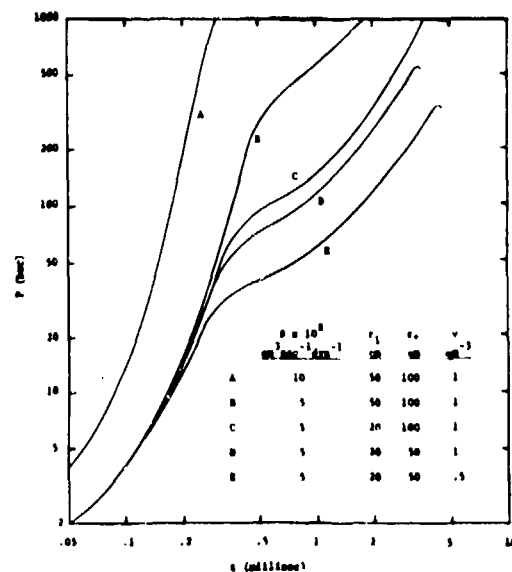

Fig. 2. Calculated bubble pressure vs time for various values of parameters

121

It is obviously not possible at present to test in detail the validity of this model, since realistic values of the pertinent parameters are largely unknown, as are the results of the type of experiment that would be required to test it. Furthermore, the limitations of the model at this stage are obvious; namely, the use of the Abel equation-of-state, and the assumptions that the liquid is incompressible, that the bubble expansion is isothermal, and that increases in the surface area of the bubbles due to hydrodynamic effects can be accounted for simply by using an enhanced value of the effective burning rate. These simplifications require future elaboration. What is offered here is a framework of a model for a process which the authors feel deserves considerably more attention, both theoretically and experimentally, for its inherent scientific interest as well as its relevance to hazard prediction.

CONCLUSIONS

A test has been described that demonstrates that cavitated, marginally explosive liquids, when subjected to relatively weak shocks under the confinement provided by the inertia of a large mass, can react in a way that resembles a low-velocity detonation. A simplified theoretical model of such an event has been developed which, in principle, permits the prediction of the development of explosive reaction in large masses of such material. The theoretical model indicates, in agreement with experiment, that the development of explosion is critically dependent on the dependence of burning rate on pressure, and also increases both with bubble density, and importantly, with scale size. The results of both the experiment and the model indicate that the hazard potential of a large mass of marginally explosive liquid can be estimated from experiments of the type described herein, or from the basic properties of the liquid, in particular, the burning rate-vs-pressure relationship.

ACKNOWLEDGMENTS

The authors wish to thank Mr. J. T. Naughton, who did some of the calculations, and Messrs J. A. Brandis, A. E. Page, A. D. Prokop, and D. A. Voigt, who executed the experiments.

REFERENCES

1. Ribovich, J., R. W. Watson, and F. C. Gibson. Instrumented Card-Gap Test. AIAA Journal, v. 6, No. 7, July 1968, pp. 1260-1263.

2. Gibson, F. C., C. R. Summers, C. M. Mason, and R. W. Van Dolah. Initiation and Growth of Detonation in Liquid Explosives. Proc. Third Symposium on Detonation, Princeton, NJ, September 26-28, 1960, pp. 436-454.

3. Watson, R. W., C. R. Summers, F. C. Gibson, and R. W. Van Dolah. Detonation in Liquid Explosives: The Low-Velocity Regime. Proc. Fourth Symposium (International) on Detonation, White Oak, MD, October 12-15, 1965, pp. 117-125.

4. Hay, J. E., and R. W. Watson. Mechanisms Relevant to the Initiation of Low-Velocity Detonations. Ann. NY Academy Sci., v. 152, 1968, pp. 621-635.

5. Watson, R. W., J. Ribovich, J. E. Hay, and R. W. Van Dolah. The Stability of Low-Velocity Detonation Waves. Proc. Fifth Symposium (International) on Detonation, Pasadena, CA, August 18-21, 1970, pp. 81-88.

6. Hay, J. E., J. Ribovich, F. H. Scott, and F. C. Gibson. The Effect of Physical and Chemical Properties on the Sensitivity of Liquid Explosives. Proc. Fourth Symposium (International) on Detonation, White Oak, MD, October 12-15, 1965, pp. 412-425.

7. Watson, R. W. The Structure of Low-Velocity Detonation Waves. Twelfth Symposium (International) on Detonation, The Combustion Institute, Pittsburgh, PA, 1969, pp. 723-729.

8. Chaiken, R. F. On the Mechanism of Low-Velocity Detonation in Liquid Explosives. Astronautica Acta, v. 17, 1972, pp. 575-587.

9. Hildebrand, D. L., and A. G. Whittaker. J. Phys. Chem., v. 59, 1955, pp. 10.

10. Ordzhorikidze, S. K., A. D. Margolin, P. F. Pokhil, and E. Yu. Shuridin. Combustion of

Liquid Explosives in a Field of Inertial Forces. Fizika Goreniya i Vzryva, v. 9, 1973, pp. 391-394.

11. National Transportation Safety Board. Railroad Accident Report, Burlington Northern Inc., Monomethylamine Nitrate Explosion, Wenatchee, Washington, August 6, 1974. Report No. NTSB-RAR-76-1.

12. Interstate Commerce Commission. ExParte 213. Accident Near Mount Pulaski, Illinois. 305 I.C.C., 1959, pp. 81-87.

13. Watson, R. W. Guage for Determining Shock Pressures. Review of Scientific Instruments, v. 38, 1967, pp. 978-980.

DISCUSSION

R. I. SOLOUKHIN
Heat and Mass Transfer Institute
BSSR Grad. Sci. MINSK 220728 USSR

The effects of an asymmetric collapse should be taken into account when the bubble in question is subjected to shock compression. These effects appear basically due to the shock-to-surface reflection interactions when asymmetrical bubble surface velocity distributions are generated before the gas sphere begins to collapse. Finally, this can result in an accumulating liquid jet which develops and propagates in the direction of the shock wave.

CELLULAR STRUCTURE OF DETONATION IN NITROMETHANE
CONTAINING ALUMINUM PARTICLES

Y. Kato and C. Brochet
Laboratoire d'Energétique et de Détonique
(Associé au C.N.R.S.)
E.N.S.M.A., Université de Poitiers
86034 Poitiers, France

The detonations of NM-PMMA/Al mixtures (PMMA is added as gelling agent) have been investigated. The detonation velocity in tubes of various diameters has been measured to determine the "infinite diameter velocity" D_∞ in terms of Al concentration. The detonation waves have been observed with the high speed framing camera technique. The observation through side tube wall has shown the regular repetition of failure and reignition processes revealed owing to aluminum combustion. The butt-end record has demonstrated the origin and mechanism of these processes. The failure and reignition processes have been interpreted on the basis of cellular structure. It has also been shown that the increase of Al concentration sensitizes the explosive mixtures.

INTRODUCTION

The complex structure of the detonation wave can be expected for detonating media such as liquids and solids, since it is well known in gaseous mixtures. A survey paper (1) has been presented recently to emphasize the progress made in this field through the preceding works of Campbell et al. (2), Dremin et al. (3,4,5), Watson (6), Persson et al. (7), Urtiew et al. (8) and Presles et al. (9,10). Moreover difficulties have appeared because the attention was focused at first on phenomena described as dark waves and failure waves, and later, on the fine structure left on heavy walls. One of the aims of this work is an attempt to continue, on the idea of Urtiew's paper (1), bringing experimental support to the postulate that the failure process and cellular structure are strongly connected. The difficulty in studying the detonation in heterogeneous explosives has also led us to investigate the liquid explosive-metal particles system (NM-Al) which may give us the advantage of simulating solid explosive. This system is particularly interesting for

reactivity of metal particles in detonation processes. The thermodynamic-hydrodynamic code calculations (11,12) have been performed for the detonation in solid explosive-Al system assuming two extreme cases (Al stays inert or Al reacts completely to Al_2O_3 at C-J plane). The results show the strong dependence of the C-J temperature on the Al reactivity.

Recently, Teychenne de Blazi et al. (13) have measured the brightness temperature of the detonation in NM-PMMA/Al mixtures. The measured brightness temperature is slightly higher than that measured when adding inert particles instead of Al. At the present stage, it is not clear whether or not this is entirely due to the combustion of small part of Al at C-J plane. Finally, we want to determine, with higher precision, the detonation characteristics of NM-PMMA/Al mixtures: the infinite diameter velocity, diameter dependence of detonation velocity, the effect of Al addition on detonation sensitivity (14,15), and the effect of Al addition on brightness temperature.

1. Characteristics of the Explosive Mixtures

We realised the charges of nitromethane (NM) containing aluminum particles (Al) in the range of concentration 5-15% in mass. The addition of 3% in mass of polymethylmethacrylate (PMMA) to NM increased its viscosity sufficiently to obtain stable suspension of Al in it. To avoid air bubbles, the explosive mixtures were prepared by mixing Al with homogeneous, viscous NM-PMMA mixture at least several hours before the shot.

Because of the opacity of the explosive mixtures, the uniformity of Al distribution was not verified accurately, but checked to be unvarying.

The composition of the explosive mixtures NM-PMMA/Al was defined by the mass fraction x of Al to NM-PMMA. The main physical properties of the components are given in Table 1. We have measured the initial density ρ_o of the explosive mixtures as a function of x. The measurements were performed within 0.1% at the temperature range 10-25°C.

Table 1 also gives these measured initial densities at $T_o = 288°K$, with those computed assuming ideal mixtures ρ_{th}. It must be emphasized that the measured initial densities are about 0.5% higher than those computed assuming ideal mixtures.

2. Measurements of the Detonation Velocity

To determine the "infinite diameter velocity" D∞, we investigated the influence of the charge diameter on the detonation velocity when all other parameters are known (mechanical and geometrical configuration of tubes, position of the ionization probes). The standard detonation tube, as shown in Fig. 1, is a hollow, internally polished brass cylinder (290 mm in length, 0.5 mm in thickness) with the ionization probes very accurately set inside polypropylene holders. The upper part of the tube is capped by a cylindrically confined donor charge, initiated by an exploding detonator. The detonation tube has 5 ionization probes, separated by 50 mm from each other, so that 4 propagation times at different test zone lengths are measured successively in one shot.

TABLE 1

Some informations about the components of the explosive mixtures

Nitromethane	CH_3NO_2, 96% commercial grade main impurities: $C_2H_5NO_2$(2 – 2.5%), $C_3H_7NO_2$(1.5 – 1.7%) initial density: 1.140 g/cm³ (at $T_o = 288°K$)
Aluminum	99%, main impurities: Cu, Fe, Mn and grease particle form: sphere, particle diameter 8-15 μm initial density: 2.70 g/cm³
PMMA	(C5 – H8 – O2)$_n$, initial density: 1.180 g/cm³

Initial densities of the explosive mixtures $T_o = 288°K$.

	ρ_o (g/cm³)	ρ_{th} (g/cm³)
x = 0	1.147	1.141
0.05	1.180	1.175
0.10	1.216	1.211
0.15	1.251	1.249
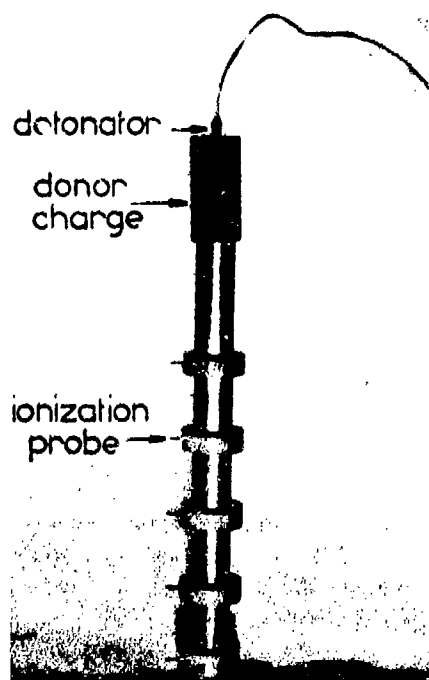
Fig. 1. Standard detonation tube.
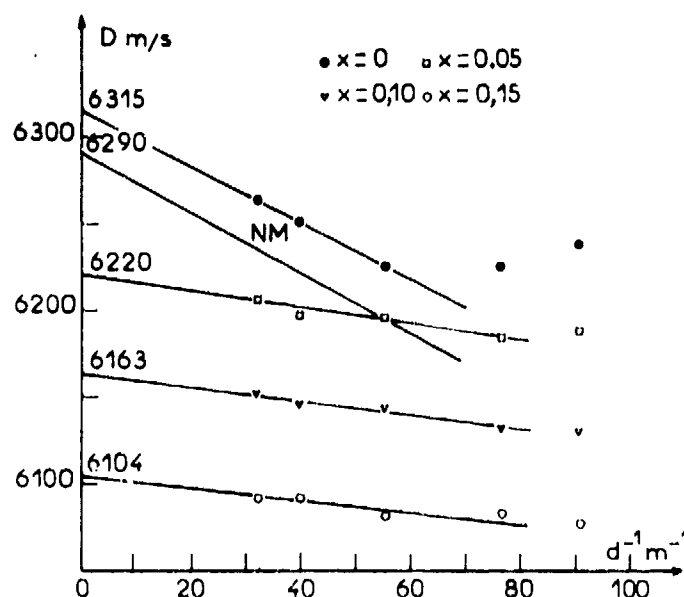
Fig. 2. Detonation velocity of NM-PMMA/Al mixtures versus d^{-1}; $T_o = 288°K$; NM values are cited from (16).

The details of the ionization probes has been described in (16).

Propagation times were measured to within 10 ns with a "time interval electronic counter" connected with pins through a signal converter (17), so that the detonation velocity is computed to within 0.1% at 150 mm test zone length. Thus, detonation velocity measurements in tubes of various diameters ($d = 11$, 13, 18, 25 and 31 mm) for different values of x have yielded the variation of D versus d^{-1}, and thanks to the least square linear approximation, we obtain finally the D_∞ values. The maximum deviation of the so defined measured values from linear approximation does not exceed 1 m/sec in the case of $x = 0$, and 6 m/sec in the case of $x = 0.05, 0.10, 0.15$. The D_∞ values may be considered to be known to within 1 m/sec in the first case, and 6 m/sec in the latter case.

The results, given in Fig. 2 (Detonation velocity versus d^{-1}) and Fig. 3 (variation of D_∞ value in function of x) show the following particular features.

1. We observe a deviation of measured values from the linear approximation at small diameter ($d = 11$
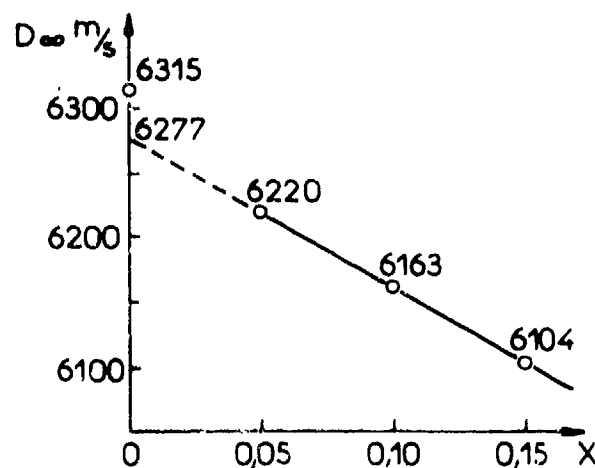
Fig. 3. Infinite diameter velocity D_∞ of NM-PMMA/Al mixtures versus x; $T_o = 288°K$.

and 13 mm) in the case $x = 0$. In other cases ($x = 0.05, 0.10, 0.15$), we distinguish slight deviation at diameter $d = 11$ mm. These measured values were neglected in the least square approximation to determine D_∞.

126

2. The D_∞ value of NM-PMMA mixtures is 25 m/sec higher than that of commercial grade NM (16).

3. The addition of Al noticeably diminishes the slope $|\partial D/\partial(d^{-1})|$.

4. Within the measured x range, the detonation velocity decreases in proportion to Al fraction x.

5. The linear extrapolation of $D_\infty(x)$ to $x = 0$ gives 6277 m/sec as $D_\infty(0)$. This value is evidently different from the measured value 6315 m/sec within the experimental error (Fig. 3).

It may be emphasized that the precision of velocity measurements has been improved with a new experimental set-up. Taking into account the higher measured initial density shown in Table 1, the fact described in (2) seems to be the result of a molecular interaction between NM and PMMA. The accuracy of the whole results seems to us to confirm the Al distribution uniformity in the mixtures.

According to the author's knowledge, there are no exactly comparable data for aluminized explosives. Cited by Price et al. (18), Coleburn et al. have studied the effect of Al on the detonation velocity at a fixed diameter (d = 50.8 mm) of TNT, RDX and TNETB. Their results show that in aluminized TNT, the detonation velocity decreases proportionally to Al concentration, but not in proportion to Al concentration in aluminized RDX and TNETB.

We cannot apply the empirical equations suggested by Kamlet and Jacobs (19) to NM-PMMA/Al mixtures owing to the difficulty cited by Kamlet and Ablard (20).

3. The High Speed Framing Camera Observations

3.1 The butt-end observations.

We observed the detonation waves through end glass plate with high speed electronic framing camera IMACON (10^7 frames/sec, exposure time 20 ns).

The detonation tube was a 100 mm long polished brass cylinder (inside diameter 18 mm, wall thickness 1 mm), or 140 mm long polyvinylchloride (PVC) cylinder (inside diameter 18 mm wall thickness 4 mm). One end of both tubes was covered with a 6 mm thick glass plate. The explosive mixtures were initiated by a 50 mm long, cylindrically confined donor charge through a 2 mm thick teflon barrier. The camera view was directed along the axis of the tube normal to the detonation wave front. Because of the opacity of the explosive mixtures, we observed the evolution of detonation phenomena in the thin layer of explosive in contact with end glass plate. Our observations time was limited to about 1 μsec. Mallory and McEvan (21) have studied the transparency of glass and certain plastics under shock attack, and they have shown that these materials stay transparent until shattered by tension waves. Our observations confirmed their experimental results.

Figure 4 shows the sequence of the butt-end record of the detonation wave in NM-PMMA/Al (x = 0.10) confined in PVC tube. Figure 5 shows the enlargement of 4th frame in Fig. 4.

As shown by Persson and Sjolin (22), the detonation light loses its intensity rapidly upon impact on end glass plate.
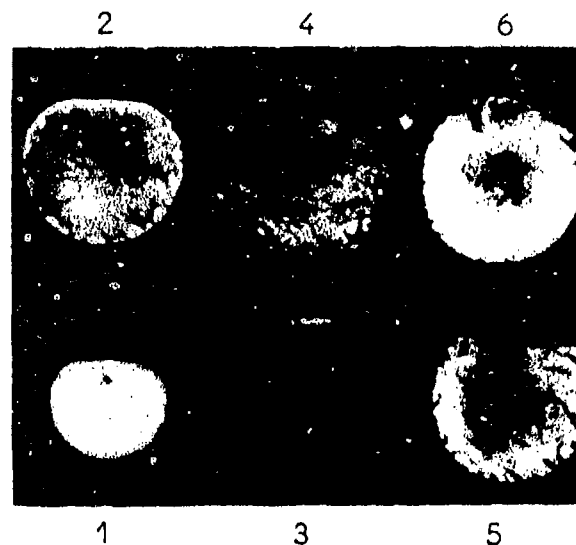
Fig. 4. Sequence of the butt-end record of the detonation in NM-PMMA/Al (x = 0.10) confined in PVC tube; time interval is 100 ns; the detonation front is curved and its upper part (1st and 2nd frame) is disturbed by ionization probe located 5 mm from the end glass plate triggering the camera; the dark point in the center of each frame is due to the defect of photocathode of camera IMACON.

With certain delay, the luminous zones corresponding to aluminum combustion appear. Particular features are observed on the charge periphery. In the 2nd frame, we observe the failure waves in half-circular band shape which are produced at the wall, and behind them, reinitiation waves. In the 3rd frame, the light of reinitiation waves is quenched upon impact on end plate. In the 4th frame, the luminous zones due to aluminum combustion appear in the same place where reinitiation waves have been generated just before. The penetration of the failure waves is limited to charge periphery.

Figure 6 shows the sequence of butt-end record of the detonation wave in the same explosive mixture confined in brass tube. The general aspects are similar to those described for Fig. 4. However, considering the resolving power of polaroid film, we cannot observe any failure wave in this case.

3.2 The observations through lateral window.

To get additional information, we observed the detonation waves through a side PMMA wall with a high speed framing camera C14 (10^6 frames/sec, exposure time $0.3 \, \mu sec$). The experiments were carried out with a 100 mm long, cross-section ($20 \times 20 \, mm^2$) tube composed of 1.5 mm thick upper and lower brass walls and 6 mm thick PMMA side walls. PMMA was used because it has about the similar shock impedance of PVC. Figure 7 shows the sequence of development of the detonation wave in NM-PMMA/Al ($x = 0.10$) mixture. The very fine, regular criss-cross pattern composed of bright and dark lines is characteristic of records. Comparing with Fig. 4 we can identify the dark lines to be the traces of failure waves generated at the wall and the bright lines correspond to aluminum combustion initiated in the re-initiation waves. Persson and Bjarnholt (7) have succeeded in demonstrating the long life failure and re-ignition processes in NM detonation confined in glass tube with the open-shutter aquarium technique. In our experiments, the regular repetition of failure and reignition processes was revealed owing to the aluminum combustion. It is also remarked that, near the detonation front, the traces of failure waves are straight and their angle between charge axis are constant, but far behind the front, they are slightly curved toward charge periphery along the expansion of the tube. These facts lead us to the conclusion that the transverse velocity of the failure waves is constant, and also give us the possibility of measuring the transverse velocity of failure waves.

Figure 8 shows the effects of aluminum concentration on the failure and reignition processes. In the case of $x = 0.05$, the criss-cross pattern size is rather enlarged and the dark lines are predominant. On the

Fig. 5. Enlargement of 4th frame in Fig. 4.
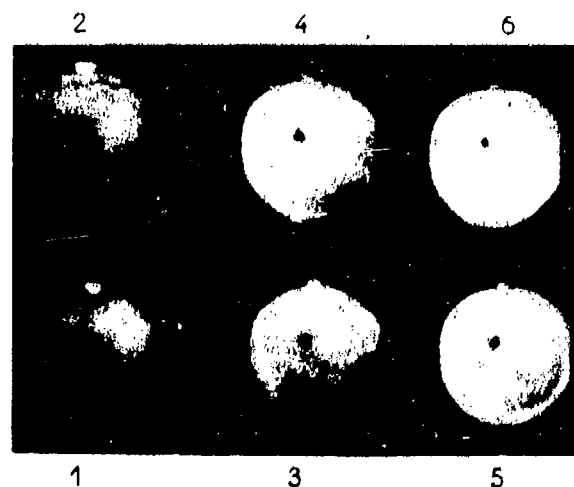
Fig. 6. Sequence of the butt-end record of the detonation in NM-PMMA/Al (x = 0.10) confined in brass tube; time interval is 100 ns and exposure time is 20 ns; on the top of the charge, the luminous point due to shock wave in air bubble is observed; the dark point in the center of each frame is due to the defect of photocathode of camera IMACON.
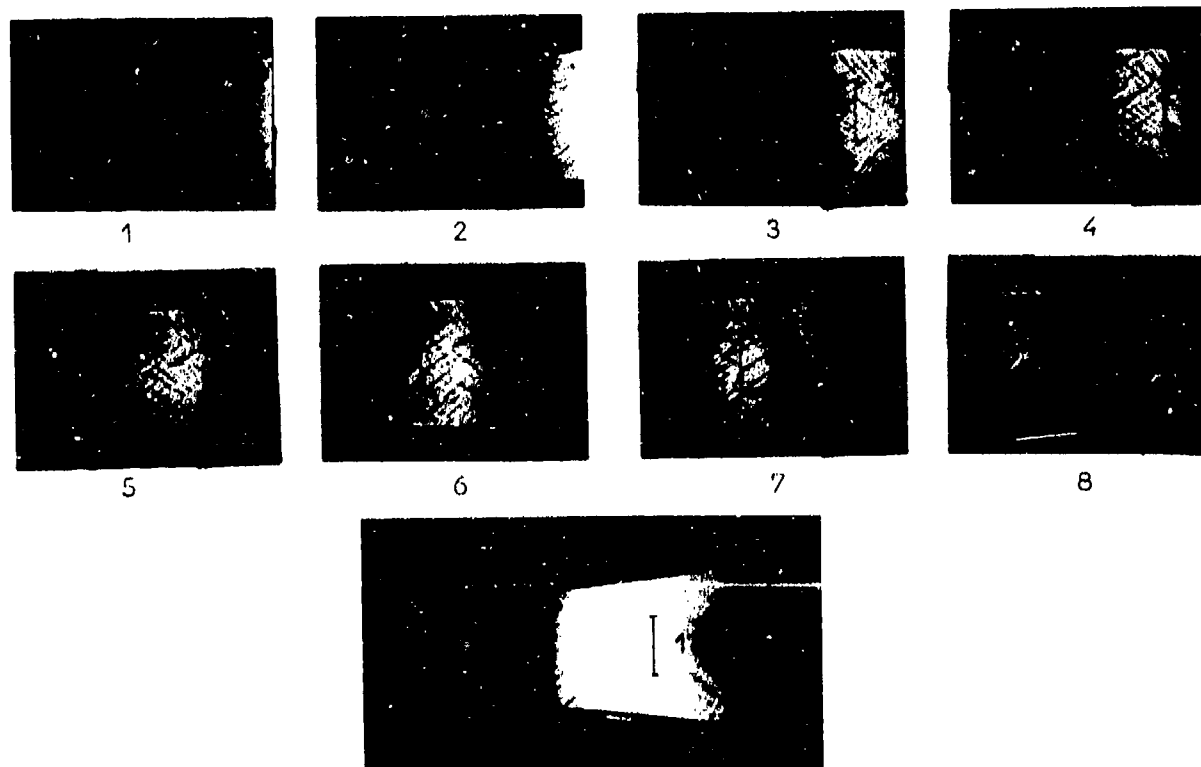
Fig. 7. Framing camera views of the development of the detonation wave in NM-PMMA/Al (x = 0.10) and scheme explaining the framing views; time interval 1 μs and exposure time 0.3 μs.
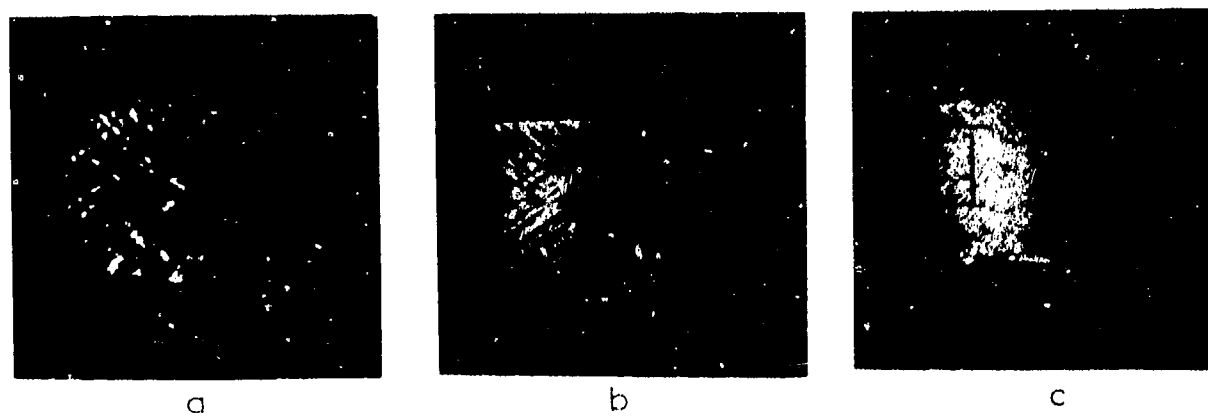
Fig. 8. Effect of Al concentration; (a) x = 0.05, (b) x = 0.10, (c) x = 0.15.

contrary, in the case of 'x = 0.15, the criss-cross pattern size is indistinguishably small, and bright lines are prevalent.

To estimate the critical conditions of NM-PMMA/Al (x = 0.10) mixture, the experiment was performed with a tube of the same size except cross-section (4 x 20 mm^2). The records show that the detonation wave propagates at constant velocity. We also confirmed that the criss-cross pattern appears just after the initiation behind teflon barrier.

3.3 Tentative interpretation.

Recently, Urtiew (1) has clearly interpreted the failure process described as dark waves or failure waves on the basis of the cellular structure of the detonation front. Our explanation is based on the model proposed by Urtiew.

Because of the weak shock impedence of PVC tube, the elementary triple-wave intersection fails to reflect off the wall (a rarefaction wave penetrates inside the reaction zone). This lack of reflection generates the failure wave which concentrically propagates inward at the constant velocity weakening the next triple-wave intersection. Because of high sensitivity of NM-PMMA/Al mixtures, the reignition sites appear after short induction time in the shock compressed mixture and catch-up the leading shock. In this reini-

tiation wave, the aluminum combustion takes place on the charge periphery. Because the reinitiation wave takes place in overdriven mode, the failure wave does not appear immediately after the catch up of leading shock by reinitiation wave, as shown on Fig. 9. The failure and reignition processes are repeated, thus printing the regular pattern observed in lateral observations.

In a brass tube, the elementary triple-wave intersection can be reflected owing to higher shock impedance of the wall. After the reflection from the wall, the triple-wave intersection is in overdriven mode, so aluminum combustion takes place and no failure wave is generated on the charge periphery.

The effect of Al concentration shown in Fig. 8 also may be explained as follows:

In the case of x = 0.05, the induction time in shocked condition is longer than in the case of x > 0.05, so, the failure waves can propagate over a rather long distance before the reinitiation waves catch-up the leading shock waves. On the contrary, in the case of x = 0.15, because of the very short induction time, the reinitiation wave catch-up the leading shock waves much sooner. From this fact, it seems that the increase of Al concentration diminishes the induction time in shocked condition and increases sensitivity of explosive mixtures.
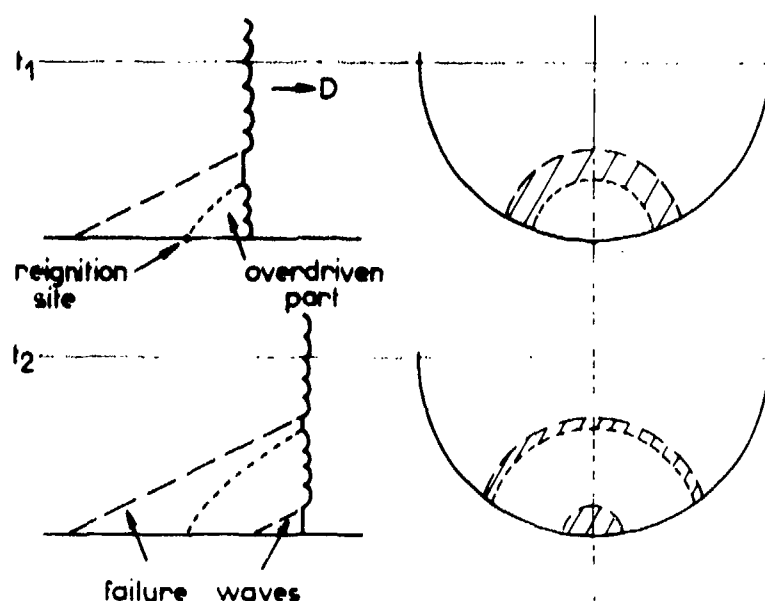
Fig. 9. Scheme of the regular repetition of failure and reignition processes.

130

4. Discussion

We have explained the failure and reignition processes of the detonation in NM-PMMA/Al mixtures on the basis of cellular structure. We believe that our observations support the postulate by Dremin (3) and Urtiew (1); the detonations in other liquid explosives, where the constant velocity failure waves have been observed have a cellular structure. At the present stage, we cannot advance detailed considerations on cellular structure because our experiments have been limited to qualitative observations. It seems possible however to draw some conclusions:

1. The transverse velocity of failure waves is about 70% of the detonation velocity in all cases ($x = 0.05$, $0.10, 0.15$). As shown by Urtiew and Kusubov (8), the transverse velocity of triple point is about the same as the detonation velocity in the NM-Acetone detonations.

2. The increase of Al concentration sensitizes the explosive mixtures, and this is coherent with the noticeable decrease of the slope $|\partial D/\partial(d^{-1})|$.

3. According to Dremin et al. (3), the critical diameter is approximately similar to the detonation limit in a weak tube, so we can estimate the critical diameter for $x = 0.10$ to be inferior to 4 mm.

4. The delay of Al combustion may be estimated to be several hundred of nanoseconds.

REFERENCES

1. P. A. Urtiew, "From cellular structure to Failure Waves in Liquid Detonations," Combust. Flame, Vol. 25, pp. 241-245, 1975.

2. A. W. Campbell, T. E. Holland, M. E. Malin and T. P. Cotter, Nature, vol. 178, pp. 38-39, July 1956.

3. A. N. Dremin, O. K. Rozanov and V. S. Trofimov, Combust. Flame, vol. 7, pp. 153-162, June 1963.

4. A. N. Dremin and V. S. Trofimov, 10th Symp. (Int.) on Combustion, pp. 839-843, The Combustion Institute, Pittsburgh, Pa., 1965.

5. A. N. Dremin, 12th Symp. (Int.) on Combustion, pp. 691-699, The Combustion Institute, Pittsburgh, Pa., 1969.

6. R. W. Watson, 5th Symp. (Int.) on Detonation, pp. 169-174, ACR-184 ONR, Dept. of the Navy, Arlington, Va., 1972.

7. P. A. Persson and G. Bjarnholt, 5th Symp. (Int.) on Detonation, pp. 115-118, ACR-184, ONR Dept. of the Navy, Arlington, Va., 1972.

8. P. A. Urtiew and A. S. Kusubov, 5th Symp. (Int.) on Detonation, pp. 105-114, ACR-184, ONR Dept. of the Navy, Arlington, Va., 1972.

9. H. Presles and C. Brochet, Astronautica Acta, vol. 17, pp. 567-573, 1972.

10. H. Presles and C. Brochet, "Instabilités de la Détonation dans les Mélanges Nitrométhane-Chloroforme et Nitrométhane-Bromoforme," Acta Astronautica, vol. 3, pp. 531-540, 1976.

11. C. L. Mader, Los Alamos Scientific Laboratory Report LA-2900, July 1963.

12. R. Chéret, Acta Astronautica, vol. 1, pp. 893-898, 1974.

13. P. Teychenne de Blazi, C. Malaval and J. M. Lombard, "Etude spectroscopique de la Température de Détonation d'un Explosif contenant de l'Aluminum," Rapport final S75-01 CEG, 1975.

14. C. L. Mader, "Initiation of Detonation by the Interaction of Shocks with Density Discontinuities," 4th Symp. (Int.) on Detonation, ACR-126, ONR Dept. of the Navy, 1966.

15. J. R. Travis, "Experimental Observations of initiation of Nitromethane by Shock Interactions at Discontinuities," 4th Symp. (Int.) on Detonation, ACR-126, ONR Dept. of the Navy, 1966.

16. C. Brochet, H. Presles and R. Chéret, 15th Symp. (Int.) on Combustion, pp. 29-40, The Combustion Institute, Pittsburgh, Pa., 1975.

17. M. Moreau, Rapport interne, E.N.S.M.A., Poitiers, 1976.

18. D. Price, A. R. Clairmont, Jr. and J. O. Erkman, Combust. Flame, vol. 20, pp. 389-400, June 1973.

19. M. J. Kamlet and S.J. Jacobs, J. Chem. Phys. vol. 48, n°1, pp. 23-35, Jan. 1968.

20. M. J. Kamlet and J. E. Ablard, J. Chem. Phys. vol. 48, n°1, pp. 36-42, Jan. 1968.

21. H. D. Mallory and W. S. McEvan, J. Appl. Phys., vol. 32, n°11, pp. 2421-2424, Nov. 1961.

22. P. A. Persson and T. Sjölin, 5th Symp. (Int.) on Detonation, pp. 153-168, ACR-184, ONR Dept. of the Navy, Arlington, Va., 1972.

EFFECTS OF LIQUID DILUENTS ON DETONATION
PROPAGATION IN NITROMETHANE

Masao Kusakabe and Shuzo Fujiwara
National Chemical Laboratory for Industry, Eighth Division
Nishiyawata 1-3-4, Hiratsuka City,
Kanagawa, JAPAN

*Acetone, nitroethane, chloroform, and carbontetrachloride were mixed with
nitromethane. Critical diameters in brass tube were determined for these mixtures
at 25°C. Detonation velocities at infinite diameter and coefficients of diameter
dependence of the detonation velocity were also estimated by applying least square
method to the values obtained by accurate measurements in various charge diam-
eters. C-J detonation parameters were calculated and compared with the observed
velocities. The effects of these diluents were summarized and peculiarities found
in carbontetrachloride and so on were explained clearly by assuming three condi-
tions for the effectiveness of the additives on the detonation propagation in the
mixture.*

INTRODUCTION

Liquid explosives are homogeneous and isotropic,
so are much simpler in their nature than the inhomog-
eneous solid explosives. This is the reason why they
are suitable to investigate the detonation propagation
mechanism in condensed phase. Nitromethane is one
of the most typical liquid explosives and is able to be
observed their detonation behaviors optically owing
to their transparency. So its explosive behaviors
have been well established by many workers
(1,2,3,4,5). Effects of addition of inert diluents to
nitromethane have also been investigated especially
in relation to the so-called pulsating detonation. In
nitromethane, the detonation front is not smooth,
but has cellular structure. The size of the structure
increases with the content of the inert diluents, this
is just like as in gaseous explosives (6,7,8,9,10,11,12).
Recently the similarity between the detonation in
liquid and that in gas has been reported (6,10,11).
Addition of inert gas such as argon and nitrogen
affects the detonation characteristics of the gaseous
explosives and is useful to clarify the detonation
mechanism in it. Addition of inert liquid diluents

to liquid explosives also affects detonation behaviors
such as detonation velocity, detonation pressure,
critical initiation shock pressure, critical diameter,
and so on. These inert diluent effects are closely
relating to the detonation propagation mechanism, so
it will be fruitful to study them in elucidating the
detonation mechanism in condensed explosives.

EXPERIMENTAL

Four kinds of inert liquids: acetone, nitroethane,
chloroform, and carbontetrachloride were mixed with
pure nitromethane. (It will be shown later that nitro-
ethane behaves as if it is an inert liquid on the detona-
tion propagation in nitromethane.) All the liquids
including nitromethane were purified from extra pure
grade liquids, by adding anhydrous calciumchloride
to them and distilled once. Mixtures were prepared
by mixing proper quantities of ingredients weighed
with a balance, so as to be attained due ratios in
volume. The ratios are accurate within the error
of ± 0.1 % in volume. Densities of these liquids and
the mixtures were measured with Digital Precision
Densimeter Model 10 (Anton Paar K. G. Austria).

Table 1 shows the observed densities of the ingredient liquids. Densities of the mixtures are listed in Table 2.

Detonation velocities of these mixtures were measured by the diagonal wave pick-up method which is illustrated in the Fig. 1. A brass container tube is assembled from three parts: bottom tube, middle tube, and upper one. Each part is cut from a long tube and machined with a lathe neatly in a proper length. The length of the middle tube is measured with the calipers within the error of ± 0.05 mm. Two pick-up gaps which are made by twisting a pair of 0.1 mm diameter magnet wire are cemented to both butt ends of the middle tube diagonally in taut as illustrated in Fig. 1. Then the other two tubes and a bottom PMMA plate are cemented with epoxy bond to each other to form a container.

The detonation wave which passes through the explosive mixture in the container shortens the magnet wire wave pick-ups successively. This causes the successive discharge of capacitors in the pulse forming circuit connected to the pick-ups and the signals generated in the circuit are sent to an electronic counter with a time measuring plug-in unit through two coaxial cables with the same length, and the time interval between the signals is measured digitally. The time resolution of the apparatus is 10 nsec.

The merit of this method lies partly in the accuracy of the measurement of detonation transit length owing to the use of calipers to measure it, and partly in freeness from the error caused by the disturbance in the detonation wave (13). This is desirable especially in the charge near critical diameter. In such a case, detonation wave is so seriously disturbed by the rarefaction wave emanating at tube wall and penetrating into the charge, that considerable error may be introduced in transit time measurement if the pick-ups are placed near charge periphery only. But, with this diagonal pick-ups, such a disturbance cannot affect seriously, because the central part of the charge hardly is disturbed by it (14).

We used the middle tubes of the lengths between ca. 150 mm and ca. 250 mm. In this case both observed transit time and observed length have values with four effective figures. And the derived detonation velocity has the accuracy within the error of ± 0.2 %.

TABLE 1

Density of the Liquid Measured at 25°C

Liquid	Density (gr/c.c.)
Nitromethane	1.1278 ± 0.0005
Carbontetrachloride	1.5844 ± 0.0005
Chloroform	1.4781 ± 0.0005
Nitroethane	1.0425 ± 0.0005
Acetone	0.7846 ± 0.0005
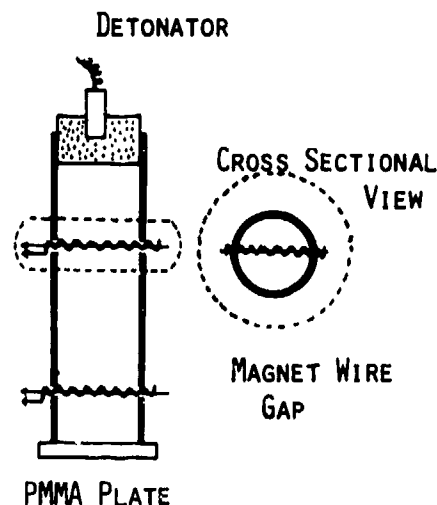
Fig. 1. Schematic diagram of a container tube with the diagonal gaps used to measure the detonation velocity.

RESULTS

In Fig. 2, the results of the test shots are plotted in a diagram with ordinate of charge diameter and abscissa of diluent content in volume percent. Dark mark represents failed case and light one does exploded case. A critical diameter curve for each group of the mixtures with a specific liquid diluent is drawn through the middle points between these failed and detonated cases. From Fig. 2, it is clear that the order of the ability of diluent to affect the critical diameter conforms to the inverse order of the density of the diluents. The lighter the liquid is, the more it affects (13,15). Except for carbontetrachloride group, the critical diameter gradually increases along

134
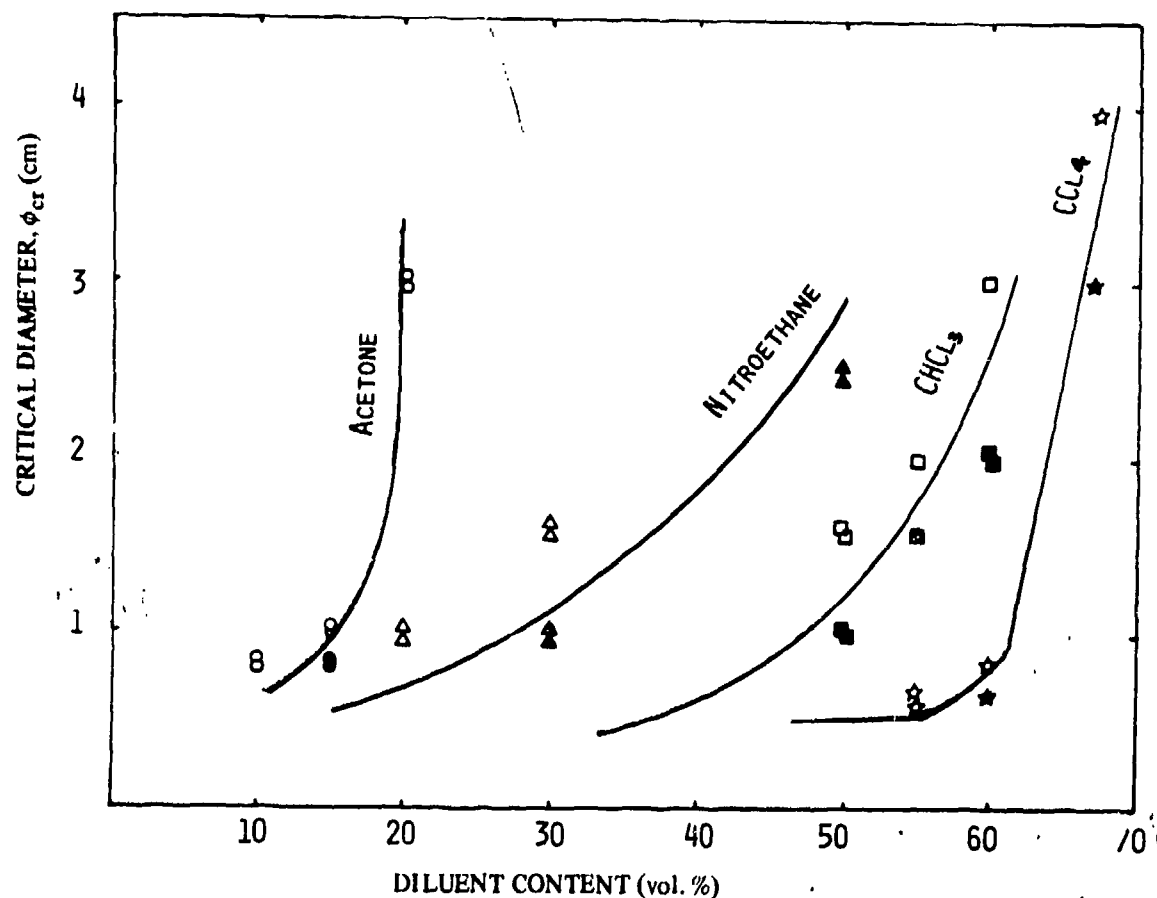
Fig. 2. Critical diameter curves for nitromethane-diluent mixture at 25°C in brass tube.

a curve with upwardly concave shape. In nitromethane-carbontrachloride mixture, critical diameter does not increase and remains almost constant with the value near 6 mm until the diluent content reaches as much as about 55 volume percent. From that point the critical diameter increases very steeply.

Detonation velocities of nitromethane in brass tubes with various diameters were measured at the temperature between ca. 20°C and ca. 30°C. These velocities were calibrated to give the velocities at 25°C using the coefficient of $dD/dT = -3.9$ m/sec/°C obtained by Davis et al. (3). Figure 3 shows the detonation velocity dependence on inverse charge diameter. The least square fit of these data gives following equation for the detonation velocity of nitromethane at 25°C.

$$D = 6.2601 - 0.0405 \cdot (1/\phi)$$

D = Detonation velocity, km/sec
ϕ = Charge diameter, cm.

Then the detonation velocity in infinite diameter of nitromethane is 6260.1 ± 5 m/sec at 25°C which leads to 6343.4 ± 5 m/sec at 4°C. This value is about 30 m/sec lower than the value of 6374.0 ± 8.7 m/sec obtained by Davis et al. (3). This difference shows our nitromethane still contains some impurities such as nitroethane and so on. One percent dilution in volume by these liquids will result in reduction of detonation velocity about 10 m/sec.

Mixture explosives were also shot in brass tubes in various diameters and the detonation velocites were measured. Each composition was tested in tubes with at least two and mostly four different diameters, and in each diameter at least two and mostly three shots were examined. The temperature of the charge ranged from ca. 20°C to ca. 30°C. Obtained velocities were reduced to the values at 25°C by using the same correction coefficient -3.9 m/sec/°C as in the case of pure nitromethane. For each mixture, the mean detonation velocities at 25°C for respective charge diameters were plotted against the inverse of the

135

TABLE 2

Detonation Parameters for the Mixtures of Nitromethane with Diluent

Composition (vol. %)	Density (gr/c.c.)	Detonation Velocity Observed (km/sec)	Detonation Velocity Calc. (km/sec)	Diameter Dependence Coefficient (cm·m/sec)	Detonation Pressure (kbar)
pure NM	1.128	6.260	6.328	40.5	118.0
NM/CCl$_4$:90/10	1.170	6.099	6.171	44.0	116.7
NM/CCl$_4$:80/20	1.212	5.932	6.002	43.6	111.9
NM/CCl$_4$:70/30	1.258	5.781	5.849	49.0	109.4
NM/CCl$_4$:60/40	1.294	5.649	5.676	53.1	107.1
NM/CCl$_4$:50/50	1.350	5.525	5.529	118.8	106.1
NM/CCl$_4$:40/60	1.397	5.277	5.107	239.8	99.4
NM/CHCl$_3$:95/5	1.145		6.234	—	119.1
NM/CHCl$_3$:90/10	1.163	6.102	6.130	53.0	115.1
NM/CHCl$_3$:85/15	1.182		6.029	-	111.5
NM/CHCl$_3$:80/20	1.199	5.896	5.924	68.6	107.3
NM/CHCl$_3$:70/30	1.230	—	5.702	—	103.0
NM/CHCl$_3$:65/35	1.250	5.599	...	86.0	--
NM/CHCl$_3$:60/40	1.269	--	5.509	—	98.3
NM/CHCl$_3$:50/50	1.301	5.302	5.298	185.0	91.4
NM/NE :90/10	1.117	6.183	6.238	52.5	116.
NM/NE :80/20	1.108	6.118	6.140	90.3	114.
NM/NE :70/30	1.100	6.001	6.046	86.8	108.
NM/Acet. :95/5	1.109	6.107	6.210	—	115.6
NM/Acet. :90/10	1.094	5.980	6.091	59.7	108.6
NM/Acet. :85/15	1.077	5.839	5.965	146.6	101.9
NM/Acet. :80/20	1.060	--	5.842	---	93.2

Detonation velocity observed: at 25°C

Fig. 3. Detonation velocity of NM at 25°C, against inverse charge diameter.

charge diameter just likely as in Fig. 3. Least square
fits of these data with a linear equation

$$D = D_\infty - A(1/\phi) \qquad (1)$$

was obtained for each group of mixture. Where D is
the detonation velocity in any charge diameter ϕ.
Detonation velocities at an infinite diameter D_∞ and
diameter dependence coefficients A, thus obtained,
are listed in the Table 2.
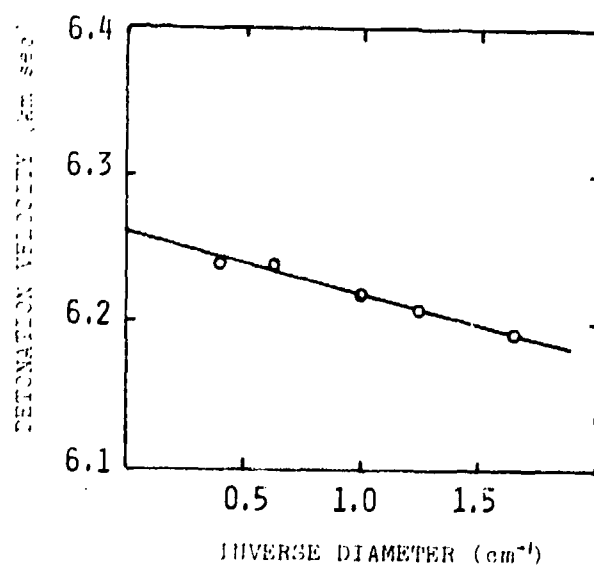
CALCULATION OF DETONATION PARAMETERS

Detonation parameters for these mixtures were
computed with Mader's code. We used Kihara-Hikita's
equation (16) in place of BKW equation of state for
the detonation products. For nitromethane, calcula-
tion which uses K-H equation with the parameters
usually adopted for calculation of solid CHNO explo-
sives gives considerably higher detonation velocity
than the observed one. The coefficient of repulsive
force in K-H equation must be changed to reduce the
discrepancy.

For calculating the detonation parameters of the
mixtures containing chlorine, it was necessary to
determine the parameters of gaseous chlorine species
under high pressure. They were determined so as to
make the calculated detonation velocity agree with
the observed one for nitromethane-chloroform mix-
ture with the dilution of 50 volume percent by trial
and error method. In Table 3, calculated detonation
parameters and CJ composition of the detonation
products for the mixture are shown. The parameters
thus determined were used to calculate the detona-
tion parameters of all the other chlorine containing
mixtures. In all these calculations, heat of mixing
were neglected.

DISCUSSION

In Fig. 4 the coefficient A in an equation (1) is
plotted against inert diluent content in volume per-
cent. These coefficients for four groups increase with
the diluent content, and both shape and the mutual
location of variation curves are very similar to those of
the critical diameter variation curves in Fig. 2. In the
case of carbontetrachloride, the diameter dependence
coefficient A remains almost constant until the diluent
content reaches a high value just likely as in the
critical diameter.

TABLE 3

*Detonation parameters and CJ composition of the
detonation products, calculated for the 50/50 mixture
of NM and CHCl$_3$ (density:1.301, heat of formation
at 0°K: -20281.3 cal/formular weight)*

CJ detonation Pressure	91.384 kbar
CJ Detonation Velocity	5297.964 m/sec
CJ Temperature	2604.917 °K
CJ Volume	0.57629 c.c./g
Vol. of gaseous product	2.996 c.c./mol
Vol. of gaseous product	18.379 c.c./mol
Mol number of the gas	2.4825 mols/gr
Solid C	0.3769 c.c./gr

CJ-composition of the Detonation Products			
Species	No. of mol	Species	No. of mol
H_2O	0.43	N_2	0.298
H_2	0.0603	OH	0.455×10^{-4}
O_2	0.1×10^{-5}	Cl_2	0.134×10^{-2}
CO_2	0.278	CCl_4	0.129×10^{-3}
CO	0.204	HCl	1.211
H	0.913×10^{-5}	C	0.517
NO	0.243×10^{-5}		

For homogeneous explosives, such as gaseous or
liquid explosives, chemical reaction which sustains the
detonation is considered to be activated by shock
heating (2,17,18). That is, so-called shock thermal
explosion theory will be applied in the detonation
propagation. Figure 5 illustrates typical pressure
profile of detonation wave based on that reaction
mechanism. P_N refers to the pressure in thê detona-
tion front and CJ does to CJ-point where reaction
just completes. The distance between the wavefront
and the CJ-point is a reaction zone length which is
denoted as l_0 in the figure. If we denote the mean
particle velocity inthe reaction zone as U. Reaction
zone length is expressed as

$$l_0 = (D - U)\tau \qquad (2)$$

Where τ is a reaction time, and nearly equal to the
induction time of the reaction.

Following the discussion by Gordon (19), critical
diameter ϕ_{cr} is almost proportional to reaction
zone length l_0, that is,

137
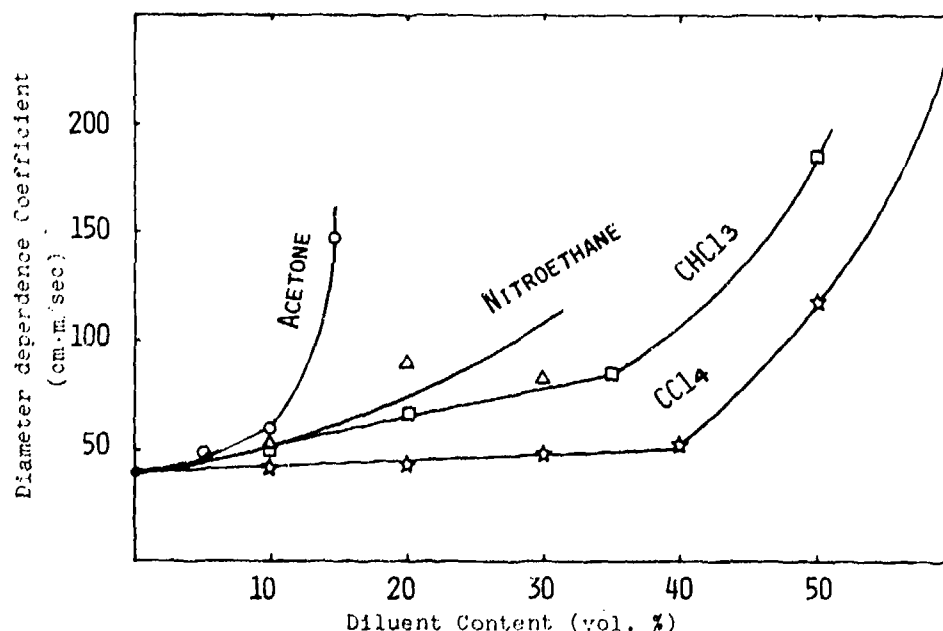
Fig. 4. Diameter dependence coefficients of detonation velocity against diluent content.
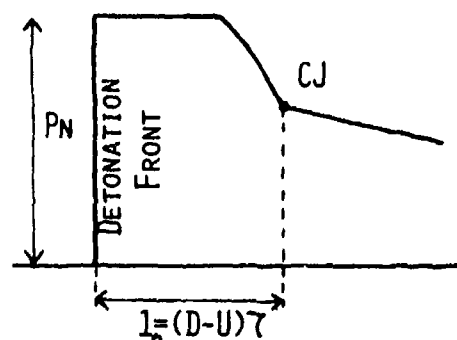
Fig. 5. Pressure profile of the detonation wave based on shock thermal explosion theory

$$\phi_{cr} \doteq K_1 l_0 \qquad (3)$$

Where K_1 is a constant. The quantity $(D-U)$ in the eq. (2) is thought to be constant as compared to the variations in l_0 or τ. Then,

$$l_0 \doteq K_2 \tau \qquad (4)$$

Where K_2 is a constant. From the analysis by Gordon, the diameter dependence coefficient A can be related to critical diameter as

$$A \doteq K_3 \phi_{cr} \qquad (5)$$

Where K_3 is another proportionality constant. Eqs. (3), (4), and (5) lead to the following relation,

$$\phi_{cr} \propto A \propto l_0 \propto \tau \qquad (6)$$

That is, there is proportionarity between these four quantities. Observed similarity between Fig. 2 and Fig. 4 is a clear evidence for this relation.

The reason why the lighter liquid diluent hinders detonation propagation more than the denser one will be explained by the difference of heat sinking ability between them. Lighter liquid will be compressed more easily and so sink more energy under the detonation pressure than denser one.

Nitroethane is able to detonate by itself and is usually thought to be active, but it behaves as if it is an inert liquid for the critical diameter variation of its mixture with nitromethane. We shall treat this peculiar feature later.

Following the relation (6), Fig. 2 and Fig. 4, reaction zone length l_0 and induction time τ are thought to remain almost constant by the addition of carbon-tetrachloride. This peculiarity will also be treated later.

138

Observed detonation velocity at infinite diameter D_∞ and calculated detonation velocity D_{cJ} are plotted against diluent content in volume percent in Figs. 6 and 7. As clearly seen in the Figures, observed and calculated velocities vary almost linearly with diluent content. The absolute values of the slopes, $|dD/dn|$, where n is diluent content, of these curves are 30 m/sec/% for acetone, 9 m/sec/% for nitroethane, 18 m/sec/% for chloroform, and 15 m/sec/% for carbontetrachloride.

In general, detonation velocity D is proportional to initial density ρ of the explosives and square root of the heat of explosion Q (20), that is

$$D \propto \rho Q^{1/2} \qquad (7)$$

If we denote the dilution ratio in volume as n $(1 \geqslant n \geqslant 0)$, the density and heat of explosion for the mixture with the dilution ratio n will be expressed as (ρ_0 and Q_0 refer to NM)
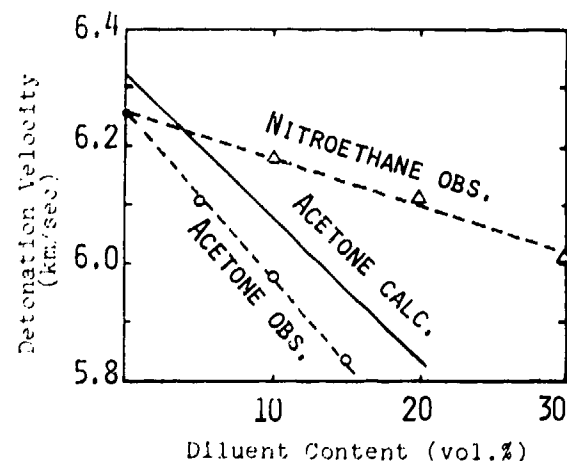
Fig. 6. Detonation velocity at infinite diameter against diluent content for the mixtures NM with acetone and nitroethane.
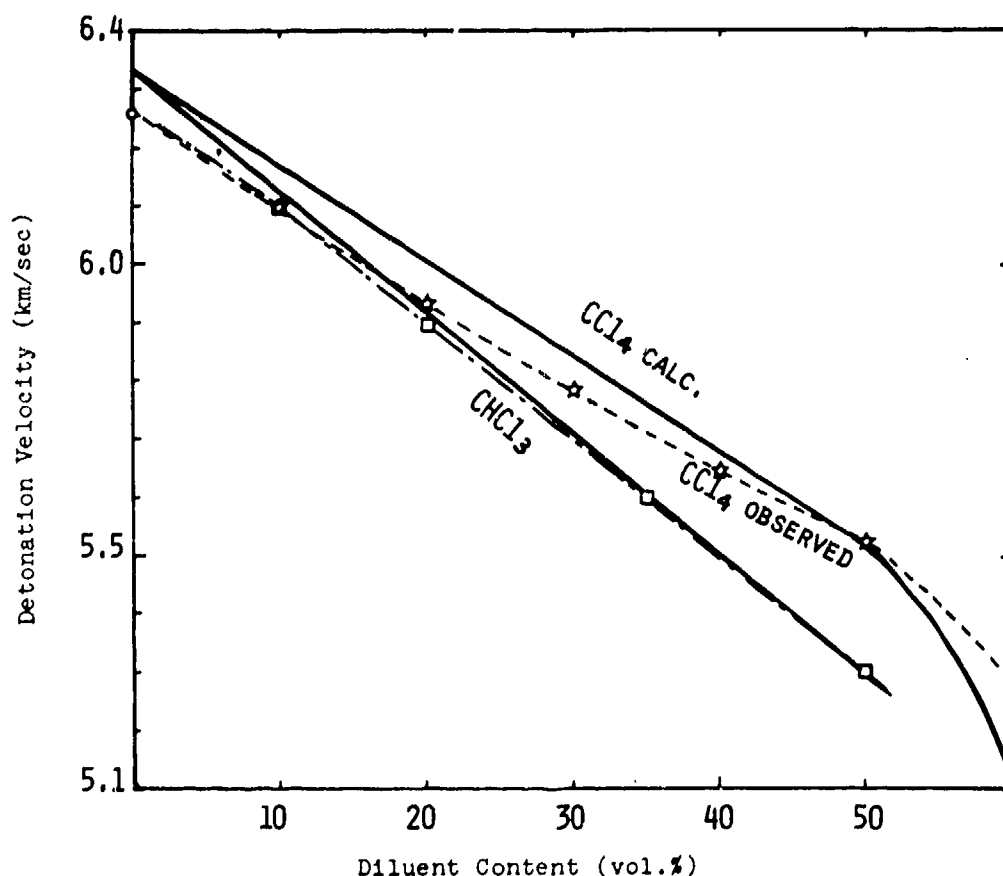
Fig. 7. Detonation velocity at infinite diameter against diluent content for the mixtures NM with CHCl and CCl.

$$\rho = \rho_0(1 - m_1 n) \tag{8}$$

$$Q = Q_0(1 - m_2 n)^{1/2} \tag{9}$$

where m_1 and m_2 are constant parameters specific to each diluent. The parameter m_1 may change its sign along with the difference between the density of nitromethane and that of diluent. From eqs. (7), (8), and (9), for small n,

$$D/D_0 = (1 - m_1 n)(1 - m_2 n)^{1/2}$$

$$= 1 - (m_1 + m_2/2)n - \ldots \tag{10}$$

That is, for small diluent content, detonation velocity varys linearly with diluent content, and its slope becomes $-(m_1 + m_2/2)$.

$$dD/dn = -(m_1 + m_2/2) \tag{11}$$

For an active additive, parameter m_2 becomes small. From eq. (11), it is natural that the absolute slope of the detonation velocity is the greatest in acetone, and becomes considerably small for nitroethane which can react exothermically. It will be true that nitroethane reacts and contributes to accelerate detonation in the mixture. That is, nitroethane behaves as an active additive for the detonation velocity variation, but on the contrary to this it does as an inert diluent for the critical diameter variation of the mixture.

Difference between the observed and calculated velocities for the mixture containing carbontetrachloride is large and cannot be neglected as experimental errors. The absolute slope of the observed velocity curve is significantly smaller than that of the calculated. This discrepancy suggests that some heat release occurs in the mixture.

To explain these experimental results in the diluent effect on detonation propagation in nitromethane, we have adopted following assumption, that is: there are three factors that determine the effect of an additive on the detonation propagation in the mixture. They are: I. Whether the additive can react exothermically or not? II. Whether the reaction (heat release change) can be initiated by the detonation shock or not? III. Whether induction time of this heat release change is shorte .han that of the reaction of the main explosives (nitrom thane in this case) or not?

To be able to contribute detonation propagation, the additive must be active (I) under the detonation

pressure of the main explosives (II) and the heat release of the reaction must be rapid enough (III). In the case of nitroethane, the requirement (I) is satisfied and requirement (II) is also satisfied too, but the reaction is not so rapid comparing to the reaction of nitromethane, (nitroethane cannot transmit detonation even at $30°C$ in 4 cm brass tube.) i.e. requirement (III) fails. So Nitroethane cannot contribute to sustain detonation in the mixture even if it reacts in the mixture.

Peculiar effect of carbontetrachloride either on detonation velocity variation or on critical diameter may be explained if the liquid has an exothermic change that can occur under the detonation pressure and the change is rapid enough to be able to contribute the detonation propagation. The heat release of this change seems not so large as that of the chemical reaction of nitromethane, considering the small deviation between the observed and calculated velocity variations.

Dick found a shock transition in carbontetrachloride occuring near 164 kbar of shock pressure. He thought it as liquid polymerization occuring under the shock pressure from ca. 70 kbar to ca. 160 kbar (21). Polymerization is usually an exothermic change even if the heat release is not so large as that of the usual detonation reaction. The induction time of this polymerization is sufficiently short with no doubt because the change is found as shock transition.

Then, can this polymerization occur in the mixture with nitromethane? The mixture looks transparent, therefore the diluent disperses in the mixture into micro-phases with the dimension less than the wave length of visible light. But the dimension will be not so small as molecular order and it may range from 100 A to 1000 A in order, since carbontetrachloride is nonpolar. Then, it can polymerize in the micro-phase under the shock transmitted from detonating nitromethane phase. This transition satisfies the three requirement to contribute the detonation propagation, and so is effective to sustain the detonation up to high content of the diluent.

Carbondisulfide and tintetrachloride have similar effects to those of carbontetrachloride on the detonation propagation in the mixture with nitromethane (15). They do not hinder the detonation in the mixture up to a high diluent content, just like as carbontetrachloride does not. Dick found a shock

transition at the pressure near 62 kbar in carbondisulfide (21). If this is an exothermic change, effects of the liquid may be also explained with it. For tintetrachloride, we can assume the existence of rapid exothermic transition near the detonation pressure in nitromethane to explain its effects.

A shock transition has been found by Dick for chloroform, which occurs between 260 kbar and 310 kbar. (private communication) This transition is sufficiently rapid but the pressure at which it occurs is much higher than that of detonation in nitromethane. That is, pressure requirement (II) fails. Therefore, chloroform behaves as an utterly inert diluent in nitromethane.

Forshey et al. reported that hydrazine was very active in the mixture with nitromethane (22). They concluded that the activity owes to the formation of so-called aci-form of the nitromethane by the additon of hydrazine. We may also consider that this active effect of hydrazine owes to its inherent characteristics under shock load, that is, hydrazine satisfies our three requirements and the heat release is very high compared to that of carbontetrachloride.

ACKNOWLEDGEMENTS

REFERENCES

1. A. W. Campbell, M. E. Malin, and T. E. Holland, "Detonation Phenomena in Homogeneous Explosives" Nature, 178, pp 38-39 (1956)

2. A. W. Campbell et al., "Shock Initiation of Detonation in Liquid Explosives" Phys. Fluids, 4, pp 498-510 (1961)

3. W. C. Davis et al., "Failure of Chapman Jouguet Theory for Liquid and Solid Explosives" Phys. Fluids, 8, pp 2169-2182, (1965)

4. J. W. Enig and F. J. Petrone, "Equation of State and Derived Shock Initiation Criticality Conditions for Liquid Explosives" Phys. Fluids, 9, pp 398-408 (1966)

5. F. J. Petrone, "Validity of the Classical Detonation Wave Structure for Condensed Explosives" Phys. Fluids, 11, pp 1473-1478 (1968)

6. A. N. Dremin and O. K. Rozanov, "Similarity of Detonation of Gaseous and Liquid Explosives" Comb. Expl. and Shock Waves, 1, pp 63-68 (1965)

7. C. Brochet and H. Presles, "Detonation Characteristics of Some Liquid Mixture of Nitromethane and Chloroform or Brmoform", Fifteenth Symp (Intern.) on Combustion, pp 29-40. The Combustion Institute, 1974

8. H. D. Mallory, "Detonation Zone Observation in Nitromethane Solutions", J. Appl. Phys., 14, pp 1361-1365 (1971)

9. V. A. Veretennikov et al., "Applicability of Hydrodynamic Theory of the Detonation of Condensed Phase" Comb. Expl. and Shock Waves, 3, pp 1-5 (1967)

10. P. A. Urtiew and A. S. Kusbov, "Wall Traces of Detonation in Nitromethane-Acetone Mixtures" Fifth symp. (Intrn.) on Detonation, pp 105-114, ONR 1970

11. P. A. Urtiew and A. S. Kusbov, "Cellular Structure of Detonation in Nitromethane" Combustion and Flame, 14, pp 117-122 (1970)

12. S. Fujiwara, M. Kusakabe, and T. Hikita, "The Study of Detonation in Multi-Component Condenced Phase. II. On Solutions of Nitromethane and Inert Solvents" J. Ind. Expl. Soc. Japan, 30, pp 77-80 (1969)

13. S. Fujiwara and M, Kusakabe, "Accurate Measurements of Detonation Velocity" J. Ind. Expl. Soc. Japan, 34, pp 276-280 (1973)

14. R. W. Watson, "Dark Waves in Liquid Explosive Systems: their Role in Detonation Failure" Fifth Symp. (Intrn.) on Detonation, pp 169-174, ONR, 1970

15. T. Hikita, S. Fujiwara, and M. Kusakabe, "Two-Phase Model of Detonation Propagation in Condensed Explosives with Inert Diluent" Thirteenth Symp. (Intrn.) on Combustion, pp 1165-1170, The Combustion Institute, 1971

16. H. Kihara and T. Hikita, Fourth symp. (Intrn.) on Combustion, p. 458, The Combustion Institute, 1953

17. K. I. Shchelkin, "Instability of Combustion and Detonation of Gases" Soviet Phys. USPEKHI, 8, pp 765-769 (1966)

18. H. W. Hubbard and M. H. Johnson, "Initiation of Detonations", J. Appl. Phys., 30, pp 765-769 (1959)

19. W. E. Gordon, "Detonation Limits in Condensed Explosives" Fourth Symp. (Intrn.) on Detonation, pp 178-197, ONR, 1965

20. H. Eyring et al., "The Stability of Detonation" Chem. Rev., 45, pp 69-181 (1949)

21. R. D. Dick, "Shock Wave Compression of Benzene, CS, CS_2, CCl_4, $CHCl_3$ CCl, CHCl, liquid nitrogen" J. Chem. Phys., 52, pp 6021 6032 (1970)

22. D. R. Forshey et al., "Detonability of the NM-Hydrazine-Methanol System", Explosivstoffe, 17, pp 125-128 (1969)

DISCUSSION

A. W. CAMPBELL, C. L. MADER, J. B. RAMSAY, L. C. SMITH
Los Alamos Scientific Laboratory
Los Alamos, New Mexico

We must admit to viewing with skepticism the report presented in this paper that solutions of nitromethane in CCL_4 detonate. We have fired two shots which confirm the result for 50/50 vol % solutions. A detonation velocity of 5.2 ± 0.1 mm/μs was obtained for a solution confined in a 12-mm diameter, 12-mm wall thickness brass tube over a length of 800-mm. A standard plate dent test with a diameter of 42-mm gave an estimated pressure of 92 kbar compared to 134 kbar for nitromethane. A BKW calculation gave a detonation velocity of 5.08 m/μs and a pressure of 106 kbar.

Kusakabe and Fujiwara suggest that an exothermic polymerization reaction of CCl_4 may contribute energy to the detonation front. Product yields presented in their Table 3 for $HCCl_3$/Nitromethane (50/50 Vol. %) show that HCl is a major component in the products. The formation of HCl is exothermic and also competes for hydrogen in the H, C, O equilibria tending to improve the oxygen blance. This reaction may explain why the solutions can detonate with large fractions of chlorinated material.

AUTHORS' REPLY

"Detonation velocities observed" presented in table 2 are ideal ones at 25°C which are obtained from the linear relationship between observed velocity and inverse diameter. The detonation velocity of 50/50 vol ratio NM-CCl_4 mixture at 25°C in a brass tube of inner diameter 12 mm can be calculated to give the value of 5.42 km/sec by the use of ideal velocity in the table, and the value is 0.2 ± 0.1 km/sec higher than the value observed by Campbell et al.

We think the discrepency may be due to impurity in both mixtures and/or due to the difference in mixing ratio. As shown in this report, impurity such as acetone will reduce the detonation velocity about 0.03 km/sec with 1 vol. % content, and 1 vol. % difference in mixing ratio will result in the difference of about 0.015 km/sec in the detonation velocity.

Campbell et al suggest the contribution of HCl formation to the detonation propagation in NM-CCl_4 mixture. If the reaction rate of HCl formation is rapid enough to satisfy our requirements given in this paper, the formation of HCl will be able to play a role of importance in the detonation propagation.

SHOCK-INDUCED ELECTRICAL POLARIZATION OF HOMOGENEOUS EXPLOSIVES

A. N. Dremin, A. G. Antipenko and V. V. Yakushev
Institute of Chemical Physics Academy of
Sciences USSR, Chernogolovka, Moscow
Region, 142432, USSR

*Results of electric signals investigations at shock compression and homogeneous ex-
plosives detonation are presented. If shock pressure is insufficient to initiate
detonation, explosive polarization does not differ from that of inert dielectrics.
The polarization signal shape at explosive detonation is related to the effect of high
electroconductivity occuring with some time delay behind the detonation wave
shock front. It is shown that in some cases the time delay magnitude can be de-
termined from the polarization experimental data. For example, the electro-
conductivity originates behind the shock front of NB powder detonation wave in
$6.7 \cdot 10^{-10}$ sec. At nitromethane detonation the dependence of the electrical sig-
nals amplitude on the nature of the metals of electrodes has been pointed out. The
dependence testifies that the factor arising at the electrode-sample interface is of
certain significance. More complex shape of the polarization signals at the shock
detonation initiation is due to manystage nature of detonation developing process.
In this case the polarization signals pecularities are caused by changes both of the
polarization probe capacity and the explosives polarization in volume.*

Shock-induced electrical polarization is defined as a dipol moment origin in a dielectric sample volume due to velocity and thermodynamical values gradients in shock front.

Since Eichelberger's and Hauver's paper (1) the experimental arrangement (Fig. 1) has been usually used for study of this phenomenon. The polarization signal is registered when the shock wave front moves through the sample 2 from the electrode 1 to the electrode 3. The signal contains both some information on shock transition processes and that on the compressed substance state.

In 1967 Hayes (2) discovered that at the detonation of explosives between the electrodes electric signals originated in the load of circuit like in the case of inert dielectrics. Hayes used the similar experimental arrangement (Fig. 1) which had the second

electrode of spherical form. The signal magnitude increased from some hundredth of volt up to order of one volt when the detonation wave was moving to the second electrode. The signal magnitude practically did not change during the process of the detonation products flow-around of the electrode. Hayes called the phenomenon "the detonation electric effect" and noted that it could be used for study both the stationary detonation and the transitional processes of explosive initiation.

The electric signals during the shock initiation of detonation in liquid explosives were experimentally investigated earlier by Travis (3). He suggested that the polarization probe should be used to reveal the space—time relation of the process parameters. The papers by Hayes and Travis stimulated the study of the electric effects under detonation and shock compression of explosives in our laboratory.
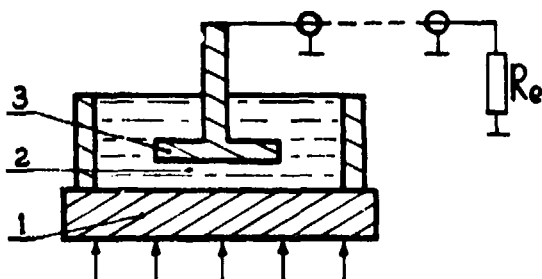
This paper is devoted to homogeneous explosives investigation. The experimental arrangement shown in Fig. 1 was used in the investigation too. The electrode 1 (8 mm thick, 80 mm diameter) and the electrode 3 (15 mm diameter) were made of aluminium AD-1 type. In some experiments the layer of 0.05 mm thick copper foil was cemented onto the electrode 1 surface. In these experiments the electrode 3 was made of copper. The distance between the electrodes x_0, was 2.5-3 mm. The electrode 1 surface faced to the explosive was polished. The oscillograph OK-33 type with the inlet resistance of 75Ω and the time response of 20 nsec was used for the electric signals registration. In some experiments to measure the polarization emf the resistance of 50-70 kΩ was applied to connect the polarization probe and the cable.

The explosive charges of 80 mm diameter and 120 mm height were used to obtain approximately one-dimensional shock loading of the samples. To calculate the dynamical pressure values in the explosives their adiabats (nitromethane (4), nitroglycerine (5), NB powder (6)) and the state of the electrode 1 material were employed.

Nitromethane of trade-mark "pure" was refined in vacuum just before the experiment; to separate nitroglycerine from methanol some volume of water was added to their mixture. The obtained nitroglycerine was dried.

SHOCK COMPRESSION OF THE EXPLOSIVES

If the dynamic pressure is lower than that of the detonation origin the shock-induced polarization of the explosives doesn't vary from that of inert polar dielectrics. Nitromethane and nitroglycerine at the pressures up to those of the detonation origin remain

still perfect dielectrics during the registration time ∼1 mksec. It has been observed in the experiments designed for this purpose.

Therefore, the polarization current dependence on time i(t) is determined by the following parameters: the polarization relaxation time τ; the time constant of the circuit $R_e C_0$; the transit time of the shock through the sample t_1; the time difference t_2 of the shock front entering in the sample due to the front convex and the value

$$\mathcal{H} = \frac{\epsilon_2}{\epsilon_1} \frac{U}{U - u}$$

ϵ_1 and ϵ_2 are dielectrics permittivities of the initial and compressed substance, U–the shock velocity, u–the particle velocity. At the pressure region from 8 kbar to 87 kbar the relaxation time of the nitromethane polarization is $\tau \leqslant 3 \cdot 10^{-11}$ sec, $\mathcal{H} \simeq 1$ (7). The t_2 value was $5 \cdot 10^{-8} \div 1.5 \cdot 10^{-7}$ sec and $R_e C_0 \simeq 3.7 \cdot 10^{-9}$ sec. Since the relaxation time τ is much less than the time constant of the circuit $R_e C_0$ the probe circuit can not be considered as a short circuit. It has been shown (8) that at $\mathcal{H} = 1$.

$$i = \begin{cases} \dfrac{E_0 C_0}{t_2} \left(1 - e^{-\frac{t}{R_e C_0}}\right), & 0 \leqslant t \leqslant t_2 \\ \\ \dfrac{E_0 C_0'}{t_2} \left(1 - e^{-\frac{t_2}{R_e C_0}}\right) e^{-\frac{t-t_2}{R_e C_0}}, & t_2 \leqslant t \leqslant t_1 \end{cases} \tag{1}$$

where

$$E_0 = \frac{P_0 \tau (U - u)}{\epsilon_0 \epsilon_2} \tag{2}$$

is an effective emf. P_0 is the initial polarization at the shock front; ϵ_0 is the permittivity of free space.

The experimental points and the calculated from Eq. 1 (solid line) polarization signals from nitromethane at the pressure p = 68 kbar are presented in Fig. 2. In this case the effective emf was equal to ∼2 volts. From the relation (2) it follows that $P_0 \simeq 1.2 \cdot 10^{-2}$ K/m². The shock front orientation ∼6% of nitromethane molecules corresponds to the very value of the initial polarizaton, the latter exceeding the

144

initial polarizaton of plastics (9) by two orders of value at the same pressure.

The information on the shock-induced polarization and electric properties of nitroglycerine behind the shock front has been published in our earlier paper (10). It has been shown that τ is less than 8 nsec and $\mathcal{H}$ is approximately equal to the unit at pressures $14 \div 122$ kbar. Accordingly, the polarization current oscillograms for nitroglycerine are fairly similar to those of nitromethane. The dependence of the initial polarization P_0 on pressure p is a steady increasing function.

The experimental arrangement described in (11) has been employed in the study of NB powder shock polarization. It has allowed us to obtain both the polarization and the relaxation signals. Fig. 3 shows a characteristic oscillogram at the pressure 44 kbar.

Unlike liquid explosives the dependence i(t) for NB powder is similar to that of plastics (1,9). In this
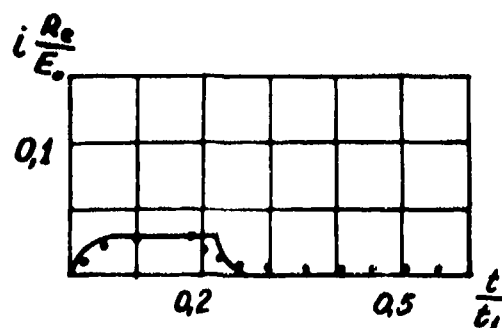
Fig. 2. Nitromethane polarization signal. Solid line presents data calculated with Eq. 1. Points are experimental data at p = 68 kbar.
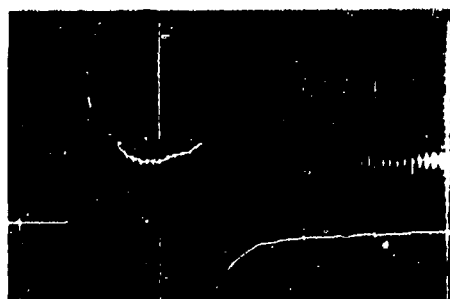
Fig. 3. The polarization and relaxation signals oscillogram of NB powder, p = 44 kbar. Time and voltage scales: 0.6 mksec/div; 1.2 V/div.

case the relaxation signal examination reveals the presence of two polarization mechanisms. The relaxation times of the mechanisms differ from each other by approximately one order of value, e.g., τ_1 being 0.2 mksec, and τ_2 being 1.5 mksec at 44 kbar. The parameters appear to correspond to the polarization of nitroglycerine and nitrocellulose, both being key components of NB powder. The Fig. 4 shows the pressure dependence of the initial density of the polarization current j_0 per unit the dielectric thickness. The dashed line is the extrapolation of the dependence in the shock pressure region up to 370 kbar, the latter corresponding to the pressure behind the shock front of NB powder stationary detonation. To calculate this pressure the shock adiabat (6) and the detonation velocity (12) have been used.

DETONATION

We shall consider the electric signals at the shock initiation of detonation with undetectable time delay.

It is known (13, 14) that condensed explosive detonation products exhibit a high electroconductivity, the latter being caused by electrolytic dissociation of water and other components of the products (15, 16). As a result of a finite rate of explosive decomposition, one can assume that the electroconductivity behind the shock front of the detonation wave arises with some time delay t_3 (8). The time t_3 must coincide approximately with the explosive decomposition induction time.

If the polarization relaxation time is much more than the electroconductivity time delay ($\tau \gg t_3$), the magnitude of t_3 can be determined from the shock
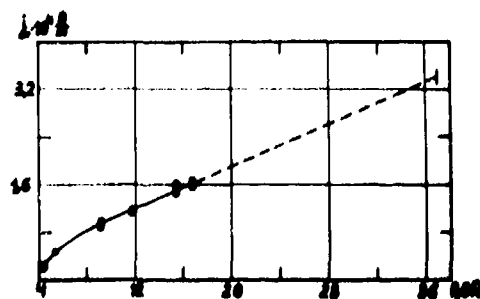
Fig. 4. The initial polarization current density dependence on pressure for NB powder.

145

polarization data. In accordance with Allison's theory for the open circuit, the polarization emf is

$$E = E_o (1 - e^{-t/\tau}) \qquad (3)$$

If we expand the exponent when t is equal to t_3, and deal only with first two temrs of the expansion and take into account the formula (2) for E_o we shall obtain:

$$E = \frac{P_o t_3 (U - u)}{\epsilon_o \epsilon_2} \qquad (4)$$

The polarization current density per unit of the dielectric thickness (17) is equal to:

$$j_o = \frac{P_o \epsilon_1 (U - u)}{\epsilon_2} \qquad (5)$$

From (4) and (5) we shall have:

$$t_3 = \frac{E \epsilon_o \epsilon_1}{j_o} \qquad (6)$$

For NB powder normal detonation the value of t_3 is approximately equal to $6.7 \cdot 10^{-10}$ sec. To calculate t_3 the values of the polarization emf ($E = 28.5$ volt) and the dielectric permittivity ($\epsilon_1 = 9.1$) experimentally measured have been used; however, the polarization current density j_o have been obtained by the extrapolation as shown in Fig. 4.

We shall consider the electric effects at nitromethane detonation in detail. It has been shown by Hayes (18) that nitromethane specific electric resistivity ρ_2 behind the shock front of the detonation wave decreases sharply in some nsec and reaches minimum magnitude approximately $6.2 \cdot 10^{-3}$ Ωm. Therefore in the experiments the following conditions:

$$\rho_2 \epsilon_o \epsilon_2 \ll t_1 \text{ and } \tau \ll t_3$$

are satisfied.

The first condition implies that at any moment the electric field in conducting zone is about zero, and, therefore, the surface of the electroconductivity origin can be regarded as a moving condenser plate. The second condition implies that the polarization re-

laxation is over before the electroconductivity origin, and hence the polarization emf is independent of time; the formula (2) relating to the polarization emf and the initial polarization. To put it another way, the polarization signal shape is determined by a condenser complex resistance change at the shock compression process. When the electroconductivity arises with a time delay the mentioned above conditions permit to apply the polarization probe current expression from the publication (8) for the interpretation of nitromethane detonation electric signals. The curve calculated and experimental points are shown in Fig. 5. The initial current impulse amplitude and time duration were employed to evaluate the emf value (19). The value accounted for 2.5 volt. It should be noted, however, that the contact potential (20) and electrochemical processes (21) could contribute to the emf value. If the electrodes are made of the similar metals, the contact potential presumably can be neglected. The electrode metal ions transition into the detonation products, on the one hand, and selected adsorption of the product ions by the electrode, on the other, are probably responsible for the electrochemical potential origin. The potential value must depend on the electrode metal nature. Hayes (2,20) when studying the detonation electric effect has observed the dependence of the registered signals value on the metal nature of both electrodes. It has been found in (19) that at nitromethane detonation in the arrangement shown in Fig. 1 the final current and the accumulated charge (for the time interval from t_2 to t_1) are larger for aluminum electrode than those of for copper one. This finding is readily accounted for by the data published in (21). It has been shown in (21) that unlike cooper ions, aluminum ions transit easily into the detonation products,
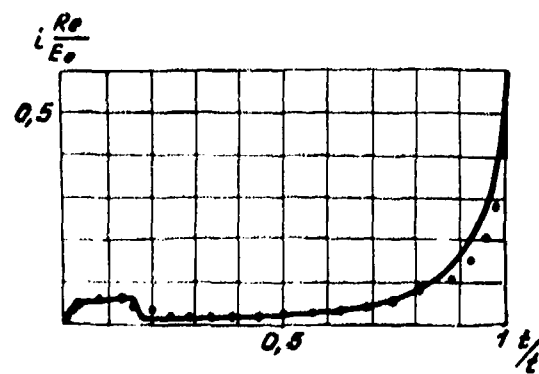
Fig. 5. Nitromethane detonation polarization signal. Solid line is the calculated data from (8); the points are experimental data at p = 157 kbar.

the latter obtaining a positive charge with reference to metal.

SHOCK INITIATION OF DETONATION

It is known (3,22) that at the shock initiation of detonation with some time delay the electric signals have more complex shape than those of during the normal detonation or during the shock explosive compression.

Fig. 6a presents the electric signal oscillogram at the shock initiation of nitroglycerine detonation. The signal shape does differ from that of the normal detonation (Fig. 5). The first impulse occurs at the moment of the shock entrance into the sample. The arrow denotes some small additional positive impulse. It is followed by the negative impulse.

To realize the nature of these constituents, we shall analyze the space-time diagram of the one-dimentional scheme of the shock initiation of detonation in a homogeneous explosive (23). OA line corresponds to the shock wave motion through the sample. The polarization layer width in time is equal to τ and is shown shading. At the metal-explosive interface (OB line) the chemical explosive decomposition occurs in some time delay t_4. It results in origin of supervelocity detonation in shock compressed explosive (CD line). The supervelocity detonation reaction products have a high electroconductivity. Therefore, this detonation front can be considered as a moving plate of the polarization probe. The detonation wave motion is responsible for a sharp increasing of the condenser capacity and, hence, for the origin of positive current impulse. When the supervelocity wave approaches the shock wave front at the distance of $\sim\tau(U - u)$, the polarization emf will start to decrease because of the electric relaxation. At the time t_5 the supervelocity wave overtakes the initiating shock wave front and as a result the overcompression detonation wave arises. For simplicity, we shall take the overcompressed detonation wave to transform into the normal detonation at the very time t_5. As it has been mentioned above, the electroconductivity arises behind the shock front of the detonation wave in time delay t_3. The polarization signal ceases at the t_1--time of reaching the second electrode by the detonation front.

The reaction does not arise simultaneously all over the electrode surface at the real experiment condi-

tions. Therefore, the polarization emf and the capacity of the probe per unit of the surface depend on the radius r. If the force lines bending is neglected, the expression for the current in the circuit of external load will be the following:

$$i = \frac{d}{dt} \int_s E(\tau,t) \, c(\tau,t) \, ds \qquad (7)$$

Fig. 6. The data on shock initiation of detonation in nitroglycerine.

a) an experimental oscillogram at p = 167 kbar. Time and voltage scales: 0.25 mksec/div; 0.4 V/div.

b) space-time diagram of the initiation process.

c) the calculated dependence of $i/i(t_2)$ on t at the following magnitudes of the parameters: $\mathcal{K} = 1$; $\tau/t_1 = 0.01$; $t_2/t_1 = 0.1$; $t_3/t_1 = 0.002$; $t_4/t_1 = 0.3$; $t_5/t_1 = 0.5$; $t_6/t_1 = 0.67$.

The integration is performed all over the probe surface S. To calculate the polarization current from (7) the reaction surface shape should be prescribed. We took it as a paraboloid of rotation.

Fig. 6c shows the calculated signal obtained under the same conditions as the oscillogram shown in Fig. 6a. The time parameters in the calculation have been used from the oscillogram (Fig. 6a). The calculated signal displays all features of the experimental oscillogram. The first positive impulse of the signal corresponds to the ordinary shock polarization of the initial explosives. Diversification t_2 of the shock wave front entrance into the sample determines the time duration of the impulse. The reaction occurs at time t_4. As in this very case, the relaxation time τ is much less than the time of the reaction beginning t_4, the reaction spreads onto the substance that has already relaxed and due to the capacity change the positive current flows through the external circuit. As the supervelocity detonation approaches the initiating shock wave front it enters the polarized substance layer and the electric relaxation effect becomes prevailing the capacity change effect, the former causing the negative current. In the one-dimensional case, the negative impulse of the signal would disappear at the moment of the normal detonation origin t_5. However, due to the supervelocity detonation wave front curvature the normal detonation building-up occurs all over the probe surface for some time interval. The negative impulse time duration is determined by the time interval denoted as $t_6 - t_5$ in Fig. 6c. The impulse shape depends on the shape of the reaction surface. Then the positive current increases because of the capacity effect as in the case of the normal detonation till the signal end time t_1.

Figure 7 illustrates the experimental oscillogram, the space-time diagram and the polarization signal calculated for NB powder. It is the larger time of relaxation when $\tau \gg t_4$ in this case that differs from the case described above. It implies that the chemical reaction occurs inside the polarized substance. The electric relaxation of the polarization occurs and at the moment of the chemical reaction origin as a consequence of it the negative current appears. Further progress of the electric signal occurs similar to nitroglycerine case.

In nitromethane case (Fig. 8) the relaxation time is very small. In the experiments the relaxation time τ is much less than the chemical reaction induction

time t_4 and time delay t_3 of the electroconductivity origin behind the shock front of the detonation wave. It means that there is no electric relaxation effect and the polarization mechanical relaxation process occurs in the dielectric medium. Hence, the
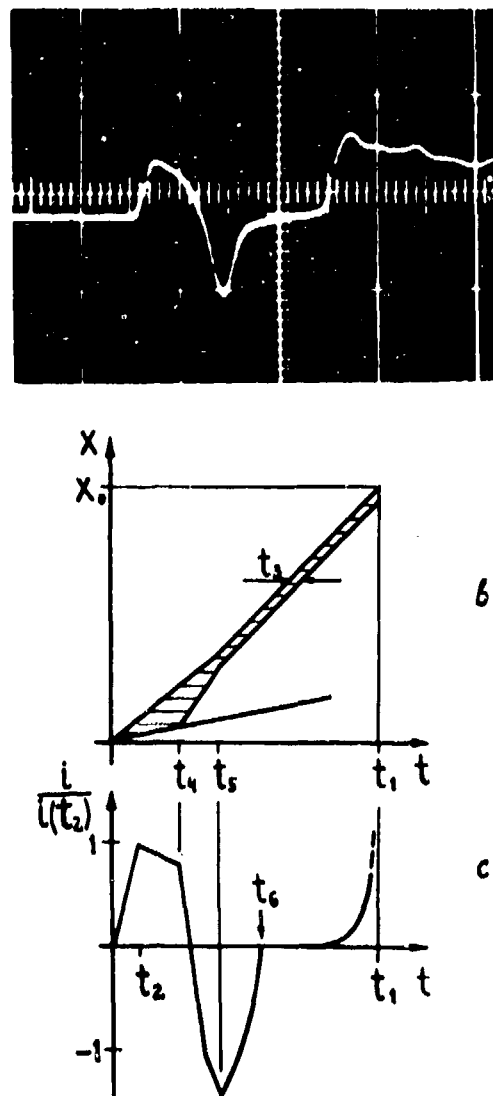
Fig. 7. The data on shock initiation of NB powder detonation.

a) *an experimental oscillogram at p = 165 kbar. Time and voltage scales: 0.25 mksec/div; 1.32 V/div.*

b) *space-time diagram of the initiation process.*

c) *the calculated dependence $i/i(t_2)$ on t at the following magnitudes of the parameters: $\mathcal{K} = 1$; $\tau/t_1 = 1$; $t_2/t_1 = 0.1$; $t_3/t_1 = 0.002$; $t_4/t_1 = 0.25$; $t_5/t_1 = 0.4$; $t_6/t_1 = 0.56$.*

supervelocity detonation motion causes only the positive current due to the capacity change effect.

So, all features of the polarization signals registered at the shock initiation of homogeneous explosives can be interpreted by the competition of the two effects, i.e., the capacity change and the electric relaxation; the signals features being determined by the relation of the times: t_3, t_4 and τ.

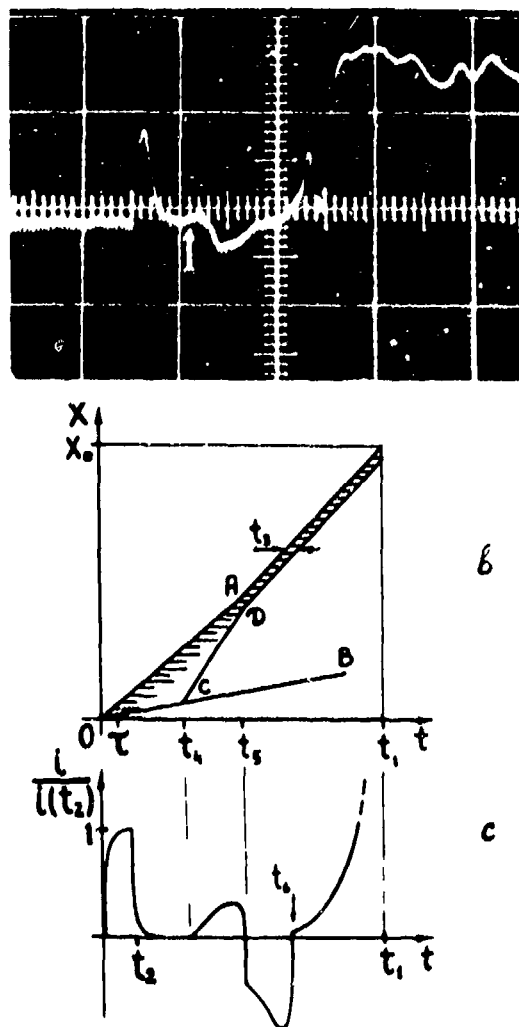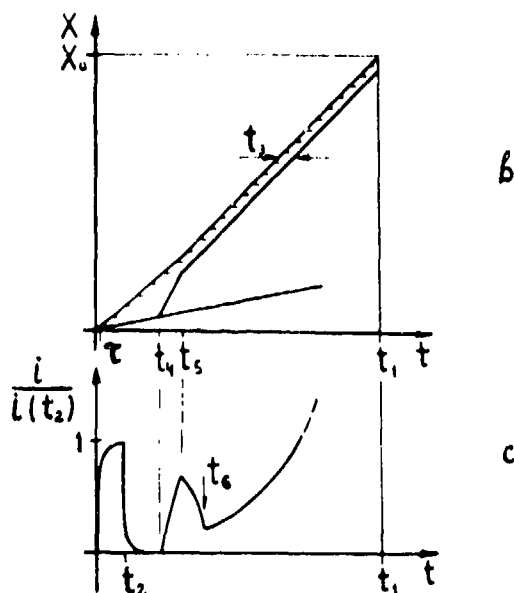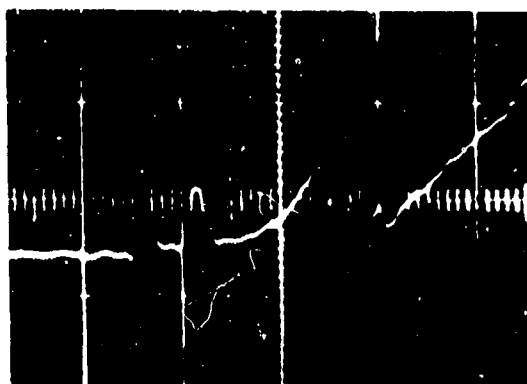*Fig. 8. The data on shock initiation of nitromethane detonation.*

a) *an experimental oscillogram at p = 105 kbar. Time and voltage scales: 0.25 mksec; 0.2 V/div.*
b) *space-time diagram of the initiation process.*
c) *the calculated dependence $i/i(t_2)$ on t at the following magnitudes of the parameters: $\mathcal{K} = 1$; $\tau/t_1 = 10$; $t_2/t_1 = 0.1$; $t_3/t_1 = 0.002$; $t_4/t_1 = 0.23$; $t_5/t_1 = 0.31$; $t_6/t_1 = 0.38$.*

It should be noted that in the overcompressed detonation wave time delay t_3^* of the electroconductivity origin can be much less than t_3 in the normal detonation. If in nitromethane case, t_3^* is of the same order of value as that of τ the polarization signal will be negative at time t_5. The signals observed can be partially determined by the compressed substance polarization in the supervelocity detonation front and by the appearance of the electrochemical emf at the moment of the electroconductivity origin. In our experiments factors did not display qualitatively. It could be due to the marked non-onedimention both of the initiating shock wave and particularly of the occurring chemical reaction surface. However, the factors could be of significance in the experiments by Travis (3) and it is, presumably, the cause of some difference of polarization signals shapes in our experiments and those of the work (3).

CONCLUSION

As a result of this study one can make a conclusion that in all investigated cases the electric signals were caused by the polarization of substance in volume. Given the electroconducting detonation products, electrochemical processes at the metal electrode-detonation products interface make some certain contribution to signals.

REFERENCES

1. R. I. Eichelberger, G. E. Hauver. "Solid State Transducers for Recording of Intense Pressure Pulses," Colloq. Internat. Centre Nat. Rech. Sci., No. 109, pp. 363-381, 1962.

2. B. Hayes, "The Detonation Electric Effect." J. Appl. Phys., Vol. 38, No. 2, pp. 507-511, 1967.

3. I. R. Travis, "Electrical Transducer Studies of Initiation of Liquid Explosives," Proceeding Fourth Symposium (International) on Detonation, pp. 609-615, Washington, 1965.

4. Compendium of shock wave data, Univ. Calif., Vol. 11, 1966.

5. A. N. Dremin, O. K. Rozanov, S. D. Savrov, V. V. Yakushev, "The Shock Initiation of Nitroglycerine Detonation," Fiz. Gor. i Vzr., Vol. 3, No. 1, pp. 11-18, 1967.

6. A. N. Dremin, S. D. Savrov, V. S. Trofimov and K. K. Shvedov, "Detonation Waves in Condensed Media." Nauka, Moscow, 1970.

7. S. S. Nabatov, V. V. Yakushev, A. N. Dremin, "Electrical Properties of Nitromethane under Shock Compression," Fiz. Gor. i. Vzr., Vol. 11, No. 2, pp. 300-304, 1975.

8. A. G. Antipenko, S. S. Nabatov, V. V. Yakushev, "Electrical Polarization of the Fast Relaxing Dielectrics at Shock Compression," Fiz. Gor. i Vzr., Vol. 11, No. 3, pp. 462-467, 1975.

9. G. E. Hauver, "Shock-Induced Polarization in Plastics. II. Experimental Study of Plexiglas and Polystyrene," J. Appl. Phys., Vol. 36, No. 7, pp. 2113-2118, 1965.

10. S. S. Nabatov, V. V. Yakushev, A. N. Dremin, "Electrical Polarization of Nitroglycerine Induced by Shock Wave," Fiz. Gor. i Vzr., Vol. 12 No. 2, pp. 251-255, 1976.

11. V. V. Yakushev, O. K. Rozanov, A. N. Dremin, "On the Measurement of the Polarization Relaxation Time in a Shock Wave," Zh. Experim. Teor. Fiz., Vol. 54, II, pp. 396-400, 1968.

12. A. J. Apin, I. D. Kostin, L. N. Stesik, "Detonation of Ballistic Powders," Dokl. Acad. Nauk SSSR, Vol. 137, No. 3, pp. 652-653, 1961.

13. A. A. Brish, M. S. Tarasov, V. A. Tsukerman, "Electrical Conductivity of the Explosion Products of Condensed Explosives," Zh. Experim. Teor. Fiz., Vol. 37, No. 6(12), pp. 1543-1550, 1959.

14. M. A. Cook, "The Science of High Explosives," London, 1958.

15. V. V. Yakushev, A. N. Dremin, "The Nature of Electric Conductivity of Detonation Products of Condensed Explosives," Dokl. Acad. Nauk SSSR, Vol. 221, No. 5, pp. 1143-1144, 1975.

16. A. G. Antipenko, A. N. Dremin, V. V. Yakushev, "On the Electric Conductivity at the Detonation of Condensed Explosives," Dokl. Acad. Nauk SSSR, Vol. 225, pp. 1086-1088, 1975.

17. F. E. Allison, "Shock-Induced Polarization in Plastics. I. Theory," J. Appl. Phys., Vol. 36, No. 7, pp. 2111-2113, 1965.

18. B. Hayes, "Electrical Measurements in Reaction Zones of High Explosives," Tenth Symposium (International) on Combustion, Combustion Inst., pp. 869-874, Pittsburgh, 1965.

19. A. G. Antipenko, A. N. Dremin, S. S. Nabatov, V. V. Yakushev, "Electrical Effects at Shock Compression and Detonation of Liquid Explosives," Fiz. Gor. i Vzr., Vol. 11, No. 3, pp. 438-443, 1975.

20. B. Hayes, "Dependence of Detonation Electric Effect on Electrode Metal," Private Communication.

21. A. N. Dremin, V. V. Yakushev, "Electrochemical Effects of Nitromethane Detonation," Acta Astronautica, I, 885, 1974.

22. I. Morvan, H. Pujols, "Shock-induced Electrical Polarization of a solid Explosive," Proceedings— Fifth Symposium (International) on Detonation, pp. 429-434, Pasadena, California, 1970.

23. R. F. Chaiken, J. Chem. Phys., Vol. 33, 760, 1960.

SOME APPLICATIONS OF THE ELECTRICAL JUNCTION EFFECT IN EXPERIMENTAL SHOCK STUDIES*

Behavior of Al-Cu composite materials under shock loading.
Detection of a phase transition in bismuth and Hugoniot elastic limits in Al-Cu alloys.

J. P. Romain and J. Jacquesson
Laboratoire d'Energétique et de Détonique (L.A. CNR S n° 193)
ENSMA—CEAT—Université de Poitiers—Rue Guillaume VII
86034—POITIERS Cédex—France

The electrical effect produced by the passage of a shock wave through a bimetallic junction gives the basis of an experimental method used for vizualising the shock front propagation in lamellar Al-Cu composites. These materials are found to behave under shock loading like homogeneous materials. Explanation for the shock front steadiness is given by an analysis of the stress-time history resulting from multiple reverberations at Al-Cu interfaces. The same experimental method is applied for the detection of double-wave shock configurations resulting from an Hugoniot elastic limit in an Al-Cu alloy and from a phase change in bismuth at 70 kbar. The slope of the phase line in the pressure-temperature plane is derived from the measurements. Comparison with static data indicates that this dynamic phase transformation corresponds to the Bi I—Bi V transition.

INTRODUCTION

The electrical effect produced by the passage of a shock wave through a bimetallic junction, first reported by Jacquesson (1) in 1959, has been experimentally and theoretically studied by several investigators mainly in France (2) and in U.S.S.R. (3,4,5). The basic features of this effect have been described in previous papers (2) and the most comprehensive theoretical interpretation has been given by Migault (6).

Some attempts were made in the past in order to study the shock behavior of dense materials with the use of experimental methods based on this effect. Results obtained on germanium and bismuth were presented at the 5th symposium on detonation in 1970 (7). This work was later on extended and new results were obtained showing the availability of the method for investigating materials under shock loading. This paper presents a review of some applications recently developed in our laboratory about the behavior of lamellar Al-Cu composites under shock and the detection of shock front instabilities resulting from an Hugoniot elastic limit of an Al-Cu alloy and from a phase transformation in bismuth.

I—SHOCK BEHAVIOR OF LAMELLAR COMPOSITE MATERIALS

(1) Studied Materials

The studied materials were Al-Cu composites constituted by alternate layers of aluminum and copper, a few tens microns in thickness, piled up and pressed together, constituting samples of total thickness between 1.7 mm and 3.5 mm. Two composites characterized by their average composition were studied: composite E (33% Cu, 67% Al) and composite I (45% Cu, 55% Al) in weight composition. Composite I was

151

TABLE 1

Al-Cu Samples: Composition and Structure

Sample type	E	I_1	I_2	I_3
Weight composition	33% Cu, 67% Al		45% Cu, 55% Al	
Density (g/cm³)	3.51		3.93	
Cu lamellas thickness (mm)	0.03	0.03	0.05	0.05
Al lamellas thickness (mm)	0.20	0.12	0.20	0.20
Total number of Al-Cu pairs	8	14	7	14
Sample total thickness (mm)	1.84	2.10	1.75	3.50
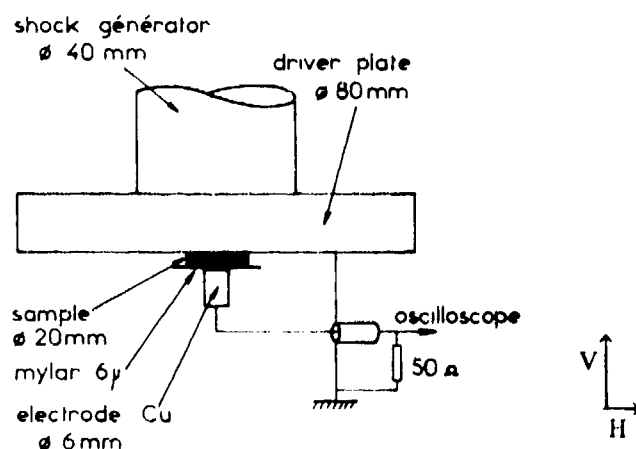
Fig. 1. Schematic of an experimental arrangement for shock behavior investigation of lamellar Al-Cu composites.

elaborated in three forms I_1, I_2 and I_3 differentiated by the thickness and total number of the lamellas constituting the samples. The composition and structure of the investigated samples are listed in Table 1.

(2) Experimental Method

The samples were submitted to plane shock waves of known amplitude propagating in a direction perpendicular to the plane of the layers. Figure 1 shows the schematic of an experimental arrangement. Shock waves were generated by explosive charges put on a metallic driver plate transmitting the incident shock into the sample pressed on the opposite face. Various initial pressures were obtained by changing the nature of the explosive and the nature of the driver plate
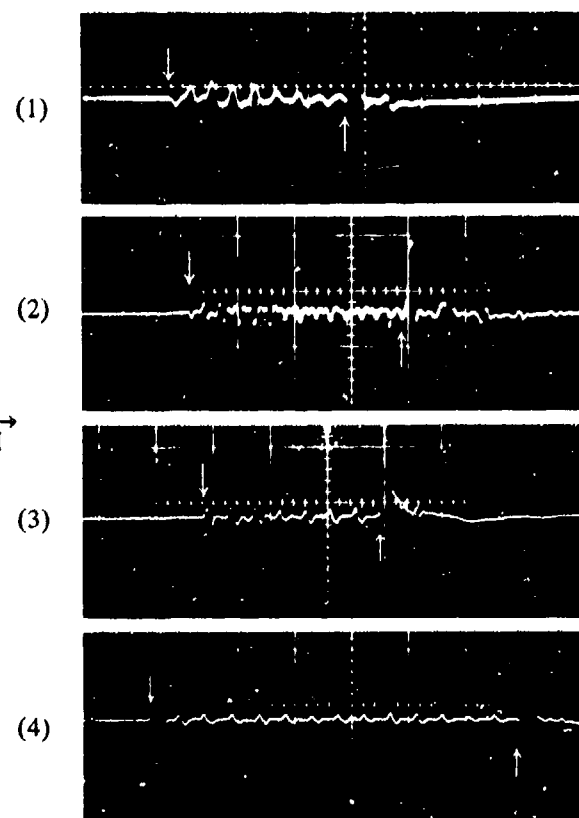
Fig. 2. Typical records of the shock wave propagation in lamellar Al-Cu samples.

Sample type: E (1); I_1 (2); I_2 (3); I_3 (4). Loading stress in the aluminium driver plate: 97 kbar (1); 107 kbar (2); 145 kbar (3); 107 kbar (4).
V: 100 mV (1, 2): 50 mV (3, 4)
H: 0,1 μs (1, 2, 3, 4)
The arrows show the instants of entrance and emergence of the shock wave into and from the sample.

(aluminium or copper) or its thickness. The pressure of the incident wave in the driver plate, just before entering the sample, was previously determined by experimental calibration and the Hugoniot curves for aluminium and copper were used as reference for the determination of the transmitted shock amplitude in the sample. A vizualisation of the shock propagation through the sample was obtained from the electrical signals generated by the passage of the shock front at the successive Al-Cu interfaces. A thin mylar sheet (6 microns) was introduced between the sample and the back-up electrode. The dielectric polarization of mylar under shock produces an electrical signal of the order of 100 mV amplitude and a few nanoseconds in rise-time, quite distinguishable from the Al-Cu junction signals of only some 10 mV amplitude, and giving precisely the arrival time of the shock at the back face of the sample. Figure 2 shows a set of typical oscillograms obtained with the various Al-Cu investigated composites. The periodical Al-Cu junction signals clearly reveal the time when the shock front crosses the successive Al-Cu interfaces and allow a precise chronometric study of the shock propagation through the sample. In comparison with other electrical or optical techniques currently used, the great advantage of this system derives from the
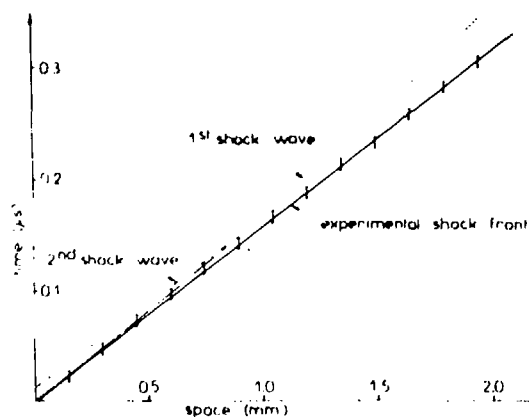
Fig. 3. Space-time diagram showing the shock front stability in a lamellar Al-Cu sample.

possibility of vizualising the shock propagation within the studied material, in addition with a very good time resolution.

(3) Experimental Results

Shock stability. Analysis of the records shows that the shock front velocity is constant through the
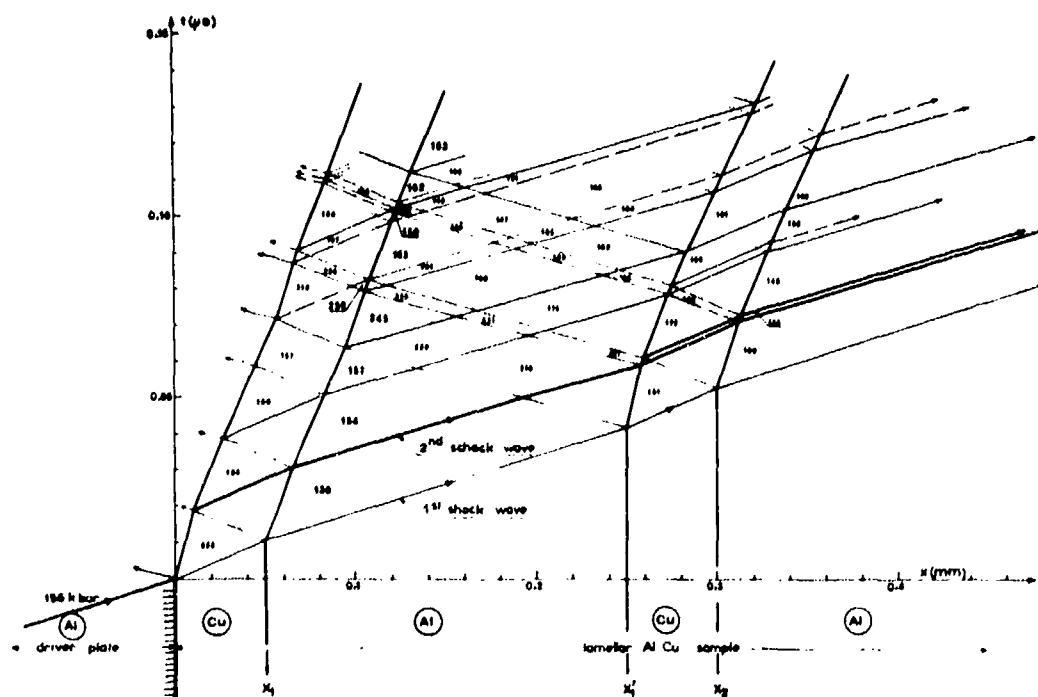
Fig. 4. Space time diagram in the first layers of a type I_2-I_3 sample shock-loaded at 155 kbar. Numbers denote the pressure in kbar units.
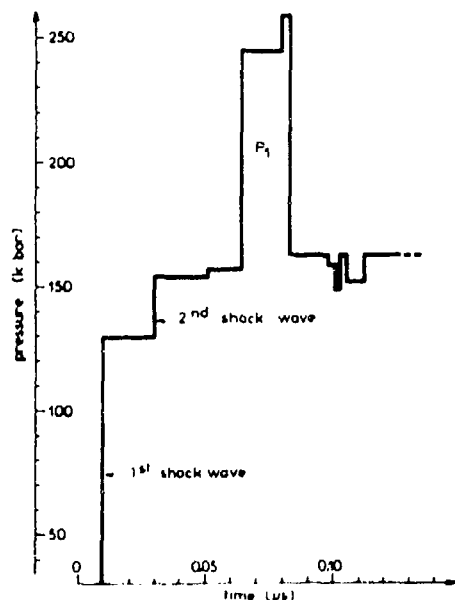
Fig. 5. Shock wave configuration at X_1 interface.

sample. Illustration of this result is given in Fig. 3 by the space-time (x, t) diagram relative to an experiment performed on a type l_1 sample. Taking into account uncertainties in the measurements, it appears that the experimental points lie on a straight line, the slope of which yields the velocity of the shock front. In the lamellar Al-Cu composite, the direction of shock propagation being perpendicular to the plane of the layers, the formation of a stable shock front necessarily results from an interaction between multiple shock and relief waves generated at Al-Cu interfaces. The propagation of the first shock wave begins at time t_0 when the shock issued from the driver plate enters the sample. The amplitude and velocity of this wave steadily decrease in the course of its propagation because of the successive transmissions from aluminium to copper. The corresponding (x, t) curve separates from that relative to the experimental shock front. After some delay, the interval between both curves becomes larger than the uncertainties in the measurements. This result gives evidence that a steady shock is already formed in the early stages of the propagation.

In order to have some informations about the process leading to the formation of a steady shock, we have constructed the (x, t) diagram of the multiple wave propagation in the first layers of a type I_2-I_3 sample. The construction shown in Fig. 4 was done

for an initial stress level of 155 kbar in aluminium, corresponding to an average value in the studied pressure range. The shock profile in pressure-time (P, t) coordinates at the first Al-Cu interface designed by X_1 in Fig. 4 is deduced from this construction and shown in Fig. 5. The point of primary interest to be noted is that the second shock wave following the first one at 20 ns interval brings the material in a pressure state near equilibrium. The pressure increase behind this wave is slow, except peak P_1 resulting from a reverberation of the first shock wave at X'_1 interface. Similar peaks of decreasing amplitude occur periodically at about 100 ns interval. They result from reverberations at the successive Al-Cu interfaces X'_2, X'_3, ... and do not appear on Fig. 5 limited to the first 120 ns of the pressure evolution. The role of these irregularities in the establishment of equilibrium state is not significant. However, because of their high amplitide they travel through the sample with a significantly faster velocity and may accelerate the process. A similar analysis at X_2 interface shows that the second wave is in fact constituted of two close successive shocks, and more generally at X_n interface of n close successive waves. Because of the approximations made in the construction, it is quite likely that these successive waves, separated by only a few nanoseconds, form into an unique shock front which brings the material near the equilibrium pressure. So, the first result given by this analysis concerns the equilibrium regime establishment, which appears to be essentially governed by the two first shock waves.

Another important feature revealed by the diagram of Fig. 4 concerns the velocity of the second shock. During its propagation through the first aluminium layer, this wave interacts with the backward reflected first shock at X_1 interface. As a consequence, the amplitude and velocity of this wave are increased. The same process occurs in each aluminium layer, so that the mean velocity of the second shock through the sample does not decrease. In the same time, the first shock wave velocity decreases. This results in a convergence of both waves, the second wave overtaking the first one at a distance evaluated at 5 or 6 pairs of Al-Cu layers. At that distance, Fig. 3 shows that the first shock wave and the experimental shock front are still close to another. This result explains the reason why the first shock wave and the experimental shock front are quite distinct after some delay. It is worth noting here the differences in the notion of "shock front" for an homogeneous material and for a lamellar composite. In the latter case, a stable shock front proceeds from an accumulation

154

of several shock waves bringing the material in its equilibrium state, instead of a single wave in the case of an homogeneous material.

Hugoniot curves. The existence of a steady shock front in the Al-Cu composites demonstrates that the shock behavior of these materials is similar to that of homogeneous materials. As a consequence, it is possible to determine their experimental Hugoniot curves. This was made by an impedance matching method, from the known amplitude of the incident shock in the driver plate and the measured shock velocity in the samples. The detailed numerical results are given in a previous paper (8), where it is also demonstrated that the shock compressibility of the investigated composites satisfies to a linear relationship between shock velocity D and particle velocity u. The extrapolation of the D(u) relation at u = 0 yields experimental values for the bulk sound velocities which are in good agreement with those calculated from the known properties of the constituents.

Fig. 6. *Hugoniot curves for the lamellar Al-Cu composites. Full lines are calculated curves.*

The experimental Hugoniot curves for the composites may be compared with those computed from the known Hugoniot curves for the constituents. In view of this calculation, several models may be used. They differ essentially by the assumptions made on thermal interactions between constituents. When the shock amplitude does not exceed one or two megabars, the thermal effects on the total pressure in the sample are small in comparison with the pure mechanical effects, so that the Hugoniot curves obtained from different calculational models are close one another. We have developed a model similar to the model of mixtures derived by Mc Queen et al (9), but using a particular form for the Grüneisen parameter characterized by a constant specific of each solid and determined either from the experimental Hugoniot curve or from the elastic properties of the solid (10). This model presented in a previous paper (11) is applied here to the Al-Cu composites and yields a satisfactory agreement between the experimental and calculated Hugoniot curves, as shown in Fig. 6.

II–DETECTION OF HUGONIOT ELASTIC LIMITS AND PHASE TRANSITIONS

(1) Experimental Method

The experimental method described above was applied with some modifications to the detection of

multiple wave structures induced by Hugoniot elastic limits (H.E.L.) or phase transitions. The experimental arrangement is shown in Fig. 7. In this modified system the mylar sheet was introduced between the driver plate and the sample in order to determine with precision the arrival time of the incident shock at the front face of the sample. The electrical response of the sample-electrode junction was used to obtain a vizualisation of the shock wave configuration at the sample issue, and to establish shock wave transit-times from which shock wave velocities were calculated. The Hugoniot curves for the investigated materials could be then determined by means of an impedance match solution. In these experiments the back-up electrode was made out of constantan (CTE) instead of copper, because the signal amplitude is higher when CTE is used.

(2) Hugoniot Elastic Limit of an Al-Cu Alloy

The initial weight composition of the investigated material was 49% Cu, 51% Al. This corresponds to an alloy composed of about 92% Al_2 Cu defined compound and 8% Al. The shock behavior of this material was studied in the pressure range from 30 kbar to 150 kbar with the use of aluminium as reference material. Figure 8 shows a set of oscillograms revealing the shock wave structure in the investigated material and its evolution with the loading pressure. At high pressure (record 1) a single electrical front is
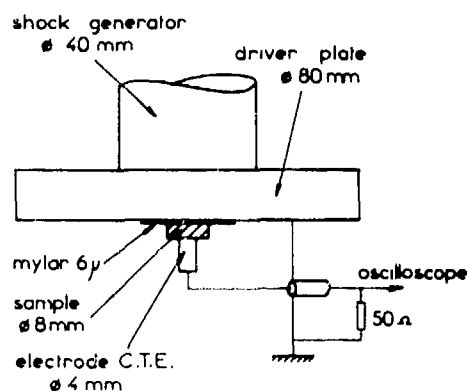
Fig. 7. Schematic of an experimental arrangement for detection of multiple-wave shock structures.

observed. It is generated by the shock arrival at the sample-electrode interface, indicating that the pressure profile is composed of a single wave. In a lower pressure range (records 2-5), two electrical fronts are observed indicating that the initial shock breaks up into two successive waves in the course of its propagation through the sample. Finally, at very low pressure (record 6) a single wave is observed again. This evolution characterizes materials exhibiting a shock instability due either to a dynamic yield point (H.E.L.) or a phase transformation.

The present instability is later identified as an H.E.L. Analysis of experimental results listed in Table 2 shows that the shock front becomes instable for a loading stress between 38 kbar and 41 kbar in the aluminium driver plate. Assuming that the transition occurs at a reference pressure of 40 kbar, we obtain the coordinates of the transition point in the Al-Cu alloy from the measured velocity of the first wave: (5.95 ± 0.10) mm/μs. These coordinates are:

P: pressure	49 kbar
D: wave velocity	5.95 mm/μs
u: particle velocity	0.199 mm/μs
ρ: density	4.24 g/cm^3

The uncertainty on the transition pressure was evaluated to ± 5 kbar resulting partly from the uncertainty on the corresponding reference pressure in the aluminium driver plate and partly from the uncertainty on the measured wave velocity. The Hugoniot curve for the investigated alloy is given on Fig. 9.

The shock instability at 49 kbar was identified as an H.E.L. for the following reasons:

• in the assumption of a phase transition, this should be observed also under static pressure. But the variations of electrical resistivity of this alloy recorded under static compression up to 100 kbar did not reveal any irregularity which could be related to a phase transformation.

• in the assumption of an H.E.L., the first wave velocity should be close to the longitudinal sound velocity. This velocity was measured by ultrasonic techniques and the obtained value of 5886 m/s ± 5 m/s agrees with the shock value of 5950 m/s ± 100 m/s.

For these reasons we conclude that the shock instability is to be attributed to an H.E.L. This conclusion was further confirmed by an investigation of Al-Cu alloys having various proportions of their constituents Al$_2$Cu and Al (12).

(3) Detection of a Phase Transformation in Bismuth

The phase diagram for bismuth, Fig. 10, established under static compression reveals several polymorphic transitions. Up to the present work, only the Bi I-Bi II transformation at 25 kbar was reported under dynamic compression (14,15). The transition Bi III-Bi V at 78 kbar and room temperature was never observed under dynamic pressure loading. This pressure is easily attainable with the use of our shock generating systems, therefore we studied the shock behavior of bismuth in a pressure range allowing the detection of a possible shock induced phase change related to the Bi III-Bi V transition. The experimental procedure used was identical to that used in the study of Al-Cu alloys.

Double-wave structures were observed in bismuth from 70 kbar to 86 kbar demonstrating that a phase transition takes place at 70 kbar. Figure 11 shows records of the shock profile and its typical evolution with the loading stress. The coordinates of the transition point in bismuth are:

P = 70 kbar,	D = 2.195 mm/μs,
u = 0.3253 mm/μs,	ρ = 11.505 g/cm^3.

As before, the uncertainty on the transition pressure was estimated to be ± 5 kbar. The Hugoniot curve for bismuth determined from our experimental results is shown in Fig. 12. Complete experimental results and their detailed analysis may be found in
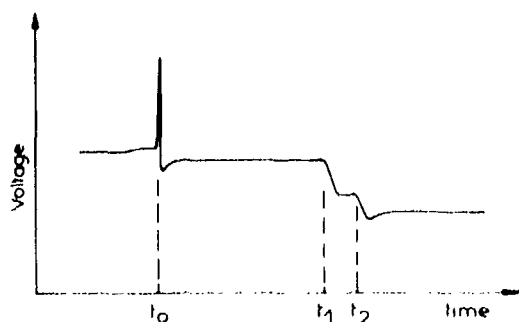
Typical oscillogram

t_0: arrival time of the incident shock wave at the front face of the sample (mylar polarization signal)

t_1, t_2: arrival time of the elastic wave (t_1) and shock wave (t_2) at the back face of the sample (AlCu-CTE junction signal)

V: 20 mV (1-5); 50 mV (6)
H: 0.1 μs (1-5); 0.2 μs (6)
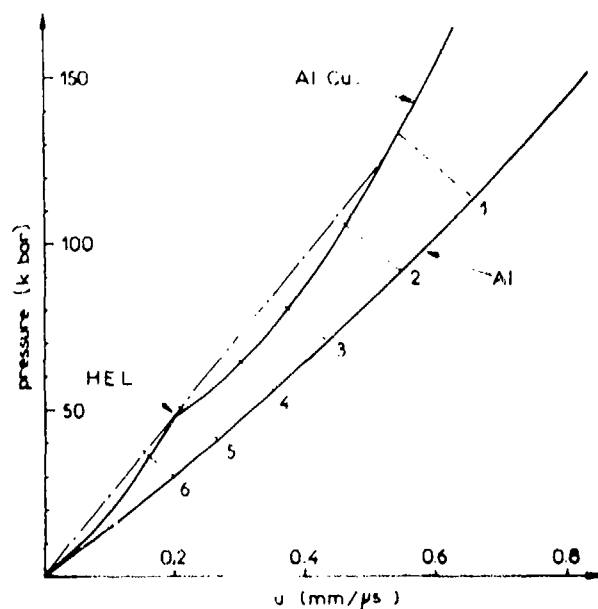
Hugoniot curve in (P, u) coordinates. The curvature is accentuated in order to make more apparent the limits of the instability region.

(1) P_R = 114 kbar
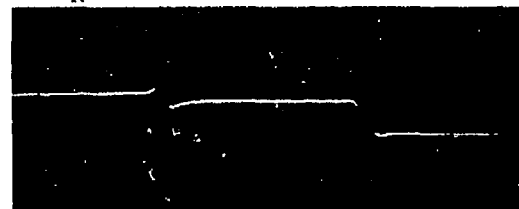
(2) P_R = 92 kbar
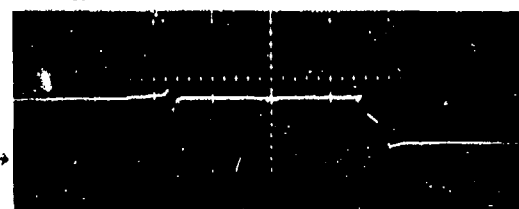
(3) P_R = 71 kbar

(4) P_R = 55 kbar
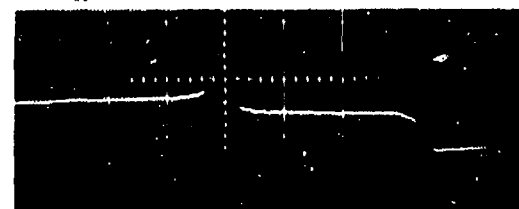
(5) P_R = 41 kbar
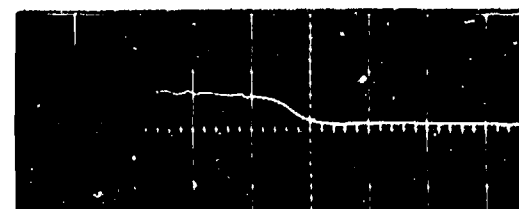
(6) P_R = 30 kbar

Fig. 8. Records of the shock wave structure in an Al-Cu alloy. Evolution with loading pressure P_R in the aluminium driver plate.

TABLE 2

Al-Cu Alloy Experimental Shock Results

P_R (kbar)	x_o (mm)	D_1 (mm/µs)	u_1 (mm/µs)	P_1 (kbar)	D_2 (mm/µs)	u_2 (mm/µs)	P_2 (kbar)
30	2.37	5.5 *	0.158	36			
38	2.00	5.5 *	0.200	45			
41	2.01	6.05			5.51	0.207	51
56	2.02	5.85	0.199	49	5.30	0.282	67
71	2.00	5.92			5.53	0.360	85
92	2.01	6.00			5.59	0.462	109
114	2.00	5.85	0.567	136			
145	2.01	6.00	0.696	176			

P_R: shock pressure in the aluminium driver plate; x_o: sample thickness; $D_1, u_1, P_1, D_2, u_2, P_2$: wave velocity, particle velocity and pressure for the first wave (subscript 1) and for the second wave (subscript 2), *: precision on $D_1 \pm 0.5$ mm/µs, for all other experiments ± 0.10 mm/µs.

ref. (16) where it is also demonstrated that the observed dynamic phase change is related to the Bi III-Bi V transition. The difference between the static value of 78 kbar and the dynamic value of 70 kbar for the transition pressure is accounted for by the temperature increase in the samples submitted to shock compression. In addition to the analysis given in ref. (16), we have calculated from our experimental results the slope dP/dT of the phase line in the pressure temperature plane corresponding to the observed shock induced transition. We used for this purpose the following equation demonstrated by Duff and Minshall (14):

$$\left(\frac{dP}{dT}\right)^2 + \frac{2\alpha}{K_A^{-1} - K^{-1}} \frac{dP}{dT} - \frac{C_P}{TV(K_A^{-1} - K^{-1})} = 0 \quad (1)$$

where all quantities are evaluated at the transition point: pressure P, specific volume V, temperature T, thermal expansion coefficient α, specific heat at constant pressure C_P and bulk modulus K of the initial phase; bulk modulus K_A of the mixed phase just above the transition point. The values of these parameters are listed in Table 3.

P and V are obtained from our experimental results. T is estimated, assuming that a low shock pressure, the Hugoniot and the isentrope are essentially the same. The following expression for isentropic compression is used:

$$T = T_o \exp\frac{\gamma_o}{V_o}(V_o - V) \quad (2)$$

where subscript o refers to the initial state. The ratio γ/V, where γ is the Grüneisen coefficient, is assumed to be constant. We consider also that under shock loading, bismuth transforms directly from phase I to phase V when the shock amplitude exceeds 70 kbar.
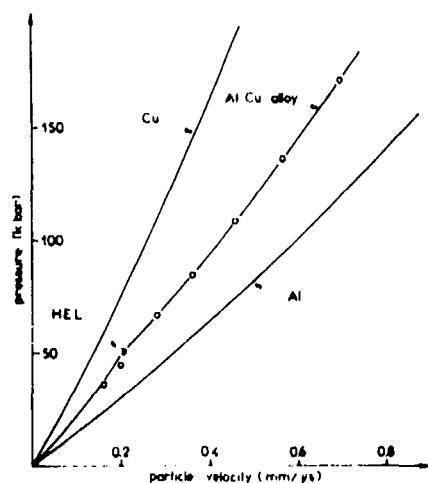
Fig. 9. Hugoniot curve for the investigated Al-Cu alloy.
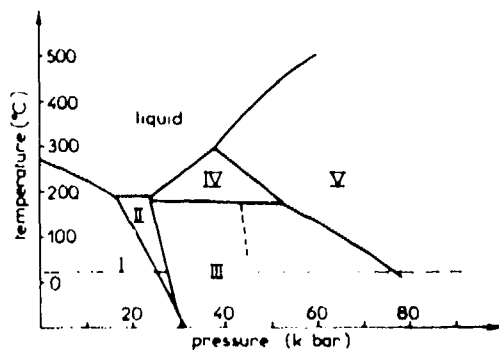
Fig. 10. Phase diagram for bismuth (13).

The initial conditions are

$$T_o = 293\ ^\circ K; \quad V_o = 0.10204\ g/cm^3$$

γ_o is deduced from the thermodynamic relation:

(1) $P_R = 79$ kbar
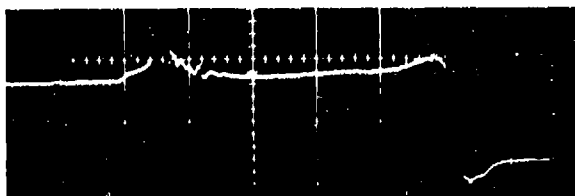
(2) $P_R = 75$ kbar
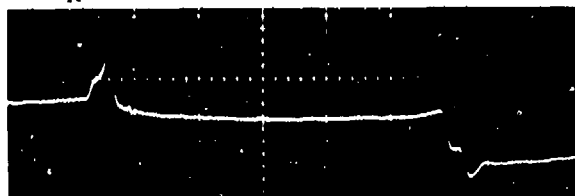
(3) $P_R = 60$ kbar
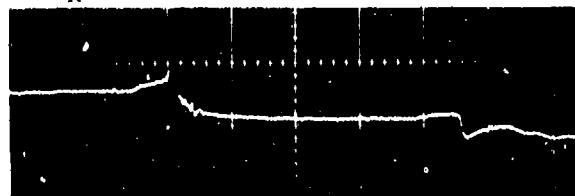
Fig. 11. Records of the shock wave structure in bismuth and evolution with loading pressure P_R in the aluminium driver plate.

V: 10 mV (1, 2, 3)
H: 0.1 μs (1): 0.2 μs (2, 3)
Sample thickness: 105 mm (1); 2.30 mm (2);
1.97 mm (3).

$$\gamma_o = \frac{\alpha_o\ K_o\ V_o}{C_V} \qquad (3)$$

The values of α_o and K_o are taken from recent data of Fritz (17) about the variations of elastic moduli of bismuth with pressure and temperature:

$$\alpha_o \approx 4.2\ 10^{-5}\ ^\circ C^{-1}$$

$$K_o = 3.620\ 10^{11}\ dynes/cm^2$$

The value of the specific heat at constant volume C_V is taken from data of Gschneidner (18): $C_V = 6.12$ cal/at.g. The value of K at 70 kbar is extrapolated from measurements made by Fritz on the Bi I phase stable up to 25 kbar, and the value of α is deduced from Eq. (3) where all quantities are then taken at 70 kbar pressure and C_V is assumed independent of pressure. Finally the value of K_A is derived from our shock measurements as schematically illustrated by Fig. 13, where point A refers to the phase transition, M to a point in the mixed phase region and D_M to the velocity of the second shock wave. Our experimental results yield:

$$\lim_{M \to A} D_M = 1.925\ mm/\mu s$$
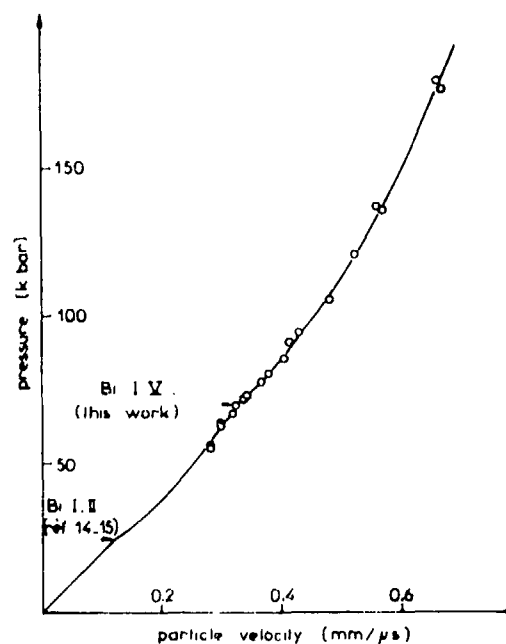
Fig. 12. Hugoniot curve for bismuth.

159

TABLE 3

Parameters for Bi at the Transition Pressure of 70 kbar

P (kbar)	V (cm³/g)	T (°K)	α	K (dynes/cm²)	C_P (cal/at.g)	K_A (dynes/cm²)
70	0.0869	353	$1.89 \ 10^{-5}$	8.10^{11}	6.20	$2.043 \ 10^{11}$

$$K_A = V_A \lim_{M \to A} \frac{P_M - P_A}{V_A - V_M}$$

$$= \frac{1}{V_A} \lim_{M \to A} (D_M - u_A)^2$$
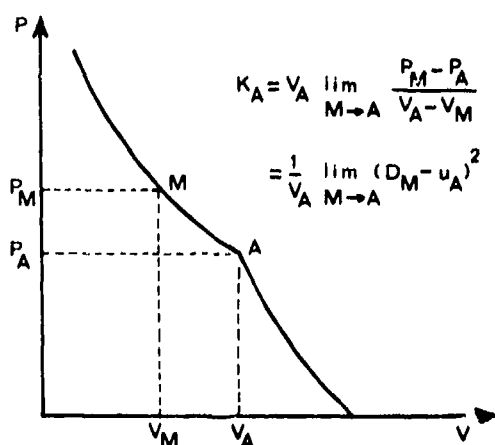
Fig. 13. Determination of the bulk modulus K_A in the mixed phase region.

The corresponding value of K_A is reported in Table 3. The value of the phase line slope derived from Eq. (1) at 70 kbar is:

$$\frac{dP}{dT} = -1.47 \ 10^8 \text{ dynes cm}^{-2} \text{ }^\circ K^{-1}$$

This value may be compared to the slope of the Bi III-V phase line, the equation of which was established from measurements under static pressure by Haygarth et al. (19).

$$P_{III-V} = 96.048 - 2.0949 \ 10^{-4} \ T^2 \qquad (4)$$

where units are kbar for P and °K for T. It must be first noticed that at 353 °K, which is the calculated temperature in bismuth shock-loaded at 70 kbar, Eq. (4) predicts $P_{III-V} = 70$ kbar. This is exactly the same value as that determined for dynamic transition pressure. This result obtained with the recent data of Fritz improves the former result given in ref. (16).

From Eq. (4), the slope of the Bi III-V phase line at 70 kbar is:

$$\left(\frac{dP}{dT}\right)_{III-V} = -1.48 \ 10^8 \text{ dynes cm}^{-2} \text{ }^\circ K^{-1}$$

This value differs only of 0.7% from the slope derived from shock measurements. Taking into account the approximations made in the calculations, the agreement between both values may be considered as excellent and confirms that under shock loading, bismuth transforms directly from phase I to phase V when the applied stress exceeds 70 kbar, and that the dynamic Bi I-V phase line is identical to the static Bi III-V phase line.

CONCLUSION

The electrical effect produced by the passage of a shock wave through a bimetallic junction gives the basis of a simple and efficient procedure for investigating the properties of solids submitted to dynamic compression. With the use of this method, we could obtain a vizualisation of the shock front propagation through samples of lamellar Al-Cu composites and accomplish a detailed study of the shock behavior of these materials. The same technique used for the vizualisation of shock front instabilities allowed us to detect the Hugoniot elastic limit of an Al-Cu alloy and the Bi I→V phase transition at 70 kbar in bismuth. This shock induced phase transformation was never previously observed, perhaps because of the narrow pressure range in which the resulting double-shock configuration appears (from 70 kbar to 86 kbar). The good precision and time resolution of our experimental method made this detection possible. These qualities of the method appear as a great advantage in comparison to the possibilities of other experimental methods used in shock wave physics.

REFERENCES

1. J. Jacquesson, Bulletin du GAMAC, 4, 4, 33, 1959.

2. J. Crosnier, J. Jacquesson and A. Migault, Proceedings of the 4th symposium on Detonation, p. 627, 1965.

3. U. S. Illyukhin and V. N, Kologrivov, Zhur. Fiz. 5, p. 175, 1962.

4. S. A. Bordzylovski, S. M. Karakhanov, Sov. Phys. Tech. Phys. 18, 9, p. 1246, 1974.

5. S. A. Bordzylovski, S. M. Karakhanov, and V. V. Polinbov, The Physics of Combustion and explosion, 4, p. 586, 1972.

6. A. Migault and J. Jacquesson, Le Journal de Physique, 33, p. 599, 1972.

7. J. Jacquesson, J. P. Romain, M. Hallouin and J. C. Desoyer, Proceedings of the 5th symposium on detonation, p. 403, 1970.

8. J. P. Romain et J. Jacquesson, Revue de Physique appliquée, 8, p. 157, 1973.

9. R. G. Mc Queen, S. P. Marsh, J. W. Taylor, J. N. Fritz and W. J. Carter, High impact Velocity Phenomena, Academic Press, p. 293, 1970.

10. J. P. Romain, A. Migault and J. Jacquesson, J. Phys. Chem. Solids, 37, p. 1159, 1976.

11. J. P. Romain, M. Hallouin, A. Migault and J. Jacquesson, C.R.A.S., B, 274, p. 1432, 1972.

12. J. P. Romain and J. Jacquesson, to be published.

13. J. F. Cannon, J. Phys. Chem. Ref. Data, 3, 3, p. 781, 1974.

14. R. E. Duff and F. S. Minshall, Phys. Rev. 108, p. 1207, 1957.

15. D. B. Larson, J. Appl. Phys. 38, p. 1541, 1967.

16. J. P. Romain, J. Appl. Phys., 45, p. 135, 1974.

17. J. J. Fritz, J. Appl. Phys. 45, p. 60, 1974.

18. K. A. Gschneidner, Sol. St. Phys. 16, Academic Press, 1964.

19. J. C. Haygarth, H. D. Luedmann, I. C. Getting and G. C. Kennedy, J. Phys. Chem. Solids, 30, p. 1417, 1969.

THE JCZ EQUATIONS OF STATE FOR DETONATION PRODUCTS
AND THEIR INCORPORATION INTO THE TIGER CODE

M. Cowperthwaite and W. H. Zwisler
Stanford Research Institute
Menlo Park, California 94025

The Jacobs equations of state, J1, J2, and J3, based on intermolecular potentials for a single species, were rewritten for a mixture containing n moles of s species, labeled JCZ1, JCZ2, and JCZ3, and programmed into the TIGER code so that they could be used to make detonation calculations. Calculations were made on RDX and TNT at different loading densities to provide a means of testing these equations of state, the values of the molecular potential constants used in their formulation, and the sensitivity of the calculated results to changes in the molecular potential constants. Comparison of calculated and experimental Chapman-Jouguet parameters showed that the exponential 13.5-6 potential is more satisfactory for treating detonation products than the Mie 9-6 potential and led to the conclusion that with appropriate adjustments of molecular parameters the JCZ3 equation of state will provide a realistic description of detonation products.

INTRODUCTION

Codes for calculating realistic detonation properties are important for predicting the performance of high explosives and for assessing the usefulness of new explosive formulations. The TIGER code (1) for making such calculations was originally developed and documented for the Ballistic Research Laboratories (BRL). Further code work was carried out in conjunction with Lawrence Livermore Laboratory (LLL), Picatinny Arsenal (PA), and the Naval Surface Weapons Center (NSWC). The present paper presents the portion of this work concerned with the equation of state of the detonation products, which was carried out in collaboration with Dr. S. J. Jacobs of NSWC.

A more fundamental equation of state is required to perform more realistic detonation calculations on condensed explosives with a hydrothermodynamic code such as TIGER because the thermodynamic description of detonation products provided by the Becker-Kistiakowsky-Wilson (BKW) (1) equation is limited. The more fundamental Jacobs-Cowperthwaite-Zwisler equations of state for detonation products (JCZ1, JCZ2, and JCZ3) were formulated by incorporating mixture rules for n moles of s species into the pressure-volume-temperature (p-v-T) relationships (J1, J2, and J3) developed by Jacobs for a single species considered as a fluid. (2) (3)

The thermodynamic functions needed to calculate detonation properties with JCZ1, JCZ2, and JCZ3 in TIGER were derived and programmed to interface with the STATE G routine. And the resulting JCZ options were debugged and tested by performing detonation calculations for RDX and TNT at different loading densities.

THE JACOBS EQUATIONS OF STATE J1, J2, AND J3

J1, J2, and J3 are based on a (p-v-T) relationship for 1 mole of fluid of the form

$$p = p_o(v) + G(v, T) RT/v \qquad (1)$$

where $p_0(v)$ denotes the lattice pressure along the zero degree isotherm, R is the universal gas constant, and the G factor accounts for the thermal contribution to the pressure arising from intermolecular forces. The problem of formulating the (p-v-T) equation for a single species can be considered as that of constructing expressions for $p_0(v)$ and $G(v, T)$ with the pair potential describing the forces of interaction between the molecules. Since Eq. (1) must describe states ranging from the ideal gas to the dense compressed state, the G factor must reduce to the virial expansion at low density and must approach the value determined by the repulsive potential at the high density limit. Dr. Jacobs took a semiempirical approach to this problem and used the results of Monte Carlo (MC) and Lennard-Jones and Devonshire (LJD) calculations to determine unknown parameters in theoretical expressions for $p_0(v)$ and $G(v, T)$.

The expression for $p_0 = - dE_0/dv$ where $E_0(v)$ denotes the volume potential of a face-centered cubic (FCC) lattice. The Madelung constants in this expression were changed to obtain agreement with MC calculations in the fluid region to account for the fact that the detonation products behave more like a fluid than a solid. The J1 and J2 expressions for $E_0(v)$ were based on the Mie potential $(\ell - m) \varphi/e_0 = m(r^*/r)^\ell - \ell(r^*/r)^m$, where r denotes the intermolecular distance, ℓ and m denote the repulsive and attractive exponents, and e_0 denotes the depth of the potential well at the equilibrium distance r^*. The J3 expression for $E_0(v)$ was based on the exponential potential which can be obtained simply by substituting $\exp[\ell(1 - r/r^*)]$ for $(r^*/r)^\ell$ in the Mie potential. The G factors were formulated in terms of the non-dimensional density $\rho = v^*/v = (r^*/r)^3$ and the non-dimensional temperature $\theta = RT/e_0$ where $e_0 = Ne_0$, N denotes Avogadro's number, and $v = (N/\sqrt{2})r^3$. The parameter θ is also written as T/T^* with $T^* = e_0/k$ and Boltzmann's constant $k = R/N$.

The G factor was constructed so that the Helmholtz free energy A could be written explicitly in terms of $E_0(v)$, the Helmholtz free energy of an ideal gas A_i, and an f factor as

$$A = A_i + E_0(v) + RT \ln f(v, T) \quad (2)$$

For notational simplicity $I = \ell nf$ is used here for all the equations of state. The relationship between G and f is obtained simply as

$$G = 1 - v/f \, (\partial f/\partial v)_T \quad (3)$$

by differentiating Eq. (2) to obtain the (p-v-T) equation of state with the identify $p = - (\partial A/\partial v)_T$. The f factor was written as a power series so that the expression for G calculated with Eq. (3) has the correct limiting behavior at high and low densities and agrees within computational error with the numerical results of the MC and LJD calculations. The power series for the J1 f factor was constructed empirically, but those for the J2 and J3 f factors were constructed with f defined in terms of the molar free volume v_f as $f = v/v_f$.

The free volume was introduced theoretically by considering the physical assumptions that simplify the classical canonical partition function Ω, so that the equation for A

$$A(v, T) = - RT \ln \Omega \quad (4)$$

can be transformed into Eq. (2). At high densities the value of v_f are determined by the lattice vibrations, and at low densities $v_f \rightarrow v$ as the system becomes ideal and $f \rightarrow 1$. The f factor was assumed to be the sum of a gaseous f factor f_g and a solid f factor f_s and written simply as

$$f = f_g + f_s \quad (5)$$

It was constructed so that f_g dominated the sum at low densities, and the f_s term dominated the sum at high densities. The expressions for f_g were formulated with virial coefficients calculated with the repulsive potential, those for f_s with Einstein's harmonic approximation for a solid, and the repulsive potential for a FCC lattice.

THE JACOBS-COWPERTHWAITE-ZWISLER EQUATIONS OF STATE

Equations of state for a single species cannot be used to calculate realistic detonation parameters because the detonation products are composed of different species. The first step in our equation-of-state task was therefore to incorporate relationships for a mixture of species into J1, J2, and J3. A mixture of volume V containing n moles of s different species with mole number $n_i(n = 1 ... s)$ was considered. It was necessary to consider the mole numbers describing the composition of the mixture

163

as independent variables and modify J1, J2, and J3 accordingly. The modification was based on the assumption that the equations for the pressure $p(V, T, n_1 \ldots n_s)$ and the lattice energy $E_o(V, n_1 \ldots n_s)$ of the mixture have the same form as those for J1, J2, and J3. Equation (1), for example, was rewritten formally for the mixture as

$$p = p_o(V, n_1 \ldots n_s) + G(T, V, n_1 \ldots n_s)nRT/V \quad (6)$$

with

$$n = \sum_{i=1}^{s} n_i$$

Since J1, J2, and J3 were formulated with the non-dimensional variables v/v^* and $T/T^* = RT/e_o$, the mole numbers were introduced explicitly by formulating expressions for the e_o and the V^* of the mixture. These expressions were based on the assumption that the properties of the detonation products can be adequately described by considering pair-pair interactions. The potential functions describing $i - i$ interactions had therefore to be generalized to describe $i - j$ interactions. The parameters e_{ij} or $T_{ij}^* = e_{ij}/k$ were used to denote the depth of the potential well for unlike molecules, and r_{ij}^* and v_{ij}^* were used to denote the corresponding equilibrium distance and associated volume. But for notational simplicity, the double subscript was not used for $i - i$ interactions, and e_o used previously for one species was written as e_i. The equations for e_o and V^* must satisfy the thermodynamic identify (4)

$$\nu = \sum_{i=1}^{s} n_i \left(\partial \nu / \partial n_i \right)_{T,p,n_1,\hat{n}_i,n_s} \quad (7)$$

that is valid for an extensive variable ν. The following equations were considered in the present work:

$$e_o = 1/n \sum_i \sum_j n_i n_j e_{ij} \quad i = 1 \ldots s, \; j = 1 \ldots s \quad (8)$$

with

$$e_{ij} = N\epsilon_{ij}$$

$$V^* = 1/n \sum_i \sum_j n_i n_j v_{ij}^* \quad i = 1 \ldots s, \; j = 1 \ldots s \quad (9)$$

with

$$v_{ij}^* = N(r_{ij}^*)^3 / \sqrt{2} \quad (10)$$

and

$$V^* = N(R^*)^3 / \sqrt{2} \quad (11)$$

with

$$R^* = 1/n^{5/3} \sum_i \sum_j n_i n_j r_{ij}^* \quad i = 1 \ldots s, \; j = 1 \ldots s \quad (12)$$

but Eqs. (9) and (10) were used instead of Eqs. (11) and (12). JZ1, JZ2, and JZ3 were generated from J1, J2, and J3 by replacing v/v^* and $T/T_i^* = RT/e_i$ with V/V^* and $T/T^* = nRT/e_o$ with V^* and e_o defined by Eqs. (8), (9), and (10). The additional relationships, $e_{ij} = f(\epsilon_i, \epsilon_j)$ and $r_{ij}^* = g(r_i^*, r_j^*)$, needed to perform calculations were assumed to be

$$\frac{e_{ij}}{R} = \left(\frac{\epsilon_i \epsilon_j}{k^2} \right)^{1/2} \quad (13)$$

and

$$r_{ij}^* = \frac{r_i^* + r_j^*}{2} \quad (14)$$

but the derivatives used in the calculations were derived in terms of e_{ij} and r_{ij}^* so that relationships other than Eqs. (13) and (14) could be introduced into the equations of state and used without difficulty.

INCORPORATION OF AN EQUATION OF STATE INTO TIGER

The introduction of a new equation of state into the TIGER code is by no means a trivial task. The $p = p(V, T, n_1 \ldots n_s)$ relationship must be rewritten in the form used in the code and then used to derive the expressions needed to perform thermodynamic calculations. The form used in the code is

$$p = \frac{nRT}{M_o} \hat{\rho} \Phi \quad (15)$$

where $v = M_o/\hat{\rho}$; M_o denotes the mass of the system including condensed phases, and Φ is the imperfection term, which has a value of 1 for the ideal gas. It is

164

necessary to derive expressions for Φ, the frozen partial derivatives $\partial\ln\Phi/\partial\ln T$, $\partial\ln\Phi/\partial\ln\hat\rho$, $\partial\ln\Phi/\partial n_i$, the activity coefficients

$$\Gamma_i = \int_0^{\hat\rho} \left[\frac{M_o}{RT\hat\rho} \frac{\partial p}{\partial n_i} - 1 \right] \frac{d\hat\rho}{\hat\rho} \quad i = 1 \ldots s \quad (16)$$

and their frozen partial derivatives $\partial\Gamma_i/\partial\ln T$, $\partial\Gamma_i/\partial\ln\hat\rho$, and $\partial\Gamma_i/\partial n_j$, and the imperfection integrals

$$\epsilon = \int_0^{\hat\rho} \frac{M_o}{RT\hat\rho} \left[p - T \left(\frac{\partial p}{\partial T} \right) \right] \frac{d\hat\rho}{\hat\rho} \quad (17)$$

$$\epsilon_T' = - \int_0^{\hat\rho} \frac{M_o T}{R\hat\rho} \left(\frac{\partial^2 p}{\partial T^2} \right) \frac{d\hat\rho}{\hat\rho} \quad . \quad (18)$$

It is convenient to derive general expressions for these quantities, for the JCZ equation of state using Eq. (2), with all the terms considered to be a function of the composition. The following equations were derived for the JCZ equation of state:

$$\Phi = 1 - V \frac{\partial I}{\partial V} - \frac{V}{nRT} \frac{\partial E_o}{\partial V} \quad (19)$$

$$\frac{\partial\ln\Phi}{\partial\ln T} = \frac{1}{\Phi} \left(\frac{V}{nRT} \frac{\partial E_o}{\partial V} - TV \frac{\partial^2 I}{\partial T\partial V} \right) \quad (20)$$

$$\frac{\partial\ln\Phi}{\partial\ln\hat\rho} = \frac{1}{\Phi} \left(1 - \Phi + \frac{V^2}{nRT} \frac{\partial^2 E_o}{\partial V^2} + V^2 \frac{\partial^2 I}{\partial V^2} \right) \quad (21)$$

$$\frac{\partial\ln\Phi}{\partial n_i} = \frac{1}{n\Phi} \left(\frac{V}{nRT} \frac{\partial E_o}{\partial V} - \frac{V}{RT} \frac{\partial^2 E_o}{\partial V\partial n_i} - Vn \frac{\partial^2 I}{\partial V\partial n_i} \right) \quad (22)$$

$$\Gamma_i = \frac{1}{RT} \frac{\partial E_o}{\partial n_i} + 1 + n \frac{\partial I}{\partial n_i} \quad (23)$$

$$\frac{\partial\Gamma_i}{\partial\ln T} = - \frac{1}{RT} \frac{\partial E_o}{\partial n_i} + T \frac{\partial I}{\partial T} + nT \frac{\partial^2 I}{\partial n_i\partial T} \quad (24)$$

$$\frac{\partial\Gamma_i}{\partial\ln\hat\rho} = - \frac{V}{RT} \frac{\partial^2 E_o}{\partial V\partial n_i} - V \frac{\partial I}{\partial V} - nV \frac{\partial^2 I}{\partial V\partial n_i} \quad (25)$$

$$\frac{\partial\Gamma_i}{\partial n_j} = \frac{1}{n} \left(\frac{n}{RT} \frac{\partial^2 E_o}{\partial n_i\partial n_j} + n \frac{\partial I}{\partial n_j} + n \frac{\partial I}{\partial n_i} \right.$$

$$\left. + n^2 \frac{\partial^2 I}{\partial n_i\partial n_j} \right) \quad (26)$$

$$\epsilon = n \left(\frac{E_o}{nRT} - T \frac{\partial I}{\partial T} \right) \quad (27)$$

$$\epsilon_T' = - n \left(2T \frac{\partial I}{\partial T} + T^2 \frac{\partial^2 I}{\partial T^2} \right) \quad (28)$$

Incorporation of an equation of state into TIGER is tested by checking the values of the partial derivatives against those computed by differencing techniques and checking the values of Γ_i, ϵ, and ϵ_T' against those computed by numerical integration of the equations. It should be noted that the expressions for Γ_i, ϵ, and ϵ_T' can be obtained more easily by differentiation than by integration in the present case because the form of the Helmholtz free energy is known explicitly. The equations were used to derive expressions for all the JCZ equations of state in terms of the nondimensional variables. Only the equations used to incorporate JCZ3 into the TIGER code are given here, however, because of space limitations.

CALCULATIONS AND CONCLUSIONS

The JCZ equations of state for nine molecular species were used to calculate Chapman-Jouguet (CJ) states and the isentropes passing through them for RDX at loading densities of 1.8, 1.4, and 1.0 g/cm³ and for TNT at loading densities of 1.6, 1.4, 1.2, and 1.0 g/cm³. The potential constants used in the calculations were standardized by adopting the values given by Fickett (5) and by assuming that the constants for NH_3 were the same as those for H_2O. The standard ideal gas state and solid carbon were treated with the data already in the TIGER library. The results of these detonation calculations were compared with experimental values to test the validity of the JC2 equations of state, the values used for their potential constants, and the sensitivity of the calculated parameters to changes in the potential constants. This comparison showed that the CJ values calculated with the standardized potential constants agree

165

reasonably well with the experimental values and lead to the following conclusions:

- JCZ2 and JCZ3, based on the harmonic approximation, provide a better description of detonation products than JCZ1.

- JCZ3, based on the exponential 13.5-6 potential, is more satisfactory for treating detonation products than JCZ2 based on the Mie (9-6) potential.

- Modification of the potential constants should lead to better agreement with experiment because the calculated CJ state is sensitive to the values chosen for the potential constants.

The results of the present paper lead to the conclusion that further work to develop a realistic equation of state of detonation products should be based on JCZ3 or a similar equation of state. Additional work on JCZ3 should include a parameter study to determine the best set of values of the potential constants and the evaluation of potential constants for species not considered in the present calculations.

REFERENCES

1. M. Cowperthwaite and W. H. Zwisler, "TIGER Computer Program Documentation," SRI publication No. Z106, January 1973.

2. S. J. Jacobs, "The Equation of State for Detonation Products at High Density," p. 501, 12th Symposium (International) on Combustion, Combustion Institute, 1969.

3. S. J. Jacobs, "On the Equation of State of Compressed Liquids and Solids," NOL Tech. Rept. NOLTR-68-214, 15 Dec 1963.

4. I. Prigogine and R. Defay, *Chemical Thermodynamics,* p. 6, Longmans Green and Co., New York, 1954.

5. W. Fickett, "Detonation Properties of Condensed Explosives Calculated with an Equation of State Based on Intermolecular Potentials," Los Alamos Rept. LA-2712, 14 Dec 1962.

Appendix

JCZ3 EQUATIONS FOR TIGER

The JCZ3 equation of state for a mixture of n moles of s species was formulated with the exponential ℓ - m pair potential in terms of

$$y = \frac{V^*}{V} \left(\frac{F}{\ell}\right)^3 \tag{A1}$$

with F given by the equation

$$F = c_1 - \ell n \left[\frac{T(\ell - m)}{m(e_o/nR)}\right] \tag{A2}$$

where $c_1 = c + \ell$ and c denotes Euler's constant. The parameters V^* and e_o are defined by Eqs. (7) and (8). The equation for E_o was written as

$$E_o = e_o Z \tag{A3}$$

with $Z = \hat{s}(r_\ell - r_m)$, $\hat{s} = m\ell/2(\ell - m)$, and $r_m = (B_m/m)$ $(V^*/V)^m$ defined for JCZ2, but with r_ℓ given by the equations

$$r_\ell = (B_\ell/\ell) \exp(\ell - z) \tag{A4}$$

$$z = \ell(V^*/V)^{-1/3}. \tag{A5}$$

The f factor was written as $f = f_g + f_s$ with f_g defined by the expression used for JCZ2

$$f_g = 1 + a_1 y + a_2 y^2 + \dots a_q y^q \tag{A6}$$

and f_s by the equation

$$f_s = 2 \left[\frac{e_o}{nRT} \left(\frac{m}{\ell - m}\right)\frac{z}{\pi} (z - 2) \exp(\ell - z)\right]^{3/2} \tag{A7}$$

Additional parameters s_r and s_e were introduced into the equations for r_{ij} and e_{ij}

$$r_{ij}^{*3} = \left[s_r \frac{(r_i^* + r_j^*)}{2}\right]^3 \tag{A8}$$

$$\frac{e_{ij}}{R} = s_e \left(\frac{\epsilon_i}{k} \frac{\epsilon_j}{k}\right)^{1/2} \tag{A9}$$

so that calculations could be made with modified values of all the r_i^* and/or modified values of all the ϵ_i. With Eqs. (A8) and (A9), the set of parameters in JCZ3 is $(\ell, m, B_\ell, B_m, q, a_1 \dots a_q, c, s_r, s_e, r_j^*, \epsilon_i)$ with $i = 1, \dots s$, and all of these parameters must be known in order to make thermodynamic calculations with JCZ3. The set of constants $(a_1, \dots, a_q)$ are defined by a set of recurrence relations in terms of coefficients in the virial expansion determined by MC calculations. The recurrence relations are the conditions for the G factor to reduce to the virial expansion as y approaches zero.

As for JCZ2, Eqs. (18) to (27) had to be rewritten for JCZ3. Derivatives of e_o, V^*, used to rewrite these equations are as follows:

$$\frac{n}{e_o} \frac{\partial e_o}{\partial n_i} = \frac{2(\Sigma_k n_k e_{ik}/R)}{(e_o/R)} - 1 \quad k = 1 \dots s \quad (A10)$$

$$\frac{n^2}{e_o} \frac{\partial^2 e_o}{\partial n_i \partial n_j} = \frac{2n(e_{ij}/R)}{(e_o/R)} - \frac{n}{e_o} \frac{\partial e_o}{\partial n_i} - \frac{n}{e_o} \frac{\partial e_o}{\partial n_j} \quad (A11)$$

$$\frac{n}{V^*} \frac{\partial V^*}{\partial n_i} = \frac{2(\Sigma_k n_k v_{ik}^*)}{V^*} - 1 \quad k = 1 \dots s \quad (A12)$$

$$\frac{n^2}{V^*} \frac{\partial^2 V^*}{\partial n_i \partial n_j} = \frac{2n(v_{ij}^*)}{V^*} - \frac{n}{V^*} \frac{\partial V^*}{\partial n_i} - \frac{n}{V^*} \frac{\partial V^*}{\partial n_j} \quad (A13)$$

The equations for the partial derivatives of E_o with respect to the volume and the mole numbers and for the partial derivatives of Z are

$$\frac{V}{nRT} \frac{\partial E_o}{\partial V} = \frac{e_o V}{nRT} \frac{\partial Z}{\partial V} \quad (A14)$$

$$\frac{1}{RT} \frac{\partial E_o}{\partial n_i} = \frac{e_o}{nRT} \left(Z \frac{n}{e_o} \frac{\partial e_o}{\partial n_i} + V^* \frac{\partial Z}{\partial V^*} \frac{n}{V^*} \frac{\partial V^*}{\partial n_i} \right) \quad (A15)$$

$$\frac{V^2}{nRT} \frac{\partial^2 E_o}{\partial V^2} = \frac{e_o V^2}{nRT} \frac{\partial^2 Z}{\partial V^2} \quad (A16)$$

$$\frac{V}{RT} \frac{\partial^2 E_o}{\partial n_i \partial V} = \frac{e_o}{nRT} \left(\frac{n}{e_o} \frac{\partial e_o}{\partial n_i} V \frac{\partial Z}{\partial V} + \frac{n}{V^*} \frac{\partial V^*}{\partial n_i} \right.$$
$$\left. \times VV^* \frac{\partial^2 Z}{\partial V \partial V^*} \right) \quad (A17)$$

$$\frac{n}{RT} \frac{\partial^2 E_o}{\partial n_i \partial n_j} = \frac{e_o}{nRT} \left(\frac{n^2}{e_o} \frac{\partial^2 e_o}{\partial n_i \partial n_j} Z + V^{*2} \frac{\partial^2 Z}{\partial V^{*2}} \frac{n}{V^*} \right.$$
$$\times \frac{\partial V^*}{\partial n_i} \frac{n}{V^*} \frac{\partial V^*}{\partial n_j} \right) + \frac{e_o V^*}{nRT} \frac{\partial Z}{\partial V^*} \left(\frac{n^2}{V^*} \frac{\partial^2 V^*}{\partial n_i \partial n_j} \right.$$
$$+ \frac{n}{e_o} \frac{\partial e_o}{\partial n_j} \frac{n}{V^*} \frac{\partial V^*}{\partial n_i} + \frac{n}{e_o} \frac{\partial e_o}{\partial n_i} \frac{n}{V^*} \frac{\partial V^*}{\partial n_j} \right) \quad (A18)$$

and

$$V \frac{\partial Z}{\partial V} = - \frac{\hat{s}}{3} (r_\ell z - r_m m) = - V^* \frac{\partial Z}{\partial V^*} \quad (A19)$$

$$V^2 \frac{\partial^2 Z}{\partial V^2} = \frac{\hat{s}}{9} [r_\ell z(z + 2) - r_m m(m + 3)] \quad (A20)$$

$$V^{*2} \frac{\partial^2 Z}{\partial V^{*2}} = \frac{\hat{s}}{9} [r_\ell z(z - 4) - r_m m(m - 3)] \quad (A21)$$

$$VV^* \frac{\partial^2 Z}{\partial V \partial V^*} = - \frac{\hat{s}}{9} [r_\ell z(z - 1) - r_m m^2]. \quad (A22)$$

The equations for the partial derivatives of y are as follows:

$$\frac{V}{y} \frac{\partial y}{\partial V} = - 1 \quad (A23)$$

$$\frac{T}{y} \frac{\partial y}{\partial T} = - \frac{3}{F} \quad (A24)$$

$$\frac{T^2}{y} \frac{\partial^2 y}{\partial T^2} = \frac{3}{F} \left(\frac{2}{F} + 1 \right) \quad (A25)$$

167

$$\frac{n}{y}\frac{\partial y}{\partial n_i} = \frac{n}{V^*}\frac{\partial V^*}{\partial n_i} + \frac{3}{F}\left(\frac{n}{e_o}\frac{\partial e_o}{\partial n_i} - 1\right) \quad (A26)$$

$$VT\frac{\partial^2 f_g}{\partial V \partial T} = -\frac{T}{y}\frac{\partial y}{\partial T}(y^2 f_g'' + y f_g') \quad (A35)$$

$$\frac{nT}{y}\left(\frac{\partial^2 y}{\partial T \partial n_i}\right) = \frac{T}{y}\frac{\partial y}{\partial T}\frac{n}{y}\frac{\partial y}{\partial n_i} + \frac{3}{F^2}\left(\frac{n}{e_o}\frac{\partial e_o}{\partial n_i} - 1\right) \quad (A27)$$

$$V^2\frac{\partial^2 f_g}{\partial V^2} = 2y f_g' + y^2 f_g' \quad (A36)$$

$$\frac{nV}{y}\left(\frac{\partial^2 y}{\partial V \partial n_i}\right) = \frac{V}{y}\frac{\partial y}{\partial V}\frac{n}{y}\frac{\partial y}{\partial n_i} \quad (A28)$$

$$Vn\frac{\partial^2 f_g}{\partial V \partial n_i} = -\frac{n}{y}\frac{\partial y}{\partial n_i}(y^2 f_g'' + y f_g') \quad (A37)$$

$$\frac{n^2}{y}\left(\frac{\partial^2 y}{\partial n_i \partial n_j}\right) = \frac{n}{y}\frac{\partial y}{\partial n_i}\frac{n}{y}\frac{\partial y}{\partial n_j} - \frac{n}{V^*}\frac{\partial V^*}{\partial n_i}\frac{n}{V^*}\frac{\partial V^*}{\partial n_j}$$

$$T^2\frac{\partial^2 f_g}{\partial T^2} = y^2 f_g''\left(\frac{T}{y}\frac{\partial y}{\partial T}\right)^2 + y f_g'\left(\frac{T^2}{y}\frac{\partial^2 y}{\partial T^2}\right) \quad (A38)$$

$$+ \frac{n^2}{V^*}\frac{\partial^2 V^*}{\partial n_i \partial n_j} - \frac{3}{F^2}\left(\frac{n}{e_o}\frac{\partial e_o}{\partial n_i} - 1\right)$$

$$nT\frac{\partial^2 f_g}{\partial T \partial n_i} = \frac{n}{y}\frac{\partial y}{\partial n_i}\frac{T}{y}\frac{\partial y}{\partial T}(y^2 f_g'' + y f_g')$$

$$\times \left(\frac{n}{e_o}\frac{\partial e_o}{\partial n_j} - 1\right) + \frac{3}{F}\left(\frac{n^2}{e_o}\frac{\partial^2 e_o}{\partial n_i \partial n_j}\right)$$

$$+ y f_g'\frac{3}{F^2}\left(\frac{n}{e_o}\frac{\partial e_o}{\partial n_i} - 1\right) \quad (A39)$$

$$- \frac{n}{e_o}\frac{\partial e_o}{\partial n_i}\frac{n}{e_o}\frac{\partial e_o}{\partial n_j} + 1\right) . \quad (A29)$$

$$n^2\frac{\partial^2 f_g}{\partial n_i \partial n_j} = y^2 f_g''\frac{n}{y}\frac{\partial y}{\partial n_i}\frac{n}{y}\frac{\partial y}{\partial n_j} + y f_g'\frac{n^2}{y}\frac{\partial^2 y}{\partial n_i \partial n_j} . \quad (A40)$$

It is convenient to treat the f_g and f_s factors separately for JCZ3 because f_s cannot be treated as another term in the polynomial for f_g as it was for JCZ2. The equations for the first (f_g') and second (f_g'') derivatives of f_g with respect to y are

The corresponding expressions for f_s written with z_1 and z_2 defined by

$$y f_g' = a_1 y + 2a_2 y^2 + \ldots q a_q y^q \quad (A30)$$

$$z_1 = (2 - z) - \frac{2}{(2 - z)} \quad (A41)$$

$$y^2 f_g'' = 2a_2 y^2 + \ldots + q(q - 1)a_q y^q \quad (A31)$$

$$z_2 = \frac{z}{2} + \frac{z}{(2 - z)^2} \quad (A42)$$

The other equations for f_g are as follows:

are as follows:

$$\frac{V \partial f_g}{\partial V} = -y f_g' \quad (A32)$$

$$\frac{V}{f_s}\frac{\partial f_s}{\partial V} = \frac{z_1}{2} \quad (A43)$$

$$T\frac{\partial f_g}{\partial T} = y f_g'\frac{T}{y}\frac{\partial y}{\partial T} \quad (A33)$$

$$\frac{T}{f_s}\frac{\partial f_s}{\partial T} = -\frac{3}{2} \quad (A44)$$

$$n\frac{\partial f_g}{\partial n_i} = y f_g'\frac{n}{y}\frac{\partial y}{\partial n_i} \quad (A34)$$

$$\frac{n}{f_s}\frac{\partial f_s}{\partial n_i} = -\frac{z_1}{2}\frac{n}{V^*}\frac{\partial V^*}{\partial n_i} + \frac{3}{2}\left(\frac{n}{e_o}\frac{\partial e_o}{\partial n_i} - 1\right) \quad (A45)$$

168

$$\frac{VT}{f_s} \frac{\partial^2 f_s}{\partial V \partial T} = \frac{V}{f_s} \frac{\partial f_s}{\partial V} \frac{T}{f_s} \frac{\partial f_s}{\partial T} \qquad (A46)$$

$$\frac{V^2}{f_s} \frac{\partial^2 f_s}{\partial V^2} = \frac{z_1^2}{4} - \frac{z_1}{2} - \frac{z_2}{3} \qquad (A47)$$

$$\frac{Vn}{f_s} \frac{\partial^2 f_s}{\partial V \partial n_i} = \frac{n}{f_s} \frac{\partial f_s}{\partial n_i} \frac{V}{f_s} \frac{\partial f_s}{\partial V} + \frac{z_2}{3} \frac{n}{V^*} \frac{\partial V^*}{\partial n_i} \qquad (A48)$$

$$\frac{T^2}{f_s} \frac{\partial^2 f_s}{\partial T^2} = \frac{15}{4} \qquad (A49)$$

$$\frac{nT}{f_s} \frac{\partial^2 f_s}{\partial T \partial n_i} = \frac{n}{f_2} \frac{\partial f_s}{\partial n_i} \frac{T}{f_s} \frac{\partial f_s}{\partial T} \qquad (A50)$$

$$\frac{n^2}{f_s} \frac{\partial^2 f_s}{\partial n_i \partial n_j} = \frac{n}{f_s} \frac{\partial f_s}{\partial n_j} \frac{n}{f_s} \frac{\partial f_s}{\partial n_i}$$

$$- \frac{3}{2} \left(\frac{n}{e_o} \frac{\partial e_o}{\partial n_i} \frac{n}{e_o} \frac{\partial e_o}{\partial n_j} - \frac{n^2}{e_o} \frac{\partial^2 e_o}{\partial n_i \partial n_j} - 1 \right)$$

$$+ z_1 \left(\frac{n}{V^*} \frac{\partial V^*}{\partial n_i} \frac{n}{V^*} \frac{\partial V^*}{\partial n_j} - \frac{n^2}{V^*} \frac{\partial^2 V^*}{\partial n_i \partial n_j} \right)$$

$$- \frac{z_2}{3} \frac{n}{V^*} \frac{\partial V^*}{\partial n_i} \frac{n}{V^*} \frac{\partial V^*}{\partial n_j} . \qquad (A51)$$

The equations for $I = \ell n f$ were written as

$$V \frac{\partial I}{\partial V} = \frac{V}{f} \frac{\partial}{\partial V} (f_g + f_s) \qquad (A52)$$

$$T \frac{\partial I}{\partial T} = \frac{T}{f} \frac{\partial}{\partial T} (f_g + f_s) \qquad (A53)$$

$$n \frac{\partial I}{\partial n_i} = \frac{n}{f} \frac{\partial}{\partial n_i} (f_g + f_s) \qquad (A54)$$

$$VT \frac{\partial^2 I}{\partial T \partial V} = - \frac{V \partial I}{\partial V} \frac{T \partial I}{\partial T} + \frac{VT}{f} \frac{\partial^2}{\partial V \partial T} (f_g + f_s) \qquad (A55)$$

$$V^2 \frac{\partial^2 I}{\partial V^2} = - \left(V \frac{\partial I}{\partial V} \right)^2 + \frac{V^2}{f} \frac{\partial^2}{\partial V^2} (f_g + f_s) \qquad (A56)$$

$$Vn \frac{\partial^2 I}{\partial V \partial n_i} = - V \frac{\partial I}{\partial V} n \frac{\partial I}{\partial n_i} + \frac{n}{f} V \frac{\partial^2}{\partial n_i \partial V} (f_g + f_s) \qquad (A57)$$

$$T^2 \left(\frac{\partial^2 I}{\partial T^2} \right) = - \left(T \frac{\partial I}{\partial T} \right)^2 + \frac{T^2}{f} \frac{\partial^2}{\partial T^2} (f_g + f_s) \qquad (A58)$$

$$nT \left(\frac{\partial^2 I}{\partial T \partial n_i} \right) = - n \frac{\partial I}{\partial n_i} T \frac{\partial I}{\partial T} + \frac{nT}{f} \frac{\partial^2}{\partial T \partial n_i} (f_g + f_s) \qquad (A59)$$

$$n^2 \frac{\partial^2 I}{\partial n_i \partial n_j} = - n \frac{\partial I}{\partial n_i} n \frac{\partial I}{\partial n_j} + \frac{n^2}{f} \frac{\partial^2}{\partial n_i \partial n_j} (f_g + f_s). \qquad (A60)$$

And Eqs. (18) to (27) were rewritten in terms of these derivatives of JCZ3 as:

$$\Phi = 1 - \frac{V}{nRT} \frac{\partial E_o}{\partial V} - V \frac{\partial I}{\partial V} \qquad (A61)$$

$$\frac{\partial \ell n \Phi}{\partial \ell n T} = \frac{1}{\Phi} \left(\frac{V}{nRT} \frac{\partial E_o}{\partial V} - TV \frac{\partial^2 I}{\partial T \partial V} \right) \qquad (A62)$$

$$\frac{\partial \ell n \Phi}{\partial \ell n \hat{\rho}} = \frac{1}{\Phi} \left(1 - \Phi + \frac{V^2}{nRT} \frac{\partial^2 E_o}{\partial V^2} + V^2 \frac{\partial^2 I}{\partial V^2} \right) \qquad (A63)$$

$$\frac{\partial \ell n \Phi}{\partial n_i} = \frac{1}{n\Phi} \left(- \frac{V}{RT} \frac{\partial^2 E_o}{\partial V \partial n_i} + \frac{V}{nRT} \frac{\partial E_o}{\partial V} - Vn \frac{\partial^2 I}{\partial V \partial n_i} \right) \qquad (A64)$$

$$\Gamma_i = \frac{1}{RT} \frac{\partial E_o}{\partial n_i} + I + n \frac{\partial I}{\partial n_i} \qquad (A65)$$

$$\frac{\partial \Gamma_i}{\partial \ell n T} = - \frac{1}{RT} \frac{\partial E_o}{\partial n_i} + T \frac{\partial I}{\partial T} + nT \frac{\partial^2 I}{\partial T \partial n_i} \qquad (A66)$$

169

$$\frac{\partial \Gamma_i}{\partial \ell n \hat{\rho}} = -\frac{V}{RT} \frac{\partial^2 E_o}{\partial V \partial n_i} - V \frac{\partial I}{\partial V} - nV \frac{\partial^2 I}{\partial V \partial n_i} \quad \text{(A67)}$$

$$\epsilon = n \left(\frac{E_o}{nRT} - T \frac{\partial I}{\partial T} \right) \quad \text{(A69)}$$

$$\frac{\partial \Gamma_i}{\partial n_j} = \frac{1}{n} \left(\frac{n}{RT} \frac{\partial^2 E_o}{\partial n_i \partial n_j} + n \frac{\partial I}{\partial n_i} + n \frac{\partial I}{\partial n_j} \right. $$
$$\left. + n^2 \frac{\partial^2 I}{\partial n_i \partial n_j} \right) \quad \text{(A68)}$$

$$\epsilon'_T = -n \left[2 \left(T \frac{\partial I}{\partial T} \right) + T^2 \frac{\partial^2 I}{\partial T^2} \right] \quad \text{(A70)}$$

DISCUSSION

S.J. JACOBS
U.S. Naval Surface Weapons Center

As the J of the JCZ equations of state, EOS, I would like to make a few amplifying comments on the paper by Cowperthwaite and Zwisler, CZ. References CZ 2 and 3 represent my very early thinking about the EOS problem. At that time the amount of Monte Carlo calculations were quite limited but I recognized the possibility that the EOS results in them might be described by a free volume approach as used by Lennard-Jones and Devonshire, LJD, (Ref. J1). This was confirmed with the MC results of Wood (Ref. J2) for the Lennard-Jones 12-6 potential. At that time I actually considered only the representation of the imperfection term in the thermal contribution to the EOS and a volume dependent term. When I took up the study again several years later it became apparent that the Helmohltz free energy would be more useful. With it all important terms for both the EOS and the other thermodynamic variables could be derived by straight-forward differentiation of the free energy. At the same time new results of the MC method became available, principally Hoover (Ref. 3, 4) and Ross (Ref. 5). At that time I also had the benefit of some LJD calculations made for me by Fickett for various Mie and Buckingham (expo-m,n) potentials. The main problem I had was to describe the free volume in the Helmholtz free energy in closed form. It was desired that this term describe a quasi-harmonic oscillator model at high density, a moderately non-ideal gas at intermediate density, and give a limiting ideal gas at very low density. The trick turned out to be to define the "f" function (CZ Equ. 5) as a sum of two terms as described by CZ. The result of this approach permits the use of potential functions other than those used in the MC method with a fair degree of assurance that the result will approximate, at least, the results that MC would give for spherically symmetric molecules. This is roughly what was found in the case of the expo-m,n potential. In this case the amount of MC work is very limited but the agreement to this work (Ref. 5) was reasonably good. The imperfection term, G, (Equ. CZ3) is a sensitive term for comparing the present EOS's with such work as MC or LJD. Our result for the expo potential is also in fairly good agreement wit Fickett's LJD calculations in this comparison.

A second problem that arose was the explanation of the two branches, fluid and solid, in the MC outputs. It was suggested by D. J. Pastine that the important difference between these states would be the alteration of the volume potential and hence the volume dependent pressure. An appropriate correction to the volume potential based on MC data was able to correlate the two states. I have used the fluid stage for the detonation problem since order is undoubtedly lacking. It turns out that LJD had already considered the problem in a similar light (Ref. J6). The work of LJD suggests that, in the absence of MC data, it is possible to make a reasonable correction in terms of the difference in volume produced at the normal melting point.

In the final checkout of the EOS substantial use was made of Fickett's work (Ref. J7). LJD is a pretty acceptable EOS for the detonation state but has the mathematical difficulty of requiring a considerable amount of numerical integration.

I wish to commend Cowperthwaite and Zwisler for the successful execution of the difficult task of extending the work I did to the description of a complex equilibrium system and getting it coded into a workable TIGER code.

REFERENCES

J1. J. E. Lennard-Jones and A. F. Devonshire, "Critical Phenomena in Gases – I", Proc. Royal Soc., **A163**, p153 (1937).

J2. W. W. Wood, "Monte Carlo Studies of Simple Liquid Models", Chap. 5 in "Physics of Simple Liquids", H. N. Temperley, et al., ed. Wiley Interscience Div. of John Wiley and Sons, New York (1968).

J3. W. G. Hoover, et al., "Soft Sphere Equation of State", J. Chem. Phys. **52**, 4931 (1970).

J4. W. G. Hoover, et al., "Thermodynamic Properties of the Fluid and Solid Phases for Inverse Power Potentials", J. Chem. Phys. **55**, 1128 (1971).

J5. M. Ross, and W. G. Hoover, "Shock Compression of Argon. II.", J. Chem. Phys. **46**, 4203 (1967).

J6. J. E. Lennard-Jones and A. F. Devonshire, "Critical and Co-operative Phenomena - III. A Theory of Melting and the Structure of Liquids", Proc. Royal Soc., **A109**, 317 (1939).

J7. W. Fickett, "Detonation Properties of Condensed Explosives Calculated with an Equation of State Based on Intermolecular Potentials", Los Alamos Laboratory Report LA-2712 (Dec 1962).

SYMPATHETIC DETONATION OF AMMONIUM PERCHLORATE
BY SMALL AMOUNTS OF NITROGUANIDINE

Allen J. Tulis
IIT Research Institute
Chicago, Illinois 60616

Investigations into the detonation characteristics of very low density explosives has
led to the development of an explosive composite of small amounts of nitroguani-
dine (NQ) in ammonium perchlorate (AP). Near ideal detonation of NQ at densities
of 0.18 to 0.015 g/cc heavily diluted in AP have been achieved and evidently induce
a sympathetic detonation in the major AP component. Amounts of NQ as low as 1
percent in AP will control the detonation rate of such NQ-AP composites. It ap-
pears that the full energy of the AP is released in the detonation of these com-
posites. It also appears that charge diameters and confinement do not influence
these results except when conditions become such that the AP itself can undergo
nonideal detonation. Similar effects in other explosive composites are suggested.

INTRODUCTION

The purpose of this paper is to present some in-
teresting results in the behavior of ammonium per-
chlorate (AP) in a detonative reaction and to advance
some theories on the detonation mechanism in com-
posite explosives. Gordon (1) described the con-
trasting behavior of composite and molecular ex-
plosives wherein composite explosives were mixtures
of self-explosive oxidizers such as AP and an inert
fuel. Although we have investigated various cor·bi-
nations of mixed explosive-fuel-oxidizer composites,
this paper will be concerned only with AP mixed with
various amounts of nitroguanidine (NQ). The reason
for this is that this particular combination of two ex-
plosive materials appears to have some unique char-
acteristics. An initial supposition was that both of
these explosive materials have a decreased critical
charge diameter with decreasing density, which is con-
trary to most explosive materials. Cook (2) explains
this effect, in fuel-oxidizer composites, by a slowing
down of the diffusion reaction with increasing
density.

The detonation velocity of condensed phase ex-
plosives is a function of the chemical energy released

in the detonation, the rate at which this energy is re-
leased, the initial density of the explosive, the ex-
plosive charge diameter and the degree of confine-
ment. Provided the charge diameter is adequate, the
detonation velocity becomes a function of initial ex-
plosive density only and is completely determined by
the thermohydrodynamics of the explosive. Such high
velocity detonations (HVD) are constant and unique
for each explosive at constant density and are termed
ideal detonation velocities (D_i). Although there exist
much greater intricacies in the detonation velocity
behavior of explosives with density and with the
detonation wave front (2,3), this paper will be con-
cerned with a relatively simplistic approach concern-
ing the empirical linear relationship of solid explo-
sives detonation velocity versus density and the impli-
cation of this relationship to experimental results
obtained with composite explosives, specifically AP
with small amount of NQ added.

THEORETICAL

It has been known for some time that certain ex-
plosives can detonate at two distinct velocities; the
normal HVD which corresponds to the thermohydro-
dynamic theory and a much lower velocity, termed

low velocity detonation (LVD) which propagates at about the sonic velocity for the unreacted explosive. In the case of nitroglycerine, for which these dual propagation rates were first observed (4), the HVD is about 8 mm/μsec whereas the LVD is about 2 mm/μsec. There is a dependence on charge diameter, confinement and severity of initiation, amongst other factors, that determines which velocity will event. In general, LVD is much harder to achieve reproducibly and often results in a transition to HVD. The mechanism of LVD is basically attributed to a grain burning in solid particulates and shock-induced cavitation, leading to bubble formation in liquid explosives such as nitroglycerine.

Ideal detonation occurs in explosives when adequately initiated and when the charge diameter is sufficiently large; the D_i is then only a function of initial explosive density. The minimum diameter for ideal detonation (d^*) is then a function of the density. Below this d^* constant velocity detonation (termed nonideal) will still event, at progressively lesser vecolities, until the critical diameter (d_c) is reached. Below d_c the detonation decays and/or does not event. In general, this nonideal detonation velocity is proportional to the inverse of the charge diameter in the range $d_c < d < d^*$. Nonideal detonation is also a function of explosive particle size and confinement, and of course density. The mechanism of nonideal detonation is generally associated with lateral energy losses due to rarefaction wave interaction with the reaction zone.

Previous work with pressed granular explosive charges has shown that the resultant density versus d_c behavior can be divided into two contrasting groups. Figure 1 illustrates the typical Group I behavior for TNT and most molecular explosives (5). Figure 2 illustrates the typical Group II behavior for AP (6). Group II explosives are generally composite fuel-oxidizer mixtures although there are some molecular explosives in this group also such as the AP illustrated in Fig. 2 and hydrazine mononitrate, NQ, dinitrotoluene and dinitrophenol (6). The inclusion of NQ in this group is uncertain; in later investigations Price and Clairmont (7) studied the behavior of NQ rather extensively, specifically for density-critical diameter-detonation velocity relationships as functions of bulk density type (low bulk and high bulk) and particle size and shape. In the density range of 0.4 to 1.63 g/cc NQ was relagated to Group I be-

havior. However, sub-detonation but supersonic and constant velocity reaction fronts were obtained with NQ at low densities; e.g., 0.4 to 1.2 g/cc. This pseudo-detonation was termed LVD and explained in terms of an ignition wave coupled to a shock wave in such manner that the shock is supported by the reaction of a small fraction of the explosive at multiple hot spots.

REF. 5 DATA; TNT, GRAIN SIZE 0.07 TO 0.20MM
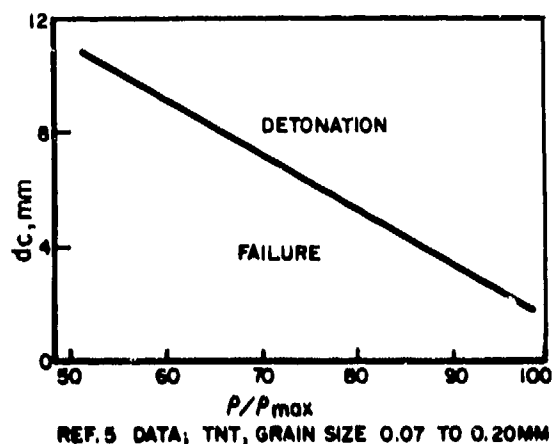
Fig. 1. Critical diameter decreasing with increasing explosive charge density, typical Group I characteristic.

REF. 7. DATA; AP, AVERAGE PARTICLE SIZE 10μ
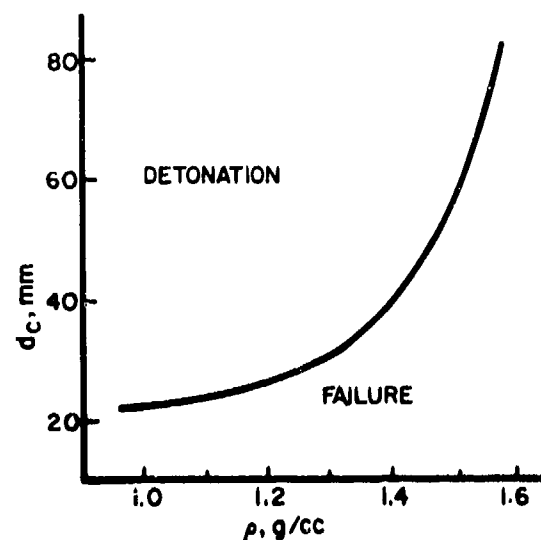
Fig. 2. Critical diameter decreasing with decreasing explosive charge density, typical Group II characteristic.

174

We have conducted extensive experiments in the development of low velocity, low detonation pressure explosive formulations. The approach has been to decrease the explosive density substantially, which means well below bulk density. One technique was to suspend the explosive particles in an expanded polyurethane foam. In this manner we achieved explosive charge densities to below 0.1 g/cc (8). However, because the explosive particles were for the most part embedded in the polyurethane the d_c increased greatly as the explosive charge density decreased, and furthermore the explosive loadings had to be substantial. Several other approaches were taken, one of the most successful being the composite NQ-AP, with small amounts of the NQ being required. The basis for this approach was that both components were purported to be Group II explosives. It was surmised that reducing NQ density by extensive dilution with AP would allow detonation to take place at very small d_c and that the AP should supplement the detonative energy output

There is not much information available on the detonation of AP. Figure 3 illustrates the d_c versus density relationship for two different particle sizes of AP as determined by Andersen and Pesante (9). Note that for both particle sizes the d_c decreases with decreasing density and additionally the d_c decreases with smaller particle size. In a later work Price et al. (10) conducted a more extensive investigation into the explosive behavior of AP, studying three weight-median particle sizes of 10, 25 and 200 μ, which corresponded to lowest density charges of 0.6, 0.9 and 1.3 g/cc, respectively. An interesting observation of this work was that although the AP failed to detonate at subcritical charge diameters, a highly luminous and vigorous reaction nevertheless initiated and persisted for some time. For example, with 200 μ AP at 1.29 g/cc the AP failed to detonate at a charge diameter of 7.62 cm but this vigorous reaction persisted for 16 cm down the length of the charge. The authors stated that there was little doubt from the experiments conducted that this fading reaction is subcritical charges of AP represented an appreciable amount of chemical reaction capable of generating high pressures.

Our initial effort with NQ-AP composites was for the purpose of obtaining low d_c of a low density explosive composition. This was achieved and proved to be effective for the requirements intended (11). In a subsequent effort, it was desired to obtain high

energy output from relatively large charge diameters. However, direct detonation of AP would have resulted in excessive shock energies. Figure 4 illustrates the linear d* versus density relationships for both NQ (12) and AP (9). The common calculation for the detonation pressure is:

$$P = 2.5\rho \, D^2 \text{ kbar} \qquad (1)$$

where ρ = density in g/cc and D = detonation velocity in mm/μsec. As indicated in Fig. 4, the empirical d* relationships for NQ and AP are:
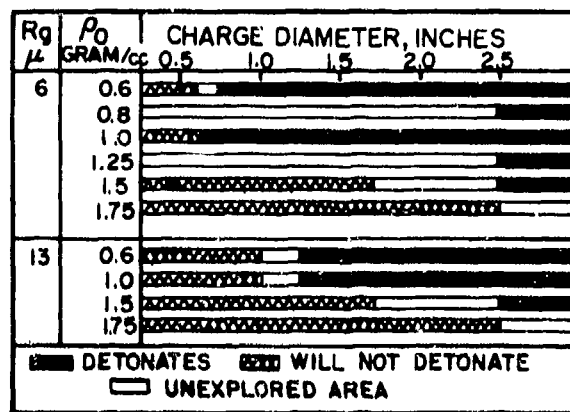
REF. 9 DATA

Fig. 3. Effect of particle size and loading density on the critical diameter of ammonium perchlorate.
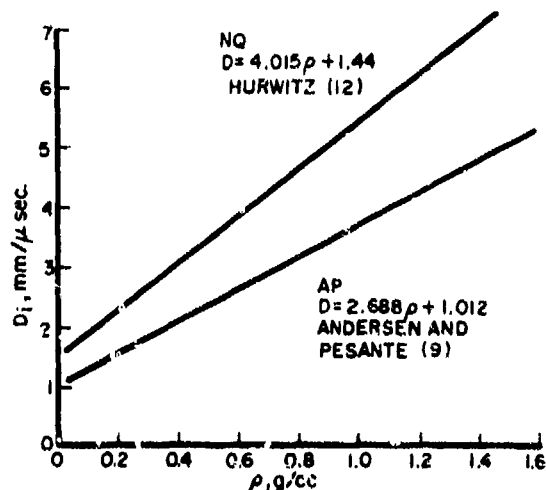
Fig. 4. Ideal detonation velocity (D_i) as a function of density for nitroguanidine (NQ) and ammonium perchlorate (AP).

175

$$\text{NQ: } D_i = 1.440 + 4.015\rho \text{ mm/}\mu\text{sec} \qquad (2)$$

$$\text{AP: } D_i = 1.012 + 2.688\rho \text{ mm/}\mu\text{sec} \qquad (3)$$

If the AP at 1.29 g/cc would detonate, the resultant D_i would be 4.48 mm/μsec corresponding to a detonation pressure of 64.7 kbar. However, if the same density NQ-AP composite would detonate at, say, 1.5 mm/μsec (based on the NQ component) then the detonation pressure should be no greater than 7.26 kbar, dependent on the extent and mechanism of the AP reaction in the detonation zone. Thus an order of magnitude reduction in pressure could be anticipated.

We therefore considered explosive composites consisting of AP with small amounts of NQ added. Under the conditions of this evaluation there would be little probability of initiating detonation of AP. However, we anticipated high probability of achieving detonation of the very low density NQ component, particularly in small charge diameters where other techniques had failed.

EXPERIMENTAL

Procedure

Figure 5 illustrates a typical experimental setup. In this test series the NQ-AP composite was loaded into Plexiglass tubes nominally 4 cm diameter by 15 cm long. The NQ-AP composite was tamp-packed by hand, in 1 inch increments with weight checks throughout to ascertain uniformity in loading. Instrumentation consisted of: (a) fiber optic probes, at 1 inch intervals, in conjunction with a photocell light detector monitor to measure the detonation velocity and (b) a carbon resistor pressure gauge (in most later tests) to obtain some indication of detonation pressure. The technique for measuring the detonation velocities was straightforward and accurate. The technique for estimating detonation pressures was identical to that described in our previous work with foamed explosives (8) fashioned after the original technique reported by Watson (13) and described by Ribovich et al (14). Initiation of the explosive composites was achieved by using either 1 or 2 tetryl pellets, 0.5 inch diameter by 0.5 inch long in conjunction with a No. 6 electric blasting cap (EBC). The
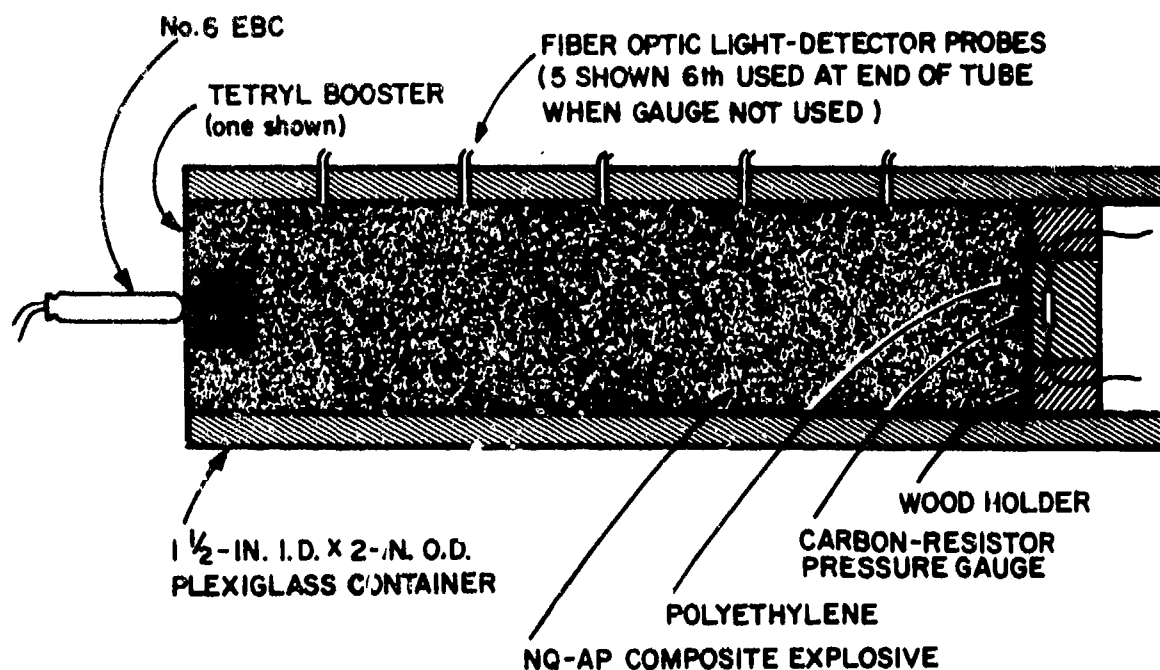
Fig. 5. Experimental test item utilized to measure detonation velocities and to estimate detonation pressures of nitroguanidine-ammonium perchlorate composites.

176

tetryl booster was embedded in the explosive composite as illustrated. One tetryl pellet was determined to be adequate although 2 were used in some tests; e.g., tests involving attempts to initiate detonation in pure AP and tests wherein the NQ component was very low.

Experiments were conducted with NQ-AP composites wherein the NQ component amount ranged from pure NQ to less than 1 percent by weight, with charge diameters from 4 to 0.6 cm, under confinement ranging from heavy to moderate to none. (No confinement refers to tests using thin-walled Plexiglass to hold the charge.) The experimental procedure for tests in steel tubes and under other geometric conditions was comparable to that described above and illustrated in Fig. 5, except as follows. In the case of charge confinement in small diameter steel tubes, the booster was considerably smaller, generally of the same diameter as the NQ-AP explosive charge. Additionally, in these small diameter charges the coupling to the carbon resistor pressure gauge was poor; the resistor size was physically too large for the small diameters of the charge. In some instances pressure records were obtained independently, utilizing larger 1 inch diameter charges for this purpose.

The NQ-AP composites were prepared from mil spec NQ and AP (15). The composites were prepared in nominally 600 g batches, placed in a roller mill and milled with 10 stones for 8 hours. In some cases, particularly those involving the small diameter charges, a small amount of Silanox (16) was added to prevent agglomeration and allow free flow of the charge powders. Figure 6 illustrates a 5 percent NQ in AP composite powder at 65X magnification. In this photo the NQ and AP particles appear to be mostly separated. In some other cases we observed that the NQ particles coated the AP particles extensively. This latter observation was made in some early tests and the reason for such coating was believed to be excessive moisture. The AP is hygroscopic and is generally handled so as to preclude excessive moisture uptake. There did not appear to be any variation in results obtained due to considerable moisture uptake or in the use of Silanox to prevent moisture uptake. In most experiments, particularly those reported here, due care was taken to prevent excessive moisture uptake.

Results

Table 1 gives the results of a test series conducted with NQ-AP composites confined in 0.6-cm diameter steel tubes. In these experiments the tube lengths were about 90 cm long and the fiber optic probes were spaced at about 15 cm intervals. The detonation velocity results for the composites are unerringly close to the D_i for the NQ component density. In the case of the pure NQ, the results are more scattered. The reason for this is believed to be experimental error; without the AP, NQ charge densities at 0.30, 0.25 and 0.19 g/cc are very low and loading of such low bulk powder was rather difficult. Note that the result with the greatest deviation from D_i was that for NQ at 0.19 g/cc, the lowest density explosive tested. Since any handling would be expected to compact the charge, the higher detonation velocity obtained is in line with this reasoning. The charges were fired upright, with the booster at the top. Thus, decrease in density near the top would be overdriven with the booster and would not necessarily be averaged out. In these experiments the velocities reported were those for the latter portion of the tubes, where the detonation had stabilized and booster effects were no longer present.

Table 2 gives the results of a test series conducted with NQ-AP composites in the test apparatus illustrated previously in Fig. 5. The detonation velocity oscillograph records for these tests are illustrated in Fig. 7. In these tests the overall density
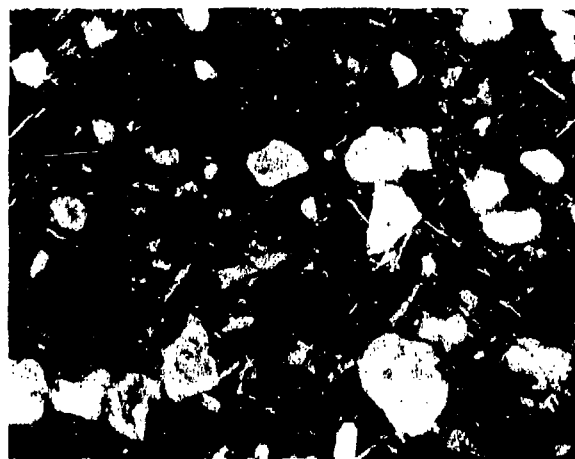
Fig. 6. Microscopic examination of NQ-AP composite. Example is 5% NQ in AP at 65X magnification.

177

TABLE 1

Detonation Velocities of Various NQ-AP Composites *

| Density, g/cc | | | %NQ | Detonation Velocity, mm/μsec | |
NQ	AP	Total		Ideal (12)	Measured
0.30	0.00	0.30	100	2.63	2.72
0.25	0.00	0.25	100	2.45	2.50
0.19	0.00	0.19	100	2.20	2.43
0.18	0.36	0.54	33	2.16	2.16
0.17	0.86	1.03	16	2.12	2.13
0.11	1.03	1.14	10	1.88	2.00
0.06	1.14	1.20	5	1.68	< 2.00
0.00	1.31	1.31	0	0.00	0.00

*0.6 cm diameter steel confinement.

TABLE 2

Detonation Velocities of Various NQ-AP Composites *

| Density, g/cc | | | %NQ | Detonation Velocity, mm/μsec | |
NQ	AP	Total		Ideal (12)	Measured
0.060	1.130	1.19	5	1.68	2.03
0.030	1.180	1.21	2.5	1.56	1.69
0.015	1.195	1.21	1.25	1.50	1.34
0.008	1.242	1.25	0.625	1.47	1.27**
0.000	1.310	1.31	0	0.00	0.00

*4 cm diameter Plexiglass confinement.
**unstable; detonation died.

averaged about 1.2 g/cc. It can be reasonably concluded that NQ in the vicinity of 0.01 g/cc detonated at near D_i in an explosive composite with about 9? percent AP. Figure 8 illustrates the carbon resistor pressure gauge responses of pure NQ at 0.5 g/cc and several NQ-AP composites tested in steel tubing of 1 inch nominal diameter. The results of these tests are listed in Table 3, based on a rough pressure gauge calibration using the calculated detonation pressure for NQ at 0.5 g/cc and assuming linearity of pressure with reciprocal ohms of the carbon resistor. These data are listed under the gauge column in the table. Under the NQ column are listed the calculated detonation pressures based on the detonation of the NQ at D_i, neglecting the AP. Under the NQ + AP column are listed the calculated detonation pressures based

on the detonation of both NQ and AP at the D_i for the NQ density of the composite. Although the gauge pressures listed are rough estimates at best, there can be little doubt but that the AP is detonating, evidently at the D_i of the NQ. We therefore conclude that the detonating NQ imposed a sympathetic detonation of the AP at the D_i of the NQ. Note in Fig. 8 that the peak pressures are realized in 0.8 μsec for the pure NQ, 1.3 μsec for the 5 percent NQ in AP, 1.4 μsec for the 2.5 percent NQ in AP and 1.6 μsec for the 1.25 percent NQ in AP. Additionally, the shock durations are more than twice as long for the NQ-AP composites as for the pure NQ. The AP energy is therefore released in the detonation zone of the reaction although the reaction zone is extended somewhat. This is in accord with the results obtained by

(a) 0% NQ in AP, overall 1.31 g/cc, 10 μsec/cm sweep, 0.1 v/cm sensitivity. RESULT: output of booster only—the pure AP did not detonate.
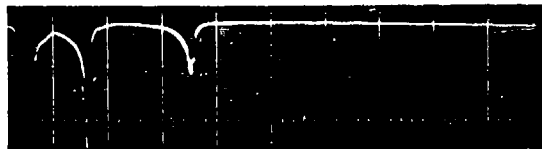
,b) 0.625% NQ in AP, overall 1.25 g/cc, 10 μsec/cm sweep, 0.2 v/cm sensitivity. RESULT: booster overdrive at start—dying detonation estimated 1.27 mm/μsec.
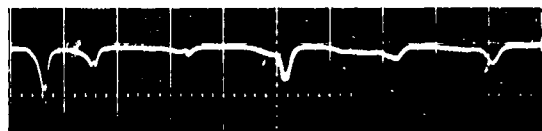
(c) 1.25% NQ in AP, overall 1.21 g/cc, 10 μsec/cm sweep, 0.5 v/cm sensitivity. RESULT: booster overdrive at start—sustained detonation at 1.34 mm/μsec.
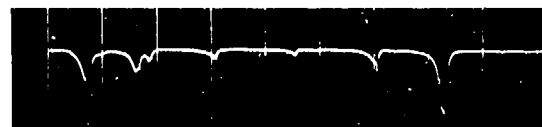
(d) 2.5% NQ in AP, overall 1.21 g/cc. 10 μsec/cm sweep, 1 v/cm sensitivity. RESULT: sustained detonation at 1.69 mm/μsec.
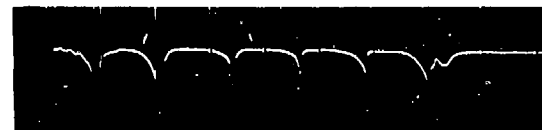
(e) 5% NQ in AP, overall 1.19 g/cc, 10 μsec/cm sweep, 0.5 v/cm sensitivity. RESULT: sustained detonation at 2.03 mm/μsec.

Fig. 7. Detonation velocity measurements of various NQ-AP composites utilizing fiber optics at six stations.
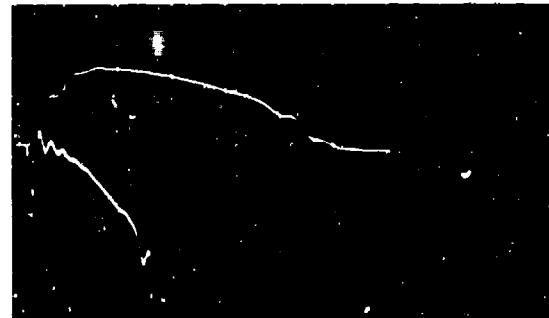
(a) 100% NQ.
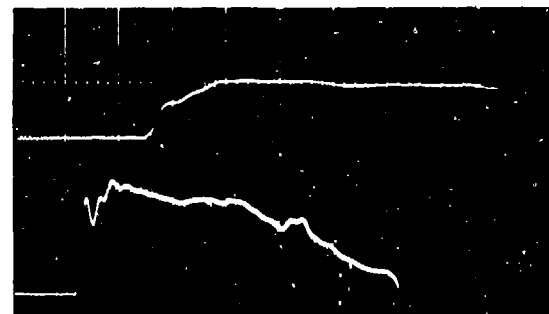
(b) 5% NQ in AP.
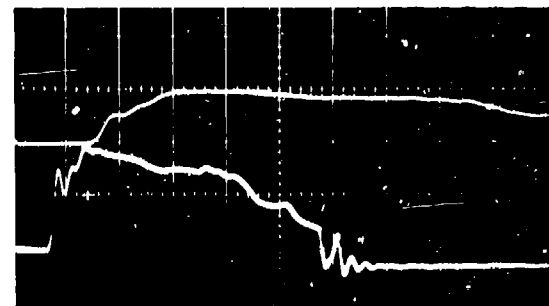
(c) 2.5% NQ in AP.
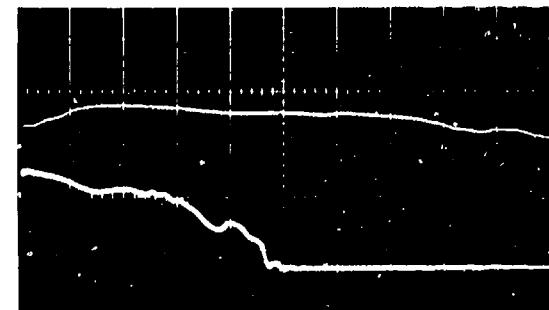
(d) 1.25% NQ in AP.

Fig. 8. Carbon-resistor pressure gauge responses for various NQ-AP composites confined in 1 inch steel tubes. All sweeps left to right; upper trace is 1 μsec/cm at 1 v/cm and lower trace is 2 μsec/cm at 0.5 v/cm.

179

Table 3

Detonation Pressures for Various NQ-AP Composites[*]

Density, g/cc			Pressure Gauge		Detonation Pressure, kbar		
NQ	AP	Total	$volt_{max}$	ohm^{-1}_{min}	NQ	NQ + AP	Gauge
0.5	0.000	0.50	1.60	0.031	14.8	—	14.8[*]
0.060	1.130	1.19	1.10	0.021	0.4	8.4	10.0
0.030	1.180	1.21	1.00	0.019	0.2	7.4	9.1
0.015	1.195	1.21	0.85	0.016	0.1	6.8	7.6

[*]The gauge pressures were based on the pure NQ gauge response, assuming linearity of pressure with reciprocal ohms of the carbon resistor gauge.

Finger et al. (17) in their studies of explosive composites involving perchlorates and other materials.

DISCUSSION

The data presented here indicate that: (a) small amounts of NQ in AP will cause such explosive composite to detonate at or near the D_i of the NQ based on the actual NQ density in the composite and (b) the AP component will also detonate, at the same velocity, in a sympathetic detonation mechanism. This has been demonstrated in this work, within the constraints of the experimental conditions utilized, for the NQ-AP composite. The reason these components were selected was because both were purported to have a decreasing d_c with decreasing density. The need of this for the NQ is probably real. The need of this for the AP, or other insensitive explosive material, is unknown. In addition, it is highly probable that similar effects can be achieved with other combinations of explosives; e.g., NQ and ammonium nitrate, dinitrotoluene and AP, etc.

Table 4 gives the results of microscopic examination of some NQ-AP composites tested. Results of some exploratory tests not reported here indicated that with substantially decreased AP particle size and/or AP density, increased detonation velocities would event independent of the NQ. This was to be expected as we were entering the nonideal detonation region of AP. From the relatively few and diverse experiments conducted with NQ-AP composites containing a fuel also, such as ethyl cellulose, and/or very small AP particle sizes it was evident that no simple treatment could be anticipated and that the

TABLE 4

Particle Size Analysis of Some NQ-AP Composites

Sample	NQ, μ (mode)[*]	AP, μ (mode)[*]
5.000 % NQ	55	110
2.500 % NQ	46	110
1.250 % NQ	50	115
0.625 % NQ	42	100

[*]Because the NQ particles are needles and the AP particles are clumps, these particle sizes must not be confused with particle mass—the particle mass of the AP was about 100 times as great as the NQ.

resultant detonation reactions were quite complex. However, in all of these composite exploratory tests containing NQ and which detonated, the resultant detonation velocity was always about D_i for the NQ actual density or higher. Thus it would appear that in NQ-AP composites wherein the AP itself was nondetonable due to subcritical diameter, large particle size or high density; or had nonideal detonation velocity lower than the D_i of the NQ present; then the NQ would induce sympathetic detonation at D_i of the NQ in the AP. On the other hand, if the AP conditions were such that a higher nonideal detonation velocity would take place in the AP than the D_i of the NQ, the NQ-AP would detonate at the higher nonideal detonation velocity. However, at this point there is no basis for determining whether or not, under critical conditions of nonideal AP detonation and near ideal NQ detonation, the overall mechanisms were acting independently or if synergistic effects

were taking place. Finally, it is not known whether or not the highly luminous and vigorous reaction induced in nondetonable AP charges, as reported by Price et al. (10) and discussed previously, was responsible for the propagation of this sympathetic detonation in AP. If that would be the case, then AP composites would be unique.

In the experiments conducted in steel tubes, the NQ-AP composites detonated at velocities that corresponded to the D_i of the NQ component. Note in Table 1 that the AP component, at 0, 0.36, 0.86 and 1.03 g/cc did not appear to alter the detonation velocity. At this small diameter the AP by itself would not detonate, which was confirmed by the last test in Table 1. At the other extreme, in experiments conducted in Plexiglass, the NQ-AP composites again detonated at velocities that corresponded closely to the D_i of the NQ component. In these experiments the explosive diameters were about 4 cm, which is in the range of d_c for AP of fine particle size and/or under heavy confinement. In several experiments under very heavy steel confinement and in an isochoric bomb experiment (18) there was some indication that the detonation velocity increased slightly; from 1.34 mm/μsec in Plexiglass to possibly as high as 1.57 mm/μsec in 1 inch wall thickness steel tubing. In this latter test the detonation velocity was estimated from the time between the booster detonation (ion probe) to the response of the carbon resistor pressure gauge—thus the effect of booster overdrive could not be eliminated and may have contributed to the higher indicated detonation velocity. The response of the carbon resistor pressure gauge was almost identical to that listed in Table 3 for the comparable NQ-AP composite; i.e., 1.25 percent NQ. However, the possibility of initiation of nonideal detonation of the AP directly cannot be discounted.

There can be no doubt, though, that this NQ-AP composite and probably numerous other combinations of explosives can prove to be most interesting explosive composites that could lead to a whole new class of "tailored" explosive compositions. For example, not only AP but ammonium nitrate and other "insensitive" explosive materials, that presently either deflagrate at rates below 1 m/sec or detonate high order, could be sensitized with a "control" explosive of less than 1 percent to achieve very rapid, low velocity detonation in the latter, particularly of small charges. The trend appears to be correct; the insensitive explosives such as AP are Group II explosives, so that very heavy loading leads to nondetonability. On the other hand, the sensitive components, NQ here and nitroglycerine in Cook's (19) work with ammonium nitrate, appear to also behave as Group II explosives but are utilized at the other extreme; i.e., at very low density to enhance their detonability, possibly at D_i.

In conclusion, we have shown that it is feasible to induce a sympathetic detonation in AP with amounts of NQ less than 1 percent. The detonation velocity is determined by the density of the NQ present. The sympathetic detonation of the AP is of course non-ideal and it is not known to what extent the AP detonates. However, from the detonation pressures estimated and from the obvious work output from these NQ-AP composites it appears that the full energy of the AP is released in the detonation reaction.

ACKNOWLEDGEMENTS

REFERENCES

1. W. E. Gordon, "Detonation Limits in Composite Explosives," Tenth Int. Symp. Combust., pp. 833-838, The Comb. Inst., Pittsburgh, Pa., 1965.

2. M. A. Cook, The Science of High Explosives, Reinhold, New York, 1958.

3. J. A. Brown and M. Collins, "Explosion Phenomena Intermediate Between Deflagration and Detonation," ESSO, ARO STAF, October 1967.

4. A. Stettbacker, Schiess-u. Sprengstoffe, 14, pg. 125, 1919.

5. V. K. Bobolev, Dokl. Akad. Nauk SSSR, 57, pg. 789, 1947. JPRS:4026.

6. D. Price, "Contrasting Patterns in the Behavior of High Explosives," Eleventh Int. Symp. Combust., pp. 693-702, The Comb. Inst., Pittsburgh, Pa., 1967.

7. D. Price and A. R. Clairmont, Jr., "Explosive Behavior of Nitroguanidine," Twelfth Int. Symp. Combust., pp. 761-770, The Comb. Inst., Pittsburgh, Pa., 1969.

8. J. L. Austing, A. J. Tulis, and C. D. Johnson, "Detonation Characteristics of Very Low Density Explosive Systems," Fifth Int. Symp. on Detonation, ONR, ACR-184, pp. 47-58, 1970.

9. W. H. Andersen and R E. Pesante, "Reaction Rate and Characteristics of Ammonium Perchlorate in Detonation," Eight Int. Symp. Combust., pp. 705-710, Williams and Wilkins, Baltimore, 1962.

10. D. Price, A. R. Clairmont, Jr., and I. Jaffe, "Explosive Behavior of Ammonium Perchlorate," Comb. and Flame, 11, No. 5, pp. 415-425, Oct. 1967.

11. A. J. Tulis, D. Morita, and C. J. Dahn, "Low Detonation Velocity Explosives for Propellant Applications," ADPA Meeting, Seattle, 1973. conf.

12. M. D. Hurwitz, OSRD 5611. (See also Ref. 7).

13. R. W. Watson, Rev. Sci. Inst., 38, pg. 978. 1967.

14. J. Ribovich, R. W. Watson, and F. C. Gibson, AIAA J., 6, pg. 1260, 1968.

15. NQ: 99.8% purity, Lot No. CCL-9-796, Cyanamid Welland Plant; AP: TRONA 99.5% min NH_4ClO_4, Lot No. 5025, Kerr-McGee Chem. Corp.

16. Silanox is a hydrobhobic agent of exceedingly small particle size that is effective in preventing agglomeration, even in hygroscopic materials, when utilized in concentrations well below 1 percent.

17. M. Finger, H. C. Hornig, E. L. Lee, and J. W. Kury, "Metal Acceleration by Composite Explosives," Fifth Int. Symp. on Detonation, ONR, ACR-184, pp. 137-151, 1970.

18. R. Nelson, ARMCOM, Rock Island Arsenal, U.S. Army, personal communication.

19. U.S. Patent 2, 149, 218.

182

FURTHER STUDIES ON THE DETONATION CHARACTERISTICS
OF VERY LOW DENSITY EXPLOSIVE SYSTEMS

Allen J. Tulis and James L. Austing
IIT Research Institute
Chicago, Illinois 60616

A technique has been developed in which inert witness foams in contact with a detonating foamed explosive charge are utilized to measure the detonation state of the explosive. The witness foams contain a tungstic oxide additive to control the overall density and make the foam clearly visible in flash x-ray, which is focused on the interface between the explosive and witness foam. The particle velocity of the interface, is monitored by recording the displacement of the interface. The pressure behind the shock wave in the witness foam is calculated from the expression for conservation of momentum. The pressure-particle velocity point that is obtained represents both one point on the Hugoniot of the witness foam and one point of the cross-curve of the explosive reaction products. By conducting several such experiments in which the impedance of the witness foam is varied, the cross-curve of the explosive reaction products can be traced. The detonation state is represented by the intersection of this curve with a line whose slope is the impedance of the explosive. Preliminary results for foamed PETN at explosive densities of 0.09 and 0.11 g/cc indicate that the detonation pressure is on the other of 0.5 kilobar, which is encouraging for applications requiring low-performance explosives.

INTRODUCTION

The work discussed in this paper represents a continuation of the effort reported by Austing et al. at the Fifth Symposium (International) on Detonation (1). In that effort the authors measured the detonation state of very low density explosive systems, defined as having explosive loading densities below 0.25 g/cc. Such values are considerably below the minimum densities that can be obtained with pure powdered explosives. These low densities were obtained by utilizing polyurethane foams in which the explosive was dispersed throughout the given volume so as to yield a very low apparent explosive density Foamed PETN and foamed nitrocellulose/nitroglycerine were studied extensively, and some work was performed on a commercial expanded nitrocellulose product. Detonation stability was studied and an attempt was made to measure

the detonation pressure of the explosives. Sufficient reliable detonation velocity data were obtained to establish the lowest densities at which stable detonation would occur. However, the detonation pressure measurements were not satisfactory, and in some instances produced results that had no physical significance.

Measurement of detonation pressure usually requires that the response of a witness material in contact with the explosive be recorded at the time the detonation wave arrives at the interface and drives a shock wave into the witness material. The witness material, be it water in an aquarium technique or a carbon resistor mounted in a polystyrene cylinder, must be calibrated from the available Hugoniot data. The detonation pressure is then generally calculated from the impedance mismatch equation. Most accurate results are obtained when the detonation

impedance (ρ_0 D) of the explosive is about equal to the shock impedance (ρ_0 U) of the witness material. In evaluating common military explosives, this latter requirement is easily met. However, in the evaluation of the foamed explosives in Ref 1 wherein the carbon resistor pressure gage was utilized, the two impedances were vastly different from each other, simply because of the large density difference that existed between the explosive and the witness. Hence, for foamed explosives very poor results were obtained. The major effort in the present work, threfore, was to develop a reliable way to measure the detonation state of very low density explosives. Initially it appeared that direct measurement of the particle velocity of the explosive by observing the motion of thin metal foils embedded in the charge would provide reliable data. However, this method failed when applied to low density foamed explosives. Hence an alternative technique h..i to be developed. This technique made use of inert witness foams in contact with the explosive charge. Successful preliminary measurements were made for foamed PETN. However, a greater number of experiments are needed in order to substantiate the efficacy of this technique. One definite attribute of this technique is that prior calibration of the witness foam is not necessary.

and that no reaction had occurred between the explosive and foaming agents.

For the charges in the present work, a premixed polyurethane system, Isonate CPR 323*, was utilized. This system foams to a predetermined density of 0.07 g/cc when the two components are combined and contains Freon to serve as the blowing agent, catalysts to promote the foaming action at the proper rate, and surfactants to control the size of the cells. Since this system had the advantage that it permitted evaluation of the effects of type of explosive and explosive loading without variation in the properties of the foam, its use for the foaming of the required charges was desirable.

Although foamed PETN had been evaluated extensively previously (1), charges had not been prepared utilizing the CPR foaming system. Hence the initial effort here was to generate foaming data for 10-12 micron PETN** foamed with the CPR polyurethane. The results are presented in Fig. 1. The quoted particle size of the PETN is probably a calculated average value because miroscopic examination revealed crystals 5-10 microns in diameter by 20-50

EXPERIMENTAL

Charge Preparation

The essential details in the preparation of foamed explosives utilizing polyurethane foams are available in Ref. 1. Briefly, polyurethane foams are produced by the exothermic reaction between a polyol and an isocyanate which crosslink and, under influence of a blowing agent, expand to produce a cellular structure with a possible density range from below 0.02 to about 1.12 g/cc. To prepare a foamed explosive charge then, the required quantities of explosive, polyol, and isocyanate were quickly mixed in a disposable beaker and then poured into the confining tube, in which the foaming subsequently occurred. After foaming had ceased and the form had cured, excess material that had foamed out of the tube was evenly removed from the ends of the tube. The density of the explosive and foam was calculated from the weight of materials remaining in the tube and the known internal volume of the tube, under the assumption that all ingredients were evenly distributed

Fig. 1. Design Curve for Preparation of Foamed PETN Utilizing 10-12 Micron PETN and Isonate CPR 323.

---

*CPR Division, The Upjohn Company, Torrance, California 90503.

**Hercules, Inc., Wilmington, Delaware.

microns long. The points in the figure are taken from actual foamings; thus, the curve represents a design curve for proper selection of the weight of foaming agents required to achieve a final explosive density.

Continuous Probe

In the work discussed in Ref. 1, ion probes inserted at intervals in the charge were utilized to measure detonation velocity. Although it was not specifically discussed in that paper, these probes did not always perform satisfactorily, especially for the very low density foamed explosive systems. Hence, for the present work, a continuous probe modeled after the type IIb probe (2) was utilized. This probe consists of 0.508 mm O.D. soft aluminum tubing with a 0.0508 mm wall; on the inside of the tubing is a 0.0508 mm Tophet-C resistance wire that is insulated from the tube by a skip-winding of nylon threads*. The probe functions by means of the pressure of the detonation continually collapsing the tube onto the wire, thereby progressively shorting out the probe. The change in voltage drop across the probe is directly related to the probe resistance, which in turn is a function of the effective length of undisturbed probe. This voltage drop can be recorded on oscilloscopes or magnetic tape and provides a continuous distance-time record of the advancing detonation, from which detonation velocity may be computed as a function of distance and time.

Best and most easily interpreted results are obtained if the current through the probe is unaffectd by the change in probe resistance. This is accomplished by utilizing a power supply that provides a constant current regardless of the laod (3). This type of power supply was utilized in this work.

Measurement of Chaptman-Jouguet Conditions

Each of the charges that were fired in the previous work (1) included a carbon resistor pressure gage for measurement of the Chapman-Jouguet (CJ) pressure. Although the gage pressures correlated with the explosive densities, in the case of the foamed explosives calculation of the CJ parameters by utilizing the impedance mismatch equation yielded results that had no physical significance. Hence, the objective in this work was to measure the CJ conditions for

foamed explosives by means of a radically different method. The most obvious method was to study the motion of foils embedded in the charge; this will be referred to as the foil motion technique. However, because this method did not work for the foamed explosives, an alternative method was developed; this will be referred to as the witness foam technique.

● foil motion technique

The foil motion technique permits direct measurement of the particle velocity behind a detonation wave, from which the pressure and density can be calculated utilizing the conservation equations. A version of this technique is described by Rivard et al. (4). One or more very thin metal foils that are opaque to flash x-ray are embedded in an explosive charge perpendicular to the direction of detonation propagation. The flash x-ray views the charge perpendicular to the detonation travel, and hence the foils appear as very thin reference lines on the flash radiograph film. The foils are swept into motion at the local particle velocity by the advancing detonation. By properly sequencing the flash x-ray, the displacement of each foil can be recorded over a given time interval, from which the particle velocity can be computed. The success of the method requires that the explosive on the downstream side of each foil be shock-initiated to stable detonation in a time interval shorter than can be resolved in the time frame of the experiment. For the high density charges and thin foils utilized by Rivard et al., this readily occurred.

Figure 2 shows the experimental arrangement that we utilized to verify the applicability of the foil
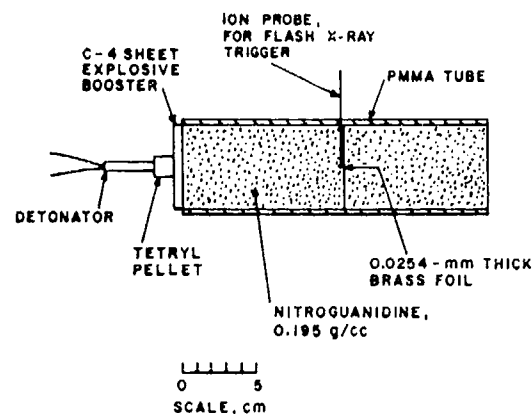
Fig. 2. Foil Motion Technique for Measurement of Particle Velocity in Detonating Low Density Explosives.

185

motion technique to very low density explosives. For the nitroguanidine, the method yielded excellent results. The ion probe was positioned against the upstream side of the foil, which in turn was prepositioned in the polymethyl methacrylate (PMMA) tube. Weighed quantities of nitroguanidine were then loaded ot the specified density from each end of the tube. The advancing detonation triggered the flash x-ray* which then flashed 3.9 μsec later. As shown in Fig. 3, the foil was displaced 4.8 mm in this time, which is equivalent to a particle velocity of 1.2 mm/μsec. Other pertinent data for this test, No. 156, are summarized in Table 1.** All evidence had indicated that the most critical aspect of instantaneous shock-initiation of the downstream nitroguanidine had been achieved.

Table 1 also presents the results when the foil motion technique was applied to the study of detonating foamed PETN. The experimental arrangement was similar to that depicted previously in Fig. 2, with the inclusion of the continuous probe positioned at the axis of the charge for measurement of detonation veolicty. As shown in the table, no particle velocities were obtained because the foil evidently prevented

reinitiation and propagation of the detonation on the downstream side of the foil. The flash x-ray films revealed that the foil had not been displaced by the foamed PETN detonation. A complicating feature of this technique as applied to foamed explosive was in loading of the device. Both the brass foil and the continuous probe were very fragile. The explosive had to be foamed carefully from both ends, and this may have introduced inhomogeniety at the interface with the brass foil. An alternative procedure would have been to foam a compelete charge, saw the cured charge in half, and then insert the brass foil. However, sawing these charges was considered to be hazardous and would have precluded use of the continuous probe.

● witness foam technique

The witness foam technique is a method whereby inert foamed materials in contact with the detonating foamed explosive are utilized to measure the detonation properties of the explosive. In this respect, this technique is similar to methods developed for evaluation of condensed explosives. However, the witness foam technique as employed in the present work precludes the necessity of prior calibration of the witness material.

The experimental arrangement for the witness foam technique is depicted in Fig. 4. The witness foam is made from the Isonate CPR 323, with an additive of tungstic oxide to adjust the density and to make the foam clearly visible in flash x-ray. The flash x-ray is focused on the interface between the foamed explosive and the witness foam. The detonation velocity in the explosive and the shock velocity in the witness foam are monitored by the continuous probe. The particle velocity in the witness foam, which is equal to the particle velocity of the interface, is monitored by recording the displacement of the interface with the flash x-ray. The flash x-ray is triggered by the pressure contact probe at the interface, and is delayed for a specified time interval of approximately 15 μsec. A typical radiograph showing the displacement of the interface is presented in Fig. 5. The displacement of 4.1 mm in 14.8 μsec corresponds to a calculated particle velocity of 0.28 mm/μsec. The two dark objects in each picture are hardware associated with construction of the continuous and pressure contact probes, and have no significance in interpreting the records.

DE TONATION
PROPAGATION

FOIL DISPLACEMENT
= 4.8 mm
IN 3.9 μsec
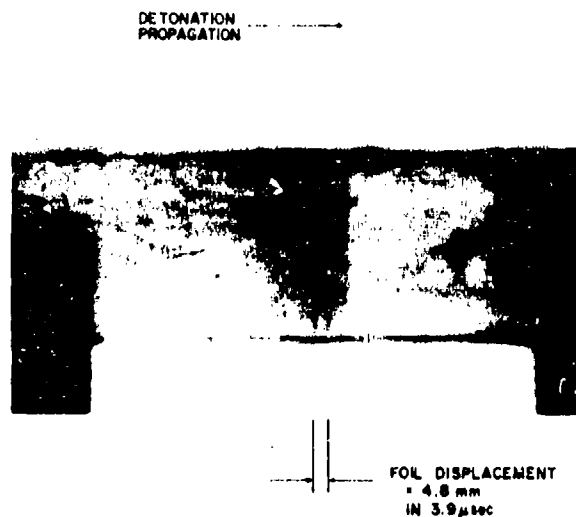
Fig. 3. Flash Radiograph Showing Displacement of Foil in Low-Density Nitroguanidine.

---

*Foxitron Model 515, 300-Kv.

**Detonation velocity was recorded with other ion probes that are not shown in Fig. 2.

TABLE 1

Foil-Motion Method for Measurement of Chapman-Jouguet Conditions In Low-Density Explosives*

System	Test No.	Charge Density, g/cc		Detonation Velocity mm/μsec	Particle Velocity mm/μsec	CJ Pressure, Kilobars
		Explosive	Foam			
Nitroguanidine	156	0.195	—	2.7	1.2	6.3
Foamed PETN	162	0.14	.16	0.8	No record	—
Foamed PETN	163	0.12	0.15	1.0	No record	—

*Experimental arrangement is depicted in Figure 2.
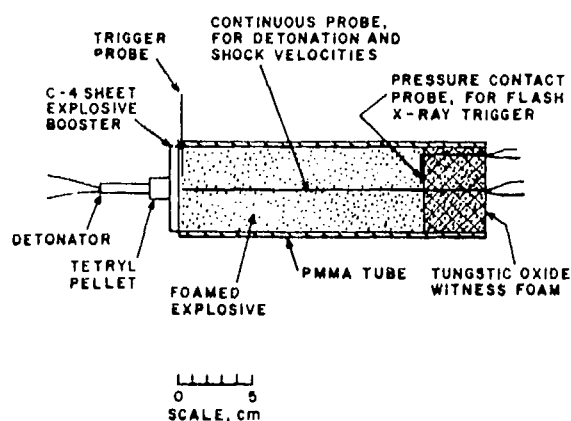
Fig. 4. Witness Foam Technique for Measurement of Chapman-Jouguet Parameters in Detonating Foamed Explosives.

The pressure behind the shock wave induced in the witness foam can now be calculated from the equation for conservation of momentum:

$$P_1 = \rho_0 U u_1 \qquad (1)$$

where:

P_1 = the shock pressure
ρ_0 = the initial density
U = the shock velocity
u_1 = the particle velocity

This pressure-particle velocity point represents both one point on the Hugoniot of the witness foam and one point on the cross-curve of the explosive reaction products, from the requirement that pressure and particle velocity are continuous across an interface.
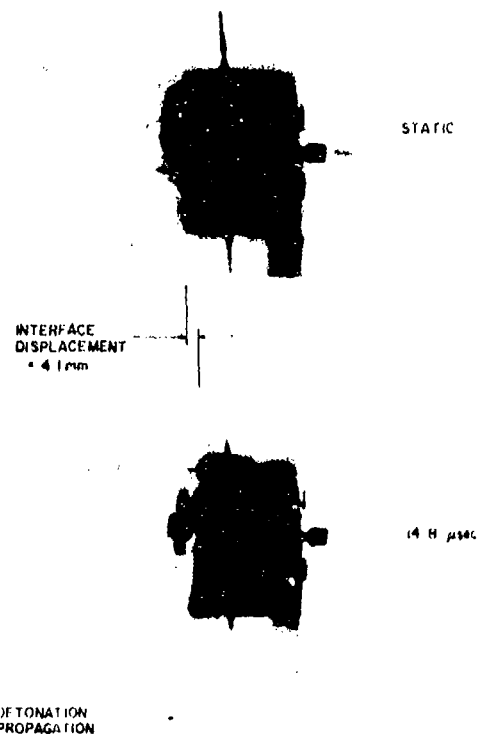
Fig. 5. Flash Radiograph Showing Displacement of Explosive-Witness Foam Interface for Foamed PETN Charge. Test No. 166 Result.

For a given explosive system, at least three such experiments should be conducted in which the shock impedance ($\rho_0 U$) of the witness foam is varied. From the results of these experiments, the cross-curve of the explosive products can be traced, and the CJ state is represented by the intersection of this curve with a line whose slope is the product of density and detonation velocity of the explosive.

187

The construction of the pressure contact probe indicated in Fig. 4 is identical to that of the continuous probe described earlier, with the exception that initially only a voltage potential exists in the open circuit. The flash x-ray, then, is triggered by the first flow of current, as the probe is crushed by the pressure of the detonating foamed explosive. The pressure contact probe served as an alternative to the use of ion probes, which in previous work did not perform well with foamed explosives.

Figure 6 shows a design curve for the preparation of the witness foams utilized in this investigation. The tungstic oxide was the so-called TO-1 grade,* which has a quoted particle size of 3 microns maximum.

Results for Foamed PETN

A total of six charges are required for the evaluation of foamed PETN at two explosive densities, viz. 0.11 and 0.09 g/cc, respectively. The experimental data for two of these experiments are summarized in Table 2, i.e., Tests 166 and 168. Time thus far has permitted only these two charges to be fired, but as shown in the following discussion the data that were obtained permitted an approximate estimate of the CJ conditions for foamed PETN at these two densities. Thus, although the validity of the experimental

*Sylvania Electric Products Corporation, Towanda, Pennsylvania.

method has been demonstrated, the remaining four tests in the table should be conducted in order to completely characterize each explosive system.

The data for Test Nos. 166 and 168 are plotted in the pressure-particle velocity plane in Figs. 7 and 8, respectively. Since data from the other experiments presented in Table 2 are not as yet available, the exact locus of the cross-curves are not known, and the CJ states must be calculated as follows. It is observed that in both figures the impedance of the witness foam was less than that of the explosive. Hence, a rarefaction was reflected back into the explosive products from the explosive-witness foam interface, and Deal's equation (5) which expresses the reflected
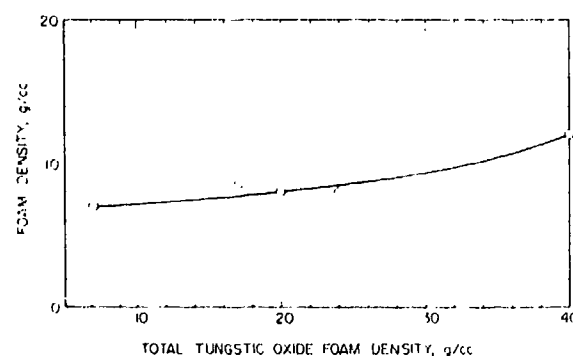
Fig. 6. Design curve for Preparation of Tungstic Oxide Witness Foams Utilizing 3-μ Tungstic Oxide and Isonate CPR 323.

TABLE 2

*Witness Foam Method for Measurement of Chapman-Jouguet Conditions in Foamed PETN**

Test No.	Charge Density, g/cc			Detonation Velocity mm/μsec	Witness Foam			
	Explosive	Foam	Total		Density g/cc	Shock Velocity mm/μsec	Particle Velocity mm/μsec	Pressure Kilobars
166	0.11	0.13	0.24	0.93	0.18	0.82	0.28	0.41
168	0.09	0.11	0.20	1.20	0.19	0.82	0.30	0.47
169	0.11	0.13	0.24		0.12			
170	0.11	0.13	0.24		0.30			
171	0.09	0.11	0.20		0.12			
172	0.09	0.11	0.20		0.30			

*Experimental arrangement is depicted in Fig. 7. 10-12 micron PETN was utilized in the foaming.

188
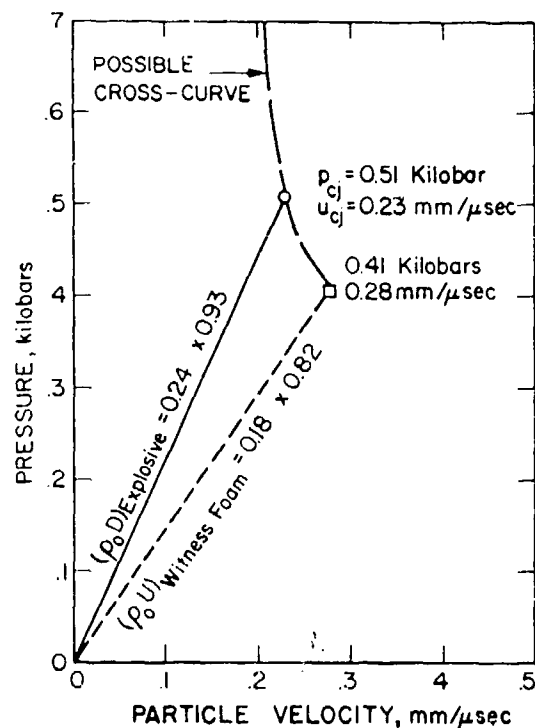
Fig. 7. Possible Calculation of Chapman-Jouguet State for Foamed PETN at Explosive Density of 0.11 g/cc. Numerical Values are Taken from the Test Results of Test No. 166.
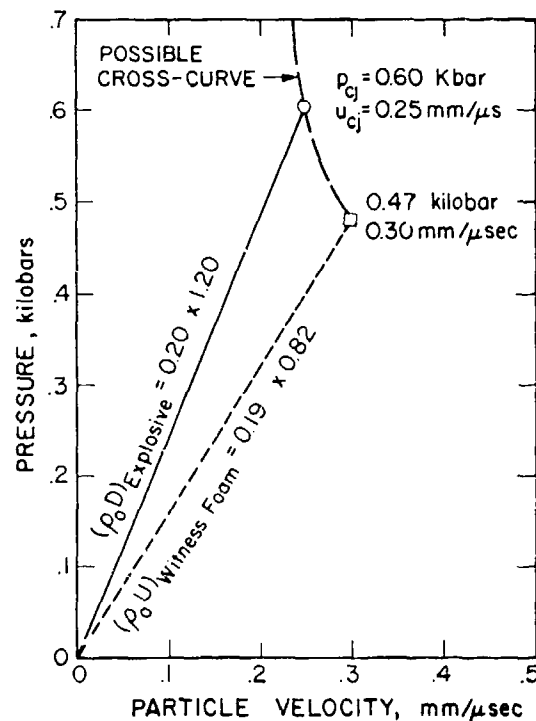
Fig. 8. Possible Calculation of Chapman-Jouguet State for Foamed PETN at Explosive Density of 0.09 g/cc. Numerical Values are Taken from the Test Results of Test No. 168.

particle velocity as a function of reflected pressure for the explosive products isentrope can be utilized:

$$u_r = \frac{P_{cj}}{\alpha \rho_o D}\left[1 + \alpha - \left(\frac{P_r}{P_{cj}}\right)^\alpha\right] \qquad (2)$$

where:

$$\alpha = 1/2\left(1 - \frac{P_{cj}}{\rho_o D^2 - P_{cj}}\right)$$

u_r = the reflected particle velocity
P_r = the reflected pressure
P_{cj} = the Chapman-Jouguet pressure
ρ_o = the initial total explosive density
D = the detonation velocity

In the present problem, the reflected pressure and particle velocity are respectively equal to the pressure and particle velocity of the witness foam, and hence are known. The value of P_{cj} can thus be calculated by trial-by-error from Eq. 2. This has been done, and the results are indicated in Figs. 7 and 8. Possible cross-curves have been drawn. Since the general form of the cross-curve appears reasonable, it is obvious that slightly alternative forms would have a small effect on the magnitude of the CJ parameters.

The estimated Chapman-Jouguet conditions for foamed PETN at two densities utilizing the pressures as calculated above are summarized in Table 3. The CJ density was calculated from the expression for conservation of mass:

$$\rho_{cj} = \frac{D}{D - u_{cj}}\,\rho_o \qquad (3)$$

TABLE 3

Estimated Chapman-Jouguet Conditions for Foamed PETN

Initial Density, g/cc		Detonation Velocity mm/μsec	CJ Density, g/cc	CJ Pressure, Kilobars	Particle Velocity, mm/μsec	Polytropic Exponent, γ
Explosive	Total					
0.11	0.24	0.93	0.32	0.51	0.23	3.1
0.09	0.20	1.20	0.25	0.60	0.25	3.8

and the polytropic exponent from the expression

$$\gamma = \frac{\rho_o D^2}{P_{cj}} - 1$$

$$= \frac{D}{u_{cj}} - 1 \qquad (4)$$

In these expressions, ρ_o is understood to mean the initial total explosive system density, i.e., the sum of the explosive and foam components. The results in Table 3 are completely consistent, and a CJ pressure on the order of 0.5 kilobar is encouraging from the standpoint that such a value is reasonable for these explosives.

DISCUSSION

The work described in Ref. 1 in part consisted of the use of a polystyrene-carbon resistor pressure gage to estimate the detonation pressure. Although the attempted calculation of detonation pressure from the measured gage pressures yielded unrealistic answers for foamed PETN, nevertheless the gage pressures correlated with the explosive densities according to the following empirical equation:

$$P = -3.0 + 105.09 \rho_o - 248.06 \rho_o^2 \qquad (5)$$

This pressure, of course, represents the shock pressure induced in the polystyrene through a PMMA attenuator that separated the charge from the gage. It is of interest to calculate such a pressure for the experiments conducted in the present work (Table 2) and from this an additional point on the cross-curve of the explosive reaction products can be obtained. The results of this calculation are presented in Figs. 9 and 10; the cross-curve in each figure has been

drawn to pass through this point on the PMMA Hugoniot and through the CJ point as determined in the previous section.

The interesting aspect is that the cross-curves for foamed PETN rise rather sharply to the left of the CJ point. The sharpness of the rise is unexpected and as yet unexplainable, but if real would account for the higher-than-expected gage pressures that were obtained for foamed PETN in Ref. 1. We have given
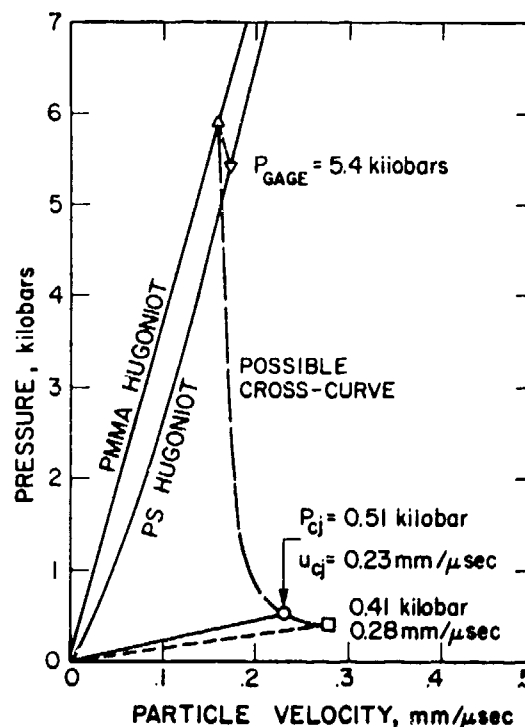
Fig. 9. Extrapolation of Cross-Curve for Foamed PETN at 0.11 g/cc to Higher Pressures. PMMA and PS are Abbreviations for Polymethyl Methacrylate and Polystyrene, Respectively.
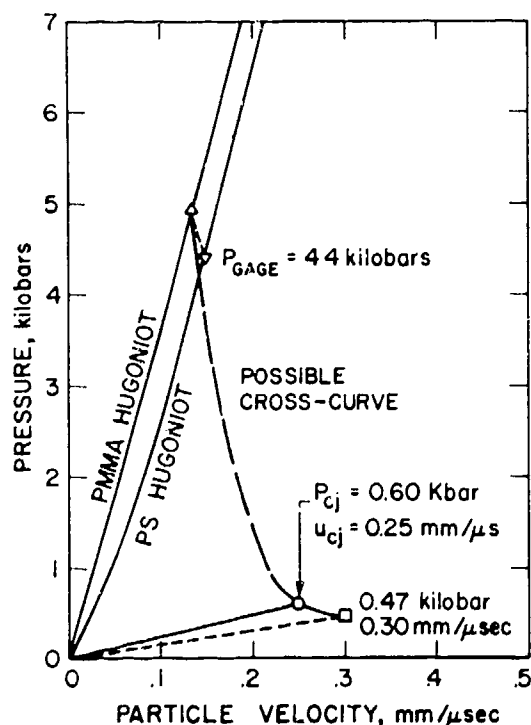
Fig. 10. Extrapolation of Cross-Curve for Foamed PETN at 0.09 g/cc to Higher Pressures. PMMA and PS are abbreviations for Polymethyl Methacrylate and Polystyrene, Respectively.

careful thought to the validity of the experimental technique utilized in that effort, but it appears to be valid since this same technique yielded realistic results for the expanded nitrocellulose charges. Further insight into the nature of cross-curve for foamed PETN will be obtained when more experimental data are available. Table 2 indicates four such experiments

that should be conducted; two of these would have witness foams with impedance higher than that of the explosive. Additional tests utilizing still higher impedance foams will trace out the cross curve in the upper regions at 4-5 kbar.

ACKNOWLEDGEMENTS

REFERENCES

1. J. L. Austing, A. J. Tulis, and C. D. Johnson, "Detonation Characteristics of Very Low Density Explosive Systems," Proceedings, Fifth Symposium (International) on Detonation, Pasadena, California, August 18-21, 1970, Report No. ACR-184.

2. J. Ribovich, R. W. Watson, and F. C. Gibson, *AIAA J.*, 6, 1260, 1968.

3. F. C. Gibson, M. L. Bowser, and C. M. Mason, *Rev. Sci. Inst.*, 30, 916, 1959.

4. W. C. Rivard, D. Venable, W. Fickett, and W. C. Davis, "Flash X-Ray Observation of Marked Mass Points in Explosive Products," Proceedings, Fifth Symposium (International) on Detonation, Pasadena, California, August 18-21, 1970.

5. Deal, W. E., *Phys. of Fluids*, 1, 523, 1958.

191

Session III
DEFLAGRATION-TO-DETONATION
TRANSITION STUDIES

Chairman: Adolph B. Amster
            Naval Sea Systems Command
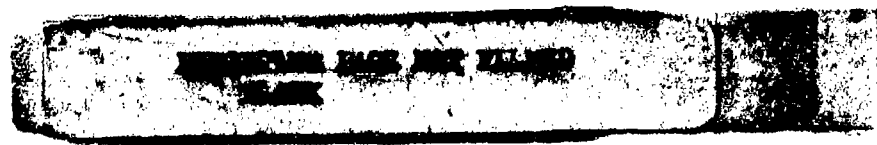
DEFLAGRATION RATE OF COMPOSITE HIGH EXPLOSIVE AND COMPOSITE PROPELLANTS AT PRESSURE ABOVE 1 KILOBAR

Pierre Benhaim and Jean Goliger
"Le Bouchet" Research Center
Societe Nationale des Poudres et Explosifs – SNPE
91710 Vert-le-Petit, France

This paper presents experimental results on determination of deflagration rate of compact composite high explosives and propellants in a closed vessel at high pressure. The closed bomb has been designed to be only partially destroyed by a possible DDT and has a combustion chamber of 100 cm³. It resists at pressure up to 15 kilobars. Computer gives DP/dt and v, i.e., the deflagration rate of the tested material. Post-fire observations of extinguished grains support validity of assumption of a uniform regression rate. First results obtained on tested material are presented; they show a quasi-linear curve v(p) up to 7000 bars. At 5000 bars, for example, we obtain a regression rate of 530 mm/s on a composition with 90% HMX. These rates will be used to foresee the evolution of ignited compact blocks in closed vessels, and enable a ranking of products according to the possibility of a rapid pressure build-up.

INTRODUCTION

Actual knowledge of high pressure deflagration rate of explosive material would be useful for modeling the beginning of pressure buildup of compact explosives after an ignition. Previous work on closed-vessel burning has allowed us to determine mechanical behavior of products under high pressure and to obtain regression rates. Thus, we designed, built, and used a special high-pressure vessel resisting up to 15 kbars, for studying high-pressure burning of compact explosive material.

1. MEASUREMENT DEVICES

1.1. Description of the Closed Vessel

The closed vessel used in this study has a design similar to those presented by other authors (1,2).

The wiring diagram is shown in Fig. 1. The volume of the combustion chamber is 100 cm³. It consists of a hollow cylinder of 36 mm interior diameter and 140 mm exterior diameter. The gas tightness comes from metallic joints and viton o-ring.

One of the closing blocks comprises the ignition electrode and a duct for the pressure transducer. The second closing block has a valve permitting the gas to escape after the test. This set is placed in a hollow cylinder with walls 60 mm thick, 720 mm high, and 450 mm in exterior diameter. This cylinder permits pressurization and is also used as a safety device in case the composition chamber breaks.

1.2. Testing Procedure

The tests have been made on parallelopiped samples weighting about 40 to 55 g. The ignition is obtained by 1 g of fine black powder.
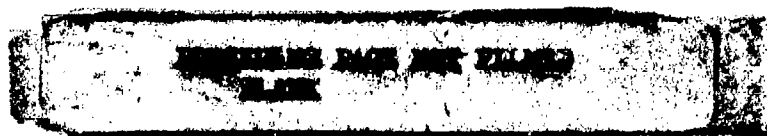
In case the combustion chamber breaks, the gas is expanded in the space situated between the chamber and the exterior cylinder.

We have used this possibility of fast expansion to execute extinction tests with a combustion chamber fragilized so as to obtain a breaking at fixed pressure.

1.3. Data Capture and Processing Equipment

The recording of pressure vs time is obtained with piezoelectric transducer KISTLER 6211, which permits measuring the pressure up to 8 250 bars. Electric charges are transmitted by an amplifier KISTLER 5001 to an analogue digital converter whose frequency was adjusted on 200 μs. The amplitude resolution is 1024 bits, and the memory records 16 000 values.

2. ANALYSIS

There are two kinds of analysis, qualitative and quantitative by the determination of the regression rate.
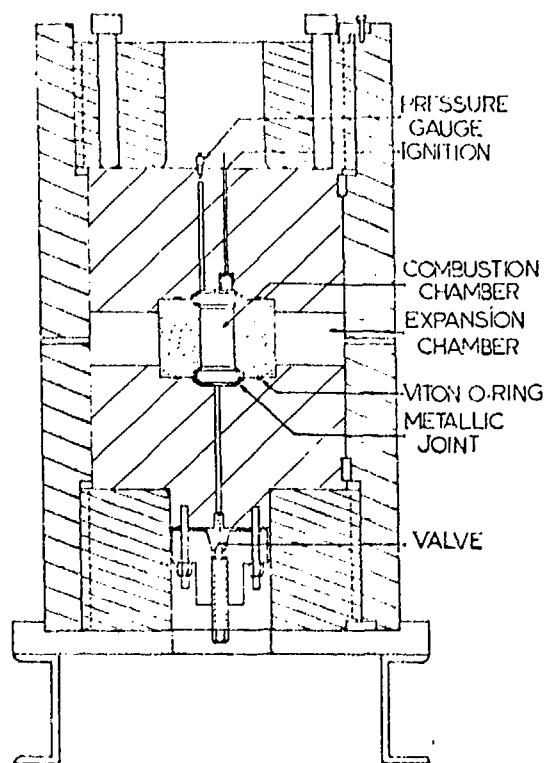
Fig. 1. *Schematic cross section of the high pressure vessel.*

2.1. Qualitative Analysis

The curve $P(t)$ permits some assumptions on the combustion of the product. The determination of the curve $dP/dt = F(P)$ simplifies the analysis. A sudden increasing of the derivate means a cracking of the product, a sudden change of the combustion running, or a probable detonation.

Another possibility is the extinction of the product during the combustion. The form of the remaining product after extinction permits analysis the combustion.

2.2. Regression Rate

We want to determine the law of burning rate of the product according to the pressure. For that we assume the combustion is linear and the ignition perfect (all the faces are ignited at the same time).

To obtain the regression rate we need $-dP/dt = F(P/Pm)$

— form function of the tested product

— state equation of combustion gas

2.2.1. $dP/dt = F(P/Pm)$

From the curve $P(t)$ recording, a program permits smoothing this function and obtaining the curve $P' = F(Pm)$ where Pm is the maximum pressure.

2.2.2. Form Function of the Tested Product

The assumption of linear combustion is expressed by writing that weight of burned material as a function of burned thickness.

In case of a parallelopiped we obtain

$$\frac{w}{w_o} = 1 - \frac{(a-e)(b-e)(c-e)}{abc}$$

w = weight of burned propellant

w_o = initial weight of propellant

a , b , c , · dimensions of the block

e   : total burned thickness

196

2.2.3. State Equation of Gas Combustion

The state equation generally used in combustion under high pressure is the Noble-Abel equation: $P(v - \eta) = f$ where η is the covolume of the combustion gas and f is the propellant force.

If we write this equation during the combustion in a closed vessel, we obtain.

$$P = \frac{fw}{c - w_0/\delta - w\left(\eta - \frac{1}{\delta}\right)}$$

P : pressure produced by the combustion

c : total volume of the combustion chamber

δ : specific weight of the product

The determination of the parameters f and η is made by performing some tests in closed vessels at different loading densities. We used the equation

$$Pm/\Delta = \eta\, Pm + f$$

Pm = maximum pressure

Δ = loading density

by representating Pm/Δ vs Pm and determining the equation of the straight line passing on these points we obtain f and η.

When we have these equations the calculation of regression rate is made by writing

$$v(P) = \frac{1}{2}\frac{de}{dt}$$

$$\frac{de}{dt} = \frac{de}{dw} \cdot \frac{dw}{dP} \cdot \frac{dP}{dt}$$

v(P) : regression rate function of pressure

t : time

3. EXPERIMENTAL RESULTS

3.1. Tested Products

For our study we made samples of several composite materials. All these formulations can detonate in small diameter.

Tested products are presented in Table 1; all the samples were controlled by X-rays before testing.

3.2. Results

Results are presented in Table 2. The first composition was tested in the form of little cubes; then we have adopted a new mode of operation using a unic grain.

On the Figs. 2 through 6 an example of curve P(t) and P'(P/Pm) is presented for each composition (test number A2, B1, C3, D2, E3).

We present the values of force and covolume obtained from tests on Table 3.

The curves of regression rate for the five compositions are shown in Fig. 7.

In Table 4 we supply the values of rate in millimeters per second for different values of pressure.

3.3. Extinction Tests

For the C composition we performed two extinction tests. For that purpose we used a fragmenting combustion chamber which was designed to break at a pre-determined pressure.

We recovered the sample after the test. In Fig. 8 we show the state of the composition chamber after breaking.

In Fig. 9 we compare samples before and after extinction of the test C4.

Test results are in Table 5.

DISCUSSION

Results show a good regularity of combustion; no violent phenomena does happen. The grain is not disaggregated; it resists to the sudden pressure build up. It had been previously found at some point that the combustion of HMX (or RDX) was able to propagate into the propellant to considerable depths and alter surface (4). However, the possibility of a disaggregation of the grain by a cracking combustion has not been observed in our tests. Extinction tests, nevertheless, show that the grain at the end of the

197

combustion has an actual surface, slightly larger than the parallelopiped geometric one.

A steady-state burning law can be used to describe the curve v(P),

$$v(P) = aP^n .$$

Corresponding parameters are given in Table 6 and curves in log-log presentation are given in Fig. 10 in the 1 000-10 000 bars area.

The exponent n is almost the same for compositions A and B. This was expected since both compositions were similar. Difference in values of regression rate would need more experimentation (the sizes of samples are not the same, and dP/dt are very different).

Composition E (CMDB) is quite different from the four other ones; its pressure exponent decreases regularly.

Comparison With Previous Results

In Fig. 11, we compare v(P) obtained on high explosives with Wachtell's results.

For the latter, the results obtained in strandburner are represented by continuous lines. Tests in closed vessel had shown that tolite and hexolite, above 500 bars, presented an apparent increase in burning rate consistent with an increase in burning surface (due to crazing or cracking); cracking seemed to be reproducible; the results of the closed vessel tests are represented by the dashed lines. Corresponding values of a and n for the five explosives are given in Table 7.

TABLE 1
Explosive Formulation and Physical Data

Product	Composition	Density	Failure Diameter of Detonation	Size and Form of the Grain
A High explosive	RDX 86% Binder 14% (polybutadiene)	1,61	6 mm	Small cubes of 10 mm Number of cubes suitable for required loading density
B High explosive	RDX 84% Binder 16% (polybutadiene)	1,59	8 mm	1 parallelopiped grain 24 mm × 24 mm Length suitable for loading density
C High explosive	HMX 90% Binder 10% (polybutadiene)	1,73	6 mm	1 parallelopiped grain 24 mm × 24 mm Length suitable for loading density
D Composite propellant with HMX	HMX 24% Binder 10% (polybutadiene)	1,82	30 mm	1 parallelopiped grain 22 mm × 22 mm Length suitable for loading density
E Composite modified double base	Alu-AP 70% Double base 30% binder	1,80	30 mm	1 parallelopiped grain 24 mm × 24 mm Length suitable for loading density
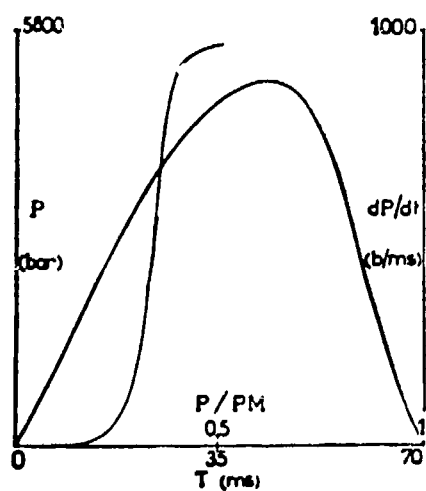
Fig. 2. Test A2.
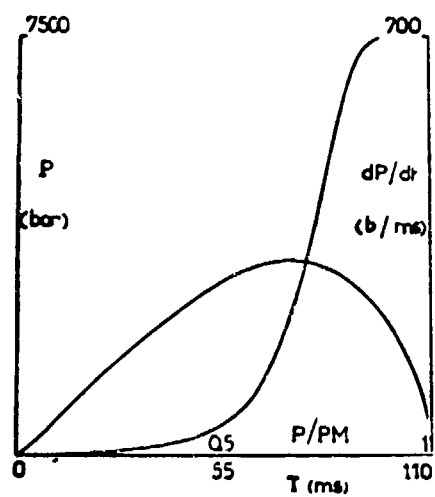
Fig. 3. Test B1.
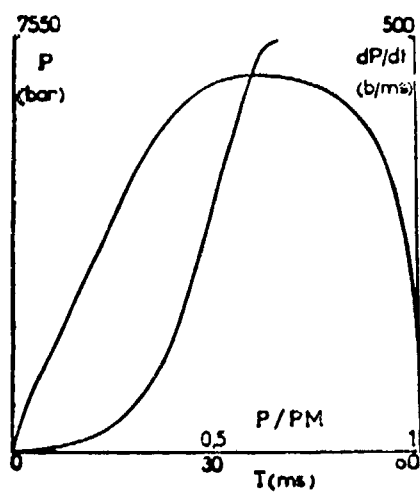
Fig. 4. Test C3.
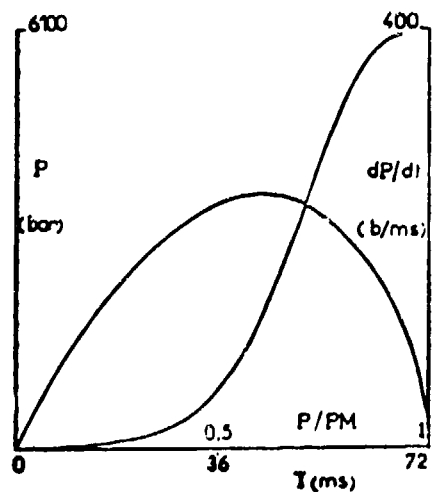
Fig. 5. Test D2.
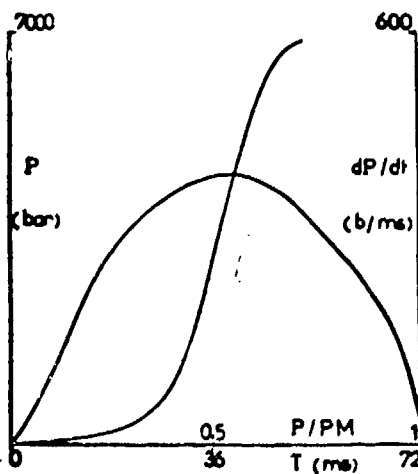
Fig. 6. Test E3.

TABLE 2
Bursting Pressure

Products	Test Number	Volume of Combustion Chamber (cm^3)	Mass of Product (g)	Loading Density (g/cm^3)	P_{max} (bar)	P'_{max} (bar/ms)	Observations
A	A1	100	33	0,33	3540		Regular burning
	A2	100	47	0,47	5660	875	Regular burning
B	B1	100	55	0,55	7430	325	Regular burning
	B2	93,5	40	0,43	4915		Regular burning
	B3	93,5	45,1	0,48	6280		Regular burning
	B4	93,5	50,1	0,54	6980		Regular burning
	B5	93,5	45,1	0,48	5900		Regular burning
	B6	93,5	39,9	0,43	5100		Regular burning
C	C1	100	45,1	0,45	5910		Regular burning
	C2	100	50,1	0,50	6930		Regular burning
	C3	93,5	49,9	0,53	7500	450	Regular burning
	C4	100	40	0,40	4670*		Regular burning
	C5	94	45	0,48	5790*		Regular burning
D	D1	100	40	0,40	4320		Regular burning
	D2	100	50,2	0,50	6040	240	Regular burning
E	E1	93,5	39,6	0,42	4220		Regular burning
	E2	93,5	49,8	0,53	6000		Regular burning
	E3	93,5	55	0,59	6850	390	Regular burning

*Tests with extinction

TABLE 3
Force and Covolume

Products	Force (MJ/kg)	Covolume (cm^3/g)
A	0,85	0,627
B	0,823	0,702
C	0,955	0,605
D	0,77	0,715
E	0,726	0,639

TABLE 4
Regression Rates

Products	1 000 Bars	2 000 Bars	3 000 Bars	4 000 Bars	5 000 Bars	6 000 Bars
	Regression Rates en mm/s					
A	110	250	430			
B	70	150	245	340	450	540
C	110	220	360	465	530	730
D	100	190	275	350	420	475
E	140	290	400	485	530	
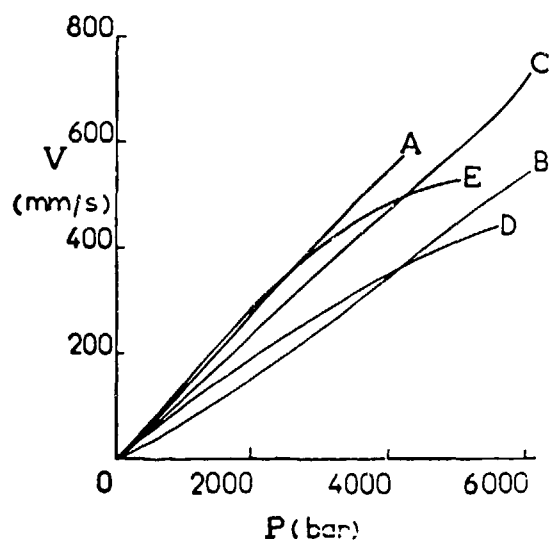
Fig. 7. *Regression rate in closed vessel.*

Fig. 8. *Combustion chamber after extinction.*
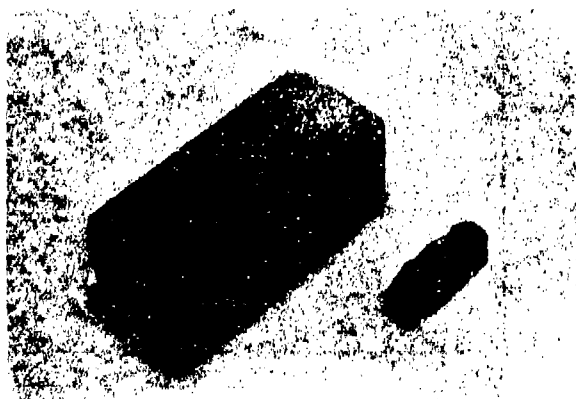
Fig. 9. *Test C4. Explosive sample before burning and after extinction.*

TABLE 5
Extinction Tests

	C4 Test	C5 Test
Initial size of grain in mm	24 × 24 × 39,9	24 × 24 × 44,8
Size after extinction in mm	6,5 × 6,5 × 21	3 × 3 × 26
Burned thickness in mm	17,5; 17,5; 18,9	21; 21; 18,8
Bursting pressure in bars	4670	5790
Post-fire observation	(See Fig. 9) parallelopiped size is very clear and visible. Some little pits 2 mm in diameter and 1 mm deep are visible.	Parallelopiped size is preserved; However one pit makes a hole of 2 mm
Theoretical pressure corresponding to burning thickness	e p 17,5 4830 17,90 4920	e p 21 6380 18,8 6260
Average	4870	6320
Theoretical burned thickness corresponding to bursting	15,7	14,80

201

	TABLE 6				

<div align="center">

TABLE 6
Parameters a and n

</div>

	a	n	
A	0,036	1,17	
B	0,019	1,18	
C	0,065	1,07	
D	0,20	0,90	
	0,14	1,0	(from 1 000 to 2 000 bars)
E	0,72	0,79	(from 2 000 to 3 500 bars)
	20,8	0,38	(from 3 500 to 5 000 bars)

<div align="center">

TABLE 7
Parameters a and n for High Explosives

</div>

Products	a	n	
A	0,036	1,17	
B	0,19	1,18	
C	0,065	1,07	
Tolite	0,027	1,11	x
Hexolite	0,075	1,07	x

(x Strandburner <1 500 bars)
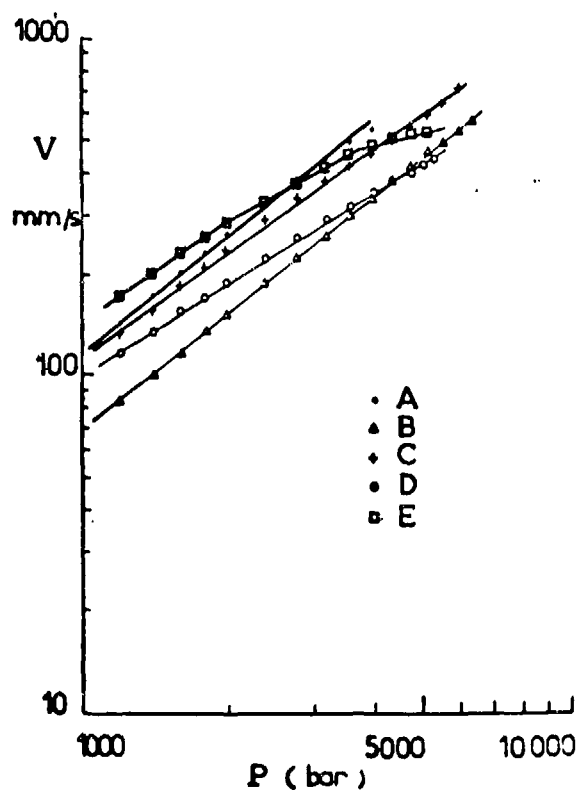
Fig. 10. Regression rate data in log/log presentation.
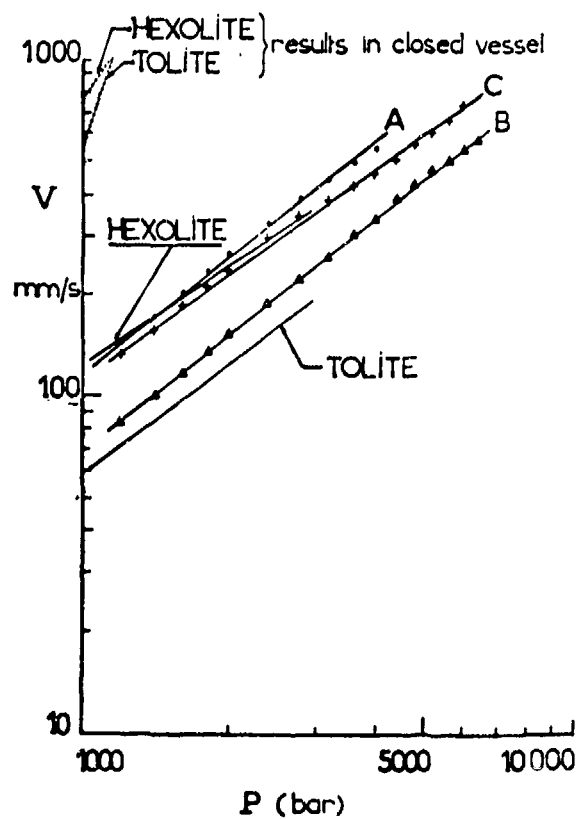
Fig. 11. Regression rate curves on high explosives.

Ranking of Products

In the DDT process, the 1 000 to 10 000 bars area is in the low-pressure part. However, it is useful to know if a rapid pressure buildup in this area is possible. We use these experiments first to obtain information on mechanical behavior of grains of approximately 1 in. × 1 in. × 2 in. Then, thanks to parameters a, n, f, and η, we are able to obtain actual information on a pressure buildup in a closed vessel.

If we schematize an experimental DDT device such as this one (Fig. 12), we can calculate (with a slight extrapolation of regression data)

t = time to reach a pressure of 10 000 bars

$$\frac{dP}{dt} = \text{at } 10\,000 \text{ bars}$$

v = regression rate at 10 000 bars.

We have assumed that the combustion is linear and starts with an initial pressure of 1 000 bars.

Values are given in Table 8.
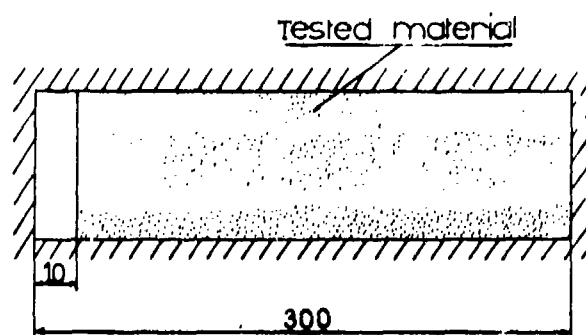
Fig. 12. Experimental DDT device.

ACKNOWLEDGMENTS

The authors would like to thank MM. Perut, Nicolas and Rohmer for fruitful discussion and members of formulation and combustion laboratories of "Centre de Recherches du Bouchet" for their contribution in fabrication and measurements of explosive samples.

TABLE 8
Provision of Situation at 10 000 Bars

Products	Cracking Pressure in Closed Bomb	t (ms)	$\frac{dP}{dt}$ (bar/ms)	v (mm/s)
A		11,9	2 400	1 750
B		20,6	1 440	1 000
C		11,9	2 100	1 230
D		16,2	1 590	800
Hexolite	500			
Tolite	500			

REFERENCES

1. S. Wachtell and L. Shulman, "Development and use of ultra-high pressure test vessel for characterizing propellants and explosives" in "Prevention of and protection against accidental explosion of munitions, fuels and other hazardous mixtures"—New York Academy of Sciences 1968.

2. M. Nicolas, "Study of the behavior of propellant combustion products at high pressure," International Symposium on Gun Propellants—Picatinny Arsenal—Oct. 1973.

3. S. Wachtell and C. E. McKnight, "A method for determination of detonability of propellants and explosives"—Third Symp. on Det'n. P 635-658.

4. N. S. Cohen and C. F. Price, "Combustion of nitramine propellants," 1975—AD-A-004-815-AIAA Paper for the 1975 Aerospace Sciences meeting.

203

EFFECTS OF CONFINEMENT AND INITIAL PRESSURE ON THE DEFLAGRATION OF SOME HIGH EXPLOSIVES

Ola Listh
Swedish National Defence Research Institute
Stockholm 80, Sweden

Deflagration of various explosives has been studied at varying confinements and initial pressures. Deflagration was initiated by discharging a capacitor through a bridgewire in contact with the explosive. The apparent pressure rise in the sample was recorded, and the capacitor potential necessary to cause a self-sustained reaction could thus be determined. With a 10-μF capacitor, voltages in the range of 200-800 V were needed to cause self-sustained reactions in cast and pressed Comp.B and in pressed TNT. The critical pressure rise in the explosive was normally of the order of a few MPa, occasionally up to 20 MPa. Ignition delay times ranged from a few hundred microseconds to some milliseconds. Increasing confinement and increasing initial pressure favored the development of self-sustained reactions. Pressed explosives of low density were easier to initiate than cast explosives, and Comp.B was easier to initiate than TNT.

INTRODUCTION

Deflagration in confined explosives is an important source of hazard, as it is the normal reaction of a secondary explosive accidentally ignited by non-shock stimulus or by weak shocks. This process may in a later stage accelerate to a detonation. A deflagration in an explosive is often considered less dangerous than a detonation. However, considerable damage can be caused by a deflagration, especially if the explosive is confined so that the pressure is not relieved until a large part of the explosive has been consumed. Some prematures, for example, have been deflagrations initiated by imperfections in the explosive charge or in the shell.

The purpose of this work was to study how confinement and initial pressure affect the possibility of starting propagating deflagrations in confined explosives. Explosives normally used in artillery ammunition, i.e. Comp.B and TNT, were selected for this study. Pressed and cast charges have been studied.

The early formation of cracks in the explosive sample could be studied in cases of non-sustained reactions.

EXPERIMENTAL

The experimental setup consists of a steel yoke, in which the confined charge is tightly mounted. The charge is initiated by discharging a capacitor through a bridgewire in the center of the charge. The reaction of the explosive is transmitted as force to the yoke, and the strain of the yoke is recorded on an oscilloscope. Confinement, initial pressure in the charge, and capacitor voltage can be varied.

Steel yoke—The yoke consists of three parts, the main body and two charge holders (Fig. 1). The yoke is made from a rigid steel cylinder, 240 mm high and 250 mm in diameter. A cylindrical space, 116 mm high and 100 mm in diameter, is made along the cylinder axis in the center of the body. A 116 mm wide hole is drilled perpendicularly to the cylinder axis and through the cylinder center.

The lower charge holder rests upon a plane horizontal surface in the yoke. In the center of the holder there is a 10 mm deep and 20 mm wide boring to fit the end of the charge. In the bottom of the boring a hole is drilled for the leads to the bridgewire.

The upper charge holder is made as a big screw and has the same boring for the charge end as the lower holder. A 5 mm wide hole is drilled axially through this holder to a nipple at the top, which is connected to a tube of pressurized nitrogen. Thus a high initial pressure (presently up to 25 MPa) in the charge can be used. A thin teflon washer is used as a seal between the charge and the upper holder.

Charges—Confined charges were made by filling steel tubes with an explosive and sealing both ends with copper plugs. The charge was initiated by a bridgewire. Figure 2 shows a section of such a charge.

The steel tubes had a length of 80 mm and an outer diameter of 20 mm. The inner diameter was 14, 15, 16, or 17 mm, implying wall thicknesses of 1.5 to 3.0 mm. The tubes used were made from cold-drawn steel (SIS No. 1232) containing 0.18% carbon. The tubes with 1.5 mm wall thickness are supposed to stand an internal pressure of 30 MPa, and

tubes with 3.0 mm walls 60 MPa. The inside of the tubes was sand-blasted to improve adherence of the explosive to the walls.

The tube ends were sealed with 15 mm long copper plugs (SIS No. 5010). One of the plugs had a gas inlet, and the other had an inlet for the leads to the bridgewire. The end plugs were made to fit accurately in the tube. To make a good seal the plugs were glued into the tube with Araldite. When the explosive is initiated the glue seal breaks, and the end plugs act as pistons that transmit the pressure caused by the deflagration to the steel yoke.

The bridgewire used was the same as in commercial electric detonators and had a resistance of approximately 0.18 ohm. The bridgewire, which was about 1 mm long and had a diameter of 0.1 mm, was for cast explosives placed in the middle of the charge. For pressed explosives the bridgewire had to be placed as near the bottom as possible to allow uniform density of the charge when pressing.

Circuitry—The firing circuit is a simple capacitor discharge circuit with a mercury switch (Fig. 3). The capacitance is 10 microfarads ($\pm$ 10%), the bridgewire resistance is 0.18 ohm, and the circuit resistance is 0.18 ohm. The nominal time constant is thus about 4 microseconds. The circuit inductance has not been measured but is believed to be some microhenries. The energy delivered by the capacitor is assumed to be equal to 0.5 CV^2, where C is the capacitance and V is a variable voltage. Figure 4 shows the voltage over the bridgewire as a function of time.

Force recordings—The force exerted on the yoke by the copper plugs was measured by a crystal strain gage glued to the yoke (Fig. 1). The strain-gage signal was amplified and recorded on both channels of a Tektronix dual-beam oscilloscope. The sensitivity ratio of the two channels was 100:1, so that both the
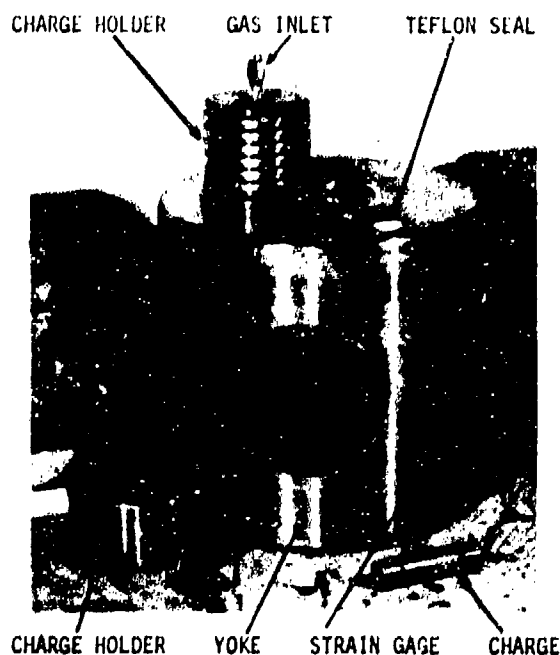
Fig. 1. Steel yoke.
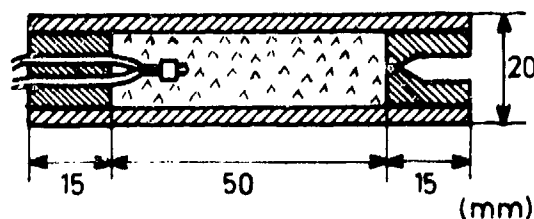
Fig. 2. Section of a confined charge.

gross reaction and the fine structure could be seen. The oscilloscope was triggered by the pulse from the discharging capacitor. The strain gage was statically and dynamically calibrated to a crystal force gage. Force was then converted to apparent pressure in the steel tube by using the known area of the end plugs.

RESULTS

Explosives studied were TNT and Comp.B, cast and pressed. Cast Comp.B charges were allowed to solidify fast, so that a fine-crystalline structure was formed. TNT charges were allowed to solidify very slowly and formed coarse-crystalline structures.

Pressed charges were compacted in the tube (with the bridgewire mounted) in three steps. TNT charges were pressed of flaked TNT. Some Comp.B charges were pressed of the usual fraction 6/60, and some were pressed of a special fine-grained fraction with the following grain-size distribution:

> 40 mesh	0%
40-60	10
60-100	25
100-140	30
140-200	10
< 200	25

Experiments were performed on cast Comp.B at normal atmospheric pressure to study the role of the confinement. To study the effect of initial pressure on the propagation of the deflagration, charges of the same sort were also fired at pressures of 5 MPa and 10 MPa in a nitrogen atmosphere. Cast and pressed charges with different grain/crystal sizes were studied to find out their ability to support reactions in confined charges. Table 1 shows the minimum capacitor voltage that caused self-sustained reactions and the maximum capacitor voltage that did not cause self-sustained reactions for confined Comp.B charges. Table 2 shows the same parameters for confined TNT charges.

Figures 5-11 show photographs of some charges that exploded and sections of charges that did not.

The energy delivered to the bridgewire causes some pressure rise in the explosive probably due to beginning deflagration. If the energy input is too low the deflagration fades out, and the pressure decreases. From the fine-structure curve of the oscilloscope record we can determine at what apparent pressure the deflagration is self-sustained. Figures 12-14 show force recordings for some charges.

The critical apparent pressure rise for cast Comp.B usually is of the order of 1-7 MPa when charges are fired at normal atmospheric pressure. When charges are fired in nitrogen atmosphere at a pressure of 5 MPa the apparent pressure rise can sometimes reach a value of 20 MPa and still cause no self-sustained reaction.

C ·CAPACITOR - 10 MICROFARAD
S - MERCURY SWITCH
L - CIRCUIT INDUCTANCE
R_1 -CIRCUIT RESISTANCE - 0.18 OHM
R_2 - BRIDGE WIRE - 0.18 OHM

Fig. 3. Capacitor discharging circuit.
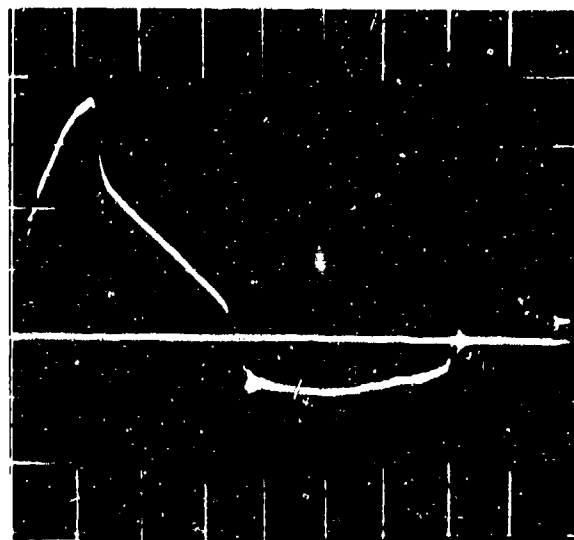
Fig. 4. Voltage pulse shape over the bridgewire when capacitor discharged at a potential of 500 V. Scale: 40 V/div; Sweep: 5 µs/div.

TABLE 1

Critical Capacitor Voltage* for Confined Comp.B Charges

Physical State of the Explosive	Tube Wall Thickness (mm)	Initial Pressure (MPa)	Minimum Voltage for Propagation (V)	Maximum Voltage for Fade Out (V)	No. of Shots
Cast	1.5	0.1	800	800	7
	2.0		488	600	6
	2.5		577	565	8
	3.0		580	650	9
	1.5	5	600	500	3
	2.0		450	430	3
	2.5		500	520	5
	3.0		450	445	4
	2.0	10	400	300	3
	2.5		334	325	3
Pressed at 50 MPa, fine-grained	1.5		285	250	5
	3.0		210	200	5
Pressed at 90 MPa, fine-grained	1.5		310	285	2
Pressed at 100 MPa, fine-grained	3.0		256	250	5
Pressed at 100 MPa, fraction 6/60	2.0	0.1	300	250	5

*With 10 μF capacitor

TABLE 2

Critical Capacitor Voltage* for Confined TNT Charges

Physical State of the Explosive	Tube Wall Thickness (mm)	Initial Pressure (MPa)	Minimum Voltage for Propagation (V)	Maximum Voltage for Fade Out (V)	No. of Shots
Flaked, pressed at 50 MPa	1.5	10	603	625	3
	3.0	10	560	530	8
Flaked, pressed at 100 MPa	3.0	10	570	568	6
	2.0	0.1	—	> 600	4
Cast, coarse-crystalline	3.0	0.1	—	> 1000	3
	3.0	10	—	> 1000	3

*With 10 μF capacitor

Firing voltage: 488 V. Wall thickness: 2.0 mm.   Firing voltage: 565 V. Wall thickness: 2.5 mm.

Fig. 5. Examples of cast Comp.B charges after firing at atmospheric pressure.
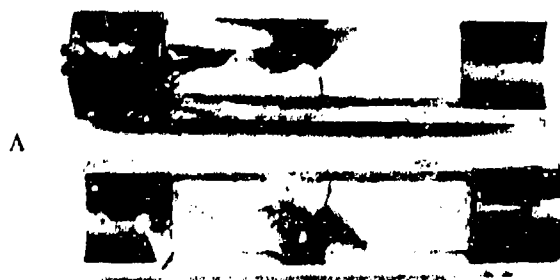
Firing voltage: 520 V. Wall thickness: 2.5 mm.   Firing voltage: 448 V. Wall thickness: 1.5 mm.

Fig. 6. Examples of cast Comp.B charges after firing at 5 MPa initial pressure.

Firing voltage: 350 V. Wall thickness: 2.5 mm.   Firing voltage: 325 V. Wall thickness: 2.5 mm.
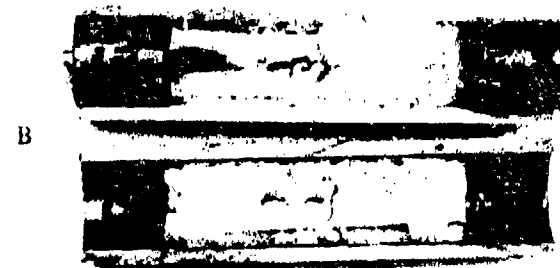
Fig. 7. Examples of cast Comp.B charges after firing at 10 MPa initial pressure.

208

Firing voltage: 210 V. Wall thickness: 3.0 mm.   Firing voltage: 285 V. Wall thickness: 1.5 mm.

Fig. 8. Examples of Comp.B charges, pressed at 50 MPa, after firing at 10 MPa initial pressure.
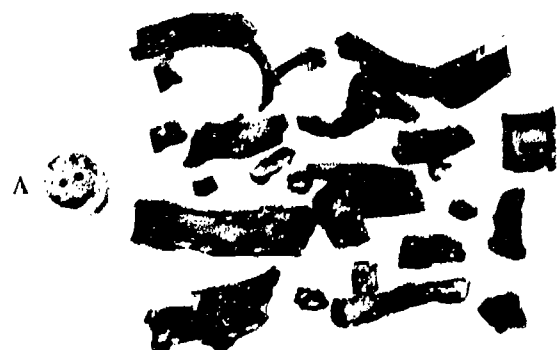
Firing voltage: 256 V. Wall thickness: 3.0 mm.   Firing voltage: 285 V. Wall thickness: 1.5 mm.
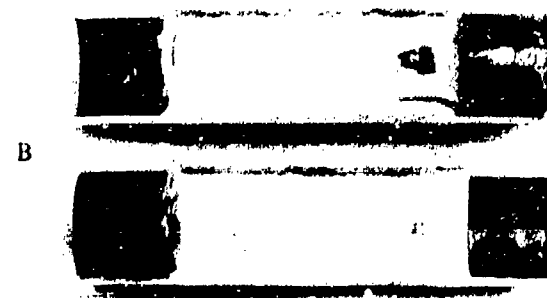
Fig. 9. Examples of Comp.B charges, pressed at 100 MPa (A) and 90 MPa (B), after firing at 10 MPa initial pressure.

Firing voltage: 300 V. Wall thickness: 2.0 mm.

Fig. 10. Comp.B charge, pressed of fraction 6/60 at 100 MPa, after firing at atmospheric pressure.
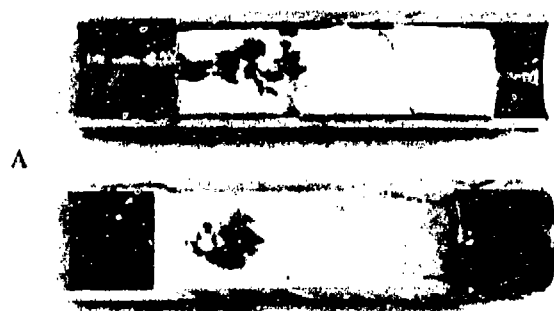
A

Flaked, pressed at 100 MPa.
Wall thickness: 2.0 mm. Firing voltage: 600 V.

B

Flaked, pressed at 50 MPa.
Wall thickness: 3.0 mm. Firing voltage: 900 V.

C

Cast, coarse-crystalline.
Wall thickness: 3.0 mm. Firing voltage: 850 V.

Fig. 11. Various TNT charges after firing at atmospheric pressure (A, C) and at 10 MPa (B).
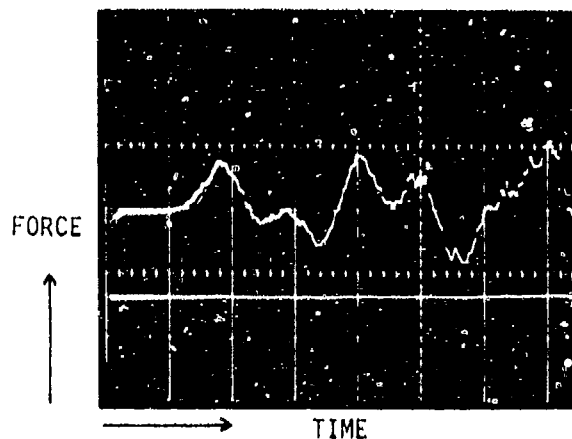
A. 3.0 mm confinement, 0.1 MPa initial pressure,
fired at 573 V. Scales: upper = 8.1 MPa/div,
lower = 810 MPa/div, time = 100 μs/div.
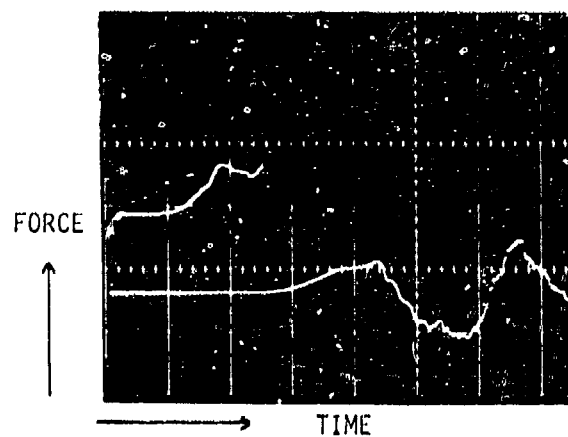
B. 2.0 mm confinement, 5 MPa initial pressure, fired
at 450 V. Scales: upper = 6.2 MPa/div, lower =
620 MPa/div, time = 100 μs/div.

Fig. 12. Force recordings for exploded (B) and non-exploded (A) cast Comp.B charges.
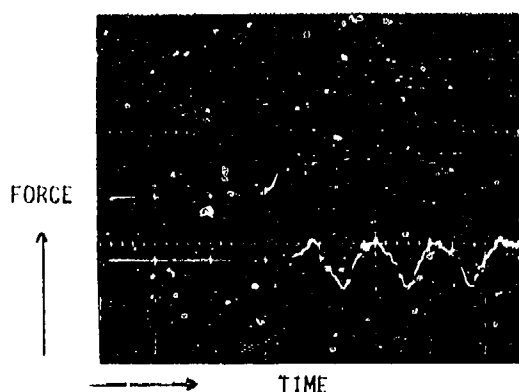
Fig. 13. Force recording for exploded pressed (50 MPa) Comp.B charge. Confinement 1.5 mm. Initial pressure 10 MPa, fired at 300 V. Scales: upper = 5.5 MPa/div, lower = 550 MPa/div, time = 200 μs/div.
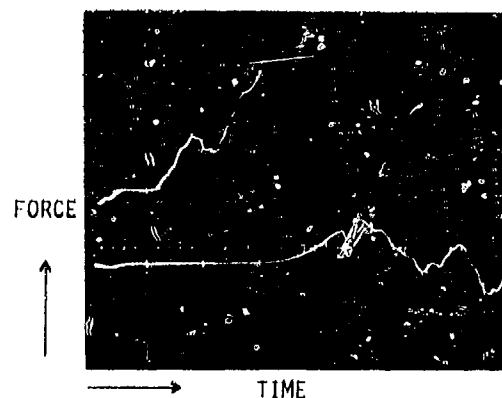
Fig. 14. Force recording for exploded pressed TNT charge. Confinement 3.0 mm. Initial pressure 10 MPa, fired at 900 V. Scales: upper = 8.1 MPa/div, lower = 810 MPa/div, time = 100 μs/div.

For pressed Comp.B the critical apparent pressure rise is too small to be recorded, whereas for pressed flaked TNT it can amount up to 15 MPa. For cast coarse-crystalline TNT the apparent pressure rise is about 3 MPa when fired at 1000 V at atmospheric pressure.

The critical apparent pressure rise tends to increase with increasing confinement and increasing initial pressure. The critical apparent pressure rise is much higher for cast charges than for pressed charges, at least for Comp.B. Table 3 gives some examples of apparent pressure rise in various charges.

The delay time from discharging the capacitor to a noticeable rise in the fine-structure curve of the force recordings is usually of the order of 80-200 microseconds for Comp.B charges fired at 400 V or more. For pressed Comp.B, which needs only 250-300 V for initiation, the delay is from 100 microseconds to 2.5 milliseconds. For pressed Comp.B charges which needs only about 200 V for initiation, the delay can be as long as 8 milliseconds. For pressed TNT, which needs about 600 V for initiation, the delay is from 100 microseconds to 4 milliseconds.

If the deflagration propagates, the time from the first indication of a reaction start until the reaction is self-sustained can be estimated by comparing the time lag between the fine-structure curve and the gross-structure curve. The gross-structure curve has a sensitivity that gives no reading unless the reaction is self-sustained. Time differences measured that way, e.g.

TABLE 3

Examples of Apparent Pressure Rise in Some Confined Charges

Explosive	Con-fine-ment (mm)	Initial Pres-sure (MPa)	Apparent Pressure Rise (MPa)
Comp.B. Cast	2.0	0.1	3.7
	2.5		2.8
	2.5		6.0
	3.0		6.5
	1.5	5	3.8
	2.0		4.4
	2.0		5.0
	2.5		7.7
	3.0		16.2
TNT press. 50 MPa	1.5	10	7.7
	3.0		13.8
	3.0		14.5
TNT press. 100 MPa	3.0		8.0
	3.0		16.0
TNT, cast coarse-crystalline	3.0	0.1	3.2

211

from Figures 12-14, give values of 100 - 300 microseconds for cast Comp.B, 50-150 microseconds for pressed Comp.B, and 200-3000 microseconds for pressed TNT. Figure 15 shows an exploding cast Comp.B charge with 2.0 mm confinement fired at atmospheric pressure. The time elapsed to sudden tube deformation (280 microsec.) in the figure is consistent with the time elapsed from ignition pulse to apparent pressure rise in the corresponding gross-structure curve.

DISCUSSION

The energy in the capacitor is taken as $0.5 \, CV^2$, where C is the capacitance and V is the capacitor potential. However, all this energy is not delivered to the bridgewire, because of the circuit inductance and the circuit resistance. As can be seen from Figure 4, the peak voltage over the bridgewire is only about 30% of the capacitor potential. Several measurements confirm that the peak voltage over the bridgewire is only 25-30% of the capacitor potential. Thus the energy stored in the capacitor cannot be taken as the quantity of energy delivered to the explosive sample. To adequately determine the energy input, it would be necessary to simultaneously measure the voltage and the current through the bridgewire. The nominal time constant of 4 microseconds should be compared with the pulse duration in Figure 4, which is about 20 microseconds.

The ignition delay time, estimated from the force recordings as the time interval from discharge of the capacitor to apparent pressure rise, was in the range of from 80 microseconds to a few milliseconds (Figs. 12-14). However, the time taken for a disturbance in the middle of the charge to travel through the charge, the copper plugs and the yoke to the strain gage is estimated to be of the order of 30-40 microseconds. That means that the shortest delay times (for pressed Comp.B) should be only some ten microseconds.

From Table 1 we can evaluate the effect of confinement on the capacitor voltages needed to start propagating deflagrations in cast Comp.B. A confinement of 1.5 mm steel seems to be unfavorable, whereas a wall thickness of more than 2.0 mm does not appreciably lower the critical capacitor voltage. This trend is the same whether atmospheric pressure or elevated initial pressure is used.

We also conclude from Table 1 that increasing the initial pressure lowers the necessary capacitor voltage for the development of propagating reactions. This is expected, because deflagrations increase their reaction rate with increasing pressure.

Table 1 also shows that it is easier to start a propagating reaction in pressed Comp.B than in cast Comp. B, at least at atmospheric pressure. The density of the charge is obviously an important parameter, which affects the possibility of starting propagating deflagrations in confined charges. Table 1 shows that a charge pressed at 50 MPa develops propagating reactions more easily than a charge pressed at 90 or 100 MPa.

Table 2 shows that pressed TNT needs higher voltages to develop propagating reactions than does pressed fine-grained Comp.B. Like pressed Comp.B, pressed TNT develops propagating reactions more easily when pressed at lower compaction pressures. TNT shows the same pattern regarding initial pressure and confinement as Comp.B. It is obvious from Table 2 that cast coarse-crystalline TNT is very hard to initiate to propagating deflagration with a hot bridgewire.

Charges that did not burst were cut and examined. Some samples are shown in Figs. 5-11. Cast Comp.B charges usually showed numerous and far-reaching cracks emanating from the bridgewire. The cracks often reached out to the tube wall (Fig. 6). It could

| t = 0 | 40 | 80 | 120 | 160 | 200 | 240 | 280 | 320 | 360 |
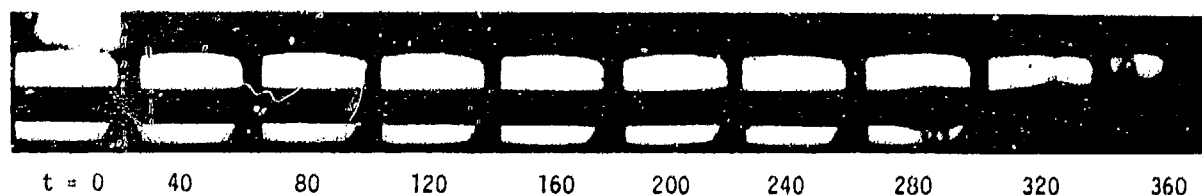
Fig. 15. High-speed photographs of exploding charge (cast Comp.B), 40 μs between each frame.

212

be seen that burning had taken place along these cracks, because soot was deposited along them. Pressed Comp. B charges that did not burst showed no signs of any reaction having taken place (Fig. 9B). On the contrary, pressed TNT charges that did not burst showed local but heavy reactions around the bridge-wire (Fig. 11A). Cast TNT charges that were cut showed signs of heavy reactions in a large area around the bridgewire (Fig. 11C). Figure 11C also shows that the charge was destroyed to form a loose pack of long, needle-shaped TNT crystals.

The results of the examination of cut charges support the theory that flame spreading along cracks and between grains of explosive is an important mechanism in the deflagration of confined charges.

Because of the greater surface area of pressed charges it should thus be easier to start propagating reactions in pressed explosives than in cast explosives. The results found are in agreement with this assumption. It could also explain why cast, coarse-crystalline TNT is so hard to initiate to propagating reactions. This theory is further supported by the fact that increasing initial pressure favors the development of self-sustained reactions. It also explains why Comp.B, which contains small and more heat-sensitive RDX crystals, more easily develops propagating deflagrations than does TNT.

The incidence of explosive events (Figs. 5A, 7A, 8, 9A, 10, 11B) shows that the reactions differ widely in strength. For cast Comp.B charges the steel tube broke into only a few large pieces, regardless of confinement and initial pressure (Figs. 5A, 7A). Pressed Comp.B charges showed the same pattern when fired at atmospheric pressure and poor confinement (Fig. 10). For pressed Comp.B, heavily confined and fired at 10 MPa initial pressure, the steel tube split into numerous fragments (Figs. 8A, 9A). For pressed Comp.B charges with poor confinement the tube just split open (Fig. 8B) or broke into large pieces.

For flaked, pressed TNT charges the tube only split open and gave no fragments regardless of confinement (Fig. 11B). Sometimes a good part of the finement (Fig. 11B). Sometimes a good part of the

explosive column remained in the tube, which did not burst but only got barrel-shaped. On the contrary, for pressed Comp.B the tube always burst, but often large amounts of explosive were thrown out as a fine powder. Figures 8A and 9A show some signs considered as typical for detonations, like small and numerous fragments, wall-thickness reduction, and shear fractures at an angle of 45 degrees to the main stress directions. However, in all those shots some unreacted explosive was recovered, either on the bottom copper plug or on the inside of the yoke.

It is possible that the deflagration in pressed Comp.B has built up to a detonation, but this hypothesis has not been further examined.

CONCLUSIONS

Tests by this technique show that increasing confinement and increasing initial pressure favors the development of self-sustained deflagrations. Pressed explosives of low density more easily develop such reactions than do cast explosives. Coarse-crystalline explosives are harder to initiate than fine-crystalline ones. Comp.B more easily develops self-sustained reactions than does TNT.

Whether the initiated deflagration will fade out or propagate is determined at very low apparent pressures (a few MPa) in the explosive sample. If the deflagration propagates, the apparent pressure rises very slowly up to a critical value, and then a very steep pressure rise occurs. From the examination of cut charges it is believed that the deflagration proceeds very rapidly along cracks, which could be formed at the velocity of sound by stresses in the explosive sample.

The results obtained can be used for the assessment of hazards related to violent deflagration in various combinations of explosives, confinements, and initial pressures, e.g. for classification purposes as well as in several important practical applications, and also as a basis for safer construction of ammunition.

THE THERMAL DECOMPOSITION AND REACTION OF CONFINED EXPLOSIVES*

E. Catalano, R. McGuire, E. Lee,
E. Wrenn, D. Ornellas and J. Walton
Lawrence Livermore Laboratory
University of California
Livermore, California 94550

This paper describes some new experiments designed to accurately determine the time interval required to produce a reactive event in confined explosives subjected to temperatures which will cause decomposition. Geometry and boundary conditions were both well defined so that these experiments on the rapid thermal decomposition of HE are amenable to predictive modelling.

Experiments have been carried out on TNT, TATB and on two plastic-bonded HMX-based high explosives, LX-04 and LX-10. When the results of these experiments are plotted as the logarithm of the time to explosion versus $1/T$ K (Arrhenius plot), the curves produced are remarkably linear. This is in contradiction to the results obtained by an iterative solution of the Laplace equation for a system with a first order rate heat source. Such calculations produce plots which display considerable curvature. The experiments have also shown that the time to explosion is strongly influenced by the void volume in the containment vessel.

We have compared the results of the experiments with calculations based on the heat flow equations coupled with first-order models of chemical decomposition. The comparisons demonstrate the need for a more realistic reaction model.

INTRODUCTION

A number of experimental tests have been developed to measure "time to explosion". (1,2,3.) We will describe here our effort to develop a new experimental system which, though relatively simple and inexpensive, is well defined and controlled so as to be amenable to computer modelling. The objective of using the generated experimental data directly, in order to define reactive source terms in a heat flow computer code, dictated that the sample be one dimensional so as to simplify geometric effects in the heat flow calculation. We will present here data gathered on TNT, TATB and two HMX-based plastic

bonded explosives, LX-10 and LX-04. Finally, we will briefly discuss our progress in the modelling of the TNT system.

EXPERIMENTAL

The central element of the experimental design is a set of cylindrical aluminum anvils which are preheated to the desired operating temperature. An anvil face is shown in Fig. 1. The anvils are 7.62 cm. in diameter and 5.08 cm. high. A hemispherical cavity is machined into the face of each anvil in order to accept spherical samples. Recessed knife edges are likewise machined into each face. These knife edges close on a copper sealing ring during the experiment. Sample sizes, for reasons of safety, have been limited in the laboratory to 1.27 cm. in diameter. This is

Fig. 1. Detail of anvil face.

Fig. 2. Experimental apparatus showing vacuum chuck.

approximately 2.2 grams of explosive. The anvils are electrically heated. The temperature is controlled to ± 0.2 K by thermocouples.

The instrument, without ancillary equipment, is shown in Fig. 2. When the operating temperature is attained, the sample is placed in a vacuum chuck. The remainder of the experiment is performed remotely. The vacuum chuck emplaces the sample in the cavity in the face of the lower anvil. The upper anvil is then driven down by a preloaded pressure accumulator, sealing the sample cavity. This process requires approximately 0.6 seconds. Both the closing pressure and the confinement pressure, i.e., the pressure maintained on the anvils during the experiment, are determined by the operator and can be varied through the hydraulic system. Experiments performed to determine the integrity of the seal have shown that there is no leak of the decomposition product gases prior to the violent rupture of the seal which marks the end point of the experiment. Experiments have also shown that if the closing pressure is not sufficiently high, the flats of the anvils between the sample cavity and the sealing ring do not make metal to metal contact, even though sealing is accomplished, leaving a small void space as shown in Fig. 3. The significance of this void space will be discussed below. The principal measurement is the time to

Fig. 3. Detail showing (a) void space caused by low pressure closure of anvils and (b) high pressure closure.

215

"explosion" which is measured from the closure of the anvils. The event which marks the endpoint is sensed by a sensitive microphone and by an accelerometer which is mounted on the anvils.

This unique and rather simple system thus provides a spherically symmetric, well characterized, nearly isothermal boundary; and a well defined, variable confinement. The purpose in developing this experimental approach was to allow us to utilize the experimental results in fixing various parameters in the chemical reaction model so that calculational predictive methods could be applied more widely and with a greater measure of confidence.

THE EXTENT AND VIOLENCE OF THE REACTION

The violence of the event as determined by post inspection of the anvils, varies both with the material and the temperature. A low order event, probably a rupture of the seals caused by gas pressure, yields little or no damage to the anvils; indeed the copper sealing ring is generally still in place and the majority of the explosive sample unconsumed though charred. An example is shown in Fig. 4. A high order event, on the other hand, causes considerable metal flow in the aluminum anvil and twisting and fragmentation of the copper seal. See Fig. 5. To date, in the small samples investigated, we have seen no high order events in TNT. LX-10 and LX-04, however, give high order events at intermediate temperatures in samples as small as 0.284 cm. radius. Low order events occur for LX-10 and LX-04 at high temperature and at temperatures near the critical temperature.

In an experiment involving LX-04, an 0.08 cm. hole was drilled into the flat of the lower anvil between the sealing ring and the sample cavity. The pressure was monitored at 483 K until gas evolution ceased. The sample did not explode in six hours, although similar samples at 483 K without the hole explode in 110-115 minutes. A plot of pressure vs. time shows the familiar sigmoidal shape, Fig. 6. The significance of this "non-event" will be discussed below. However, it should be noted that the normal explosion point of 110-115 minutes for fully confined samples occurs when about 4.5% of the reaction has taken place and where the gas evolution is accelerating.
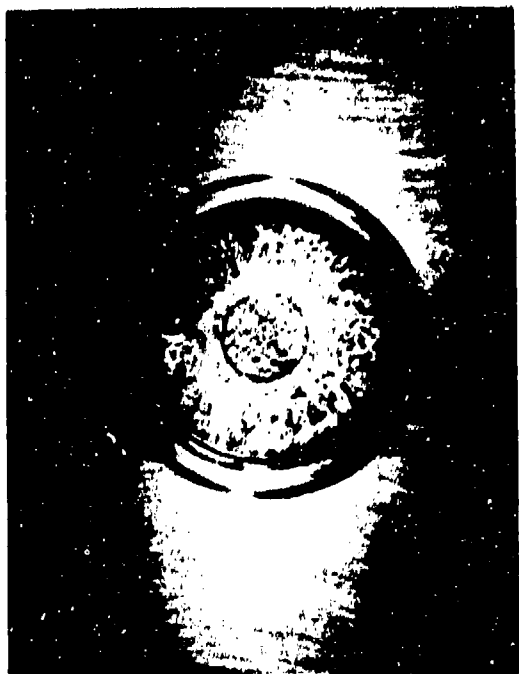
Fig. 4. An anvil following a low order event.

Fig. 5. An anvil following a high order event.

TIMES TO EXPLOSION

Plots of time to explosion versus reciprocal temperature are essentially linear for the materials investigated viz. TNT and LX-10, over the range of temperatures from 623 K to the critical temperature. This finding is in contradiction to previously reported data which showed significant curvature. Indeed mathematical treatments such as those by Frank-Kamenetskii (4), Zinn (1,5) and others based on single source term simple Arrhenius kinetics, Fig. 7 and Eq. (1),

$$ - \lambda \nabla^2 T + \rho C (\partial T / \partial t) = \rho \Delta H Z e^{-E_a/RT} \quad (1) $$

predict significant curvature to these plots. Here T is temperature in K, λ is thermal conductivity (cal deg^{-1} cm^{-1} sec^{-1}), ρ is density (g cm^{-3}), C is heat capacity (cal $g^{-1} deg^{-1}$), ΔH is heat of decomposition (cal g^{-1}), Z is the pre-exponential factor (sec^{-1}), E_a is the activation energy (cal M^{-1}), R is the gas constant (1.98715 cal M^{-1} deg^{-1}), ∇^2 is the LaPlacian operator and t is the time (sec).

The major difference between our experiments and those previously performed is that none of the gaseous decomposition products were allowed to escape from contact with the HE sample in our test. The significance of this containment is shown in Table 1 and again in Fig. 8.

Table 1 shows that the time to explosion of samples closed (sealed) at 1500 atm. is essentially

Fig. 7. Comparison of experimental time to explosion curve vs. that predicted by single source term Arrhenius kinetics.

Fig. 8. Time to explosion vs. temperature for LX-10. Comparison of low pressure closure (500 atm.) and high pressure closure (1500 atm.).
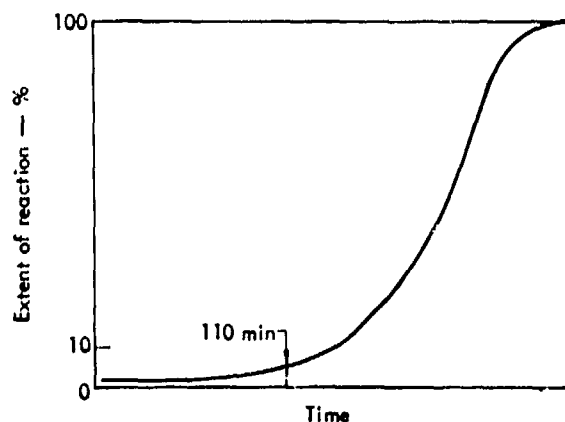
Fig. 6. Extent of reaction $(\Delta P/\Delta P_\infty)$ vs. time for HMX decomposition at 483 K.

217

TABLE 1

Effect of Closing Pressure on Time to Explosion at 483 K of LX-04. (a, c)

Closing Pressure	Holding Pressure	Time to Explosion
1500 atm.	1500 atm.	≈ 110 min.
1500 atm.	500 atm.	≈ 115 min.
500 atm.	500 atm.	≈ 210 min.
500 atm.	500 atm. (b)	Did not explode in six hrs.

a. LX-04 is also a HMX-based PBX but has 15% binder vs. 5% for LX-10
b. Anvil had a 0.08 cm. hole drilled in it to allow gaseous products to escape.
c. Sample – 0.284 cm. radius sphere, mass ≈ 0.22 gm.

Fig. 9. Time to explosion vs. temperature for TNT. Scaling is an order of magnitude in mass of HE.

constant regardless of the pressure of the experiment. However, if the anvils are closed at the lower pressure, leaving a small gap (void space) between the anvils, the time to explosion is almost doubled. If a small hole is drilled into the anvil, essentially increasing the void space to infinity, the sample fails to explode. This last observation agrees with Rogers (6) who found the critical temperature for HMX to be 250 K for this size sample.

Figure 8 shows the effect of confinement, or closing pressure on the time to explosion and critical temperature for LX-10. Lowering the closing pressure, and leaving a small void volume, lengthens the time to explosion at any given temperature and raises the critical temperature. It is interesting to note that the lines are truly parallel showing that thermal conductivity, heat capacity and the activation energy are unchanged.

CRITICAL TEMPERATURE SCALING AND EFFECT OF CONTAINMENT

Figure 9 shows the time to explosion curves for two sizes of TNT samples. This represents an order of magnitude difference in mass. The lines are divergent toward lower temperatures and the critical temperature is lowered with increase in mass. Attempts to predict the critical temperatures using kinetic constants proposed by Rogers (6) in a Frank-Kamenetskii

model gave significantly higher temperatures than those we experimentally determined. If, however, we derived a pseudo activation energy and pre-exponential factor from experiments of one size, we could successfully predict the critical temperature of the larger size. This data is summarized in Table 2.

We believe that this decrease in observed critical temperature from that predicted using Rogers' (6) treatment is a result of maintaining the gaseous decomposition products in contact with themselves and with the solid explosive. This allows the gases to continue reacting and to more effectively feed the energy back to the solid HE. This results in an increase in the heat of reaction.

The effect was similarly illustrated above in Table 1. That is, by providing a small void or expansion volume, we have effectively decreased the gas concentration and the heat flow and increased the time to explosion for any given size and temperature.

218

TABLE 2

Comparison of Predicted and Observed Critical Temperatures (T_c)

Explosive	Charge Radius (cm)	Predicted T_c Classical (a)	Predicted T_c Experiment	Observed T_c Experiment
		K	K	K
TNT	0.284	515	508	508
	0.635	490	482	478
TATB (b)	0.284	572	529	529
	0.635	554	504	503
LX-10	0.284	596	464	464
	0.635	478	457	–

a. Ref. 6.
b. TATB = Triaminotrinitrobenzene.

COMPUTER MODELLING

We first attempted to model the experimental linear dependence for the times to explosion/temperature data on TNT by varying such parameters as heat capacity, thermal conductivity and the reaction terms E_a and Z in Eq. (1). These results are summarized in Figs. 10, 11 and 12. While the initial portions of these curves are fairly linear, indeed we have represented them as straight lines, they take on considerable curvature at lower temperatures. Even so, using reasonable values for the parameters we failed to match the experimental slope even at the higher temperatures. It was obvious then that we could not successfully model the experiment using a single source term, Arrhenius kinetics.

The single source term models a reaction sequence such as Eq. (2).

$$A \xrightarrow{\hspace{2cm}} B. \qquad (2)$$
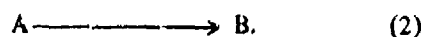
This simple approach does reasonably well at predicting critical temperatures since that quantity is determined by the accelerating exotherm, i.e., the steeply rising portion of the reaction curve in Fig. 6. It is, however, the induction period which determines, for the most part, the time to explosion. The simple model of Eq. (1) does not model this.
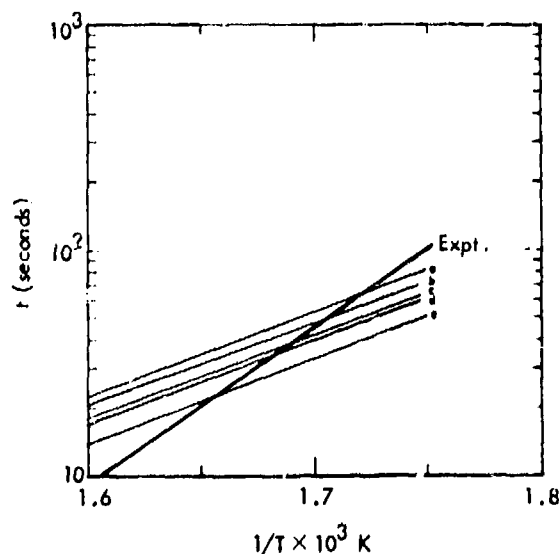
Fig. 10. The effect on predicted times to explosion by variation of heat capacity (C) and thermal conductivity (λ) in equation 1. (a) $C = 0.5 - 0.6$, $\lambda = .0005 - .0001$; (b) $C = 0.5$, $\lambda = .0005 - .0001$; (c) $C = 0.5 - 0.6$, $\lambda = .0005 - .0003$; (d) $C = 0.5 - 0.7$, $\lambda = .0005$; (e) $C = 0.5$, $\lambda = .0005$.

We have done some preliminary analysis on two models to include this induction period. One of these, a sequential model, is shown in Eq. (3). This leads to the source term

219
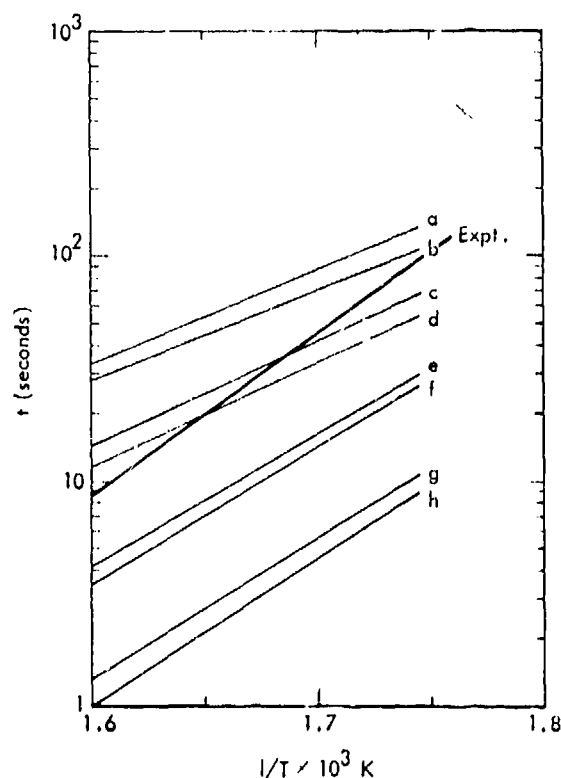
Fig. 11. The effect on predicted times to explosion by variation of activation energy, E_a, in equation 1. (a) $E_a = 46$ kcal M^{-1}, $\ln Z = 32$; (b) $E_a = 48$ kcal M^{-1}, $\ln Z = 34$; (c) $E_a = 44$ kcal M^{-1}, $\ln Z = 32$; (d) $E_a = 46$ kcal M^{-1}, $\ln Z = 34$; (e) $E_a = 42$ kcal M^{-1}, $\ln Z = 32$; (f) $E_a = 44$ kcal M^{-1}, $\ln Z = 34$; (g) $E_a = 40$ kcal M^{-1} $\ln Z = 32$; (h) $E_a = 42$ kcal M^{-1}, $\ln Z = 34$.

Fig. 12. The effect on predicted times to explosion by variation of pre-exponential factor (Z) in equation 1. (a) $E_a = 44$ kcal M^{-1}, $\ln Z = 30$; (b) $E_a = 46$ kcal M^{-1}, $\ln Z = 32$; (c) $E_a = 44$ kcal M^{-1}, $\ln Z = 32$; (d) $E_a = 46$ kcal M^{-1}, $\ln Z = 34$; (e) $E_a = 44$ kcal M^{-1}, $\ln Z = 34$; (f) $E_a = 46$ kcal M^{-1}, $\ln Z = 36$; (g) $E_a = 44$ kcal M^{-1}, $\ln Z = 36$; (h) $E_a = 46$ kcal M^{-1}, $\ln Z = 38$.

$$A \xrightarrow{1} B \xrightarrow{2} C \qquad (3)$$

expression in Eq. (4).

$$\Delta H_1 N_A Z_1 e^{-E_{a1}/RT} + \Delta H_2 N_B Z_2 e^{-E_{a2}/RT}. \quad (4)$$

Here the subscripts 1 refer to step 1, subscripts 2 to step 2 and $N_{A,B,C}$ are mole fractions such that $N_A + N_B + N_C = 1$. The results of preliminary calculations using this model are shown in Figs. 13, 14 and 15. These show that it is possible to approximate the early slope using slightly endothermic values for the heat of reaction of step 1. This could be a nucleation step of the formation of a reactive intermediate.

The second model under consideration includes a growth or autocatalytic step as Eq. (5).

$$A \xrightarrow{1} B$$
$$B + A \text{ or } B + B \xrightarrow{2} C \qquad (5)$$
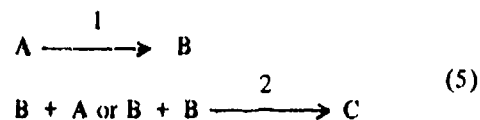
This leads to a reactive term as expressed in Eq. (6).

220
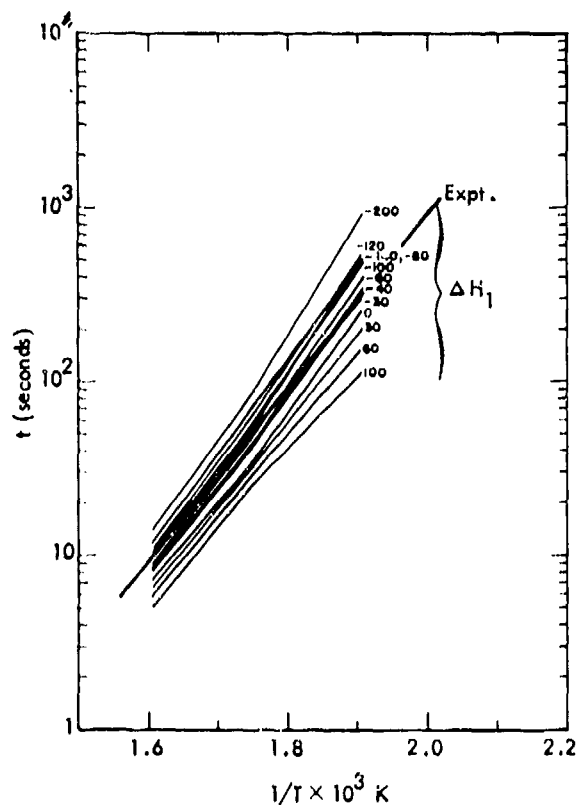
Fig. 13. Effect of changing heat of reaction of precursor step (ΔH_1) in sequential reaction model.

Fig. 14. Effect of changing activation energy of precursor step (E_{a1}) in sequential model.

$$\Delta H_1 N_A Z_1 e^{-E_{a1}/RT} + \Delta H_2(N_A + N_B)$$

$$(1 - N_B)Z_2 e^{-E_{a2}/RT} \quad (6)$$

We have only initiated work on this model and will not report at this time.

We hope to be able to independently measure reaction parameters and thus to realistically model the response of explosives to thermal stimulus.

This test gives results which are significantly different than those given by tests in which the gaseous products are vented.

The amount of expansion volume, even in a totally contained system, has a pronounced effect in the time to explosion for any given sample size and temperature.

A heat flow model which uses a single Arrhenius source term does not adequately model the results of time to explosion tests.

SUMMARY AND CONCLUSIONS

We have designed and constructed an instrument to study the time to explosion of one dimensional samples where the gaseous decomposition products are totally contained.

REFERENCES

1. J. Zinn and C. L. Mader, J. Appl. Phys. 31, 323 (1960).

2. J. Wenograd, Trans. Faraday Soc. 57, 1612 (1961).

221
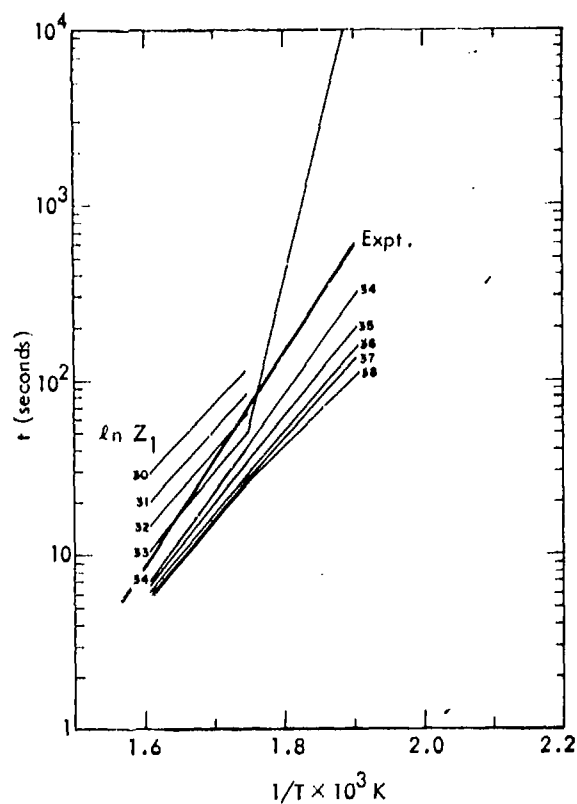
Fig. 15. Effect of changing pre-exponential factor of precursor step (1n Z_1) in sequential model.

3. H. Henkin and R. McGill, Ind. Eng. Chem. **44**, 1391 (1952).

4. D. A. Frank-Kamenetskii, Acta Physicochem. USSR, **10**, 363 (1939).

5. J. Zinn and R. N. Rogers, J. Phys. Chem. **66**, 2646 (1962).

6. R. N. Rogers, Thermochimica Acta, **11**, 131 (1975).

Session IV

DEFLAGRATION-TO-DETONATION
TRANSITION STUDIES

Chairmen: G. D. Coley
Atomic Weapons Research Establishment
D. B. Hayes
Sandia Laboratories

RETARDED DETONATION

M. Held, D. Ludwig, and P. Nikowitsch
Messerschmitt Bölkow Blohm GmbH
8898 Schrobenhausen, West Germany

INTRODUCTION

It is well known that the thrust S of a rocket is given by exhaust velocity of the reaction products v_a times mass flux G. G is given by the burning rate and the geometry of the propellant, Fig. 1.

The state of art of modern rocket combustion chambers is, that much higher working pressures and alongside higher effectivity could be attained unless the reaction mechanism of up to date propellants would limite sufficient burning rates.

At the present time the burning rate of solid propellants is about 10^{-2} m/s or slightly higher. The mass flux is increased by using special geometries of the propellant to get larger burning surfaces, Fig. 2. An often used type of geometry is the so-called star shaped burner which is used instead of end-burners. But even with this type of propellant geometry physical limits are set by the rather poor loading density and maximum possible gas velocities within the inside channels of the propellant. For an end-burner using an explosive material with high burning rate these problems would not occur.

The regime of stable detonation at which gas is produced with reaction velocities of km/s nearly instantly accompanied by pressures far beyond the level any combustion chamber could withstand, is not promising for this purpose. Another regime adjoining the burning phase at the low reaction side and detonation on the rapid reaction side, the instationary deflagration regime, is more adequate for solving the problem of higher burning rates. One could also define this regime as "accelerated burning" or "retarded detonation." The pending problem is to turn the reaction process appearing only as a transition phase into a stationary process.

The following basic possibilities exist in principle for the accelerated burning or retarded detonation respectively, Fig. 3:

- The detonable material will be phlegmatized by inert material in such a way that the detonation phase is not reached any more but burning is increased substantially such that a "stable regime" of deflagration is obtained.

- It is very difficult to control the transition phase by additives, as the burning rate increases rapidly with increasing pressure. Therefore a possible means to limit the pressure to adequate levels is to insert inactive barriers into the propellant.

- It is known that the detonation results in a highly directed very rapid flow, which cannot run around a given edge with deliberately small radius of curvature. This fact may be used to decrease the reaction velocities in order to stay within the limits of a stable deflagration regime.

In some basic experiments all three possibilities were checked. Six materials, as shown in Fig. 4, were investigated in a first step.

RETARDED DETONATION OF THE HOMOGENEOUS TYPE

The experimental set up consists of a perspex body with the cross section of 70 × 70 mm² and 180 mm length with a central bore of 32 mm diameter. Top and bottom were covered by 10 respectively 20 mm thick steel discs. Burst membranes of 0.1 mm copper foil close simple holes of 8, 16 and 32 mm diameter at the end where ignition is started. In some

cases we did not have holes for the depressuration at all, Fig. 5. The reaction was started by the squib Mk 1, 3.4 gramms lightly packed and 2.8 gramms pressed blackpowder. The explosive material to be tested was filled into the reaction chamber under slight shaking resulting in an adequately low loading density. The flanges were fixed with 4 or 6 rigid bolts

The events were observed by means of HYCAM and a rotating mirror camera (Type CORDIN modell 330) and were registered in frames and streak recordings. The HYCAM was operated at 13 000 to 16 000 f/s and at writing speeds of about 50 m/s for the streak recordings. The rotating mirror camera on the other hand was run at about 500 000 f/s and at 3 000 m/s streak writing speed.

The evaluation of the HYCAM recordings yields run-up-times of 4 to 10 ms depending on type of material, grain size and free hole diameter. The corresponding distances within the sample up to the onset of the detonation or the break-up of the test chamber are situated in the range between 30 and 140 mm including the case where the chamber was completely closed, Figs. 6 and 7.

Detonation was observed only in the case of PETN, in the rest of the cases the chamber just broke up. HYCAM streak recordings are shown in Fig. 8. In the upper part of the figure we see the result of a test with RDX with grain size $<200\,\mu$ in a completely closed reaction chamber. After a run up time of 5,5 ms corresponding to a distance of about 30 mm a very strong reaction occurred accompanied by the break-up of the chamber.

In the lower part of Fig. 8 we see the recording of a test with PETN of grain size $<500\,\mu$, which turned into a detonation after a run-up-time of 11 ms corresponding to a run-up-distance of 70 mm. Beneath the streak photo the resulting reaction velocities are noted.

The transition zone from deflagration to detonation of PETN sample is shown magnified in Fig. 9. Here it is possible to compare the HYCAM streak recordings at a streak writing speed of 42 m/s with the streak recording of the rotating mirror camera taken at a writing speed of 560 m/s. From the recordings you can see the onset of the detonation in forward direction and a clear cut reaction wave propagating backward into the partly burnt PETN.

Figure 10 again shows the rotating mirror streak recording in a view where the different reaction phases are pointed out. Since the initiation starts near the center of the cylindrical sample and because of the spherical shape of the detonation wave we record on the streak photo a phase velocity on the surface, which is greater than the actual velocity of the detonation wave. This region is often referred to as super detonation. Adjacent to the region of phase velocity on the streak photo the streak line represents the time—distance history of the stationary detonation wave. Of vital interest is a two phase regime, where a backward detonation or retonation wave propagates into the partly burnt part of the explosive medium and a second wave propagates in form of a reaction wave into the burnt section of the PETN. The retonation wave has a propagation velocity of 3 650 m/s and the reaction wave propagates with a velocity of 2 310 m/s.

TESTS WITH INSERTED BARRIERS

The propagation of shock waves in inert bodies as well as run-up-time and run-up-distance of the reaction wave up to the detonation of the explosive charges as a function of shock wave pressure have been subject of extensive studies so far. These experiments were done in a set up as shown in Fig. 11. Figure 12 shows a typical recording and evaluation, where similar events in the acceptor charge are recorded as earlier mentioned. These events are sudden transitions of the reaction wave into a detonation wave in the center of the acceptor charge, a so called super detonation and a retonation at the surface of the explosive charge. As an example we present in Fig. 13 the run-up-distances of different pressed and casted explosive charges versus the thickness of the barrier. In this type of set up a defined shock wave pressure of the detonation of the donor charge—a tetryl booster—is coupled to the barrier.

TESTS WITH SCHIKANES

As mentioned earlier the detonation wave cannot run around an obstacle having deliberately small radius of curvature. This phenomena is tied to the fact that the detonation is inherently linked to a flow, which in the first place builds up a corresponding ram pressure only in the direction of the flow. According to this model some other phenomena may

226

be explained. On the other hand this effect can be used to interrupt the detonation or slow down the reaction rate.

In basic experiments detonability of casted TNT/ RDX explosive charges of the composition 35/65 were tested. The initiation was inserted into a coaxial bore of 8 mm diameter within a cylindrical explosive charge with various outer diameters. The initiation chain consisted of an electrical detonator HX 20, detonator F8A and a booster of H 5 (RDX with 5% wax) having a diameter of 8 mm and a length of 15 mm. The space adjacent to the booster was filled with an aluminum rod of 8 mm diameter, the bore on the side of the electrical detonator was left open, Fig. 14. The streak recording of a test with a cylindrical high explosive charge of 25 mm outer diameter shows that a forward detonation but no backward detonation occurred.

This fact can also be clearly seen on the framings in the upper part of Fig. 15. However, if we regard the streak recording from a cylindrical explosive charge of 64 mm outer diameter (Fig. 15, lower part), we find forward detonation as well as retonation. The critical diameter at which retonation does not occur anymore was found to be about 42 mm for this type of high explosive charge. This corresponds to a wall thickness of 17 mm.

The diagram, Fig. 16, presents the location of the detonation breakthrough to the surface of the explosive charge as a function of wall thickness, along with the length of retonation visuable on the respective streak recordings. The effect of the locally delayed onset of the detonation wave after passing a curved obstacle can already be seen on the photo showing an aluminum rod, Fig. 17. The part which

was in direct contact with the booster charge exhibits a relatively smooth surface. Only after a distance of about 12 mm the surface gets rough in a manner typical for detonative loading. In other words, this is a direct projection of the run-up-distance of 12 mm.

This effect is also observed with thin foils of explosive material (85% PETN) which detonates around an edge. Again we get an area of smallest radius of curvature in the order of magnitude of about 10 mm close to the edge which does not react detonative. This effect has been used already for detonative valve arrangements (1). We have visualized this on the recordings of the detonation of a 2 mm thick explosive foil, Fig. 18. Besides the other possibilities mentioned, this schikane-effect can be used to control the deflagration regime in the earlier sense mentioned in this paper.

SUMMARY

Ideas and some possible solutions were discussed, on how the detonation starting after a certain run-up-distance may be stopped and the reaction depressed by the use of barriers and schikanes to such a level that reaction velocities are attained which are far beyond the burning rates of ordinary solid propellants.

REFERENCES

1. Held, M., "Streak Technique as a Diagnostic Method Method in Detonics," Proceedings of the First International Symposium on Ballistics IV 177-210, 1974.

ROCKET THRUST S

$$S = v_a \times \dot{G}$$

v_a = nozzle outlet velocity

$\dot{G}$ = mass flux

$\dot{G}$ = f (burning rate, propellant geometry)

MBB
4235

AF 233
4 0 76
Meyer H

Fig. 1.

227

INCREASE OF MASS FLUX

Linear burning rate
(mass / time)

propellant geometry

Fig. 2.

EXPERIMENTAL SET UP
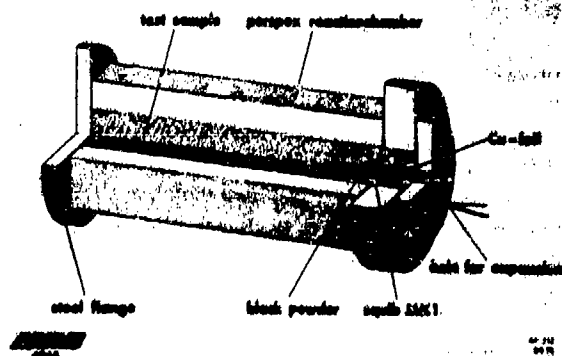
Fig. 3.

EXPLOSIVE MATERIALS

PETN Nitroguanidine	Aromatics
TNT Tetryl	Aliphatics
RDX HMX	Nitramins

Fig. 4.

RETARDED DETONATION

homogeneous

barrier

schlieren
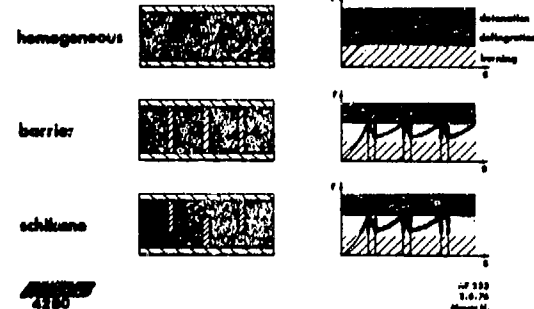
Fig. 5.

RUN UP TIME
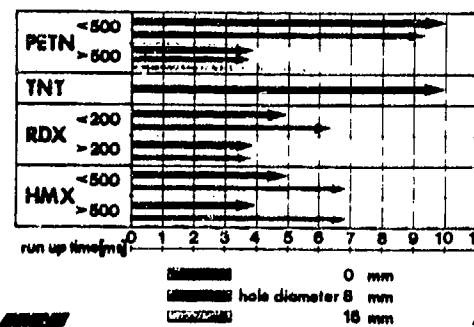
Fig. 6.

RUN UP DISTANCE

Fig. 7.

228
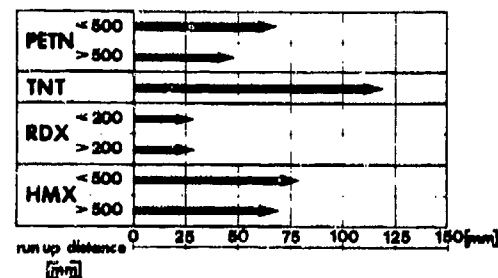
RUN UP VELOCITIES V

Fig. 8.
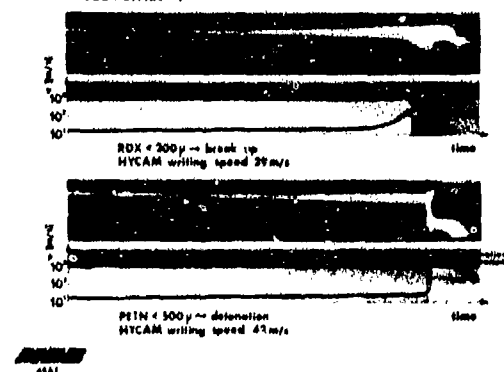
OPTICAL SET UP

Fig. 11.

DETONATION PETN ~500µ D23789

Fig. 9.
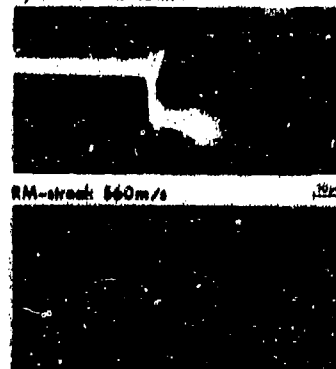
GAP TEST DET. 13419

Fig. 12.

DETONATION ~ RETONATION
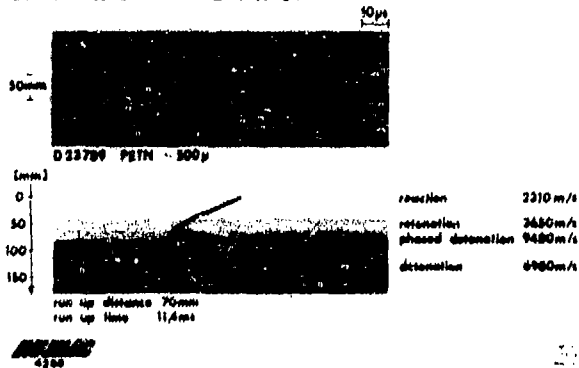
Fig. 10.
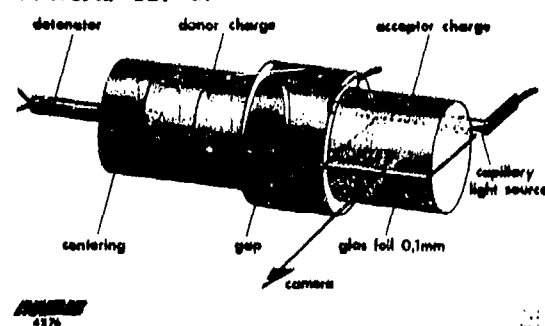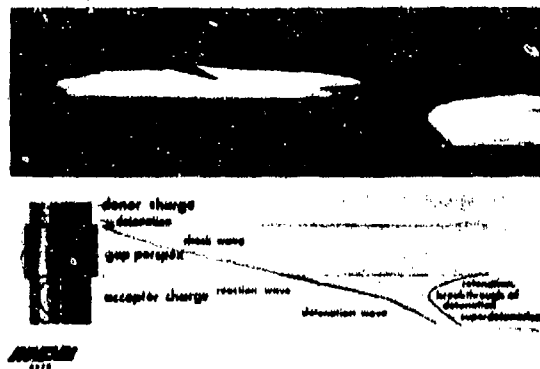
EXPLOSIVE CHARGE

Fig. 13.

229
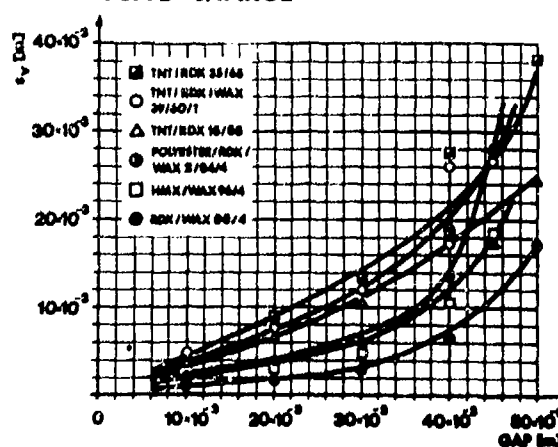
EXPERIMENTAL SET UP: SCHIKANE

Fig. 14.

RETONATION TNT/RDX 35/65
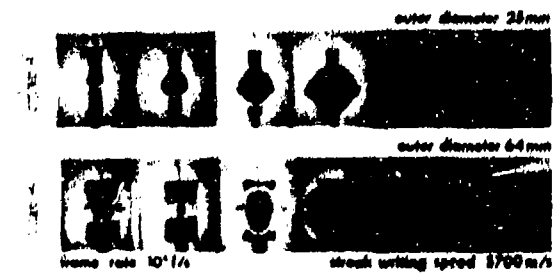
Fig. 15.
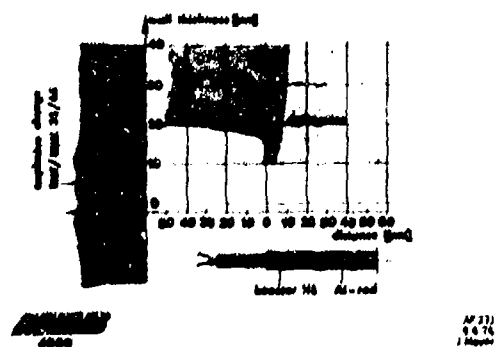
Fig. 16.

ALUMINUM ROD
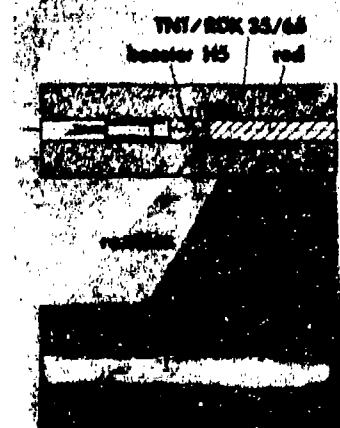
Fig. 17.

EXPLOSIVE FOIL
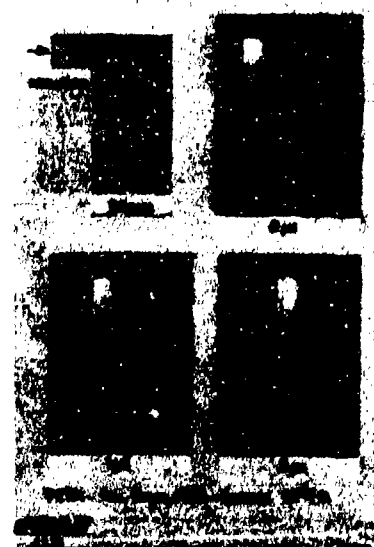
Fig. 18.

DEFLAGRATION-TO-DETONATION TRANSITION STUDIES FOR TWO POTENTIAL ISOMERIC CAST PRIMARY EXPLOSIVES*

C. M. Tarver, T. C. Goodale, R. Shaw,[†] and M. Cowperthwaite
Stanford Research Institute
Menlo Park, California 94025

A combined experimental and theoretical study of the deflagration-to-detonation transition (DDT) was undertaken for two potential isomeric cast primary explosives, 1-methyl-5-nitrotetrazole (1-MNT) and 2-methyl-5-nitrotetrazole (2-MNT). The measured threshold voltages for ignition by a hot bridgewire were 110 volts for cast 2-MNT and 375 volts for cast 1-MNT. Critical times and distances for DDT in cast 2-MNT of 8 μs and 2-3 mm, respectively, were determined by performing experiments on charges of different lengths. In the theoretical study, Macek's model for DDT in cast explosives was modified to provide a more realistic treatment of the accelerating flame. Calculations were made with the deflagration treated as a reactive discontinuity whose burnt state satisfied either the Chapman-Jouguet (CJ) condition or the condition of zero particle velocity to determine upper and lower limits for the deflagration velocity as functions of pressure in the unburned explosive. The predicted times and distances for DDT in cast pentolite and crystalline lead azide agree well with the meager experimental data available.

INTRODUCTION

The long-range objective of the present combined experimental and theoretical program is to develop a relationship between chemical structure and primary explosive behavior as a research tool for assessing the potential of primary explosives. After numerous discussions with experts in the field of explosives and an extensive literature review, a research plan was developed (1), which is based on the following conclusions:

- The most important distinction between a primary and a secondary explosive is that a primary explosive undergoes very much faster deflagration-to-detonation transition (DDT).

- The difference between primaries and secondaries is one of degree rather than kind; therefore, all that has been learned about DDT in secondaries can be applied to primaries.

- It will be easier to develop a quantitative model for DDT in cast explosives than in porous explosives.

The first assumption is based on the prime functions of primary and secondary explosives. Primaries are required to detonate rapidly when ignited, whereas detonations in secondaries are initiated by shock waves. In general, the faster the DDT, the better the primary. This rapid DDT of a primary is also its weakness because accidental initiation of deflagration will result in detonation.

The second assumption is based on observations of the many similarities between primary and secondary explosives (2). Both primaries and secondaries will

[†]Present address: 1162 Quince Avenue, Sunnyvale, California 94087.

undergo DDT, although the transition takes longer and requires heavier confinement for secondaries. The existence of near primaries, such as some of the hydroxynitroaromatic compounds, and sensitive secondaries like PETN suggests that there may be many other compounds between the main body of primaries and the main body of secondaries that have received little attention because there is no obvious practical use for them.

The third assumption is based on the results of DDT research on secondary explosives. A first-generation model that gives order of magnitude agreement with experimentally determined times and distances for DDT in cast secondaries has been formulated by Macek (3). No equivalent model of DDT in porous secondaries exists. The work of Bernecker and Price (4) indicates that the formation of a convective flame front over a large surface area and a resulting complex flow field precede DDT in a porous explosive. Because of the current research effort on DDT in porous explosive-based propellants, a clearer understanding of the role of convective burning in DDT in porous explosives may eventually be developed. However, at present, the basic physical processes involved in DDT have been determined only for cast explosives in which convective burning does not occur.

The first experimental task in this research plan is to measure the threshold voltages for hot bridgewire initiation and the times and distances for DDT in two potential isomeric cast primary explosives, 1-methyl-5-nitrotetrazole (1-MNT) and 2-methyl-5-nitro-tetrazole (2-MNT). Isomeric cast explosives are most convenient for isolating the effects of chemical structure in primaries because isomers have different molecular structures but essentially the same physical properties; because inhomogeneities leading to increased sensitivity are minimized by the casting process; and because the mechanism of DDT is more fully understood in cast explosives than in porous explosives. The first theoretical task is to analyze Macek's model for DDT in cast secondary explosives and apply it to DDT in cast primaries. This paper presents the experimental DDT measurements for cast 1-MNT and cast 2-MNT and a modified version of Macek's model that provides a more realistic treatment of accelerating flames.

DDT MEASUREMENTS ON CAST 1-MNT AND 2-MNT

The threshold voltages for ignition were measured for cast 1-MNT and 2-MNT by using the technique developed by Leopold (5) and modified by Goodale (6). The initiator plug and charge holder are shown in Fig. 1. The bridgewires were 1-mil Nichrome wires soldered across the center of the charge holder.

A plastic monofilament light pipe of 40-mils diameter was placed in the phenolic plug with its upper surface
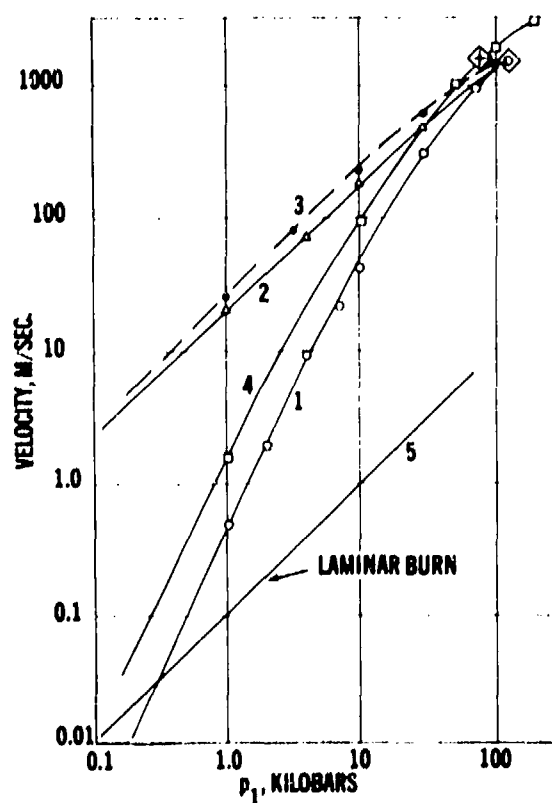
Fig. J1. Deflagration and Particle Velocities. 1). $W - u_1$ $(u_2 = 0)$; 2). $W - u_1$ (CJ); 3). u_1; Tarver, et al. 4). $W - u_1$ $(u_2 = 0)$, Coffey and Jacobs. 5). Laminar flame velocity (approximate).

Fig. 1. Initiator Plug and Charge Holder

232

immediately under the bridgewire to determine the time of initiation of burning in the explosive by observing the first light emission near the bridgewi.e. A second light pipe was inserted into the top of the charge holder and placed directly on the upper surface of the cast explosive to detect the light emitted by the detonation wave as it reached the top of the charge. A capacity-discharge firing circuit was used to ignite the explosive charges. The waveform of the current discharge through the bridgewire, as represented by the voltage drop across a constant non-inductive resistance close to the bridgewire in the bridgewire in the circuit, was monitored in each test on an oscilloscope. Reproducible current pulses free from anomalous irregularities required the use of a vacuum fix this "switch of high" current capacity. The resistance of each bridgewire was measured before each test to ensure that the bridgwire connections remained intact and that the resistance remained in the normal range of 4.5 to 7.5 ohms.

Accurately weighed 5-, 10-, 20-, and 40-mg charges of 1-MNT and 2-MNT were transferred into charge holders and pressed at 5000 psi. These pressed charges were then melted to obtain cast, fully dense charges. The resulting cast 2-MNT charges had extremely flat upper surfaces and an average density of 1.672 g/cm³. Considering the small weights (5-40 mg) and measured charge lengths (0.5-5 mm), this average density was in good agreement with the literature value (7) of 1.64 g/cm³.

Because of its low melting point (58°C compared with 86°C for 2-MNT), molten 1-MNT cooled relatively slowly and exhibited a large degree of supercooling before solidifying into a glass. By using a faster cooling rate, fully dense, crystalline charges of 1-MNT were finally produced in the forms of microcrystals and relatively coarse crystals. All these forms of cast 1-MNT (glassy, microcrystalline, and coarse crystalline) were tested. The average density of the cast 1-MNT charges (1.775 g/cm³) closely agreed with the value of 1.76 g/cm³ predicted by the group additivity approach (2).

Since both cast 1-MNT and 2-MNT were found to be somewhat transparent to light, the tops of all charges were blackened with a thin film of India ink to prevent premature triggering of the upper phot ultiplier by light transmitted from inside the reacting charge before the detonation wave reached the top surface of the charge.

Two series of cast 20-mg charges were fired at various capacitor charging voltages to determine the threshold voltages for initiation of 1-MNT and 2-MNT. For cast 2-MNT, the threshold voltage for 20-mg charges was approximately 100 volts, while discharges of 110 volts reliably detonated every 20-mg cast 2-MNT charge fired. Therefore, capacitor charging voltages of 110 volts were used to make the quantitative measurements of time for DDT as a function of charge length for cast 2-MNT. Although it was expected that cast 1-MNT would have a similar threshold voltage, cast 1-MNT charges failed to explode at capacitor charging voltages of less than 375 volts and only one-fourth of the charges exploded at that voltage. In most tests, sufficient pressure was generated to blow the charge holder off the plug. Usually unreacted 1-MNT remained in the charge holder and no audible explosive effects were produced. At capacitor charging voltages above 200 volts, the light emitted by the glowing bridgewire was sufficient to trigger the sensitive lower photomultiplier before the explosive actually ignited. Thus the measured times for DDT for these high voltage tests were upper limits because they included the ignition delay time of cast 1-MNT. Therefore, quantitative time to DDT versus charge length measurements could not be obtained for cast 1-MNT. However, the large difference in threshold capacitor charging voltages for two cast isomers, 1-MNT and 2-MNT, is an important result because it indicates that chemical structure can play a major role in the performance of potential primaries. Because the threshold voltage of cast 2-MNT is approximately the same as that of pressed lead azide (6), cast 2-MNT, based solely on this test, appears to be a promising candidate primary explosive, while cast 1-MNT appears to be a very poor primary.

Quantitative data on time for DDT as a function of charge length were obtained for cast 2-MNT using a capacitor charging voltage of 110 volts. These cast charges varied in weight from 4 to 47 mg and in length from 0.4 to 5 mm. Charges weighing less than 5 mg failed to detonate, while approximately two-thirds of the 10-mg charges detonated. Charges exceeding 20 mg definitely detonated and damaged the aluminum charge holder to roughly the same extent as an equivalent mass of pressed lead azide. The experimental results for the fifteen cast 2-MNT charges that produced good oscilloscope records are summarized in Table 1. The actual oscilloscope records of one of these shots (Shot 2M-19 in Table 1)

233

are reproduced £3 Fig. 2. Figure 2a is the dual-beam oscilloscope record of the bridgewire current waveform and the light produced by the ignition of cast 2-MNT near the bridgewire. Practically all of the energy from the capacitor discharge was deposited in the bridgewire in 4-6 μsec, and ignition occurred 12 μsec after the discharge began. The average time from the beginning of the energy pulse to the onset of burning for the cast 2-MNT charges listed in Table 1 was 13.7 μsec. The corresponding time to ignition for pressed lead azide at 105.9 volts was on the order of 50 μsec (6). Figure 2b is the single-beam oscilloscope record of the light output detected by the lower photomultiplier after it had been triggered by the first light of ignition near the bridgewire. A reference pulse with a 0.6-μsec time delay and a time delay circuit of 1.57 μsec for the trace allowed observation of the entire lower photomultiplier output with a known time reference.

Figure 2c represents the single-beam oscilloscope record of the light output detected by the upper photomultiplier after it had been triggered by the ignition of the charge. The 0.6 μsec reference peak also appeared on this record, which measured the time between ignition and the appearance of light at the top of the charge. This light was assumed to be caused by a detonation wave produced inside the charge that propagated through the remainder of the charge. The measured time was then taken as the time for DDT for that charge. The time for DDT in Fig. 2c is 8.6 μsec. The mean time for DDT and the standard deviation from this mean for the fifteen cast 2-MNT charges listed in Table 1 were found to be 4.60 and 2.68 μsec, respectively. These values are compared with previously determined values (6) for three other primaries in Table 2. All of the primaries

TABLE 1

Summary of Time to Ignition and Time for DDT Experiments on Cast 2-MNT

Charge Number	Capacitor Charging Voltage (volts)	Charge Length (mm)	Time to Ignition of Charge (μsec)	Time from Ignition to Detection of Light at Top of Charge (μsec)
2M-16	110	0.488	12.8	4.4
2M-27	110	0.632	>20.0	2.6
2M-26	110	0.904	16.0	2.4
2M-24	110	1.214	19.0	4.0
2M-10	110	1.621	12.4	2.0
2M-14	110	1.717	12.5	2.0
2M-33	150	1.796	>10.0	3.6
2M-45	110	1.923	11.2	2.7
2M-35	110	1.991	13.1	3.2
2M-34	100	2.042	13.5	6.3
2M-46	110	2.223	12.2	1.9
2M-37	110	4.270	15.8	8.8
2M-19	110	4.425	11.8	8.6
2M-38	135	4.493	--	7.5
2M-20	110	4.877	14.3	9.0

TABLE 2

Comparison of Time for DDT Measurements for Cast 2-MNT with Other Primary Explosives

	Primary Explosive			
	Lead Azide	Lead Styphnate	FDIPAM	Cast 2-MNT
Number of charges fired	20	29	27	15
Capacitor voltages, volts	105.9	67.8	131.2	110.0
Average charge length, mm	1.43	1.94	2.74	2.31
Average density, g/cm^3	2.33	1.88	1.36	1.67
Mean times from ignition to detection light at the top of the charge, μsec	0.65	11.20	9.81	4.60
Standard deviations of times from ignition to detection of light at the top of the charge	0.115	1.110	1.660	2.68

Bridgewire Current Waveform
  Horizontal Scale: 2 μsec/cm
  Vertical Scale: 0.2 volts/cm
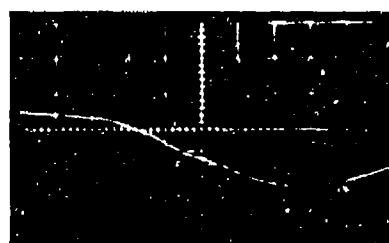
Photomultiplier Monitoring
Light Near Bridgewire
  Horizontal Scale: 2 μsec/cm
  Vertical Scale: 0.2 volts/cm

Lower Photomultiplier
Triggered By First Light
Near Bridgewire
  Horizontal Scale: 0.5 μsec/cm
  Vertical Scale: 0.2 volts/cm
Reference Peak At 0.6 μsec
Time Delay Of 1.57 μsec

Upper Photomultiplier
Triggered By First Light
Near Bridgewire
  Horizontal Scale: 1 μsec/cm
  Vertical Scale: 0.2 volts/cm
Reference Peak At 0.6 μsec

Fig. 2. Oscilloscope Records for Shot 2M-19

tested in this apparatus exhibited significant standard deviations in time for DDT. The absence of confinement on the upper surface of the explosive may result in upward movement of the charge during deflagration. This motion could contribute to the variation in burning times. Cast 2-MNT exhibits a much larger standard deviation in the times for DDT than the other three primaries. However, its mean time for DDT is less than that of lead styphnate and FDIPAM and, therefore, cast 2-MNT qualifies as a good primary based on relative DDT times.

Ideally, the standard deviation in the times for DDT for charges of equal length is small, and a plot of times for DDT at various charge lengths yields two lines of distinctly different slopes. For charge lengths less than the critical length for DDT, the times for DDT increase rapidly with charge length because the entire charge is consumed by the deflagration wave. For longer charges, the detonation wave propagates at a high velocity over some distance in the charge, and the times for DDT increase very slowly with charge length. The relationship between time for

DDT and charge length for these longer charges would yield a good estimate of the detonation velocity in such an ideal primary.

The experimental times for DDT listed in Table 1 for cast 2-MNT are plotted as a function of charge length in Fig. 3. The times for DDT vary greatly for charge lengths of less than 2 mm, while the times for DDT for 4-5 mm charges appear to be more consistent. The longer charge (Shot 2M-38), which had a relatively short time for DDT (7.5 μsec), failed to ignite at 110 volts and was fired a second time at 135 volts. This double firing probably affected the performance of this shot. Omitting this result, a straight line with a slope of 3 mm/μsec is drawn in Fig. 3 through the results for the remaining three longer charges. The detonation velocity of cast 2-MNT is considerably higher than 3 mm/μsec [a TIGER code calculation (2) resulted in a detonation velocity of 7.8 mm/μsec], but the scatter in the measured times for DDT prohibits an accurate determination of the detonation velocity.

235
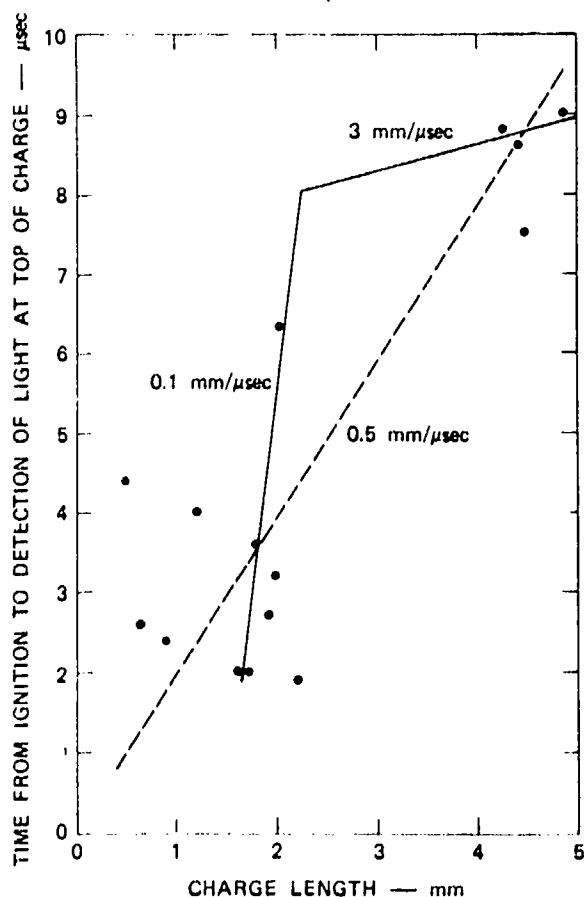
Fig. 3. Time for DDT as a Function of Charge Length for Cast 2-MNT

Using the 3 mm/μsec line in Fig. 3, we can draw another line with a much less steep slope through the shorter charge length results. A line with a slope of 0.1 mm/μsec is shown in Fig. 3, although the large variation in times for DDT for these charges prohibits any quantitative conclusions. In fact, a line with a slope of 0.5 mm/μsec (the dashed line in Fig. 3) can be drawn through all of the data. However, three observations indicate that the time-for-DDT behavior of cast 2-MNT is governed by a time-for-DDT versus charge-length relationship with an abrupt change in slope (such as the solid line in Fig. 3). First, cast 2-MNT charges of approximately 1-mm length sometimes failed to explode, indicating that the critical length for full development of detonation is more than 1 mm. Second, charges between 1.6 and 2 mm did show a trend toward large increases in time for DDT over this small range of lengths. Third, the three reliable sets of data for 4-5 mm charge

lengths showed the relatively small deviation (8.8 ± 0.2 μsec) typical of a fully developed detonation wave that had traveled some distance.

These three observations lead to the conclusion that the critical charge length for DDT is approximately 2-3 mm in this experiment. This critical distance agrees qualitatively with two results for lead azide. In a thin flyer-plate impact study of shock-to-detonation transition (SDT) in pressed lead azide, Davies et al. (8) found that the transition occurred between 1 and 3 mm for shock waves that did not cause immediate detonation at the explosive surface, but did cause buildup to detonation within the explosive sample. Chaudhri and Field (9) concluded that single crystals of lead azide less than 2 mm thick deflagrated rapidly but could not make the transition to detonation that thicker crystals made.

MODIFICATION OF MACEK'S MODEL FOR DDT IN CAST EXPLOSIVES

Early work (10,11) on the transition from deflagration (slow pressure-dependent burning) to detonation led to the hypothesis that the sequence of events in the transition can be divided into three parts: a rapid pressure increase behind the burning front that sends compression waves through the front and into the unreacted explosive, the coalescence of these compression waves into a shock wave in the unreacted explosive some distance ahead of the flame, and the shock initiation of a detonation wave in the unreacted explosive. Macek (3,12-14) then developed a first-generation experimental and theoretical approach to the study of DDT in cast secondary explosives that included experimental measurements of the pressure-time history in the deflagration region and of the time and position where detonation first appeared. A strain gage positioned on the outside of the tube was used to measure the pressure-time history in the deflagrating explosive near the bridgewire. Ionization probes were located at regular intervals to record the passage of the deflagration wave or compression waves in the unreacted explosive. The measured pressure-time rise was of the form

$$P = P_0 e^{kt} \qquad (1)$$

where P_0 is the initial pressure, t is the time, k is an experimentally determined constant, and P is the pressure in the reaction product gages. This pressure

236

was assumed to be equal to the pressure in the unreacted solid explosive, which obeyed the modified Tait compression equation

$$P = \frac{\rho_o c_o^2}{n}\left[\left(\frac{\rho}{\rho_o}\right)^n - 1\right] \qquad (2)$$

where ρ_o is the initial density, c_o is the initial sound velocity, ρ is the density of the compressed explosive, and n is a constant (generally n – 3). The propagation of the flame and its associated high-pressure gases into the solid explosive creates compression waves. The motion of these compression waves through the reacted solid was calculated by the method of characteristics (15), which is illustrated in a distance-time diagram such as Fig. 4.

When the velocities of the compression waves were calculated at various pressures, and drawn in Fig. 4 as C_+ characteristics (u + c), the characteristics intersected at a distance of about 12 cm into the unreacted explosive. This intersection of the characteristics was assumed to represent the formation of a shock wave of sufficient magnitude and duration to cause initiation of detonation in that region of the solid explosive. Once initiated, the detonation wave traveled through the unreacted explosive in the direction of flame propagation (detonation) and also toward the flame front (retonation).

Using this approach, Macek obtained qualitative agreement between calculated times and distances required for DDT and observed times ($\sim$100 μsec) and distances ($\sim$12 cm) for two cast secondaries, diethylnitramine dinitrate (DINA) and pentolite 50/50 (3). Macek also attempted to explain the observed exponential pressure-time relationship [Eq. (1)] behind the burning front on the basis of one-dimensional, adiabatic flame model. This flame had a burning-rate law of the form

$$R = \beta p^\lambda \qquad (3)$$

where R was the burning rate, β was a constant equal to 10 cm/sec-kbar, and λ was a constant equal to one. This type of burning-rate law has been observed for several explosives over a range of ambient pressures up to a kilobar by Andreev and Chuiko (16). Macek normalized the pressure-time relationship derived for this burning-rate law to Eq. (1) through an adjustable proportionality constant that included the surface area of the burning front.

Although Macek's approach gave qualitative agreement with DDT experiments and contained many of the physical processes involved in DDT, it has several weak points that require modification. In the DDT experiments, Macek used strain gages placed on the outside of the tube to measure pressure-time histories. Recent advances in the use of in-material stress and particle velocity gages make it possible to use these gages in DDT experiments on cast explosives. In particular, multiple Lagrange particle velocity gages have been successfully used in reacting explosives (17) and stress gages have been used near exploding bridgewires to measure detonator output (18). Experiments using these stress gages to measure pressure-time histories during DDT would quantitatively determine the constants in Eq. (1) for each explosive. In addition to better pressure measurements, deflagration velocity measurements must be much more accurate than in Macek's experiments to determine the actual burning rate and surface area of burning as functions of time.

On the theoretical side of Macek's approach, three problems exist. By assuming that the pressures in the burned gages and in the unreacted explosive were equal, Macek neglected the pressure drop across a deflagration wave, which can be very large if the flame approaches a Chapman-Jouguet (CJ) deflagration. Thus the pressure in the unreacted explosive ahead of the flame may have been much higher than the pressures measured near the bridgewire in Macek's apparatus.
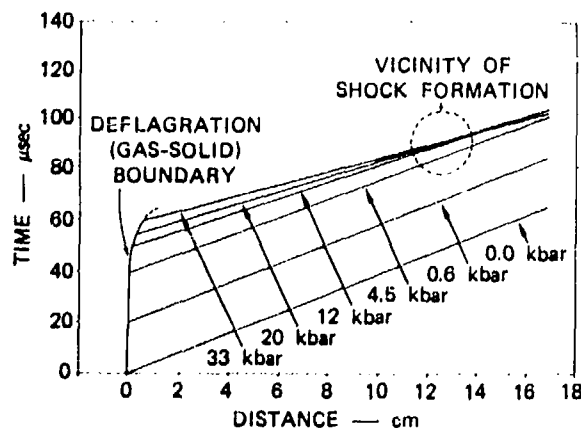
Fig. 4. *Characteristics Diagram (C_+) for the Development of a Compression Wave from Deflagration in a Rigidly Confined High Explosive (3)*

237

The second problem was pointed out by Jacobs (19), who noticed that the linear pressure-burning rate relationship derived by Macek cannot describe the pressure-particle velocity buildup at pressures above one kilobar. A calculation of the magnitude of the burning surface area showed that Macek's linear pressure/burning rate relationship can account for the experimental pressure/time relationship only when the surface area of the burning front is 20,000 times the original surface area of the cast explosive. Even the introduction of mechanical means of increasing the surface area available to the flame, such as fracture and induced porosity, cannot account for that magnitude of surface area increase. Therefore, the actual burning rate-pressure relationship in accelerating deflagrations that cause detonation must be very different from the linear burning rate-pressure law observed for explosives burning at high ambient pressures and low ambient temperatures (16).

The third problem with Macek's analysis is that the momentum imparted to the burnt gages by the deflagration wave is neglected. In a closed tube, this momentum participates in the flame acceleration mechanism. Figure 5 shows the detonation and deflagration branches of the Hugoniot curves in the pressure-volume and pressure-particle velocity planes. When the deflagration wave is ignited in a closed tube, it travels up the tube burning the explosive and creating a flow of burnt gases in the opposite direction (i.e., toward the rear wall). As these gases contact the wall, their kinetic energy is converted into internal energy. The resulting pressure increase creates compression waves that interact with the deflagration wave, thereby establishing a mechanism of flame acceleration. Because the accelerating deflagration wave is creating a compression field in the unreacted explosive, a complicated nonsteady flow develops.

This complex flow is illustrated by a series of particle velocity-distance diagrams in Fig. 6 (20). In Fig. 6, the deflagration wave is shown as a discontinuity for simplicity but it actually has a finite width. In Figures 6a and 6b, the positive particle velocity of the compressed, unreacted explosive is less than the negative particle velocity imparted by deflagration, so a compression zone is required to bring the particle velocity to zero at the rear boundary. Figure 6c shows the unique case in which the particle velocity lost in deflagration exactly balances the particle velocity previously gained in compres-

sion. At later times, as illustrated in Fig. 6d, the forward momentum is not totally destroyed by deflagration, and a rarefaction wave is created behind the flame to satisfy the rare boundary condition. However, once the compression zone behind the flame no longer exists, this flame acceleration mechanism also vanishes. The associated compression field preceding the flame must then be strong enough to shock-initiate the unreacted explosive for DDT to occur.

Although an exact solution of the complex nonsteady flow field resulting from deflagration in a closed tube is extremely difficult, two analytical models of flame acceleration that provide upper and lower deflagration velocity limits have been formulated by considering the nature of the deflagration process. For a detonation wave, the CJ state represents the only stable end state for the products (21), but the end state of a deflagration wave may be represented by any point on the weak deflagration

(a) PRESSURE-VOLUME

(b) PRESSURE-PARTICLE VELOCITY
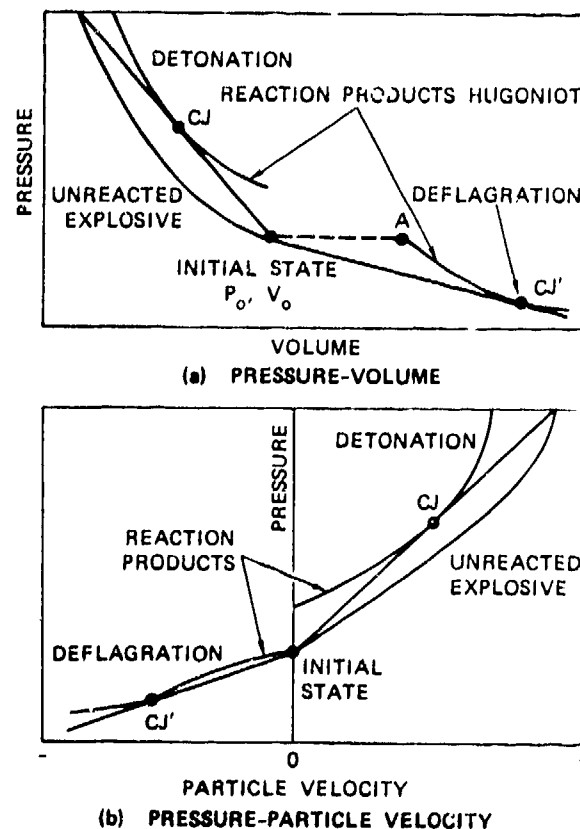
Fig. 5. Pressure-Volume and Pressure-Particle Velocity Diagrams for Deflagration and Detonation

238
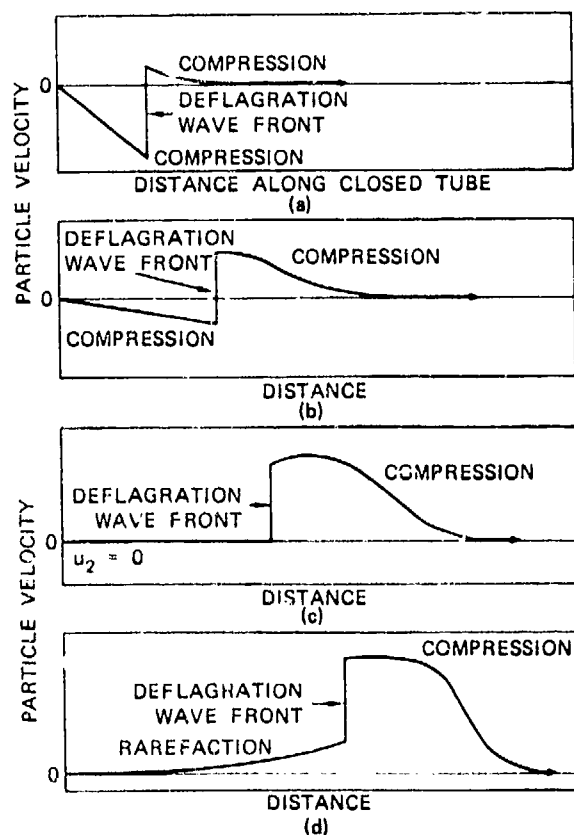
Fig. 6. Particle Velocity-Distance Diagrams for Accelerating Deflagration Waves

branch of the Hugoniot curve (22), which is bounded by points A and CJ' in Fig. 5. Point A corresponds to a constant pressure deflagration in which no particle velocity is produced and point CJ' corresponds to the maximum possible deflagration and particle velocities and pressure drop.

Combining the flame acceleration mechanism and the properties of deflagration waves led to the formulation of two analytical models of flame acceleration that treat deflagration waves as reactive discontinuities. One model, originally used by Adams and Pack (23) for DDT calculations in gases, consists of the compression region followed by deflagration wave whose velocity is always such that the forward momentum imparted to the explosive by the compression waves is exactly canceled out by the loss in forward momentum caused by deflagration. The Adams and Pack model does not require a rarefaction or compression wave to satisfy the rear boundary

condition, and all of its states are represented by Fig. 6c. Since the change in particle velocity with distance behind the flame is zero, the change in pressure at the rear boundary with time must also be zero. Although this model conserves momentum, it is not physically correct because it contains no flame acceleration or rear wall pressure-time increase mechanisms. However, the Adams and Pack model provides lower limits of the deflagration velocity and pressure drop across an accelerating deflagration wave, because any faster deflagration produces negative particle velocity and thus possesses the buildup mechanisms.

The second model of flame acceleration assumes that the deflagration is always a CJ deflagration with the largest possible velocity and pressure drop associated with a certain initial pressure. This model definitely includes the flame-acceleration and rear-wall pressure-increase mechanisms exhibiting all of the flow situations shown in Fig. 6. This CJ deflagration model was discussed for DDT in gases by Troshin (24). An interesting state where the two models predict the same velocity and brunt gas pressure is represented by Fig. 6c. For the CJ deflagration, this state corresponds to the end of the flame acceleration mechanism of compression waves overtaking the deflagration wave. Table 3 shows the calculated properties of this state behind a shock wave in cast TNT and cast pentolite 50/50. The resulting shock pressures, 95 kbar for cast TNT and 129.5 kbar for cast pentolite 50/50, are too high to indicate a criterion for DDT, because pentolite, which readily undergoes DDT, has a shock sensitivity of about 20 kbar (25) and cast TNT, which does not undergo DDT, can be initiated by a 60-kbar shock (17).

TABLE 3

Conditions Required for a CJ Deflagration to a Zero Particle Velocity End State Behind a Shock Wave

	Cast TNT	Cast Pentolite 50/50
Shock pressure in explosive (kbar)	95.0	129.5
CJ deflagration velocity (mm/μsec)	3.116	3.504
CJ pressure after deflagration (kbar)	43.5	63.4

239

Therefore, some other criterion for flame acceleration determines whether a cast explosive undergoes DDT.

These two analytical models of flame acceleration were used to make DDT calculations for cast pentolite, which is the only explosive for which a complete set of the required data was available. The method-of-characteristics part of Macek's analysis was used to predict the time and distance to shock formation ahead of the flame. The pressure-time histories used were those of Macek (3) up to one kilobar

$$P_2 = (0.08 \text{ kbar})e^{0.12t} \qquad (4)$$

and the more recent data of Price and Wehner (25) above one kilobar

$$P_2 = (1 \text{ kbar})e^{0.08856(t - 21.05)} \qquad (5)$$

where P_2 is the pressure behind the deflagration and t is in microseconds.

The conditions ahead of the flame were determined by the equations for an isentropic compression with n = 3 in the modified Tait equation. The equations for the density ρ_1, particle velocity u_1, C_+ characteristics ($u_1 + c_1$), and internal energy E_1 in terms of the pressure P_1 in the compressed unreacted explosive are

$$\rho_0 = \rho_1 \left(1 + \frac{3P_1}{\rho_0 c_0^2} \right)^{-1/3} \qquad (6)$$

$$u_1 = c_0 \left[\left(1 + \frac{3P_1}{\rho_0 c_0^2} \right)^{1/3} - 1 \right] \qquad (7)$$

$$u_1 + c_1 = c_0 \left[2 \left(1 + \frac{3P_1}{\rho_0 c_0^2} \right)^{1/3} - 1 \right] \qquad (8)$$

$$E_1 - E_0 = \frac{P_1}{2\rho_1} - \frac{c_0^2}{2} \left(1 - \frac{\rho_0}{\rho_1} \right) \qquad (9)$$

The conservation equations across the deflagration wave are

$$(\text{MASS}) \ \rho_1(W - u_1) = \rho_2(W - u_2) \qquad (10)$$

$$(\text{MOMENTUM}) \ P_1 + \rho_1(W - u_1)^2 = P_2 \\ + \rho_2(W - u_2)^2 \qquad (11)$$

$$(\text{ENERGY}) \ E_1 + \frac{P_1}{\rho_1} + \frac{(W - u_1)^2}{2} + Q = E_2 \\ + \frac{P_2}{\rho_2} + \frac{(W - u_2)^2}{2} \qquad (12)$$

where the subscript 2 denotes the state behind the deflagration wave, W is the deflagration velocity and Q is the heat of reaction. The equation of state for reaction products is

$$P_2 \rho_2^{-K} = \text{constant} \qquad (13)$$

and

$$E_2 + P_2/\rho_2 = \frac{K}{K - 1} \frac{P_2}{\rho_2} \qquad (14)$$

where K is the adiabatic expansion coefficient determined at the CJ detonation state through the equation

$$P_{CJ} = \frac{\rho_0 D^2}{K + 1} = 2(K - 1)Q \qquad (15)$$

where D is the detonation velocity.

In the Adams and Pack model of zero particle velocity behind the deflagration, u_2 is set equal to zero and the resulting equation for the deflagration velocity in terms of state 1 is

$$W^2 + \frac{W}{u_1} \left[(K - 1)(Q + E_1) - \frac{P_1}{\rho_1} + \frac{K - 3}{2} u_1^2 \right] \\ - (K - 1) \left(Q + E_1 + \frac{P_1}{\rho_1} + \frac{u_1^2}{2} \right) = 0 \qquad (16)$$

240

The pressure P_2 and density ρ_2 are then calculated from Eqs. (10) and (11) with $u_2 = 0$. Table 4 lists the input data on pentolite 50/50 required for the calculations and the calculated values of u_1, $u_1 + c_1$, W, and P_2 for various values of P_1, the pressure in the compressed, unreacted explosive. As shown in Table 4, the calculated deflagration velocities W are roughly 300 times faster than predicted by the linear pressure-burning rate relationship, Eq. (3). Gibson and Macek (12) actually observed deflagration wave velocities of $10^5 - 2 \times 10^5$ cm/sec, so these calculated velocities appear to be of the correct magnitude. The closeness of the values for P_1 and P_2 clearly shows that the flame in the Adams and Pack model is a nearly constant pressure deflagration (corresponding to point A in Fig. 5) for pressures below 20 kbar.

The only other quantity required for a distance-time plot for DDT similar to that in Fig. 4 for pentolite using this model is the position of the flame front as a function of time, $x(t)$, which is derived from

$$x(t) = \int_0^t W(t)\, dt \qquad (17)$$

where $W(t)$ is determined from the dependence of W on P_2 in Table 4 and the dependence of P_2 on time from Eqs. (4) and (5). Figure 7 shows the resulting distance-time plot for pentolite using the Adams and Pack model of deflagration behind an isentropic compression. In comparing Fig. 7 with Fig. 4, the Adams and Pack model predicts a much more rapid deflagration and thus a greater penetration of the flame into the explosive. However, the time and distance required for shock formation are approximately the same in both diagrams.

These DDT predictions must also be compared with those for a CJ deflagration following an isentropic compression. At the CJ state, $W = u_2 + c_2$, or

$$(W - u_2)^2 = K\, \frac{P_2}{\rho_2} \qquad (18)$$

TABLE 4

Input Data for Pentolite and Results for Deflagration Waves in Pentolite (Adams and Pack Model)

P_1 (kbar)	P_2 (kbar)	u_1 (cm/sec)	W (cm/sec)	$u_1 + c_1$ (cm/sec)
1	0.9998	2.440×10^3	2.489×10^3	2.479×10^5
2	1.9984	4.831×10^3	5.023×10^3	2.527×10^5
4	3.988	9.481×10^3	1.0228×10^4	2.620×10^5
7	6.937	1.6151×10^4	1.8358×10^4	2.753×10^5
10	9.815	2.249×10^4	2.700×10^4	2.880×10^5
20	18.75	4.171×10^4	5.700×10^4	3.264×10^5
30	26.36	5.864×10^4	8.860×10^4	3.603×10^5
40	32.56	7.385×10^4	1.201×10^5	3.907×10^5
70	44.47	1.1244×10^5	2.054×10^5	4.678×10^5
100	50.28	1.4410×10^5	2.738×10^5	5.311×10^5
123.8 (CJ state)	52.62	1.6597×10^5	3.186×10^5	5.749×10^5

Data on Pentolite
Density = 1.67 g/cm^3
C_o = 2.43 × 10^5 cm/sec
D = 7.47 × 10^5 cm/sec
PCJ = 259 kbar
K = 2.598
Q = 1.16 kcal/g

Substituting Eq. (18) into the conservation Eqs. (10)-(12) and solving for P_2 yields the following relationship

$$P_2 = (K - 1)\rho_1(Q + E_1)$$

$$\left[1 - \sqrt{1 - \frac{(2Q + 2E_1 + P_1/\rho_1)P_1}{\rho_1(K^2 - 1)(Q + E_1)^2}} \right]. \quad (19)$$

and solving for ρ_2 gives

$$\rho_2^{-1} = \frac{(K - 1)(Q + E_1 + P_1/\rho_1)}{KP_1}$$

$$\left[1 + \sqrt{1 - \frac{K^2(2Q + 2E_1 + P_1/\rho_1)P_1}{\rho_1(K^2 - 1)(Q + E_1 + P_1/\rho_1)^2}} \right]. \quad (20)$$

The particle velocity u_2 behind the deflagration and the deflagration velocity W are then calculated from Eq. (18) and

$$W - u_1 = (W - u_2) \frac{\rho_2}{\rho_1} = \left(\frac{KP_2}{\rho_2}\right)^{1/2} \frac{\rho_2}{\rho_1} \quad (21)$$

Table 5 lists the calculated states for a CJ deflagration in isentropically compressed pentolite at various pressures and Fig. 8 is the distance-time plot for DDT for the CJ deflagration model. The pressures P_2

behind the CJ deflagration wave are much lower than the corresponding values for the Adams and Pack model at low initial pressures P_1, and the CJ deflagration velocities are nearly twice as large as those in Table 4. In terms of the time and distance to DDT, the CJ deflagration front moves a greater distance into the explosive, and the shock formation occurs in a shorter time (about 80 μsec in Fig. 8 compared with 90 μsec in Fig. 7), whereas the distance to shock formation increases (about 14 cm in Fig. 8 compared with about 13 cm in Fig. 7). Since these two analytical models represent upper and lower limits to the deflagration rate, the critical time and distance for DDT in cast pentolite 50/50 should be bracketed by these results if the isentropic compression of cast pentolite 50/50 obeys Eq. (2) with n = 3. More fully instrumented DDT experiments on pentolite are required to test the validity of these results.

Because the objective of this study is to formulate a DDT model for primary explosives, calculations using the modified Macek model were made for lead azide, the only primary for which some of the required data exist. The processes of SDT (8) and DDT (9) have been studied to a limited extent in lead azide. Chaudhri and Field (9) observed very fast deflagration waves in hot-wire initiation tests on single lead azide crystals of thicknesses below the critical thickness for DDT. By photographing the deflagrating crystals under water, the velocities and pressures of the shock waves produced in the surrounding water by the rapid deflagration of lead azide were measured. These pressure data, combined with Chaudhri and Field's framing camera records of the
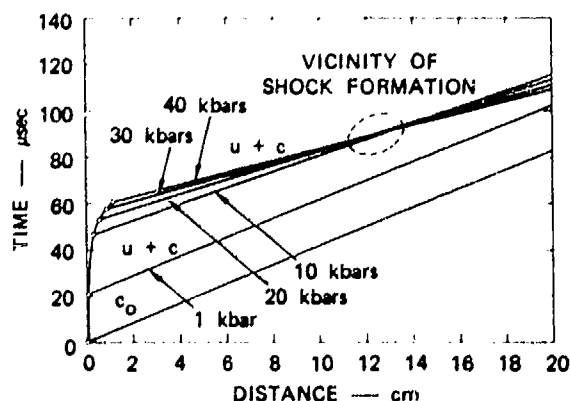
Fig. 7. Distance-Time Diagram for Shock Formation in Cast Pentolite 50/50 Using the Adams and Pack Model of Deflagration
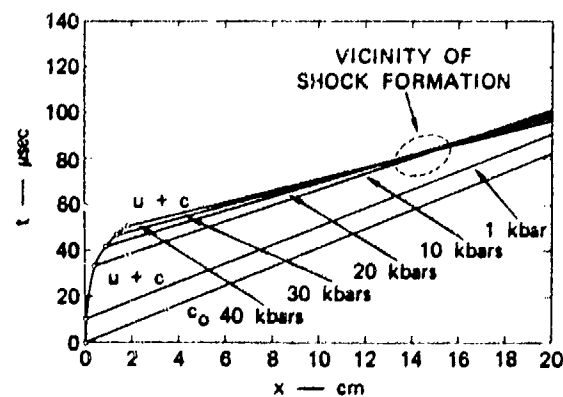
Fig. 8. Distance-Time Diagram for Shock Formation in Cast Pentolite 50/50 Ahead of a CJ Deflagration Wave

242

ignition process, provided a rough estimate of the pressure-time history in the deflagration region. Chaudhri's measurements (26) of the sound velocity and shock initiation of lead azide crystals and Davies' measurements (8) of the unreacted Hugoniot and sound velocity in lead azide pressed to a density of 3.4 g/cm³ provided data on the properties of lead azide in the compression zone ahead of the deflagration wave. These data were used in the two models of deflagration discussed in the previous section to make calculations of the times and distances for DDT in lead azide crystals and pressed lead azide and for SDT in pressed azide.

To calculate the time and distance required for DDT in lead azide crystals, the pressure data obtained by Chaudhri and Field (9) were related to the time after ignition. The actual pressures measured were those of the shock waves produced in water as the lead azide deflagration front reached the end of the crystal. The acoustic approximation developed by Deal (27) for a detonation wave propagating into an inert material is used for the pressure in the lead azide, P_{LA}, given by

$$P_{LA} = P_W \left(0.5 + \frac{\rho_{LA} U_{LA}}{\rho_W U_W} \right) \qquad (22)$$

where P_W is the measured water pressure, ρ_W is the density of the water, U_W is the measured shock velocity in the water, ρ_{LA} is the measured density of α-lead azide crystals (4.60 g/cm³), and U_{LA} is the measured velocity of propagation of the reaction front in the lead azide. Table 6 lists the measured values and the calculated pressures in the lead azide

TABLE 5

CJ Deflagration Wave Calculations for Isentropically Compressed Pentolite

P_1 (kbar)	P_2 (kbar)	u_2 (cm/sec)	W (cm/sec)
1	0.2799	-2.044×10^5	4.500×10^3
2	0.5637	-2.019×10^5	8.910×10^3
4	1.1426	-1.958×10^5	1.7503×10^4
7	2.038	-1.870×10^5	2.986×10^4
10	2.966	-1.782×10^5	4.170×10^4
20	6.261	-1.5253×10^5	7.767×10^4
30	9.835	-1.3208×10^5	1.0962×10^5
40	13.65	-1.1304×10^5	1.3862×10^5
70	26.32	-6.539×10^4	2.130×10^5
100	38.54	-2.247×10^4	2.719×10^5
123.8	52.62	0	3.186×10^5

TABLE 6

Pressures and Wave Velocities from Chaudhri and Field's (9) Experiments on α-Lead Azide Crystals

Crystal Thickness (μm)	Lead Azide Deflagration Velocity (mm/μsec)	Water Shock Velocity (mm/μsec)	Water Shock Pressure (kbar)	Calculated Lead Azide Pressure (kbar)
310	2.50	1.67	1.3	5.14
560	2.90	1.72	2.0	8.76
670	2.62	1.90	3.5	12.85

crystals. Since P_{LA} is the pressure at the front of the wave, it corresponds to P_1, the pressure in the unreacted explosive. These pressures were related to the time after ignition by examination of Chaudhri and Field's framing camera records of these reactions. In these records, the framing rate was 0.7 μsec between frames and the transition from ignition to full development of the steady deflagration velocity for a certain crystal thickness took less than one frame. Thus the calculated pressures P_{LA} were assumed to be attained in less than 0.7 μsec. The largest pressure P_{LA} (12.85 kbar) was assumed to be developed in exactly 0.7 μsec, and the other two pressures were assumed to occur at times of 0.7 μsec minus the difference in crystal thicknesses divided by the average deflagration velocity (2.7 mm/μsec) in these experiments. The resulting pressure-time curve was of the form

$$P_{LA} = P_1 = (0.1 \text{ kbar}) e^{6.94t} \qquad (23)$$

where t is in microseconds.

The particle velocity u_1 in the unreacted lead azide was related to P_1 using the relationship

$$P_1 = \rho_0 c_0 u_1 \qquad (24)$$

which was found by Davies et al. (8) to hold for pressed lead azide at pressures below 10 kbar.

Chaudhri and Field (9) reported a propagation rate for a low amplitude longitudinal stress wave in lead azide crystals of 2.15 $\pm$ 0.3 mm/μsec. This value was taken for c_0 in these calculations. Actually, if the sound velocity is 2.15 mm/μsec, the waves that Chaudhri and Field (9) refer to as fast deflagration waves are supersonic and therefore represent low-velocity detonation waves (LVD) that cannot develop into high-velocity detonation (HVD) because of rapid pressure decay at the edges of the crystal. A phenomenon similar to LVD has been observed by Leopold (28) for lead azide pressed to high densities (3.75 g/cm^3).

Table 7 lists the input data for crystalline lead azide and the results of calculations at various initial pressures for the two deflagration models, the Adams and Pack model and the CJ deflagration model. The calculated deflagration velocities for both models are an order of magnitude lower than those observed by Chaudhri and Field (9), while the velocities of C_+ characteristics ($u_1 + c_1$) are of that magnitude ($\sim 2.5 \times 10^5$ cm/sec). Figures 9 and 10 show the distance-time diagrams for DDT in α-lead crystals predicted by the Adams and Pack and the CJ deflagration models, respectively. The calculated distances for DDT are approximately 2 mm. This agrees with the observed behavior of lead azide crystals of varying thickness. Crystals less than 2 mm thick cannot undergo the DDT that thicker crystals readily make.

TABLE 7

Input Data for α-Lead Azide Crystals and Deflagration Velocity Calculations

Data on α-Lead Azide

$\rho_0 = 4.60$ g/cm^3 $\qquad\qquad$ $K = 3,199$

$Q = 115$ kcal/m $= 1.652 \times 10^{10}$ erg/g $\quad c_0 = 2.15$ mm/μsec

DDT Calculations

P_1 (kbar)	u_1 (cm/sec)	$u_1 + c_1$ (cm/sec)	Adams and Pack Model ($u_2 = 0$)		CJ Deflagration Model	
			P_2 (kbar)	W (cm/sec)	P_2 (kbar)	W (cm/sec)
5.14	5197	2.252×10^5	5.127	5.711×10^3	1.269	1.154×10^4
8.76	8857	2.324×10^5	8.698	1.032×10^4	2.214	1.943×10^4
12.85	1.299×10^4	2.403×10^5	12.65	1.608×10^4	3.325	2.813×10^4
25.78	2.607×10^4	2.644×10^5	24.31	3.712×10^4	7.080	5.388×10^4
101.7	1.0283×10^5	—	38.68	2.019×10^5	(CJ + u_2 = 0 models coincide)	
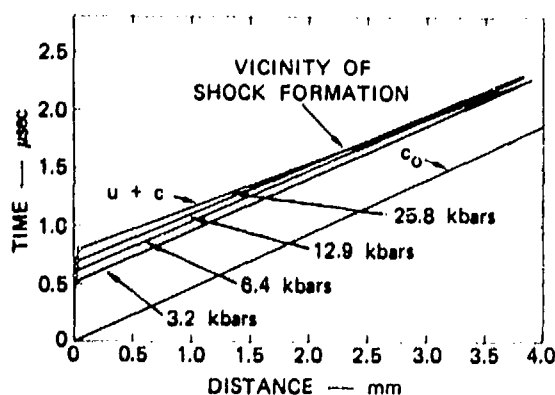
Fig. 9. Distance-Time Diagram for DDT in α-Lead Azide Crystals Using Adams and Pack Deflagration Model
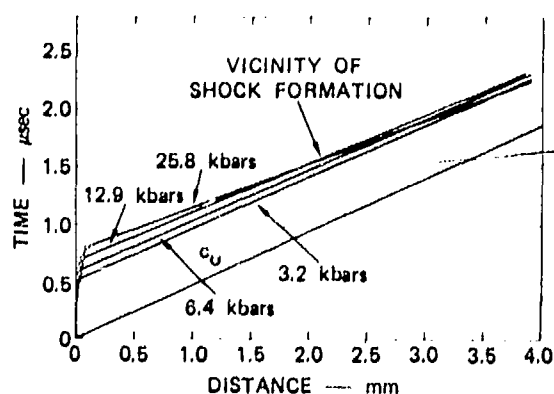
Fig. 10. Distance-Time Diagram for DDT in α-Lead Azide Crystals Using a CJ Deflagration Model

The calculated times to DDT are approximately 2 μsec and thus agree with the preliminary results of Slagg (29), who has measured times for DDT of 3 ± 2 μsec for lead azide crystals.

The DDT calculations for crystalline lead azide exhibit order-of-magnitude agreement with the experimental results, and this is all that can be expected at the present time. The exact nature of the rapid deflagration or LVD waves in lead azide crystals is unknown. The framing camera records of the process indicate that some reaction occurs at the front of the wave (9). The overall description of DDT appears to be valid, but the effect of reaction on the characteristics used in the shock formation part of the model needs to be considered.

The recent SDT experiments on pressed lead azide by Davies et al. (8) pioneered the use of stress gages in thin flyer plate impacts of primary explosives and also yielded data on the unreacted Hugoniot and on the time and distance for SDT. For lead azide pressed to a density of 3.4 g/cm^3, Davies found that stress waves propagate at 1.23 mm/μsec, which implies that the Hugoniot curve is

$$P_1 = 41.7 \, u_1 \qquad (25)$$

For both long pulses (3.5 μsec) and short pulses (0.1 μsec), in the 6-9 kbar range, Davies (8) observed that the transition to detonation took about 2 μsec and occurred 1-3 mm into the sample of pressed lead azide. To determine whether the theoretical approach to DDT developed in this report would predict similar times and distances, this unreacted Hugoniot for pressed lead azide and the pressure-time relationship of Eq. (23) were used in the CJ deflagration model to calculate the distance-time diagram shown in Fig. 11. This calculation predicts a shorter time (1.2 μsec) and distance (0.9 mm) for pressed lead azide than for crystalline lead azide. This is mainly due to the lower sound velocity in pressed lead azide, which allows the compression waves to overtake each other more quickly. To compare a prediction of the CJ deflagration model to Davies' results, the SDT calculation shown in Fig. 12 was made for an 8-kbar shock that causes the deflagration to begin about 0.6 μsec later in agreement with Eq. (23). This calculation resulted in the formation of a second shock wave caused by the crossing of the characteristics ahead of the flame. This second
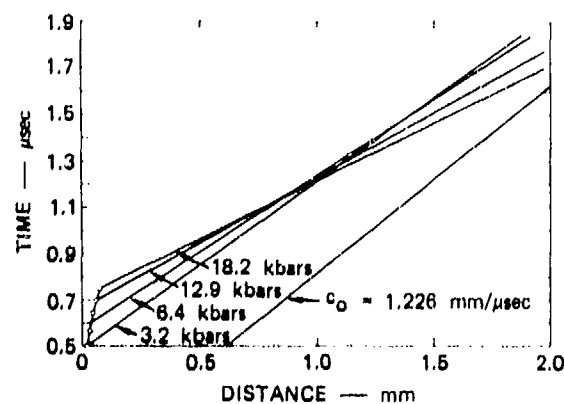
Fig. 11. Distance-Time Diagram for DDT in Pressed Lead Azide ($\rho_o = 3.4 \, g/cm^3$) Using a CJ Deflagration Model
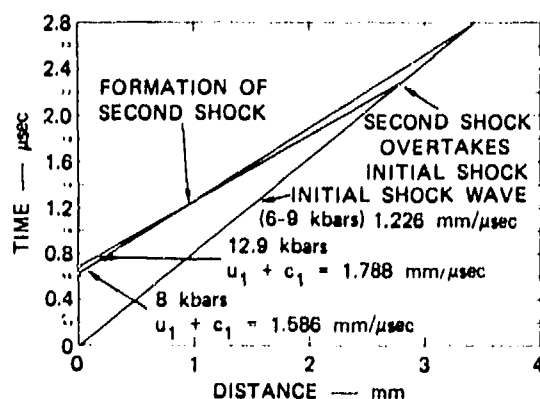
Fig. 12. Distance-Time Diagram for SDT in Pressed Lead Azide

shock wave may cause detonation at $1.3~\mu sec$ and 1.1 mm, or detonation may result when the second shock overtakes the initial shock at $2.3~\mu sec$ and 2.8 mm. Some of Davies' (8) gage records did appear to detect two finite strength shocks at 1 or 2 mm into the explosive in tests where detonation occurred at 3-4 mm. Again the order of magnitude agreement between the SDT calculation and Davies' (8) results is all that can be expected at the present time.

CONCLUSIONS

The main conclusions derived from the results of the DDT experiments on cast 1-MNT and cast 2-MNT are:

- Cast 2-MNT is a much better primary than cast 1-MNT because 2-MNT charges were readily initiated by a capacitor charging voltage of 110 volts, whereas 1-MNT charges were rarely initiated even at 375 volts.

- Cast 2-MNT is a good primary in its ignition and DDT properties since its threshold voltage is close to that of pressed lead azide, its time to ignition is less than that of pressed lead azide, and the mean time required for DDT is longer than that of the lead azide but shorter than that of lead styphnate.

- The critical length for DDT in cast 2-MNT is approximately 2-3 mm, and the critical time

required for the full development of detonation in the DDT process is roughly $8~\mu sec$.

The analysis of Macek's model for DDT in cast explosives revealed a physically unrealistic description of the accelerating flame. Modification of Macek's model to include the limiting cases of a nearly constant pressure deflagration and a CJ deflagration showed that the deflagration velocities in cast pentolite during DDT must be 250-500 times faster than the burning velocities in explosives at high ambient pressures (16). Deflagration velocities of this order of magnitude have been observed in cast explosives by Gibson and Macek (12) and in porous explosives by Bernecker and Price (4). From the results of the DDT and SDT calculations on pentolite and lead azide, it is apparent that reliable experimental data on pressure-time histories in the deflagration region, on deflagration velocity, and on shock formation ahead of the flame are scarce. Thus a good test of the modified Macek approach to DDT cannot be made on primary or secondary explosives. Well-instrumented DDT experiments on primary explosives are critically needed to provide the next step toward an understanding of DDT in primaries.

REFERENCES

1. R. Shaw, "Structure-Property Correlations in Primary Explosives," paper presented at the International Conference on Research in Primary Explosives at the Explosives Research and Development Establishment, Waltham Abbey, England, Mar. 1975.

2. J. M. Guimont, M. E. Hill, R. Shaw, and C. M. Tarver, "Structure/Property Correlations in Primary Explosives," SRI Technical Progress Report 75-2 (Annual), Project PYU-3692, Menlo Park, CA, Sept. 1975.

3. A. Macek, "Transition from Deflagration to Detonation in Cast Explosives," *J. Chem. Phys.* 31, 162, 1959.

4. R. R. Bernecker and D. Price, "Studies in the Transition from Deflagration to Detonation in Granular Explosives—III. Proposed Mechanisms for Transition and Comparison with Other Proposals in the Literature," *Combust. Flame* 22, 161, 1974.

5. H. S. Leopold, "A New Technique for Detecting the Initial Reaction of Primary Explosives Initiated by Hot Wire," NOLTR 69-148, Nov. 7, 1969.

6. H. M. Peters, R. L. Simon, Jr., W. G. Blucher, D. L. Ross, and T. C. Goodale, "Synthesis and Testing of Primary Explosives," Final Report, Project PYU-2044, Menlo Park, CA, Dec. 1972.

7. R. A. Henry and W. G. Finnigan, "Mono-Alkylation of Sodium 5-Aminotetrazole in Aqueous Medium," *J. Amer. Chem. Soc.* **76**, 923, 1954.

8. F. W. Davies, A. B. Zimmerschied, F. G. Borgardt, and L. Avrami, "The Hugoniot and Shock Initiation Threshold of Lead Azide," *J. Chem. Phys.* **64**, 2295, 1976.

9. M. M. Chaudhri and J. E. Field, "Deflagration in Single Crystals of Lead Azide," Fifth Symposium (International) on Detonation, Office of Naval Research, ACR-184, Pasadena, CA, 1970, p. 301.

10. G. B. Kistiakowsky, "Initiation of Detonation of Explosives," Third Symposium on Combustion, Flame, and Explosion Phenomena, Williams and Wilkins, Baltimore, MD, 1949, p. 560.

11. A. R. Ubbeholde, "Transition from Deflagration to Detonation," Third Symposium on Combustion, Flame, and Explosion Phenomena, Williams and Wilkins, Baltimore, MD, 1959, p. 566.

12. R. W. Gibson and A. Macek, "Flame Fronts and Compression Waves During Transition from Deflagration to Detonation in Solids," Eighth Symposium (International) on Combustion, Williams and Wilkins, Baltimore, MD, 1962, p. 847.

13. C. T. Zovko and A. Macek, "A Computational Treatmer : of the Transition from Deflagration to Detonation in Solids," Third Symposium (International) on Detonation, Office of Naval Research, 1960, p. 606.

14. A. Macek, "Sensitivity of Explosives," *Chem. Rev.* **62**, 41, 1962.

15. R. Courant and F. Ol Friedricks, *Supersonic Flow and Shock Waves,* Interscience Publishers, Inc., New York, 1948, p. 87.

16. K. K. Andreev and S. V. Chuiko, "Transition of the Burning of Explosives into an Explosion. I. Burning of Powdered Explosives at Constant High Pressures," *Russian J. Phys. Chem.* **37**, 695, 1963.

17. M. Cowperthwaite and J. T. Rosenberg, "A Multiple Lagrange Gage Study of the Shock Initiation Process in Cast TNT," Sixth Symposium (International) on Detonation, 1976.

18. J. T. Rosenberg and D. F. Walter, "Development of Two Improved Output Tests and Detonator-Detonating Fuse Devices," SRI Final Report on Project PYU-2691, Menlo Park, CA, May 1974.

19. S. J. Jacobs, private communication.

20. Ya. B. Zel'dovich and A. S. Kompaneets, *Theory of Detonation,* Academic Press, New York, 1960, p. 112.

21. J. Taylor, *Detonation in Condensed Explosives,* Clarendon Press, Oxford, 1952, Chapter VI.

22. B. Lewis and G. Von Elbe, *Combustion, Flames and Explosions of Gases,* Academic Press, New York, 1960, Chapter V.

23. G. K. Adams and D. C. Pack, "Some Observations on the Problem of Transition Between Deflagration and Detonation," Seventh Symposium (International) on Combustion, Butterworths, London, 1959, p. 812.

24. Ya. K. Troshin, "The Generalized Hugoniot Adiabatic Curve," ibid, p. 789.

25. D. Price and J. F. Wehner, "The Transition from Burning to Detonation in Cast Explosives," *Combust. Flame* **9**, 73, 1965.

26. M. M. Chaudhri, "Shock Initiation of Fast Decomposition in Crystalline Solids," *Combust. Flame* **19**, 419, 1972.

27. W. E. Deal, "Measurement of Chapman-Jouguet Pressure for Explosives," *J. Chem. Phys.* **27**, 796, 1957.

28. H. S. Leibpold, "The Growth to Detonation of Binary Explosive Mixtures," NOLTR63-129, April 16, 1963.

29. N. Slagg, private communication.

DISCUSSION

S. J. JACOBS
U.S. Naval Surface Weapons Center

I find the authors' calculations of the deflagration speeds required to produce an exponentially rising pressure in the unreacted explosive most interesting. It appears to me that for each pressure in an isentropic compression the authors have computed the necessary deflagration speed to create that pressure for either the product state at rest or the product state satisfying the conditions of a CJ deflagration. The solutions are then put together to approximate a continuous build-up relation. This is a novel approach which appears to be plausible. Steven Coffey and I have solved a related problem to get an estimate of the deflagration rates which would be needed to maintain a given pressure in a shock ahead of the burn rather than in a compression wave. The model is that in Figure 1 of Adams and Pack (authors' Ref. 23). The input data and equations which we used are fairly similar to those used by the authors and the results, deflagration speed as a function of pressure, are not too different from the authors' results for the case where the particle flow is zero behind the deflagration. I would like to point out, however, that deflagration speed should be defined relative to the moving compressed medium ahead of the burn. This is the speed which must be related to reaction rates. In fact it would be more appropriate to use mass burning rates, $\rho(W - u_1)$, as given in the authors' Equation (10) as a basis for defining the decomposition. This is the common practice in the Russian literature. My figure shows the results of the authors' work and ours when the rate, $W - u_1$, is plotted against the pressure. We see that at pressures below about 20 kilobars the required burning rate varies approximately as the square of the pressure for the case in which the flow comes to rest behind the deflagration. The CJ rates are considerably higher at these pressures. It seems to me that the CJ condition is unlikely to be approached at the lower pressures. Most experiments require a fair amount of confinement to establish DDT and this confinement, even though not perfect, would limit the flow behind the deflagration at low pressures to a very small value.

I must take exception to the statement that "Macek's linear pressure/burning rate relationship can account for the experimental p - t relation only when the surface area of the burning front is 20,000 times the original surface area of the cast explosive". I have plotted on my figure the approximate linear burning rate used by Macek. It can be seen that the linear burning rate curve would intersect the required curve at about 300 bars. The required rate and corresponding surface increase at 10 kilobars is about 50 to 100 times that given by the linear burning rate curve. Above 10 kilobars reaction initiated by the shock or compression wave is likely to make any discussion of burning rates relatively meaningless. In the range 0.3 to 10 kilobars the implication is that the anomolous effect on mass deflagration increases the effective pressure exponent from one to two. It is unlikely that his increase can be related to an unusual reaction which starts with heat transfer as the only stimulus. I think the mechanical means can account for the runaway burn. Obviously further study is needed.

REPLY BY C. TRAVER

I would like to clarify the final point raised by Dr. Jacobs concerning Dr. Macek's attempt to account for the experimental pressure-time data with a linear pressure-burning rate relationship. In his original DDT paper (our reference 3), Dr. Macek developed an adiabatic flame model based on the linear pressure-burning relationship shown as line 5 in Figure J1. This adiabatic flame model was fitted to the experimental pressure history with an adjustable parameter that included the burning surface area. The numerical value of this burning surface area required to match the experimental pressures was more than 20,000 times the original surface area of the cast explosive. To predict these experimental pressure histories and the rapid deflagration velocities observed by Gibson and Macek (our reference 12), I believe that a realistic model of DDT in cast explosives should include both the mechanical means of increasing the burning surface and an effective pressure exponent of approximately two.

ON THE MECHANISM OF DEFLAGRATION TO DETONATION TRANSITION
IN GAS-PERMEABLE HIGH EXPLOSIVE

A. A. Sulimov, B. S. Ermolaev, A. A. Borisov
A. I. Korotkov, B. A. Khasainov, V. E. Khrapovsky
Institute of Chemical Physics
USSR Academy of Sciences, Moscow, 117334

Main stages of deflagration to detonation transition in porous PETN are considered, including gas penetrative (convective) burning (CB) and low velocity detonations (LVD). The propagation velocity of the process is shown to be determined substantially by the pressure in a lead zone and exhibited only a slight dependence on the rate of pressure rise. The critical pressures of normal burning-CB-LVD-normal detonations transitions are given. Using streak camera and pressure gauges the CB and LVD processes are studied, and the conditions of the steady-state regimes are determined. The propagation velocity is found to be highly dependent on the pressure in lead zone. Experimental results are compared with the theoretical models.

INTRODUCTION

Deflagration in porous high explosives confined in metal tubes is known to tend to accelerate when the charge is ignited with a relatively weak ignition source. This acceleration eventually results in detonation if the charge is long enough. The main transient stages between the normal layer-by-layer combustion and the normal detonation are convective burning (CB) and low velocity detonation (LVD). The mechanisms of the latter two are still far from complete understanding because of the poor reproducibility and stability of the process and its strong dependence on the experimental conditions. CB and LVD differ in the mechanism of the reaction initiation. Combustion products in the case of CB penetrate through pores into the unreacted explosive overtake the flame front and preheat the walls of pores up to the ignition point (1). The initiation of the reaction in LVD is due to collapse of pores and to the plastic flow in the compression (shock) wave, which leads the LVD (1). However there is one common feature which makes CB and LVD different from normal burning and normal detonations, that is a rather small part of the total energy released in the vicinity of the front (less than

10-20%). The rest of the heat is released in an extended burn-up zone due to surface burning of the grains or cavities formed in the explosive and ignited at the first stage.

The intention in undertaking this study was to determine the conditions under which CB or LVD could be stabilized (at least approximately and in charges of limited sizes) and could be investigated in details in order to elucidate the basic characteristics of these transient (in a general case) processes. It has been shown experimentally that the quasi-steady CB and LVD could not be observed over the whole range of possible propagation velocities. For instance in the case of PETN these ranges are 1-10 m/sec for CB and 1000-3300 m/sec for LVD.

CRITICAL PRESSURES

It is convenient to depict these transient processes in the $W - P_m$ plane, where W is the propagation velocity and P_m the pressure in the lead zone. In the case of CB this zone corresponds to a narrow region adjacent to the ignition front, and P_m could be

chosen as the maximum pressure in the convective burning wave. For the LVD it is reasonable to take P_m as the pressure immediately behind the lead compression wave. The $W - P_m$ plane is convenient because one can point out definite critical pressures on it: P_{tr}, P_{min}, and P_{cr}. Region $P_{tr} \leqslant P_m \leqslant P_{min}$ corresponds to CB and $P_{min} \leqslant P_m < P_{cr}$ corresponds to LVD. These critical pressures are functions of the nature of the explosive, its structure (gas permeability porosity and grain sizes), of the charge diameter, and confinement parameters.

Experimental values of W can be plotted as a single curve $W(P_m)$ for a certain range of experimental conditions and for a given explosive. This curve represents the evolution of the explosion in a porous high explosive and usually consists of several sections with markedly different sensitivity of the process to pressure variations. The effective pressure exponent of W calculated as $\nu = d \ln W/d \ln P_m$ is about 2-3 near P_{tr} and then decreases to 1.5 (and even lower in the region of nonsteady regimes) when P_m is increasing. In the LVD region $\nu = 4$ nearby P_{min} and then drops abruptly to 0.25 when the wave becomes stronger. The high value of ν is one of the causes of the poor stability of CB and LVD. Generally speaking W is a function not only of P_m, but of the time derivative of P_m as well. However, the experimental observations show that $d P_m/dt$ has only a minor influence on the critical pressure P_{tr}, and that the generation of the normal detonation is also determined mainly by the pressure in the wave and is practically independent of the wave profile in a reasonably limited range (3). This relative weak sensitivity of the CB process with respect to the pressure-time history could be understood from approximate theoretical analysis given in (4). According to (4)

$$W \sim \sqrt{r} \; P_m^{3/2} \qquad (1)$$

when the pressure in the combustion zone is proportional to $\exp(rt)$. This relation is valid when $1/r$ is assumed to be of the order of and/or less than the characteristic time of the filtration zone (that is the time of the pressure decay in the preignition region) yet much greater than the characteristic times of the preheating and ignition zones. Relation (1) shows a weak dependence of W on r. The dependence of W on P_m for PETN with the initial porosity 0.1 is illustrated in Fig. 1.
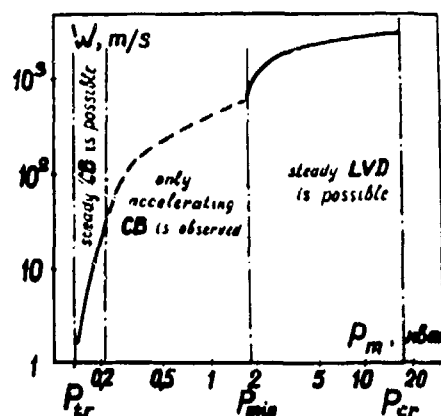
Fig. 1. Velocity of convective burning and low velocity detonation as a function of pressure (PETN, $\phi_o = 0.1$, grain size $d_o = 0.5$ mm).

Thus even from those scarce experimental and theoretical results reported one can conclude that the evolution of the explosion in porous high explosives is determined mainly by the pressure level rather than by the rate of pressure change. Certainly this is true in the case of quasi-steady stages of the process when the pressure changes caused by external sources are decoupled from the pressure changes due to CB or LVD themselves. However, the rate of pressure changes is very important in estimating the actual pressure (or velocity)-time histories of the deflagration to detonation transition but not the gross characteristics of the quasi-steady stages of the process.

Measurements of the critical pressures have been carried out for pressed PETN having a relatively low initial porosity ($\phi_o = 0.03 - 0.2$). The PETN with a narrow distribution of grain sizes around $d_o = 0.5$ mm was pressed in pellets. The lateral surfaces of the pellets were covered with a thin layer of epoxy. The charge was mounted in metal or plexiglass tubes. The constant volume bomb technique (1,2) has been used in order to measure P_{tr}. Critical pressures P_{min} and P_{cr} (for initiation of LVD and of normal detonation, respectively) have been measured using the conventional technique of shock wave initiation. Shock waves from the donor charge passed through an inert plate into the test charge. The intensity of the compression wave was regulated by changing the thickness of the plate. The experimental results are shown in Table 1.

251

TABLE I

Critical Pressures for PETN
(Charge diameter 5 mm)

Initial Porosity (ϕ_o)	P_{tr} (kbar)	P_{min} (kbar)	P_{cr} (kbar)
0.2	0.09	2.5	5.5
0.1	0.13	2.5	8.5
0.025	0.45	3.0	17.0

Unlike P_{tr} and P_{cr}, the value of P_{min} is only slightly dependent on porosity. As a consequence of this fact P_{min} is several times less than P_{cr} at lower porosities, however, the difference decreases with increasing ϕ_o.

CONVECTIVE BURNING

Nomenclature:

a — nondimensional coefficient dependent on the geometry of junction of small and large pores

c — specific heat

E — see Eq. (7)

g — see Eq. (4)

k — gas permeability

l — averaged spacing of large pores

P — pressure

Q — heat of combustion

R — universal gas constant divided by molecular weight

T_i — ignition temperature of the explosive

T_o — initial temperature

T_{ad} — adiabatic flame temperature

u — gas velocity

u_n — rate of normal burning

W — velocity of propagation of the ignition front

t — time

x — spatial coordinate

γ — specific heats ratio

δ — diameter of pores

λ — thermal conductivity

μ — viscosity

ν — pressure exponent, $d \ln W / d \ln P$

ρ — density

ϕ — porosity

ξ_f — thickness of the filtration zone

Indexes: s — solid phase, g — gas phase, 1 — larger pores, 2 — smaller pores, o — boundary between ignition and filtration zones, m — lead zone

Experiments were carried out in a transparent combustion chamber made of plexiglass. Photographic technique and piezoelectric gauges were applied in order to monitor the propagation velocity W and the pressure profiles at different points along the charge. The charge was ignited at the open end of the tube by a fast burning igniter. The igniter created a sharp jump of pressure, and then the pressure in the combustion products was maintained at a constant level within 10%. The CB proved to propagate with an approximately constant velocity when the following conditions were fulfilled:

a) porosity and gas permeability of the charge lower than certain threshold values,

b) the maximum pressure in the combustion zone and that in the combustion products maintained constant,

c) a subsonic flow of the combustion products.

Figure 2 shows W as a function of P_m for PETN with porosity 0.1. As one can see the average value of ν in the tested region is 2.7. At higher velocities and
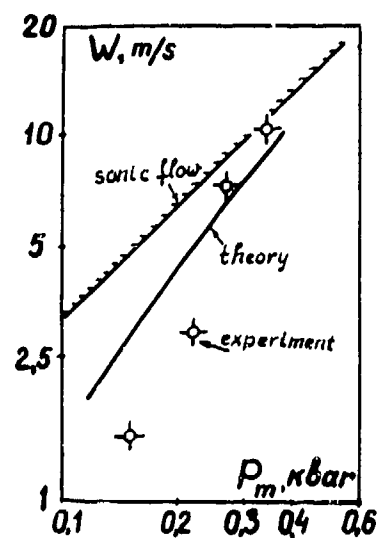
Fig. 2. Experimental (points) and theoretical dependencies of W on P_m for PETN. Shaded line corresponds to sonic flow of the combustion products.

pressures the CB accelerates very fast. Rough esti-
mations made using the streak camera and pressure
records suggest the value of ν between 1 and 1.5 in
this region.

A typical streak camera record of tne quasi-steady
CB is presented in Fig. 3

It follows from this record that CB is non-onedi-
mensional and pulsating in its nature. The periodical
decrease in the light emission at the flame front and
dark striations in the combustion products are e.-
dence of an intensive fragmentation of the explosive
in the combustion zone. Such a behavior of the defla-
gration wave is presumably caused by advanced pene-
tration of the hot gases through larger pores and by a
fast pressure rise inside the latter. Measured depths
of the pulsations (several mm) are longer than the size
of the preheat zone but less than the size of the filtra-
tion zone. The frequency is proportional to W and is
of the order of a hundred Hz.

An analytical model is suggested which gives an
approximate (at least qualitative) description of the
steady CB process. The model is based on the experi-
mental evidence that CB is led by hot gases penetrating
through larger pores. This fact was confirmed by anal-
ysis of the quenched specimens. Size distribution
curves obtained by direct microscopic measurements
of pores at cross-sections of pressed charges demon-
strated that pores with sizes ten times higher than the
average exist, and that their volume is not more than
10% of the total volume of voids. The estimated
values of relative volumes of larger pores are given in
Table 2.

The estimations are made using the data on gas
permeability (k_{exp}) for different porosities in charges

TABLE 2

Estimated Volumes of Large Pores in Pressed PETN

Porosity ϕ_0	0.45	0.3	0.25	0.1
Gas permeability ratio $k_{theor.}/k_{exp.}$	1	25	60	1100
Volume of large pores ϕ_1	0.45	(12	0.07	0.01
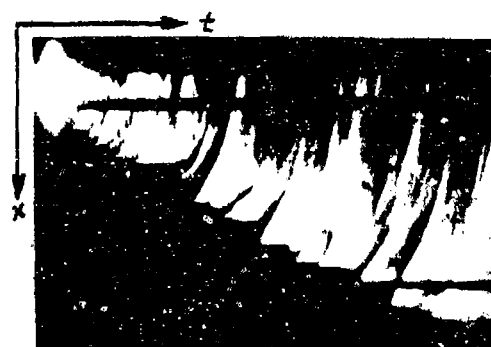
Fig. 3. Streak camera photograph of convective burning of pressed PETN.

of pressed PETN (1,2). The difference between the
experimental $k_{exp}(\phi_0)$ curve and that calculated
from the Cozeni-Karman relation is assumed to be a
consequence of the fact that the volumetric portion
of larger pores which determine the effective gas
permeability of a real charge is small compared to
ϕ_0. Smaller pores have high filtration resistance,
ignition of the explosive inside those pores is much
less probable than in larger ones because of the very
small amount of heat stored in the gas which fills up
the pore. Thus the smaller pores form an effective
sink of the gas from the larger pores. This means
that the main objection against the possibility of
steady one dimensional regimes of CB with advanced
gas penetration (13) can be avoided. Kuo, and Sum-
merfield (6), and Dubovitsky, et al. (7) have obtained
steady-state solutions for the regimes where the flow
rate of gases did not exceed the velocity of the igni-
tion front, i.e., the solid was preheated in their case
by another mechanism than the advanced filtration
of combustion products.

In the suggested model the gas is allowed to flow
through the ignition front into the unreacted sub-
stance in the steady-state case if all the gas that has
penetrated into the unreacted explosive through large
pores is accumulated in smaller pores. For conven-
ience we consider a system with two types of pores:
larger ones having diameter δ_1, gas permeability k_1,
and porosity ϕ_1 and smaller ones with the relevant
para ters δ_2, k_2, ϕ_2. It is assumed that $\delta_1 \gg \delta_2$,
$k_1 \gg k_2, \phi_1 \ll \phi_2$. The basic principles and equa-
tions for filtration in a medium having dual porosity
are given in (5). According to Barenblatt et al. (5)
the two values of pressure in gas phase are referred
to each spatial point P_1 and P_2 for large and small
pores, respectively. The equations which describe

the filtration in a system with dual porosity can be written as follows:

$$\frac{d^3\sigma}{dz^3} + \frac{d}{dz}\left(\sigma\,\frac{d\sigma}{dz}\right) - \frac{d\sigma}{dz} = 0 \qquad (2)$$

$$\pi^2 = \sigma^2 + \frac{d\sigma}{dz}. \qquad (3)$$

Here the zero point of the coordinate system is travel-ing at the velocity of CB at the boundary between the filtration zone and the preheat zone. The boundary conditions are:

$$\text{at } z = -\infty: \quad \sigma = \frac{d\sigma}{dz} = \frac{d^2\sigma}{dz^2}$$

$$\text{at } z = 0: \quad \pi = \pi_0, \quad \frac{d\pi}{dz} = \left(\frac{d\pi}{dz}\right)_0$$

where

$$\pi = P_1/P_x$$
$$\sigma = P_2/P_x$$
$$z = \xi/\xi_x$$
$$\xi = Wt - x$$
$$\xi_x = 1\sqrt{k_1/ak_2}$$
$$P_x = gW$$

$$g = 2\mu_g\phi_2\ell/\sqrt{ak_1k_2}. \qquad (4)$$

The initial pressure in the pores is neglected when writing the boundary conditions. Equations (2) and (3) are to be solved for the filtration zone only, since it is much longer than the preheat zone and the amount of gas accumulated in smaller pores can be neglected in the preheat zone. Thus the preheat zone and the subsequent ones are described by the relations derived in (4) for the case of monoporous explosives. Using the expression for the mass flow of the filtrating gas given in (4) one gets:

$$\left(\frac{d\pi}{dz}\right)_0 = \frac{\phi_1 u_0}{2\phi_2 W} \qquad (5)$$

where $u_0 = u_{z=0}$. Furthermore it was shown in (4) that

$$\frac{u_0}{W} = 1 + \frac{E}{P_0} \qquad (6)$$

where

$$E = \left(\frac{T_1 - T_0}{T_{ad} - T_0}\right)^2 \frac{c_s\lambda_s\rho_s(\gamma - 1)T_0}{c_p\mu_g\gamma}. \qquad (7)$$

The solution of Eqs. (2) and (3) can be expressed analytically in terms of parameter $q = d\sigma/dz$

$$\sigma^2 = -2\left[\ln(1 - q) + q\right] \qquad (8)$$

$$\pi^2 = -2\left[\ln(1 - q) + q/2\right]. \qquad (9)$$

At $z = 0$ this gives

$$\pi_0^2 = -2\left[\ln(1 - q_0) + q_0/2\right] \qquad (10)$$

$$\sigma_0^2 = -2\left[\ln(1 - q_0) + q_0\right] \qquad (11)$$

$$\left(\frac{d\pi}{dz}\right)_0 = \sigma_0(1 + q_0)/2\pi_0. \qquad (12)$$

The value of q_0 varies over the range of $0 - 1$. Ex-cluding u_0/W from Eqs. (5), (6), and (12) one finds that

$$W = \frac{E}{g[\sigma_0(1 + q_0)\phi_2/\phi_1 - \pi_0]}. \qquad (13)$$

Equations (13), (4), (10), and (11) give a parametric relation between W and P_0 in terms of q_0. The ana-lytical expression for $W(P_0)$ can be obtained if $q_0 \ll 1$. Expansion of $\ln(1 - q_0)$ in series up to the q_0^2 term yields a simple formula:

$$W = \frac{\phi_2 P_0^2}{\phi_1 g(E + P_0)}. \qquad (14)$$

This expression is valid for

$$[(1 + E/P_0)(\phi_1/\phi_2)]^2 \ll 1.$$

In order to replace an uncertain parameter P_0 for the P_{max} (or P_m) measured experimentally it is rea-sonable to use the equation for P_m derived in (4):

254

$$P_m^2 = P_0^2 + (8, 6 + f)\gamma RT_{ad} \left[\rho_s W \frac{\lambda_g}{\lambda_g} \left(\frac{T_1 - T_0}{T_{ad} - T_0} \right)^2 \right]^2$$

(15)

where

$$f = \mu_g \sqrt{4, 2(\phi_1/k_1)}/\rho_s u_n .$$

(16)

Equation (15) in most practical cases can be simplified, since usually $P_{max} - P_0 \ll P_0$. If $q_0 \ll 1$, the characteristic size of the filtration zone is expressed as follows:

$$\xi_f = 2\ell \sqrt{k_1/ak_2} .$$

(17)

Equation (17) predicts substantially thinner filtration zones than those in the case of monoporous charges. For pressed PETN with grain size of 0.5 mm experimental values of ξ_f (several cm) can be obtained if ℓ is assumed to be of the order of several grain sizes.

An example of a calculated $W(P_{max})$ curve shown in Fig. 2 (solid line) is illustrated further in Table 3.

TABLE 3

Calculated Parameters of Convective Burning of PETN

P_m bar	100	200	300	400
W m/sec	1.6	4.3	7.2	10
Length of pre-heat zone, cm	0.3	0.5	1.4	2.0
P_1/P_2 at $z = 0$	0.2	0.155	0.14	0.13

LOW VELOCITY DETONATIONS

As the amplitude of the nonelastic wave increases the more probable becomes the initiation of the reaction in hot spots. Eventually it results in transition of CB to LVD. Special experiments with metal diaphragms which separated two parts of a charge have demonstrated that the gas filtration is dominant until W exceeds the level of 700-800 m/sec. The process propagating at higher velocities can be easily transmitted through a metal diaphragm and should be regarded as LVD. For this stage of transient process there also exist certain conditions where LVD propagates at nearly constant velocity.

Experiments were carried out with charges of PETN ($\rho_s = 1.73$ g/cc) confined in steel tubes (9,10). The tubes were of 5 mm i.d. and of different wall thickness. A pyrotechnic igniter or a weak shock wave were used to initiate LVD. The propagation velocity was measured using a photographic technique. The results are shown in Fig. 4 (points). Because of an insufficient frequency response of the applied transducer the pressure P_m was measured indirectly in special experiments point P_m is assumed to be approximately equal to the maximum pressure which the tube with a given wall thickness can withstand when a charge of explosive is burned up in the tube. The rate of pressure rise in these experiments was about 0.5 kbar/μsec. Velocity of LVD grows from 1300 to 3300 m/sec when a stronger confinement (higher pressure in the compression wave) is used. In a certain region W is much less than the longitudinal acoustic velocity of the solid phase (2250 m/sec).

The experimental data on the propagation of LVD (1,9) and on the compressibility of PETN in weak shock waves (10) show that the velocity of LVD depends on profiles of the compression wave in the explosive and its amplitudes. Transition from elastic deformation to a nonelastic flow is very important in determining the conditions under which LVD arises. For pressed high explosives the plastic yield strengths lie in the range of 1-3 kbar. When $P > P_T(P_T$ is the yield strength) the compression wave consists of two waves (elastic and plastic), which may propagate with different velocities. The reaction starts in the nonelastic wave which can propagate much slower than the elastic (acoustic) precursor. In order to find the conditions where both waves are separated experiments were made with pressed TNT ($\rho = 1.6$ g/cc) using the conventional technique of electromagnetic measurements. A two wave configuration was observed for pressures lower than 7 kbar, at higher pressures the pressure profile corresponded to a single shock wave. It was demonstrated in (11) and (12) that LVD propagates at a supersonic speed with respect to the two-phase medium behind the elastic precursor, and hence it could be called a detonation phenomenon.

255

Figure 4 (solid curve) shows the calculated dependence of velocity on pressure. The calculations were made using simple estimations of wave parameters given in (12). These estimations account for the bifurcation of the wave and collapse of pores in the plastic wave.
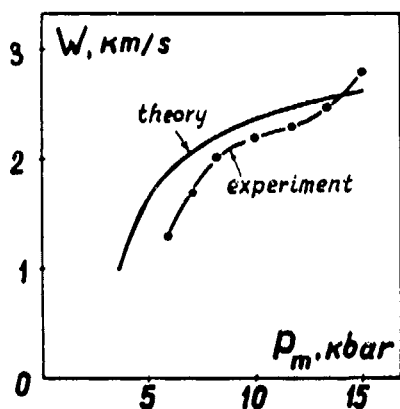
Fig. 4. Velocity of low velocity detonation in pressed PETN as a function of pressure in the compression wave. Calculated values - solid line, experimental results - points. Charge diameter 5 mm, confinement - steel tubes.

When comparing the calculations with the experimental results the following values of parameters were used: $\phi_o = 0.1$; $\phi_1 = 0.01$; grain size 0.5 mm; $k_1 = 10^{-11}$ cm^2; $E = 8 \cdot 10^7$ g/cm sec^2; $g = 2 \cdot 10^6$ g/cm^2 sec. The range of reasonable values of E and g calculated using the available literature data is $4 - 15 \cdot 10^7$ g/cm sec^2 and $1 - 6 \cdot 10^6$ g/cm^2 sec. As mentioned before the length of the filtration zone is several cm. Noteworthy is the high sensitivity of the CB velocity to pressure variations, the exponent ν is everywhere higher than 1. The results of calculations are in reasonable agreement with the experimental data. The agreement could be made better if one accounts for the possible turbulent filtration of the gas through pores.

The model of a steady-state CB considered is not unique. There could be found other nondimensional effects which would result in effective gas losses upstream to the ignition front. For instance, Margolin and Margulis (8) have shown that U-shaped pores generate a swirled filtration of the gas and make the spontaneous penetration of a flame into pores easier. The role of this process in a forced CB is to be elucidated.

Besides the high pressure exponent of W there is another destabilizing factor in CB which restricts the region of steady regimes at high propagation velocities. This factor is the appearance of a region of sonic flow in the combustion products (flow choking) and, as a consequence, generation of compression waves. The critical condition of flow choking is calculated by integrating the steady-state conservation equations for a two-phase reacting flow. Suppose that the starting point for integration is $P = P_{max}$, $u_s = u_g = 0$; $\phi = \phi_m$; $T_g = T_{ad}$; $T_s = T_o$, and the terminal point is $\phi = 1$, $P = P_\infty$. Assuming that flow tubes have a constant cross-section and neglecting the interaction of the flow with the confinement wall one can come to the expression:

$$\frac{P_\infty}{P_m} = \frac{1}{\gamma + 1} \pm \sqrt{\left(\frac{\gamma}{\gamma + 1}\right)^2 - \left(\frac{b}{P_m}\right)^2} \qquad (18)$$

$$b = \rho_s(1 - \phi_m)W \sqrt{2\gamma RT_{ad}/(\gamma + 1)}. \qquad (19)$$

The condition $b \geqslant P_m \gamma/(\gamma + 1)$ means that the process becomes nonstationary (accelerating). The calculated upper limiting values of W for steady regimes of CB are shown in Fig. 2 (shaded line). This effect together with the strong pressure dependence of W explain why CB in pressed PETN charges under confinement is highly unstable, and that CB propagating at velocities greater than 10 m/sec is impossible.

Acceleration of CB up to velocities of 100 m/sec and higher results in formation of a nonelastic compression wave in the unreacted explosive. This nonelastic wave is expected to affect the CB process in different ways:

to decrease the porosity,

to change the ratio of large and small pores,

to preheat the gas and create hot spots in the solid,

to change the conditions for fragmentation.

The analytical models which account for the effects of fragmentation of the solid in a CB wave and of the compression of the unreacted porous explosive would complete the description of the transient process, if they were worked out. However, this is still a problem for future studies.

A theoretical approach to the problem of stabilization of LVD (14) has shown that lateral expansion of confinement wall provides the energy losses needed for making the process steady. However, the analysis given in (14) has to be further developed if one wants to understand the mechanism of the transition from low velocity detonation to normal detonations. Extremely important in this process is the influence of heat release in the burn up zone on the flow parameters nearby the LVD front. This problem is under investigation at the present time.

REFERENCES

1. A. F. Belyaev, V. K. Bobolev, A. A. Sulimov, A. I. Korotkov, and S. V. Chuiko, "Perekhod goreniya kondesirovannykh sistem vo vzryv," Moskva, "Nauka," 1973.

2. A. F. Belyaev, A. I. Korotkov, and A. A. Sulimov, "Fizika goreniya i vzryva," 3, p. 476, 1966.

3. A. N. Afanasenkov, V. M. Bogomolov, and I. M. Voskoboinikov, "Obobschennaya udarnaya adiabata organicheskikh zidkostei, Fizika goreniya i vzryva," 3, No. 4 (1967), pp. 585-594.

4. B. E. Ermolaev, B. A. Khasainov, A. A. Borisov, and A. I. Korotkov, "Rasprostranenie konvektivnogo goreniya v poristykh porokhakh i VV, Fizika goreniya i vzryva," 11, No. 5, 1975, pp. 720-730.

5. G. I. Barenblatt, V. N. Entev, and V. M. Ryžik, "Teoriya nestacionarnoi fil'tracižidkosti i gasa," Moskva, Nedra, Chapter YIII.

6. K. K. Kuo and M. Summerfield, "Theory of steady-state burning of gas-permeable propellants, AIAA Journal, 12, No. 1, 1974, pp. 49-56.

7. V. F. Dubovitsky, V. G. Korostelev, A. I. Korotkov, Yu. V. Frolov, A. N. Firsov, K. G. Shkadinsky, and S. V. Khomik, "Burning of porous condensed systems," Fizika goreniya i vzryva, No. 6, 1974, pp. 811-818.

8. A. D. Margolin and V. N. Margulis, "On the penetration of combustion into a single pore," Fizika goreniya i vsryva, 5, No. 1, pp. 15-16.

9. A. V. Obmenin, V. A. Balykov, A. I. Korotkov, and A. A. Sulimov, "The role of confinement in the evolution of explosion in PETN of high density," Fizika goreniya i vzryva, 6, No. 4, 1970, pp. 571-573.

10. A. A. Sulimov, A. V. Obmenin, and A. I. Korotkov, "On the low velocity regime of explosion reactions in dense charges of solid high explosives," Trudy III Vsesoyusnogo simposiuma po pogoreniyu i vsryvu, Moskva, Nauka, 1972, pp. 464-469.

11. N. M. Kusnetsov, "On the theory of detonations in weak condensed explosives," Zurnal prikladnoi mekhaniki i tekhnicheskoi fiziki, No. 1, 1975, pp. 69-75.

12. B. S. Ermolaev, B. A. Khasainov, and A. I. Korotkov, "Propagation of plastic compression waves in dense high explosives," Fizika goreniya i vzryva, 11, No. 2, 1975, pp. 325-327.

13. B. S. Ermolaev, A. A. Borisov, and B. A. Khasainov, "Comments on the theory of steady-state burning of gas-permeable propellants," AIAA Journ., 13, No. 8.

14. B. S. Ermolaev, B. A. Khasainov, A. A. Borisov, and A. I. Korotkov, "Low velocity detonations in cast and pressed high explosives," paper presented at the Fifth International Colloquium on Gas Dynamics of Explosions and Reactive Systems, Bourge, France, 1975.

A COMPARISON OF MODEL PREDICTIONS
AND EXPERIMENTAL RESULTS OF DDT TESTS

D. T. Pilcher, M. W. Beckstead, L. W. Christensen, and A. J. King
Hercules Incorporated, Bacchus Works, Magna, Utah

*A model describing convective burning in porous beds based upon the Krier/Van
Tassell gun combustion computer code has been developed and applied to a
variety of tests investigating the transition from deflagration to detonation (DDT)
in porous beds of propellant. The tests included numerous bed configurations
in steel and Kevlar pipes. Agreement between model predictions and experi-
mental results has been excellent. The general structure of the Krier model and
its integration scheme were retained, but a number of alterations were made
to the model to make it applicable to DDT investigations. The computer
combustion model was then coupled with a structural dynamics code to sim-
ulate motion of the confining media. This combination of programs, called
HONDO/Krier, is proving to be an invaluable tool, providing much insight into
the details of the DDT phenomenon.*

INTRODUCTION

The transition from normal burning to detona-
tion in a gas-permeable explosive system has been a
topic of investigation for some time (1-4), but only
recently have there been attempts to model the de-
tails of this phenomenon using a full system of
conservative equations of two-phase flow. Such a
model has an advantage as it provides detailed informa-
tion of flow parameters throughout the entire bed,
whereas experimentally obtaining pressure, tempera-
ture, flame speed, and other details of the event, even
at a few points, is a difficult task. Researchers (5-9)
have recently made significant advances in describing
flame spread in porous beds of gun propellants. Their
work provided a starting point for the investigations
of DDT.

The phenomenon of DDT in porous beds of granu-
lated propellant is being studied using the dual approach
of experimentation and computer modeling. As the
experimental program progressed, it became evident
that differences in confinement of the gases offered
by various test vehicles was a critical factor in test
outcome. The combustion model by itself was not
adequate to analyze the test results thoroughly. As a
consequence, the combustion model was coupled to a
dynamic structural analysis program to simulate the
motion of the material enclosing the porous bed of pro-
pellant. A much better understanding of the complex
DDT process has thus been achieved. Although the
DDT model must be considered to be in a develop-
mental stage, it has proven to be extremely valuable
in analysis of explosive systems where DDT is possible.

Ten tests of varying design were simulated using the
DDT model in an attempt to verify the model, at least
in the ability to differentiate between detonation and
no-detonation, and to better understand the details of
the DDT process. The tests were part of a series con-
ducted to determine experimentally under what
conditions various types of propellants (explosives)
would undergo DDT before the test vehicle ruptured
sufficiently to stop the process. Table 1 provides
a brief overview of the tests, showing that model pre-
dictions agreed with test results in 9 of 10 cases.

In the one case where agreement was not achieved, the model predicted a detonation, and the result of the experiment was classified as a very violent reaction—possibly a detonation. Thus, even in this instance, the prediction and the test result were basically similar. Use of the model has not only increased the ability to predict situations where a detonation might occur, but it has provided insight into the various mechanisms which affect DDT.

THE MODEL

The Hercules DDT model consists of two computer programs linked together; one modeling combustion in a porous bed, the other modeling motion of the confining walls of the bed. The combustion model was developed from the Krier and Van Tassel (7) gun combustion program. The integration scheme with numerical smoothing was retained, but numerous

other changes were necessary to make the program operate satisfactorily for the extreme conditions of DDT. A variable covolume was added to the equation of state. Boundary conditions and start conditions were changed. The 'diffusion' terms were removed and time variations in bed cross-sectional area were included. In its present form, the model is a one-dimensional continuum model of two-phase flow, in which the area varies with both space and time. The conservation equations for the gas and solid phases (Eq. 1-6) are shown below.

Gas Phase

$$\frac{\partial}{\partial t}\,(\phi\rho_g A) + \frac{\partial}{\partial x}\,(\phi\rho_g U_g A) = \Gamma_g A + \text{Ign} \qquad (1)$$

$$\frac{\partial}{\partial t}\,(\phi\rho_g U_g) + \frac{\partial}{\partial x}\,(\phi\rho_g U_g^2) = \phi\,\frac{\partial p}{\partial x} - D + \Gamma_s(U_g - U_s)$$
$$+ \text{Ign } U_g \qquad (2)$$

TABLE 1

Comparison of Analytical and Experimental Results

Motor	Bed Type	Bed Length (in.)	Void Length (in.)	%TMD	Propellant	Particle Size (μ)	D_t (in.)	Reaction	Model Prediction
1	CORE	24.0	0.25	70	Class A HMX	200	0.00	No DDT	No DDT
2	FD	1.0	4.50	75	Class A HMX	200	0.65	DDT	DDT
3	FD	0.25	1.00	49	Class A HMX	200	0.25	No DDT	No DDT
4	FD	0.50	0.25	50	Class A HMX	200	0.25	DDT	DDT
5	FD	5.0	0.25	71	Type B	1200	0.00	DDT	DDT
6	FD	1.0	4.50	80	Type B	1200	0.65	No DDT	No DDT
7	FD	2.0	0.25	73	Type B	1200	0.25	No DDT	DDT
8	Annulus	19.5	0.50	59	Class A HMX	200	0.00	DDT	DDT
9	Annulus	19.5	0.50	65	Type B	1200	0.00	No DDT	No DDT
10	Annulus	19.5	0.50	63	Type A	~800	0.00	No DDT	No DDT

FD	— A full diameter bed of particles backed by a solid cylinder of propellant in a Schedule 160, 6-inch steel pipe
CORE	— A center core of particles in an annulus of undamaged propellant encased in a Schedule 160, 6-inch steel pipe
Annulus	— An 0.8-inch-thick annulus of particles between a 10-inch-diameter Kevlar (fiber) case and a cylinder of undamaged propellant
D_t	— Initial throat diameter of the nozzle
% TMD	— Percent theoretical mean density
DDT	— Deflagration to detonation transition

$$\phi\rho_g \ \frac{\partial E_g}{\partial t} + \phi\rho_g U_g \ \frac{\partial E_g}{\partial x} = \frac{1}{A} \frac{\partial}{\partial x} \ (p\phi U_g A) - Q - Q_w +$$

$$\Gamma_s \ [(1 - X) E_{chem} - E_g] +$$

$$\text{Ign} \ (E_{ign} - E_g) \qquad (3)$$

Solid Phase

$$\frac{\partial}{\partial t} \ [(1 - \phi)\rho_s A] + \frac{\partial}{\partial x} \ [(1 - \phi)\rho_s U_s A] = \Gamma_s A(1 - \phi) \quad (4)$$

$$\frac{\partial}{\partial t} \ [(1 - \phi)\rho_s U_s] + \frac{\partial}{\partial x} \ [(1 - \phi)\rho_s U_s^2] = - (1 - \phi) A\sigma] + D$$

$$+ \Gamma_s (U - U_g) \quad (5)$$

$$\rho_s \ \frac{\partial E_s}{\partial t} + \rho_s U_s \ \frac{\partial E_s}{\partial x} = \Gamma_s \ X \ E_{chem} + Q \qquad (6)$$

where:

ϕ = A_g/total cross-sectional area
ρ = Density
A = Cross-sectional area of bed
U = Velocity
P = Pressure
D = Drag
Ign = Igniter mass generation rate
Γ = mass generation rate
Q = Heat transfer
σ = Stress
x = Endo thermic fraction
Subscript g = Gas phase
Subscript s = Solid phase
Subscript w = Wall

For most applications, the geometry of the solid particles has been approximated with a sphere. Drag and heat transfer correlations are those used by Krier (7). The fixed bulk temperature of Krier has been used as an ignition criterion for the particles, as has the fixed surface temperature of Kitchens (5). The most satisfactory results have been obtained using a variable bulk temperature criterion for which the bulk ignition temperature is a function of particle size and burn rate. The particles at a given station are ignited when the solid phase temperature at that point reaches the value T* given by equation (7).

$$T^* = T_0 - 3 (\lambda)^{-3} \ (T_s - T_0) \ \{e^{-\lambda} \ [\lambda^2 + 2\lambda + 2]$$

$$- 2\} \qquad (7)$$

where:

λ = (particle radius $\times$ burn rate)/thermal diffusivity

This ignition criterion is given support by the work of Derr (10) who showed a strong correlation between ignition temperature and burn rate for a group of composite propellants.

A significant problem has been the determination of initiation of detonation. The present level of refinement of the model does not lend itself to a flame velocity criterion as discussed in Reference (1) where Belyayev, et al. established 3000 to 4000 m/sec as the beginning of a full detonation, the last of four DDT stages. A fundamental definition in terms of pressure, temperature, and other variables is not available; therefore, a semi-empirical criterion is used. A detonation is said to have occurred when $P^2\tau$ exceeds a prescribed value:

$$P^2\tau = \int_{t_0}^{t} p^2 \ dt \qquad (8)$$

Based on HMX explosives (11), a value of $P^2\tau$ of 10^5 psi^2-sec ($\sim$ 500 kb^2 - μsec) was used.

The structural program HONDO (12), a finite element program for large deformation dynamic response developed by Sandia Laboratories, has been modified so the two programs can be linked together. To further assist in modeling more complicated tests, the capability of multiple-defined nodes to allow for separation of pieces of the structure and of altering node constraints during execution was added. The additions were used in modeling tests where an end closure broke free from the test vehicle when chamber pressure exceeded a specified value. The model describes axisymmetric structures, but planar structures can be approximated with some additional effort. Figure 1 is a schematic of the input and output of each program and the data passed between them.

TEST MATRIX

Three basic configurations were used in the tests discussed. All were basically go/no-go tests with little instrumentation. In one, a thick annulus of undamaged propellant 24-inches-long was encased in a 6-inch Schedule 160 steel pipe. The center core was filled with Class A HMX, thus forming a porous bed. Forward
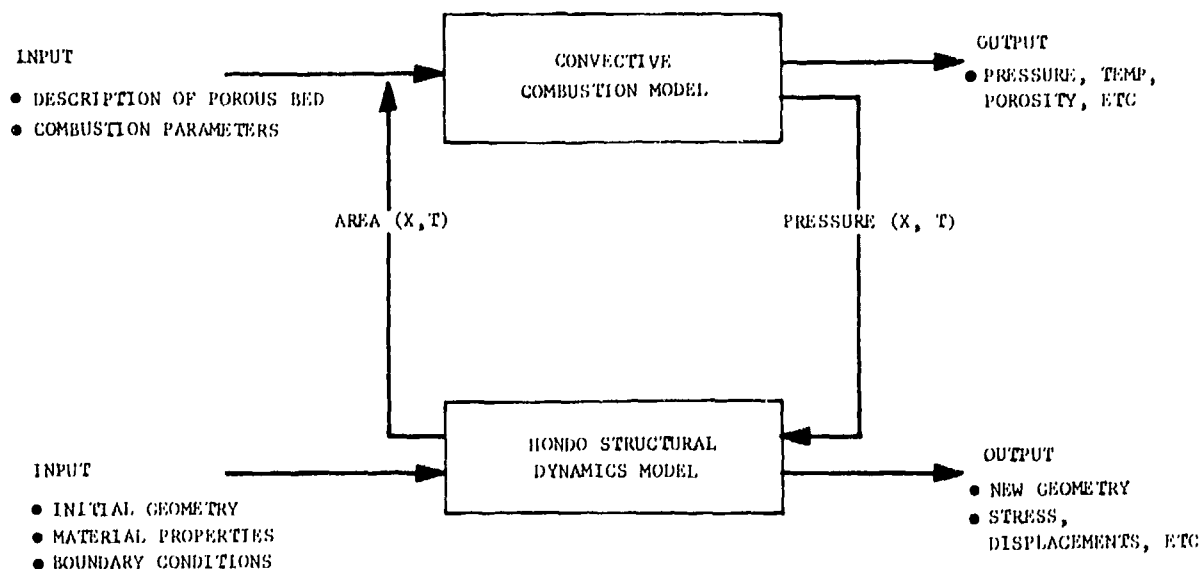
Fig. 1. Description of DDT model

and aft closures were attached by bolts which yielded at a chamber pressure of approximately 12,000 psi. This first configuration analyzed is shown in Figure 2 and designated Motor 1.

A similar pipe was used in the second configuration motors, numbered Motors 2 to 7, each used a full-diameter bed of granulated propellant backed by a cylinder of undamaged propellant. Bed length, void length, particle size, and nozzle throat diameter varied in the tests, but the same type of bag igniter was used (Table 1). Motor 5 was the only one of this configuration that was not vented. Figure 3 shows the basic

configuration of the motors and the idealization used in the analysis. For motor 5, the tapered portion of the model was removed and a rigid wall boundary was assumed to be present.

The third set of tests, Motors 8 to 10, investigated DDT characteristics of relatively weak test vehicles. An annular bed of propellant was confined between a thin filament-wound Kevlar chamber and a solid propellant grain, as shown in Figure 4. The body of the case was
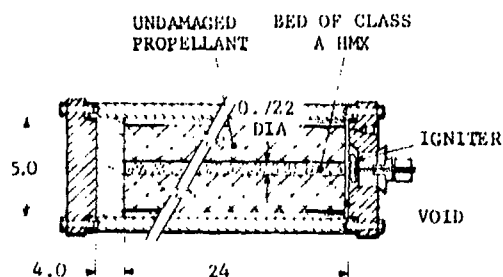
Fig. 2. Six-inch pipe tests, core of HMX (dimensions in inches)
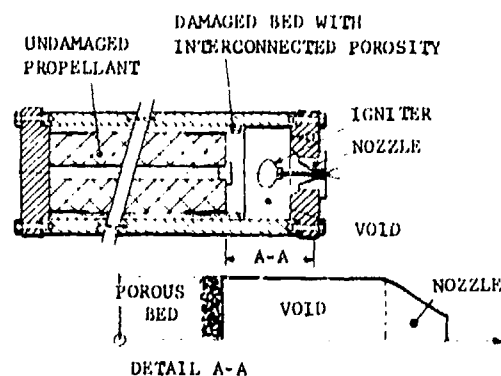
Fig. 3. Six-inch pipe tests, full-diameter bed

261

0.122-inch thick but increased to 0.54 inch at the ends to accommodate the closures. The static burst strength of the case was estimated to be 3500 psi. The motors were not vented. A bag igniter was located in the 0.5-inch void between the propellant and the end closure. The igniter strength for Motor 8 was approximately one-third of that used in the other two tests of this configuration.

TEST ANALYSES

Discussion of the firing of Motor 1 and the subsequent analysis will illustrate the extent of information provided by the math model. The propellant grain of Motor 1 had a 0.722-inch-diameter center bore filled with unground Class A HMX. A bag igniter was located in an 0.25-inch-long void between the propellant and the aft closure. The test results indicated that flame from the bag igniter initiated the column of HMX, and shortly thereafter both forward and aft closures were blown off after failure of the retaining bolts. DDT did not occur as evidenced by the fact that 3 large pieces of propellant approximately 8.0-, 6.0-, and 3.0-inches-long by the full diameter were recovered.

To simulate the test using the model, certain assumptions were made. The igniter sequence was bypassed by assuming the first 0.25-inch of the bed was pressurized to 1450 psi and ignited. The pressure decreased linearly to atmospheric conditions at 0.7-inch into the bed. Initia porosity of the bed was 0.30. The resulting calculations show that when the

pressure at the igniter end of the vehicle was sufficient to release the closure, most of the bed was still at ambient conditions; only 0.4-inch of the bed had ignited, and the radius of the bed increased only 9.2×10^{-3}-inch at the bed entrance. Figure 5 shows how the bed expanded as the pressure front moved into the bed. The 'continental divide' commonly seen in the analysis of run-up length experiments (13) was clearly evident by 30 μsec after start time. Pressure had stopped rising at the bed entrance by 48.5 μsec due to the bed expansion. The pressure peak continued to rise until it reached 92,000 psi at 1.2 inches in the interior of the bed. At this time, 1.6 inches of the bed were ignited. The gas

Fig. 4. Fiber case with annular bed
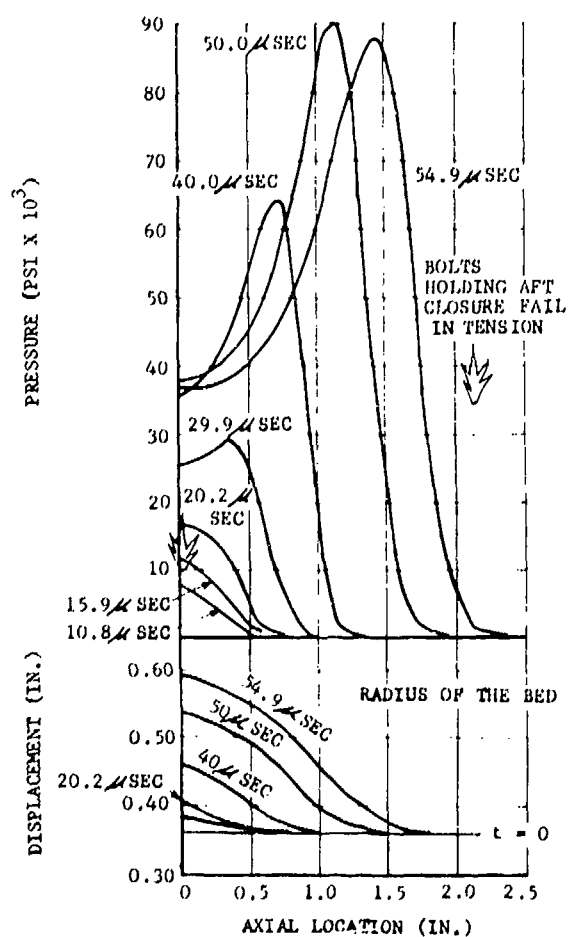
Fig. 5. Pressure history of bed (Motor 1)

262

volume at the front of the bed had increased by 627 percent due mainly to expansion of the bed, but also due to motion and burning of the particles. The change in volume at 1.2 inches was 154 percent. There was not sufficient mass being generated behind the pressure peak to sustain it, so the peak began to fall rapidly even though the flame front and pressure front continued to move into the bed. It was judged that no detonation would occur.

MOTORS WITH FULL-DIAMETER BEDS

In the analysis of the motors containing a full-diameter porous bed, the ignition sequence was included and rigid pipe walls were assumed. Calculations for Motor 5, using both rigid and elastic walls, indicated this assumption did not introduce gross errors. The aft closure was represented by a 20 pound projectile which was free to move when the pressure against it reached 12,000 psi. Three bed lengths were tested and analyzed for 200 μ HMX particles. Three bed lengths for 1200 μ particles of type B propellant (which has a comparable burn rate) were also tested and analyzed. Each set of three tests exhibited both a detonation and a nondetonation. Detonation predictions agreed with test results in all cases except for Motor 7, a 2-inch bed of 1200 μ particles. In each set of tests, the intermediate bed length was near the minimum length for which DDT would occur.

Figure 6 illustrates the variation in calculated pressures for the HMX motors. Motors 2 and 4 detonated, Motor 3 did not. It was observed that differences in porosity, bed length, and void length were the major factors in determining if a detonation would occur. The increased porosity of the 0.25-inch bed of Motor 3 effected a three-fold decrease in the mass generated per unit time compared with Motor 2. Venting of gases into the void adjoining the short bed also contributed to keeping pressures low. Calculations showed that following ignition of the 1.0-inch bed, pressures rose quickly to the detonation level within the bed, yet there was little venting of gas into the void. This agreed with previous analyses of beds of RDX which showed that once flame was well established in a 'long' bed of particles with high S/V, the void had little influence on whether or not DDT occurred. For this 1.0-inch bed, detonation

was predicted to occur before the aft closure broke loose.

In the 0.5-inch bed, the pressure peak quickly moved to the solid-granule interface. A pressure oscillation developed but had essentially damped out by the time the pressure reached 60,000 psi. From this time on, the pressure rise was nearly uniform throughout the bed. Restriction of flow through the bed was sufficient that detonation occurred before the aft closure had moved 0.05 inch.

Motors 5, 6, and 7 contained beds of propellant particles of approximately 1200 μ diameter. Because of the six-fold decrease in the S/V compared to the 200 μ HMX, the DDT sequence was considerably slower and there was a greater chance of losing the end closures before a detonation occurred. The dominant mechanisms noted in the HMX motors were also observed. Since all motors had a porosity between 0.20 and 0.30, the significant parameters affecting DDT for the three Type B propellant motors were the bed and void lengths. A small void region and absence of a nozzle gave the 5-inch bed a more vigorous start than the other two motors (Figure 7). However, the greater bed length was more important. Once the flame was established well into this long bed, the combustion products could not escape fast enough to prevent DDT. The small 1/4-inch-long void between the 2-inch bed and the end closure of Motor 7 was definitely a factor in the extremely high pressures seen in this motor. Figure 8 compares pressure-time
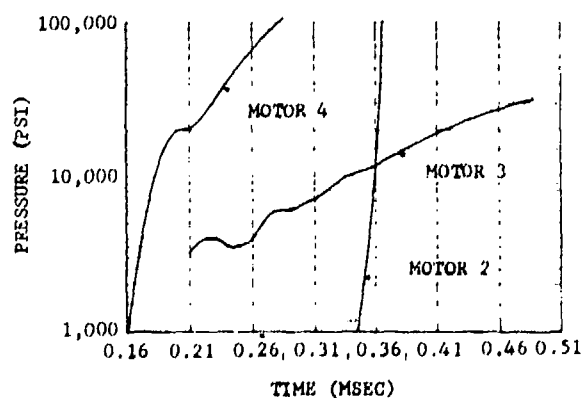
Fig. 6. *Maximum pressure-time plots for 6-inch HMX motors*
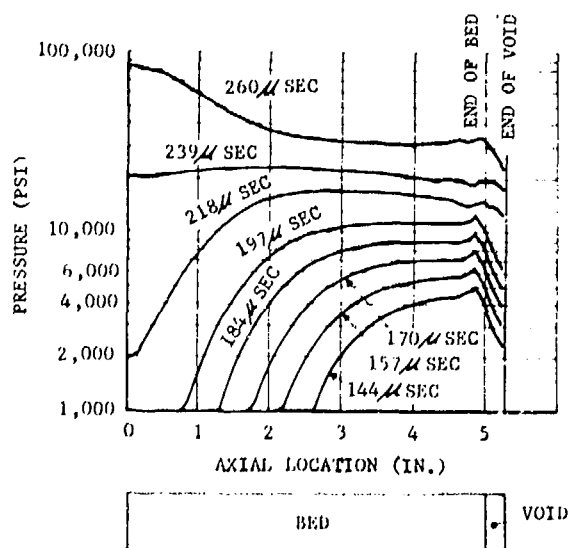
Fig. 7. Pressure-distance curves for Motor 5
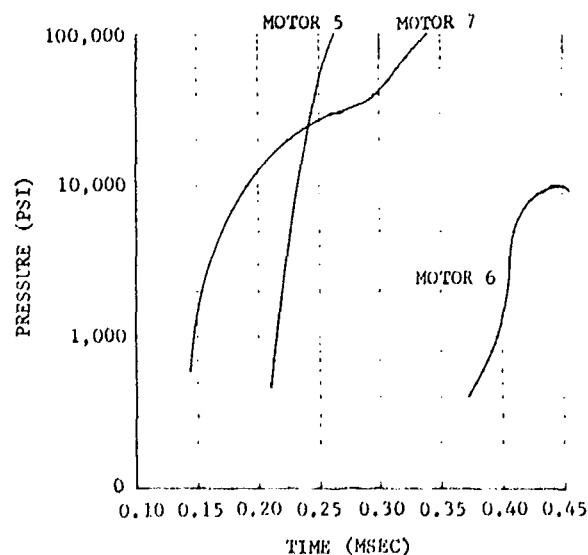
Fig. 8. Maximum pressure-time plots for Motors 5, 6, and 7

plots for Motors 5, 6, and 7. A large void such as that of Motor 6 would have significantly reduced the pressure.

LIGHTWEIGHT MOTORS WITH ANNULAR POROUS BEDS

The relatively low strength of the light-weight fiber cases made the tradeoff between mass generation and expansion of the case critical for Motors 8 to 10. The analyses of these motors, using the combined combustion and structural models, were performed early in the development of the DDT model and did not include the void volume present in the motors. Omission of the void and igniter sequences had some influence upon the model predictions, but there was sufficient agreement between analysis and experiment to demonstrate the reliability of the DDT model when structural confinement is a critical factor.

Motors 8 to 10 were nearly the same except for variations in particle sizes. Only Motor 8, loaded with 200 μ HMX, detonated. The detonation was avoided in Motors 9 and 10 because a slower mass

generation rate allowed sufficient time for expansion of the bed by motion of the propellant grain and the case. The expansion slowed the reaction rate sufficiently to allow the case to rupture before pressure was so high DDT could not be stopped. Figure 9 shows the deformation of the chamber and grain of Motor 9 immediately prior to case failure. For the Type A or Type B particles to detonate in these lightweight motors, they would need to be a size close to that of the HMX.

Test results for Motor 9 indicated chamber failure began at a point approximately 1.5 inches into the porous bed between 2.0 and 2.5 msec after ignition. Calculations showed that the case failure would occur just short of the end of the reinforcement of the case; approximately 3.0 inches into the bed, at 1.0 to 1.2 msec. Since the ignition sequence was bypassed in the analysis by assuming approximate start conditions and the void was omitted, it is felt agreement between predicted and test results was good. Test results and predictions for Motor 10 were very similar to those of Motor 9 (Figure 10).

In the HMX motor, case failure began at the end of the case, but not soon enough to prevent detonation.

264
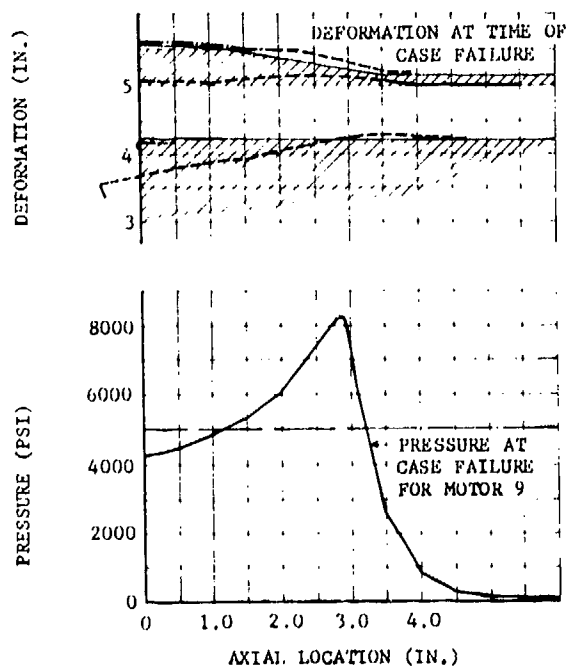
Fig. 9. Pressure and deformation of lightweight case

Fig. 10. Comparison of pressure-distance traces of Motors 8 and 9

Just as indicated by test data, case failure was calculated to begin at the end of the case 60 μ sec after start. At this time a pressure peak of 81,000 psi was located 1.0 inch into the bed. Pressure continued to rise ahead of the case failure until a wave of approximately 100,000 psi began moving through the bed. A detonation followed.

CONCLUSIONS

The combustion model has been used to study the effects of variable parameters, such as porosity and particle size, which strongly influence DDT (13). The analytical predictions are in good agreement with published experimental results. The analyses of DDT tests, using the full model described in the report, cover a wide range of test configurations and provide further evidence that the DDT model is a reliable analytical tool. The model not only provides a means of predicting situations where detonation may occur, but also yields much detailed information about the

combustion process and the dynamic response of the test vehicle. The model cannot be applied to situations where two-dimensional effects are dominant. The detonation criteria must be improved; generation of heat within the particles due to stresses experienced is a critical mechanism to be investigated and other improvements can certainly be made. The model has, however, greatly increased the understanding of the highly complex phenomenon of DDT.

REFERENCES

1. Belyayev, A. F., Bobolev, V. K., et al., "Transition of the Combustion of Condensed Systems into an Explosion," Perekhod Goreniya Kondenserovannyh Sistem Vo Vzeyv, Izd Vo "Nanka," 1973, pp. 1-292.

2. Bernecker, R. R., and Price, D., "Studies in the Transition from Deflagration to Detonation in Granular Explosives—I, Experimental Arrangement

265

and Behavior of Explosives Which Failed to Detonate," Combustion and Flame, Vol 22, (1974). pp. 111-118.

3. Bernecker, R. R., and Price, D., "Studies in the Transition from Deflagration to Detonation in Granular Explosives—II, Transition Characteristics and Mechanisms Observed in 91/9 RDX/Wax," Combustion and Flame, Vol 22, (1974), pp. 119-129.

4. Bernecker, R. R., and Price, D., "Studies in the Transition from Deflagration to Detonation in Granular Explosives—III, Proposed Mechanism for Transition and Comparison with Other Proposals in the Literature," Combustion and Flame, Vol 22, (1974), pp. 161-170.

5. Gough, P. J., "Fundamental Investigation of Interior Ballistics of Guns," Final Report, Indian Head Contract Report 74-1, Naval Ordnance Station, Indian Head, Maryland, July 1974.

6. Kitchens, C. W., "Flame Spreading in Small Arms Ball Propellant," BRL Report No. 1604, August 1972, Ballistic Research Laboratories, Aberdeen Proving Grounds, Maryland.

7. Krier, H., Van Tassell, W., Rajan, S., Ver Shaw, J. T., "Model of Gun Propellant Flame Spreading and Combustion," BRL Contract Report No. 147, March 1974, to IBL, BRL, APG, Md.

8. Kuo, K. K., Vichnevetsky, R., Summerfield, M., "Theory of Flame Front Propagation in Porous Propellant Charges Under Confinement," AIAA J., Vol I No. 4, pp. 444, April, 1973.

9. Dubovitski, V. F., et al., "Burning of Porous Condensed Systems and Powders," Fizika, Goreniya i Vzryva, Vol 10, No. 6, Nov-Dec 1974, pp. 811-818.

10. Derr, R. L., and Fleming, R. W., "A Correlation of Solid Propellant Arc-Image Ignition Data," 10th JANNAF Combustion Meeting, Naval War College, Newport, Rhode Island, 6-10 August 1973.

11. Walker, F. E., and Wasley, R. J., "Critical Energy for Shock Initiation of Hetrogeneous Explosives," Explosivestooffe, 1969, 17(1), pp. 9-13.

12. Key, S. W., "HONDO—A Finite Element Computer Program for the Large Deformation Dynamic Response of Axisymmetric Solids," SLA-72-0039, Sandia Laboratories, Albuquerque, New Mexico.

13. Beckstead, M. W., Peterson, N. L., Pilcher, D. T., Hopkins, B. D., Krier, H., "Convective Combustion Modeling Applied to Deflagration-to-Detonation Transition of HMX, submitted to Combustion and Flame Journal.

SHOCKS RETARDATION AND PRESENCE OF CRACKS IN MATERIALS

B. M. Belgaumkar
Technical Consultant, I.A.E.C. (Bom.) Pvt. Ltd., Bombay, India
Formerly, Professor & Head, Dept. Mech. Engg.,
Indian Institute of Technology, Kharagpur, India

An analytical method, based on the recent progress made in the areas of Shock Waves, Dislocation Dynamics, and Fracture Mechanics, is presented for the estimation of plane elastic precursor decay in the presence of cracks in a principally elastic material. Extension of the method is suggested for the studies of Elastic-plastic Waves, Elastic-Visco-Plastic Waves and other aspects of Shock-Waves in such materials.

INTRODUCTION

Shock Waves in solids are most often produced by explosion or high-speed impact on a material boundary. Shock growth and retardation studies in the existing literature seems to be restricted to those effects due to reflection at the free surface, or to reflection and refraction at the interface. The attenuation of plane elastic precursor shock has played a significant role in the Dislocation Dynamics studies. Nonetheless, it appears that very scanty attention has been diverted to the studies of interaction of dislocation on the shock propagation, etc. Similarly, good many advances have been made recently in the Fracture Mechanics. Studies of shock waves in solids have made distinctive contribution in understanding the crack propagation in metals, rocks, and other solids. But, the converse, namely, the effect of cracks in a material on shock propagation and interaction on crack nucleation and its propagation, seems to have not attracted any attention.

It is generally assumed in shock analysis, the material to be homogeneous and isotropic. But, it is well-known that flawlessness in a material is only a relative term when applied to actual solids. The presence of cracks in solids cannot be neglected in any serious investigation having important practical applications.

The purpose of the present paper is to discuss what may happen when a shock wave is to propagate itself through a material having crack flaws, to propose an analytical method to estimate the precursor decay, and to suggest avenues for future research.

Before we take up the analysis of the problem stated above, it may not be out of place to very briefly describe the state of art in the studies of shock wave mechanics, dislocation dynamics, and fracture mechanics, as the discussion is centered round the recent progresses made in these areas.

SHOCK WAVE MECHANICS

For our purpose, shock wave may preferably be described as finite amplitude stress wave consisting of regions of essentially stable, discontinuous or nearly discontinuous stress change, called shock fronts, or briefly shocks. For simplifying, it is assumed that the compression or rarefaction phase of a shock wave to be a single discontinuous shock front. Various solids, however, have properties which produce multiple shock fronts travelling at different velocities. In carefully conducted experiments, it is possible to generate a plane shock wave with a single discontinuous shock front. Important applications of shock waves in the study of solids are reviewed in (1). Reflection and

267

refraction of plane waves at interface and free surface in a solid are discussed in (2).

DISLOCATION DYNAMICS

The role of the theory of dislocations in explaining the an-elasticity and other properties, is well recognized. The nature of the study and advances in the theory are summarized in (3). The single strain rate equation for plasticity is used to explain the microscopic creep, stress-strain, and shock wave tests. A straight dislocation line in dynamical equilibrium has three forces acting on it. Discussing these forces, it is shown in (4) that the steady state velocity is determined by the ratio of the driving force to the damping constant. As a dislocation moves past a point, the material there receives a cycle of shear strain or shear plus dilatation.

FRACTURE MECHANICS

Fracture mechanics deals mainly with nucleation, propagation, etc. of different types of cracks and the various conditions under which there is likelihood of setting in of instability in the growth of cracks and resulting in complete fracture of the material. An excellent advanced treatise in seven volumes of (5) deals with various aspects of fracture mechanics studies.

A survey of the contribution that dislocation theory has made to the understanding of the process of fracture in solids, particularly in crystalline solids, will show that not only does crystal dislocation play an important role in fracture process but also the dislocation concept is of considerably wider value in understanding fracture mechanics of solids. Dislocations serve as convenient basic elements in the microscopic treatment of fracture. Crack is equivalent to a continuous array of dislocations. The basic problem in the theory of cracks is the determination of the way in which a crack modifies the applied stress field. Knowledge of how cracks propagate, branch, and interact with boundaries is important in many areas. In addition to the crack propagation problems that arise from engineering application of materials, knowledge of fracturing has an important bearing on problems ranging from the performance of solid-fuel propellants to methods of excavating rocks.

Griffith, (6,7) laid the theoretical foundation for the study of brittle fracture of ideal brittle materials. Griffith's concept has been extended (8,9,10) to include the case of brittle fracture of actual materials. The analysis of Griffith fracture model based on the thermodynamic criterion for crack propagation leads to a necessary condition but not sufficient one. Sharfuddin (11) has shown that the necessary and sufficient criterion is that there should occur at the crack edge total stress which are sufficient to rupture the atomic bonds. The tensile rupture of atomic bonds requires a stress of approximately one-fifth of the elastic modulus, whereas brittle solids commonly rupture at about one-hundredth of atomic cohesive force. It is now recognized almost without contradiction that the relatively low strength of materials is due to the presence of cracks, either nucleated by microscopic dislocation processes or to inhomogeneity of composition. Expressions for fracture toughness for various types of deformations applied to cracks of complicated shapes are given in (12).

MECHANISM OF SHOCK RETARDATION IN THE PRESENCE OF CRACKS

For studying the mechanism involved, we consider crack as a flat separation bounded within the material by a leading edge which is approximated as a simple curve. At a relatively small uniaxial stress across the cracked region, plastic strains are confined to a small zone which is regarded as a line disturbance zone. The natural locus for the leading edge of the linear analysis model crack is a central position within the plastic zone where the stress distribution is two-dimensional. The tensile crack stress field near the leading edge of a crack is regarded as either of plane-strain or of plane-stress type. A general mathematical treatment would refer to mode I (tensile) stress equation in order to represent opening of crack surface displacements and mode II (forward shear) and mode III (parallel shear) stress equations in order to represent stresses developed by application of shear parallel to the crack plane.

It may be said without contradiction that the analytical aspects of shock wave studies are complete relative to homogenous-isotropic-linear elastic media. A similar statement should hold good in respect of linear fracture mechanics relative to basic formulation and two-dimensional static problems. We accordingly

wish to confine our discussions that follow only to those problems that come under the purview of the above statements. We assume that the size, shape, distribution, properties and behavior of cracks are random in nature and their description is governed by either statistical averages or by known distribution functions.

The object of this paper being to examine the effects of crack on the retardation of shock, it is assumed that the elastic precursor is a simple unidimensional plane shock of single narrow rectangular pulse of low intensity such that the stresses produced in the material are below the dynamic yield and fracture strengths. It is also assumed that before the arrival of the shock, the material is stress free, the cracks are stable and are due to previous history, and the temperature is below NDT (nil-ductility-temperature) of the material.

What happens when the shock approaches the crack will depend on the orientation of the crack with respect to the shock, on type of deformation of the crack, and on the phase of the shock—compressive or rarefaction. The behavior of the shock at the cracked surfaces will be in effect that of a free surface. But in the case of slit crack with compression phase, the behavior will be that of at the interface.

At the free surface, if the incidence is direct, the shock will be reflected with phase reversal. On the other hand, if the incidence is oblique, it gives rise to two reflected waves, one of dilatation and the other of distortion. At the interface, a part of the shock will be reflected and other part will be refracted, both with reduced intensity.

It is well recognized that plane wave theory is an oversimplification of the reality even for unidimensional small strain elastic problems, like the one under discussion. We can rarely handle finite boundaries where end reflections and internal interactions of wave take place in large numbers. It is therefore evident that we should find a different approach to the problem. We have Hooke's law for elastic response and strain rate equation for plasticity. If we can establish a constitutive relation for crack-sensitive elastic-plastic solids, we may break the ice. The general approach we are going to propose here parallels the method used for obtaining the rate dependent stress-strain relationships in dislocation dynamics

THEORETICAL ANALYSIS

Our guiding equation is the counterpart of the one derived and discussed by various authors following the original verbal exposition by Orowan, (13,14)

$$\dot{\gamma} = bNv \qquad (1)$$

where
- $\dot{\gamma} \equiv$ avg. plastic shear strain rate in the vicinity of the crack tip,
- $b \equiv$ avg. interflaw spacing,
- $N \equiv$ running crack density, and
- $v \equiv$ avg. running crack velocity.

The constitutive relation, termed dynamic by Curran (15), may be obtained by combining Eq. (1) with the incremental Hooke's law under the assumption that the total strain is the sum of elastic and plastic components and the plastic strain to cause no volume change and after taking time derivative, as given below:

$$\dot{6}_x - (\lambda + 2\mu)\dot{e}_x = -(8/3)\mu bNv \qquad (2)$$

where λ and μ are the usual Lame constants.

Equation (2) is derived for a loading geometry of plate-impact test under conditions of uniaxial strain and the plane of maximum shear stress in isotropic media is inclined at 45° to the direction of shock propagation.

Analytical solutions of Eq. (2) have been obtained for elastic precursor decay and plastic shock-wave propagation for dislocation-dynamics models, (16,17, 18). Corrections for the anisotropy in polycrystalline samples have been calculated in (19). The crack density, size, orientation, and formation have been statistically investigated in (20). The Lame constants can be taken from the dynamic elastic properties of the material. If b and v are evaluated from the known principles of fracture mechanics, combining Eq. (2) with Lagrangian equations for unidimensional wave motion,

$$(\partial u/\partial t) + (\partial 6/\partial x) = 0 \qquad (3)$$

$$(\partial u/\partial x) + (\partial \epsilon/\partial t) = 0 \qquad (4)$$

269

where u is the mass velocity, yield a complete system which can, in principle, be solved to obtain wave profiles in materials in presence of cracks.

Fracture calculation method in an existing computer program that solves the equations of continuum mechanics is two space dimensions and time is described in (21), which can be modified to effectively handle the present problem in a high-speed computer. One can thus extricate enough information analytically to allow comparison with results obtained experimentally on test samples with and without cracks.

DISCUSSION ON v, b, N & $\dot{\epsilon}_x$

Once the crack has started to spread, its tip will be moving at some velocity $v = da/dt$, where $2a$ is the length of the crack. As 'a' becomes large, the limiting crack velocity is about 0.4 of the elastic longitudinal wave velocity for the material. This has been observed experimentally in a number of materials.

The velocity, v, of a running crack can be correlated to a linear dependence in shear stress as below:

$$v = b\frac{\tau}{B} \qquad (5)$$

where B is the damping coefficient. Analytical investigation of material damping characteristics is discussed in (22) and it is shown that the net dissipated energy in the material can be expressed as a product of four factors representing geometry of specimen, material constant, excitation amplitude and mode shape parameters.

The average interflaw spacing, b, is the Cinderella of this analysis. It has been considered as a material characteristic following statistical distribution. But no suitable correlation has been found to date to allow a separation of its effects from the distribution of flaw concentration factor, (23).

For mobile crack models which specify N and v, simple correlation is to be obtained of crack properties with dislocation models of the material on the assumption that the crack properties depend not on the statistical population of crack models but on the magnitude of a single value of the statistically dispersed model parameter. Such a key parameter is

provided by the exponent, m, of the Weibull's special distribution function for tensile strength of solids (24).

$$\alpha_F(V) = \text{Const.} \; (V)^{-1/m} \qquad (6)$$

where α_F is the tensile strength and V the test volumes. A qualitative physical interpretation of the 'm' value is that it increases with increasing homogeneity. Low 'm' value indicates inhomogeneous materials.

Finally, the strain rate for the running crack is given by

$$\dot{\epsilon} = \dot{a} \, \dot{\epsilon}_1/\delta \qquad (7)$$

where
$\dot{a} \equiv$ constant crack speed (relatively low)
$\dot{\epsilon}_1 \equiv$ the critical strain at the crack tip.
$\delta \equiv$ Crack opening dislocation.

CONCLUSIONS

It is thus possible to estimate the shock retardation in the presence of cracks in a principally elastic media, except for the small plastic zone near the crack tip. The method proposed is based on the progress made in the recent past in the areas of shock wave mechanics, dislocation dynamics, and fracture mechanics studies. The analysis presented is applicable for the decay of the precursor. It can be extended to the studies of elastic-plastic stress waves, elastic-visco-plastic waves and other aspects of shock waves in the presence of cracks in a material. Conversely, the decay of shock wave in a material may be used to evaluate the existence of cracks in a material and their average properties, as against the evaluation of individual cracks by the usual ultrasonic method. The utility or otherwise of the method proposed for further researches in different areas depends on getting an experimental verification of the results predicted by the proposed method.

REFERENCES

1. G. E. Duval, Ap. Mech., Revs., 15, Nov. 1962, 849.

2. Y. C. Fung, "Foundations of Solid Mechanics," Pb. Prentice-Hall, India, 1968.

3. J. J. Gilman, Proc. V U.S. Natl. Cong. Ap. Mech., June 1966.

4. J. J. Gilman, Ap. Mech. Revs., **21**, Aug. 1968, 767.

5. M. Liebowitz, Ed., "Fracture" v. I-VII, Acad. Press, 1971.

6. A. A. Griffith, Phil. Tr. Roy. Soc., Lond., 1920, Ser. A 220.

7. A. A. Griffith, Proc. Int. Cong. Ap. Mech., Delft., 1924, 55-63.

8. G. R. Irwin, "Fracture Dynamics" in "Fracturing of Metals." ASM. Cleveland, Ohio, 1948.

9. E. Orowan, Rept. Progr. Phys. **12**, 1949, 185-232.

10. J. J. Gilman, In "Plasticity," Pergamon, N.Y., 1960, 43.

11. S. M. Sharfuddin, Jour. Engg. Maths. **9** n. 3, July 1975.

12. P. C. Paris and G. C. M. Sih, "Fracture Toughness Testing." ASTM, Pa. STP. No. 381. 1965, 30.

13. E. Orowan, Z. Physik **89**, 1934.

14. P. P. Gillies and J. J. Gilman, *J. Ap. Phy.* **36**, 1965, 3370.

15. D. R. Curran, In "Shock Waves," Proc. 17th SAMR Conf., Syracuse Univ. Press, 1971, 121.

16. J. W. Taylor, *J. Ap. Phy.* **36**, 1965, 3146.

17. J. N. Johnson and L. M. Barker, *J. Ap. Phy.* **40**, 1969, 4321.

18. J. N. Johnson et al., *J. Ap. Phy.* **41**, 1970, 2330.

19. J. N. Johnson, *J. Ap. Phy.* **40**, 1969, 2287.

20. L. E. Kaechele and A. S. Teleman, Acta. Met., **17**, 1969, 463.

21. M. L. Wilkins, in "Shock Waves," Proc. 17th SAMR Conf. Syracuse Univ. Press, 1971, 387.

22. B. M. De   and A. S. R. Murty, I World Conf. Ina   , New Delhi, 1972.

23. V. Weis   . Trans. ASME, Ser. D, 1966, 675-681.

24. W. Weibull, Roy. Swed. Inst. Eng. Res. Proc. **193**, 1939, 151.

DISCUSSION

J. J. DICK
Washington State University
Pullman, Washington

As I understand it, the author suggests that plastic strain rate is proportional to average distance between flaws b (Eq. 1). This does not make sense to me since this implies that the greater the spacing (fewer flaws) the greater the strain rate.

AUTHOR'S REPLY

While thanking the discussor for taking interest in the paper, the author would like to point out the fallacy in assuming "the greater the spacing (fewer flaws)." The flaw density is defined by the term N in equation (1) and is independent of b, the inter flaw facing.

SENSITIVITY OF EXPLOSIVE SUBSTANCES
A MULTIVARIATE APPROACH

Stig Ek
Swedish National Defense Research Institute
Stockholm, Sweden

A new philosophy in sensitivity testing and risk evaluation is presented. An explosive substance should be tested by a test battery comprising many and varied tests. The test battery should be designed and the information in the results extracted with the aid of multivariate statistical methods. This will give

a. An understanding of the meaning of the tests.
b. A certain possibility to evaluate the risks directly from à priori information about the substance.
c. A characterization of the sensitivity of a substance by a few figures.

Future risks can be estimated from the relative positions of a substance and known substances, e.g. TNT and PETN, in a space with these characteristic figures as coordinates.

The methods are demonstrated by an analysis of an experimental material from BAM in Berlin comprising homogeneous substances and pyrotechnic mixtures tested in several tests.

INTRODUCTION

When triggered by a suitable, sufficiently energetic impulse an explosive substance reacts chemically with the liberation of energy. The input of energy needed to start the reaction is very different for different substances. To start the reaction with a high degree of certainty the various explosive devices therefore need ignition systems designed to transfer the proper amount of energy in proper form.

During its production and handling an explosive substance is exposed to unwanted input of various kinds of energy. This can under unfavourable circumstances lead to ignition of the substance and possibly to accidents. Since the consequences of such accidents can be very severe, we must take effective precautions to keep the probability of such unintentional ignitions at a very low level. This is possible only if we know enough about the behaviour of the substances in various situations.

We get such knowledge mainly in three ways: through various types of fundamental studies, through different kinds of sensitivity tests, and from statistics concerning accidents and exceptional behaviour in production and handling.

Whatever method we use to predict possible accidents, we have one fundamental problem. The substances can be subjected to so many different situations, each with its own pattern of different kinds of stress, that it is impossible to imagine them all. With more theoretical understanding we can make theoretical predictions of risks in more and more situations, but a *wholly* complete understanding and description of all potential risk situations will never

272

be possible. Therefore systems for sensitivity testing will always be one important basis for our decisions.

SENSITIVITY TESTING IN RISK ASSESSMENT

To predict the behaviour of a certain substance under "natural" stress one can observe its behaviour in a number of sensitivity tests, each designed to show its reaction in a certain situation. A test relevant to this situation will rank the explosives according to their risks in just this case.

To create meaningful sensitivity tests, one must analyze the situation, describe it in appropriate categories, and then design the test to give a result relevant to just this situation. As always in sensitivity testing many replications of the test are needed before we can guarantee a really small accident risk. Since the possible combinations of situations and substances are very numerous, it would be prohibitively expensive and time-consuming to design and perform such "tailor made" tests in more than a few really important cases.

For a long time we have therefore used "standard tests". These are simple to perform and are supposed to give an indication of the sensitivity in some typical situations e.g. impact and friction. Many of them are carefully standardized and prescribed for the legal classification of explosive substances.

The standard tests can give an indication of possible risks without too much work, but we must have in mind their limitations. They are neither close duplications (simulation) of specific hazardous situations, nor physically "pure" tests. They have been designed often in an intuitive way to resemble some "type situations". Therefore most specific practical situations can neither be closely paralleled by one of the tests (e.g. drop weight test) nor estimated from the test via fundamental physical and chemical characteristics.

We can, nevertheless, often correctly estimate the risks in "conventional" risk situations for explosives of well-known types from such test results. This is possible, since we have a vast experience as regards the common types of explosives, both from such testing and from statistics concerning accidents and exceptional behaviour in "standard situations".

MULTIVARIATE METHODS IN TESTING AND EVALUATION

As the possibly hazardous situations are very numerous and varied, we need a wide and representative basis for our decisions. We need rather many tests of very different kinds (1).

The testing of many substances in many tests tells us the behaviour of every explosive in every test, but this is only one aspect of the information contained in the results. The relation between the sensitivities of the substances is different for the different tests (and this is of course the reason why we need many tests). The test results form a rather complicated pattern. With the aid of suitable multivariate statistical methods we can analyze this pattern and present the information it contains in a compact and lucid way.

Such methods are much used in the social sciencies, but much less so in the physical sciences, e.g. the explosives field, perhaps because we can often interpret our experimental results from reliable theories, whereas in the social sciences the theoretical foundation is less precise and more controversial and the systems studied very complex.

In spite of our rather well developed theoretical knowledge I think it is rational to make extended use of multivariate statistical methods in our work. The analysis of a material with these methods is not only a statistically efficient way to condense the experimental results. Used in an intelligent way it can represent an independent way of thinking in our field and a fair chance to discover new facts and relations fundamental for our understanding.

TESTING IN GENERAL

Testing is done extensively in many fields to get information about the behaviour of e.g., mechanical units or people in different situations. The general problem here is to design and use a battery of tests that is relevant to some important situations the test battery must have a high validity.

Since the aim of testing is about the same in different fields, it must be profitable for us to study some of the methods used and the results obtained in other fields. I think this is especially true about some branches of psychological testing.

Thus in ability testing--e.g. IQ tests and their equivalents--a tremendous amount of work has been done during the last 100 years or so. One of the most important multivariate methods, factor analysis, has been developed and extensively used in connection with ability testing and the search for meaningful categories to describe the function of the human mind (2).

To use the knowledge and experience from the psychological field as well as possible we can I think without change adopt many statistical methods of a general character and some test strategies that have been fruitful there. Because our problems can be more strictly defined and our theoretical background is better, I think we can also profitably modify some methods and develop new, even more effective ones, in our field.

IMPORTANT MULTIVARIATE METHODS

Some of the multivariate methods are fundamental for an understanding founded on statistical criteria: Multiple regression, discriminant analysis, and factor analysis with the special case of principal components analysis.

Multiple regression analysis can tell us how certain parameters affect the behaviour of the substances under various conditions. These parameters can be the composition of the substances or characteristic values as regards the special environments, etc.

Discriminant analysis gives the most efficient measure of the difference between two or more groups of substances that is possible with a linear combination of the variables tested. If we think that two or more groups of substances in our material differ in some respect, we can test this hypothesis with the aid of discriminant analysis using all the tests or a suitable subgroup of tests.

Factor analysis gives information about the structure in the relations between substances and tests and between the various tests. It tells us the dimensionality of our system and thus gives a measure of its complexity. It can help us design rational test batteries, and factor analysis or principal components analysis gives an effective mean for evaluating the results from a test battery. The information about the structure contributes to our understanding of the

mechanisms at work and can give valuable ideas for new fundamental research (3, 4, 5).

Basic Data for the Analyses

The results from the various sensitivity tests can be of very different character, and they are often measured in units that are not directly comparable (time, temperature, pressure, length, etc.). In psychological testing the "standard score" is very much used. It is defined as $(X-M)/\sigma$ where X is the measurement at hand, M its mean value in the material, and σ the standard deviation of this measure in the material. In this way, each substance will have a "score" in a test that tells how many standard deviations its value is higher or lower than the group mean. The signs are chosen so that a positive standard score means a relatively sensitive substance, a negative one a relatively insensitive. In some cases a transformation of the values has been performed to give a more nearly normal distribution.

In this way, the results from all the tests are comparable, and the information can be conveniently described as correlations in the system. Two sets of such correlations are of special interest here.

1. Between results from various tests with different substances.

2. Between some parameters possibly relevant to the substances and their behavior in the tests.

ANALYSIS OF AN EXPERIMENTAL MATERIAL

To test the use of multivariate methods in sensitivity testing we have analyzed results obtained by BAM in Berlin and published during 1961-70 (6). This material consists of results in a number of sensitivity tests of nearly 100 different explosive substances. 40 of the substances are homogeneous--both normal explosives and other chemical compounds with some explosive properties--and nearly 60 pyrotechnic compositions.

The tests subject the substances to heat in different forms--open or in different states of confinement--and to impact, friction, detonative shock in steel tubes, and measure the explosive strength in a lead block.

274

After a lot of tentative analyses we have mainly analyzed a subset of rather well-known substances, 29 homogeneous ones, 18 chlorate mixtures and 18 aluminium mixtures.

The 4 tests for ignitability by sparks of two kinds, flame and red hot iron were conveniently combined into one figure of ignitability, and the 2 tests of detonability in steel tubes could without loss of information also be condensed into one figure.

We have used the following tests in our analyses:

9. Time for reaction in a red hot steel bowl.
10. Behaviour in a heated glass capillary.
11. Behaviour in a heated steel box $8 \times 8 \times 8$ cm.
12. Largest orifice in the BAM apparatus (Koenen test) for bursting of the steel crucible.
14. Time from beginning of reaction in test 12 to explosion.
15. Friction sensitivity in the BAM apparatus.
16. Impact sensitivity in the BAM drop weight test.
17. Lead block expansion according to BAM.
20. Above mentioned index of ignitability.
21. Detonability in 1″ or 2″ steel tube.

In some analyses we have also included

1. Ignition temperature in a Wood metal bath.
13. Time from beginning of heating in the Koenen test to first sign of reaction.

To make possible a less confused presentation of the results the tests are often grouped as below.

A.	Ignition temperature and equivalent	1, 13
B.	Heat supplied to open substance	9, 20
C.	Heat supplied to partially enclosed substance	10, 12, 14
D.	Heat supplied to totally enclosed substance	11
E.	Impact test	16
F.	Friction test	15
G.	Lead block and detonability	17, 21

The tests in each one of these (natural) groups have rather high intercorrelations within the group and usually follow each other in the analyses.

Multiple Regression

We have chosen 3 measures as independent variables to explain the behaviour of the 18 chlorate mixtures in 12 tests. They are:

1. The total amount of available energy per unit weight represented by the amount of oxygen that can be transferred from an oxidizer to a fuel.

2. The part of this energy that can be liberated more easily, represented by the amount of oxygen that can be transferred from a *chlorate* to a fuel.

3. The part of this latter energy that can be developed through transfer of oxygen from a chlorate to a subclass of the fuels.

The analysis shows that the most important of these variables is number 2. This is in agreement with our general experience that a high chlorate content gives a higher sensitivity.

Multiple regressions are obtained that explain between 49 and 92% of the variance in the 12 tests. I think this is a good result considering the difficulty of obtaining exact results in sensitivity testing.

To get a largely independent result we performed a factor analysis on the same material and extracted 3 factors. The factor analysis does *not* use the information about the values of our independent variables, but gives its results only on the basis of the intercorrelation between tests. On the other hand, the multiple regression computes the results for each test without regard to these intercorrelations. If therefore the results from the two analyses agree reasonably well, the results must be of some significance.

The factor analysis explains between 25 and 99% of the variance in the tests. The mean value explained is 70% in the regression analysis and 73% in the factor analysis.

In Fig. 1 the *pattern* in the results from the two analysis are compared. Both results can be represented as vectors in a 3-dimensional space. A test vector has a length equal to the square root of the part of variance explained. The correlations between each of our independent variables and a test vector in the regression model and between two test vectors in the factor analysis model are represented by their sscalar products. Two vectors at right angles have zero
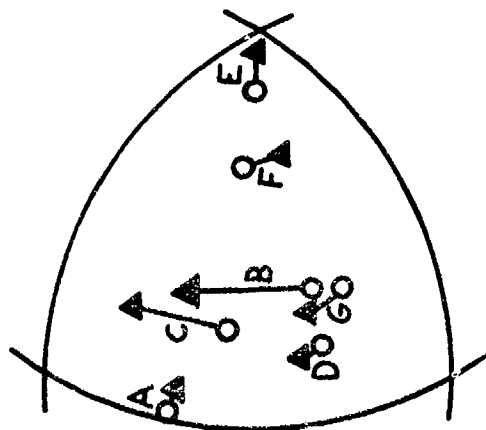
Fig. 1. Comparison between multiple regression and factor analysis for 18 chlorate mixtures.

correlation, two vectors close to each other a high correlation. The test vectors are extended to unit length to meet the surface of a sphere. A map of the points where the test vectors meet the surface of a unit the sphere is then made.

Filled triangles represent the results from the factor analysis, open circles the results from the multiple regression. The regression solution has been rotated to coincide as well as possible with the factor analysis. The 3 circular arcs represent the 3 great circles enclosing the positive octant of the unit sphere. The letters represent the group means above. The lines represent the discrepancy between the two solutions.

As both the explained part of the variance in the tests and the picture of the relative intercorrelations between the tests coincide rather closely, we have shown it is possible to compute the results in several tests and their relation to each other from a few fundamental (chemical and /or physical) parameters.

All these relations between cause and effect, between various tests, and between the two kinds of solution are of course much better seen in a 3-dimensional model.

Discriminant Analysis

In our material we have homogeneous substances and pyrotechnic mixtures. These two groups might behave differently because the energy-producing

reaction in pyrotechnic mixtures is a transfer of oxygen from a grain of oxidizer to a grain of fuel, whereas in the homogeneous substances the energy-producing reaction can take place within the same molecule.

Are we able to demonstrate a clear-cut difference between the two groups from the 10 test results chosen? To answer this question we have performed a discriminant analysis. In such an analysis each substance is characterized by a value in a discriminant function. In Fig. 2 the distribution of these values is given for the substances.

As can be seen the substances are divided into two distinct groups. We can ask whether we really need all these tests or whether a subgroup of them will discriminate as well. To answer this question we have performed a stepwise discriminant analysis, which shows that a group of 7 tests, 14, 17, 11, 20, 15, 16, and 9, discriminate as well as all the 10 tests. Their discriminative effects are in the order given with number 14 the most effective, followed by number 17.

Principal Components Analysis

The results from the various tests are rather strongly correlated in our material. One can therefore effectively condense the results in many tests without losing a significant amount of information. Through the averaging effect in this process these new functions can also be more precise than the original test result.

Such a condensation can effectively be done with the aid of principal components. The first such component is computed so as to explain as much as possible of the variance in the results, the second
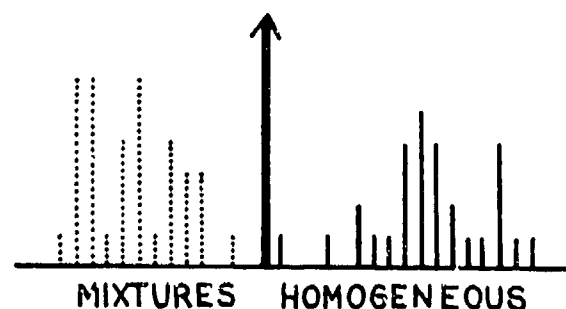
Fig. 2. Discriminant analysis.

component as much as possible of the remaining variance etc. These components are constructed to be orthogonal. The original results are in this way explained as well as possible for a certain number of functions.

We performed a principal components analysis on the results from the 65 substances tested in 10 tests. 83% of the total variance can be explained by the first 3 components and 75% by the first 2. One can thus give a good picture of the results in 3 dimensions, and even a picture in 2 dimensions contains most of the information, see Fig. 3.

The first component represents mainly the sensitivity in all tests except the detonability tests 17 and 21. The second component represents above all these two tests. As a very crude approximation one can regard the first component as representative of the sensitivity to heat and low intensity mechanical stress, the second component of detonability and sensitivity to high intensity shock waves. The third component is of a more mixed character.

The homogeneous substances, the chlorate mixtures, and the aluminum mixtures form 3 distinct groups where the typical substances in each group lie rather close to the 3 lines in the figure. This means that the homogeneous substances are relatively more sensitive to high intensity shocks of short duration than to low intensity energy input with longer duration. For pyrotechnic mixtures it is vice versa and most pronouncedly for the aluminum mixtures. This is well in accordance with the difference in reaction kinetics mentioned above and to the fact that both the pyrotechnic compositions and the homogeneous explosives have been designed and selected to act this way.
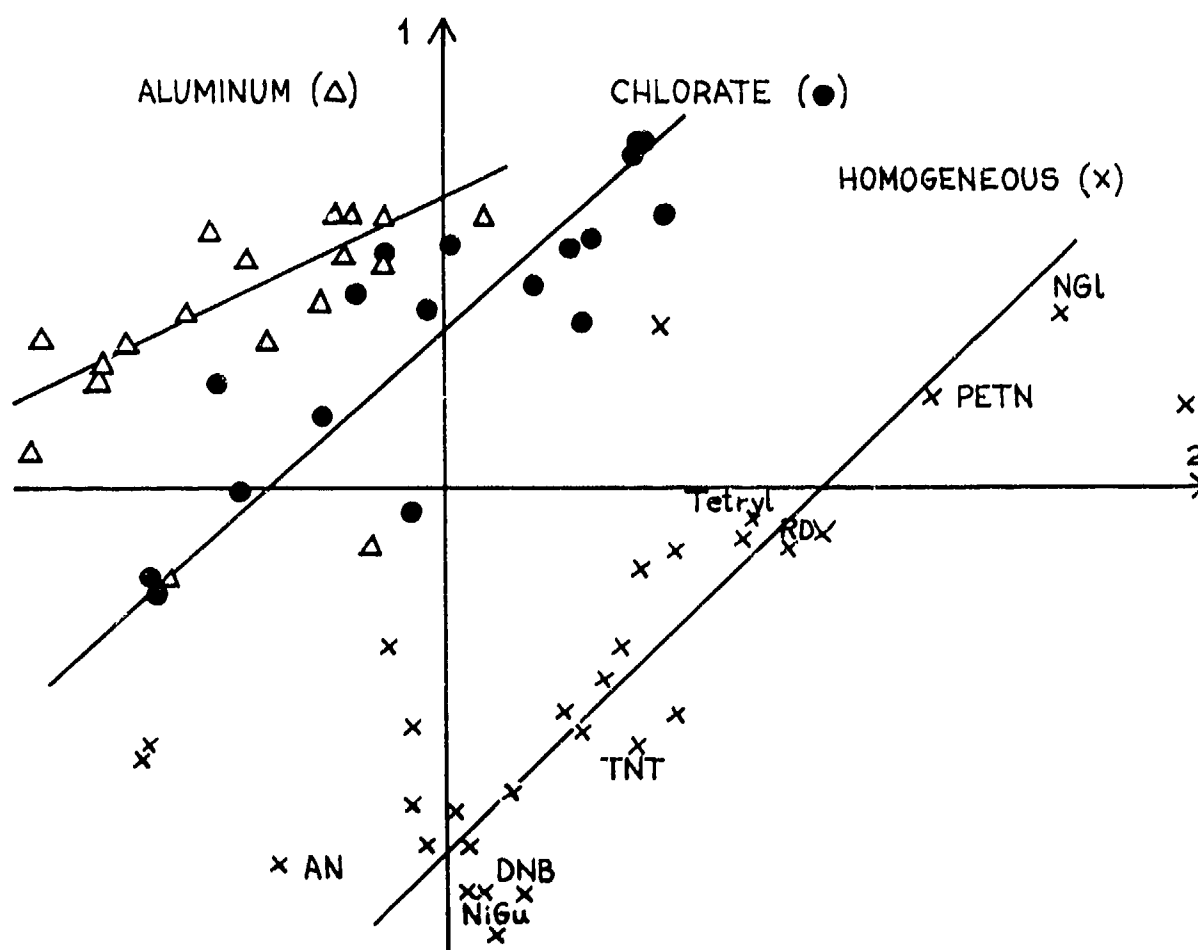
Fig. 3. Principal components.

In each group the most sensitive substances lie close to the upper right part of the lines, with the others following in descending order to the least sensitive at the lower left. For the pyrotechnic mixtures the order along the lines corresponds to the general rating of sensitivity made by BAM. For the homogeneous substances this order is evident from the position of some well-known substances indicated in the figure, from the most sensitive Nitroglycerine and PETN at the upper right over Tetryl and RDX to the insensitive Dinitrobenzene, Nitroguanidine, and Ammonium nitrate at the lower left.

Even if the principal components in such a system do not represent intuitively simple concepts (which, however, the first two components do here) one can estimate the risks for a newly tested substance from its place relative the well-known ones.

Factor Analysis

A principal components analysis tries to explain as much as possible of the total variance in the test results and thus gives a compact description of these results. A factor analysis on the other hand, tries to explain as much as possible of the intercorrelations between the tests in the system. If therefore gives an insight into the structure of the system and may possibly disclose some important new categories in the field.

We have made such analyses, first with the whole material 65 substances in 10 tests—and then with different subgroups of the substances in the same 10 tests.

The Whole Material

The factor analysis shows that 3 dimensions are needed to explain the relations. This is in good agreement with the result above from the principal components analysis. Fig. 4 gives a map of the relations between the test groups B—G. It is constructed in the same way as in Fig. 1.

The corners of the triangle give the positions of the factors rotated according to the (in connection with factor analysis conventional) varimax principle. Such a rotation is of great importance in the social sciences as an aid in identifying unknown basic factors, especially in solutions in many dimensions, but is not as important here. We have a better chance
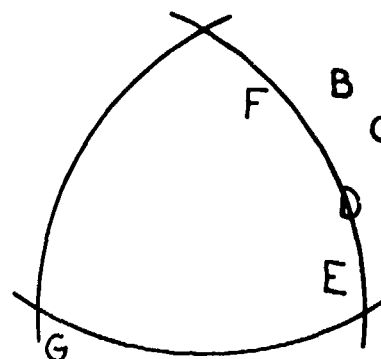
Fig. 4. Factor pattern. All substances.

to identify the findings with the aid of our physical and chemical knowledge.

It is immediately seen that the tests in groups B F are more or less correlated in this material, but group G, the behaviour when subjected to a shock wave, is uncorrelated to the others, and even negatively correlated to B and C, the reactions to heat unenclosed and lightly enclosed respectively.

This negative correlation depends on the fact that the homogeneous substances as a group are relatively more sensitive to shock waves than to heat in open condition, and the pyrotechnic compositions on the other hand are relatively more sensitive to heat in free conditions than to detonative shock. *Within* each of these two groups the sensitivity to detonative shock is—more or less—positively correlated to the unconfined heat tests.

Subgroups

Separate factor analyses have been performed for the homogeneous substances and for the pyrotechnic mixtures. In each case 2 dimensions are needed. The test vectors are shown in Fig. 5a and b. The patterns are about the same, with the open or partially closed heat tests B and C as one extreme type of tests, and the detonability tests G as the other extreme. There are some irregularities however, which I think are mainly caused by the too low dynamic range in some of the tests. This is very obvious in 2 tests as regards the homogeneous substances.

Only 5 of our 29 homogeneous substances did react at all in the friction machine used—3 of them

278
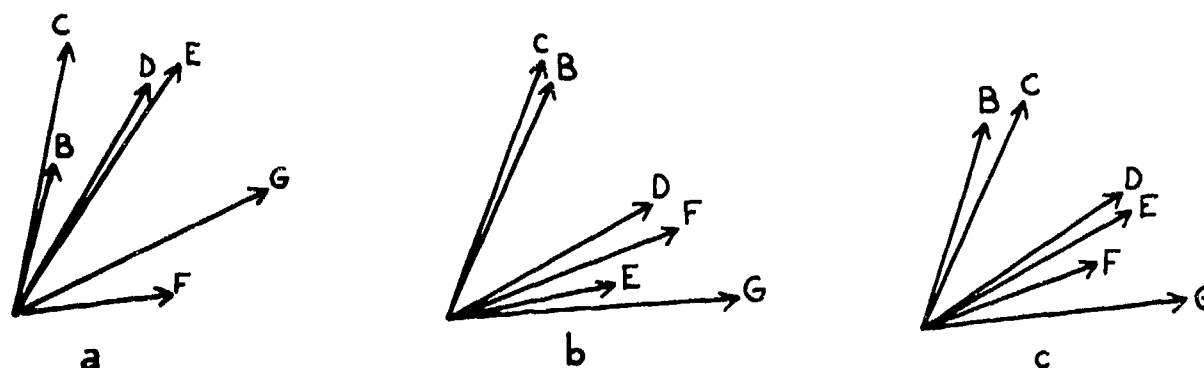
Fig. 5. Factor patterns. a: Homogeneous substances; b: Pyrotechnic mixtures; c: All substances.

only for the maximum stress possible. The correlations in this subgroup between test F and the others are therefore biased compared to what a friction test with ample dynamic range would give. The correlations are all very low and the test vector F is badly explained in the analysis and probably wrongly situated.

We have the reverse problem as regards the detonability tests for the homogeneous substances. All but 4 of them detonated completely in the 1″ steel tube. An effective classification is obviously not possible. If (or when) we design a completely new test battery it is important to have tests with sufficient dynamic range to get reliable results in this kind of analyses.

A way to diminish the effect of too low dynamic range in our tests is to compute correlation coefficients in the 2 subgroups, as a basis for a factor analysis. Since some tests have low dynamic range in one group, some tests in the other, we will in this way have a fair chance to avoid too much biased correlation coefficients.

We have performed a factor analysis on these correlations. The test vectors are shown in Fig. 5c.

This factor structure has the same general appearance as the structures for the 2 subgroups. It is however very different from the pattern in Fig. 4, because here we have the structure *within* the 2 groups.

I think this structure in Fig. 5c is the best general picture we can give of explosive substances in a test battery as this. We can distinguish two factors: sensitivity to heat unconfined and detonability. The other tests measure something in between. All kinds of

sensitivity are positively correlated *(within* groups) and the nature of the tests changes stepwise in the direction B C D-E-F-G.

Worth noting is that D and E, the heat test in a closed steel box and the impact test, according to this and other analyses seem to measure about the same type of sensitivity. This is a little puzzling and not à priori obvious.

DISCUSSION

The analysis of the experimental material from BAM has shown that it is possible to get valuable information of new kinds with the aid of multivariate statistical analyses. A new insight into the structure of the substances--tests relations has been obtained and a method to describe the risks for a substance on the basis of test results has been demonstrated.

To make full use of the methods it is, however, not enough to analyze a material already at hand. It is necessary to do experimental work with new tests to develop really effective test batteries.

The clear division between groups of explosive substances and the relatively simple structure *within* groups make it seem rational to develop new test strategies as a kind of stepwise testing. The first step would be a decision *to what group* the substance should belong. In this step the known chemical and physical parameters for the substance are obviously very important. The next step would consist of applying a battery of tests especially suited for this particular group.

279

A presentation of the sensitivity of the substance in this battery as principal components, as has been done here, is probably one of the most efficient ways. Since this kind of averaging gives figures that normally are much more reliable than the results of the single tests in the battery and a large variety of tests is necessary to avoid "unconventional" accidents, it will be optimal to divide a certain amount of experimental work between as many tests as possible with only rather few replications in each test. That the results from each of the tests will be very uncertain does not matter in such a system.

If one really needs a point information for a special case the problem is of course different. Then one needs a kind of tailor made test.

ACKNOWLEDGEMENT

REFERENCES

1. Stig Ek, "Determination of risks in relation to sensitivity of explosives" OECD, IGUS report, Nov 1969.

2. J. P. Guilford, The Nature of Human Intelligence, McGraw-Hill, New York 1967.

3. L. L. Thurstone, Multiple Factor Analysis. University of Chicago Press, 1947.

4. H. H. Harman, Modern Factor Analysis. University of Chicago Press, 1967.

5. SPSS, Statistical package for the social sciences. McGraw-Hill, 1975.

6. H. Koenen et al., "Sicherheitstechnische Kenndaten explosionsfähiger Stoffe", Explosivstoffe Nr. 1, 1961, Nr. 9, 1961, Nr. 12 1965, Nr. 3, 1970.

INSTABILITY OF HETEROGENEOUS DEFLAGRATION WAVES

Luigi De Luca

Istituto di Macchine, Politecnico di Milano,
32 Piazza L. da Vinci - 20133 Milano, Italy

The static and dynamic stability of heterogeneous deflagration waves for finite size disturbances is examined. In order to retain the important nonlinearities, an approximate formulation of the problem has been written by means of a standard integral method. At a given pressure, a minimum surface heat release exists above which upper dynamic instability shows up. This leads to abrupt accelerations of the monodimensional deflagration processes. The burning rate may increase by orders of magnitude even at pressures of few tens of atm. For further increases of surface heat release, stationary configurations are no longer allowed and steady oscillating burning rates are observed as solutions. For even larger increases of surface heat release, the only allowed steady solution is the trivial nonreacting configuration. The predictive capability of the proposed approach is well verified by computer simulated experiments.

INTRODUCTION

The purpose of this study is to analyze the heterogeneous deflagration wave stability properties peculiar to the essentially nonlinear character of the relevant phenomena. These are described by a strongly nonlinear second order partial differential equation of parabolic type. There is today no rigorous analytical way for dealing in general with such a problem.

In order to ascertain general properties of the governing set of equations, an approximate formulation of the problem in terms of an ordinary differential equation has been written (1). This allows one to define stability boundaries for finite size disturbances of burning rate, not only at constant pressure (static stability) but also following timewise monotonic changes of the controlling parameters (dynamic stability). In principle, the proposed approach may be applied to deflagration waves associated with any substance initially in a condensed phase, provided a proper flame model is furnished. However, in the sequence of papers (1-3) prepared by this writer,

quantitative applications are made with reference to a tative applications are made with reference to a solid, ammonium perchlorate based, composite propellant indicated as AP/PBAA #941 by the Princeton group. For this cl~ f heterogeneous deflagration waves very satisfa.. / flame models have been developed by Summerfield and coworkers (4).

In this paper attention is focused on the existence (for finite size disturbances) of dynamic stability boundaries in contrast to the static stability boundary. A survey of the Literature (1) shows a quite confused state of affairs in this respect. Emphasis is given to conditions leading to heterogeneous deflagration wave transition toward faster regimes and to the existence of an upper dynamic stability boundary. This can also be considered a first step in the complicated patterns involved in the deflagration detonation transition (5). Indeed, the possible existence of an upper dynamic stability boundary would imply that an abrupt transition from an initial stable reacting configuration may occur at any instant during the deflagration history, if a sufficiently vigorous disturbance process is somehow triggered.

Burning rate increases may be obtained in several ways, e.g. by increasing ambient temperature or external radiant flux. For sake of brevity, in this paper only the burning rate dependence on pressure and surface heat release will be considered. It will be shown that, at a given pressure, any heterogeneous deflagration wave with an appropriate value of surface heat release is intrinsically able to undergo dramatic accelerations. Basically, this is due to an unstable energy coupling of the condensed with the gas phase through the burning surface.

The strategy in this paper is to evaluate the stability properties of heterogeneous deflagration waves directly from the structure of the approximate ordinary differential equation describing the problem. The predictive capability of the proposed approach will, then, be verified by computer simulated experiments performed by numerical integration of the complete set of the governing equations.

BACKGROUND

For a review of the current literature on solid propellant combustion stability, the reader is referred to (1). Here only some brief comments will be given. Although widely debated in the technical literature, the burning stability problem has been largely limited to the question of dyanmic extinction by depressurization. The work by T'ien (6-7) is among the very few aiming directly at establishing an extinction criterion for fast depressurization. On the other hand, no criterion has been formulated so far for the case of dynamic extinction by fast deradiation reported by the Princeton group (8). Likewise, very little work has been done on the upper dynamic stability question (9).

T'ien (6) found that "for depressurization transients, if the instantaneous burning rate drops below r_b (the unstable burning rate solution at the final pressure), extinction will occur". T'ien derived his quantitative criterion from another study (7) by him of flammability limits of premixed flames under the influence of environmental disturbances. A somewhat similar result has been obtained by the writer following a completely different approach (2).

The line of research evolved within the framework of the mechanistic (Zel'dovich) approach (10-12) has been unable to reach meaningful conclusions about the dynamic stability problem. Novozhilov observed (p. 216 of Ref. 12) that this "question requires certain information about the properties of the system outside the area of smooth burning. Such information cannot be obtained from experiments on steady state combustion. For the calculation of unsteady conditions in the unstable region it is necessary to draw on certain schemes of combustion, which make it possible to predict the properties of propellants beyond the (static) stability limit".

The question of a possible early warning of extinction during a depressurization transient, evaluated via the Zel'dovich method, was examined also by the Princeton group (13-14). The possibility was checked that crossing of the static stability boundary is sufficient to subsequently produce dynamic extinction. Although correct, only a qualitative answer to this question was given: "the dynamic conditions of extinguishment tend to shift the stability line" (p. 257 of Ref. 14). It is the opinion of this writer that the static stability boundary has only secondary relevance in a dynamic situation.

AN INTEGRAL APPROACH

The basic mathematics consists in an approximate transformation of the governing nonlinear parabolic partial differential equation to a nonlinear initial value ordinary differential equation based on a well known "integral method" (15). A similar approach has been already applied to droplet burning (16). The application to heterogeneous deflagration wave models is described in detail in (2). The important assumptions made are: quasi-steady gas phase, opaque and inert condensed phase, and condensed reacting layer collapsed to the burning surface.

It is found that at constant pressure the instantaneous response of the system, when subjected to finite departures from the initial configuration, is described (2) by

$$\frac{du_s}{d\tau} = -\frac{2}{3} \frac{(u_x)_{c,s}}{u_s} \frac{R \cdot u_s - (u_x)_{c,s} + \Delta \dfrac{d\bar{\theta}_i}{dx} - R \cdot \Delta\bar{\theta}_i}{1 - \dfrac{1}{2} \dfrac{u_s}{(u_x)_{c,s}} \left[\dfrac{\partial(u_x)_{c,s}}{\partial u_s}\right]_\tau}$$

(1)

282

where $u_s(\tau)$ is the finite size surface temperature disturbance (Fig. 1). Following Lyapunov (17), the above equation can be re-written as

$$\frac{d\theta_s}{d\tau} = -\frac{du_s}{d\tau} = + f(\bar{\theta}_{i,s} - \theta_s) \qquad (2)$$
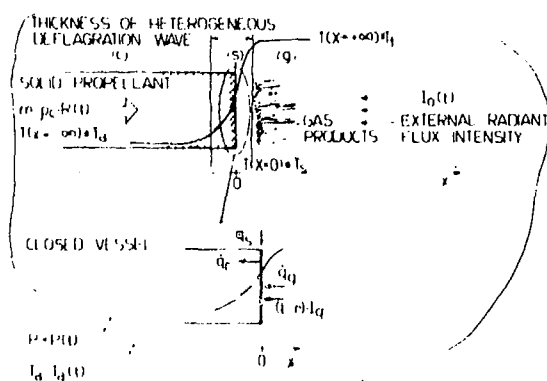
Fig. 1. Schematic diagram of the physical problem and energy balance at the surface of the condensed phase.

The function $f(\bar{\theta}_{i,s} - \theta_s)$, called the static restoring function, is qualitatively sketched in Fig. 2. For a
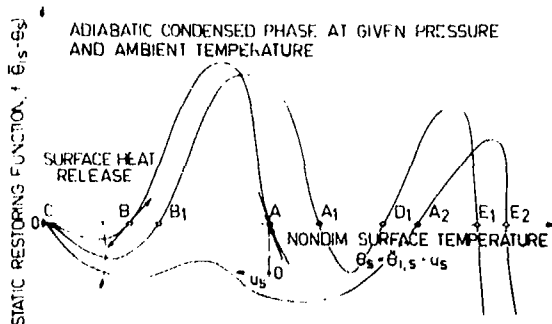
Fig. 2. Qualitative sketch of the nonlinear static restoring function illustrating the existence of three roots A, B (reacting mode) and C (unreacting mode) for a standard set of operating conditions. For the reacting mode, only solution A is statically stable and can be observed in steady state experiments. Increasing of surface heat release makes D and E type of roots appear (upper dynamic instability) and the reacting equilibrium configuration become unstable (root A_2).

standard set of parameters (say: pressure P = 30 atm, ambient temperature T_a = 300 K, no external radiant flux, no heat loss, heat release at the surface Q_s = − 158.2 cal/g), the curve connecting points A-B-C is obtained. It was shown in (2) that:

1. at a given pressure, besides the trivial $\theta_s = 0$ corresponding to the statically stable nonreacting configuration (root C), two more roots A and B are found. Of these

2. root A (statically stable) corresponds to the steady state reacting configuration $\bar{\theta}_s$, while root B (statically unstable) is the lower dynamic instability point θ_s^L.

3. At a given pressure, a branching point θ_s^S exists where the two nontrivial roots A and B coalesce.

4. The static stability boundary for finite size disturbances is the locus of the branching points θ_s^S.

5. The lower dynamic stability boundary, for finite size disturbances consequent to timewise monotonic changes of the controlling parameters, is the locus of the statically unstable points θ_s^L at the final pressure.

The static stability boundary defines the line of separation between a region where stable steady state solutions are allowed and a region where no steady solutions can be found. The lower dynamic stability boundary defines that ultimate burning condition beyond which extinction necessarily follows. The meaning and the existence of an upper dynamic stability boundary will be discussed in next section.

UPPER DYNAMIC STABILITY OF HETERO- GENEOUS DEFLAGRATION WAVES

Any self-sustained reactive system is capable of exothermic reactions. These occur both in gas (Q_f, cal/g) and condensed (Q_s, cal/g) phases. The total energy release $Q_f(P) + Q_s$ is determined by the energy balance at ambient temperature of the steadily burning adiabatic propellant. The effect of the surface heat release Q_s on the static restoring function is qualitatively illustrated in Fig. 2. As mentioned in the previous section, for a standard set of parameters only A - B - C roots are found. For increasing Q_s values, the following facts are observed:

283

1. a new pair of roots, D_1 (unstable) and E_1 (stable), appears in the high burning rate region (see Fig. 2).

2. roots A and D approach until coalescence (with stability character exchange) occurs. The steady state reacting solution (root A), stable before coalescence, is unstable after.

3. roots B and D approach until they merge and disappear.

4. only $C - A_2 - E_2$ roots are left (see Fig. 2)

For all cases, the overall steady energy balance is satisfied only at roots C (unreacting mode) and A (reacting mode). Therefore, these are in general the only allowed stationary solutions and can be observed either experimentally or theoretically as long as they are stable. But increasing Q_s displaces the reacting parameters toward faster regimes with loss of stability of root A; this also, then, becomes unobservable.

A quantitative plot, with Q_s ranging from -170 to -200 cal/g, is shown in Fig. 3 for a solid propellant deflagrating at P = 30 atm. Compare also with the curve $Q_s = -158.2$ cal/g shown in Fig. 4. It is inferred from Fig. 3 that coalescence of A and D roots, with loss of stability of the stationary reacting mode,

Fig. 4. Influence of pressure on nonlinear static restoring function for $Q_s = -158.2$ cal/g showing upper dynamic instability at P = 10 atm.

occurs at $Q_s = -190$ cal/g for the standard conditions of $T_a = 300$ K and adiabatic sample. By similar plots, the coalescence value of Q_s can be defined for any other pressure. The results obtained are listed in Table 1. Increasing pressure implies increasing Q_f, which in turn requires larger values of Q_s for destabilizing the stationary reacting mode. Therefore, larger pressures require larger coalescence values of Q_s.

The effect of pressure on the static restoring function, at a fixed value of $Q_s = -158.2$ cal/gr, is illustrated in Fig. 4 for P ranging from 10 atm to 40 atm. Roots are of A, B and C type for pressure not

TABLE 1

Surface heat release values, at which coalescence of A and D roots occurs, in function of pressure. For increasing pressure, stable stationary reacting configurations are observed for a larger Q_s range. See also Fig. 4.

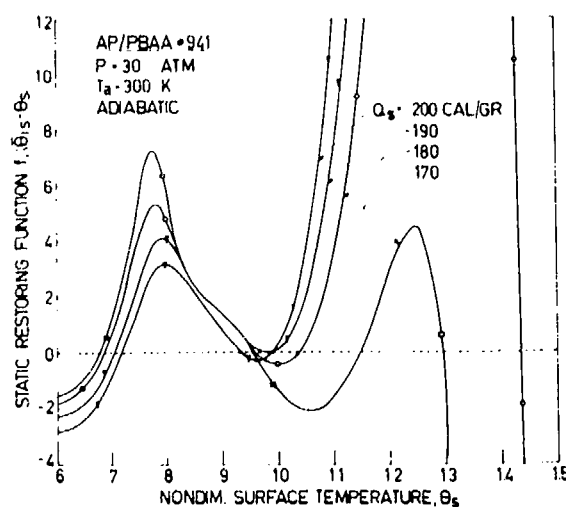| Pressure, P, atm	surface heat release, Q_s, cal/g
6	-158.2
10	-170.
20	-180.
30	-190.
40	-196.

Fig. 3. Influence of surface heat release on nonlinear static restoring function showing loss of stability of reacting equilibrium configuration for $Q_s = -190$ cal/g.
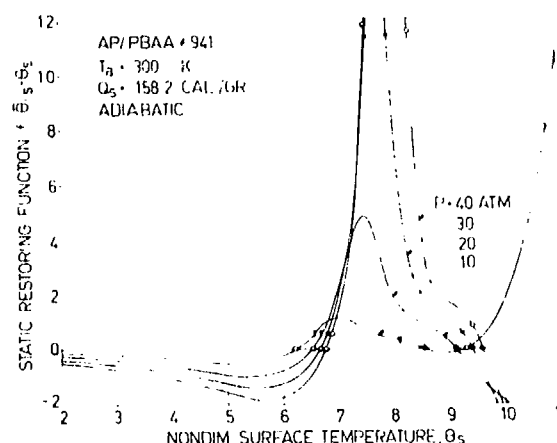
less than 20 atm. At $P = 10$ atm a pair of roots D and E appears.

The two roots B_1 and D_1 (Fig. 2), located on either side of the stable steady state configuration A_1, represent dynamically unstable points. If the surface temperature during a transient goes past B_1 or D_1, the heterogeneous deflagration wave will accelerate respectively toward C (lower dynamic instability) or E_1 (upper dynamic instability). In the case of lower dynamic instability, the fate of the heterogeneous deflagration wave is defined by the stable unreacting steady state configuration corresponding to root C (trivial solution). This is called dynamic extinction and is a well known phenomenon in solid propellant combustion not only for depressurization but also for deradiation (6-8). In the case of upper dynamic instability, the fate of the heterogeneous deflagration wave is more involved. As soon as point D_1 is passed a vigorous acceleration occurs. The increase of burning rate may be orders of magnitude. Point E_1, although strongly stable, is not allowed as a stationary solution. Therefore, after reaching E_1, the heterogeneous deflagration wave is violently recalled back toward a stable steady state configuration. Depending on the dynamics of the whole process, this can be either the reacting mode A_1 or the unreacting mode C (dynamic extinction).

After coalescence of A and D roots, the static restoring function features two stable roots (D and E) neither of which is allowed as a stationary solution, while the stationary solution A is unstable. Under these conditions, the two roots B and A, located on either side of D, represent dynamically unstable points. All previous considerations are valid, except as to the fate of the heterogeneous deflagration wave. Depending on the dynamics of the whole process, this can be either the unreacting mode C (dynamic extinction) or self-sustained oscillations peaking at D and E and centered around A. This suggests, under the specified conditions, the existence of a limit cycle. If so, since a limit cycle is an overall property of the governing differential equation, once triggered this oscillatory behavior would not depend on the initial conditions of the system.

In the case of a static restoring function featuring only $C - A_2 - E_2$ roots (Fig. 2), the fate of the heterogeneous deflagration wave is always extinction.

The above properties have been verified by computer simulated transients evaluated by numerical integration of the governing partial differential equation. The finite difference scheme implemented is discussed in (1). Typical, but by no means mandatory, laws used for the controlling parameters are:

$$\tau(\tau) = \tau_i - (\tau_i - \tau_f) \cdot (1 - e^{-B_p \cdot \tau}), \tau \geqslant 0 \qquad (3)$$

$$F(\tau) = F_i - (F_i - F_f) \cdot (1 - e^{-B_r \cdot \tau}), \tau \geqslant 0 \qquad (4)$$

describing the exponential change in time of the non-dimensional parameters (pressure τ or radiant flux intensity F) from an assigned initial value to an assigned final value according to assigned positive coefficients B_p or B_r. In particular, relaxation transients and go/no-go type of runs have been performed in order to check respectively the static and dynamic stability limits (otherwise unobservable). Some results concerning the lower dynamic stability limits are illustrated in Table 2. The evaluated limits are in good agreement with the expected values.

Some results concerning the upper dynamic stability limits are illustrated in Figs. 5 - 6. Go/no-go type of runs with exponential increase of pressure from $P_i = 10$ atm to $P_f = 30$ atm are plotted for several values of Q_s. Compare with Table 3. For Q_s sufficiently low, one observes a smooth transition from the initial to the final steady state equilibrium configuration (see, for example, $Q_s = -158.2$ cal/g). For larger values of Q_s, a vigorous acceleration of the wave occurs (Fig. 5). Following this, the heterogeneous deflagration wave will relax toward a steady solution (Fig. 6). This is the stable stationary reacting configuration for Q_s less than the coalescence value ($Q_s = -180$ cal/g), self-sustained oscillations for Q_s larger than the coalescence value ($Q_s = -200$ cal/g) and the stable stationary unreacting configuration ($Q_s = -220$ cal/g).

Self-sustained oscillations have been observed in several different situations. The nature of these oscillations depends only on the static restoring function associated with the final burning conditions. For example, the same self-sustained oscillations have been found with $B_p = 1$ and $B_p = 200$ for the pressurization transient shown in Fig. 6. Oscillatory behaviour has been found also in the computer simulated tests reported in (18).

<p style="text-align:center">TABLE 2</p>

Computer simulated go/no-go transient tests showing agreement with the predicted lower dynamic stability boundary and strong dependence of dynamic extinction on the initial conditions. All runs performed for adiabatic opaque strands with $T_a = 300\ K$ and $Q_s = -158.2\ cal/g$. Pressure measured in atm and radiant flux intensity in $cal/cm^2 - s$. The rate constants B_p and B_r are nondimensional. See (2).

Controlling parameter		Constant parameters			Nondim. burning rate		
no occurrence of dynamic extinction	occurrence of dynamic extinction			rate constants	observed lower dynamic limit	predicted lower dynamic limit	static limit
$I_{0,i} = 44.52$	$I_{0,i} = 44.55$	$I_{0,f} = 0$	$P = 10$	$B_r = 10$	0.057	0.053	0.15
96.26	96.27	0	20	19	0.083	0.070	0.23
156.85	156.87	0	30	10	0.093	0.083	0.29
$P_i = 34.42$	$P_i = 34.43$	$P_f = 10$	$I_0 = 0$	$B_p = 10$	0.051	0.053	0.15
$B_p = 3.336$	$B_p = 3.337$	$I_0 = 0$	$P_i = 40$	$P_f = 10$	0.054	0.053	0.15
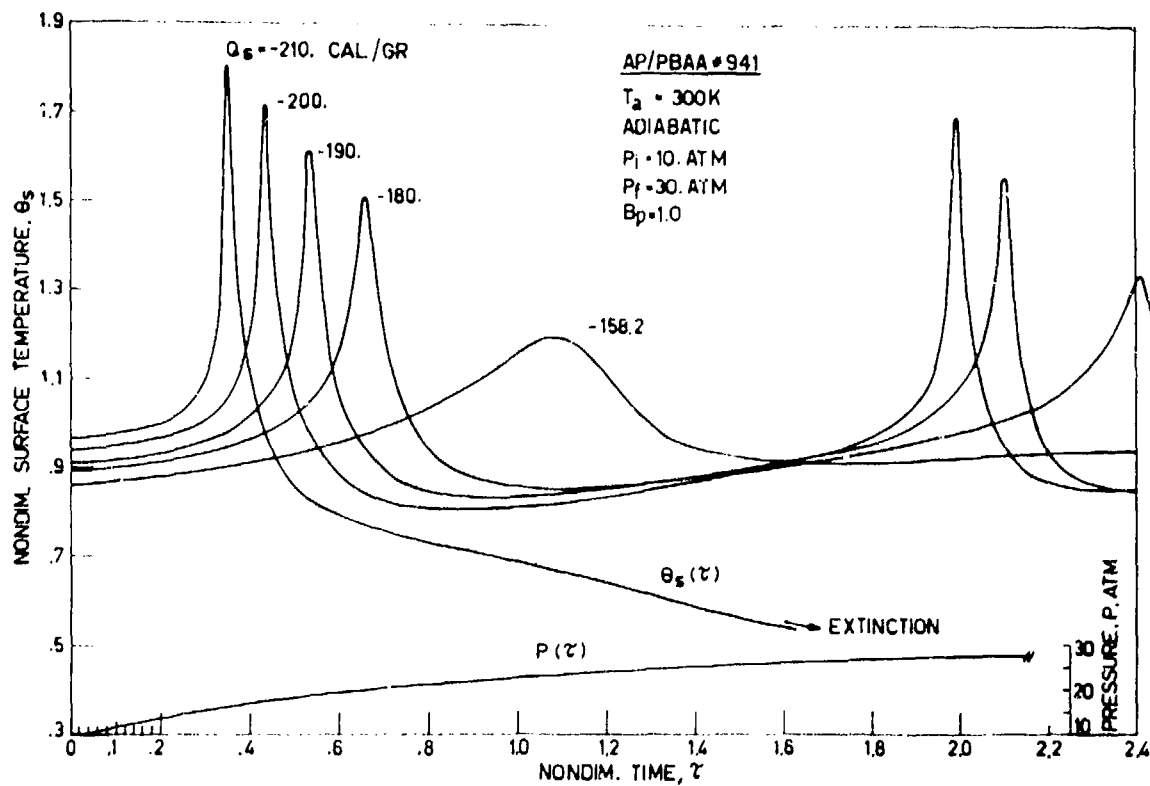
Fig. 5. Computer simulated pressurization tests showing destabilizing effect of large surface heat release.
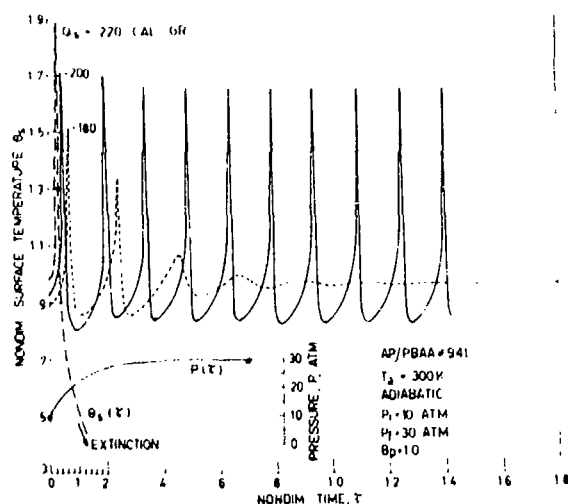
Fig. 6. Computer simulated pressurization tests showing self-sustained surface temperature oscillations.

At any pressure, above the coalescence value of Q_s no stable stationary reacting configuration is allowed

(static instability). Border values are listed in Table 1. This has been verified by computer simulated relaxation type of runs from assigned initial burning configurations (corresponding to the stationary solution at the investigated conditions). Typical results are shown in Fig. 7. At a constant pressure $P = 10$ atm, the initial burning configuration is stable for Q_s less than the coalescence value (negligible oscillations are observed for $Q_s = -158.2$ cal/g) but is unstable for Q_s larger than the coalescence value (e.g., $Q_s = -180$ cal/g). Notice the larger overshoot associated to $Q_s = -200$ cal/g due to upper dynamic instability. Just at the coalescence value of $Q_s = -170$ cal/g static instability only takes more "induction" time to show up. For all cases of instability, the final solution is the trivial nonreacting configuration.

CONCLUSIONS

The stability problem of adiabatic heterogeneous deflagration waves for finite size disturbances has been dealt with. In order to retain the important non-linearities of the problem, an approximate formulation of the condensed phase energy equation in terms

TABLE 3

Roots associated with the static nonlinear restoring function for an adiabatic opaque strand deflagrating at $P = 30$ atm and $T_a = 300$ K. For all cases root C, corresponding to the trivial solution $\theta_s = 0$, is also found. For $Q_s = -190$ cal/g coalescence of A and D roots occurs. The stationary unreacting configuration (root C) is always stable, while the stationary reacting configuration (root A) becomes unstable after coalescence with root D. See Fig. 3.

surface heat release, Q_s, cal/g	Nondimensional surface temperature, θ_s			
	root B	root A	root D	root E
-150	0.66	0.929	—	—
-158.2	0.67	0.937	—	—
-170	0.68	0.949	1.15	1.29
-180	0.69	0.962	1.04	1.43
-190	0.70	0.976	0.976	1.53
-200	0.72	0.992	0.93	1.61
-210	0.74	1.011	0.90	1.68
-220	0.78	1.032	0.86	1.75
-230	—	1.057	—	1.81

287
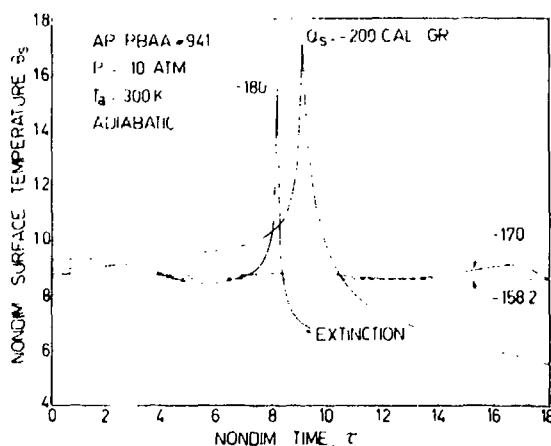
Fig. 7. Computer simulated relaxation tests showing that equilibrium reacting configurations are unstable for surface heat release above the coalescence value (See Table 1).

of an ordinary differential equation has been written by means of a standard integral approach. It has been shown that the surface heat release strongly affects the static and dynamic (upper and lower) stability limits.

In particular, the following points have been discussed. For increasing values of Q_s:

1. the lower dynamic stability point moves toward larger burning rate (easier dynamic extinction).

2. an upper dynamic stability point appears (acceleration).

3. the stationary reacting mode configuration becomes unstable (static instability).

4. self-sustained oscillations occur.

5. only the trivial solution is allowed.

Further work concerning the influence of ambient temperature and nonadiabaticity of the condensed phase is being done (3). In particular, this allows one to define the pressure deflagration limit of any given heterogeneous flame. Furthermore, it will be of interest to predict the pressure dependent frequency of the observed self-sustained oscillations.

NOMENCLATURE

Latin symbols

B_p = depressurization rate coefficient (see Eq. 3)
B_r = deradiation rate coefficient (see Eq. 4)
F = nondimensional thermal flux intensity
H = nondimensional surface heat release
I_0 = radiant flux intensity impinging at the condensed phase surface, $cal/cm^2 - s$
P = pressure, atm
τ = nondimensional pressure
q = energy flux intensity, $cal/cm^2 - s$
Q = heat release, cal/g
R = burning rate, cm/s
R = nondimensional burning rate
t = time, s
T = temperature, K
u = nondimensional finite size disturbance of temperature
u_s = nondimensional finite size disturbance of surface temperature
u_x = nondimensional finite size disturbance of thermal gradient
$(u_x)_{c,s}$ = nondimensional surface thermal gradient disturbance at the condensed phase side
x = space variable, cm
X = nondimensional space variable

Greek symbols

δ = nondimensional thermal layer penetration
Δ = finite difference of a quantity evaluated between $X = 0$ and $X = -\delta$
θ = nondimensional temperature
τ = non-dimensional time

Subscript and Superscripts

a = ambient value
c = condensed phase value
f = final value
g = gas
i = initial value
L = lower dynamic stability
p = pressure
r = radiant
s = surface value
$-$ = steady state value of a parameter
$-\infty$ = condition far upstream
$+\infty$ = condition far downstream

288

Abbreviations

AP = ammonium perchlorate
PBAA = polybutadiene - acrylic acid

REFERENCES

1. De Luca, L., "Ignition and Other Unsteady Combustion Phenomena Induced by Radiation", Ph.D. Thesis, Princeton University, 15 Nov. 1976.

2. De Luca, L., "Nonlinear Stability Analysis of Solid Propellant Combustion", 2nd International Symposium on Dynamics of Chemical Reactions, University of Padova, 15-17 Dec. 1975.

3. De Luca, L., "Nonlinear Static Stability Limits of Heterogeneous Deflagration Waves", in preparation.

4a. Merkle, C.L., Turk, S.L. and Summerfield, M., "Extinguishment of Solid Propellants by Depressurization: Effects of Propellant Parameters", AIAA Paper No. 69-176, 1969.

4b. Merkle, C. L., Turk, S. L. and Summerfield, M., "Extinguishment of Solid Propellants by Rapid Depressurization", AMS Report No. 880, July 1969, Princeton University, N. J.

5. Belyaev, A. F., Bodolev, V. K., Korotkov, A. I., Sulimov, A. A. and Chuiko, S. V., *Transition from deflagration to detonation in condensed phases,* translated from Russian, Israel Program for Scientific Translations, Jerusalem 1975, distributed by J. Wiley & Sons.

6. T'ien, J. S., "A Theoretical Criterion for Dynamic Extinction of Solid Propellants by Fast Depressurization", *Combustion Science and Technology,* Vol. 9, 1974, pp. 37-39.

7. T'ien, J. S., "The Effects of Perturbation on the Flammability Limits", *Combustions Science and Technology,* Vol. 7, 1973, pp. 185-188.

8. Ohlemiller, T. J., Caveny, L. H., De Luca, L. and Summerfield, M., "Dynamic Effects on Ignitability Limits of Solid Propellants Subjected to Radiative Heating", XIV Symposium (International) on Combustion, 1973, pp. 1297-1307.

9. Strahle, W. C., "One-Dimensional Stability of AP Deflagrations", *AIAA Journal,* Vol. 9, No. 4, April 1971, pp. 565-569.

10. Istratov, A. G., Librovich, V. B. and Novozhilov, B. V., "An Approximate Method in the Theory of Unsteady Burning Velocity of Powder", PMTF, No. 3, 1964. Translation AFSC FTD-MT-64-319, pp. 233-242.

11. Novozhilov, B. V., "Nonstationary Burning of Powder Having a Variable Surface Temperature", PMTF, No. 1, pp. 54-63, 1967, Translation AFSC FTD-MT-24-376-68.

12. Novozhilov, B. V., *Nonstationary Combustion of Solid Rocket Fuels,* 1973. Translation FTD-MT-24-317-74.

13. Summerfield, M., Caveny, L. H., Battista, R. A., Kubota, N., Gostintsev, Yu.A. and Isoda, H., "Theory of Dynamic Extinguishment of Solid Propellant with Special Reference to Non Steady Heat Feedback Law", *Journal of Spacecraft and Rockets,* Vol. 8, No. 3, March 1971, pp. 251-258.

14. Battista, R. A., Caveny, L. H. and Summerfield, M., "Non Steady Combustion of Solid Propellants", AMS Report No. 1049, October 1972, Princeton University, N. J.

15. Goodman, T. R., "Application of Integral Methods to Transient Nonlinear Heat Transfer", *Advances in Heat Transfer,* Vol. 1, 1964, Academic Press, New York, pp. 51-122.

16. Peters, N., "Theory of Heterogeneous Combustion Instabilities of Spherical Particles", XV Symposium (International) on Combustion, 1975, pp. 363-375.

17. Andronow, A. A., Vitt, A. A. and Khaikin, S. E., *Theory of Oscillators,* English edition by Pergamon Press Ltd., London; USA edition distributed by Addison-Wesley, Mass. 1966.

18. Barrows, A. W., Kooker, D. E. and W. Nelson, "Solid Propellant Unsteady Combustion", 2nd International Symposium on Dynamics of Chemical Reactions, University of Padova, 15-17 Dec. 1975.

THE GROWTH OF REACTION IN SECONDARY EXPLOSIVES
UNDER TRANSIENT CONFINEMENT

G. D. Coley,
MOD (PE) AWRE,
Reading, Berkshire, England.

ABSTRACT A quantitative method has been developed to study the growth of re-action in small high explosive (HE) charges (weight about 17 g), initiated under conditions related to accidental impact. Explosive yield was assessed from the peak force impressed on a load cell by the reacting HE. Maximum peak forces measured for PBX 9404 (HMX/NC/TCEP 94/3/3), Octol-A (HMX/TNT/Wax 80/20/1) and HW4 (HMX/Wax 95/5) were 977 kN, 460 kN and 140 kN respectively, for similar conditions of charge confinement. This ranking of event size is in good qualitative agreement with the explosiveness ranking in the Skid Test for these compositions. The relationship between charge confinement and the violence of the explosive re-action has been investigated for each composition, and the importance of both the strength and the inertial components of confinement has been demonstrated.

1. INTRODUCTION

Accidents have occurred with secondary explosive charges, in which the yield has approached that appropriate to detonation of the charge, even though the initiating stimulus would not have been expected to have initiated detonation by normal shock initiation processes. Recognition of the hazards associated with HE formulations in charge form has led to the introduction of a wide range of charge hazard tests, designed to simulate handling and transportation accident situations of practical importance. Sensitiveness and explosiveness of HE systems are determined from their response in these tests.

Although a number of mechanisms for initiation by thermal and mechanical accident stimuli have been studied and confirmed, the mechanisms for growth of reaction are not well understood. Beedham, Dyer and Holmes (1) reported a series of small scale tests designed to investigate the sensitiveness aspects of charge hazard. Charges were initiated in a controlled manner by the conduction of heat from hot surfaces,

in contact with the HE, under impact loading conditions.

The work reported now extends these studies to the development of a quantitative method to study the growth of reaction in laboratory scale charges, and to the investigation of the effects of charge confinement on the explosiveness of HE systems. This work is a prelude to a more comprehensive study of the physical conditions and HE properties, which limit the growth of reaction in an HE system, and result in the partial events commonly experienced in accidents. A laboratory scale explosiveness test, based on the work, could replace the Skid Test (2,3) as a more economic and quantitative explosiveness screening test in HE formulations development programmes.

2. EXPERIMENTAL

HE charges, confined in metal cups, were transiently loaded in a drop weight apparatus, and thermally initiated, at a predetermined point in the

loading cycle by a hot wire, in contact with the bare face of the charge. Impact conditions were chosen to simulate the Skid Test (2,3), where impact pressures up to 0.1-0.2 GPa with impact times of 1.0-2.0 msec can occur (1) depending on the drop height and the mechanical properties of the explosive. The violence of the explosive event was assessed from the output of strain gauges fitted to a load cell mounted beneath the explosive charge.

2.1 Explosive Samples

Three HE compositions were selected for study. These were HW4 (HMX/Wax 95/5 by wt), Octol-A (HMX/TNT/Wax 80/20/1 by wt) and PBX 9404 (HMX/NC/TCEP 94/3/3 by wt). They were chosen because they were known to give small partial reaction, large partial reaction and high order reaction respectively in the AWRE Skid Test (2,3).

Discs of HE weighing approximately 17 g and measuring 28.6 mm diameter X 14.3 mm thick were machined from pressed charges and assembled into metal cups, with the bare face of the charge protruding 1.5 mm (Fig. 1). Different strengths and inertias of confinement were obtained by using steel or aluminium alloy for the cup material and by varying the cup wall thickness.

2.2 Drop Weight Apparatus

The apparatus is shown schematically in Fig. 2. The charge assembly (A) was impacted by a 22.7 kg drop weight (B), falling through 305 mm in a guide tube (C). Impact loading pulses with maxima in the
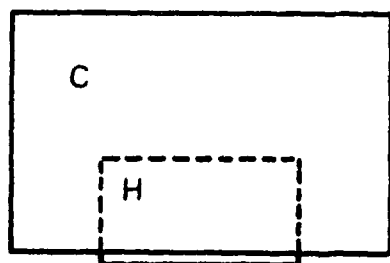
Fig. 1. Explosive charge assembly—schematic view of an explosive disc (H) (28.6 mm diameter X 14.3 mm thick) mounted in a steel or aluminium alloy cup (C) (height 31.8 mm, thickness of base 19.0 mm). The HE protruded 1.5 mm from the metal cup. The wall thickness of the cup was varied as described in the text.
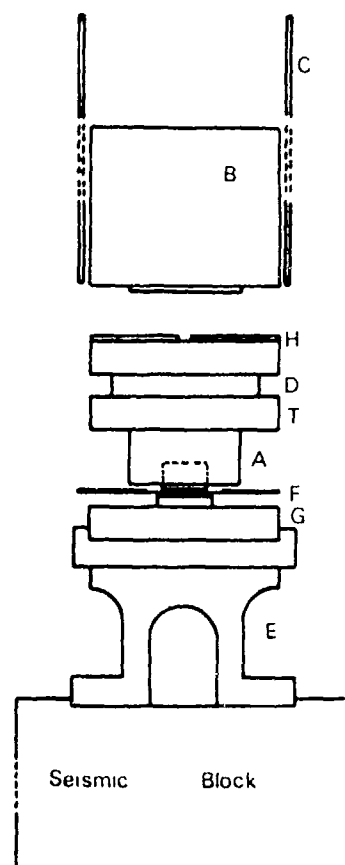
Fig. 2. Drop weight apparatus—a schematic view. (A) Charge assembly, (B) Drop weight (22.7 kg), (C) Guide tube, (D) Pulse shaper, (E) Load cell, (F) Heater wire soldered between copper leads, (G) Spigot, (H) Impact switch, (T) Load spreading plate.

range 25.0-35.0 kN and impact durations of approximately 2.0 msec were achieved by the incorporation of a felt pulse shaper (D), 12.7 mm thick X 75 mm diameter, mounted on a tufnol (a resin bonded fabric) load spreading plate (T), above the explosive charge. These loading pulses, although of lower amplitude than in the Skid Test, were chosen in order that the dynamic compressive strengths of the test charges were not exceeded before initiation. The felt also served to smooth the loading pulse by damping stress wave reverberations in the drop weight. The forces, arising from both the impact of the drop weight and any explosive event, were measured by strain gauges mounted on a load cell (E) beneath the charge assembly and displayed as a function of time on an oscilloscope.

291

A constantan resistance wire (F) 0.152 mm diameter X 38.1 mm long was positioned along a diameter between the bare face of the explosive charge and a tufnol spigot (G).

The wire was heated for 80 μsec, during the loading cycle, by the rapid discharge of a 25 μF capacitor bank charged to 600 V. Using a similar hot wire device and transient loading, Beedham, Dyer and Holmes (1) reported that the heating pulse produced by the discharge of a 16 μF capacitor charged to 500 V reliably initiated HW4, Octol-A and PBX 9404.

A simple switch (H), which was constructed from a sheet of copper foil, with a 2.54 mm diametrical gap, mounted on a tufnol plate on top of the pulse shaper, was connected in series with a 15 V battery and a 10 K ohm resistor. When the switch was closed by a thin copper disc mounted on the front face of the drop weight a reference pulse was produced at the start of the loading cycle, which was used to trigger the time base of the oscilloscope, and after a delay the hot wire power pack. The delay was chosen to achieve loads of 20-30 ' N on the rising portion of the pulse at the time of th hot wire discharge.

A typical load/time record is shown in Fig. 3.1. This record was obtained from a PBX 9404 charge
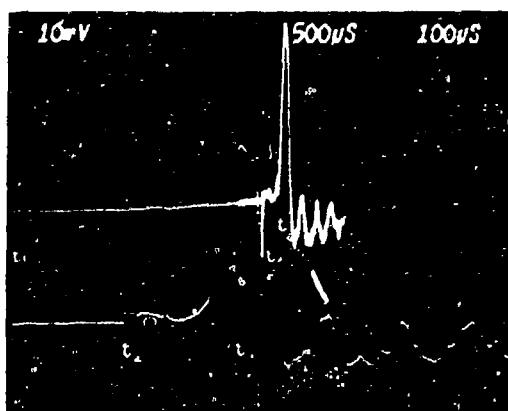
Fig. 3.1. An oscilloscope record of the load cell output for a PBX 9404 charge confined in an aluminium alloy cup (wall thickness 23.8 mm). Upper trace: Complete load/time history – sweep 500 μsec/div. Lower trace: An expanded section of the upper trace – sweep 100 μsec/div. (t_1) impact of drop weight, (t_2) discharge of heater power pack, (t_3) explosive event.

confined in an aluminium alloy cup with a wall thickness of 23.8 mm. The lower trace corresponds to the intensified portion of the upper trace and shows the event with improved time resolution. The start of the loading cycle is indicated by t_1 and from t_1 the load increases smoothly, as the drop weight decelerates compressing the felt pulse shaper. The signal at t_2 is noise produced by the discharge of the heater power pack and does not represent the shape of the pressure pulse. All attempts to remove this noise signal were unsuccessful. However the perturbation of the load cell record was minimal and it did serve to indicate the conditions at the time of initiation. The peak load produced by reaction in the HE occurred at t_3, and this load was taken as a measure of the explosiveness of the system under investigation. Following t_3 the drop weight rebounded and the load cell record terminated in mechanical ringing.

In the absence of an explosive event the load rises smoothly to a peak of 25-35 kN and then decreases smoothly to zero as shown in Fig. 3.2. Variations in the peak load in the absence of an event arise from differences in strength between charge assemblies with different cup wall thicknesses.

In some of the experiments reaction phenomena were observed with a high speed cine camera, operated at a framing rate of 4500 frames sec^{-1}. Frames corresponding approximately to t_1, t_2 and t_3 in Fig. 3.1 are shown for the same experiment in Fig. 3.3.

2.3 Experiments

The peak force, impressed on the load cell (e.g., the load at t_3 in Fig. 3.1), was determined for a
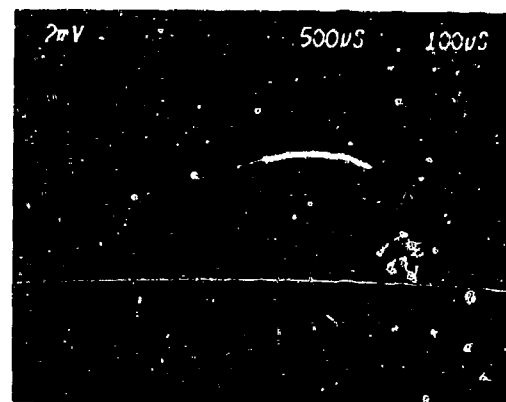
Fig. 3.2. A typical oscilloscope record of the load cell output obtained when the charge was not ignited.

Fig. 3.3. Three frames selected from a high speed camera sequence to correspond with times t_1, t_2, and t_3 in Fig. 3.1. (A) Charge assembly, (F) Heater leads, (D) Pulse sharper, (R) Product gases.

range of cup wall thicknesses, when each of the compositions HW4, Octol-A and PBX 9404 were confined in mild steel and in aluminium alloy cups. Confinements with wall thicknesses of 4.76, 7.94, 11.11, 17.46, 23.81 and 36 51 mm were investigated. The weights of the steel and aluminium charge assemblies for each of these wall thicknesses are shown in Table 1. These values include the mass of the tufnol plate beneath the pulse shaper (0.300 kg).

In additional experiments, Octol-A charges were confined in steel cups which had a mild steel plate 152.0 mm diameter bonded to the back face. The

Mass (kg) of the experimental charge assemblies including the mass of the tufnol plate beneath the pulse shaper (0.300 kg).

Wall Thickness mm	Cup Material	
	Steel	Aluminium Alloy
4.76	0.536	0.391
7.94	--	0.426
11.11	--	0.461
17.46	1.039	0.562
23.81	--	0.678
36.51	2.270	0.978

thickness of the plate was chosen to make the total weight of each charge assembly 5.0 kg. Three different wall thicknesses 4.76, 17.46 and 36.51 mm were investigated.

3. EXPERIMENTAL RESULTS

3.1 HW4

The variation of peak force (F) with confinement wall thickness is shown in Fig. 4. Peak force increased slightly when the wall thickness was increased from 4.8 mm to 36.5 mm for both materials, and for a given size of confinement larger events were observed with steel compared with aluminium alloy. Very small explosive yields were obtained with HW4 compared with the other compositions. The metal confinements and tufnol base plates were always recovered undamaged and most of the HE was unreacted and retained in the confinement after an experiment. A typical round recovered after firing is shown in Fig. 7.1. The confinement was aluminium alloy and the wall thickness was 4.8 mm. Maximum peak forces, measured when the confinement was varied were 140 kN and 43.2 kN for steel and aluminium alloy respectively.

3.2 OCTOL-A

The experimental results are shown in Fig. 5. Peak force increased when the wall thickness was increased from 4.8 mm to approximately 25.0 mm, for both steel and aluminium confinements. However

293
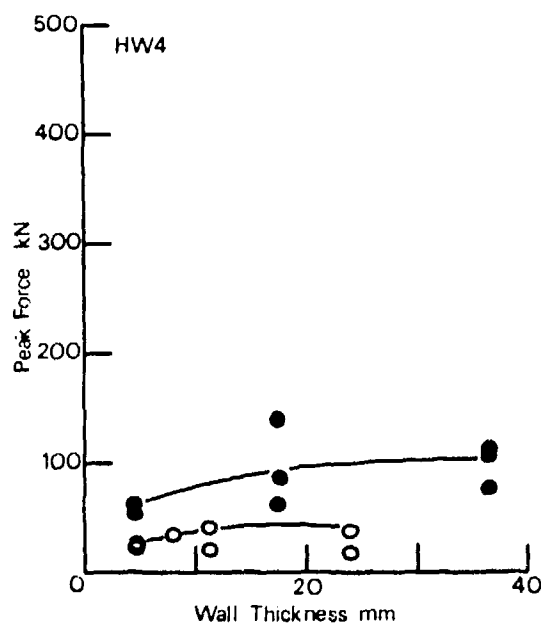
Fig. 4. The variation of peak force with confinement wall thickness for HW4 charges confined by steel (●) and aluminium alloy (○) cups.

Fig. 6. The variation of peak force with confinement wall thickness for PBX 9404 charges confined by steel (●) and aluminium alloy cups (○).

Fig. 5. The variation of peak force with confinement wall thickness for Octol-A charges confined by steel cups (●), aluminium alloy cups (○) and steel cups with a total assembly weight of 5 kg (X).

further increases in wall thickness above 25.0 mm produced little further increase in yield. The maximum peak forces measured were 460.2 kN and 296.6 kN for steel and aluminium respectively. Confinements with wall thicknesses not exceeding 11.1 mm for steel and 17.5 mm for aluminium were recovered undamaged, but with more HE reacted than shown in Fig. 7.1 for HW4. For rounds with wall thicknesses greater than these values, plastic deformation of the inner wall of the confinement together with severe erosion of the tufnol spigot was observed. A charge which had been confined in aluminium alloy with a wall thickness of 36.5 mm is shown after firing in Fig. 7.4, and this result is typical for the thick walled confinement. Unreacted fragments of HE were recovered from the bomb chamber, and most of the explosive had been ejected from the confining cup.

The results for the steel confinement experiments in which the charge weight was maintained at 5 kg are also shown in Fig. 5 for comparison with the experiments described above in which the mass of the explosive assembly varied with wall thickness. For wall thicknesses in excess of 11.1 mm the results

294

Fig. 7.1. An HW4 charge assembly after firing. Confinement aluminum alloy, wall thickness 4.8 mm.

Fig. 7.2. An Octol-A charge assembly after firing. Confinement steel, wall thickness 4.8 mm. Total assembly weight 5 kg including the steel make weight visible in the lower half of the figure. In the upper half the tufnol spigot can be seen, forced into the mouth of the cup.

from the two series of experiments with steel confinement were very similar. However, for wall thicknesses less than 11.1 mm significantly larger events were observed in the 5 kg series. Comparing results for confinements with wall thicknesses of 4.8 mm, peak forces of (152 ± 40) kN were measured when the experimental mass was 0.536 kg, and (269 ± 11) kN for the experiments in which the mass was 5 kg. The increased violence of reaction was also apparent from an examination of the round after the experiment. Figure 7.2 shows a 5 kg round with a 4.8 mm wall thickness, after firing. Pronounced distortion of the walls of the confinement occurred. The tufnol spigot can be seen to be forced into the opened mouth of the cup and this probably happened on the second impact of the drop weight. In contrast, the 0.536 kg round with the same wall thickness was recovered undamaged.

3.3 PBX 9404

Plastic deformation of the metal confinements was observed for all wall thicknesses investigated. Steel and aluminium alloy confinements with wall thicknesses not exceeding 11.1 mm were deformed as shown in Fig. 7.3, which shows a steel confinement, with 4.8 mm wall, recovered after firing. Significant belling of the confinement had occurred, which was similar to the distortion observed for Octol-A in Fig. 7.2. When the wall thicknesses exceeded 11.1 mm plastic deformation of the confinement occurred at the internal radius only, as shown in Fig. 7.4 for Octol-A. Experimental results are shown in Fig. 6 as a function of confinement wall thickness. The variations of peak impressed force with confinement wall
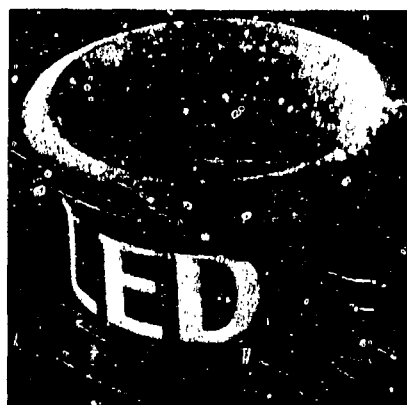
Fig. 7.3. A PBX 9404 charge assembly after firing. Confinement steel. Wall thickness 4.8 mm.

thickness for both steel and aluminium alloy were qualitatively similar to the results previously described for Octol-A. Maximum peak forces of 977 kN and 475 kN have been recorded for steel and aluminium alloy confinements respectively.

4. DISCUSSION

Reaction was initiated in these experiments under conditions of transient loading which simulated the impact conditions in the AWRE Skid Test. Partial reaction of the HE was observed in all cases with the
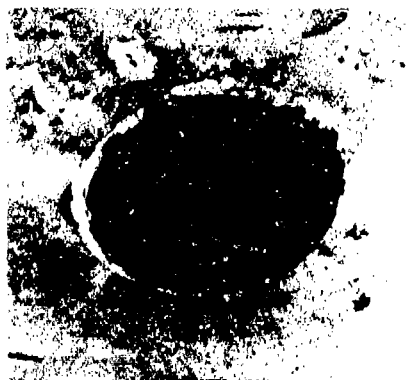
Fig. 7.4. An Octol-A charge assembly after firing. Confinement aluminium alloy, wall thickness 36.5 mm. The central portion of the cup near the inside wall is shown. The outside wall (not shown) was not deformed. Most of the tufnol spigot can be seen inside the cup.

unreacted explosive either retained in the confinement or dispersed in the test area, depending upon the severity of the reaction. For any given confinement the experimental results in Figs. 4, 5, and 6 show that the ranking of explosiveness for the compositions investigated was HW 4 < Octol-A < PBX 9404. Differences were least pronounced when the charges were confined in thin walled aluminum vessels, and most pronounced for charges confined in thick walled steel vessels. The maximum peak impressed forces obtained for HW4, Octol-A and PBX 9404 in both steel and aluminium confinements are shown in Table 2, together with the response of 50 lb hemispherical charges in the AWRE Skid Test for comparison.

The results in Figs. 4, 5, and 6 indicate that both the strength and the inertial components of confinement can be important, in varying proportions, depending on the experimental conditions. For any explosive/cup material combination, the explosiveness increased with increasing wall thickness up to a limiting value. This suggests that the strength of the confining cup is a factor controlling the event size, since the maximum internal stress to cause plastic deformation of the cup walls increases in this way with increasing wall thickness. Yield stresses for the aluminium alloy and the steel were both of the order of 0.28 GPa. The strengths of aluminium and steel confining cups of the same size should therefore be similar. However in all experiments larger events were

TABLE 2

Maximum peak impressed forces for steel and aluminium confinements compared with Skid Test results (Unit kN).

	HW4	Octol-A	PBX 9404
Aluminium	43.0	297.0	475.0
Steel	140.0	460.0	977.0
Skid	Small Partial	Large Partial	High Order

obtained with the steel than with the aluminium suggesting that the inertia of the confinement was also important.

Following the model proposed by Macek (4), build up to detonation, in a system with no venting, would be determined by (a) the relation between burning rate and pressure, (b) the shock sensitivity of the composition in an appropriate geometry and (c) geometrical factors. Venting did occur in the present experiments, and the relative rates of product gas formation and venting must also be taken into account. Three different venting processes were identified by examining rounds recovered after firing:

(i) acceleration of the charge assembly under the action of the force exerted by the reaction products, with the resulting vertical displacement of the round allowing the escape of product gases. At the time of the initiation the felt pulse shaper is compressed by a force of 20-25 kN and the high speed photographic sequence shown in Fig. 3.3 indicates that the felt is strained approximately 50%. Static compression tests were made on the felt pulse shaper and a load/displacement curve is shown in Fig. 8 for a sample which was prestressed by a load of 12 kN. The point P on the curve at 22 kN indicates typical initiation conditions. From the curve it may be deduced that additional loads of 10, 20 and 30 kN produced by a developing reaction could give rise to additional compressions in the felt of 0.29, 0.54, and 0.73 mm respectively. From these measurements it would appear that sufficient relative movement between the drop weight and the experimental assembly can occur following initiation of the HE to allow venting of product gases. The initial stages of the vertical acceleration of the charge assembly will therefore be governed by the mass of the charge assembly and not
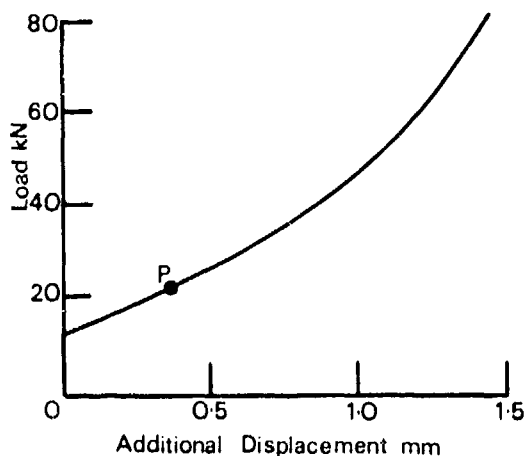
Fig. 8. A static load-displacement curve for a felt pulse shaper, 12.7 mm thick × 75 mm diameter prestressed by a load of 12 kN. (The strain for a load of 12 kN was approximately 50%). The point P indicates the degree of compression of the pulse shaper corresponding to typical initiation conditions in the explosiveness experiments.

that of the drop weight, since these are effectively decoupled by the pulse shaper. Increases in the mass of the round will therefore lead to an increased event size for this venting mechanism.

(ii) Plastic deformation of the confinements involving a displacement of all of the wall material. This type of deformation is illustrated in Figs. 7.2 and 7.3, and would occur when the internal stress in the confinement was such that the maximum hoop stress in the wall exceeded the yield stress of the confinement material. The maximum internal stress to cause failure will increase with increasing wall thickness, for a given confinement, until the internal stress approaches the yield stress for the confinement material. Venting will occur at a rate which depends on the radial motion of the wall material which in turn will be related to the inertia of the wall. Event size will thus increase with increasing wall strength and wall mass up to a maximum value determined by the yield stress of the material.

(iii) Plastic deformation of the confinement in which the internal radius is increased whilst the external radius remains unchanged. This mechanism may be seen as the limiting case of mechanism (ii), above, when the internal stress in the confinement approaches the yield stress of the material. Further increases in wall mass and thickness will then have no

further influence on event size. An example of this type of deformation is given in Fig. 7.4.

The influence of these venting mechanisms and hence the strength and inertia of the confinement on the build up of reaction may be illustrated by the experimental results for Octol-A shown in Fig. 5. Peak impressed force has been replotted as a function of the mass of the charge assembly in Fig. 9 in which the results for the 5 kg series of experiments have been omitted. In region I a single curve may be fitted to the steel and aluminium confinement data. All the confinements were recovered undamaged in this region, and the results are clearly in agreement with venting by mechanism (i). In region II the peak impressed forces measured for each confinement material tend to limiting values with increasing mass (and therefore wall thickness) and all confinements recovered were deformed on their internal radius only. Venting by mechanism (iii) is consistent with this data, with the strength of the confinement material limiting the event size. The results for steel tend to a higher limiting value than those for aluminium since for a given strength steel is heavier than aluminium.
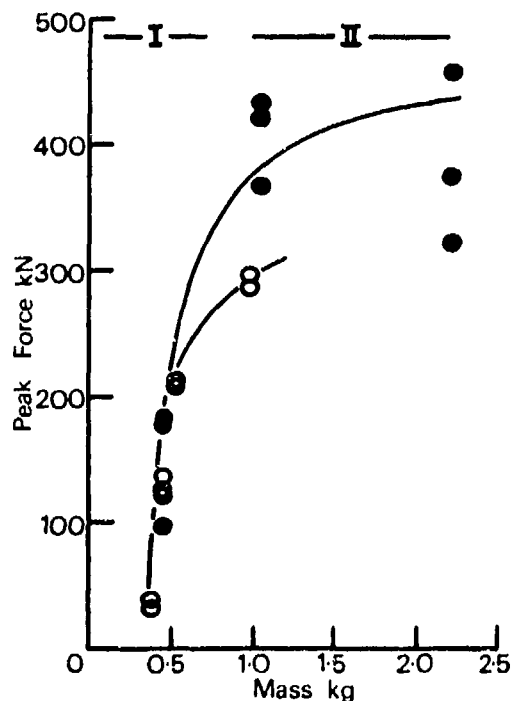
Fig. 9. The variation of peak force with the mass of the charge assembly for Octol-A. (○) Aluminium alloy confinement (●) Steel confinement.

297

In the 5 kg series of experiments venting by mechanism (i) was not observed, for any confinement. Increasing the mass of the round for the thin walled confinements reduced the effectiveness of venting by mechanism (i) and reaction pressures sufficiently to cause plastic deformation of the confinement occur. The increase in mass for the thick walled confinement is not effective in increasing the event size since the major venting mechanism for these confinements was mechanism (iii).

Factors responsible for differences in explosiveness include mechanical processes, and the ignition and burning characteristics of the explosive. The work reported here has concentrated on the mechanical aspects. However differences in the burning rate/pressure relationship between HW4, Octol-A and PBX 9404 may be inferred from the results. In the experiments with HW4 the confinements were recovered undamaged in all cases and therefore either (a) the venting rate by mechanism (i) exceeds the rate cf product gas formation or (b) the impact time is short compared with the build up time for the reaction.

With PBX 9404 plastic deformation of the confinement was always observed implying that the rate of product gas formation appropriate to the experimental impact conditions always exceeded the rate of venting by mechanism (i). Venting by mechanism (i) was predominant for Octol-A for rounds weighing 0.1-0.5 kg. However, when the mass was increased mechanisms (ii) and (iii) predominated, indicating that the reaction rate increases significantly with increasing pressure.

5. SUMMARY

In a small scale test, designe1 to simulate the impact conditions in the AWRE Skid Test, the ranking with increasing explosiveness for three test compositions was found to be HW4 < Octol-A < PBX 9404, in good qualitative agreement with the full scale test.

Explosiveness is a property of an HE and its confinement. The importance of both the strength and inertial components of confinement has been demonstrated.

6. REFERENCES

1. K. Beedham, A. S. Dyer, and W. I. Holmes, Fifth Symposium (International) on Detonation 224, 1970.

2. S. C. C. No. 3 Explosives Hazard Assessment. Manual of Tests, ERDE, Sept. 1968.

3. A. S. Dyer and J. W. Taylor, Fifth Symposium (International) on Detonation 235, 1970.

4. A. Macek, J. Chem. Phys. 31 1 162, 1959.

7. ACKNOWLEDGEMENT

PROPELLANT DETONATION RISK TESTING

E. E. A. Cruysberg, H. J. Pasman and Th. M. Groothuizen
Technological Laboratory TNO
P.O. B. 45, Rijswijk 2100, The Netherlands

For various propellants the possibility of detonation on flame ignition has been investigated in field trials. Single-base multiperforated propellant failed to detonate under the test conditions. Double-base single-perforated propellant and porous single-base propellant did detonate indeed. On the basis of pressure measurements TNT equivalences have been determined. A laboratory test has been developed whose results agree well with those of the field tests.

INTRODUCTION

In 1972 an explosion occurred during the manufacturing process of porous propellant (1). Altogether more than 2 tons of porous nitrocellulose powder were involved in this explosion. Electrostatic discharge in propellant dust during a drying operation may be regarded as the most likely cause of ignition. The effect of the violent explosion was such that considerable window pane failure was encountered in a nearby residential area at a distance of at least 500 m from the explosion point.

After this explosion the authorities prescribed that the quantities of propellant in process and storage should be reduced to such an extent as to diminish the damage to the relevant residential area to a maximum of 5 to 10 per cent of window pane failure in the event of another explosion.

In order to comply with this condition and also to safeguard continuation of the works' activities a safety plan has been designed with the principal objective to arrive at a hazard classification of the various propellants. To this end field tests have been conducted with various types of propellants.

Previous investigations had shown that all types of propellants (single base, double base and triple base) are capable of detonation if they are initiated by a

HEchange. Since in the case of an incident initiation will mainly be by some thermal source, a deflagration will take place initially. The question is whether a deflagration to detonation transition will occur.

DEFLAGRATION TO DETONATION TRANSITION IN PROPELLANTS

In the first series of field tests it was assessed whether the various types of propellant were capable of burning to detonation under the conditions comparable with those prevailing in actual practice in the factory.

To this end the propellant under investigation was introduced into a cylindrical aluminum container (Fig. 1) of the following dimensions: height 90 cm, diameter 80 cm, plate gage 3 mm.

Ignition was effectuated by means of a squib and 2 g of a pyrotechnic mixture. This mixture consisted of potassium nitrate, propellant dust, silicon powder and binder in a 4:2:4:3 ratio. The ignition source was submerged in the propellant and that at 1/3 from the filling point. The charge depth of the propellant in the container was approximately 75 cm. The occurrence of blast was measured by means of piëzo-electric pressure transducers, placed about 1 m above ground level at distances of 25, 50, 75 and 100 m from the explosion point.

Fig. 1. Cylindrical aluminium container.

No blast occurred on ignition of 350 kg of multi-perforated single-base propellant with a web size of 1.3 mm, nor with 350 kg of single-perforated single-base propellant with a web size of 0.8 mm, nor with 350 kg of single-perforated double-base propellant (NG content 9 per cent) with a web size of 0.48 mm, and the propellant was simply burnt down.

On ignition of porous propellant, however, blast was measured. Based on peak pressure measurements blast effects corresponded with a TNT mass equivalence between 20 and 60 per cent (TNT = 100%). (Table 1). The data at various distances showed considerable scatter without a distinct trend; the impulse data showed lower equivalence values than peak pressures, viz. 10 to 25 per cent.

The container was completely fragmented. The rather fine aluminum fragments travelled over a distance of at least 100 m.

With single-perforated single-base propellant with a web size of 0.6 mm that was loosely filled in the container and ignited halfway the charge depth the container was burnt out. However, when this type of propellant was vibrated into a compact mass and ignition was effectuated at 1/3 from the filling point an explosion occurred with a TNT equivalence of 5-15 per cent (or based on impulse 2-6 per cent).

It is apparent from this test series that the various types of propellant react quite differently when ignited with a flame, and can be divided into three hazard groups, viz.

TABLE 1

TNT Equivalence of Propellants on Flame Ignition

Type of propellant	Web size (mm)	TNT equivalence (based on peak pressure at 25 m)
multiperforated single base	1.3	no detonation
single perforated single-base	0.8	no detonation
single perforated single-base	0.6	no detonation* 5-15 per cent
single-perforated double-base (9 per cent NG)	0.48	no detonation
porous nc.	–	20-60 per cent

*Ignition halfway the charge depth.

(i) propellants that do not detonate under the test conditions and only present a mass fire hazard

(ii) propellants that have a low TNT-equivalence if and when they explode

(iii) propellants that apparently detonate and have a high TNT-equivalence

Moreover it appears from the tests with the single-perforated single-base propellant (with a web size of 0.6 mm) that density and the location of ignition of in other words the degree of confinement plays an important part.

This gave cause to a second test series with the parameters: type of container and level at which ignition takes place in the charge depth. Besides the existing cylindrical aluminium container an oblong aluminium container with the dimensions 1.25 m long × 0.66 m wide × 0.71 m high and a plate thickness of 3 mm was used, and also fibre-board drums (0.60 m high × 0.36 m ⌀). Capacities of the oblong container and fibre-board drums were 350 kg and 25 kg respectively. It is apparent from the results (Table 2) that, with the exception of porous nitrocellulose propellant, explosion fails to take place when the tested propellants are ignited at a maximum of 0.55

300

TABLE 2

*TNT Equivalence at Varying Degree
of Confinement*

Type of propellant	Web size (mm)	Type of container	Ignition depth (m)	% TNT-equivalence (based on peak pressure)
single-perforated single-base	0.8	R	0.5	0
single-perforated single-base	0.6	R	0.55	0
single-perforated double-base (9 per cent NG)	0.48	R	0.45	0
		C	0.55	0
porous nc	-	F	0.35	17 (at 37 m)

R = oblong aluminium container, max. 350 kg

C = cylindrical aluminium container, max. 350 kg

F = fibre-board drum, 25 kg.

m below the surface irrespective of the type of container . The porous nitrocellulose propellant did explode and the blast corresponded with a TNT equivalence of 17 per cent.

Then it was examined whether the explosion that occurred with two types of propellant was indeed a detonation. To this end a detonation of 50 kg of single-perforated single-base propellant (with a web size of 0.6 mm), and of 25 kg of porous nitrocellulose propellant in a fibre-board drum was initiated purposely with the aid of 375 g of plastic explosive. The blast of the single perforated single-base propellant corresponded with a TNT equivalence of 36 per cent, while that of the porous propellant corresponded with 50 per cent.

From this it follows that whereas the explosion on flame ignition of single-perforated single-base propellant is not a full detonation that of porous propellant is.

This test series indicates, and in particular the tests with the single-perforated single-base propellant (with a web size of 0.6 mm), that transition to detonation has taken place in the final phase of the explosive burning of the propellant. For every condition and type of propellant there is a so-called

critical layer thickness above which the propellant detonates and below which it fails when ignited by means of a flame.

COMPARTMENTATION

The purpose of the following series of field tests was to determine the minimum barrier thickness whereby sympathetic detonation just fails to occur. This thickness is an important parameter in safe storage of propellants that are capable of detonation even at small thickness of the layer, in view of compartmentation.

It is clear that the thickness of the layer is related to the quantity that detonates, but since the scaling laws apply to this thickness (third power of the energy release), relatively small quantities have been used in these tests (max. 200 kg).

The test set-up (Fig. 2) comprised two compartments with a sand-filled timbered partition in between.

Dimensions of each compartment were: length 1.50 m × width 1.40 m × height 1.70 m. The thickness of the backwall was 0.60 m and that of the separation

301

wass was 0.40 m, 0.60 m and 0.80 respectively in three different set-ups. (Fig. 3A).
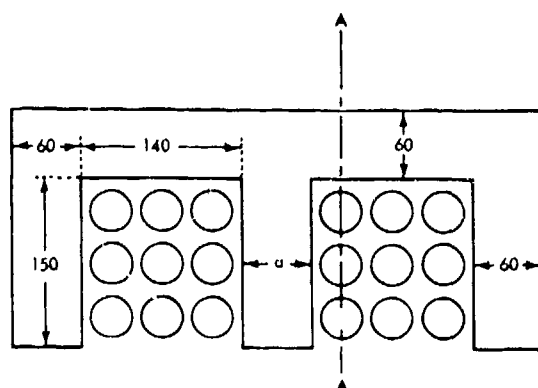
Fig. 3A. Arrangement of drums in compartments.
a = 0.40, 0.60 and 0.80 m respectively.

Each compartment contained two tiers of three by three fibre-board drums of a capacity of 25 kg, of which four drums that were placed against the separation wall were filled with porous propellant (Fig. 3B). The remaining ones were filled with sand.
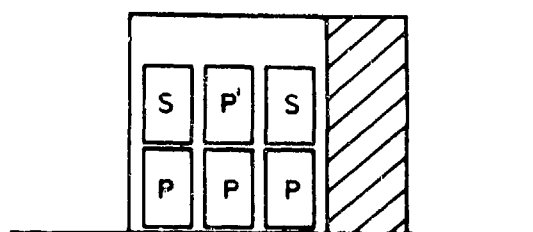
Fig. 3B. Section A-A. Arrangement of two tiers of drums against separation wall.

In the top 'donor' drum detonation was initiated with 375 g of plastic explosive. The possible occurrence of a sympathetic detonation in the adjoining compartment was evidenced by means of

(i) a detonation of primacord with one end in the 'acceptor' drum (parallel to its axis), witnessed by a lead plate at the other end

(ii) pressure transducers, installed at a distance of 50 m from the open side of the compartments

In the case of a 0.40 m thick separation wall a sympathetic detonation occurred (Table 3), whereas no sympathetic detonation was encountered with the 0.60 and 0.80 m thick separation walls and after the last two trials unburned propellant was found back in the proving grounds. An earthen wall of a thickness of 0.60 m may therefore be considered the minimum thickness whereby no sympathetic detonation takes place on detonation of 100 kg of porous nitro-cellulose propellant. Upscaling to larger quantities is done by the cubic root of the quantity of propellant.

TABLE 3

Minimum Barrier Thickness

Thickness separation wall	Lead witness plate	TNT-equivalence % peak pressure at 50 m
0.40	Sympathetic	58, based on 200 kg of donor + acceptor propellant
0.60	No detonation	65, based on 100 kg of donor propellant
0.80	No detonation	70, based on 100 kg of donor propellant

The barrier tests showed also that the TNT equivalence of propellants is dependent on the distance at which the peak pressure has been measured. A pressure versus distance diagram has been constructed on the basis of the experimental results with porous propellant. This diagram is compared with an equivalent quantity of TNT (Fig. 4).

302
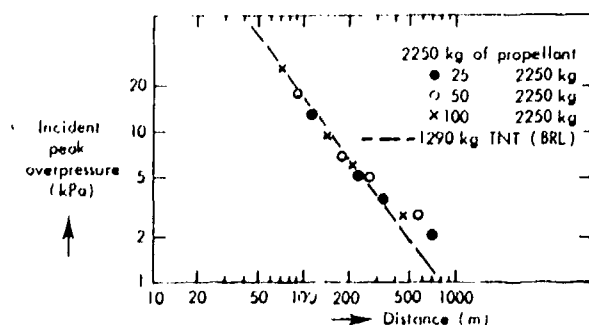
Fig. 4. Peak pressure versus distance diagram.

It shows that the two profiles are in good agreement when the pressure is high. At pressures below 4 kPa the peak pressure of the propellant exceeds that of TNT at the same distance. This implies that the propellant equivalence increases with increasing distance.

LABORATORY TEST

Since the execution of field tests is a costly proposition the search for a laboratory test which would yield the same hazard classification as the field tests seems a logical step. The propellant to be investigated is confined in a steel tube (Fig. 5) with the dimensions: length 1.18 m × I.D. 0.03 or 0.05 m, wall thickness 0.01 m. The tube is closed at one end. The propellant is ignited at the closed end with the
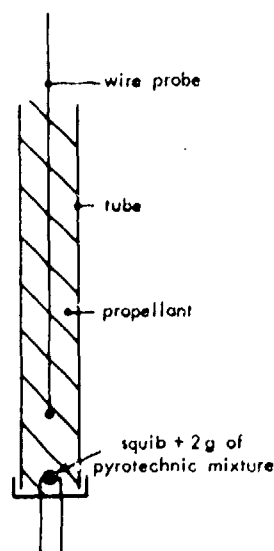
Fig. 5. Set up laboratory test.

aid of a squib in a few grams of pyrotechnic mixture, or by means of plastic explosive. In the longitudinal axis of the tube a wire is fitted. This probe consists of a bare copper wire round which an intermittently nylon-insulated resistance wire is skipwound. After short-circuiting the ends of the two wires the assembly is wrapped in aluminum foil, and fitted in the centre of the tube to a depth of approximately 10 cm above the ignition point.

On ignition the voltage drop in the circuit, which is proportional to the reaction rate in the substance, is monitored. When the propellant is initiated by means of a squib an initial increase in the rate of the reaction front is observed which will then level off to a constant value (Fig. 6).
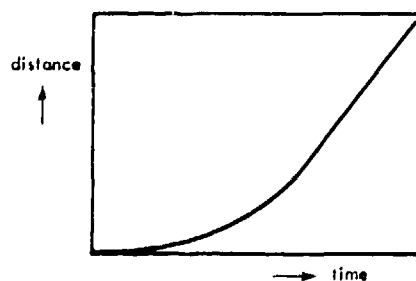
Fig. 6. Reaction rate curve on electric initiation.

Not all types of propellant will attain this constant value. If, on the other hand, initiation is effectuated by plastic explosive, then a constant rate is attained at once.

On the basis of these rate measurements the propellants may be divided into three groups (Table 4).

TABLE 4

*Hazard Classification Based on
Velocity Measurements in
the Laboratory Test*

Hazard group	Velocity m/s	
	flame ignition	booster ignition
1	max. 600 m/s	6000 m/s
2	1300 m/s	4000 m/s
3	3200 m/s	4000 m/s

303

(i) propellants not attaining a constant rate, and having a detonation rate which is many times higher

(ii) propellants attaining a constant rate which is considerably lower than the detonation rate

(iii) propellants having a high reaction front propagation rate in excess of 3000 m/s—which is almost equal to the detonation rate

As compared with the division into hazard groups following the field blast measurements this sub-division shows a striking resemblance, so that the laboratory test seems to be well suitable for hazard classification.

In order to determine the critical layer thickness of the various propellants also the distance has been determined at which the constant rate is attained in the laboratory test. For the propellants belonging to the first hazard group holds that this distance is larger than 1.18 m. For the propellants of both the second and the third hazard group holds that this distance is about constant, viz. about 0.30 m. In view of the results of the forementioned field tests where pro-pellants from hazard group 3 detonate almost completely at a layer thickness of 0.50 m, and those of the second group show no or incomplete detona-tion, the critical layer thickness and this distance cannot directly be correlated. The objective of the present investigation is to try and find a correlation as yet on the basis of the laboratory test.

CONCLUSIONS

The various types of propellants can in practice be divided into three hazard groups

(i) mass fire hazardous

(ii) mass detonable

(iii) detonable, depending on the thickness of the layer

The laboratory test is well suited to establish the hazard group of the propellant.

The investigation to determine the critical layer thickness with the aid of the laboratory test with be continued. An earthen wall with a minimum thickness of 0.6 m proved to be capable of preventing a sympathetic detonation when 100 kg of the tested porous nitrocellulose propellant detonated.

REFERENCE

1. Dr. J. W. Hartgerink. Investigation into the cause of an explosion during the drying of porous nitrocellulose powder. I Chem. E. Symposium no. 39, 6 (1974).

VOLUME AND PRESSURE DEPENDENCE OF SOME KINETIC PROCESSES IN EXPLOSIVES

D. J. Pastine, M. J. Kamlet and S. J. Jacobs
Naval Surface Weapons Center
W: `: Oak Laboratory
Silver S₁ ing, Maryland 20910

*Qualitative formulae are developed which describe the volume and pressure
dependence of certain kinetic processes thought to occur in explosives. The volume
and pressure dependences of the monomolecular, bond breaking, process and of one
possible bimolecular reaction process are specifically described, and the possible
relationship between these processes and explosive phenomena, such as explosion
time, are discussed.*

INTRODUCTION

It should be clear that energy barriers exist to the formation of explosive products. Were this not so, explosives would not exist for long in the unreacted state. The reactions, therefore, which occur in explosives and their concomitant rate constants should always be associated with a barrier or energy of activation. In what follows we try to construct qualitative models and expressions for the rate constants and activation energies of various kinds of decomposition processes. We do this to ascertain the volume and temperature dependence of these quantities for the purpose of improving our understanding of initiation and detonation phenomena and of explosive sensitivity in general. It is important to note that the models which we do construct differ from earlier work in that the volume dependence of kinetic processes in solids and liquids is specifically formulated and the physical basis for this dependence is elucidated.

It was Evans and Polanyi (1) who first constructed a theory of volume effects on reaction kinetics. In their early paper they described such effects in terms of a volume of activation, ΔV^*, which is the difference between the sum of the normal volumes of reactant molecules and the volume of Eyrings (2) activated complex. Here, we have taken a somewhat different approach and describe kinetic processes in terms of other fundamental phenomena and from these descriptions we derive expressions for ΔV^*.

Since the work of Evans and Polanyi, a number of investigators (3,4) have done work substantiating the significant effects of volume (or pressure) on many types of kinetic processes. The most recent indications that such effects are important in explosives have been given by the work of Lee et al. (5), who showed that the time to explosion at any given temperature can have a significant pressure dependence.

Clearly then, for any description of explosive behavior to be complete, the volume and pressure effects on kinetics must be taken into account. It is toward this end that we have made a beginning in the modeling of such effects for the liquid and solid states.

In the process of constructing our models, some convenient assumptions have been made. For example, we assume that rate controlling reactions proceed in one direction only. This assumption may be very close to the truth. In addition to this, thermodynamic equilibrium is assumed, and, it is also assumed that whenever a molecule or a pair of adjacent molecules have sufficient energy to react or

305

disintegrate, that they always do so. These assumptions are not necessarily true but this inaccuracy should not detract much from the qualitative description of monomolecular and bimolecular decomposition processes given below.

MONOMOLECULAR DECOMPOSITION

Two types of monomolecular decomposition can easily be distinguished. We refer to these as types A and B. We define the Type A decomposition as one which can occur because one or several internal modes of molecular vibration achieve amplitudes sufficient to cause either internal reaction or the breaking of bonds. The C-N bond, for example, will lose its strength if it is streached beyond a certain point. Since there will always be one or more normal modes of natural vibration which require the stretching of this bond, one can safely assert, assuming the validity of Boltzmann statistics, that any temperature, T, a certain number of these vibrations should have amplitudes sufficient to cause the breaking up of the molecule. Likewise, certain modes of vibration by virtue of their large amplitudes can bring otherwise unbonded atoms of the molecule into such proximity that they produce internal reaction. In nitromethane for example, the scissorlike motion of the oxygens relative to their companion nitrogen, could conceivably bring one of the oxygens close enough to a neighboring hydrogen atom to produce the reaction.

$$CH_3NO_2 \rightarrow CH_2N = 0 + HO\cdot + energy.$$
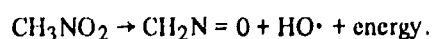
Type B decompositions are quite different and may have little connection with intramolecular vibrations. This type may be viewed as the result of a change in the electronic state of the molecules. One can picture a molecule raised in energy from its electronic ground state to some higher energy level from which it may readily decompose into products. Excited levels such as this can be achieved by the absorption of either thermal or electromagnetic energy. It should be clear then that explosives which can disintegrate by the type B process will also exhibit the property of photodecomposition at certain frequencies of light, a fact which enables us to directly determine the activation energies associated with this process.

Of the two types of monomolecular decomposition mentioned thus far, we investigate type A

processes only and below we construct the simplest possible model which will qualitively describe the related decomposition rates as functions of temperature, T, and specific volume, v.

Classically, the potential energy ψ_i of the ith normal mode of molecular oscillation is given by,

$$\psi_i = \frac{1}{2} w_i^2 \zeta_i^2 \tag{1}$$

where w_i is the angular frequency and ζ_i is the normal coordinate (6) for the ith mode. Since the normal coordinates are linear combinations of the Cartesian displacements of the atoms from their equilibrium positions, we expect that decomposition can occur whenever ζ_i reaches a particular value (amplitude), ζ_i^*. The potential energy associated with this amplitude will be

$$\psi_i^* = \frac{1}{2} w_i^2 \zeta_i^{*2} \tag{2}$$

Only molecules in which ψ_i can exceed ψ_i^* will be able to decompose through the ith oscillation mode. These molecules must, therefore have enough energy E_i in the ith mode such that $E_i \geqslant \psi_i^*$. According to equilibrium Boltzmann statistics (7), the fraction f_i of molecules which have (in the ith mode) an energy greater than ψ_i^* is given by

$$f_i = exp(-\psi_i^*/kT) = exp(-w_i^2 \zeta_i^{*2}/2kT) \tag{3}$$

where k is the Boltzmann constant. The total number per gram, n_i, of molecules having $E_i > \psi_i^*$ is simply nf_i where n is the total number of molecules per gram. Since each mode of vibration can achieve ζ_i^* only once per cycle, then on the average, a molecule with sufficient energy will decompose, approximately, in the time $\tau_i/2$ where τ_i is the period of the ith mode (i.e., $\tau_i = 2\pi/w_i$). The maximum rate at which molecules can decompose through the ith mode is given by the relation,

$$\left(\frac{dn}{dt}\right)_i = \frac{2bn_i}{\tau_i} = -\frac{bw_i}{\pi} n \, exp\{(-w_i^2 \zeta_i^{*2}/2kT)\} \tag{4}$$

where b is a proportionality constant of the order of unity. From equation (4) we can extract the rate constant, κ_i for the process,

306

$$\kappa_i \simeq \frac{bw_i}{\pi} \exp\{-w_i^2 \zeta_1^{*2}/2kT\} \qquad (5)$$

Since there are in general 3ν-6 internal vibrational modes for a molecule of ν atoms, the effective rate constant, κ, which governs the disintegration rate arising from all modes of vibration is given by the sum of the κ_i. That is,

$$\kappa = \sum_{i=1}^{3\nu\text{-}6} \kappa_i \qquad (6)$$

The total rate of disintegration via monomolecular vibrations is then

$$\frac{dn}{dt} = -\kappa n. \qquad (7)$$

Since the w_i's will be affected by the molecular environment, that is, since they will be influenced or perturbed by neighboring molecules, we must consequently expect that the w_i's will change with changing volume. This happens because smaller volumes bring neighboring molecules closer on the average and increases their perturbing effect on the normal mode frequencies. The 's, due to anharmonic effects, will also depend on it but that problem will not be addressed at this time.

It is interesting to examine the logarithmic volume derivative, $(\partial \ln \kappa_i/\partial \ln v)_T$ of equation (5). Taking this derivative, one finds

$$\left(\frac{\partial \ln \kappa_i}{\partial \ln v}\right)_T = \gamma_i \left[\frac{w_i^2 \zeta_i^{*2}}{kT} - 1\right] \qquad (8)$$

where $\nu_i = -d \ln w_i/d \ln v$, is the Grüneisen parameter for the ith mode. Since $w_i^2 \zeta_i^{*2}$ is just twice the activation energy, ΔE_i, for the decomposition process, equation (8) may be rewritten in the form,

$$\left(\frac{\partial \ln \kappa_i}{\partial \ln v}\right)_T = \gamma_i \left[\frac{2\Delta E_i}{kT} - 1\right] \qquad (9)$$

Through the identity, $(\partial \ln \kappa_i/\partial \ln v)_T = -B_T(\partial \ln \kappa_i/\partial P)_T$, where B_T is the isothermal bulk modulus, we may write equation (9) in terms of pressure changes, i.e.,

$$\left(\frac{\partial \ln \kappa_i}{\partial P}\right)_T = -\frac{\gamma_i}{B_T} \left[\frac{2\Delta E_i}{kT} - 1\right] \qquad (10)$$

Equation (10) is very interesting because it implies that near ambient temperatures most vibrationally induced decomposition process will be suppressed by pressure. This is so because the γ_i's, with a few exceptions, are generally positive (i.e., the w_i's usually increase with decreasing v) and in addition, $2\Delta E_i/kT$ is almost always greater than unity. A relatively low value of $\Delta E_i/kT$ which is associated with the C-N bond breaking process (8), is 25,000/T. This information, along with some information on the infrared spectra of explosives, can be used to calculate the order of magnitude of the pressure dependence of κ_i for the C-N (and the similar N-N) bond breaking process in secondary explosives. Infrared spectra (9) of high explosives indicate that, over a pressure range of about 60 kbar, normal mode frequencies in the region of 2.5×10^{13} to 3×10^{13} hertz increase by about 1.5%. Since these frequencies should be close to that for the C-N bond vibration (10) we expect $\Delta w_i/w_i$ to be about .015 as pressure increases from 1 atm to 60 kbars. Theoretical work (11) on TATB indicates that $\Delta v/v$ should typically be about -0.18 over the same pressure range. Therefore,

$$\gamma_i \simeq -\frac{\Delta w_i}{w_i} \frac{v}{\Delta v} = 0.083$$

is a reasonable estimate of the Grüneisen Parameter for the bond breaking process. Using a rather typical (12) value of 100 kbars for B_T we have, for the C-N bond breaking decomposition,

$$\left(\frac{\partial \ln \kappa_i}{\partial P}\right)_T = -0.00083 \left[\frac{50,000}{T} - 1\right] \text{kbar}^{-1}. \quad (11)$$

Equation (11) is a crude estimate but it should provide a reasonable value for the pressure dependence of the bond breaking process which may very well dominate (8) the reaction kinetics of some explosives at low P and T. In fact, its predictions agree surprisingly well with values which may be derived from time to explosion measurements (5). Assuming the time to explosion, τ, is proportional to $1/\kappa$, we find from experiments at 555°K that for dinitropropane, $(\partial \ln \kappa/\partial P) \simeq -0.050 \text{ kbar}^{-1}$ and for HMX, $(\partial \ln \kappa/\partial P) \simeq -.074 \text{ kbar}^{-1}$. Putting T = 555°K into equation (11), we find $(\partial \ln \kappa/\partial P) \simeq -.074$ kbar^{-1} for C-N bond breaking. Since there is good reason (8) to suspect that the bond breaking process

can dominate kinetics in this region of T, the qualitative agreement between theory and experiment trends to support the theory presented thus far.

If more than one vibrational mode is competitive in the decomposition at a given T, then it becomes necessary to sum the effects of different modes to obtain the pressure dependence of the effective rate constant, κ. That is

$$\left(\frac{\partial \ln \kappa}{\partial P}\right)_T = \frac{\sum_{i=1}^{3\nu-6} \kappa_i \gamma_i \left[\frac{2\Delta E_i}{kT} - 1\right]}{\beta_T \sum_{i=1}^{3\nu-6} \kappa_i} \quad (12)$$

If one of the κ_i's, say κ_j, is much larger than all the rest (which also implies a larger γ_i), then equation (12) reduces to $(\partial \ln \kappa/\partial P) \simeq {}_T (\partial \ln \kappa_j/\partial P)_T$. Therefore if one vibrational process dominates the decompositional kinetics, then its pressure dependence will determine the pressure dependence of the kinetics.

From what has been done so far we can come to a few tentative conclusions about vibrationally induced decomposition process. Equation (5) implies that $\kappa_i \propto w_i$ when $\Delta E/kT \ll 1$. Since $\Delta E_i, \propto w_i 2$, this suggests that, as T increases, the processes with higher and higher activation energies begin to dominate the decomposition process. Equation (5) also suggests that the precoefficient (w_i/π) for each process is proportional to the square root of the activation energy, ΔE_i, for that process. This means that unless there are very large differences between all the ΔE_i associated with a single molecule, (so that a single decomposition mode can be dominant over a broad range of P and T) the value of κ at temperatures associated with detonation will be considerably higher than would be assumed from ambient temperature measurements. This casts doubt on the validity of simple Arrhenius kinetics when applied to initiation and detonation phenomena.

Equations (10) and (12) are also interesting because they imply that, if there are no processes of importance with negative γ_i, then there will be a region of shock pressures in which it is impossible to initiate an explosive through Type A monomolecular processes. The demarcation point is determined by the shock pressure, P^*, which raises the temperature sufficiently to offset the rate suppression caused by

the pressure itself. The value of P^* is hard to estimate. It will depend heavily on the physical properties of the explosive and the values of γ_i and ΔE_i for the rate controlling processes. It is safe to say, however, that for the C-N bond breaking process, P^* should be less than a few kbar (13).

Another interesting aspect of equation (10) is that it may be used to calculate, ΔV^*, a quantity thought of as the effective difference between the normal molecular volume and an activated state volume (1) from which decomposition may occur. This quantity is defined by the equation

$$\left(\frac{\partial \ln \kappa}{\partial P}\right)_T = -\frac{\Delta V^*}{kT} \quad (13)$$

Combining equation (13) with equation (1) we find, for vibrational decompositions,

$$\Delta V^* = \frac{kT\gamma_i}{B_T} \left[\frac{2\Delta E_i}{kT} - 1\right] \quad (14)$$

Using the earlier results for C-N bond breaking at $555°K$, one finds

$$\Delta V^* = 5.6 \times 10^{-24} \text{ cc/molecule} = 3.4 \text{ cc/mole.}$$

This calculated value of ΔV^* is quite typical of those measured for organic reactions which usually lie (3) between -5 and 15 cc/mole. The last result, therefore, further substantiates the validity of equation (1).

At this point, we can say little more about Type A or Type B processes without detailed calculations on specific molecules. This we save for future work.

BIMOLECULAR DECOMPOSITION

Bimolecular reactions should result from the proximity of molecules. It is reasonable to believe that reaction is possible when two (or more) specific atoms on different molecules come to within a distance, δ, of one another. Because the molecules repel one another at close range, this will require a certain amount of energy to activate the reaction process. To qualitatively describe the rates associated with these reactions, we will, for the time being, limit ourselves to the simplest possible molecular model.

308

Assume we have a solid or liquid of roughly spherical molecules, radius $\simeq a$, which perform many oscillations about a given site before changing position in a laboratory frame. Assume also, that these oscillations are completely harmonic at any given specific volume, v, for the system. The outer atoms of two neighboring molecules will then be able to come to within a distance δ of one another, only if their vibrational amplitudes are sufficiently large, or, if v is so small that the molecules are forced to be in close proximity. If R_0 is the mean separation between one molecule and a nearest neighbor, then reaction can occur when the amplitude of vibration, $\eta = (R - R_0)$, along the line of centers has a maximum value, η^*, of at least $\eta^* = (R_0 - 2a - \delta)$. If the associated frequency of vibration is $(w/2\pi)$, then the energy, ΔE^*, required to achieve η^* is $\Delta E^* = mw^2\eta^{*2}/4$ where m is the molecular mass. Assuming thermodynamic equilibrium, the fraction of the z nearest neighbors with which a molecule will share this energy is* $\exp(- \Delta E^*/kT)$ and the probability that a given molecule shares sufficient energy with a neighbor to react is †z $\exp(- \Delta E^*/kT)$. As in the case of monomolecular decomposition, the reaction rate for n molecules per gram is then

$$\frac{dn}{dt} \propto \frac{wzn}{\pi} \exp\left(\frac{- \Delta E^*}{kT}\right) \quad (15)$$

Equation (15) assumes that reaction occurs at the first opportunity whenever sufficient energy exists. The rate constant, κ, is therefore,

$$\kappa \propto \frac{wz}{\pi} \exp\left(\frac{- \Delta E^*}{kT}\right)$$

$$= \frac{wz}{\pi} \exp\left[\frac{mw^2(R_0 - 2a - \delta)^2}{4kT}\right]. \quad (16)$$

Now, as before, w will depend on v. Note also that $R_0 = \alpha v^{(1/3)}$, where α is a proportionality constant so that it is convenient to set $\eta^* = \alpha(v^{1/3} - v_c^{1/3})$, where $v_c^{1/3} = (2a - \delta)/\alpha$, is a critical volume at which all neighbors can immediately react with one another. This volume is the volume for which $\Delta E^* = $

0. Keeping this in mind, we take the logarithmic derivative of κ with respect to v and obtain

$$\left(\frac{\partial \ln \kappa}{\partial \ln v}\right)_T = \gamma \left[\frac{2\Delta E^*}{kT} - 1\right] - \frac{2\Delta E^*}{3kT} \left[1 - \left(\frac{v_c}{v}\right)^{1/3}\right]^{-1} \quad (17)$$

where $\gamma = - d \ln w/d \ln v$. In terms of pressure changes we have

$$\left(\frac{\partial \ln \kappa}{\partial P}\right)_T = - \frac{\gamma}{B_T} \left[\frac{2\Delta E^*}{kT} - 1\right]$$

$$+ \frac{2\Delta E^*}{3B_T kT} \left[1 - \left(\frac{v_c}{v}\right)^{1/3}\right]^{-1} \quad (18)$$

This last relation is very interesting because there are two competing terms on the right-hand side. The first term is identical in form to equation (10) for monomolecular processes. Here, however, γ is expected to have a value of two or greater if the molecules of the system are bound together primarily by Van der Waals bonds (14). This will frequently be the case for explosives.

Assuming $\Delta E^*/kT \gg 1$, the first term in equation (18) indicates strong pressure suppression. The magnitude of the second (rate enhancing) term depends heavily on the value of v_c/v. It is clear that this term will eventually dominate in equation (17) as $v_c/v \to 1$. If we neglect unity compared to $2\Delta E^*/kT$, then the two terms in equation (18) exactly balance when

$$\gamma \simeq \frac{1}{3[1 - (v_c/v)^{1/3}]} \quad (19)$$

Thus, if γ is in the neighborhood of two, then the bimolecular reaction rate will be enhanced with pressure only for compressed volumes such that $v_c/v \geqslant .57$. It is interesting to pursue the question as to whether or not an explosive may acquire a volume, $v \simeq v_c$, in a detonation wave. Before we consider this question, we must first dispose of the spherical symmetry assumed earlier, since most explosives are not composed of spherical molecules.

In a solid explosive it is reasonable to assume that reaction can occur when the extremities of two neighboring molecules vibrating along their line of centers come to within a distance δ of one another.

---

*Here it is assumed that a molecule forms an independent oscillator with each nearest neighbor. This model is over-simplified and is used only because it facilitates the calculation of volume dependent effects.

†It should be noted that z is not assumed to be a function of n.

This model also leads to equations (16), (17), and (18) as before except that now, a is half the molecular diameter in the direction of oscillation and ν is associated with the value of w for that direction. One can therefore find a value of v_c for every direction of oscillation for which bimolecular reaction is possible. Now, since in some reactive directions in some explosives the value of $(2a + \delta)$ will be a large fraction of the distance, R_0, between centers, then, it is entirely conceivable that a critical volume can be reached behind a detonation wave, since for such waves a compression, relative to the original explosive volume, v_0, of $v/v_0 < 0.75$ is not unusual.

In liquid explosives, bimolecular reaction rates will be affected by molecular rotations. The nitromethane molecule, for example, will normally tend to rotate about axes passing through its center of gravity which is close to the nitrogen atom.

This rotation will make it difficult, for example, for the carbon of one molecule to come to within 1Å (the approximate C = 0 bond distance) of the oxygens of another molecule in order to form CO or CO_2. This implies a very high effective activation energy for this reaction if almost all the molecules are freely rotating. With compression, however, rotations will be suppressed (hindered) and the effective activation energy for the process will drop accordingly. This is an interesting effect because it connects reaction rates with the hindering of rotations. The existence of the phenomena would imply that the relaxation time associated with the transition from rotation to vibration may be an important factor in the shock initiation and detonation of liquid explosives.

At this point, little more can be said without further analysis and calculations on specific explosives. The results obtained thus far are summarized in the discussion below.

DISCUSSION AND CONCLUSIONS

We have constructed plausible models to describe qualitatively, the pressure and temperature dependence of monomolecular (Type A; internal reaction or bond breaking) and bimolecular reactions in explosives. In both cases we find that the reaction rates are volume dependent (and therefore they are, indirectly, pressure dependent). In the case of monomolecular, Type A, processes, only a slight volume or pressure

dependence is anticipated. For those processes, different rates are associated with different vibrational modes and the decomposition modes of higher activation energy are expected to dominate at the higher temperatures. In addition, we expect that the precoefficient associated with a particular decomposition mode should be roughly proportional to the square root of the activation energy for that decomposition mode. These results lead us to conclude that a simple Arrhenius rate law may describe detonation processes only very crudely and that activation energies determined under ambient conditions may have little bearing on detonation processes.

In the case of bimolecular reactions, strong pressure suppression of the rate is indicated until the system nears some critical volume v_c. The approach to this volume signals the onset of extremely rapid reaction which can occur at relatively low temperature. We expect that this may be a significant initiating mechanism in some explosives. In the case of liquid explosives, we suggest that free molecular rotations can impede bimolecular reaction rates and that this rate can be enhanced in such cases by the hindering of rotations through compression of the system. In the case of rapid shock compression, the relaxation time associated with the rotation to vibration transition may have an important bearing on the sensitivity of liquid explosives to the duration of applied shocks. For that matter, subsequent to a shock, any relaxation processes of sufficient length which slow the rate of internal temperature increase of explosive molecules will have an equally important bearing on shock sensitivity.

One general implication of all these results is that more effort should be spent on high pressure experimentation. The high pressure infrared and Raman spectra of explosives would tell us more about the values of w_i, γ_i and the relative values of the ΔE_i, for monomolecular decomposition processes. Likewise, very high pressure (>100 kbar) experiments done at ambient temperature would shed light on whether or not any critical volumes may be associated with bimolecular decomposition processes. Such experiments are now possible as a result of new measuring techniques associated with the use of the diamond anvil press. (15)

Before closing, we caution the reader as to the qualitative nature of the results described above. Harmonic oscillations (at constant v) have been

assumed throughout. This is an unrealistic assumption in most cases and consequently, the precoefficients for the theoretical rate constants are only roughly proportional to the square root of the associated activation energies and not exactly proportional as indicated by equations (5) and (16). For the same reason, if a particular w_i and ζ_i^+ were known, then an activation energy calculated by means of $\Delta E_i = (1/2)w_i\zeta_i^{+2}$ would probably be seriously in error. It is better for the time being to use experimental values for the ΔE_i. It will be part of our future work to develop more accurate theoretical expressions for these quantities.

REFERENCES

1. M. G. Evans and M. Polanyi, Trans. Faraday Soc., **31**, 875, 1935.

2. H. Eyring, D. Henderson, B. J. Stover and E. M. Eyring, Statistical Mechanics and Dynamics, (John Wiley and Sons Inc., New York, London and Sidney, 1964).

3. See for example, S. D. Hamann, Physico-Chemical Effects of Pressure, (Academic Press, Effects of Pressure, (Academic Press, New York and London, 1957).

4. L. V. Barabe, A. N. Penshin and V. V. Yakovlev, Fizika Gorniya, **5**, 528, 1969.

5. E. L. Lee, R. H. Sandborn and H. D. Stromberg, Proceedings of the Fifth Symposium (International) on Detonation, Pasadena, California, Aug. 18-21, 1970. Sponsored by the Naval Surface Weapons Center (Naval Ordnance Laboratory) and the Office of Naval Research.

6. These normal coordinates are linear combinations of cartesian coordinates each of which is multiplied by the square root of the atomic mass which it locates. The atomic masses therefore do not appear in equation (1) since they are contained in the definition of the ζ_i. See, for example, K. R. Symon, Mechanics (Addison-Wesley, Reading and London, 1961) Chapter 12.

7. See, for example, J. E. Mayer and M. G. Mayer, Statistical Mechanics, (John Wiley and Sons, New York and London, 1961).

8. T. L. Cottrell, T. E. Graham, and T. Y. Reid, Trans. Faraday Soc. **47**, 584 (1951).

9. R. J. Jakobsen, Battelle Memoral Institute (USA) Technical Report, 11 March 1971 (unpublished).

10. G. Herzberg, Infrared and Raman Spectra of Polyatomic Molecules, BD. Van Nostrand, New York, 1945). The frequencies associated with the $C = N$, $C = C$ and $C - C$ bonds are given in the reference above (p. 195). The frequency associated with the $C - N$ bond has been estimated by assuming that it has about the same ratio to the $C = N$ frequency as the $C - C$ stretching vibrations has to the $C = C$ vibration. The calculated result for the $C - N$ vibration is 2.75×10^{13} hertz.

11. D. John Pastine and R. R. Bernecker, J. Appl. Phys, **45**, 4458, (1974).

12. S. P. Marsh (Private Communication) Mr. Marsh has kindly provided us with the ultrasonic data from which the bulk sound speed may be calculated in various explosives. These sound speeds were used to determine the isentropic bulk moduli. The latter, which ranged from 40 to 150 kbar, were used in place of B_T.

13. The low estimate of P^* results from the observation that a temperature rise of only a few degrees is sufficient to offset the rate suppression caused by shock compression. This may be seen by comparing $(\partial \ln \kappa / \partial T) \Delta T_{P=0}$ and $\partial(\ln \kappa / \partial P)$ $P_{T=293°K}$ at points on the explosive shock Hugoniot given in reference (6).

14. D. John Pastine, Phys. Rev. **138** A767 (1965). An indication of the relationship between γ and the character of the attractive, central forces between atoms or molecules is given in this paper.

15. See, for example, C. E. Weir, S. Block, and G. J. Piermarini, J. Chem Phys **53** 4265 (1970).

16. SRI Progress Report 37-1, Semiannual 1 Sep 1972 to 28 Feb 1973, on ONR Contract N00014-70-0190.

17. M. J. Kamlet, L. A. Kaplan and J. C. Dacons, J. Org. Chem., **26**, 4371 (1961) and references cited therein.

18. Among others, V. V. Dubhikin, G. M. Nazin and G. B. Manelis, Izv. Akad. Nauk SSSR, 1412 (1971).

THE RELATIONSHIP OF IMPACT SENSITIVITY WITH STRUCTURE OF ORGANIC HIGH EXPLOSIVES. I. POLYNITROALIPHATIC EXPLOSIVES

Mortimer J. Kamlet
Naval Surface Weapons Center
White Oak Laboratory
Silver Spring, Maryland 20910

Impact sensitivities of organic high explosives are primarily functions of their thermal decomposition rates at the temperatures generated under the impact hammer. For classes of explosives with similar decomposition mechanisms, there appear to be rough linear relationships (sensitivity-structure trends) between logarithmic 50% impact heights and values of OB_{100}, a measure of oxidant balance. It is shown that polynitroaliphatic explosives containing at least one N-nitro linkage are more sensitive as a class than nitroaliphatic explosives containing only C-nitro linkages.

Factors which influence the sensitivity of high explosives have long been of interest to the United States Navy. An ongoing approach to the problem at the Naval Surface Weapons Center, NSWC (ex Naval Ordnance Laboratory, NOL) has been to investigate the reactions governing sensitivity in much the same manner as the physical organic chemist usually studies any reaction, i. e., by determining the effect of structure on reactivity. We wish now to describe this approach as it applies to several types of nitroaliphatic explosive compounds.

Of the many means of evaluating sensitivity of high explosives, the impact test is by far the most common. The test involves subjecting samples of the explosives to the force of a series of hammer blows caused by a standard weight falling from varying heights. The sensitivity is reported as that height which has a 50% probability of causing an explosion.

As carried out at the Naval Surface Weapons Center, the technique is a modification of that developed at the Explosives Research Laboratory, Bruceton, Pennsylvania during World War II. The salient features which distinguish the ERL-NSWC machine and method from other such tests are: the particular tool design, the criterion of explosion, the use of flint paper to rest the sample on, and the statistical procedure used to conduct the experiment and reduce the data (1).

Because the machine can distinguish between explosives with 50% impact heights of 15 and 20 cm about equally as well as between 150 and 200 cm, the logarithm of the 50% height is usually considered to be the best measure of relative impact sensitivity. Impact sensitivities (or 50% heights) for some standard explosives are: 1, 3-diamino-2, 4, 6-trinitrobenzene, 320 cm (top of scale); TNT, 160 cm; Comp. A-3, 60-70 cm; Comp B, 60-70 cm; tetryl, 32-35 cm; RDX, 22-24 cm; HMX, 24-26 cm; bis (2, 2, 2-trinitroethyl) urea, 14-16 cm; PETN, 10-13 cm; bis (2, 2, 2-trinitroethyl) nitramine, 4-6 cm; lead azide, 2-4 cm.

The test, which has the advantage of requiring relatively small quantities of material (*ca* 700 mg), may be carried out rapidly and conveniently, and it has proven reasonably successful in separating high explosives into classes of generally similar handling hazards. The machine, however, has neither the resolution nor the reproducibility required of a research tool, and only limited reliability may be attributed to any individual 25-shot impact result. TNT, a standard, illustrates the poor reproducibility.

Separate 25-shot determinations on twice recrystal-lized material have given 50% impact heights ranging from below 100 cm to above 250 cm. Such varia-tions have been attributed to operator technique, particle size distribution in the sample, atmospheric conditions (humidity, etc.), and multifold other causes.

In view of the unreliability of individual results, it was felt that any correlation of impact sensitivity with structure would necessarily depend on a large body of data determined for classes of chemically related compounds. It was hoped that errors in the individual determinations would tend to cancel ou and that a plot of the data as a function of the structural parameter chosen for comparison would show the data points distributing about a meaningful *sensitivity-structure trend*. This trend might then serve as a tool for predicting impact behavior of con-templated new synthesis candidates. We were fortu-nate in that the large body of impact information had already been assembled at NOL during the period 1950-1960, and that a majority of the determinations had been carried out by the same competent opera-tor.

A convenient structural parameter chosen for comparison with log $h_{50\%}$ was oxidant balance, OB_{100}, a term which we define as the number of equivalents of oxidant per hundred grams of explo-sive about the amount required to burn all hydrogen to water and all carbon to carbon monoxide. In cal-culating OB_{100}, an atom of oxygen represents two equivalents of oxidant, an atom of hydrogen one equivalent of reductant, and an atom of carbon two equivalents of reductant (2). Since carboxyl groups are considered to be "dead weight", two equivalents of oxidant were subtracted for each such group in the molecule (3). For C-H-N-O explosives, the applica-ble equation is,

$$OB_{100} = \frac{100(2n_O - n_H - 2n_C - 2n_{COO})}{Mol. Wt.}, \quad (1)$$

where n_O, n_H, and n_c represent the number of atoms of the respective elements in the molecule, and n_{COO} is the number of carboxyl groups. For explosives balanced to the CO-level of oxygen balance, $OB_{100} = 0$; at the CO_2-level of oxygen balance, $OB_{100} = ca + 2.5$ (4). Values of OB_{100} are additive for mixtures of explosives, of for explosive plus nonexplosive diluent.

A number of criteria were set for explosive com-pounds included in the correlations: the compound was solid at room temperature; contained no hetero-aromatic ring such as triazole, tetrazole, etc.; con-tained no acetylenic or azido groups; and was not a salt. Impact sensitivities for seventy eight polyni-troaliphatic and alicyclic explosives which meet these requirements are listed in Table 1, together with molecular formulas and values of OB_{100}. The com-pounds are divided into eight categories as follows: *A*) eight compounds with nitro groups exclusively in nitramine linkages; Tetryl is included to avoid set-ting up a separate category for this single example; *B*) seven compounds with nitro groups in both nitra-mine and *gem*-dinitro linkages; *C*) seventeen examples containing both nitramine and trinitromethyl linkages. Some also contain *gem*-dinitro groups; *D*) three com-pounds having nitramine and nitrate ester functions. They may also contain trinitromethyl or *gem*-dinitro functions; *E*) ten nitramides, all having present some other of the above functions; *F*) nineteen examples having trinitromethyl groups. These may have mono-nitro but not *gem*-dinitro functions; *G*) nine trini-tromethyl compounds also having *gem*-dinitro func-tions; and *H*) six examples having *gem*-dinitro groups only.

Fifty percent impact heights on a logarithmic scale are plotted against corresponding OB_{100} values in Fig. 1. If all data points are considered equally, it is seen that, as might be expected, they fall within a rather broad band of increasing $H_{50\%}$ values with decreasing OB_{100}. Sensitivities range from 5 to 16 cm at $OB_{100} = ca + 3.0$, from 11 to 72 cm at $OB_{100} = ca\ 0.0$ and from 53 to > 320 cm at $OB_{100} = ca - 3.0$.

If now we make a distinction between the explo-sive compounds based on the nature of the "trigger linkage", some further regularities begin to appear. Data points for all compounds containing at least one N-nitro grouping in their structures (classes *A-E* in Table 1, represented by filled circles in Fig. 1) are seen to cluster toward the lower side of the broad band; data points representing trinitromethyl compounds containing only C-nitro linkages (classes *F* and *G*, open circles) cluster toward the upper por-tion of the plot. Indeed, if the two categories are considered separately, most of the points can be seen to distribute about separate straight lines which might be considered to represent the hoped-for *sensitivity-structure trends*.

313

TABLE 1

Impact Sensitivity and CB_{100} of Selected Explosives.

No.	Compound Name	Molecular Formula	CB_{100}	$H_{50\%}$, cm*
	A. Nitramines			
1.	methylenedinitramine (MEDINA)	$C_4H_4N_4O_4$	+1.47	13
2.	ethylenedinitramine (EDNA)	$C_2H_6N_6O_6$	-1.33	34
3.	RDX	$C_3H_6N_6O_6$	0	24
4.	N-methyl EDNA	$C_3H_8N_4O_4$	-3.65	114
5.	HMX	$C_4H_8N_8O_8$	0	26
6.	3-nitraza-1, 5-pentanedinitramine	$C_4H_{10}N_6O_6$	-2.52	39
7.	3, 6-dinitraza-1, 8-octanedinitramine	$C_6H_{14}N_8O_8$	-3.07	53
8.	Tetryl	$C_7H_5N_5O_8$	-1.04	32
	B. Nitramine plus gem-Dinitro			
9.	3, 3-dinitro-1, 5-pentanedinitramine	$C_5H_{10}N_6O_8$	-1.42	35
10.	N, 3, 3, 5, 5-pentanitropiperidine	$C_5H_6N_6O_{10}$	+1.29	14
11.	bis (2, 2-dinitropropyl) nitramine	$C_6H_{10}N_6O_{10}$	-0.61	29
12.	bis (2, 2-dinitrobutyl) nitramine	$C_3H_{14}N_6O_{10}$	-2.82	80
13.	2, 2, 4, 7, 9, 9-hexanitro-4, 7-diazadecane	$C_8H_{14}N_8O_{12}$	-1.45	72
14.	2, 2, 4, 7, 7, 10, 12, 12-octanitro-4, 7-diazatridecane	$C_{11}H_{18}N_{10}O_{16}$	-1.47	44
15.	2, 2, 5, 7, 7, 9, 12, 12-octanitro-4, 7-diazatridecane	$C_{11}H_{18}N_{10}O_{16}$	-1.47	37
	C. Nitramine plus Trinitromethyl			
16.	methyl 2, 2, 2-trinitroethyl nitramine	$C_3H_5N_5O_8$	+2.09	9
17.	bis (2, 2, 2-trinitroethyl) nitramine	$C_4H_4N_8O_{14}$	+4.12	5
18.	2, 2, 2-trinitroethyl 3, 3, 3-trinitropropyl nitramine	$C_5H_6N_8O_{14}$	+2.98	6
19.	N, N'-bis (2, 2, 2-trinitroethyl) MEDINA	$C_5H_6N_{10}O_{11}$	+3.46	5
20.	N-methyl-N'-trinitroethyl EDNA	$C_5H_9N_7O_{10}$	+0.30	11
21.	2, 2, 2-trinitroethyl N-(2, 2, 2-trinitroethyl) nitraminoacetate	$C_6H_6N_8O_{16}$	+2.69	9
22.	2, 2, 2-trinitroethyl 4-nitrazavalerate	$C_6H_9N_5O_{10}$	-0.97	35
23.	2, 2, 2-trinitroethyl 3, 3-dinitrobutyl nitramine	$C_6H_9N_7O_{12}$	+0.81	20
24.	bis (2, 2, 2-trinitroethyl) 3-nitrazaglutarate	$C_8H_8N_8O_{18}$	+1.58	14
25.	1, 1, 1, 3, 6, 9, 11, 11, 11-nonanitro-3, 6, 9-triazaundecane	$C_8H_{12}N_{12}O_{18}$	+1.42	12
26.	1, 1, 1, 3, 6, 6, 9, 11, 11, 11-decanitro-3, 9-diazaundecane	$C_9H_{12}N_{12}O_{20}$	+1.64	10
27.	1, 1, 1, 4, 6, 6, 8, 11, 11, 11-decanitro-4, 8-diazaundecane	$C_9H_{12}N_{12}O_{20}$	+1.64	11
28.	bis (2, 2, 2,-trinitroethyl) 4-nitraza-1, 7-heptanedioate	$C_{10}H_{12}N_8O_{18}$	0	29
29.	1, 1, 1, 3, 6, 9, 12, 14, 14, 14-decanitro-3, 6, 9, 12-tetrazatetradecane	$C_{10}H_{16}N_{14}O_{20}$	+0.61	19

*25-shot determinations on Type-12 tools.

TABLE 1

Impact Sensitivity and CB_{100} of Selected Explosives. (Continued)

No.	Compound Name	Molecular Formula	CB_{100}	$H_{50\%}$, cm*
30.	bis (2, 2, 2-trinitroethyl)3, 6-dinitraza-1, 8-octanedioate	$C_{10}H_{12}N_{10}O_{20}$	+0.67	29
31.	1, 1, 1, 3, 6, 6, 8, 10, 10, 13, 15, 15, 15-tridecanitro-3, 8, 13-triazapentadecane	$C_{12}H_{16}N_{16}O_{26}$	+1.50	23
	D. Nitramine plus Nitrate Ester			
32.	N-(2, 2, 2-trinitroethyl) nitraminoethyl nitrate	$C_4H_6N_6O_{11}$	+3.19	7
33.	3-[N(-2, 2, 2-trinitroethyl)nitramino] -propyl nitrate	$C_5H_8N_6O_{11}$	+1.83	12
34.	3, 5, 5-trinitro-3-azahexyl nitrate	$C_5H_9N_5O_9$	–0.35	21
	E. Nitramides			
35.	N-nitro-N-(3, 3, 3-trinitropropyl) 2, 2, 2-trinitroethyl carbamate	$C_6H_6N_6O_{16}$	+2.70	9
36.	2, 2, 2-trinitroethyl 2, 5-dinitrazahexanoate	$C_6H_9N_7O_{12}$	+0.27	15
37.	2, 2, 2-trinitroethyl 2, 5, 5-trinitro-2-azahexanoate	$C_7H_9N_7O_{14}$	+0.72	22
38.	2, 2, 2-trinitroethyl 2, 4, 6, 6-tetranitro-2, 4-diazaheptanoate	$C_7H_9N_9O_{16}$	+1.47	18
39.	N, N'-dinitro-N, N'-bis (3, 3, 3-trinitropropyl) oxamide	$C_8H_8N_{10}O_{18}$	+2.26	9
40.	2, 2, 6, 9, 9-pentanitro-4-oxa-5-oxo-6-azadecane	$C_8H_{12}N_6O_{12}$	–1.56	47
41.	1, 1, 1, 5, 7, 10, 14, 14, 14-nonanitro-3, 12-dioxa-4, 11,-dioxo-5, 7, 10-triazatetradecane	$C_9H_{10}N_{12}O_{22}$	+1.88	11
42.	N, N'-dinitro-N, N'-bis (3, 3-dinitrobutyl) oxamide	$C_{10}H_{14}N_8O_{14}$	–1.28	37
43.	1, 1, 1, 5, 8, 11, 14, 18, 18, 18-decanitro-3, 16-dioxa-4, 15-dioxo-5, 8, 11, 14-tetrazaoctadecane	$C_{12}H_{16}N_{14}O_{24}$	+0.54	19
44.	N, N'-dinitro-N, N'-bis (3-nitrazabutyl) oxamide	$C_8H_{14}N_8O_{10}$	–2.61	90
	F. Trinitromethyl Compounds			
45.	2, 2, 2-trinitroethyl carbamate	$C_3H_4N_4O_8$	+1.79	18
46.	methyl 2, 2, 2-trinitroethyl carbonate	$C_4H_5N_3O_9$	+1.25	28
47.	1, 1, 1, 3-tetranitrobutane	$C_4H_6N_4O_8$	+0.84	33
48.	methylenebis (2, 2, 2-trinitroacetamide)	$C_5H_4N_8O_{14}$	+3.50	9
49.	1, 1, 1, 3, 5, 5, 5-heptanitropentane	$C_5H_5N_7O_{14}$	+3.36	8
50.	bis (2, 2, 2-trinitroethyl) carbonate	$C_5H_4N_6O_{15}$	+3.60	16
51.	N, N'-bis (2, 2, 2-trinitroethyl) urea	$C_5H_6N_8O_{13}$	+2.60	17
52.	5, 5, 5-trinitropentanone-2	$C_5H_7N_3O_7$	–1.36	125
53.	2, 2, 2-trinitroethyl 4, 4, 4-trinitrobutyrate	$C_6H_6N_6O_{14}$	+2.07	18
54.	ethyl 2, 2, 2-trinitroethyl carbonate	$C_5H_7N_3O_9$	–0.39	81
55.	tris (2, 2, 2-trinitroethyl) orthoformate	$C_7H_7N_9O_{21}$	+3.80	7
56.	1, 1, 1, 7, 7, 7-hexanitroheptanone-2	$C_7H_8N_6O_{13}$	+1.04	34

TABLE 1

Impact Sensitivity and CB_{100} of Selected Explosives. (Continued)

No.	Compound Name	Molecular Formula	CB_{100}	$H_{50\%}$, cm*
57.	nitroisobutyl 4, 4, 4-trinitrobutyrate	$C_8H_{12}N_4O_{10}$	–3.09	279
58.	4, 4, 4-trinitrobutyric anhydride	$C_8H_8N_6O_{15}$	+0.93	30
59.	N, N'-bis (3, 3, 3-trinitropropyl) oxamide	$C_8H_{10}N_8O_{14}$	+0.45	45
60.	bis (2, 2, 2-trinitroethyl) succinate	$C_8H_8N_6O_{16}$	+0.90	30
61.	tetrakis (2, 2, 2-trinitroethyl) orthocarbonate	$C_9H_8N_{12}O_{28}$	+3.83	7
62.	methylenebis (4, 4, 4-trinitrobutyramide)	$C_9H_{12}N_8O_{14}$	–0.44	113
63.	ethylene bis (4, 4, 4-trinitrobuyrate)	$C_{10}H_{10}N_6O_{16}$	–0.43	120
	G. Trinitromethyl plus gem-Dinitro			
64.	N-(2, 2, 2-trinitroethyl)-3, 3, 5, 5-tetranitropiperidine	$C_7H_8N_6O_{14}$	+1.40	18
65.	2, 2, 2-trinitroethyl 4, 4-dinitrovalerate	$C_7H_9N_5O_{12}$	–0.28	70
66.	2, 2-dinitropropyl 4, 4, 4-trinitrobutyramide	$C_7H_{10}N_6O_{11}$	–0.57	72
67.	2, 2-dinitrobutyl 4, 4, 4-trinitrobutyrate	$C_8H_{11}N_5O_{12}$	–1.33	101
68.	2, 2, 2-trinitroethyl, 4, 4-dinitrohexanoate	$C_8H_{11}N_5O_{12}$	–1.33	138
69.	N, N-bis (2, 2-dinitropropyl) 4, 4, 4-trinitrobutyramide	$C_{10}H_{14}N_8O_{15}$	–0.82	72
70.	2, 2-dinitropropane-1, 3-diol bis (4, 4, 4-trinitrobutyrate)	$C_{11}H_{12}N_8O_{20}$	+0.35	50
71.	bis (2, 2, 2-trinitroethyl) 4, 4-dinitroheptanedioate	$C_{11}H_{12}N_8O_{20}$	+0.35	68
72.	bis (2, 2, 2-trinitroethyl) 4, 4, 6, 6, 8, 8-hexanitroundecanedioate	$C_{15}H_{16}N_{12}O_{28}$	+0.74	32
	H. gem-Dinitro Compounds			
73.	3, 3, 4, 4,-tetranitrohexane	$C_6H_{10}N_4O_8$	–2.25	80
74.	2, 2, 4, 6, 6-pentanitroheptane	$C_7H_{11}N_5O_{10}$	–1.54	56
75.	2, 2, 4, 4, 6, 6-hexanitroheptane	$C_7H_{10}N_6O_{12}$	0	29
76.	bis (2, 2-dinitropropyl) oxalate	$C_8H_{10}N_4O_{12}$	–1.70	227
77.	2, 2-dinitropropyl 4, 4-dinitrovalerate	$C_8H_{12}N_4O_{10}$	–3.09	>320
78.	3, 3, 9, 9-tetranitro-1, 5, 7, 11-tetraoxaspiro [5, 5] undecane	$C_7H_8N_4O_{12}$	+0.59	66

*25-shot determinations on Type-12 tools.

To ascribe this apparent separation of the data points to differences in chemical structure in the light of the intrinsic inexactness of the impact machine, we should first demonstrate some independent or *a priori* basis for the distinction between the categories. For this purpose it is first necessary to consider the phenomena occurring under the impact hammer in a more detailed manner.

The impact explosion of a high explosive is not a stable detonation. This can be demonstrated by comparing damage to the impact tools by *primary* and *secondary* explosives. The less powerful *primaries*, which on initiation rapidly go over to stable C-J detonations, do far more severe damage than the more energetic *secondary* explosives. Further, while products of Chapman-Jouguet detonations of C-H-N-O explosives are primarily water, nitrogen and the carbon oxides (5), analysis of products of impact explosions show relatively large amounts of nitrogen oxides and simple organic molecules such as formaldehyde (6). This suggests that the impact explosion
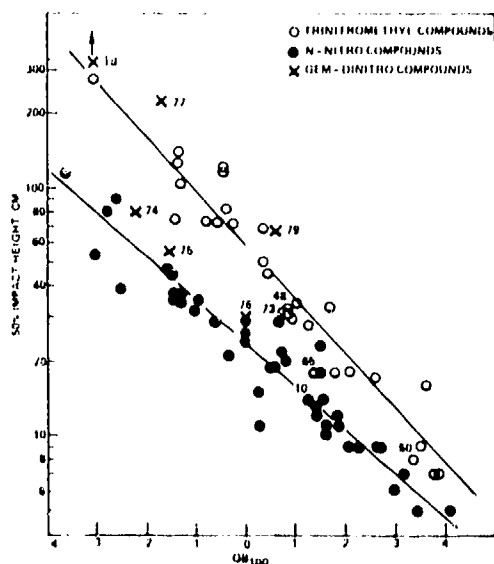
Fig. 1. 50% impact height (on logarithmic scale) plotted again OB_{100} for several classes of nitro-aliphatic explosives

of a high explosive is a phenomenon resembling more closely a relatively low temperature thermal decomposition than a detonation. It further suggests that reaction kinetics, which do not affect the velocities of stable detonations (7), may play an important role under the impact hammer.

Groups working with Bowden (8) and Ubbelohde (9) have devoted considerable attention to the mechanism of initiation of explosion by impact. Bowden has proposed that initiations stem from *hot spots* in the explosive mass formed by a number of possible routes including adiabatic compression of entrapped gases, viscous heating and frictional heating. He has concluded that to cause fires in pentaerythritol tetranitrate and nitroglycerine these *hot spots* must reach temperatures of at least 430-500°C.

The birth of *hot spots* and their development into explosions may be governed by a wide variety of physical and chemical properties. In addition to the kinetics of the initial thermal decomposition reaction, these may include: *a*) the heat evolved in the decomposition reaction, *b*) the heat capacity, *c*) thermal conductivity, and *d*) latent heats of fusion and evaporation of the explosive, *e*) crystal hardness, *f*) crystal shape, etc. In the case of liquids, surface tension, vapor pressure, and dissolved gases may also play a part.

By limiting the correlations to solid explosives, and by proper design of the impact experiment, the contributions of several of these properties to sensitivity may be minimized. Thus, resting the samples on flint paper submerges the effects of crystal hardness and crystal shape. The formation of *hot spots* is governed more by the physical properties of the sandpaper than by those of the explosive, and sensitivity differences between polymorphs, which are discernable on bare tools, can often no longer be observed.

Other properties such as (*b*), (*c*), and (*d*) may differ from explosive to explosive, but if consideration is limited to organic compounds the range of variation is small. The variation in heat evolved is also relatively small among organic explosives. The range 0.3 to 1.6 Kcal/g covers thermal decompositions, low order explosions, and full-scale stable detonations.

Parameters governing rates of thermal decomposition, however, are subject to far greater variation among the types of compounds being considered. Activation energies ranging from 20 to 50 Kcal/mole and pre-exponential factors from 10^{12} to 10^{20} sec^{-1} have been reported. It would seem, therefore, that, while the part played by the other properties may not be ignored, the most likely correlations with impact sensitivity would necessarily depend on chemical reactivity in the classical sense.

This view has been corroborated in a convincing manner by Wenograd's (10) experimental measurements of initiation delays in thermal explosions in the 260 to 1100°C range. He found that the temperature at which an explosion would occur within a time comparable to the interval available under the impact hammer (250 μsec) varied greatly among explosives. He then demonstrated a monotonic variation of these "critical temperatures" with measured impact sensitivities for a variety of explosives, suggesting that he had, in effect, simulated an impact experiment by a non-mechanical rate measurement.

With the above as background, we may now consider whether the separation of the open and filled data points in Fig. 1 is the result of some fundamental difference between the two classes of compounds being considered or whether simply an accidental consequence of the inexactness of the measurement technique. In an earlier report on this subject (11),

we proposed a "trigger linkage" hypothesis, suggesting that the fundamental difference was in the fact that the nitrogen-nitrogen bonds in nitramine compounds were intrinsically weaker than carbon-nitrogen bonds in trinitromethyl derivatives. We believed that thermal decompositions of both classes of compounds followed similar rate laws, and that rate-controlling steps involved thermolytic cleavage of weakest or "trigger" linkages. This rationale would require that activation energies for thermal decompositions should be lower, and rates more rapid for N-nitro than for C-nitro compounds.

More recent kinetic results by several groups of Russian workers now lead us to consider that this earlier view was overly simplistic. Pertinent data are summarized in Table 2 in the form of Arrhenius parameters for first order thermal decomposition reactions of some trinitromethyl compounds and some nitramines. It may be seen that activation energies are of similar magnitudes for both classes of compounds and that, if any conclusion were to be drawn from comparison of Arrhenius parameters for the first order processes, it would be that thermal decompositions of the C-nitro compounds should be more rapid because of generally higher pre-exponential factors.

The same reports do, however, provide experimental evidence to support an alternative, somewhat modified "trigger linkage" rationale (12-15). Nazin, Manelis and coworkers have shown that thermal de-

compositions of most aliphatic C-nitro compounds proceed by radical, *non-chain* mechanisms in which the rate-controlling steps are the initial thermolyses of C-N bonds (16, 17). There is only minor auto-catalysis by NO_2 or other product species, and usual rate experiments follow nicely uncomplicated first-order kinetics to greater than 70% completion, with no dependence of k on mass/volume (m/V) ratios.

In marked contrast, the N-nitro derivatives follow first-order kinetics only during the first few percent of reaction. Typical rate curves are S-shaped, indicating strong autocatalysis, which Dubovitskii and co-workers show is by the NO_2 generated in the first bond-breakings (14, 18). Along similar lines, Samoilenko and coworkers (15) have shown that when the liquid phase thermal decomposition of di-(2-nitroxyethyl) nitramine is carried out in open reaction vessels, or at low values of m/V, the reaction takes place without autocatalysis and obeys first-order kinetics. At higher m/V ratios, however, strong autocatalytic effects are observed, leading to a roughly hundred-fold increase in rate, a decrease in activation energy from 45 to 32 Kcal/mole, and an increase in the heat of reaction by about 50%.

On this basis, N-nitro bonds may be regarded as "trigger linkages", not because they are intrinsically weaker than C-nitro bonds, but because they provide alternative autocatalytic routes in thermal decomposition processes, which lead to manyfold rate accelerations, which are not usually observed with C-nitro

TABLE 2

Kinetic Parameters for First-Order Thermal Decomposition Reactions of
N-Nitro and C-Nitro Compounds in Gas and Liquid Phases

Compound	Phase	$\Delta E^{\ddagger}$, Kcal/mole	log A, (A, sec^{-1})	Ref.
trinitromethane	gas	41.9	15.40	12
fluorotrinitromethane	gas	42.4	15.94	12
1, 1, 1-trinitroethane	gas	43.2	17.18	12
1, 1, 1-trinitroethane	liq.	42.6	16.93	13
1, 1, 1-trinitropropane	gas	42.3	16.86	12
1, 1, 1-trinitrobutane	gas	43.6	17.70	12
diethylinitramine	gas	41.6	15.1	14
N-nitropiperidine	gas	42.1	14.8	14
di (2-nitroxyethyl) nitramine	liq.	45.0	18.67	15

compounds (17), and which should be quite important in the confined conditions under the impact hammer.

It is significant that among the compounds in Table 1, there are a number which contain as many as six $C-NO_2$, but which nevertheless fall into the $N-NO_2$ family of explosives insofar as their impact sensitivity behavior is concerned. One may conjecture that these materials begin to decompose under the impact hammer by thermolysis of C-N bonds, but that the NO_2 formed in these primary steps serves to accelerate reactions at or near N-N sites, so that the nature of the rate controlling step changes and the overall process goes over rapidly to the autocatalytic decomposition mechanism characteristic of N-nitro derivatives.

An alternative explanation, which has been advanced to account for the separation into families of the data points in Fig. 1, deserves some discussion. N-nitro compounds generally have more favorable (more endothermic) heats of formation than C-nitro compounds at equal values of OB_{100}, and hence are more energetic. The rationale, according to this line of reasoning, is that the lower 50% impact heights of the $N-NO_2$ derivatives are a consequence of the higher heats of reaction in the thermal explosions under the impact hammer. To assesses this possibility, it is instructive to compare impact sensitivities, values of OB_{100}, and calculated heats of detonation (estimated according to the $H_2O-CO-CO_2$ "arbitrary") (19) for pairs of compounds which are structurally identical with the exception that in each case a $-C(NO_2)_2$ group replaces an $-N(NO_2)-$group. The data are assembled in Table 3, where it is seen that in both instances the $N-NO_2$ compound has a more negative value of OB_{100} and a lower calculated heat of detonation, but is still more sensitive.

It should be kept in mind, however, that products and heats of thermal explosions do not necessarily coincide with products and heats of detonations, and that Samoilenko and coworkers (15) have reported an appreciable increase in heat of reaction in going from noncatalyzed to autocatalyzed thermal decomposition of bis (2-nitroxyethyl) nitramine. On this basis, higher heats of reaction may indeed contribute to the greater sensitivities of the nitramines, although it is very unlikely that they are the dominant effect.

Having satisfied ourselves that there is some meaningful kinetic basis for the separation of the explosives in Table 1 and Fig. 1 into the categories indicated, we may now return to the rough linear relationships that appear to exist between $\log h_{50\%}$ and OB_{100} within each family. In order that these relationships may be used to describe *sensitivity-structure trends*, rather than to imply that correlations based on such inexact measurements are quantitative, the data have been subjected to least squares regression analysis.

For the forty five $N-NO_2$ compounds (classes A-E in Table 1), the *sensitivity-structure trend* is described by the regression equation,

$$\log h_{50\%} = 1.372 - 0.1681\ OB_{100}, \qquad (2)$$

with r (the correlation coefficient) = 0.950 and sd (the standard deviation) = 0.105 log units, corresponding to an sd of 26% in impact height.

For the twenty eight $C(NO_2)_3$ compounds (classes F and G in Table 1) the least squares linear regression equation is,

$$\log h_{50\%} = 1.753 - 0.233\ OB_{100}, \qquad (3)$$

with r = 0.968 and sd = 0.106 log units, corresponding to a 27% sd in impact height. Drop height settings on the impact machine are at 0.100 log unit intervals, so that the sd in both instances corresponds to a ± one level uncertainty in impact sensitivities.

Sensitivities of gem-Dinitro Compounds. With the *sensitivity-structure trends* for the N-nitro and C-trinitro families of explosives to provide a framework of reference, it becomes instructive to examine variation of impact sensitivity with structure for other classes of compounds. It has been mentioned (Table 2) that Nazin and Manelis reported activation energies of 42-44 Kcal/mole for the first order thermal decompositions of a number of $R-C(NO_2)_3$ compounds (12). These same workers have also shown that *geminal*-dinitro compounds, $R-C(NO_2)_2-R'$, follow similar first order kinetics in their thermal decompositions, (17) with activation energies in the range 47.1-50.5 Kcal/mole, (12, 20) *i.e.*, *ca* 6 Kcal/mole higher than for trinitromethyl derivatives. In the light of these findings, the "trigger linkage" concept would require that 50% impact heights be significantly higher for

TABLE 3

Impact Sensitivities and Calculated Heats of Detonation of Some Nitroaliphatic Explosives

Number	Explosive	OB_{100}	Heat of Detonation (cal/g*)	$H_{50\%}$ (cm)
66	$CH_3C(NO_2)_2CH_2CH_2COOCH_2C(NO_2)_3$	–0.28	1,035	70
23	$CH_3N(NO_2)CH_2CH_2COOCH_2C(NO_2)_3$	–0.97	970	35
72	$[C(NO_2)_3CH_2OCOCH_2CH_2]_2C(NO_2)_2$	+0.35	1,115	68
29	$[C(NO_2)_3CH_2OCOCH_2CH_2]_2N\text{-}NO_2$	0	1,065	29

*Calculated according to the $H_2O\text{-}CO\text{-}CO_2$ arbitrary assumption of detonation product composition. (19)

$-C(NO_2)_2$-compounds than for $-C(NO_2)_3$ derivatives at similar values of OB_{100}.

Data for six *gem*-dinitro compounds are included in Table 1 (subclass *II*) and plotted as crosses in Fig. 1. It is seen that three data points (compounds 77-79) fall well above the *sensitivity-structure trend* for trinitromethyl explosives, and three (74-76) fall well below. We can readily rationalize these results in terms of steric effects.

Compounds 77-79, which have their *gem*-dinitro groups in relatively uncrowded situations, show the higher 50% impact heights than the trinitromethyl compounds, and there is good reason to believe that this represents normal behavior for $-C(NO_2)_2$-derivatives (21). The three more sensitive *gem*-dinitro compounds, 74-76, on the other hand, all have $-C(NO_2)_2$-functions adjacent to, or one carbon atom removed from, other $-C(NO_2)_2$-or-$CH(NO_2)$-groupings. Examination of molecular models show that structures of the latter types of sterically rather constrained, with many rotational modes of freedom "frozen out" (22).

To ascertain whether such steric effects are general, we re-examined the data for the trinitromethyl explosives and found two $C(NO_2)_3CH_2CH(NO_2)$- and two $-C(NO_2)_2CH_2C(NO_2)_2$-examples (compounds 48, 50, 65, 67). The data points for these compounds are indicated in Fig. 1, and it is seen that $h_{50\%}$ values in all four instances are lower than predicted by the *sensitivity-structure trend* for $-C(NO_2)_3$ compounds. On this basis, we suggest that $-C(NO_2)_2C(NO_2)_2$-,

$-C(NO_2)_2CH_2C(NO_2)_2$-, and $-C(NO_2)_2CH_2CH(NO_2)$- structural moieties are seats of thermolytic instability (and hence increased impact sensitivity) relative to less crowded combinations of polynitroaliphatic linkages (23).

Additional fragmentary evidence is available to support this view. The normal surveillance temperature at which we assess the thermal stability of polynitroaliphatic explosives in our Center is $100°C$; most material of this class evolve less than 2.0 cc of gas per gram in 48 hours at this temperature. For comparison, 1, 1, 1, 3, 5, 5, 5-heptanitropentane evolves 6.1 cc gas per gram in 48 hours at $90°C$ (23).

Also, Nazin and Manelis (12, 24) have reported that uncrowded $R\text{-}C(NO_2)_2F$ derivatives have activation energies for thermal decomposition in the same range as other $R\text{-}C(NO_2)_2\text{-}R'$ derivatives, *i. e.*, *ca* 47.5 Kcal/mole, but with $FC(NO_2)_2C(NO_2)_2F$ the $\Delta E^{\neq}$ goes down to 42.2 Kcal/mole and with $C(NO_2)_3C(NO_2)_2F$ it goes down to 36.5 Kcal/mole. These results serve as part of a self-consistent picture wherein increased steric crowding leads to lowered activation energies in thermal decomposition reactions which, in turn, lead to decreased 50% impact heights.

In contradistinction to the behavior of the C-nitro explosives, the one example containing any of the above structural features, which we could find among the nitramines (compound *10*), falls almost directly on the *sensitivity-structure trend line* for N-nitro compounds. This implies that, although steric crowding may indeed sensitize the C-nitro linkages, the N-nitro bond remains the "trigger linkage".

EXPERIMENTAL SECTION

The Impact Test

The impact tools (type 12) consist of a 3.50 inch long striker and a 1.25 inch long anvil machined to 1.25 inches diameter from "Ketos" tool steel and hardened to Rockwell C-60-63. The contacting surfaces are polished. When, after successive repolishing, the length of the striker falls below 3.47 inches it is discarded.

A conical heap, comprising about 35 mg of the granular explosive, is centered on the anvil on a piece of 5/0 flint paper. The flat surface of the striker is rested on the sample through a closely fitted guide ring. The striker is then hit by a 2.50 Kg weight dropped from heights which are varied according to the "up-down" experimental design described by Dixon and Massey (25). This design permits the calculation of a height from which drops will cause explosions 50% of the time.

The impact sensitivities reported in Table 1 are 50% heights as generally determined from twenty five shot sequences. A microphone-actuated noise-meter, set to record sounds louder than a preset intensity, decides whether a given shot has resulted in an explosion. The noisemeter is calibrated at that value which will cause TNT to have a 50% height of 160 cm.

Materials

Most of the explosives in Table 1 were prepared at the Naval Surface Weapons Center, White Oak Laboratory (formerly the Naval Ordnance Laboratory) under a Properties of Explosives Task, or at Aerojet General Corporation, Rocketdyne Corporation, and the U. S. Rubber Company under ONR Power Branch contracts during the period 1950-1960. They were purified by conventional methods to meet conventional journal standards of purity. The physical properties and methods of preparation of many of these are included in an excellent 1964 review article (26).

ACKNOWLEDGEMENTS

REFERENCES AND FOOTNOTES

1. E. H. Eyster and L. C. Smith, "Studies of the ERL Type 12 Dropweight Impact Machine at NOL," NOLM-10003, 25 Jan 1949; H. D. Mallory, ED., "The Development of Impact Sensitivity Testing at the Explosives Research Laboratory, Bruceton, Pennsylvania During the Years 1942-1945," NAVORD Report 4236, 16 Mar. 1956. The technique appears not to have been described in the general literature, but similar machines are described in "Military Explosives," Department of the Army Technical Manual TM 9-1910, Washington, D. C., April 1955.

2. In fluorinated explosives, an atom of fluorine represents one equivalent of oxidant.

3. We also considered subtracting 0.25 or 0.5 equivalent for other non-energetic oxygens, but the imprecision of the method discouraged such additional refinements.

4. CO-Balanced explosives contain sufficient oxygen to burn their hydrogen to H_2O and their carbon to CO. CO_2-Balanced explosives contain enough additional oxygen to burn the CO to CO_2.

5. M. J. Kamlet and J. E. Ablard, J. Chem. Phys., 48, 36 (1968).

6. A. J. B. Robertson and A. D. Yoffee, Nature, 161, 806 (1948).

7. M. J. Kamlet and H. Hurwitz, J. Chem. Phys., 48, 3685 (1968).

8. F. P. Bowden and A. D. Yoffee, "Initiation and Growth of Explosions in Liquids and Solids," Cambridge University Press, 1952.

9. J. L. Copp, S. E. Napier, T. Nash, W. J. Powell, H. Skelley, A. R. Ubbelohde, and P. Woodward, *Phil. Trans. Roy. Soc.*, **A 241**, 197 (1948).

10. J. Wenograd, *Trans. Faraday Soc.*, **57**, 1612 (1961).

11. M. J. Kamlet, "Sensitivity Relationships," *Proc. Third Symp. Detonations*, Princeton University (1960), ONR Symposium Report ARC-52, Vol. III.

12. G. M. Nazin and G. B. Manelis, *Izv. Akad. Nauk SSSR, Ser. Khim.*, 811 (1972).

13. G. M. Nazin, G. B. Manelis, and F. I. Dubovitskii, *Ibid.*, 2628 (1968).

14. B. L. Korsunskii, F. I. Dubovitskii, and E. A. Shurygin, *Ibid.*, 1452 (1967).

15. N. G. Samoilenko, A. A. Vinokurov, V. G. Abramov, and A. G. Merzhanov, *Zhur. Fiz. Khim.* **44**, 22 (1970). The page given is that in the English Translation.

16. G. M. Nazin, G. N. Nechiporenko, D. N. Sokolov, G. B. Manelis, and F. I. Dubovitskii, *Izv. Akad. Nauk SSSR, Ser. Khim.*, 315 (1968).

17. However, compounds which have a hydrogen atom on the same carbon as one or two nitro groups have been shown to also undergo a wall-catalyzed reaction which is also weakly auto-catalytic. This complicates the kinetics of thermal decomposition somewhat at lower temperatures but becomes insignificant at temperatures as high as those which lead to explosions under the impact hammer. The wall catalyzed reaction probably involves conversion of a nitro group to the *aci*-nitro form and facile decomposition of the latter to the carboxylic acid, e. g., $R\text{-}C(NO_2)_2H \rightarrow R\text{-}C(NO_2) = NOOH \rightarrow R\text{-}COOH$.

18. The first-order character of the thermal decomposition of diethylnitramine can be maintained if a "getter" like formaldehyde is added to react with the NO_2 as it is formed (14).

19. In calculating heats of detonation by the $H_2O\text{-}CO\text{-}CO_2$ "arbitrary", oxygen, as available, first burns hydrogen to water, then carbon to CO, then CO to CO_2. Such calculated values correspond reasonably closely to heats of detonation determined by detonation calorimetry (5). Other "arbitraries" are $H_2O\text{-}CO_2$, and $CO\text{-}H_2O\text{-}CO_2$.

20. G. M. Nazin, G. B. Manelis, and F. I. Dubovitskii, *Izv. Akad. Nauk SSSR, Ser. Khim.*, 2629 (1968).

21. We shall show in future paper that $R\text{-}C(NO_2)_2F$ compounds, an uncrowded sub-family of this category, follow a *sensitivity-structure trend* which lies well above that described by Eq. 2, and that compounds 77-79 fall within the precision limits of that trend.

22. In the later paper we shall also suggest that steric effects on thermal decomposition rates and sensitivities are primarily a consequence of redistribution of energy between vibrational and rotational modes.

23. In the case of the $\text{-}C(NO_2)_2CH_2CH(NO_2)\text{-}$ compounds, we cannot exclude the possibility that rearrangements to the *aci*-nitro forms, and facile decompositions thereof, contribute to the greater sensitivities (17).

24. G. M. Nazin, G. B. Manelis, and F. I. Dubovitskii, *Izv. Akad. Nauk SSSR, Ser. Khim.*, 2631 (1968).

25. Dixon and Massey, "Introduction to Statistical Analysis," McGraw Hill Book Co., New York, 1951, Chapter 19.

26. P. Noble, Jr., F. G. Borgardt, and W. L. Reed, *Chem. Rev.*, **61**, 19 (1964).

Session V
MOSTLY THEORETICAL STUDIES

Chairmen: P. A. Persson
    Swedish Detonic Research Foundation
    G. Abrahamson
    Stanford Research Institute

INITIATION OF VIOLENT REACTION BY PROJECTILE IMPACT

R. Frey, G. Melani, M. Chawla, and J. Trimble
Detonation & Deflagration Dynamics Laboratory
Ballistic Research Laboratories
Aberdeen Proving Ground, Maryland 21005

The initiation of low order explosive reactions by projectile impact has been investigated in confined composition B, octol, and PBX 9404 charges. All three explosives are subject to such reactions, but the degree of confinement which is required is greater for composition B than it is for PBX 9404 or octol. The onset of explosion as projectile velocity is increased is quite abrupt. To understand the phenomenon, we have measured pressure time histories in charges undergoing low order initiation. The records show that pressure rises in an approximately exponential fashion, but there is evidence for an abrupt transition to a more rapid rate at about 60 MPa in composition B. We have also performed calculations to determine the relative importance of plastic work and shock heating in the initiation of low order reactions. Plastic work is favored relative to shock by thick casings, low velocity, and small diameter.

INTRODUCTION

When a projectile impacts on a bare explosive charge, one normally observes either that the charge detonates or that it is scattered and the result is recorded as no reaction. The same is true for charges which are confined on the front (impacted) face but are unconfined elsewhere. In this situation Dewey and Slade (1), and Brown and Whitbread (2), demonstrated that the mechanism of initiation is shock initiation. The projectile generates a strong shock in the explosive, which causes reaction to take place, which feeds energy into the shock and accelerates the shock towards detonation. The process is very rapid and detonation generally occurs before the shock has propagated more than two or three projectile diameters or, in most cases, in less then 10 usec. Confinement has no effect on the results except for conditioning the shock which reaches the explosive.

On the other hand, when a projectile impacts on a fully confined explosive charge, a variety of results

are possible. Sometimes explosions which are quite violent, but clearly not detonations, are observed. As will be demonstrated here, the time to explosion in these situations can be hundreds of microseconds and confinement can have a marked effect on the results. Such reactions can be quite important when one considers problems of explosive safety and handling, but there are few systematic studies of the phenomenon and little understanding of the factors which control the violence of the reaction. In this paper we will discuss some preliminary work which we have done in this area.

SHOCK INITIATION

It will be useful to compare the conditions required for low order explosions with those required for shock initiation to detonation. Gittings (3) demonstrated that the minimum shock pressure which will just cause detonation is dependent on the duration of the shock pressure. Walker and Wasley (4) expressed this relationship in the form of a

critical energy criterion. This criterion states that there is a critical energy per unit area which must be delivered to the explosive to obtain detonation. It may be expressed in the form Put = constant or $p^2t/\rho_0 U$ = constant, where P is shock pressure, u is the particle velocity behind the shock in the explosive, t is the duration of the shock pressure, ρ_0 is the initial explosive density, and U is the shock velocity in the explosive. In a separate paper in this symposium, we (Howe, Frey, Taylor, and Boyle) make some comments about the critical energy criterion and note that a P^2t criterion may be better. In this paper we will use the criterion in the form stated by Walker and Wasley.

Under projectile impact conditions, the duration, t, of the shock pressure is generally controlled by rarefactions coming from the periphery of the projectile. We shall demonstrate that the critical energy criterion in the Put form can be used to predict the results of experiments. We have demonstrated this by analyzing some old data due to Dewey and Slade (1). This data gives the 50% velocity for initiation of composition B and tetryl targets, both bare and covered by steel plates, when impacted end on by right circular cylinders of steel. The covered targets were unconfined except for the cover plate on the impacted surface. We have evaluated the quantity Put at the 50% velocity for each case. P and u were determined by Hugoniot calculations; t was determined as the time for a rarefaction to propagate from the periphery of the projectile to a point at the explosive metal interface lying along the axis of the projectile. For the bare charges, t was computed using the sound speed in the metal computed by Jacobs' formula (5), as follows:

$$c = \frac{(U - u)(U + u\,s)}{U}$$

where c is the sound speed, U is the shock velocity, u is the particle velocity and s is a Hugoniot parameter determined by the relation,

$$U = a + s\,u$$

To evaluate t for the cased charges it was necessary to consider the particle velocity in the casing and the reflected wave coming back from the casing explosive interface. A sketch illustrating the velocities which must be considered is shown in Figure 1. In this sketch, the point A is a point on the periphery of the

EXPLOSIVE
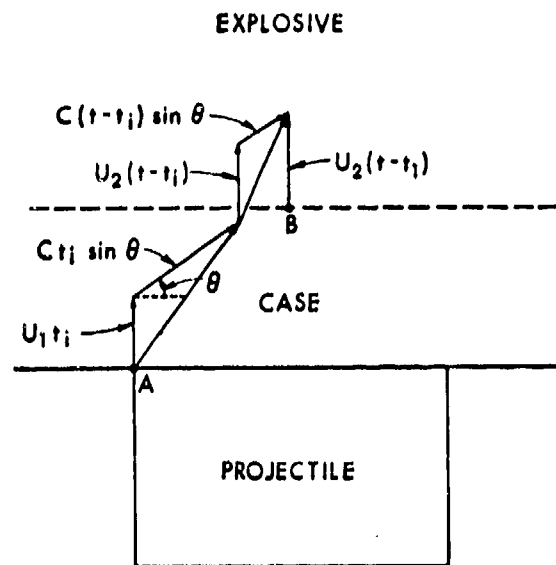
Fig. 1. Velocities to be considered in the propagation of a rarefaction from Point A to Point B are shown schematically.

projectile and B is the point on the axis of the projectile where Put is to be evaluated; U_1 is the initial particle velocity at the projectile casing interface; U_2 is the particle velocity in the casing after a rarefaction is reflected back from the explosive-casing interface; c is the sound velocity in the casing; t_1 is the shock transit time across the casing; t_i is the time at which the rarefaction reflected from the explosive casing interface reaches the advancing rarefaction wave, and t is the time for the rarefaction to reach point B. The equations for evaluating t are the following:

$$U_1 t_i + U_2(t - t_i) + ct\sin\theta = y + U_2(t - t_1)$$

$$ct\cos\theta = r$$

$$U_1 t_i + t_i\,c\sin\theta + (c - U_1)(t_i - t_1) = y$$

*The critical energy, Put, is shown in Tables 1 and 2 for the tetryl and composition B experiments. The values are reasonably constant, and this demonstrates that the criterion can be applied to impact experiments. We should note that the function Put is a strong function of impact velocity, so a small error in velocity can make a larger error in the critical energy.

---

*See comment on last page.

326

TABLE 1

Critical Energies in Cal/cm² Calculated from Projectile Impact Data on Tetryl

Projectile Diameter, cm	Cover Plate Thickness, cm				
	0	0.15	0.27	0.64	0.78
0.76	26.6	31.0	31.4		
1.27	27.4	30.4	30.4	31.4	33.7
1.49	25.4				
0.32 (brass)	25.4				

TABLE 2

Critical Energies in Cal/cm² Calculated from Projectile Impact Data on Comp B

Projectile Diameter, cm	Cover Plate Thickness, cm		
	0	0.15	0.27
0.64	156		
1.27	137	144	143
1.49	145		

This information can be used in a crude, but simple procedure for comparing the vulnerability of an explosive to detonation and to low order explosions. For any target, the procedure is to compute the projectile striking velocity which will produce a residual velocity at the surface of the explosive just capable of initiating detonation in bare explosive. For brevity, we will refer to the velocities computed in this way as predictions, although in fact they have little predictive value. From the preceding paragraph, we can see that the predicted velocity should be lower than the velocity required for detonation. We shall see that it is greater than the velocity required for low order explosions. The velocity difference between the low order explosion point (to be defined later) and the predicted velocity is a crude measure of the susceptibility of an explosive to low order reactions. If the difference is large, it implies that the explosive is much more susceptible to low order explosions than to detonation.

In this paper the calculation of residual velocity was made using the equations from Project Thor (6). The velocity required to initiate bare explosive depends on fragment shape and size. In determining the velocity required to initiate bare explosive, we used the initial projectile shape. For size, we had a choice of using either the initial mass or the residual

Using the critical energy criterion, one can determine how the projectile velocity necessary to achieve detonation varies as a function of casing thickness. Figure 2 is a plot of Dewey and Slade's data for steel cylinders, 1.27 centimeters in diameter, impacting tetryl charges which were protected with steel plates of varying thickness. On the same figure we have plotted the striking velocity necessary to have a constant residual projectile velocity after perforating the steel layer. For this purpose we assume that the projectiles were cylinders with a length to diameter ratio of one. The figure demonstrates that the ability of the casing to protect against the initiation of detonation is much greater than its ability to protect against penetration. This will always be true for projectiles whose length to diameter ratio is about one or for projectiles which impact with their long axis parallel to the direction of motion. This statement assumes that the casing is in direct contact with the explosive.
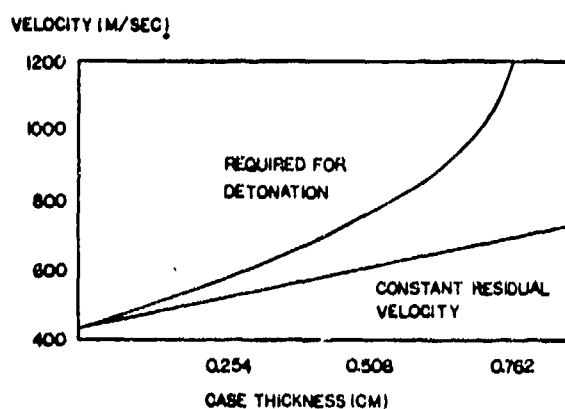
VELOCITY (M/SEC)

Fig. 2. The impact velocity required for detonation and the impact velocity required to maintain a constant residual velocity are shown as a function of case thickness. The explosive is tetryl, and the projectile is 1.27 cm long and 1.27 cm in diameter. The case and the projectile are steel.

327

mass after perforating the confinement on the charge. We did the calculations in both ways and present both results. To obtain values for the velocity required to initiate bare explosive we used Dewey and Slade's data for composition B and conducted our own firings on PBX 9404 and octol. Our firings were consistent with a critical energy of 16 cal/cm^2 for PBX 9404 of density 1.83 and 145 cal/cm^2 for octol of density 1.81.

LOW ORDER EXPLOSIONS

In this section we present the results of some impact experiments involving composition B, octol, and PBX 9404 explosives. The targets were all right circular cylinders of aluminum with either steel or aluminum plates on the front (impacted) end and steel plates on rear end. The cylinders were 10 centimeters in diameter and were constructed of 0.23 centimeter thick aluminum. The length was varied from 10 to 20 centimeters. The targets were held together with four bolts, 0.64 centimeters in diameter. The projectiles were steel cubes which hit the target in a flat, or nearly flat, orientation.

In assessing the damage to the target, we found that there was a transition from essentially no reaction to a violent explosion over a fairly narrow range of velocities. Consequently, we were led to define a low order explosion limit velocity, which is the velocity at which low order explosions begin to occur. The exact definition of a low order explosion is arbitrary, but the limit velocity is only weakly dependent on the exact definition. In our tests we considered the result to be an explosion if we fragmented the side confinement into three or more pieces.

Results for PBX 9404, octol, and composition B targets are shown in Figures 3, 4, 5, respectively. In the figures, the low order limit velocity is plotted as a function of projectile mass and compared to the predictions which were described earlier. The figures show that PBX 9404 is exceptionally vulnerable to low order explosions. Octol is less so, and with composition B a velocity close to the predicted number is required. The observed reactions above the low order limit were probably not detonations, but there were very violent nevertheless. The casing of the target was fragmented into small pieces. Some of the tests were conducted in an enclosed chamber,

and in these tests we were able to verify that little or no explosive remained unburned. In some of the tests we measured the time interval from the moment of impact until the case expanded 0.64 centimeters. This time varied from 140 to 200 usec. This is more than enough time for several shock reverberations in the charge and indicates that the mechanism is not shock initiation in the usual sense.

As has already been mentioned, the transition from no reaction to a violent explosion was quite abrupt. For instance, with the composition B target a 19.5 gram fragment at 1830 m/sec initiated a reaction which was just violent enough to blow the front plate of the charge. At 2000 m/sec the sleeve was fragmented into small pieces and a casual observer might have thought that a detonation had occurred. In all tests, the transition from essentially no reaction to a violent explosion occurred over no more than 200 m/sec.
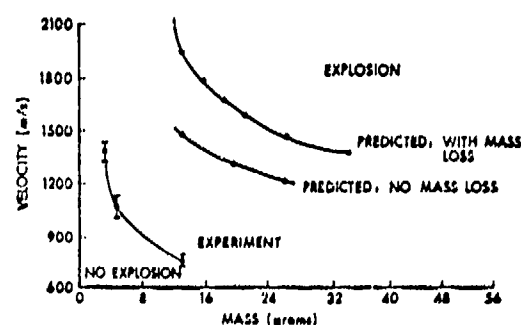
Fig. 3. The velocity for low order initiation of a PBX 9404 target is plotted as a function of projectile mass.
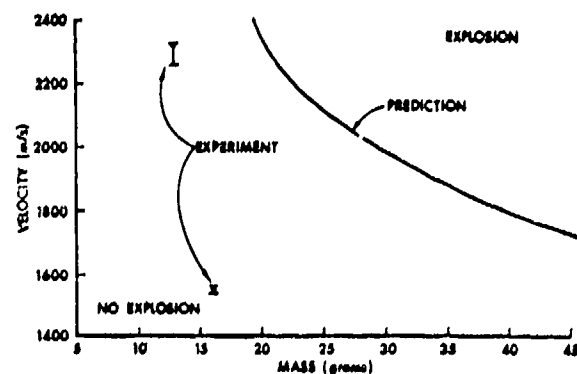
Fig. 4. The velocity for low order initiation of an octol target is plotted as a function of projectile mass.
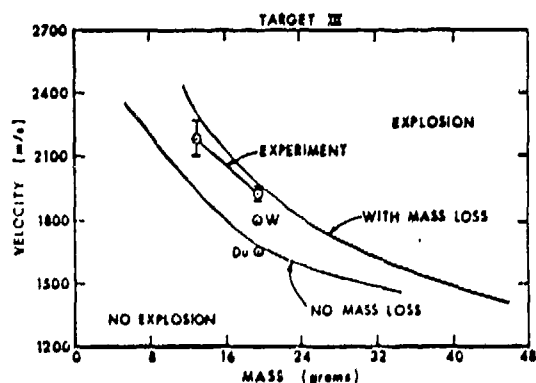
Fig. 5. *The velocity for low order initiation of a composition B target is plotted as a function of projectile mass.*
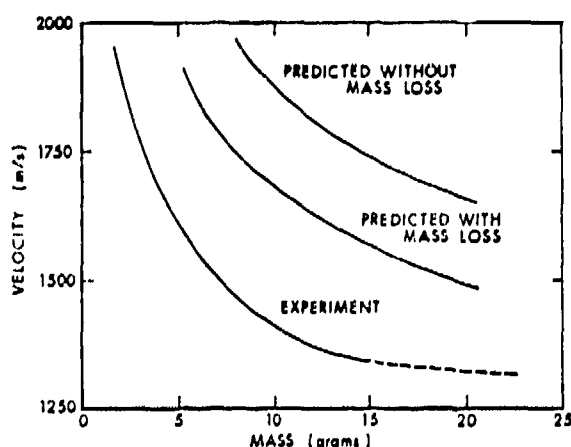
Fig. 6. *The velocity for low order initiation of a heavily confined composition B target is plotted as a function of projectile mass.*

From these tests, it is apparent that it is much more difficult to initiate low order reactions in composition B than it is in the HMX based explosives. However, such reactions can be initiated in composition B if the confinement is sufficiently strong. This is demonstrated by some data given us by Reeves (7). He fired at the curved surface of cylindrical targets which were constructed from a single piece of steel. The wall thickness at the point of impact in his test was 1.02 cm of steel as compared to 1.27 cm of steel in our tests. His fragments were right circular cylinders of steel with a length to diameter ratio of one. His data is presented in Figure 6 along with predicted values for comparison. He did not attempt

to distinguish between detonations and low order reactions, so we cannot be sure which were observed. Nevertheless, it is apparent that the heavily confined composition B is very susceptible to explosive reactions under conditions where shock initiation cannot be operative.

PRESSURE MEASUREMENTS IN INITIATING CHARGES

It is apparent that all three of the explosives we have studied are susceptible to low order explosions. With PBX 9404 the phenomenon occurs even with extremely light confinement, but with composition B moderately heavy confinement is required. In an effort to explain these observations, we have attempted to record the pressure time history in charges which are undergoing a low order explosion. The measurements are made difficult by the fact that we require long recording times (several hundred usec) and by the fact that the flow may be divergent. We are employing two techniques to make these measurements. The first involves the use of a manganin piezoresistive foil gage. Such gages have been described by Wackerle (8). Because of the flow divergence which is possible in our experiments, we had to adopt a technique suggested by Rosenburg (9). In Rosenburg's technique a constantan strain gage is used in conjunction with the manganin gage. The manganin responds to both stress and strain. The constantan has a near zero piezoresistive coefficient and responds only to strain. By placing the gages in equivalent positions, we are able to determine how much the manganin gage has strained and to correct the measurement accordingly. The foil gages we are using were manufactured by Micromeasurements. The manganin gage has a foil element approximately 0.6 cm square with a resistance of 48.5 ohms. It is designated as UM-55-MG130-48 by Micromeasurements. The constantan gage has a foil element approximately 0.5 cm square with a resistance of 120 ohms. It is designated as EP-08-250AF120. The gages were mounted in equivalent positions on flat metal surfaces to minimize the amount of strain. They were used in conjunction with a standard bridge circuit which was pulsed for 500 usec at 200 volts.

We are also attempting to measure the pressure with tourmaline piezoelectric gages. However, we have fired only one successful shot with this gage,

329

and we will reserve discussion of it for another occasion.

Our measurements to date have been made in composition B charges confined in thick walled steel cylinders. The explosive cavity is 7.5 cm in diameter and 15 cm long. The cylinder walls and ends are 2.54 cm thick, and one of the ends is a screw on cap. The manganin and constantan gages were mounted either on the flat ends of the cylinder or on a flat surface on the side of the cylinder which was created by adding a steel insert to the inside of the cylinder. The explosive is cast over the gages. In our shots to date we have simulated projectile impact with a tetryl booster. The booster in the shots to be described was 1.27 cm in diameter and 2.54 cm long and was placed in a hole which drilled in the cylinder wall. This hole was 1.9 cm deep (leaving 0.64 cm of steel) and was tapered in diameter from 2.54 cm at the top to 1.27 cm at the bottom. We have also drilled the hole all of the way through the cylinder wall and filled in the bottom with a 0.64 cm steel plug. There is no appreciable difference in the reactions obtained in this way.

Our results to date are preliminary, but nevertheless interesting. Figures 7 and 8 show the gage records for one of our shots. Figure 7 shows the manganin (left) and constantan (right) gage records. Figure 8 shows the variable baseline for both gages (manganin on left; constantan on the right). The variable baseline is a characteristic of the particular pulsing circuit which we use and is due to heating of the resistors in the circuit. We are unable to interpret the early time behavior of the records and will consider only measurements made after 100 usec. Figures 9 and 10 show pressure time histories for two shots. Figures 11 and 12 show the natural logarithm of the pressure as a function of time. The pressure appears to rise in an approximately exponential fashion. However, in both records, but especially in Figures 9 and 11, there is evidence for a change in slope at about 60 MPa. This may be significant in explaining the effect of confinement.

CALCULATIONS ON PROJECTILE IMPACT

Several investigators have attempted to simulate numerically the processes occurring during projectile impact (10, 11). In all studies of which we are aware, the phenomenon investigated was really shock initia-

Fig. 7. Gage records from manganin (left) and constantan (right) gages.

Fig. 8. Baseline records from manganin (left) and constantan (right).
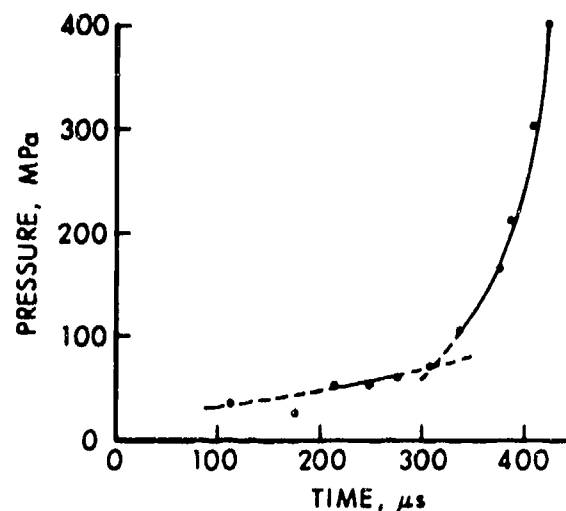
Fig. 9. Pressure versus time for low order initiation in composition B.

tion. Under low order initiation conditions, it is possible that plastic work of the explosive, the projectile, or the case may contribute to ignition. In order to determine the relative importance of plastic work and shock heating, we have performed a series of calculations utilizing the HELP computer code. HELP is a mixed Eulerian-Lagrangian hydrodynamic, elastic-plastic code which was developed by Systems, Science, and Software and which has been described by Hageman and Walsh (12). The basic mesh is

Eulerian, but it contains Lagrangian tracer particles which can be used to follow particular material points.

In the calculations, the P-V equation of state of the explosive had the following form:

$$P = au + bu^2 + cu^3 + \rho \Gamma E$$

$$u = \frac{\rho}{\rho_0} - 1$$

$a = 0.135 \times 10^{12}$ dynes/cm^2

$b = 0.95 \times 10^{11}$ dynes/cm^2

$c = 1.01 \times 10^{12}$ dynes/cm^2

$\Gamma = 0.947$

ρ = density

ρ_0 = initial density

P = pressure

E = internal energy.

This equation was derived from the following Hugoniot with the assumption that the Gruneisen gamma is constant:

$$U = 2.71 + 1.86 \, u$$

U = shock velocity in mm/usec

u = particle velocity in mm/usec,

Fig. 10. *Pressure versus time for low order initiation in composition B.*

Fig. 11. *Natural logarithm of pressure versus time for low order initiation of composition B.*

A Tillotson equation of state, described in Reference 12, was used for the steel. Both the steel and the explosive were treated as being elastic-perfectly plastic. The Von Mises yield condition, also described in Reference 12, was used. The code has a failure condition which causes all stresses to be zeroed when the ratio of the specific volume to the initial specific volume exceeds a value which is determined from the ultimate tensile strength. We do not believe that the choice of this parameter is critical to the results reported here, but we have not checked this point.
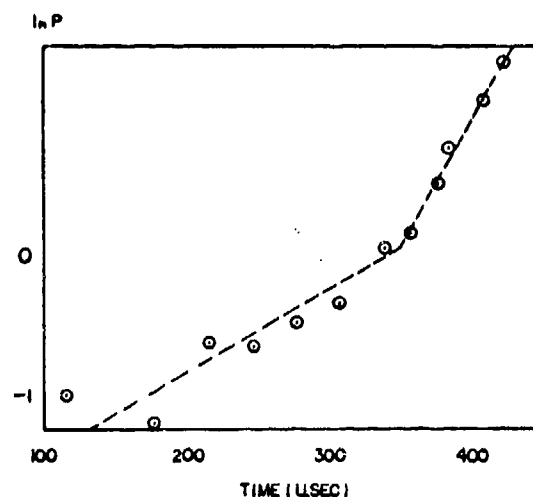
We have numerically simulated the processes occurring when right circular cylinders of steel impact composition B targets which are covered with 0.5 cm thick steel plates. The projectiles were 2 cm long and varied from 0.5 to 2 cm in diameter. The projectile impacted with the axis of the cylinder perpendicular to face of the target and with no yaw. We computed the maximum pressure occurring at the explosive-metal interface and used the Walsh-Christian technique (13) to convert this to a shock temperature. We also computed the total plastic work occurring at

331
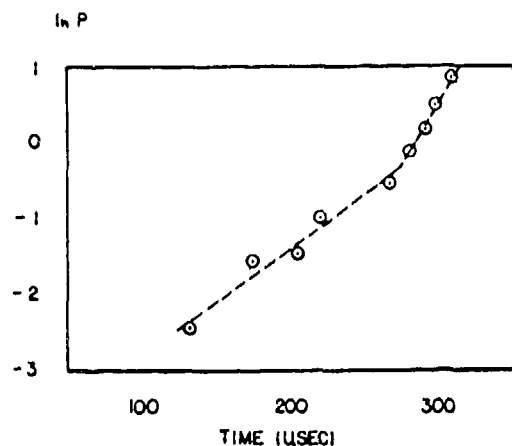
Fig. 12. Natural logarithm of pressure versus time for low order initiation of composition B.

a number of Lagrangian tracer points in the explosive and the metal. This number was converted to a temperature and is referred to as the plastic work temperature. We should comment immediately that both of these quantities really represent averages over small regions of space. In the case of shock heating, small voids and density variations will cause large fluctuations in the local temperature (14). With regard to plastic work, there are clearly small regions along the axis of the projectile, and perhaps elsewhere, which obtain very high total strains. Our ability to resolve these regions is limited by the number of mesh points which we can economically handle. In these calculations the cell dimensions were 0.1 cm X 0.2 cm. A finer grid would probably have resulted in higher temperatures being attained by tracer particles close to the axis. A further qualification should be made with regard to brittle explosives. In such explosives, heating probably occurs along localized fracture surfaces and could lead to high temperatures over small regions. The code cannot handle this problem. For these reasons, the exact numerical values of temperatures which we report here are not significant. What is important are the general trends and the relative values of shock temperature and plastic work temperature.

In Figure 13 we have plotted the maximum plastic work temperature of both metal and explosive and the maximum shock temperature of the explosive as a function of projectile velocity. We should note that the plastic work associated with the tracer

particles levels out at long times because failure occurs. The maximum plastic work temperature is determined after this leveling has occurred. The projectile diameter was 0.5 cm. The figure shows that the maximum plastic work in both the metal and the explosive is nearly independent of velocity. The explanation for this is that the total deformation is only a weak function of the velocity in this velocity region. Since the shear stresses are independent of strain rate in this code, the result follows. The metal experiences a much larger temperature rise due to plastic work than does the explosive. This is due to the higher strength and lower heat capacity of the steel. The highest plastic work temperatures were always attained by the tracer particles whose initial location was closest to the projectile axis. In the metal the hottest tracer particle was located at the front of the projectile, where it would eventually make contact with the explosive. In the explosive, the hottest tracer particle was the one near the explosive-metal interface. The implication of these results is that plastic work can be a dominant effect only at low impact velocities. However, one should keep in mind the fact that thicker cases will tend to increase the relative importance of plastic work by decreasing the peak shock pressure reaching the explosive (if the casing is sufficiently thick) and by

Fig. 13. Shock and plastic work temperatures as a function of projectile velocity. Projectile diameter was 1 cm; case thickness was 0.5 cm.

increasing the plastic work which the projectile will experience in penetrating the case.

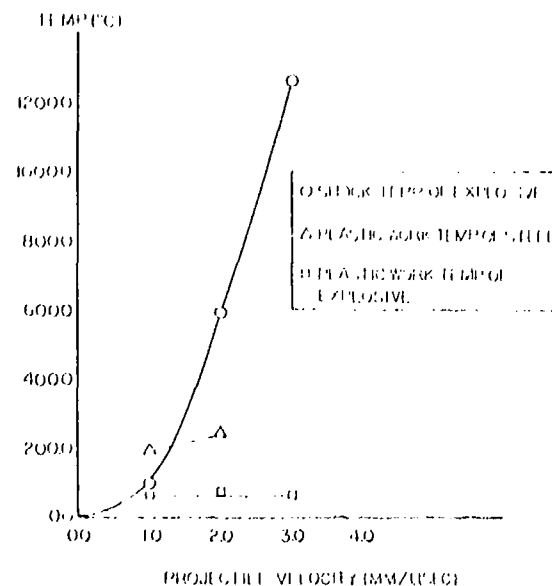Figure 14 shows the maximum plastic work temperature and shock temperature as a function of projectile diameter. The velocity for these calculations was 1 mm/usec. Again, the plastic work temperature is nearly independent of diameter, but the shock temperature increases with diameter in this range. Again, we should note that the plastic work would be relatively more important if the case thickness were greater. The implication of this figure is that plastic work will be dominant for small diameters, and shock will be dominant for large diameters if other things are equal.

Fig. 14. Shock and plastic work temperatures as a function of projectile diameter. Impact velocity was 1 mm/usec; case thickness was 0.5 cm.

DISCUSSION

It has long been known that a variety of reactions are possible in explosive charges under projectile impact. What seems to have escaped general observation is that there is a rather sharply defined set of conditions which separate explosions and less violent reactions in confined charges. All of the explosives which we have studied seem to be susceptible to low order explosions under conditions which are much less severe than those required for detonation. However, the conditions under which low order explosions are observed are dependent on confinement, and PBX 9404 requires much less confinement than does composition B. From a theoretical point of view, the problem is to explain the sharp onset of explosive reactions and the way in which confinement influences the limit point.

We believe the problem must be separated into an ignition phase and a buildup phase. Ignition probably occurs under very mild conditions, but we have little evidence on the minimum conditions required. Shock heating and heat transfer from the hot fragment are both possible mechanisms. The calculations reported here indicate that the latter mechanism will be favored by thick confinement (at the impacted point), low velocity, and small radius.

If the buildup does not occur by a shock process, which would lead to detonation, it must be controlled by the competing processes of gas evolution (burning)

and venting. At the risk of oversimplification, we can use steady state equations for the explosive burning rate and for venting. From strand burner experiments, the burning rate per unit of ignited surface area is proportional to P^n, where P is pressure. If we assume choked flow, the venting rate is proportional to the area of the nozzle times chamber pressure to the first power. The time derivative of the pressure will obey an equation such as follows:

$$\frac{dP}{dt} = A P^n - BP,$$

where A and B are parameters depending on the ignited surface area, the size of the hole in the wall of the charge, and other factors. For n less than 1, this equation leads to stable burning rates, and permits a constant pressure to be obtained; for n greater than 1 an explosive increase in pressure is possible. For most explosives, n seems to be about 1 (15, 16, 17). Under these conditions the stability of the burning rate is determined by the parameters A and B which are in turn determined by the amount of ignited area and the size of the hole through which venting occurs. If A is greater than B, the pressure will rise until the confinement fails. In this case the pressure should

333

rise in an approximately exponential fashion with time, and this is in general accord with the pressure records we have obtained. The pressure rise would not be expected to be perfectly exponential since the burning area will increase with time. One might expect that the maximum pressure obtained would be equal to the pressure required to burst the confinement. This is clearly not the case. On the other hand, if the pressure is rising rapidly, it may overshoot the rupture pressure because of inertial confinement. In this case, the violence of the explosion will depend on the rate of pressure rise at the time of case rupture.

The change in slope in our pressure time curves may be important in this consideration. If the rupture pressure of the confinement is above the transition point, a violent explosion would be much more likely. The composition B targets in which we observed low order explosions all had rupture pressures above 70MPa. The target in which we did not observe low order explosions, had a very low rupture pressure. The transition point may be determined by the point at which the explosive begins to fracture exposing more area to burning. Wachtell (17) suggested this as the explanation for a similar phenomenon observed when explosive was burned in a closed bomb. The transition pressures measured by Wachtell were lower than ours, but his rate of pressure rise was also much lower.

ACKNOWLEDGEMENTS

REFERENCES

1. Dewey and D. Slade, BRL Report 1021 (1967).

2. S. Brown and E. Whitbread, les Ondes de Detonation, 1961.

3. E. F. Gittings, Initiation of a Solid Explosive by a Short Duration Shock, Fourth Symposium on Detonation (1965).

4. F. Walker and R. Wasley, Critical Energy for Shock Initiation of Heterogeneous Explosives, Explosivestoffe 17, 9 (1969).

5. S. Jacobs, as reported by F. Allison, BRL Report No. 1294 (1965).

6. Ballistic Analysis Laboratory, Johns Hopkins University, "The Resistance of Various Metallic Materials to Perforation by Steel Fragments, Empirical Relationships for Fragment Residual Velocity and Weight, Project Thor Technical Report No. 41 (1961).

7. H. Reeves, USA Ballistic Research Laboratories, private communication.

8. J. Wackerle, J. Johnson and P. Halleck, Projectile Velocity Measurements and Quartz and Manganin Gauge Pressure Determinations in Gas Gun Experiments, LA 5844 (1975).

9. J. Rosenburg, Development of a Piezo-resistant Transducer to Measure Stress-Time Output of Small Detonators, Report by Stanford Research Institute to Picatinny Arsenal, Contract DAAA21-71-C-0845.

10. B. Trott and R. Jung, Effect of Pulse Duration on the Impact Sensitivity of Solid Explosives, Fifth Symposium on Detonation (1970).

11. C. Kot, H. Napadensky, Y. Shikari, A. Wiedermann, A Numerical Study of Impact Phenomena in Explosives and Propellants, Computational Methods in Non Linear Mechanics, Texas Institute for Computational Mechanics, Austin, Texas (1973).

12. L. Hageman and J. M. Walsh, HELP, A Multi-Material Eulerian Program for Compressible Flow and Elastic-Plastic Flows in Two Space Dimensions and Time, Report by Systems, Science, and Software to Eglin Air Force Base on Contract DAAG-07-68-C-0931.

13. J. Walsh and R. Christian, Equation of State of Metals from Shock Wave Measurements, Physical Review of 97, 1944 (1955).

14. C. Mader, Initiation of Detonation by Interaction of Shocks with Density Discontinuities, The Physics of Fluids 8, 1811 (1965).

15. F. A. Baum, K. P. Stanyukovich, and B. I. Shekhter, Physics of Explosion, Moscow (1959).

16. J. Taylor, The Rapid Burning of Secondary Explosives by a Convective Mechanism, Third Symposium on Detonation (1960).

17. S. Wachtell and C. McKnight, A Method for Determination of Detonability of Explosives and Propellants, Third Symposium on Detonation (1960).

AUTHORS NOTE: On the second page of this paper, the variables y and r are the case thickness and projectile radius respectively. In the calculation of the critical energy on the same page, the quantity Put should be $Pu(t - t_1)$.

335

A NUMERICAL STUDY OF IMPACT PHENOMENA IN EXPLOSIVES
AND PROPELLANTS

A. H. Wiedermann, C. A. Kot,[*] H. S. Napadensky, and Y. Shikari
ITT Research Institute
Chicago, Illinois 60616

The mechanical and thermal response of explosive and propellant materials during moderate speed impact, typical for accident conditions, is investigated numerically. The objective is to determine the mechanisms which may lead to the initiation of detonation or chemical decomposition reactions. The dynamic impact problem is formulated in the Lagrangian frame of reference for two-dimensional and cylindrically symmetric geometries. Calculations are carried out for unconfined and partially confined impact. It is found that both for homogeneous and inhomogeneous materials the major mechanism leading to energy focusing and temperature increases is the adiabatic shock compression. Friction, dissipation due to distortion, and heat transfer are of small importance. While in unconfined impact temperature rises are moderate, confinement or the presence of low density inhomogeneities or gas bubbles produces local heating thought to be sufficient for the initiation of chemical reaction. In particular gas inclusions are prone to cause the formation of hot spots. The thermal effect of high density inclusions on the other hand is found to be minimal. The calculated material distortions qualitatively agree with experimental observations of impact phenomena.

INTRODUCTION

In order to evaluate the hazards associated with the impact of solid explosive and propellant materials, it is essential to obtain an understanding of the phenomena which may lead to the initiation of detonation during dynamic compression. Existing detonation theories are primarily concerned with the response of explosives to strong shock waves. However, detonation and subdetonation reactions of these materials often occur (Napadensky and Kennedy, 1964) at impact speeds and pressures which are well below those predicted by classical detonation theorie. Therefore, in the current investigation interest is focused on moderate impact stimuli which are representative of typical accident conditions.

Experiments indicate (Napadensky and Kennedy, 1964) that prior to initiation by impact, solid explosives and propellants undergo large deformations. Thus to understand the mechanisms leading to ignition, it is necessary to delineate the material flow and energy conversion and focusing processes caused by dynamic compression. Instrumentation difficulties, in general, limit the results of experimental studies to gross observations and to the establishment of initiation thresholds. To obtain better insight into the impact processes requires detailed analytical investigations. This then provides the motivation for the numerical study and the development of a computer program capable of calculating the essential impact phenomena.

The present paper outlines the theoretical formulation and the numerical method, and briefly describes the capabilities of the computer program. Typical

computational results for impact calculations in homogeneous and nonhomogeneous materials are presented, and their implications relative to initiation mechanisms in solid explosives and propellants are discussed.

COMPUTATIONAL APPROACH

A two-dimensional unsteady model of the impact phenomena was developed for cylindrically symmetric and plane geometries. Elastic-plastic or purely hydrodynamic material representation can be used. The formulation is in Lagrangian coordinates to permit the treatment of multiple materials and interfaces. Since details of the approach were given elsewhere (Napadensky et al., 1970) only a brief outline follows.

Governing Equations

The conservation equations describing the impact behavior are:

Mass

$$\rho J = \rho_0 \tag{1}$$

Momentum

$$\rho \frac{Du}{Dt} = \frac{\partial \sigma_{xx}}{\partial x} + \frac{\partial \sigma_{xz}}{\partial z} + \nu \frac{\sigma_{xx} - \sigma_{\theta\theta}}{x} \tag{2}$$

$$\rho \frac{Dw}{Dt} = \frac{\partial \sigma_{xz}}{\partial x} + \frac{\partial \sigma_{zz}}{\partial z} + \nu \frac{\sigma_{xz}}{x} \tag{3}$$

Energy

$$\frac{De}{Dt} - \frac{p}{\rho^2} \frac{Dp}{Dt} = \frac{Db}{Dt} + q \tag{4}$$

Here the following notation has been used: x z, θ - current radial (horizontal), axial (vertical), and angular coordinates; u, w - radial and axial velocity; ρ, ρ_0 - current and initial density; σ_{xx}, σ_{zz}, $\sigma_{\theta\theta}$ - normal stress components; σ_{xz} shear stress; p pressure (negative average normal stress); e - internal energy; b - strain energy of distortion; q - heat release; D/Dt - Lagrangian time derivative; $\nu = 0, 1$ for plane and axially symmetric geometries respectively; J - limit of the ratio of a differential element of current volume to that occupied by the same mass initially.

The stress and strain rate tensors are split into isotropic (hydrostatic) and antisymmetric (deviatoric)

parts. Constitutive equations describe the stress-strain relationship for the latter. The thermodynamic variables are related by a caloric equation of state, of the form:

$$p = A + Be \tag{5}$$

where A and B are functions of density. Temperatures are computed from a given thermal equation of state. The boundary conditions which can be treated include free and rigid surfaces and the impact of a flyer plate.

Numerical Procedures

The numerical solution follows closely a procedure developed by Wilkins (1964). A grid of straight lines divides the plane of motion into rectangular zones which deform into quadrilaterals as the motion progresses. The node indices of the grid serve as discrete Lagrangian variables. Accelerations, velocities, and displacements are defined at the nodes. State properties such as stress, density and energy are associated with the zones. Velocity is defined at mid-timestep while all other variables are defined at the end of a timestep. To permit the ready computation of the spatial derivatives in a distorted grid, use is made of an integral definition of the partial derivatives. Fictitious edge zones are used to compute the boundary conditions.

During each time step the accelerations are evaluated first, using finite difference forms of the momentum equations (2) and (3). Integrations with respect to time then yield the velocities and displacements. New zone volumes are computed and the densities are evaluated from the fixed zone masses; this is equivalent to using equation (1). Strain rates, deviatoric stress components, and distortion energies are calculated next, using the constitutive relations. Finally the internal energy and pressure are obtained by simultaneous solution of the energy equation (4) and the equation of state (5).

Shock waves are treated by introducing an artificial viscosity in regions of compression and computational stability is insured by choosing timesteps consistent with the Courant criterion (Richtmeyer and Morton, 1967). Detonation processes, using classical Chapman-Jouget theory, can be calculated. The grid size may be variable. Friction can be included at a rigid boundary and inertial effects of

casings around the explosive can be taken into account.

RESULTS AND CONCLUSIONS

Numerical experiments and parameter studies were carried out both for unconfined and partially confined impact (see Fig. 1). The latter represents the most common experimental configuration in which a cylinder of the tested material rests on an anvil surface and is impacted by a metal flyer plate. Both in unconfined and semiconfined impact the motion behind the initial shock is one-dimensional. Rarefaction waves originating at the lateral surfaces relieve the pressure and form a two-dimensional flow field. Interactions of these waves along the centerline can lead to strong tension in the material, particularly for unconfined impact.

Preliminary studies with a number of explosives and propellants indicated that their qualitative behavior is very much alike, and that only small quantitative differences exist, e.g., twenty percent differences in peak temperatures (Napadensky and Kot, 1971). Therefore, results for only a single material are presented here, namely TNT having a normal density of 1.58 gm/cc. The equations of state used are those given by Enig and Metcalf (1962). Elastic-perfectly plastic behavior is assumed when material strength is taken into account, and yielding occurs according to the von Mises criterion. The elastic modulus and the yield strength are 80.5 and 1.21 kilobars respectively. The impact velocity for both unconfined and flyer plate impact was held constant at 21 cm/msec (~700 fps). A cylinder height of 5 cm was used for all calculations while the diameter was varied in order to study geometric effects.

Large differences in the mechanical material response are observed, when comparing hydrodynamic modeling with an elastic-plastic treatment. For unconfined impact, particle velocities and displacements, in regions of significant material flow, are two times larger for the hydrodynamic case (see Fig. 2). However, the influence on the thermal response is much smaller, peak temperature being about ten percent higher for the hydrodynamic case, as shown in Fig. 3. The maximum temperatures in unconfined impact are quite moderate (~200°C) and occur directly behind the main shock wave in regions of maximum compression. Energies of distortion associated with elastic-plastic material response contribute little to the temperature rise. Also the effect of surface friction on temperature response was found to be minimal. More significant is the reduction of radial velocity and displacement along the impacting surface.

Flyer plate impact on cylinders of the same size (5 cm radius) and at the same velocity as for the unconfined case produces significantly higher (by a factor of two) temperature increases (see Fig. 4). These temperature maxima occur directly behind the shock reflecting from the rigid anvil surface. Therefore, it appears that the primary mechanism responsible for the temperature increases in a homogeneous material is the adiabatic shock compression. This was further substantiated by the results of numerical experiments with cylinders of various aspect ratios, subjected to flyer plate impact. Long and slender cylinders experience small temperature rises because the shock pressure is relieved by rarefaction waves from the lateral free surface before reflection takes place, as can be seen in Fig. 4 for the cylinder having a radius of 2.5 cm.
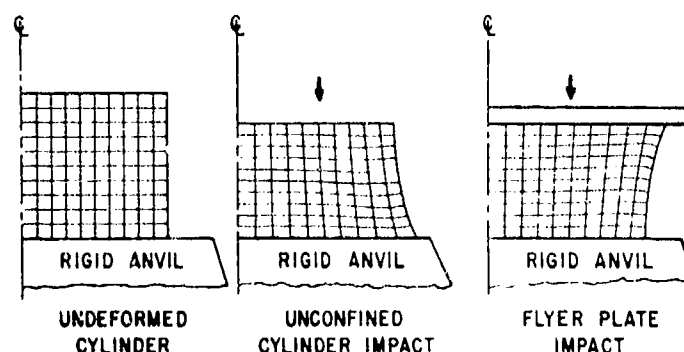
Fig. 1. Impact configurations.
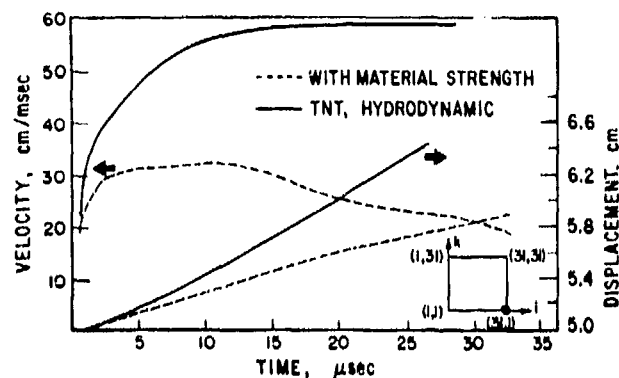
Fig. 2. *Effect of material strength on velocity and displacement. (unconfined impact, i = 31, k = 1)*
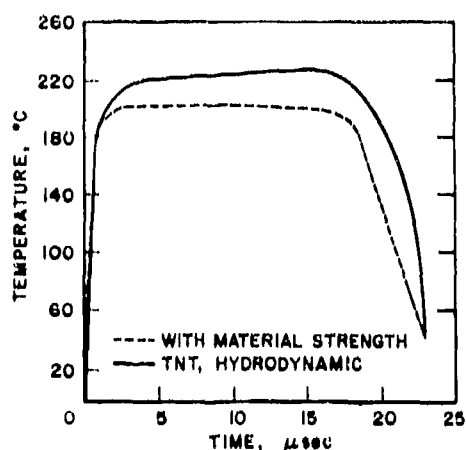
Fig. 3. *Effect of material strength on maximum temperature. (unconfined impact)*

Fig. 4. *Maximum temperature variations (elastic-plastic).*

The computational results indicate that significant energy focusing and temperature increases are possible in partially confined homogeneous materials at moderate impact speeds. While the substantial material heating is limited to small spatial regions (~0.16 cm diameter) and short durations (a few microseconds), it has been shown (Bowden and Yoffe, 1952), that at the calculated peak temperatures (~400°C), ignition sources of these dimensions and durations are sufficient to initiate chemical reaction. Since the large temperature increases are very localized, the effect of computational mesh size was evaluated. Adequate temperature predictions were obtained for grid sizes equal to or smaller than the formed hot spots. A computational mesh which is

too coarse predicts erroneously low temperatures as illustrated by the dashed curve in Fig. 4.

Experimental evidence indicates that the presence of material inhomogeneities such as impurities, gas bubbles and voids, enhances the production of hot spots or loci of initiation in propellants and explosives. The effect of such material inclusions was therefore investigated numerically. Specifically evaluated were the effect of gas bubbles and the influence of small inclusions consisting of either high or low density inhomogeneities. The calculations were carried out neglecting heat transfer and therefore

339

over estimate the temperature increases. However, they are indicative of the qualitative thermal response. The geometrical arrangement in all calculations was that shown in Fig. 5 for the case of an air inclusion.

It is found that soft (low density, $\rho = 0.5 \rho_0$ where ρ_0 is the normal density) inclusions and gas bubbles undergo very substantial temperature increases during shock compression. Due to the impedance mismatch at their boundary the inclusions are strongly compressed and energy is focused in these regions. Hard (higher density, $\rho = 2\rho_0$) inclusions act as small reflecting surfaces increasing the temperature slightly in the immediately adjacent material. However, their overall effect on the thermal response is minimal. Figure 6 shows the variation of maximum temperature with time for all three types of inhomogeneities. For comparison the curve for the homogeneous material is included. Only the first temperature peak is of interest here, since it is caused by the inclusion, the second peak results from the shock reflection at the anvil surface. It can be seen that the thermal effect of a soft inclusion is equivalent to that of a confining surface. The average air cavity temperature is found to be in excess of $3000^\circ C$ when using a perfect gas equation of state. Obviously real gas effects and heat transfer should be taken into account at these temperatures. Due to excessive distortion and partial collapse of the computational mesh the calculation with the air inclusion had to be terminated shortly after the shock passed the inhomogeneity. The shape of the air cavity and the grid distortion at that time can be seen in Fig. 5.

Figure 7 presents typical pressure and temperature profiles for the soft and the air inclusion at the time of maximum temperature occurrence. Again for comparison the profiles for the homogeneous material are also shown. The vertical profile for the latter, along the centerline, is characteristic of one-dimensional motion behind the downward moving shock wave. The rapid decreases of pressure and temperature towards the lateral surface in the horizontal profile are due to the rarefaction waves originating at that surface. Significant distortions of the profiles are caused by the presence of the inclusions. Of particular interest is the fact that while the temperature in the air cavity is extremely high the pressure is still but a small fraction of the value prevailing in the surrounding material. Thus, further collapse of the cavity accompanied by an additional temperature increase should be expected.

An auxiliary analysis was conducted to study in detail the phenomena in the vicinity of a single collapsing gas bubble or void. The materials of interest in their sensitive range generally experienced rather small strains during shock passage and the subsequent cavity collapse process was relatively symmetric with respect to a coordinate system moving with the apparent center of mass of the cavity. This indicated that the associated two-dimensional effects

Fig. 5. Deformation of a TNT cylinder with an air inclusion (hydrodynamic).
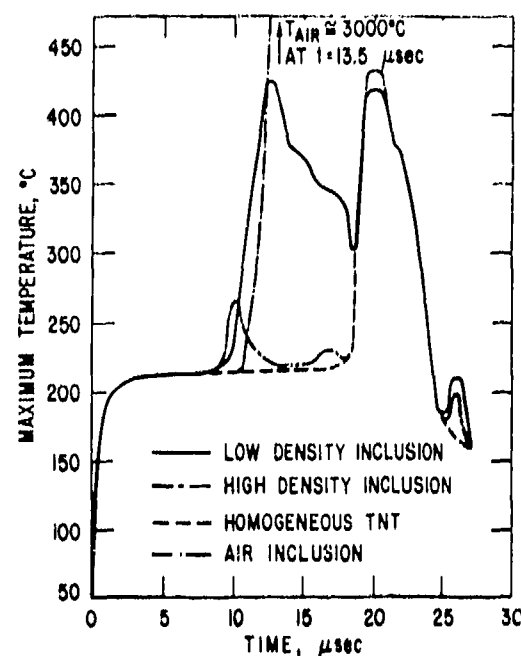
Fig. 6. Effect of inclusions on maximum temperature (hydrodynamic).

340
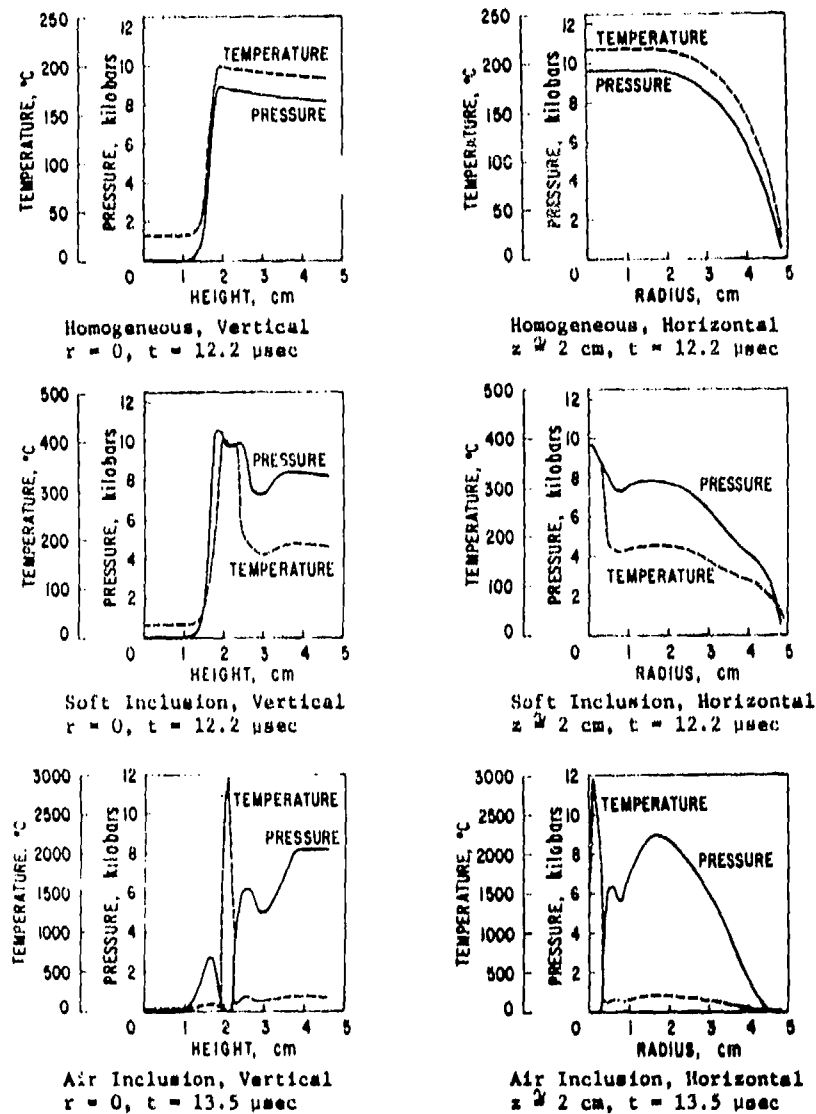
Fig. 7. Effect of inhomogeneities on pressure and temperature profiles (hydrodynamic).

were relatively weak and suggested that a one-dimensional spherically symmetric analysis could be used to evaluate the collapse process with improved fidelity. The analysis was limited to hydrodynamic material behavior. The process is started by instantaneously pressurizing a volume of material to the desired shock pressure level using the appropriate material properties. A low pressure gas filled or empty cavity is located at the origin of this region and the stress imbalance at the cavity boundary initi-

ates the cavity collapse process. The pressure at the cavity boundary was related to the instantaneous average gas pressure using a simple isentropic law for a perfect gas. In the case of a void the boundary was maintained at a zero pressure level.

The pressure and temperature histories, in the gas bubble and the immediately adjacent material are shown in Fig. 8. It can be seen that the temperature rise in the gas precedes the pressure increase and that

341

both are of very short duration (a few μsec), since the bubble reexpands. Using these adiabatic results an estimate of the heat transfer was obtained by solving the unsteady heat conduction equation. For the short durations indicated above, penetration of significant temperature increases was limited to depths of the order of one micron. It was concluded from these observations that the heat transfer mechanism was not a significant factor in concentrating energy within an adequate region of the material.

Much more important is the heating due to shock compression alone. As shown in Fig. 8 the temperature in the material immediately adjacent to the gas cavity rises to approximately 700°C. The time and spatial distribution of the temperature in the explosive material is given in Fig. 9 which presents the wave diagram isotherms and the path of the cavity boundary during collapse and reexpansion. A similar result is obtained for the case of a void indicating that the response of the gas within the cavity is not an important factor. The collapse process is governed primarily by the geometrically controlled dynamic response of the material itself.

In summary the results show that both for homogeneous and inhomogeneous materials the major mechanism leading to energy focusing and temperature increases is the adiabatic shock compression. Friction, dissipation due to distortion, and heat transfer are of small importance. While in unconfined impact temperature rises are moderate, confinement or the presence of low density inhomogeneities or gas bubbles produces local heating thought to be sufficient for the initiation of chemical reaction. In particular gas inclusions are prone to cause the formation of hot spots. The thermal effect of high density inclusions on the other hand is found to be minimal.

While no quantitative comparison with experiments was possible, due to the lack of appropriate test data, the computed material distortions agree qualitatively with high speed photography observations (Napadensky and Kennedy, 1964). Finally, the understanding of impact processes gained from the computational results amply demonstrates the value of the numerical modeling approach.

ACKNOWLEDGMENT

REFERENCES

Bowden, F. P., and Yoffe, A. D., (1952), *Initiation and Growth of Explosion in Liquids and Solids*, Cambridge University Press, Cambridge.
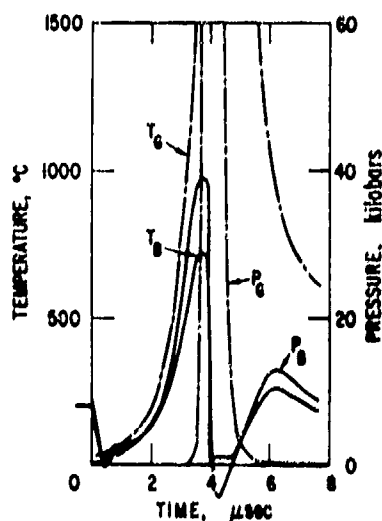
Fig. 8. Pressure (P) and temperature (T) histories, spherical bubble collapse (B· boundary, G· ·gas).
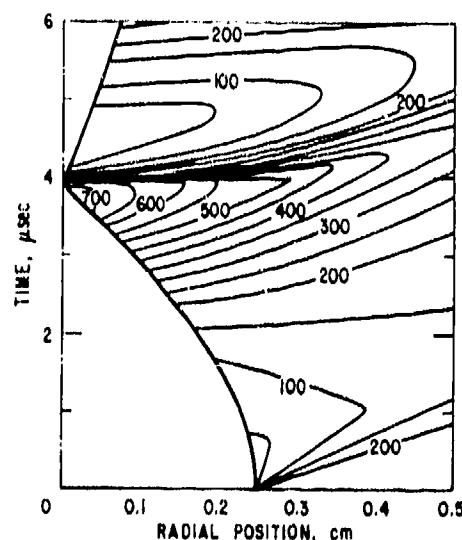
Fig. 9. Isotherms (°C) and gas bubble boundary path in the radius-time plane.

342

Enig, J. W., and Metcalf, F. T., (Aug. 24, 1962), "Theoretical Calculations on the Shock Initiation of Solid Explosives," NOLTR 62-160.

Napadensky, H. S., and Kennedy, J. E., (August 1964), "A Criterion for Predicting Impact Initiation of Explosive Systems," Minutes of the Sixth Explosive Safety Seminar of the Armed Services Explosive Safety Board.

Napadensky, H. S., Eichler, T. V., Kot, C. A., and Zaker, T. A., (1970), "Deformation of a Cylinder of Explosive Material in Unconfined Impact," Proceedings Fifth Symposium (International) on Detonation, Pasadena, California, pp. 313-320.

Napadensky, H. S., and Kot, C. A., (November 1971), "Initiation Mechanisms of Solid Rocket Propellant Detonation," AFOSR-TR-71-3028.

Richtmeyer, R. D., and Morton, K. W., (1967), *Difference Methods for Initial Value Problems*, Second Edition, Interscience Publishers, New York.

Wilkins, M. L., (1964), "Calculation of Elastic-Plastic Flow," *Methods in Computational Physics 3*, Academic Press, New York, pp. 211-263.

A KINETIC LATTICE APPROACH TO DETONATION IN HETEROGENEOUS EXPLOSIVES

Robert F. Chaiken and John C. Edwards
Pittsburgh Mining and Safety Research Center
Bureau of Mines
U.S. Department of the Interior
Pittsburgh, Pennsylvania 15213

In a previous paper, a kinetic lattice model of detonation was coupled with
Chapman-Jouguet Theory and Eyring Curved Front Theory to describe the critical
detonation characteristics of heterogeneous condensed explosives. In the present
work, non-ideal detonation behavior resulting from lateral energy loss is incorpo-
rated directly into the kinetic lattice model obviating the use of other failure
theories. The resulting equations are solved numerically to give the relationship
between detonation velocity, charge diameter and loading density. The results not
only describe the contrasting Group I/Group II behavior patterns reported by Price,
but also yield low velocity steady-state detonation solutions which resemble LVD
phenomena in solids. Critical diameter are also calculated for the specific case of an
RDX/AP Propellant explosive system. The generated data compare quite favorably
with experiment.

INTRODUCTION

In a previous paper (1), we outlined a kinetic
lattice approach to determining the detonation reac-
tion time of heterogeneous explosives, which when
incorporated into the detonation failure theory of
Eyring et al. (2) yielded a good accounting of
observed critical diameter phenomena. Of particular
interest is the fact that we were able to predict (albeit
a posteriori) the Group I/Group II type explosive
behavior as described by Price (3). This earlier treat-
ment of the lattice model assumed ad hoc the results
of Curved Front Theory (2) for describing the non-
ideal detonation condition.

In the present work, we describe how non-ideal
detonation behavior resulting from lateral rarefaction
energy loss can be incorporated directly into the
kinetic lattice model, obviating the use of other
failure theories. This treatment can be considered to
be an adaptation of Dremin's concept of a quenching
wave (4). The resulting kinetic lattice equations

when coupled with Chapman-Jouguet Theory again
leads to an initial value problem that defines the
regions of stable detonation for heterogeneous
explosives.

Numerical calculations with the present treatment
of the lattice model not only lead to good agreement
with experimental data on detonation velocity vs.
charge diameter, but also indicate the existence of
stable detonations at very low velocities, i.e., LVD
phenomena (5).

THE KINETIC LATTICE MODEL

Following our earlier treatment (1), we consider a
heterogeneous explosive to be composed of a uniform
distribution of spherical sites. These sites represent
the various types of explosive components; for
example, explosive particles, inert particles, and
potential hot-spots such as air voids, crystal defects,
and contact surfaces. For a one-dimensional treat-
ment of this model, we define a 1-D lattice composed

344

of an array of sites along a line drawn through the diameter of a cylindrical explosive charge. Considering the explosive to contain M-components, we denote for each type of site $i = 1, 2, \ldots M$ a mass density ρ_i, an effective diameter ℓ_i, and a total initial number $N_i(o)$. The charge diameter, d, and charge (loading) density ρ_0 is then expressed as

$$d = \sum_{i=1}^{M} \ell_i N_i(o) \qquad (1)$$

and

$$\rho_0 = \sum_{i=1}^{M} \frac{\pi}{6} \ell_i^3 N_i(o) \rho_i \bigg/ \sum_{i=1}^{M} \frac{\pi}{6} \ell_i^3 N_i(o) \qquad (2)$$

Passage of a detonation wave through the explosive is considered to result in decomposition (or activation) of the sites along the lattice to form hot-spots (i.e., ignition centers). If $N_i^*(t)$ is the number of hot-spots formed from sites of type i at time t after passage of the detonation front, then the total number of hot-spots formed is simply

$$N_T^*(t) = \sum_{i=1}^{M} N_i^*(t) \qquad (3)$$

Assuming a first order reaction process with a rate constant k_i for each type of site, we have

$$dN_i^*/dt = k_i N_i \qquad (4)$$

and

$$dN_T^*/dt = \sum_{i=1}^{M} k_i N_i \qquad (5)$$

We now consider that each hot-spot formed becomes the origin of a grain burning (i.e., deflagration) wave which consumes unreacted sites as it spreads outwardly from its origin along the lattice.

The grain burning wave leads to an effective first order consumption of sites given by

$$-(dN_i/dt) \text{ Grain Burn} = 2BN_T^* N_i \bigg/ \sum_{j=1}^{M} \ell_j N_j(t), \quad (6)$$

where B is the linear velocity of the grain burning wave.

The above processes of hot-spot formation and grain burning are essentially the energy liberating reactions which support the detonation, and lead to a set of M rate equations that describes the consumption of sites:

$$-dN_i/dt = \left[k_i + \frac{2BN_T^*}{\sum_j' \ell_j N_j} \right] N_i \qquad (7)$$

This is essentially the equation we derived in our earlier work (1) where Arrhenius rate constants for k_i and B were assumed, i.e.,

$$k_i = A_i \exp(-E_i/RT) \sec^{-1} \qquad (8)$$

and

$$B = A_s \exp(-E_s/RT) \text{ cm/sec}, \qquad (9)$$

and where temperature was taken as the Chapman-Jouguet value.

Our previous use of equations 7-9 to define the detonation reaction time tacitly assumed that every site will react in the detonation reaction zone even when lateral rarefaction energy losses occur (i.e., non-ideal detonation). We believe a more realistic approach to defining the detonation reaction time would be to identify the lateral rarefaction as a reaction quenching wave which originates at the two ends of the 1-D lattice (i.e., at the surface of the explosive charge), just after passage of the detonation front, and spreads inwardly to the center of the charge. The velocity of this quenching wave could be approximately the local velocity of sound for uncased charges and somewhat less than that for cased charges. Unreacted sites overtaken by this quenching wave will no longer be able to react, thereby decreasing the energy available for propagating the detonation. In the context of site consumption, the quenching reaction will have an effective first order reaction rate given by

$$-(dN_i/dt) \text{quench} = 2CN_i \bigg/ \sum_{j=1}^{M} \ell_j N_j \qquad (10)$$

where for uncased charges, C is taken as the local velocity of sound.

345

Incorporating equation 10 into equation 7, the total rate of consumption of sites of type i (i = 1, ..., M) is then

$$-\frac{dN_i}{dt} = \left[k_i + \frac{2(BN_i^* + C)}{\sum_j \ell_j N_j} \right] N_i, \qquad (11)$$

and the time to consume all sites is the detonation time, τ.

With this approach, lateral rarefaction leads to a certain number of unreacted sites of type i in the detonation zone, viz.,

$$(N_i)_{unreacted} = \int_0^{\tau_i} \frac{2CN_i}{\sum \ell_j N_j} dt, \qquad (12)$$

with an associated total fractional energy loss, f given by

$$f = \frac{\sum \frac{\pi}{6} \ell_i^3 \rho_i q_i \int_0^{\tau_i} \frac{2CN_i}{\sum \ell_j N_j} dt}{\sum \frac{\pi}{6} \ell_i^3 \rho_i q_i N_i(o)} \qquad (13)$$

where q_i is the heat of detonation per unit mass of sites of type i.

The overall heat of detonation of the explosive Q_d is simply

$$Q_d = (1 - f)Q_I \qquad (14)$$

where Q_I is the ideal heat of detonation (i.e., for the infinite diameter charge.

It is interesting to compare equation 14 for the case of a single component explosive with the results of other failure theories (2,6). Taking M = 1, equation 13 with C time independent leads to

$$f = 2C\tau/\ell_i N_i = 2C\tau/d \qquad (15)$$

Assuming C to be the Chapman-Jouguet sound velocity, (D-u), and recognizing that the length of the detonation reaction zone, $a = \tau (D\text{-}u)$, yields

*For purposes of numerical calculation, it is useful to set N_i = zero when the calculated $N_i(t) < 1$.

$$Q_d/Q_I = 1 - 2a/d \qquad (16)$$

This equation is somewhat similar in form to the simple approximate velocity vs. diameter equation of Curved Front Theory for uncased charges, i.e.,

$$D/D_I = 1 - a/d \qquad (17)$$

The relation between the heat of detonation, Q_d, and detonation velocity, D, through C-J theory is generally complex as will be shown later in this paper; however, a useful approximation for comparison purposes is $Q_d \propto D^2$, so that equation 16 becomes

$$(D/D_I)^2 \simeq 1 - 2a/d \qquad (18)$$

Figure 1 shows a plot of D/D_I vs. a/d for equations 17 and 18. Also included are the results of Jones' Nozzle theory for uncased charges taken from reference 2. The various theories are in rough numerical agreement; however, the downward curvature represented by the Nozzle theory has been found to be in keeping with some experimental data (7).

The numerical calculations are based on the argument that the kinetic reaction time (equations 7-9) is to be evaluated at the Chapman-Jouguet temperature, which in principle can be determined from Chapman-Jouguet Theory. From our previous simplified treatment of one-dimensional C-J theory, we set down directly the following detonation equations:
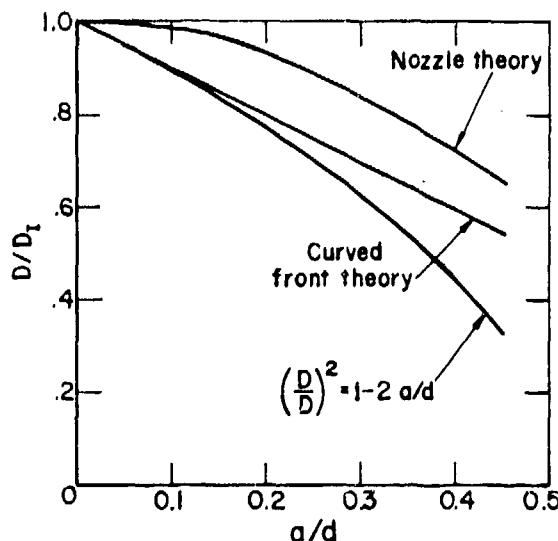
Fig. 1. D/D_I vs. a/d for Various Failure Theories.

346

Conservation of mass, momentum and energy (neglecting initial pressure terms) (1,2):

$$D^2 = \frac{P}{\rho_o(1 - \rho_o/\rho)} \qquad (19)$$

$$u = P/\rho_o D \qquad (20)$$

$$C_v T - C_v T_o = Q_d + \frac{1}{2}P\left(\frac{1}{\rho_o} - \frac{1}{\rho}\right) \qquad (21)$$

Chapman-Jouguet Condition:

$$C = D - u \qquad (22)$$

where D is the detonation velocity; u, the particle velocity, P, the pressure; ρ, the density; C_v, an averaged constant heat capacity; C, the speed of sound = $(\partial P/\partial \rho)_s^{1/2}$; T, the temperature; and the subscript zero refers to the initial state of the explosive.

Equation-of-state of the detonation products (taken as a single component gas):

$$P(1 - \alpha\rho) = \rho(\gamma - 1)C_v T \qquad (23)$$

$$\alpha = (1 - e^{-b\rho})/\rho \qquad (24)$$

where α is a volume dependent covolume; and b, a constant (= 1 cm³/gm).

The P-ρ-T equation of state is due to Cook (8), and its validity can be questioned in connection with C-J calculations for condensed explosives. Our use of this equation-of-state is primarily for computational convenience, although as an approximation, it is probably in keeping with our simplified approach, and our uncertainty in kinetic constants.

The detonation equations can be solved explicitly to yield a "hydrodynamic" Q_d, which can be compared with a "kinetic" Q_d determined from equations 11, 13 and 14. This comparison is repeated over a temperature range up to the maximum temperature defined by Q_1. Solutions are determined when the "hydrodynamic" Q_d is equal to the "kinetic" Q_d.

NUMERICAL RESULTS

In this section, we examine several solutions of the kinetic lattice model to demonstrate the effect of reaction kinetics on detonation behavior. Also, we present a comparison of calculated and experimental critical diameter data for one of the explosive systems treated in our earlier paper.

Two-Component Explosive System

Here we consider the same "hypothetical standard" granular explosive as given in reference 1. One component of the explosive is the explosive particles themselves (i = 1); the other component is the air voids (i = 2). Table 1 lists the various input parameters for the calculations. Several items can be pointed out:

1. For convenience, the air voids and explosive particles are considered equal in size.

2. Due to the strong shock heating characteristics of air, the activation energy E_2 is taken as zero to reflect high localized shock temperatures, and A_2 is chosen to yield a fast constant heating time ($\sim 10^{-10}$ sec).

3. The decomposition and grain burning kinetics for the explosive particles are similar to those of ammonium nitrate (AN). The heat of detonation is about four times that of AN.

4. γ was chosen to yield $D_1 \sim 7000$ m/sec at $\rho_o = 1$ gm/cm³.

TABLE 1

Input Parameters for "Hypothetical Standard" Explosive

ρ_1 = 1.725 g/cm³	C_v = 0.4 cal/g°K
ρ_2 = 1.176 × 10⁻³ g/cm³	γ = 1.5
$\ell_1 = \ell_2$ = 2.5 × 10⁻³ cm	q_1 = 880 cal/g
T_o = 300°K	q_2 = 0
$k_1 = 5.56 \times 10^9$ exp (-40000/RT) sec⁻¹	(a)
$k_2 = 5 \times 10^{10}$ sec⁻¹	
B = 300 exp (-7100/RT) cm/sec	(a)

(a) Reference 9 cites $k = 10^{12.28}$ exp (-38300/RT) and B = 0.23T exp (-7100/RT) cm/sec for NH_4NO_3.

Figure 2 depicts a plot of the numerical data for D vs. ρ_0 for various charge diameters. It is recognized that the calculated values of D at large ρ_0 are not representative of real explosives; however, the trends shown by the curves are believed to be significant. The curves represent steady-state solutions, and we see that not only are there limited regions of detonation for a given diameter, but the detonation velocity is multivalued.

Addressing our attention to the higher velocity parabolic shaped curves at constant d, we see that the apex of the curves defines a critical diameter-density condition where no high velocity solution occurs for ρ_0 less than the apex point. The dashed line through these points establishes a failure curve in d vs ρ_0 space which indicates an explosive behavior similar to that of the Group I explosives by Price (3), viz., d_{cr} decreasing with increasing ρ_0. At large diameters (e.g. d = 40 cm), the higher velocity solutions while still multivalued have no apex point indicating stable detonation at all densities.
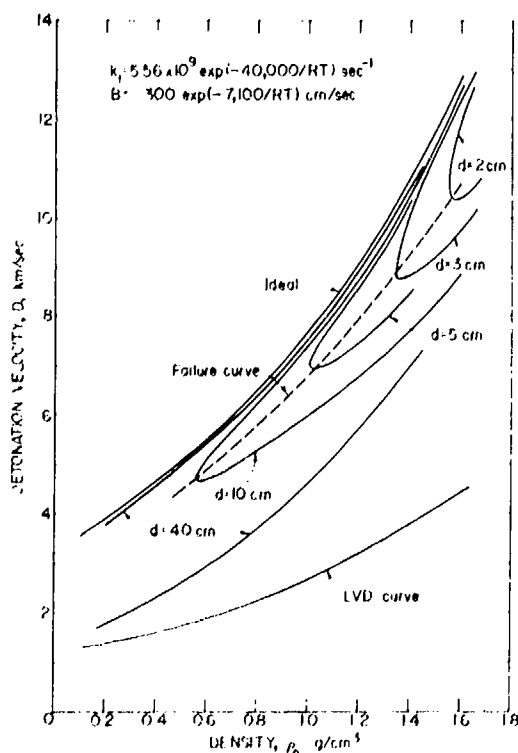
Still referring to the parabolic shaped solutions, the failure curve defines two velocity regimes of detonation. This is identical to that found in our earlier work (1), and also in the failure theories of Eyring et al. (2) and Evans (10). It was pointed out then that the physical reality of the solutions below the failure curve is in question; however, the solutions above the failure curve should represent the "normal" non-ideal steady-state detonation wave. Indeed, the portion of the parabolic curves above the failure curve does exhibit Group I explosive behavior (viz., D approaching D_I as ρ_0 increases) consistent with the critical diameter results.

Let us now give our attention to the single curve at lower velocity, which indicates a D vs. ρ_0 dependence which is far less steep than the "normal" high velocity solutions, and which appears to be independent of charge diameter. This curve was not obtained in our previous treatment of the lattice model. The calculated fraction of energy release for these cases is quite small (~ 0.5 pct), corresponding to low C-J temperatures (~ 400 to $600^\circ K$) and long reaction times (~ 10 μsec). These values can be compared with $T_{C-J} \sim 2800^\circ K$ and $\tau \sim 0.5$ μsec for the high velocity case. The behavior of the lower velocity solutions appears to resemble the few experimental data attributed to low velocity detonation (LVD) in granular explosives (5); in particular, the relative constancy of the LVD wave velocity with changes in d and ρ_0 and the fact that only small amounts of explosive reaction are involved in its propagation.

It would appear that the current kinetic lattice model now yields solutions for both HVD and LVD non-ideal detonations. However, it should be pointed out that in this case, an apparent inconsistency arises in our treatment of the lattice model. Namely, we have assumed a single component gas equation-of-state to describe the C-J products; yet, small fractions of reaction such as ascribed to LVD imply the detonation products to be mostly unreacted solid explosive. At this time we are not certain how the results of our lattice model treatment depend on the equation-of-state, particularly for a system of solid detonation products.

It is now of interest to examine the effects of altering the kinetic constants for the "standard" explosive so as to enhance the rate of grain burning relative to that of bulk decomposition. Figure 3 shows a plot of D vs. ρ_0 for the data of Table 1

except that k_1 (i.e., A_1) has been decreased by a factor of 10 and B (i.e., A_s) increased by a factor of 10. We note a rather significant change in the position of the parabolic shaped curves. The curves at constant small d (<10 cm) still have apex points which define a failure curve, but the resulting d_{cr} vs. ρ_o relationship is opposite to that of Fig. 2, viz., d_{cr} increases with increasing ρ_o. This is exactly one of the contrasting behavior patterns which defines Group II type explosives (3). The "normal" detonation solutions (i.e., above the failure curve in Fig. 2) likewise exhibit Group II behavior in that D approaches D_I as ρ_o decreases. Again, we attribute no physical significance to that portion of the parabolic curves below the failure curve (at least for the present).

We also note that Fig. 3 shows the same type of LVD curve as depicted in Fig. 2. Numerically, they are almost identical, thus indicating the LVD wave to be insensitive to the HVD reaction kinetics.
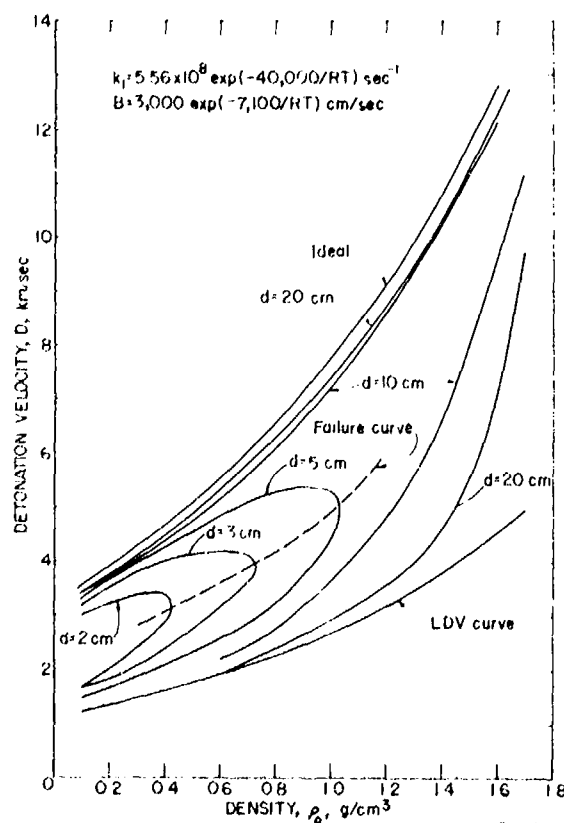
Fig. 3. *Variation of Detonation Velocity With Loading Density "Modified Hypothetical" Explosive: Effect of Enhanced Grain Burning.*

The above numerical results for the "standard" explosive strongly suggest that Price's Group I/Group II behavior can still be accounted for by the kinetic lattice model, and that the behavior depends upon whether bulk decomposition or grain burning is the dominant mechanism in the detonation reaction. The current failure mechanism introduced into the kinetic lattice model suggests that the model can also account for the existence of a stable LVD wave in solid explosives. Unfortunately there is too little quantitative data on stable LVD in solids to afford us a detailed comparison of the properties of such detonation waves.

RDX Adulterated Composite Propellant

The attempt here is to calculate the dependency of detonation velocity and critical diameter of a solid composite propellant which is sensitized with varying amounts of RDX. The propellant is composed of 60-70 wt pct ammonium perchlorate (AP), $\sim$ 15 wt pct aluminum, and $\sim$ 15 wt pct rubber binder, with varying amounts of 15 μ spherical grain RDX replacing the AP. There are extensive data on the detonation characteristics of this system (11,12), and it is one of the examples described in our earlier treatment of the kinetic lattice model.

The lattice is constructed by assuming the propellant to consist of spherical propellant particles (i = 1) with dimensions and reaction characteristics defined by the large particle AP component of the propellant. The RDX particles and air voids (0 and 2 wt. pct) form second (i = 2) and third (i = 3) components respectively. Table 2 lists the values of the input parameters. Here γ and C_v have been chosen to yield an ideal detonation velocity of 4620 meters/sec for the 9.2 wt. pct RDX mixture. The kinetic expressions for k_1 and B are approximately those reported for AP, having been adjusted somewhat to fit the experimental critical diameter at an RDX mass fraction $f_{RDX} = 0.0475$. It is noted that the RDX kinetics are those reported by Robertson (14), which in light of more recent kinetic studies (16), may not be applicable to detonation conditions. However, for the propellant system, the RDX undoubtedly reacts much faster than the AP; hence the exact choice of values for A_2 and E_2 is not too important. This was verified by the fact that calculations with A_2 several orders of magnitude smaller than 10^{18} sec^{-1} did not alter the numerical results.

TABLE 2

Input Parameters for
RDX/AP Propellant Explosive

$\rho_1 = \rho_2 = 1.6 \text{ g/cm}^3$	$C_v = 0.3 \text{ cal/g-}^\circ\text{K}$
$\rho_3 = 1.176 \times 10^{-3} \text{ g/cm}^3$	$\gamma = 1.2$
$\ell_1 = 1.2 \times 10^{-2} \text{ cm}$	$q_1 = 260 \text{ cal/g}$
$\ell_2 = \ell_3 = 3 \times 10^{-3} \text{ cm}$	$q_2 = 1500 \text{ cal/g}$
$T_0 = 300^\circ\text{K}$	$q_3 = 0$
$k_1 = 2.15 \times 10^9 \exp$	
$(-29000/RT) \text{ sec}^{-1}$	(a)
$k_2 = 3.2 \times 10^{18} \exp$	
$(-47500/RT) \text{ sec}^{-1}$	(b)
$k_3 = 1 \times 10^{10} \text{ sec}^{-1}$	
$B = 6.2 \times 10^4 \exp$	
$(-18000/RT) \text{ cm-sec}^{-1}$	(c)

(a) Reference 13 cites $k = 7.16 \times 10^{10} \exp(-26000/RT)$ cal/g/sec for AP propellant.

(b) Reference 14 cites $k = 3.2 \times 10^{18} \exp(47500/RT)$ sec^{-1} for RDX.

(c) Reference 15 cites $B = 31T \exp(-22000/RT)$ cm/sec for AP.

Figure 4 shows the experimental and calculated curves for the velocity-diameter dependence of the 9.2 wt. pct RDX case, and Table 3 lists the results for the variation of critical diameter with mass fraction of RDX content ($0 \leqslant f_{RDX} \leqslant 0.092$). The agreement between experiment and theory is quite good considering the fact that only two data points (viz., D_1 for $f_{RDX} = 0.092$, and d_{cr} for $f_{RDX} = 0.0475$) were used for evaluating the many parameters. No attempt was made to optimize this curve fit by further adjustments in the AP kinetic constants. While this probably could be readily accomplished, it was felt the result would not be too meaningful in view of the simplifications involved in our treatment of the C-J state.

It is noted from Table 3, that somewhat better agreement with experiment is obtained if the propellant is assumed to contain 2 wt pct air voids. This result is identical to our previous findings and consistent with the data interpretations presented by the original experimental investigators (12).

CONCLUSIONS

The inclusion of a first order quenching wave term in the kinetic lattice model equations has been shown

TABLE 3

Comparison of Critical Diameter
Data for RDX-Adulterated Propellant

f_{RDX}	d_{cr}, cm		
	Exp't (a)	Calculated (2% Porosity)	Calculated (0% Porosity)
.092	6.8	8.6	8.7
.071	13.3	--	..
.0475	28.6	28	29
.021	59.7	--	--
.00375	122	127	160
0 (b)	152 No-Go 183 Go	153	196

(a) Reference 12

(b) Single test at each diameter.
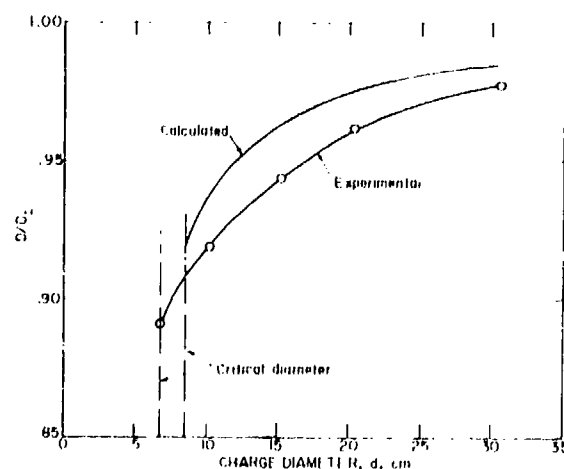
Fig. 4. Comparison of Velocity-Diameter Dependence for 9.2 wt pct RDX-Adulterated Propellant.

to result in a self-contained failure theory for the detonation of heterogeneous explosives. While our calculations to date with the model are quite limited and involve many simplifications, the results can be deemed very promising on the basis that the observed non-ideal detonation behavior of granular solid explosives is encompassed by the model. This includes not only the contrasting Group I/Group II patterns described by Price, but also as a distinct possibility, the phenomena of Low Velocity Detonation. This

latter point, however, must be considered in much further detail than we have undertaken here, particularly with regard to the nature of the P-ρ-T relation for the Chapman-Jouquet state, which appears to be a solid/gas mixture.

With regard to *a priori* prediction of non-ideal detonation behavior of arbitrary explosive mixtures, that is still a long way off, particularly in view of the dearth of required chemical kinetic data. However, the results to date would indicate that the kinetic lattice approach offers a possible direction to pursue in achieving this goal.

ACKNOWLEDGEMENT

The authors are grateful to Mr. J. E. Hay, U.S. Bureau of Mines-PMSRC Explosives Group, for many helpful discussions.

REFERENCES

1. R. F. Chaiken and J. C. Edwards. "Detonation and Critical Diameter of Heterogeneous Explosives," in press. Acta Astronautica (1976).

2. H. Eyring, R. E. Powell, G. H. Duffy and R. B. Parlin. "The Stability of Detonation," Chem. Rev., vol. 45, pp. 69-181 (1949).

3. D. Price. "Contrasting Patterns in the Behavior of High Explosives," Eleventh Symposium (International) on Combustion, pp. 693-701, The Combustion Institute, Pittsburgh, Pa. (1967).

4. See J. W. Enig and F. J. Petrone, "The Failure Diameter Theory of Dremin," Fifth Symposium (International) on Detonation, pp. 99-104, Office of Naval Research ACR-184 (1970).

5. See e.g., L. V. Babaitsev, B. N. Kondrikov and V. F. Tyshevich. "Low Velocity Detonation of Cast Explosive Charges," Vzryvnoe Delo Collection No. 68/25, B. D. Rossi, editor, pp. 194-201, Moskva (1970); Israel Program for Scientific Translation TT 70-50163 (1971), available from U.S. Department of Commerce.

6. H. Jones. "A Theory of the Dependence of the Rate of Detonation of Solid Explosives on the Diameter of the Charge," Proc. Roy. Soc. (London), Vol. A189, pp. 415-426 (1947).

7. M. E. Malin, A. W. Campbell and C. W. Mautz, "Particle Size Effects in One- and Two-Component Explosives," Preprints of the Second ONR Symposium on Detonation, pp. 360-381, Office of Naval Research Report (1955).

8. M. A. Cook. "The Science of High Explosives," pp. 63-64, Reinhold Publishing Corp., New York (1958).

9. W. H. Andersen and R. F. Chaiken. "Application of Surface Decomposition Kinetics to Detonation of Ammonium Nitrate," ARS Journal, vol. 29, pp. 49-51 (1959).

10. M. W. Evans. "Detonation Sensitivity and Failure Diameter in Homogeneous Condensed Materials," J. Chem. Phys., vol. 36, pp. 193-200 (1962).

11. O. R. Irwin, G. L. Roark and P. K. Salzman. "Large Solid-Propellant Boosters Explosive Hazards Study Program (Project SOPHY)," AFRPL-TR-65-211 (24 Nov. 1965); available from NTIS AD476617.

12. R. B. Elwell, O. R. Irwin and R. W. Vail, Jr., Project SOPHY, Solid Propellant Hazards Program, AFRPL-TR-66-25 (28 June 1966); also AFRPL-TR-67-211, vol. 1 (Aug. 1967).

13. D. Gross and A. B. Amster. "Thermal Explosions: Adiabatic Self-Heating of Explosives and Propellants," Eighth Symposium (International) on Combustion, pp. 728-734, Williams and Wilkins Co., Baltimore, Md. (1962).

14. A. J. B. Robertson. Trans. Faraday Soc., vol. 44, p. 977 (1948).

15. W. H. Andersen and R. F. Chaiken. "Detonability of Solid Composite Propellants," ARS Journal, vol. 31, pp. 1379-1387 (1961).

16. J. J. Batten and D. C. Murdie. "The Thermal Decomposition of RDX at Temperatures Below the Melting Point," Aust. J. Chem., vol. 23, pp. 749-55 (1970).

PERTURBATION METHODS APPLIED TO PROBLEMS IN DETONATION PHYSICS[*]

J. B. Bdzil
Los Alamos Scientific Laboratory
University of California
Los Alamos, New Mexico 87545

A theoretical study of an explosive which releases a small fraction, δ^2, of its total energy via resolved reactions is presented. Two separate problems are treated. First, a time-dependent one-dimensional unsupported detonation is considered. It is shown that to $0(\delta)$ the detonation is a reactive simple wave. The particle velocity profiles are calculated for a model explosive. Second, the detonation edge effect for a steady-state semi-infinite unconfined detonation is considered. It is shown that the near-field flow is dominated by the Prandtl-Meyer singularity, whereas the far-field flow is controlled by the reactivity and streamline divergence. The shock locus, sonic locus, and limiting characteristic are calculated and the effects of confinement are discussed.

I. INTRODUCTION

Detonation physics is primarily concerned with understanding the rather complex subject of reactive nonlinear hydrodynamics. As a result of this, the number of analytic solutions describing detonation problems is very small. In part, this has led to a heavy reliance on numerical solution methods for these problems. By their very nature, these methods are only marginally suitable for parameter variation studies; thus they often provide little or no guidance as to the nature of the governing physics.

For a small class of problems, analytical solutions can be found using modern singular perturbation theory. The purpose of this paper is to describe the underlying scaling principles of these methods, and to show how they filter the relevant physics from the full governing equations. As examples, we consider two problems that have as a small parameter δ^2, the fraction of the total energy released via resolved reactions.

In section II, we examine a one-dimensional time-dependent detonation. We show that to lowest order in the perturbation (δ), the evolution of the detonation proceeds as if it were a simple wave with independent variables x and δt. A straightforward application of the method of characteristics to the resulting equations allows us to study a wide class of simple wave problems.

In section III, we examine a steady two-dimensional detonation. We show that for an unconfined semi-infinite detonation, the physical space divides itself into two distinct regions. Very near the edge (inner problem) the flow is nearly a free unreactive expansion with $x/\delta^{1/3}$ and $\delta^{1/3}y$ being the independent variables, where y is the distance into the charge from the edge. Away from the edge (outer problem) the reactivity and streamline divergence enter equally with x and δy being the independent variables. We determine the shape of the shock and sonic loci and study the effects of confinement on the detonation.

II. A TIME-DEPENDENT DETONATION

A. Statement of the Problem

Most of the experiments that have been performed on explosives were designed to measure the parameters contained in the Chapman-Jouguet theory. When applied to unsupported detonations, this theory makes the following assumptions: (1) initially the right half-space $(x > 0)$ is occupied by a quiescent fluid at a density ρ_0 which is in a state of metastable chemical equilibrium; (2) at time $t = 0$ a piston, which is originally at $x = 0$, is impulsively brought to a velocity $u^* > 0$ and then withdrawn producing a planar shock wave followed by a rarefaction; (3) on passing over the initially quiescent fluid the shock initiates an instantaneous chemical reaction, of specific internal energy $q(1 - \delta^2)$, which then supports a classical detonation with a pressure P^* and a velocity $\mathcal{D}^*$; (4) in terms of this model the parameters ρ_0, $\mathcal{D}^*$, and P^* completely characterize the flow. In this section, we will consider the consequences of releasing an additional small amount of energy $q\delta^2$ to the flow on a relatively slow time scale.

We limit our discussion to the following constitutive relations: a polytrope equation of state

$$E = \frac{1}{\gamma - 1} \frac{P}{\rho} + q\delta^2(1 - \lambda) \quad q, \quad (2.1)$$

where E is the specific internal energy, P is the pressure, ρ is the density, γ is the adiabatic exponent, and a state-independent square-root rate law $(0 \leqslant \lambda \leqslant 1)$

$$r = k(1 - \lambda)^{1/2}, \quad (2.2)$$

where k is a constant rate multiplier. Neglecting all transport processes, the field equations for our time-dependent one-dimensional flow (shock fixed coordinates) are

$$\frac{D_0}{Dt'} \ln(P'/\rho'^\gamma) = \frac{\gamma + 1}{2\gamma} \frac{\delta^2 r'}{c'^2} \quad (2.3)$$

$$\frac{D_\pm}{Dt'} P' \pm \gamma\rho'c' \frac{D_\pm}{Dt'} u' = \frac{\gamma + 1}{2\gamma} \rho'\delta^2 r' \quad (2.4)$$

$$\frac{D_0}{Dt'} \lambda = r', \quad (2.5)$$

where

$$\frac{D_\pm}{Dt'} = \frac{\partial}{\partial t'} + [\mathcal{D}, -(u' \pm c')] \frac{\partial}{\partial\zeta'} \quad (2.6a)$$

$$\frac{D_0}{Dt'} = \frac{\partial}{\partial t'} + (\mathcal{D}' - u') \frac{\partial}{\partial\zeta'} \quad (2.6b)$$

$$\zeta = \mathcal{D}(t)dt - x. \quad (2.7)$$

In the above equations t' is the scaled time (kt), ζ' is the scaled distance coordinate in the shock frame $(\gamma + 1)k\zeta/\gamma\mathcal{D}^*$, u' is the scaled particle velocity in the laboratory frame, c' is the scaled sound speed, ρ' is the scaled density $\gamma/(\gamma + 1)\rho_0$, and $\mathcal{D}'(t')$ is the scaled detonation velocity. To simplify the notation, the primes will be dropped.

Equations (2.3), (2.4), (2.5), the initial condition of an impulsive piston, and the shock conditions serve to completely describe the problem we wish to consider. In the limit $\delta \to 0$ the solution is a simple wave known as a Taylor wave. We will show that for δ sufficiently small the solution is a reactive simple wave.

B. Reactive Simple Wave

Since we are considering a system for which δ is small, it is natural to seek a solution to the stated problem as a regular asymptotic expansion in δ

$$u = \frac{1}{\gamma} + u^{(0)} + \delta u^{(1)} + \delta^2 u^{(2)} + \dots \quad (2.8)$$

$$c = c^{(0)} + \delta c^{(1)} + \delta^2 c^{(2)} + \dots, \text{ etc.} \quad (2.9)$$

A straightforward calculation gives us $u^{(2)} \sim t$ for t large. Thus, for times greater than δ^{-2} Eq. (2.8) no longer gives us an asymptotic representation of the solution. Examining the governing differential equations, we find that the secularity in $u^{(2)}$ arises because the equations for the perturbations are linear. It follows that for long times they do not contain the nonlinear convective effects that bound reactive growth. Physically, we can understand this with the aid of the Master Equation (1). It states that the growth of the shock pressure is the difference between the rate of energy input of the reactions minus the rate of energy loss to the following flow.

353

When the flow is sonic, as it is in our unperturbed flow, the loss rate is zero. Introducing δt as a time scale into the Master Equation leads to bounded solutions (1). This suggests that in addition to t, we should include δt as a time scale. Using the method of multiple time scales, we will show that a bounded solution can be found to our differential system (2).

We begin by formally integrating Eq. (2.3) and then using the results to rewrite Eqs. (2.4) as

$$\frac{D_\pm}{Dt} R_\pm = \frac{\gamma+1}{2\gamma} \frac{c}{\gamma(\gamma-1)}$$

$$\times \left(\gamma \frac{\delta^2 r}{c^2} \mp \frac{\partial}{\partial \zeta} \int \frac{\delta^2 r}{c^2} dt_o\right) + O(\delta^2), \quad (2.10)$$

where $R_\pm$ are the Riemann variables

$$R_\pm = \frac{2}{\gamma-1} c \pm u \qquad (2.11)$$

and $\int dt_o$ denotes an integral taken along a particle path. Following in the spirit of the multiple time scale method, we introduce the time scales

$$y^{(i)} = \frac{\gamma+1}{2} \delta^i t; \qquad i = 0, 1, 2, \ldots \quad (2.12)$$

and assume that Eqs. (2.8) and (2.9) depend explicitly on all of these times as well as ζ. The characteristic derivatives become

$$\frac{2}{\gamma+1} \frac{D_\pm}{Dt} = \frac{\partial}{\partial y^{(0)}} + [1 - (u^{(0)} \pm c^{(0)})] \frac{\partial}{\partial \zeta}$$

$$+ \delta \left[\frac{\partial}{\partial y^{(1)}} - \frac{2}{\gamma+1}(u^{(1)} \pm c^{(1)})\frac{\partial}{\partial \zeta}\right] + \ldots \quad (2.13)$$

Focusing our attention on the negative Riemann variable, we find that at $O(1)$ Eq. (2.10) is easily integrated. Since all the negative characteristics emanate from a region whose state is at most specified by the variables $y^{(1)}, y^{(2)}, \ldots$

$$R_-^{(0)} = g^{(0)}(y^{(1)}, y^{(2)}, \ldots). \qquad (2.14)$$

At $O(\delta)$, we find

$$R_-^{(1)} = -y^{(0)}\left(\frac{\partial g^{(0)}}{\partial y^{(1)}}\right) + g^{(1)}(y^{(1)}, y^{(2)}, \ldots). \qquad (2.15)$$

To avoid the secular behavior in Eq. (2.15), we set

$$R_-^{(0)} = g^{(0)}(y^{(2)}, \ldots). \qquad (2.16)$$

Proceeding to $O(\delta^2)$, we get

$$R_-^{(2)} = g^{(2)}(y^{(1)}, y^{(2)}, \ldots)$$

$$+ \frac{1}{\gamma^2(\gamma-1)} \int \left[c\left(\frac{\gamma r}{c^2}\right.\right.$$

$$\left.\left. + \frac{\partial}{\partial \zeta} \int \frac{r}{c^2} dt_o\right)\right] dy^{(0)}\bigg|_{\zeta = f(y^{(0)})}, \quad (2.17)$$

where

$$\frac{df}{dy^{(0)}} = \frac{2}{\gamma+1}(1 - u^{(0)} + c^{(0)}), \qquad (2.18)$$

and we have taken

$$\frac{\partial g^{(0)}}{\partial y^{(2)}} + \frac{\partial g^{(1)}}{\partial y^{(1)}} = 0 \qquad (2.19)$$

to avoid the appearance of a secularity. Using these results, the positive Riemann variables can be written as

$$R_+^{(0)} = 2u^{(0)} + g^{(0)}(y^{(2)}, \ldots) \qquad (2.20)$$

$$R_+^{(1)} = 2u^{(1)} - y^{(1)}\left(\frac{\partial g^{(0)}}{\partial y^{(2)}}\right) + \tilde{g}_1(y^{(2)}, \ldots). \qquad (2.21)$$

Requiring Eq. (2.21) to remain bounded, we are forced to set $(\partial g^{(0)}/\partial y^{(2)}) = 0$, which gives

$$R_-^{(0)} = g^{(0)}(y^{(3)}, \ldots), \quad R_-^{(1)} = g^{(1)}(y^{(2)}, \ldots). \qquad (2.22)$$

Therefore, to $O(\delta)$ the flow is a simple wave for the scales $y^{(0)}$ and $y^{(1)}$.

354

Turning our attention to the equations governing the positive Riemann variables and arbitrarily setting $u^{(0)} = 0$ and $c^{(0)} = 1$, we find

$$\frac{\partial U^{(1)}}{\partial y^{(1)}} - u^{(1)} \frac{\partial U^{(1)}}{\partial \zeta} = \frac{1}{2\gamma^2}$$

$$\times \left\{ \begin{array}{ll} \left(1 - \frac{1}{2}\zeta\right), & 0 < \zeta < 2 \\ \\ 0 & , \ 2 < \zeta \end{array} \right\} . \tag{2.23}$$

Solving Eq. (2.23) subject to the relevant boundary and initial conditions, we find

$$u^{(1)} = \frac{1}{\gamma} \tanh\left(\frac{y^{(1)}}{4\gamma}\right) - \frac{\zeta}{2\gamma} \coth\left(\frac{y^{(1)}}{2\gamma}\right),$$

$$0 < \zeta < 2$$

$$u^{(1)} = -\frac{\zeta}{y^{(1)}} + \frac{2}{y^{(1)}} \left[1 + \gamma u^{(1)} \ln\left(-(\gamma u^{(1)})^{-1}\right.\right.$$

$$\left.\left. + \sqrt{1 + (\gamma u^{(1)})^{-2}}\right)\right], \ 2 < \zeta . \tag{2.24}$$

Substituting Eq. (2.24) into Eq. (2.8) gives us an asymptotic representation of the solution which is valid over the entire physical region.

C. Discussion

The effects that a small fraction of resolved energy release can have on a detonation can best be appreciated by considering an example. We take

$$\mathcal{D}^* = 8.8 \text{ mm/}\mu s, \quad \gamma = 3.0 \tag{2.25}$$

$$\delta^2 = 0.06 \qquad , \quad k = 2\,\mu s^{-1} . \tag{2.26}$$

Figures 2.1 and 2.2 compare the particle velocity profiles to the reference Chapman-Jouguet detonation for 6 μs and 30 μs of run. Two features of the flow deserve special attention: (1) adding only 6% of the total energy via a slow reaction results in a 27% increase in the particle velocity at the shock, and (2) after 30 μs of run, the final steady-state has not been reached. Therefore, changes of $O(\delta^2)$ in the detonation energy (i.e., the Chapman-Jouguet state) produce changes of $O(\delta)$ in the shock state.
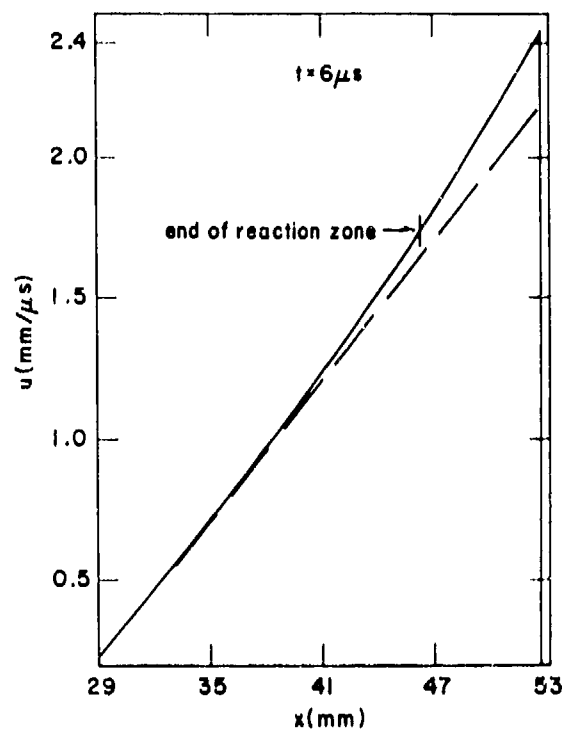

Fig. 2.1. A comparison of particle velocity vs distance profiles for a Chapman-Jouguet detonation (- -) and Eq. (2.24) (—).

Fig. 2.2. See Fig. 2.1.

355
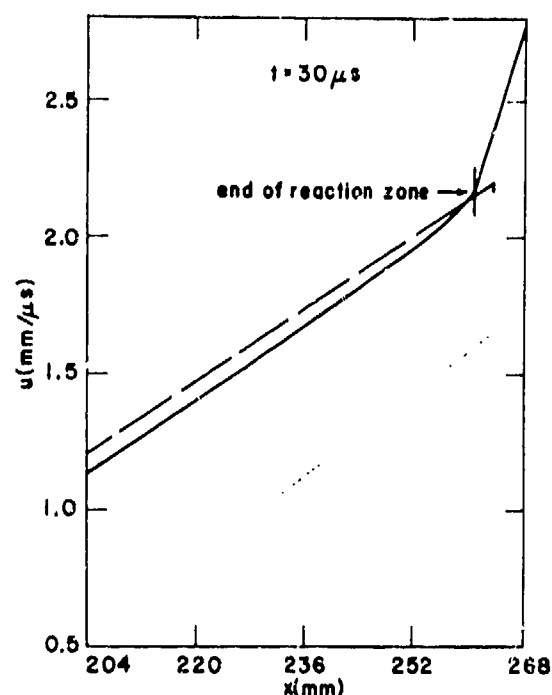
Also, the rate at which the steady-state is approached is measured in units of $(\delta k)^{-1}$. Consequently, even if only a small amount of the available energy in a detonation is released relatively slowly, the deviations from the Chapman-Jouguet model will be large.

III. EDGE EFFECTS

A. Statement of the Problem

Consider a *steady* detonation of velocity $\mathcal{D}$ propagating in the positive x-direction. The explosive supporting the wave is taken to be semi-infinite with explosive occupying the half-space $y < 0$ and a vacuum for $y > 0$ (see Fig. 3.1).

If we assume a Chapman-Jouguet detonation, an observer riding with the shock would see a flat shock (y-axis), along which the flow would be exactly sonic. Behind the shock he would see a Prandtl-Meyer fan originating from a singularity at $y = 0$.
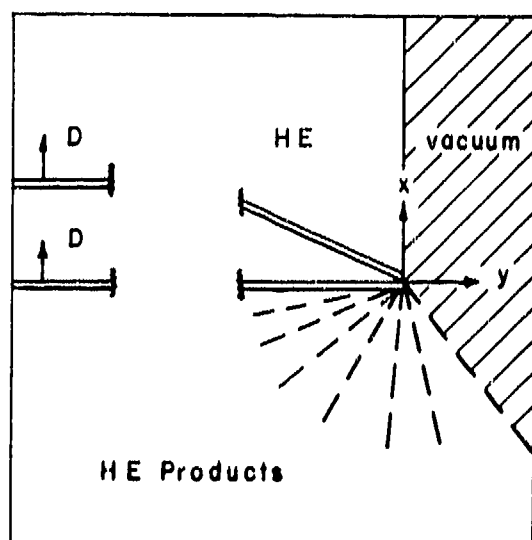
Fig. 3.1. A schematic representation of the detonation edge effect. The shocks (both C-J and resolved) are double lines. The Prandtl-Meyer fan is represented by the dashed lines.

For the case of a resolved reaction zone, the flow at the intersection of the shock with the x-axis must again be locally described by the Prandtl-Meyer singularity. This requires that the flow at the shock be sonic at $y = 0$, which in turn, requires that the shock make an acute angle with the positive x-axis. Proceeding into the explosive along the shock, the effects of the singularity diminish, and leave in the limit an undisturbed one-dimensional flow with a subsonic shock which is parallel to the y-axis. In the intervening region $(-\infty < y < 0)$ the shock must smoothly connect these two limits with some analytic form. The purpose of this section is to describe the structure of the region of reactive flow, including the determination of the shock shape, sonic locus, and limiting characteristic. For the general case, the analysis of this problem is difficult. However, we will again find that in the limit of small δ^2 (the resolved energy release fraction) a perturbation solution is possible. In this limit, progress becomes possible because we are dealing with a nearly sonic transonic flow.

B. Preliminary Considerations

Assuming that all transport processes can be neglected, the field equations for our steady two-dimensional plane flow (shock fixed coordinates) are

$$\Delta \cdot (\rho \underline{u}) = 0 \qquad (3.1)$$

$$\underline{u} \cdot \Delta \underline{u} = -\frac{1}{\rho} \underline{\Delta} P \qquad (3.2)$$

$$\underline{u} \cdot \underline{\Delta} P - c^2 \underline{u} \cdot \Delta \rho = \frac{1}{E_p} q \delta^2 r \qquad (3.3)$$

$$\underline{u} \cdot \underline{\Delta} \lambda = r, \qquad (3.4)$$

where ρ is the density, $\underline{u}$ is the particle velocity relative to the shock velocity, P is the pressure, c is the sound speed, E is the specific internal energy, q is to total energy release due to chemical reaction, r is the rate of reaction and λ is the reaction progress variable ($\lambda = 1$ at the end of reaction). Since we wish to study the general features of the flow, we limit our discussion to the following constitutive relations: a polytropic equation of state

$$E = \frac{1}{\gamma + 1} \frac{P}{\rho} + q \delta^2 (1 - \lambda) - q, \qquad (3.5)$$

where γ is the adiabatic exponent, and a state-independent square-root rate law

$$r = k(1 - \lambda)^{1/2} , \qquad (3.6)$$

where k is a constant rate multiplier. After a straightforward transformation (see Serrin (3)), Eqs. (3.2) and (3.3) become

$$H + \frac{1}{2} |\underline{u}|^2 = \frac{1}{2} \mathfrak{D}^2 , \qquad (3.7)$$

where $H = E + P/\rho$ and we have assumed the flow ahead of the shock is both homoenergetic and at zero pressure, and

$$\underline{u} \cdot \Delta \left(\frac{\Omega}{\rho}\right) = -\frac{1}{\gamma} \left(\frac{\partial \rho^{-1}}{\partial x} \frac{\partial c^2}{\partial y} - \frac{\partial \rho^{-1}}{\partial y} \frac{\partial c^2}{\partial x}\right), \qquad (3.8)$$

where and $\Omega = (\partial u_y/\partial x) - (\partial u_x/\partial y)$ is the vorticity which is directed into the plane of the paper. Using Eqs. (3.2), (3.3), and (3.7) we can rewrite Eq. (3.1) as

$$(c^2 - u_x^2) \frac{\partial u_x}{\partial x} - 2u_x u_y \frac{\partial u_y}{\partial x} + (c^2 - u_y^2) \frac{\partial u_y}{\partial y}$$

$$= (\gamma - 1)q\delta^2 r - u_x u_y \Omega . \qquad (3.9)$$

Equations (3.6), (3.7), (3.8), and (3.9) serve as the working equations for our analysis. They are partial differential equations of mixed type. In regions of supersonic flow, they are of hyperbolic type; whereas in regions of subsonic flow they are of elliptic type. Formulating the boundary value problem for such a system requires some care. The Tricomi equation

$$\Xi_{xx} + x\Xi_{yy} = 0 , \qquad (3.10)$$

which is the simplest equation of mixed type, serves as a guide (4). It can be shown that if the potential Ξ is specified along some smooth curve in the subsonic region $(x > 0)$, which originates and terminates on the sonic locus $(x = 0)$, and also along a characteristic in the supersonic region $(x < 0)$, which is joined to one of the end points of the boundary for $x > 0$, then Eq. (3.10) has a unique solution. Translated to the problem at hand, we are led to require that:
(1) along the shock (free boundary) both the normal

and tangential jump conditions are satisfied (curve 1); (2) at $y \to -\infty$ the streamline flow is that of the corresponding one-dimensional problem (curve 2); and (3) along the cross characteristic encircling the Prandtl-Meyer singularity, the flow is that of an inert simple wave (curve 3). A schematic representation of the boundary is shown in Fig. 3.2. From a physical standpoint, applying these boundary conditions seems quite natural.
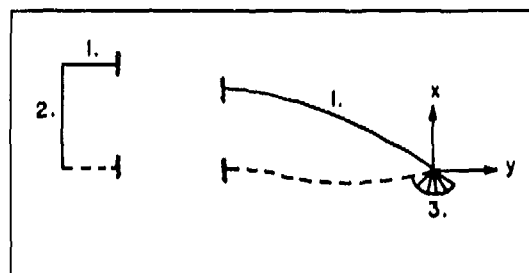
Fig. 3.2. A schematic representation of the boundary curves for the edge effect on a reaction zone; (1) the shock, (2) streamline at infinity, (3) cross characteristic. The dashed line represents the sonic locus.

Of these, the shock conditions need some special consideration. We begin by defining the equation for the shock locus

$$x = -\psi(y) , \qquad (3.11)$$

in terms of which the tangent, $\underline{t}$ and the normal, $\underline{n}$ to the shock surface are

$$\underline{t} = \left(-\frac{d\psi}{dy} \underline{i} + \underline{j}\right) \Big/ \left(1 + \frac{d\psi}{dy}^2\right)^{1/2} \qquad (3.12)$$

$$\underline{n} = \left(\underline{i} + \frac{d\psi}{dy} \underline{j}\right) \Big/ \left(1 + \frac{d\psi}{dy}^2\right)^{1/2} . \qquad (3.13)$$

The jump conditions across the shock require that the following relations hold:

$$\rho_+(\underline{u} \cdot \underline{n})_+ = \rho_0(\underline{u} \cdot \underline{n})_0 \qquad (3.14a)$$

$$(\underline{u} \cdot \underline{t})_+ = (\underline{u} \cdot \underline{t})_0 \qquad (3.14b)$$

$$P_+ + \rho_+(\underline{u} \cdot \underline{n})_+^2 = \rho_o(\underline{u} \cdot \underline{n})_o^2 . \quad (3.14c)$$

Since the state ahead of the shock is quiescent in the laboratory frame, Eqs. (3.14) may be rewritten as

$$\frac{\rho_o}{\rho_+} = \frac{\gamma}{\gamma+1} - \frac{1}{\gamma+1} \sqrt{1 - (1-\delta^2)\left(1 + \left(\frac{d\psi}{dy}\right)^2\right)} \quad (3.15a)$$

$$u_{y+} = (u_{x+} + \mathcal{D}) \frac{d\psi}{dy} \quad (3.15b)$$

$$u_{x+} = \mathcal{D}\left[-\left(\frac{d\psi}{dy}\right)^2 - \frac{\gamma}{\gamma+1}\right.$$

$$\left. + \frac{1}{\gamma+1}\sqrt{1 - (1-\delta^2)\left(1 + \left(\frac{d\psi}{dy}\right)^2\right)}\left(1 + \left(\frac{d\psi}{dy}\right)^2\right)\right]. \quad (3.15c)$$

Using the result of Hayes (5), the vorticity jump across the shock is

$$\Omega_+ = \frac{(1 - \rho_o/\rho_+)^2 \mathcal{D}(d\psi/dy)(d^2\psi/dy^2)}{\rho_o/\rho_+[1 + (d\psi/dy)^2]^2} , \quad (3.16)$$

where the flow ahead of the shock is irrotational. Equations (3.15) and (3.16) provide all the necessary boundary conditions along the shock. Unfortunately, the shape of the shock is not known *a priori*, so that at this point in the calculation, they are of only limited usefulness. The slope at the sonic point on the shock can be calculated by substituting Eqs. (3.15b) and (3.15c) into Bernoulli's law [Eq. (3.7)], and setting $c^2 = |\underline{u}|^2$. We obtain

$$\left(\frac{d\psi}{dy}\right)_{\text{sonic}} = \delta \frac{(\gamma^2 - \delta^2)^{1/2}}{(\gamma + \delta^2)} , \quad (3.17)$$

where for later convenience we introduce

$$\frac{d\psi}{dy} = (1 - \epsilon)\left(\frac{d\psi}{dy}\right)_{\text{sonic}} . \quad (3.18)$$

Since we must require that the shock shape is a smooth convex function, Eq. (3.17) serves as an upper bound on the shock slope. Recalling that the energy release fraction is δ^2, Eq. (3.17) shows that the shock slope is sensitive to the amount of resolved energy release, particularly for small values of δ^2. From the vorticity jump condition we find that Ω_+ is proportional to the product $(d\psi/dy)(d^2\psi/dy^2)$. Assuming that the shock curvature, $d^2\psi/dy^2$, is also $O(\delta)$ then Ω_+ is $O(\delta^2)$. Since the right-hand-side of Eq. (3.8) is at most $O(\delta^2)$, Eq. (3.8) requires that the velocity be $<O(\delta^2)$. Therefore, it seems likely that for δ sufficiently small we will be able to consider the flow as irrotational.

In the analysis of the flow equations, we will find it convenient to be in a coordinate system in which the flow at the edge $(y = 0)$ is directed along a single coordinate axis. We select the direction of flow at the sonic point on the shock as our new x-axis (x_w) with the new y-axis (y_w) being perpendicular to it. Because the flow is locally a Prandtl-Meyer expansion, the sonic locus coincides with y_w at $y = 0$. In this system, the velocities are

$$u_{xw} = u_x \cos \omega - u_y \sin \omega \quad (3.19a)$$

$$u_{yw} = u_x \sin \omega + u_y \cos \omega , \quad (3.19b)$$

with the rotation angle given by

$$\sin \omega = \delta/\gamma . \quad (3.19c)$$

In these new coordinates, the shock velocity jump conditions are

$$\tilde{u}_{xw+} = \frac{(\gamma + \delta^2)}{\gamma[(\gamma + \delta^2)^2 + \delta^2(\gamma^2 - \delta^2)(1 - \epsilon)^2]}$$

$$\times\left[-\delta^2(1 - \epsilon) - \frac{\delta^2(\gamma^2 - \delta^2)(1 - \epsilon)^2}{(\gamma + \delta^2)}\right.$$

$$\left. + \delta \frac{(\gamma + \delta^2\epsilon)}{(\gamma + \delta^2)} \sqrt{(\gamma + \delta^2)^2 - (1 - \delta^2)(\gamma^2 - \delta^2)(1 - \epsilon)^2}\right] \quad (3.20)$$

$$\tilde{u}_{yw+} = \frac{\delta}{(\gamma^2 - \delta^2)^{1/2}}\left[\frac{(\gamma + \delta^2) + (\gamma^2 - \delta^2)(1 - \epsilon)}{(\gamma + \delta^2) - \delta^2(1 - \epsilon)}\right]\tilde{u}_{xw+}$$

$$- \frac{\delta(\gamma + \delta^2)\epsilon}{(\gamma^2 - \delta^2)^{1/2}[(\gamma + \delta^2) - \delta^2(1 - \epsilon)]} , \quad (3.21)$$

where

$$\tilde{u}_{xw} \equiv 1 + u_{xw} \qquad (3.22)$$

and the velocities in Eqs. (3.20), (3.21), and (3.22) have been scaled by $\mathcal{D}(\gamma^2 - \delta^2)^{1/2}/(\gamma + 1)$. In the following sections, we will use the method of matched asymptotic expansions to find a solution to the stated problem in the limit of δ small. To simplify the notation, the subscript w and tildes will be dropped.

C. The Outer Problem

In applying a perturbation method to the solution of a problem, there are two essentially unique steps. The first is the determination of the form of the expansion of the dependent variable in terms of the small parameter. The second is the scaling by the small parameter of the independent variables. For the problem we are considering, the shock jump conditions argue strongly that an expansion of the dependent variables in integral powers of δ should be tried. Requiring that any solution that we generate include a sonic transition, the effects of reactivity, and streamline divergence, suggests that the independent variables be x and δy. Physically, we can understand the scaling of the independent variables as follows. Far from the edge we can expect the distance from the shock locus to the sonic locus to be near the undisturbed one-dimensional value which goes as x. Since the reaction zone is only slightly subsonic in the small δ limit, the flow at the shock changes from sonic at the edge to only slightly subsonic at great distances from the edge. Therefore, the sonic character of the flow is nearly the same everywhere so that there is little to differentiate the near from the far fields. The scale δy has this property.

We proceed with the perturbation solution by assuming that the dependent variables possess the following asymptotic expansions

$$u_x = \delta u_x^{(1)} + \delta^2 u_x^{(2)} + \dots \qquad (3.23)$$

$$u_y = \delta u_y^{(1)} + \delta^2 u_y^{(2)} + \dots \qquad (3.24)$$

$$c^2 = 1 + \delta(c^2)^{(1)} + \delta^2(c^2)^{(2)} + \dots \qquad (3.25)$$

$$\frac{\rho_0}{\rho} = \frac{\gamma}{\gamma + 1} + \delta\left(\frac{\rho_0}{\rho}\right)^{(1)} + \delta^2\left(\frac{\rho_0}{\rho}\right)^{(2)} + \dots \qquad (3.26)$$

$$\lambda = \lambda^{(0)} + \delta\lambda^{(1)} + \delta^2\lambda^{(2)} + \dots \qquad (3.27)$$

$$\epsilon = \epsilon^{(0)} + \delta\epsilon^{(1)} + \delta^2\epsilon^{(2)} + \dots, \qquad (3.28)$$

where c^2 has been scaled by $\mathcal{D}^2(\gamma^2 - \delta^2)/(\gamma + 1)^2$. The independent variables are taken to be

$$x^* = \frac{(\gamma + 1)k}{\mathcal{D}(\gamma^2 - \delta^2)^{1/2}} x \qquad (3.29)$$

$$\bar{y}^* = \delta \frac{(\gamma + 1)k}{\mathcal{D}(\gamma^2 - \delta^2)^{1/2}} y. \qquad (3.30)$$

(The asterisks will be deleted from our notation). Since the reaction zone we are considering is of finite length, it is necessary to transform to $\lambda, \bar{y}$ as the independent variable set to insure that the amount of energy added in the reaction zone is compatible with the value of $\mathcal{D}$. The differential operators are thus replaced by

$$\frac{\partial}{\partial x} = \left(\frac{\partial \lambda^{(0)}}{\partial x} + \delta \frac{\partial \lambda^{(1)}}{\partial x} + \dots\right) \frac{\partial}{\partial \lambda} \qquad (3.31)$$

$$\frac{\partial}{\partial y} = \delta \frac{\partial}{\partial \bar{y}} + \delta \left(\frac{\partial \lambda^{(0)}}{\partial \bar{y}} + \delta \frac{\partial \lambda^{(1)}}{\partial \bar{y}} + \dots\right) \frac{\partial}{\partial \lambda}. \qquad (3.32)$$

Substituting Eqs. (3.27) and (3.6) into Eq. (3.4) and setting to zero the terms of $O(1)$ and $O(\delta)$, we get equations for $\lambda^{(0)}$ and $\lambda^{(1)}$

$$\underline{O(1)} \quad \frac{\partial \lambda^{(0)}}{\partial x} = -(1 - \lambda^{(0)})^{1/2} \qquad (3.33)$$

$$\underline{O(\delta)} \quad \frac{\partial \lambda^{(1)}}{\partial x} = u_x^{(1)} \frac{\partial \lambda^{(0)}}{\partial x} + \frac{1}{2} \lambda^{(1)}(1 - \lambda^{(0)})^{-1/2}. \qquad (3.34)$$

Equation (3.33) can easily be solved, yielding

$$\lambda^{(0)} = 1 - \left[1 - \frac{1}{2}(x_s - x)\right]^2, \qquad (3.35)$$

where $x_s(\bar{y})$ is the shock locus. Before we can integrate Eq. (3.34) $u_x^{(1)}$ must be found.

We begin the analysis of our system by first eliminating c^2 by applying Bernoulli's law [Eq. (3.7)]

359

$$\underline{O(\delta)} \quad (c^2)^{(1)} = (\gamma - 1)u_x^{(1)} \tag{3.36}$$

$$\underline{O(\delta^2)} \ (c^2)^{(2)} = (\gamma - 1)\left[u_x^{(2)} - \frac{1}{2}(u_x^{(1)})^2\right.$$
$$\left. - \frac{1}{2}(u_y^{(1)})^2 + \frac{1}{2}\frac{\gamma + 1}{\gamma - 1}\frac{\lambda}{(\gamma^2 - \delta^2)}\right].$$
$$\tag{3.37}$$

Using Eqs. (3.28) and (3.32) it follows that the vorticity jump is $O(\delta^3)$. From the definition of the vorticity it then follows that

$$\underline{O(\delta)} \quad \frac{\partial u_y^{(1)}}{\partial \lambda} = 0 \tag{3.38}$$

$$\underline{O(\delta^2)} \quad \frac{\partial \lambda^{(0)}}{\partial x}\frac{\partial \lambda_y^{(0)}}{\partial \lambda} - \frac{\partial u_x^{(1)}}{\partial \bar{y}} - \frac{\partial \lambda^{(0)}}{\partial \bar{y}}\frac{\partial u_x^{(1)}}{\partial \lambda} = 0. \tag{3.39}$$

Making use of Eqs. (3.33) through (3.39), we find that Eq. (3.9) becomes

$$\underline{O(\delta^2)}$$

$$u_x^{(1)}\frac{\partial u_x^{(1)}}{\partial \lambda} - \frac{1}{(\gamma + 1)(1 - \lambda)^{1/2}}\frac{\partial u_y^{(1)}}{\partial \bar{y}} = -\frac{1}{2\gamma^2} \tag{3.40}$$

$$\underline{O(\delta^3)}$$

$$u_x^{(1)}\left(\frac{\partial \lambda^{(1)}}{\partial x}\frac{\partial u_x^{(1)}}{\partial \lambda} + \frac{\partial \lambda^{(0)}}{\partial x}\frac{\partial u_x^{(2)}}{\partial \lambda}\right)$$

$$+ \left[u_x^{(2)} - \frac{1}{2}(u_x^{(1)})^2 - \frac{1}{2}\left(\frac{\gamma - 1}{\gamma + 1}\right)(u_y^{(1)})^2\right.$$

$$\left. + \frac{\lambda}{2\gamma^2}\right]\frac{\partial \lambda^{(0)}}{\partial x}\frac{\partial u_x^{(1)}}{\partial \lambda} + \frac{2}{\gamma + 1}u_y^{(1)}\frac{\partial \lambda^{(0)}}{\partial x}\frac{\partial u_y^{(2)}}{\partial \lambda}$$

$$+ \frac{1}{\gamma + 1}\left(\frac{\partial u_y^{(2)}}{\partial \bar{y}} + \frac{\partial \lambda^{(0)}}{\partial \bar{y}}\frac{\partial u_y^{(2)}}{\partial \lambda}\right)$$

$$+ \left(\frac{\gamma - 1}{\gamma + 1}\right)u_x^{(1)}\frac{\partial u_y^{(1)}}{\partial \bar{y}} = 0 \tag{3.41}$$

plus higher order terms. Expanding the shock conditions [Eqs. (3.20) and (3.21)], we get

$$\underline{O(\delta)} \qquad u_{x+}^{(1)} = \frac{1}{\gamma}\sqrt{1 - (1 - \epsilon^{(0)})^2} \tag{3.42}$$

$$u_{y+}^{(1)} = -\frac{1}{\gamma}\epsilon^{(0)} \tag{3.43}$$

$$\underline{O(\delta^2)} \ u_{x+}^{(1)}u_{x+}^{(2)} = -\frac{1}{\gamma}(1 - \epsilon^{(0)})u_{y+}^{(2)} \tag{3.44}$$

$$u_{y+}^{(2)} = \left(\frac{\gamma + 1}{\gamma} - \epsilon^{(0)}\right)u_x^{(1)} - \frac{1}{\gamma}\epsilon^{(1)}. \tag{3.45}$$

The remaining boundary conditions require that the flow approach the one-dimensional limit as $\bar{y} \to -\infty$ and a Prandtl-Meyer singularity at $\bar{y} = 0$, $x \leqslant 0$.

The lowest order equations [Eqs. (3.38) and (3.40)] can be integrated without difficulty. Since $u_y^{(1)}$ is independent of λ, Eq. (3.40) can be treated as a first order ordinary differential equation (O.D.E.) in λ. As such it can satisfy only one boundary condition (shock condition) and the Prandtl-Meyer condition must be dropped. This then serves as the definition of the outer limit of the full problem:

Outer Problem. The system of O.D.E. [Eqs. (3.40), (3.41), etc.] and the shock boundary conditions which together describe the flow far from the Prandtl-Meyer singularity.

Solving Eq. (3.40), we get

$$(u_x^{(1)})^2 = (u_{x+}^{(1)})^2 + \frac{4}{\gamma + 1}\frac{du_y^{(1)}}{dy}[1 - (1 - \lambda)^{1/2}]$$

$$- \frac{1}{\gamma^2}[1 - (1 - \lambda)], \tag{3.46}$$

where $u_{x+}^{(1)}$ and $u_y^{(1)}$ are known functions of $\epsilon^{(0)}(\bar{y})$. Now, if Eq. (3.46) is to be an acceptable solution to our reactive flow problem, it must have the following properties: (1) $u_x^{(1)}$ must be real, and (2) $u_x^{(1)}$ must be equal to zero (sonic flow) at some point in the reaction zone. These can be considered as a generalized Chapman-Jouguet condition. Requiring this of Eq. (3.46) gives us a differential condition on $\epsilon^{(0)}$

360

$$\frac{d\epsilon^{(0)}}{dz} = 1 - \sqrt{1 - (1 - \epsilon^{(0)})^2}\,, \quad (3.47)$$

where $z \equiv -(\gamma + 1)\bar{y}/2\gamma$. Integrating Eq. (3.47) and requiring that $\epsilon^{(0)}(0) = 0$ gives us an implicit expression for the shock slope

$$\tan\left(\frac{\pi}{4} + \frac{\theta}{2}\right) - (1 + \theta) = z\,, \quad (3.48)$$

where $\cos\theta = 1 - \epsilon^{(0)}$. Transforming Eq. (3.18) into the edge sonic-line-fixed coordinates and integrating, we get a first approximation to the shock locus

$$x_s = \frac{2}{\gamma + 1}\left[\tan\left(\frac{\pi}{4} + \frac{\theta}{2}\right) - (1 + \theta) - \gamma\sin\theta\right.$$

$$\left. - \gamma\ln(1 - \sin\theta)\right]. \quad (3.49)$$

Therefore, the first approximation to the outer velocity field is

$$u_x^{(1)} = \frac{1}{\gamma}\sin\theta - \frac{1}{\gamma}[1 - (1 - \lambda)^{1/2}] \quad (3.50)$$

$$u_y^{(1)} = -\frac{1}{\gamma}(1 - \cos\theta)\,, \quad (3.51)$$

where $\lambda = 0$ at the shock.

We find that the above solution has the following properties:

(1) The solution merges into the one-dimensional flow as $\bar{y} \to -\infty$.

(2) The distance (along the laboratory x-coordinate) from $(0, 0)$ to the lead point on the shock is infinite (for the square-root rate law).

(3) The sonic line enters $(0, 0)$ with infinite slope instead of the required zero slope.

A plot of the shock locus and sonic locus is shown in Fig. 3.3. Therefore, we find that the outer solution agrees with both, the shock conditions and those at
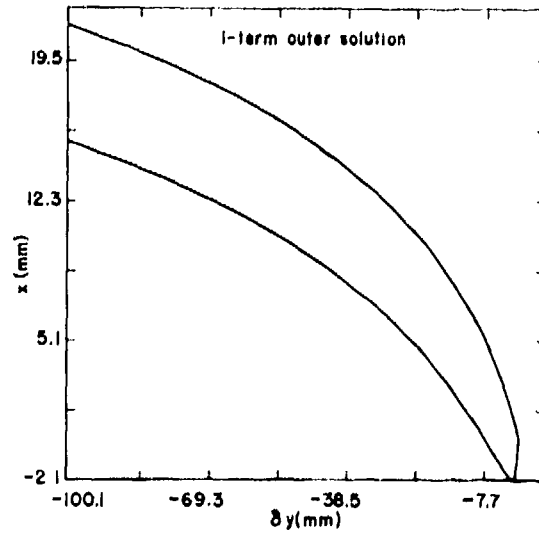
Fig. 3.3. 1-term outer solution. The shock locus (upper curve) and the sonic locus (lower curve) in edge fixed coordinates. The parameter values are $\mathcal{D} = 8\ mm/\mu s$, $\gamma = 3$, and $k = 2\ \mu s^{-1}$.

$\bar{y} \to -\infty$, but violates the conditions at the Prandtl-Meyer singularity. This is a substantial shortcoming.

Going on to the next order of the outer problem, matters become even worse. Solving Eqs. (3.34), (3.39), and (3.41) subject to Eq. (3.44), we find

$$u_x^{(2)} = u_{x+}^{(2)} + \frac{1}{2\gamma^2}\left[(\gamma - 2)(1 - \sin\theta)\right.$$

$$\left. - (\gamma + 1)(\csc\theta - 1)\left(\csc^2\theta - \frac{2\gamma + 1}{\gamma + 1}\sin\theta\right)\right]$$

$$\times [1 - (1 - \lambda)^{1/2}] \quad (3.52)$$

$$u_y^{(2)} = u_{y+}^{(2)} + \frac{\gamma + 1}{\gamma^2}\left[(1 - \sin\theta)\cot\theta - \frac{1 + \gamma\cos\theta}{\gamma + 1}\right]$$

$$\times [1 - (1 - \lambda)^{1/2}]\,, \quad (3.53)$$

where

$$u_{x+}^{(2)} = -u_{y+}^{(2)}\cot\theta \quad (3.54)$$

361

$$u_{y+}^{(2)} = \mathcal{C}'(1 - \sin\theta) + \frac{\gamma+1}{2\gamma^2}(1-\sin\theta)\ln\left(\tan\frac{\theta}{2}\right)$$

$$+ \frac{2}{\gamma}\cos\theta - \frac{5\gamma+3}{2\gamma^2}(1-\sin\theta)\theta$$

$$+ \frac{3}{2}\frac{\gamma+1}{\gamma^2}(1-\sin\theta)\cos\theta + \frac{1}{\gamma^2}, \qquad (3.55)$$

and $\mathcal{C}$ is an arbitrary constant. In the limit $\overline{y} \to -\infty$ ($\theta \to \pi/2$) the solution is well-behaved. However, near the edge ($\theta \to 0$) Eqs. (3.52), (3.53), (3.54), and (3.55) all become singular. To resolve this difficulty, we must examine the vicinity of the Prandtl-Meyer singularity in some detail. In the next section, we formulate the inner limit of our problem and show how the singularities in the outer problem can be removed.

D. The Inner Problem

The problem encountered at the end of the last section is similar in principle to that treated by Cole (6). There as here the singularity arises because the O.D.E. being studied has singular coefficients. However, in our case the resolution of the difficulty proceeds somewhat differently. The principal short-coming of the outer limit is that the O.D.E.'s which are obtained are capable of handling only a very restricted class of transonic flows. Since the reactivity is of secondary importance near the edge (relative to the Prandtl-Meyer singularity), let us neglect it and the vorticity for the moment and obtain the kernel transonic partial differential operator contained in Eq. (3.9). The object of this exercise is to obtain a partial differential equation (P.D.E.) which is capable of satisfying all of the applicable boundary conditions near the edge. We proceed by introducing a potential and scaled independent variables

$$\Psi = -x + \delta^m\phi(x,y) \qquad (3.56)$$

$$\widetilde{x} = x\delta^{-\nu}, \quad \widetilde{y} = y\delta^{-\mu}. \qquad (3.57)$$

Using Eqs. (3.56) and (3.57) to calculate the velocities and Bernoulli's law to eliminate c^2, the dominant terms in Eq. (3.9) yield the equation

$$(\gamma+1)\frac{\partial\phi}{\partial\widetilde{x}}\frac{\partial^2\phi}{\partial\widetilde{x}^2} + \frac{\partial^2\phi}{\partial\widetilde{y}^2} = 0, \qquad (3.58)$$

where we have the constraint

$$3(m-\nu) = 2(m-\mu). \qquad (3.59)$$

Equation (3.58) is the model equation for transonic flow (7). It is capable of describing the flow in the neighborhood of a Prandtl-Meyer singularity imbedded in a mixed flow. In fact, the specification of a unique solution of Eq. (3.58) requires that ϕ be given along the shock, a curve connecting the shock to the sonic locus, as well as the Prandtl-Meyer condition. To determine the parameters m, ν, and μ, we require that the orders of magnitude of the velocities calculated from Eq. (3.58) match the dominant singularities found in the outer solution. This can be thought of as satisfying the boundary conditions along a curve connecting the shock locus to the sonic locus in an order of magnitude sense. The most singular terms in $u_x^{(2)}$ and $u_y^{(2)}$ are

$$\delta^2 u_x^{(2)} = 0(\delta^{1/2+\nu-3\mu/2})\frac{\widetilde{x}}{(-\widetilde{y})^{3/2}} \qquad (3.60)$$

$$\delta^2 u_y^{(2)} = 0(\delta^{1/2+\nu-3\mu/2})\frac{\widetilde{x}}{(-\widetilde{y})^{1/2}}, \qquad (3.61)$$

so that we get the conditions

$$\frac{1}{2} + \nu - \frac{3}{2}\mu = m - \nu \qquad (3.62)$$

$$\frac{3}{2} + \nu - \frac{1}{2}\mu = m - \mu. \qquad (3.63)$$

Solving Eqs. (3.59), (3.62), and (3.63), we get

$$\phi = O(\delta^{5/3}), \quad \widetilde{x} = x/\delta^{1/3}, \quad \widetilde{y} = \delta^{1/3}y \qquad (3.64)$$

$$u_x = O(\delta^{4/3}), \quad u_y = O(\delta^2). \qquad (3.65)$$

In terms of the variables of Eq. (3.64) the remaining singular terms in the outer $u_x^{(2)}$ and $u_y^{(2)}$ are

$$\delta^2 u_x^{(2)}: \quad \delta^{5/3}\frac{\ln(-\widetilde{y})}{(-\widetilde{y})^{1/2}} + \frac{2}{3}\delta^{5/3}\frac{\ln\delta}{(-\widetilde{y})^{1/2}} \qquad (3.66)$$

$$\delta^2 u_y^{(2)}: \quad \delta^2\ln(-\widetilde{y}) + \frac{2}{3}\delta^2\ln\delta. \qquad (3.67)$$

362

When expressed in terms of Eq. (3.64), the dominant terms in the outer $u_x^{(1)}$ and $u_y^{(1)}$ are $O(\delta^{4/3})$ and $O(\delta^{5/3})$ respectively.

Using this information as a guide, we assume that the flow potential can be expressed as the following asymptotic sequence

$$\phi = \delta^{4/3}\phi^{(4/3)} + \delta^{5/3} \ln\delta \, \phi^{(\ell 5/3)} + \delta^{5/3}\phi^{(5/3)}$$
$$+\delta^2 \ln\delta \, \phi^{(\ell 2)} + \delta^2\phi^{(2)} + \delta^{7/3} \ln\delta \, \phi^{(\ell 7/3)}$$
$$+\delta^{7/3}\phi^{(7/3)} + \dots, \tag{3.68}$$

which is valid for velocities up to at least $O(\delta^{7/3})$ since Eq. (3.16) gives

$$\Omega_+ = O(\delta^{7/3}) \, \frac{d(1-\epsilon)^2}{d\tilde{y}} \,. \tag{3.69}$$

For this set of dependent and independent scales, the reaction progress variable must be

$$\lambda = \delta^{1/3}\lambda^{(1/3)} + \delta^{2/3}\lambda^{(2/3)} + \dots, \tag{3.70}$$

where $\lambda^{(1/3)}$ and $\lambda^{(2/3)}$ satisfy

$$\frac{\partial\lambda^{(1/3)}}{\partial\tilde{x}} = -1 \tag{3.71}$$

$$\frac{\partial\lambda^{(2/3)}}{\partial\tilde{x}} = \frac{1}{2}\,\lambda^{(1/3)}\,, \tag{3.72}$$

so that

$$\lambda^{(1/3)} = \tilde{x}_s - \tilde{y} \tag{3.73}$$

$$\lambda^{(2/3)} = -\frac{1}{4}\,(\tilde{x}_s - \tilde{x})^2 \,. \tag{3.74}$$

Introducing $\tilde{\lambda} \equiv \lambda/\delta^{1/3}$ and $\tilde{y}$ as the independent variables, Eqs. (3.7) and (3.9) yield the following set of equations for ϕ:

$\underline{O(\delta^{5/3})}$

$$\frac{\partial}{\partial\tilde{\lambda}}\left(\frac{\partial\phi^{(4/3)}}{\partial\tilde{\lambda}}\right)^2 = 0 \tag{3.75}$$

$\underline{O(\delta^2 \ln \delta)}$

$$\frac{\partial}{\partial\tilde{\lambda}}\left(\frac{\partial\phi^{(4/3)}}{\partial\tilde{\lambda}}\,\frac{\partial\phi^{(\ell 5/3)}}{\partial\tilde{\lambda}}\right) = 0 \tag{3.76}$$

$\underline{O(\delta^2)}$

$$-(\gamma+1)\,\frac{\partial}{\partial\tilde{\lambda}}\left(\frac{\partial\phi^{(4/3)}}{\partial\tilde{\lambda}}\,\frac{\partial\phi^{(5/3)}}{\partial\tilde{\lambda}}\right)$$
$$+\frac{1}{2}\,(\gamma+1)\left(\frac{\partial\phi^{(4/3)}}{\partial\tilde{\lambda}}\right)^2 + \frac{\partial^2\phi^{(4/3)}}{\partial\tilde{y}^2} = \frac{(\gamma+1)}{2\gamma^2} \tag{3.77}$$

$\underline{O(\delta^{7/3}(\ln \delta)^2)}$

$$\frac{\partial}{\partial\tilde{\lambda}}\left(\frac{\partial\phi^{(\ell 5/3)}}{\partial\tilde{\lambda}}\right)^2 = 0 \tag{3.78}$$

$\underline{O(\delta^{7/3} \ln \delta)}$

$$-(\gamma+1)\,\frac{\partial}{\partial\tilde{\lambda}}\left(\frac{\partial\phi^{(4/3)}}{\partial\tilde{\lambda}}\,\frac{\partial\phi^{(\ell 2)}}{\partial\tilde{\lambda}} + \frac{\partial\phi^{(\ell 5/3)}}{\partial\tilde{\lambda}}\,\frac{\partial\phi^{(5/3)}}{\partial\tilde{\lambda}}\right)$$
$$+\frac{1}{2}\,(\gamma+1)\left(\frac{\partial\phi^{(\ell 5/3)}}{\partial\tilde{\lambda}}\,\frac{\partial\phi^{(4/3)}}{\partial\tilde{\lambda}}\right) + \frac{\partial^2\phi^{(\ell 5/3)}}{\partial\tilde{y}^2} = 0 \tag{3.79}$$

$\underline{O(\delta^{7/3})}$

$$-(\gamma+1)\,\frac{\partial}{\partial\tilde{\lambda}}\left[\frac{1}{2}\left(\frac{\partial\phi^{(5/3)}}{\partial\tilde{\lambda}}\right)^2 + \frac{\partial\phi^{(4/3)}}{\partial\tilde{\lambda}}\,\frac{\partial\phi^{(2)}}{\partial\tilde{\lambda}}\right.$$
$$\left.-\tilde{\lambda}\,\frac{\partial\phi^{(4/3)}}{\partial\tilde{\lambda}}\,\frac{\partial\phi^{(5/3)}}{\partial\tilde{\lambda}} - \frac{1}{2}\,\frac{\partial\phi^{(4/3)}}{\partial\tilde{\lambda}}\,\frac{\partial\phi^{(5/3)}}{\partial\tilde{\lambda}}\right]$$
$$-\frac{1}{2}\,(\gamma+1)\tilde{\lambda}\left(\frac{\partial\phi^{(4/3)}}{\partial\tilde{\lambda}}\right)^2 + \frac{\partial^2\phi^{(5/3)}}{\partial\tilde{y}^2}$$
$$-\tilde{\lambda}\,\frac{d\tilde{x}_s}{d\tilde{y}}\,\frac{\partial^2\phi^{(4/3)}}{\partial\tilde{y}\partial\tilde{\lambda}} = -\frac{(\gamma+1)}{4\gamma^2}\,\tilde{\lambda}\,. \tag{3.80}$$

363

Since the higher order equations are increasingly more complex, we will not consider them here. Doing so will not affect the first approximation to the uniformly valid solution.

Let us now obtain the boundary conditions for Eqs. (3.75)–(3.80). Given the potential of Eq. (3.68) and the shock condition of Eq. (3.21), we take

$$\epsilon = \delta^{2/3} \epsilon^{(2/3)} + \delta \ln\delta \, \epsilon^{(\ell 1)} + \delta \epsilon^{(1)}$$

$$+ \delta^{4/3} \ln\delta \, \epsilon^{(\ell 4/3)} + \dots \tag{3.81}$$

Substituting Eq. (3.81) and the velocities into Eqs. (3.20) and (3.21), we get the shock boundary conditions

$$O(\delta^{5/3}) \quad \left(\frac{\partial\phi^{(4/3)}}{\partial\tilde{\lambda}}\right)_+ = 0 \tag{3.82}$$

$$O(\delta^{7/3}(\ln\delta)^2) \quad \left(\frac{\partial\phi^{(\ell 5/3)}}{\partial\tilde{\lambda}}\right)_+ = 0 \tag{3.83}$$

$$O(\delta^{7/3}) \quad \left(\frac{\partial\phi^{(5/3)}}{\partial\tilde{\lambda}}\right)_+^2 = -\frac{2}{\gamma}\left(\frac{\partial\phi^{(4/3)}}{\partial\tilde{y}}\right)_+ \tag{3.84}$$

$$O(\delta^{5/3} \ln\delta) \quad \left(\frac{\partial\phi^{(\ell 2)}}{\partial\tilde{\lambda}}\right)_+ = 0 \tag{3.85}$$

$$O(\delta^{8/3}) \quad \left(\frac{\partial\phi^{(5/3)}}{\partial\tilde{\lambda}}\right)_+ \left(\frac{\partial\phi^{(2)}}{\partial\tilde{\lambda}}\right)_+ = -\frac{1}{\gamma}\left(\frac{\partial\phi^{(5/3)}}{\partial\tilde{y}}\right)_+ , \tag{3.86}$$

where the terms in the shock slope are

$$\epsilon^{(2/3)} = -\gamma\left(\frac{\partial\phi^{(4/3)}}{\partial\tilde{y}}\right)_+ , \quad \epsilon^{(\ell 1)} = 0 \tag{3.87}$$

$$\epsilon^{(1)} = -\gamma\left(\frac{\partial\phi^{(5/3)}}{\partial\tilde{y}}\right)_+ , \quad \epsilon^{(\ell 4/3)} = -\gamma\left(\frac{\partial\phi^{(\ell 2)}}{\partial\tilde{y}}\right)_+ .$$

Far from the edge (i.e., $-\tilde{y}$ large), the flow calculated for the inner problem must match that of the outer problem. Calculating the outer potential from

Eqs. (3.50), (3.51), (3.52), and (3.53) and then taking the inner limit of this outer potential gives us the match potential for the inner problem

$$\phi = \delta^{4/3} \frac{\gamma+1}{4\gamma^2} \tilde{y}^2 + \delta^{5/3}\left\{-\frac{1}{\gamma}\left(\frac{\gamma+1}{\gamma}\right)^{1/2}(-\tilde{y})^{1/2}\tilde{\lambda}\right.$$

$$+\frac{1}{4\gamma}\tilde{\lambda}^2 - \frac{\gamma+1}{4\gamma^2}(-\tilde{y})\ln(-\tilde{y})$$

$$\left. -\frac{2}{15}\frac{1}{\gamma}\left(\frac{\gamma+1}{\gamma}\right)^{3/2}(-\tilde{y})^{5/2}\right\}$$

$$+\delta^2\left\{\frac{1}{2}\frac{\gamma+1}{\gamma^2}(-\tilde{y})\tilde{\lambda} - \frac{1}{4\gamma}\left(\frac{\gamma+1}{\gamma}\right)^{1/2}(-\tilde{y})^{1/2}\tilde{\lambda}^2\right.$$

$$+\frac{1}{8\gamma}\tilde{\lambda}^3 + \frac{1}{6\gamma}\left(\frac{\gamma+1}{\gamma}\right)^{3/2}(-\tilde{y})^{3/2}[\ln(-\tilde{y})+7]$$

$$\left. +\frac{1}{36\gamma}\left(\frac{\gamma+1}{\gamma}\right)^2(-\tilde{y})^3\right\} , \tag{3.88}$$

where we have set the arbitrary constant in Eq. (3.55) equal to

$$\mathcal{C} = -\frac{\gamma+1}{4\gamma^2}\left[\ln\left(\frac{\gamma+1}{4\gamma}\delta^{2/3}\right)-1\right] - \frac{7\gamma+5}{2\gamma^2} .$$

Lastly we have the Prandtl-Meyer condition at $\tilde{y} = 0^-$, $\tilde{x} = 0^-$. Thus, the inner limit of the full problem is:

Inner Problem. – The system of P.D.E. [Eqs. (3.75), (3.76), (3.77), (3.78), (3.79), (3.80), etc.], the shock boundary conditions [Eqs. (3.82), (3.83), (3.84), (3.85), (3.86), (3.87), etc.], the match into the outer problem [Eq. (3.88)], and the Prandtl-Meyer singularity which together describe the flow near the edge.

Finding the solution of Eqs. (3.75), (3.76), (3.77), (3.78), and (3.79) subject to the appropriate boundary conditions is straightforward. We obtain

$$\phi^{(4/3)} = \frac{\gamma + 1}{4\gamma^2}\ \tilde{y}^2 \qquad (3.89)$$

$$\phi^{(\ell 5/3)} = 0\ . \qquad (3.90)$$

Using these results to simplify Eq. (3.80), we get

$$-(\gamma + 1)\ \frac{\partial\phi^{(5/3)}}{\partial\tilde{\lambda}}\ \frac{\partial^2\phi^{(5/3)}}{\partial\tilde{\lambda}^2} + \frac{\partial^2\phi^{(5/3)}}{\partial\tilde{y}^2} = -\frac{\gamma + 1}{4\gamma^2}\ \tilde{\lambda}\ . \qquad (3.91)$$

Equation (3.91) is an inhomogeneous transonic P.D.E. Finding an analytic solution to it subject to the shock, match, and Prandtl-Meyer boundary conditions is not a simple matter. Since the reactivity is not a dominant effect near the edge, we will first examine the homogeneous form of Eq. (3.91). The simplest approach is to seek a similarity solution to Eq. (3.91). The drawback with this method is that one may not be able to satisfy all of the boundary conditions.

The most general similarity solution to the homogeneous form of Eq. (3.91) is that solution which is invariant under an infinitesimal one-parameter Lie group of transformations. We find

$$\phi_h = -(-\tilde{y} + b_2)^{3\eta - 2}G(s) + (-\tilde{y} + b_2)B_1 + B_2 \qquad (3.92)$$

$$\frac{\partial\phi_h}{\partial\tilde{\lambda}} = (\gamma + 1)^{-1/3}(-\tilde{y} + b_2)^{2\eta - 2}G'(s) \qquad (3.93)$$

$$s = \frac{-\tilde{\lambda}(\gamma + 1)^{-1/3} + b_1}{(-\tilde{y} + b_2)^\eta}\ , \qquad (3.94)$$

where $\eta, b_1, b_2, B_1, \dots, B_2$ are constants and $G(s)$ satisfies the O.D.E.

$$(G' - \eta^2 s^2)G'' + 5\eta(\eta - 1)sG' - 3(\eta - 1)(3\eta - 2)G = 0. \qquad (3.95)$$

(See Bluman and Cole (8).) Setting B_1, B_2, b_2 to zero, $\eta = 5/4$, and assuming that $b_1 = O(\delta^{1/3})$, we find that Eq. (3.93) satisfies Eq. (3.84) to within a distance $O(\delta^{-/3})$ of the shock. Analyzing the singular points of Eq. (3.95) we find a Prandtl-Meyer singularity at $\tilde{\lambda} = 0^+, \tilde{y} = 0^-$ (i.e., $s \to -\infty$) when

$b_1 = 0$ at the edge. Taking b_1 to be a function of $\tilde{y}$ which behaves like $(\gamma + 1)^{-1/3}\tilde{x}_s$ near the edge and never exceeding $O(\delta^{1/3})$ far from the edge, the sonic line leaves the singularity along the $-\tilde{y}$ axis as required. Since $b_1 = O(\delta^{1/3})$ the error made in Eq. (3.91) is of higher order and will be recovered as the higher order equations are considered. Fortunately, for $\eta = 5/4$ the solution to Eq. (3.95) can be found in closed form (9,10)

$$\phi_h = \frac{9}{56}\ \alpha^{-3}(-\tilde{y})^{7/4}\left(-\frac{3}{5}\ \xi\right)^{-9/8}\left(\xi^2 + \frac{14}{3}\ \xi + \frac{7}{27}\right), \qquad (3.96)$$

where α is an arbitrary scaling constant and

$$\left(\frac{3}{5}\ \xi + 1\right)\left(-\frac{3}{5}\ \xi\right)^{-3/8} = -2\alpha s\ . \qquad (3.97)$$

Therefore, we find that an analytic solution of the homogeneous form of Eq. (3.91) can be found that satisfies both the shock and the Prandtl-Meyer boundary conditions.

Finding a solution to the inhomogeneous form of Eq. (3.91) is more difficult. One possibility is to express $\phi^{(5/3)}$ as an infinite power series in $(-\tilde{y})$

$$\phi^{(5/3)} = \phi_h + \sum_\nu (-\tilde{y})^\nu f_\nu(\xi)\ , \qquad (3.98)$$

with the ν's being selected so that the inhomogeneity in Eq. (3.91) is accounted for. Proceeding in this fashion, we find that the $f_\nu(\xi)$'s satisfy an inhomogeneous hypergeometric equation whose homogeneous solutions are terminating series in ξ. Therefore, as a practical matter, the $f_\nu(\xi)$'s are obtainable. The sonic locus computed from the inner solution, $\phi^{(5/3)} = \phi_h + (-\tilde{y})^{1\ 3/4}f_{1\ 3/4}(\xi)$, is shown in Fig. 3.5. Now, if Eq. (3.98) is to be a useful inner solution, it must be valid for $\tilde{y} \to -\infty$. Clearly, any finite sum does not have this property. As an alternative, let us consider the expression

$$\phi^{(5/3)} \simeq \psi \equiv \phi_h + \frac{1}{4\gamma}\ \tilde{\lambda}^2$$

$$-\frac{2}{15}\ \frac{\gamma + 1}{\gamma}\ \alpha^{-2}(\gamma + 1)^{-1/3}(-\tilde{y})^{5/2} \qquad (3.99)$$

365

as a possible approximate solution valid for $-\infty \leqslant \tilde{y} \leqslant 0$. The motivation for selecting Eq. (3.99) is that it yields the same $\tilde{x}$ – velocity component as the match potential of Eq. (3.88) and in addition, satisfies the shock and Prandtl-Meyer conditions. Substituting Eq. (3.99) into Eq. (3.91), we find that ψ satisfies

$$-(\gamma + 1)\frac{\partial \psi}{\partial \tilde{\lambda}} \frac{\partial^2 \psi}{\partial \tilde{\lambda}^2} + \frac{\partial^2 \psi}{\partial \tilde{y}^2} = -\frac{\gamma + 1}{4\gamma^2}\tilde{\lambda} - R,$$

$$(3.100)$$

where the remainder is

$$R = \frac{\gamma + 1}{2\gamma}\, \alpha^{-2}(\gamma + 1)^{-1/3}(-\tilde{y})^{1/2}$$

$$\times \left[1 + \frac{3}{4}\left(-\frac{3}{5}\xi\right)^{-3/4}\left(\frac{7}{5}\xi + 1\right)\right]. \quad (3.101)$$

Although it would be difficult to get a rigorous error bound on $|\phi^{(5/3)} - \psi|$, we can get some estimates of the degree to which ψ satisfies Eq. (3.91) in a global sense. Writing Eq. (3.100) in divergence form and then integrating over some closed region $\mathfrak{a}$ in $\tilde{\lambda}$, $\tilde{y}$, we get

$$\oint \underline{m} \cdot \left[-\underline{i}\,\frac{\gamma + 1}{2}\left(\frac{\partial \psi}{\partial \tilde{\lambda}}\right)^2 + \underline{j}\,\frac{\partial \psi}{\partial \tilde{y}}\right] d\ell =$$

$$-\iint_{\mathfrak{a}}\left[\frac{\gamma + 1}{4\gamma^2}\tilde{\lambda} + R\right]d\tilde{\lambda}d\tilde{y}, \quad (3.102)$$

where $\underline{m}$ is the outward normal to the boundary of $\mathfrak{a}$. We first consider the region $\mathfrak{a}_1$ near the Prandtl-Meyer singularity (see Fig. 3.4). There we readily find that the source due to the Prandtl-Meyer singularity, S_{pm}

$$S_{pm} = O\left(\frac{\sin^4\theta}{\cos^3\theta}\right), \quad (3.103)$$

is stronger than the effective reactive source

$$-\iint_{\mathfrak{a}_1}\left[\frac{\gamma + 1}{4\gamma^2}\tilde{\lambda} + R\right]d\tilde{\lambda}d\tilde{y} = O\left(\tilde{\lambda}^2\,\frac{\sin\theta}{\cos\theta}\right),$$

$$(3.104)$$
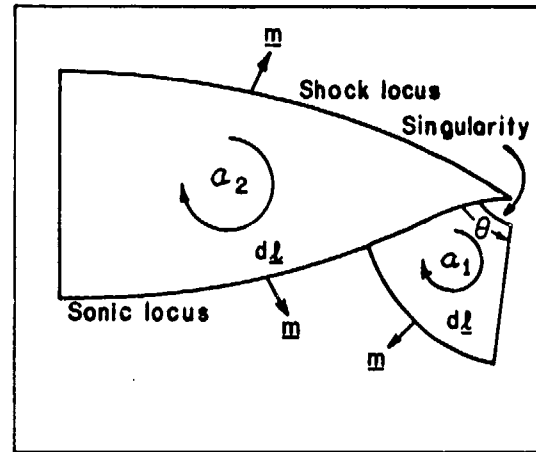
Fig. 3.4. Regions of the flow over which the global accuracy of the flow ψ is examined. $\mathfrak{a}_1$ is the neighborhood of the P-M singularity. $\mathfrak{a}_2$ is the region of subsonic flow.

in the region of the singularity. Focusing our attention on region $\mathfrak{a}_2$, we find that

$$\iint_{\mathfrak{a}_2} R\,d\tilde{\lambda}d\tilde{y} = 0, \quad (3.105)$$

when the lower boundary (sonic locus) is taken as either the sonic locus for the near-field homogeneous flow given in Eq. (3.96) ($\xi = -1/3$) or the sonic locus for the far-field flow given in Eq. (3.88). For any other lower boundary of region $\mathfrak{a}_2$

$$\iint_{\mathfrak{a}_2} \tilde{\lambda}\,d\tilde{\lambda}d\tilde{y} = O((-\tilde{y})^{7/2}) \quad (3.106)$$

$$\iint_{\mathfrak{a}_2} R\,d\bar{\tilde{\lambda}}d\tilde{y} = O((-\tilde{y})^{11/4}). \quad (3.107)$$

Therefore, ψ represents a reasonable approximation to Eq. (3.91) in a global sense. Comparing the inner sonic locus calculated via Eq. (3.98) (one term past the homogeneous solution) to that calculated via Eq. (3.99), we find little difference in the range $-0.8 \leq \tilde{y} \leq 0$ (see Fig. 3.5). Thus we conclude that Eq. (3.99) provides a reasonable approximation to the velocity $\partial\phi^{(5/3)}/\partial\tilde{\lambda}$. Since $\partial\phi^{(5/3)}/\partial\tilde{\lambda}$ contributes

366
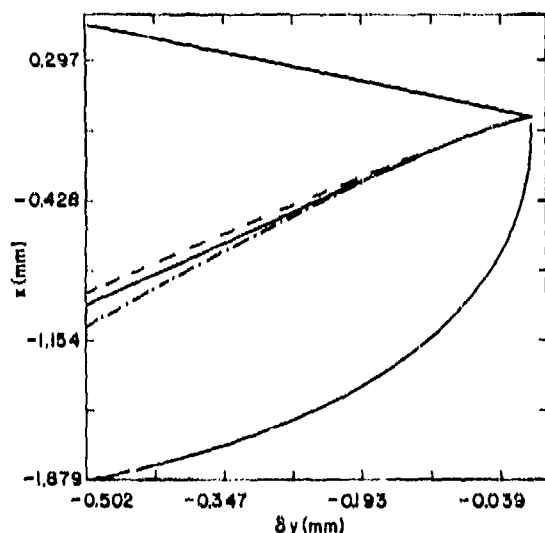
Fig. 3.5. A comparison of the inner sonic locus as calculated with the flow of Eq. (3.96) (−·−), Eq. (3.98) (—), and Eq. (3.99) (− −) displayed in edge fixed coordinates. In all cases $b_1 = (\gamma + 1)^{-1/3}\tilde{x}_s$. The 1-term outer shock locus (upper curve) and sonic locus (lower curve) appear as references. The parameter values are $\mathcal{D} = 8$ mm/μs, $\gamma = 3$, $k = 2$ μs^{-1}, $\delta = 0.1$.

to the velocity at $O(\delta^{4/3})$, and whereas $\partial\phi^{(5/3)}/\partial\tilde{y}$ contributes at $O(\delta^{5/3})$, it follows that the boundary terms in Eq. (3.88) that have been omitted will not influence the solution up to and including $O(\delta^{4/3})$ in the velocity. If a solution valid to $O(\delta^{5/3})$ in the velocities is desired, the equation governing $\phi^{(2)}$ must be found (a simple matter), and Eq. (3.99) must be discarded in favor of a $\phi^{(5/3)}$ that satisfies all of the match conditions in Eq. (3.88).

Summarizing, we find that the inner velocities [i.e., Eqs. (3.89), (3.90), and (3.99)] have been calculated up to and including $O(\delta^{4/3})$. To this order, the shock locus is given by the 1-term outer solution [Eq. (3.49)]. However, probably the most important result is qualitative rather than quantitative. We find that the features of the inner flow depend on $\delta^{1/3}y$ and thus can penetrate well into the explosive.

E. The Composite Solution

The outer and inner solutions found in the previous sections are valid over only restricted regions in

y. To get a uniformly valid asymptotic expansion of the solution, the two limiting solutions must be matched in a region of overlapping validity. Following Van Dyke's matching procedure, we express the outer solution in inner variables, the inner solution in outer variables, and then match at each order in δ (11). The composite expansion is then formed as the inner expansion plus the outer expansion minus the terms that are common to both in the overlap region. Retaining terms up to and including $O(\delta^{4/3})$ in the velocities, the composite velocity expansions are

$$u_x = \delta \frac{1}{\gamma} \{\sin\theta - [1 - (1-\lambda)^{1/2}]\}$$

$$-\delta^{4/3} \frac{1}{\gamma}\left(\frac{\gamma+1}{\gamma}\right)^{1/2} (-\tilde{y})^{1/2} \frac{3}{4}\left(\xi + \frac{1}{3}\right)\left(-\frac{3}{5}\xi\right)^{-3/4}$$

$$-\delta \frac{1}{\gamma}\left(\frac{\gamma+1}{\gamma}\right)^{1/2} (-\bar{y})^{1/2} \qquad (3.108)$$

$$u_y = -\delta \frac{1}{\gamma} (1 - \cos\theta) , \qquad (3.109)$$

where the match requires that

$$\alpha = \frac{\gamma^{3/4}}{(\gamma+1)^{5/12}} . \qquad (3.110)$$

To this order the shock locus is given by Eq. (3.49).

Equations (3.108), (3.109) and the required auxiliary equations constitute a full solution to $O(\delta^{4/3})$ of the boundary value problem posed in part A. of this section. Using it we will now determine some of the salient features of the flow. In all of the examples, we will take the function b_1 appearing in the similarity variable to be

$$b_1 = \delta^{1/3} \frac{k(\gamma+1)^{5/3}}{D\gamma^2} \tanh\left(-\frac{\mathcal{D}\gamma}{k(\gamma+1)}\tilde{y}\right). \qquad (3.111)$$

Figures 3.6 and 3.7 show a comparison of the outer and composite solutions in the far and near fields respectively. To $O(\delta^{4/3})$, the shock loci for the two solutions are identical. The sonic loci, however, are quite dissimilar. Unlike the outer solution,

Fig. 3.6. $O(\delta^{4/3})$ composite solution. The shock locus (upper curve), composite sonic locus (middle curve), and outer sonic locus (lower curve) in edge fixed coordinates. The parameter values are $\mathcal{D} = 8\ mm/\mu s$, $\gamma = 3$, $k = 2\ \mu s^{-1}$, and $\delta = 0.1$.
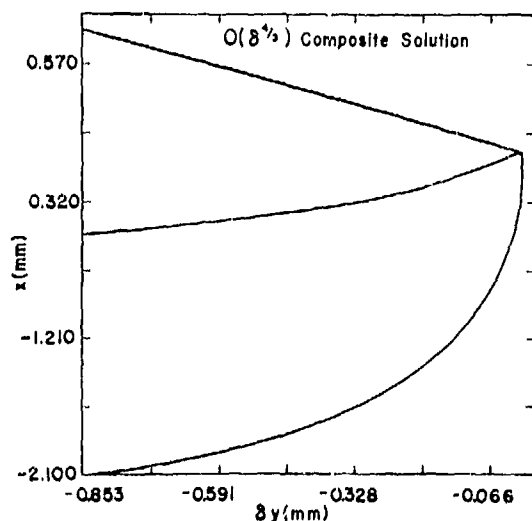
Fig. 3.7. $O(\delta^{4/3})$ composite solution. See Fig. 3.6.

the composite solution satisfies the conditions at the Prandtl-Meyer singularity (see Fig. 3.7). Perhaps the most striking feature of the composite flow is the range over which the edge, through the inner solution,

influences the flow. Figure 3.8 shows that the influence propagates in $\simeq 50$ reaction zone lengths. Considering that the inner scale is $\delta^{1/3}y$ and that $\delta^{1/3}$ changes by only a factor of two for $0.01 \leqslant \delta^2 \leqslant 1$, the range of influence of the inner solution (in real sapce) is nearly the same for large and small values of δ. However, since the outer scale is δy, the inner solution becomes relatively more important as δ is increased. Figure 3.9 shows that increasing δ from 0.1 to 0.33 makes the inner solution relatively more important.

Although the sonic locus is not a flow property which is physically as apparent as the shock locus, it is of greater importance in determining the flow. This is because only the chemical energy released in the subsonic region is effective in driving the detonation. It is for this reason that proper satisfaction of the Prandtl-Meyer condition is crucial to any calculation. As an example, consider the case of an explosive charge of finite size. Including the energy released in the shaded area of Fig. 3.8 (unavailable energy) in the calculation of the detonation velocity would lead to a substantial error. More important perhaps is the effect that the form of the inner solution has on the problem of confinement. Considering the family of characteristics emanating from the Prandtl-Meyer singularity, we find a characteristic (the limiting characteristic) which is just tangent to the sonic locus (see Fig. 3.10). All the characteristics leaving the singularity downstream of the limiting
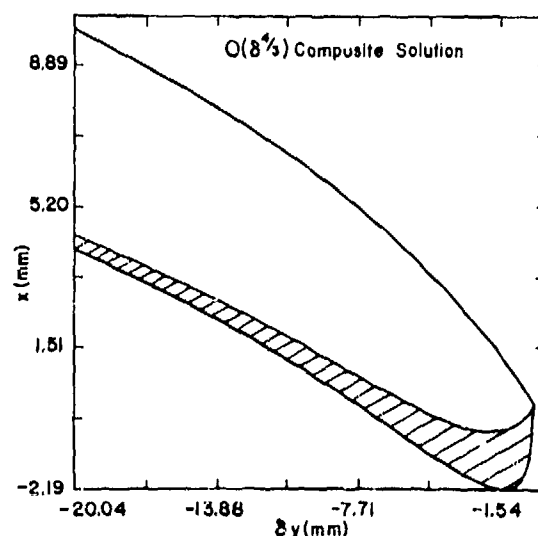
Fig. 3.8. $O(\delta^{4/3})$ composite solution. See Fig. 3.6.

368
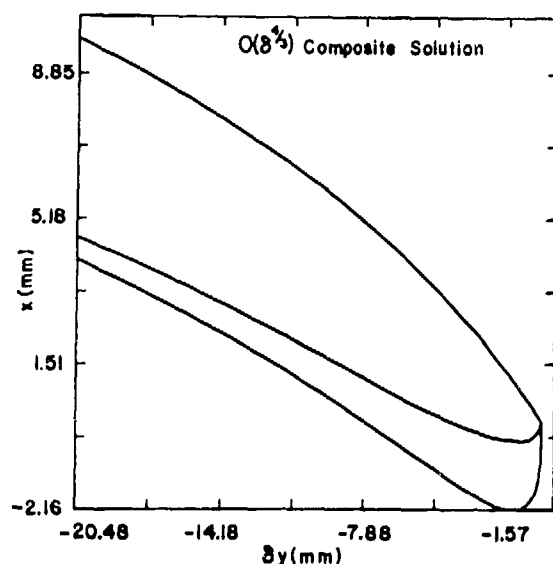
Fig. 3.9. $O(\delta^{4/3})$ composite solution. The parameter values are $D = 8\ mm/\mu s$, $\gamma = 3$, $k = 2\ \mu s^{-1}$, and $\delta = 0.33$.
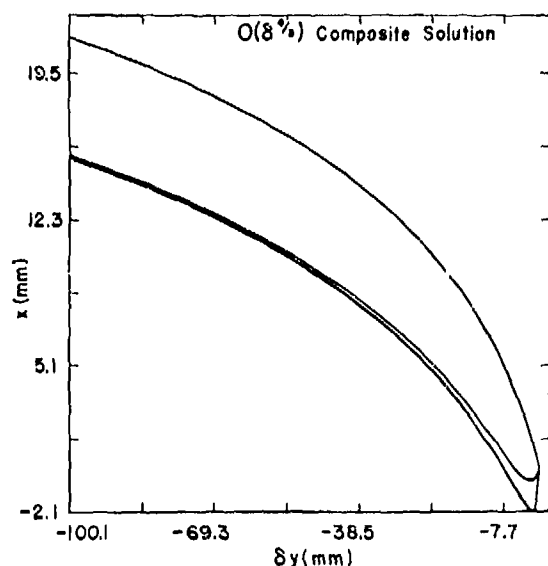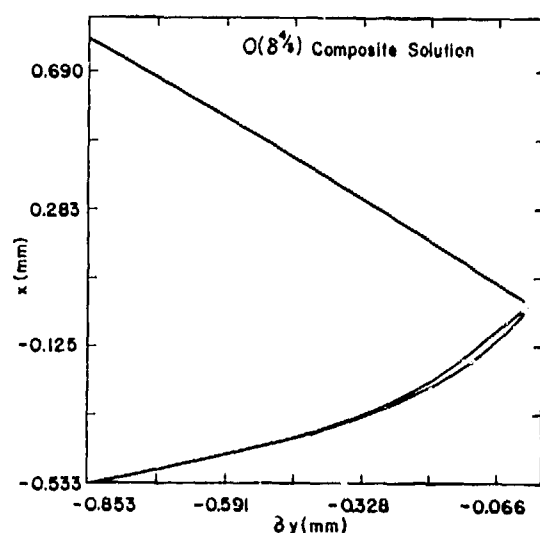

Fig. 3.10. $O(\delta^{4/3})$ composite solution. The shock locus (upper curve), composite sonic locus (middle curve) and limiting characteristic (lower curve) in edge fixed coordinates. The parameter values are $\mathfrak{D} = 8\ mm/\mu s$, $\gamma = 3$, $k = 2\ \mu s^{-1}$, and $\delta = 0.1$.

characteristic never contact the sonic locus. Therefore, information about confinement traveling along them cannot influence the structure of the subsonic flow. Put another way, the limiting characteristic defines the critical degree of confinement below which the confinement has no influence on the structure of the subsonic flow. For the example considered in Fig. 3.10 the critical confinement angle (i.e., the angle that the wall makes with the x-axis) for a sufficiently smooth wall is 1.94^0. For a system with the parameter values given in Fig. 3.9 (i.e., increasing δ to 0.33) the critical confinement angle is 6.63^0. In both cases, these angles are equal to the streamline angle at the sonic point on the shock. Therefore, we find that the resolved-δ^2 portion of the reaction zone for a system with an edge proceeds as an essentially unconfined detonation unless the confinement is heavy (i.e., aluminum or heavier).

F. Summary

Reviewing the results of this section, we find:
(1) Far from the edge (outer region) the flow is governed by O.D.E.'s (with independent variables x, δy) and the shock boundary conditions. The outer problem determines the shock locus to $O(\delta^{4/3})$ for $-\infty \leqslant y \leqslant 0$ and the sonic locus in the very far field. (2) Near the edge (inner region) the flow is governed by P.D.E.'s (with the independent variables $x/\delta^{1/3}$, $\delta^{1/3}y$) and the boundary conditions along the shock locus, at the Prandtl-Meyer singularity, and the match into the outer solution. The inner problem, which is strongly influenced by the singularity, has a long range influence on the sonic locus and properties which depend on it. (3) The critical confinement angle is equal to the angle that the streamlines at the sonic point on the shock make with the edge.

ACKNOWLEDGMENTS

REFERENCES

1. J. B. Bdzil and W. C. Davis, Los Alamos Report, LA-5926-MS, p. 14 (1975).

2. A. H. Nayfeh, *Perturbation Methods*, p. 228, Wiley, New York (1973).

3. James Serrin, *The Encyclopedia of Physics*, Vol. VIII/1, p. 125, S. Flügge, Ed. Springer Verlag, Berlin (1959).

4. K. G. Guderley, *The Theory of Transonic Flow*, p. 112, Pergamon Press, Oxford (1962).

5. W. D. Hayes, *J. Fluid Mech.* 2, 595-600 (1957).

6. J. D. Cole, *Perturbation Methods in Applied Mathematics,* p. 21, Blaisdell, Waltham, Massachusetts (1968).

7. Lipman Bers, *Mathematical Aspects of Subsonic and Transonic Gas Dynamics*, p. 21, Wiley, New York (1958).

8. G. W. Bluman and J. D. Cole, *Similarity Methods for Differential Equations*, p. 143, Springer-Verlag, New York (1974).

9. R. Vaglio-Laurin, *J. Fluid Mech.* 9, 81-103 (1960).

10. S. V. Falkovich and I. A. Chernov, *J. Appl. Math. Mech.* 28, 342-347 (1964).

11. Milton Van Dyke, *Perturbation Methods in Fluid Mechanics*, p. 89, Academic, New York (1964).

370

A SIMPLE MODEL FOR THE SIMULATION OF THE INITIATION OF
DETONATION BY A SHOCK WAVE IN A HETEROGENEOUS EXPLOSIVE

A. A. Schilperoord
Technological Laboratory TNO
P.O. Box 45, Rijswijk-2100
The Netherlands

A model has been developed for the shock wave initiation of detonation in a heterogeneous explosive. The model is based on chemical reaction of the explosive through both a hot spot mechanism and a bulk reaction mechanism. The hot spot reaction may strengthen the initiating shock wave to such an extent as to initiate a bulk reaction. Results are presented of calculations of initiation distance vs initiating pressure for two densities of PETN.

INTRODUCTION

The mechanism of the initiation of detonation by a shock wave in a so-called heterogeneous explosive is still poorly understood. For homogeneous explosives the gross features of the mechanism are well-known (1), though refinement may be necessary for a detailed analysis (2).

For heterogeneous explosives it is generally accepted--see e.g. (3)--that under the action of the initiating shock wave at discontinuities in the explosive hot spots arise, whose reaction strengthen the shock wave, so that initiation is facilitated compared to homogeneous explosives.

How these spots arise is hardly known; it could be, for instance by a shock focussing (4) or jetting mechanism (5). It could be that owing to the reaction of the hot spots, the initiating shock wave gradually builds up to a detonation wave. There are indications on the other hand--see e.g. (6)--that a reaction mechanism as in homogeneous explosives--reaction throughout the bulk behind the shock wave front--may play a role.

For simulation of the gradual build up of a shock wave to a detonation wave in a one-dimensional

theoretical model a pressure dependent term can be introduced into the Arrhenius' kinetics--see e.g. (7)--which without this term simulates the shock wave initiation in homogeneous explosives very well--see e.g. (8). This procedure is not very satisfying from a physical point of view. Therefore a model was developed, based on both a hot spot and a homogeneous explosives reaction mechanism where the hot spots are supposed to arise through a shock focussing mechanism.

DESCRIPTION OF THE MODEL

Suppose a model of a heterogeneous explosive with voids and grains, for instance granular or pressed explosive. When a shock wave passes through this explosive it is assumed that under the action of the shock wave at each void after its collapse through a shock focussing mechanism as described by Mader (4), a hot spot is created. The size of the hot spot is about equal to the size of the original void, as was shown to be true by two-dimensional calculations for a spherical void in nitromethane by Mader (4). Throughout the hot spot there is a non-uniform temperature distribution. For the sake of simplicity it is assumed that a certain fraction of the original

371

void volume transforms into a hot spot with a uniform temperature distribution. After its formation the hot spot will explode after a delay time τ, which can be calculated from the Arrhenius' kinetics for a homogeneous explosive, provided the temperature of the hot spot is known. During this time τ, rarefaction waves travel into the hot spot which cool it, so that the effective size of the hot spot decreases. It is assumed, that in rarefied regions of the hot spot reaction is completely quenched, and that the explosion of the non-rarefied part of the hot spot will not lead to immediate further reaction in the surrounding explosive. After explosion of the hot spot, the size of which is corrected for rarefaction, a pressure wave will be formed, which overtakes the initiating shock wave. Summing over all hot spots this situation is similar to that of a shock with a partly reacted explosive in its wake. The strengthened shock wave is capable of forming hotter hot spots, which thus react in a shorter time, and therefore have a larger contribution towards strengthening the shock wave. This process will continue until the contribution of the hot spots will be constant (e.g. when τ is so small, that the influence of the rarefaction waves can be neglected). The shock wave is now sufficiently strong to initiate a bulk reaction as is observed in homogeneous explosives.

During the initiation process the reacted fraction of the explosive f can be calculated from:

$$f = f_{HOM} + f_{HS} \qquad (1)$$

where f_{HOM} and f_{HS} are the reacted fraction of explosive calculated from the Arrhenius' kinetics for the homogeneous explosive and from the hot spot contribution respectively

The Arrhenius' kinetics equation is:

$$\frac{df_{HOM}}{dt} = k(1 - f_{HOM}) e^{-E_a/RT} \qquad (2)$$

The hot spot volume fraction f_{HS} can be written:

$$f_{HS} = \alpha \cdot n \cdot 4/3 \, \pi (R_o - c\tau)^3 \qquad (3)$$

where

f_{HS} = hot spot volume fraction of explosive
α = fraction of hot spot that reacts

n = number of hot spots/unity of volume
R_o = radius of original spherical void
c = sound velocity (velocity of penetrating rarefaction wave)
τ = induction time of the hot spot

Equation (3) represents the volume fraction of hot spots in the explosive, corrected for rarefaction influence. It is assumed, that the voids are homogeneously distributed, spherical and equally sized. R_o can be regarded as the radius of a sphere having the same volume as the original void. If we assume in

LIST OF SYMBOLS

f = reacted fraction of explosive
t = time
k = frequency factor
E_a = activation energy
R = gas constant
T = temperature
α = fraction of hot spot that reacts
n = number of hot spots/unity of volume
R_o = radius of original spherical void
c = sound velocity
τ = induction time of the hot spot
R_g = radius of spherical grain
ρ_{HE} = density of the non-porous explosive
ρ = density of porous explosive
β = void size distribution function
V = specific volume
u = particle velocity
y = mass-coordinate
p = pressure
E = specific energy (total)
Q = explosion energy
C_v = specific heat at constant volume
e = specific internal energy
γ = constant in ideal gas equation of state
U = shock wave velocity
a = constant in Hugoniot equation
b = constant in Hugoniot equation
F_{HS} = energy concentration factor in hot spot
S = entropy
D = detonation velocity
A = constant in t_{HOM}, P_i equation
B = constant in t_{HOM}, P_i equation
σ = standard deviation
x = distance

372

the same way R_g as the radius of a spherical grain, having the same volume as the grain, the following relation can be derived (if the number of voids is equal to the number of grains in a volume element):

$$R_o = R_g \left(\frac{\rho_{HE} - \rho}{\rho} \right)^{1/3} \quad (4)$$

where

ρ_{HE} = density of the non-porous explosive
ρ = density of porous explosive

In deriving Eq. (4) it is assumed, that the density of the gas in the voids can be neglected. On the same assumption we can write for n:

$$n = \frac{\rho}{4/3 \, \pi R_g^{\,3} \rho_{HE}} \quad (5)$$

Combining Eqs. (3), (4) and (5) yields

$$f_{HS} = \frac{\alpha \rho}{\rho_{HE}} \left[\left(\frac{\rho_{HE} - \rho}{\rho} \right)^{1/3} - \frac{c\tau}{R_g} \right]^3 \quad (6)$$

From Eq. (6) some interesting conclusions can be drawn with respect to the hot spot contribution to the reacted fraction of explosive. It can be seen, that this contribution will be larger for smaller ρ (more porosity) and smaller τ (higher pressure). Moreover there is a critical condition for f_{HS} being greater than zero:

$$c\tau < R_g \left(\frac{\rho_{HE} - \rho}{\rho} \right)^{1/3} \quad (7)$$

which leads to critical conditions for pressure, particle size and density.

It is important to realize, that τ is not a function of particle size or density, for the hot spot temperature is not a function of void size (9) but is calculated from the shock strength in the grains (and not from the overall shock conditions in the porous explosive).

If a particle size distribution is assumed Eq. (6) becomes:

$$f_{HS} = \frac{\alpha(\rho_{HE} - \rho) \int (R_o - c\tau)^3 \beta dR_o}{\rho_{HE} \int R_o^3 \beta dR_o} \quad (8)$$

Here β is the void size distribution function, while the integration is performed over all void sizes. In the calculations the distribution curve of R_o is assumed to be Gaussian.

CALCULATIONS

The calculations concerning the shock wave initiation of detonation in a heterogeneous explosive, based on the model described, were performed in two ways:

1. One-dimensional calculations with integration of the conservation equations in partial differential conservative form by means of the Lax scheme in order to be able to deal with shock waves (10). In these calculations the explosive is divided into small elements (layers perpendicular to the shock propagation direction), and after each time step, the value of which is determined by stability conditions, the specific volume V, particle velocity u, and specific energy E of each element is calculated from the conservation equations:

$$\frac{\partial V}{\partial t} = \frac{\partial u}{\partial y} \quad (9)$$

$$\frac{\partial u}{\partial t} = -\frac{\partial p}{\partial y} \quad (10)$$

$$\frac{\partial E}{\partial t} = \frac{-\partial(pu)}{\partial y} + Q \frac{\partial f}{\partial t} \quad (11)$$

The shock wave in the explosive was generated by impact of a thick plate.

The reacted fraction f is calculated from Eq. (1), where the temperature in Eq. (2) is calculated from the specific internal energy e:

$$e = C_v(T - T_o) \quad (12)$$

where

C_v = specific heat at constant volume
T_o = temperature of uncompressed explosive

Further

$$e = E - 1/2 \, u^2 \quad (13)$$

373

The pressure p is calculated by combining the state equations of the gaseous and solid phase, an ideal gas equation of state and the Hugoniot respectively. If the pressure in the gas phase equals that of the solid state phase, these equations are:

$$e = fe_g + (1 - f)e_s \qquad (14)$$

$$V = fV_g + (1 - f)V_s \qquad (15)$$

$$e_g = pV_g/(\gamma - 1) \qquad (16)$$

$$e_s = 1/2\,p\,(V_o - V_s) \qquad (17)$$

where g and s indicate gas phase and solid state phase. V_o = volume of uncompressed explosive and γ is a constant. Combining equations (14) through (17) leads to an expression for V_s:

$$V_s = \frac{2(\gamma - 1)}{(1 - f)(\gamma + 1)p} \left(\frac{pV}{\gamma - 1} - e\right) + \frac{\gamma - 1}{\gamma + 1} V_o \qquad (18)$$

Further we can obtain a relation between V_s and p through the conservation equations of mass and momentum over the shock front:

$$p = \frac{b^2(V_o - V_s)}{(V_o - a\,V_o + a\,V_s)^2} \qquad (19)$$

using the empirical relation:

$$U = b + a\,u \qquad (20)$$

where U = shock wave velocity and u = particle velocity. So p can be calculated from Eqs. (18) and (19), when V, e, f, V_o, γ, a and b are known.

For calculating the hot spot condition, a certain energy concentration F_{HS} in the hot spot is assumed:

$$e_{HS} = F_{HS}\,e \qquad (21)$$

As stated earlier, e is the energy of the shock wave in the non-porous explosive. With the aid of e_{HS}, c and τ are calculated:

$$c^2 = -V^2 \left(\frac{dp}{dV}\right)_s \qquad (ref. 11) \qquad (22)$$

where $(dp/dV)_s$ may be derived from the Hugoniot equation (19)

$$\tau = \frac{R(e_{HS} + C_vT_o)^2}{C_v\,Q\,E_a k}\,\exp\left(\frac{C_vE_a}{R(e_{HS} + C_vT_o)}\right) \qquad (23)$$

which is the equation for the adiabatic induction time (12). Repetitively after a time period equal to the sum of induction period and time needed for the pressure pulse from a reacting hot spot to reach the shock front, the values of c and τ in the equation for f_{HS} are updated.

All calculations with the Lax-scheme had to be performed with the Hugoniot-equation for the non-porous explosive, so that all results are strictly true for the non-porous explosive only. Further only semi-quantitative results could be obtained because of small oscillations at the shock wave front due to the existence of two different media (non-reactive and reactive) there.

2. The conservation equations can be simplified by assuming the specific change in volume to be negligible during the initiation process. So in the conservation of energy equation

$$de = -pdV + Qdf \qquad (24)$$

$$dV = 0, \quad \text{leading to:}$$

$$de = Qdf \qquad (25)$$

With this approximation, the induction time formula (23) can be derived for shock wave initiation of detonation in a homogeneous explosive (12). This same equation (25) can be used with the calculations for heterogeneous explosives with the model described. When Eq. (25) is used the calculated induction times will be too short. Alternatively an equation in dp instead of dV can be derived from equation (14) through (17), and (24), leading to:

$$de = \left(Q + pV_s + \frac{1}{2}(\gamma - 1)pV_s - \frac{1}{2}(\gamma - 1)pV_o\right)df\Big/\gamma \qquad (26)$$

when $dp = dV_s = 0$

Equation (26) gives induction times which are too long. So the real induction time will be in between the values, calculated by Eqs. (25) and (26). By calculating during the Lax calculation process the terms, which are neglected when deriving (25) or (26), an impression can be gained which equation should be used in an approximative calculation.

374

In these calculations the reacted fraction f is calculated from Eq. (1) after a time lapse equal to the induction time τ of the hot spots, and the time the pressure wave needs to overtake the shock wave. Then the new e is calculated from Eq. (25) or (26) and subsequently the new c and τ, after which the process is repeated. At each cycle f_{HS} and f_{HOM} increase, but f_{HS} tends to a constant value—reached at time t_{HS}--since the induction period becomes very short, while f_{HOM} is becoming relatively more important. At time $t_{HOM} + t_{HS}$ the bulk explosive subjected to maximum compression due to hot spot reaction has gone through induction and reacts. This is the start of detonation. Initiation times and distances can be derived (Fig. 1) from

$$t_{HS}U_s + t_{HOM}u_p + D^*(t_i - t_{HOM} - t_{HS}) = x_i \quad (27)$$

$$x_i = U_s t_i \quad (28)$$

t_{HS} = time necessary for f_{HS} to become constant
t_{HOM} = induction time for bulk reaction
t_i = initiation time
x_i = initiation distance
U_s = shock wave velocity
u_p = particle velocity
D^* = detonation velocity in compressed medium
D = detonation velocity in uncompressed medium.

U_s and u_p are the shock wave velocity and particle velocity for a shock wave in a porous explosive. These quantities are assumed to be constant throughout the initiation process. They are calculated from the conditions of the non-porous explosive with the
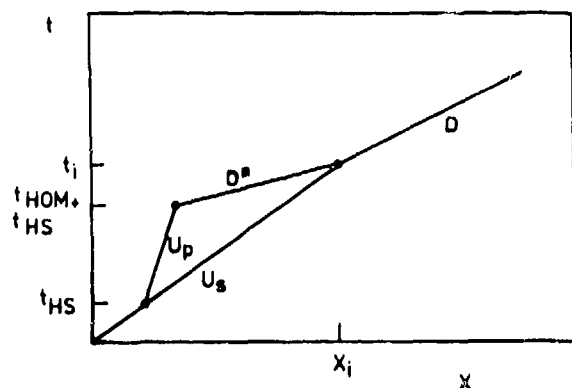
method of Thouvenin (13) as modified in (14). D^* is the detonation velocity of a detonation, travelling through a compressed explosive. It was evaluated from the conservation equations and the Chapman-Jouguet-condition over this detonation wave, assuming an ideal gas equation of state for the detonation reaction products. It is further assumed that the reaction takes place near the shock front until the hot spot contribution f_{HS} has become constant.

Eliminating t_i from Eqs. (27) and (28) leads to an expression for x_i:

$$x_i = t_{HS}U_s + \frac{t_{HOM}U_s(D^* - u_p)}{(D^* - U_s)} \quad (29)$$

It will be clear, that with this second method the computation process can be very much simplified.

The calculations were performed for PETN with three densities, based on the experimental work of Stirpe et al. (6) and Seay et al. (15). These shock wave initiation experiments were done with wedge-shaped pressed PETN samples, initiated with a plane wave lens/attenuator-donor system. The data are given as distance to detonation vs. initiating shock wave pressure. The data for the highest density (1720 kg/m^3) were used to derive a relationship between the induction time and the initiating pressure. With this derivation it was assumed, that the high density material reacted according to a homogeneous explosives mechanism, i.e. the reaction starts behind the initiating shock wave in the place, where the shock wave entered the explosive. This will not be exactly true, but it appeared that there was a "second wave phenomenon" (so reaction behind the initiating shock wave) for the PETN of the highest density.

The t_{HOM}, P_i-relationship can be extracted from Eq. (29), putting $t_{HS} = 0$ and using the experimental data of x_i vs. p_i and the Hugoniot. With Eq. (23) (induction time equation) and a curve-fitting procedure (16), several sets of kinetic parameters E_a, k and C_v could be determined, which simulate the experimental data. This procedure was felt to give more realistic values for the kinetic parameters, than by using the literature values, determined at relatively low temperatures (rate of gassing).

Fig. 1. t/x diagram of an idealised initiation process in a heterogeneous explosive.

An interesting result was, that the t_{HOM}, P_i-relationship could be written as:

375

$$\log t_{HOM} = A + B \log p_i \qquad (30)$$

$A = -4.80$ and $B = -2.79$ for p_i between 0.01 and 0.1 Mbar and t_{HOM} in μs.

For $B = -2$ Eq. (30) resembles the constant energy initiation hypothesis of Walker et al. (17) ($p_i^2 t$), and is identical if t_{HOM} is equal to the critical shock wave pressure duration (t) of the initiating shock wave.

With the input data of table 1, it was tried to simulate the experimental shock wave initiation data of PETN at the lower densities of 1000 kg/m^3 and 1600 kg/m^3, using the second calculation method described. With the first method a good idea of the initiation process can be obtained.

The values of $\bar{R}_g$, σ_{R_g}, α and F_{HS} were chosen arbitrarily. This was one set of parameters which gave a good correlation with the experimental data.

The precise values of $\bar{R}_g$ and σ_{R_g} are not known, because the influence of the pressing operation on the particle size distribution is not known. Moreover, it can be expected, that the velocity of the wave, which effectively cools the hot spot so that no reaction will occur, will be smaller than c, which is equivalent to a smaller effective $\bar{R}_g$.

RESULTS

The results of the approximative calculations (method 2) for PETN with densities of 1600 and 1000 kg/m^3 with the input data of table 1 are shown in Fig. 2, together with the experimental results of Stirpe et al. (6). The approximative calculations were performed on the assumption $dV = 0$, because in the Lax-scheme calculations this proves to be the best approximation. With the Lax-scheme calculations the expected initiation process was found: near the shock front hot spot reaction and reaction according to a homogeneous explosives mechanism behind it.

TABLE 1

Input data for shock wave initiation to detonation calculations for PETN with densities of 1000 kg/m^3 and 1600 kg/m^3

$$\rho_{HE} = 1720 \text{ kg/m}^3 \quad (6)$$

$$\bar{R}_g = 1.5 \text{ mm}$$

$$\sigma_{R_g} = 0.75 \text{ mm}$$

$$a = 3.45 \quad (6)$$

$$b = 1.83 \text{ km/s} \quad (6)$$

$$\gamma = 2.63 \quad (18)$$

$$k = 1215 \times 10^6 \text{ s}^{-1} \quad (19)$$

$$E_a = 36763 \text{ J/mole} \quad (19)$$

$$R = 8.3136 \text{ J/(mole K)}$$

$$C_v = 343 \text{ J/(mole K)} \quad (19)$$

$$Q = 1.83 \times 10^6 \text{ J/mole} \quad (20)$$

$$\alpha = 0.25$$

$$T_0 = 300 \text{ K}$$

$$F_{HS} = 3$$

NOTE: $\bar{R}_g$ is the particle size which goes with the mean volume of the grains and σ_{R_g} is the standard deviation of R_g which corresponds to the standard deviation of the grain volume. In the same way $\bar{R}_0$ and σ_{R_0} are defined, whereby $\bar{R}_0$ is calculated from Eq. (4), assuming the same relation between σ_{R_g} and σ_{R_0}.
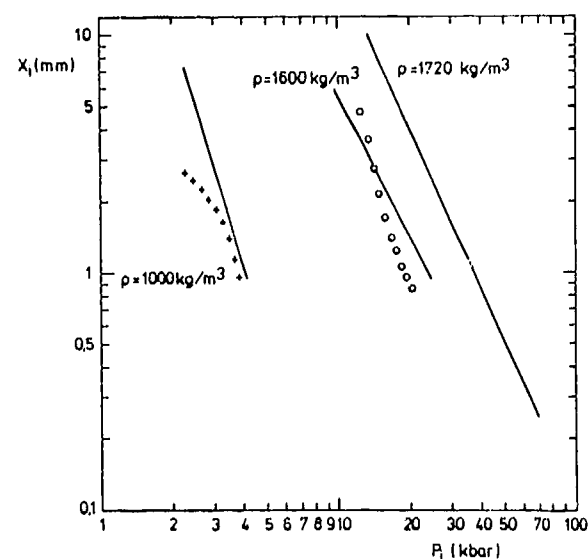

Fig. 2. Log-Log plot of initiation distance vs. initiating pressure for shock wave initiation of pressed PETN with densities of 1000, 1600 and 1720 kg/m^3. Full lines represent fitted curves for experimental data (6), the crosses and open dots were calculated.

The place where the detonation started depended on the degree of hot spot reaction, and thus on the density of the explosive. In Fig. 3 the situation is given for explosives of several densities just before detonation sets in; the position of this place with respect to the shock wave front is quite different indeed.

As can be gathered from Fig. 2, the fit is reasonably good for this set of parameters, though other sets could also give a close resemblance with the experiments. It appeared, however, that reaction of a part of the hot spot volume with high energy concentration gave the best results (small α, large F_{HS}). Calculations were also performed with a different set of kinetic parameters, which gave about the same results as produced above (within about 10%) (19).

DISCUSSION AND CONCLUSIONS

The one-dimensional model described, based on both hot spot reaction and bulk reaction as is ob-
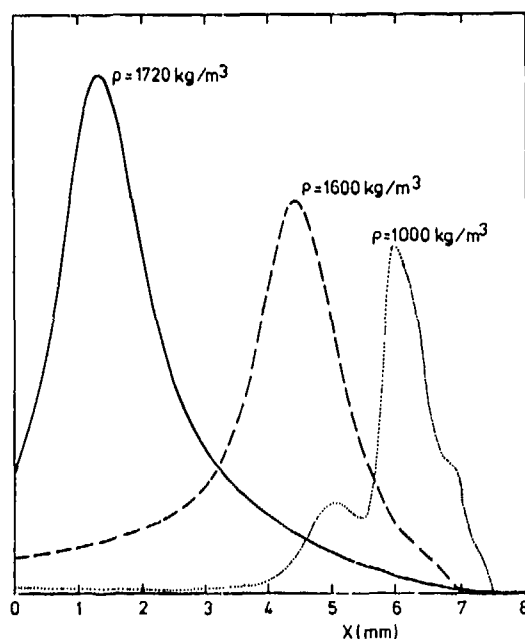
Fig. 3. Reacted fraction f (f between 0 and 1 and different scale uni's for the three curves) as a function of distance in explosive, 0.04, 0.03 and 0.02 μs before detonation sets in, for the densities 1720, 1600 and 1000 kg/m³ respectively.

served for homogeneous explosives, predicts the following features for shock wave initiation of heterogeneous explosives (voids):

1. There is a critical condition for hot spot reaction to occur (Eq. 7) or, in case of a particle size distribution, to be of any importance. The hot spot reaction is facilitated by larger particle size and smaller density of the explosive. This is in confirmation with the experimental observation that an explosive is more sensitive with larger particle size and lower density—see e.g. (5). The particle size effect disappears with large initiating pressures when τ becomes very short.

2. Once a certain fraction of the explosive decomposes through hot spot reaction under the influence of the initiating shock wave, the shock wave will be continuously strengthened till the maximum hot spot contribution will be attained. This process will be more continuous than described by the model because of the different geometries and sizes of the hot spots, leading to different energy concentrations, reaction times and reacted fractions. The time needed to reach the maximum hot spot contribution will also depend on the hot spot parameters (geometry, size etc.). The reacted wave thus obtained could be similar to a low velocity detonation wave. In the one-dimensional model, however, (without rarefaction influence) the strengthened shock wave will initiate a bulk reaction which starts behind this shock wave. The place where this reaction starts will depend on the degree of strengthening of the shock wave, hence on the density. So the "second wave phenomenon" should be observed with the highest densities, whereas with the lower densities the bulk reaction can be so close to the shock wave front, that it seems to be a continuous build-up process. This is in agreement with the experimental results of Stirpe et.al. (6).

It is clear, that during the hot spot build-up process, "single curve build-up" (21) is explained by the model and it is striking, that Boyle (22) could explain the shock wave initiation experiments with tetryl of Lindstrom (21) with a hot spot initiation model with single curve build-up except for the highest density.

3. There is a good deal of simplification in the model, in describing the hot spot (temperature, size etc.) and in the method of formation of the hot spot

377

(shock focussing when a void collapses). In practice the hot spot size, temperature and geometry will be much more complicated, while also other hot spot formation processes could be operative. In spite of this, there will be no change in the fundamental principles of the model and the accuracy with which the hot spots can be described will be of influence on the results.

4. For a set of input data, partially derived from shock wave initiation of detonation experiments for PETN at high density, the data for two other densities could be simulated reasonably well.

REFERENCES

1. A. W. Campbell et al., Phys. Fluids **4** (4), 498 (1961).

2. F. E. Walker et al., Combustion and Flame **15**, 233 (1970).

3. A. W. Campbell et al., Phys. Fluids **4** (4), 511 (1961).

4. C. L. Mader, Phys. Fluids **8** (10), 1811 (1965).

5. L. B. Seeley, 4th Electric initiator symp., paper 27 (1963).

6. D. Stirpe et al., J. Appl. Phys. **41** (9), 3884 (1970).

7. F. J. Warner, 9th Symp. on Combustion, p 536 (1962).

8. C. L. Mader, Phys. Fluids **6** (3), 375, (1963).

9. C. L. Mader, The two-dimensional hydrodynamic hot spot, volume IV, LA report 3771, July 1967.

10. P. D. Lax, Comm. Pure and Appl. Math. VII, 159 (1954).

11. R. Courant and K. O. Friedrichs, Supersonic flow and shock waves, Interscience Publ. Inc., New York (1948).

12. H. W. Hubbard et al. J. Appl. Phys. **30** (5), 765 (1959).

13. J. Thouvenin, 4th Symp. on detonation ACR 126, p. 258 (1965).

14. J. F. Heyda, Plate-gap model of a porous solid and its application to impact by reduced density projectiles, report NASA-CR-1140.

15. G. E. Seay et al., J. Appl. Phys. **32** (6), 1092 (1961).

16. In this curve-fitting procedure values of E_a and k were varied with a fixed value of C_v to determine one set of values of E_a, k and C_v that fitted Eq. (23) with derived t_{HOM}, P_i relationship. In this way several sets of E_a, k and C_v were generated.

17. F. E. Walker et al., Explosivstoffe 1, 9 (1969).

18. γ was calculated from: $\gamma^2 - 1 = D^2/(2Q)$. This equation can be derived for a CJ-detonation, using an ideal gas equation of state. D = detonation velocity = 8.3 km/s (density 1700 kg/m^3) (20), Q = explosion energy.

19. This set of kinetic parameters was chosen, because C_v was the same as the value in (20). As C_v is expected to be larger at higher temperatures, also another set with larger C_v was used: $C_v = 500$ J/mole, $E_a = 42033$ J/mole, k = 16×10^9 s^{-1}.

20. W. R. Tomlinson, Properties of explosives of military interest, Technical Report no. 1740 (April 1958).

21. I. E. Lindstrom, J. Appl. Phys. **41** (1) 337 (1970).

22. Ph. M. Howe, A simplistic approach to the shock initiation of detonation in heterogeneous explosives, BRL MR report 2151, Jan. 1972.

CHEMICAL KINETIC AND CURVATURE EFFECTS
ON SHOCK WAVE EVOLUTION IN EXPLOSIVES

Peter J. Chen and James E. Kennedy
Sandia Laboratories
Albuquerque, New Mexico 87115

The properties of shock waves in explosives are considered here with particular attention given to the effects of chemical kinetics and arbitrary wave surface curvatures on the evolutionary behavior of these waves. The analysis treats a shock surface as a propagating singular surface across which the particle velocity suffers a finite jump; possible jumps in the extents and rates of reactions are also taken into account. The reactions may be exothermic or endothermic, and the shock strengths need not be uniform over each shock surface.

The objective of this analysis is to examine the conditions for which the amplitude of a shock may grow, decay, or remain constant. The results are applicable to shock initiation and detonation processes. We also consider various limiting cases of our general results, including the Zel'dovich-von Neumann-Doering and Chapman-Jouguet models of detonation. The effects of wave surface curvature on shock evolution are illustrated with the aid of data for the explosives PBX-9404 and X-0219.

1. INTRODUCTION

This paper is an attempt to develop a broad frame-work for the study of shock waves in explosive materials in that we examine the effects of chemical kinetics and arbitrary wave surface curvatures on the evolutionary behavior of the amplitudes of these waves. We do not assume *a priori* that the shock strengths are uniform over each shock surface; and across the shock surfaces, regarded as propagating singular surfaces, we allow for possible changes in the extents and rates of reaction. The results of this work extend and generalize those of rumerous previous authors. It (i) includes the alternative classical treatments of detonation, viz., the Chapman-Jouguet model and the Zel'dovich-von Neumann-Doering model, and (ii) provides alternative treatments of local wave amplitude growth or decay in shock initiation calculations.

Such a broad framework is of value in that it places the existing approaches to explosive problems in perspective, and it clearly points out the types of information which must be determined, either theoretically or experimentally, in order to employ a given model in practice. The terms involving changes in the *extents* and *rates* of reaction appear as a sum in the general expression, and this sum may be determined using experimentally determined Hugoniot and shock amplitude evolution data. However, we cannot determine explicitly the individual contributions of these two terms. In view of this difficulty, we examine the consequences of the existence of a known function giving the extents of reaction behind a shock, and show how this function can be used to ascertain the influences of the various parameters. We also examine the contribution of wave surface curvature toward the strengthening or weakening of a shock and this contribution is shown to be a term

379

which can simply be added to the results derived from plane shock experiments.

2. PRELIMINARIES AND CONSTITUTIVE ASSUMPTIONS

In this paper we consider a curved shock wave propagating in a chemically reacting but nondiffusing fluid mixture, and examine, in particular, the effects of chemical kinetics and curvature on the evolutionary behavior of its amplitude. To this end, we presume that the internal energy e, the pressure p, and the absolute temperature θ are determined by the specific volume v, the entropy s, and an N-vector ξ, i.e., (1)

$$e = \hat{e}(v, s, \xi) ,$$

$$p = \hat{p}(v, s, \xi) , \qquad (2.1)$$

$$\theta = \hat{\theta}(v, s, \xi) ,$$

The components $(\xi_1, \xi_2, ..., \xi_N)$ of ξ characterize the extents of reaction of the N independent chemical reactions taking place in the fluid. In addition, the rate of reaction vector $\dot{\xi}$ is given by

$$\dot{\xi} = \omega(v, s, \xi) . \qquad (2.2)$$

The response functions $\hat{e}$, $\hat{p}$, and $\hat{\theta}$ are not independent. Indeed, the second law of thermodynamics requires that

$$\hat{p} = -\hat{e}_v , \quad \hat{\theta} = \hat{e}_s ; \qquad (2.3)$$

and that

$$\sigma \cdot \omega \geqslant 0 , \qquad (2.4)$$

where $\sigma = \hat{\sigma}(v, s, \xi)$ is the chemical affinity defined by

$$\hat{\sigma} = -\hat{e}_\xi . \qquad (2.5)$$

The quantity h, defined by

$$h = -\frac{\theta}{\hat{p}_s} \hat{p}_\xi - \sigma , \qquad (2.6)$$

is called the heat of reaction. The reactions taking place in the mixture are said to be exothermic if $h \cdot \omega < 0$ or endothermic if $h \cdot \omega > 0$.

In addition to the preceding properties we presume, as is physically reasonable in most cases, that the response function of the pressure has the properties

$$\hat{p}_v < 0 , \quad \hat{p}_{vv} > 0 , \quad \hat{p}_s > 0 \qquad (2.7)$$

for all (v, s, ξ). Clearly, the inequalities (2.7) are the usual conditions which ensure that the fluid mixture can support a compressive shock.

The motion of the fluid is described by the function χ which gives the present position $x = \chi(X, t)$ of the material point X at time t. As is customary, we identify each material point X with its position in a fixed homogeneous configuration with mass density ρ_0. The particle velocity $\dot{x}$ and the deformation gradient F are

$$\dot{x} = \frac{\partial \chi}{\partial t}, \quad F = \nabla_X \chi . \qquad (2.8)$$

We presume that the motion of the fluid contains a shock. Its speed of propagation, a measure of the speed with which the shock traverses the fluid, is denoted by U_N. In addition, across the shock the motion is continuous, but the velocity, the deformation gradient and the higher order derivatives of the motion suffer finite jump discontinuities. In particular,

$$[\dot{x}] = u , \quad [F] = -\frac{1}{U_N} u \otimes N , \qquad (2.9)$$

where u is called the amplitude vector and N is the unit normal to the shock surface in the reference configuration (2). In writing (2.9) we have made use of the usual notation to denote the jump $[\psi]$ of any quantity ψ across the shock, i.e., $[\psi] = \psi^- - \psi^+$ with ψ^- and ψ^+ being the limiting values of ψ immediately behind and just in front of the shock. In the spatial configuration the unit normal to the shock surface is denoted by n, and its speed of displacement, a measure of the speed with which the shock traverses space, is denoted by U_n. The relations between the speeds and the normals are simply

$$U_N = (U_n - \dot{x}^+ \cdot n) \frac{1}{|F^{-\top} n|}, \qquad (2.10)$$

380

$$N = \frac{F^{T\mp} n}{|F^{T\mp} n|}. \tag{2.11}$$

The relation between the specific volume v and the mass density ρ is, of course, $v = 1/\rho$, and it follows from the requirement of balance of mass

$$[\rho(U_n - \dot{x} \cdot n)] = 0 \tag{2.12}$$

that

$$[v] = -\frac{v_0 J^\mp}{U_n - \dot{x}^\mp \cdot n} \, u \cdot n. \tag{2.13}$$

where $J = \rho_0/\rho$. Further, balance of linear momentum asserts that

$$[p] n = \rho^\mp (U_n - \dot{x}^\mp \cdot n)[\dot{x}] ; \tag{2.14}$$

and, in view of $(2.9)_1$ and (2.14), we see that the amplitude vector u is proportional to the normal n, i.e.,

$$u = un. \tag{2.15}$$

We call u the amplitude, and it corresponds to the particle velocity jump across the shock. Clearly, it follows from (2.13) and (2.15) that

$$[v] = -\frac{v_0 J^\mp}{U_n - \dot{x}^\mp \cdot n} \, u. \tag{2.16}$$

That is, the jump in the specific volume across the shock is proportional to the amplitude. Further, it follows from $(2.9)_1$, (2.14), and (2.16), that

$$(\rho^\mp)^2 (U_n - \dot{x}^\mp \cdot n)^2 = -\frac{[p]}{[v]} . \tag{2.17}$$

3. EVOLUTIONARY BEHAVIOR OF THE AMPLITUDE

Before we derive the differential equation which describes the evolutionary behavior of the amplitude, let us consider the properties of the entropy s and the extents of reaction ξ. It seems natural that the entropy is discontinuous across the shock, i.e., $[s] \neq 0$. However, whether the shock induces abrupt changes

in the extents of reaction remains an open question. At present, there are two schools of thought. The first maintains that reaction times are large compared to the shock rise time. Hence it may be assumed that there is no jump in the extents of reaction across the shock and that chemical reactions occur only in the regions immediately behind the shock front. The second asserts that the shock induces at least partial chemical reactions which progress to completion in the regions behind the shock front. As we shall see, studies of the evolutionary behavior of the shock do not resolve this question.

We now record the differential equation which the amplitude u, or equivalently $[v]$, must obey. We assume, in general, that $[\xi] \neq 0$ and $\dot{\xi}^- \neq 0$; and the cases (i) when $[\xi] = 0$ and $\dot{\xi}^- \neq 0$ or (ii) when $[\xi] \neq 0$ and $\dot{\xi}^- = 0$ follow as special cases. We also assume that the fluid mixture is initially at rest in a fixed homogeneous configuration, and, for convenience, we take this configuration to be the reference configuration. Since the derivation of this equation is quite tedious as well as technical and since derivations of some of its special cases have appeared in the literature $(3,4)$, we will not repeat the analysis, but will simply record the results. It can be shown that the jump in the specific volume across the shock must obey the equation

$$\frac{\delta[v]}{\delta t} = \frac{v_0 U_N (1 - \mu)(2\tau - 1)}{(3\mu + 1)\tau - (3\mu - 1)} (\lambda - c_n), \tag{3.1}$$

where

$$\lambda = -\frac{\hat{p}_s^-}{v_0 \hat{p}_v^- (1 - \mu) U_N \theta^-} \, h^- \cdot \left(\dot{\xi}^- - \frac{3\tau}{2\tau - 1} \frac{\delta[\xi]}{\delta t} \right) \tag{3.2}$$

$$+ \frac{(1 + [v]/v_0)[v]/v_0}{1 - \mu} \, b_\Gamma^\Gamma ,$$

$$c_n = n \cdot c , \tag{3.3}$$

with $c^i = [\dot{x}^i_{,\alpha\beta}] N^\alpha N^\beta$. In (3.1) $\delta/\delta t$ denotes the displacement derivative which gives the time rate of change of a quantity associated with the shock surface, and

$$\mu = -\frac{\rho_0^2 U_N^2}{\hat{p}_v^-}, \quad \tau = -\frac{\theta^-}{\hat{p}_s^-[v]} ; \tag{3.4}$$

and, in (3.2), b_Γ^Γ is the mean curvature of the shock surface (5). Formula (3.1) applies at each point on the shock surface; it indicates that the time rate of change of the jump [v] is proportional to the difference $\lambda - c_n$. c_n, of course, characterizes the wave form immediately behind the shock. λ depends, in particular, on the thermal, chemical and mechanical properties of the fluid mixture and the mean curvature of the shock surface.

We should also remark that in writing (3.1) we do not assume that the shock strength is uniform over the entire shock surface. Hence (3.1) indicates that the evolutionary behavior of the amplitude at some point on the shock surface, in general, differs from that at any other point. It should also be clear that the only curved shocks which may persist in time are cylindrical and spherical shocks of uniform amplitudes.

Formula (3.1) may be rewritten in terms of the amplitude u and the normal component of the acceleration immediately behind the front (6), viz.,

$$\frac{\delta u}{\delta t} = \frac{\alpha}{\beta + \alpha(\beta + 1)} (n \cdot \ddot{x}^- - \hat{\lambda}), \qquad (3.5)$$

where

$$\alpha = \frac{(1 - \mu)(2\tau - 1)}{(3\mu + 1)\tau - (3\mu - 1)},$$

$$\beta = \frac{\mu(2\tau - 1)}{\mu(2\tau - 1) + \tau(1 - \mu)} \qquad (3.6)$$

and

$$\hat{\lambda} = -\frac{\hat{p}_s^- U_N}{v_o \hat{p}_v^-(1 - \mu)\theta^-} h^- \cdot \left(\dot{\xi}^- - \frac{3\tau}{2\tau - 1} \frac{\delta[\xi]}{\delta t}\right)$$

$$-\frac{(U_N - u)u}{1 - \mu} b_\Gamma^\Gamma. \qquad (3.7)$$

The result (3.5) is much more useful in the interpretation of experimental data in that the amplitude u and the normal component of the acceleration may be obtained directly from experimental data. Henceforth, we shall restrict our discussions to (3.5) rather than (3.1).

4. FURTHER IMPLICATIONS OF THE SHOCK AMPLITUDE EQUATION

Formula (3.5) which governs the evolutionary behavior of the shock amplitude is, of course, quite general. in that it contains as special cases a number of results which are of interest. In particular, the quantity $\hat{\lambda}$, defined by (3.7) and sometimes referred to as the critical acceleration, may be rewritten in the form

$$\hat{\lambda} = \hat{\lambda}_{chem} + \hat{\lambda}_{curv}, \qquad (4.1)$$

where

$$\hat{\lambda}_{chem} = -\frac{\hat{p}_s^- U_N}{v_o \hat{p}_v^-(1 - \mu)\theta^-} h^- \cdot \left(\dot{\xi}^- - \frac{3\tau}{2\tau - 1} \frac{\delta[\xi]}{\delta t}\right) \qquad (4.2)$$

is the critical acceleration due to the thermal, chemical and mechanical properties of the fluid mixture; and

$$\hat{\lambda}_{curv} = -\frac{(U_N - u)u}{1 - \mu} b_\Gamma^\Gamma \qquad (4.3)$$

is the critical acceleration due to the geometrical properties of the shock surface. Clearly, if we have a plane shock, then $b_\Gamma^\Gamma = 0$ and $\hat{\lambda}_{curv} = 0$; and if we have a cylindrical shock or a spherical shock, then $b_\Gamma^\Gamma = \mp 1/r$ or $b_\Gamma^\Gamma = \mp 2/r$ with r being the radius of the cylindrical or spherical shock surface (7). As we have remarked earlier, only these shocks with uniform amplitudes may persist in time.

We now turn our attention to the consideration of the critical acceleration $\hat{\lambda}_{chem}$. Here, we recall that in our derivation of (3.5) we presume that the shock induces at least partial reactions which progress to completion in the regions behind the shock. The consequences of this assumption are manifested in the definition of $\hat{\lambda}_{chem}$ in that it depends, in particular, on $\dot{\xi}^-$ and $\delta[\xi]/\delta t$. The term involving $\dot{\xi}^-$ characterizes the ongoing reactions in the regions behind the shock while the term involving $\delta[\xi]/\delta t$ exhibits the fact that the shock induces at least partial chemical reactions.

There are important implications to the possibility of a finite jump in the extents of reaction. When [ξ] $\neq$ 0, any measured Hugoniot will

implicitly contain the effects of the reaction jump, but this will not necessarily be obvious in the inspection or usage of the data. Further, experimental results on shock amplitude evolution can, in principle, be properly applied to determine $\hat{\lambda}_{chem}$ through the usage of the measured Hugoniot properties without regard to whether or not $[\xi] = 0$ at all shock amplitudes. However, information on $\hat{\lambda}_{chem}$ cannot, in general, be used to evaluate the terms involving $\delta[\xi]/\delta t$ and $\dot{\xi}^-$. In the absence of any quantitative experimental verification, Mader (8) has judiciously included the effects of both of these terms in his model for shock initiation of explosives, based on the experimental observations of Dremin and Koldunov (9), Craig and Marshall (10), Kennedy (11,12), and Wackerle and Johnson (13,14).

Zel'dovich-von Neumann-Doering Model

The classical Zel'dovich-von Neumann-Doering (ZND) model of a detonation wave is based on two assumptions, i.e., (i) a nonreactive shock followed by (ii) reactions which are complete at the Chapman-Jouguet (C-J) sonic plane. Recent work by Bdzil and Davis (15) discusses evidence which suggests that the second assumption of completion of reactions at the sonic plane is inadequate to explain all the observed phenomena in the detonation of explosives. We note that assumption (i), viz., $[\xi] = 0$, should also be considered open to question. The equation governing the evolutionary behavior of the shock amplitude within the context of the ZND model follows as a special case of (3.5). In fact, (3.5) is still the governing differential equation, but now $\hat{\lambda}_{chem}$ has the obvious reduced form (3.16)

$$\hat{\lambda}_{chem} \rightarrow \hat{\lambda}_{chem}^* = -\frac{\hat{p}_s^- U_N}{v_o \hat{p}_v^- (1-\mu)\theta^-} h^- \cdot \dot{\xi}^- . \qquad (4.4)$$

The classical arguments regarding the properties of shock transition may now be adapted to show that the shock must be compressive, i.e., $u > 0$, and that μ, defined by $(3.4)_1$, must satisfy the inequality $0 < \mu < 1$. Hence (4.4) with (2.7) implies that $\hat{\lambda}_{chem}^* < 0$ if the reactions occurring in the regions behind the shock are exothermic, and $\hat{\lambda}_{chem}^* > 0$ if the reactions occurring in the regions behind the shock are endothermic. It also follows from (4.3) that for a shock with negative mean curvature (e.g.,

a spherically diverging shock) $\hat{\lambda}_{curv} > 0$, and for a shock with positive mean curvature (e.g., a spherically converging shock) $\hat{\lambda}_{curv} < 0$.

Chapman-Jouguet Model

Another classical model of a detonation wave hinges on the assumptions that the shock induces instantaneous chemical reactions, and that there are no ongoing reactions in the regions behind the shock. Within this context, it is clear that the jump $[\xi] \neq 0$ and $\dot{\xi}^- = 0$. The propagation properties of such a shock have been presented by Courant and Friedrichs (17); its evolutionary behavior is described by an obvious special case of (3.5). In effect, Courant and Friedrichs also assumed that the regions behind the shock are in a state of strong thermochemical equilibrium, i.e., $\sigma = 0$. This assumption then allows us to solve for the extents of reaction ξ^- behind the shock in terms of v^- and s^- (18). In view of this observation, further simplification of (3.5) results. In a recent paper Bowen and Chen (19) presented an extended discussion of the evolutionary behavior of plane waves within this context. However, since the consequences of the Chapman-Jouguet model are not the main thrust of this paper, we will not repeat here their analysis for the three dimensional problem.

We now return to the consideration of (3.5). As we have remarked earlier, experimental results on shock amplitude evolution can, in principle, be applied to determine $\hat{\lambda}_{chem}$ through the use of measured Hugoniot properties. In effect, experimenters measure the particle velocity histories of a mechanical disturbance at several material points of an explosive of interest. From these data, we can then deduce the shock amplitude u, its time rate of change $\delta u/\delta t$, and the normal component $n \cdot \dot{x}^-$ of the acceleration behind the shock. Also, the measured Hugoniot data may be expressed as a known function of the shock amplitude, i.e.,

$$U_N = f(u) . \qquad (4.5)$$

Now, an examination of (3.5) reveals that if we know the value of the coefficient of its right-hand member, then these experimentally determined data will permit us to calculate $\hat{\lambda}$; and, in order that we may determine this coefficient we must know the quantities μ and τ, defined by (3.4).

The quantity τ may be rewritten in the form

$$\tau = - \frac{1}{\gamma^- - \frac{\hat{p}_s}{\theta^-} v_0} , \qquad (4.6)$$

where

$$\gamma = \frac{\hat{p}_s}{\theta} v , \qquad (4.7)$$

is the well-known Grüneisen parameter. Hence, if we can specify γ corresponding to the state behind the shock and assume that $\rho\gamma$ = constant, then τ may be determined. In view of (4.5), we see that μ may be determined provided that we know $\hat{p}_v^-$. As we shall see, the determination of $\hat{p}_v^-$ is quite complex, but most interesting.

In view of our assumption, viz., the fluid mixture is initially at rest in a fixed homogeneous reference configuration, balance of linear momentum (2.14) with (2.15) reduces to

$$p^- - p^+ = \rho_0 U_N u . \qquad (4.8)$$

Formulae (4.5) and (4.8) imply that there exists a function p_H such that

$$p^- = p_H(u) = \rho_0 f(u)u + p^+ . \qquad (4.9)$$

Further, formulae (2.13) and (2.15) imply that

$$v^- = v_0 \frac{U_N - u}{U_N} , \qquad (4.10)$$

which together with (4.5) indicates that v^- is given by a known function of u. Hence, we may assume that there exists a function $\bar{p}_H$ such that

$$p^- = \bar{p}_H(v^-) . \qquad (4.11)$$

By (4.9) and (4.11), we have

$$p'_H(u) = \bar{p}'_H(v^-) \frac{dv^-}{du} . \qquad (4.12)$$

Since $p'_H(u)$ and dv^-/du are known, we now have an explicit expression for $\bar{p}'_H(v^-)$ in terms of u.

Balance of energy states that across the shock

$$[e] + \frac{1}{2} (p^- + p^+)[v] = 0 , \qquad (4.13)$$

and, in view of $(2.1)_1$, we have

$$\hat{e}(v^-, s^-, \xi^-) - \hat{e}(v_0, s^+, \xi^+) + \frac{1}{2} (p^- + p^+)[v] = 0 . \qquad (4.14)$$

We assume that there exists a function ξ_H such that

$$\xi^- = \xi_H(v^-) ; \qquad (4.15)$$

and since $\hat{p}_s > 0$, we have via $(2.1)_2$

$$s = \hat{p}^{-1}(v, p, \xi) , \qquad (4.16)$$

where $\hat{p}^{-1}(v, \cdot, \xi)$ denotes the inverse of $\hat{p}(v, \cdot, \xi)$. We now define the function H such that

$$H(v^-, p^-) = \hat{e}(v^-, \hat{p}^{-1}(v^-, p^-, \xi_H(v^-)), \xi_H(v^-))$$

$$-\hat{e}(v_0, \hat{p}^{-1}(v_0, \hat{p}^+, \xi^+), \xi^+) \qquad (4.17)$$

$$+\frac{1}{2} (p^- + p^+)[v] .$$

Notice that H depends on the underlying state (v_0, p^+, ξ^+); this dependence, however, need not be rendered explicit. In view of (4.14) and (4.17), we have

$$H(v^-, p^-) = 0 , \qquad (4.18)$$

which together with (4.11) implies that

$$\frac{dH}{dv^-} = \frac{\partial H}{\partial v^-} + \frac{\partial H}{\partial p^-} \bar{p}'_H(v^-) , \qquad (4.19)$$

and consequently

$$\bar{p}'_H(v^-) = -(\partial H/\partial v^-)/(\partial H/\partial p^-) . \qquad (4.20)$$

It can readily be shown that

$$\frac{\partial H}{\partial v^-} = \frac{\theta^-}{\hat{p}_s^-} + \frac{1}{2} [v] , \qquad (4.21)$$

and

384

$$\frac{\partial H}{\partial v^-} = -\frac{\hat{p}_v^-\theta^-}{\hat{p}_s^-} - \frac{1}{2}\,[p] + h^- \cdot \xi_H'(v^-). \quad (4.22)$$

Hence, (4.20) with (4.21) and (4.22) implies

$$\bar{p}_H'(v^-) = \frac{\hat{p}_v^-(2\tau - \mu)}{2\tau - 1} + 2\,\frac{h^- \cdot \xi_H'(v^-)}{(2\tau - 1)[v]}. \quad (4.23)$$

Formula (4.23) gives another expression for $\bar{p}_H'(v^-)$. Clearly, if we can specify the heat of reaction h, the function ξ_H and the Grüneisen parameter γ corresponding to the condition behind the shock, we may then determine $\hat{p}_v^-$ by substituting (4.23) into (4.12).

In view of the preceding results, we see that we are now in the position to calculate $\hat{\lambda}$ using experimental information concerning shock amplitude evolution. Further, since knowledge of μ and Hugoniot data also allows us to determine $\hat{\lambda}_{curv}$ for any given mean curvature, formula (4.1) indicates that $\hat{\lambda}_{chem}$ can now be determined. Perhaps, the most interesting aspect of our results follows from our assumption of the existence of the function ξ_H, defined by (4.15). Since (4.15) implies

$$\frac{\delta[\xi]}{\delta t} = \xi_H'\,\frac{\delta[v]}{\delta t}, \quad (4.24)$$

and since $\delta[v]/\delta$ ... y be rewritten, via (4.5) and (4.10), in terms of u and $\delta u/\delta t$, it is quite evident that the individual contributions of the terms involving $\delta[\xi]/\delta t$ and $\dot{\xi}^-$ in the definition of $\hat{\lambda}_{chem}$ can be ascertained.

The existence of the function ξ_H and, consequently (4.24), allows us to rewrite (3.1) in the form

$$\frac{\delta[v]}{\delta t} = \frac{v_0 U_N \hat{p}_v^-[v](1-\mu)(2\tau-1)}{\hat{p}_v^-[v]\{(3\mu+1)\tau - (3\mu-1)\} + 3h^- \cdot \xi_H'}$$

$$\times(\lambda^\dagger - c_n)\,, \quad (4.25)$$

where

$$\lambda^\dagger = -\frac{\hat{p}_s^-}{v_0\hat{p}_v^-(1-\mu)U_N\theta^-}\,h^- \cdot \xi^-$$

$$+ \frac{(1 + [v]/v_0)[v]/v_0}{1 - \mu}\,b_\Gamma^\Gamma\,. \quad (4.26)$$

Formula (4.25) gives the explicit expression for the evolutionary behavior of the shock when the function ξ_H is specified. Clearly, an equivalent relation for (3.5) could be readily derived. In view of our preceding discussions the usefulness of (4.25) should be quite evident.

5. APPLICATIONS OF OUR RESULTS

It would now be interesting to evaluate certain aspects of our results with respect to the explosives PBX-9404 and X-0219. PBX-9404 is a somewhat sensitive explosive in that it is not difficult to initiate, and X-0219 is quite insensitive. In the sequel we hope to offer some reasons for this difference in sensitivity.

First, let us assume there is no jump in the extents of reaction across the shocks and evaluate the effect of the shock surface curvature, i.e., we are adopting the ZND model. In particular, we shall compare the values of

$$-\frac{\hat{\lambda}_{curv}}{b_\Gamma^\Gamma} = \frac{(U_N - u)u}{1 - \mu} \quad (5.1)$$

for various shock amplitudes. Table 1 lists the relevant information required for the evaluation of the right-hand member of (5.1).

The results shown graphically in Fig. 1 indicate that for the same mean curvature b_Γ^Γ the damping effect due to $\hat{\lambda}_{curv}$ for X-0219 is somewhat less than that for PBX-9404. This is a most curious observation in that it is known that shocks in X-0219 have great difficulty in corner turning and this has been conjectured to be due to strong curvature effects. We then evaluate the coefficient

$$-\frac{\hat{p}_s^- U_N}{v_0\hat{p}_v^-(1-\mu)\theta^-} \quad (5.2)$$

which appears in the definition of $\hat{\lambda}_{chem}$ and $\hat{\lambda}_{chem}^*$. Clearly, this coefficient is a manifestation of the thermomechanical properties of an explosive. Its values, determined using the same information given in Table 1, are shown graphically in Fig. 2. These results indicate that the thermomechanical properties of X-0219 lower the amplifying effects due to chemical heat release by half an order of magnitude compared with those of PBX-9404. In view of the fact

385

that the chemical heat release rate of X-0219 is also less than that of PBX-9404, it seems it is this combination of effects which causes X-0219 to be difficult to initiate.

In Fig. 3, we illustrate the effect of curvature on the critical acceleration, $\hat{\lambda}$. $\hat{\lambda}^*_{chem}$ for plane shock waves in PBX-9404 is taken from the results of Kennedy and Nunziato (20), and we use (3.7) to evaluate $\hat{\lambda}$ for spherically diverging shocks of two finite radii of curvature. Notice that in some instances the damping effect due to $\hat{\lambda}_{curv}$ is sufficient to overcome the amplifying effect due to $\hat{\lambda}^*_{chem}$ so that $\hat{\lambda} > 0$ whereas $\hat{\lambda}^*_{chem} < 0$.

We also consider an example of the situation when the jump in extents of reaction is not zero for the explosive PBX-9404. Here, we take the extents of reaction to be a single parameter ξ characterizing the products of reaction. Mader and Forest (23) have

recently proposed a model whereby they specify ξ_H and ξ^- as functions of shock strength. In this situation the heat of reaction h is given by the single parameter (22)

$$h = -1.370 \text{ kcal/g} , \qquad (5.3)$$

and we have the reactive Hugoniot (24)

$$U_N(\text{cm}/\mu\text{s}) = 0.246 + 2.53u . \qquad (5.4)$$

We now consider plane waves and determine, using experimental values (20) of $\delta u/\delta t$ and $n \cdot \ddot{x}^-$ versus t, the values of $\hat{\lambda}_{chem}$ via (3.5) with $b_H^\Gamma \equiv 0$. The values of $\hat{\lambda}_{chem}$ so determined can be viewed via (4.2) as restrictions between the jump $[\xi]$ in the products of reaction and the rate of reaction $\dot{\xi}^-$ behind the shock, in that specification of either one of these quantities leads to the specification of the other. That is, the jump $[\xi]$ and the rate $\dot{\xi}^-$ cannot be independent of each other. Hence we may adopt Mader's (8) function ξ_H, which is consistent with
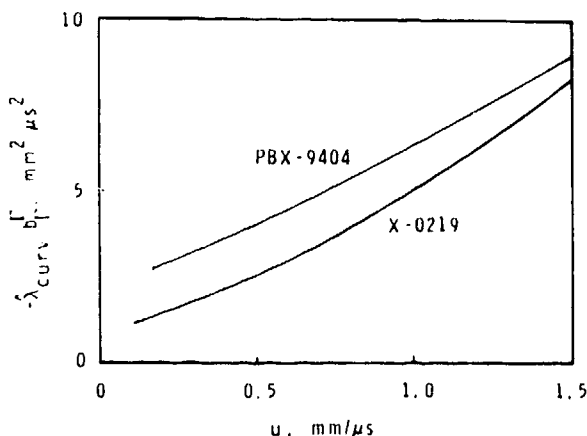
Fig. 1. Generalized critical acceleration due to curvature, $-\hat{\lambda}_{curv}/b_H^\Gamma$, as a function of shock amplitude, u, for unreactive PBX-9404 and X-0219. Note that the values are comparable for the two explosives.
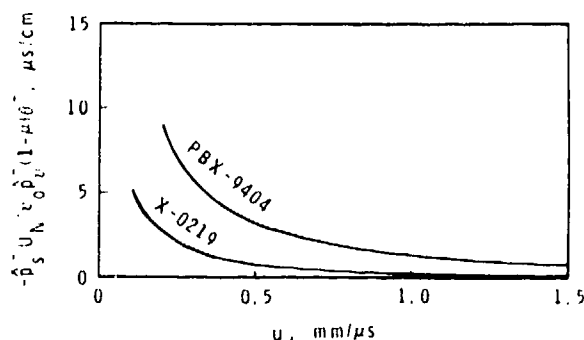
Fig. 2. Thermomechanical coefficient, $-\hat{p}_s^- U_N/v_o \hat{p}_v^-(1-\mu)\theta^-$, as a function of shock amplitude for unreactive PBX-9404 and X-0219. This coefficient couples the chemical energy release to the critical acceleration, $\hat{\lambda}$, per (4.2).

TABLE 1

Explosive	ρ_o, g/cm^3	γ	(Ref.)	Unreactive Hugoniot U_N, cm/μs	(Ref.)
PBX-9404	1.84	0.675	(8)	0.269 + 1.72u	(20)
X-0219	1.92	0.29	(21)	0.2037 + 2.497u	(22)
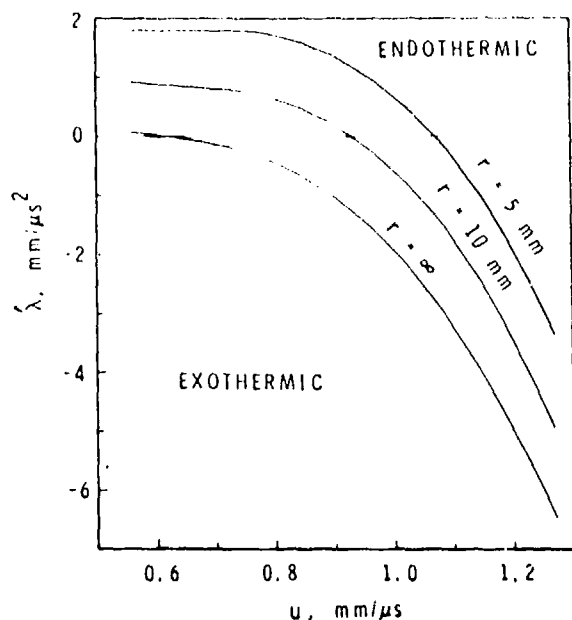
Fig. 3. Critical acceleration, $\hat{\lambda}$, for various radii of curvature for unreactive PBX-9404. The plane shock response $(r = \infty)$ is taken from the data of Kennedy and Nunziato (20).

Fig. 4. Reaction rate, $\dot{\xi}^-$, immediately behind the shock front as a function of shock amplitude for several models of shock response of PBX-9404. Kennedy and Nunziato (20) adopted the ZND model, i.e., $[\xi] = 0$. We used Mader's function ξ_H together with the data of Kennedy and Nunziato to derive the upper curve, via (4.2).

the reactive Hugoniot (5.4), and make use of (4.2) along with the values of $\hat{\lambda}_{chem}$ to determine the rate of reaction $\dot{\xi}^-$. The results are shown graphically in Fig. 4 and compared with those determined by Kennedy and Nunziato (20), who adopted the ZND model. It is of interest to note that these two curves agree at the lower values of u for which we have data. For larger shock amplitudes, the values of $\dot{\xi}^-$ which are consistent with Mader's function ξ_H are greater than those of Kennedy and Nunziato; this is a direct consequence of the influence of the term $\delta[\xi]/\delta t$ in (4.2). In Fig. 4 we also show the values of the function $\dot{\xi}^-$ recently proposed by Mader and Forest (23), and we observe that it lies between the two curves based on alternative interpretations of experimental data.

ACKNOWLEDGEMENTS

We gratefully acknowledge helpful discussions with D. B. Hayes concerning the properties of TATB, the principal ingredient of X-0219. C. L. Mader and C. Forest have graciously made available details of their model for shock initiation calculations on PBX-9404.

FOOTNOTES AND REFERENCES

1. The constitutive relations which we propose are quite standard; see, e.g., I. Prigogine, Thermodynamics of Irreversible Processes, 2nd ed., Interscience, New York, 1961.

2. Our analysis is based on the method of the theory of singular surfaces, see, e.g., C. Truesdell and R. A. Toupin, "The Classical Field Theories," in Handbuch der Physik, Band III/1, Springer-Verlag, Berlin, Göttingen and Heidelberg, 1960.

3. P. J. Chen and M. E. Gurtin, Phys. Fluids, Vol. 14, p. 1091, 1971.

4. P. J. Chen and T. W. Wright, Meccanica Vol. X, p. 232, 1975.

5. The mean curvature b_1^Γ is simply the sum of the principal curvatures, see, e.g., T. Y. Thomas, Concepts from Tensor Analysis and Differential Geometry, 2nd ed., Academic Press, New York and London, 1965.

6. In view of our assumption that the fluid mixture is initially at rest in a fixed homogeneous configuration, the amplitude u is now the particle velocity behind the shock.

7. The negative sign refers to diverging shock surfaces and the positive sign refers to converging shock surfaces.

8. C. L. Mader, Los Alamos Scientific Laboratory Rept. LA-4475, 1970.

9. A. N. Dremin and S. A. Koldunov, Vzryvnoye delo, Vol. 63, p. 37, 1967.

10. B. G. Craig and E. F. Marshall, Proc., Fifth Symp. (Intl.) on Detonation, p. 321, ACR-184, O.N.R., Arlington, VA, 1970.

11. J. E. Kennedy, Proc., Fifth Symp. (Intl.) on Detonation, p. 435, ACR-184, O.N.R., Arlington, VA, 1970.

12. J. E. Kennedy, Proc., Fourteenth Symp. (Intl.) on Combustion, p. 1251, Combustion Inst., Pittsburgh, PA, 1973.

13. J. Wackerle and J. O. Johnson, Los Alamos Scientific Laboratory Rept., LA-DC-72-1015, 1972.

14. J. Wackerle and J. O. Johnson, Los Alamos Scientific Laboratory Rept., LA-5131, 1973.

15. J. Bdzil and W. C. Davis, Los Alamos Scientific Laboratory Rept. LA-5926-MS, 1975.

16. J. W. Nunziato, J. Chem. Phys., Vol. 58, p. 961, 1973.

17. R. Courant and K. O. Friedrichs, Supersonic Flow and Shock Waves, Interscience, New York, 1948.

18. Clearly, specification of ξ^- and v^- corresponds to specification of the concentrations of all chemical species.

19. R. M. Bowen and P. J. Chen, Arch. Mech. (in press).

20. J. E. Kennedy and J. W. Nunziato, J. Mech. Phys. Solids, Vol. 24, p. 107, 1976.

21. D. J. Pastine and R. R. Bernecker, J. Appl. Phys., Vol. 45, p. 4458, 1974.

22. B. M. Dobratz, Lawrence Livermore Laboratory Rept. UCID-51319 Rev. 1, 1974.

23. C. L. Mader and C. Forest, private communication, 1976.

24. J. B. Ramsay, private communication, 1976, cited by Mader and Forest (23).

THE HUGONIOT AND SHOCK INITIATION THRESHOLD OF LEAD AZIDE

F. W. Davies and A. B. Zimmerschied
Boeing Aerospace Company
Seattle, Washington 98124

F. G. Borgardt
Lockheed Palo Alto Research Laboratory
Palo Alto, California 94304

Louis Avrami
Explosives Division
Feltman Research Laboratory
Picatinny Arsenal
Dover, New Jersey 07801

The Hugo. iiot of unreacted dextrinated lead azide has been determined using a 2.5 inch bore gas gun. The Hugoniot is linear up to 10 kbar and can be represented by the equation $\sigma = 41.7 \, U_p$ (σ in kbar and U_p in mm/μsec). The initiation threshold to long duration (3.5 μsec) shocks was 6.0 kbar. For short duration (0.1 μsec) shocks the lead azide was inpacted by thin flyers accelerated by exploding foils. The short-pulse initiation threshold for polyvinyl lead azide is 4.2 kbar for a density of 3.6 gm/cc, and 2.1 kbar for dextrinated lead azide for a density of 2.9 gm/cc. Comparison of the initiation threshold measurements suggest that there is a minimum thickness, or a run-up distance, before detonation occurs which is independent of pulse width with stresses up to 10 kbar. The explosive shows a gradual transition from an unreactive shock to a stable detonation which is similar to that observed for heterogeneous secondary explosives.

ELECTRIC FIELD INITIATION OF EXPLOSIVE AZIDES

Thaddeus Gora, David S. Downs, and Harry D. Fair, Jr.
Energetic Materials Division
Large Caliber Weapon Systems Laboratory
ARRADCOM
Dover, New Jersey 07801

Peter Mark
Princeton University
Princeton, New Jersey 08540

A number of explosive azides, including lead azide, can be initiated by the application of sufficient voltage via conducting electrical contacts. Such electric field initiation phenomena have been intensively studied because of relevance to safety problems and to potential new fuzing applications. It has not been possible, however, to relate the results of experiments conducted under different conditions on different sample forms. We summarize here new theoretical and experimental results on the electric field initiation of explosive azides. They further characterize and elucidate field initiation phenomena. A broader analysis of the individual results leads to the genera' conclusion that field initiation is strongly affected by the nature of the electrical contact made to the explosives. This enables one to understand and relate seemingly inconsistent experimental results.

INTRODUCTION

A number of explosive azides, including lead azide, can be initiated by the application of sufficient voltage *via* conducting electrical contacts. This occurs for both single crystal (1-4) and pressed pellet (5,6) samples. The effect is normally referred to as electric field initiation and we shall adopt that terminology here. The related problem of the sensitivity of azide compounds to static electric charging and electric discharge has also received considerable attention (7). These phenomena are relevant to safety in the storage and handling of munitions items (lead azide is the Army's prevalent primary explosive), and to novel initiation mechanisms for potential fuzing applications (1,2).

A great deal of work has been done to characterize field initiation effects in explosives (3,5,6) and to

understand them on the basis of the fundamental electronic, decomposition and conductivity properties (1,2) of the materials. But it has been difficult to relate experiments using single crystals (easiest to reproduce and understand) to experiments on pressed pellets and powders. Our recent results and analysis, reported here, indicate that contact and surface effects are central to understanding the electric field initiation of explosives and to relating the results of experiments performed under different conditions and on different sample forms.

a. Concepts and Techniques

Certain basic concepts involving the electronic structure of solids and the nature of the interface at sample-metal contacts are briefly reviewed here, as they will be extensively employed in the analysis and interpretation of electric field initiation experiments.

The electronic energy levels of a solid are arranged in a fashion similar to their arrangement in the free atoms or molecules which comprise the solid with several critically important differences. In the solid all of the electronic particles interact, perturbing the atomic or molecular electronic states so that they appear as energy bands rather than discrete levels of energy (8). The bands of energy are separated by energy regions for which no electron energy states are allowed; such forbidden regions are called energy gaps or band gaps. The highest energy band filled with electrons is called the valence band and the next higher band (which is not completely filled) is called the conduction band. Electrons excited to the latter band may move under the influence of an electric field, giving rise to electronic conduction. The widths of the energy bands, the band-gap separation between them, and other features of the bands are referred to as the electronic band structure or the electronic energy level structure. The (explosive) azides of lead, thallium and silver are insulating solids with large band gaps (approximately 4 eV) (1). Measurements of conductivity and of photoconductivity usually require the application of electrical contacts, most often formed by applying metallic electrodes to the sample. However, the results of the measurements may be strongly influenced by the nature of the junction at the metal-insulator interface. The contacts may be "ohmic" (injecting), in which case a reservoir of carriers is provided by the metal to freely enter the semiconductor or insulator as needed (9). Or, as is more commonly the case with large band-gap solids, the contacts may be "blocking" (non-injecting), resulting in extreme nonlinearities in the electric field within the metal-insulator interface. The current through a material is then controlled entirely by the conditions at the metal-insulator contact, yielding little information about the bulk electronic properties of the material. The current characteristics resulting from blocking contacts (also called Schottky-barrier contacts) have been extensively analyzed for semiconductors with band gaps up to 1-2 eV, but the properties of such contacts on larger band-gap materials are not as clearly defined.

The energy level diagram for a metal-semiconductor blocking contact is shown in Fig. 1. Near the interface, the energy bands in the semiconductor or insulator bend over a distance d, the thickness of the Schottky-barrier region. The extent of the band bending (the surface potential V_s) may be appreciable, in which case an electric field applied to the
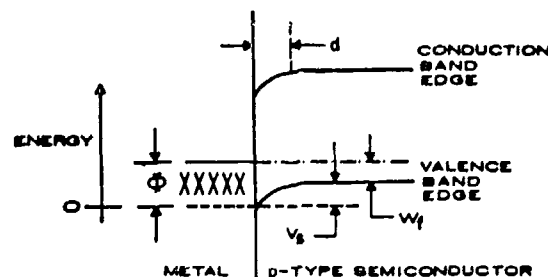
Fig. 1. Energy band diagram for a p-type semiconductor-metal Schottky-barrier contact with thickness d, barrier height Φ, surface potential V_s and Fermi energy W_f.

material may be distributed primarily over the barrier thickness d rather than over the bulk of the material.

An experiment which measures the threshold voltage for electric field initiation of an explosive is basically straightforward. A sample is placed between two electrical contacts and a voltage applied in some prescribed manner until initiation is observed. On the other hand the analysis of the experiment is not at all straightforward; the effects of several parameters (such as the dielectric and conductivity properties of the explosive, the nature of the electrical contact and the particular sample-electrode geometry) must be taken into account. Only by considering these parameters can the electric field intensity, in the sample, be determined as a function of position. As we will show, it is a detailed knowledge of the field distribution which leads to an understanding of electric field initiation.

b. Background

Our previous experiments (1-3) on lead azide [$Pb(N_3)_2$] using gold contacts and a sandwich geometry showed the following: Single crystals initiate upon the application of a voltage corresponding to an average threshold electric field (voltage/sample thickness) of 3.5×10^4 V/cm. Gold forms a blocking (non-injecting) contact to $Pb(N_3)_2$ under the conditions of the experiments. The voltage drop across the sample is relatively uniform near threshold voltages, i.e., the bulk of the sample experiences an electric field near the average field. The pressed pellet threshold average field approximates the single crystal value. Simultaneous application of low-intensity band-gap radiation decreases the single crystal (but

391

not the pressed pellet) threshold average field by a factor of two; this was explained qualitatively in terms of free charge motion and a consequent field redistribution resulting in a higher electric field at the metal-explosive surface. Finally, the conductivity of $Pb(N_3)_2$ is very low, $\sim 10^{-12}$ (ohm-cm)$^{-1}$, while photoconductivity is up to four orders of magnitude higher.

Russian experiments (6) on cupric azide $[Cu(N_3)_2]$ and thallous azide $[TlN_3]$ pressed pellets found that threshold field values depend on the electronic work function of the metal contacts. This was interpreted to be evidence for the injection of charge. Experiments by Leopold (5) on $Pb(N_3)_2$ pressed pellets showed that no initiation occurs, even at much higher fields, if either or both of the electrodes are separated from the sample by thin mylar sheets.

In the analysis of experiments the dielectric constant of lead azide was generally taken to be ~ 5, based on pressed pellet data (10).

RECENT RESULTS

a. Theoretical

Our theoretical aims were twofold: to understand and model the Russian field initiation experiments, and to form a quantitative basis for understanding internal field distributions in azide explosives. The average threshold field value (voltage/sample thickness) simply does not provide sufficient information for comparative purposes.

The experiments, performed by Zakharov and Sukhushin (6), revealed that the threshold initiation field for *pressed pellets* of $Cu(N_3)_2$ and TlN_3 depends on the electrode material: its value increases with increasing work function of the anode metal in the case of $Cu(N_3)_2$, and decreases with increasing work function of the cathode metal in the case of TlN_3. The effect was associated with "injection" of electronic carriers, but it is difficult to understand how variations in the contacts' work functions could play a significant role in a model based on current injection. With the ohmic contacts that injection specifically requires, current limitation is a bulk phenomenon, and the electrodes play no role other than to provide current carriers as the volume field conditions demand (9).

We have proposed a carrier emission model in which initiation is associated with a critical interface field at the Schottky-barrier contact between the metal electrode and the azide (11). Electric fields at the interface are shown to explicitly depend on properties of the sample and on the work function of the electrode, and are larger than the applied voltage divided by sample thickness. The model predicts an effect for *uniform* samples which is qualitatively consistent with experiment, but whose magnitude would be too small to observe. However, the experimental samples were pressed pellets composed of individual grains which are likely to be separated by potential barriers (12). Taking this into account, the model is consistent with experiment if initiation occurs at a critical interface field of about 2×10^5 V/cm. This is a plausible value, in that fields in excess of 10^5-10^6 V/cm applied to surfaces of wide band-gap semiconductors commonly result in destructive breakdown due to carrier emission into the bulk. The important conclusion is that initiation is determined by details of the electric field distribution rather than by the average field (applied voltage/sample thickness).

Figure 2 depicts the one-dimensional sample-electrode configuration used in experiments where the electrodes are not in contact with the azide sample. The sample is a slab with parallel sides and thickness d, located symmetrically a distance $\ell/2$ away from two parallel capacitively coupled electrodes (electrode spacing is L). The static dielectric
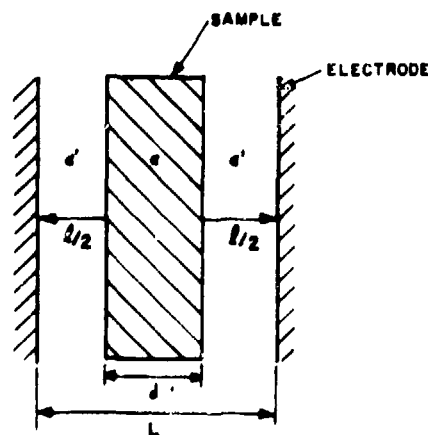

Fig. 2. Sample of thickness d and dielectric constant e between two electrodes, and spacing material of dielectric constant e'.

392

constant of the sample is ϵ, and that of the spacing material ϵ' (ϵ_0 in free space). In order to understand such experiments, complete field distributions were determined theoretically for three assumptions as to the nature of the specimen: perfect insulator, intrinsic semiconductor and extrinsic semiconductor (uniform photo-excitation can be included in the last two cases) (13).

In the perfect insulator case, the field is uniform throughout the sample and so is equal to the surface field E_s, which is simply

$$E_s = \frac{V}{\kappa_r \ell + d},\tag{1}$$

where $\kappa_r = \epsilon/\epsilon'$, the dielectric constant of the sample relative to that of the spacing medium. The expression is used below to determine values of E_s attained in our experiments. Note that for given values of ℓ and d, increasing κ_r leads to a decreasing E_s.

Our results for the intrinsic and extrinsic semiconductor cases have been summarized elsewhere (14). The important qualitative features are that the presence of a uniform mobile charge distribution of both carrier types (the definition of the intrinsic semiconductor case) can only lower the value of E_s from the perfect insulator case (for constant V); whereas E_s-values are larger for the extrinsic semiconductor case, where it is assumed that only one carrier type is mobile. The increase can be dramatic for sufficiently large charge density.

b. Experimental

All experiments were performed in the sandwich geometry of Fig. 2. Prior results with direct explosive-metal contact were summarized above, and only the non-contacted experiments ($\ell \neq 0$ in Fig. 2) are discussed here. The importance of using single crystal as well as pressed pellet samples is evident from the fact that the Schottky-barrier model presented earlier explicitly requires the presence of intergrain barriers (for semiquantitative agreement with the Russian experiments). In the analysis of experiments with single crystals, only the barriers at the azide metal contacts are considered.

Samples were mounted between mylar insulators in a vacuum chamber at 2×10^{-5} torr. (The high voltage experiments reported by Leopold (5) were performed with the samples immersed in oil.) Care was taken to avoid discharges from the high voltage points of the sample holder to ground. The voltage was increased in steps of 500 volts to a maximum of 5 kV, and was held constant for 30 sec at each step.

The expression appropriate to calculating the average electric field *in the sample* $\bar{E}$ is Eq. (1), which is also the expression for the surface field if the field is uniform throughout the sample. Lead azide's dielectric constant (ϵ/ϵ_0) was taken to be 5 for the values quoted in this Section.

No initiation occurred in the pressed pellet samples (~ 3.5 gm/cm^3 density, $1-3 \times 10^{-2}$ cm thick), using the insulated electrodes, up to the highest $\bar{E}$-values applied, 1.4×10^5 V/cm. This corresponds to the upper limit (5 kV) of the power supply for the sample dimensions used. It is a factor of four greater than the $\bar{E}$-values that lead to initiation in contacted samples (1-3), and a factor of two greater than the highest $\bar{E}$-value reported by Leopold (5). The same result (no initiation) held for single crystal samples (grown by the method of Garrett (15), and cut and polished to provide parallel flat surfaces), with the highest $\bar{E}$-value attained being 1.02×10^5 V/cm. The highest $\bar{E}$-values were maintained on the sample for about a half-hour. Some samples were subjected to combinations of 400.0 nm irradiation (strongly absorbed by $Pb(N_3)_2$) and a strong field, for both polarities, again with no initiation.

The results lead us to conclude that electrode interface effects dominate the field initiation of $Pb(N_3)_2$ single crystals and pressed pellets, with or without simultaneous low-level, strongly absorbed radiation, when the samples are directly contacted with the electrodes. Samples not directly contacted can sustain rather higher fields without initiation. It will be clear from the discussion below that only relative values of $\bar{E}$ are reliable from these experiments; they were performed without determining crystallographic orientation, and the dielectric constant has since been found to be strongly anisotropic.

DISCUSSION

The important general conclusion is that contact effects dominate the electric field initiation properties of explosive azides, and that this can explain apparent

discrepancies when comparing experiments performed under dissimilar conditions. The detailed mechanisms involved are not fully understood, but the nature of the crucial experiments and calculations are now clear.

The Russian field initiation experiments (6) provided an important clue to the role of interface contacts. Our theoretical model shows that the experiments using non-ohmic metal contacts can be explained if initiation is the result of a critical threshold field $E_s(crit)$ at the metal-explosive interface. A different value of $E_s(crit)$ would then be associated with each explosive azide, and be independent of the nature of the non-ohmic metal contact (so long as a contact is available); its magnitude is of the order of 10^5 V/cm in $Cu(N_3)_2$ and TlN_3. Recall that our model cannot explain these experimental results without explicitly taking the pressed pellet nature of the samples into account. The field initiation experiments on contacted $Pb(N_3)_2$ samples appear also to require a critical interface field (3).

These conclusions point to an initiation model involving carrier emission from a barrier contact. Two alternative mechanisms are suggested for this emission model based on field breakdown mechanisms in the literature. Both rely on high local internal fields to generate hot electrons, which can then cause impact ionization. The first, due to O'Dwyer (16), assumes that the impact ionization leads to avalanche multiplication with eventual breakdown at the exit electrode, where most of the energy of impact-generated carriers is dissipated. The second mechanism, due to DiStefano and Shatzkes (17), suggests that impact ionization generates a space charge in the volume of the sample which concentrates the internal field at the emitting electrode; this in turn produces an increase in the emission current, with eventual catastrophic power dissipation at the entrance electrode. The choice between the two mechanisms (for a given explosive azide) can thus be made on the basis of experiments that determine whether initiation occurs near the entrance or exit electrode.

The experiments of Leopold (5), and their extensions reported here, showed that no initiation occurs without direct metallic contact up to the limits of the experimental apparatus. This is consistent with the emission model just presented. Values for the interface fields E_s attained can be calculated from Eq. (1)

by using the appropriate dielectric constant κ_r. Lead azide's dielectric constant has recently been found to be large and highly anisotropic (18). Thus single crystal experiments on oriented samples must be performed to establish reliable values of the highest E_s attained in the samples; and other experiments testing at what value of E_s initiation occurs, without direct contact, would be valuable.

Our previous model for the photo-electronic initiation effect (decrease in average threshold field for initiation when strongly absorbed light is applied simultaneously) involved a redistribution of the electric field as a consequence of the illumination (2). The analysis of the field initiation experiments provides a more quantitative basis for this model. We assume that $Pb(N_3)_2$ is highly insulating (a perfect dielectric), and acts as an extrinsic semiconductor upon irradiation. This determines the increase in E_s that results from a uniformly absorbed radiation pulse, in the absence of contacts. The analysis must be expanded to include non-uniformly absorbed irradiation (which is straightforward), and also the direct ($\ell = 0$) metallic contact situation (as in the Schottky-barrier analysis).

Finally, recent surface studies of explosive azides (19) have found contamination, and the absence of stoichiometry, in the topmost several layers of even laboratory-quality samples. This may explain why attempts to find injecting contacts have not been successful, and also how to overcome this problem. It also suggests closer scrutiny of the relation between prior treatment of azide surfaces and the sensitivity of explosive azide powders.

CONCLUSIONS

An integrated experimental and theoretical program to understand the field initiation properties of explosive azides has resulted in an important broad conclusion. Contact and surface effects dominate the electric field initiation properties of these materials. This realization has been successfully used to relate the results of experiments performed under different sample forms.

The results and understanding are directly relevant to a number of novel fuzing device applications (e.g., fuzes that require more than one stimulus to fire), and to safety against electrical and electrostatic hazards in the storage and handling of munitions.

REFERENCES

1. H. D. Fair, Jr., D. S. Downs, A. C. Forsyth, W. Garrett, M. Blais, T. Gora and F. E. Williams, Picatinny Arsenal Technical Report 4607, December 1973.

2. D. S. Downs, W. Garrett, D. A. Wiegand, T. Gora, M. Blais, A. C. Forsyth and H. D. Fair, Jr., Picatinny Arsenal Technical Report 4711, September 1974.

3. D. S. Downs, T. Gora, M. Blais and W. L. Garrett, Picatinny Arsenal Technical Report 4874, November 1975.

4. F. P. Bowden and A. C. McLaren, Proc. Roy. Soc. A246, 197 (1958).

5. H. S. Leopold, Naval Ordnance Laboratory Technical Report 73-125 (1973).

6. Y. A. Zakharov and Y. N. Sukhushin, Izv. Tomsk Politeck.. Inst. 251, 213 (1970). Y. N. Sukhushin, Y. A. Zakharov and F. I. Ivanov, Khim. Vys. Energiy 7, 216 (1973).

7. M. S. Kirshenbaum, Picatinny Arsenal Technical Report 4559 (1973).

8. C. Kittel, *Introduction to Solid State Physics* (Wiley, New York, 1968).

9. M. A. Lampert and P. Mark, *Current Injection in Solids*, Chapter 1 (Academic Press, New York, 1970).

10. J. E. Schiviner, Sandia Laboratories, Report No. 73-5001 (1973).

11. P. Mark and T. Gora, J. Solid State Chem. 15, 79 (1975).

12. R. H. Bube, J. Appl. Phys. 31, 2239 (1960); P. Mark and B. W. Lee, J. Phys. Chem. Solids 35, 865 (1974).

13. T. Gora and P. Mark (unpublished calculations).

14. T. Gora, J. Sharma, D. A. Wiegand, W. L. Garrett and D. S. Downs, *Proceedings of the 1976 Army Science Conference* (West Point, New York, June 1976).

15. W. L. Garrett, Mat. Res. Bull. 7, 949 (1972).

16. J. J. O'Dwyer, J. Appl. Phys. 40, 3887 (1969).

17. T. H. DiStefano and M. Shatzkes, Appl. Phys. Lett. 25, 685 (1974); J. Vac. Sci. Tech. 12, 493 (1975).

18. W. L. Garrett, Mat. Res. Bull. (to be submitted); private communication.

19. P. DiBona, D. A. Wiegand and J. Sharma, J. Vac. Sci Tech. 13, 45 (1976).

395

ADIABATIC ELASTIC MODULI OF SINGLE CRYSTAL PENTAERYTHRITOL TETRANITRATE (PETN)

C. E. Morris
Los Alamos Scientific Laboratory
University of California
Los Alamos, New Mexico 87545

The six elastic moduli which are required to characterize the tetragonal crystal structure of PETN were determined from ultrasonic wave velocity measurements at ambient conditions. A sufficient number of velocity measurements were made to provide cross-checks, and a detailed error analysis was done to estimate the probable error in the calculated moduli. The magnitudes of the elastic stiffness moduli in units of GPa (1 GPa = 10 kbar) along with the probable errors are given below.

$$c_{11} = 17.18 \pm 0.6\% \qquad c_{66} = 3.93 \pm 0.5\%$$
$$c_{33} = 12.14 \pm 0.5\% \qquad c_{12} = 5.43 \pm 1.8\%$$
$$c_{44} = 5.03 \pm 0.5\% \qquad c_{13} = 7.48 \pm 11.5\%$$

INTRODUCTION

The Los Alamos Scientific Laboratory now has the capability of growing large (10-20 mm) single crystals of some high explosives. This has enabled the measurement of some physical properties of explosives which until now have been impossible to determine. In particular, the fundamental elastic moduli can be measured. These moduli are important for the theoretical study of explosives. PETN is a commonly used secondary explosive. As such, its physical properties are of interest. From the ultrasonic viewpoint, it is an ideal high explosive to study since the single crystals are relatively easy to grow and have one of the simplest crystal structures (tetragonal, 42m symmetry).

SAMPLE DESCRIPTION

The large single crystals used were grown slowly from a PETN-ethyl acetate solution. Typical linear dimensions of the crystals were 25 mm on edge. Due to the low density of PETN, the Laue back reflection method could not be used to align the crystals. A two-circle goniometer that utilized a laser beam reflected from a natural crystal face (101 or 110 direction) was used to align the crystals for cutting on a small circular saw. To insure proper alignment, the orientation was checked before and after cutting. All the samples were aligned to within 0.5°. Final surface preparation was done by hand-lapping on 40 μm sandpaper. Typical dimensions of the finished samples were 3 to 5 mm thick with lateral dimensions of about 25 mm. The sample faces were parallel to within 0.01°. Howard H. Cady of Group WX-2, Los Alamos Scientific Laboratory, grew the single crystals and fabricated the samples.

The PETN crystals had two unusual characteristics worth mentioning. On some of the natural faces, a conical growth center existed which had a depression at its center. The vertex angles of the cones varied from face to face and especially from crystal to crystal. Cone vertex angles ranged from 179.8° to 178.5°. Every large crystal examined had at least

two conical growth faces. These conical growth centers were accidently discovered when it was observed that the spot projected on a natural face by a laser was reflected back on the wall as a cylindrical arc or circle. The other unusual characteristic of these crystals was their sensitivity to thermal shock. A freshly grown crystal when picked up in your hand would sometimes shatter. This thermal sensitivity diminished with age.

EXPERIMENTAL METHOD

Wave Propagation in Single Crystals

PETN has a tetragonal crystal structure with 42m symmetry. Six elastic stiffness moduli c_{11}, c_{33}, c_{44}, c_{66}, c_{12}, and c_{13} are needed to specify its elastic properties (1). The equations relating ρV^2 to the elastic moduli are given by the Christoffel relations (2). From these relations, it can be shown that for a given propagation direction in any single crystal, three plane-wave modes exist, each traveling with a characteristic velocity and particle displacement direction. Each wave velocity is a function of one or more elastic stiffness moduli and the density. Because of the Hermitian property of the Christoffel matrix, each particle displacement direction of the three modes is mutually orthogonal. Depending on the symmetry of the crystal in the direction of propagation, the particle displacement may or may not be precisely parallel or perpendicular to the propagation direction. For example, for the PETN crystals A, B, and C in Table 1, L and S denote respectively pure longitudinal and shear modes for which the particle displacement directions are exactly parallel and perpendicular to the propagation direction. For crystal D, QL, and QS denote respectively quasi-longitudinal and quasi-shear modes. For these modes, the particle displacements are not exactly parallel and perpendicular to the propagation direction, the misalignment being $5.7°$.

The orientations of the crystal faces were selected to provide the most direct relations between the measured wave velocities and the six elastic moduli. Crystals A and B are oriented for wave propagation along the principal crystallographic directions, to obtain the four diagonal moduli, c_{11}, c_{33}, c_{44}, and c_{66}. The remaining two orientations were chosen to derive the two cross-coupling moduli c_{12} and c_{13}. These cross-coupling moduli can be derived from velocities propagated in any direction which is perpendicular

to one principal axis and inclined to one of the other two principal axes at some angle θ. The angle θ is normally chosen close to $45°$ to minimize the deviation of the particle displacement direction from the propagation direction for quasi-longitudinal modes (3). This reduces the possibility that the quasi-longitudinal and quasi-shear waves will interfere with each other when their respective velocities are being measured. This orientation also yields the most direct relations for the cross-coupling moduli.

Experimental Geometry

A schematic diagram of the experimental geometry is shown in Fig. 1. This geometry was chosen because it facilitated sample assembly, isolated the high voltage impressed on the quartz crystals from the explosive, and aided in making accurate velocity measurements. Quartz crystals were used to generate and detect ultrasonic waves which travelled through the fused quartz buffer rod and resonated in the sample. 20 MHz, X-cut, quartz crystals were used to excite the longitudinal modes and 10 Mhz, Y-cut, quartz crystals, oriented with their vibration direction parallel to a shear normal mode direction, were used to excite separately each shear mode.

The buffer rod was approximately 65 mm long, 25 mm in diameter and had a working area at the sample end of 250 mm^2. To suppress spurious trailing pulses generated at the rod's surface, its periphery was threaded (1 thread/mm, 1 mm deep). A light lubricating oil was used as a seal material to couple longitudinal waves into the buffer rod and sample while a viscous resin, poly-α-methylstyrene, was used for shear waves. Normally, to get a thin viscous resin seal, the buffer rod and sample are heated to about $60°C$ and then the sample is "wrung" onto the rod. Since the explosive sample could not be heated, a moderately thin seal was obtained by first heating the rod without the explosive and then spreading as thin
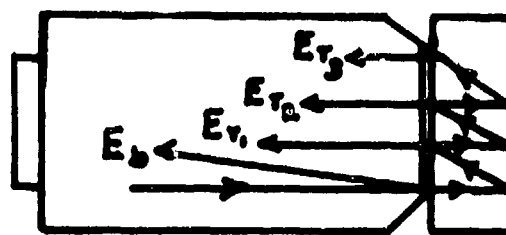

Fig. 1. Schematic Diagram of Experimental Geometry.

397

a film as possible with a flat plate. The rod was allowed to cool before the explosive was put into position. A spring loaded plunger held the explosive on the rod and further aided in extruding the resin.

Phase Comparison Technique

The phase comparison technique of McSkimin (4) was used for transit time measurements. These measurements are made by sending a finite length ultrasonic wave-train through the buffer rod to resonate in the sample (Fig. 1). This wave train has an accurately measured, but variable, RF carrier frequency. The wave-train length is purposely made longer than the sample transit time so that the echoes will phase-interfere with each other but less than the round-trip transit time in the buffer rod to isolate the sample resonance from the buffer rod resonance. At each impedance discontinuity the ultrasonic wave splits up into a reflected and transmitted wave. Figure

1 shows, in schematic form, the build-up process due to the reflections. At discrete RF frequencies, f_n, the sample-waves E_{T_1}, E_{T_2}, etc. are in phase with each other, but precisely out of phase with the strong interface reflection E_b. The velocity of propagation is given by

$$V = 2df_n/(n + a_n/360) \tag{1}$$

where d is the explosive thickness, n is an integer and a_n is the phase shift in degrees associated with the reflection of the wave from the sample-seal interface. The integer n can be determined without ambiguity by the equation

$$n = f_n/[(f_n - f_{n-m})/m] - 1/2 \tag{2}$$

where m is determined by counting the number of times the "in-phase" condition occurs as the frequency is varied from f_{n-m} to f_n. Typically n was about 40 for

TABLE 1

Summary of Wave Velocity – Elastic Stiffness Modulus Relations

Velocity Number	Crystal	Type Mode	Direction of Particle Motion	ρV^2	V km/s
1	A	L	100	c_{11}	3.1140
2	A	S	001	c_{44}	1.6841
3	A	S	010	c_{66}	1.4893
4	B	L	001	c_{33}	2.6167
5	B	S	010	c_{44}	1.6822
6	B	S	100	c_{44}	1.6822
7	C	L	110	$(c_{11} + c_{12})/2 + c_{66}$	2.9308
8	C	S	-110	$(c_{11} - c_{12})/2$	1.8197
9	C	S	001	c_{44}	1.6866
10	D	QL	101*	$\{(c_{11} + c_{33} + 2c_{44}) + [4(c_{13} + c_{44})^2 + (c_{11} - c_{33})^2]^{1/2}\}/4$	2.9636
11	D	QS	-101*	$\{(c_{11} + c_{33} + 2c_{44}) - [4(c_{13} + c_{44})^2 + (c_{11} - c_{33})^2]^{1/2}\}/4$	1.3588
12	D	S	010	$(c_{44} + c_{66})/2$	1.6306

*approximate direction

$\rho = 1.773$ kg/m^3

for the PETN samples. Equation (2) differs from the one given by McSkimin (4) because the acoustical impedance $(Z = \rho V)$ of explosives is less than fused silica. Consequently, the phase shift for zero seal thickness is $180°$ rather than $0°$ (see Fig. 2).

A good first order approximation for the velocity is to assume $a_n = 180°$ (zero seal thickness approximation). This gives a velocity accurate to about 0.4%. A much better procedure is to experimentally measure the relative amplitudes of E_b, E_{T_1}, E_{T_2}, etc. at resonance. One is then able to determine a_n precisely. The phase shift a_n is given by (4)

$$a_n = a_n(Z_1, Z_2, Z_3, \theta) \qquad (3)$$

where Z_1, Z_2, and Z_3 are respectively the acoustical impedances of the explosive sample, fused quartz buffer rod, and the seal material, and θ is the seal thickness expressed in degrees $[\theta = 360 (l/\lambda) = 360 (lf_n/V)]$. Typical seal thicknesses range from $5°$ to $15°$. The function $a_n (\theta)$ is shown in Fig. 2 for the case of a longitudinal wave traveling in the (100) direction in PETN. The relative amplitudes of the waves at resonance can also be expressed in terms of the above variables plus the attenuation coefficient α.

$$E_{T_1}/E_b = - A(Z_1, Z_2, Z_3, \theta) \exp(-2\alpha d) = - X \qquad (4)$$

$$E_{T_2}/E_{T_1} = E_{T_3}/E_{T_2} = B(Z_1, Z_2, Z_3, \theta) \times$$

$$\exp(-2\alpha d) = Y \qquad (5)$$

The functions $a_n (Z_1, Z_2, Z_3, \theta)$, $A (Z_1, Z_2, Z_3, \theta)$ and $B (Z_1, Z_2, Z_3, \theta)$ are given in Ref. (4). Since A and B are positive valued functions, it is evident from Eqs. (4) and (5) that frequencies which place the specimen waves E_{T_1}, E_{T_2}, etc. in phase also place E_{T_1} and E_b out of phase. McSkimin's (4) recipe to determine θ is to measure E_{T_1}/E_b in this experiment and measure α in a different experimental geometry. The seal thickness can then be calculated from Eq. (4). To minimize the handling of explosives, an alternate approach was used. Eqs. (4) and (5) can be combined to given an expression independent of α.

$$X/Y = A(Z_1, Z_2, Z_3, \theta)/B(Z_1, Z_2, Z_3, \theta) \qquad (6)$$

The function X/Y is shown in Fig. 3 for the case of a longitudinal wave traveling in the (100) direction in

PETN. Experimentally, a_n is determined by measuring the amplitudes of E_b, E_{T_1}, E_{T_2}, etc. from which a value of X/Y can be calculated. The value of θ can then be obtained from Eq. 6 which in turn can be used in Eq. 3 to calculate a_n.

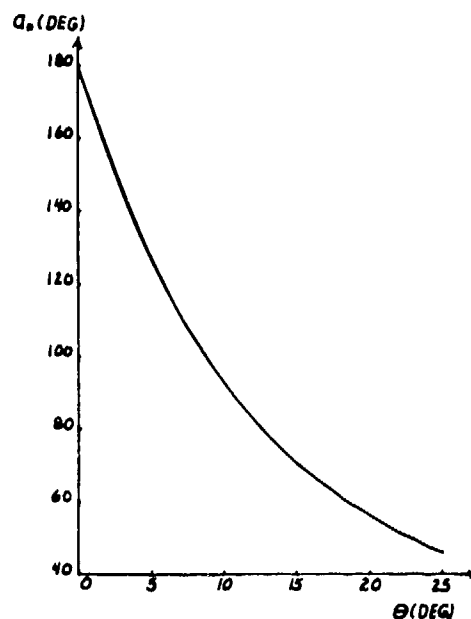
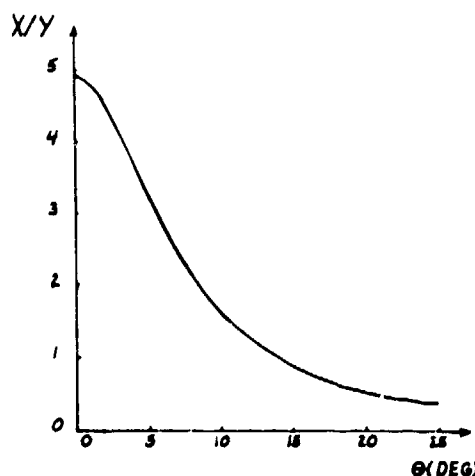Fig. 2. Variation of Phase Shift as a Function of Seal Thickness.

Fig. 3. Variation of X/Y as a Function of Seal Thickness.

EXPERIMENTAL RESULTS

Calculation of Moduli

The measured velocities given in Table 1 for the various modes of propagation are the average of three independent sets of velocity data. The density of PETN, inferred from x-ray lattice parameter measurements (5), is 1.773 kg/m^3. Using this density along with the measured plane-wave velocities, the elastic moduli can be evaluated by inverting the equations in Table 1. In general, there are at least two independent ways to calculate each modulus. The calculated moduli are listed in Table 2. Where the evaluation of a modulus was dependent on ρV^2 and other moduli, the weighted mean values of the required moduli were used. In the calculations of c_{13}, a square root needs to be taken which involves the appropriate choice of algebraic sign. The plus sign results in a positive value of c_{13} whereas the sign results in a positive value of c_{13} whereas the

negative sign gives a negative value. It can be shown from crystal stability arguments (6) that the plus sign is the correct choice.

Error Analysis

It is informative in analyzing the elastic moduli data, to calculate the probable error in each calculated modulus. This gives a method of weighting the various calculated moduli and also provides information relative to the self consistency of the measured velocities. Since it's impractical to make enough velocity measurements to be statistically significant, it seems more reasonable to estimate the possible errors in each factor involved in a velocity measurement, sum up the errors and arrive at an estimated probable error. Using these probable velocity errors, the probable error in the elastic moduli can be calculated using the standard equations (7) for the propagation of independent, random errors.

TABLE 2

Summary of Calculated Elastic Moduli

Modulus	Velocity Equation	Calculated Modulus (GPa)	Probable Error %	Weighted Modulus (GPa)	Experimental Error %	Recommended Modulus (GPa)
c_{11}	1	17.193	0.72	17.177	0.09	17.18
c_{11}	7 + 8	17.167	0.56		0.06	(0.6%)
c_{33}	4	12.140	0.53	12.002	1.15	12.14
c_{33}	10 + 11	10.454	1.75		11.44	(0.5%)
c_{44}	2	5.029	0.56	5.030	0.02	5.03
c_{44}	5	5.017	0.52		0.26	(0.5%)
c_{44}	9	5.044	0.54		0.28	
c_{66}	3	3.933	0.54	3.993	1.49	3.93
c_{66}	12	4.398	1.41		10.16	(0.5%)
c_{12}	7	5.416	3.83	5.428	0.22	5.43
c_{12}	8	5.435	2.14		0.13	(1.8%)
c_{12}	7 - 8	5.425	1.79		0.06	
c_{13}	10	6.145	2.83	7.477	17.81	7.48
c_{13}	11	7.868	0.97		5.23	(11.5%)
c_{13}	10 - 11	7.008	1.37		6.27	

The probable error in each velocity measurement, which takes into account the error in the resonant frequency measurement, thickness measurement and seal thickness determination is

$$\left(\frac{\Delta V}{V}\right)^2 = \left(\frac{\Delta d}{d}\right)^2 + \left(\frac{\Delta f_n}{f_n}\right)^2 + \left(\frac{\Delta a_n/360}{n + 1/2}\right)^2 \quad (7)$$

The estimated percent error for sample thickness, resonant frequency, and phase shift are respectively 0.20%, 0.10%, and 0.14%. This results in a velocity error of 0.26%. In three cases where the measured transit times had a slightly larger variation than given by the last two terms in Eq. (7), the larger values for these quantities were used. Using the above probable velocity errors, the estimated errors in the calculated moduli are given by

$$\Delta c_{ij} = \left[\sum_{k,1 \neq i,j} \left(\frac{\partial c_{ij}}{\partial c_{k1}} \Delta c_{k1}\right)^2 + \left(\frac{\partial c_{ij}}{\partial(\rho V^2)} \Delta(\rho V^2)\right)^2 + \left(\frac{\partial c_{ij}}{\partial \phi} \Delta\phi\right)^2 \right]^{1/2} . \quad (8)$$

The first two terms in Eq. (8) can be straightforwardly calculated. The last term is the orientation error due to the misalignment $\Delta\phi$ of the crystal face. For all crystal cuts used, $\Delta\phi$ was equal to $0.5°$. Direct calculation of the last term is extremely arduous. However, it can be evaluated rather easily by realizing that the effect of misorientation is to perturb the velocity. The amount of perturbation can be calculated by solving for the eigenvalues of the Christoffel matrix for which the propagation direction is inclined at an angle $\Delta\phi$ with respect to the intended direction. Since the magnitude of the perturbation is dependent on the direction of misalignment, the maximum perturbation value was chosen for evaluation of Eq. 8. In cases where more than one ρV^2 term is involved in the calculation of a modulus an additional velocity and orientation term should be added to Eq. (8).

The probable error deduced from Eq. (8) for each calculated modulus is given in Table 2. The weighted modulus is also given and is computed by weighting each calculated modulus by a factor that is inversely proportional to the square of the probable error. This

ideally results in the best estimation for a given modulus. The experimental error listed in Table 2 is the percent deviation of each independently calculated modulus from the weighted modulus.

It is evident from Table 2 that in some cases, there is good agreement between the probable error and the experimental error, while in other cases, the experimental error is considerably greater than the probable error. Closer examination of the data reveals that the velocity data for crystals A, B, and C (velocities 1 through 9) are in excellent agreement. In most cases, the agreement of the calculated moduli is considerably better than the predicted probable error. However, the moduli calculated from the velocities measured on crystal D (velocities 10, 11 and 12) do not show good agreement amongst themselves in the calculation of c_{13} or with crystals A, B, and C in the calculation of c_{33} and c_{66}. Even though there were three independent evaluations of each propagation velocity on crystal D, the measurements were repeated on a different crystal because of this disagreement with the probable error calculation. The velocities on the second crystal agreed to within 0.1% of the measured velocities on the first crystal. It was implicitly assumed in the derivation of the equations relating ρV^2 to the elastic moduli that the PETN crystal was a perfect single crystal in which all unit cells were perfectly aligned relative to each other. A possible reason for the lack of agreement might be that there is a crystal defect such that the velocities are slightly perturbed in the 101 direction so that the equations in Table 1 are not perfectly valid. Alton and Barlow (8) have reported measurements on calcium molybdate, a single crystal with tetragonal symmetry, in which a similar discrepancy occurred in the cross-coupling moduli. The cross-coupling moduli had a 50% error that could not be accounted for using standard error theory for perfect single crystals.

Because of the poor agreement between the predicted probable error and the experimental error, the weighted modulus values of c_{33} and c_{66} are unrealistic. A more plausible approach would be to assume the directly measured values of these moduli are correct to within the predicted probable error and ignore the values of these moduli calculated from velocities 10, 11, and 12. These directly measured values of c_{33} and c_{66} are listed under recommended modulus in Table 2. As far as the recommended modulus values for c_{11}, c_{44}, and c_{12} are concerned,

the weighted values are probably the best since the experimental error is entirely consistent with the predicted probable error. The listed errors for these moduli are chosen to be the lowest values of their respective probable errors. This should be a conservative estimate since the experimental agreement is much better. Even though the probable error car. .t account for the range of c_{13} values, the weig. ed modulus is still the best estimate for c_{13}, if fo: no other reason than the probable error is a good estimation of the sensitivity of each calculated modulus to variation of the other moduli and the propagation velocity. As such, the calculated modulus least affected by small variations in the other moduli and measured velocity would also be the least affected by crystal imperfections. The percent error in c_{13} was estimated by dividing the range of measured c_{13} values by $2 c_{13}$.

Calculation of Bulk Modulus

One thermodynamic variable of direct interest in shock wave studies is the adiabatic bulk modulus. The bulk modulus for tetragonal crystais of 42m symmetry is given by

$$B_s = \frac{c_{33}(c_{11} + c_{12}) - 2c_{13}^2}{c_{11} + c_{12} + 2c_{33} - 4c_{13}} \qquad (9)$$

It is interesting to note that a knowledge of all the elastic constants is not required to calculate the bulk modulus. Evaluation of Eq. (9) in terms of the recommended moduli listed in Table 2 yields a value of 9.58 GPa with an estimated erroi of 4.6%. The majority of the error in B_s is due to the error in c_{13}. The bulk modulus was also measured on polycrystalline PETN samples which were 99% of theoretical density. The bulk modulus on these pressed samples varied between 9.24 to 9.45 GPa. The polycrystalline data is consistent with the single crystal data since it should provide a lower bound for the bulk modulus.

SUMMARY

The adiabatic elastic moduli for tetragonal single crystal PETN were measured using the phase comparison technique of McSkimin with minor variations. Measurements on four different crystal orientations yielded twelve wave velocities from which the six moduli were calculated. The self-consistency cross-

checks on c_{11}, c_{12}, and c_{44} were excellent while the cross-checks on c_{33}, c_{66}, and c_{13} were not. The only modulus with appreciable error was c_{13} which was estimated to be 11.5%. The single crystal bulk modulus agrees rather well with the bulk modulus of polycrystalline specimens indicating the value of c_{13} is probably within its estimated error.

REFERENCES

1. Walter Guyton Cady, Piezoelectricity, pp. 17-20, 53-57, McGraw-Hill, New York, 1946

2. Warren P. Mason, Physical Acoustics and the Properties of Solids, pp. 368-373, D. Van Nostrand, New York, 1958

3. E. S. Fisher and H. J. McSkimin, "Adiabatic Elastic Moduli of Single Crystal Alpha-Uranium," J. Appl. Phys. Vol. 29, No. 10, pp. 1473-1484, Oct 1958

4. H. J. McSkimin, "Use of High Frequency Ultrasound for Determining the Elastic Moduli of Small Specimens," IRE Trans. on Ultrasonic Eng., PGUE-5, pp. 25-43, 1957

5. Howard H. Cady, "The PETN-DiPEHN TriPEON System," LASL Rept. LA-4486-MS, Dec 1972

6. G. A. Alers and J. R. Neighbours, "Crystal Stability and Elastic Constants," J. Appl. Phys., Vol. 28, No. 12, p. 1514, Dec 1957

7. Yardley Beers, Introduction to the Theory of Error, pp. 26-36, Addison-Wesley, Reading, Mass., 1958

8. W. J. Alton and A. J. Barlow, "Acoustic-Wave Propagation in Tetragonal Crystals and Measurements of the Elastic Constants of Calcium Molybdate," J. Appl. Phys., Vol. 38, No. 10, pp. 3817-3820, Sept 1967

Session VI
DETONATION AND INITIATION

Chairman: R. W. Van Dolah
U. S. Bureau of Mines

TWO DIMENSIONAL HOMOGENEOUS AND HETEROGENEOUS
DETONATION WAVE PROPAGATION

Charles L. Mader
Los Alamos Scientific Laboratory
University of California
Los Alamos, New Mexico 87545

*The process of detonation propagation of homogeneous explosives along surfaces
may be described using resolved reaction zones, Arrhenius rate laws and two dimen-
sional reactive hydrodymanic calculations. The wave curvature increases with
increasing reaction zone thickness. The process of detonation propagation and
failure of heterogeneous explosives along surfaces and around corners may be
described if the decomposition that occurs from hot spots formed by shock inter-
actions with density discontinuities is described by a burn rate determined from the
experimentally measured distance of run to detonation as a function of shock
pressure, the reactive and nonreactive Hugoniot and the assumption that the reac-
tion rate derived near the front can be applied throughout the flow.*

INTRODUCTION

The time-dependent behavior of detonations with
resolved reaction zones in condensed homogeneous
explosives has been described (1,2), using an Arrhe-
nius rate law. The failure of a nitromethane detona-
tion, resulting from a side rarefaction cooling the
explosive inside its reaction zone, was calculated and
the experimentally observed rarefaction velocity was
reproduced. We shall extend the study to nitro-
methane detonations proceeding perpendicular to
metal surfaces and examine wave curvature and
failure as a function of reaction zone thickness.

Experimental observations (3) of detonation waves
in heterogeneous explosives proceeding perpendicular
to metal plates showed very little wave curvature
after a large plane-wave-initiated cylindrical explosive
charge had run several charge diameters. An empiri-
cal model with an unresolved explosive reaction zone
and programmed to maintain a constant velocity,
plane detonation front reproduced the experimental
observations. Because the basic mechanism of hetero-
geneous shock initiation is shock interaction at

density discontinuities producing local hot spots that
decompose and add their energy to the flow, models
such as the heterogeneous-sharp-shock-partial-reaction
burn model, have been developed to model the flow
(4). They have not been useful for solving two
dimensional reactive flows because they did not re-
spond to local state variables in a realistic manner.
We used a new model called Forest Fire (5) to
describe the hot spot reaction rate in the bulk of the
heterogeneous explosive to detonations proceeding
perpendicular to metal plates, to detonations turning
corners and to detonations proceeding along free sur-
faces for shock sensitive and insensitive explosives.

HOMOGENEOUS DETONATIONS

Reference 1 shows that the reaction zone of nitro-
methane is ~2500 A long and that it is probably
pulsating about the steady-state values if the usual
activation energies (E) and frequency factors (Z) are
appropriate. It is impossible to make calculations
with such small reaction zones being resolved for
systems the size usually studied experimentally. We

405

can study the effect the size of the reaction zone has on the flow by increasing the frequency factor to scale up the size of the reaction zone. We can also eliminate the pulsating nature of the reaction zone by choosing an activation energy that results in steady nonpulsating flow. As shown in Ref. 1, an activation energy of 30 kcal/mole results in steady flow, and by varying the frequency factor, we can have various thickness reaction zones. However, because such scaling results in unrealistically large reaction zones, care is required in extrapolating the calculated results to real experiments.

Experimental measurements of the detonation wave arrival of nitromethane across the surface of a charge have shown that there is remarkably little wave curvature even after the wave has run many charge diameters in a large plane-wave-initiated cylindrical charge. In our first study we investigated how a resolved reaction zone in nitromethane proceeds perpendicular to a copper surface. Figure 1 shows that the larger reaction zone resulted in an increased wave curvature. The calcula. .s were performed using the 2DL reactive hydrodynamic code (6) with a mesh of 0.01 cm square. The equation-of-state parameters used for nitromethane are described in Ref. 7 and those for copper aluminum and Plexiglas are described in Ref. 8. The detonation wave was started using the same steady-state piston described in Ref. 6. The absolute value of pressure is plotted and the slight discontinuity at the nitromethane-copper interface is from the different amounts of artificial viscosity in the two materials.

Because the detonation wave curvature decreases with decreasing reaction zone thickness, it is not surprising that nitromethane, with its very thin reaction zone, shows very little curvature. The reason for this result appears to be that although the head of the rarefaction goes into the reaction zone at the same speed regardless of the reaction zone thickness, the wave curvature depends upon how much the confining surface or wall moves out during passage of the reaction zone. Because lower density walls permit more outward motion than higher density walls, the lower density walls result in more curved fronts. Shortening the reaction zone keeps the wall from moving outward as much during transit which results in less shock curvature. The two critical parameters are the rarefaction speed and the reaction zone length.

Figure 2 shows that the increased divergence resulting from cylindrical geometry permits the outward moving surface to be more effective in increasing the wave curvature. The effect of changing the density of the confining wall is shown in Fig. 3, where the detonation wave proceeds along a copper and then an aluminum wall. Compared with the copper wall in Fig. 1, the curvature increases and the reaction zone becomes thicker as the reaction proceeds along the aluminum wall. These results qualitatively agree with the experimental observations.

Campbell, Malin and Holland (9) observed that thin foils of metal were as effective at confining the nitromethane detonation wave as were thick cylinders of the same metal. In Fig. 4 the thickness of the confining copper wall is decreased but the shockfront and reaction zone profile is the same as in Fig. 1. Other calculations showed that the reaction zone must be thick enough for the rarefaction from the outer copper surface to arrive back at the nitromethane-copper interface before passage of the reaction zone for the reaction zone and wave curvature to be effected by the thickness of the confining metal.

The detonation wave curvature increases with increasing reaction zone thickness. A thin metal cylinder may prevent detonation failure if the reaction zone is thin enough for the rarefaction from the outside metal surface to arrive in the detonation products after passage of the reaction zone. The observed failure and reignition of nitromethane detonation by holes in confining surfaces can be reproduced qualitatively by the Arrhenius kinetic model as shown in Ref. 5.

HETEROGENEOUS DETONATIONS

Heterogeneous explosives such as PBX-9404 or Composition B show a different behavior than homogeneous explosives when propagating along confining surfaces. A heterogeneous explosive can turn sharp corners and propagate outward. A heterogeneous explosive, depending upon its sensitivity, may exhibit either very little or a lot of curvature when propagating along a metal surface. The mechanism of initiation for heterogeneous explosives is different than the Arrhenius kinetic model found adequate for homogeneous explosives. Heterogeneous explosives
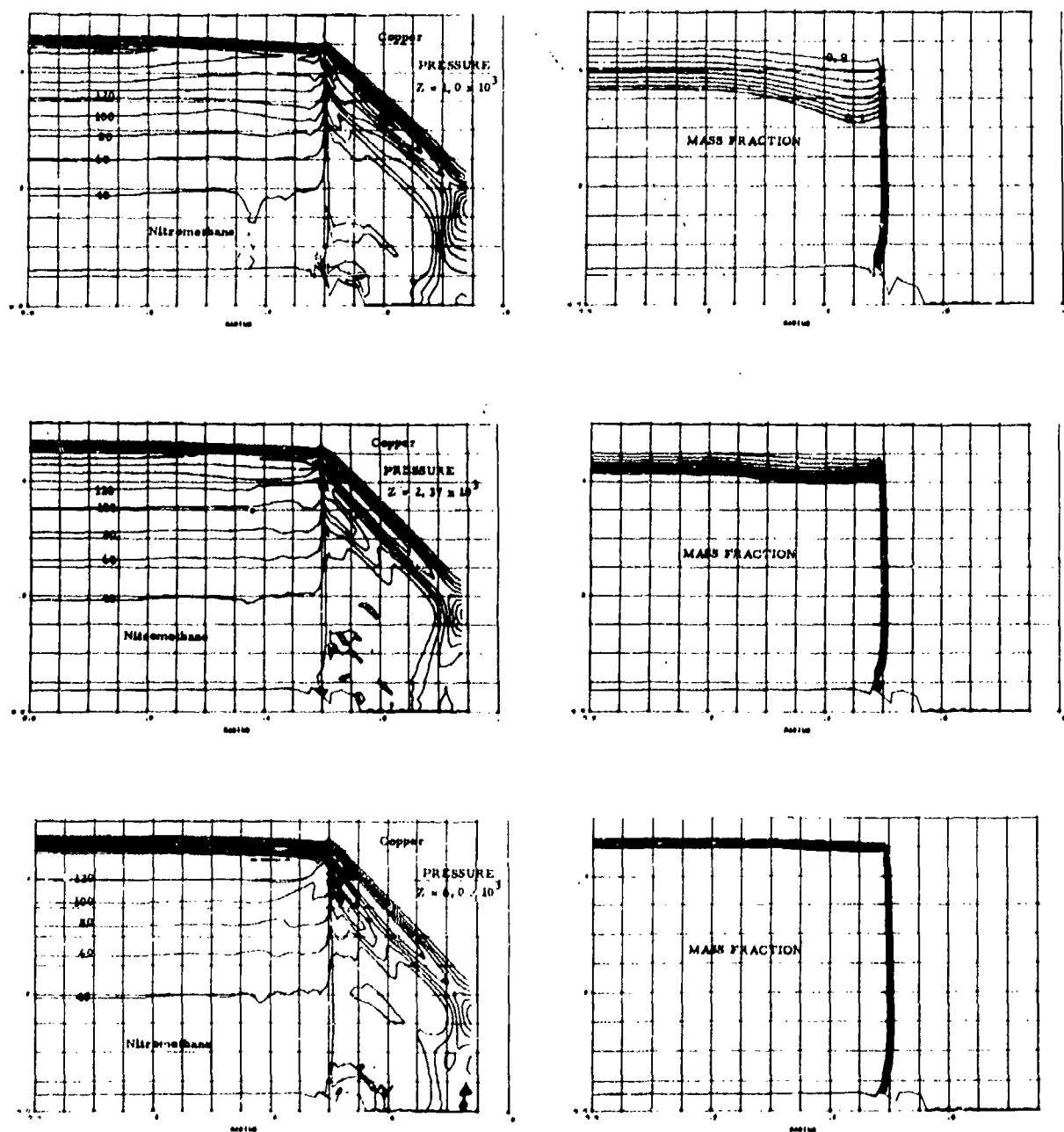
Fig. 1. A resolved nitromethane reaction zone of various thickness proceeding perpendicular to a copper plate. The nitromethane activation energy was 30 kcal/mole. The pressure profiles are shown at 20 kilobar intervals and the mass fraction of undecomposed explosive interval is 0.1. $Z = 1.0, 2.37$ and 6.0×10^3.
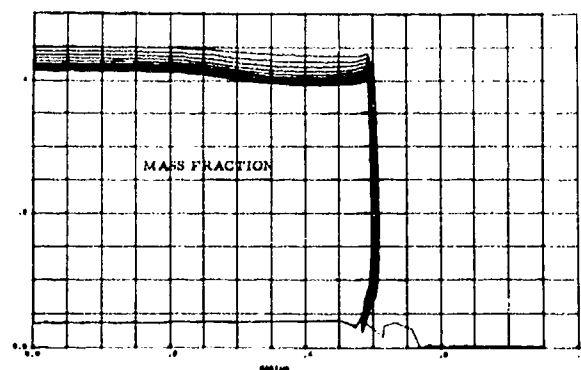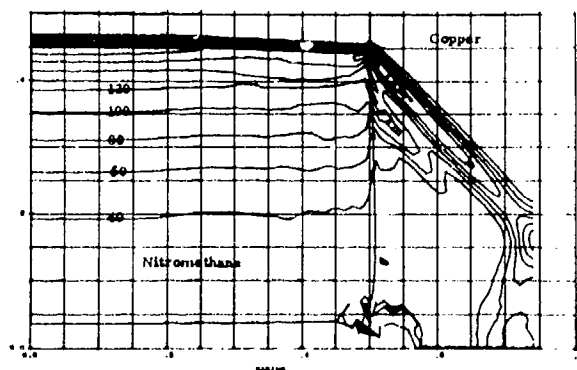
Fig. 2. A resolved nitromethane zone proceeding perpendicular to a copper cylinder. $Z = 2.37 \times 10^3$, $E = 30$.
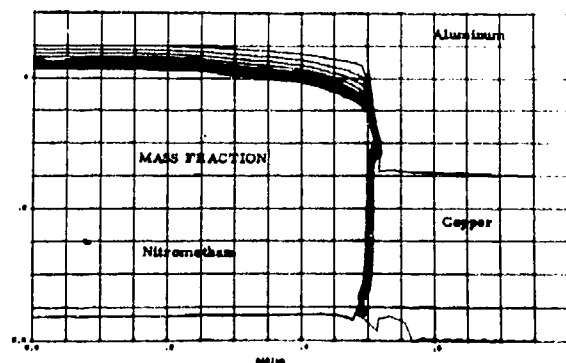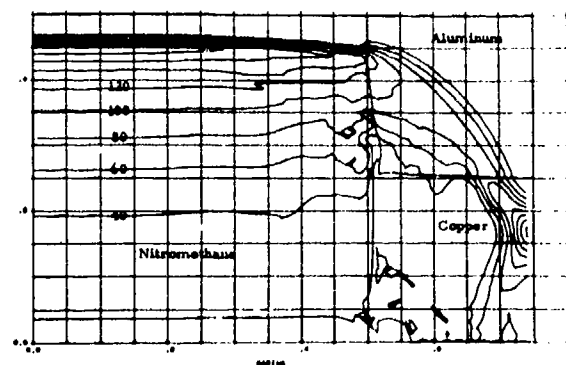
Fig. 3. A resolved nitromethane zone proceeding perpendicular to wall of copper and aluminum. $Z = 2.37 \times 10^3$, $E = 30$.
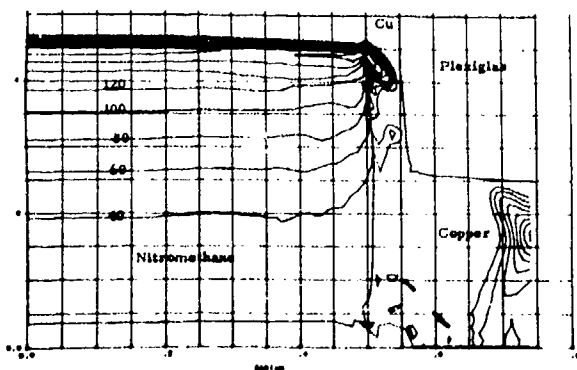

Fig. 4. A resolved nitromethane reaction zone proceeding perpendicular to a copper plate that becomes about as thin as the reaction zone thickness. $Z = 2.37 \times 10^3$, $E = 30$.

408

are initiated and may propagate by the process of shock interaction with density discontinuities such as voids. These interactions result in hot regions that decompose and give increasing pressures that cause more and hotter decomposing regions. Some heterogeneous explosives may require hot spots even for the propagation of the detonation wave.

Because previous modeling of heterogeneous shock initiation of explosives has proved useful only for certain applications (4), a more general model for the bulk decomposition of a heterogeneous explosive has been developed. It may be used to reproduce the explosive behavior in many one- and two-dimensional situations for which data is available. It is called the Forest Fire model and is described in Ref. 5. The model gives the rate of explosive decomposition as a function of the local pressure (or any other state variable) in the explosive shown in Fig. 5. In this section we shall describe the results of applying the Forest Fire description of heterogeneous explosive detonation propagation to detonation propagation along surfaces and around corners.
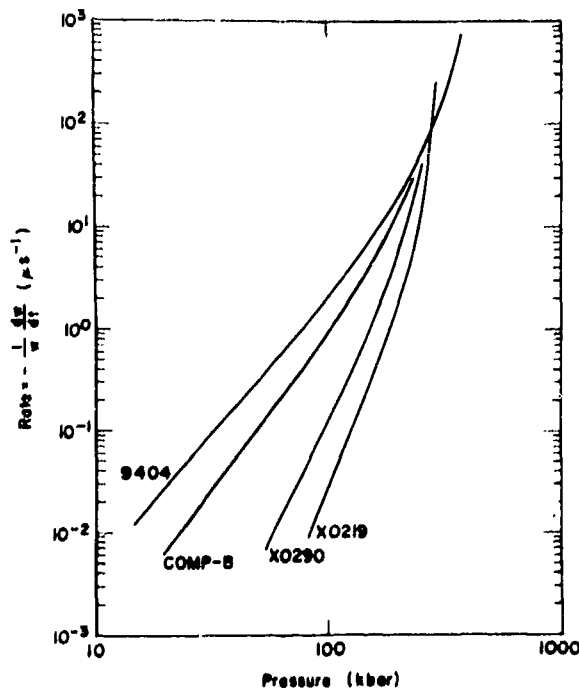
The Los Alamos Scientific Laboratory radiographic facility, PHERMEX (10) was used to study the detonation wave profile in heterogeneous explosives as it proceeds up metal surfaces (3,10). It has also been used to study the profiles when a detonation wave in Composition B or X0219 turns a corner (11,12).

As described in Ref. 3, a radiographic study was made of a 10.16-cm cube of Composition B, with and without tantalum foils, initiated by a plane wave lens confined by 2.54 cm-thick aluminum plates. The radiographs show a remarkably flat detonation front followed by a large decrease in density originating near the front of the wave as it intersects the metal plate.

A numerical calculation using Arrhenius kinetics results in considerable curvature of the detonating wave if realistic kinetic parameters are used. The Forest Fire model of heterogeneous shock initiation results in a calculated flow closely resembling that observed experimentally as shown in Fig. 6. This suggests that the observed detonation behavior is a result of the heterogeneous shock initiation processes.

Fig. 5. The rate of decomposition as a function of the pressure from the Forest Fire model.
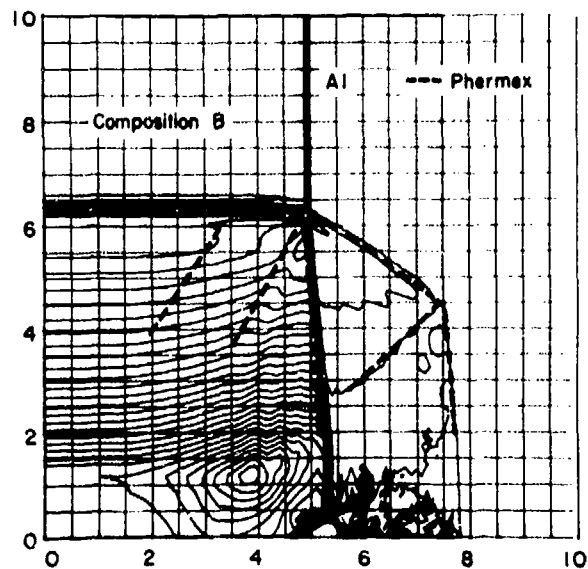

Fig. 6. The constant density profiles at 8 μsec for a 5-cm-half-thickness slab of Composition B detonating by the Forest Fire model up an aluminum plate 2.5-cm-thick. The prominent features of a radiograph of the flow are shown with dashed lines.

409

Therefore, the more insensitive explosives should give greater wave curvature and have larger failure diameters. Explosives initiated and burned with a heterogeneous shock initiation model, such as Forest Fire, do not exhibit scaling behavior and hence failure depends upon the pressure magnitude and how long it can be maintained. The Forest Fire model results agreed with experimental observations for many explosives.

Venable (11,5) performed a radiographic study of a Baratol plane-wave-initiated Composition B slab detonation proceeding perpendicular to an aluminum block and up a 45 degree wedge. Calculations using the Forest Fire model reproduced the features of the radiographs as shown in Fig. 7. This was not a very significant test of the Forest Fire model because the C-J volume burn technique or programmed burn technique of burning explosives can give also similar profiles to those observed experimentally. An Arrhenius burn with a resolved reaction zone will not give detonation wave behavior such as observed experimentally.

Dick (12) performed a radiographic study of a detonation wave proceeding up a block of a very insensitive triamino trinitrobenzene (TATB) based explosive, called X0219 (90% TATB, 10% KelF, ρ_0 = 1.914), and its failure to propagate completely around a corner. Dick's experimental profiles and the calculated profiles using the Forest Fire model are shown in Fig. 8. The agreement shown is encouraging. However, the amount of explosive that remains undecomposed after passage of the shock wave depends primarily upon the curvature of the detonation wave before it turns the corner. If the wave is sufficiently curved, the detonation proceeds like a diverging detonation wave and little or no explosive remains undecomposed. If the wave is flat, or nearly so, when it arrives at the corner then much more partially decomposed explosive will remain after shock passage. The actual experiment was performed with air in the corner so the Lagrangian calculation which required some low density material in the corner (we used Plexiglas) underestimates the amount of explosive that remains undecomposed. An aluminum corner results in very little undecomposed
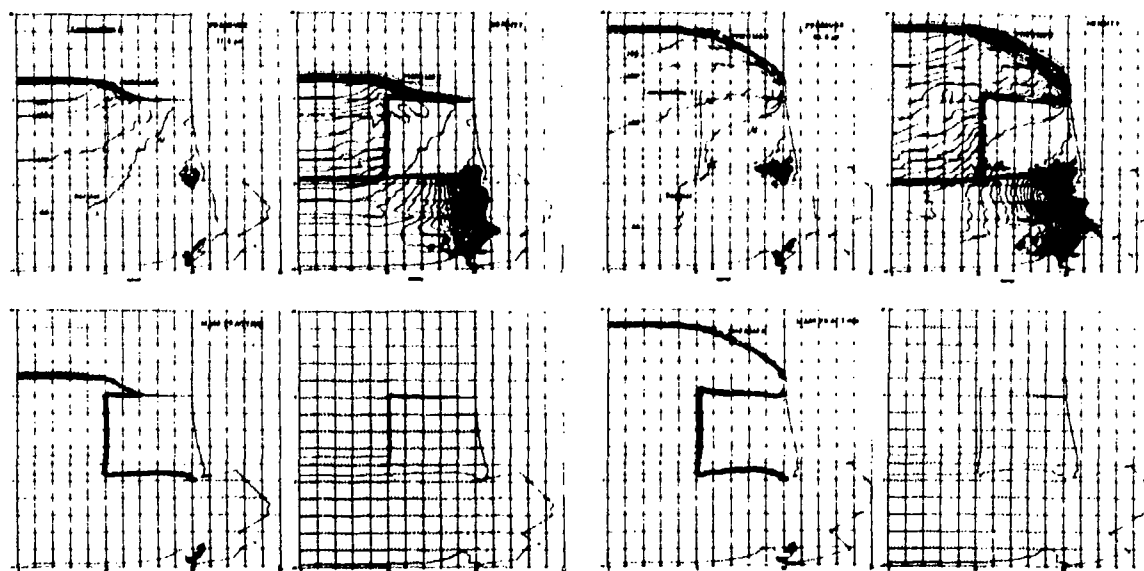

Fig. 7. Calculated profiles of a Composition B Forest Fire detonation proceeding around a 90° corner formed by an aluminum block. The pressure profile interval is 50 kbar, the density profile is 0.02 cc/gm, the mass fraction interval is 0.1 and the last figure is the mesh used in the calculation. The PHERMEX profiles are shown by dashed lines.

410

explosive, and a lower density material slightly increases the amount of undecomposed explosive.

To study this system in a more realistic geometry, we used the Eulerian code 2DE (13) because it can handle large distortion problems such as an explosive-air interface. The calculated results using Forest Fire burn are similar to those calculated with the 2DL code in Fig. 8. Again, the results depend upon the detonation wave profile before it reaches the corner. An interesting aspect of the calculational study was that if the wave was started out flat, the explosive region near the explosive-air interface remained partially decomposed and the detonation wave never completely burned across the front until the wave became sufficiently curved at the front and near the interface. The failure process of a heterogeneous

explosive must be a complicated interaction of the effective reaction zone thickness (presumably dependent upon the void and resulting hot spot size and decomposition rate) determining how flat the wave should be and the curvature required for decomposition to occur near the surface of the charge. Because the details of the hot spot reaction zone are missing from our calculation and model, much remains to be done before realistic calculations of failure radius can be achieved.

Calculations were performed using the Forest Fire burn in 2DL for 0.7- and 1.3-cm-radius cylinders of X0219 confined by Plexiglas and for half thickness slabs of 1.3 and 2.6 cm. The thinner charges developed greater curvature and the 0.7-cm-radius cylinder failed to propagate. Calculations were also performed using the Forest Fire burn in 2DE for 0.65 and 1.3-cm-radius cylinders of X0219 confined by air. The 0.65-cm-radius cylinder failed to propagate as shown in Fig. 9. The experimentally observed failure radius of X0219 is 0.75 cm. The results of similar calculations for 9404, Composition B, and X0290 are compared with the experimental failure radius of Campbell and Engelke (14) in Table 1. These results are
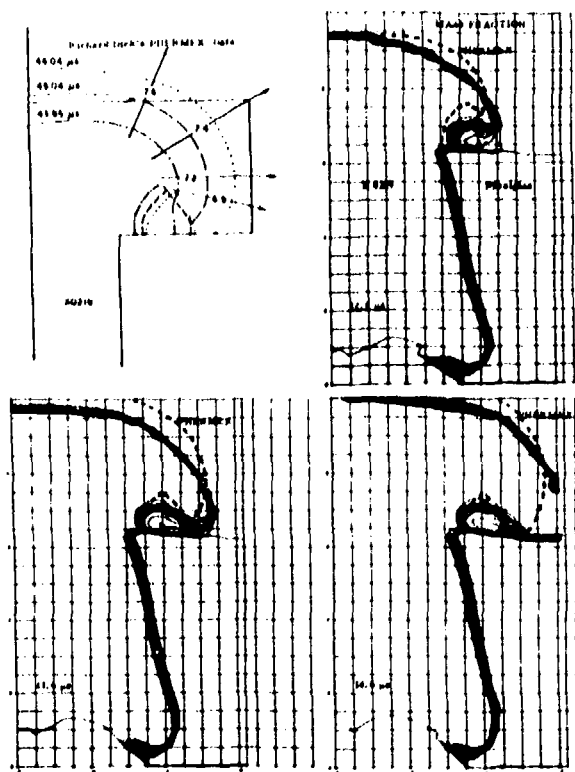

Fig. 8. The radiographic and calculated 2DL profiles of a detonation wave propagating around a corner of insensitive explosive X0219. The corner is filled with air in the experiment and with Plexiglas in the calculation.
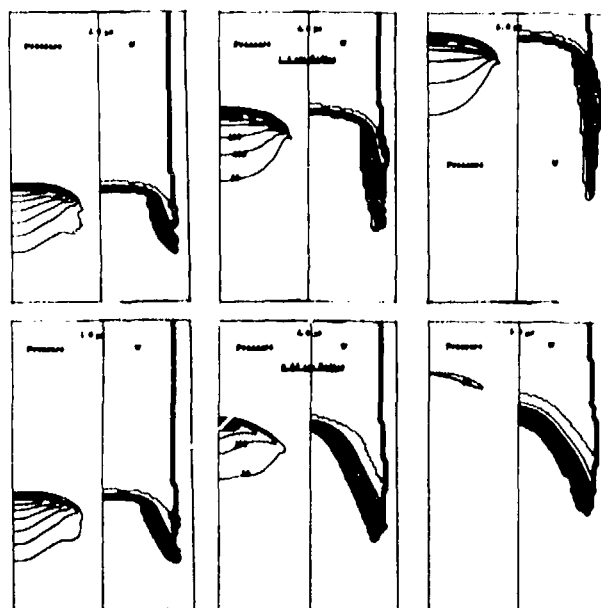

Fig. 9. The pressure and mass fraction profiles for a 0.65 and a 1.3-cm-radius cylinder of X0219 in air calculated using the 2DE code with the Forest Fire burn model.

411

TABLE 1

Experimental and Calculated Failure Radii

	Experimental Failure Radius (cm)	Calculated Results
X0219	0.75 ± .05	1.3 propagated 0.7 failed
X0290	0.45 ± .05	0.50 propagated 0.30 failed
Comp B	0.214 ± .03	0.30 propagated 0.20 failed
9404	0.06 ± .01	0.10 propagated 0.05 failed

a heterogeneous detonation wave depends upon the interrelated effects of the wave curvature and the shock sensitivity of the explosive. Some of the basic differences have been established between homogeneous and heterogeneous explosive propagation and failure.

ACKNOWLEDGMENTS

dependent upon the initiation method and the burn resolution. The dominate feature of failure in heterogeneous explosives appears to be the same hot spot decomposition reaction that determines the shock initiation behavior.

CONCULSIONS

The process of detonation initiation and propagation of homogeneous explosives along surfaces may be qualitaively described using Arrhenius kinetics. Because the reaction zone scale is orders of magnitude smaller than the scale of the experiments of interest, quantitative calculations are difficult to achieve. The ability of thin metal cylinders to prevent detonation failure in nitromethane and the observed failure and reignition of nitromethane by changes in confinement geometry may be qualitatively reproduced by numerical reactive fluid dynamics with Arrhenius kinetics.

Detonation initiation and propagation of heterogeneous explosives cannot be described adequately using Arrhenius kinetics. A new model can describe the decomposition that occurs from hot spots formed by shock interactions with density discontinuities in heterogeneous explosives and can also describe the passage of heterogeneous detonation waves around corners and along surfaces. Failure or propagation of

REFERENCES

1. Charles L. Mader, "One- and Two-Dimensional Flow Calculations of the Reaction Zones of Ideal Gas, Nitromethane, and Liquid TNT Detonations," in *Twelfth Int. Symp. on Combustion*, (The Williams and Wilkins Co., Baltimore, MD), pp. 701-709, 1968.

2. Charles L. Mader, "Numerical Calculations of Explosive Phenomena," in *Computers and Their Role in the Physical Sciences*, (Gordon and Breach Science Publishers, New York), pp. 385-401, 1970.

3. Charles L. Mader, "Detonation Induced Two-Dimensional Flows," Acta Astronautica, Vol. 1, pp. 373-383, 1974.

4. Charles L. Mader, "An Empirical Model of Heterogeneous Shock Initiation of 9404," Los Alamos Scientific Laboratory report LA-4475, Oct. 1970.

5. Charles L. Mader and Charles A. Forest, "Two Dimensional Homogeneous and Heterogeneous Detonation Wave Propagation," Los Alamos Scientific Laboratory report LA-6259, June 1976.

6. Charles L. Mader, "The Two-Dimensional Hydrodynamic Hot Spot," Vol. 3, Los Alamos Scientific Laboratory report LA-3450, April 1966.

7. Charles L. Mader, "A Study of the One-Dimensional Time-Dependent Reaction Zone of Nitromethane and Liquid TNT," Los Alamos Scientific Laboratory report LA-3297, August 1965.

8. Charles L. Mader, "An equation of State for Shocked Copper Foam," Los Alamos Scientific Laboratory report LA-4381, May 1970.

9. A. W. Campbell, M. E. Malin and T. E. Holland, "Detonation in Homogeneous Explosives," Second ONR Symposium on Detonation, Washington, D.C., February 1955.

10. Douglas Venable, "PHERMEX," Physics Today, Vol. 17, pp. 19-22, 1964.

11. Douglas Venable, Los Alamos Scientific Laboratory, private communication, 1968.

12. Richard Dick, Los Alamos Scientific Laboratory, private communication, 1975.

13. James D. Kershner and Charles L. Mader, "2DE: A Two-Dimensional Continuous Eulerian Hydrodynamic Code for Computing Multicomponent Reactive Hydrodynamic Problems," Los Alamos Scientific Laboratory report LA-4846, March 1972.

14. A. W. Campbell and Ray Engelke, "The Diameter Effect in High-Density Heterogeneous Explosives," Sixth Symposium (International) on Detonation, San Diego, CA, August 1976.

HIGH RESOLUTION PHOTOGRAPHY OF TRANSVERSE WAVE
EFFECTS IN THE DETONATION OF CONDENSED EXPLOSIVES

Per-Anders Persson and Gunnar Persson
Swedish Detonic Research Foundation
Box 32058, 126 11 Stockholm, Sweden

Dark-wave effects of different kinds (cellular structure, transverse waves, convergent and divergent dark waves) that occur in the detonation of homogeneous liquid explosives have been studied by Kerr-cell, streak camera, and open camera high resolution photography.

Interaction between chemical reaction and transverse waves gives a common explanation for these seemingly different kinds of dark-wave effects.

Similar wave-like dark-and-light patterns first observed in the 1920s by Urbanski in open camera photographs of plastic and powder explosives detonating in glass tubes are found to be strongly dependent on the mode of fracturing of the glass envelope.

INTRODUCTION

The detonation wave front in many homogeneous liquids has a complex structure of transverse waves, caused by the rapidly pulsating, intermittent separation of the zone of chemical reaction from the wave front. The development and frequency of this structure depend on the rate constants of the chemical reaction and the general level of shock compression temperatures of unreacted explosives behind the wave front. The transverse wave structure develops when these conditions are such that the chemical reaction has a marked induction period.

This relatively recent discovery is as important a contribution to the understanding of explosives as was the formulation of the Chapman-Jouget theory.

As with the Chapman-Jouget theory, the transverse wave theory was first verified in gas detonation experiments and could later be applied successfully to condensed explosives, Shchelkin 1959 (5), Dremin et al. 1963 (2).

In contrast to gas detonations, where repeated reflections of the transverse waves at the containing walls can create a regular network of interacting triple-wave intersections, condensed phase detonations normally seem to have a more irregular pattern of transverse waves of randomly distributed strength. Particularly with walls of low or medium shock impedance such as plexiglass or glass, reaction break-down phenomena caused by rarefactions originating at the wall dominate the wave pattern to such an extent that they were long considered to be separate phenomena of a different nature from the transverse wave structure.

The purpose of this paper is to present some photographic evidence to show how all these effects are interrelated. They are really only different manifestations of the same phenomenon, that of local transient separation of the zone of reaction from the wave front.

414

EXPERIMENTAL

The experimental techniques used in these experiments will be described below to give some details of the optical systems and photographic techniques used to obtain an improved resolution.

In general, great care was taken to use a high optical quality glass bunker window and object mirror and not to use thicker bunker windows than necessary. To decrease the airblast pressure on the bunker window, a heavy steel blast screen was placed between the object mirror and the window, having an opening only sufficiently large to transmit the object light. The window was of mirror glass quality and was collimator tested to ascertain parallellity of surfaces and to avoid glass defects. The mirror was 6-8 mm thick, of optical flat quality with front surface vapor deposited aluminum and silicon reflecting material.

KERR-CELL PHOTOGRAPHY

The 15.5/18-mm-diameter glass tube filled with nitromethane used in the Kerr-cell photography was placed vertically with the TNT booster charge at the bottom. The mirror was placed at an angle of $45°$ above and close to the object so that the camera regarded the charge from above along the charge axis. To avoid the effect of surface tension at the liquid surface by the tube wall, a conical nitromethane-filled container was glued on at the top end of the tube so that there was a flat liquid surface over the whole of the cross sectional area of the tube. The camera was equipped with a 1:2.9/200 mm objective lens and the full aperture was used. The object-to-film scale was 4:1, and the distance between the 6-mm-thick glass window and the objective lens was about 50 mm.

A description of the camera and shutter was given by Aronzon in 1957 (12).

The Kerr-cell was triggered by triple mechanically shortcircuiting trigger wires taped on to the outside of the glass tube. As the depth of field was only about 1 mm, high demands on triggering accuracy had to be met.

STREAK CAMERA PHOTOGRAPHY

The experimental setup used for the streak photography was similar to that used in the Kerr-cell photo-graphy except that the initiation of the charge was triggered electronically from the Brixton type rotating mirror camera. A detailed description of the camera, built at the Swedish Research Institute of National Defense has been given by Axelsson and Beijer 1959 (11). For this series of experiments, the objective lens was a high resolution repro-lens (Voightländer Apo-Skopar 1:9/450 mm). In the experiments with 15.5-mm-diameter charges of neat nitromethane and also those with 30-mm-diameter charges of acetone-diluted nitromethane the film-to-object scale was 1:1 (the camera has a slit-to-film enlargement factor of 1.52/:1), and we obtained the best time- and space-resolution by using a slit of 0.1 mm (0.15 mm in the film plane) and a writing speed about 2.7 mm/μsec. In the experiments with acetone-diluted nitromethane in a brass cell, the object-to-film scale was 3:1, the slit 0.3 mm (0.45 on the film), and the writing speed 2.7 mm/μsec.

The weak film exposure obtained under these conditions by the light emitted from detonating nitromethane, and especially by the faint light emitted by the detonation in the shock-compressed material, made it necessary to use a relatively fast film material that gave a fine grain even after forced development. The optimal combination was found to be Kodak 4164 sheet film developed in Agfa Refinal for 15 min at 20°C. This gave a film density around 0.1 above basic fog for the light of regular detonation in neat nitromethane in a small diameter glass tube.

THE OPEN CAMERA TECHNIQUE

The open camera technique for recording the total light emission from a detonating charge was pioneered by Urbanski in 1927 (4). The charges, contained in a transparent tube surrounded by air or, as in later applications, (See Persson and Bjarnholt 1970 [15]) in a waterfilled aquarium, is placed in a darkened space and an ordinary mechanical shutter camera is focussed to see the whole charge. The detonation is allowed to pass through the charge while the shutter is open, thus giving a time-integrated picture of the self-luminosity of the detonation. The luminous reaction zone is often quite thin, so there is little motion of the reacting explosive during the time it emits light. Therefore any local variations in light emission will result in a pattern of light and dark regions on the surface of the charge.

In a further development of this technique the setup is combined with a short duration explosive argon flash arranged to give a background illumination through the unreacted transparent liquid explosive. As the reaction products are normally opaque, the usual dark wave pattern can be seen in that part of the charge that has detonated before the time of the light flash. The position of the shock wave and detonation fronts at the instant of the flash are well outlined against the background light. Where the shock-compressed liquid is transparent, the borderline between reacted and unreacted material can be detected.

The camera used in all these experiments was a Hasselblad 500 C (60 X 60 mm), with a 1:4/150 mm Sonnar objective lens. The aperture used was 1:11 and the film was Agfa AP 25 developed in Agfa Refinal for 3.5 min at 20°C to decrease contrast.

DARK WAVES

In 1956, Campbell, Holland, Malin, and Cotter (1) reported streak camera records of detonating nitromethane and nitromethane-acetone mixtures showing regions of low luminosity that they named "dark waves." The waves were thought to be associated with hydrodynamic rarefactions originating at the charge boundary. Similar waves were observed in diethylene glycol dinitrate, ethyl nitrate, and also in single crystals of PETN.

In agreement with the theory of Shchelkin 1959 (5) of unstable combustion leading to pulsating detonations, Dremin and co-workers in 1963 (2) concluded that the wave patterns observed in their streak camera records of detonating nitromethane diluted with acetone, nitroglycerine diluted with methyl alcohol and also ethylene glycol dinitrate mixed with acetone, were indeed due to transverse wave disturbances, interacting with each other and with the chemical reaction, in the manner proposed by Shchelkin.

CONVERGENT DARK WAVES

Figure 1a and 1b show end-on streak camera records of detonating neat nitromethane in glass tubes of internal/external diameter 15.5/18 mm and with a length of 50 mm. Initiation was made by a 85-mm-long charge of pressed TNT of 30 mm

diameter through a 0.25-mm sheet of black PVC. Previous studies have shown (Persson & Sjölin 1970 [7]) that pressed TNT at this charge diameter gives almost immediate initiation with negligible overdrive effects in nitromethane when initiating through a 0.25-mm sheet of PVC.

In the experiment of Fig. 1a the glass tube was positioned at an angle to the optical axis of the camera so that the camera slit was off-center in the lower part of the tube. The tube appears conical because of this and the dark waves near the wall are mirrored by optical reflexion of light at the inner wall of the tube. The upper surface of nitromethane was in contact with atmospheric air.

In the experiment of Fig. 1b the column of nitromethane was completely interrupted by a 0.1-mm-thick sheet of glass at right angles to the tube axis at a position 30 mm from the PVC sheet. The upper surface of nitromethane was separated from the air by another glass sheet, 0.3 mm thick, to avoid the air shock light seen in Fig. 1a.

Figure 2 shows a Kerr-cell photograph of the oncoming detonation front in a glass tube of neat nitromethane of the same dimensions and initiated exactly in the same way as in the experiments of Fig. 1. We see two large dark waves and numerous small ones. In the larger ones, the faintly luminous zone of the detonation in the shock compressed nitromethane can be seen, as well as the narrow band of increased light intensity of the overdriven detonation.

In all three photographs, most of the dark waves are seen to originate at the tube wall, and they converge as they travel inwards. Characteristic for these waves, that we suggest should be called convergent dark waves, is that the line of reinitiation is preceeded by a faint light and followed by a short duration intense light that quickly decays into the intensity level of the undisturbed detonation. The process is explained in Fig. 3 where the "dark" region is enclosed between the failure line F-F and the reinitiation line R-R. After failure, that always originates at the tube wall, reinitiation occurs first at a point in the liquid C' originally positioned at C on or close to the failure line F-F and some distance away from the wall.

In Fig. 3, the lines 0-0, 1-1, 2-2, and 3-3 represent the positions of the detonation front at five different
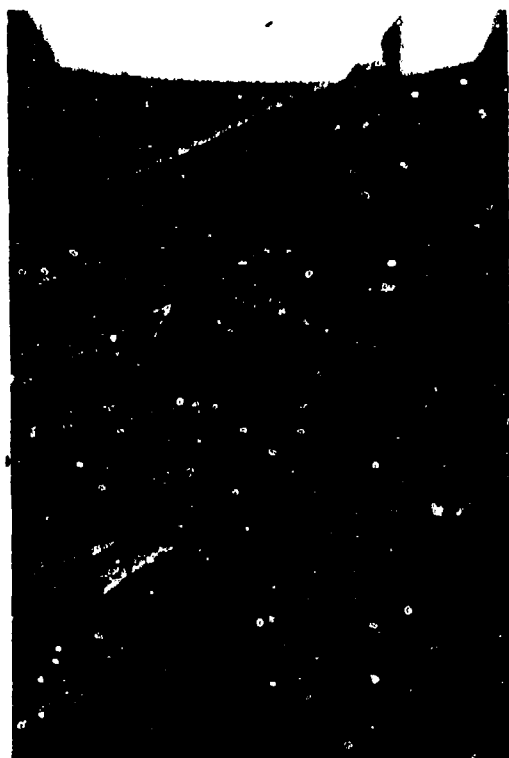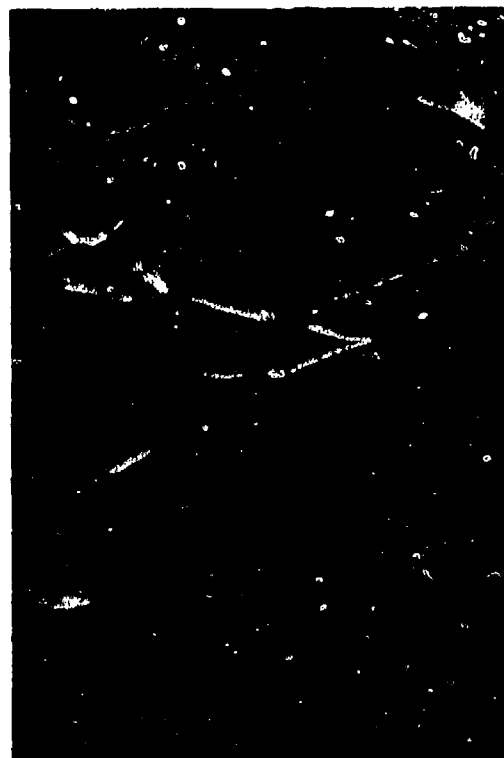
a.   b.

Fig. 1. Streak camera records of dark waves in neat nitromethane in 15.5-mm-diameter glass tube at initial temperatures a. Shot No. 12119, 14°C, b. Shot No. 12122, 6.5°C.

Fig. 2. Kerr-cell camera photo of the instantaneous self-luminosity of an oncoming detonation wave in neat nitromethane.

times during the development of a convergent wall failure wave. At time 0, a detonation failure develops at the point F at the wall. As the detonation proceeds, the failure spreads into the explosive, bounded by the failure line and the oblique shock front. At time 1 a detonation front that originated at the centre of initiation C' has just caught up with the shock front. The detonation in the shock compressed material successively intersects the shock front along the line R-R' as the detonation and failure proceeds. Because of its higher pressure and velocity, the detonation in the shock compressed explosive will overdrive the detonation immediately on the other side of R-R', but because of the wave curvature this overdrive quickly decays into a regular detonation. No light is emitted from the shock compressed unreacted explosive. A faint light, weaker than that from a regular detonation is sent out from the detonation front in the shock-compressed explosive. A short duration intense light, brighter than that of the regular detonation, is sent out by the overdriven detonation. These
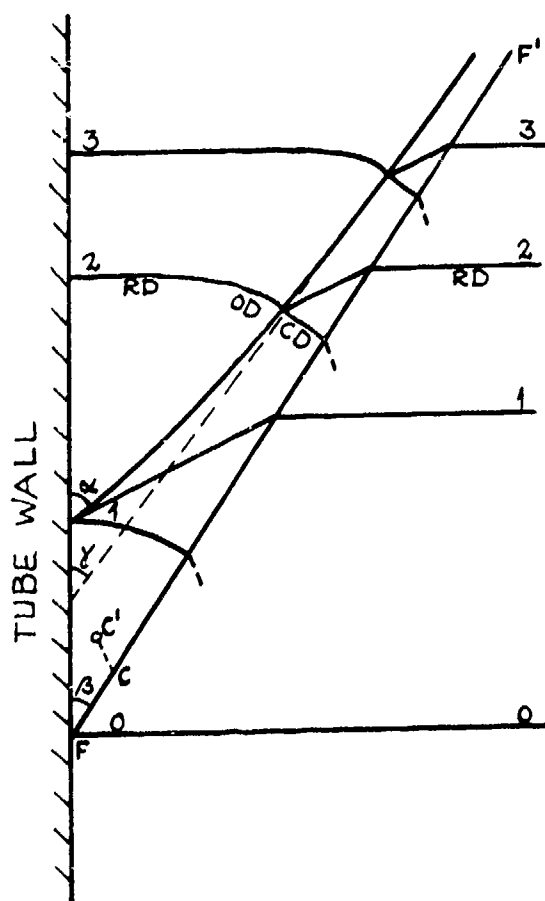
417

Fig. 3. Schematic diagram of triple wave interactions in a single convergent dark wave. F-F': failure line, R-R': strong reinitiation line, RD: regular detonation front, OD: overdriven detonation front, CD: detonation front in shock compressed material, S: shock front.

features can be seen in the large failure wave in the upper left hand part of the record in figure 1a, and in the upper right hand part of figure 1b. We will call this kind of reinitiation a strong reinitiation, because it is always accompanied by an overdrive of the detonation along the line of reinitiation.

Note also the fine-structure of narrow failure waves that create a criss-cross network of lines just visible in the upper half of each recording, where the camera is focussed. We would suggest that this fine-structure is only a small fraction of the total fine-structure present, most of which is too finely detailed to be visible, even with the improved resolution

afforded by these records. The upper left hand part of the record in Fig. 1b strongly suggests this, and it also shows the random size distribution of the failure lines.

Within the resolution of these records, of the order of 0.04 mm in the object, the failure line F-F' and the reinitiation line R-R' gradually approach each other and become almost parallell, but they never meet, and the dark wave propagates, visible as a narrow dark band, for long distances across the charge.

It is interesting to note the close similarity between these narrow dark waves in neat nitromethane with those recorded by Brochet, Presles, and Cheret 1974 (6) in nitromethane mixed with the high density liquids chloroform or bromoform.

THE PROPAGATION OF A FAILURE WAVE AND THE ASSOCIATED SHOCK

The evaluation of propagation velocities from streak camera recordings using cylindrical charges can lead to an over-estimate of the velocity unless the point of origin of the failure at the wall and the point of reinitiation both happen to fall on the slit.

To get a better estimate of the lateral propagation velocity v of the failure wave, the associated shock wave velocity u_s, and the lateral reinitiation wave velocity u, we have made use of two different kinds of experiment that will be described in the following.

Figure 4 shows two photographs obtained by superimposing a 0.1-μsec-duration argon flash back-lighting on the open camera picture of a rectangular cross-section cuvet containing neat nitromethane. The back and front walls of the cuvet was glass of 2 mm thickness, the left side wall and the lower part of the right side wall was made of steel foil of thickness 0.1 mm while the upper part of the right hand side wall was 0.06 mm mylar foil. The size of the cuvet was 9.7 X 20 mm cross section and 80 mm length, with the 20-mm side facing the camera. At the point on the left hand wall where the steel foil ends, 30.5 mm from the rectangular 12 X 24 mm cross section TNT booster charge, a failure wave begins. The background flash gives an outline of the detonation wave, the shock wave in the nitromethane and the shock wave in the surrounding water. It also shows, with a slight distortion because of refraction in the

418

Fig. 4. Combined flash and open camera photos of self-luminosity of neat nitromethane detonating in a rectangular cross section glass cuvet where the lower part of the right hand side wall is steel foil. Superimposed on photo is 0.1 µsec argon flash backlightning, showing outline of detonation front and shock fronts. Cuvet size: 9.7 X 20.0 X 80 mm, length of steel foil, 30.5 mm. a. Shot No. 10281, b. Shot No. 10282. Photo: G. Bjarnholt.

water shock, the position of the reaction products of the booster charge and the lower part of the nitro-methane. In the following, let α be the angle between the original surface of the wall and the nitromethane shock wave front. Let β be the angle between the wall and the failure line, and let γ be the angle between the wall and the line of reinitiation. We find from geometrical considerations (see Fig. 5).

$$v = D \, tg \, \beta,$$

$$u_s = \{D \sin{(\alpha-\beta)}\}/\cos \beta$$

Table 1 shows some values of the angles α and β and the associated velocities u_s and v evaluated from records like those in Fig. 4, assuming the detonation velocity is 6.3 km/sec. We notice that some of the v-values are lower than those found previously. Davis

1964 (8) reported $v = 3.72$ km/s using plane wave initiated charges, whereas Dremin and Trofimov 1964 (9) reported 4.75 km/s using axisymmetric charges. Because the charges in this series of experiments were close to critical dimensions, it is not surprising that the average v-and u_s values are low. A close scrutiny of the pictures shows that there is a curvature both to the regular detonation front, the failure line (F-F'), the shock front, and the reinitiation line. If we try to estimate the values of α and β at the failure line intersection with the shock and detonation fronts, we find approximately $\alpha = 64°$ and $\beta = 35°$ corresponding to $v = 4.41$ km/s and $u_s = 3.73$ km/s at an assumed detonation velocity $D = 6.3$ km/s. The corresponding pressure in the shock compressed, unreacted explosive close to the failure line is found to be 87 kb, using the shock adiabat

$$u_s = 2.00 + 1.38u_p$$

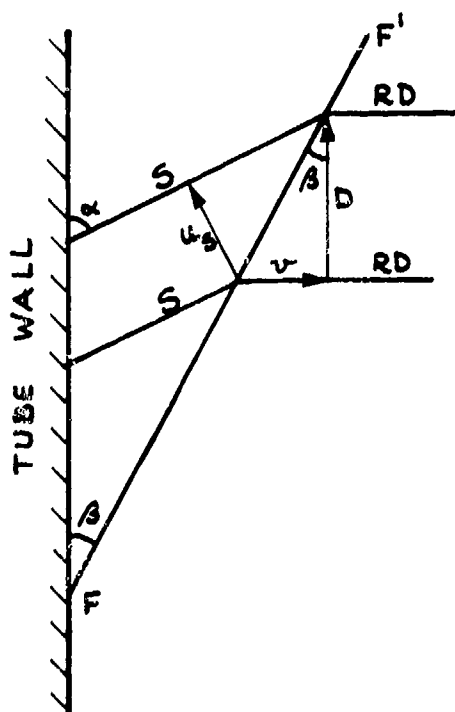for unreacted nitromethane given by Ilyukhin et al. 1966 (10).

Fig. 5. Relations between detonation velocity D, shock velocity u_s, and lateral failure velocity v. S: shock wave front, RD: regular detonation front, F-F': failure line.
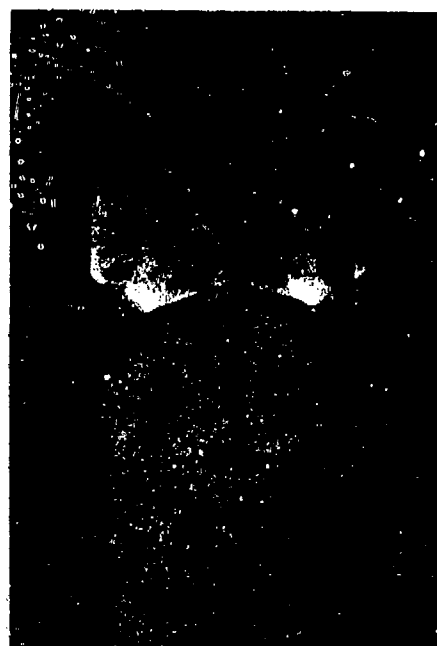

Fig. 6. Streak camera record of divergent dark waves in the detonation of neat nitromethane in a 10-mm-diameter brass tube with two internal grooves. Initial temperature 21°C. Shot No. 12150.

DIVERGENT DARK WAVES

Figure 6 shows a streak camera record of neat nitromethane detonating in a brass tube of diameter 11 mm. The camera looks along the axis of the tube at the oncoming detonation front with the camera slit exposing a diameter. The length of the tube was 120 mm, and initiation was by a no 6 detonator initiating

TABLE 1

shot no	α deg	β deg	v km/s	u_s km/s	
10282	59.7	26.3	3.09	3.90	(average)
10281	63.8	29.1	3.53	3.41	(average)
10278		35.6	4.51		(center)
10278		28.1	3.37		(wall)
10278		34.2	4.27		(average)

a 20 mm diameter 80 mm long pressed TNT charge, separated from the nitromethane by a 0.25 mm thick black PVC foil. The downstream end of the tube opened into a 36-mm diameter 24-mm-long tube. Both tubes were filled with neat nitromethane.

In the experiment of Fig. 6 two grooves were turned into the inside wall of the tube, 12 mm from the downstream end of the tube, 15 mm and 10 mm respectively from the downstream end of the tube. The first of these had a depth equal to its width of 0.75 mm. (Because of the small tube diameter, and possibly also because of the additional disturbance of the second groove, the detonation in the experiment of figure 6 did not reinitiate after being extinguished on passing out into the larger tube, as it did in some of the other experiments.) The most prominent feature of figure 6 is the symmetrically occurring dark zones spreading inward from the upstream corner of each groove. Because the dark zone widens as it moves towards the charge axis we will call it a divergent dark wave.

420

WEAK AND STRONG REINITIATIONS

We see from the experiments in Fig. 6 that the weak reinitiation caused by the reappearance of the metal wall support downstream of the groove has an entirely different appearance and a lower propagation velocity than the strong reinitiation dealt with above. For reasons that will become obvious later we will call this a weak reinitiation. In the weak reinitiation, there is no evidence of detonation in the shock compressed material and no overdrive.

The failure line in these experiments appears to have a similar slope to that found in the wall failures, i.e. in the range $3.75 < v < 4.25$ km/sec, where the lateral propagation velocity v of the failure increases as the failure travels towards the charge axis.

Table 6 shows some average lateral propagation velocities of the failure wave and the weak reinitiation wave evaluated from the streak record in Fig. 6.

Just at the limit of resolution, there is evidence of a fine-structure of failures and reinitiations in several of our pictures of this kind even though the explosive is neat nitromethane. This fine-structure often occurs in regions downstream of a large failure. Some of it can be seen in Fig. 6. We take this as further evidence of the existence, in a normal nitromethane detonation, of a network of very fine failures and reinitiations. This supports the conclusions drawn by Dremin and co-workers 1970 (13) from experiments

TABLE 6

Lateral Velocities of Failure Wave and Weak Reinitiation in Neat Nitromethane in 10 mm Diameter Brass Tube with Internal Grooves (Fig. 6). Shot No 12150.

Groove no	Position	Lateral failure velocity km/sec	Lateral reinitiation velocity km/sec	Axial groove width mm	Axial length of failure mm
1	left	3.75	3.78	0.4	0.8
	right	3.86	3.24		
2	left	3.59		0.75	1.04
	right	3.73			
Mean value		3.73	3.01		

that showed the detonation front of nitroglycerine to be specularly light reflecting whereas that of nitromethane was not. They concluded that nitromethane, in contrast to nitroglycerine, has a transverse wave structure in the detonation front, of a wave length greater than that of visible light.

In Table 2 is also given the time interval of darkness and the distance of no detonation along the wall from the beginning of each groove in the experiment of Fig. 6. We see that the origin of the reinitiation at the wall is some distance downstream of the end of the groove, a distance about equal to the width of the groove. In deriving this distance from the recorded time interval, we have assumed a constant shock wave velocity and a detonation wave with no curvature.

Figure 7 shows the relative positions of the detonation front and the front of the shock wave in the divergent dark wave at two different times, where (1) is the moment of reinitiation at the wall, and (2)
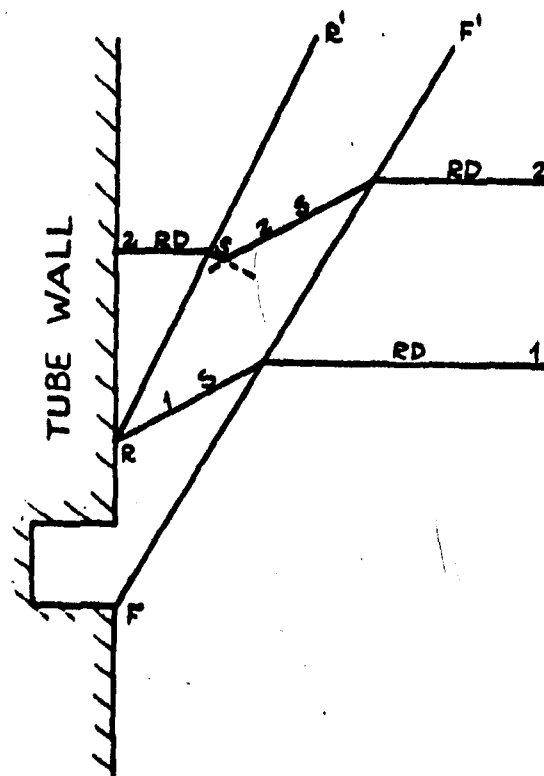

Fig. 7. Schematic diagram of detonation and shock fronts in a divergent dark wave created by a groove in the containing tube wall. RD:regular detonation front, S:shock wave front, F-F':inward-going failure line, R-R':outward going failure line.

421

is after the two detonations have propagated some distance. From Fig. 7 we may predict, because of the divergence of the dark wave, that the detonation to the left of the dark wave will outrun the leftgoing shock in the dark region and will create a right-going shock also in the dark region. In consequence, we must expect our "weak reinitiation" not to be the locus of reinitiation at all but an inward-going failure of the detonation. The detonation is more stable at the metal wall where it has the added support of the left-going shock at the rear.

In spite of trying a great number of combinations of brass tube diameters and groove sizes, we were not able to create conditions for this "weak reinitiation" line to continue all the way to the axis of the charge. Instead, there was always a transition into a strong reinitiation, accompanied by the strong light of an overdriven detonation. In several of the records this was preceeded by the narrow zone of faint light indicating the presence of a detonation in the precompressed material behind the shock front in the dark zone. We are led to assume that the transition to strong reinitiation is a result of interaction between the inward-going and the outward-going shock waves in the dark region.

A further insight into the nature of the "weak reinitiation" can be obtained by repeating the experiment of Fig. 6 in a larger dimension grooved metal tube using acetone diluted nitromethane. Fig. 8 shows an end-on streak record of the divergent failure produced in 16/84 weight % acetone/nitromethane by a 2.5 mm wide and 2.5 mm deep groove 30 mm from the end of a 30 mm inside diameter steel tube. (The tube ends in a 60 mm diameter tube filled with the same mixture, and, as in Fig. 6, the detonation fails completely upon leaving the 30 mm tube).

We notice the divergence of the dark zone from the wall inwards, as in neat nitromethane. We also see from the wave structure that the locus or reinitiation is along the wall in the region downstream of the dark zone, and we see how the "weak reinitiation" is in fact an inward-going failure wave of the same kind as the outward-going initial failure wave.

CELLULAR STRUCTURE IN LIQUIDS

Figure 9 shows a streak camera record of the oncoming detonation wave in 19/81 weight % acetone/
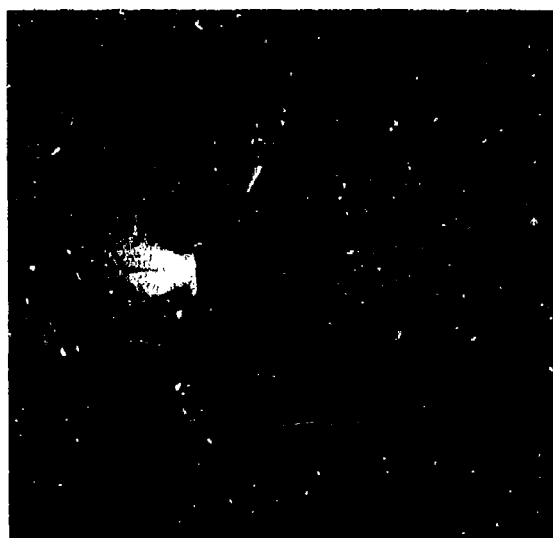


Fig. 8. Streak camera record of divergent dark waves in the detonation of 16/84 weight% acetone/nitromethane in a 30 mm steel tube with an internal groove. Initial temperature 19°C. Shot No. 12143.

nitromethane contained in a 20 X 80 mm rectangular cross-section 4 mm wall thickness brass cuvet of 200 mm length. The camera looks down into the cuvet with the slit parallell to the 80-mm sides of the cuvet.

The width of the cuvet was exactly four times its thickness in order to facilitate the development of a regular cellular structure by interference between waves from different directions. By varying the initial temperature or the acetone content, the coarseness of the structure could be varied within wide limits. In all the experiments made, however, the structure was random as in Fig. 9. We must conclude that reflexion at the wall plays a less important role in liquids than in gases.

We see in Fig. 9 the close connection between the random cellular wave structure and the two types of dark waves discussed previously. We can follow a dark wave across the width of the cuvet and see how it changes from a convergent character to a divergent and back again, the convergent mode being accompained by the intense light of overdrive, the divergent mode without it.

We can also see many examples of particularly bright spots of light indicating overdriven detona-
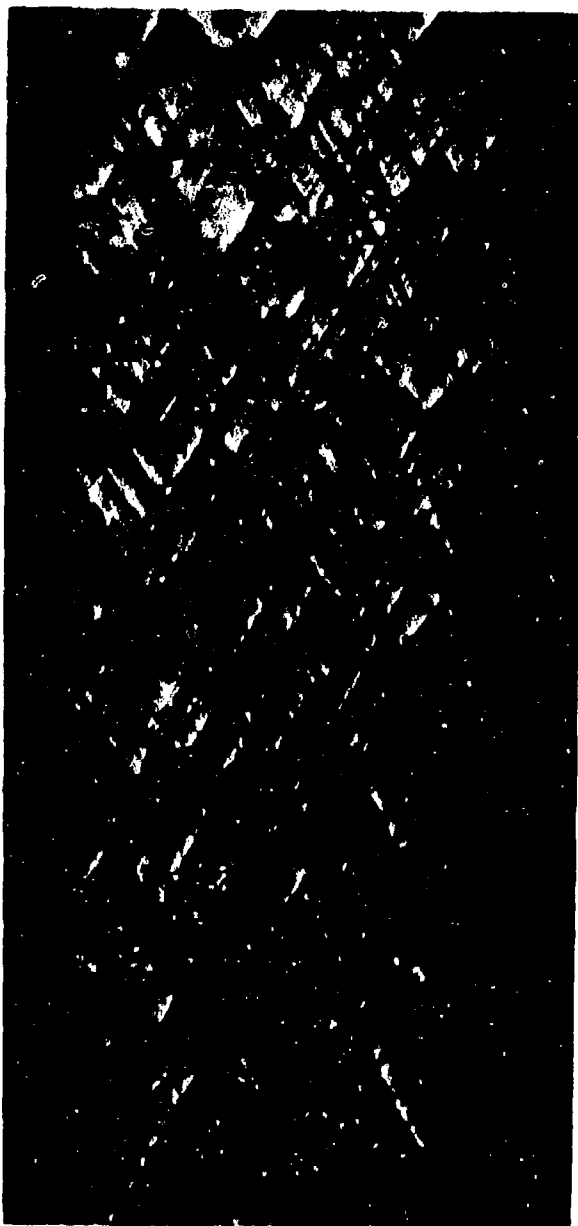
Fig. 9. Streak-camera record of random dark waves or cellular structure in the detonation of 20.5/79.5 weight% acetone/nitromethane in a rectangular 20 × 80 mm cross section brass cuvet. Initial temperature 12°C. Shot No. 12156.

of the overdrive areas, there is a fine structure of very narrow dark waves, closely spaced in a fine criss-cross network.

All this is evidence that interaction between lateral waves and chemical reaction plays a vital role in the propagation of detonation in diluted nitromethane. The simple two-dimensional model of the process, with two sets of equally strong waves interacting to geneate cells that are all of equal size as described by Urtiew 1975 (14), is a good picture to start out from, but the 3-dimensional reality is a great deal more complex.

The fact that a disturbance in the form of a short interruption of the chemical reaction at the wave front can propagate laterally across the charge is in itself a sign that the sonic condition of the Chapman-Jouget theory, $c = D - u_p$, cannot be fulfilled. If such disturbances exist also in neat nitromethane then we may expect that the sonic condition is not fulfilled there either.

We then need a new theory to show why the detonation velocity in liquids in such a remarkably stable parameter.

DETONATION LIGHT PATTERNS IN POWDER AND PLASTIC EXPLOSIVES

In 1927 Urbanski (4) reported wave-like dark-and-light patterns found in open camera photographs of powder and plastic mining explosives enclosed in glass tubes. He noted that these patterns were sometimes of a spiral nature and suggested a spiral mode of propagation of the detonation.

In repeating his experiments, we have found the wave structure to be strongly dependent on the tube material and its mode of fracturing. Fig. 10 shows open camera photos of the same powder explosive, 94.4/5.6 weight% ammonium nitrate/fuel oil (ANFO), detonating in three different containers, glass, plexiglass (PMMA), and 0.04 mm thick mylar surrounded by water. We note that the weakest container, and that with the lowest shock impedance, i.e. the thin mylar surrounded by water, gives very little evidence of a wave pattern.

An important part of the explanation of the pattern obtained with the glass container is seen in Fig.

tions where two dark waves coming from different directions collide.

We finally see how there are several size ranges of wave structure overlapping such that even in some

a.　　　　　b.　　　　　c.

Fig. 10. Open camera photos of the self-luminosity
of ANFO at density 900 kg/m³ and charge diameter
30 mm enclosed in a glass tube of wall thickness 3
mm, shot No. 12200, b. plexiglass tube of wall
thickness 5 mm surrounded by water, shot No. 12194,
c. mylar film (40 μm) surrounded by water, shot No.
12195.

11a. This is a Kerr-cell picture of the same type of
glass tube filled with ANFO. The detonation velocity
of ANFO in a 32 mm i.d. glass tube is about 2.500 m/
sec, while the stress wave velocity of glass is around
4.500 m/sec. Obviously the glass fractures a long way
ahead of the detonation front. This leads to scattering
of the detonation light and also to an irregular expan-
sion of the reaction products. We suggest that this,
rather than a spiral detonation, is the main cause of
the light patterns observed by Urbanski. In the record
of the mylar-enclosed charge, there is a faint trace of
a criss-cross pattern that could possibly be evidence
of a lateral wave structure.

As a warning against the use of glass tubes as a
containing material for medium detonation velocity
explosives we finally show a Kerr-cell picture (Fig.
11b) of 10/90 weight% acetone/nitromethane detona-

a.　　　　　　　b.

Fig. 11. Kerr-cell camera pictures of detonating
30 mm diameter charges a. ANFO, density 900
kg/m³, in glass tube with 3 mm wall thickness,
b. 10/90 weight% acetone/nitromethane in glass
tube with 3 mm wall thickness.

ting in a glass tube. Apparently, the stress wave
velocity of the glass is higher than the detonation
velocity in this case, too, and the glass fractures ahead
of the detonation front.

CONCLUSIONS

The experiments have given additional support to
the belief that there exists a fine-structure of lateral
waves in the detonation front of neat nitromethane.
The phenomenological interrelation between such
lateral waves, dark waves, failure waves, and cellular
structure of detonation has been illustrated.

The presence of a cellular structure of dark waves
at the detonation front indicates that the sonic condi-
tion $c = D - u_p$ of the Chapman-Jouguet theory is not
fulfilled.

No strong evidence has been found for the theory
that there should exist a lateral wave structure in the

detonation of powder and plastic explosives, but further studies of this ought to be made.

ACKNOWLEDGMENTS

REFERENCES

1. A. W. Campbell, T. E. Holland, M. E. Malin, and T. P. Cotter, jun., "Detonation Phenomena in Homogeneous Expolsives," Nature, Vol. 178, No 4523, pp. 38-39, July 1956.

2. A. N. Dremin, O. K. Rozanov, and V. S. Trofimov, "On the Detonation of Nitromethane," Combustion and Flame, Vol. 7, pp. 153-162, June 1963.

3. R. W. Watson, "Dark Waves in Liquid Explosive System: Their Role in Detonation," Proc. 5th Symp. Detonation, Pasadena, 1970. ACR-184, p. 169.

4. T. Urbanski, "Photographische Untersuchungen des Detonationsverlaufes brisanter Sprengstoffe," Z.fd ges. Schiess- und Sprengstoffw. Vol. XXII, nr 10, October 1927.

5. K. I. Shchelkin, "Two cases of unstable combustion," J. Exptl. Theoret, Phys (USSR) Vol. 36, p. 600-606, (1959) (in Russian), Soviet Physics JETP, Vol. 36, p. 416 (1959) (in English).

6. C. Brochet, H. Presles, and R. Cheret, "Detonation Characteristics of some liquid mixtures of Nitromethane and Cloroform or Bromoform," 15th Symposium on Combustion, The Combustion Institute, Pittsburgh, Pennsylvania, 1974, p. 29.

7. P. A. Persson and T. Sjölin, "Light Emission During Initiation of Liquid Explosives," Proc. 5th Symp. Detonation, Pasadena, 1970, ACR-184, p. 153.

8. W. C. Davis, Private communication (1964) Se C. L. Mader, Los Alamos Scientific Laboratory Report No LA-3077 (June 1964).

9. A. N. Dremin and V. S. Trofimov, Zhur Prikl. Mek i Tekn. Fiz. No 1, (1964). (English translation in: Clearinghouse for Federal Scientific and Technical Information, US Dept of Commerce, Report No AD 615211, pp. 205-216 (March 1965)).

10. V. S. Ilyukhin, P. E. Pokhil, D. K. Rozanov, and N. S. Shvedova, "Measurement of the Shock Adiabatic Curves for Cast TNT, Crystalline RDX and Nitromethane," Doklady Akad. Nauk USSR, Vol. 131, p. 793 (1960).

11. G. Axelsson, U. Beijer, "Streak Camera 8 mm/ μsec," Research Institute of National Defence, Stockholm, Report FOA A 2008-2017 February 1959 (In Swedish).

12. A. Aronzon, "Kerr Cell Shutter," Research Institute of National Defence, Stockholm, FOA, Dnr 2578-2051, 19 August 1957 (In Swedish).

13. A. N. Dremin, C. D. Savrov, V. C. Trofimov, "Detonic waves in Condensed Media," Nauka, Moscow 1970, p. 35 ff (In Russian). English translation: Swedish Detonic Research Foundation Report 1971.

14. P. A. Urtiew, "From Cellular Structure to Failure Waves in Liquid Detonations," Combustion and Flame, Vol. 25, p. 241-245 (1975).

15. P. A. Persson and G. Bjarnholt, "A Photographic Technique for Mapping Failure Waves and other Instability Phenomena in Liquid Explosives Detonation," Proc. 5th Symp. Detonation, Pasadena, 1970, ACR-184, p. 115.

DEFLAGRATION TO DETONATION TRANSITION BEHAVIOR OF TETRYL

R. R. Bernecker, Donna Price, J. O. Erkman, and A. R. Clairmont, Jr.
Naval Surface Weapons Center
White Oak Laboratory .
Silver Spring, Maryland 20910

In this study of the deflagration to detonation transition (DDT) behavior of tetryl, results are reported for the compaction range of 63-90% theoretical maximum density (TMD) for coarse (470μ) tetryl and 46-85% TMD for fine (20μ) tetryl. Although all tetryl charges below 85% TMD exhibited a transition, their behavior differed from that found in earlier studies on RDX and RDX/wax in two ways: (1) the decomposition products formed shortly after ignition had such a high electrical resistance that ionization probes frequently failed to respond to them and (2) the onset of accelerated burning was located nearer the onset of detonation than the ignition region. Both differences are attributed to the low temperature decomposition of tetryl. Coarse and fine tetryl both showed the same qualitative effect of compaction on predetonation column length (ℓ), a nearly constant ℓ at high porosity with increasing values as the % TMD increases above 75%. At the same density values, the fine tetryl had a greater ℓ value than the coarse as well as a longer relative time to detonation.

INTRODUCTION

In our effort to elucidate the mechanism of the deflagration to detonation transition (DDT) in porous, granular explosives, we first studied 91/9 RDX/wax. A physical model was proposed for the transitions observed in this explosive (1); the model's first necessary condition for such a transition was a rapid pressure buildup in the ignition region. Because the behavior of a mixture rather than a pure compound provided the basis for our model, it seemed desirable to see how widely applicable the model is - in particular, how applicable it is to neat explosives. We have now studied six different pure explosives at various compactions, and have started an investigation of the effect of particle size on DDT. Both charge permeability and reactive surface area are determined by particle size and compaction; moreover, both are obviously important factors in any burning process and hence to a resultant pressure buildup and subsequent transition to detonation.

This paper presents the results of the study of fine (20μ) and coarse (470μ) tetryl. Tetryl does not conform to the original model (1) in that its rapid pressure buildup occurs nearer to the site of detonation onset than to the ignition region. It also shows other uncommon explosive behavior which seems best explained in terms of its chemistry of decomposition.

EXPERIMENTAL ARRANGEMENT AND PROCEDURE

The experimental setup and procedures have been described in detail elsewhere (1, 2). A schematic of the arrangement is shown in Fig. 1. It consists of a seamless steel tube with heavy end closures. The column length of the 0.35 g of 25/75 B/KNO$_3$ ignitor is 6.3 mm; the length of the explosive column is 295.4 mm.

Coarse tetryl with an average particle size $\delta \sim$ 470μ is from a commercial lot satisfying the military

specifications. The 20μ tetryl was prepared from the coarse by a turbulent mixing of its acetone solution with water to form a very fine grained precipitate.

The DDT tube is instrumented with ionization probes and strain gages to monitor ionization fronts and internal pressure, respectively. For brevity, henceforth ionization probes will be referred to as probes; strain gages, as gages. As before (1), both custom-made and commercial probes are used; distance-time (x-t) data from each are distinguished on the graphs. The number of gage locations for monitoring internal pressure is now an average of four or five per tube. The gage output is reported in strain (ϵ) or microstrain ($\mu\epsilon$). In a static calibration of the tube, the gradient is 112 $\mu\epsilon$/kbar up to the elastic limit at 2.2 kbar. From 2 to 4.7 kbar, the microstrain increases from 225 to 788.

One difference in procedure from that reported in reference (1) is in the determination of the predetonation column length, ℓ. In the case of 91/9 RDX/wax, it was possible to use the intersection of the postconvective wave front with the extrapolated detonation front to locate ℓ in the x-t plane; the value was confirmed by that obtained from tube fragments. Here, and, in general for HE other than 91/9 RDX/wax, ℓ is more reliably determined from markings on the tube fragments; it is checked for consistency with the probe and gage records in the x-t plane. Unless otherwise indicated, ℓ values are measured to ±3 mm.

EXPERIMENTAL RESULTS AND DISCUSSIONS

Tetryl 1

Tetryl, N-methyl-N-nitro-2, 4, 6-trinitroaniline $CH_3N[C_6H_2(NO_2)_3]NO_2$ or $C_7H_5N_5O_8$, was originally chosen for study because it is one of the relatively few neat explosives commercially available as well as being a widely used military explosive. Utilizing instrumentation and techniques developed in previous DDT studies, we rapidly found that the behavior of tetryl in our setup differed from that of other HE we have studied. First, rapid pressure buildup occurred nearer the point of onset of detonation than the ignition area. Second, in the case of very porous charges, early decomposition seemed to be associated with such high electrical resistance that
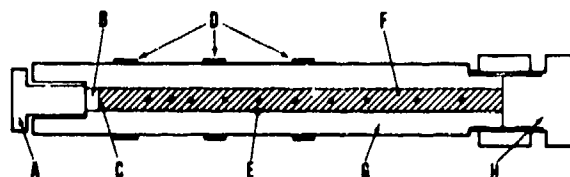

Fig. 1. Cross section of DDT tube. (A - ignitor bolt; B - ignitor; C - ignitor/explosive interface; D - strain gages; E - ionization probe location; F - explosive charge; G - tube; H - bottom closure. Inner diameter = 16.3 mm, outer diameter - 50.8 mm. Distance from ignitor/explosive interface to bottom closure = 295.4 mm.)

our probes did not register the reaction. Hence we had difficulty in triggering the oscilloscopes to follow early reaction as well as inadequate guidance about where to place our gages to obtain useful strain time (ϵ-t) records. In addition, almost all ϵ-t records were much more difficult to read and interpret; they contained many more perturbations that could cause ambiguity in interpretation than the records we have been obtaining over the last five years. Under these circumstances, our knowledge of the DDT behavior of tetryl has been built up from studying many records, most of which supplied incomplete information. Only two of the most complete sets of records will be reproduced here; the remainder will be found in reference (3).

Figure 2 presents the data for coarse tetryl compacted to 85.0% theoretical maximum density (TMD); Fig. 3, those for fine tetryl compacted to 76.6% TMD. Each figure is a composite with (a) distance-time data and (b) strain-time data. Fig. 2a shows that the first front *detected* in this shot was a compressive front travelling at 1.25 mm/μsec, about the sound velocity for this density of coarse tetryl (4). In other words, this front is the first compressive front that in other materials is called the postconvective wave; here it is the result of a confined burning which produces only a mild linear increase in pressure with time (see Fig. 2b). The front must have been preceded by some flow of product gases from the ignitor and the burning tetryl, but such gases were evidently of too low a temperature to cause a probe response. Instead, the probes responded about 10 μsec after the passage of the pressure front; their response was presumably to a pressure-induced electrical conductivity.
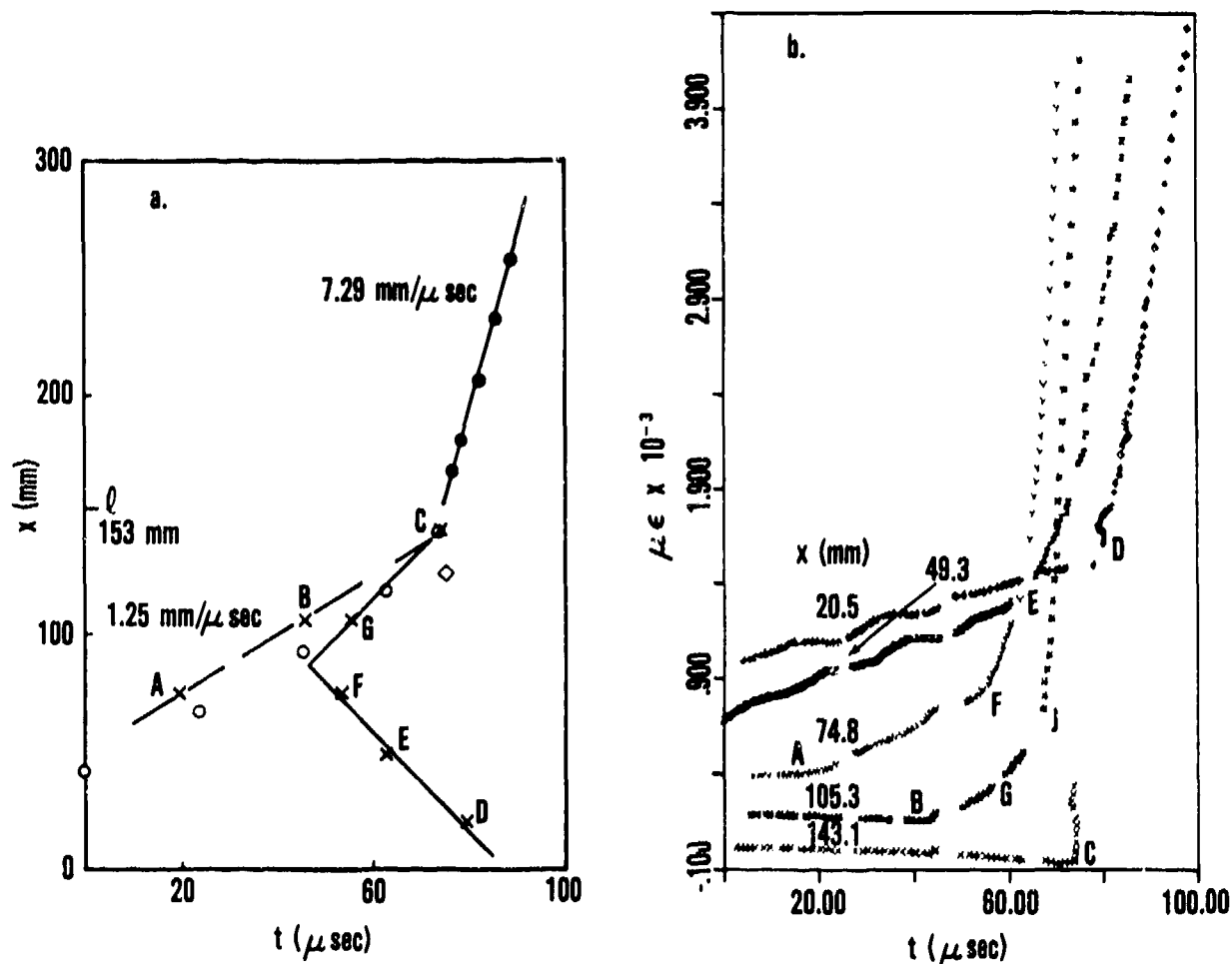
427

Fig. 2. Data for shot 613 on 470μ tetryl at 85% TMD, ρ_0 = 1.47 g/cc. [a. distance-time plot (○ custom-made probes, ● commercial probes, × change in slope of ε-t curve of b, ◇ coalescence of isobars); b. strain-time plots (change of slope shown by letters which also appear in a. Each curve except the lowest has been raised 0.2 × 10⁻³ μϵ, or an integral multiple thereof, for better data display.)]

Although the initial compressive wave appears to originate near the ignition area, as it does in other studies, it does not mark the beginning of an accelerated burning (Fig. 2b will make this clearer), and hence does not seem to lead directly to the production of a shock necessary for the shock to detonation transition (SDT) that terminates each deflagration to detonation transition (DDT). On the other hand, some event has occurred at about x = 87 mm, and it has created compressive fronts travelling both forward and backward at about 2 mm/μsec. The former front is followed within 10 μsec by an extremely accelerated burning and hence may well contribute

to shock formation and subsequent onset of detonation at x = ℓ = 153 mm.

Figure 2b contains the strain-time curves produced by the five gages at the tube locations shown. The third and fourth gages produce similar, information curves. For that at 105 mm, we have a period of mild burning (linear increase of ϵ with t) BG; it is followed by a second interval of slightly faster but still mild pressure increase GJ; that in turn is followed by greatly accelerated burning beyond J. The first two gages might have shown a similar initial pattern if the oscilloscopes had been triggered earlier, but the onset
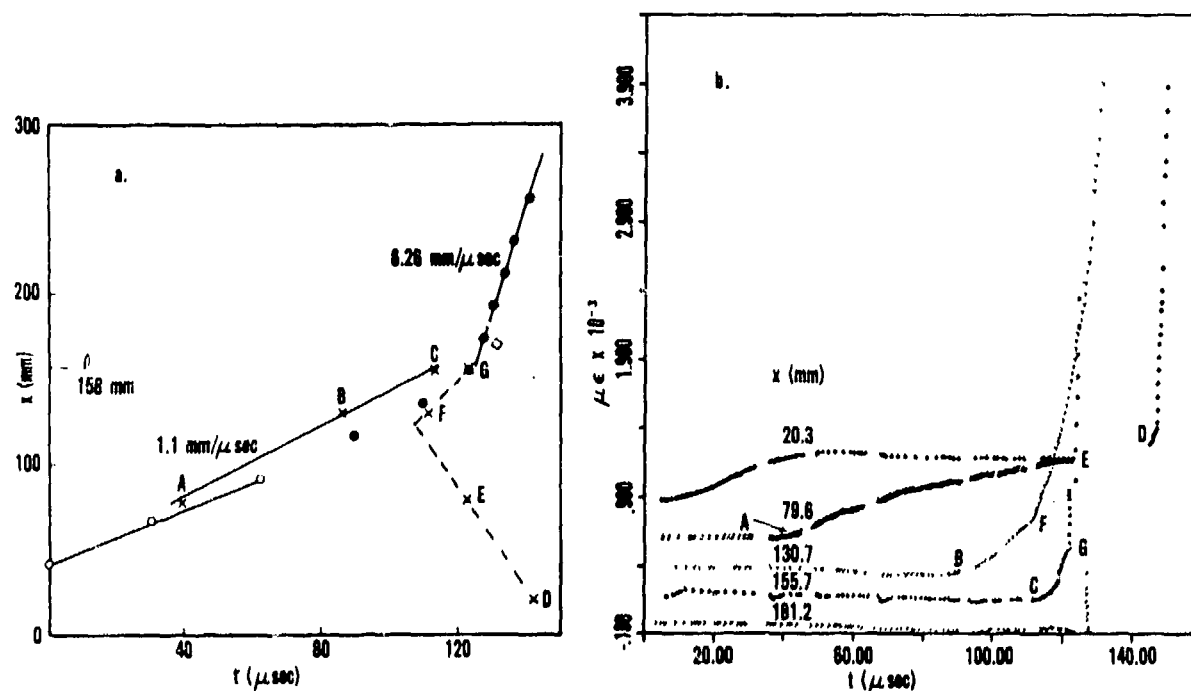
428

Fig. 3. Data for shot 813 on 20µ tetryl at 76.6% TMD, $\rho_0 = 1.33$ g/cc. a. Space-time plot (key of Figure 2a); b. Strain-time plots (key of Figure 2b).

of accelerated burning comes much later, e.g., point D on the ε-t curve of the first gage (x = 20 mm) occurs after detonation has begun at x = 153 mm.

The gage records were used to construct isobars in the elastic range of the DDT tube (50-250 µε). As in the case of 91/9 RDX/wax, the x-t isobars, constructed from ε-t curves produced by the third and fourth gage, coalesced when extrapolated. However, the point of coalescence was 125 mm, 75.4 µsec; it is marked by a diamond on Fig. 2a. Hence, although isobars formed near the ignition region might coalesce into a shock, the coalescence appears in this case too late to effect either detonation or the event at x = 87 mm. It should be kept in mind that these are isobars associated with the 1.25 mm/µsec compressive front. They were examined, in part, as a possible source of shock that could lead to the accelerated burning observed at x = 87 mm. The regions beyond F and G in Fig. 2b, where accelerated buildup of pressure occurs and would be expected to produce shock formation, were not similarly examined because they were at pressures greater than the elastic limit of our tube.

Seven other shots were made on the coarse tetryl over the range of 63-90% TMD. Table 1 gives summary data; the records appear in reference (3). For Shots 513 and 612, incomplete data permitted the estimate of a predetonation event such as that shown in Fig. 2b for Shot 613; the estimates appear in Table 1. In addition to Shot 613, the coalescence of isobars was examined for four other shots. Coalescence occurred in three cases, but did not in any case seem the likely starting point for the initiating shock in an SDT. Hence the immediate cause of the transition seems to be that event at x = 87 mm which we will now call the explosive event. A second weak compressive front, not associated with an explosive event, was observed in two cases (Shots 602 and 504); it may be the result of the unusual decomposition processes of tetryl that will be described later. The other three velocities listed in Table 1, under "second compressive front" are those associated with an explosive event.

Figure 3 shows the data for one of the most informative shots on fine tetryl. In this case, the initial

429

TABLE 1

Summary of Shots on Coarse Tetryl

Shot No.	ρ_0 g/cc	% TMD	Front Velocity, mm/μsec				Predet. column length ℓ, mm[b]	Event site x_c mm	$\frac{x_c}{\ell}$	Det. time Δt_{41} μsec
			Con-vect-ive[a]	Com-press-ive	2nd Com-press.	Det-ona-tion				
602	1.55	89.5	---	0.9	2.4	F	—	–	—	—
504	1.48	85.5	0.4	d	1.4	7.26	207	---	--	279
613	1.47	85.0	--	1.2	2.0	7.29	153	87	.57	75
513	1.40	81.0	—	1.3	~1.6	7.22	118	71[c]	.60	77
604	1.29	74.6	--	~1.0	—	6.65	68	---	---	18
506	1.21	70.1	0.7[c]	d	—	6.41	64	—	--	24
612	1.20	69.5	---	0.8	--	6.34	67	50[c]	.75	17
607	1.09	63.2	0.2	1.3	~3.2	5.82	75	---	—	56

a. Whenever observed, this was first front.

b. Values to ± 3mm.

c. Despite relatively high velocity, pressure registered seemed too low for compressive front.

d. Record inadequate to give value.

e. Approximated from sparse data.

charge was 76.6% TMD, and, as before, the x-t plot and the ϵ-t plots appear in parts a and b, respectively. The information from the shot on fine tetryl parallels that from the coarse: the first observed front is again compressive (at 1.1 mm/μsec); it, in turn, creates a following ionic front. Again the extrapolated low pressure isobars from the ignition region coalesce, but too late to initiate the detonation or to cause the explosive event. Finally, an explosive event occurs near the onset of detonation (here at x = 122 mm while ℓ = 158 mm); the event seems to lead to the onset of detonation as well as to send a compressive disturbance back into the burning explosive, and again the forward moving compressive front marks the beginning of accelerated burning. Thus the disturbance from the explosive event resembles the postconvective wave in other explosives undergoing transition much more closely than does the first compressive wave observed.

Table 2 contains the summary of shots on the fine tetryl; the records appear in reference (3). Three sets of records in addition to those of Fig. 3 contained enough data to locate the explosive event approximately. Although there was still difficulty in obtaining probe response to the initial reaction front, the response was much better in the fine than in the

coarse tetryl. Thus Table 2 shows that the convective front was observed in over half the shots; the custom-made probes were used for triggering. In addition to Shot 813 (Fig. 3), Shots 1004, 815, and 1007 were analyzed for convergence of isobars; no convergence was found. This, in addition to the negative results observed on the coarse tetryl, strongly indicates that the compressive waves formed by the initial burning of the tetryl in the ignition area do not contribute directly to the onset of detonation or to the appearance of the explosive event.

For burning tetryl we have found the following patterns of reaction: a linear ϵ-t rise, followed by a slightly faster linear ϵ-t rise, followed by an accelerating strain increase. Despite high electrical resistance of the initial reaction front, decomposition does start in the ignition area as would be expected. It produces sufficient gas to create a compressive front, but one which shows only a linear increase of ϵ with t followed by a second period of linear increase that was absent in other HE studied. These patterns could be produced by a multistage decomposition mechanism.

Tetryl begins to decompose at a relatively low temperature; its decomposition at 140-160°C and up to 20-25 atm pressure of gas products has been

430

TABLE 2

Summary of Shots on Fine Tetryl

Shot No.	ρ_0 g/cc	% TMD	Front Velocity, mm/μsec Convect- ive.[a]	Com- press- ive	2nd Com- press.	Det- ona- tion	Predet. Column Length ℓ, mm[b]	Event site x_e, mm	$\frac{x_e}{\ell}$	Det. time Δt_{60} μsec
713	1.48	85.4	0.6	—	—	F	—	—	—	—
1117	1.44	83.4	—	1.1,-	—	b	583[d]	—	—	560
104	1.36	77.8	—	0.9,-	—	b	259	—	—	220
813	1.33	76.6	—	1.05,-	2.0	6.26	158	124	.78	101
807	1.29	74.5	0.3	1.4,0.8[f]	~1.1	~6.3[c]	200±7	158[e]	.79	170
815	1.21	70.1	—	1.9,0.9[f]	~3.0	6.34	201	131[e]	.65	139
1007	1.17	67.7	0.2	1.4,1.1[f]	~1.4	5.86	175	142[c]	.81	137
1311	1.09	63.0	0.2	-,0.6	—	~4.6[c]	237	—	—	317
1111	1.02	59.0	0.3	1.8,0.8[f]	—	5.55	190	—	—	225
1312	0.87	50.3	0.5	1.1,0.6[f]	—	5.21	196	—	—	269
1208	0.79	45.8	0.3	1.4,0.6[f]	—	5.13	147	—	—	228

a. Whenever observed, this was first front.

b. Values of ±3mm, unless otherwise indicated.

c. Insufficient data.

d. Double length, coupled tube.

e. Estimated from inadequate data.

f. Compressive front starts near ignition area and changes slope after overtaking convective front. Second velocity that of compressive front after change or of the associated ionization front.

studied in some detail (5, 6). Dubovitskii and his colleagues found that within this temperature range, "the decomposition proceeds via three parallel routes" with the respective solid products of picric acid (PA), 2, 4, 6-trinitroanisole, and N-methyl-2, 4, 6-trinitroaniline. Of these, picric acid was shown to catalyze the slow decomposition—indeed, to account quantitatively for the self-acceleration. The gaseous products were also analyzed (e.g., chiefly NO_2 at 18% decomposition), and the effect of the ratio (mass of explosive/volume of container, m/V) examined. In general, the higher m/V (and the gas pressure to which it is proportional) the greater the rate of decomposition. In fact, earlier investigators were reported to have observed a critical value of this variable at which slow decomposition changed to explosion.

The supplementary information on tetryl decomposition justifies assuming a multi-stage decomposition. For example, very slow decomposition to picric acid, $C_6H_2(NO_2)_3OH$, and NO_2 followed by a much more rapid, high pressure decomposition. In the first stage reaction, temperature is low and products non-ionic; hence our difficulty in response of the ionization probes. The postulated second stage should lead to a very rapid pressure rise and what we have so far called an explosive event.

A more detailed examination of Figs. 2 and 3 shows that the strain gage nearest the location of the event is in each case the third from th ignition end of the tube, and that at the time (F) that the e-t curve shows a marked increase in slope (from about 10 to about 70 μe/μsec), the strain corresponds to about 400 μe or 3 1/4 kbar. Seven microseconds later, the strain is about 900 μe. In other words, an accelerated burning seems to start at the location of the "explosive event".

When the output of the third gage indicated 3 1/4 kbar, those of the first and second gages were 400 μe or somewhat greater. Although these outputs are still within the range of the static calibration, they are beyond the level at which the tube behaves elastically.

Moreover, the gages record total stress, not just internal gas pressure. (The velocity data have indicated compaction near the ignition area, and that could affect stress transmission to the tube.) We have not yet any data on the effect of gage location or of lag in gage response on the observed output. In view of these uncertainties, we suggest that the location of the explosive event is at that point where the gas pressure and burning surface area become critical for a runaway reaction; that this happens to be nearer the point of onset of detonation than to the ignition area is merely because of the complexity of the tetryl decomposition, and its difference from that of other HE in being able to sustain low-temperature decomposition. Once accelerated burning starts at the location of the event, it can travel in both directions. Tetryl in the ignition end of the tube would have been undergoing only a slow decomposition for a time of the order of magnitude of a millisecond. Hence, very little of the tetryl should be decomposed prior to the beginning of accelerated burning. Once accelerated burning began, however, it could rapidly lead to shock formation and initiation of detonation in either direction. Although tube fragmentation, indicating onset of detonation, was not found in the ignition end of the tube, the fragments from this part of the tube were smaller than those recovered from other explosives (physically comparable charges) which showed accelerated burning starting near the ignition region instead of traveling back into it.

Korotkov and coworkers (7) have, from optical observation of DDT in porous PETN, suggested "the explosion of a limited volume of the explosive" as a source of the initiating shock wave. We do not believe that our explosive event is a thermal explosion of an appreciable quantity of tetryl because the pressure records do not show the sharp rise to be expected for such an occurrence. Instead, as explained above, they suggest the start of an accelerated burning that leads to shock formation and subsequent detonation as it does in the model.

There is no discernable pattern with increasing initial charge density of the velocities of either the convective or the first compressive front. Each could be represented by an average value with large scatter at individual points within the range covered. Nor does there seem to be a detectable difference in these velocities caused by the particle size of the tetryl.

The detonation velocities of Tables 1 and 2 that have been determined from three or more probe responses fit the relation

$$D(mm/\mu sec) = 2.036 + 3.400\, \rho_0(g/cc) \qquad (1)$$

to within 6% or less. Equation (1) is the straight line between the value of 7.17 mm/μsec for tetryl at 1.51 g/cc (8) and the value 7.85 mm/μsec at 1.71 g/cc (9). The agreement is quite adequate to show that steady state detonation has been achieved.

Relative time to detonation (Δt) is also listed in Tables 1 and 2; it is relative to the discharge of a probe at 41 mm and one at 60 mm, respectively. It is not surprising that the trend of Δt with compaction seems a bit erratic in view of the difficulties we experienced with probe response. The Δt_{41} for coarse tetryl is appreciably less than Δt_{60} for fine. Since the different starting points would be expected to have the opposite effect, we can assume the difference is real unless the values of Table 1 have been excessively shortened by lack of probe response to the convective front. The Δt of both tables show an increase with increased compaction; this trend is the opposite of that observed for 91/9 RDX/wax (10). Moreover, at 70% TMD, Δt of fine tetryl is comparable to that of 94/6 RDX/wax and less than that of the 91/9 mix whereas Δt of coarse tetryl is somewhat less than that of 97/3 RDX/-wax. In fact, both ℓ and Δt_{41} of 470μ tetryl at 70% TMD are very close to those found for Class E RDX also at 70% TMD (11).

The predetonation column length (plotted as a function of compaction in Fig. 4. A ut 75% TMD and less, ℓ seems to remain essentially constant down to as porous a charge as can be prepared and handled. As the compaction increases above 75% TMD, ℓ also increases and, in the case of fine tetryl, increases very sharply. In contrast to 91/9 RDX/wax, there seems to be no well defined minimum in ℓ. In fact, the sharp rise of ℓ with increased compaction suggests that decreased permeability hinders DDT in tetryl to a far greater extent than it does in 91/9 RDX (200μ)/wax which exhibits transition at all compactions up to and including 97% TMD (11). At all compactions $\ell(20\mu$ tetryl) $> \ell(470\mu$ tetryl). This particle size effect is in the same direction as that reported by Calzia (12) for RDX. If as we have assumed, the explosive event is directly responsible for the onset of detonation, there should be a close dependence
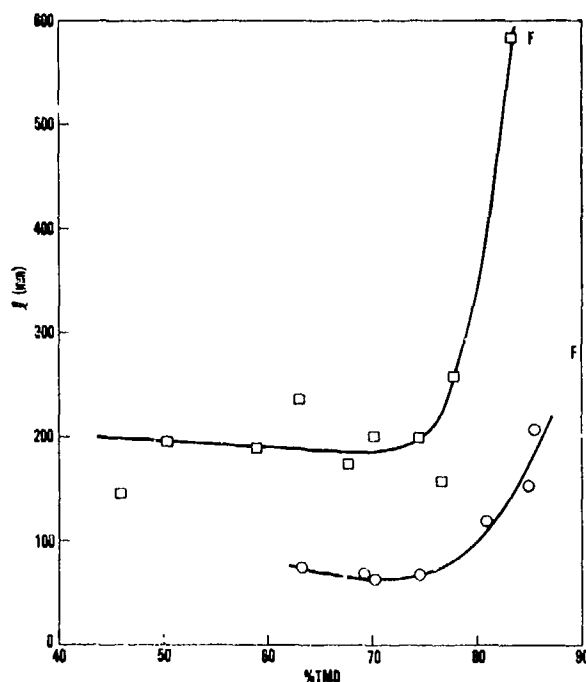
Fig. 4. Effect of compaction on predetonation column length of tetryl. (□ 20μ, ○ 470μ).

between the location of the event (x_c) and ℓ. Figs. 2 and 3 give x_c/ℓ values of 0.6 (coarse) and 0.8 (fine). Using more limited gage data to approximate x_c on other shots, we have one value (of two) that checks the former; two (of three) for the latter.

The literature provides only fragmentary data on the transitional behavior of tetryl (13-15). If it is assumed that the literature reports are for a coarse tetryl comparable to that used here, there are no obvious inconsistencies between the present data and those of earlier work. On the contrary, there is fair agreement between ℓ values and front velocities (3).

Because of the difficulty we encountered with probe response in the coarse, porous tetryl, we have started a study of the electrical resistance of the commercial probe when it is in a burning porous bed contained in an open ended tube. We found that with porous 91/9 RDX/wax, PETN, and TNT, the probe resistance dropped from a high value to less than 100 ohms in one μsec or less (16). Cast TNT showed the same drop in 2-4 μsec whereas our porous ignitor mixture (25/75 B/KNO₃) and porous coarse tetryl required more than 20 μsec for the same decrease in

resistance. Thus tetryl burns initially more like our ignitor mixture than a typical HE.

It is of interest that Dremin and coworkers (17) investigated changes in the electrical conductivity of porous tetryl and porous TNT when shocked at intensities of 8-25 kbar. For the lower amplitude, TNT reached a resistance below 100 ohms in 8-10 μsec whereas tetryl had exhibited no significant conductivity after 15 μsec. If we assume the shock initiation mechanism is thermal, these results should parallel those found above with an ignitor, as they do.

Finally, we should like to present the results for two shots on 97/3, tetryl (470μ)/wax. Earlier work on RDX showed that addition of wax slowed down and stretched out the DDT process. Thus for 70% TMD Class A RDX, ℓ = 40-45 mm (11), and for 70% TMD 97/3 RDX (Class A)/wax, ℓ = 95 mm (1). Hence 3% wax was added to tetryl (470μ) in the hope of obtaining better resolution of the transition process. Two shots were made at 66.5% TMD; the more complete set of records is shown in Fig. 5. The increase in ℓ was from about 70 mm (Fig. 4) to 238 mm and 248 mm, a much greater increase than the 2-fold one observed for RDX. The corresponding increase in Δt_{41} was from 18-56 μsec to 416 μsec.

Even more interesting than the effect of 3% wax on ℓ and Δt_{41} is its apparent ability to change the initial low temperature decomposition of tetryl into one more typical of other explosives. Although selection of the compressive front(s) from Fig. 5b may be difficult, there seems little doubt that their origin is nearer the ignition region than the onset of detonation (see Fig. 5a). Moreover, low pressure isobars from records of the third and fourth gage extrapolate to show a fair coalescence at a location (Fig. 5a) at which the shock could be a factor in SDT. In other words, 97/3 tetryl/wax appears to conform to the physical model of DDT (1) although unwaxed tetryl does not. Further work on waxed tetryl will, of course, be necessary to substantiate this result. It should also be mentioned at this point that we have succeeded in resolving the PC front in one shot on pure RDX. There seems to be no difference in mechanism between the waxed and unwaxed RDX.

Another feature of interest in Fig. 5a is the initially high velocity (~1.5 mm/μsec) of the compressive front, followed by the lower velocity (0.64 mm/μsec)
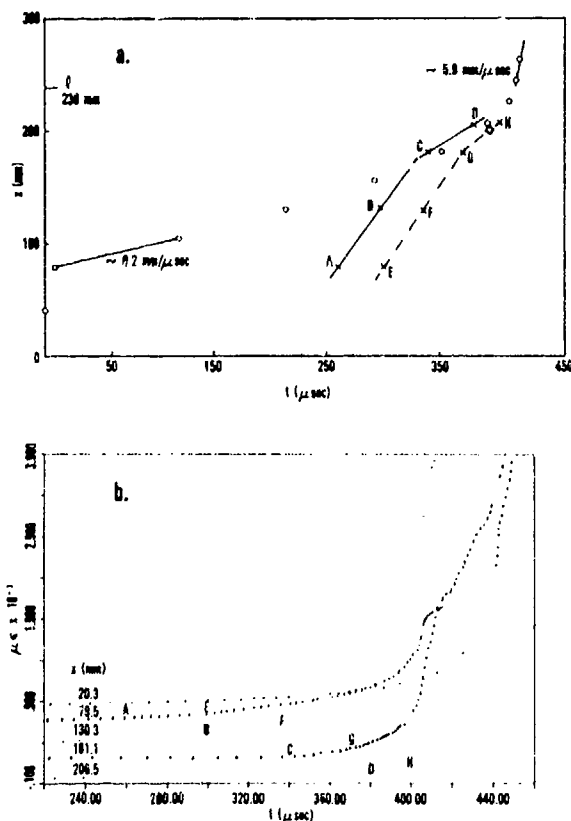
433

Fig. 5. Data for shot 1310 on 97/3 tetryl (470μ)/wax at 66.5% TMD, $\rho_0 = 1.17$ g/cc. a. Distance-time plot (key of Figure 2a); b. Strain-time plots (key of Figure 2b).

to be expected as the sound velocity in this high porosity charge. It therefore appears that some compaction of the charge occurs near the ignition area as a result of the moderate pressurization necessary for formation of the convective front. The compressive front that is subsequently formed, as the result of post-ignition but slow burning, travels through the compressed explosive rapidly. When it emerges into explosive which has not yet been compressed, its rate drops to that to be expected at the original compaction.

This phenomenon is not unique to waxed tetryl. We found evidence that it occurred in 90% of the shot records of fine, high porosity (>25%) tetryl. (See Figs. B11-B17 of reference (3)).

CONCLUSIONS

1. Tetryl decomposition in the DDT tube appears to start at a relatively low temperature. It progresses slowly for some time at a lower temperature than that of the initial decomposition of other explosives studied.

2. The initial slow decomposition replaces the convective front of the 91/9 RDX/wax model with a gas front that is not always detectable by ionization probes. However, it causes a linear increase of pressure with time, and also causes compression of the very porous charges.

3. Accelerated burning begins at a location x_c, closer to the onset of detonation than to the ignition region. Compressive waves are sent out in both directions from x_c. The forward traveling wave corresponds to the postconvective wave in the earlier model in that it marks the onset of accelerated burning shortly after its passage.

4. The curve, predetonation column length versus % TMD of tetryl, shows no well defined minimum as did that of 91/9 RDX/wax. In fact, ℓ decreases with compaction to 75% TMD, and remains nearly constant as the porosity increases above 25%.

5. Larger particle size shortens ℓ (and apparently Δt) for tetryl.

6. Addition of a small amount (3%) of wax has a greater effect on the DDT behavior of tetryl than that of RDX. In particular, the waxed tetryl appears to follow the DDT model typical of other explosives, but not of pure tetryl.

REFERENCES

1. R. R. Bernecker and D. Price, "Studies in the Transition from Deflagration to Detonation in Granular Explosives" II and III, Combust. Flame 22, 119-129 and 161-170 (1974). See also NOLTR 72-202.

2. D. Price and R. R. Bernecker, "Sensitivity of Porous Explosives to Transition from Deflagration to Detonation," Combust. Flame 25, 91-100 (1975). See also NOLTR 74-86.

3. D. Price, R. R. Bernecker, J. O. Erkman and A. R. Clairmont, Jr., "DDT Behavior of Tetryl and Picric Acid," NSWC/WOL/TR 76-31 (31 May 1976).

4. I. E. Lindstrom, "Planar Shock Initiation of Porous Tetryl," J. Appl. Phys. **41** (1), 337-350 (1970).

5. F. I. Dubovitskii, V. A. Strunin, G. B. Manelis, and A. G. Merzhanov, "Thermal Decomposition of Tetryl at Varying m/V Values," Russ. J. Phys. Chem. **35** (2), 148-152 (1961).

6. F. I. Dubovitskii, G. B. Manelis, and L. P. Smirnov, "Kinetics of the Thermal Decomposition of N-Methyl- N, 2, 4, 6-tetranitroaniline (Tetryl)," Russ. J. Phys. Chem. **35** (3), 255-260 (1961).

7. A. I. Korotkov, A. A. Sulimov, A. V. Obmenin, V. F. Dubovitskii and A. I. Kurkin, "Transition from Combustion to Detonation in Porous Explosives," Combusion, Explosion and Shock Waves **5**, 216-222 (1969).

8. A. R. Clairmont, Jr. and I. Jaffe, "Analysis of Optical Determination of Detonation Velocity in Short Charges," S.P.I.E. Journal **5**, 18-21 (1966). See also NOLTR 64-23.

9. Military Explosives, TM 9-1300-214, Nov 1967.

10. R. R. Bernecker and D. Price, "Transition from Deflagration to Detonation in Granular Explosives," NOLTR 72-202 (13 Dec 1972).

11. R. R. Bernecker and D. Price, unreported work.

12. J. Calzia, "Experiments on the Deflagration-Detonation Transition in Condensed Explosives," Compt Rendu **276**, 1397-1399 (1973).

13. G. F. Cawsey, J. L. Farrands, and S. Thomas, "Observations of Detonation in Solid Explosives by Microwave Interferometry," Proc. Roy. Soc. **248A**, 499-521 (1958).

14. N. Griffiths and J. M. Groocock "The Burning to Detonation of Solid Explosives," J. Chem. Soc., 4154-62 (1960).

15. L. V. Afonina, I. V. Babaitsev, and B. N. Kondrikov, "Method for Determining the Tendency of an Explosive to Pass from Combustion to Detonation," Vzryvnoe Delo Collection No. 68/25, Translation, Jerusalem 1971: pp. 136-143.

16. J. O. Erkman, unreported work.

17. A. N. Dremin, S. A. Koldunov, and K. K. Shvedov, "Changes in the Electrical Conductivity of Shock-Initiated Explosives," Combustion, Explosion, and Shock Waves **8** (1), 123-125 (1972).

435

Session VII
NEW EXPLOSIVE PROPERTIES

Chairman: M. Kamlet
         Naval Surface Weapons Center

IMPROVEMENT OF PERFORMANCE OF COMPOSITE EXPLOSIVES CONTAINING AMMONIUM NITRATE BY PHYSICAL SYNTHESIS

J. Hershkowitz and I. Akst*
Picatinny Arsenal
Dover, N.J. 07801

The performance of explosives containing ammonium nitrate (AN) has been improved by combining AN with either methylammonium nitrate (MAN) or ethylenediamine dinitrate (EDD) in the eutectic and other ratios by cosolidification techniques. Confined small-scale (9.65mm) dent and detonation velocity tests were conducted on these compositions and combined with RDX. Depths of dents for some compositions, containing up to 40 weight percent AN, were comparable to those for Composition B. Cylinder tests at 101.6 mm explosive diameter were done for RDX/AN/MAN, 40/60/0, 40/45/15, 40/30/30 and for RDX/TNT/ AN, 60/40/0, 40/40/20, 20/40/40. Cylinder wall kinetic energy for RDX/AN/ MAN, 40/30/30 was 95% of the Composition B value. Results were compared with predictions based on the BKW equation of state and Chapman-Jouguet theory to show that the improved performance corresponded to a move toward ideal explosive behavior. This move was related to an increase in AN contribution by solving for the AN value in an equation setting the cylinder wall kinetic energy for the composition equal to a volume fraction weighted sum of wall kinetic energies for individual constituents.

INTRODUCTION

The timing and extent of energy release of composite explosives is often limited by rate controlling factors (e.g. diffusion) and elemental imbalances between components (e.g. fuel rich). To overcome these limitations, extremely close juxtaposition of complementary energetic materials by various cosolidification techniques is proposed. This approach, which is called physical synthesis, spans the various levels of intimacy achieved in eutectics, substitutional and interstitial solid solutions, mixed crystals and intimately blended crystallites of various sizes. The selection of complementary constituents is guided by predicted ideal performance, existence of eutectics, etc., kinetic role, and other considerations. Physical synthesis can lead to new composite explosives and

casting matrices, improved performance due to synergism of components, and the use of inexpensive, readily available energetic materials. A program has been conducted (1, 2, 3) to provide information on the value of this approach.

Ammonium nitrate (AN) was selected because composite explosives containing AN do not achieve their predicted potential (4), possibly due to limited diffusion (5) and/or to the need for kinetically active species to interact with those of AN decomposition. In addition, AN is a readily available low cost energetic material and eutectics exist that could serve as casting matrices. Methylammonium nitrate (MAN), tetramethylammonium nitrate (QMAN) and ethylenediamine dinitrate (EDD) were selected to complement AN. RDX was selected to alter the pressure, temperature and species environment in which the cosolidified combinations would function.

*Now at Idos Corp., P.O. Box 285, Pampa, Texas 79065

PROCEDURES

Performance was first evaluated by confined small-scale dent and detonation velocity tests. This test uses a brass or steel cylinder 76.2 mm (3″) long with an inner diameter of 9.65 mm (3/8″) and an outer diameter of 25.4 mm to confine a stack of explosive pellets totalling at least 63.5 mm in height. A Comp B pellet was generally used for initiation. Ionization probes passing through the wall were used to measure detonation velocity. The loaded cylinder was placed directly on the thick steel dent plate. Two slightly different testing configurations (2,3) were used. Combining the data was justified by comparision of data on the same explosives, experiments varying one of the configurations, and available information (6 or 7) on the effect of dent test parameters. Results of these small-scale tests are of direct interest for comparable dimension applications and serve as screening tests to select compositions for further studies at larger diameters. The standard cylinder test (8) was used at an explosive diameter of 101.6 mm which is comparable to configurations of interest and is considered sufficiently large to have a limited residual diameter effect. The cylinder was 914 mm (36″) long and had a wall thickness of 10 mm (0.4″). Radial displacement of the wall was recorded with a slit camera. Detonation velocity was measured using contactors that responded to initial displacement, spaced along the wall exterior.

Different methods were tried in preparing compositions for the small scale tests, which also served to provide data on the influence of method of preparation. The combinations of AN with MAN, or QMAN, or EDD were prepared by the following procedures: comelting with rapid cooling by pouring onto a stainless steel sheet or into Freon TF, or injecting the latter into the melt; corecrystallization from water solution with rapid vacuum evaporation; this last procedure followed by melting and quick solidification; slurry preparation by melting in perchlorethylene with additional perchlorethylene used for chilling; dry mixing. Each of the resulting materials was pulverized and screened (350 μm) as necessary. In some cases the eutectic ratio compositions (with wt. % and $T^\circ C$ as follows: MAN/AN, 62.5/37.5, 57°; QMAN/AN 17/83, 133°; EDD/AN, 50/50, 102°) were first prepared by one of the above procedures and additional AN was added by dry mixing to achieve the desired proportions. These combinations

were dry mixed with RDX to achieve the final composition. All mixes were pressed into pellets.

The RDX/MAN/AN for the cylinder tests (2) was prepared as follows. The MAN/AN eutectic ratio composition was made from aqueous solution using vacuum evaporation in an oven, followed by melting into layers 6 mm thick that were quickly solidified. This material was crushed, mixed with AN, reground and passed through a 177 μm mesh opening (No. 80) sieve. This product was dry blended with the required weight of RDX. The charges were pressed to diameter and machined to length to provide pellets for the cylinder test. The RDX/TNT/AN, 40/40/20 and some of the 20/40/40, 60/40/0 were cast compositions (9). The remaining 20/40/40, 60/40 and 64/36 were pressed.

RESULTS

The results of the confined small scale dent and detonation velocity tests at an explosive diameter of 9.65 mm (3/8″) are given in Table 1. The depth of dent data for binary combinations (Fig. 1, left) of RDX and EDD, MAN, TNT overlap, whereas those of RDX with AN and INERT (an inert substitute for AN) produce lesser dents. The data on depth of dent for binary and ternary composites containing AN is plotted in Fig. 1, right. TNT and EDD, which gave similar results with RDX, show distinctly different results with AN. An AN is increased in AN/EDD, the dent depth does not decrease, but instead increases slightly peaking at 20% AN. In the more active environments of RDX 20/EDD and RDX 40/EDD, there is a marked increase in dent depth as AN content is increased. The peak is now at about 40% AN and as more AN is added the curve remains above that for RDX/AN. The curve for the RDX 40/MAN environment shows the same improvement of dent producing performance with AN content as for the environments containing EDD. In addition, data from confined small-scale dent tests at 8.08 mm explosive diameter (1) for other environments containing MAN/AN and QMAN/AN showed similar behavior. The results for environments containing EDD and MAN demonstrate enhanced participation of AN over the time period involved in forming the dent.

The small scale detonation velocity results are shown in Fig. 2. In all environments, except that

440

TABLE 1

Results of Confined Small Scale Dent and Detonation Velocity Test
(Explosive Diameter = 9.65 mm)

TNT	RDX	AN	MAN	QMAN	EDD	$\bar{\rho}$	Depth of Dent (mm)				Avg.	Det. Vel. (mm/μsec)			Avg.
	100					1.72	3.58	3.61	3.47	3.47	3.53	8.66	8.59	8.46	
												8.55			8.57
20	80					1.66	3.43	3.28			3.36				
40	60					1.67	3.33	3.20	3.10	3.23	3.22	7.73			7.73
60	40					1.64	2.95	2.90			2.93				
80	20					1.63	2.79	2.84			2.82				
100						1.59	2.53	2.57	2.41	2.46		6.92	6.92	6.69	6.84
							2.49	2.44	2.46		2.48				
	80		20			1.67	3.40	3.35			3.38				
	60		40			1.59	2.90	2.95			2.92				
	40		60			1.53	2.84	2.84			2.84	7.37	7.27		7.32
	20		80			1.46	2.57	2.72			2.65	6.41	6.49		6.45
			100			1.40	0.05	0.10			f				
	60				40	1.67	3.25	3.18			3.22				
	40				60	1.64	2.90	2.82			2.86	7.96	7.66		7.81
	20				80	1.59	2.69	2.72			2.71	7.56	7.52		7.54
					100	1.55	2.72	2.46	2.59	2.64	2.60	6.77			6.77
	80	20				1.70	3.30	3.20			3.25				
	60	40				1.73	2.69	2.77			2.73				
	40	60				1.71	1.89	1.93	2.21	2.26		7.17	7.17	7.12	7.15
							2.26				2.11				
	20	80				1.66	1.19	1.22			1.21				
	80			120		1.69	3.00	3.07			3.04				
	60			140		1.70	2.31	2.26			2.29				
	40			160		1.66	1.47	1.35			1.41				
40					60	1.57	2.69	2.57			2.63				
		20			80	1.48	2.67	2.69			2.68	6.18	6.58		6.38
		30			70	1.51	2.64	2.49	2.49	2.72		5.85	5.60	5.90	5.78
							2.74				2.61				
		40			60	1.47	2.52	2.57			2.54	5.90	5.69		5.80
		50			50	1.55	1.52	1.70	2.18	1.52		5.17	5.18	5.20	5.19
							0.76	0.86	1.96		1.50				
		56			44	1.58	0.91	2.13	2.72	0.40		5.81	5.23		5.52
							1.98	2.52	0.15	f	1.20				
		60			40	1.55	1.70	1.32	1.52	1.83	1.59				
70		30				1.63	2.01	2.03			2.02	6.48	6.25		6.37

TABLE 1–Continued

TNT	RDX	AN	MAN	QMAN	EDD	$\bar{\rho}$	Depth of Dent (mm)				Avg.	Det. Vel. (mm/μsec)			Avg.
	40	45	15			1.66	2.97	2.97	2.96		2.97	7.34	7.31	7.07	7.24
	40	30	30			1.62	3.05	3.07	2.99		3.04	7.49	7.51	7.16	7.39
	40	15	45			1.57	2.97				2.97	7.57			7.57
	40	48		12		1.64	2.41	2.36			2.39	6.99	7.06		7.03
	40	40		20		1.59	2.29	2.46			2.38	6.94	6.97		6.96
	40	30		30		1.53	2.21	2.21			2.21	6.77	6.86		6.82
	40	34			26	1.67	3.22	3.25	3.28	3.23	3.25				
	40	30			30	1.66	3.28	3.15	3.30	3.20	3.23	7.38			7.38
	20	60			20	1.67	2.29	2.36			2.33				
	20	45			35	1.62	2.95	2.92			2.94	6.16			6.16
	20	40			40	1.61	3.05	3.02	3.30	3.23	3.15	6.39			6.39
	20	24			56	1.51	2.90	2.84			2.87	6.93			6.93
40	20	40				1.65	2.54	2.46	2.71	2.67	2.60	7.10			7.10
40		34			26	1.61	2.79	2.82			2.81				

Compositions given in weight percents. AN = ammonium nitrate; MAN = methylammonium nitrate; QMAN = tetramethyl-ammonium nitrate; EDD = ethylenediamine dinitrate; I = inert = 90/10 ammonium sulfate/ammonium sulfite monohydrate. $\bar{\rho}$ = average density in g/cm^3; f = fails to propagate; AN = 100 and AN/EDD = 75/25 did not propagate. Data on RDX 40/AN/MAN or QMAN, RDX/MAN 20/80 and first two values for RDX are from Ref 2, balance from Ref 3.

with QMAN, the velocity decreases as AN content is increased. (The exception is simply due to the non-explosive character of QMAN, and its lower density). However, the velocity decrease with increase in AN is at two rates, with a lower rate for the more active environments RDX 40/MAN and RDX 40/EDD. (Note the same slope for 101.6 mm as for 9.65 mm explosive diameter of RDX 40/MAN/AN. In the shorter time frame of the detonation zone, the AN contribution though small is enhanced by more active environments.

The results of the 101.6 mm explosive diameter cylinder tests are given in Table 2, together with sources (2, 8, 9, 10, 11, 12) and necessary descriptions. The wall velocities at the 20 and 76 mm wall displacements (R-R_0) correspond to the volume occupied by products being twice and seven times respectively that of the uninitiated explosive. The wall kinetic energy ratios for different explosives are formed by squaring the wall velocity and dividing it by a similar quantity for RDX/TNT 64/36 (standard). Note first that as the ratio of MAN to AN increases in the RDX 40/AN/MAN the metal accelerating

ability of the explosive increases significantly, reaching 95% of that of the standard explosive for equal parts of MAN and AN. This must be assessed in terms of the fact that the standard explosive has more RDX (64 wt %), and the balance TNT, whereas this composition uses only 40 parts RDX. Comparison with RDX/TNT/AN 40/40/20 and 20/40/40 (Amatex 20) show that the MAN/AN combination provides highest wall kinetic energy for minimum use of RDX and TNT. A comparison of data in Table 2 for displacements of 20 and 76 mm shows that the compositions containing MAN/AN also provide greater acceleration at earlier times than those containing TNT/AN. The detonation velocity data show the same trends as the wall kinetic energies. For example, RDX/AN/MAN, 40/30/30 has a detonation velocity of 7.88 mm/μsec compared to 7.99 for the standard and 7.04 for RDX/TNT/AN 20/40/40 and 7.53 for 40/40/20. Since MAN is an explosive and the improved performance occurred as MAN was increased, the results are due to substitution of MAN for AN, enhancement of the AN contribution, and the more active environment in which the balance of the AN functions (see DISCUSSION).
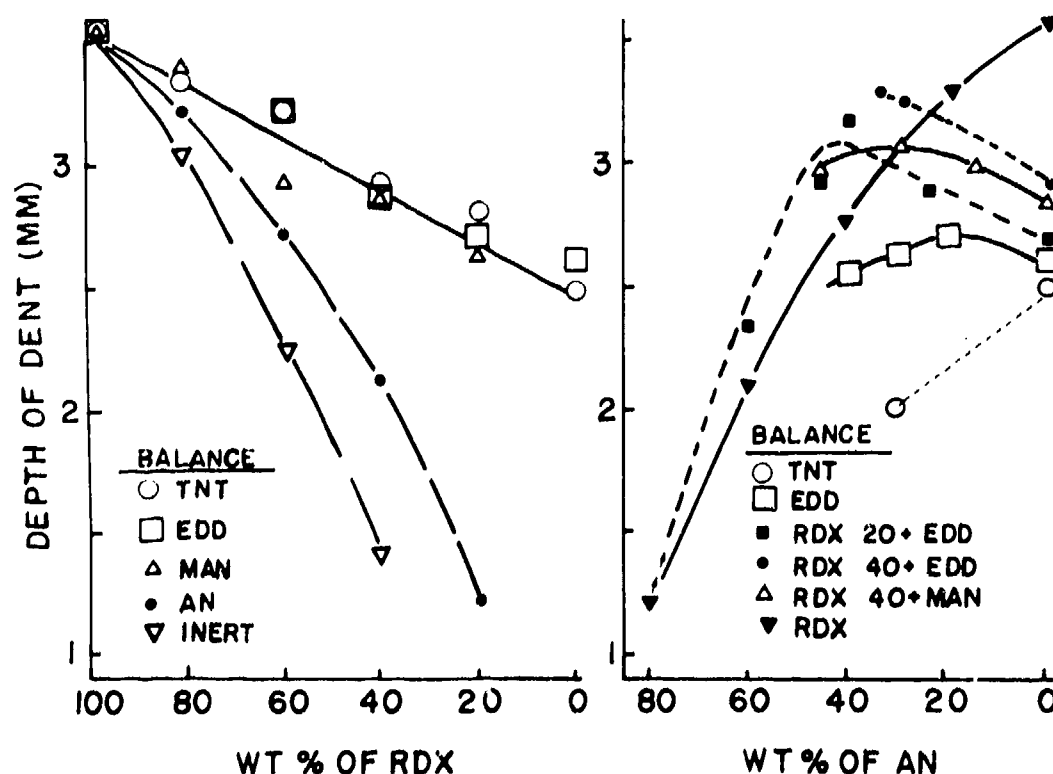
442

Fig. 1. Depth of dent results for confined small scale test (9.65 mm).

The data in Table 2 also show the effect of sub-stituting AN for RDX holding TNT at 40 wt %. Average kinetic energy ratios 1.0, 0.93, 0.86 and average detonation velocities 7.91, 7.53, 7.04 correspond to 0, 20, 40 AN in TNT 40/RDX/AN. These trends and those presented previously for the RDX/AN/MAN system are shown in Fig. 3 by the open circles and triangles. The RDX 40/MAN/AN points fall above and have a lower rate of decrease with increase of AN than the TNT 40/RDX/AN system, demonstrating the earlier stated superiority of systems containing MAN/AN.

Before leaving Table 2, note that data is also presented showing that use of prills or very coarse AN (below dashed line) results in lower detonation velocity and cylinder wall velocities. It is possible that in longer time frames (e.g. blast waves, cratering, rock blasting) these particle size effects would be reduced. The performance of AN/FO (12) is listed for comparison.

The results of calculations of ideal detonation and expansion properties using the TIGER computer
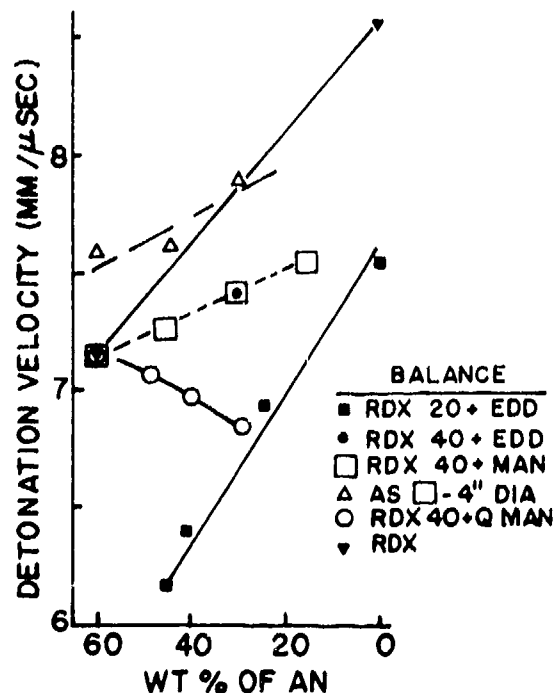
Fig. 2. Detonation velocity results for confined small scale test (9.65 mm).

443

TABLE 2

Results of Cylinder Tests for 101.6 mm Explosive Diameter

Composition Wt. %					ρ	Wall Velocity (mm/μsec) at $R\text{-}R_0$(mm)		Ratios of (Wall Velocity)^2		Detonation Velocity (mm/μsec)			Ref.
TNT	RDX	AN	MAN	FO		20	76	20	76				
36	64				1.717	1.390	1.630	1.0	1.0	7.99			8
40	60				1.700	1.380	1.645	0.986	1.018	7.89	7.90	7.91	9
					1.701	1.378	1.625	0.983	0.994	7.92			10
40	40	20			1.677	1.327	1.587	0.911	0.948	7.55			9a
					1.672	1.311	1.558	0.890	0.914	7.55	7.56		9b
					1.669	1.313	1.568	0.892	0.925	7.50	7.50		9b
	40	60			1.720	1.325	1.534	0.909	0.886	7.58	7.59		2c
	40	45	15		1.673	1.348	1.572	0.940	0.930	7.64	7.65		2d
	40	30	30		1.630	1.360	1.589	0.957	0.950	7.88	7.88		2d
40	20	40			1.634	1.269	1.517	0.833	0.866	7.03	7.03		9e
					1.624	1.276	1.509	0.843	0.857	7.03	7.06		9e
					1.572	1.217	1.468	0.767	0.811	6.81			10i
					1.613	1.237	1.471	0.792	0.814	6.95			11g
					1.604	1.266	1.508	0.830	0.856	6.95	6.96		9a
		94		6	0.782	--	0.866	--	0.282	3.89			12h

Cylinder test is described in Ref. 8. Expansion velocity of the 10 mm thick copper wall is given for wall displacements, $R\text{-}R_0$. Detonation velocity is simultaneously measured by multiple pin signals along wall. Detonation values listed first correspond to 10 mm wall case; other D values are for walls 5 mm thick. The ratios of wall velocities squared uses RDX/TNT 64/36 as standard. Ref. 9 compositions were cast, others pressed (except AN/FO prills). Last column gives source of data (numbers) and notes (letters) on particle size of AN as follows - a - AN coarse (75% 177-800 μm); b - AN fine (85% 62-177 μm); c - AN extra-fine (median < 40 μm); d - AN/MAN eutectic melt (see text); e - AN medium, equal parts coarse and fine; f - AN prills; g - AN prills (median ~ 500 μm); h - AN prills with No. 6 diesel fuel oil.

program (13) with the BKW equation of state are presented in Table 3. Subject to applicability of Chapman-Jouguet (CJ) theory and the equation of state, the values represent an upper bound on performance of the compositions. The footnotes in Table 3 explain the column headings. Note that R_2'' and R_7'' are predicted ratios of wall kinetic energy to the standard explosive while the ratios of velocity squared in Table 2 are the experimental counterparts. Calculations for theoretical maximum densities and for experimental densities were made and the former set selected for Table 3 as of more general use. (Con-

clusions of analyses are not altered by this choice). One can estimate that a 0.1 g/cm^3 increase in density increases detonation velocity about 330 m/sec.

To compare depth-of-dent data (Table 1, Fig. 1) with Table 3 one can use the CJ pressure or R_2'' as representing very short time frames. For the binaries containing RDX, instead of the overlap of dent of depth results (left side of Fig. 1), three separate curves are predicted with performance decreasing in the order RDX/EDD, RDX/TNT, RDX/MAN. For the ternaries containing AN (right side of Fig. 1) the

TABLE 3

Properties Predicted for Explosives Using TIGER Computer Program

TNT	RDX	AN	MAN	QMAN	EDD	ρ_{TMD}	D	P	T	Γ	Gas	C	$-E_f$	$-E_2$	$-E_7$	R_2''	R_7''
	100					1.802	8774	346	2631	2.96	33.8	6.7	-96	880	1250	1.209	1.188
20	80					1.770	8453	318	2694	2.93	32.2	9.9	-61	850	1205	1.109	1.097
40	60					1.740	8148	291	2739	2.92	30.5	13.2	-26	821	1159	1.014	1.010
*60	40					1.710	7517	253	2933	2.77	29.0	16.3	9	785	1119	0.913	0.929
*80	20					1.682	7262	231	2921	2.79	27.3	19.5	44	762	1076	0.830	0.850
*100						1.654	7001	209	2901	2.82	25.7	22.7	78	738	1032	0.750	0.772
	80		20			1.710	8505	308	2442	2.96	35.6	7.5	95	999	1356	1.063	1.056
	60		40			1.627	8247	275	2257	2.97	37.3	8.3	285	1141	1468	0.957	0.942
	40		60			1.552	7999	246	2078	2.99	39.0	9.1	476	1275	1579	0.853	0.838
	20		80			1.483	7753	220	1904	3.01	40.8	9.8	666	1410	1690	0.758	0.743
			100			1.420	7513	196	1733	3.03	42.6	10.6	857	1547	1801	0.674	0.656
	60				40	1.713	8516	305	2143	3.02	36.4	7.6	277	1162	1480	1.042	1.008
	40				60	1.672	8382	286	1923	3.06	37.7	7.5	464	1302	1591	0.964	0.922
	20				80	1.633	8242	267	1717	3.10	39.0	7.8	650	1441	1699	0.887	0.839
					100	1.595	8090	249	1526	3.14	40.3	8.1	837	1577	1805	0.812	0.756
	80	20				1.786	8832	341	2264	3.04	35.8	4.1	143	1100	1442	1.175	1.136
	60	40				1.770	8888	335	1923	3.12	37.8	1.6	381	1315	1622	1.136	1.075
	40	60				1.755	8815	316	1466	3.26	39.7	0.0	620	1473	1710	1.030	0.936
	20	80				1.740	8463	272	894	3.52	41.7	0.0	859	1524		0.796	
		100				1.725	7836	210	470	3.97	43.7	0.0	1097	.	.	--	-
40					60	1.618	7788	240	1986	3.04	34.3	14.1	534	1257	1526	0.805	0.786
		20			80	1.619	8252	260	1442	3.18	41.0	5.2	889	1647	1857	0.844	0.775
		30			70	1.632	8340	266	1398	3.21	41.3	3.8	915	1682	1898	0.860	0.785
		40			60	1.645	8429	272	1354	3.24	41.7	2.3	941	1716		0.877	
		50			50	1.657	8515	278	1312	3.27	42.0	0.9	967	1750		0.892	
		56			44	1.665	8571	282	1285	3.29	42.2	0.1	983	1770		0.902	
		60			40	1.671	8540	278	1200	3.32	42.4	0.0	993	1757		0.877	
70		30				1.675	7766	249	2255	3.00	30.9	14.3	384	1119	1403	0.846	0.835
	40	45	15			1.699	8667	304	1747	3.14	39.6	1.5	584	1461	1741	1.025	0.962
	40	30	30			1.647	8424	283	1869	3.07	39.4	4.0	548	1399	1688	0.964	0.919
	40	15	45			1.598	8203	264	1979	3.02	39.2	6.5	512	1337	1634	0.906	0.878
	40	48		12		1.677	8536	294	1781	3.10	39.3	4.5	561	1416	1695	0.986	0.931
	40	40		20		1.629	8297	273	1878	3.05	39.1	8.3	522	1344	1628	0.921	0.882
	40	30		30		1.573	8022	249	1981	3.01	38.8	12.9	473	1253	1543	0.844	0.824
	40	34			26	1.718	8685	309	1751	3.14	38.9	2.7	552	1429	1707	1.035	0.971
	40	30			30	1.712	8646	306	1773	3.13	38.7	3.2	542	1414	1693	1.026	0.965
	20	60			20	1.712	8681	297	1329	3.29	41.1	0.0	807	1615		0.952	
	20	45			35	1.691	8634	296	1507	3.21	40.5	1.4	768	1602	1844	0.970	0.981
	20	40			40	1.684	8587	292	1532	3.19	40.4	2.1	755	1584	1828	0.961	0.885
	20	24			56	1.663	8443	282	1608	3.15	39.8	4.4	713	1527	1779	0.931	0.867
40	20	40				1.710	8239	283	2035	3.05	34.4	8.1	451	1266	1556	0.958	0.924
40	40	20				1.725	8205	288	2372	2.98	32.4	10.7	212	1040	1364	0.990	0.973
40		34			26	1.661	7906	259	2433	2.96	32.2	13.6	216	1000	1311	0.894	0.890

Compositions are as described with Table 1. ρ_{TMD} = theoretical maximum densities of explosives. Chapman-Jouguet values are D = detonation velocity in meters/sec.; P = pressure in kiloatm.; T = temperature in degrees Kelvin, $\Gamma = -d(\ln P)/d(\ln V)_s$; Gas = gaseous detonation products; C = carbon solid, both in moles/kg of explosive. Energies are in cal/g with E_f = explosive formation at STP; E_2, E_7 = energy of products on isentrope from CJ point at specific volumes two and seven times, respectively, that of the undetonated explosive. R_2'' = ratio of $\rho(E_f - E_2)$ to -1454.25 which is for RDX/TNT 64/36 at ρ = 1.717. R_7'' = similar ratio (with E_7) to -2042.94. *indicates that TNT constants were used in the BKW eqn. - indicates that temperatures at those isentrope points were too low.

445

performance predictions with increase of AN content correspond to the trends observed in the depth of dent data, except for TNT/AN. For the detonation velocities of the confined small-scale test, the predicted trend as AN is increased corresponds for all except TNT/AN and RDX/AN. These exceptions are due to the predictions showing an increase in detonation velocity as the carbon in the products combines with oxygen from AN, which prediction is evidently not realized for the experimental conditions. Because of the strong diameter and confinement effects involved in composition performance in the small-scale test configuration, no effort has been made to further correlate these data (Table 1) with the predictions in Table 3.

Figure 3 provides a comparison of cylinder test data at 101.6 mm explosive diameter (Table 2) and predictions (Table 3). The predicted and experimental detonation velocities (Fig. 3, left) are of opposite slope, with the experimental velocities diverging from the predicted as the AN content is increased. This divergence may be attributed to AN not contributing significantly within the time frame of the detonation zone. The predicted increase in detonation velocity

with increase of AN content in RDX/40/MAN/AN is related, as described previously, to oxidation of carbon in the products. Experimental results for relative wall kinetic energy (Fig. 3, right) are represented by the ratios of wall velocity squared at 76 mm wall displacement ($7V_0$) whereas the predictions are represented by R_7'' (see footnote Table 3). Comparison of the experimental and predicted wall kinetic energies can only be made as to trends, not absolute values because of the different sources of the ratios (e.g. experimental involves reshocking). Further, the predicted point for RDX/AN 40/60 must be used with caution because the sevenfold volume expansion on the isentrope corresponds to a predicted temperature of $266°K$ and 613 atmospheres and the behavior of the BKW equation of state in this range is not known. Both the experimental and predicted relative wall energy for TNT 40/RDX/AN decrease as AN content increases, with the experimental line diverging from the predicted. As for the detonation velocity comparison, this behavior may be attributed to AN not contributing significantly within this composite explosive. For RDX 40/MAN/AN the experimental relative wall kinetic energy increases as AN content is decreased to 30 wt %. Using the nonabsolute
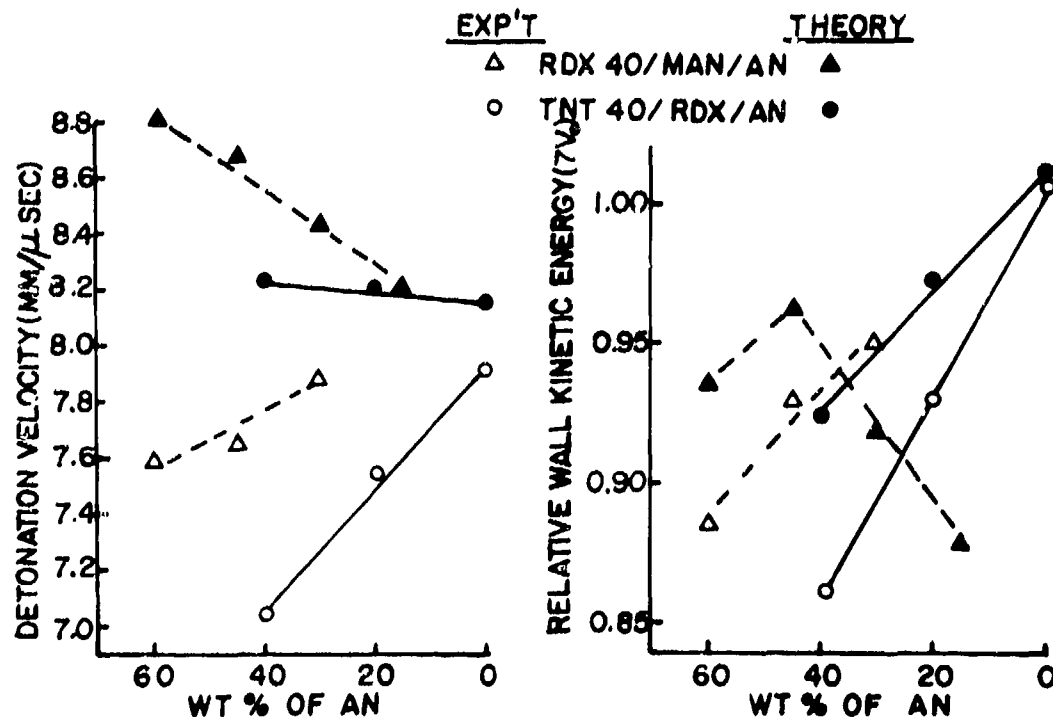
Fig. 3. Cylinder test (101.6 mm) results and ideal explosive predictions.

446

character of the ordinate scales for prediction and experiment as justification, one can imagine the curves shifted so that performance is always below prediction for ideal behavior. It follows, that as AN was decreased to 30 wt % performance improved, approaching ideal behavior. In the DISCUSSION this conclusion is given a quantitative examination. Data for less than 30 wt% AN and improved correlation between experimental and predicted measures of performance are required for further interpretation.

The effect of preparation procedures on performance was studied in connection with the small-scale tests on compositions containing AN, EDD, and RDX (3). The following were found to be key parameters: weight percent of AN, the environment provided by the balance of the explosive, and the importance to performance of AN behavior (e.g., near critical diameter). Data in Table 4 illustrate the change in dent depth as a function of composition and preparation procedure.

DISCUSSION

The results of both the confined small-scale tests and the cylinder tests have shown that performance of explosives containing AN is significantly improved when the composition also contains MAN or EDD. The analyses of the data made use of trends with changing weight percent of AN, and comparison with predictions of pressure, detonation velocity and wall energy obtained with the TIGER computer program using the BKW equation of state. For ideal explosives the ratio of experimental wall kinetic energy to that of standard explosive at sevenfold volume expansion of the products from the uninitiated state has been shown (8) to correspond to an analogous computer derived ratio, R_7'' (see Table 3). Mader (4) has shown that predicted CJ pressure is a linear function of experimental wall kinetic energy for ideal explosives. In applying these methods to non-ideal explosives the underlying assumption is that use of CJ theory and the BKW equation of state is a good approximation. The correlation of Mader also requires that the locus of the explosive

TABLE 4

Small-Scale Confined Dent Test Results as a Function of Composition Preparation Procedures*

RDX/AN/EDD	Procedure	Dents (mm)	
0/50/50	Melt into Freon	1.52	1.52
	Melt onto Plate	0.76	0.86
	Inject Freon	2.54	2.46
	Recrystallize	2.11	2.21
	Slurry	0.64	0.61
	Dry Mix	1.70	
0/30/70	Melt into Freon	2.49	2.79
	Melt onto Plate	2.72	2.74
	Recrystallize	2.64	2.49
20/40/40	Melt into Freon	3.05	3.02
	Slurry	3.23	3.30
40/30/30	Melt onto Plate	3.15	3.28
	Slurry	3.20	3.30

*Described in procedure section of this paper and in greater detail in Ref. 3.

product expansion from the CJ pressure scale with that pressure for different explosives functioning in the cylinder test configuration. The difficulty with both approaches stems from the time dependent energy release of non-ideal explosives. It is for these reasons that emphasis was placed on trends rather than absolute values for analyzing the results.

To determine whether improvements in performance are due to substitution of a superior explosive (e.g. MAN for AN) or to enhanced performance of a component (e.g. AN) an inversion procedure is proposed and applied to the cylinder test results. It is known (14, 15) that the detonation velocity and cylinder wall kinetic energy of some composite explosives may be estimated by a sum of volume-fraction weighted detonation velocities and wall kinetic energies respectively of the constituents. Thus when the experimental detonation velocity of the composite explosive and those for all but one constituent are known, one can invert this summation equation to derive an effective detonation velocity for that one constituent in that composite explosive. An analogous approach is also suggested for cylinder wall kinetic energies of non-ideal explosives. It is asserted based on the expressibility of R_7'' for ideal composite explosives, in terms of constituent contributions and on the correspondence that exists between computed and experimental wall energy ratios that this approach is as valid as the analysis techniques discussed in the

previous paragraph. Thus, the summation over volume-fraction weighted wall kinetic energies has been set equal to the experimental value for each composite explosive and the equation inverted to derive an index to the behavior of AN in that explosive. A further use of this approach is to characterize the environment in which AN functions by using the summation without the term for AN, directly or normalized to unit volume (by division by the volume fraction represented). By doing the described calculations for the compositions containing AN, one can observe the extent of enhanced participation of AN and the relationship to the environment. Results for RDX/AN/MAN and RDX/TNT/AN are in Table 5. It is seen that the AN detonation velocity and wall kinetic energy indices increase as AN decreases to 30 wt % in RDX 40/AN/MAN. Note that a constant value (magnitude is not critical to trend) has been used for MAN in the calculation. Detailed interpretation of Table 5 requires additional exploration of the approach.

The performance observed (Tables 1, 2) should have been related to the intimacy achieved in a particular cosolidification. To date, no satisfactory measure of intimacy has been found. For this reason, the approach was to use eutectics and rapid cooling of melts insofar as possible, and to use the small-scale tests to observe the effect of preparation procedure as a guide for further work.

TABLE 5

Inverse Method Indices*

WEIGHT		PERCENT		DET. VEL. INDEX		(VEL)^2 INDEX	
TNT	RDX	AN	MAN	AN	ENV	AN	ENV
40	20	40		6851	4585	2.21	1.41
40	40	20		6980	6308	2.13	2.04
	40	60		7022	3418	1.79	1.26
	40	45	15	6934	4657	2.14	1.52
	40	30	30	7381	5821	2.64	1.77

*Experimental values of detonation velocity or (wall velocity)^2 (at $7V_0$) are set equal to volume fraction weighted sum of same quantities for constituents. Equation is inverted to obtain value for AN. ENV is weighted sum in equation for balance (environment). Values used in calculation for Det Vel and for (Vel)^2 are respectively: RDX, 8774, 3.229; TNT, 7065, 1.9285; MAN, 7512, 1.6875.

448

CONCLUSIONS AND FUTURE WORK

Significantly improved performance has been achieved for composite explosives containing AN by the physical synthesis approach. This is attributed, in part, to enhanced contribution of the AN and represents a move toward ideal behavior. Results of small-scale tests on systems containing EDD/AN are sufficiently promising to justify cylinder test evaluations. Work to define a measure of the intimacy of constituents achieved by cosolidification or by other methods of physical synthesis will be pursued. The proposed approach to an index of participation of AN in a composite explosive and to characterizing the role of the environment in which the AN functions requires further study.

ACKNOWLEDGEMENTS

REFERENCES

1. J. Hershkowitz, I. Akst, "A New Approach to Improving the Performance of Non-Ideal Explosives Containing Ammonium Nitrate," Picatinny Arsenal Technical Report 4789, March 1975.

2. B. G. Craig, J. Hershkowitz, A. W. Campbell, Ray Engelke, "The Effects of Cosolidifying MAN/AN and QMAN/AN on the Performance of a Non-ideal Explosive," Los Alamos Scientific Laboratory Report LA-6585-MS, Dec 1976.

3. I. Akst, J. Hershkowitz, "Explosive Performance Modification by Cosolidification of Ammonium Nitrate with Fuels," Picatinny Arsenal Technical Report 4987, October 1976.

4. C. L. Mader. "An Equation of State for Nonideal Explosives," Los Alamos Scientific Report LA-5864, Apr 1975.

5. H. Cheung, "Kinetics of Energy Release of Heterogeneous High Explosives," Lawrence Livermore Laboratory Report UCID-15962, Dec 1971.

6. W. M. Slie, R. Stresau, "Small Scale Dent Test for Confined Charges," Naval Ordnance Laboratory Report 2422, April 1952.

7. L. J. Montesi, "Steel Dent Output of a Number of Common Explosives," Naval Ordnance Laboratory NOLTR 72-92, May 1972 (see Fig. 2).

8. J. W. Kury, H. C. Hornig, E. L. Lee, J. L. McDonnel, D. L. Ornellas, M. Finger, F. M. Strange, M. L. Wilkins, "Metal Acceleration of Chemical Explosives," Proc. Symp. Detonation, 4th, Office of Naval Research, Rept. ACR-126, pp 3-13, U.S. Govt. Printing Office, Washington, D. C. 1965.

9. J. Hershkowitz, J. Rigdon, "Evaluation by a Modified Cylinder Test of Metal Acceleration by Non-Ideal Explosives Containing Ammonium Nitrate," Picatinny Arsenal Technical Report 4611, April 1974.

10. A. Popolato, A. W. Campbell, T. Rivera, H. L. Flaugh, "Some Properties of Amatex/20K," Los Alamos Scientific Laboratory Report LA-6243-MS, March 1976.

11. A. Popolato, A. W. Campbell, L. W. Haniel, H. R. Lewis, P. G. Salgado, B. G. Craig, "Properties of Amatex/20," Los Alamos Scientific Laboratory Report LA-5516-MS, March 1974.

12. L. Penn, F. Helm, M. Finger, E. Lee, "Determination of Equation of State Parameters for Four Types of Explosive," Lawrence Livermore Laboratory Report UCRL-51892, August 1975.

13. M. Cowperthwaite, W. H. Zwisler, "Tiger Computer Program Documentation," Stanford Research Institute Projects 1182, 1281, 1397, March 1974.

14. C. L. Mader, "Theoretical Estimates of the Detonation Velocities of Explosives Containing Inert Diluents," Defense Standards Laboratories (Australia) Technical Memorandum 29, August 1969.

15. B. M. Dobratz, "Properties of Chemical Explosives and Explosive Simulants" Lawrence Livermore Laboratory UCRL-51319 Rev. 1, July 31, 1974 (see p 8-2, 8-12)

HOMOGENEOUS LIQUID EXPLOSIVES CONTAINING UREAPERCHLORATE

Shuzo Fujiwara, Masao Kusakabe, and Kazuo Shiino
National Chemical Laboratory for
Industry, Eighth Division
Nishiyawata 1-3-4, Hiratsuka City,
Kanagawa, JAPAN

Ureamonoperchlorate (UP) is remarkably soluble in water and its high concentrated aqueous solution can dissolve many kinds of organic substances readily. Some of its homogeneous mixtures with the organic substances can propagate the reaction waves, and their explosive behaviors were investigated. These detonable mixtures were generally insensitive to impact and their light emission during detonation reaction was rather weak. Mixtures with detonable substances, such as picric acid or nitromethane were very powerful explosives and showed two modes of detonation, i.e. LVD and HVD. On the other hand, mixtures with non-detonable substances such as nitrobenzene or dimethylformamide showed only LVD. This LVD in the mixture with dimethylformamide was clearly different from usual LVD observed in nitroglycerine or methylnitrate.

INTRODUCTION

It is well known that some perchlorates or their mixtures with fuels are good explosives, for instance, ammoniumperchlorate is generally used as a component of explosives or rocket propellants. Though explosive properties of these perchlorates have been studied well (1), ureamonoperchlorate (UP) is unknown.

UP is hygroscopic and highly deliquescent. This may be the reason why the substance has not been interested in and not studied as an explosive material. UP is soluble into water in a great amount and its aqueous solution is a good solvent of various kinds of organic substances. Although aqueous solution of UP has not so much detonability itself, some of its homogeneous mixtures with the organic substances can transmit detonation wave. This work has been undertaken to study the explosive behaviors of these liquid mixtures.

PREPARATION OF UP

UP was prepared by the process shown in Fig. 1 (2). Twenty-five parts (weight) of urea were added to 45 parts of aqueous hydrochloric acid (35 weight percent) and dissolved under agitation. Then aqueous solution of sodiumperchlorate (51 weight percent) was added and the mixture was stirred for about 10 minutes at 40°C and then cooled to 20°C. The precipitates which were mostly sodiumchloride were separated by filtration. The filtered solution was concentrated under the reduced pressure at a temperature below 80°C and then the precipitated sodiumchloride was filtered again. By repeating this purifying procedure, crystals of UP were obtained in a high yield from the resulted high concentrated solution.

This substance is a colorless crystal in the form of thin plate. It is a chemically stable and highly hygroscopic explosive substance which is not so dangerous
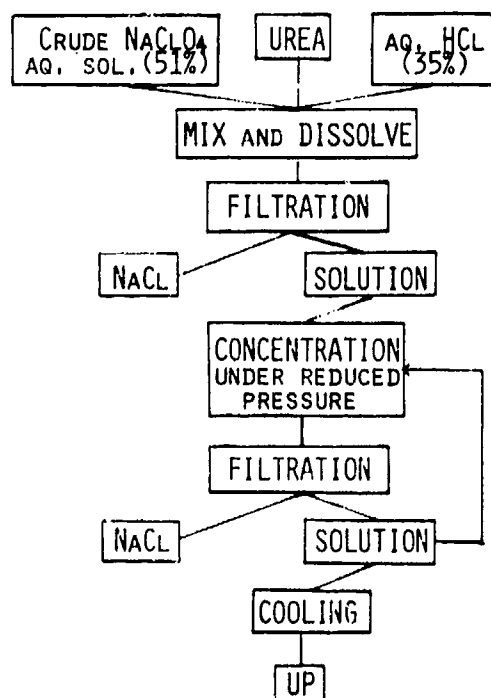
Fig. 1. Flow diagram of UP preparation.

Fig. 2. Solubility of UP in water.
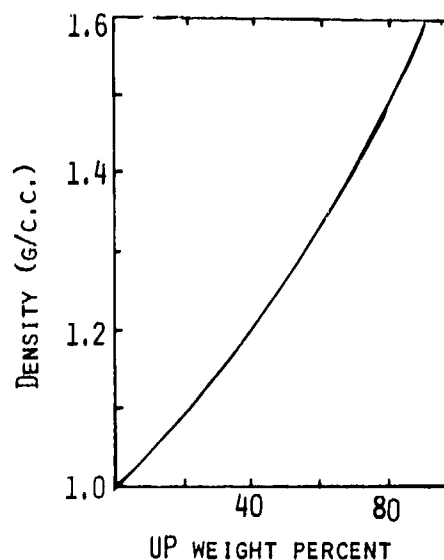
Fig. 3. Density (20°C) of aqueous solution of UP.

in handling. Properties of UP are shown in Table 1. Solubility to water against temperature and density at 20°C of its aqueous solution against UP content are shown in Fig. 2 and Fig. 3, respectively.

DETONABILITY OF UPS

Ninety weight percent aqueous solution of UP (UPS), which is almost saturated under usual ambient

TABLE 1

Properties of Ureamonoperchlorate (UP)

Molecular formula:	$CO(NH_2)_2 \cdot HClO_4$
Molecular weight:	160.52
Melting point:	83°C
Decomposition temperature:	165°C
Solubility to water (20°C):	958 in 100 water
Density of saturated aqueous solution:	1.6226 (20°C)
Oxygen balance (CO_2):	+0.099 g/g
Impact sensitivity:	0/6 (5 kg, 60 cm)

temperature (see Fig. 2), was tested for its detonability. Under our experimental conditions, no stable reaction wave was observed in this solution.

When a steel tube charge containing UPS (ϕ_{in} = 28 mm, ϕ_{out} = 36 mm, length = 250 mm) was strongly initiated with a tetryl pellet (density = 1.52 g/c.c., 10 g), the reaction wave propagation was observed only at the neighbors of the tetryl booster and then failed.

UPS was highly incombustible too. About 100 g of UPS was confined in steel tubes (ϕ_{in} = 22 mm, ϕ_{out} = 30 mm, length = 200 mm) and ignited with the thermite of 1 gramme, but no appreciable decomposition was observed.

HOMOGENEOUS MIXTURES WITH ORGANIC SUBSTANCES

Various kinds of organic substances, especially polar liquids or solids, for example, acetone, acetonitryl, nitroalkane, nitrobenzene, picric acid, dimethylform amide, etc., can be readily dissolved to UPS. Several homogeneous mixtures of UPS with these combustible substances could propagate the reaction waves. Explosive behaviors of these homogeneous liquids, i.e., critical diameter, detonation velocity, shock and impact sensitivities were investigated by various methods. Results are shown in Table 2.

Impact test with five killogramme drop hammer was done for the mixtures. About 0.1 g of the sample liquid was poured in a small shallow stainless steel cup and covered with stainless lid which had a small hole at the center. This sample assembly was placed on an anvil and tested. Although nitroglycerine (NG) showed four positive results with six trials at 5 cm

height, the mixtures listed in Table 2 showed no positive result at as high as 60 cm drop height.

Detonation velocity was measured by two methods. In the case of high velocity detonation (HVD), velocity was measured by the electronic method described in our previous report (3). In the case of low velocity detonation (LVD), however, its velocity was measured by the Dautriche's method, because of the following reasons. The detonation pressure of LVD was not high enough to cause the instantaneous electrical break-down of the ion-gap insulator. Optical measurement of the propagation velocity was also difficult for LVD of these mixtures. In general, light emitted from the reaction front of these liquids was too weak to observe it by the streak camera.

In Fig. 4, detonation velocity (HVD) and density of the mixtures of nitromethane and UPS are plotted against UPS concentration.

Sensitivity to shock wave was determined by our small scale card-gap test (4). In the method, tetryl pellet (density = 1.52 g/c.c., diameter - 20 mm, weight = 20 g) and PMMA plates were used as a donor charge and gap-materials respectively. Thick lead tubes (inner diameter = 20 mm, outer diameter = 28

TABLE 2

Explosive Properties of Typical Homogeneous Liquid Explosives Containing UP

Composition	Density (g/c.c.)	Detonation Velocity (km/sec)	Critical Initiation Pressure	Critical Diameter in brass tube
NM-UPS	se Fig. 3	HVD see Fig. 4 LVD NM/UPS = 10/90: 1.9 NM/UPS = 20/80: 2.0	HVD 60-90 kbar LVD ca. 2 kbar	
PA/UPS = 10/90	1.603 (25°C)	HVD (Pb tube, ϕ_{in} = 20 mm): 6.89, LVD: 1.9		
PA/UPS = 15/85	1.610 (25°C)	HVD (same above): 7.66		
DCB/UPS = 10/90	1.593 (25°C)	HVD (same above): 5.68		4-6 mm
NB/UPS = 10/90	1.527 (20°C)	LVD (same above): 2.2	<2 kbar	4-6 mm
DFA/UPS = 10/90	1.498 (20°C)	LVD (same above): 1.7	39-41 kbar	8-10 mm

UPS: 90 weight percent aq. solution of UP
PA: Picric acid
DCB: Dinitrochlorbenzene
NB: Nitrobenzene
DFA: Dimethylformamide
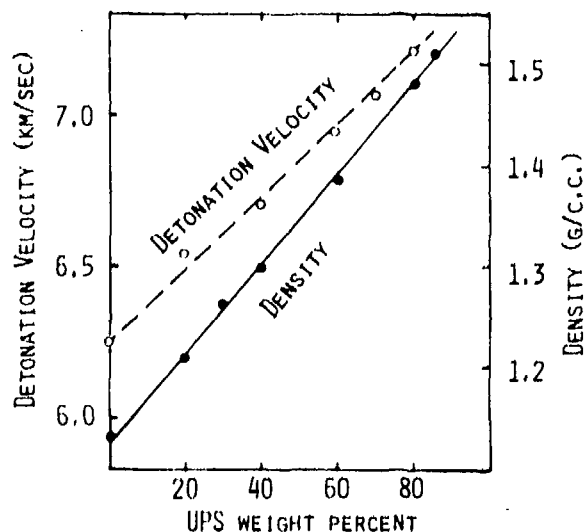
Fig. 4. Detonation velocity and density (20°C) of NM-UPS mixture.
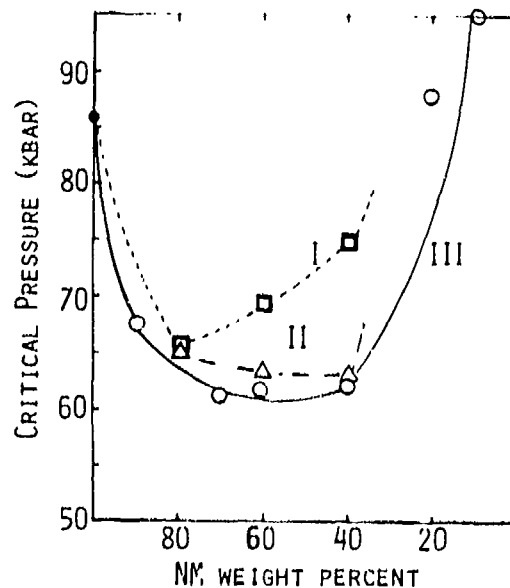

Fig. 5. Critical initiation pressures of NM-UPS-water mixtures.

I: NM-UPS (90%) mixture.
II: NM and $UPS/H_2O = 80/20$.
III: NM and $UPS/H_2O = 60/40$.

mm, length: 25-50 mm) were used as the containers for the sample liquids. From the shape of the impressed mark on the used lead witness plate, we could judge which mode of reaction had occurred, non-initiation, LVD or HVD. Shock initiation pressure was obtained from the resulted critical gap-length using gap length-pressure calibration curve, which had been determined for this system. In Fig. 5, the critical initiation pressures (for HVD) for the mixtures of nitromethane and UPS (90%) are plotted against the UPS content.

The maximum sensitivity lies at about 60 weight percent mixing ratio which is widely different from that of stoichiometric composition (CO_2 or CO).

Effect of water on the shock initiation sensitivity and propagation properties of reaction in ternary system of NM-UP-water was also examined by card gap test under the same conditions as the above mentioned. Figure 6 shows three different regions, i.e. non-initiation, HVD only, and the region both LVD and HVD can exist on the three component diagram.

DISCUSSION

UPS can be used as oxydizing agent in the explosive mixtures with fuels. Mixture with picric-acid or with nitromethane is much more powerful than nitro-

Fig. 6. Regions separated by propagation mode difference in ternary mixtures.

NI: non-initiation.
HVD: only HVD occurs.
HVD & LVD: both modes of propagation can occur.

methane itself and its brisance is almost equal to that of NG.

These explosive mixtures generally possess the following characters. At first, they are insensitive to impact as verified in the results of drop hammer test. This may be due to their poor combustibility.

Secondly, their light emission in detonation reaction is rather weak. Especially, in the case of LVD, it was impossible to record the detonation front trace with our streak camera. To the contrary, LVD of NG or methylnitrate has bright detonation front and can be recorded with our streak camera easily (5). This discrepancy may be due to low detonation temperature because of small heat of explosion or to some unknown factors.

Thirdly, UPS mixtures containing suitable amount of a detonable component such as dinitrotoluene, picric acid, or nitromethane have two modes of detonation propagation, i.e. HVD and LVD. But mixtures with a non-detonable component show only LVD at least under our experimental conditions. HVD may, however, be able to occur in the condition of further heavy confinement and/or of much larger diameter.

It is of much interest that the mixtures with liquid amides have the quite low shock sensitivity in spite of their low velocity detonation propagation. As shown in Table 2, the detonation velocity of the mixture of UPS-dimethylformamide is about 2 km/sec and it never shows HVD. Nevertheless, it has high critical initiation pressure (about 40 kbar) which can not be

explained in terms of usual concept on LVD. So it is concluded that this LVD in UPS-dimethylformamide mixture is clearly different from that in NG or methylnitrate, although further experiments will be needed to confirm this.

REFERENCES

1. T. Urbanski, "Chemistry and Technology of Explosives," Vol. 2, Pergamon Press, New York, 1965.

2. M. Kusakabe, S. Fujiwara, and K. Shiino, "Under-water Blasting Method and Explosives and Devices in therein," U.S. Patent 3,952,655, 1976

3. S. Fujiwara and M. Kusakabe, "Accurate Measurements of Detonation Velocity," *J. of Jap. Ind. Expl. Soc.*, Vol. 34, pp. 276-279, (1973).

4. S. Fujiwara et al., "Gap Test of Explosives for Under-water Blasting," *J. of Jap. Ind. Expl. Soc.*, Vol. 34, pp. 208-212, (1973).

5. M. Kusakabe and S. Fujiwara, "Explosive Behavior of Methylnitrate and its Mixtures with Liquid Diluents," Fifth Symp. (intern.) on Detonation, N.O.L., pp. 267-273, 1970.

A NEW EXPLOSIVE FOR LOW VOLTAGE
DETONATOR APPLICATIONS

W. B. Leslie, R. W. Dietzel, and J. Q. Searcy
Sandia Laboratories
Albuquerque, New Mexico 87115

A new explosive 1-(5-cyanotetrazolato)pentaammine cobalt (III) perchlorate, designated CP, is much less sensitive to accidental initiation than primary explosives such as lead azide, yet it can rapidly grow to detonation when properly confined. We have made a study of the most important parameters controlling ignition and subsequent growth to detonation of this explosive in test detonator hardware. We conclude that this new material can replace primary explosives in many hot wire detonator requirements, especially if safety considerations are of major concern.

The need for low voltage detonators made from inherently safe explosives has led to an intensive search for explosives with seemingly contradictory properties. The explosive should be so difficult to initiate that it is relatively insensitive to electrostatic discharge and impact, and yet it must be so easily initiated that the simple hot wire will suffice. It should be thermally stable enough to withstand fairly high temperature requirements, yet be reactive enough to grow to detonation rapidly. In this paper we report a new material that approaches this ideal case, and we present results from a study of certain parameters that affect functional characteristics. Hot wire detonators made with this material clearly undergo deflagration-to-detonation transition (DDT). Our interest in this material has been recently boosted by new safety requirements, and our experiments have been dictated by a parallel detonator development program.

This new material is one of a series of new explosives investigated for a number of years at Sandia Laboratories. The general chemical formula of this group of coordination compounds can be given as $[(NH_3)_4 Co^{III} XY] (ClO_4)_n$. X and Y represent other ligands. The value of n is determined by the formal electronic charge on X and Y. A large effort has been devoted to synthesizing and characterizing these compounds, but very little information has been published. Most of the work was done at Sandia Laboratories by various staff members, or at Unidynamics/Phoenix under contract to Sandia. Explosive characterization of these materials has, in general, been dictated by a particular need. Basic property studies have been neglected. For example, the CJ pressure has been determined for only one of these explosives, ICCP (isothiocyanatopentaammine cobalt III perchlorate), and the reported value of 8.9 gigapascals is suspiciously low (1). At least 30 compounds in this series have been synthesized. Since there are so many, and the chemical names are so clumsy, acronyms have been assigned to most of the compounds.

Preliminary screening of the explosive properties of these materials indicated that three seem to have a desirable combination of properties for safety and sensitivity in hot wire detonators. These are ICCP, modified CATCP (catena-μ-cyanotetraammine cobalt III perchlorate) and CP(1-5 cyanotetrazolatopentaammine cobalt III perchlorate). Modified CATCP is relatively difficult to synthesize and early development tests with it suggested a disagreeable tendency to corrode bridgewires. This compatibility problem was eventually traced to the presence of free silver ions. The bridgewire corrosion disappeared when the

explosive was synthesized by an alternate procedure (2). The explosive CP was chosen for the study reported here because it is easily synthesized, somewhat more thermally stable, and slightly less sensitive to accidental initiation than the other two candidates. Figure 1 gives the chemical structure of CP.

The CP, as supplied by Unidynamics, is a free-flowing gold or yellow-orange powder. The loose powder density is approximately 0.6 g/cm^3, and the crystal density is approximately 2.0 g/cm^3. The crystal size ranges up to approximately 500 microns. The powder can be easily pressed and forms a free standing pellet without a binder at densities greater than 1.2 g/cm^3. The explosive is slightly hygroscopic. The instantaneous autoignition temperature has been determined as 340°C, and the explosive yield is approximately equal to TNT for equal weights (3). It is more thermally stable than RDX, but somewhat less thermally stable than HNS.

In the loose powder form CP is a relatively safe explosive. In the Bureau of Mines 2 kg drop weight test, initiation occurred for one out of ten samples at 49 cm. Repetitions of this test with different lots of powder have given values as high as 65 cm. In one test, an electric match immersed in four grams of loose powder failed to give a self-sustained deflagration. A 600-pF capacitor with 500 ohms in series charged to 50 kV failed to ignite the loose powder when a spark was discharged through it (4). In fact, we have not yet initiated the loose powder by electrostatic discharge, even though a number of tests have been made.

When CP is pressed to a higher density a different situation prevails, as illustrated in Fig. 2. This curve was generated by charging a 600-pF capacitor and spark discharging it through a 500-ohm resistor and the powder in series. A specific geometry was used in which the shortest path for a spark was always 0.82 mm. The energy in the spark was somewhat arbitrarily determined by assuming 10 percent of the energy stored by the capacitor was delivered into the explosive. The magnitude of this curve is surely geometry dependent, but the general trend is clear. This material becomes increasingly sensitive to initiation by electrostatic discharge as the density increases. We also note that reliable ignition from a hot bridgewire seems to require a density near the wire of about 1.3 g/cm^3 or greater. No tests have yet been made to determine friction sensitivity (5).

Most of our experimental results were obtained using the test hardware illustrated in Fig. 3. Many variables potentially affect the performance of a detonator, and they may be interdependent. Our approach was to hold all variables constant at the values given in Fig. 3 except when a particular variable was being studied. Our data have been limited to

1-(5-cyanotetrazolato)pentaammine cobalt (III) perchlorate

Fig. 1. Chemical structure and name of the explosive CP.
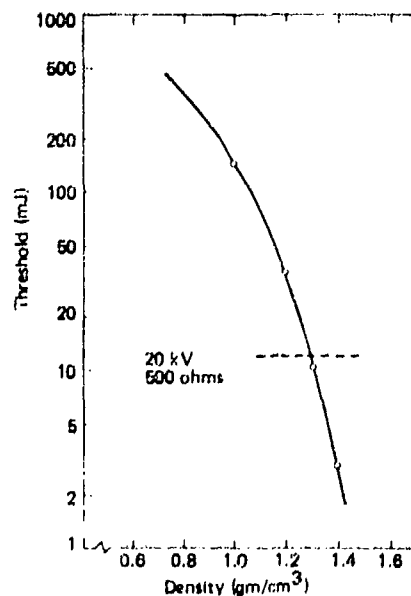
Fig. 2. Threshold values for initiation of one in ten samples at various densities.

a survey of general trends. We define an electronic function time, Te, as the time elapsed between the application of a firing pulse and the triggering of an ion probe at the output end of the explosive column. This time was determined from oscilloscope records. Most of our work was done with powder as supplied, and the density was maintained at a constant value throughout the test detonator. We have made checks with powder from different sieve fractions and find no discernable effect on Te or the output. Output was determined by measuring the depth of the dent created in a steel block.

The effect of density on functional characteristics is shown in Fig. 4 for a constant firing current of 10 A. Figure 4a gives function time vs. density and Fig. 4b gives output vs. density. The sharp drop shown by the density curve suggests that CP does not grow to detonation from a hot wire for a column of these dimensions if the density is too high. Much of the electronic function time is used in heating the bridge-wire and igniting the powder. The smooth decrease in Te on this curve probably reflects a shorter ignition due to the increasingly intimate contact between the powder and the bridgewire with increasing density, and perhaps faster deflagration rates. As a result of these curves, all further work reported here was done for a CP density of 1.4 g/cm^3.

It is interesting to speculate on a mechanism for the failure to achieve detonation at higher densities. According to Belyaev, et al., (6), DDT in a pressed explosive depends on the rate of pressure change during deflagration and the shock sensitivity of the explosive. Furthermore, above a given density, it becomes more and more difficult to shock initiate

many explosives. If the deflagration rate does not increase as fast with density as does the minimum shock initiation pressure, DDT may not occur.

The effects of changes in the containment fixture and explosive column length are given in Figs. 5 and 6. Figure 5 clearly indicates that a certain maximum wall thickness (i.e., containment) is necessary for growth to detonation in this fixture. Figure 6 suggests a column length of about 8 to 10 mm is desirable. The variation of function time with current was determined for CP and for lead azide pressed in the fixture with a pressure of 68.95 MPa. Figure 7 gives

Bridgewire is 0.033 mm by 0.51 mm
evanohm. Detonator O.D. - 0.80 cm,
I.D. - 0.190 cm, Length of Explosive
Column - 0.95 cm

Fig. 3. Test detonator hardware.

(a)

(b)
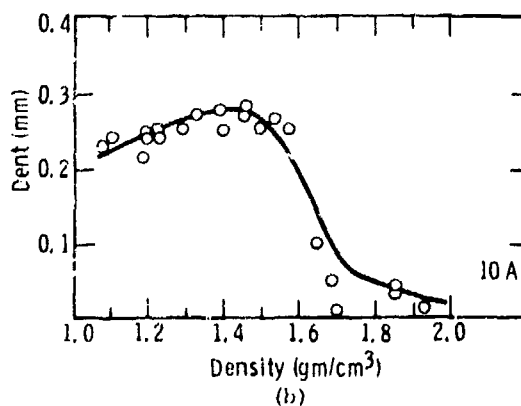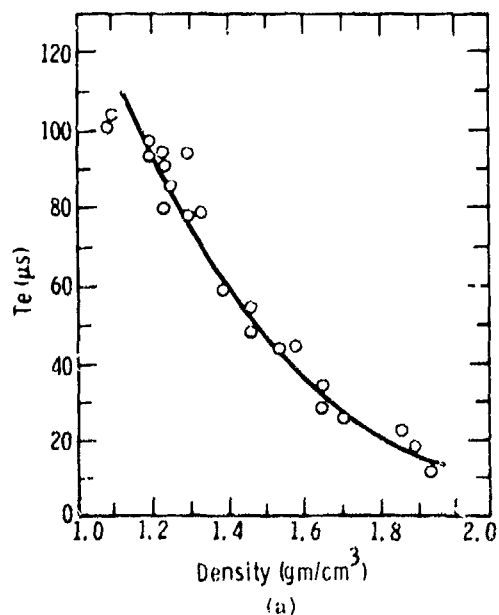
Fig. 4. The effect of density on output and function time for a 10 A firing signal.
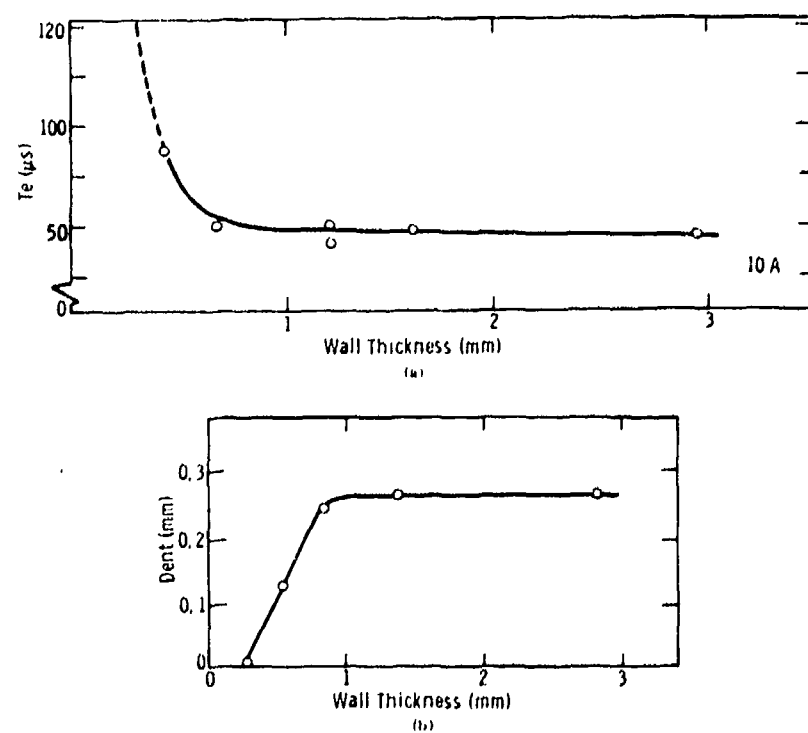
Fig. 5. The effect of wall thickness on output and function time for a 10 A firing signal.
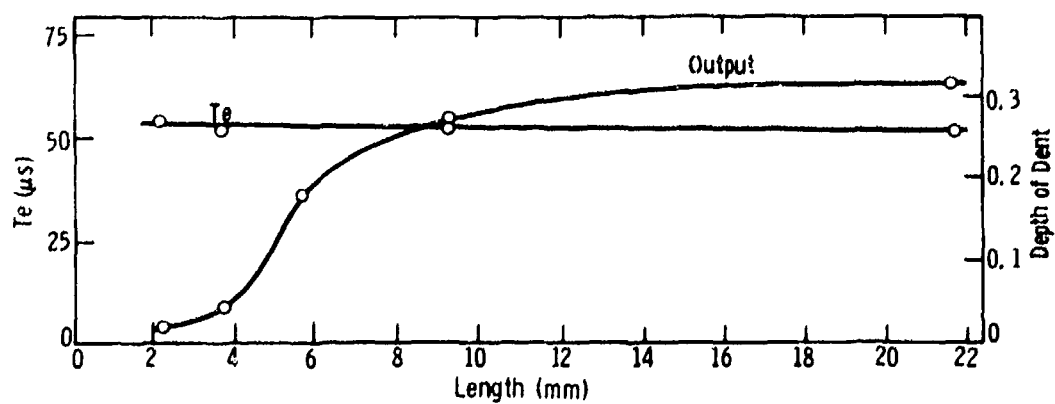
Fig. 6. The effect of column length on output and function time for a 10 A firing signal.
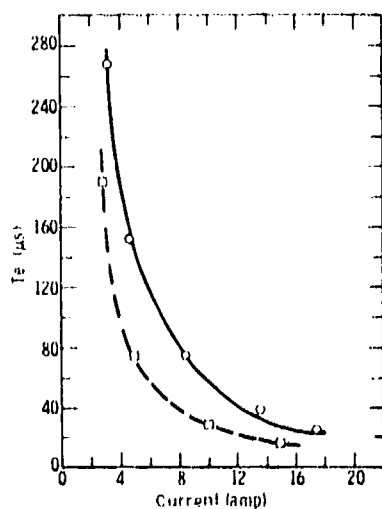
Fig. 7. The effect of different firing current on the function time of CP (open wide) and lead azide (squares).

the results. Lead azide functions about twice as fast as CP over this range.

We have also examined the effect of temperature and bridgewire diameter on T_e. Temperature has a small effect. For a 10-A firing signal, T_e varies by only about 10 percent within the temperature range of 75 to 475 K. In order to explore the minimum T_e, smaller and smaller bridgewires were used with a constant 10-A firing signal. The results are shown in Fig. 8. Extrapolation of the curve-to-zero wire diameter suggests that the ignition and subsequent growth to detonation (assuming zero time required for heating the bridgewire) is very short, perhaps less than 10 μs at a density of 1.4 g/cm^3.

Any hot wire detonator using CP would be a DDT device. With this consideration, a large standard deviation in function time for a given detonator configuration might be expected. We have fired a number of prototype units designed to function at about 75 μs and a standard deviation of 12 μs was determined.

CP is a very well behaved and interesting material. It can apparently replace more sensitive materials such as lead azide in many applications, especially if
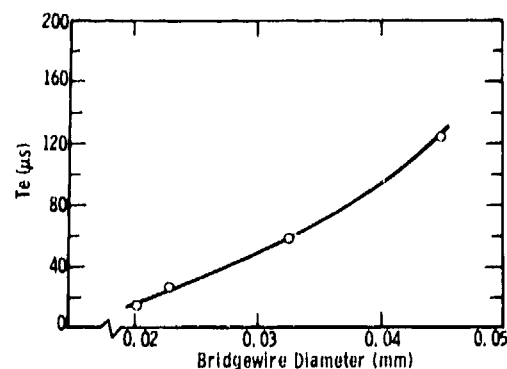
Fig. 8. The effect of bridgewire diameter on function time for a constant firing current of 10 A.

safety is of major concern. It is not clear that very small hot wire detonators can be made with it but we have made no effort to minimize size. We hope to pursue a more basic study of this material and more closely examine the DDT process and determine the Hugoniot, CJ parameters, physical properties, and chemical thermodynamic and kinetic properties.

REFERENCES

1. W. C. Thompson, *Characteristics and Initiation of the Secondary Explosive Isothiocyanatopenta-ammine Cobalt III Perchlorate*, SC-TM-66-276, Sandia Laboratories, Albuquerque, New Mexico, May 1966.

2. H. S. Schuldt, private communication, Sandia Laboratories, 1976.

3. John Fronabarger, *A New Concept In Detonators*, NCO-75, Unidynamics/Phoenix, Arizona, 1975.

4 John Fronabarger, private communication, Unidynamics, 1975.

5. Later tests indicate an increasing impact sensitivity with increasing density, and the material seems to be fairly sensitive to friction.

6. A. F. Belyaev, et al., *Transition of Combustion of Condensed Systems to Detonation*, Chapter 5, partially translated by Patricia Newman, released as SAND76-6014, SAND76-6015, SAND76-6016, and SAND76-6018, Sandia Laboratories, 1976.

BTX – A USEFUL HIGH TEMPERATURE EBW DETONATOR EXPLOSIVE*

R. H. Dinegar, L. A. Carlson, and M. D. Coburn
Los Alamos Scientific Laboratory
University of California
Los Alamos, New Mexico 87545

A high-temperature resistant exploding bridgewire detonator is described. The explosive is BTX, which shows no exotherm below the melting point 263°C, and is stable in vacuum stability tests at a temperature exposure of at least 175°C for 90 days. The energy required is higher than is used for PETN detonators. Design studies are being made.

I. INTRODUCTION

Exploding bridgewire (EBW) detonators that contain PETN have a temperature limit of 100°C or less, depending on the length of exposure and other considerations. Improved capability is obtainable with RDX, but the effective gain is small. HMX has a high melting point ($\sim$ 280°C), but above 100°C phase changes occur with important changes in crystal density. RDX and HMX have very poor vacuum stability at 150°C. HNS of high purity is heat resistant, but the energy required for its initiation by an EBW may be unacceptable for some applications. Thus, a search for a more suitable explosive has continued. This report covers a preliminary study of an explosive, BTX, which appears to make available a truly high-temperature detonator.

II. BTX EXPLOSIVE

The preparation of BTX is described by M. D. Coburn in "Nitro Derivatives of 1-Picrylbenzotriazole," J. Heterocyclic Chem **10**, p. 743 (1973).

The structure and properties of BTX are shown in Fig. 1.
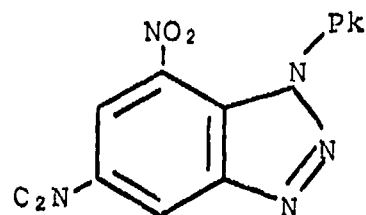
Fig. 1. (5, 7,-dinitro-1-picrylbenzotriazole).

Melting Point	263°C
DTA	Stable to melting pt.
Vacuum Stability	1.0 m³/Mg (1.0 mℓ/g) 48 h at 200°C
	1.3 m³/Mg (1.3 mℓ/g) 91 days at 175°C
Impact Sensitivity	Type 12 – 350 mm Type 12B – 330 mm
Spark Sensitivity	0.48 J, 76-μm foil
Friction Sensitivity	Neg. at all angles
Crystal Density	1.74 Mg/m³
Detonation Velocity (calc)	7170 m/s
C-J Pressure (calc)	23.4 GPa

The differential thermal analysis (DTA) for BTX used in this work is shown in Fig. 2.
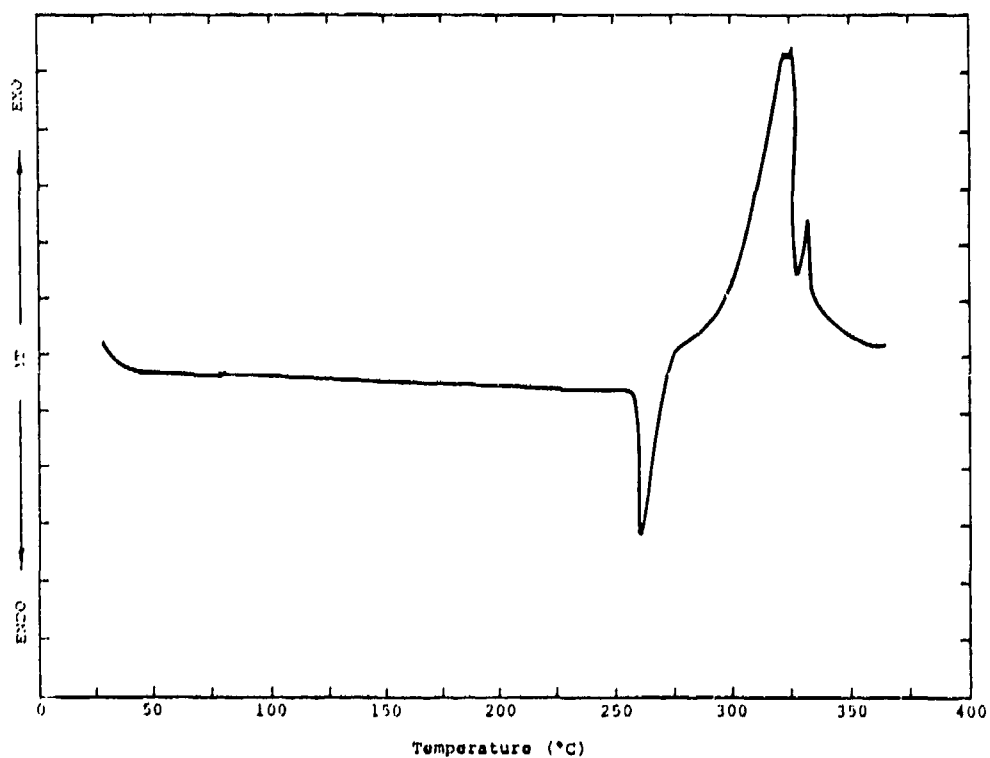
Fig. 2. BTX DTA. 20°C/min heating rate.

TABLE 1

175°C Temperature Vacuum Stability Tests (1)
Time of Exposure (days)

Material	Total Gas Evolved (m³/Mg at STP. Average of two samples.)													
	2	7	14	21	28	35	42	49	56	63	70	77	84	91
BTX	0.2	0.3	0.4	0.4	0.5	0.6	0.7	0.8	1.0	1.1	1.1	1.2	1.2	1.3
HMX	3.1	31.2												
HNS	0.2	0.4	0.5	0.6	0.7	0.8	0.8	0.9	1.0	1.1	1.1	1.2	1.2	1.2
RDX	4.2	15.1												
TATB	0.3	0.4	0.4	0.5	0.6	0.7	0.8	0.9	1.0	1.1	1.2	1.4	1.5	1.6

Vacuum stability test data at 175°C are given below in Table 1 for BTX and four other explosives.

When BTX is prepared originally it is formed in large platelet crystals of less than 100-m²/kg specific surface. BTX is soluble in acetone, but insoluble in water, and the original BTX was recrystallized by the rapid addition of water to a BTX/acetone solution.

Batches of various specific surfaces then were produced for evaluation. BTX scanning electron micrographs are shown in Fig. 3.

III. FIRING CONDITION

The firing unit used a 3-µf capacitor charged to 7 kV to initiate one detonator in the preliminary

461

1000 X
~100-m²/kg specific surface
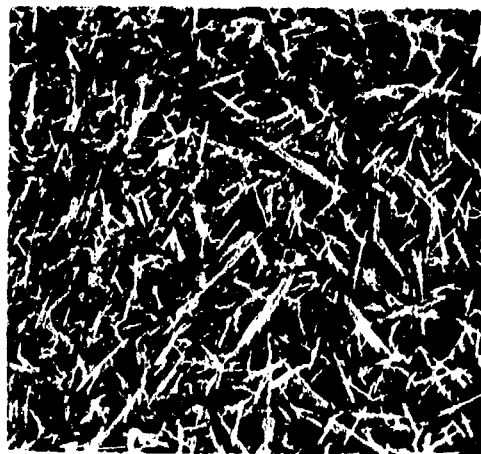
1000 X
~2200-m²/kg specific surface

Fig. 3. Scanning electron micrographs of BTX.

work. In subsequent tests the voltage was reduced, and two detonators were initiated by the same firing unit.

IV. EXPERIMENTAL DETONATOR

The work was done with SE-1 assemblies which were modified to have larger diameter bridgewires than normal. The configuration is shown in Fig. 4.

V. EBW INITIATION STUDIES

It first was determined that the BTX could be initiated by a bridgewire. An ionization pin was placed over the face of the initial pressing in place of the pellets shown in Fig. 4, and the transit time (t_T) from start of current to closure of the pin was measured.

BTX Pellets

7.6-mm diam by 2.5-mm long
1.6-Mg/m³ density
1.4-Mg/m³ density
1.2-Mg/m³ density

BTX Initial Pressing

7.6-mm diam by 6.4-mm long
Density varied

Au Bridgewire

130-µm diam
Bridgewire length varied

SE-1 Brass Sleeve, Plastic
Head, and Electrical Leads
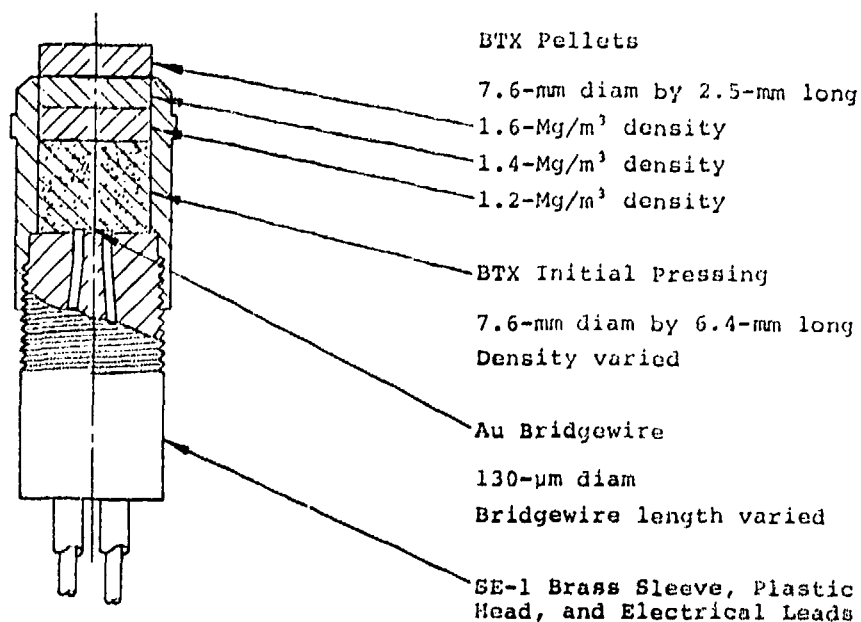
Fig. 4. Modified SE-1 detonator, BTX study.

462

With an initial pressing density of 0.90 Mg/m^3, the transit time was found to average 2.2 μs when two detonators were fired in parallel at a 7.0-kV firing voltage. For comparison, the time for PETN initial pressings loaded into identical assemblies and fired in the same way was 2.0 μs. From this it was concluded that the BTX was initiated promptly.

Most of the tests were made with a BTX specific surface of approximately 2200 m^2/kg; transit time varied slightly from batch to batch. With a 900-m^2/kg specific surface the detonator performance was poor and indicated a high threshold. With the ∿100-m^2/kg platelet crystals of the originally prepared BTX, using the EBW test condition described above, all detonators failed.

Electrical measurements were made at one test condition. The bridgewire burst current at 7.0 kV was found to be 7 kA and the burst power was 15 MW, using two detonators in parallel and a 130-μm-diam by 1-mm-long gold bridgewire.

A bridgewire length study was made which showed that the voltage threshold with a 0.5-mm-long bridge was 5.0 kV, but with a 1-mm length it was reduced to 3.0 kV. With a 1.5-mm length the initiation delay at the bridge was reduced for the firing voltages below 7.0 kV, although threshold remained at 3.0 kV. At 2.5-mm length no further improvement was seen.

VI. BOOSTER PELLET INITIATION

The ability of a BTX initial pressing to initiate a high-density pellet was studied. The initiation of a 1.60-Mg/m^3 density BTX pellet was marginal. The staged pellet density arrangement shown in Fig. 4 was found to perform acceptably in most tests; simpler designs probably can be made. Initiation delay in the 1.2-Mg/m^3 pellet was ∿0.2 μs, but was small in the other pellets.

VII. PLATE DENT

A comparison is shown in Fig. 5 of the plate dent produced in a 6-mm-thick Dural plate by a BTX detonator and a PETN detonator, both built as shown in Fig. 4. The dent from the PETN detonator is a little larger due to its higher detonation pressure (33 GPa) compared to the pressure for BTX (23.4 GPa).

VIII. HIGH-TEMPERATURE EXPOSURE

BTX powder was heated at 175°C for 50 hours, and then was loaded into SE-1 detonators. The test was done in this manner since we wanted to assess the effect on BTX alone and not that in combination with the SE-1 detonator. In addition, we do not have detonator hardware capable of withstanding high
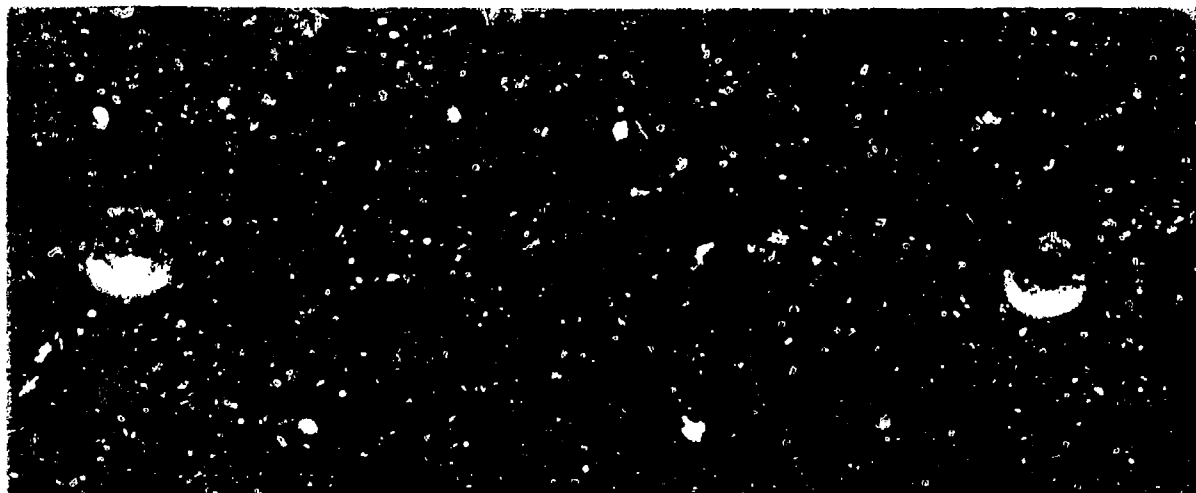
BTX Detonator   PETN Detonator

Fig. 5. Plate dent comparison.

463

temperatures. With PETN the effect of heating is nearly the same whether the powder is heated before or after loading. The test data are shown in the t_T vs voltage curves of Fig. 6. After the heat exposure the specific surface changed to 1700 m²/kg. Only a small effect was observed on detonator timing and on voltage threshold in comparison with the unheated material.

IX. DENSITY THRESHOLD

Using the firing condition that was described previously, the density threshold of BTX was determined for two test conditions: two detonators per test, or one detonator per test, at ambient temperature. The data are shown in the curves of Fig. 7. A higher initial pressing density than 0.90 Mg/m³ is feasible with BTX, depending on other design requirements.

X. CONCLUSION

It is believed that a practical EBW detonator which contains only BTX can be made for applications that require a high-temperature capability. The BTX detonator probably will require a larger, higher voltage firing unit than is required for PETN EBW

HIGH-TEMPERATURE DETONATOR STUDY

t_T vs Firing Voltage

BTX explosive. Modified SE-1 detonator, 130-μm-diam x 1-mm-long Au bridgewire. 0.90-Mg/m³ density initial pressing + electronic gap switch. Batch BTX-7. BTX heated in bulk then loaded into SE-1. TSD-4 firing unit (3 μF) + 610-mm C-cable + 460-mm L-cable + SE-1. 1-2 detonators per data point.

Fig. 6.

BTX DENSITY THRESHOLD

t_T vs Initial Pressing Density
One Detonator vs Two Detonators Per Test

Modified SE-1 detonator, initial pressing, 130-μm
-diam x 1.52-mm-long Au bridgewire. Batch BTX-8,
2200 m²/kg. TSD-4 firing unit (3 μF at 7.0 kV)
+ 610-mm C-cable + 460-mm L-cable + SE-1 + elec-
tronic gap switch, branches in parallel when two
detonators tested. t_m from nanosecond counter.
Ambient temperature. Three dets/point.

Fig. 7.

detonators. It appears that the BTX detonator itself will need to be somewhat larger than PETN detonators. We are conducting design studies to improve the configuration of detonator components and to reduce the initiation delays. Tests that use the flying plate mode also are being done since it is believed to be more efficient than the EBW mode for the less sensitive explosives.

ACKNOWLEDGMENTS

REFERENCE

1. J. F. Baytos, "High-Temperature Vacuum Thermal Stability Tests of Explosives," Los Alamos Scientific Laboratory report LA-5829-MS (January 1975).

465

PHYSICAL, STABILITY, AND SENSITIVITY PROPERTIES
OF LIQUID EXPLOSIVES*

K. Scribner, R. Elson, R. Fyfe, and J. P. Cramer
Lawrence Livermore Laboratory
University of California
Livermore, California 94550

Liquid explosives are of interest as carriers for a new class of extrudable explosives. Thirty-six liquids, most of them new, are characterized as to physical properties, stability, and sensitivity. ADDF (1, 4, 4, 10, 10, 13-hexafluoro-1, 1, 7, 7, 13, 13-hexanitro-3, 5, 9, 11-tetraoxotridecane) and the eutectic mixture of MFF and TFMFF (1, 4, 4, 7, 7-pentafluoro-1, 1, 7-trinitro-3, 5-dioxoheptane and 1, 1, 1, 4, 4, 7-hexafluoro-7, 7-dinitro-3, 5-dioxoheptane) are the most useful carrier liquids of those studied. They both are characterized by a melting point near -50°C, density of 1.65 g/cm³ or greater, excellent thermal stability, low vapor pressure, and very low sensitivity when tested on our drop hammer and by means of a new low-velocity-detonation (LVD) screening test.

INTRODUCTION

Extrudable compliant explosives can be made by mixing a crystalline explosive with an energy-contributing liquid and a gelling agent. They are of interest for several reasons:

- They are much less sensitive to impact than rigid explosives of comparable energy. With the proper selection of the crystalline explosive and the liquid carrier, compliant explosives have been made with 120% of the energy of Comp B, Grade A.
- They are simpler to fabricate and use than plastic-bonded explosives that must be pressed, machined, and assembled.
- They can have unique applications. In nuclear weapons, for example, the explosive can be stored away from the fissile material so that in case of accidental detonation, the toxic fissile material would not be scattered over the countryside.

We screened certain existing and newly synthesized liquids for use as carrier liquids for compliant explosives. This report presents some of the physical, stability, and sensitivity properties of these liquids. For simplicity of reference, we use a designator rather than the full chemical name of the liquid. These abbreviations are listed in Table 1, which also gives the chemical name, the atomic composition, and the synthesizer of each.

PHYSICAL PROPERTIES

The physical properties of the liquids are listed in Table 2. They were determined on material purified by a simple vacuum-line distillation or by thorough removal of solvent by heating on the vacuum line.

- *Purity.* Analysis for purity was done by chromatographic methods and, in several cases,

TABLE 1

Designator Identification

Designator	Chemical Name	Atomic Composition	Source
ADDF	1, 4, 4, 10, 10, 13-hexafluoro-1, 1, 7, 7, 13, 13-hexanitro-3, 5, 9, 11-tetraoxotridecane	$C_9H_8F_6O_{16}N_6$	SRI
BTFMA	1-fluoro-1, 1-dinitro-4, 4-bis(trifluoro... ... dioxohexane	$C_6H_5F_7O_6N_2$	NSWC
DFB	2, 2-difluoro-2-nitroethyl-5, 5-difluoro-2-(3' ... oro-3'-nitro-1-oxopropyl)-5, 5-dinitro-3-ox... ...nonate	$C_8H_7F_6O_{10}N_3$	NSWC
DFF	Bis(2-fluoro-2, 2-dinitroethyl)difluoroformal	$C_5H_4F_4O_{10}N_4$	SRI
DFNT	2, 2-difluoro-2-nitroethyl trifluoromethane-sulfonate	$C_3H_2F_5O_5NS$	FLUOROCHEM
DNPP	2, 2-dinitropropyl perchlorate	$C_3H_5O_8N_2Cl$	FLUOROCHEM
EDNP	Ethyl 4, 4-dinitropentanoate	$C_7H_{12}O_6N_2$	CORDOVA
FDA	Bis(2-fluoro-2, 2-dinitroethyl) acetal	$C_6H_8F_2O_{10}N_4$	NSWC
FDE	1, 1, 4-trifluoro-1, 4, 4-trinitro-3-oxobutane	$C_3H_2F_3O_7N_3$	NSWC
FDEE	1, 5-difluoro-1, 1, 5, 5-tetranitro-3-oxopentane	$C_4H_4F_2O_9N_4$	FLUOROCHEM
FDNE-A	1, 9-difluoro-1, 1, 5, 5, 9, 9-hexanitro-3, 7-dioxononane	$C_7H_8F_2O_{14}N_6$	FLUOROCHEM
FDNE-N	2-fluoro-2, 2-dinitroethyl nitrate	$C_2H_2FO_7N_3$	FLUOROCHEM
FDNE-S	Bis(2-fluoro-2, 2-dinitroethyl) sulfate	$C_4H_4F_2O_{11}N_4S$	FLUOROCHEM
FDNEP	2-fluoro-2, 2-dinitroethyl perchlorate	$C_2H_2FO_8N_2Cl$	FLUOROCHEM
FEFO	Bis(2-fluoro-2, 2-dinitroethyl) formal	$C_5H_6F_2O_{10}N_4$	ROCKETDYNE
FTE	1, 1, 1, 4-tetrafluoro-4, 4-dinitro-3-oxobutane	$C_3H_2F_4O_5N_2$	NSWC
GBFO	1, 12-difluoro-1, 1, 12, 12-tetranitro-3, 5, 8, 10-tetraoxododecane	$C_8H_{12}F_2O_{12}N_4$	ROCKETDYNE
MA	1, 1, 7-trifluoro-4-methyl-1, 7, 7-trinitro-3, 5-dioxoheptane	$C_6H_8F_3O_8N_3$	NSWC
MF	1, 1, 7-trifluoro-1, 7, 7-trinitro-3, 5-dioxoheptane	$C_5H_6F_3O_8N_3$	NSWC
MFDNB	Methyl 4-fluoro-4, 4-dinitrobutyrate	$C_5H_7FO_6N_2$	NSWC
M-FEFO	1, 7-difluoro-4-(1-oxomethyl)-1, 1, 7, 7-tetranitro-3, 5-dioxoheptane	$C_6H_8F_2O_{11}N_4$	FLUOROCHEM
MFF	1, 4, 4, 7, 7-pentafluoro-1, 1, 7-trinitro-3, 5-dioxoheptane	$C_5H_4F_5O_8N_3$	SRI
OTTO	1, 1, 1, 7, 7, 13, 13, 13-octafluoro-4, 4, 10, 10-tetranitro-2, 6, 8, 12-tetraoxotridecane	$C_9H_8F_8O_{12}N_4$	SRI
REX-20	2, 2, 2-trifluoroethyl-4-fluoro-4, 4-dinitrobutyrate	$C_6H_6F_4O_6N_2$	ROCKETDYNE
SRI-1	1, 1, 1-trifluoro-4, 4, 4-trinitro-2-oxobutane	$C_3H_2F_3O_7N_3$	SRI
SRI-2	1, 1, 1, 4-tetrafluoro-4, 4-dinitro-2-oxobutane	$C_3H_2F_4O_5N_2$	SRI

467

TABLE 1

Designator Identification – Continued

SRI-3	1, 1, 1-trifluoro-4, 4-dinitro-2-oxopentane	$C_4H_5F_3O_5N_2$	SRI
SRI-4	1, 1, 1, 7, 7, 7-hexafluoro-4, 4-dinitro-2, 6-dioxoheptane	$C_5H_4F_6O_6N_2$	SRI
SRI-5	1-fluoro-1, 1, 3, 3-tetranitro-5-oxohexane	$C_5H_7FO_9N_4$	SRI
SYEP	4, 4-Bis(difluoramino)-1, 7-difluoro-1, 1, 7, 7-tetranitro-3, 5-dioxoheptane	$C_5H_4F_6O_{10}N_4$	SRI
TDPF	1, 1, 1, 13, 13, 13-hexafluoro-4, 4, 10, 10-tetranitro-2, 6, 8, 12-tetraoxotridecane	$C_9H_{10}F_6O_{12}N_4$	SRI
TFA	1, 7-difluoro-1, 1, 7, 7-tetranitro-4-trifluoromethyl-3, 5-dioxoheptane	$C_6H_5F_5O_{10}N_4$	NSWC
TFMA	1-fluoro-1, 1-dinitro-4-trifluoromethyl-3, 5-dioxohexane	$C_5H_6F_4O_6N_2$	NSWC
TFMDA	1-fluoro-4-difluoronitromethyl-1, 1-dinitro-4-trifluoromethyl-3, 5-dioxoheptane	$C_6H_5F_6O_8N_3$	NSWC
TFMFF	1, 1, 1, 4, 4, 7-hexafluoro-7, 7-dinitro-3, 5-dioxoheptane	$C_5H_4F_6O_6N_2$	SRI
TTF	1, 1, 1-trifluoro-7, 7, 7-trinitro-3, 5-dioxoheptane	$C_5H_6F_3O_8N_3$	NSWC

it was checked by proton and/or fluorine NMR.

- *Density*. Densities were either reported by the source or determined by weighing in a micro-pipette.
- *Melting Point*. The melting point was determined by crystallizing the material in 3-mm capillaries and warming at $1°C$ per min in a stirred, clear Dewar. The reported temperature is that of last melting.
- *Boiling Point*. Boiling points, or vapor pressures, are those reported by the synthesizer of the material.
- K_f. The molal freezing-point lowering constant K_f (1) was determined using two diluents at concentrations of 2, 4, and 6 volume percent.
- *Viscosity*. Viscosities were determined using a Haake Roto Visco RV 3* at shear rates of 0.5 to 5364 per second. They are shown in Fig. 1.

The melting point of ADDF is of considerable interest. Although the material was probably never obtained in a crystalline form, a number of bits of indirect evidence strongly suggest a melting point of $-50 ± 10°C$.

The trends in these physical properties confirm the known effects of substituent groups (i.e., replacement of H by F or NF_2 lowers the melting point, raises the density, and, for F, lowers the boiling point). Also, asymmetric molecules melt at lower temperatures than symmetric ones. Many of the new liquids synthesized in the latter portion of the program were designed to take advantage of these effects.

A number of binary mixtures were examined for melting points. These are listed in Table 3.

STABILITY AND SENSITIVITY PROPERTIES

The results of the chemical reactivity test (CRT), differential thermal analysis (DTA) and drop hammer tests are listed in Table 4.

TABLE 2

Physical Properties of the Liquids

Designator	Purity (%)	Density (g/cm^3)	M.P. (°C)	B.P. (°C/Torr)	K_f
ADDF	>96	1.700	-50?	$85/10^{-6}$	—
BTFMA	—	1.59	-19	—	—
DFB	—	1.63	-2	—	—
DFF	99^+	1.670	-17.5	83/0.3	3.5
DFNT	>95	1.690	-50	48/13	—
DNP	—	1.629	-25	25/0.01	5.6
EDNP	99^+	1.28	-5	83/0.05	14
FDA	>98	1.52	-7	—	—
FDE	>97	1.650	-33	200/760	—
FDEE	>97	1.629	9.5	100/0.4	—
FDNE-A	>95	1.640	21	$100/10^{-3}$	—
FDNE-N	97	1.642	-1	62/5	—
FDNE-S	98	1.704	-14	$100/2.5 \times 10^{-2}$	—
FDNEP	—	1.704	-35	20/0.01	4
FEFO	99^+	1.607	14.5	110/0.3	~80
FTE	—	1.60	-47	150/760	—
GBFO	—	1.495	-40?	$149/5 \times 10^{-3}$	—
MA	>97	1.500	-43?	—	—
MF	>98	1.560	-22	80/0.1	—
MFDNB	95	1.400	3	75/0.2	—
M-FEFO	>97	1.540	-0?	127/0.3	—
MFF	99^+	1.680	-34	$39/6 \times 10^{-3}$	—
OTTO	98	1.665	—	81/0.01	—
REX-20	95	1.534	8	80/15	—
SRI-1	—	1.650	—	65/15	—
SRI-2	—	1.590	-63	51/35	—
SRI-3	—	1.480	-21	25/0.4	—
SRI-4	—	1.620	-38	27/1	—
SRI-5	—	1.550	~15	85/0.4	—
SYEP	97.5	1.691	-2	$110/10^{-5}$	—
TDPF	—	1.590	(1) 6.5* (2) 15	135/0.01	—
TFA	—	1.65	-1	—	—
TFMA	—	1.53	-17	—	—
TFMDA	—	1.65	-11	—	—
TFMFF	99^+	1.620	-36	$21/6 \times 10^{-3}$	—
TTF	—	1.54	-14	—	—

*Appeared to exist in two modifications.

CRT. In CRT (2), a 0.25-g sample is heated at 393 K (120°C) for 22 h in an atmosphere of He. A two-stage chromatography unit is used to measure the volumes of $N_2 + O_2$, NO + CO, N_2O and CO_2 evolved.

DTA. The DTA compares the temperature of the (10- to 20-mg) test sample to that of a similar reference sample while both are being heated in the same environment at 10°C/min. Differences in

temperature reflect heat absorption or evolution by the test sample.

Drop Hammer. Our drop hammer is an ERL-type impact machine using a 2.5-kg weight. A series of drops are made from different heights, and a go or no-go criterion is based on an arbitrary sound level produced on impact. The result of the test is summarized as H_{50}, the height in cm at which the probability of explosion is 50%.

As has been noted by others, fluorodinitro and difluoronitro groups are generally more thermally stable than trinitro, difluoramino, or nitrate groups, and formals and acetals are more stable than ethers and esters. The drop hammer, although considered only qualitative, did show gross differences similar to the results of the low-velocity detonation (LVD) test. It should be noted that the two perchlorates tested were extremely sensitive, but that all other liquids tested were less sensitive than FEFO, a plasticizer used at the Lawrence Livermore Laboratory and elsewhere.
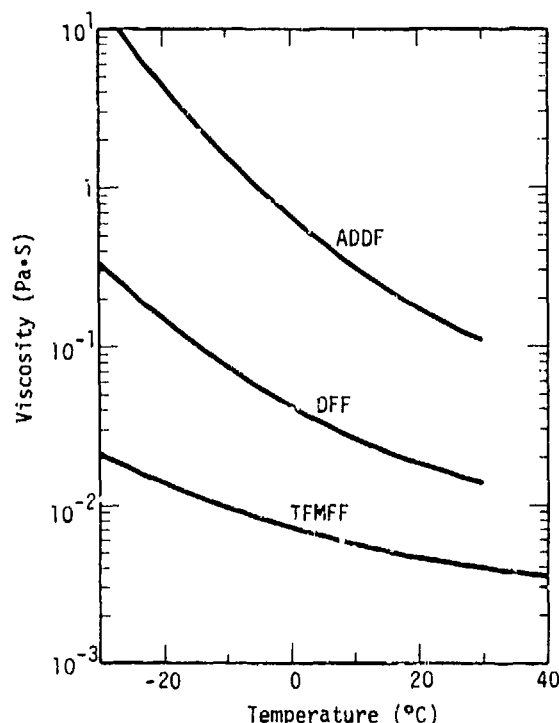
Fig. 1. Viscosity as a function of temperature of three liquid high explosives.

LOW-VELOCITY DETONATION: A SCREENING TEST (3)

We initiated the compliant-explosives program using FEFO and EDNP as carrier liquids. During the processing, particularly with FEFO, we noticed thin films of the liquid carrier forming on the processing equipment. We became concerned about safety, since nearly all liquid HE's can undergo LVD in thin films. None of the available screening tests for sensitivity to LVD were definitive enough for our purposes, so we developed a new test based on the tapered-thickness-film work of Ribovich (4). We chose to use a variable-output donor system with near

TABLE 3

Melting Point of Binary Mixtures

Component A	Mole % A	Component B	M.P. (°C)	Comments
DFF	53	FDA	-29	Eutectic
FEFO	25	FDA	-15	Eutectic
FEFO	~14	DFF	-23	Eutectic
FEFO	~82	DFF	-25	Eutectic
FEFO	–	EDNP	-24	Lowest melting composition
DFF	–	EDNP	-22	Lowest melting composition
FDNEP	~50	DNPP	-50	Eutectic?
MFF	~50	TFMFF	-53	Eutectic?

470

TABLE 4

Stability Properties of Liquids

Designator	CRT, (cm^3)					DTA, 1st exotherm		
	$N_2 + O_2$	NO + CO	N_2O	CO_2	Total	Starts (°C)	Max (°C)	H_{50} (cm)
ADDF	0.013	0.019	0.003	0.017	0.052	221	224	158
BTFMA	—	—	—	—	—	—	—	—
DFB	—	—	—	—	—	—	—	—
DFF	0.01	0.02	0.002	0.012	0.044	224	260	⩾177
DFNT	0.006	0.008	0.	0.009	0.023	none	none	⩾177
DNPP	0.02	0.39	0.09	0.50	1.00	160	200	<3.2
EDNP	0.006	0.021	0.004	0.009	0.04	165	200	⩾177
FDA	—	—	—	—	—	—	—	—
FDE	0.027	0.14	0.01	0.12	0.30	—	—	—
FDEE	0.06	0.27	0.08	0.20	0.61	150	160	~75
FDNE-A	0.048	0.123	0.033	0.096	0.30	175	268	~158
FDNE-N	—	—	—	—	—	—	—	⩾100
FDNE-S	0.021	0.075	0.015	0.022	0.130	208	226	~160
FDNEP	0.01	0.06	0.01	0.67	0.75	165	180	<2.0
FEFO	0.006	0.015	0.002	0.012	0.035	105	115	28
FTE	—	—	—	—	—	—	—	—
GBFO	0.03	0.14	0.02	0.11	0.30	144	165	⩾110
MA	—	—	—	—	—	—	—	—
MF	0.005	0.026	0.002	0.011	0.044	none	none	⩾177
MFDNB	0.021	0.070	0.010	0.049	0.150	none	none	⩾177
M-FEFO	—	—	—	—	—	202	228	~110
MFF	0.008	0.034	0.007	0.033	0.082	none	none	⩾177
OTTO	0.010	0.015	0.002	0.015	0.042	214	243	⩾177
REX-20	0.014	0.060	0.007	0.034	0.115	none	none	⩾177
SRI-1	0.37	0.96	0.53	1.25	3.11	none	none	⩾177
SRI-2	0.19	1.00	0.19	1.03	2.41	none	none	⩾177
SRI-3	—	—	—	—	—	none	none	⩾177
SRI-4	0.04	0.019	<0.001	0.028	0.087	none	none	⩾177
SRI-5	—	—	—	—	—	124	150	⩾177
SYEP	0.43	0.75	0.052	0.034	1.27	157	245	⩾141
TDPF	0.012	0.042	0.006	0.029	0.089	—	—	—
TFA	—	—	—	—	—	—	—	—
TFMA	—	—	—	—	—	—	—	—
TFMDA	—	—	—	—	—	—	—	—
TFMFF	0.010	0.038	0.010	0.033	0.091	none	none	⩾177
TTF	0.2	0.7	0.1	0.5	1.5	—	—	—

zero attenuation, whereas Ribovich used a constant donor with variable attenuation.

Six liquids of potential interest as carriers were tested along with nitroglycerine, which was used as a reference. The results are listed in Table 5. The pressures shown are those in the attenuator at the liquid-attenuator interface. W is the weight percent PETN in the donor pellet (defined later); the last two columns indicate whether HVD or LVD occurred in a

471

TABLE 5

Results of the LVD Screening Test

Liquid	d-max (mm)	W (wt%)	P (GPa)	HVD	LVD	Threshold
NG	1.6	20	4.9	Yes	Yes	
FEFO	1.6	30	6.5	No	No	
		40	8.1	No	No	
		45	8.9	No	Yes	LVD
		50	9.8	No	Yes	
		55	10.6	No	Yes	
		60	11.4	$-^a$	Yes	
		75	13.8	$-^a$	Yes	
		90	16.3	$-^a$	Yes	
		95	17.1	Yes	Yes	HVD
		100	17.9	Yes	No	
DFF	1.6	100	17.9	No	No	
	3.2	50	9.8	No	No	
		60	11.4	No	No	
		65	12.2	No	No	
		70	13.0	$-^a$	No	
		75	13.8	$-^a$	No	
		85	15.5	$-^a$	$-^b$	
		90	16.3	$-^a$	Yes	LVD
		95	17.1	$-^a$	$-^b$	
		100	17.9	Yes	No	HVD
ADDF	1.6	100	17.9	No	No	
	3.2	70	13.0	No	No	
		80	14.6	No	No	
		90	16.3	No	No	
		100	17.9	No	No	
MFF	1.6	100	17.9	No	No	
	3.2	100	17.9	No	No	
TFMFF	1.6	100	17.9	No	No	
	3.2	100	17.9	No	No	
50/50 Eutectic of MFF/ TFMFF	3.2	100	17.9	No	No	

[a]HVD ignited then quenched without ever spreading the full width of the shot tray. See Fig. 3.
[b]Inconclusive evidence.

particular test: d-max is the liquid thickness at the donor-liquid interface.

Table 6 lists the minimum liquid film thickness below which HVD or LVD failed to propagate.

THE TEST ARRANGEMENT AND PROCEDURE

The base for our shot tray was a flat 6061-T6 aluminum alloy plate, 12.7 mm thick, 50.8 mm wide, and 380 mm long. Polymethylmethacrylate (PMMA)

472

TABLE 6

Detonation Failure Thickness

Liquid	HVD (mm)	LVD (mm)
NG	0.6	0.0
FEFO	0.9	0.0
DEF	2.8	0.2

was used on the sides and a 0.5-mm thick piece of epoxy was fixed to one end to confine the liquid on the plate. A PMMA fixture was used to align the detonator-booster assembly on the closed end of the plate with its center on the liquid-aluminum interface (Fig. 2).

The shot tray was leveled on the table and then shimmed so that the open end was elevated either 1.6 or 3.2 mm. Liquid was added to form a long thin wedge tapering from either 1.6 or 3.2 mm at the initiator end to zero thickness 305 mm along the plate. The aluminum base became a witness plate that clearly showed the various reactions that occur during the test.

Our donor system consisted of an exploding bridgewire detonator filled with low-density PETN ($\rho = 0.95$ g/cm^3), a booster pellet 12.7 mm in diameter by 12.7 mm long, and a 0.5-mm epoxy attenuator. The booster pellets consisted of blends of PETN and pentaerythritol pressed to $90.0 \pm 0.5\%$ of their theoretical maximum density. The PETN concentration ranged from 20 to 100 wt% in 5% increments, giving us a variable output donor. Lower concentrations of PETN could not be made to detonate reliably.

The pressure pulse of the donors was characterized by using π-type manganin gages. The active manganin element was 3.2 mm long, and it was potted behind 0.50 mm of epoxy. As described above, this same thickness was used for the attenuator. The pressure observed via the manganin gage was the pressure at the epoxy side of the attenuator-liquid interface as the donor shock passed during the experiment.

A series of shots were fired with each liquid to be tested. After each shot, we examined the witness

plate for HVD, LVD, transitions, and failure. We selected the pressure of each successive booster pellet after examining the results of the previous shot. Where HVD occurred, the witness plate surface was depressed about 1 mm. LVD was revealed by a fine pitting on the surface. Areas where no reaction occurred remained smooth (Fig. 3).

Two anomalies were observed on examination of some witness plates. In one, DFF detonated HVD with a 17.9-GPa input, but it did not convert to LVD, even though LVD was observed with a 16.3-GPa input. In 11 of the tests with FEFO, DFF, and ADDF, a partial HVD was initiated. It projected about 40 mm
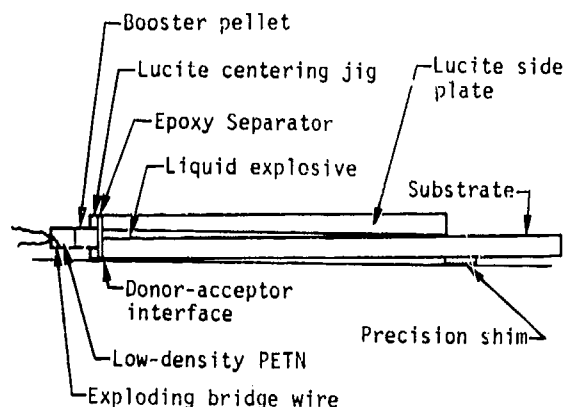
Fig. 2. *Schematic of the shot arrangement.*
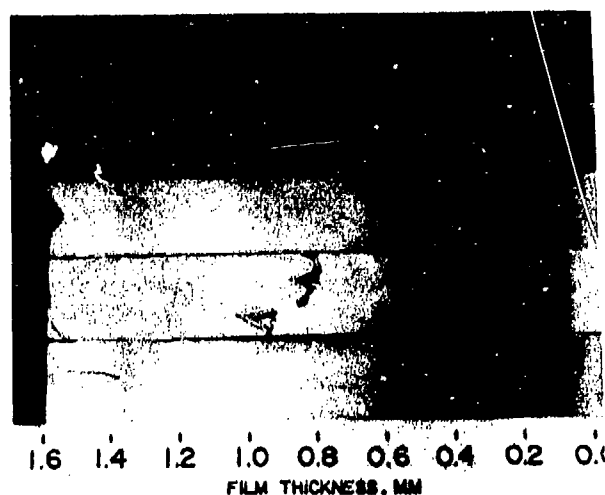
Fig. 3. *Witness plates demonstrating: top - donor only, no initiation; middle - HVD, LVD, and transitions; bottom - partial HVD as the only response.*

473

in a flame shape directly in line with the booster but did not spread the full width of the tray.

agent. Several of these had most of the desirable properties.

DISCUSSION AND CONCLUSIONS

Our compliant explosive program had, as its prime objective, the development of an explosive that would be comparable in its performance to those used in nuclear weapons, but that would remain stable and extrudable to at least $-30°C$ (and preferably to $-54°C$). To accomplish this, we needed a liquid carrier with some unique characteristics:

- Energy/density comparable to TNT.
- Melting point below $-30°C$.
- Excellent thermal stability in the CRT (< 0.5 cm^3 total).
- Lower sensitivity than main charge explosives currently in use in nuclear weapons (H_{50} values should be $\geqslant 50$ cm and less sensitive to LVD than FEFO).
- Compatibility for twenty years or more with all materials that the explosive would contact.
- Low viscosity, particularly at low temperature.
- Low vapor pressure at ambient temperature.

Two liquid systems were developed that are prime candidates as a carrier fluid for a compliant explosive. They are ADDF and the eutectic mixture of MFF and TEMFF. Each liquid nearly fits the requirements, but has one defect according to the above list. ADDF is too viscous at low temperature, and the eutectic has a slightly higher vapor pressure than is desirable. It is possible that the ideal liquid carrier could be a multicomponent mixture of some of these new liquids.

Stable, high-energy, extrudable explosives have been prepared with several of the most attractive liquids at 65 to 70 vol.% HMX with 1 to 2% gelling

REFERENCES

1. The molal freezing-point lowering constant is defined as

$$K_f = \frac{\Delta T}{m} ,$$

where ΔT is the change in melting point in $°C$ and m is the moles of solute added per 1000 g of solvent.

2. J. Frazer and K. Ernst, "Chemical Reactivity Testing of Explosives," Lawrence Livermore Laboratory, Rept. UCRL-7438, 1963.

3. Some of the material in this report was submitted to Explosivstoffe. R. R. Fyfe, "A Screening Test for Low Velocity Detonation in Thin Films of Liquid Explosives," Lawrence Livermore Laboratory, Rept. UCRL-75120, Aug. 1973.

4. J. Ribovich, "A Wedge Technique for Evaluation of Detonation Hazards of Liquid Explosives," Annals of the New York Academy of Sciences, Vol. 152, Art. 1, pp. 766-772, (1968).

Session VIII
EXPLOSIVELY DRIVEN SHOCKS IN INERT MEDIA

Chairmen: Prof. G. Duval
                Washington State University
            M. Wilkens
                Lawrence Livermore Laboratory

DYNAMIC DETECTION OF THE ONSET OF SPALLING
IN STAINLESS STEEL ON COMP. B

C. P. M. Smith, G. Eden, and B. D. Lambourn
Atomic Weapons Research Establishment,
AWRE, Aldermaston, Berks, England

A simple experimental method is described for determining whether spalling has occurred in a plate in contact with an explosive charge. The total reflection method has been used to determine the time interval between the arrival of the first shock and the next main wave at the plate free surface. For thin plates the time interval is the plate reverberation and increases nearly linearly with plate thickness. Above a critical plate thickness, the time interval exceeds the corresponding non-spalling value by a successively greater amount, and the second wave is the shock from the recollision of the spalled surfaces.

Critical thicknesses of stainless steel plates in contact with 25.4-, 50.8- and 76.2-mm-thick Composition B charges are respectively 2.8, 3.5, and 4.4 mm.

The experiments have been analysed using the 1D hydro-code RICSHAW. Best fits to the experimental time intervals give spall strength of 91 kb, 64 kb and 56 kb for the three Composition B thicknesses.

1. INTRODUCTION

When a plane detonation wave in a finite thickness of explosive is incident on the rear surface of a metal plate, the velocity of the front (free surface) of the plate rises in a series of steps as the plate oscillates in a succession of reverberations. If the plate is strong and cohesive, the amplitude of each step is related to the relative shock impedances of the plate and the detonation products. The time interval between velocity jumps depends on the wave velocities in the plate. Between these accelerations, the free surface decelerates steadily under the influence of the Taylor wave transmitted into the plate from the explosive.

The thickness of charge determines the steepness of the Taylor rarefaction following the initial shock. This controls stress rates and stress gradients in the plate after the shock is reflected at the free surface.

As the rarefaction returns through the plate, down the ramp of the Taylor wave, the maximum tension in the plate increases. This is relieved by its reflection as a compression at the rear surface of the plate. Hence, for a given charge thickness, the maximum tension in the plate is governed by its own thickness.

For a thin plate the time interval Δt between the first two accelerations (i.e. the first shock and its reflection arriving at the free surface) may be measured. Time Δt increases linearly (or very nearly so) with x, the plate thickness, provided the reflected rarefaction and compression travel in a continuous medium. If the plate material parts under the tension in the first reverberation, then the x, Δt point departs from the original cohesive line, since the shock due to recollision of the parent plate and spall arrive progressively later, as x increases. This is due to the extra time taken for the parent to be accelerated by the detonation products and close the gap. The magnitude of the recollision-shock is similar to a normal reverberation and its arrival is easily measured.

The change in the x, Δt curve provides a purely experimental method of determining the geometry at which spalling starts.

A number of such experiments have been fired using Comp. B and stainless steel EN58B (18 Cr: 8 Ni) and the x, Δt data has been collected, to demonstrate how this method may be used to determine the onset of spalling. This 18/8 steel is one of the few iron alloys which show negligible phase transition effects near 130 kb.

Some earlier experiments in the series were compared with calculations by Lambourn and Hartley (Refs. 1,2) using a characteristics code NIP, and a finite difference code. It was shown that, based on the delay in the arrival of the main reverberation, the critical thickness of steel plate which just spalled was 3.0 mm for a 50.8 mm thick Composition B charge, corresponding to a spall strength of about 65 kb. However the spall thickness of a 12.7 mm steel plate driven by a 76.2 mm Comp. B charge determined by flash radiography seemed to correspond to a spall strength of ~53 kb. This difference in spall strength led to additional experiments on various thicknesses of explosive charge.

2. EXPERIMENTAL METHOD

A standard Baratol/Comp. B plane wave lens, 127 mm dia, was used to initiate 127 mm dia Comp. B cylinders of lengths 25.4 mm, 50.8 mm, or 76.2 mm. The results of many experiments using this system have demonstrated that the shock wave transmitted into an inert plate has axial symmetry and is plane within 0.5 mm over a 50 mm radius. Care was taken to ensure the flatness of the steel plates, which had a ground surface finish of better than 0.25 μm and were plane and parallel within 25 μm over the area used.

The thicknesses of stainless steel plates placed on the Comp. B cylinder gave ratios of plate thickness/ charge thickness in the range 0.02 to 0.20. To give a little data on thin charge geometry, two additional shots were fired in which the explosive lens initiated a 50.8 mm cylinder of Comp. B driving a plane shock into a 3.35 mm EN58B plate. This shock initiated a 10 mm thickness of Comp. B on which a test plate was placed.

Free surface velocity measurements of the early motion of each metal plate were made using a Barr and Stroud S4 str a': camera and the inclined block

total reflection method, as described in Ref. 2. In many experiments two independent traces were obtained by using two parallel slits in the streak camera focal plane. Velocities were obtained from the resulting trace (see e.g. Figs. 4 and 5 of Ref. 2) by measuring at least 100 co-ordinate points on each streak camera record. A computer programme was used to scale the values to give true distance versus time points and to perform least squares regressions to fit linear or quadratic curves to the parts of the trace showing steady velocities or accelerations.

Two types of analysis were used, one (a) in which the whole of each deceleration phase is fitted with a single quadratic curve, and the other (b) in which a chosen number of points 1 to N are selected at the start of the trace, fitted analytically and differentiated to give a velocity at their mid-value. The points 1 to 5 are then discarded and the points (N+1) to (N+6) are taken into the regression to give a velocity at the new mid-value. The degree of smoothing which is introduced by this process is therefore controlled by the choice of N. Both types of analysis are shown applied to the same experiment in Fig. 9 in which the full line is the result of the first type, and the individual points were obtained from the second type, taking N = 10.

3. EXPERIMENTAL RESULTS

The way i   iich the measured value of Δt begins to increase disproportionately when the relative plate thickness R rises above a certain critical value is shown in Fig. 1 for 50.8 mm charges. Here some of the experimental results are compared with calculations in which the plate is assumed to be infinitely strong.

Results of all the experiments are summarised in Table 1, in which

L = charge thickness
x = plate thickness
R = the ratio of (plate thickness)/(charge thickness)
Δt = the time interval between first motion of the steel free surface and the 50% velocity rise caused by the arrival of either a whole plate reverberation or the parent recollision shock, i.e. the next major acceleration.

478

TABLE 1

Shot No.	L (mm)	x (mm)	R	$\Delta t_{(EXPT)}$ (μs)	Duration (μs)	$\Delta t_{(CALC)}$ (μs)	Duration (μs)
C82	76.2	1.52	0.020	0.514	0.05(5)		
				0.539			
C93		2.03	0.0267	0.735	0.13		
				0.745	0.13		
81		3.05	0.040	1.154	0.16	1.17	0.11
				1.160			
C83		3.81	0.050	1.512	0.12	} 1.47	0.14
				1.505	0.17		
C84		4.57	0.060	1.890	0.11		
				1.905			
80		5.10	0.067	2.25	~0.4		
				2.29	~0.4		
C85		6.10	0.080	2.674	0.28		
				2.675	0.24		
C90		8.46	0.111	4.9	~0.4		
				4.7			
64A	50.8	1.98	0.0390	0.698	0.14	} 0.78	0.074
				0.732	0.10		
64		2.06	0.0405	0.753	0.15		
66		3.17	0.0625	1.28	0.22		
67		3.38	0.0665	1.338	0.16		
68		3.63	0.0715	1.497	0.06		
63		3.90	0.0767	1.722	0.03		
63A		3.91	0.077	1.630	0.04		
				1.600			
62		5.03	0.099	2.535	0.2	2.45	
60		6.35	0.125	>3.67			
C86	25.4	1.02	0.040	0.390	0.04	0.39	0.037
				0.393	0.03		
83		1.63	0.064	0.565	0.06		
				0.607	0.08		
C87		2.03	0.080	0.800	0.02	0.81	0.075
82		2.54	0.100	1.086	0.12	} 1.03	0.095
				1.095	0.08		
C88		3.05	0.120	1.46	0.10		
				1.38	0.08		
C89A		3.78	0.149	2.17	0.16		
61		5.00	0.197	3.36	0.14		
85	10.0	0.84	0.084	0.336	0.028		
				0.341	0.032		
84		1.68	0.168	0.675	0.06		
				0.675			
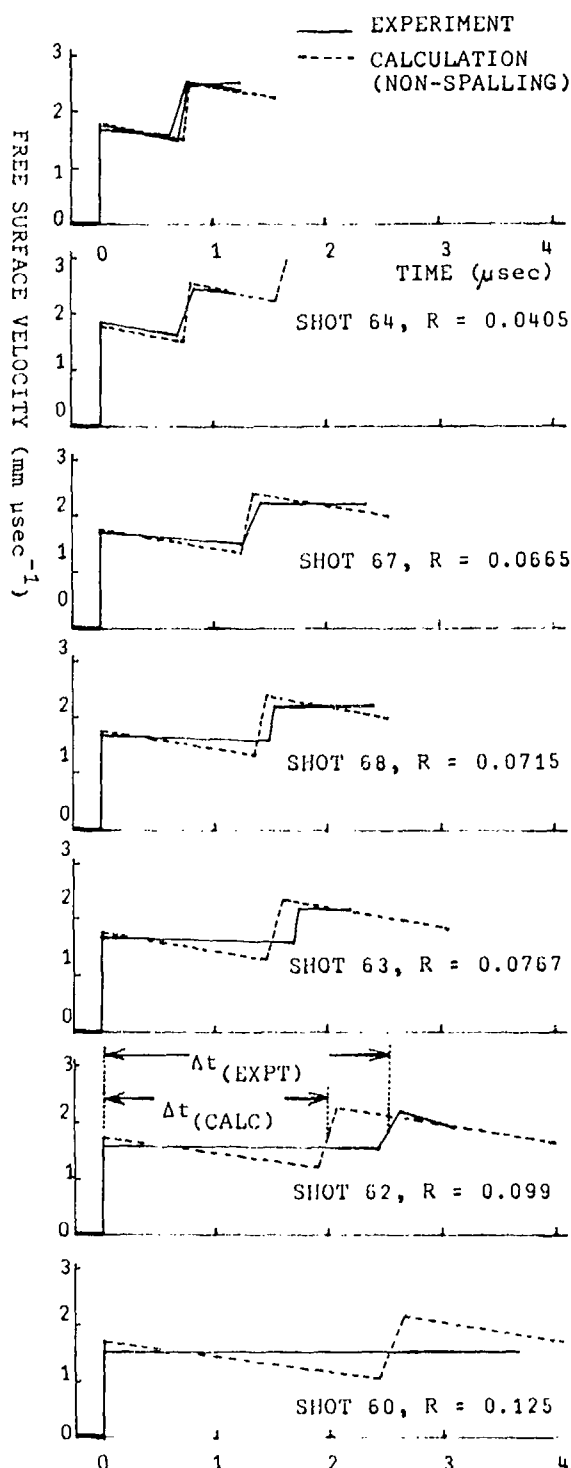
Fig. 1. Disproportionate rise of $(\Delta t)_{EXPT}$ with ratio R for L = 50.8 mm.

Duration of the major acceleration is also shown in Table 1 and is normally about 0.1. Δt, and repeatability of the time to 50% velocity rise is usually within 0.1 μs.

The Δt vs. x plot for one charge thickness (Fig. 2) shows the deviation of the experimental points from the nearly linear non-spalling curve.

The point of deviation, i.e. onset of spalling, does not scale with charge thickness, but since non-spalling results may be scaled (approximately), data from shots having short charge lengths (in wh   apparent strength of the plate is high) may be use   to extend the non-spalling 'line' beyond the point of deviation for a greater charge length, as shown in Fig. 2.

This provides a purely experimental method of defining the geometry on which spalling starts in a material when a given triangular pulse reflects at its free surface. But unless something is known about the form of curve on which the deviating points lie, then a large number of shots would be needed to locate accurately the point of deviation. To make this assessment, and to make estimates of spall strength, the experimental systems were computed, using code RICSHAW.

4. COMPARISON OF THE EXPERIMENTS WITH COMPUTATION

4.1. Method of Calculation

Lambourn and Hartley (1) used a one-dimensional method of characteristics code NIP to analyse some of the earlier experiments. NIP was used to indicate peak tension and hence spall strength at the spall plane, but it was necessary to use a finite difference code to calculate the motion subsequent to spalling.

NIP was superceded by a more sophisticated code, RICSHAW, which was presented at the 5th Symposium (3) and is very briefly outlined in another paper in this symposium (4). Essentially RICSHAW is a 1D unsteady compressible fluid flow code which can deal with multiple materials with a wide variety of equations of state. All shock waves are treated as discontinuities; and because they are characteristics, the edges of rarefaction and compression waves are marked as wave boun.'aries and followed. As arranged at present, spalling must occur at an interface

already in the calculation. It is therefore usually necessary to carry out two calculations, one without spalling, to determine the position of the spall plane, and then one with spalling included. Any plausible spalling criterion can be used, but, in fact, in the calculations described here it was assumed that spalling occurred when the particle at the chosen spall plane first exceeded a chosen critical tension.

The edge of the Taylor wave following the detonation wave in the explosive was defined at a pressure of 149 kb, corresponding to the pressure arising at the interaction of the Baratol in the plane wave lens with the Composition B. In some of the calculations it was necessary to include the Baratol because the flow in the steel plate was affected by its Taylor wave.

The equation of state assumed for the Composition B was of constant β form with pressure (p), specific volume (v), specific internal energy (E) relation

$$p = \frac{wE}{v} + \frac{wA}{v^\delta}$$

where $w = 0.797, \delta = 2.95, A = 0.0179$ Mbcm$^{3\delta}$ g$^{-\delta}$. With an initial density of 1.651 g cm^{-3}, this leads to a detonation pressure of 250.8 kb and a detonation velocity of 7.75 mm μs^{-1}.

For baratol a polytropic gas equation of state was assumed with initial density 2.61 g cm^{-3}, a γ of 3.52 and a detonation velocity of 4.925 mm μs^{-1}, giving a detonation pressure of 140 kb.

A linear shock velocity-particle velocity relationship was assumed for the EN58B stainless steel

$$W = 4.48 + 1.639 u \text{ mm } \mu s^{-1}$$

with initial density 7.90 gcm^{-3} and Gruneisen Gamma equal to 2.025.

No evidence has been observed of a polymorphic phase transition in EN58B.

4.2. Calculation with No Spalling

Figure 3 is a wave diagram for a calculation with no spalling (76.2 mm Comp. B, 3.05 mm stainless steel) in which is seen the primary shock in the steel, AB, which is reflected at the free surface as a rarefaction (BC,BDE). The rarefaction fan takes the form of a series of diverging characteristics of which only the edge characteristics (wave boundaries) are plotted. When the rarefaction meets the interface with the detonation products it is reflected as a compression wave (CDF,EG) which is a converging set of characteristics. It is this compression wave meeting the free surface which causes the free surface to accelerate rapidly.

The calculated free surface velocity history is compared with experiment in Fig. 4. The deceleration after the arrival of the shock wave is due to part of the Taylor wave being propagated through the plate. The arrival of the compression wave is spread out over a short time interval. For comparison purposes later, the reverberation time in the steel is taken to be
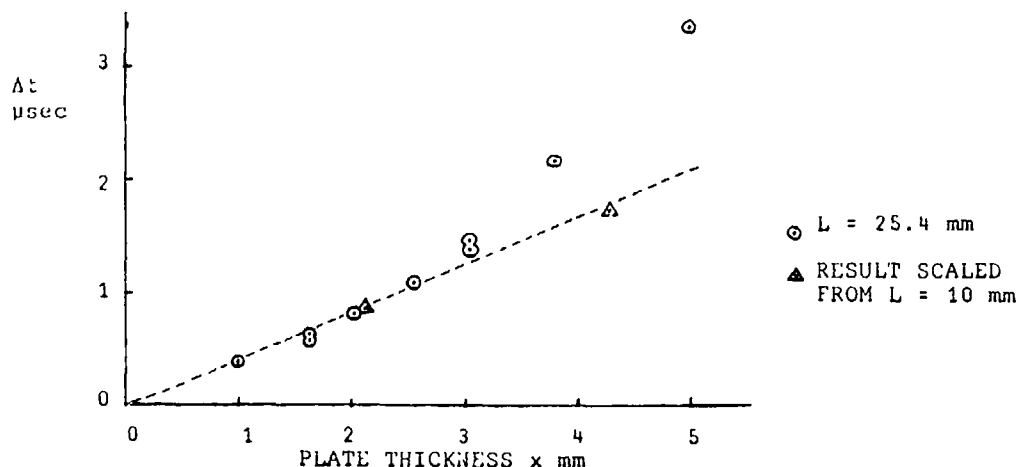
Fig. 2. Δt versus x for stainless steel plate on Comp. B, L = 25.4 mm.

481

the mean of the times of arrival of the leading and tailing characteristic of the compression wave.

Agreement between calculation and experiment is good, although the rather low value of initial velocity calculated suggests that the detonation pressure assumed for the Comp. B (251 kb) may be too low.

The tension in the steel arises from the interaction between the rarefaction reflected when the primary shock meets the free surface and the Taylor wave transmitted into the plate from the explosive. Peak tension for any particle of the plate first occurs on the tailing characteristic of the rarefaction wave. Peak tension increases with distance from the free surface, reaching a maximum where the tailing characteristic intersects the leading characteristic of the compression wave (point D in Fig. 3).

Figure 5 shows how the tension along the tailing edge of the compression wave varies with Lagrangian mass co-ordinate (a = $\int \rho dx$, with origin at the free surface) for a range of different plate to charge thick-

ness ratios. It will be seen that with the exception of a thickness ratio 0.20, the $-p$ vs. a graphs have closely the same slope, a slope which is mainly dependent on the rate of change of pressure in the Taylor wave. Thus if plates of different thickness spall at the same critical tension, then the spall thickness will be nearly constant. The kink in the slope for thickness ratios of 0.15 and 0.2 corresponds to the arrival of the edge of the Taylor wave. For points with Lagrangian co-ordinate greater than 4.4, the tailing edge of the rarefaction is affected by the presence of the baratol in the plane wave lens. The
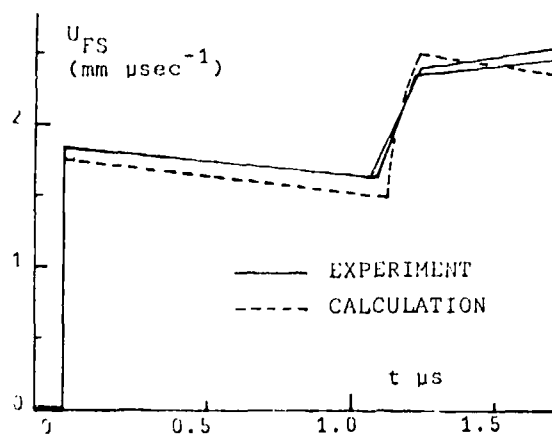
Fig. 4. Free surface velocity history of non-spalling plate (76.2 mm Comp. B, 3.05 mm steel).

Fig. 3. Wave diagram - no spalling (76.2 mm Comp. B, 3.05 mm steel).
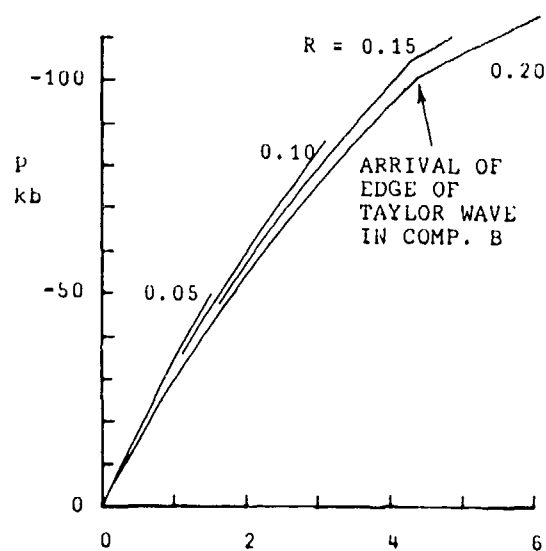
Fig. 5. Pressure on tail of rarefaction vs. Lagrangian mass coordinate for various values of plate/charge thickness ratio R.

482

maximum tension is plotted as a function of plate to charge thickness ratio in Fig. 6.

4.3. Spalling Calculations

Because of the way RICSHAW is currently written, a spalling calculation has to have an artificial interface inserted in the steel. Spalling then occurs when the chosen tension is first exceeded at that interface.

Figures 7(a) and (b) are wave diagrams for steel plates of relative thicknesses 0.08 and 0.12, spalling at a critical tension of 64 kb, which is appropriate to a 50.8 mm Composition B charge. It will be seen that the spall thickness is the same in both calculations, but of course the parent part of the plate increases in thickness.

Taking a thickness ratio of 0.12 as an example (Fig. 7(b)), when the plate spalls at 64 kb spall shocks
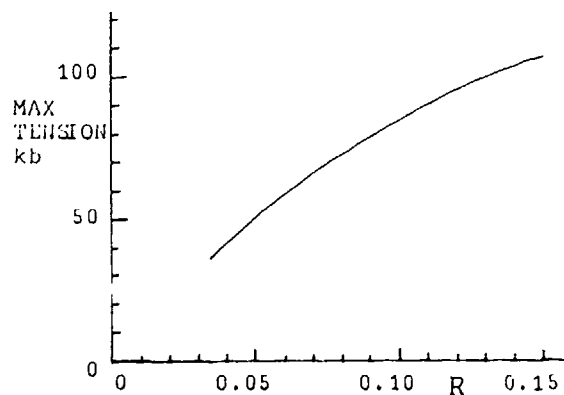
Fig. 6. Maximum tension vs. plate/charge thickness ratio R.
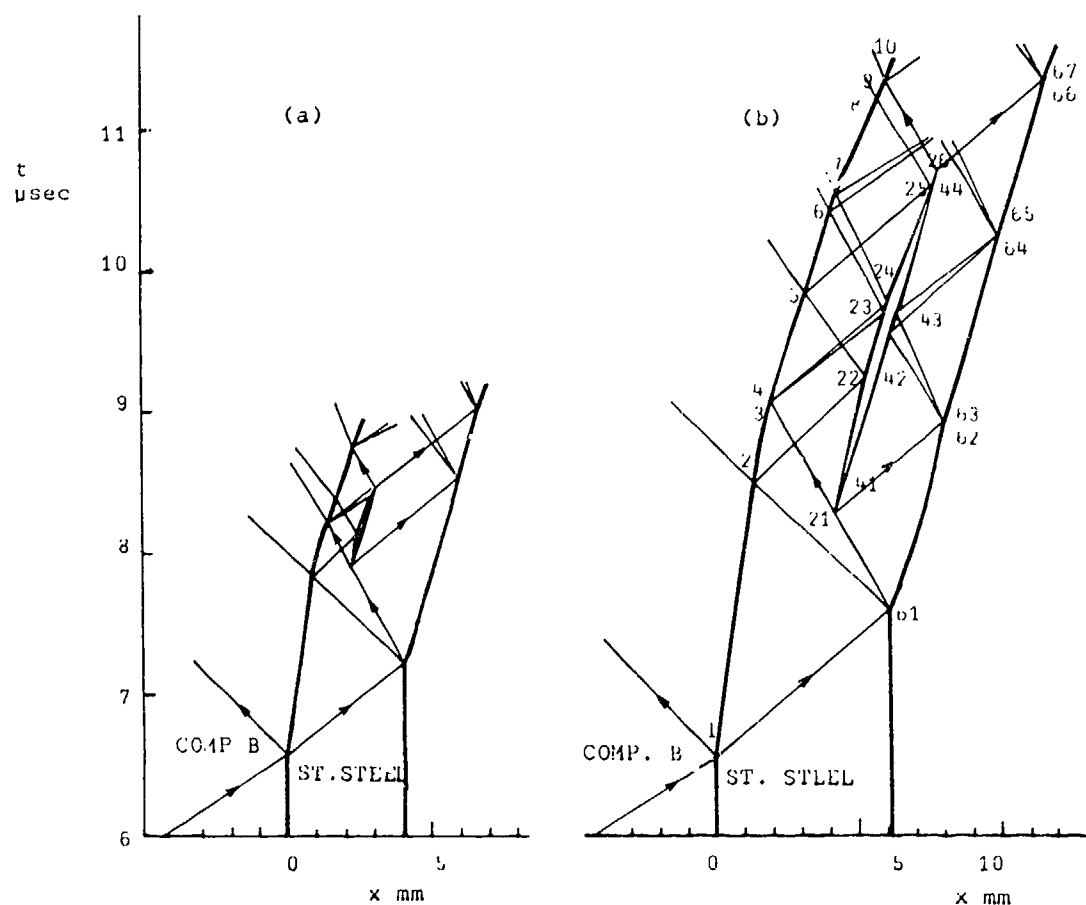
Fig. 7. Wave diagrams for R = 0.08 and R = 0.12 (50.8 mm Comp. B).

483

are emitted into both the spall and the parent plate and these raise the pressure at the spall plane from the critical spall tension to zero. As a result, the spall surfaces separate.

Taking first the spall, when the spalling shock meets the free surface it is reflected as a rarefaction and this wave reverberates alternately as forward-moving compression and backward-moving rarefaction until recollision takes place. Figure 8(a) shows the velocity histories of the two surfaces of the spall. Each has sawtooth form with constant mean velocity until they are affected by the re-collision shock. Corresponding points in Figs. 7(b) and 8 are numbered similarly.

The backward-moving spalling shock in the parent plate cuts off part of the main rarefaction and slows down the parent plate. As was shown by Lambourn and Hartley (1), the line of constant fracture tension has higher velocity than the spalling shock, so the shock has ever-increasing tension ahead of it until it meets the leading edge of compression. When the spalling shock meets the detonation products it is reflected as a rarefaction wave and this wave reverberates in the parent on the back of the main compression wave. However, the main compression wave moves forward and kicks the free surface of the parent forward, and is reflected as a rarefaction wave. It is one or other of the reverberations of this main

compression wave which causes the spall surfaces to re-close. Essentially the parent plate is still extracting energy from the detonation products. Figure 8(b) shows the velocity histories of the two surfaces of the parent plate.

On recollision of the parent and spall, a recollision shock is propagated backwards and forwards and it is the arrival of this recollision shock at the free surface which is measured experimentally and gives Δt.

The wave diagrams in Fig. 7 show that the thicker the parent plate, the longer it takes the spall planes to re-collide, essentially because the parent needs to extract more momentum from the detonation products, or, looked at in another way, the spall surfaces have more time to separate before the arrival of the main compression wave kicks the free surface of the parent towards the spall.

The free surface velocity history after the recollision shock is complicated by the particular waves propagating forward from the parent plate just after the collision. The strength of the recollision shock is also a variable, depending on the relative velocity of the impacting surfaces at the instant of collision.

4.4. Comparison of Calculations with Spalling Experimental Results

In Fig. 9, an experimental free surface velocity history for a 25.4 mm Comp. B charge, 3.05 mm

Fig. 8(a). Front and rear surface velocities of spall, R = 0.12.
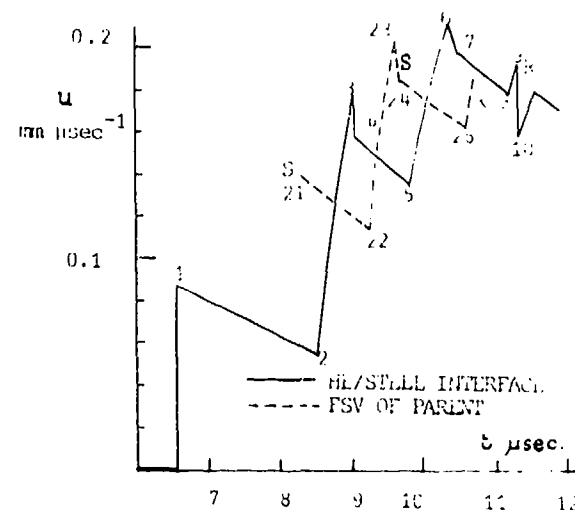
Fig. 8(b). Front and rear surface velocities of parent, R = 0.12.

484

stainless steel plate, is compared with calculations assuming various spall strengths in the steel. As the assumed spall strength is reduced, the spalling shock arrives earlier, but the recollision shock arrives later. The best match to the experiment for the recollision shock would be to assume a spall strength of about 94 kb.

Although Table 1 contains data on the major accelerations only, i.e. cohesive plate reverberation or spalled plate recollision shock, in some experiments, the analysis of motion indicated smaller accelerations within the time interval Δt and these were interpreted as due to the spalling shock. Their amplitudes were always smaller than expected from computation and this put their measurement near the limit of resolution of the experimental method. Any raggedness of the real spall surface, or possibly incomplete fracture, would tend to increase the duration of the compression wave generated in parting and reduce its amplitude, making it a less reliable indicator, but, in general, the effects which were observed arrived earlier at the free surface than the deduced 'deviation point,' suggesting a lower spall strength.

Good fits can be obtained for most of the recollision shock times. These are shown in Figs. 10(a), (b) and (c) for 25.4, 50.8, 76.2 mm. Composition B charges. The later kink in the calculated variation of Δt with thickness ratio is due to the different number

of reverberations required of the main compression wave to cause recollision.

Taking the points of deviation from these figures, Table 2 shows the geometry at which spalling starts for each charge thickness.

TABLE 2

Comp. B Thickness L (mm)	Thickness of EN58B which just spalls)/L
25.4	0.112 ± 0.005
50.8	0.068 ± 0.005
76.2	0.058 ± 0.005

5. CONCLUSIONS AND DISCUSSION

A purely experimental method has been proposed and demonstrated to determine the onset of spalling in a metal plate when an explosively genera ed triangular pulse reflects at its free surface.

The method depends on observation of the arrival time of the shock generated by recollision of the
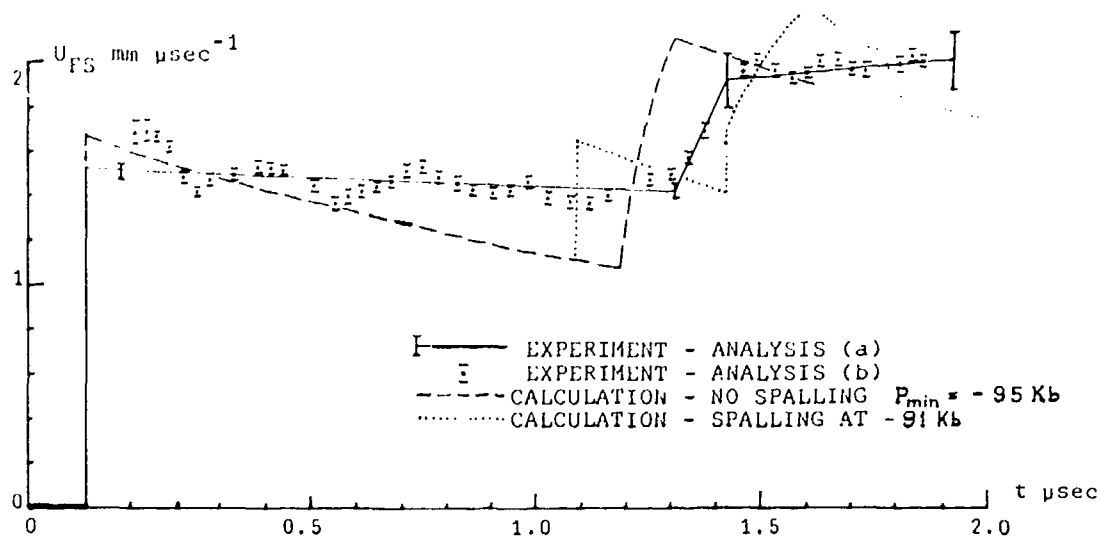
Fig. 9. Comparison of calculation with experiment for free surface velocity of spalling plate (25.4 mm Comp. B, 3.05 mm st. steel).

485
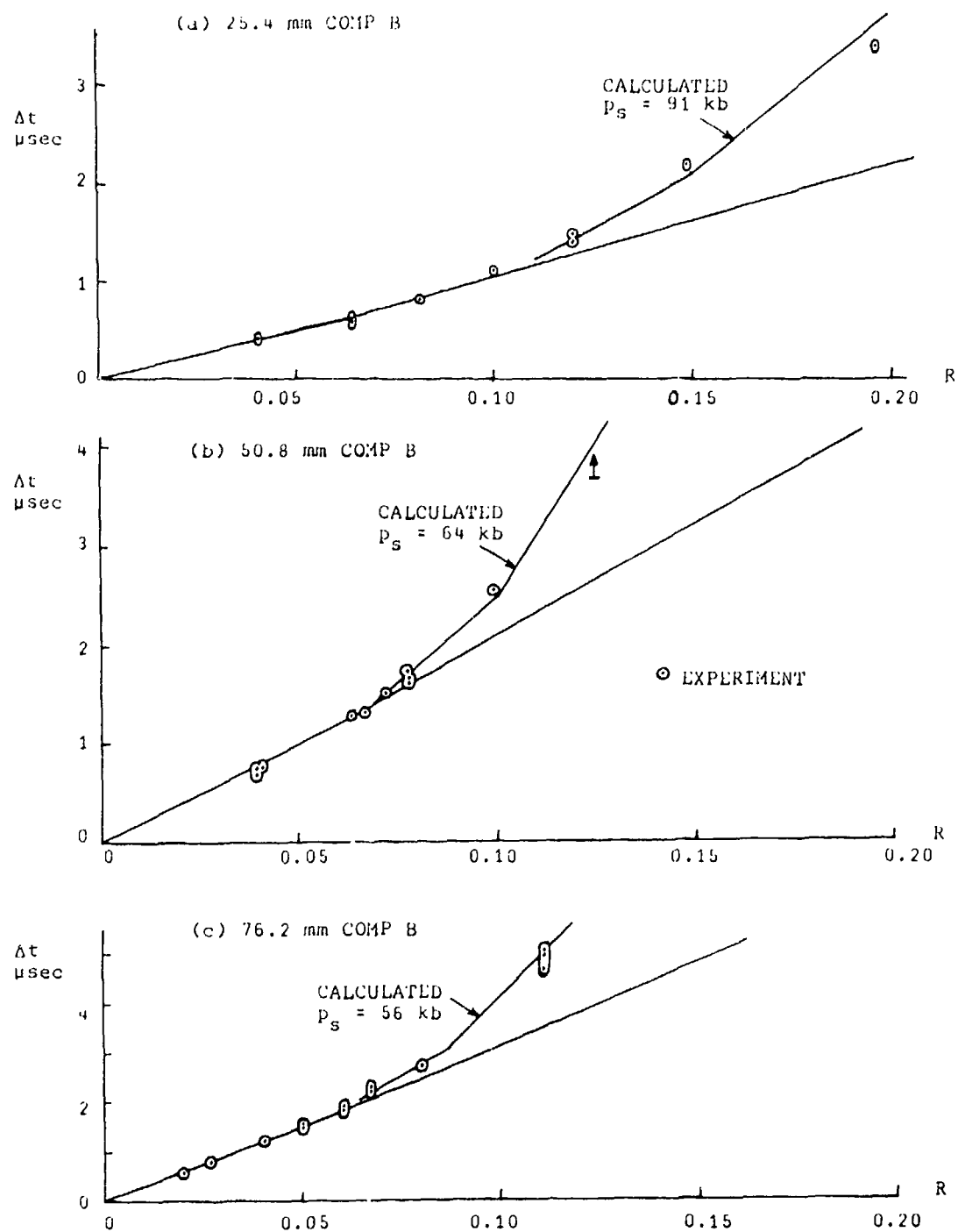
Fig. 10. Reverberation time in non-spalled and spalled plates.

486

parent plate and spall, which is more clearly defined than the lower amplitude spalling shock. The start of spalling has been shown to depend on absolute charge thickness, and not to scale according to the ratio of plate to charge thickness. Since charge thickness controls the steepness of the Taylor rarefaction following the initial shock, and hence the tensile stress rates and gradients in the plate, the lack of scaling confirms that the mechanism of spalling is rate or time dependent.

The number of experiments needed to deduce the critical geometry can be reduced by comparing the results with computation, in this case a one-dimensional characteristic code RICSHAW, which can deal with spalling. The recollision shock time has been shown to be a fairly sensitive indicator of what spall strength should be chosen for the calculation in which a simple spalling criterion is assumed—in this case instantaneous parting at a plane in the plate when its tensile stress reaches the selected value.

The inferred best fit spall strengths deduced from the time of arrival of the recollision shocks, are summarised in Table 3.

TABLE 3

Comp. B Charge Thickness (mm)	Spall Strength of EN58B (kb)
25.4	91 ± 3
50.8	64 ± 3
76.2	56 ± 3

The estimated spall strength for 50.8 mm charges, using RICSHAW, is in close agreement with the value of 65 kb estimated in Ref. (2), using somewhat different equations of state. It is also interesting to note that the strength for 76.2 mm charges deduced from the delay in the reverberation time is in very good agreement with the value deduced in Ref. (1) from a flash radiograph of a spalled plate in flight, i.e. the thickness of the spall deduced from the reverberation delay is in sensible agreement with that observed by flash radiography.

The only other data on spalling of explosively driven stainless steel plates is given by Thurston and Mudd (5) who re-analysed the radiographic experiments of Breed, Mader and Venable (6). Thurston and Mudd, following Mader, correlated the calculated spall strength with the calculated stress gradient $\Delta p/\Delta x$ between the spall plane and free surface in the form

$$-p_s = \sigma_0 + A\left(\frac{\Delta p}{\Delta x}\right)^B$$

where for 347 stainless steel Thurston finds the best fit parameters to be

$$\sigma_0 = 6\,kb, \quad A = 125, \quad B = 0.55$$

where the units of A are such that $\Delta p/\Delta x$ is in Mb cm^{-1} and the spall strength is in kilobars. (The chromium:nickel content of 347 steel is specified as 17-19:9-13 whereas EN58B has 17-20:7-10.)

Figure 11 shows that the current results for EN58B stainless steel based on reverberation time delay are in substantial agreement with the form of Thurston and Mudd's best fit to the radiographic results, but have slightly higher spall strength.

Further information on the spalling process may be obtained in future work with such a system by
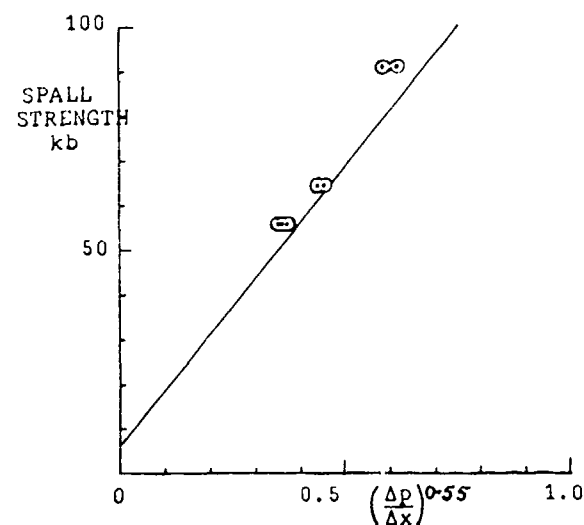
Fig. 11. Comparison between the experimental data and the best fit to Thurston's stress gradient model.

487

varying some of its parameters, e.g. initial shock strength by using different explosives, combined with variations in stress gradient.

ACKNOWLEDGEMENT

6. REFERENCES

1. B. D. Lambourn, J. E. Hartley: 'Code calculation of the hydrodynamic behaviour of plane one-dimensional explosive/metal systems.' Proc. 4th Symp. on Detonation, USNOL, White Oak, Maryland, Oct. 1965. ACR-126, p. 538.

2. G. Eden, P. W. Wright: 'A technique for the precise measurement of the motion of a plane free surface.' Proc. 4th Symp. on Detonation USNOL, White Oak, Maryland, Oct. 1965, ACR-126, p. 573.

3. B. D. Lambourn, N. E. Hoskin: 'The computation of general problems in one-dimensional unsteady flow by the method of characteristics.' Proc. 5th Symp. on Detonation, Pasadena, Calif., Aug. 1970. ACR-184, p. 501.

4. K. Burrows, D. K. Chilvers, R. Gyton, B. D. Lambourn, A. A. Wallace: 'Determination of detonation pressure using a manganin wire technique.' 6th Symp. on Detonation, San Diego, Calif., Aug. 1976.

5. R. S. Thurston, W. L. Mudd: 'Spallation Criteria for Numerical Computations.' LA 4013 (Nov. 1968).

6. B. R. Breed, C. L. Mader, D. Venable: J. App. Phys. 38, 3271-3275 (July 1967).

DISCUSSION

STEPHEN COCHRAN
Lawrence Livermore Laboratory
Livermore, California

I have performed calculations on experiments similar to those described as well as plate impact spall experiments. I have found that it is important to include the time it takes for fracture to occur. If one calculates spall as a continuous process and includes its influence on the stress correctly, the spall strength becomes more nearly a property of the material, independent of experimental geometry.

THE CRITICAL ANGLE FOR MACH BRIDGE FORMATION BETWEEN OPPOSING SHOCK WAVES IN POLYURETHANE FOAM

R. M. James, P. W. J. Moore and B. D. Lambourn
Atomic Weapons Research Establishment
Aldermaston, Berks

Hugoniot data in the pressure range 0.75 to 26 kbar has been obtained for three polyurethane foams of initial densities 0.3, 0.187 and 0.036 g cm^{-3} by flash radiography of symmetrically crushed blocks of foam. Both regular and Mach interactions have been observed at the intersection of the two crushing shock waves. It has been shown both experimentally and theoretically that, in contrast to normal materials, the critical angle of incidence for Mach reflection increases with increasing incident shock strength.

1. INTRODUCTION

When equal strength shock waves intersect at small angles of incidence, the reflected shocks emanate from the point of intersection and the reflection is said to be regular. As the angle of incidence is increased a critical angle is reached, beyond which the reflected waves do not intersect the incident waves on the plane of symmetry and a Mach bridge is formed connecting the points of intersection. The Mach bridge grows with time. In many materials it is found (e.g., 1,2) that the critical angle of incidence decreases with increasing incident shock strength. It is the purpose of this paper to examine the variation of critical angle of incidence with incident shock strength for polyurethane foam.

Amongst a set of experiments designed to determine shock wave velocity and mean compression in dynamically crushed polyurethane foam blocks, Mach bridge formation was detected in some instances at a collision plane between opposing shock fronts within the foam specimen. Steady state shock interaction theory has been used to evaluate the critical angle of incidence for Mach reflection as a function of incident shock pressure. The theory predicts that the critical angle of incidence increases with pressure for the porous foam. Additional experiments

with suitable values of incident angle and shock pressure were designed to yield a Mach bridge or to preclude its formation and so test the theoretical prediction.

2. EXPERIMENTAL METHOD

The method used was a straightforward application of single shot flash radiography. A block of polyurethane foam was crushed along two opposite surfaces by explosively driven flat brass plates, which were set up to crush the foam symmetrically and progressively from one end of the block to the other. The timing of the flash x-ray pulse and the angle between both plates and the foam block surfaces were chosen to display:

i. Whenever possible, a portion of the flying plates which had not struck the foam, showing the (apparent) plate flight angle and the uncrushed foam surfaces. When this was not possible, the plate flight angle was derived from other similar experiments x-rayed at earlier times,

ii. A region in which the interface between crushed and uncrushed foam was visible over a substantial fraction of the length of the foam block; and

iii. The region in which the opposing shock fronts interacted, displaying reflected waves into shocked material and, in some experiments, a Mach bridge at the interaction plane.

All this information was displayed in a single radiograph taken at right angles to the direction of motion of the shock fronts in the foam block. Timing probes attached to the two faces of the block attacked by the flying plates were correlated with the flash x-ray time from initiation of the explosive, and gave plate velocities before striking the foam, from which were deduced mean velocities of incremental segments of each plate after striking the foam.
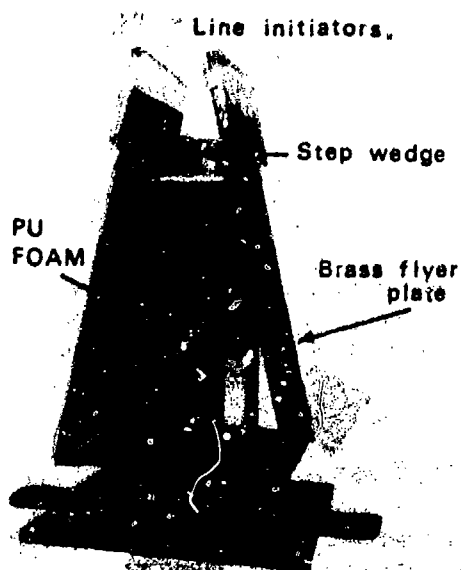
Fig. 1a.

A photograph of the assembly is shown in Fig. 1a. Foam density was usually 0.3 g cm^{-3}; some lower density foams were used in a few experiments. Each block was 27 cm × 22.5 cm × 10 cm, and the opposite 27 cm × 22.5 cm faces were crushed by 1.25-mm-thick brass plates, driven by line-initiated sheets of explosive varying between 3 mm and 18 mm thickness in different experiments.

Both plates and explosive sheets were identical for a particular experiment so that the system was symmetrical. The 27 cm × 10 cm surfaces (viewed by the flash x-ray generator) were confined within 4-mm-thick aluminum alloy plates (reasonably transparent to the x-rays) with a slight angular run-in towards the

Simultaneity (both sides) ± 0.1 μs
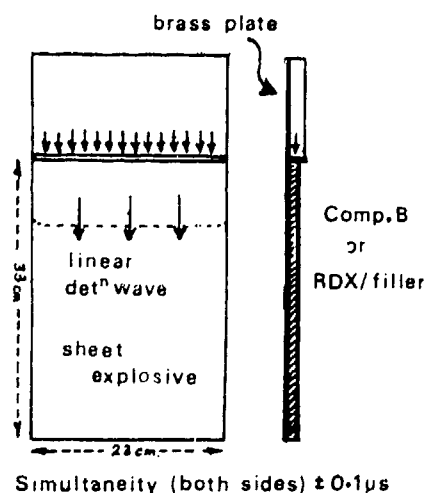
Fig. 1b. Line initiator and explosive.
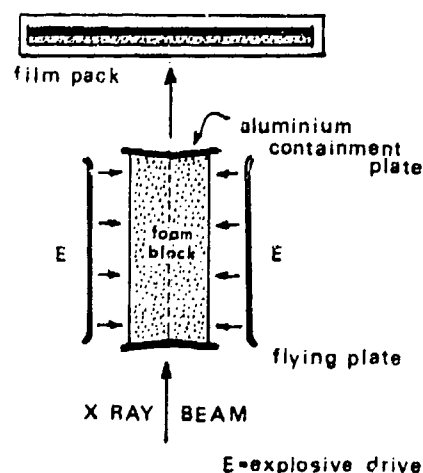
Fig. 1c. Plan view.

central vertical plane, in order to maintain shock pressure as far as possible at the edges of the block.

In some experiments (e.g., F26, F36, F37), similar brass "acceptor" plates were placed in contact with the foam, which was crushed by both plates after the collision phase.

Considerable care was taken to align the block and plates accurately in the x-ray beam, choosing the centre of the polar diagram to fall at the expected

490

interaction point between the opposing shock waves. The initial angle of each plate to the block (measured in the static radiograph) and the apparent angle of incidence of each plate to it in the dynamic radiograph gave the true flight attitude of each plate as the mean of these two angles. These aspects are shown in Figs. 2a, 2b, and Appendix A.
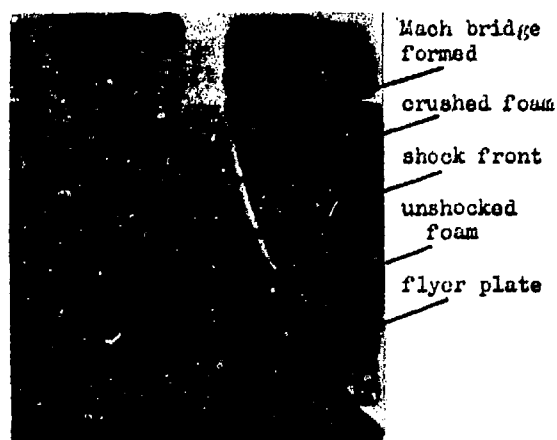
vacuum shot

Fig. 2a. Expt F42 radiograph – typical dynamic, 50 ns exposure
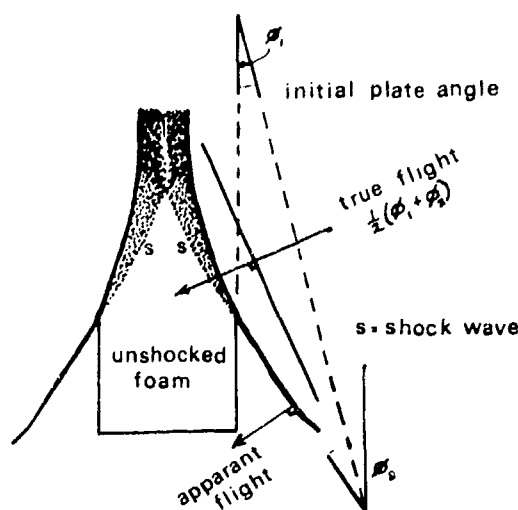
Fig. 2b. Plate flight direction from dynamic radiograph.

The plates remained flat during flight and as they compressed the foam. Shock wave fronts and plate

positions were well defined on the radiographs. Motion blur was insignificant with a 50-ns duration x-ray exposure. Spot size and film/screen effects introduce errors of about ±0.5 mm.

There was some concern about the effect trapped air might cause between the flying plates and the foam block. Several experiments were fired inside thin steel vacuum vessels, which were exhausted before firing. Foam blocks in these experiments were wrapped in thin aluminium foil, attached to the polyurethane foam by epoxy resin, to ˄vent gas escaping from the foam itself. In the event, no discernible effects due to presence or absence of air were recorded. Figure 3 shows the vacuum arrangement.

E = explosive (3 mm to 18 mm in different experiments)

F = flyer plate. 1.25 mm brass
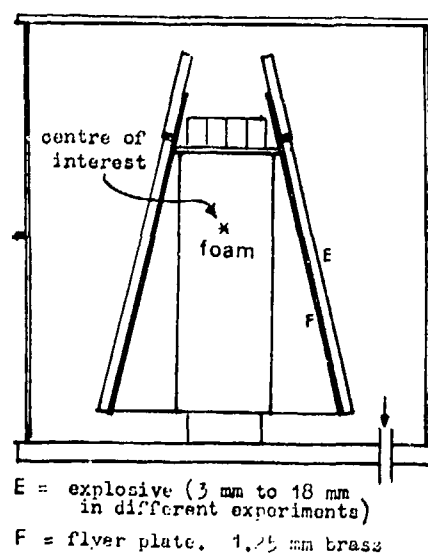
Fig. 3. Vacuum assembly.

3. TREATMENT OF HUGONIOT DATA

3.1. Experimental Data

The basic information necessary to construct a Hugoniot curve was determined from measurements taken on the radiographs. Knowing the true flight attitude of each plate (by taking the mean value of angles of incidence of the plate to the block in static and dynamic radiographs, as described above), a set of lines could be drawn dividing the shocked foam region into an arbitrary number of zones in which foam compression was approximately uniaxial (Fig. 4).

491
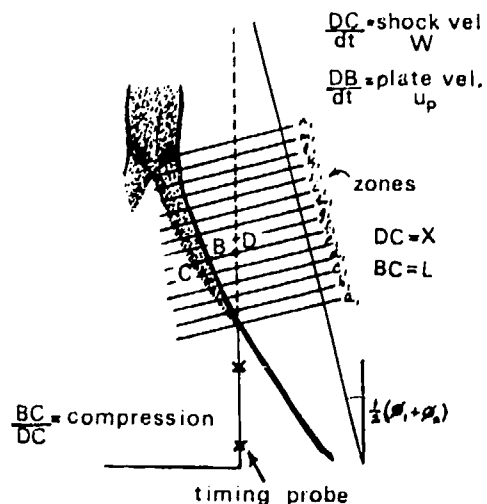
Fig. 4. Measurements from radiograph.

In practice these lines were usually drawn at 1-cm intervals, normal to the plate flight attitude line, to intersect the plate in its various positions below the original foam surface, and the shock wave front ahead of the plate.

Taking L as the thickness of shocked foam in each zone, these direct measurements from the radiographs gave:

   i. The distance the shock wave had travelled into the foam (X).

   ii. The distance the plate had travelled into the foam (X − L).

   iii. The average compression of the foam (L/X ≡ ρ/ρ_0) – for continually varying values of X and t (time).

Derivatives with time are then calculated:

   iv. The shock wave velocity (W).

   v. The plate velocity (u_p or u_0 at t = 0).

As a first approximation, the particle velocity u was taken as the plate velocity (u_p) computed for the central point in each zone. Therefore the pressure p and the dynamic compression ρ/ρ_0 could be computed at time steps related to each consecutive zone of shocked foam in the radiograph, from close to

initial impact time to the time at which the opposing shock waves interacted, from:

$$p = \rho_0 W u$$

and

$$\rho/\rho_0 = \frac{W}{W - u}.$$

Since at t = 0 the particle velocity u *is* the plate velocity (i.e., u = u_0 at time of impact), this time resolved computed data for p and ρ/ρ_0 (expressed as v/v_{0s}) can be extrapolated back to t = 0 to give an experimental point on the Hugoniot curve (Fig. 5).
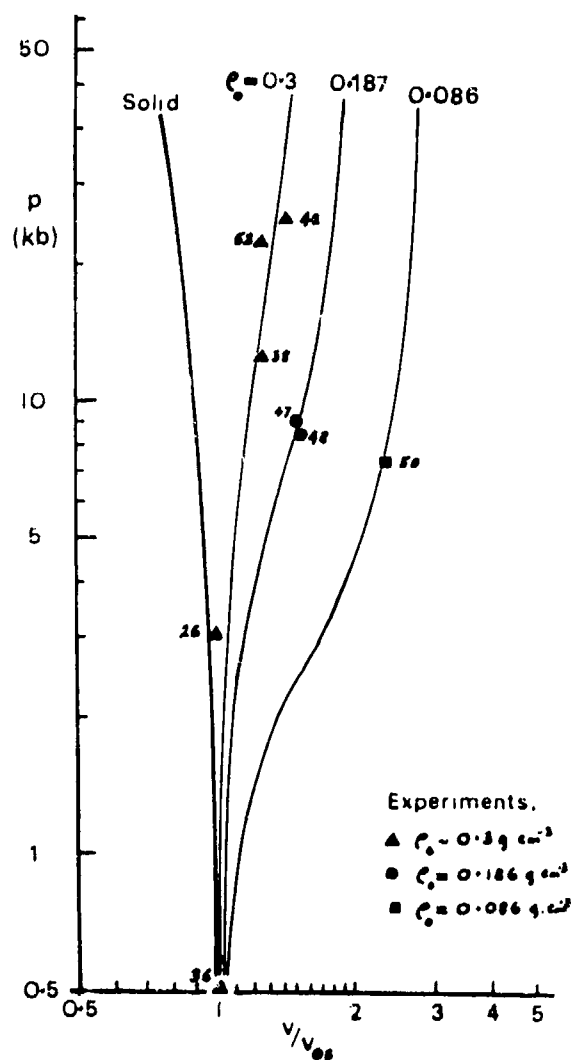
Fig. 5. Hugoniot curves for polyurethane foams.

492

TABLE 1

Experiment No.	F26	F36	F37	F38	F42	F47	F48	F52
Foam density (g cm^{-3})	.294	.300	.285	.294	.286	.186	.186	.292
Explosive, thickness	SX2 9 mm	SX2 3 mm	SX2 3 mm	Comp.B 9 mm	Comp.B 18 mm	Comp.B 9 mm	Comp.B 9 mm	Comp.B 18 mm
Flyer plate initial angle	12½°	12½°	12½°	13°	13°	11½°	11½°	2½°
Flyer plate velocity (mm μs^{-1})	2.14 *(1.07)	1.0 *(0.5)	1.0 *(0.5)	1.93	2.60	1.91	1.90	2.66
Interaction zone pressure p_1 (kbar)	1.9	0.4	0.12	2.5	6.5	2.7	2.9	6.3
Shock wave Angle of incidence[†]	12°	9°	7°	16°	20°	17°	18°	13½°
Angle of reflection[‡]	69°	Not observed	12°	46°	36°	33°	39°	26°
Peak pressure at shock front (at t = 0) p_{max} (kbar)	3.1	0.51	0.32	12.5	25.1	9.0	8.4	22.5
v/v_{os} at peak pressure	1.0	1.01	1.2	1.27	1.43	1.50	1.55	1.27
Mach bridge observation; remarks	YES Clear low density zone at interaction	NO (Vacuum shot)	NO Similar to F36, later	YES Faster plates (vacuum shot)	YES Further increase in plate velocity (vacuum shot)	PARTLY	PARTLY (Vacuum shot)	NO Reduced plate angle

*Bracketed figures giving half flyer plate velocity indicate equal mass acceptor plates at foam surface.
[†]SX2 is plastic explosive in sheet form (RDX/filler).
[‡]Comp.B ~60% RDX, ~40% TNT, ~1% wax.

Similar p, v/v_{os} points derived from other experiments enabled the EOS data to be checked over a wide variety of pressure values, using foams of different densities.

In order to obtain the pressure at the interaction plane between the opposing shock waves, which is lower than the peak pressure value at the initial impact (t = 0), a computed value of p was obtained from the plate (i.e., particle) velocity and the shock velocity for the particular zone where the interaction occurs. Smoothed data for the shock wave and plate positions were used in these calculations, and veloci-

ties derived from data relating to the incremental time steps corresponding to the boundaries of each zone (Fig. 4).

A typical set of results computed from measured data on the radiographs of experiment F48 ($\rho_o = 0.186$ g cm^{-3}, initial plate velocity $u_o = 1.9$ mm μs^{-1}) is given in Appendix B.

The experimentally derived p, v/v_{os} point is shown in Fig. 5. Peak pressure by extrapolation in this experiment was 8.4 kbar; pressure at the interaction point was 2.9 kbar. A Mach bridge was partially formed.

3.2. Equation of State

In order to analyse the shock wave interaction data, it was necessary to find an equation of state which fitted the Hugoniot data. McQueen et al. (3) have determined a Hugoniot for solid polyurethane of density

$$\rho_{os} = 1.265 \text{ g cm}^{-3} \tag{1}$$

in the usual linear shock velocity (W) – particle velocity (u) form

$$W = a + bu \tag{2}$$

where $a = 2.486 \text{ mm } \mu s^{-1}$, $b = 1.577$, and the Gruneisen Gamma at normal density is

$$\Gamma_o = 1.55 . \tag{3}$$

Taking the Hugoniot for solid polyurethane as a basis, one can construct a Gruneisen form of equation of state relating pressure (p), specific volume (v) and specific internal energy (E):

$$p = p_H(v) + \frac{\Gamma(v)}{v} (E - E_H(v)) \tag{4}$$

based on the variation of pressure $p_H(v)$ and specific internal energy $E_H(v)$ on the Hugoniot curve. For any reasonable variation of Gruneisen Gamma with volume, this equation of state is valid for densities greater than ρ_{os}. It may be extrapolated plausibly to densities just less than ρ_{os}, but with foams of initial density <25% of ρ_{os}, the density on the Hugoniot for shock pressures >1 kbar is significantly less than ρ_{os}.

It was decided, therefore, to use a modified PUFF (4) form of equation of state for the expansion states of polyurethane. This equation of state is still of Gruneisen form but the reference curve is now the isobar $p = 0$, along which the internal energy is assumed to vary with v according to the relation

$$E_r(v) = E_s \left[1 - \left(\frac{v_{os}}{v} \right)^{\delta} \right] \tag{5}$$

where v_{os} is the initial specific volume of solid polyurethane, E_s is the sublimation energy and δ is a dimensionless parameter, which is chosen so that the

derivative $(\partial E/\partial v)_p$ and hence the sound speed is identical for the two forms of equation of state at $v = v_{os}$.

$$\delta = \frac{a^2}{\Gamma_o E_s} . \tag{6}$$

The form chosen for the variation of Gruneisen Gamma with specific volume was proposed by Parish (5) and is

$$\Gamma(v) = \gamma + \alpha \exp \left[-\beta \left\{ \ln \left(\frac{v}{v_m} \right)^2 \right] \right] \tag{7}$$

where α, β, γ are dimensionless constants and v_m is the specific volume at which Γ takes a maximum value $\gamma + \alpha$. As v tends to zero or infinity, Gruneisen Gamma tends to γ.

Of the five parameters E_s, γ, α, β and v_m in the expansion equation of state, v_m was assumed equal to v_{os} and γ to be 0.3 so that

$$\alpha = \Gamma_o - \gamma = 1.25 . \tag{8}$$

E_s and β were selected by choosing values which gave satisfactory fits to the experimental Hugoniot data shown on Fig. 5 with particular care taken to fit the foam of initial density 0.3 g cm^{-3}. The values chosen were

$$E_s = 0.017 \text{ Mb. cc g}^{-1}(1700 \text{ Jg}^{-1})$$
$$\beta = 1.7 . \tag{9}$$

4. ANALYSIS OF INTERACTION DATA

At the interaction plane, reflected shock waves occurred, and radiographic dose and energy were chosen such that the reflected waves could be observed. Conditions similar to reflection at a semi-infinite oblique wall gave the opportunity to observe Mach bridge formation under better conditions than obtainable with a single reflection at a high density boundary. When a Mach bridge was formed, radiography revealed a strip of lower density material at the interaction plane, indicating the lateral boundaries of the Mach reflection zone (see Fig. 6). The relevant experiments which straddled conditions for Mach bridge formation are listed on Table 1. Polyurethane foam

494

EXPERIMENT 26
Clear Mach bridge
formed throughout the
interaction region.

PU foam
$\rho = 0.294$ g cm^{-3}

Plate velocity
$u_o = 2.14$ mm μsec^{-1}

Acceptor plates at
foam surface

High shock reflection
angle (α')

Static radiograph
(9 mm thick explosive)

Dynamic radiograph
117.5 µs after initiation

Mach reflection at
central plane

EXPERIMENT F38
Clear Mach bridge
formed.

PU foam
$\rho = 0.294$ g cm^{-3}

Plate velocity
$u_o = 1.93$ mm μsec^{-1}

Fired in vacuum

Static radiograph
(9 mm thick explosive)

Dynamic radiograph
99.0 µs after initiation

Mach reflection at
central plane

EXPERIMENT F52
Reduced initial
plate angle:
No Mach bridge.

PU foam
$\rho = 0.292$ g cm^{-3}

Plate velocity
$u_o = 2.66$ mm μsec^{-1}

Low angle of incidence
(α) between shock
fronts

Static radiograph
(18 mm thick explosive)

Dynamic radiograph
83.5 µs after
initiation

Regular reflection at
central plane

Fig. 6. Radiographs from three experiments.

495

of density 0.3 g cm^{-3} was used in six experiments, and density 0.186 g cm^{-3} in two.

The shock strength was controlled by the flyer plate velocity, hence by the thickness of explosive. The angle of incidence of the shock waves in the foam was controlled by initial plate angle and its velocity.

Figures 6a, 6b, and 6c illustrate static and dynamic radiographs from three of these experiments. F52 exhibits regular reflection of the shock waves and F26 and F38 display Mach bridges. In the latter two cases it will be noted that a low density region can be discerned originating at the Mach bridge, and extending along the interaction plane into the doubly shocked material.

5. COMPARISON OF INTERACTION RESULTS WITH SHOCK INTERACTION THEORY

5.1. Regular Shock Interaction Theory

Consider the interaction of two equal strength oblique shock waves at angles of incidence 2α. The pressure p_1 behind both incident shock waves is assumed known and this gives the shock velocity W and shock compression. Following the standard procedure, it is convenient to consider an observer moving with the point of intersection of the shocks (Fig. 7), so that with respect to him the material ahead of the incident shock is flowing into the shock at velocity $q_o = W \text{ cosec } \alpha$ parallel to the plane of symmetry.
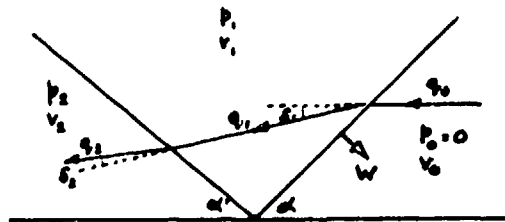
Fig. 7. Shock wave reflection.

The flow is deflected downwards through angle δ_1 by the incident shock, because the component of flow velocity normal to the shock is reduced by the shock transition, whereas the component of velocity parallel to the shock is unchanged. The deflection is given by

$$\tan(\alpha - \delta_1) = \frac{v_1}{v_o} \tan \alpha. \qquad (10)$$

Thus, knowing the strength of the incident shock, the value of δ_1 is determined, and the flow velocity behind the incident shock is given by

$$q_1 = q_o \cos \alpha \sec(\alpha - \delta_1). \qquad (11)$$

Taking the reflected shock to be at angle α' to the plane of symmetry, and the deflection upwards of the flow by the reflected shock to be δ_2, then the equation of continuity and the equality of the tangential component of velocity on either side of the reflected shock give:

$$q_2 \sin(\alpha' + \delta_1 - \delta_2) = \frac{v_2}{v_1} q_1 \sin(\alpha' + \delta_1) \qquad (12)$$

$$q_2 \cos(\alpha' + \delta_1 - \delta_2) = q_1 \cos(\alpha' + \delta_1) \qquad (13)$$

so that the total deflection $\theta = \delta_1 - \delta_2$ through both shocks is given by

$$\tan(\alpha' + \theta) = \frac{v_2}{v_1} \tan(\alpha' + \delta_1). \qquad (14)$$

In addition, the flow must satisfy conservation of momentum, and the Rankine Hugoniot equation across the reflected shock

$$p_2 - p_1 = \frac{q_1^2 \sin^2(\alpha' + \delta_1)}{v_1^2} (v_1 - v_2) \qquad (15)$$

$$E_2 - E_1 = \frac{1}{2}(p_1 + p_2)(v_1 - v_2) \qquad (16)$$

and the equation of state for the doubly shocked foam

$$p_2 = p(v_2, E_2) \qquad (17)$$

which is defined in Sec. 3.2.

The final condition required is that the total deflection θ be zero, so that the flow behind the reflected shock is parallel to the plane of symmetry.

Equations (14) through (17) need to be solved by iteration to find α', p_2, v_2 and E_2. The equations

yield two possible values of α', p_2, etc., of which the lower value is the only stable one.

Figures 8a and 8b show the angle of reflection versus the angle of incidence for solid polyurethane and polyurethane foam of initial density 0.3 g cm^{-3}. Each curve is for a different incident shock pressure. As is usual, solutions only exist for angles of incidence up to an extreme value (α_x), which is a function of incident shock pressure. But whereas for solid polyurethane α_x *decreases* as the pressure behind the incident shock increases, for polyurethane foam α_x *increases* as the incident shock strength increases.
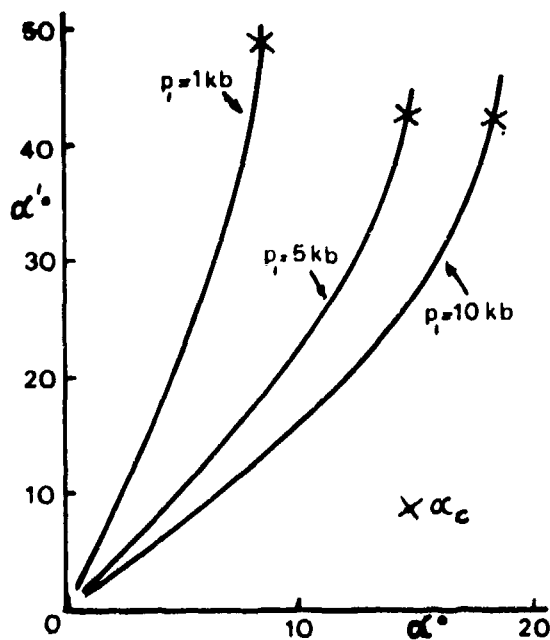
Figures 9a and 9b show the same effect in graphs of the pressure behind the reflected shock against
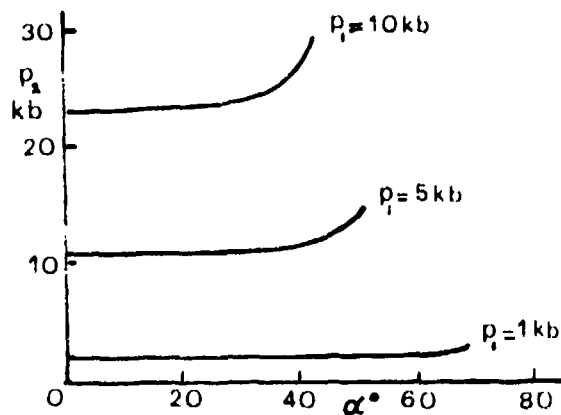
Fig. 8a. Angle of reflection vs angle of incidence. Solid polyurethane.

Fig. 9a. Reflected shock pressure vs angle of incidence. Solid polyurethane.

Fig. 8b. Angle of reflection vs angle of incidence. Foam $\rho_o = 0.3$ g cm^{-3}.
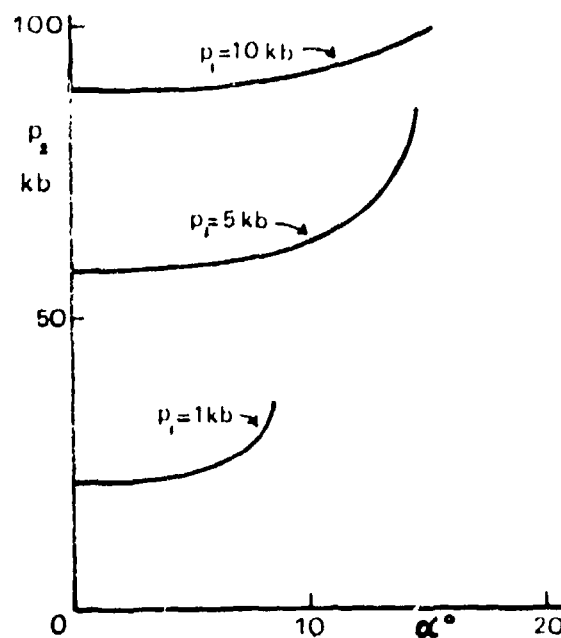
Fig. 9b. Reflected shock pressure vs angle of incidence. Foam $\rho_o = 0.3$ g cm^{-3}.

497

angle of incidence. As may be expected, the pressure ratio across the reflected shock is much greater for the foam than for the solid polyurethane.

5.2. Critical Angle for Mach Interaction

Consideration of both simple three-shock theory (e.g., [6]) and of the velocity of the disturbance arising from the point where the two incident waves first interact shows that Mach bridges begin to form at a value of α for which the flow velocity behind the reflected wave q_2 is just sonic. Points marked x in Figs. 8a and 8b are calculated angles for which the velocity is sonic.

Figure 10a shows the calculated variation of the critical angle of incidence (α_c) for Mach bridge formation as a function of incident shock pressure (p_1). For any incident shock strength, angles of incidence less than α_c should give regular reflections and angles of incidence greater than α_c should give Mach reflections. The two points marked R and the three points marked M, corresponding to experiments F36, F37; F26, F38, and F42; show that the calculated curve is in the correct place but might not be of the right shape.

The theoretical prediction that the value of α_c increases with incident shock strength was tested by an additional experiment (F52) in which the incident shock pressure was 6.3 kbar and the angle of incidence was 13½°. By comparison with the point for experiment F26 at $p_1 = 1.9$ kbar, $\alpha = 12°$, which had a Mach bridge, experiment F52 should have given a Mach reflection if α_c decreased with increasing p_1, and a regular reflection if the theory is correct. In the event no Mach bridge was formed, and the full set of experimental points is plotted in Fig. 10b with experiment F52 ringed.

6. CONCLUSIONS AND DISCUSSIONS

Hugoniot data has been obtained by a novel radiographic technique for polyurethane foams of density 0.3, 0.19, and 0.09 g cm^{-3}. It has been shown that as the pressure is increased above about 1 kbar, the density decreases. Previous reported data on polyurethane foam (3,7) has been insufficiently accurate to show this phenomenon.

It has been shown both experimentally and theoretically that whereas for fully dense materials the critical angle of incidence for Mach reflection decreases with increasing incident shock strength, for foams the critical angle increases with increasing incident shock strength. Figure 11 shows that this behavior is applicable for weak shocks in porous

(a) Before expt. F52.   (b) Including expt. F52 (ringed).
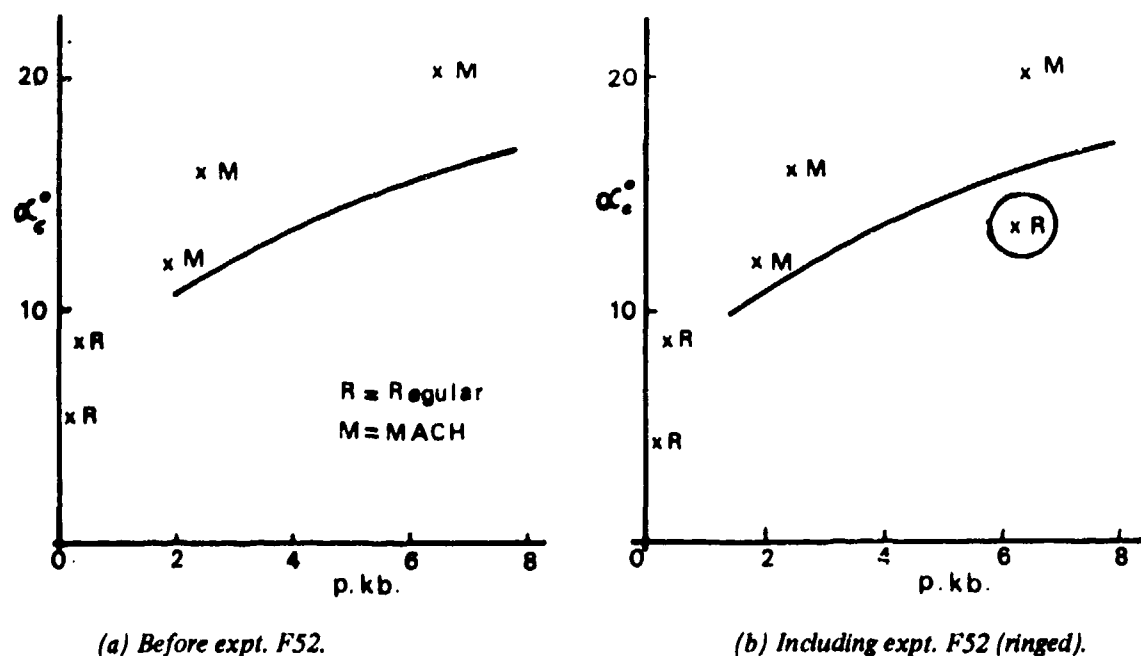
Fig. 10. Comparison of predicted critical angle with experimental results.

498
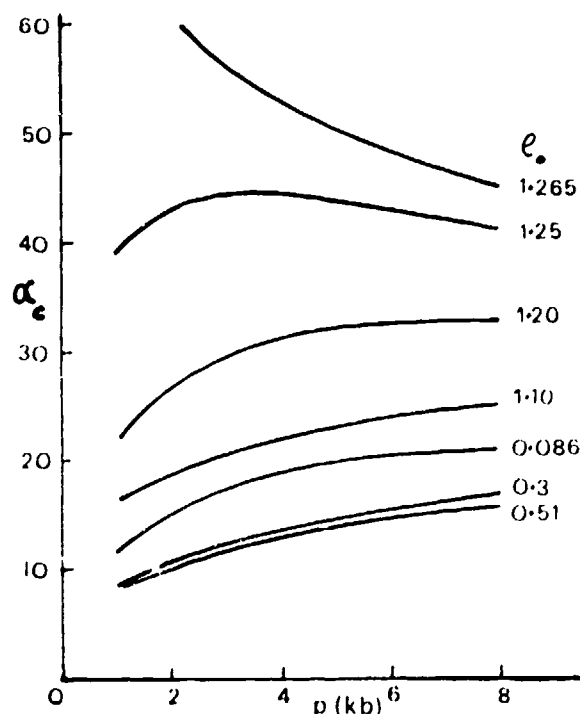
Fig. 11. Critical angle – incident shock pressure curves for various foam densities.

polyurethane of all initial densities. The critical angle of incidence at given shock pressure is a minimum for that porous density for which the Hugoniot is vertical, i.e., the material is shocked to solid volume at all pressures. The initial density ρ_{om} in this case is given by

$$\rho_{om} = \frac{\Gamma_0}{\Gamma_0 + 2}\, \rho_{os},$$

which is 0.51 g cm^{-3} for polyurethane.

ACKNOWLEDGMENTS

The authors would like to thank Mr. M. P. Tuck and Mr. C. J. Ham for calculating the regular shock interactions and Mr. G. E. Griffin for assisting with the experimental work.

REFERENCES

1. R. Courant and K. O. Friedrichs, "Supersonic Flow and Shock Waves" (Interscience (1948)) p. 326.

2. N. L. Coleburn and L. A. Roslund, "Interactions of Spherical Shock Waves in Water," 5th Symposium (International) on Detonation. ACR-184, 581-588 (1970).

3. R. G. McQueen, S. P. Marsh, J. W. Taylor, J. N. Fritz, and W. J. Carter, "The Equation of State of Solids from Shock Wave Studies," *High Velocity Impact Phenomena* (ed. R. Kinslow), Academic Press (1970), Ch. VII.

4. L. Seaman: "SRI, PUFF 3 Computer Code for Stress Wave Propagation," AFWL. Con. No. F20601-70-C-0001.

5. P. G. Parish (AWRE), private communication.

6. B. D. Lambourn and P. W. Wright, "Mach Interaction of Two Plane Detonation Waves," 4th Symposium (International) on Detonation. ACR-126, 142-152 (1965).

7. I. C. Skidmore and E. Morris, "Thermodynamics of Nuclear Materials," pp 173-216, Intern. AEA, Vienna (1962).

APPENDIX A

Calculation of Plate Flight Velocity

Measurements taken from the radiographs alluded to under "treatment of Hugoniot data," Sec. 3 and in Appendix B, depend upon the true direction of flight being known for the plate elements. Since the plates are driven under sideburn conditions (the explosive is initiated linearly at one end) the true flight altitude is neither the static angle of incidence to the foam block, nor the angle observed in the dynamic radiographs between the plates and the uncrushed portion of the block.

If AD is the static plate position, and BD is the part of the plate still visible in free flight at the time

499

of the flash x-ray, and AC represents the surface of the foam block, then

in the triangle BDC, V_c is the velocity of the plate contact along the foam block surface (timed by probes) and V_p is the plate velocity; hence

$$\frac{V_p}{\sin \phi_2} = \frac{V_c}{\sin B\hat{D}C}$$

$$B\hat{D}C = 90° - \left(\phi_2 - \frac{(\phi_1 + \phi_2)}{2}\right)$$

$$= \frac{1}{2}(180° + \phi_1 - \phi_2).$$

Therefore

$$V_p(\equiv u \text{ in text}) = \frac{V_c \sin \phi_2}{\sin \frac{1}{2}(180° + \phi_1 - \phi_2)}.$$

APPENDIX B

Results are listed from measurements taken on the radiographs of Experiment F48. Fired in vacuum. $\rho_o = 0.186 \text{ g cm}^{-3}$.

As shown in Fig. 4, normals a, b, c, etc., are drawn to the corrected plate flight angle on both sides of the block. Mean values are taken from each pair of similar measurements. Measurements are taken along the normals from the original foam block surface lines,

i. to the free surface of the brass plate $(X - L)$, and

ii. to the shock wave front in the foam (X), where L is the thickness of crushed foam.

Times from plate impact for each normal intersection with the original foam surface were given by probe data.

In the table below, t, W, u, p and ρ/ρ_o are calculated for points midway between the intersections of each pair of normals with the plate and shock wave front (see Fig. 4).

Normal	X (cm)	X–L (cm)	t (μs)	Shock Velocity W (mm μs^{-1})	Particle Velocity u_p (mm μs^{-1})	Shock Pressure $p = \rho_0 W u$ (kbar)	Compression $\rho/\rho_0 = \dfrac{W}{W - u_p}$	$V/V_{os} = \dfrac{\rho_{os}}{\rho_0}\dfrac{\rho_0}{\rho}$	Other Data
a_1a_2	0.55	0.43							
			3.16	2.19	1.67	6.82	4.24	1.53	Initial plate velocity
b_1b_2	1.08	0.83							
			5.26	2.05	1.61	6.13	4.71	1.38	$u_0 = 1.90$ mm μs^{-1}
c_1c_2	1.57	1.22							
			7.37	1.92	1.55	5.54	5.17	1.26	Time interval between zone
d_1d_2	2.04	1.60							boundaries ~2.11 μs
			9.47	1.82	1.51	5.10	5.87	1.28	
e_1e_2	2.48	1.96							
			11.58	1.76	1.38	4.52	4.72	1.38	
f_1f_2	2.90	2.30							
			13.68	1.69	1.36	4.30	5.12	1.27	$\rho_0 = 0.186$ g cm^{-3}
g_1g_2	3.31	2.63							
			15.79	1.61	1.30	3.90	5.20	1.25	$\rho_{os} = 1.210$ g cm^{-3}
h_1h_2	3.70	2.94							
			17.92	1.59	1.32	3.91	5.92	1.10	
i_1i_2	4.09	3.26							
			20.00	1.51	1.16	3.25	4.29	1.52	$\dfrac{v}{v_{os}} = 1.30$
j_1j_2	4.45	3.54							
			22.10	1.47	1.18	3.22	5.07	1.28	
k_1k_2	4.81	3.83							$\dfrac{v}{v_{os}}\,(t=0) = 1.54$
			24.21	1.51	1.16	3.25	4.29	1.52	
l_1l_2	5.20	4.11							
			26.31	1.32	1.11	2.75	6.40	1.02	$p_{max}(t=0) = 8.4$ kbar
m_1m_2	5.49	4.38							
			28.42	1.38	1.16	2.98	6.09	1.07	$p(t=31.5$ μs$) = 2.9$ kbar
n_1n_2	5.83	4.66							

NOTE:

(1) Lines a_1a_2 are near the initial impact end of the shocked foam; n_1n_2 are near the interaction plane between the shock waves.

(2) Plotting $1/p$ against t, and extrapolating to $t = 0$ gives $p_{max} = 8.4$ kbar at the position of first contact.

(3) Plotting $1/p$ against t, and extrapolating to $t = 31.5$ μs (at interaction) = 2.9 kbar. (In this experiment a Mach bridge was partly visible.) The p_{max} figure (8.4 kbar) is plotted on the Hugoniot at $v/v_{os} = 1.54$ (see Fig. 5).

(4) Angle of incidence between the shock waves and the central plane was 18°.

(5) X and (X − L) are dimensions taken from the radiograph, unscaled. Scaling factor = 0.87.

ON BLAST WAVES IN LIQUIDS

M. Kamel,[1] G. E. Abouseif,[2] R. H. Guirguis,[3]
S. A. Farag,[4] and A. K. Oppenheim[5]
Cairo University, Egypt
and
University of California, Berkeley, USA

An analysis of initial stages of explosion in liquids is presented. First a simple method for determining the trajectory of the shock front in the time-space domain is introduced. It is based on the postulate that the shock velocity is practically identical to that of the positive characteristic at the head of the flow field. Then the evolution of the structure of the non-steady flow field is determined on the basis of an experimentally observed trajectory of the gas bubble formed by the explosion initiating charge. This, in turn, is based on the postulate that the density profile obeys a power law dependence on radius. The exponent of the law is determined from the mass integral. Pressure profiles are obtained directly from the Tait equation of state, while velocity profiles are evaluated by integrating the continuity equation. The solution provides an insight into the role of the gas bubble formed by the explosive charge in driving the blast wave.

INTRODUCTION

Knowledge of blast waves in liquids is of primary importance to the theory of explosions in two respects: 1) evaluation of the effects of explosions, especially with reference to underwater events, and 2) enhanced understanding of micro-explosions in condensed phase explosives prior to their ignition. In both cases, the front of the blast wave propagates through the condensed medium, while, close to the center, there is a gas bubble formed by the blast initiator.

An analytical study of such phenomena is seriously handicapped by the scarsity of data on the equation of state for the shock compressed medium. However, since the most complete set of information now available is on water, having been obtained in connection with interest in underwater explosions, we have concentrated our attention in this study essentially on this case.

The most readily observable quantities in blast waves are the trajectory and strength of the leading shock wave. In the case of underwater explosions one has in addition data on the trajectory of the gas bubble created in the course of the energy deposition process. For point explosions the front trajectory is usually determined from the energy integral, e.g. Korobeinikov (1) and Sakurai (2), a procedure which requires an a priori knowledge of the profiles of gas-dynamic parameters throughout the flow field. There is one exceptional case of an approximate method developed in Manchester by the group of Chester (3), Chisnell (4), and Whitham (5), known as the Whitman

rule which does not require this information. It is applicable when the wave front becomes decoupled from the source of explosion, rendering the energy integral essentially meaningless, as in the case of the Guderley implosion or the Kaizer-Heyes solution of explosions in an exponential atmosphere (6). The rule is based on the postulate that only positive characteristics can influence the trajectory of the front, the feed-back conveyed by negative characteristics being negligible. Preliminary studies revealed that for the initial stages of explosions in liquids, as a consequence of the relatively low Mach number of the front, one may go one step further and simply assume that the slope of the positive characteristic is in effect equal to that of the front itself.

Thus, to obtain an analytical solution for blast trajectory and shock strength in terms of the initial charge radius, the differential equation for the positive characteristic is expressed in terms of referential derivatives with respect to front velocity. The trajectory of the front in the time-space domain is then determined by integrating the characteristic equation, while the thermodynamic parameters across the shock wave are evaluated by the use of a modified Tait equation of state that takes into account the effects of dissipation across the shock. The trajectory of the shock at the front and its strength, obtained in this manner, compare favorably with experimental results reported by both Hantel and Davis (7) and Coleburn and Roslund (8).

To gain an insight into the evolution of the flow field between the lead shock front and the gas bubble in the center, an approximate solution is obtained that, in essence, utilizes the density power law developed by Mel'nikova (9) and Bach and Lee (10). The analysis presented here is applied to experimental records of Coleburn and Roslund (8) obtained by the use of spherical charges of pentolite set off in water.

Specifically, the power law postulates that the density at any point in the flow field is proportional to the ratio of the radius of this point and that of the front raised to some power α. The value of this index is determined from the principle of mass balance expressed in terms of the mass integral between the front and the inner interface between the water and the gas bubble. The continuity equation is then directly integrated yielding the velocity profiles. Moreover, since the Tait equation of state provides a direct relation between density and pressure, space profiles relation between density and pressure, space profiles

of the latter are obtained directly from those of the former.

One should observe that our simplified method of analysis obviates the use of the equations of momentum and energy. The reason for this is that the results of the first could not be sufficiently accurate since they have to be based on the knowledge of the decay coefficient that has to be evaluated by triple differentiation of the front trajectory—a procedure requiring a much more precise data than those afforded by the experiment; the second, on the other hand, becomes superfluous as a consequence of the introduction of the density power law—a well established feature of analysis based on this device.

Finally, it should be pointed out that surface or buoyancy effects have been neglected. Thus, the validity of our results is strictly limited to the initial phase of explosion when the gas bubble formed by the initiator is still expanding, and before diffusion across the interface and the feed-back effects causing its oscillations become predominant.

FRONT TRAJECTORY ANALYSIS

For a non-steady, one-dimensional isentropic, but not necessarily homentropic, flow field, the equation for the positive characteristic can be written as follows, Courant and Friedrichs (11):

$$\delta p + \rho a\, \delta u + \frac{j\rho u a^2}{u+a}\frac{\delta r}{r} = 0 \qquad (1)$$

where r is the radius playing here the role of an independent space variable, while ρ, p, u and a are the density, pressure, particle velocity, and the local speed of sound, respectively, while j is a geometric factor equal to 0, 1, and 2 for plane, cylindrical and spherical geometries, respectively. In the above d expresses a referential derivative with respect to the absolute velocity of local sound waves, i.e., $\delta(\ ) \equiv \partial(\ )/\partial t + (u+a)\,\partial(\ )/\partial r$, where t denotes time.

As pointed out in the introduction, our analysis is based on the assumption that the slope of the positive characteristic can be identified with that of the front. This means that in the above equation $u + a = w$, where $w \equiv dR/dt$, the propagation velocity of the front, while $r = R$, its radius. Thus Eq. (1) becomes reduced to

503

$$dp + \rho a\, du + \frac{j\rho u a^2}{w} \cdot \frac{dR}{R} = 0 \qquad (2)$$

where d denotes the referential derivative with respect to the wave front velocity, w.

Thermodynamic properties of the medium are expressed in terms of a modified form of the Tait equation of state that takes into account the fact that the flow field is non-homentropic, so that the effects of energy dissipation at the front are taken into account, Richardson, et al. (12), namely

$$p = B\left[\left(\frac{\rho}{\rho_a}\right)^\nu - 1\right] \qquad (3)$$

where

$$B \equiv 3.134 - \frac{1.65}{10^3}(T - 328) -$$

$$\frac{1.181}{10^4}(T - 328)^2 + \frac{5.32}{10^7}(T - 328)^3 \text{ Kbar}$$

with the temperature T measured in degrees Kelvin. Subscript a in Eq. (3) refers to conditions of the undisturbed medium while ν is an index usually taken equal to 7.

To cast the formulation of the problem into a non-dimensional form, we introduce a field variable $x \equiv r/R$, a front variable $\xi \equiv R/R_o$, where subscript o refers to the initial radius of the explosive charge, and a shock strength parameter $\pi \equiv (p_n \div B)/B$ where subscript n denotes conditions immediately behind the shock front. Gasdynamic parameters of the flow field are expressed then in terms of the following non-dimensional variables:

$$U \equiv \frac{u}{a_a}, \qquad A \equiv \frac{a}{a_a}$$

$$h \equiv \frac{\rho}{\rho_a}; \qquad P \equiv \frac{p+B}{B}; \qquad f \equiv \frac{u}{w}$$

Local velocity of sound is expressed in terms of the sound speed modulus $\Gamma \equiv (\partial \ln p / \partial \ln \rho)_s$, so that $a^2 = \Gamma p/\rho$, while a_a is obtained from Eq. (3) for $B = B(T_a)$ whence, neglecting the change in liquid temperature during the isentropic process, $a_a^2 = \nu B(T_a)/\rho_a$.

On the basis of the above expressions, parameters of state of the medium immediately behind the shock front are evaluated from the Rankine-Hugoniot conditions combined with Eq. (3). One obtains thus the following relations, establishing the boundary conditions for the flow field and providing proper basis for the determination of its structure,

$$U_n = \left[\frac{(\pi^{1/\nu} - 1)(\pi - 1)}{\nu \pi^{1/\nu}}\right] \qquad (4)$$

$$A_n = \pi^{(\nu-1)/2\nu} \qquad (5)$$

$$P_n = \pi \qquad (6)$$

$$h_n = \pi^{1/\nu} \qquad (7)$$

and

$$f_n = \frac{\pi^{1/\nu} - 1}{\pi^{1/\nu}} \qquad (8)$$

while

$$y \equiv \frac{1}{M^2} = \frac{\nu(\pi^{1/\nu} - 1)}{\pi^{1/\nu}(\pi - 1)} \qquad (9)$$

With the aid of these expressions, Eq. (2) is reduced to a quadrature relating the shock strength π to the distance ξ, as follows

$$d \ln \xi = -\frac{1 + F(\pi)}{\nu j\, (1 - \pi^{-1/\nu})} d \ln \pi \qquad (10)$$

where

$$F(\pi) \equiv \frac{y^{1/2}}{2}[1 + (y\, \pi^{\nu+1/2\nu})^{-1}]$$

This is solved, subject to initial conditions specified by the initial Mach number of the shock (i.e., y_o) at $\xi = 1$ which, for the purpose of this analysis, was taken to correspond to the value of π behind the Chapman-Jouguet detonation wave in the explosive charge.

The initial motion of the interface may now be determined by noting that

$$f_i = x_i\left(1 + \frac{d \ln x_i}{d \ln \xi}\right) \qquad (11)$$

504

where subscript i denotes the condition immediately ahead of the interface. At $\xi = 1$, one may set $f_i = f_n$ which, with the aid of Eqs. (8) and (9), yields

$$y_o = \frac{\nu(1 - \delta_o)\delta_o^{\nu}}{1 - \delta_o^{\nu}} \qquad (12)$$

where

$$\delta_o \equiv (d \ln x_i / d \ln \xi)_{\xi = 1}.$$

The decay coefficient of the wave,

$$\lambda \equiv d(\ln y)/d(\ln \xi) = -2\,\dot{R}\,\ddot{R}/\dot{R}^2$$

where dots express time differentials as used by Newton, can then be expressed in terms of the shock strength as follows:

$$\lambda = \frac{j\pi(y - \pi^{-(\nu+1)/\nu})}{1 + F(\pi)} \qquad (13)$$

FIELD STRUCTU!

Upon establishing the trajectory of the front, it is of interest to inquire into the structure of the flow field. Of particular interest in this connection is the role played by the gas bubble in the middle of the blast wave: is it acting as a piston driving the wave, or as a void around the center that is created as a consequence of the motion imparted upon the liquid by the initial force of the explosion? In order to resolve this question, a very simple analysis leading to an algebraic solution is developed. As pointed out in the introduction, it is based on the assumption that the density of the liquid at any point in the flow field can be expressed as a power function of the radius, that is, in terms of the non-dimensional variables,

$$h = h_n\,x^{\alpha} \qquad (14)$$

where α is a function of ξ. The relation between them is established on the basis of the mass balance requiring the mass of the liquid engulfed by the front to be contained within a volume bounded by the interface and the front, i.e.

$$\int_{r_i}^{R} \rho\,r^j\,dr = \int_{R_o}^{R} \rho_a\,r^j\,dr$$

or, in non-dimensional form

$$\int_{x_i}^{1} h\,x^j\,dx = \frac{1 - \xi^{-(j+1)}}{j + 1}$$

where $x_i \equiv r_i/R$. With the aid of Eq. (14), one obtains finally

$$\alpha + j + 1 = \frac{(j + 1)\,h_n\,(1 - x_i^{\alpha+j+1})}{1 - \xi^{-(j+1)}} \qquad (15)$$

In the above, x_i can be expressed simply in terms of ξ, by postulating that

$$x_i = \xi^{-\delta} \qquad (16)$$

From experimental data it appears that the exponent δ is practically constant.

By virtue of the Tait equation of state, pressure at each point in the flow field is directly related with density by Eq. (3), provided that, as it is quite reasonable at the initial stages of the process, it is assumed that $B(T) = B(T_a)$. Hence

$$P = h^{\nu} \qquad (17)$$

Velocity profiles are obtained from the continuity equation which, in non-dimensional form can be written as, Oppenheim, et al. (13),

$$(f - x)\frac{\partial h}{\partial x} + h\,\frac{\partial f}{\partial x} + j\frac{f}{x} - \frac{\partial h}{\partial \ln \xi} = 0$$

With the aid of Eq. (14), and by using the outer and inner boundary conditions at the wave front and bubble, respectively, the above equation can be integrated to give

$$f = x\left\{(f_n - \theta \ln x) + \zeta\left(\frac{x_i}{x}\right)^{\alpha+j+1}\left[1 - x^{\alpha+j+1}\right]\right\} \qquad (18)$$

where

$$\theta \equiv \frac{d \ln(\alpha + j + 1)}{d \ln \xi}$$

while

$$\zeta \equiv \frac{1}{1 - x_i^{\alpha+j+1}}\,(h_n^{-1} - \delta + \theta \ln x_i)$$

505

RESULTS

The trajectory of the blast wave is displayed in
Fig. 1, while Fig. 2 describes the decay of the pres-
sure at the front as it moves away from the center of
explosion. The time coordinate in Fig. 1 has been
normalized to $\bar{t} = 1 + tD/R_o$, where D is the detona-
tion velocity in the explosive charge, and the shock
strength in Fig. 2 by its initial value of $R = R_o$. The
analytical results based on Ews. (10) and (13) are evi-
dently in good agreement with experimental observa-
tions of Hantel and Davis (7) and of Coleburn and
Roslund (8), obtained by exploding PETN and pento-
lite charges of various sizes under water. In order to
emphasize the relatively satisfactory character of our
results, they are compared in Figs. 1 and 2 with a cor-
responding solution obtained by the use of Whitham's
rule.

Figure 3 shows the decay coefficient plotted as a
function of the shock radius. The analytical results
obtained from our analysis are again closer to the
curve based on the correlation of experimental data

Fig. 2. *Decay of the strength of shock front with its*
radius.

Fig. 1. *Analytical and experimental trajectories of*
the wave front generated by underwater explosions
during the initial stages of propagation, and experi-
mental trajectory of the gas bubble interface.
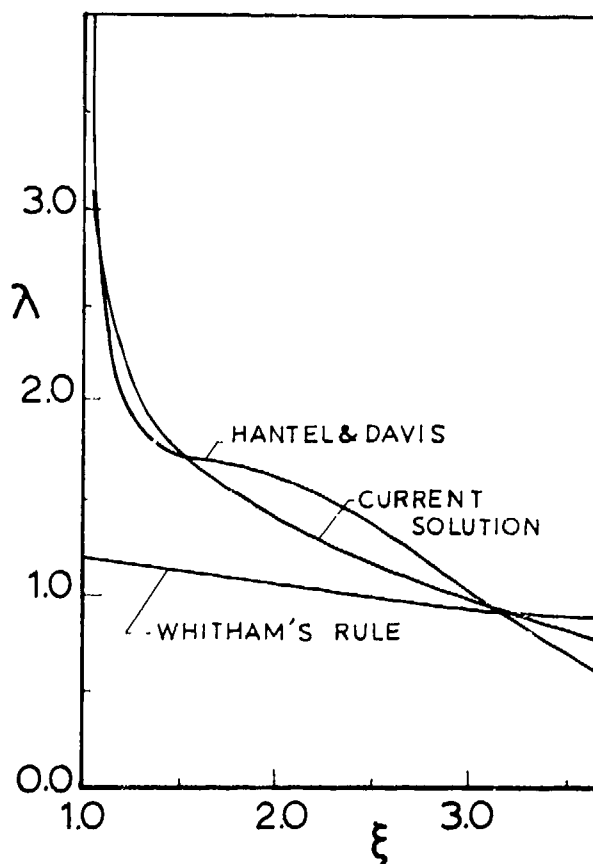
Fig. 3. *Dependence of the decay coefficient on front*
radius.

derived by Hantel and Davis, than those evaluated by the use of Whitham's rule. It is of particular interest to note the oscillatory behavior of the decay coefficient based on experimental data. As pointed out in the introduction, this annihilates effectively the utility of these data for the evaluation of the blast wave structure. Obviously, values of the slope of the undulating curve and of its derivative, that determine the magnitude of the decay coefficient on which such an evaluation crucially depends, would be most unreliable.

The trajectory of the front of the blast wave and of the interface between the gas bubble and water establish boundary conditions for equations describing the structure of the wave. Such conditions, expressed in terms of the density at the front, h_n, the front velocity parameter, y, evaluated from Eqs. (7),

(9) and (10) are shown in Fig. 4. Also displayed there is the trajectory of the interface according to experimental observations of Coleburn and Roslund (8). In the semi-log coordinates of Fig. 4 it plots as a straight line whose equation, obtained by a least square fit to experimental data, is

$$x_i = 0.99413 \, \xi^{-0.4734}$$

This yields for the exponent of Eq. (16): $\delta = 0.47$. The functional dependence of α on ξ, established on the basis of Eq. (15), has been also plotted on Fig. 4.

On this basis, the density, pressure and velocity profiles, for different values of front parameter $\ln \xi$, have been evaluated by the use of Eqs. (14), (17) and (18), respectively, and are displayed in Figs. 5-7.

CONCLUSIONS

The paper presents a simplified analysis of blast waves generated by underwater explosions. It demonstrates first the validity of extending Whitham's rule to its logical extreme by assuming that the velocity of the shock front is practically equal to that of the forward characteristic corresponding to conditions immediately behind it. The structure of the wave is then evaluated on the basis of an exponential dependence between the space coordinates of the inner interface and the front, with index determined from experimental observations.

Gasdynamic profiles exhibit a typical piston-driven nature of the blast wave, indicating that the energy of the explosion continues to be deposited into the

Fig. 4. Front parameters specifying boundary conditions for the evaluation of the flow field.
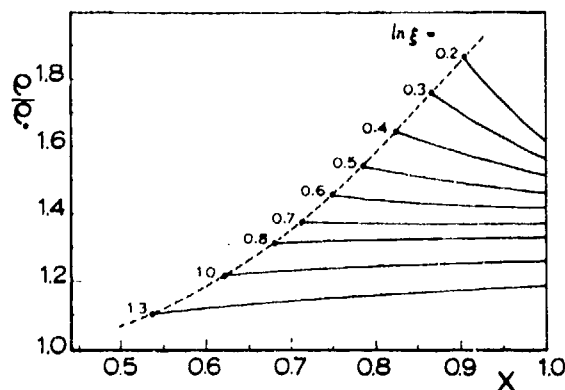
Fig. 5. Density profiles. The dashed line indicates the location of the interface.
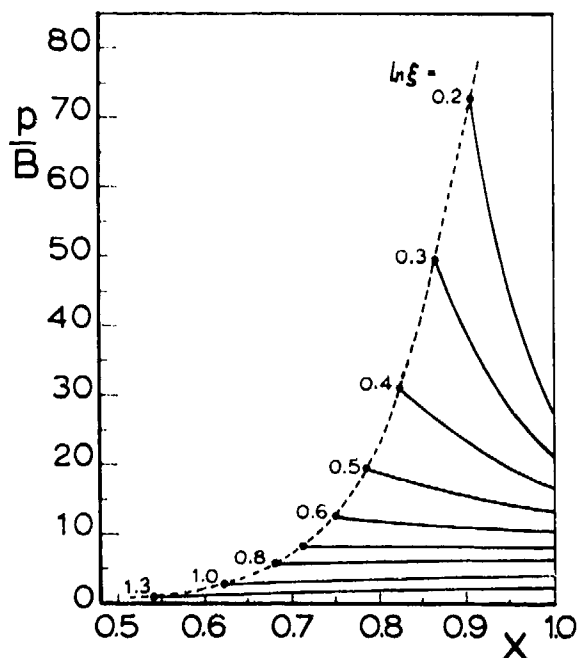
Fig. 6. Pressure profiles. The dashed line indicates the location of the interface.

Fig. 7. Particle velocity profiles. The dashed line indicates the location of the interface.

water through the action of the interface for a significant period of time after initiation. This provides an incentive for a more detailed analysis of the phenomenon, utilizing a more accurate equation of state for water and a more exact method of analysis.

Moreover, on the basis of our simplified analysis, a method could be devised for estimating the initial stages of underwater explosions from the knowledge of the energy of the ignitor as specified by its detonation velocity D, a measure of the density of exothermic energy, and its initial size, R_o. For this purpose, experimental evidence indicates that a value of 0.5 could be considered adequate to represent the interface index δ in Eq. (16), which could be used to estimate the trajectory of the interface. The front trajectory, on the other hand, may either be estimated directly from Fig. 1, by using the proper values of D and R_o, or by integrating Eqs. (9) and (10) to get $\xi = \xi$ (y), with a second integration yielding $\xi = \xi$ (t). To estimate the flow field structure between the front and interface, the value of δ may be substituted into Eq. (15) to give $\alpha = \alpha$ (ξ) which, in turn, is substituted into Eq. (14) to obtain the density distribution. The distributions of pressure and particle ve-

locity may then be determined from Eqs. (17) and (18), respectively.

REFERENCES

1. V. R. Korobeinikov, N. S. Mel'nikova and Ye. V. Ryazanov, The Theory of Point Explosion, pp. 332, Fizmatgiz, Moscow, 1961 (English translation, U.S. Department of Commerce, JPRS: 14,334 CSO: 6961-N).

2. A. Sakurai, "Blast Wave Theory," Basic Developments in Fluid Dynamics (Editor: M. Holt), Vol. 1, pp. 309-375, Academic Press, New York, 1965.

3. W. Chester, "The Quasi-Cylindrical Shock Tube," Phi. Mag. Ser. 7, Vol. 45, p. 1293, 1954.

4. R. F. Chisnell, "The Motion of a Shock Wave in a Channel, with Applications to Cylindrical and

Spherical Shock Waves," J. Fluid Mech., Vol. 2, pp. 286-298, 1957.

5. G. B. Whitham, "On the Propagation of Shock Waves Through Regions of Non-Uniform Area or Flow," J. Fluid Mech., Vol. 4, pp. 337-360, 1958.

6. G. G. Bach, A. L. Kuhl and A. K. Oppenheim, "On Blast Waves in Exponential Atmospheres," J. Fluid Mech., Vol. 71, pp. 105-122, 1975.

7. L. W. Hantel and W. C. Davis, "Spherical Explosions in Water," The Fifth Symposium (International) on Detonation, Pasadena, Office of Naval Research, ACR-184, pp. 599-604, 1970.

8. N. L. Coleburn and L. A. Roslund, "Interactions of Spherical Shock Waves in Water," The Fifth Symposium (International) on Detonation, Pasadena, Office of Naval Research, ACR-184, pp. 581-588, 1970.

9. N. S. Mel'nikova, "On a Point Explosion in a Medium with Variable Initial Density," Non-Steady Motion of Compressible Media Associated with Blast Waves (Editor: L. I. Sedow), Proc. V. A. Steklov Inst. of Math. in the Acad. of Science of the USSR, pp. 66-85, 1966.

10. G. G. Bach and J. H. Lee, "An Analytical Solution for Blast Waves," AIAA Journal, Vol. 8, No. 2, pp. 271-275, 1970.

11. R. Courant and K. O. Friedrichs, Supersonic Flow and Shock Waves, pp. 464, John Wiley and Sons, New York, 1948.

12. J. M. Richardson, A. B. Aron and R. R. Halverson, "Hydrodynamic Properties of Sea Water at the Front of a Shock Wave," J. Chem. Phys., Vol. 15, 1947.

13. A. K. Oppenheim, E. A. Lundstrom, A. L. Kuhl and M. M. Kamel, "A Systematic Exposition of

the Conservation Equtions for Blast Waves," J. of Applied Mechanics, pp. 783-794, 1971.

DISCUSSION

RUSSELL E. DUFF
Systems, Science and Software
La Jolla, California

The analysis presented is closely coupled to the observed motion of the gas bubble. Do you know if the reported motion was corrected for optical distortion caused by the spherical density field? If so, have you checked the correction with your calculated density profile? If not, how important is this neglect, based on your calculated profile, on the experimental data and on your analysis?

REPLY BY A. K. OPPENHEIM

The authors are obligated to Dr. Duff for the point he raised. They do not know whether Coleburn and Roslund have taken properly into account the refractivity effects in their observation of the motion of the interface between the gas bubble and water. However, it should be pointed out, the results of the analysis concerning the structure of the flow field depend significantly on the trajectory of the interface. Thus, if the data of Coleburn and Roslund are not accurate enough, the density profiles presented on Fig. 5, the pressure profiles presented on Fig. 6, and the particle velocity profiles presented on Fig. 7 may be in error.

EFFECTS OF ALUMINUM AND LITHIUM FLOURIDE ADMIXTURES ON METAL ACCELERATION ABILITY OF COMP B

Gert Bjarnholt
Swedish Detonic Research Foundation
Box 32058, S-126 11 Stockholm, Sweden

The ability to accelerate metal of Comp B and a cast RDX/TNT based explosive with 15% aluminum or lithium flouride admixture has been determined by streak camera recording of the radial motion of 25 mm ID copper tubes with a wall thickness of 2.28 mm loaded with explosives. Detonation data has also been calculated with a computer code using the BKW eos. From a comparison between calculations and experiments using lithium flouride to simulate aluminum inert in the explosive the aluminum reaction influence on the performance of the explosive could be studied. The first experimental evidence of a pressure increase caused by the reaction of the 30-60 μm aluminum was noticed about 4 μs behind the detonation. The final experimental aluminum reaction contribution to metal velocity was less than 35% of that predicted by expansion work calculations along the BKW CJ-isentrope.

INTRODUCTION

Detonation calorimeter experiments and thermo-dynamic calculations show that aluminum mixed into ordinary high density CHNO explosives gives a considerable increase in the chemically liberated energy of the explosive.

It is also known that the main part of the energy from the aluminum reaction can be converted to expansion work when these explosives are detonated under water (1). The products can then do work for relatively long times and to a low final pressure.

In short time high pressure applications however the performance of aluminized explosives are often disappointing.

In computer code calculations of detonation data of aluminized explosives one often finds that the isentrope through the CJ point falls below the non-aluminized explosive matrix isentrope in the high pressure region.

At some intermediate pressure along the CJ isentrope however the isentrope of the aluminized explosive crosses that of the explosive matrix and stays above during the rest of the expansion to atmospheric pressure.

The aim of this work has been to try to increase the knowledge of the mechanisms that limit the possibility to get increases in expansion work by adding aluminum to an explosive.

There are at least three possible mechanisms that can be of importance in limiting the performance of aluminized explosives.

1. A long burning time of the aluminum.
2. Nonequilibrium during the expansion between gaseous products and the main aluminum product Al_2O_3 which is present in condensed form.
3. Changes in the equation of state of the products caused by the aluminum admixture such that the internal energy is less efficiently converted to expansion work.

510

To get more information on the importance of these mechanisms we chose to study the effects of mixing aluminum and lithium flouride into a cast RDX/TNT explosive. The reason for the use of lithium flouride was that it should effect the explosive performance very much the same as aluminum if the aluminum was behaving inert in the explosive.

EXPERIMENTAL

The cylinder test was the experimental technique chosen to determine the performance of the explosives. In this test the radial motion of the walls of an explosive loaded metal cylinder detonated from one end is measured (2, 3, 4).

Our standard test consists of a 24.96 mm ID, 29.52 mm OD and 300 mm long copper cylinder filled with explosive. Specifications are given in Fig. 1. The explosive is detonated from one end and a streak camera records the radial motion of the copper wall through conventional shadowgraph technique.

The streak camera recording (Fig. 2) gives radius versus time data from which position, velocity, acceleration and energy of the cylinder wall can be calculated. From acceleration data the pressure in the products can be determined.

A high intensity argon flash driven by explosives was used as a light source behind the cylinder.

A ϕ 52 mm plane wave lens and a booster of pressed 93 PETN/7 wax was used to initiate the explosives.

The velocity of detonation was determined conventionally by measuring the interval between closure of two ionization contacts.

EXPLOSIVES MATERIAL STUDIED

The explosives chosen for this investigation were cast 60 RDX/40 TNT (hexotol 60/40, 42.5 RDX/42.5 TNT/15 Al (hexotonal 15) and 42.5 RDX/42.5 TNT/15 Lif (hexotolif 15). Data on the explosives are summarized in Table 1. The two types of aluminum powder used were both so-called atomized aluminum having irregularly shaped grains with a free Al content higher than 98.5%. The lithium flouride of purum quality was ground until it had the same particle size distribution as the coarser of the two aluminum powders. The particle size distribution of the Al and Lif is given in Fig. 3.

The explosives were cast in copper tubes with an inner diameter of 24.96 ± 0.10 mm, outer diameter 30 mm. The temperature of the explosives when casting was 83-84°C and the moulds were preheated to 85-90°C. For each type of explosive three identical charges were made. Two were used for the cylinder test experiments and one was used to check the density and the Al and LiF content at the upper and lower ends of the charge.

EVALUATION OF STREAK CAMERA RECORDINGS AND FITTING OF DATA

The streak camera recordings were evaluated by means of a coordinate microscope. About 60 points
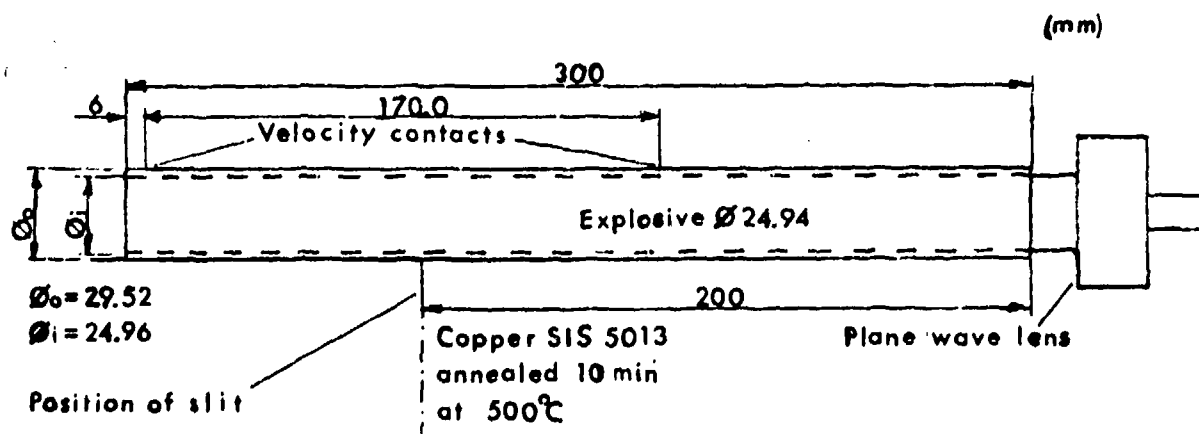
Fig. 1. Specifications on cylinder test arrangement.

511
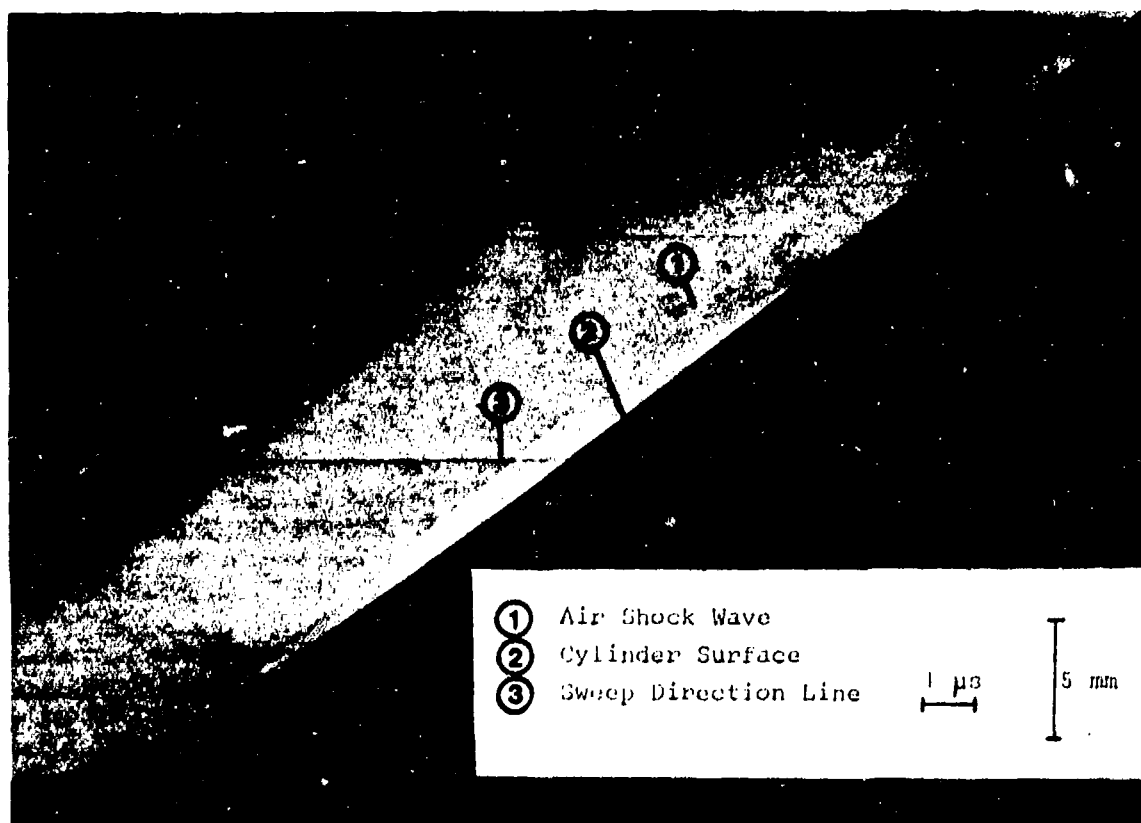
Fig. 2. Streak camera recording of cylinder test #5 (hexotol 60/40).

on the recording were transformed to displacement-time data. The displacements were then corrected for light diffraction in the air shock.

The optical observation of the expansion of the cylinder wall is disturbed by the air shock that is formed outside the expanding wall. The correction Δr needed to determine the real position of the wall from a streak camera recording is:

$$\Delta r = R' \left[\frac{\eta(n_o - 1) + 1}{n_o} \right] - 1 \qquad (1)$$

for

$$R'/R_s < \frac{n_o}{\eta(n_o - 1) + 1}$$

where R' is the apparent outer radius of the cylinder wall, R_s is the radius of the air shock formed outside the wall, n_o is the refractive index of the undisturbed

air and η is the compression (V_o/V) of the air between the cylinder wall and the air shock front.

Shock wave data for air was taken from reference (5).

The real radius R of the outer cylinder surface is then obtained from:

$$R = R' - \Delta r \qquad (2)$$

The correction Δr can be expressed as a function of the apparent displacement along the streak camera slit $(R' - R_o)$. R_o is the original outer radius of the wall. The same correction $\Delta r = f(R - R_o)$ shown in Fig. 4 was used for all shots because the compression η of the air is not very sensitive to the differences in performance of the explosives tested in this paper.

In Fig. 5 an example of the early time streak camera recording of a cylinder test is shown.

512

TABLE 1

DATA ON THE EXPLOSIVES

		Hexotol 60/40	Hexotonal 1580	Hexotonal 15100CS	Hexotolif 1580
RDX	weight%	58.9	42.1	42.1	42.1
TNT	" %	39.9	42.1	42.1	42.1
Wax	" %	1.2	0.8	0.8	0.8
Al	" %	–	15.0	15.0	–
LiF	" %	–	–	–	15.0
From analyses of test charge					
Al^* (upper end)	weight%	--	15.0	15.0	–
Al^* (lower end)	" %	–	15.2	15.2	–
LiF^* (lower end)	" %	--	–	–	15.1
Density (mean)	g/cm^3	1.691	1.758	1.758	1.758
Density (upper end)	g/cm^3	1.687	1.755	1.756	--
Density (lower end)	g/cm^3	1.690	1.762	1.762	1.760
Voids	volume%	1.1	2.3	2.3	2.1

Al and LiF particle size is given in Fig. 3.
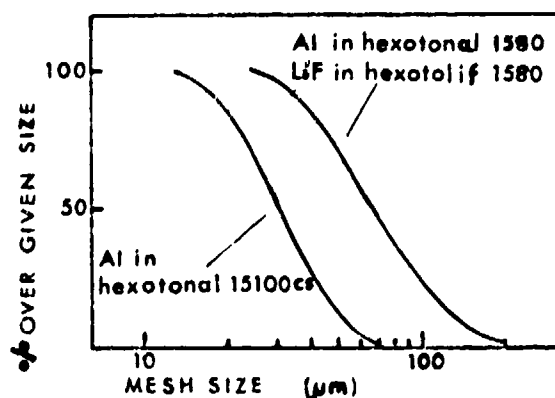
Fig. 3. Particle size distribution of Al and LiF.

The reproducibility of radius-time data in the test is normally better than 0.5%. For comparison $\Delta r/(R-R_o)$ is 1.8% for $R-R_o$ = 1 mm, 0.6% for $(R-R_o)$ = 5 mm, and 0.3% for $(R-R_o)$ = 30 mm.

The original thickness of the cylinder walls varied between 2.28 and 2.31 mm for the shots in this paper. Displacement-time data were normalized to a wall thickness of 2.28 mm the following way. If $t' = f(R-R_o)$ is valid for a wall thickness of S we have for wall thickness 2.28 mm
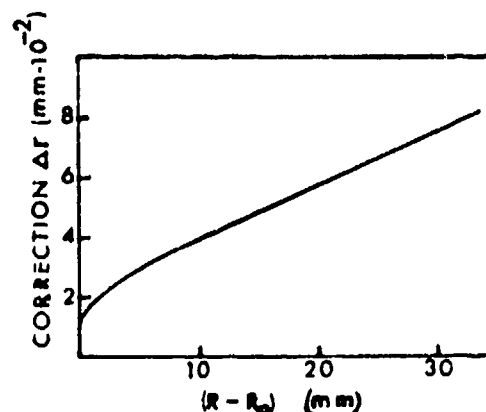
Fig. 4. Correction for light diffraction in air shock in ϕ 30 mm cylinder test.

$$t = t'\sqrt{\frac{S}{2.28}} \qquad (3)$$

An expression of the form used by Hoskin et al (6).

$$t = A + B(R-R_o) + C \exp D(R-R_o) \qquad (4)$$

was then fitted to the experimental t, $(R-R_o)$ normalized coordinates for every shot. Here t = time

513
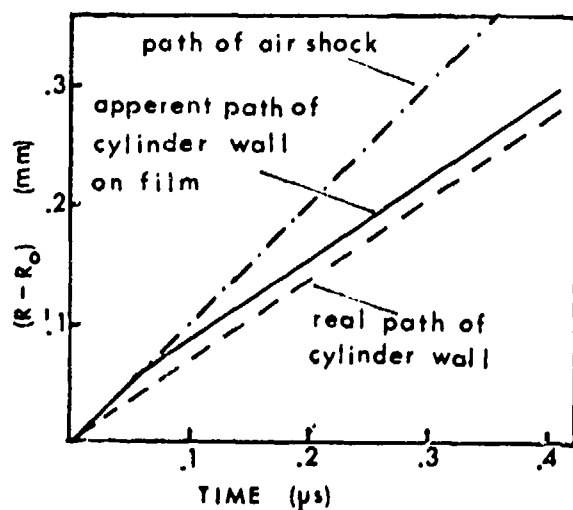
Fig. 5. Streak camera recording of cylinder test at early times with influence of air shock on recording.

from the start of the expansion and A, B, C and D are constants in the fit. This was done for $(R - R_o)$ = 5,6, ... 30 mm.

In Fig. 6a and 6b one can see how the fit is reproducing the experimental time coordinates. The first part of the expansion from $(R - R_o) = 0$ to 5 mm where internal shocks in the cylinder wall are still of importance cannot be described by formula (4). The details of the early time behaviour of the wall have been treated by Wilkins (7).

The initial velocity which stays constant for about 1 μs can be evaluated by a straight line fit to the displacement time coordinates during the first microsecond of movement.

RESULTS

Experimental Data

Two shots of respectively hexotol 60/40, hexotonal 1580 and hexotonal 15100CS were fired. For hexotolif 1580 only one experiment was made. The reproducibility of the displacement versus time coordinates was normally better than 0.5%.

As representative of the explosives tested shot #5 was chosen for hexotol 60/40, #6 for hexotonal 1580, #8 for hexotonal 15100CS and #10 for hexotolif 1580. Detonation velocity was measured

for every shot. Results are given in Table 2. The aluminum and the lithium flouride had the same lowering effect on detonation velocity. From 7630 m/s for pure hexotol 50/50 to about 7500 m/s with 15% Al or LiF.

The initial velocity of the cylinder wall calculated from a straight line fit to the displacement versus time coordinates during the first 0.75 mm of the expansion is given in Table 4. This velocity reflects the pressure at and very close to the front. It is the same within the experimental error for hexotonal 1580, hexotonal 15100CS, and hexotoilif 1580. This indicates that the front pressure in these explosives is the same. Hexotol 60/40 however gives about 9% higher velocity indicating about 10% higher front pressure.

When one compares the early time movement of the wall for the different explosives one finds that the expansion for hexotolif 1580 starts to lag behind that of hexotonal 1580 and 15100CS after about 4-5 mm of expansion corresponding to about 4 μs behind the detonation front. This indicates that a considerable part of the aluminum must have reacted within 4 μs.

For the expansion from 5 to 30 mm the expression (4) was fitted to the expansion data. Values of constants in the fit together with displacement-time, and displacement-velocity calculated from the fits are presented in Table 2 and 3 and Fig. 7.

The wall velocity was highest for hexotol 60/40 during the whole expansion to $(R - R_o) = 30$ mm. The velocities for hexotonal 15100CS and 1580 at this expansion were 3.5 respectively 4.1% lower than that for hexotol 60/40.

It should be pointed out that the displacement-time data one gets from a streak camera recording as in Fig. 2 does not describe the motion of one and the same point of the cylinder wall. Therefore the velocity one gets from direct differentiation of formula (4) is not the true particle velocity of the wall but rather a phase-velocity.

The difference between the two velocities is however so small that it can be neglected in most cases. In the experiments in this work for example the particle velocity of the wall is at the most $\cong 1.5\%$ lower than the velocity we get from direct differentiation of the streak camera data.

514
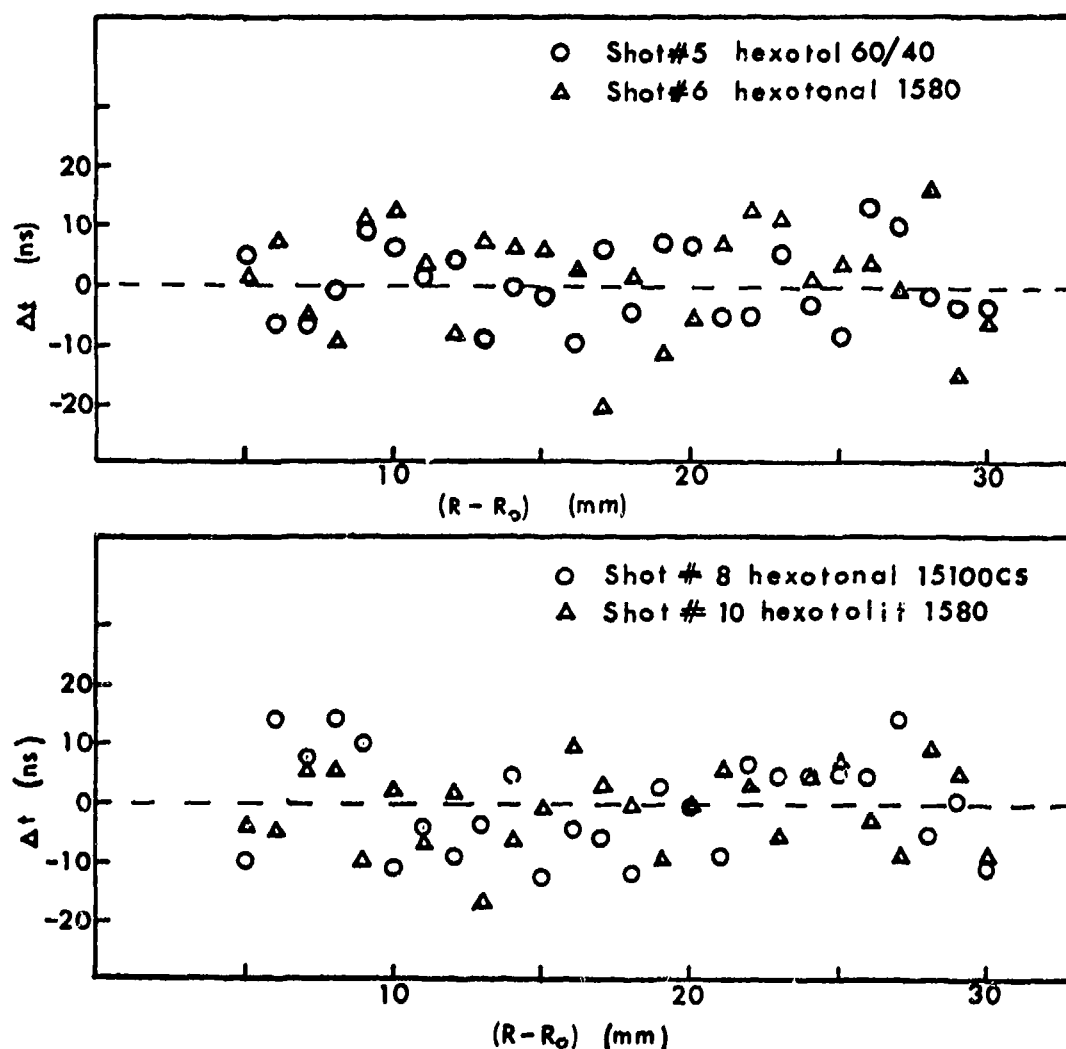
Fig. 6a and b. Difference between experimental and fitted time at given expansions.

COMPUTER CODE CALCULATIONS

Results from calculations performed by Roger Holmberg at this laboratory with a computer code for detonation data calculations developed at Los Alamos Scientific Laboratory with a BKW eos (8) are shown in Table 5.

The velocity of detonation is lowered (1%) if the aluminum is assumed to react before the CJ-plane compared to the case where it is considered inert and only melts.

In Table 5 one can also see that the aluminum reaction increases the CJ pressure about 3% and that the temperature is raised considerably by the aluminum reaction. The front of the detonation wave is thus not strengthened very much by the aluminum reaction.

The main part of the aluminum reaction energy at the front goes into thermal energy.

ESTIMATION OF THE WORK DONE BY THE EXPLOSIVES

From thermodynamic considerations one should expect the work done by most CHNO ideal explosives in a isentropic expansion from detonation conditions

515

TABLE 2

CYLINDER TEST RESULTS NORMALIZED TO COPPER CYLINDER

$\phi_i = 24.96\ mm,\ \phi_y = 29.52\ mm$

Shot #	Explosive	Density g/cm³	Detonation velocity m/s	Time t (μs)/velocity v_c(mm/μs) at (R-R$_0$) = (mm)					
				5	10	15	20	25	30
5	Hexotol 60/40	1.691	7810	4.44	7.74	10.85	13.86	16.80	19.71
				1.45	1.57	1.64	1.68	1.71	1.72
6	Hexotonal 1580	1.757	7490	4.84	8.38	11.69	14.86	17.96	21.01
				1.35	1.47	1.55	1.60	1.63	1.65
8	Hexotonal 15100CS	1.759	7510	4.77	8.31	11.59	14.73	17.79	20.81
				1.34	1.48	1.57	1.62	1.65	1.66
10	Hexotolif 1580	1.758	7510	4.81	8.45	11.87	15.19	18.44	21.66
				1.32	1.42	1.49	1.53	1.55	1.56

The explosive matrix in hexotol 15100CS and 1580 and hexotolif 1580 is 50 RDX/50 TNT. With the same void volume as in hexotonal 15 the experimental detonation velocity of this matrix is estimated to be 7630 m/s.

TABLE 3

RESULTS OF FIT TO EXPERIMENTAL
WALL EXPANSION DATA FOR
$5 \leqslant (R\text{-}R_o) \leqslant 30\ mm$

Shot #	$t = A + B(R\text{-}R_0) + C \exp D(R\text{-}R_0)$			
	A	B	C	D
5	2.573	0.5733	-1.778	-0.11424
6	3.118	0.5989	-2.240	-0.11239
8	3.038	0.5945	-2.281	-0.12204
10	2.616	0.6364	-1.845	-0.12400

TABLE 4

INITIAL RADIAL WALL VELOCITY

Shot #	Explosive	Initial velocity (m/s)
5	hexotol 60/40	721 ± 15
6	hexotonal 1580	648 ± 15
8	hexotonal 15100CS	665 ± 15
10	hexotolif 1580	663 ± 15

to atmospheric pressure in the products to be close to the heat of detonation $(-\Delta H_d)$ of the explosive. The expansion in the cylinder test can be approximated by an adiabatic expansion from the CJ-point down to that expansion where products start to leak out through cracks in the wall (3, 6).

We have found that this happens at an expansion of $(R - R_o) \cong 35$ mm in our cylinder test. The corresponding pressure in the products is then of the order of some hundred bars and the total work done is of the order of 80-90% of the work available in an expansion to atmospheric pressure.

Jacobs has proposed a model for calculation of the isentropic expansion work W to a final pressure P_o (9). With this model one gets

$$W = \int_{P_1}^{P_o} P(v)dv - \frac{u_1^2}{2} \qquad (5)$$

$P(v)$ = isentrope of the products through the CJ point

P_1 = pressure at the CJ point

TABLE 5

RESULTS FROM BKW CODE CALCULATIONS

Explosive	Hexotol 60/40	Hexotonal 15	Hexotonal 15	Hexotolif 15
Remark		$Al \rightarrow Al_2O_3$ at the CJ-plane Al, Al_2O_3 compressible	Al inert (melting only) Al compressible	LiF inert (melting only) LiF compressible
Density (g/cm^3)	1.690	1.758	1.758	1.758
Detonation velocity (CJ) (Experimental value)	7921 (7820)	7421 (7490)	7497 (7490)	7485 (7510)
CJ pressure (GPa) CJ temperature (K)	26.9 2669	24.6 4783	23.9 2363	23.7 2333
Heat of detonation[1] at the CJ-point. (MJ/kg)	5.81	7.61	4.87	4.88
On the isentrope through the CJ point at 0.1 GPa (MJ/kg)	5.70	6.71	4.76	4.78

[1] ΔH (standard state 298 K and 1 bar).

TABLE 6

EXPERIMENTAL ENERGY PARTITIONING AT $(R-R_o)$ = 30 MM IN CYLINDER TEST

Explosive			Hexotol 60/40	Hexotonal 1580	Hexotonal 15100CS	Hexotolif 1580
A.	Kinetic energy of the metal	MJ/kg[1]	3.01	2.70	2.67	2.38
B.	Kinetic energy of the reaction products	MJ/kg[1]	0.71	0.65	0.66	0.59
C.	Internal energy[2] in the metal	MJ/kg[1]	0.2	0.2	0.2	0.2
D.	PdV-work against the surrounding air	MJ/kg[1]	0.02	0.02	0.02	0.02
W =	A + B + C + D. Total work done in the expansion to $(R-R_o)$ = 30 mm	MJ/kg[1]	3.9	3.6	3.6	3.2

[1] MJ/kg of explosive
[2] Private information, C. Mader, LASL

P_0 = final pressure in the expansion

u_1 = particle velocity of the products at the CJ point.

With this model and data from the BKW calculations W has been calculated for the explosives tested in this investigation. Together with the experimentally determined work the data are presented in Fig. 8.

In Table 6 the total experimental expansion work as summed at an expansion $(R - R_0) = 30$ mm is presented.

DISCUSSION OF RESULTS

It is reasonable to assume that LiF behaves mainly inert in our explosive. Such physical properties as density, compressibility, melting point and boiling point are very similar for LiF and aluminum. LiF should thus affect the detonation properties of the explosive very similary to aluminum if aluminum behaves inert.

From Table 5 one can also see that the code predicts the same detonation velocity and detonation

pressure within 1% for hexotonal 15 with aluminum inert and hexotolif 15. Detonation pressure however is raised about 3% and detonation velocity lowered about 1% when aluminum is inert and only melts.

In the experiments the same detonation velocity within the experimental error of about ± 0.2% was recorded for hexotonal 15 and hexotolif 15. The initial wall velocity was also the same within an experimental error of about ± 2%.

According to the BKW code calculations the aluminum reaction influences the velocity and pressure conditions at the front very little. Therefore nothing can be said about the degree of aluminum reaction from the experimental detonation velocity and initial wall velocity data. It is only after some initial expansion that the aluminum reaction can give a marked pressure increase. In our experiments the wall velocity for hexotonal 15 starts to increase when compared to that of hexotolif 15 after about 4 μs of expansion.

M Finger et al (4) could also see the first effects of the aluminum reaction about 3 μs behind the front when they studied 5 μm Al in al HMX based explosive in the cylinder test. The time of the first
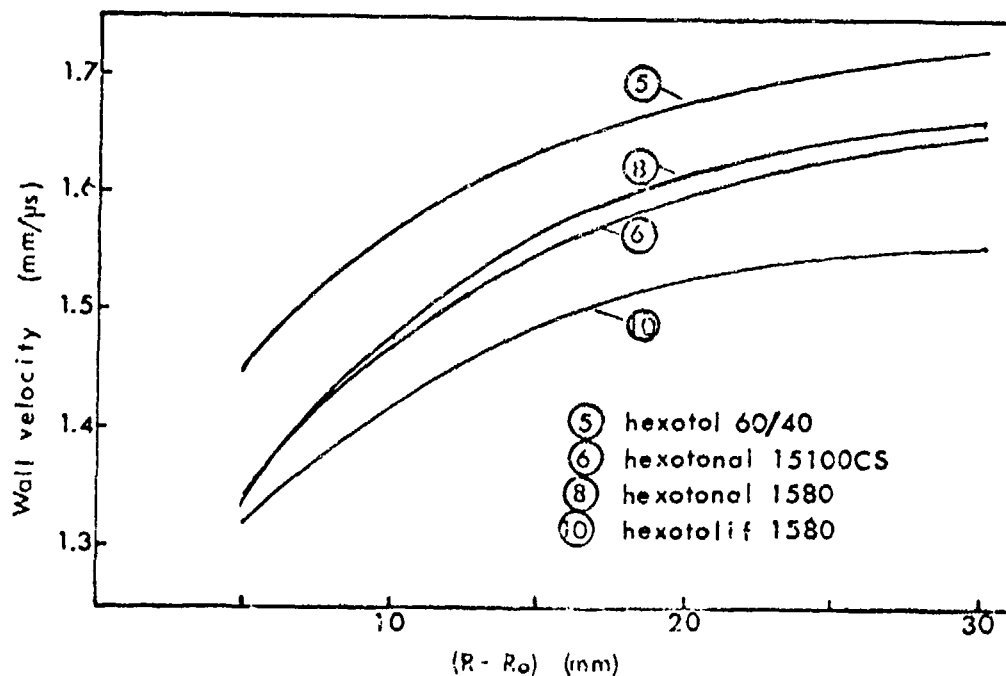
Fig. 7. Wall velocities calculated from the fit to experimental displacement-time data for
$(R - R_0)$ between 5 and 30 mm.

pressure increase does thus not seem to be changed markedly if one uses 5 μm or 30-60 μm aluminum.

If one uses the fit (4) to calculate the acceleration of the wall at an expansion of $(R - R_o) = 25$ mm, hexotonal 15100CS and 1580 shows about 55% higher acceleration than hexotolif 1580 indicating 55% higher pressure in the products at this expansion.

To summarize the question of the degree of aluminum reaction in the explosives, our data can be used to say that the first sign of aluminum reaction appears at about 4 μs behind the front. Our data does however not allow us to say anything about the degree of reaction in the region between the front and 4 μs thereafter.

The difference in performance between hexotonal 1580 and 15100CS is very slight. About 1% higher wall velocity was observed for hexotonal 15100CS than for hexotonal 1580 at expansions larger than 10 mm. The difference in performance one gets between

30 μm Al and 60 μm Al is thus just barely significant in the experiment.

The expansion work calculated along the BKW isentrope is much larger than the total expansion work from the experimental data (Fig. 8). This confirms the observation made by Kury et al (3) that metal acceleration to relatively large expansions in cylinder geometry is poorly predicted on an absolute basis by an expansion work calculation along the BKW eos isentrope. If one compares the products composition and the heat of detonation calculated along the BKW isentrope for hexotol 60/40 with experimental detonation calorimeter products composition and heat of detonation data for Comp B (11) which is very similar to hexotol 60/40 one finds that the main part of the absolute discrepancy can be explained by differences between the calculated and the experimental products composition and heat of detonation. For hexotol 60/40 the heat of detonation $(-\Delta H)$ calculated along the CJ isentrope down to 0.1 GPa varies between 5.7 and 5.8 MJ/kg. For
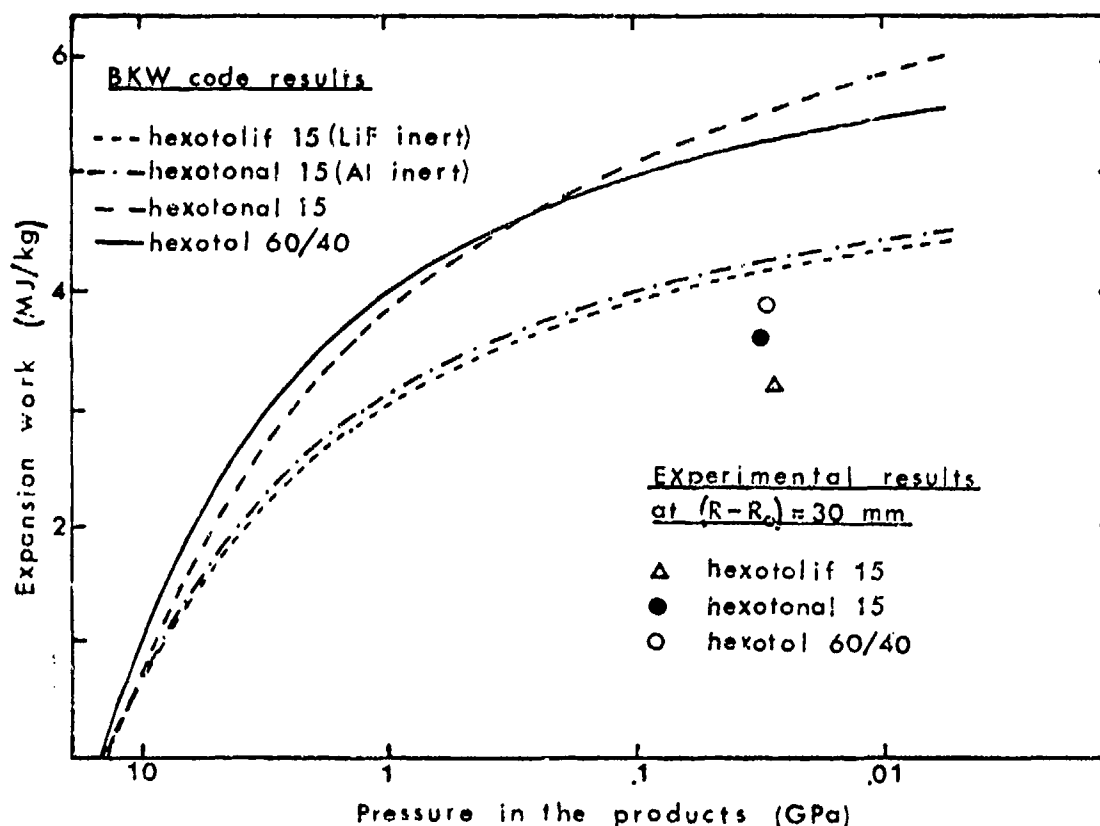
Fig. 8. Expansion work calculated along the BKW isentrope and experimental expansion work determined at $(R - R_o) = 30$ mm.

519

Comp B a heat of detonation of 4.69 MJ/kg i.e. 18% less was determined in a detonation calorimeter which allowed the products to expand fairly isentropically (11).

Fig. 8 shows that the experimental difference in expansion work between hexotonal 15 and hexotolif 15 is much smaller than that calculated by the BKW code. According to the experiments, hexotonal 15 yields only 12% more expansion work at $(R - R_o) =$ 30 mm than hexotolif 15 instead of the 31% difference calculated by the BKW code. Even if we take into account that the code tends to overestimate energies at large oxygen deficits the discrepancy is too great to be explained by this alone.

We must conclude that some assumption basic to the calculation is violated. The BKW code assumes that there is thermodynamic equilibrium between solid and gaseous reaction products and that the reactions are completed at the CJ-plane.

We conclude that under the experimental conditions either, or both of these assumptions are violated and that nonequilibrium and/or a low reaction rate of the aluminum is responsible for much of the difference between the calculated and the experimental yield of expansion work from the aluminum reaction.

ACKNOWLEDGEMENTS

REFERENCES

1. G. Bjarnholt, "Strength Testing of Explosives by Underwater Detonation," Swedish Detonic Research Foundation, Stockholm. Report DS 1975:8 (1975).

2. E. L. Lee et al, "Adiabatic Expansion of High Explosive Detonation Products," University of California, Livermore. Report UCRL 50422 (1968).

3. J. W. Kury et al, "Metal Acceleration Ability of Chemical Explosives," Proceedings Fourth Symposium (Int) on Detonation, Office of Naval Research, Report ACR-126 (1965).

4. M. Finger et al, "Metal Acceleration by Composite Explosives," Proceedings Fifth Symposium (Int) on Detonation, Office of Naval Research, Report ACR-184 (1970).

5. W. E. Deal, "Shock Hugoniot of Air," J. of Applied Physics, 28, No. 7 (1957).

6. N. E. Hoskin et al, "The Motion of Plates and Cylinders Driven by Detonation Waves at Tangential Incidence," Proceedings Fourth Symposium (Int) on Detonation, Office of Naval Research, Report ACR-126 (1965).

7. M. Wilkins, "The Use of One- and Two-Dimensional Hydrodynamic Machine Calculations in High Explosive Research," Proceedings Fourth (Int) Symposium on Detonation, Office of Naval Research, Report ACR-126 (1965).

8. C. Mader, "A Code for Computing the Detonation Properties of Explosives," Los Alamos Scientific Laboratory, Report LA 3704 (1967).

9. S. J. Jacobs, Navord Report 4366, Naval Ordnance Laboratory, White Oak, Silver Spring, Maryland (1965).

10. J. E. Kennedy, "Gurney Energy of Explosives: Estimation of the Velocity and Impulse Imparted to Driven Metal," Sandia Laboratories, Sandia Corporation, Livermore, California. Report SC-RR-70-790 (1970).

11. H. C. Hornig, Private information (1973), Lawrence Livermore Laboratory, California.

ACCELERATION OF SPHERICAL METAL SHELLS BY HIGH EXPLOSIVES: DETONATION VELOCITY ALONG THE SHELL SURFACE AND EFFICIENCY OF ENERGY TRANSFER

H. U. Freund, W. Geiger, and G. Honcia
Battelle-Institut, Frankfurt, Germany

The acceleration of spherical aluminum shells loaded on the outside with high explosive (Composition B 60:40) was investigated for various radii of the liner and various thicknesses of the explosive layer. Detonation was initiated through a small detonator at one point of the explosive surface (pole). For polar angles of 0 to 90° both the velocity of the detonation front and the liner velocity were measured. A decrease of the detonation velocity with decreasing radius of the liner is observed along the liner surface. The variation of the liner velocity with polar angle was measured for various shell radii and explosive thicknesses. From these data the efficiency of energy transfer from the explosive to the liner is deduced. The results are compared to a modified detonation head theory.

1. INTRODUCTION

For charges with curved liners it is important—e.g., for the purpose of projectile development—to know for each liner segment the time at which it is being set into motion by the explosive and what is its final velocity. The aim of the work described in this paper was to determine the dependency of the liner velocity on the charge parameters in the spherical case, mainly the radius of curvature and the explosive to liner mass ratio.

2. EXPERIMENTAL SETUP

.Spherical aluminium shells with wall thicknesses of 2 to 3 mm and radii of 30, 60 and 120 mm were loaded on the outside with high explosive (Composition B 60:40) of constant thickness in the range of 10 to 60 mm. The explosive was cast onto the shells. The charges were ignited on one point (pole) through a small detonator. The detonation front is traced for polar angles from 0° to 90° (120° in some cases) by small coaxial pin contacts inserted into the explosive

charge as shown in Fig. 1. The array of pins allows the detonation velocity to be determined along a straight line through the point of ignition in the bulk of the explosive as well as along the explosive/liner interface in the shadow region. i.e. the region not seen from the ignition point.

In addition the initial motion of the liner is measured through slightly modified pins placed inside the spherical liner. An array of such pins is shown in Fig. 2. In order to avoid mutual disturbance of the pins the bundle of pin tips had to be spread laterally as indicated. A close-up construction view of the two types of pin contacts is given in Fig. 3. A total set of 30 pins was employed. The short circuit signal of each pin allowed the measurement of the time of arrival of the detonation front and of the liner surface accurately to ±10 ns and ±20 ns respectively. The exact pin tip positions were taken from X-ray photographs for the pins embedded in the explosive and through special callipers for the pins inside the spherical shell. The estimated errors are 1/20 mm and ./10 mm respectively.
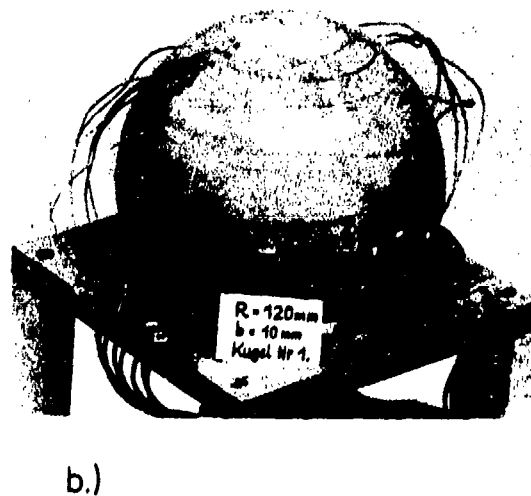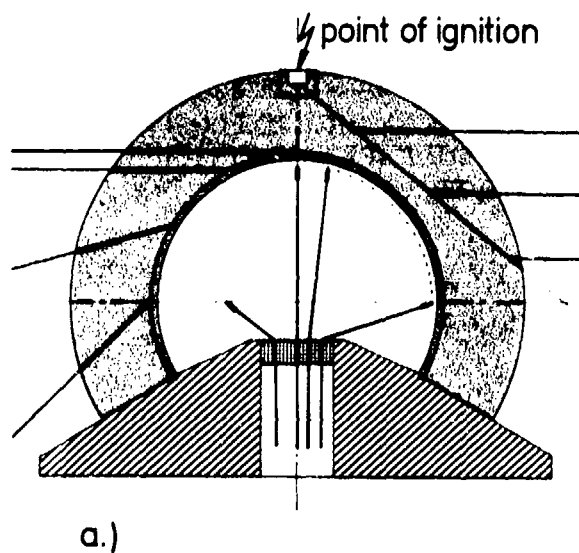
Fig. 1. Pin array to measure the detonation front velocity. a.) schematically, b.) real setup.
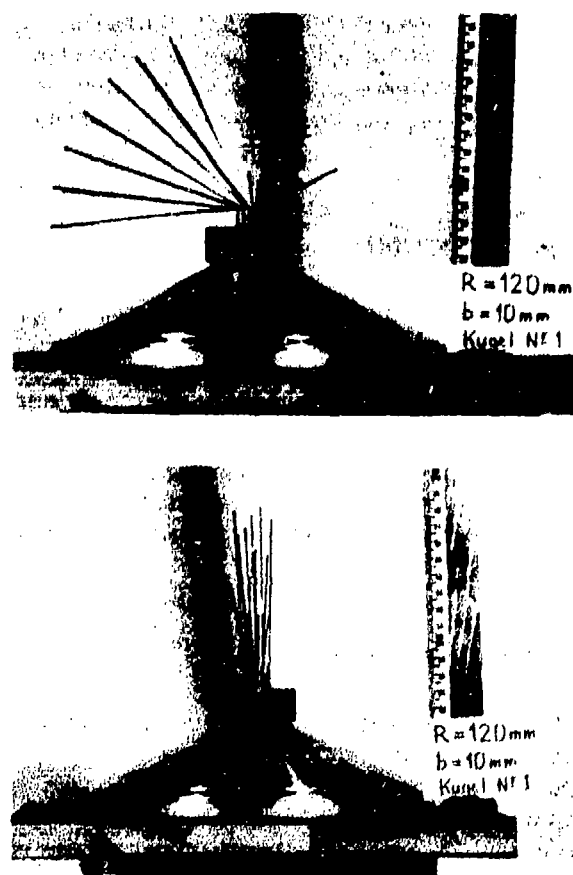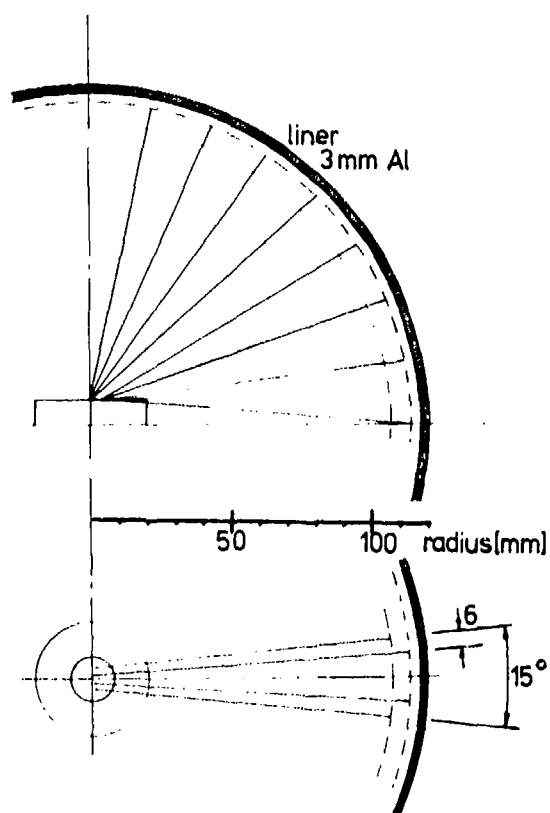
Fig. 2. Pin array to measure the liner velocity for a sphere with radius R = 120 mm and explosive layer thickness b = 10 mm. a.) schematically, b.) real setup.

522

3. RESULTS

(a) Detonation Velocity

The detonation velocity along the explosive/liner interface in the shadow region was compared to the unperturbed detonation velocity in the explosive bulk. A decrease of the detonation velocity is observed in the shadow region. The smaller the radius of the sphere the more pronounced is this effect. Within the experimental error limits this reduced detonation velocity can be regarded constant and independent of the explosive thickness. The results are summarized in Fig. 4. Also included in this figure there are experimental values obtained from cylindrical charges with point ignition at the cylinder surface. As can be expected the reduction effect is smaller and about one half of that for a sphere of the same radius. The experimental data for the variation ΔD of the detonation velocity D are well represented by a formula similar to one given by Chéret (1)

Fig. 3. Pin types used for measurement of: a.) detonation velocity and; b.) liner velocity.
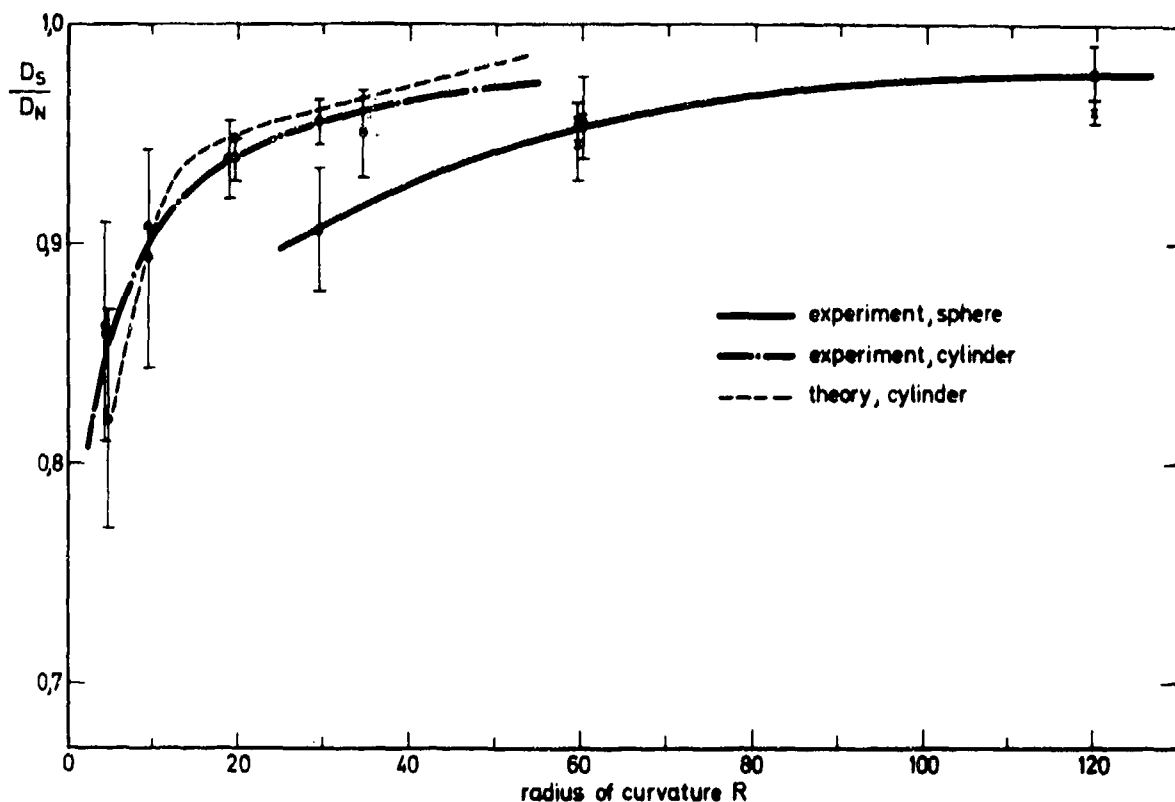
Fig. 4. Decrease of detonation velocity along curved liner surface.

523

$$\frac{\Delta D}{D} + \alpha \cdot \frac{k}{R} = 0 \qquad \text{with} \quad \alpha = 1 \text{ for cylinders}$$

$$\alpha = 2 \text{ for spheres}$$

$$\text{and} \quad k = 1 \text{ mm for Comp. B}$$

For the cylindrical case an estimate on the basis of Chapman-Jouguet's theory has been made. While the detonation proceeds along the curved surface the pressure is reduced by a certain amount due to lateral expansion of the reaction zone (i.e. the zone within which pressure determines the continuous reinitiation of the detonation front) into the shadow region. As a consequence the detonation velocity will be reduced. Assuming the reaction zone to have a thickness of 1.5 mm the theoretical curve fits the experimental data quite well as shown in Fig. 4.

(b) Initial Liner Velocity v_0

From the pin measurement inside the spherical shell the contours of the collapsing shell in the initial phase have been mapped. The liner velocity was obtained from these contours. Figure 5 shows an example of the diagrams of the liner location s versus time along the polar angle $\theta = 30°$ direction. A first order approximation for the initial velocity v_0 was obtained from the initial slope of the $s(t)$ curve. This value was corrected by taking into account the Taylor deflection angle. As can be seen there is a marked
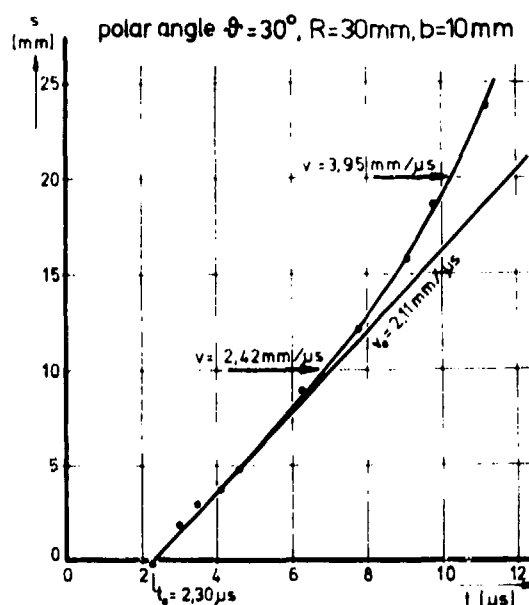
Fig. 5. Definition of initial liner velocity v_0.

increase in the liner inner surface velocity after about 4 μs due to the convergent flow of the liner material. Experimental values for the initial liner velocity v_0 were determined along the meridian for values of θ from 0 to 90°. In Fig. 6 these data have been plotted
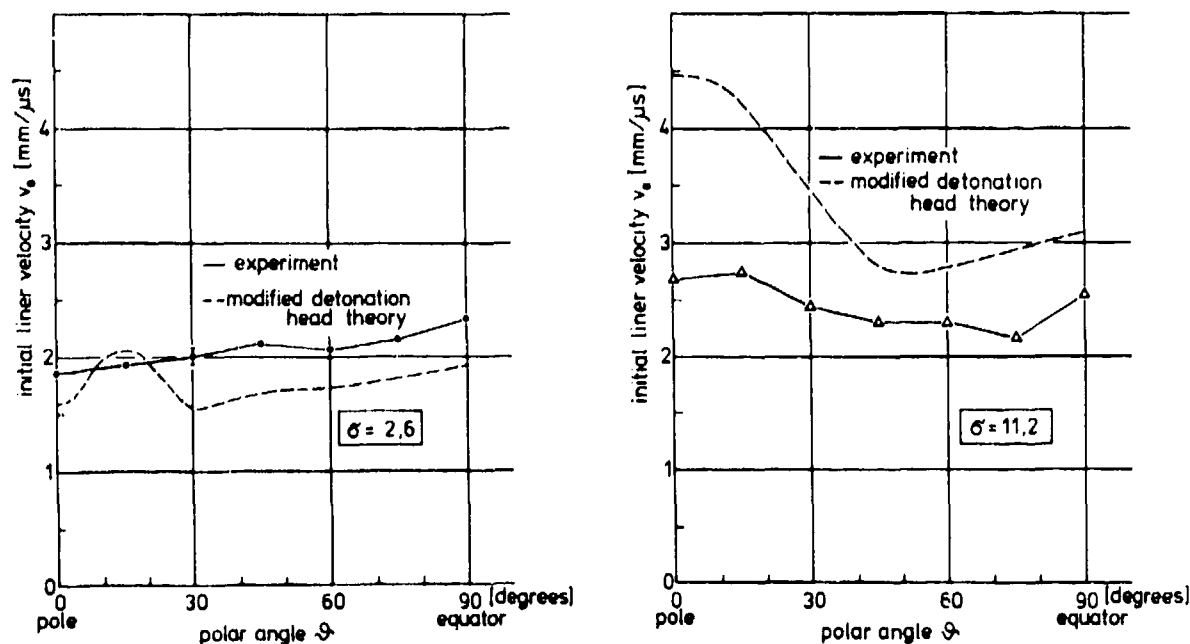
Fig. 6. Initial liner velocity v_0 as function of polar angle for spheres with $R = 60$ mm, $b = 10$ and 30 mm respectively ($\sigma = 2.6$ and 11.2, respectively).

524

for two different radii and explosive thicknesses. As can be seen there is a general tendency for increase of v_0 with increasing polar angle θ above $45°$. For large explosive thicknesses a pronounced higher velocity v_0 occurs in the polar region.

A theoretical model was used to interpret the results. As a first step the interaction time t_1 of the explosive/liner system was obtained from simple detonation head theory. It is assumed that following the detonation a rarefaction wave moves into the explosion products from the free surface(s) at a constant velocity and decreases the full detonation pressure to zero. The period of time between the arrival at the liner surface of the detonation front and the rarefaction wave is taken as t_1. The arrival time of the rarefaction wave is derived from geometrical construction as shown in Fig. 7. The detonation wave at 7.7 mm/μs is followed from the outer surface of the explosive by a rarefaction wave moving with 5.8 mm/μs. The rarefaction which originates from the explosive/liner interface as the liner is set into motion is neglected in this picture.
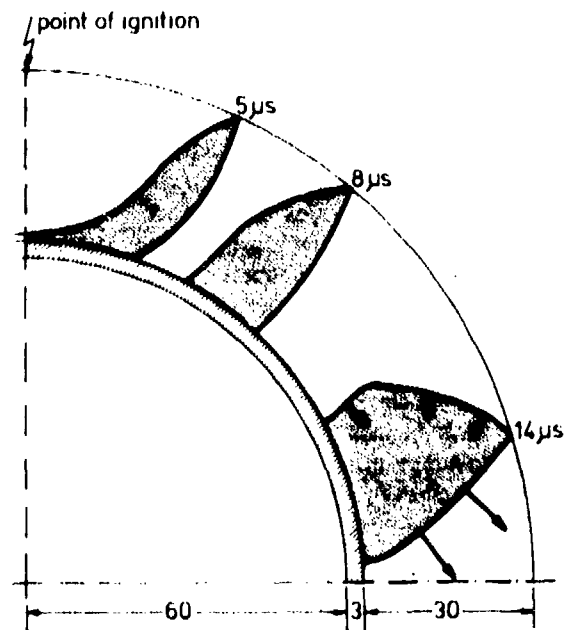
Fig. 7. Shapes of detonation head at 3 different times after ignition for a spherical shell with R = 60 mm, b = 30 mm.
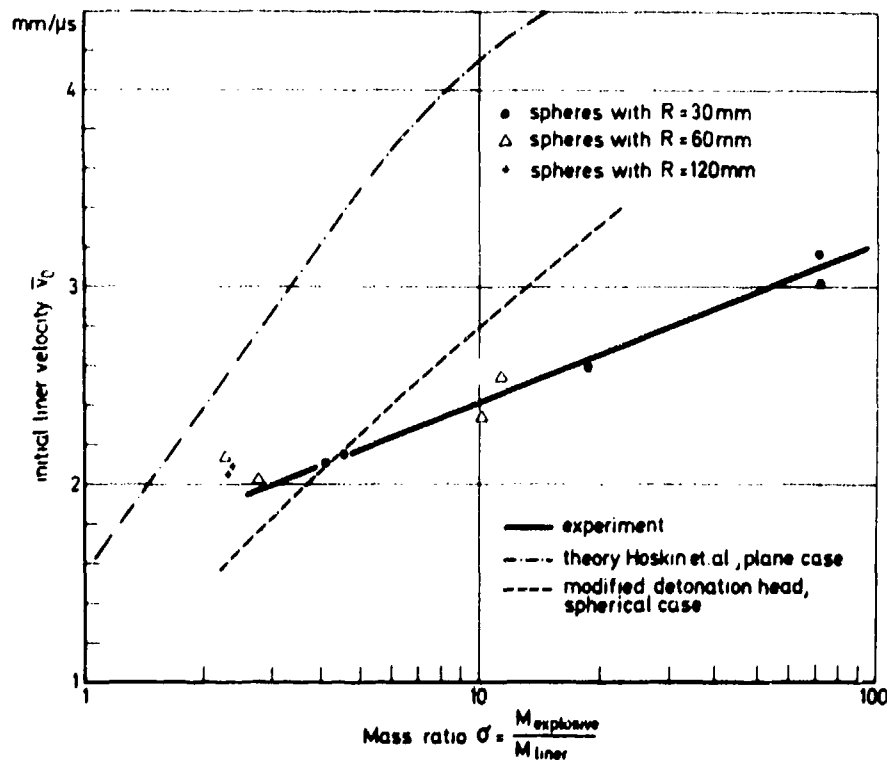
Fig. 8. Mean value of initial liner velocity as function of mass ratio.

In a second step, however, this latter rarefaction wave is taken into account. An analytical description by Schramm (2) for the acceleration of a metal sheet by an infinitely thick layer of explosive is used. The liner velocity v_0 is taken as the velocity which the liner has attained at time t_1.

The calculated values are represented by dashed lines in Fig. 6. It is obvious that in the polar region the experimental curves are much smoother than the calculated ones. Also the strong dependence of the average liner velocity (averaged over the half sphere) on the explosive thickness is not verified experimentally. This can be seen more clearly from Fig. 8 where the average initial liner velocity $\bar{v}_0$ is plotted versus the explosive to liner mass ratio σ. This ratio σ is defined analogous to the plane case mass ratio as indicated in Fig. 9. The experimental results justify this definition which includes the curvature: All experimental points for different radii are located along a smooth curve within an error bar of about 10%. This also holds when the kinetic energy of the liner is related to the explosive energy as shown in Fig. 10. A value of $E_0 = 4.1 \cdot 10^3$ J/g for the specific explosive energy has been used. The efficiency of energy transfer varies from 20% to 1% and falls below the theoretical estimates.
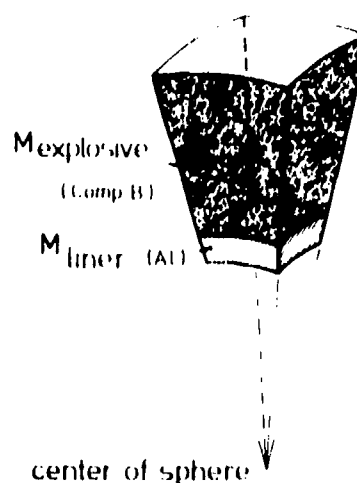
Fig. 9. *Definition of mass ratio σ for a segment of spherical charge.*

Comments on the modified detonation head model: At small polar angles the initial velocity v_0 is mainly affected by the decrease in the pressure acting on the liner with increasing angle of incidence of the detonation front. The described model seems to overemphasize this effect. Also the model yields a too strong dependence of v_0 on the explosive thick-
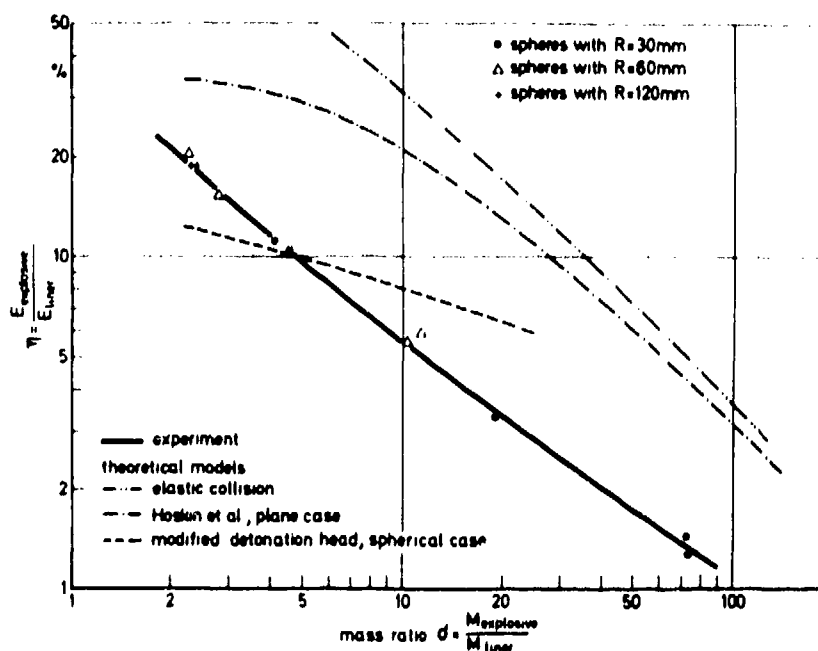
Fig. 10. *Efficiency of energy transfer as function of mass ratio.*

ness. This is probably due to the fact that the effective interaction time t_i for the radially expanding explosive products is overestimated.

REFERENCES

1. R. Chéret, "Theoretical Considerations on the Propagation of Shock and Detonation Waves," IVth Symposium on Detonation, Report ACR-126, p. 78 ff., 1965.

2. K. H. Schramm, "Dynamisches Verhalten von Metallen unter Stoßwellenbelastung," Springer Tracts in Modern Physics. Vol. 58, p. 262 ff., 1971.

DISCUSSION

M. VAN THIEL
Lawrence Livermore Laboratory
Livermore, California

We have done some 2-dimensional Lagrange calculations to see if the data presented by Dr. Freund could be predicted by our computer models. This was especially of interest, since the approximate release wave model presented by the authors suggested that some shock effects might be occurring that suggest that energy delivery scales in an unpredictable fashion, perhaps due to an unexplained physical phenomenon.

The results of the computer calculations indicated that their experiments conform to our models and that therefore there was nothing wrong or unexpected in their experiments.

We used the JWL equation of state form described by Finger, Lee, et al. with constants derived from the tabulation in the compilation of B. Dobratz. The explosive energy and density was scaled from the values for 64/36 Comp. B given in the compendium for the composition of the 60/40 Comp. B used by the authors.

Experimentalists and theoreticians who at present do not have access to a computer to do such calculations should be urged to attempt to get such access to aid their design and analysis work.

CALCULATED SPHERICAL SHOCK WAVES PRODUCED BY CONDENSED EXPLOSIVES IN AIR AND WATER

H. M. Sternberg and H. Hurwitz
Naval Surface Weapons Center
White Oak, Silver Spring, Maryland 20910

Spherical shock wave computations were made with a conventional Lagrangian artificial viscosity scheme, augmented by a sharp shock routine in which the main shock is fitted by the method of characteristics, with exact tracking of the shock inside the Lagrangian cells. It is shown that relatively small effects on air blast are produced by the use of a real air equation of state in place of an ideal gas equation, and by changing initial conditions so that initial transmitted pressures range between 170 and 720 bars. In water centrally detonated PBX 9404 is shown to produce a greater peak shock pressure than Pentolite, but a smaller impulse, because more energy is dissipated in shock heating of the water. A constant volume Pentolite explosion in water with initial density one fourth that of the solid explosive is shown to yield about 30% more usable energy than the centrally detonated charge, due to less energy dissipation. This energy comes out of the HE gas bubble slowly and is manifested mainly as an increase in impulse. At 10 charge radii from the center, a constant volume Pentolite explosion in water with initial gas density equal to that of the solid explosive produced a peak shock pressure 11% greater and a p^2dt integral 14% greater, when compared with a centrally detonated charge with the same density and energy.

INTRODUCTION

The limited possibility of a large increase in energy output from high explosives detonated in air or water has stimulated interest in the extent to which the available energy can be used more efficiently. It seems clear that if the energy is released very slowly much of it will remain in the explosive gas. On the other hand, the energy dissipated due to shock heating of the surrounding medium will increase with the strength of the transmitted shock. This has led to speculation that there is an optimum energy release for the purpose of producing a strong shock wave. The effect of energy release is examined here by hydrodynamic computation of three cases, all with the same total energy, covering a wide range of transmitted pressures. These are the shock waves produced by a centrally detonated high explosive sphere, by a constant volume sphere (explosion product gas initially at uniform pressure and density) at the density of the solid high explosive, and by a constant volume sphere with a larger initial radius and one fourth the density of the solid explosive. Other items treated here are the effects of computing with a real gas equation of state for air, instead of an ideal gas equation, and a comparison of calculated shock wave parameters obtained with Pentolite (50/50 TNT/ PETN) and the more energetic, higher detonation pressure explosive PBX 9404-3 (HMX/NC/CEF94/3/3).

The finite difference scheme, in which Lagrangian artificial viscosity method is used, and the equation of state used for water, are described in previous papers by W. A. Walker and one of the authors.[1,2] A substantial change in the computational scheme,

made recently and used in the present work, is outlined in Sec. II. This is the addition of a procedure for producing a sharp main shock in the spherical flow computations. The shock is tracked through the Lagrangian mesh by shock fitting, using the positive characteristic extended back from the shock to the previous constant time line. The method was tested against a power law similarity solution and results of this test are given.

Section III deals with explosions in air and Sec. IV with explosions in water. The differences in the nature of the explosion-produced spherical waves in air and water come about mainly from the thousand fold difference in density of the two media. It will be seen that the real air effects while large, have little influence on the shock wave from a high explosive because the total mass of air subjected to them is small.

The energy dissipated by shock heating is important because it determines the energy remaining to drive the shock. Methods which use the dissipated energy in the calculation have been quite successful in predicting peak shock pressures vs distance in air shocks from explosives, as in the work of Porzel[3], and Kirkwood and Brinkley[4]. In the present work the dissipated energies were found, after the finite difference calculations were completed, in order to complete the description of the energy partition and distribution in the wave.

II THE SHARP SHOCK

In the earlier computations[2], the smearing of the main shock over several computations cells in the artificial viscosity scheme was treated by introducing a finely zoned region which contained the shock and moved with it. Here, the shock is tracked through the Lagrangian mesh and exact values of its Lagrangian coordinate and position, and the related flow variables, are calculated at each time step. The result is a faster and more accurate computation.

For spherical flow the equations solved are

$$M(j) = 4\pi \int_{X(j_0)}^{X(j,t)} \rho X^2 dX, \qquad (1)$$

$$\partial u/\partial t = -4\pi X^2 \partial(p + q)/\partial M, \qquad (2)$$

$$\partial X/\partial t = u, \qquad (3)$$

$$\partial E/\partial t = -(p + q)\partial v/\partial t, \qquad (4)$$

$$p = p(E, v). \qquad (5)$$

Here, X is the distance from the center, ρ is the density (= 1/v), M is the mass, p is the pressure, q is the artificial viscosity, E is the internal energy, and u is the particle velocity. The independent variables are the time t and the Lagrangian label j. Equation (5) refers to the equation of state, used in conjunction with Eq. (4) to find E and p after v is gotten with Eqs. (1)-(3).

The procedure will be explained with Fig. 1. Let n be the time cycle in the finite difference computation, and let the mesh points correspond to integer values of j. Suppose everything is known at time t^n. In the advance to time t^{n+1}, one calculates, in the artificial viscosity scheme, u at $(j, n + 1/2)$, X at $(j, n + 1)$, and E, p, v, q at $(j - 1/2, n + 1)$. Denote the values of these variables at the main shock by $j_s(n)$, $X_s(n)$, $F_s(n)$, etc. Conditions ahead of the shock, being at the initial ambient state, are known. As the shock moves new mesh points are uncovered and values of the flow variables at these points must be computed. Until the shock has passed $(j + 1/2, n)$, the acceleration at (j, n) cannot be calculated from the usual finite difference formulas, which use the pressure at $(j + 1/2, n)$. Also, the specific volume at
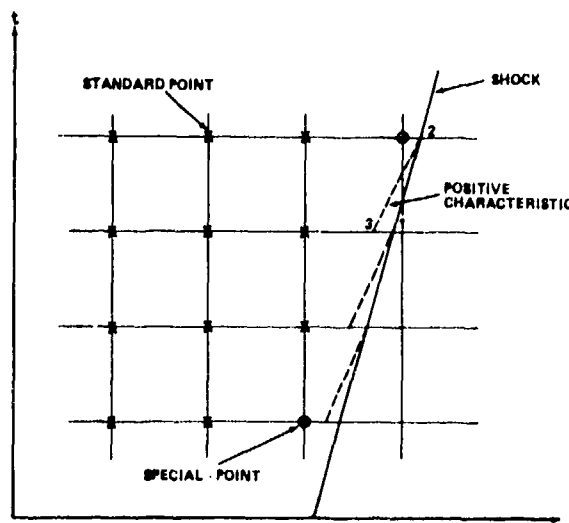
Fig. 1. Fitting the sharp shock in the Lagrangian artificial viscosity grid.

529

(j − 1/2, n + 1) cannot be calculated in the usual way if the shock is in the cell because $X(j, n + 1)$ is not available. Insofar as it was feasible the calculations for these special points were made with finite difference forms of the governing equations and not by interpolating between values at the shock and the points behind it. In Fig. 1., the mesh point (j, n) will be called a standard point, denoted by a cross, if $j_s \geq j + 1/2$. Otherwise (j, n) will be called a special point.

At each time cycle the computation begins with the calculation, for successive values of j, of the acceleration at (j, n), the velocity at $(j, n + 1/2)$, the position at $(j, n + 1)$, the relative specific volume $V(= v/v_0)$ at $(j − 1/2, n + 1)$, and the artificial viscosity at $(j − 1/2, n + 1/2)$. This is done for the standard points and followed by the sharp shock routine where the shock is fitted and values for the special points are calculated. After this, the pressures and energies at all the cell centers behind the shock are calculated, a new time step is determined from stability considerations, the total energy is checked, and a new cycle is started.

The only change from the previous scheme[1,2] in the calculation for the standard points is in the acceleration calculation where a three point formula is used. Denote the points $(j − 3/2, n)$, $(j − 1/2, n)$, $(j + 1/2, n)$, (j, n) by the subscripts 1, 2, 3, and 4 respectively. Recall that in the Lagrangian computation $M(j)$ is always known, since it is prescribed at the beginning of the calculation. Let $P = p + q$ and set

$$P = P_1 + a(M − M_1) + b(M − M_1)^2. \qquad (6)$$

The points 2 and 3 are then used to find

$$a = \frac{1}{(M_3 − M_2)} \left[\frac{M_3 − M_1}{M_2 − M_1} (P_2 − P_1) \right. \\ \left. − \frac{M_2 − M_2}{M_3 − M_1} (P_3 − P_1) \right], \qquad (7)$$

$$b = \frac{1}{(M_3 − M_2)} \left[\frac{P_3 − P_1}{M_3 − M_1} − \frac{P_2 − P_1}{M_2 − M_1} \right], \qquad (8)$$

and $(\partial P/\partial M)_j$ in Eq. (2) from

$$(\partial P/\partial M)_j = a + 2b(M_4 − M_1). \qquad (9)$$

To fit the shock the Rankine-Hugoniot conditions must be satisfied, viz,

$$E_s − E_0 = (p_s + p_0)(v_0 − v_s)/2, \qquad (10)$$

$$(u_s − u_0)^2 = (p_s − p_0)(v_0 − v_s), \qquad (11)$$

$$\rho_0(U − u_0) = \rho(U − u), \qquad (12)$$

and on the positive characteristic between the points 3 and 2 in Fig. 1

$$du + \frac{dp}{\rho c} = − \frac{2uc}{X} dt, \qquad (13)$$

$$\frac{dX}{dt} = u + c. \qquad (14)$$

Here U is the shock velocity and c is the sound speed. Starting values of U, c_s, and u_s at t^{n+1} are taken to be values at t^n. Equation (14) and interpolation of known values along t^n are then used to get X_3, u_3, c_3 in Fig. 1. The point 3 is where the positive characteristic extended back from the shock point at t^{n+1} meets the line $t = t^n$. Finite difference forms of (10), (11), (13), (5), and the sound speed formula derived from (5), are then solved simultaneously for p_s, E_s, V_s, c_s, and u_s. The shock velocity U at t^{n+1} is then gotten with Eq. (12) and the entire process, starting with the calculation of X_3, u_3, c_3, is repeated until it converges.

The exact value of j at the shock is calculated from

$$(dj/dt)_s = UX^2/(X_0^2 \partial X_0/\partial j), \qquad (15)$$

where the zero subscript refers to the initial ambient state and $X_0(j)$ is specified at the outset. Equation (15) is obtained from

$$U = (dX/dt)_s = (\partial X/\partial j)_t (dj/dt)_s + u \qquad (16)$$

combined with (12) and the mass conservation equation

$$\rho X^2(\partial X/\partial j)_t = \rho_0 X_0^2(\partial X_0/\partial j)_t. \qquad (17)$$

Calculation for the special points (open circles in Fig. 1) is done immediately after the shock fitting. Since j_s is known the mass in the partial cell between the shock and last mesh point behind it can be

calculated from the prescribed function M(j). If j, at t^n, is a special point and $j_s < j + 1/2$, the acceleration at (j, n) is calculated with Eqs. (7), (8), and (9), with M_3 and P_3 replaced by the M_s and P_s, the values at the shock, at t^n. If $j + 1/2 < j_s < j + 1$, Eqs. (7), (8), and (9) can be used directly, but a special calculation must be made for v at (j + 1/2, n + 1). The calculated mass in the partial cell and the values of X_j and X_s are used to get v at the midpoint of the partial cell. Then v at (j + 1/2, n + 1) is found by interpolation between the midpoint and the shock.

Special calculations are made to assign values to the flow variables when new integer or half integer values of j are uncovered as the shock moves outward. When the shock straddles j + 1/2, where j is an integer, E_s, P_s, v_s at j + 1/2 are gotten by interpolation between the shock points at t^n and t^{n+1}. These are then used as the previous values at j + 1/2 in calculating E and p at (j + 1/2, n + 1) with Eq. (4). The new u(i, n + 1/2) needed when the shock straddles an integer value of j is found by interpolation between the shock and j - 1.

The sharp shock procedure also includes special calculations for the initial flow at the interface between the HE gas and the surrounding medium. The initial conditions in the explosive gas sphere are either a constant state or a similarity solution for the detonation wave[1]. The exact transmitted shock conditions are calculated separately and applied at the boundary as initial conditions. The rarefaction wave in the HE gas next to the boundary is calculated, at the beginning, by the method of characteristics. This calculation is removed after a short time, so that the entire flow, except for the sharp main shock, is calculated by the artificial viscosity method. In spherical flow a second shock, with zero initial strength, forms at the tail of the rarefaction wave and moves back into the gas. In the calculations made to date this second shock was not put into the method of characteristics calculation, but formed in the artificial viscosity calculation after the special calculation was stopped.

The sharp shock scheme was tested with a known similarity solution. Suppose the pressure ahead of the shock is zero, and the equation of state of the medium is $E = pv/(\gamma - 1)$. If $\gamma = 7$, $\rho_0 = 1$, and a spherical piston with initial values $t_2 = 1$, $X_1 = 2.5$, $v = 1$, is moved into the medium with velocity $u_p = t^{-0.9}/4$, the conditions at the back of the driven shock are

$$U = t^{-0.6}, \quad p_s = t^{-1.2}/4, \quad X_s = 2.5t^{0.4} \qquad (18)$$

Table 1 contains a comparison of shock values calculated with the artificial viscosity program containing the sharp shock scheme, where the spherical psiton is constrained to move at the velocity $u_p = t^{-0.9}/4$, and the exact values calculated with Eq. (18). Note that this does not test the treatment of the interface in the computations with explosives. Also, it does not test the linear interpolation for the assigned particle velocity when the shock straddles an integer value of j, because the particle velocity in this similarity solution is linear with distance.

TABLE 1

Comparison of Shock Values Calculated with the Sharp Shock Procedure and with a Spherical Flow Similarity Solution, at t = 10087.3

	Sharp Shock Calculation	Similarity Solution
U	0.39631×10^{-2}	0.39625×10^{-2}
X_s	99.822	99.838
p_s	0.39266×10^{-5}	0.39253×10^{-5}

III EXPLOSIONS IN AIR

Spherical blast wave computations were made for the following five cases,

(1) Pentolite, centrally detonated in γ-law air ($\gamma = 1.4$),

(2) Pentolite, centrally detonated in real air, same radius as (1),

(3) PBX 9404, centrally detonated in real air, same radius as (1),

(4) Pentolite, constant volume explosion in real air, with initial HE gas density, ρ_0, of 1.65 g/cc, and the same radius and total energy as case (1),

(5) Pentolite, constant volume explosion in real air, with initial HE gas density of 0.4125 g/cc, the

531

same total energy as case (1), and initial HE gas radius of $4^{1/3}$ times that in case (1).

A comparison of cases (1) and (2) shows the effect on the calculation of the use of a real air equation where dissociation and ionization are taken into account. Cases (2) and (3), considered together, show the effect of a more energetic explosive (0.1020 mbar-cc/cc vs 0.0884 mbar-cc/cc for Pentolite) with a greater detonation pressure (370 kbar vs 245 kbar for Pentolite). Cases (2), (4), and (5) show the effect of a variation in initial conditions ranging from an initial transmitted pressure of 720 bars to a transmitted pressure of 180 bars. Except for case (5) the initial radii of the HE charges were identical, hence the PBX 9404 and Pentolite (cases (2) and (3)) are being compared on a volume basis.

The equation of state used for Pentolite was the same as that used in the earlier work[1,2], namely,

$$p = A\rho\epsilon + B\rho^4 + Ce^{-K/\rho}$$

with ρ in g/cc, ϵ the internal energy in mbar-cc/g, p in mbars, and A = 0.35, B = 0.002164, C = 2.0755, K = 6. The solid explosive density, the detonation velocity, the energy released and the Chapman-Jouguet (CJ) conditions were taken, as before, to be

$$\rho_0 = 1.65 \text{ g/cc}, \ D = 0.7655 \text{ cm}/\mu\text{sec},$$

$$E_0 = 0.0884 \text{ mbar-cc/cc}, \ p_s = 0.245 \text{ mbar},$$

$$C_s = 0.5714 \text{ cm}/\mu\text{sec}, \rho = 2.210 \text{ g/cc}.$$

For PBX 9404 the JWL equation with the constants listed for PBX 9404-3 in Ref. 5 was used. Here,

$$p = A\left(1 - \frac{\omega}{R_1 V}\right)e^{-R_1 V} + B\left(1 - \frac{\omega}{R_2 V}\right)e^{-R_2 V} + \frac{\omega E}{V},$$

where $V = v/v_0$, E is the internal energy in mbar-cc/cc, A = 8.545, B = 0.20493, R_1 = 4.60, R_2 = 1.35, ω = 0.25. The CJ parameters are ρ_0 = 1.84 g/cc, p_J = 0.370 mbar, D = 0.088 cm/μsec, c_J = 0.6513 cm/μsec, ρ_J = 2.486 g/cc.

The real air equation of state used in the calculations is that of Doan and Nickel[6]. Isentropes from various points on the shock Hugoniot from one atmosphere were calculated with this equation of state to get the dissipated energy, the excess energy remaining after expansion to one atmosphere, as a function of shock pressure. The process is explained in Ref. 2.

Some of the air results are shown in Table II, where calculated peak pressures and positive impulses (the pressure-time integral over the positive duration of the wave) are shown for the five cases considered, at times corresponding to various positions of the main shock. Notice first, from cases (1) and (2) that the effect of the real air is not large, the difference in peak pressure and positive impulse being 5% or less beyond five charge radii. Hence, for most purposes, computations with γ-law air would be satisfactory for solid high explosives. Comparison of cases (2), (4), and (5) in Table II shows that there are no significant differences in the peak pressures or positive impulses for shock positions beyond 25 charge radii, despite the variation in initial conditions. The largest differences when the shock is 25 charge radii from the center, 8% in peak pressure and 4% in positive impulse, are between cases (2) and (3), a consequence of the fact that the PBX 9404 charge contains 15% more energy than the Pentolite charge.

Figure 2 shows the calculated peak pressure vs distance for cases (2), (3), (4), and (5). Notice that the PBX 9404 curve lies a bit above the others. The shape of the curve for case (5), the constant volume explosion with ρ_0 = 0.4125 and initial radius equal to $4^{1/3}$ charge radii, is interesting, because this shape is observed experimentally when charges with metal casings are fired. The shapes are similar because there is relatively little energy transmitted into the air before the casing expands to 1.5 to 2.0 charge radii and breaks up. Except for the energy imparted to the casing, the system at the time the casing breaks up is like that in case (5).

The result that the positive impulse at 25 charge radii is essentially the same for the three Pentolite cases (2), (4), and (5) stems from virtually identical shapes of the pressure-distance curves extended from the shock back through the positive phase. This is reflected in the calculated pressure vs time curves shown in Fig. 3. On the scale shown, the positive phases for the three pentolite cases are the same. The PBX 9404 curve, case (3), lies slightly above the others.

A partial explanation for the lack of significant differences beyond 10 charge radii in the various cases considered can be found in the calculated cumulative dissipated energy vs shock position curves shown in Fig. 4. The expectation that large differences in dissipated energy per unit mass of air within the first few charge radii will result in different flows is not realized because the total mass of air in this region is small. Consequently, the total

amount of energy dissipated within the first few charge radii is small. Note in Fig. 4 that for all the cases considered, less than two percent of the total energy is dissipated by shock heating within the first three charge radii. Note, too, that the dissipated energy curves for the various cases lie close together over the entire range of the calculations (70-80 charge radii). This is used to good advantage in the work of Porzel[3].

TABLE 2

Calculated Peak Shock Pressure and Positive Impulse at Various Distances from the Center, for Spherical Explosions in Air*

	Charge Radius R/R_o	Peak Shock Pressure (mbar)	Positive Impulse $\int pdt$ (mbar-μsec)
(1) Pentolite, central detonation in γ-law air ($\gamma = 1.4$)	1	8.10×10^{-4}	
	5	1.40×10^{-4}	
	10	4.50×10^{-5}	
	25	6.92×10^{-6}	3.73×10^{-4}
	50	2.13×10^{-6}	4.64×10^{-4}
(2) Pentolite, central detonation in real air	1	7.20×10^{-4}	
	5	1.34×10^{-4}	
	10	4.27×10^{-5}	
	25	6.61×10^{-6}	3.69×10^{-4}
	50	2.09×10^{-6}	4.62×10^{-4}
(3) PBX 9404, central detonation in real air	1	$8.6 \ \times 10^{-4}$	
	5	1.56×10^{-4}	
	10	4.81×10^{-5}	
	25	7.13×10^{-6}	3.84×10^{-4}
	50	2.17×10^{-6}	4.70×10^{-4}
(4) Pentolite, constant volume explosion ($\rho o = 1.65$) in real air	1	3.05×10^{-4}	
	5	1.09×10^{-4}	
	10	4.81×10^{-5}	
	25	6.67×10^{-6}	3.72×10^{-4}
	50	2.09×10^{-6}	
(5) Pentolite, constant volume explosion ($\rho o = 0.4125$) in real air	1	1.72×10^{-4}	
	5	7.85×10^{-5}	
	10	4.07×10^{-5}	
	25	6.73×10^{-6}	3.67×10^{-4}
	50	2.09×10^{-6}	4.61×10^{-4}

*The initial radius is denoted by R_o, except when $\rho_o = 0.4125$, where the initial radius is $4^{1/3} R_o$. Charge radii are given in multiples of R_o. Hence, all comparisons for a specified value of R/R_o are made at the same distance from the center. This procedure is followed throughout the text and in all of the figures.

Insight into the process can be gained from the calculated energy partition curves shown in Fig. 5. Notice first, that for the PBX 9404 charge, Fig. 5(b), the kinetic energy of the HE gas, which is between 9 and 10 percent of the total when the detonation wave is at the charge surface, grows to 75% when the main shock is 3 charge radii from the center. At this time over 90% of the total energy is still in the HE gas. When the shock is at 50 charge radii, 11% of the total energy is in the HE gas, as internal energy. The HE gas is now separated from the main shock by a negative phase, and no longer has a part in driving the shock forward. A comparison of the energy partition curves for the centrally detonated PBX 9404 and Pentolite charges, Fig. 5(a) and 5(b), shows that the energy comes out of the HE gas in almost exactly the same way in both cases and that the energy partition in the air is almost exactly the same, although the kinetic energy, internal energy partition in the HE gas is somewhat different in the early stages. In the

constant volume case with $\rho_0 = 0.14125$, Fig. 5(c), the energy comes out of the HE gas more slowly, but the energy partition after the main shock has reached 50 charge radii is essentially the same as in the centrally detonated cases.

IV EXPLOSION IN WATER

The cases considered here cover a wide range of candidates for underwater explosives, from a high detonation pressure explosive (PBX 9404), where the initial pressure transmitted to the water is 228 kbar, to a relatively slow energy release where the initial transmitted pressure is 6 kbar. Peak pressure vs distance from the center, the integral of the pressure squared with respect to time, a measure of the energy flux[7], and the impulse, or integral of pressure with respect to time, are of interest. The results are explained in terms of the energy dissipated by shock heating of the water.
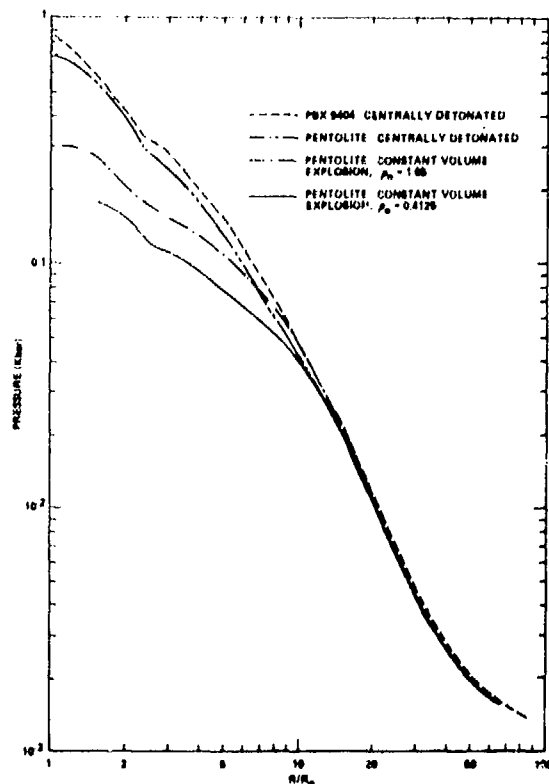
Fig. 2. Calculated peak shock pressure vs distance, for explosions in air.
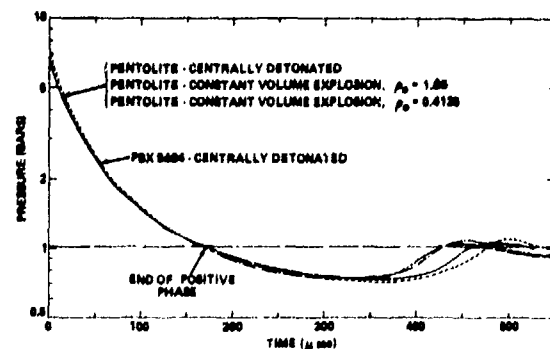
Fig. 3. Calculated pressure vs time at 25 charge radii from the center, for explosions in real air.
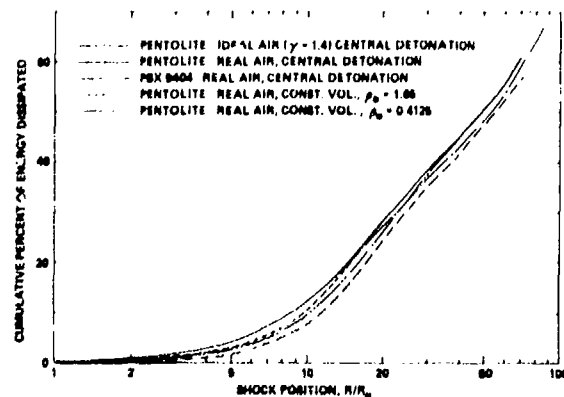
Fig. 4. Calculated cumulative percent of energy dissipated, for explosions in air.

Calculations were made for the following spherical charges in water,

(1) Pentolite, centrally detonated,

(2) PBX 9404, centrally detonated, same radius as (1),

(3) Pentolite, constant volume explosion, initial HE gas density 1.65 g/cc, same radius and total energy as (1),

(4) Pentolite, constant volume explosion, initial HE gas density 0.4125 g/cc, same total energy as (1), and initial HE gas radius $4^{1/3}$ times that in (1).

The equation of state used for Pentolite and PBX 9404 are listed in Sec. II. The equation of state used for water, and the related dissipated energy function are taken from Refs. (1) and (2).

Figure 6 shows the calculated peak shock pressures vs distance for the four types of charges. Peak pressures at several positions, together with the values of the p^2 dt integral are listed in Table III. Consider first the two centrally detonated cases. Note that the peak pressure for the PBX 9404 is consistently greater than that of the Pentolite, 15% larger at 10 charge radii and 7% larger at 20 charge radii. However, the

Fig. 5(a). Pentolite, centrally detonated
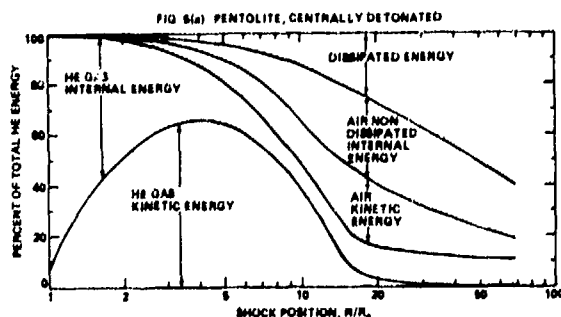
Fig. 5(b). PBX 9404, centrally detonated
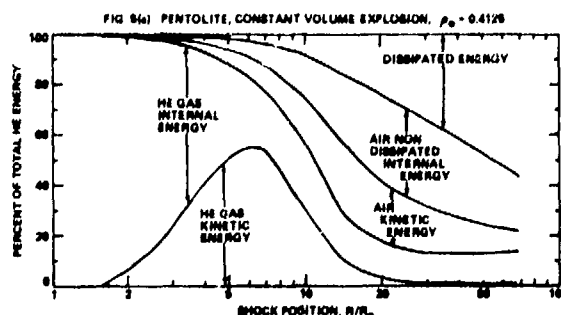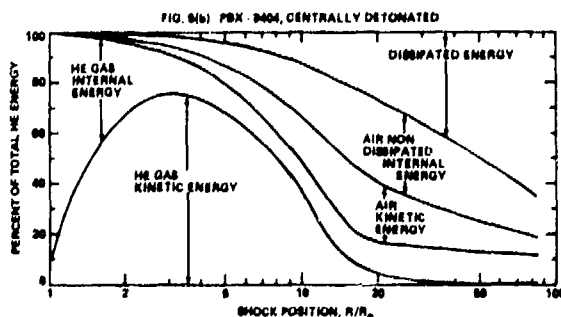
Fig. 5. Calculated energy partition vs position of the main shock, for explosions in real air.
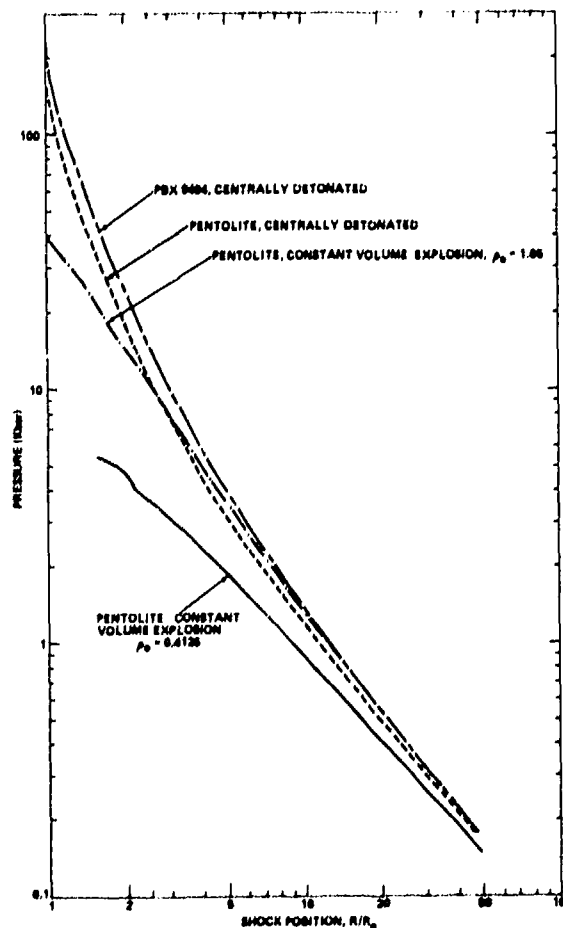
Fig. 6. Calculated peak shock pressure vs distance for explosions in water.

535

integral of p^2 dt is the same for both charges at 10 charge radii and a bit worse for the PBX 9404 at 20 charge radii. Among the three Pentolite cases, the constant volume case with the same density as the solid high explosive ($\rho_0 = 1.65$) has both the greatest peak shock pressure, 11% greater than the centrally detonated charge at 10 charge radii, and the greatest p^2 dt integral, 14% greater than the centrally detonated charge at 10 charge radii. It will be seen later that case (4), the constant volume explosion with $\rho_0 = 0.4125$, ultimately delivers the most useable energy to the water and that this is manifested in a larger impulse.

Figures 7 and 8 contain calculated pressure vs time curves at the 10 charge radii position. Notice in Fig. 7 that the p vs t curves from the centrally detonated PBX 9404 and Pentolite cross, so that the pressure from the Pentolite is greater after a short time. The p vs t curves at 10 charge radii are shown for the three Pentolite charges in Fig. 8. The constant volume case, with $\rho_0 = 0.4125$ g/cc starts at a lower pressure than the other two (see Table III for the exact values) but the pressure soon becomes the remains higher.

Integrals of p^2 dt vs time are plotted in Fig. 9. Notice that at 100 μsec the integrals are close to their maximum values. The values listed in Table III are those at 230 μsec, where the calculation ended. Case (3), the constant volume Pentolite with $\rho_0 = 1.65$ is the best here, but the constant volume case with $\rho_0 = 0.4125$ is also better than the centrally detonated case (see Table III).

The impulse, or integral of pressure with respect to time, is shown in Fig. 10 for the four cases, as a function of time at 10 charge radii. The constant volume case with $\rho_0 = 0.4125$ is the best here, the integral being 24% better than the centrally detonated case at 200 μsec. The integrals did not reach their maximum values, when the calculation ended. It appears from Fig. 10, that the improvement in impulse may be considerably better than 24% at later times. Note in Fig. 10 that the worst impulse is
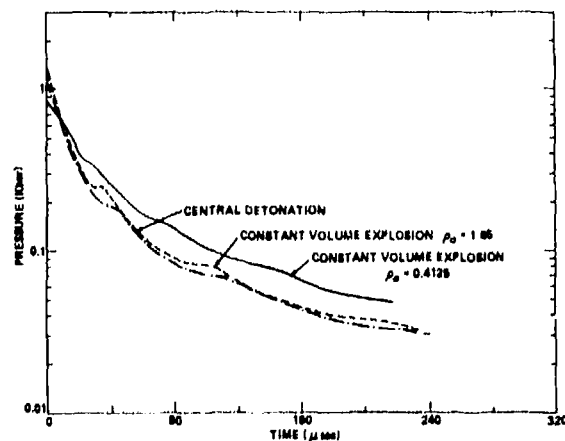
Fig. 8. Calculated pressure vs time at 10 charge radii, for pentolite explosions in water.

Fig. 7. Calculated pressure vs time at 10 charge radii, for centrally detonated PBX 9404 and pentolite, in water.
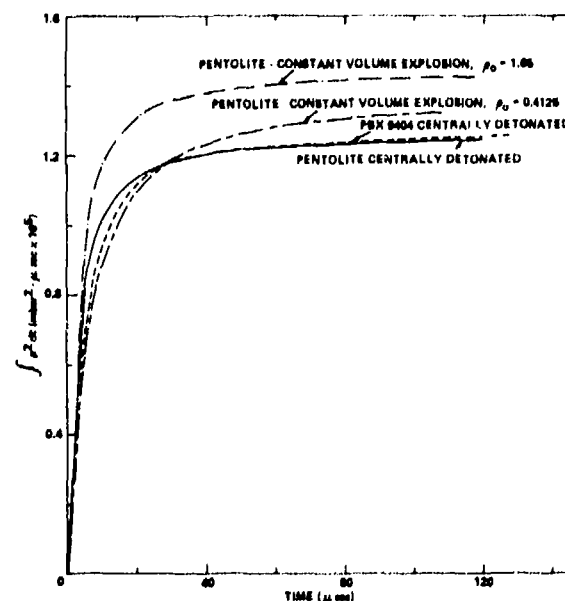
Fig. 9. Calculated integral of p^2dt vs time at 10 charge radii, for explosions in water.

536

obtained with the centrally detonated PBX 9404, in spite of its greater detonation pressure and energy.

The above results can be explained in terms of the dissipated energy due to shock heating of the water. The calculated dissipated energy values are shown in Fig. 11. It can be seen in Ref. 2, that the energy dissipated in a spherical shell of water increases rapidly with the shock pressure. This accounts for the fact that with the PBX 9404 charge, with an initial transmitted pressure of 228 kbar, 48% of the explosive energy has been dissipated when the shock is at 10 charge radii, compared to 33% dissipated for the centrally detonated Pentolic charge, which has an initial transmitted pressure of 162 kbar, and 3% dissipated by the constant volume pentolite charge with $\rho_0 = 0.4125$ and initial transmitted pressure of 6 kbar.

Calculated energy partitions vs shock position are shown in Fig. 12. The centrally detonated PBX 9404 plot, Fig. 12(b), shows that when the main shock is at 10 charge radii 13% of the HE energy is still in the bubble, 48% has been dissipated in heating the water, 29% is in kinetic energy of the water, and 10% is in nondissipated internal energy of the water. Comparison of Figs. 12(a) and (b) shows that with the centrally detonated charges there is less useable energy in the PBX 9404 system than in the Pentolite system after the shock passes 12 charge radii, due to the greater dissipation in the PBX 9404 case. Figure 12(d) shows that with the constant volume case $\rho_0 = 0.4125$ g/cc, only 6% of the HE energy has been dissipated when the main shock is at 40 charge radii from the center. Thus 30% of the total energy which is dissipated in the centrally detonated Pentolite case

TABLE 3

Calculated Peak Shock Pressure and $\int p^2 dt$ at Various Distances from the Center, for Spherical Explosions in Water

	Charge Radius R/R_0	Peak Shock Pressure (mbar)	$\int p^2 dt$ (mbar^2·µsec)
Pentolite	1	0.162	
(1) central detonation	5	3.11×10^{-3}	
	10	1.19×10^{-3}	1.25×10^{-5}
	20	4.94×10^{-4}	2.74×10^{-6}
	40	2.14×10^{-4}	
PBX 9404	1	0.228	
(2) central detonation	5	3.97×10^{-3}	
	10	1.37×10^{-3}	1.25×10^{-5}
	20	5.27×10^{-4}	2.60×10^{-6}
	40	2.21×10^{-4}	
Pentolite, constant	1	0.039	
	5	3.58×10^{-3}	
(3) volume explosion	10	1.32×10^{-3}	1.43×10^{-5}
$\rho_0 = 1.65$	20	5.26×10^{-4}	3.04×10^{-6}
	40	2.24×10^{-4}	
Pentolite, constant	1	0.006	
	5	1.86×10^{-3}	
volume explosion	10	8.79×10^{-4}	1.33×10^{-5}
(4)	20	4.10×10^{-4}	3.15×10^{-6}
$\rho_0 = 0.4125$	40	1.90×10^{-4}	

Fig. 10. Calculated impulse vs time at 10 charge radii, for explosions in water.
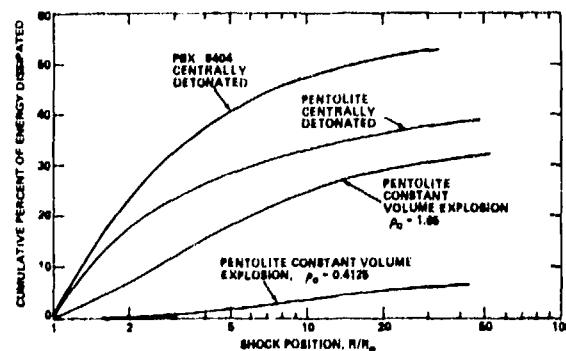
Fig. 11. Cumulative energy dissipated in water due to shock heating vs position of main shock.

(see Fig. 12(a)) is now available to do useful work. This energy comes out of the bubble relatively slowly. When the main shock is at 10 charge radii, 49% of the total energy is still in the bubble. However, most of this energy does eventually come out of the bubble (see Fig. 12(d)). This accounts for the cross over in the pressure-time curves (Fig. 8), the increase in the p^2dt integral (Fig. 9), and the large increase in the impulse (Fig. 10) relative to the centrally detonated Pentolite charge. The kinetic energy of the water is also increased.

Fig. 12(a). Pentolite, centrally detonated
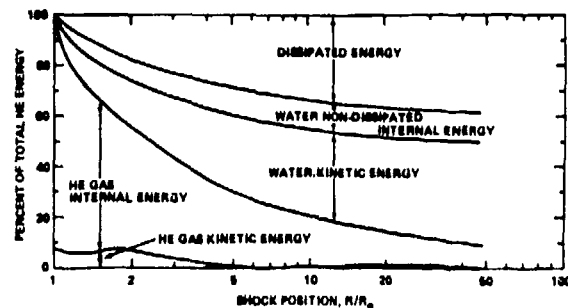
Fig. 12(b). PBX 9404, centrally detonated
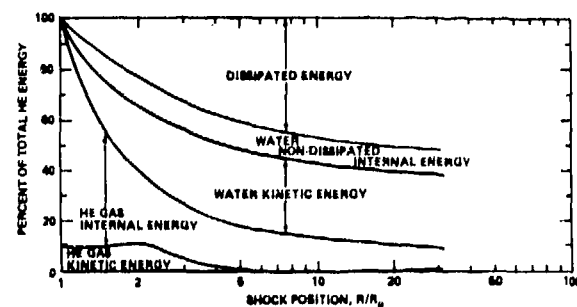
Fig. 12(c). Pentolite constant volume explosion, $\rho_o = 1.65$.
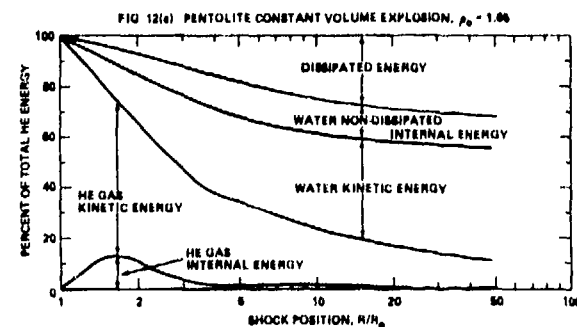
Fig. 12(d). Pentolite constant volume explosion, $\rho_o = 0.4125$.
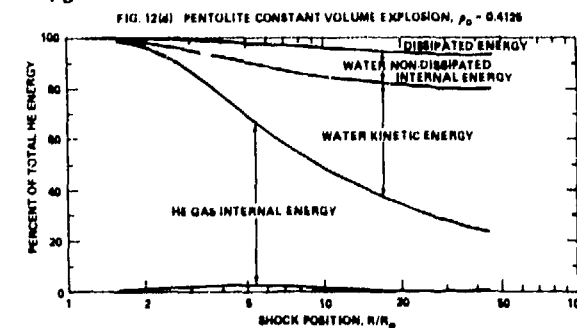
Fig. 12. Calculated energy partition vs position of the main shock, for explosions in water.

538

REFERENCES

1. W. A. Walker and H. M. Sternberg, "The Chapman-Jouguet Isentrope and the Underwater Shock Wave Performance of Pentolite," Proceedings of the 4th Symposium (International) on Detonation ACR-126, U.S. Gov't. Printing Office, Wash., D.C. pp. 27-38, 1965.

2. H. M. Sternberg and W. A. Walker, "Calculated Flow and Energy Distribution Following Under-Water Detonation of a Pentolite Sphere," Phys. Fluids, Vol. 14, No. 9, pp. 1869-1878, 1971.

3. F. B. Porzel, "Introduction to a Unified Theory of Explosions (UTE)," NOLTR 72-209, Naval Ordnance Laboratory, White Oak, Silver Spring, Maryland. 14 September 1972.

4. Stuart R. Brinkley, Jr. and John G. Kirkwood, "Theory of the Propagation of Shock Waves," Phys. Rev. Vol. 71, pp. 606-611, 1947.

5. Brigitta M. Dobratz, Ed., "Properties of Chemical Explosives and Explosive Simulants," Lawrence Livermore Laboratory, University of California/Livermore, UCRL-51319, 15 Dec. 1972.

6. L. R. Doan and G. H. Nickel, "A Subroutine for the Equation of State of Air," Technical Memorandum RTD (WLR)TM-63-2, Air Force Weapons Laboratory, Kirtland Air Force Base, New Mexico, May 1963.

7. R. H. Cole, Underwater Explosions, Princeton University Press, Princeton, N.J. 1948.

EXPLOSIVE EXPANSION WORKS IN UNDERWATER DETONATIONS

Gert Bjarnholt and Roger Holmberg
Swedish Detonic Research Foundation
Box 32058, S-126 11 Stockholm, Sweden

Shock wave energy and bubble energy for different explosives have been measured in underwater experiments. A method to determine bubble energies in cases where the free water surface and bottom boundary disturbs the bubble oscillation has been developed. The shock energy loss when the primary shock wave travels from the charge to the gage resulting in heating of the surrounding water has been estimated by correlation with data derived from detonation calorimeter experiments for some explosives. Comparison of the measured total expansion work with data from thermodynamic computer calculations show good agreement for many oxygen balanced explosives, but poor agreement for explosives with a large oxygen deficit. For explosives of the ANFO type there is a considerable effect on expansion work of initiator or booster size, charge size, and shape.

INTRODUCTION

Methods to measure the expansion work performed by explosives are valuable tools in explosives research. The underwater explosion test has several interesting characteristics. It allows the use of sufficiently large charges to ensure stable detonation even in explosives with a large critical diameter, and the reaction products are allowed to expand to a low final pressure. The pressure profile of the shock wave in the surrounding water 50-100 charge radii away can be measured accurately. From it can be derived the impulse density and the energy of the shock wave. From the bubble period, i.e., the time interval between the detonation and the first bubble implosion, the bubble energy can be determined. This energy is the work the reaction products do against the hydrostatic pressure of the surrounding water in expanding the bubble to its first maximum.

For two reasons, the underwater explosion test has previously been used mostly for comparative measurements.

Firstly, the energy dissipated as heat in the water between the charge and the pressure gage is not easily measurable.

Secondly, it is not always easy to find a large enough water pond for the bubble expansion to be undisturbed by the water surface and the containing boundaries. In a case with marked boundary effects the bubble energy is difficult to determine absolutely.

In this paper will be described a practical way to determine the dissipated energy and a method to derive the bubble energy from the bubble period, even in cases when boundary effects have a marked influence on the bubble period.

The underwater explosion test can then be used to give an absolute measure of the total expansion work done by different explosives. Results of such measurements will be presented below.

EXPERIMENTAL

The experimental arrangement used in the experiments is shown in Fig. 1. The charges were located at a depth of 2.50 m, 2.00 m from the 1/4 inch tourmaline piezoelectric gage. A second gage placed 10 cm closer to the charge was used to trigger the instruments before the primary shock reached the measuring gage. The experimental site in Fig. 1 was used for charges
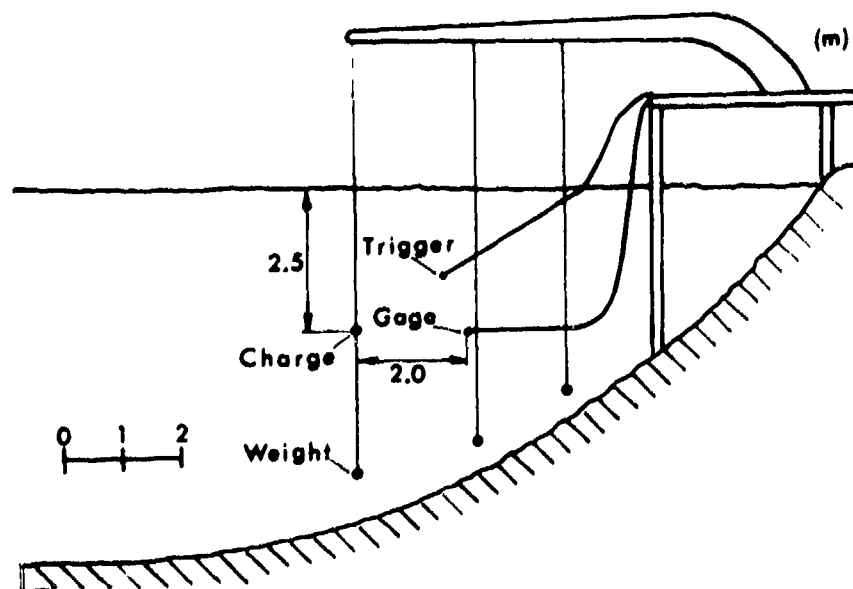
Fig. 1. Experimental site.

up to about 0.5 kg. For bigger charges, another experimental site with 10 m charge depth was used. At that site the gage was located 15.0 m from the charge. The instrumentation used to record the pressure time signals from the gage was that conventionally used for these types of measurements.

where

θ is the time constant in the measured shock

R   is the distance between the charge and the gage

c_w is the sound velocity of the water

ρ_w is the density of the water.

EVALUATION OF PRIMARY DATA

The data from the shot was registered by an oscilloscope camera which recorded the primary shock wave and by another recorder with a longer writing time where the time between the primary shock and the shock sent out at the first implosion (the first bubble period) could be determined. Fig. 2 shows an example of a recording at the site described in Fig. 1.

SHOCK ENERGY AT THE GAGE

The energy E_s in the primary water shock when it passes the gage was determined from the energy density at the gage and assuming a spherical expansion (1).

$$E_s = \frac{4\pi R^2}{\rho_w c_w} \int_0^{6.70} p^2(t)\, dt \qquad (1)$$

Fig. 2. Example of oscilloscope camera picture of pressure time and $\int p^2\, dt$ recording from a 0.255 kg TNT charge at 2.00 m distance.

p(t): 3.0 MPa/div, 100 µs/div (lower trace).

$\int p^2\, dt$: 72.6 KJ/div, 100 µs/div (uppertrace, inverted).

541

To ease evaluation of E_s the instrumentation included a squarer- and integrater unit. We determined the shock energy as proportional to the signal from the squarer and integrator unit at a time of 6.7θ. We then corrected this value for the distortion at the front of the signal caused by the recording equipment (1,3,4). This correction was about 3% for the smallest charges and about 1% for the biggest.

BUBBLE ENERGY E_b

The bubble energy E_b in the first bubble pulse can be defined as the work done in expanding the bubble to its first maximum against the hydrostatic pressure.

The so called Willis formula can be used to calculate the bubble energy from the period of oscillation t_b of the bubble in cases where we have no boundary effects. This formula can be written (1) as

$$t_b = 1.135 \rho_w^{1/2} E_b^{1/3}/p_h^{5/6} \qquad (2)$$

where

t_b is the period of the first bubble oscillation
p_h is the total hydrostatic pressure at the charge depth.

Formula (2) can be written

$$t_b = k_1 E_b^{1/3} \qquad (3a)$$

where

$$k_1 = 1.135 \rho_w^{1/2}/p_h^{5/6} . \qquad (3b)$$

Cole (1) has shown that for an experimental configuration as in Fig. 1 with boundary effects the Willis formula will be modified so that

$$t_b = k_1 E_b^{1/3} + k_2 E_b^{2/3} \qquad (4)$$

where $k_2 \neq 0$ is a constant at a given charge location and experimental site. Solving for E_b in Eq. (4) gives

$$E_b = \frac{k_1^3}{8k_2^3} \left[\pm \sqrt{1 + \frac{4k_2 t_b}{k_1^2}} - 1 \right]^3 . \qquad (5)$$

For $k_2 < 0$ the plus sign is valid and the condition $t_b < -k_1^2/4k_2$.

For $k_2 > 0$ the minus sign is valid.

For $k_2 = 0$ we have

$$E_b = t_b^3/k_1^3 . \qquad (6)$$

The constant k_2 in Eq. (4) characterizes the influence of the boundaries on the bubble period. For a case with no boundary effects $k_2 = 0$.

Cole has outlined a way to calculate k_2. The results are presented in his book Underwater Explosions (1) are however not consistent. We therefore decided to determine k_2 for our experimental sites experimentally. This was done by scaling experiments with one explosive.

If one has an explosive where the bubble energy is proportional to the charge weight of the explosive Eq. (4) may be written

$$t_b = aW^{1/3} + bW^{2/3} \qquad (7)$$

where a and b are constants at the given experimental site and charge location, and W is the charge weight of the particular explosive used. By identification between Eqs. (4) and (7) we get

$$k_2 = \frac{k_1^2 b}{a^2} . \qquad (8)$$

Equation (8) in (5) then gives

$$E_b = \frac{a^6}{8k_1^3 b^3} \left[\pm \sqrt{1 + \frac{4bt_b}{a^2}} - 1 \right]^3 . \qquad (9)$$

Putting

$$c = \frac{b}{a^2} \qquad (10)$$

Eq. (9) can be written

$$E_b = \frac{1}{8c^3 k_1^3} [\pm \sqrt{1 + 4ct_b} - 1]^3 \qquad (11)$$

and for $c = 0$ Eq. (6) is valid.

542

If we assume that at a given site the boundary effects on a given bubble period are the same irrespectively of the explosive used to generate that period, formula (11) can be used to calculate the bubble energy for any explosive from its measured bubble period at that site. As $t_b \sim p_h^{-5/6}$, normal atmospheric pressure changes from one day to the other can have a marked influence on the measured bubble period at small charge depths as in Fig. 1. The measured bubble periods should therefore be normalized to the same total hydrostatic pressure p_{hn} before they are used in Eq. (11). This normalization can be included in Eq. (11) giving

$$E_b = \frac{1}{8c^3 k_1^3} \left[\pm \sqrt{1 + 4ct_b \left(\frac{p_h}{p_{hn}}\right)^{5/6}} - 1 \right]^3 \quad (12)$$

where

$k_1 = 1.135 \rho_w^{1/2} / p_{hn}^{5/6}$

p_{hn} = the normal total hydrostatic pressure at the given charge depth.

p_h = the total hydrostatic pressure at the charge depth when t_b was measured.

c = determined from Eqs. (7) and (10) with t_b in Eq. (7) normalized to p_{hn}.

The constant c for the site in Fig. 1 was determined by firing from 15 up to 386 grams of an explosive PE composed of 86PETN/14 Wax by weight, having a density of 1.48 g/cm^3. The periods were then normalized to the same total hydrostatic pressure p_{hn}. The results are given in Table 1 and Fig. 3. The value of the constant c at the site in Fig. 1 was

$$c = -0.4464 \text{ s}^{-1} .$$

THE SHOCK ENERGY LOSS

The chemical energy liberated by the decomposition of the explosive is partitioned into various forms of energy when the products expand and do work. In an underwater detonation it is convenient to regard the energy per mass unit of explosive as partitioned into the following forms.

e_s = shock energy when the primary shock passes the gage

e_d = primary shock energy dissipated as heat in the water during travel from the charge to the gage

e_b = energy required to expand the bubble to its first maximum against the hydrostatic pressure

e_i = internal energy in the reaction products when the bubble is at its first maximum.

The total expansion work A_0 done by the explosive per mass unit is then

$$A_o = e_s + e_b + e_d . \quad (13)$$

Let

$$A_o = \mu e_s + e_b \quad (14)$$

then we obtain

$$e_d = e_s(\mu - 1) . \quad (15)$$

The dissipated energy e_d is then proportional to the measured shock energy at the gage and the factor $(\mu - 1)$.

TABLE 1

The Bubble Period t_{bn} *for Different Charge Weights W of Explosive PE at the Site in Figure 1*

W (kg)	W$^{1/3}$ (kg$^{1/3}$)	t_{bn} (s)
0.0150	0.247	0.0612
0.0289	0.307	0.0757
0.0289	0.307	0.0759
0.0900	0.448	0.1087
0.0935	0.454	0.1104
0.102	0.467	0.1138
0.182	0.567	0.136
0.183	0.568	0.136
0.310	0.677	0.160
0.318	0.683	0.161
0.381	0.725	0.170
0.386	0.728	0.171

*Periods normalized to a total hydrostatic pressure of 125.8 kPa.

543
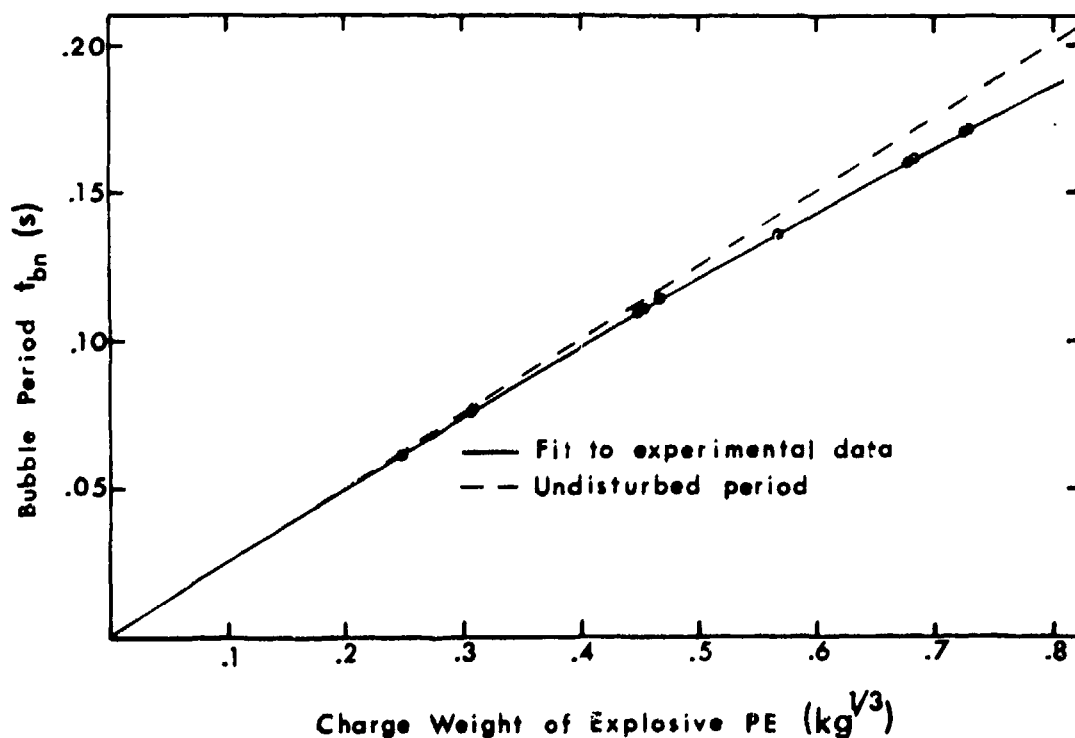
Fig. 3. The bubble period as a function of the charge weight of the explosive PE at the site in Fig. 1. Periods normalized to a total hydrostatic pressure of 125.8 kPa.

We decided to try to determine the shock energy loss factor μ by combining experimental shock and bubble energies with heat of detonation data for some ideal CHNO explosives. These explosives were chosen so that a wide range of detonation pressure would be covered.

Thermodynamic calculations with ordinary ideal CHNO explosives with a loading density of 1-2 g/cm^3 show that the expansion work the products can do when they expand isentropically from detonation conditions to atmospheric pressure usually is 97 to 100% of the calculated heat of detonation.

Data from cylinder test experiments with some ordinary ideal CHNO explosives also show that the expansion work the products do when they expand to atmospheric pressure is the same (within a couple of percent) as the heat of detonation as measured in a detonation calorimeter with an expansion similar to that in the cylinder test (5,6,7,8). As the expansion of the products in an underwater detonation is a reasonably isentropic expansion down to about atmospheric pressure, it is reasonable to assume that

these explosives should give an underwater expansion work A_o such that

$$A_o \simeq -\Delta H_d , \qquad (16)$$

where $-\Delta H_d$ is the heat of detonation as measured in a detonation calorimeter of the type described by Ornellas, et al. (5).

Equations (13) and (16) then give

$$-\Delta H_d = \mu e_s + e_b \qquad (17)$$

which can be written

$$\mu = \frac{-\Delta H_d - e_b}{e_s}. \qquad (18)$$

We assumed that the loss factor μ for any explosive is determined solely by its detonation pressure.

We determined μ as a function of the detonation pressure p_d by combining detonation calorimeter

544

ΔH_d and underwater e_s and e_b values for some explosives with a wide range of detonation pressures. The detonation pressure was estimated from

$$p_d = 0.25\rho_o D^2 \qquad (19)$$

where

ρ_o is the density of the explosive
D   is the detonation velocity.

The results are presented in Fig. 4 and Table 2.

The range of p_d values covered by these explosives was from 7.3 GPa to 25.7 GPa. To be able to extend μ as a function of p_d down to detonation pressures around 2 GPa we used the fact that $\mu \to 1$ when $p_d \to 0$ (the acoustic approximation). We also used a $(e_s, e_b, -\Delta H_d, p_d)$ - coordinate for the explosive ANFO (94.5% amoniumnitrate prills and 5.5% fuel oil) at a density of 0.9 g/cm³.
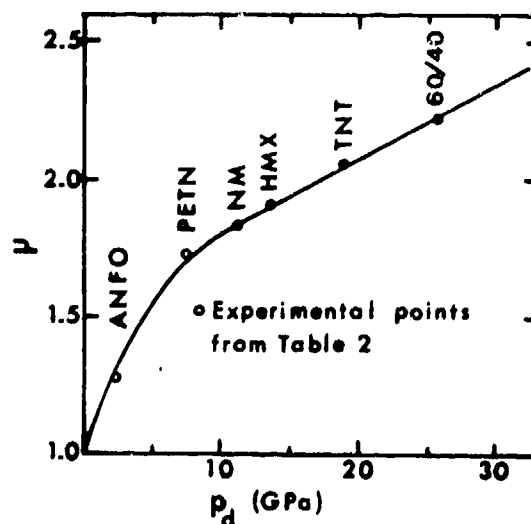
Fig. 4. Shock loss factor μ as a function of the detonation pressure p_d of the explosive.

TABLE 2

Data on Explosives Used to Determine the Shock Energy Loss Factor μ^*
as a Function of the Detonation Pressure p_d

Explosive	Charge Size Class W (kg)	Density (ρ_o) (g/cm³)	Charge Shape and Initiation‡	Charge Shape Factor k_f	Detonat. Velocity D (m/s)	Bubble Energy e_b (MJ/kg)	Shock Energy e_s (MJ/kg)	Detonat. Calorim. Heat of Detonation $-\Delta H_d$‡ (MJ/kg)	Heat of Detonat. Used to Determine $\mu^* -\Delta H'_d$ (MJ/kg)
ANFO	10	0.90	B/d + 140	1.02	3200	2.43	1.12	3.78	3.78
PETN	0.3	1.00	E/d	1.02	5400	3.00	1.44	5.73	5.61
NM	0.3	1.13	E/d + 20	1.02	6300	2.22	1.16	4.44	4.44
HMX	0.3	1.19	E/d + 6	1.02	6700	2.33	1.40	5.13	5.10
TNT	0.5	1.58	S/d + 2	1.00	6900	2.06	1.04	4.27	4.20
Hexotol 60/40	0.4	1.69	E/d + 12	1.01	7800	2.08	1.19	4.69	4.77

$$^*\mu = \left(\frac{-\Delta H'_d}{k_f} - e_b\right)e_s, \quad p_d = 0.25\,\rho_o D^2.$$

†See Fig. 5, d = detonator No. 8, d + x = detonator No. 8 plus x grams of flegm. PETN.
‡Results from Refs. (5,6,7,8). For ANFO the BKW code CJ value was used. The value for PETN was obtained at a density of 1.73 g/cm³.

The calculated ΔH_d value for ANFO was used as we had no detonation calorimeter value for this explosive. As ANFO is oxygen balanced we considered the calculated ΔH_d value to be reliable. The e_s and e_b values were determined with a 10 kg paint can type of charge initiated by a 140 g PETN primer.

COMPUTER CODE CALCULATIONS OF HEAT OF EXPLOSION AND HEAT OF DETONATION

To be able to make comparisons of experimental and calculated data for the explosives tested the heat of explosion and/or the heat of detonation was also calculated.

Heat of detonation data was calculated with a computer code called Fortran BKW obtained from Los Alamos Scientific Laboratory. This code uses the BKW equation of state (eos).

Heat of explosion data was calculated with a constant volume explosion equilibrium code called Nitrodyne using an eos described by J. Taylor (10).

RESULTS

In Table 3 formulations and properties of 13 different explosives are presented. Table 4 presents the results of experimental and calculated data for these explosives. Some of the explosives were shot with different initiation, charge size and charge shape.

The detonation pressures were estimated with formula (19) from the densities and detonation velocities of the explosives. From Fig. 4 the shock energy loss factor μ could then be determined. The experimental expansion work A_0 for the explosives was determined with formula (14) from the measured bubble and shock energy e_s and e_b, the charge shape factor k_f and the shock loss factor μ.

The charge shape factor k_f is a correction for the influence of the charge shape and casing o: the measured expansion work. Figure 5 gives values of k_f for the different types of charges based upon experiments with the same ideal explosive in different charge shapes.

Normally all our underwater experiments were made with at least two identical charges The results

TABLE 3

Composition and Properties of Explosives

Explosive	Composition (Weight %)	Density (g/cm^3)	Oxygen Balance (%)
Oxygen Balanced CHNO Explosives			
Pentanex	45PETN/37AN/2Glycol 15.5H_2O/0.5Guar	1.48	−0.3
EGDN	100EGDN	1.48	0.0
ANFO	94.6AN/5.4FO	0.90	0.1
Oxygen Deficient CHNO Explosives			
PETN	100PETN	1.00	−10.1
HMX	100HMX	1.20	−21.6
NM	100NM	1.13	−39.3
Hexotol 60/40	59RDX/40TNT/1 Wax	1.69	−46.4
86PETN/14FO	86PETN/14FO	1.08	−57.4
TNT	100TNT	1.58	−74.0
Aluminized Explosives			
ANFOAL 10	87.4AN/2.6FO/10Al	0.90	−0.5
WG 2	MMAN sensit. watergel expl. 7% Al (60 μm)	1.34	−0.3
WG 4	MMAN sensit. watergel expl. 13% Al (60 μm)	1.36	−0.5
Hexotonal 15	42.1RDX/42.1TNT/0.8 Wax/15Al (30 μm)	1.76	−56.3

EGDN – Ethylene Glycol Dinitrate.
MMAN – Mono Methyl Amine Nitrate.
  AN – Ammonium Nitrate Prills.
  FO – Fuel Oil No. 1.

presented were chosen as representative of the data. The experimental relative errors are estimated to be less than ±1.5% for bubble energy and less than ±3% for shock energy.

DISCUSSION

Shock Energy Loss Factor μ

As can be seen in Fig. 4 the shock energy loss factor μ increases rapidly with detonation pressure. This means that explosives like TNT, hexotol 60/40 and hexotonal 15 which generate high initial pressures when fully coupled to the surrounding wate. will

546

TABLE 4

Experimental and Calculated Data on Explosives

Shot No.[†]	Explosive	Charge Weight (kg)	Charge Shape[*]/ Initiat.	Charge Shape Factor k_f	Shock Energy (MJ/kg)	Bubble Energy (MJ/kg)	Deton. Press. (GPa)	Loss Factor μ	Exper. Expans. Work A_0 (MJ/kg)	$(-\Delta H_d)$ BKW Code[‡] (MJ/kg)	$(-\Delta U)$ Nitrodyne Code (MJ/kg)
Oxygen Balanced CHNO Explosives											
31L	Pentanex	1.72	C/d + 5	1.08	0.85	1.79	17.0	1.99	3.76	3.90	4.00
40L	Pentanex	1.48	B/d + 23	1.00	0.97	1.86	18.0	2.02	3.82	3.90	4.00
43L	Pentanex	7.26	B/d + 23	1.00	0.99	1.88	18.0	2.02	3.88	3.90	4.00
201	EGDN	0.392	E/d + 12	1.02	1.50	2.77	19.7	2.07	5.99	6.70	6.82
203	EGDN	0.190	E/d + 12	1.03	1.47	2.74	19.7	2.07	5.96	6.70	6.82
88	ANFO	0.360	E/d + 19	1.02	0.92	2.01	2.0	1.25	3.22	3.78	3.89
38L	ANFO	2.30	E/d + 95	1.02	0.92	2.08	2.8	1.34	3.31	3.78	3.89
36L	ANFO	2.07	C/d	1.10	0.98	1.90	2.3	1.28	3.47	3.78	3.89
37L	ANFO	2.03	C/d + 95	1.10	1.00	1.92	2.3	1.28	3.52	3.78	3.89
41L	ANFO	1.48	B/d + 23	1.00	0.67	1.73	2.0	1.25	2.55	3.78	3.89
45L	ANFO	4.93	B/d + 140	1.00	1.08	2.39	2.3	1.28	3.77	3.78	3.89
46L	ANFO	10.05	B/d + 140	1.00	1.12	2.43	2.3	1.28	3.86	3.78	3.89
47L	ANFO	9.91	B/d + 23	1.00	0.82	2.22	2.0	1.25	3.25	3.78	3.89
Oxygen Deficient CHNO Explosives											
235	PETN	0.313	E/d	1.02	1.44	3.00	7.3	1.69	5.54	5.76	5.88
281	HMX	0.340	E/d + 6	1.02	1.40	2.33	13.4	1.90	5.09	5.76	5.28
199	NM	0.294	E/d + 20	1.02	1.16	2.23	11.2	1.84	4.45	5.43	4.82
254	Hexotol 60/40	0.426	E/d + 12	1.01	1.19	2.08	25.7	2.23	4.78	5.70	5.60
253	86PETN/14FO	0.298	E/d + 12	1.02	1.11	2.19	8.2	1.74	4.20	5.22	4.53
272	TNT	0.255	S/d + 2	1.00	1.02	2.06	18.8	2.04	4.14	5.33	4.95
4L	TNT	1.97	S/d + 2	1.00	0.97	2.11	18.8	2.04	4.09	5.33	4.95
7L	TNT	4.99	S/d + 2	1.00	0.97	2.11	18.8	2.04	4.09	5.33	4.95
35L	TNT	2.34	C/d + 20	1.08	0.96	1.91	18.8	2.04	4.18	5.33	4.95
Aluminized Explosives											
53	ANFOAL 10(30)**	0.364	E/d + 19	1.02	1.27	2.93	2.0	1.25	4.61	5.45	5.56
66	ANFOAL 10 (120)	0.380	E/d + 19	1.02	1.27	2.93	2.0	1.25	4.61	5.45	5.56
81	ANFOAL 10 (600)	0.356	E/d + 19	1.02	1.13	2.80	2.0	1.25	4.19	5.45	5.56
289E	ANFOAL 10 (60)	2.20	C/d + 150	1.10	1.50	2.65	2.5	1.31	5.08	5.45	5.56
1E	WG 2	10.12	C/d + 360	1.08	1.17	2.38	7.4	1.70	4.72	–	4.71
8E	WG 4	9.74	C/d + 360	1.08	1.26	3.00	6.4	1.65	5.49	–	6.09
255	Hexotonal 15	0.255	E/d + 12	1.01	1.35	2.89	25.7	2.23	5.96	7.61	7.60

*See Fig. 5. d = detonator No. 8. d + x = detonator No. 8 + x grams of pressed flegm. PETN. Cylindrical charges had a diameter of 75 mm.

[†]Shots with an L or E after the shot No. were shot at 10 m charge depth, 15 m from the gage.

[‡]CJ values.

**Mean aluminum particle size (μm).

Towards surface ↑

B

$k_f = 1.00$

Charge in paint can

C

$k_f = 1.08 - 1.10$

Cylinder shaped charge with L/D=6

E

$k_f = 1.02 - 1.03$

Charge in erlen-meyer glass flask

S

$k_f = 1.00$

Sphere in-itiated at the center
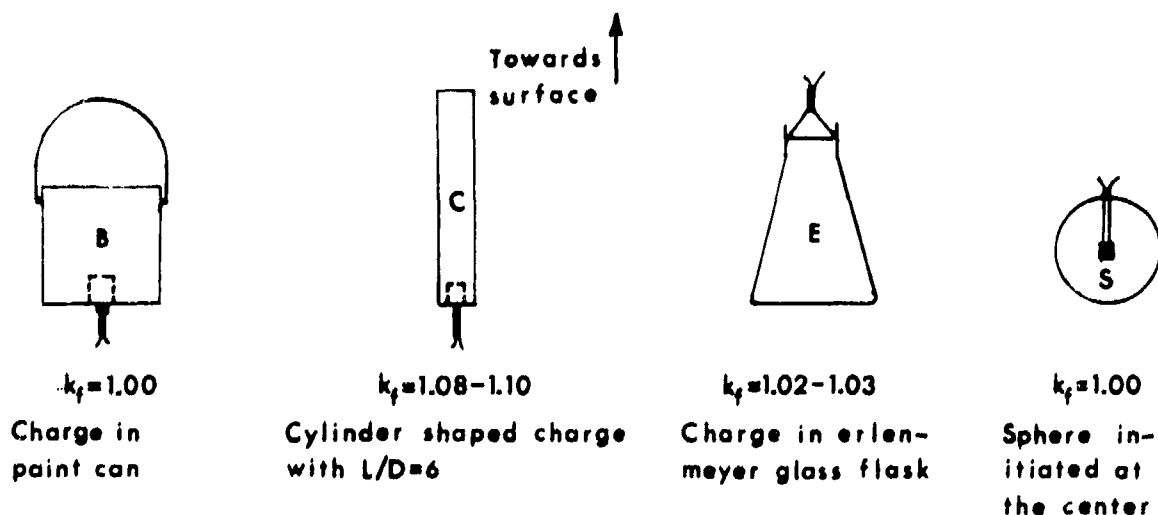
Fig. 5. Key to charge shapes and charge shape factor k_f.

loose considerably more energy as heat to the surrounding water close to the charge than explosives with lower front pressures like ANFO and ANFOAL 10. This effect is clearly demonstrated by comparing the measured shock energies for hexotonal 15 and ANFOAL 10. The detonation pressure of ANFOAL 10 is an order of magnitude smaller than that of hexotonal 15 but it gives about 9% higher measured shock energy e_s than hexotonal 15.

By decreasing the initial density of an explosive or by surrounding the charge with a cavity one should be able to decrease the energy dissipated as heat. In both cases there should also be a marked increase in bubble energy.

Oxygen Balanced CHNO Explosives

The explosive Pentanex which detonates almost ideally under the experimental conditions showed an experimental expansion work A_0 that was close to the calculated heat of detonation and heat of explosion. A_0 varied very little with charge size and the two charge geometries used. We take this observations as an indication that our loss factor μ has a correct value at the detonation pressure 17-18 GPa estimated for Pentanex and that the charge shape factor value k_f of 1.08 for cylinder shaped charges with a length to diameter ratio of 6 is correct.

The result for EGDN showed an experimental A_0 about 10% lower than the calculated $(-\Delta H_d)$ and

$(-\Delta U)$. EGDN is an oxygen balanced CHNO explosive which normally means that ΔH_d and ΔU should be easy to compute correctly. However, in the Nitrodyne code nitrogen oxide (NO) is not included as a possible reaction product and consequently assumed to be nil. The BKW code has NO as a possible reaction product and calculates 0.07 moles/mole EGDN at the CJ-point. When one compares detonation front temperature measurements (10) with CJ temperatures calculated with the BKW eos the calculated temperatures however seem to be significantly lower than the experimental. As the formation of NO is temperature sensitive the experimental NO concentration at the front in an explosive like EGDN with a combined high heat of detonation and oxygen content could be appreciably higher than that calculated with the BKW eos. As the products expand and do work they will cool and the NO concentration should decrease shifting the equilibrium towards more energetic products. However, if there is a "freeze out" of the NO concentration during the expansion at some value appreciably higher than that calculated, less energetic products would be the result.

We suggest that formation of appreciable amounts of NO (≈ 0.7 moles/mole EGDN) caused by the combined high front temperature and high oxygen content could explain the low experimental A_0 for EGDN.

The results for ANFO show large effects on A_0 of charge size and initiation. The initiation where no further increase in A_0 is obtained varies with different

548

charge size and shape. For the cylinder shaped charges with a diameter of 75 mm and a length of 450-500 mm a very small difference in A_0 was noted between initiation with a detonator No. 8 only and a high density PETN primer weighing 95 g. For the 10 kg charges of the paint can type, however, a big difference was noted between a 25 g and a 140 g PETN primer.

We attribute the large effects of charge size and initiation in ANFO to the very non-ideal detonation characteristics and slow reaction rates in this explosive. In the 10 kg charge initiated by a 140 g PETN primer we believe that ANFO gives an expansion work close to its maximum.

Oxygen Deficient CHNO Explosives

Detonation calorimeter heat of detonation values for PETN, HMX, NM, hexotol 60/40 and TNT were used to determine the shock loss factor μ as a function of detonation pressure. Naturally the expansion work A_0 determined for these explosives will be almost equal to the corresponding detonation calorimeter heat of detonation value. Consequently the difference between calculated $(-\Delta H_d)$ or $(-\Delta U)$ and measured A_0 get bigger with increasing oxygen deficiency the same way as the difference between calculated and detonation calorimeter ΔH_d or ΔU does.

We believe that much of the differences between experimental and calculated data are caused by a difference between experimental and calculated products composition. In the calculations considerably more carbon is formed in the products than in for example a detonation calorimeter experiment with confined charges. We therefore suggest that most of the difference between calculated and experimental data for explosives with large oxygen deficit is caused by computational difficulties.

Aluminized Explosives

In ANFOAL 10 a considerable difference in A_0 was noted between 0.4 kg erlenmeyer flask type of charges and 2.2 kg cylinder shaped charges. We could also notice a lowering effect on A_0 when the particle size of the aluminum was changed from 120 μm to 600 μm in the 0.4 kg erlenmeyer type of charge.

The aluminized watergel explosive WG 2 which contains 7% 60 μm Al gave an experimental expansion work almost equal to its calculated heat of explosion. WG 4 which is similar to WG 2 but has 13% aluminum did however not perform as expected from its calculated heat of explosion. The relatively high amount of such solid reaction products as Al_2O_3 and Na_2CO_3 in WG 4 may result in considerable thermodynamic nonequilibrium between solid and gaseous reaction products during the expansion causing a reduction in the expansion work yield of the explosive.

Hexotonal 15 having a large oxygen deficit did also not perform as well as its calculated data might infer.

In ANFO and ANFOAL 10 the relatively slow reaction rate may be affecting the expansion work performance for the smaller charges.

REFERENCES

1. R. H. Cole, Underwater Explosions, Princeton University Press, Princeton, New Jersey (1948).

2. H. M. Sternberg and W. A. Walker, "Calculated Flow and Energy Distribution of a Pentolite Sphere," The Physics of Fluids, Vol. 14, No. 9 (1971).

3. A. B. Arons and R. H. Cole, "Design and Use of Piezoelectric Gages of Large Transient Pressures," The Review of Scientific Instruments, Vol. 21, No. 1, Jan. 1950.

4. F. B. Jensen, "Weak Shock Waves in Water Generated by Small Detonators," Technical University of Denmark, Department of Fluid Mechanics, Copenhagen, Denmark (1972).

5. D. L. Ornellas, J. H. Carpenter, and S. R. Gunn, "Detonation Calorimeter and Results Obtained

with PETN," The Review of Scientific Instruments, Vol. 37, No. 7 (1966).

6. D. L. Ornellas, "The Heat and Products of Detonation of Cyclotetraethylenetetranitramine, 2,4,6-Trinitrotoluene, Nitromethane, and Bis[2,2-dinitro-2-fluorethyl] formal," The Journal of Physical Chemistry, Vol. 72, No. 7 (1968).

7. D. L. Ornellas, "The Heat and Products of Detonation in a Calorimeter of CNO, HNO, CHNF, CHNO, CHNOF and CHNOSi Explosives," Combustion and Flame, Vol. 23, pp. 37-46 (1974).

8. H. C. Hornig, Private information (1973).

9. C. L. Mader, "A Code for Computing the Detonation Properties of Explosives," Los Alamos Scientific Laboratory Report LA 3704, (1967), Los Alamos, New Mexico.

10. P. A. Urtiew, "Brightness Temperature of the Detonation Wave in Some Liquid Explosives," Fifth International Colloquium on Gasdynamics of Explosions and Reactive Systems, Sept. (1975). To be published in Astronautica Acta (1976).

11. C. L. Mader, "Compressible Numerical Calculations of Underwater Detonations," Los Alamos Scientific Laboratory Report LA 4594 (1971), Los Alamos, New Mexico.

OPTIMISATION OF EXPLOSIVES FOR USE UNDERWATER

A. N. Hicks
Naval Construction Research Establishment
Scotland, United Kingdom

A short series of calculations to investigate the "efficiency" of underwater explosives is described. The calculations are based on idealised adiabatics for the explosion products and investigate the changes which can be caused in the pressure signatures in the water by variations in the energy distribution under the adiabatic. The results show that modest gains are achievable for the impulse flux and bubble energy but that current explosives are probably already quite close to the optimum for energy flux.

INTRODUCTION

The most obvious way in which the damage potential of a given mass of explosive may be increased is by increasing the detonation energy of the explosive. However, it is becoming increasingly difficult to find compounds and mixtures with higher detonation energy than those currently available. In addition, increased detonation energy is often associated with increased sensitivity of the explosive so that compositions possessing it may be too dangerous for practical use.

Thus it is becoming expedient for chemists to seek more powerful explosives by attempting to reduce the sensitivity of existing high energy explosives and to improve the efficiency with which their energy is converted into mechanical energy capable of doing useful work. For example, in many modern applications, the principal objective is to impart a very high velocity to metal in contact with the explosive. High velocities of this type are associated with a very high detonation pressure in the explosive and, where it has not been practicable to increase the detonation energy significantly, modern explosive compositions have been developed which provide high detonation pressures.

However, it has been known for many years that such compositions are not efficient for use in underwater applications. As the shock wave from the explosion travels outward it heats the water it traverses. The equation of state for water is very insensitive to such heating, and practically all the shock wave energy which is transformed into heat in this way is completely lost as far as useful work is concerned. The extent of such heating is determined by the shock wave pressure and increases very sharply with pressure. Figure 1 shows, approximately, the specific energy absorbed in this way by the water as a function of the shock pressure. Since the highest shock pressures are close to the explosion, most of the energy lost in this way is absorbed by the water immediately surrounding the explosive charge. A spherically expanding shock wave in water also leaves behind a considerable amount of kinetic energy in the form of outward motion of the water around the bubble of gaseous explosion products. This energy is in a mechanical form and some of it can still contribute to the damage potential. A typical breakdown of the original energy release of an underwater explosive is shown in Fig. 2. This breakdown illustrates the large energy loss in the water. Naturally, the higher the detonation pressure of the explosive, the higher the shock pressure in the water and the greater the
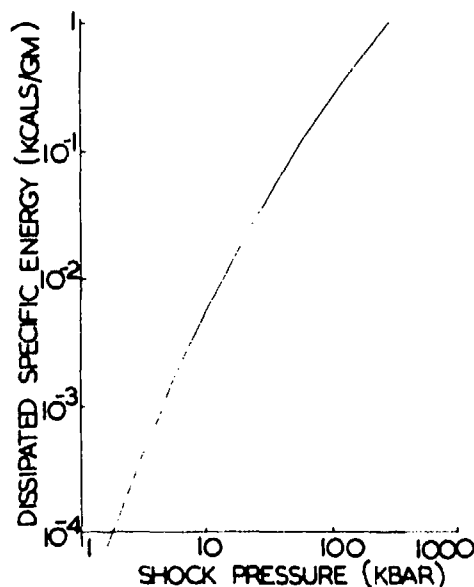
Fig. 1. Variation of energy dissipation with shock pressure.

amount of energy dissipated in the water close to the explosion. Thus, in some ways recent developments in explosives have been in exactly the wrong direction as regards underwater applications.

The aim of the present study was to provide a simple estimate of the possible improvements which might be achievable in underwater uses of explosives by seeking compositions having low detonation pressures for a given specific energy release. Such an

estimate would guide chemists on the extent to which the goal of high specific detonation energy should be modified to keep down the detonation pressure. Unless the desirability of low detonation pressures is borne in mind, they tend to rise naturally with the specific energy release.

METHOD

The shock wave emitted by an explosion is largely determined by the adiabatic expansion curve through the detonation point in the (p, v) plane of the explosion gaseous combustion products. The approach used in this paper is to select simple forms of adiabatic expansion curve, resembling genuine adiabatics, and to calculate the early pressure fields resulting. The idealised adiabatics used have been selected to give the same detonation energy and the adiabatics cover the widest possible spread of detonation pressures. In this way the results should indicate the greatest possible changes in the pressure signatures in the water which are possible from altering an adiabatic without changing the total energy release.

Figure 3 shows calculated adiabatic expansion curves for several different explosives. Theoretical curves are shown since very few experimental results are available for such adiabatics. The theory on which they are based was developed by Jones (1) and the curves were calculated as described by Haywood (2).
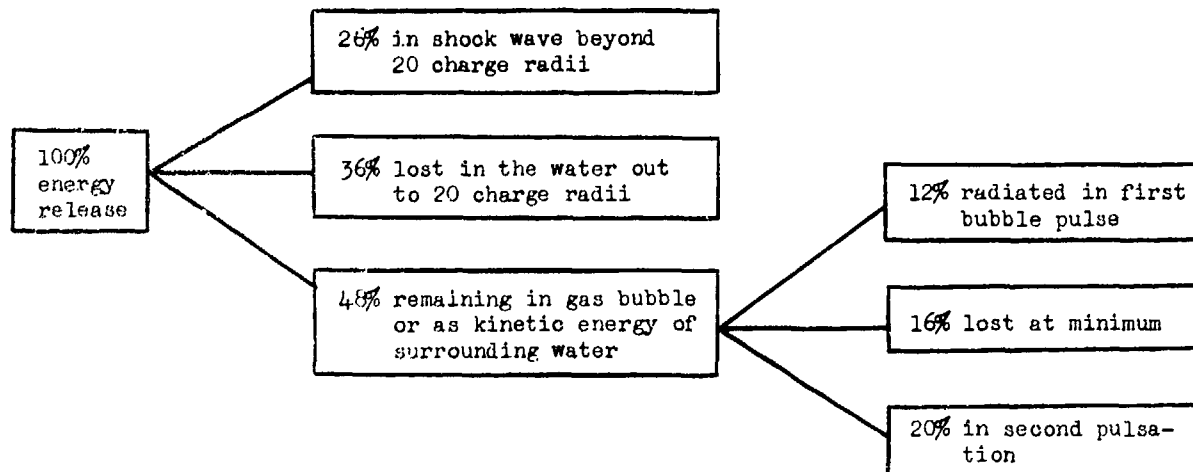
Some of the shock wave energy crossing 20 charge radii is later transformed into bubble energy so accounting for the apparent 110% total energy.

Fig. 2. Energy distribution from an underwater explosion.

552
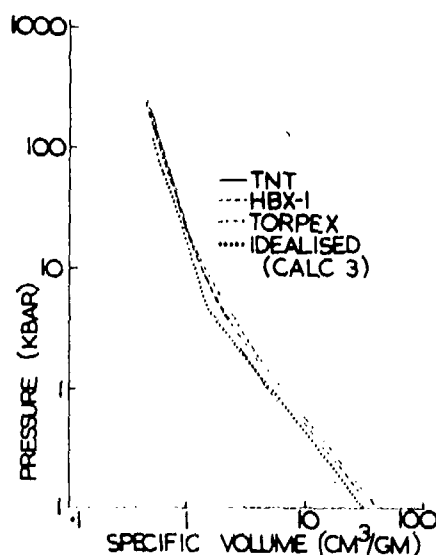
Fig. 3. Theoretical explosive adiabatics.

The curves are very similar in showing a behaviour like pv^γ = constant with γ near 3 at high pressures. At low pressures, where the temperature of the products has dropped greatly and the composition has 'frozen', a similar behaviour is evident, with γ near 1.25. Although purely theoretical, such curves are believed to be realistic, and calculated pressures in the surrounding water agree reasonably well with experimental results (3).

The simplest approximation to such curves is an adiabatic which behaves as an ideal gas with adiabatic exponent equal to 3 for all pressures above a given change-over pressure. For pressures below this change-over, the adiabatic behaves as for an ideal gas with exponent equal to 1.25. Such an adiabatic curve has been added to Fig. 3 for comparison.

For an explosive with such an adiabatic, of original specific volume v_0 and detonation specific energy release h_0, the detonation pressure p_d and pressure p_c at the adiabatic exponent change-over can be shown to be related by

$$h_0 = \frac{1}{8} p_d v_0 [2 + 21(p_c/p_d)^{2/3}]$$

The specific internal energies at the detonation front and at the change-over pressure are, respectively,

$$e_d = \frac{3}{8} p_d v_0 [1 + 7(p_c/p_d)^{2/3}]$$

$$e_c = 3 p_d v_0 (p_c/p_d)^{2/3}$$

These relations have been used to define the adiabatics summarised in Table 1. All correspond to explosives of initial density 1.5 gm/cc; four with a detonation energy of 1 kcal/gm and one of 2 kcals/gm. The detonation pressures were chosen to give the quoted values for $(e_d - e_c)/e_d$, the proportion of the specific detonation internal energy in the part of the adiabatic above the change-over pressure.

Many computer programs are now available which can calculate the flow field around an explosion. The one used here (3) is a rather primitive home-grown program based on the method of characteristics. It can follow the primary shock wave fairly accurately, although the secondary shock in the gas bubble, and the non-homentropic flow behind it, cannot be followed accurately. The calculations are all for central detonation of a sphere of explosive. A secondary program was used to integrate the "Taylor detonation wave" equations (4), to provide the initial pressure and velocity distributions for the main calculation. Typical initial distributions are shown in Fig. 4. The pressures in the penultimate row of Table 1 correspond to the central quiescent regions in such distributions. For the main calculations, a modified Tait equation of state was used for the water. The calculations were all carried out for an initial charge radius of 1 cm and were followed until the shock wave reached a radius of 30 cm.
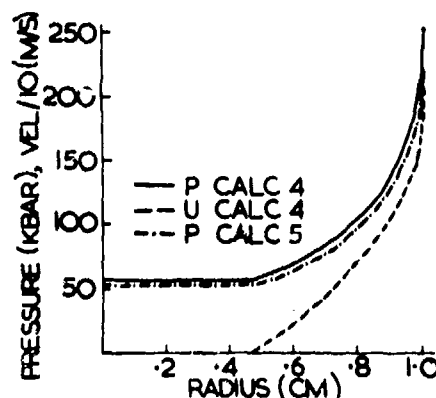
Fig. 4. Pressure and velocity distribution in detonation wave.

553

TABLE 1

Summary of Calculations and Detonation Conditions

Calculation No	1	2	3	4	5
Percentage of energy in high γ part of adiabatic	0	20	50	100	50
Detonation pressure (kbar)	21.8	55.73	115.8	250.3	231.6
Pressure at γ change-over (kbar)	21.8	10.7	4.29	0	8.58
Pressure initially transmitted into the water (kbar)	19.6	43.5	84.8	173	161
Static pressure at bubble centre (kbar)	9.10	12.45	25.9	56	51.7
Detonation energy release (kcal/gm)	1.0	1.0	1.0	1.0	2.0

RESULTS

a. Overall Energy Balance

Throughout the calculation, estimates were kept of the total energy in the gas bubble, the total mechanical energy in the water, the energy dissipated in the water as heat, the mass of gas in the bubble, and the mass of water within the shock front radius. These estimates were used to provide simple conservation checks on the overall accuracy of the calculations but they also provide useful information on the way the energy distribution changes. This is illustrated for calculation 3 in Fig. 5. The following tables, 2, 3 and 4, give comparative figures for the different energies in the five calculations. Much of the energy remainir g in the water as mechanical energy (Table 4) is in the form of kinetic energy. Much of this energy in turn is retained close to the gas bubble as 'incompressible' flow, and is available for the bubble motion, but not for the shock wave, except insofar as the bubble motion affects the pressures in the tail of the shock wave. This 'incompressible' energy can be calculated and subtracted from the water energy to leave the potential and kinetic energy associated with the compressible flow (largely the shock wave). This gives for the shock wave the values shown in Table 5.

From the above results it is clear that the percentage of energy loss as heat near the charge depends strongly on the initial detonation pressure, and that adiabatics close to 1 or 2 are preferable. The shock wave energy values suggest that some of the energy thus saved will be retained in the bubble motion and that in consequence adiabatic 2 is slightly preferable if 'shock wave energy' is to be maximised. The difference between 1 and 2 however is very small.
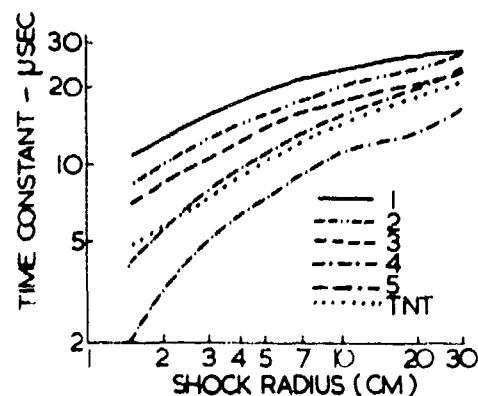
Fig. 5. Energy distribution versus time.

TABLE 2

Fraction of Initial Energy Lost as Heat

Calculation Shock Front Radius (cm)	1	2	3	4	5
5	0.067	0.084	0.195	0.509	0.230
10	0.088	0.103	0.222	0.577	0.266
15	0.097	0.113	0.233	0.603	0.282
20	0.103	0.120	0.240	0.617	0.292
25	0.108	0.124	0.245	0.627	0.298
30	0.111	0.128	0.249	0.634	0.303

TABLE 3

Fraction of Initial Energy Retained in the Bubble Gas

Calculation Shock Front Radius (cm)	1	2	3	4	5
5	0.587	0.568	0.471	0.039	0.446
10	0.448	0.437	0.381	0.021	0.354
15	0.380	0.371	0.330	0.018	0.316
20	0.344	0.337	0.305	0.017	0.288
25	0.316	0.309	0.284	0.017	0.272
30	0.297	0.291	0.270	0.016	0.259

TABLE 4

Fraction of Initial Energy Retained in the Water as Mechanical Energy

Calculation Shock Front Radius (cm)	1	2	3	4	5
5	0.346	0.348	0.334	0.452	0.324
10	0.464	0.460	0.397	0.402	0.380
15	0.523	0.516	0.437	0.379	0.402
20	0.552	0.544	0.455	0.366	0.420
25	0.576	0.567	0.470	0.357	0.430
30	0.592	0.581	0.481	0.350	0.437

TABLE 5

'Shock Wave' Energy as a Percentage of the Original Energy

Calculation Shock Front Radius (cm)	1	2	3	4	5
5	0.170	0.174	0.184	0.291	0.188
10	0.237	0.228	0.191	0.241	0.204
15	0.235	0.256	0.191	0.221	0.205
20	0.240	0.262	0.199	0.208	0.193
25	0.253	0.265	0.202	0.198	0.194
30	0.261	0.270	0.205	0.192	0.195

b. Pressure Signature Results

The 'overall energy' results described above do not correspond to any physically measurable quantities. Normally all results concerning an explosion have to be deduced solely from pressure-time signatures measured at isolated points in the water.

Experimental results usually show a pressure which rises almost instantaneously to a peak value as the shock wave crosses the gauge. The pressure then falls exponentially, thus

$$p(r, t) = p_0(r)e^{-t/\theta}$$

where $\theta(r)$, normally called the decay time constant, indicates the rate of decay. After about 1 time constant, records show a sudden change to a much slower rate of decay, typically as $t^{-4/5}$. At about the same time, the records sometimes also show a second, very small shock wave.

A similar general character for the pressure signatures is evident in the calculated results. Figure 6 shows typical early pressure signatures for calculation 4. The variation of the peak pressure p_0, with standoff is illustrated by the (pressure $\times$ radius) v (radius) curves in Fig. 7. The initial decay time constants are shown in Fig. 8.

It may be noticed that calculations 4 and 5 are very similar in the early stages. The detonation pressures are fairly close, at about 250 kbar, and the initial γ values for the adiabatics are both equal to 3 for pressures down to 8.6 kbar. In consequence, the pressure distributions in the bubble as the detonation wave reaches the water are very similar (Fig. 4). Despite this, as Fig. 8 shows, the time constants for calculation 5 are almost double those for calculation 4, even at 1.5 cm. The reason is that the pressure in the bubble falls very rapidly. In calculation 5, it takes only 3 μs for the bubble to expand to 1.37 cm radius, and the pressure at the gas/water interface has then
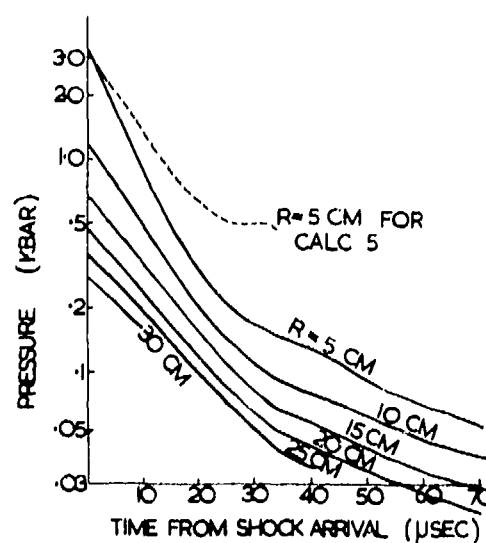
Fig. 6. Pressure signatures for calculation 4.

556
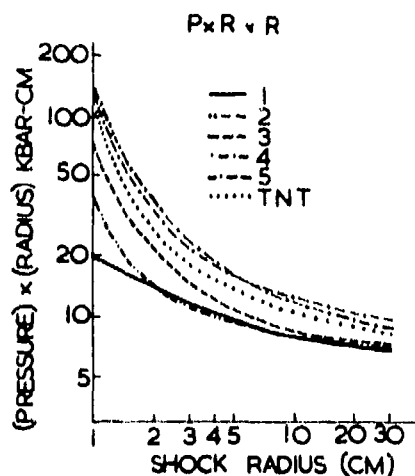
Fig. 7. *Pressure × radius versus radius.*
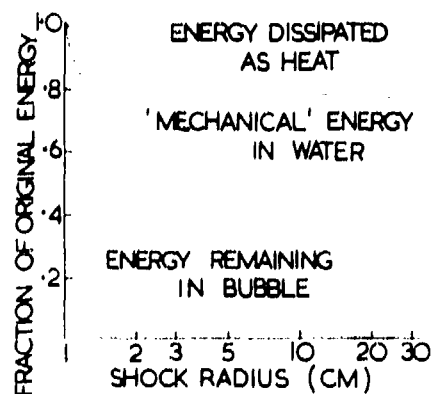
Fig. 8. *Time constants versus radius.*

fallen to about 8.5 kbar, at which level the difference in the adiabatics begins to be felt in the water. Because such effects gradually catch up to the shock wave, this time delay before the point where the pressure signatures start to diverge, steadily reduces. At 2.0 cms radius it is down to 1-1/2 μs and at 5 cms it is less than 1/2 μs, and the similarity between calculations 4 and 5 is almost entirely gone (Fig. 6). As Fig. 7 shows although the peak pressures in calculations 4 and 5 are very similar out to a shock radius of 5 cms, beyond this the difference in the adiabatics is felt even by the shock wave and the calculation 4 peak pressures decay more rapidly than those for calculation 5.

Although the peak shock wave pressure, p_0, and time constant, θ, are the physical parameters most often quoted for underwater explosives, the damage

potentials of different explosives is usually assessed by comparing their impulse and energy fluxes at the standoff concerned. The impulse and energy fluxes are calculated as the integrals

$$ I = k_1 \int_0^{5\theta} p \, dt \qquad \text{impulse} $$

$$ E = k_2 \int_0^{5\theta} p^2 \, dt \qquad \text{energy.} $$

where k_1 and k_2 are constants. For most of the standoffs covered by the present calculations, these integrals cannot be completed (close-in the bubble crosses the standoff concerned before 5θ, and further out, cutting off the calculations when the shock wave reaches 30 cm radius limits the duration available). For a standoff of 10 cms, however, the full integrals have been carried out, giving the results shown in Figs. 9, 10 and summarised in Table 6.

The table shows that, in terms of impulse, the low detonation pressure adiabatics are clearly preferable, again there being little difference between calculations 1 and 2. In terms of energy the high detonation pressure adiabatic retains a sufficiently high pressure at the head of its shock wave to show up fairly well. However, the longer duration of the low detonation pressure adiabatic just gives it an edge. Between these extremes, the energies are lower. Further out from
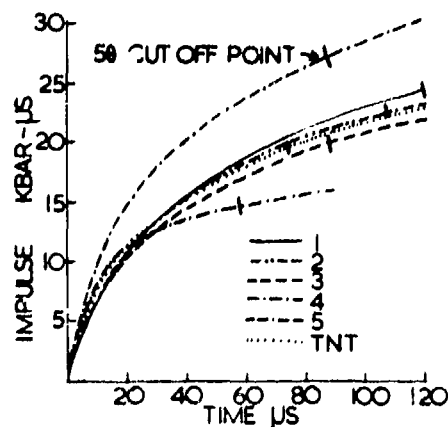
Fig. 9. *Impulse flux versus time at 10 charge radii.*
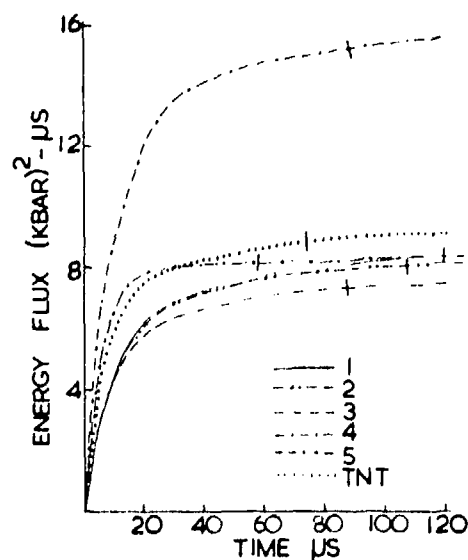
Fig. 10. Energy flux versus time at 10 charge radii.

the charge, the peak pressure in calculation 4 decays more rapidly than in calculations 1-3 (see Fig. 7) and it would probably fare less well in terms of energy flux at such ranges.

BUBBLE ENERGY

As the shock wave travels outward, it leaves behind energy in the form of an outward 'afterflow' velocity of the water. This velocity is simply the incompressible flow around the expanding bubble. Its kinetic energy, added to the energy in the gas itself gives the total bubble energy which shows itself as a vigorous pulsation which can be very damaging.

Traditionally, bubble energy is deduced, via theoretical equations for the bubble motion, from measurements of the bubble pulsation period. Bubble probes have also been used to measure the

radius of the bubble, so that its energy can be estimated as the potential energy of the hole in the water when the bubble is at its maximum size.

From the calculated conditions for the bubble when the shock wave reaches 30 cms, the maximum bubble size and the subsequent bubble minimum size can be estimated from standard incompressible theory. The pulsation energy is then the difference between the potential energies of the bubble at maximum and minimum radii. The results are shown in the following Table 7. The actual values depend slightly upon the depth of the explosion but are sensibly constant for the depths of common practical interest. The difference between the total bubble energy and the pulsation energy represents the energy irretrievably locked in the gas products.

Once again, the low detonation pressure adiabatic leads to the most efficient transfer of energy.

For the generation of bubble energy there need not even be a shock wave. Propellants from rocket motors can produce pulsating bubbles. However, it is possible to go too far in this direction. The pulsation energy is really the difference in the potential energies of the holes in the water when the bubble is at its maximum and minimum sizes. A nonpulsating bubble is relatively innocuous, even if large. Slow burning propellants can produce large bubbles, but these have large minimum radii also, and so the actual pulsation energy available is less than for an equivalent explosive. All the adiabatics used here are far from this limit as the energy of the hole at minimum size is small.

COMPARISON WITH A 'NORMAL' EXPLOSIVE

A calculation similar to the foregoing five calculations has been carried out for TNT of initial density

TABLE 6

*Impulse and Energy Flux Values
at a Radius of 10 cm*

Calculation	1	2	3	4	5
I/k_1 kbar-μs	24.4	22.2	19.9	14.6	27.1
E/k_2 kbar^2-μs	8.35	8.00	7.30	8.08	15.34

558

1.5 gm/cc and an energy release of 1.082 kcals/gm. The adiabatic used was that illustrated in Fig. 3. Results from this calculation have been added to all the figures.

The rather different shaped adiabatic leads to a detonation pressure between calculations 3 and 4 but closet to 4, the poorest performer in the other calculations. The detonation conditions corresponding to Table 1 are:

Detonation pressure	209 kbar
Pressure initially transmitted into the water	157 kbar
Bubble centre static pressure	37 kbar
Detonation energy	1.082 kcals/gm

Corresponding to Tables 2, 3, 4 and 5, TNT gave the values in Table 8. Again TNT lies between calculations 3 and 4 in terms of overall energy although this time closer to 3. For 'shock wave' energy it is roughly equal to 3. In terms of 'shock wave' energy, as defined for Table 5, an explosive with the energy release of TNT could produce nearly 30% more energy if its adiabatic were modelled to resemble that of calculation 2. In terms of mechanical energy in the water, the possible improvement is about 23%.

Figures 9 and 10 show the impulse and energy fluxes at 10 cms standoff. The corresponding values integrated to the time 5θ are:

$$I/k_1 = 19.6 \text{ kbar} - \mu s$$

$$E/k_2 = 8.96 \text{ kbar}^2 - \mu s \, (8.28 \text{ kbar}^2 - \mu s)$$

TABLE 7

Bubble Pulsation Energy as a Fraction of the Original Energy

Calculation	1	2	3	4	5
Total Bubble Energy	0.702	0.672	0.606	0.208	0.560
Pulsation Energy	0.600	0.572	0.513	0.202	0.477

TABLE 8

Overall Energy Balance for TNT

Shock Front Radius	5	10	15	20	25	30
Fraction of energy lost as heat in water	0.287	0.328	0.346	0.357	0.364	0.369
Fraction of energy remaining in bubble	0.322	0.249	0.207	0.187	0.173	0.160
Fraction of energy in water in mechanical form	0.392	0.423	0.447	0.457	0.463	0.471
Fraction of energy in 'shock wave'	0.232	0.229	0.209	0.201	0.205	0.207

559

which may be compared with Table 6. The figure in parentheses is the value obtained by reducing the TNT value to correspond to an initial energy of 1.00 kcals/gm and is a more appropriate value for direct comparision with the other calculations. In terms of impulse, TNT is about equal to calculation 3, and about a 12% improvement would result (19% allowing for the extra energy), if the calculation 2 adiabatic were modelled. In terms of energy flux, the TNT could not be greatly improved, being already very close to the calculation 1 value. At greater ranges the TNT values are probably slightly less favourable.

The pulsation energy for TNT is a fraction 0.425 of the original energy, so again a considerable improvement could be achieved (21%) by modelling the adiabatic for calculation 2.

COMPARISION WITH THE HIGHER DETONATION ENERGY ADIABATIC

The calculation for the higher detonation energy idealised adiabatic (5) shows very substantial enhancement of all the energy levels considered. It naturally has a higher detonation pressure than the comparable lower energy adiabatic (3) and so is less efficient. For the same efficiency, all energies would be exactly 2.0 times greater in calculation 5 than in calculation 3. In fact, the factor is over 1.8 for all energies. Thus, although a substantial proportion of the initial energy is 'wasted' for both these adiabatics, the proportion is not greatly increased at the higher energy.

CONCLUSIONS

The idealised adiabatics used for the calculations described here straddle a wider range than is likely to be producible in a conventional explosive.

The adiabatics all have the same energy release, a form similar to that for actual explosives, and they cover a wide range of detonation pressures.

The results suggest strongly that very high detonation pressures are undesirable from most viewpoints, except possibly the energy flux (measured to 5t). The impulse flux for the adiabatic with the highest detonation pressure was 60% less than that with the lowest detonation pressure, and the bubble energy was 66% less. The energy flux (to 5θ) however was

little different (about 3% down, although intermediate detonation pressures gave up to 10% less).

Normal explosives perform far better than this 'worst' adiabatic. Although having a comparable detonation pressure, the shape of the theoretical adiabatic for TNT at lower pressures compensates to a considerable extent, and for the same energy release, the possible improvements for a modified adiabatic are of the order:

energy flux at 10 charge radii	0%
impulse flux at 10 charge radii	20%
bubble energy	20%

Theoretical adiabatics for HBX-1 and Torpex, two explosives optimised experimentally for underwater use, are illustrated (Fig. 3) and the shape suggests that most of the energy they have in excess of that for TNT is situated well down in the adiabatic. Accordingly, it is likely that they are already quite close to the optimum as calculated here.

The additional loss of efficiency due to increasing the initial energy available to the explosive is not great and this is probably still the most promising avenue to explore in the search for greater damage potential.

REFERENCES

1. Jones, H and Miller, A R: "The detonation of solid explosives: the equilibrium conditions in the adiabatic expansion of the products of detonation." Proc Roy Soc, Ser A Vol 194, No 1039 (Nov 1948), 480.

2. Haywood, J H: "The behaviour of underwater explosions". Proceedings of the Eleventh International Congress of Applied Mechanics, Munich 1964.

3. Hicks, A N: "A numerical analysis of the early behaviour of an underwater explosion". NCRE Report R485, Jan 1964.

4. Taylor, G I: "The dynamics of the combustion products behind plane and spherical detonation fronts in explosives". Proc Roy Soc, Ser A Vol 200, No 1061 (Jan 1950), 225.

THE EFFECT OF EXPLOSIVE PROPERTIES ON THE SHOCK WAVE
PARAMETERS OF UNDERWATER EXPLOSIONS

B. D. Lambourn
Atomic Weapons Research Establishment
Aldermaston, Berkshire, England

*A series of hydro-code calculations has been carried out to find the effect of chang-
ing the parameters in a polytropic equation of state for detonation products, on the
shock pulse in water arising from an underwater explosion. It is found that after
the shock wave has reached 1½ charge radii, there is a strong correlation of shock
pressure with detonation energy, Q, and virtually no dependence on adiabatic ex-
ponent, γ. Conversely the pulse width depends mainly on γ and little on Q. The
effect of changing charge density is that the shock wave parameters scale with
charge mass in the normal way. Further calculations with different shapes for the
Chapman Jouguet adiabat have shown that over a wide range of detonation energies
a remarkably constant percentage of the energy (27-30%) is developed as kinetic
energy of the water, but bubble internal energy is sensitive to the form of equation
of state of the detonation products.*

INTRODUCTION

Two series of detailed calculations on the attenua-
tion of shock waves generated by underwater explo-
sions have been carried out in recent years. Sternberg
and Walker (1) calculated the explosion of a sphere of
pentolite. Mader (2) considered a Tetryl sphere
detonated at various depths. Neither investigation
considered the effect of changing the explosive.
Underwater explosion experiments show that at large
distances from the charge, the shock wave parameters
are not very sensitive to the nature of the explosive,
but, at least in the UK, there has been no systematic
series of calculations to find the effect of changing
explosive parameters on the shock pulse.

Some early hydrocode calculations on underwater
explosions in which the shock wave was smeared out
over several meshes by the artificial viscous pressure
method, were too insensitive to establish the effect of
changing explosive equation of state parameters on
the characteristics of the shock pulse.

The present calculations use an alternative method
of calculating both the shock and detonation waves
as mathematical discontinuities. In the first 'grid' of
calculations, a simple polytropic equation of state
was used for the detonation products, with 3 different
values for the detonation energy Q (800 cal/g, 1000
cal/g, 1200 cal/g); and 3 different values for the
adiabatic exponent γ (2.769, 3.0 and 3.317) at a
constant initial explosive density of 1.6 gcm^{-3}.

Two calculations were done to vary initial density.

Four additional calculations have been carried out
to find the effect of changing the form of the adiabatic
expansion of the detonation products. In part, the
latter series of calculations arose because the energy
distribution in the grid calculations was different
from that quoted by, for example, Penney and
Dasgupta (3).

THE CALCULATIONS

The calculations were carried out using a hydro-
code called MCCOY which has been developed by

Hoskin (4). In MCCOY the detonation wave in the explosive and the first shock wave in an inert material may be treated as a 'sharp' shock. All subsequent shock waves are smeared out by the viscous pressure method.

In the calculations, a 1 cm radius sphere of explosive divided into 25 meshes was initiated at its centre and it was planned to calculate the shock in the water out to about 20 charge radii. It would have been too expensive in computer time to have divided the water into equal thickness meshes, so a gradually increasing mesh size was used in successive regions of the water. A total of 270 meshes was used in the water, the arrangement being shown in Table 1.

The equation of state of the water was taken to be of a simple polynomial form

$$p = 0.0225\,\mu + 0.05725\,\mu\,|\mu|$$

$$+ \rho_0 E\,(0.11 + 5.61\,\mu)$$

where p is pressure in Mb, $\mu = \rho/\rho_0 - 1$, ρ_0 the initial density is 1 gcm^3, and E is the specific internal energy. The first coefficient, 0.0225 Mb, is the bulk modulus of the water. The equation of state is chosen to fit the Hugoniot fairly well, but does not fit the expansion behaviour satisfactorily for densities less than 1 gcm^3. However, it is regarded as adequate for simple comparative calculations.

As has already been noted, a simple polytropic gas equation of state

$$p = (\gamma - 1)\,pE$$

was chosen for the detonation products.

In terms of the initial density ρ_0, γ and the detonation energy per gram Q, the Chapman-Jouguet pressure p_{cj} is

$$p_{cj} = 2\,\rho_0\,(\gamma - 1)\,Q$$

The values of p_{cj} in kb are given for the chosen values of ρ_0, Q and γ in Table 2.

RESULTS

Shock Pressure

Shock pressures in the water at various radii are summarised in Table 2. The initial shock pressure in the water correlates very well with Chapman-Jouguet pressure, as is shown in Figure 1, and for given p_{cj} there is only a mild dependence on Q and γ. This behaviour is to be expected from a consideration of the shock interaction process in the pressure-particle velocity plane. Shock pressure generated in the water is largely determined by the initial conditions behind the detonation wave and changes in the shock impedance of the detonation products are only a second order effect.

The shock wave's memory of the detonation pressure rapidly fades and the striking feature of Table 2 for shock radii of 1.5 cm and greater is that whilst there is a significant increase of shock pressure with detonation energy Q, though decreasing in magnitude for larger charge radii, there is effectively no dependence on adiabatic exponent γ. In fact shock pressure increases with γ for small shock radii, is essentially independent of γ at a shock radius of 5 cm, and decreases with γ at larger radii. Hence, the higher the value of γ, the greater the rate of attenuation of the

TABLE 1

Distribution of Meshes in the Calculations

Explosive		Water			
n = 25 dR = .040	n = 20 dR = .025	n = 30 dR = .033	n = 50 dR = .050	n = 70 dR = .071	n = 100 dR = .100
R (cm) 1	1.5	2.5	5.0	10.0	20.0

TABLE 2

Shock Pressure in kb at Various Shock Radii

(Initial charge density 1.6 gcm⁻³)			
Q	800	1000	1200
γ = 2.769	p_{cj}	190	237	284
	R = 1.0	138	170	203
	1.5	34.1	41.1	47.8
	2.0	17.8	20.8	23.9
	5.0	3.14	3.52	3.89
	10.0	1.17	1.30	1.41
	14.0	0.752	0.825	0.886
γ = 3.0	p_{cj}	214	268	321
	R = 1.0	151	187	223
	1.5	35.8	42.9	50.5
	2.0	18.2	21.4	24.4
	5.0	3.13	3.50	3.90
	10.0	1.16	1.29	1.39
	14.0	0.744	0.813	0.870
γ = 3.317	p_{cj}	248	310	372
	R = 1.0	169	209	249
	1.5	37.6	45.4	53.0
	2.0	18.8	22.0	25.1
	5.0	3.12	3.49	3.86
	10.0	1.15	1.26	1.36
	14.0	0.732	0.798	0.852

Note: The header columns are Q, 800, 1000, 1200. The γ values (2.769, 3.0, 3.317) label each block in the left margin.

shock amplitude. Thus, although a larger value of γ gives a larger p_{cj}, it also implies that when the bubble has expanded to a given radius, the average bubble pressure will be smaller. Signals from the more rapidly dropping bubble pressure catch up with the shock wave and cause it to attenuate more rapidly.

Pulse Width and Impulse

Shock pulse width and approximate shock impulse are plotted as functions of Q and γ at a shock radius of 10.3 cm in Figs. 2 and 3. The radius of 10.3 cm was chosen to compare with some earlier viscous shock runs.

The pulse width θ is taken at $1/e$ times the shock pressure and an approximate shock impulse is evaluated from

$$I = \int_{t_s}^{\alpha} p_s \exp\left(- \left[t - t_s\right]/\theta\right) dt = p_s \cdot \theta$$
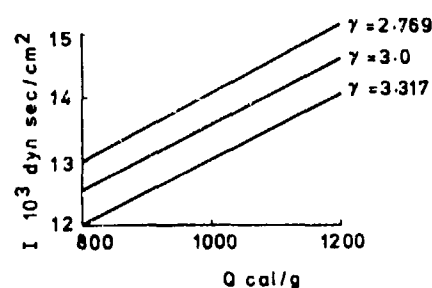
Fig. 2. *Dependence of pulse width θ on Q and γ at $R = 10.3$ cm $(\rho_o = 1.6\, g\, cm^{-3})$.*
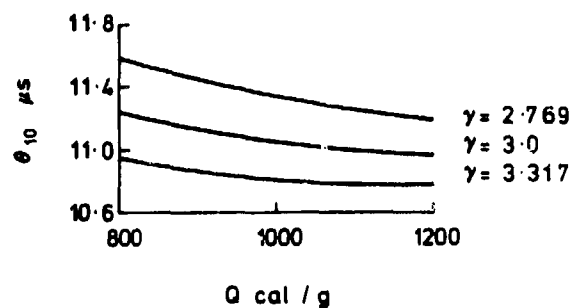
Fig. 3. *Dependence of impulse on Q and γ at $R = 10.3$ cm $(\rho_o = 1.6\, g.cm^{-3})$.*

Fig. 1. *Initial shock pressure as a function of p_{cj}*

For convenience in plotting the computer runs, the pressure-time history has been analysed assuming that the measuring station moves with the water, rather than remaining stationary. Since the water particles initially at radius 10.3 cm have only moved 0.06 cm in time θ, the error is not large. Figure 2 shows that the pulse width θ is nearly independent of Q and decreases as γ increases. This is consistent with the previous discussion on the dependence of shock pressure on γ. A faster rate of decay in pressure at the bubble surface will produce a narrower shock pulse.

As a result of the dependence of shock pressure on Q and pulse width on γ, the impulse increases w Q and decreases with γ, as shown in Fig. 3.

Effect of Change in Explosive Density

In order to explore the effect of changing the explosive density, two additional calculations have been carried out, keeping γ fixed at 3.0 and Q at 1000 cal/g. The two densities were 1.33 and 2.0 g.cm^{-3} and the calculations can be compared with the appropriate grid run, with density 1.6 g.cm^{-3}. In the calculations the charge radius was fixed at 1 cm, so that the charge mass varies in proportion to the density. In analysing the runs it seem profitable to enquire whether the results fitted the normal scaling laws. The results of the calculations were therefore tabulated at a suitable shock radius, so that they could be compared directly with the grid calculation at 10.3 charge radii, i.e., the shock pulse was evaluated at a radius of 10.3 times the cube root of the ratio of the densities,

and the corresponding pulse widths were divided by this factor.

Table 3 shows for the two runs at densities of 1.33 and 2.0 g cm^{-3} the actual shock pressure and pulse width at the appropriate scaled radius, together with the pulse width and impulse scaled to be equivalent to 10.3 charge radii for the calculation at an initial density of 1.6 g cm^{-3}. It will be seen that the shock pressures at the scaled radii agree within 2% despite the fact that the Chapman-Jouguet pressures vary by % and the initial shock pressure in the water by %.

The scaled pulse widths agree to within 3% and the scaled impulse to within 4%. Thus scaling appears to hold well for a wide range of initial explosive densities.

Energy Distribution

Figure 4 shows the distribution of kinetic and internal energy in the water for the calculation with $\rho_o = 1.6$ g cm^{-3}, Q = 1000 cal/g and $\gamma = 3$, as a function of time. Region 1 corresponds to water initially between the charge and radius 1.5 cm, and region 2 to the water outside 1.5 cm. It will be seen that the kinetic energy in region 1 is negligible. The internal energy remaining in region 1 is constant at about 20% of the total. In region 2 the internal energy is slowly increasing and is about 50% of the available energy, and the kinetic energy of region 2 is slowly decreasing and contains the remaining 30% of the energy.

TABLE 3

Effect of Initial Explosive Density

Initial Density ρ_o (g cm^{-3})	Detonation Pressure p_{cj} (kb)	Initial Shock Pressure p_1 (κb)	Actual Conditions at Scaled Radius			Scaled Conditions at scaled Radius		
			Radius R (cm)	Pressure p_s (kb)	Pulse Width θ (μs)	Radius R (cm)	Pulse Width θ' (μs)	Impulse $p_s\theta'$ (kb μs)
1.33	222	169	9.7	1.25	10.2	9.7	10.9	13.5
1.6	268	187	10.3	1.23	11.0	10.3	11.0	13.6
2.0	334	211	11.1	1.22	11.5	11.1	10.7	13.0
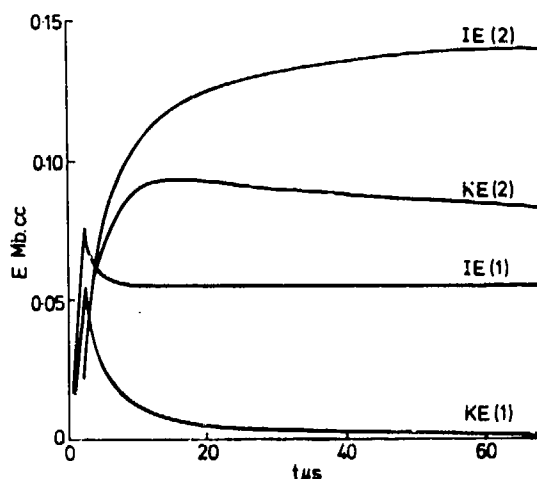
Fig. 4. Energy history in water region (1) (R < 1.5 cm) and region (2) (R > 1.5 cm) $\rho_o = 1.6$ g cm^{-3}, Q = 1000 cal g^{-1}, $\gamma = 3.0$.

When the shock radius is $\sim$ 14 cm, the percentage of the total energy as internal energy in region 1 increases slightly with both γ and Q, corresponding to an increase in shock heating, whereas the percentage of the total energy as internal energy in region 2 increases slightly with Q and is independent of γ.

The distribution of energy may be compared with the results of Penney and Dasgupta (3), and Walker and Sternberg (1), who calculated the distribution when the shock wave has reached 6 charge radii.

Table 4 compares the energy distributions when the shock has reached 6 charge radii. It will be seen that whereas the MCCOY grid calculation has less than 1% of the explosive energy remaining in the bubble, the other calculations have 25%. The proportion of energy available as kinetic energy is the same for all three calculations, and so the energy lost from the bubble is in the water as internal energy.

The MCCOY calculations have not been analysed to find how the internal energy in the water should be divided between shock heating and compressional energy, but it is likely that the shock heating is similar in the three cases.

It was at first thought that the curious energy distribution in the MCCOY calculation might be due to the rather simple equation of state assumed for the water, but a calculation with a different EOS soon showed that this was not so.

Further calculations have therefore been carried out with variations in the equation of state for the detonation products.

THE EFFECT OF EOS VARIATIONS

Description of the Equations of State

The calculations were carried out using three equations of state for the U.S. explosive PBX 9404 and for an extrapolated theoretical explosive--"high energy

TABLE 4

Comparison of Energy Distributions at 6 Charge Radii

	Penney and Dasgupta	Sternberg and Walker	MCCOY Calculations
Explosive	TNT $\rho_0 = 1.5$	Pentolite $\rho_0 = 1.65$	Q = 1000 $\gamma = 3.0$ $\rho_0 = 1.6$
Water KE	33%	34%	34%
Water IE (Shock htg) (Compressive)	27% 14%	34%) 13%)	65%
Bubble IE	25%	25%	< 1%

565

9404." Each explosive had the same Chapman-Jouguet pressure and detonation velocity, but different shapes for the adiabatic expansion in the pressure-volume plane. Analytically the adiabats were:

(a) Polytropic gas

$$p = \frac{C_1}{v^\gamma}$$

(b) Constant β equation of state (5)

$$p = \frac{A}{v^\delta} + \frac{C_2}{v^{1+w}}$$

(c) Jones-Wilkins-Lee equation of state (6)

$$p = B_1 e^{-k_1 v} + B_2 e^{-k_2 v} + \frac{C_3}{v^{1+w}}$$

where $\gamma, A, \delta, w, B_1, k_1, B_2, k_2$ are material constants and C_1, C_2, C_3 are functions of entropy which are, of course, constants for the respective Chapman-Jouguet adiabats.

Adiabats for the four equations of state are shown in the $\ln p - \ln v$ plane in Fig. 5. JWL constants for many explosives are given by Lee, Hornig and Kury (7).

The four calculations carried out were as follows:

312B–JWL equation of state with detonation energy[*] 1342 cal/g.

312C–Polytropic gas equation of state with γ equal to the value at the C-J state for PBX 9404 (γ = 2.66); detonation energy 1543 cal/g.

312E–Constant β equation of state, with the same C-J state and same low pressure behaviour as the JWL equation of state; detonation energy 1852 cal/g.

312D–Hypothetical constant β equation of state, with the same C-J state as the other calculations but 8

[*]The detonation energy is the area in the p-v plane between the C-J adiabat and the Rayleigh line joining the initial state $p = 0$, $v = v_0$, to the C-J state. It is the maximum amount of energy available for doing hydrodynamic work.

times larger pressure than 312E at large expansions; detonation energy 3678 cal/g.

Whereas runs 312B, C and E all represent, to a greater or lesser extent, the true behaviour of PBX 9404, run 312D was purely an attempt to find the effect of a markedly different expansion behaviour on the shock pulse. However, runs 312B, E and D are members of the same family of equations of state, with increasing detonation energies.

Energy Distributions

Tables 5 and 6 show the distribution of energy when the shock has reached 10 charge radii, first in terms of the distribution of calories per gram of explosive, and secondly as percentages of the detonation energy available. The water is divided into two parts—(1) that initially between the explosive and 1.5 charge radii, for which the internal energy is mainly shock heating; and (2) that outside 1.5 charge radii.
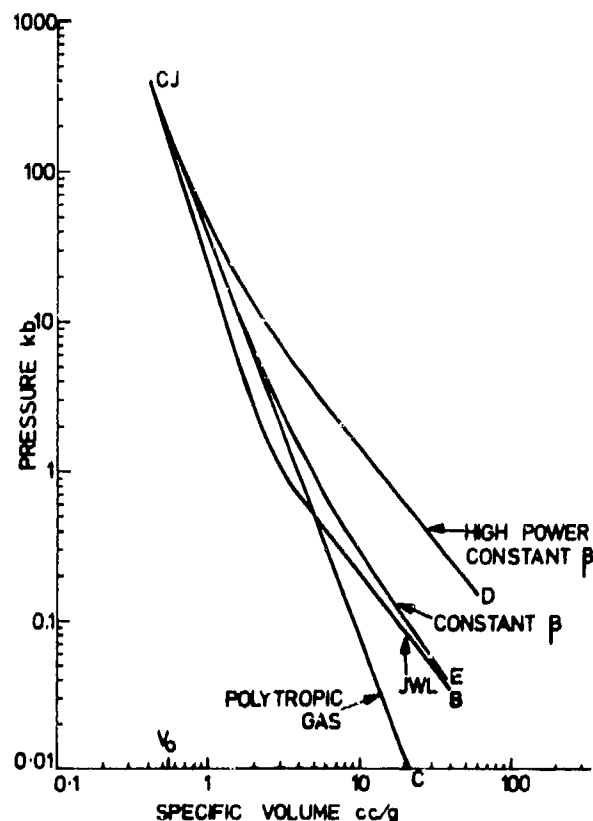
Fig. 5. Chapman-Jouguet adiabats for PBX 9404 variants.

TABLE 5

Energy Distribution for "PBX 9404" in Calories/gram

	JWL	Polytropic Gas	Constant β	High Energy Constant β
Bubble: KE	7	3	7	4
IE	162	3	154	936
Region (1): KE	5	5	6	11
IE	240	274	274	284
Region (2): KE	370	435	530	1106
IE	558	823	881	1337
Total	1342	1543	1852	3678 cal/g

TABLE 6

Energy Distribution for "PBX 9404"--Percentages

	JWL	Polytropic Gas	Constant β	High Energy Constant β
Bubble: KE	0.6	0.2	0.4	0.1
IE	12.1	0.2	8.3	25.4
Region (1): KE	0.4	0.3	0.3	0.3
IE	17.8	17.8	14.8	7.7
Region (2): KE	27.5	28.2	28.6	30.1
IE	41.6	53.3	47.6	36.4

The conclusions that may be drawn from these calculations are that

(1) the bubble internal energy is indeed a strong function of equation of state. The key to the difference lies in the low pressure behaviours of the equations of state. Each tends towards a straight line in the ln p - ln v plane (Fig. 5) and hence behaves like a perfect gas. Thus at low pressures the internal energy is of the form

$$e \sim \frac{pv}{x - 1}$$

but whereas $x - 1$ is $\gamma - 1$ for the polytropic gas EOS and is of order 2, $x - 1$ is w for the JWL and constant β equations of state and is of order 0.4. In addition,

Table 8 shows that when the shock has reached 10 charge radii, the bubble radius is nearly constant, so that v is roughly independent of the EOS. However, Fig. 6 shows that the pressure for the polytropic gas EOS is low compared with the other equations of state. These two factors account for the low internal energy in the water in the grid calculations.

(2) The internal energy in the inner region of the water is nearly independent of the equation of state and accounts for, perhaps, half of the shock heating. It is a reflection of the fact that shock pressure histories are similar in the early stages of the calculations.

(3) Ultimately the greater internal energy and greater pressure remaining in the bubble for the JWL

567

and constant β equations of state are going to have an effect on the bubble expansion. Had the calculations been taken on to a much later time, it is probable that the bubble behaviour would have been quite different for the polytropic gas EOS than for the other calculations.

Shock Wave Parameters

The shock wave parameters for the four 'PBX 9404' calculations are summarised in Tables 7 and 8.

Table 7 shows the variation of shock pressure with radius. All start with almost the same shock pressure in the water. The polytropic gas and constant β equations of state have very similar shock histories, essentially because the detonation product adiabats are closely similar, down to a few kilobars (Fig. 5).

The values of pulse width to some extent reflect the low pressure behaviour of the explosives. The polytropic gas calculation has a smaller pulse width, essentially because the bubble pressure drops more rapidly.

CONCLUSIONS

The results of the earlier grid calculations using the polytropic equation of state show that

(1) Initial shock pressure in the water increases with detonation pressure p_{cj}.

(2) In the body of the water the shock pressure depends mainly on the detonation energy Q and little on the adiabatic exponent γ of the detonation products. At 10 charge radii, the shock pressure increases by 20% for a 50% change in Q.

(3) Pulse width depends mainly on γ and not on Q, when the shock has reached 10 charge radii. A 20% increase in γ produces a 6% reduction in pulse width.

(4) The calculations suggest that about 30% of the available energy remains as internal energy of the water initially between the charge and 1½ charge radii; and that when the shock has reached 14 charge radii, about 70% of the available energy is in the form of internal energy of the water.

TABLE 7

Shock Pressure at Various Radii for "PBX 9404"

R (cm)	JWL	Polytropic Gas	Constant β	High Energy Constant β
1.0	262.4	263.9	263.7	264.2
1.5	52.4	63.2	63.4	67.2
2.0	25.1	31.5	31.8	35.1
5.0	3.85	4.84	5.02	6.35
10.0	1.39	1.68	1.75	2.23
12.5	1.02	1.22	1.27	1.61

TABLE 8

Bubble Radius and Impulse at 10.3 Charge Radii

	JWL	Polytropic Gas	Constant β	High Energy Constant β
R	3.04	3.14	3.22	3.62 cm
p_s	1.33	1.61	1.67	2.13 kb
θ	12.7	11.5	12.2	14.1 μs
$I = p_s\theta$	16.8	18.4	20.5	29.9 kb μs

Calculations on the effect of changing charge density show that, at least in the range at which the results were analysed (i.e., at ~ 10 charge radii), the shock pressure, pulse width and impulse are in satisfactory agreement, providing normal scaling with the cube root of the mass is used.

The fact that the energy distribution for the grid calculations was different from that shown by other authors has been investigated by four calculations on the explosive PBX 9404, with different shapes for the Chapman-Jouguet adiabat. The calculations show

(a) that the internal energy remaining in the bubble when the shock has reached 10 charge radii is very dependent on the low pressure adiabatic exponent of the detonation products and on the pressure in the products at large expansions;

(b) that over a very wide range of detonation energies, 800 to 3700 cal/g, a remarkably constant percentage of the energy (27-30%) is developed as kinetic energy of the water.

ACKNOWLEDGMENTS

REFERENCES

1. H. M. Sternberg and W. A. Walker: "Calculated Flow and Energy Distribution Following Underwater Detonation of a Pentolite Sphere;" Physics of Fluids 14 (9), 1869-1878, (Sept. 1971).

2. C. L. Mader: "Compressible Numerical Calculations of Underwater Detonations;" LA-4594 (March 1971).

3. W. G. Penney and H. K. Dasgupta: "Pressure-Time Curves for Sub-Marine Explosions (Second Paper);" Underwater Explosions Research, Vol. I, The Shock Wave, 289-299, Office of Naval Research, Department of the Navy, 1950.

4. N. E. Hoskin: "MCCOY and SIMLA—General Purpose Programs for One-Dimensional Unsteady Compressible Fluid Flow." AWRE Report 0-42/72, (July 1972).

5. W. Fickett and W. W. Wood: "A Detonation-Product Equation of State Obtained From Hydrodynamic Data." Physics of Fluids 1 (6), 528-534, (1958).

6. J. W. Kury et al: "Metal Acceleration by Chemical Explosives." 4th Symposium (International) on Detonation, ACR-126, 3-13, (1965).

7. E. L. Lee, H. C. Hornig, and J. W. Kury: "Adiabatic Expansion of High Explosive Detonation Products;" UCRL 50422 (1968).

THE UNSTEADY REGULAR AND MACH REFLECTION RESULTING FROM THE INTERACTION OF SPHERICAL EXPLOSION SHOCK WAVES IN WATER

Julius W. Enig

Naval Surface Weapons Center, White Oak Laboratory
White Oak, Silver Spring, Maryland 20910

Numerical solutions have been obtained for the unsteady phenomena of regular and Mach reflection occurring when two identical spherical explosive charges of pentolite, of radius a_0 and center-to-center separation distance 2ℓ, are simultaneously detonated underwater. Calculations have been performed for $3.0 < 2\ell/a_0 < 11.1$ with an equation of state of water due to Sternberg and Walker (S-W). Good agreement has been obtained between the numerical results and the existing experimental shadowgraphs for the motion of the shock waves and the development of the Mach stem. The characteristic properties of water have been analyzed in detail with the aid of oblique shock theory. The von Neumann simple three-shock solution does not occur for incident shock pressures below 5 kilobars if the S-W or the HOM equations of state are used to represent water. The use of the S-W and HOM equations in oblique shock theory correctly predicts the Mach stem pressure at the critical shock angle while a γ-law type does not.

I. INTRODUCTION

It is known from World War II experiments that regular shock reflection on the plane of symmetry, that arises when two identical explosive charges are simultaneously detonated underwater, changes abruptly to Mach reflection when the angle between the incident spherical shock front and the pla.ie of symmetry becomes sufficiently large.

At present, no analytical solutions exist which describe the effect of the unsteady flow field on the formation, growth, and strength of the Mach stem, and, in particular, on the growth angle of the triple point. In the case of Mach reflection arising from the intersection of spherical shock waves, a "growth" angle for the locus of the "triple point" has been calculated and compared with previous experimental observations. The calculated results are derived from a numerical solution of the partial differential equations. The discussion will be in the following sequence:

Three different equations of state of water and an equation of state of the detonation products of the explosive, pentolite, are given in §II. Historically, the simplest method of analyzing a problem involving unsteady oblique shocks has been to consider the unsteady oblique shock phenomena as a sequence of pseudostationary events, each of which may be treated by stationary oblique shock theory. The application of this theory to the calculation of regular and Mach reflection in water using, for the first time, the recent Sternberg-Walker (S-W) and HOM equations of state, is made in §III. A brief discussion of the experimental data on the collision of spherical shock waves in water is given in §IV and oblique shock theory is applied to some of these experiments in order to calculate the flow parameters at the critical angle for Mach reflection. In §V, the flow equations for unsteady axisymmetrical compressible flow are written in Lagrangean coordinates which consist of two families of concentric circles. Finally, the numerical solution for the problem of two simultaneously detonated explosive spheres

underwater is given in §VI. Calculations for different ratios of the charge separation to charge radius with different equations of state of water are shown and comparison is made with existing experimental results.

II. EQUATIONS OF STATE

Sternberg and Walker (S-W)

The E, p, V equation of state of water, due to Walker and Sternberg (1), is of the form

$$p = f_1/V + f_2/V^3 + f_3/V^5 + f_4/V^7 , \quad (2.1)$$

where f_1, f_2, f_3, and f_4 are polynomial functions of the specific internal energy, E, fit to both the shock Hugoniot data and the low-pressure compressibility data for fresh water, and p and V are, respectively the pressure and specific volume. The initial state of the water, denoted by superscript 0, is given by $p^0 =$ 1 atm = 1.01325 bar, $\rho^0 \cong 1/V^0 = 0.99821$ g/cm^3, and $E^0 = 0$.

γ-Law Type

In early calculations on shock waves in water, Polachek and Seeger (2) employed the E, p, V equation of state for water that resembles a γ-law gas:

$$p = [p_0 V_0 + \gamma A(V_0 - V) + (\gamma - 1)E](\gamma - 1)E/V, \quad (2.2)$$

where A = 3000 atm and γ = 7.15. Here p_0 = 1 atm and V_0 = 1.000 cm^3/g are initial values at 20°C.

HOM Equation

The HOM equation of state for water, used by Mader and Gage (3), fits the experimental data for the single shock Hugoniot to a Grüneisen equation of state.

WSH Equation

The E, p, V equation of state for the detonation products of pentolite is given by

$$p = AE/V + B/V^4 + Ce^{-KV} , \quad (2.3)$$

where A = 0.35, B = 0.002164 mbar cm^{12}/g^4, C = 2.0755 mbar, and K = 6. The functional form of Eq. (2.3) is due to Wilkins, Squier, and Halperin (4), but the method for obtaining the constants A, B, C, and K is given in Ref. 1. These values hold when the undetonated explosive has an initial density of ρ^0 = 1.65g/cm^3 and a detonation energy of 0.0536 mbar cm^3/g (1280 cal/g).

The Chapman-Jouguet (CJ) detonation conditions for pentolite are p_{CJ} = 0.2452 mbar, ρ_{CJ} = $1/V_{CJ}$ = 2.210 g/cm^3, E_{CJ} = 0.0724 mbar cm^3/g, and c_{CJ} = 0.5714 cm/μsec, where c is the sound speed.

III. REGULAR AND MACH REFLECTION

Oblique Flow Across an Incident Shock

Consider a stationary plane shock IO, and let u_0 be the fluid velocity in the vertical direction entering IO at an angle β, the shock angle, and u_1 be the fluid velocity exiting IO after being deflected by an angle θ_1, the deflection angle, as shown in Fig. 3.1. The deflection angle is positive if the acute angle that the deflected flow makes with the direction of u_0 is measured in the counterclockwise direction. Let

$$u_{0n} = u_0 \sin \beta \quad (3.1)$$

and u_{1n} be the components of these velocities normal to the shock, and u_{0t} and u_{1t} be the components tangential to it. Let p_0, ρ_0 and p_1, ρ_1 be the pressure and density "in front of" and "behind" the shock, respectively, of Fig. 3.1. The equation of continuity is

$$\rho_1 = \rho_0 u_{0n}/u_{1n} . \quad (3.2)$$
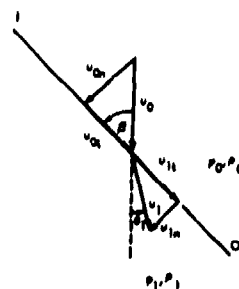
Fig. 3.1. Stationary plane shock 10 making angle β with incoming flow of velocity u_0; θ_1 is deflection angle.

The momentum equation in the normal direction is

$$p_1 - p_0 = \rho_0 u_{0n}(u_{0n} - u_{1n}) \qquad (3.3)$$

which, together with Eq. (3.2) yields

$$\rho_0^2 u_{0n}^2 = (p_1 - p_0)/(V_0 - V_1), \qquad (3.4)$$

where $V \equiv 1/\rho$. The conservation of energy across the shock requires that

$$E - E_0 = (p_1 + p_0)(V_0 - V_1)/2. \qquad (3.5)$$

In the tangential direction,

$$u_{1t} = u_{0t}. \qquad (3.6)$$

From $\tan \beta = u_{0n}/u_{0t}$, $\tan(\beta - \theta_1) = u_{1n}/u_{1t}$, and Eqs. (3.2) and (3.6) it follows that

$$\theta_1 = \beta - \tan^{-1}[(\rho_0/\rho_1)\tan \beta]. \qquad (3.7)$$

Behind the shock front,

$$u_1 = u_{1n}/\sin(\beta - \theta_1). \qquad (3.8)$$

For known p_0, V_0, and, therefore, E_0, the flow across IO involves nine variables, namely, u_0, u_{0n}, p_1, V_1, E_1, u_1, u_{1n}, θ_1, and β, connected by the equation of state $E \equiv E(p, V)$ and Eqs. (3.1), (3.2), (3.4), (3.5), (3.7), and (3.8). Thus, specification of any two yields the other seven variables.

Example 1: Assume p_1 and β are given. Equation (3.5) and $E = E(p, v)$ leads to a known Hugoniot relationship, $V_1 = V_1(p_1)$; and E_1, u_{0n}, u_0, u_{1n}, u_1, and θ_1 follow directly from Eqs. (3.5), (3.4), (3.1), (3.2), (3.8), and (3.7), respectively.

Suppose u_0 is given. Then p_1 is a function of the deflection angle θ_1. A plot of this function, the shock polar ABCD, is shown in Fig. 3.2. The shock polar ABCD is the locus of possible shocked states $p_1(\theta_1)$ when the flow ahead of the shock is in state (0). The pressure p_0 at A corresponds to $u_{0n} = c_0$, where c_0 is the sound speed of the incoming fluid; the maximum pressure $p_{1,max}$ at C corresponds to $u_{0n} \sim u_0$ in Eq. (3.4), i.e., the shock wave is normal to incoming flow. The point B corresponds to the angle of maximum possible deflection of the flow,
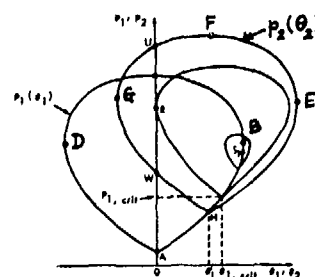
Fig. 3.2. Coelescence of the weak and strong shocks solutions W and U to the point R as $p_1' \to p_{1,crit}$ in regular reflection. S_1 is the sonic-point.

$\theta_{1,max}$. The segment ADC corresponds to flow deflections through negative angles. For each value of $\theta_1' < \theta_{1,max}$, there exist two solutions. The segment DAB corresponds to the "weak shock" solution for which β is relatively small and the downstream flow is generally supersonic. Inasmuch as S_1, the sonic point, is very close to B, there exists a small subsonic segment $S_1 B$ corresponding to the weak shock solution. BCD corresponds to the "strong shock" solution for which β is relatively large and the downstream flow is subsonic. Which of the two solutions is the physical one depends on the boundary conditions.

Oblique Flow Across a Reflected Shock

Let a uniform flow with velocity u_0 be deflected on passing through the two plane shocks IO and I'O through angles $\theta_1' \neq \theta_1' \neq \theta_1^{*'}$ as shown in Fig. 3.3. Now there are present two reflected shocks RO
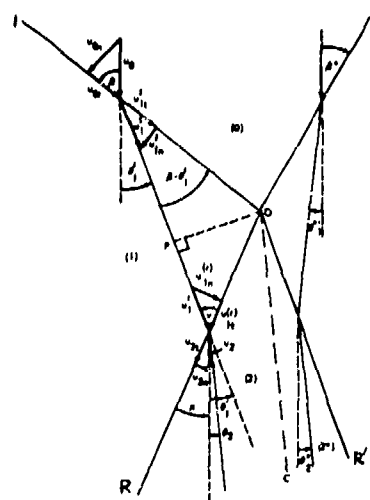
Fig. 3.3. Four-shock configuration.

572

and R'0 and a slip line 0C. The particles along the streamline passing through I0 emerge from R0 having the same direction, but different speed, as those along the streamline emerging from R'0. Both streamlines are parallel to 0C. Region R0R' has constant pressure, though R0C and R'0C have different entropies. If the shocks I0 and I'0 are of equal strength, i.e., the angles θ_1' and $\theta_1^{*\prime}$ are identical, then 0C vanishes and the flow is symmetric, being equivalent to shock reflection off a rigid wall.

In Fig. 3.3, ahead of I0, the flow variables are again denoted by subscript 0; behind I0 by subscript 1 and a prime, the latter denoting that the flow has been determined; behind R0 by the subscript 2 in R0C where the flow is to be determined. In I0R, Eqs. (3.2)-(3.8) hold, but with a prime on all variables with subscript 1.

In order to consider the flow across R0, let ν be the angle that the incoming streamline makes with R0, $\mu \equiv \nu - \theta_1'$ be the angle that R0 makes with the vertical (i.e., the direction of u_0), and θ_2 be the angle that the streamline makes with the vertical. (In Fig. 3.3, ν is an acute angle.) Therefore, $\theta_1' - \theta_2$ is the angle that the streamline is deflected on crossing R0. Let

$$u_{1n}^{(r)} \equiv u_1' \sin \nu, \quad u_{1t}^{(r)} \equiv u_1' \cos \nu$$

be, respectively, the normal and tangential components of u_1' relative to R0. Across R0, and analogous to Eqs. (3.5), (3.4), (3.2), and (3.6),

$$E_2 - E_1' = (p_2 + p_1')(V_1' - V_2)/2 \qquad (3.9)$$

$$u_{1n}^{(r)} = V_1'[(p_2 - p_1')/(V_1' - V_2)]^{1/2} \qquad (3.10)$$

$$u_{2n} = u_{1n}^{(r)}V_2/V_1', \qquad (3.11)$$

$$u_{2t} = u_{1t}^{(r)}, \qquad (3.12)$$

where u_{2n} is the normal component of u_2 relative to R0. From

$$\nu = \sin^{-1}\left(u_{1n}^{(r)}/u_1'\right), \qquad (3.13)$$

$$\frac{\tan(\mu + \theta_2)}{\tan \nu} = \frac{u_{2n}/u_{2t}}{u_{1n}^{(r)}/u_{1t}^{(r)}} = \frac{u_{2n}}{u_{1n}^{(r)}} = \frac{V_2}{V_1'},$$

where Eqs. (3.11) and (3.12) have been used, it follows that

$$\theta_2 = \theta_1' - \nu + \tan^{-1}[(V_2/V_1')\tan \nu]. \quad (3.14)$$

Once the flow in I0R has been determined, the flow in R0C is determined with the aid of another shock polar. The equation of state and Eqs. (3.9)-(3.11), (3.13), and (3.14) are six equations in the seven unknowns p_2, V_2, E_2, $u_{1n}^{(r)}$, u_{2n}, ν, and θ_2. Therefore, p_2 is a function of θ_2. A plot of this function, shown in Fig. 3.2, gives the shock polar HEFG as the locus of possible states 2 in R0C of Fig. 3.3. H corresponds to the state 1 ahead of the reflected shock, where $\theta_1 = \theta_1'$ and $p_1 = p_1'$. Another piece of information is needed in order to single out a particular state 2 from among the possible. In Fig. 3.3, 0P is the perpendicular to the direction of u_1'. If $\nu < \pi/2$ (as shown), then R0 is called *backward-facing*, and $\theta_2 < \theta_1'$. If $\nu > \pi/2$ (as in Fig. 3.4), then R0 is a *forward-facing* shock, and $\theta_2 > \theta_1'$. In Fig. 3.2, HEF corresponds to forward-facing shocks and HGF corresponds to backward-facing shocks.
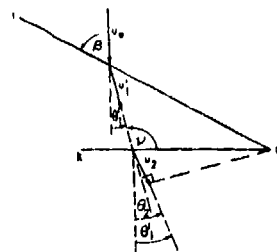
Fig. 3.4. A forward-facing reflected shock R0; $\nu < 90°$.

Regular and Mach Reflection at a Rigid Wall

The weak shock state W of Fig. 3.2 corresponds to regular reflection off a rigid wall as shown in Fig. 3.5, i.e., $\theta_2 = 0$ in Fig. 3.3. As p_1' (and, therefore, θ_1') increases for fixed u_0, the shock polar for state 2 becomes smaller as shown in Fig. 3.2, and finally shrinks to a point when H reaches the sonic point S_1 of the shock polar $p_1(\theta_1)$. For $p_1' = p_{1,crit}$, the weak and strong shock solutions W and U, respectively, coalesce to R in Fig. 3.2. For $p_1' > p_{1,crit}$

573
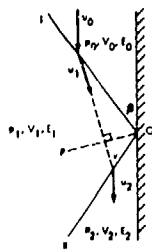
Fig. 3.5. Reflection off a rigid wall reduced to steady flow.

Fig. 3.7. Shock polar showing two Mach stem intersections.

(and, therefore, $\theta_1' > \theta_{1,\text{crit}}$), regular reflection off a rigid wall is no longer possible. Because β increases with increasing p_1' for fixed u_0, it follows that there exists a critical incident shock angle β_{crit} such that regular reflection is not possible for $\beta > \beta_{\text{crit}}$. Here, "Mach reflection" is encountered. The simplest form of Mach reflection consists of the von Neumann (5) "three-shock configuration."

Mach Reflection With "Zero Growth Angle"

In a coordinate system centered at the "triple point" T, moving parallel to u_0, the steady flow in the neighborhood of T, is depicted in Fig. 3.6. The incoming flow enters the incident shock IT at an angle β. The reflected shock RT, making an angle β_r with u_0, is shown as backward-facing. Let MT be the tangent to the Mach stem WT at T. The flow passing through IT and RT emerges parallel to the flow passing through MT and at the same pressure; the slip line CT divides RTM into two regions RTC and MTC in which the flow speeds are different. The flow in RTM is represented by the two intersections, T and T* of Fig. 3.7, which correspond to a backward-facing (see Fig. 3.6) and a forward-facing (see Fig. 3.4) reflected shock, respectively. The point T is thought to give the correct solution. The shock

Fig. 3.6. Mach stem with "zero growth angle."

polars may also have only one intersection as shown in Fig. 3.2. Since the curved Mach stem must be perpendicular to the wall at W, the flow behind WT in Fig. 3.6 is given by the segment WT of the shock polar in Fig. 3.7.

For the curved Mach stem WT, the slope of the stem at T in Fig. 3.6, i.e., the shock angle β_m of the tangent shock MT, is $\beta_m(p_2, u_0)$. Since $u_{0n}^{(m)} = u_0 \sin \beta_m$, the specific volume $V_2^{(m)}$ behind the Mach stem at T is given by

$$\rho_0 u_{0n}^{(m)} = [(p_2 - p_0)/(V_0 - V_2^{(m)})]^{1/2}. \quad (3.21)$$

If instead of the steady flow depicted in Fig. 3.6, the shock motion is pseudo-stationary, i.e., the shocks IT and TW move with constant speed $-u_0$ into stationary gas, then the locus of triple points T is a straight line parallel to the rigid wall. The angle between this locus and t' wall is obviously zero; and the flow is referred to as containing a triple point moving at "zero growth angle."

Mach Reflection With "Nonzero Growth Angle"

If a plane shock wave strikes a rigid corner such that the shock angle β exceeds β_{crit}, then the resulting unsteady flow yields the locus of triple points T as a straight line making an angle $\chi > 0$, the "growth angle," with the wall. In a coordinate system moving with T, the resulting pseudo-stationary flow in the neighborhood of T is shown in Fig. 3.8. The incoming flow enters IT at an angle $\omega \equiv \beta - \chi$. The reflected shock RT, making an angle ω_r with u_0, is shown as backward-facing. In von Neumann's model, the flow in region RTM is represented by the intersection points of the shock polars AHW' and HT'FT in

574
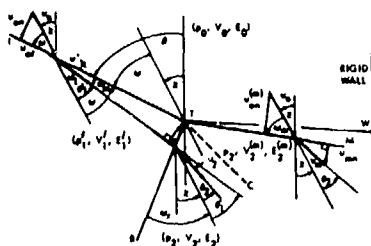
Fig. 3.8. Mach stem with "nonzero growth angle," $\chi > 0$.

Fig. 3.9. These are generated using Eqs. (3.1)-(3.14) as before, except that β is replaced by ω wherever the former appears. The point T (backward-facing shock) is thought to give the correct solution. In Fig. 3.8,

$$\omega_m = \sin^{-1} u_{0n}^{(m)}/u_0 . \qquad (3.16)$$
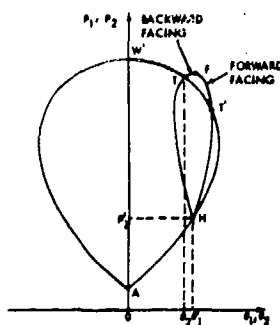
Fig. 3.9. Shock polar with $\chi > 0$.

It is important to note that, unlike the case for $\chi = 0$, the pressure at the wall W of Fig. 3.8 is *not* given by the pressure at the point W' of Fig. 3.9 for $\chi > 0$. Thus, TW' in Fig. 3.9 is not the exact image of TW of Fig. 3.8, except for the point T (6). The pressure $p_{w'}$ is given by

$$(p_{w'} - p_0)/(V_0 - V_{w'}) = [\rho_0 u_{0n}/\sin(\beta - \chi)]^2 = \rho_0^2 u_0^2 . \qquad (3.17)$$

Consider shock polars having *two or zero* intersection points as shown in Fig. 3.10* for water with the S-W equation of state given in §II. As p_1 increases

*Note that when the shock polars are computer generated, and drawn with the use of the Gould Electrostatic Plotter, as, for example, in Fig. 3.10, that portion of the incident polar for which $p < p_1$ is not drawn.
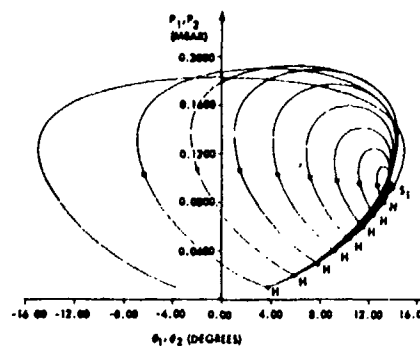
Fig. 3.10. Change in the reflected shock polars for water (S-W equation of state, Eq. 2.1) as the incident shock pressure $p_1 = p_1'$ is increased from 10 kbar in kbar increments for fixed $p_{1,max} = 183$ kbar. The sonic point for each polar is denoted by a *. S_1 is the sonic point for the incident shock polar.

while u_0 (or $p_{1,max} = 183$ kbar) is held constant, not only does regular reflection disappear for $p_1 > p_{1,crit}$, but even Mach reflection of the von Neumann type (containing a single slip line) appears not possible when the incident and reflected shock polars do not intersect (except at the point H) for sufficiently large values of p_1. Note, however, that a simple triple point solution is possible for some range of p_1.

A variant of the above is found for water with the same equation of state. Here, Mach reflection of the von Neumann type does not occur at all for fixed u_0 (or $p_{1,max} = 147.3$ kbar) as shown in Fig. 3.11. For $p_1 = 10$ kbar, the polars for increasing values of ω are shown in Fig. 3.12.

Shock polars having *one* intersection point during regular reflection are shown in Figs. 3.13 and 3.14; these polars are computed for water using the γ-law equation of state given in §II. In Fig. 3.14, a "von Neumann" Mach stem exists even as the second loop becomes small.

Critical Angle

The transition from regular to Mach reflection takes place in one of three possible ways which, following the notation of Ahrens and Urtiew (7), are denoted as Type I, II, and III. The three types of solutions are shown in Figs. 3.15 and 3.16, where all three types are defined by the relative positions of the polars when the reflected shock polar is tangent to the ordinate.
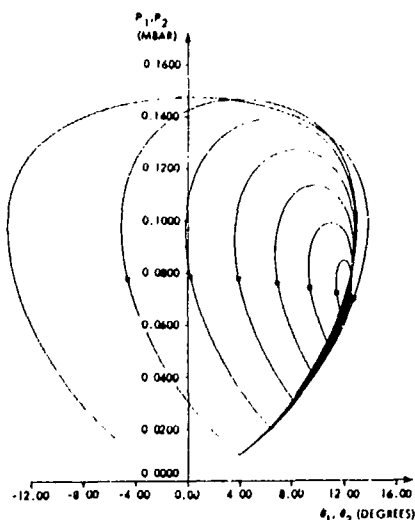
Fig. 3.11. Change in the reflected shock polars for water (S-W equation of state, Eq. 2.1) as the incident shock pressure p_1 is increased from 10 kbar in 10 kbar increments for fixed $p_{1,max} = 147.3$ kbar. The sonic point for each shock polar is denoted by an asterisk *.
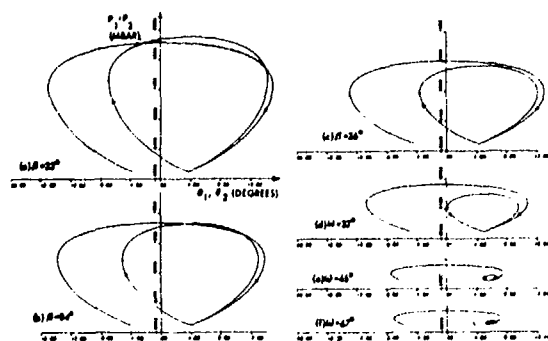
Fig. 3.12. For fixed $p_1 = 10$ kbar, change in both incident and reflected shock polars for water (S-W equation of state) as $\omega = \beta - \chi$ is increased. The sonic points are denoted by an asterisk *.

In Type I, the entire reflected shock polar lies inside the incident shock polar without crossing it at any point as seen in Figs. 3.11 and 3.12. It follows that the flow cannot be represented by a simple three shock configuration with a single slip line. The flow is more complicated involving compression waves along the Mach stem. Guderley (8) has.suggested that the flow contains a supersonic patch embedded in the subsonic flow downstream of the Mach stem as shown in the enlargement in Fig. 3.16(a). This flow requires that the reflected shock points up-
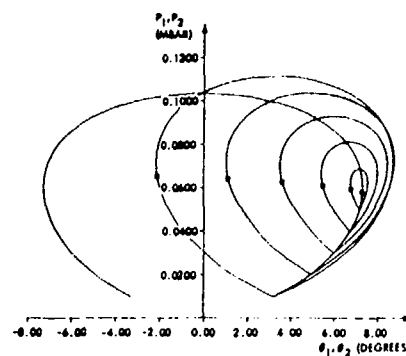
Fig. 3.13. Change in the reflected shock polars for water (γ-law equation of state, Eq. 2.2, $\gamma = 7.15$) as the incident pressure p_1 is increased from 10 kbar in 10 kbar increments for fixed $p_{1,max} = 103.5$ kbar. The sonic point for each polar is denoted by an asterisk *.
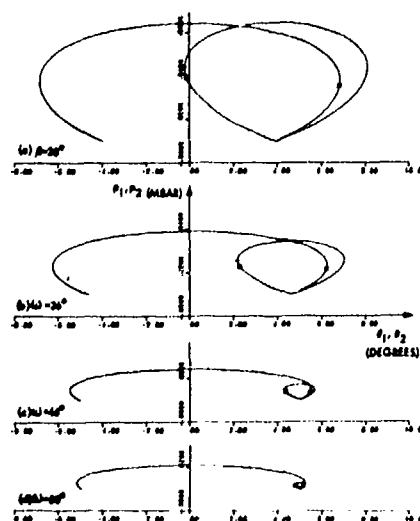
Fig. 3.14. For fixed $p_1 = 10$ kbar, change in both incident and reflected shock polars for water (γ-law equation of state, $\gamma = 7.15$) as $\omega = \beta - \chi$ is increased. The sonic points are denoted by an asterisk *.
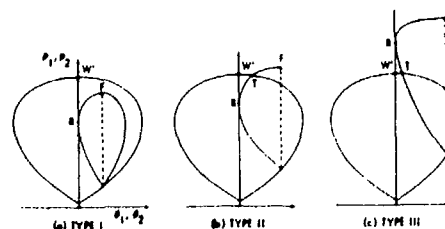
Fig. 3.15. Shock polars for the three types of Mach reflection at the critical angles, β_{crit}.
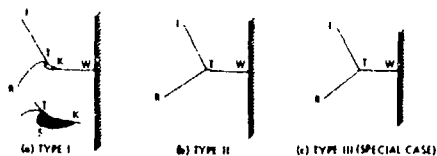
Fig. 3.16. (a) Guderley's solution for the flow at the triple point when the shock polars do not intersect. The flow in the vicinity of T is a supersonic patch (shown enlarged) embedded in a subsonic flow. (b) Mach stem at the critical angle when the flow behind the reflected shock RT is subsonic. (c) Stationary Mach stem, a special case of Type III transition.

stream at the triple point. The curved line TSK is a sonic line.

In Figs. 3.15(b) and (c), the points R and T represent the flow behind the reflected shock in regular and Mach reflection, respectively. For Type II, the Mach reflection T occurs on the "strong" (subsonic) shock part of the reflected shock polar as seen in Figs. 3.10 and 3.13, while for Type III, the reflection occurs on the "weak" (mostly supersonic) part of the reflected shock polar.

In the exceptional case for Type III, when $RW'T$ shrinks to a point, "stationary" Mach reflection appears in which the Mach stem is a straight line normal to the wall as shown in Fig. 3.16(c).

At the critical shock angle β_{crit}, let $p_{W'}$, p_R, and p_F be the pressures corresponding to the points W', R, and F of Fig. 3.15, i.e., $p_{W'}$, p_R, and p_F represent, respectively, the pressure behind the Mach stem at the wall (if $\chi = 0$, otherwise not), the pressure behind the regularly reflected shock, and the maximum possible reflected shock pressure (corresponding to $\nu = 90°$ in Fig. 3.4). Hence, for transitions of Type I, $p_R < p_F < p_{W'}$; for transitions of Type II, $p_R < p_{W'} < p_F$; and for transitions of Type III, $p_{W'} < p_R < p_F$. Theoretically, it is possible to have $p_F < p_{W'}$ for Type II but that case seldom occurs due to the characteristics of the polars. While the pressure $p_{W'}$ is not exactly the Mach stem pressure p_W at the wall, they are approximately equal when $\chi \ll \beta$ as seen from Eq. (3.17).

For fixed p_1', the variation of p_W as a function of $\omega \equiv \beta - \chi$, as the reflection process changes from regular to Mach reflection, depends in a qualitative

manner on whether the material undergoes Type I, II, or III transition at the critical shock angle β_{crit}. On the assumption that the shock pressure on the wall is always the minimum of p_R and p_W, and that $p_W \doteq p_{W'}$, it is seen from Fig. 3.15, that Type I and II transitions lead to a discontinuous increase in pressure $p_W \doteq p_{W'}$ at the wall at the transition from regular to Mach reflection, and that Type III transitions yield a continuous change in pressure.

Analysis of Water by Type

Calculations for water, similar to those in Ref. 7 for metals, have been performed for β_{crit} as a function of p_1 as shown in Fig. 3.17. The three curves are for the S-W, the $\gamma = 7.15$, and the HOM equations of state. Pairs of va: ⸴f p_1, β that fall below the curves are in the regular reflection regime; above the curves they are in the Mach reflection regime. The calculated pressure ratios at β_{crit} as functions of p_1 for the three equations of state are shown, respectively, in Figs. 3.18, 3.19, and 3.20. Over the range of pressures investigated, the S-W equation of state has a transition from Type I to Type II at 24 kbar (see Fig. 3.18); the γ-law type equation of state is Type I below 5 kbar, Type II with $p_F < p_{W'}$ for $5 \leqslant p_1 \leqslant 10.5$ kbar, and Type II with $p_F > p_{W'}$ for $p_1 > 10.5$ kbar; the HOM equation of state is of Type I.

For the S-W equation of state, p_R and $p_{W'}$ are shown as a function of $\omega \equiv \beta - \chi$ for different values of p_1 in Fig. 3.21. Similar curves for $\gamma = 7.15$ and the HOM equations of state are given in Figs. 3.22 and 3.23, respectively. The solid curve RR' is the theoretical locus of p_R/p_1 at which regular reflection just fails for different values of ω. Shock polar calculations show the relationship between ω_r and ω for the S-W equation of state; two families of curves of constant p_1 are given in Fig. 3.24. One family consists of the regular reflection curves. The asterisk* on each curve denotes the point at which $\beta = \beta_{crit}$ and divides the "weak" (mostly supersonic) reflected shock solutions (lower segments) from the "strong" (subsonic) reflected shock solutions (upper segments). The curve RR' through the asterisks is, therefore, the theoretical locus of points at which regular reflection fails and Mach reflection begins. The other family consists of the possible triple point solutions; the X denotes the largest value of ω at which a three-shock solution is possible, i.e., a point of tangency of the two shock polars in the p, θ plane.
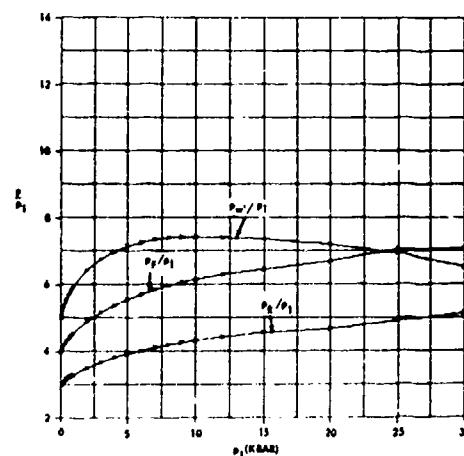
577

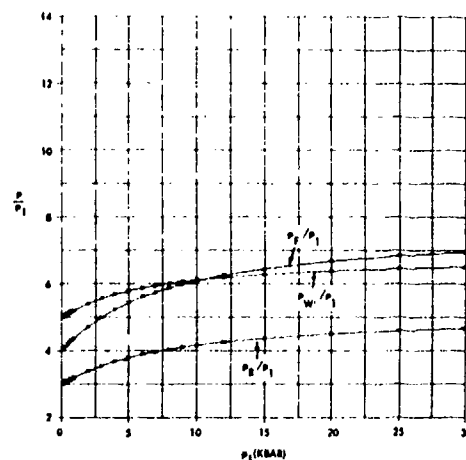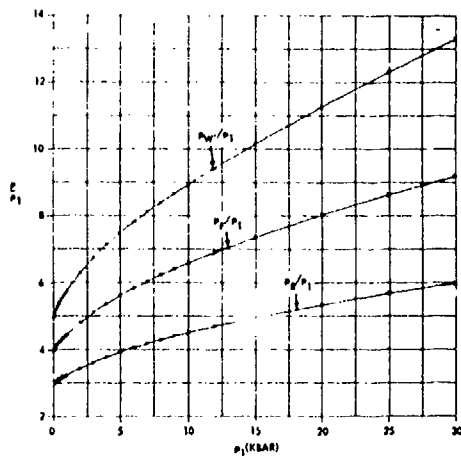Fig. 3.18. Calculated pressure ratios at β_{crit} as a function of p_1 in water with S-W equation of state.

Fig. 3.19. Calculated pressure ratios at β_{crit} as a function of p_1 in water with γ-law type $(\gamma = 7.15)$ equation of state.

The curve TT' through each X is the theoretical locus of points at which the three-shock solution fails and more complicated Mach reflection begins. For small values of p_1, e.g., a "weak" incident shock such as $p_1 = 1$ kbar, the values of β for the three-shock solution lie within the β interval for regular reflection and no three-shock solution exists. For $\beta > \beta_{crit}$, Mach reflection occurs through more complicated flows as discussed earlier for Type I solutions. Similar families of curves for $\gamma = 7.15$ and the HOM equations of state are presented in Figs. 3.25 and 3.26, respectively. These differ in a qualitative

Fig. 3.17. p_1 vs β_{crit} for (a) the S-W, (b) γ-law type $(\gamma = 7.15)$, and (c) HOM equations of state.

578

Fig. 3.20. Calculated pressure ratios at β_{crit} as a function of p_1 in water with HOM equation of state.
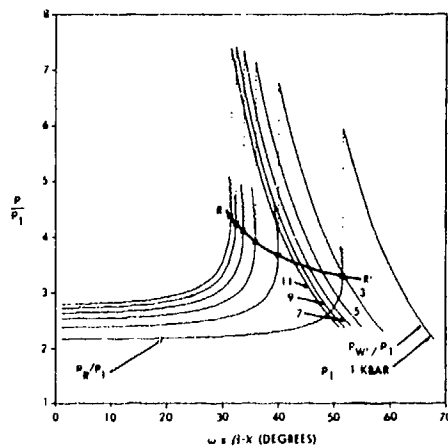
Fig. 3.21. p_R/p_1 and $p_{W'}/p_1$ versus $\omega = \beta - \chi$ at different values of p_1 for water using the S-W equation of state. RR' is the locus of points at which regular reflection fails.

manner from Fig. 3.24. For the γ-law equation of state, there exists only one three-shock value of ω_r for each ω as is seen in Fig. 3.14, a sample calculation for $p_1 = 10$ kbar. For the HOM equation of state, there are no triple point intersections at all over the range of p_1 shown.

IV. COLLISION OF UNDERWATER SHOCK WAVES

A qualitative theoretical description of colliding spherical shock waves, that should hold for chemical
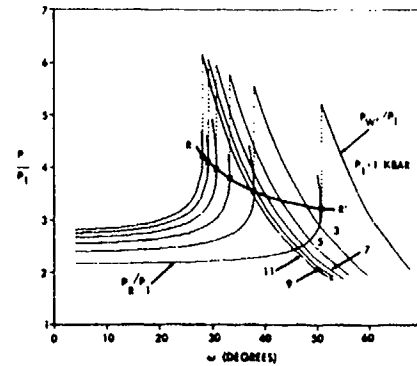
Fig. 3.22. p_R/p_1 and $p_{W'}/p_1$ versus ω at different values of p_1 for water using the γ-law type equation of state with $\gamma = 7.15$.

Fig. 3.23. p_R/p_1 and $p_{W'}/p_1$ versus ω at different values of p_1 for water using the HOM equation of state.

detonations of explosive spheres in water, was given by Reines and von Neumann (9) for a nuclear burst above the ground. Experimental work on the collision of underwater shock waves dates back to World War II (10,11,12,13) and is summarized by Cole (14) and in Ref. 2.

Experiments by Coleburn and Roslund

A very extensive series of experiments on the underwater collision of spherical shock waves arising from the simultaneous detonation of two 225 gram, 6.33 cm diameter spheres of cast pentolite was made

579
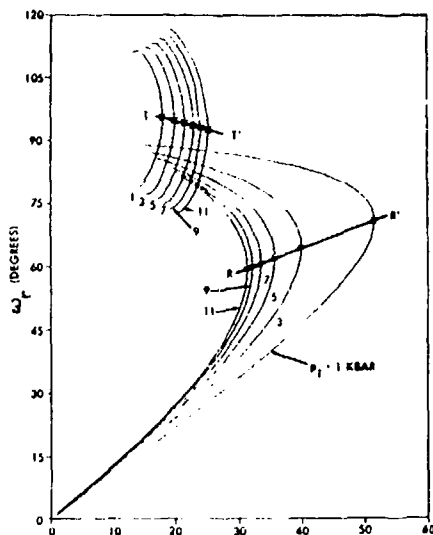
Fig. 3.24. Reflected shock angle ω_r as a function of incident shock angle ω for fixed values of p_1 for water using the S-W equation of state.
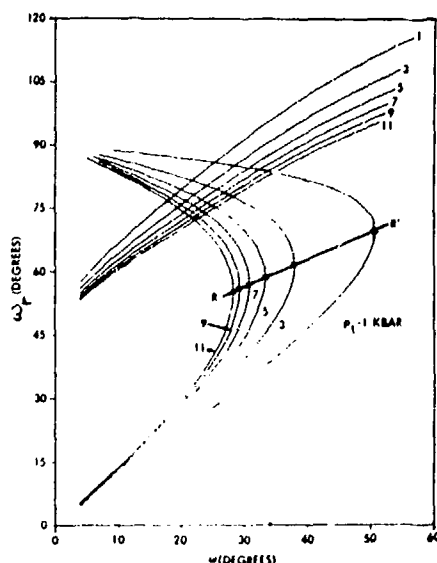
Fig. 3.25. Reflected shock angle ω_r as a function of incident shock angle ω for fixed values of p_1 for water using the γ-law type equation of state with $\gamma = 7.15$.

Fig. 3.26. Reflected shock angle ω_r as a function of incident shock angle ω for fixed values of p_1 for water using the HOM equation of state.
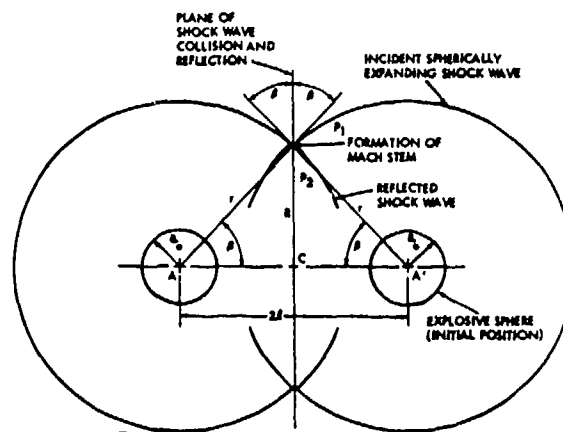
Fig. 4.1. The separated charge arrangement and a sketch of shock wave positions at the point of Mach wave formation where $\beta = \beta_{crit}$ (after Ref. 15(a)).

recently by Coleburn and Roslund (15). The center-to-center separation distance 2ℓ between the centrally initiated spheres was varied to change the incident shock pressures p_1 at the interaction plane shown in Fig. 4.1. The shock waves from the two spheres collide and reflect regularly first at point C

in the plane of symmetry and, thereafter, at increasing values of R as the shock angle β increases from zero to β_{crit}. For $\beta > \beta_{crit}$, the growth of the Mach stem is clearly seen in Fig. 4.2 traced from shadowgraph time profiles 10.9 μsec apart for a charge separation $2\ell = 7.6\ a_0$, where $a_0 = 3.165$ cm is the explosive charge radius.

In Fig. 4.3 is shown a sequence of previously unpublished shadowgraphs (16) where $2\ell = 5.6a_0$. (In Ref. 15a, Fig. 3a is erroneously represented as the case for $2\ell = 5.6a_0$; actually the shadowgraphs were for $2\ell = 7.6a_0$ (16).) At about 4.17 μsec after
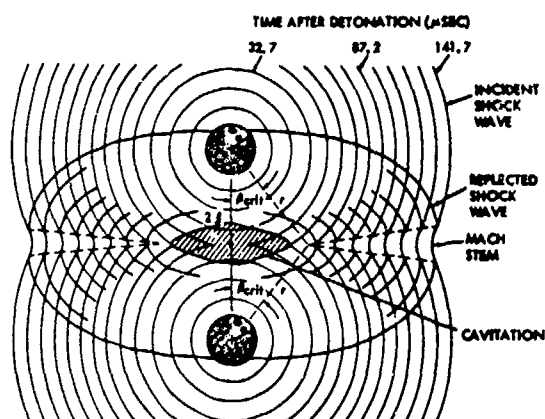
Fig. 4.2. Experimental time profiles of the collision of two equal spherically expanding underwater shock waves showing Mach wave formation; 10.9 μsec between successive wave fronts; $2\ell = 7.6a_0$; bubble motion not shown (after Ref. 15(a)).
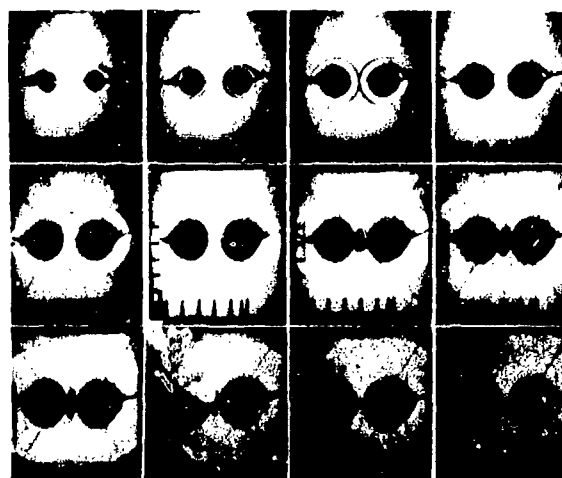
Fig. 4.3. Framing camera shadowgraphs of shock wave interactions from separated charges with $2\ell/a_0 = 5.6$ (16).

initiation, the detonation wave reaches the explosive-water interface and the product gas bubble begins to grow in size as a shock wave is transmitted into the water.

Eventually, the shock wave from each charge reaches the explosion bubble of the other resulting in a rarefaction wave moving from the interface into the water and a shock wave transmitted into the bubble. (This latter shock wave cannot be seen in the opaque products but its calculated motion is

shown in §VI.) The subsequent collision of the two rarefaction waves produces a region of cavitation seen as a growing opaque region in the shadowgraph; this region grows as a symmetrical disc between the bubbles.

They measured β_{crit} and the Mach stem velocity along the plane of symmetry of Fig. 4.2 (i.e., the velocity of W along the wall of Fig. 3.6) and calculated p_W along this plane from the Hugoniot for water; the experimental pressures p_2 for regular reflection ($\beta < \beta_{crit}$) could have but were not obtained from the shadowgraphs.

In Table 6.1, the experimental values of p_1 and p_W at the observed β_{crit} for different experimental values of the geometrical scale factor $2\ell/a_0$ are given in the first, fifth, fourth, and second columns, respectively (15a,c). r, a_0, 2ℓ, and β_{crit} are shown in Figs. 4.1 and 4.2.

Coleburn and Roslund exployed oblique shock theory to calculate the value of β_{crit} from experimental curves for p_1 versus r/a_0 for $r > \ell$ for a single charge (see Fig. 4.1). These theoretical values of β_{crit}, which are close to those shown in the seventh column of Table 6.1, are in reasonable agreement with the experimental values except at $p_1 = 1.62$ kbar. Their theoretical analysis, limited to regular reflection theory, made no attempt to analyze their experimental results from the point of view of Mach reflection. This will be done below.

From the discussion of §III, it follows that the transition from regular to Mach reflection is of Type I for all of the incident pressures p_1 of Table 6.1 when the S-W and HOM equations of state are used, and of Type I(II) below (above) 5 kbar for the γ-law type equation of state. The results from shock polar calculations are given in columns 7-19 of Table 6.1, where the regular reflection and Mach stem pressures, p_R and $p_{W'}$, are given at the computed shock angle β_{crit} for different values of the experimental incident shock pressure p_1. The pressures p_R, p_F, and $p_{W'}$, are defined in Fig. 3.15; p_T is the pressure at the triple-point. The p_R lay on the locii RR' of Figs. 3.21-3.23; the $p_{W'}$ lay on the locii (not shown) joining the upper end points of the Mach reflection curves of Figs. 3.21-3.23.

Table 6.1 shows that the values of β_{crit} in this pressure range vary little between the S-W and HOM

TABLE 6.1

Experimental and Theoretical Shock Wave Parameters for Mach Stem Formation in Water
(Values of p_1, p_W, $p_{W'}$, p_F, $p_{T'}$ and p_R are in kbars, β_{crit} in degrees)

p_1	Experimental (15)					S-W				HOM				$\gamma = 7.15$				
	$2\varrho/a_0$	r/a_0	β_{crit}	p_W	p_W/p_1	β_{crit}	p_W'	p_F	p_R	β_{crit}	p_W'	p_F	p_R	β_{crit}	p_W'	p_F	p_R	$p_{T'}$
6.5	5.1	3.1	36	46.0	7.1	33.96	47.50	37.59	26.39	31.33	51.80	38.66	26.89	31.31	38.50	36.98	25.63	39.83[a]
4.45	5.6	3.5	36	39.0	7.2	35.13	39.22	30.62	21.66	32.94	41.64	31.20	21.82	32.60	31.82	30.10	26.50	30.09[a]
4.60	6.1	3.8	37	34.0	7.4	36.35	32.59	25.23	17.88	34.55	33.84	25.43	17.85	33.97	26.49	24.69	17.30	24.68[b]
4.15	6.6	4.1	36	29.0	7.0	37.14	29.09	22.45	15.91	35.58	29.86	22.49	15.83	34.86	23.70	21.90	15.40	21.85[b]
3.63	7.1	4.4	37	26.0	7.2	38.24	25.07	19.26	13.67	36.94	25.43	19.19	13.57	36.08	20.51	18.74	13.23	18.60[b]
3.17	7.6	4.8	38	24.0	7.6	39.42	21.57	16.49	11.73	38.36	21.63	16.36	11.61	37.40	17.72	16.02	11.36	15.75[b]
2.95	8.1	5.0	37	21.5	7.3	40.07	19.91	15.19	10.82	39.13	19.87	15.05	10.69	38.12	16.40	14.74	10.47	14.40[b]
1.62	11.1	7.3	41	12.5	7.7	46.07	10.17	7.73	5.56	45.97	9.91	7.59	5.48	44.84	8.65	7.46	5.39	6.46[b]

[a]Backward-facing reflected shock.
[b]Forward-facing reflected shock.

equations of state. The same is true for $p_{W'}$, p_F, and p_R. Comparison of the theoretical β_{crit} with the experimental values of β_{crit} of Table 6.1 shows only satisfactory agreement. The theoretical values of $p_{W'}$ from the S-W equation of state are in good agreement with the experimental values p_W; the HOM equation is not as good; the γ-law equation is unsatisfactory giving values of $p_{W'}$ that are too low.

With the γ-law equation of state, the von Neumann simple three-shock solution is possible. Careful examination of enlargements of the framing camera shadowgraphs fails to show any indication of a slip-line. If the slip-line existed, there would be but a very small difference in tangential velocities u_2 and u_m (of Fig. 3.8) across the slip-line. For example, for $p_1 = 6.5$ kbar (see Table 6.1), $u_2 = 0.3440$ and $u_m = 0.3362$ cm/μsec, giving a relative slip velocity of only 0.0078 cm/μsec. The specific volume of the doubly-shocked water is 0.730 cm^3/g while that of the singly-shocked water is 0.787 cm^3/g; this is an appreciable density difference. However, it is felt that light rays from any source passing through the slip-line would not reach the camera lens due to the bending of the rays at the curved shock (17). Therefore, no conclusion can be drawn just from the absence of slip-lines from the shadowgraphs. It should be noted again that the S-W and HOM equations of state do not yield the three-shock solution and, therefore, would not show a simple slip-line through the triple point.

V. UNSTEADY FLOW EQUATIONS

For axially symmetrical isentropic continuous flow, the Eulerian equations for the conservation of mass, momentum, and energy are, respectively,

$$DV/Dt = V(\partial v/\partial Z + \partial u/\partial R + u/R)$$
$$Du/Dt = -V\partial p/\partial R$$
$$Dv/Dt = -V\partial p/\partial Z$$
$$DE/Dt + pDV/Dt = 0,$$

in cylindrical coordinates. Here, u and v are the fluid velocities in the directions of the radial coordinate R and axial coordinate Z, respectively, and

$$D/Dt \equiv \partial/\partial t + u\partial/\partial R + v\partial/\partial Z.$$

Let the Lagrangean coordinates R^0 and Z^0 denote the R and Z coordinates of a small fluid element at time $t = 0$. Then the position of that same fluid element for $t > 0$ is given by $R(R^0, Z^0, t)$ and $Z(R^0, Z^0, t)$. The continuity equation becomes

$$\frac{V}{V^0} = \frac{R}{R^0} J\left(\frac{R, Z}{R^0, Z^0}\right),$$

where J is the Jacobian of the transformation. It is convenient to replace R^0, Z^0 by a pair of arbitrary Lagrangean coordinates $\xi(R^0, Z^0)$, $\eta(R^0, Z^0)$ since

for computational purposes it may be more desirable to take lines other than $R^0 = $ constant and $Z^0 = $ constant as mesh lines.

The system of equations that determines the flow is now

$$\frac{\partial u}{\partial t} = -\frac{V^0 R}{J^0 R^0}\left(\frac{\partial P}{\partial \xi}\frac{\partial Z}{\partial \eta} - \frac{\partial P}{\partial \eta}\frac{\partial Z}{\partial \xi}\right)$$

$$\frac{\partial v}{\partial t} = -\frac{V^0 R}{J^0 R^0}\left(\frac{\partial P}{\partial \eta}\frac{\partial R}{\partial \xi} - \frac{\partial P}{\partial \xi}\frac{\partial R}{\partial \eta}\right)$$

$$u = \partial R/\partial t, \quad v = \partial Z/\partial t$$

$$J = \frac{\partial R}{\partial \xi}\frac{\partial Z}{\partial \eta} - \frac{\partial R}{\partial \eta}\frac{\partial Z}{\partial \xi},$$

$$J^0 = \frac{\partial R^0}{\partial \xi}\frac{\partial Z^0}{\partial \eta} - \frac{\partial R^0}{\partial \eta}\frac{\partial Z^0}{\partial \xi}$$

$$V = V^0 J R/J^0 R^0$$

$$P = p + q$$

$$\partial E/\partial t + P \partial V/\partial t = 0,$$

where the pseudo-viscosity q, introduced into the above equations by replacing p by $P \equiv p + q$, is defined by

$$q = \frac{\rho^0 R^0 \Delta\ell}{RV}\frac{\partial V}{\partial t}\left(\frac{\sigma_4 \rho^0 R^0 \Delta\ell}{R}\frac{\partial V}{\partial t} - \sigma_3 c_{max}^2 F\right)$$

$$\frac{\partial V}{\partial t} < 0,$$

and $q = 0$ if $\partial V/\partial t \geqslant 0$. Here, $F = 1$ in the products and $(R^0/R)^{1/2}$ in the water, σ_3 and σ_4 are constants that are adjusted to give the desired shock "sharpness," $\Delta\ell$ is a characteristic mesh width, and c_{max} is the maximum sound speed over the entire flow field at t. To these equations must be added an equation of state for each different fluid,

$$p = p(E, V).$$

Concentric Circles as Coordinates

For the spherical charges whose centers are separated by a distance 2ℓ, it is convenient to define the Lagrangean coordinates ξ and η by two families of concentric circles, one about each sphere as shown in Fig. 5.1. The families of concentric circles,

$$\xi^2 = R^{02} + Z^{02}$$

$$\eta^2 = R^{02} + (Z^0 - 2\ell)^2,$$

have their origins at the centers of charges A and A', respectively. Therefore,

$$Z^0 = \ell + (1/4)(\xi^2 - \eta^2)/\ell$$

$$R^0 = \left\{\xi^2 - [\ell + (1/4)(\xi^2 - \eta^2)/\ell]^2\right\}^{1/2}.$$

$$J^0 = -\xi\eta/\left[4\ell^2/\xi^2 - (2\ell^2 - \xi^2 + \eta^2)^2\right]^{1/2}.$$

$J^0 \to -\infty$ as $|\xi - \eta| \to 2\ell$ or $\xi + \eta \to 2\ell$, i.e., along the axis of symmetry for $\xi \neq 0$, $\eta \neq 0$. Furthermore, J^0 does not approach a uniform limit as $\xi \to 0$ or $\eta \to 0$. That the mapping is singular on the axis is expected because here the circles $\xi = $ constant and $\eta = $ constant are tangent to each other. However,

$$R^0 J^0 = -(1/2)\xi\eta/\ell < 0,$$

except at the charge centers.
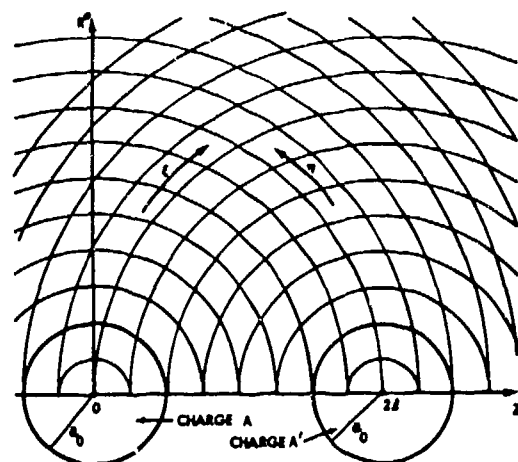
Fig. 5.1. Two families, $\xi = $ constant and $\eta = $ constant, of concentric circles (Lagrangean coordinates); one family about each pentolite sphere.

VI. NUMERICAL SOLUTION FOR TWO SIMULTANEOUSLY DETONATED EXPLOSIVE CHARGES UNDER WATER

The water and explosion products are partitioned into a number of discrete cells formed by the intersection of the two families of equally spaced concentric circles. The finite-difference mesh is formed by joining the intersections of Fig. 5.1 by straight lines as shown in Fig. 6.1, so that each cell is constrained to move as either a quadrilateral or as a triangle. Axial cells are those cells (all triangular) having the axis of symmetry as one of t... boundaries; all other cells (all quadrilaterals) are interior cells. The centers of the two charges correspond to $\xi = 0$ and $\eta = 0$, respectively.

All flow variables are computed at discrete material particles and at discrete times. The particles corresponding to the ξ and η coordinates are labeled with indices k and ℓ, respectively; time is labeled with an index n. The variables are now only defined at the mesh points and time steps as follows:

$$u_{k,\ell}^{n+1/2}, \; v_{k,\ell}^{n+1/2}; \; R_{k,\ell}^{n+1} , \; Z_{k,\ell}^{n+1}, \; J_{k,\ell}^{n+1}, \; E_{k+1/2,\ell+1/2}^{n+1},$$

$$V_{k+1/2,\ell+1/2}^{n+1}, P_{k+1/2,\ell+1/2}^{n+1}, q_{k+1/2,\ell+1/2}^{n+1/2}.$$ Here $n + 1/2$ and $n + 1$ refer to "new" values; $n - 1/2$ and n refer to "old" values. The actual details of the finite-difference method used to calculate the motion of the interior and axial points and the advancement of the solution in time will not be presented here.
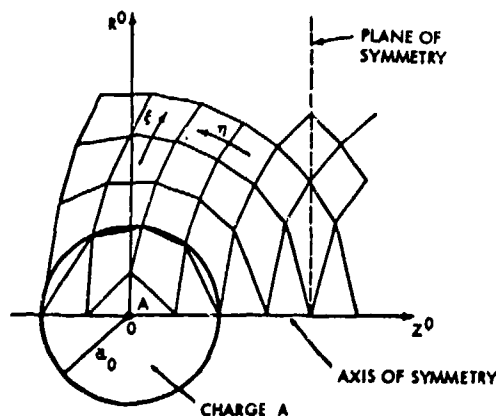
Fig. 6.1. Schematic of the finite-difference mesh corresponding to coordinates shown in Fig. 5.1.

As long as the shock wave in the water arising from the detonation of charge A in Fig. 4.1 does not reach the plane of symmetry, the flow is one-dimensional. After shock reflection has occurred, a two-dimensional flow field grows as shown in Fig. 4.2. This flow field is bounded by the plane of symmetry, the axis of symmetry, the reflected shock front, and for Mach reflection, by the Mach stem (18).

The simplest method for computing the entire flow field would be to construct a two-dimensional axisymmetrical unsteady flow code and use it to compute both the one-and-two-dimensional flow fields at each time step. However, it is clear that it is wasteful to do a two-dimensional calculation of a one-dimensional flow particularly for the shock collision problem dealt with here. It is shown schematically in Fig. 4.2 that at the moment of shock collision with the wall, the ratio of the areas of the one-dimensional to the two-dimensional flow is infinite, thereafter decreasing until it reaches zero at the time at which the Mach stem has completely fused with the incident shock. Because this ratio will always be larger than, at least, 4 for all flows computed here, it was considered essential to couple the one-dimensional spherically symmetrical flow to the outer edge of the expanding region of two-dimensional flow. One reason for the present choice of the Lagrangean ξ, η coordinates is that it is relatively easy to perform this coupling. This arises because the ξ and η coordinates are defined in exactly the same way as the one-dimensional ξ coordinate that is used to calculate the one-dimensional spherically symmetrical flow.

Calculation for Separated Charges

In a series of numerical calculations utilizing the S-W equation of state, a_0 was held constant while 2ℓ was varied over the interval $3.0 \leqslant 2\ell/a_0 \leqslant 11.1$. The initial conditions for the pentolite products are calculated using Taylor's similarity solution (1).

As an example of the flow fields calculated, consider the case for $2\ell/a_0 = 5.625$ with $k_i = 16$, where $k_i \Delta\xi = a_0$ and $\Delta\xi$, $\Delta\eta$ are the mesh widths with $\Delta\xi = \Delta\eta = $ constant over the entire mesh. There exist 91 (= 5.625 × 16 + 1) ξ coordinates (concentric circles at t = 0) about the center $\xi = 0$ of charge A that intersect the axis, R = 0, between the two charge centers, and similarly for the η coordinate about the

center $\eta = 0$ of charge A' (see Fig. 5.1). For this case, Fig. 6.2 (a)–(g) displays the positions of the various shock fronts as functions of R and Z at different times. The shock front is identified by the asterisk * plotted at the center of a cell wherever $q \geqslant 10^{-2}$ kbar and is a local maximum in the ξ or η direction.
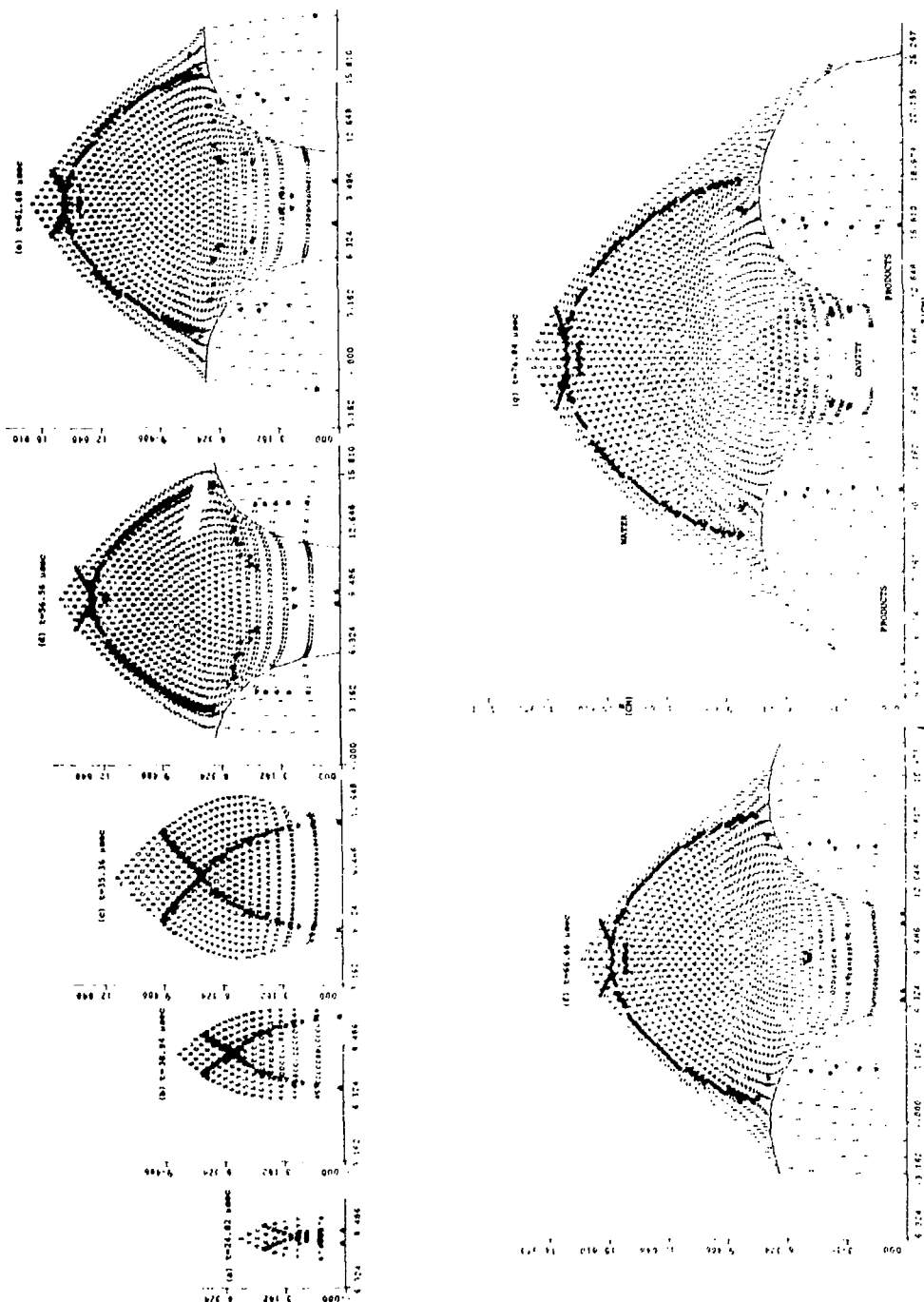

Fig. 6.2. Reflected shocks and Mach stem at different t for $2\ell/a_0 = 5.625$.

585

In (a) and (b), regular reflection exists and three regions are found as expected. These are the ambient region upstream of the incident shock, the region downstream of the incident shock, and the region downstream of the reflected shock. Mach stem formation appears to occur in (c), and the growth of the Mach stem is shown in (d)–(g). Because of the pseudo-viscosity q, the shock front thickness is 5 cells in the normal direction though fewer cells are plotted with an asterisk *.

In Fig. 6.2, the centers of the two charges are at $Z = 0$ and $Z = 2\ell = 17.96$ cm, respectively. The only ξ and η coordinates shown are the products/water interfaces.

The shocks and the interfaces are plotted only in that region of the R, Z plane where the flow was found from the solution of the two-dimensional equations. Note that the region upstream of the reflected shock is a region of one-dimensional flow (found from the two-dimensional calculation).

For a short time after shock collision, the two reflected shock fronts cannot be differentiated clearly due to the mutual spreading of each shock front into the other by the pseudo-viscosity as seen in Fig. 6.2(a). By the time corresponding to (b), the reflected shocks can be differentiated clearly. In (c), the reflected shock has just reached the products/water interface on the axis.

In all calculations presented here, no provision is made for "slippage" of the water along the product/water interface. As the expanding bubbles must force the water out as the bubbles approach each other, the cells near the axis, $R = 0$, become elongated in the R direction. With respect to the Mach stem, its curvature is positive and largest in the early phases of growth and tends to decrease with time.

In order to visualize the calculated pressure field, it is convenient to print an approximate value of p at the center of the quadrilateral for interior cells and at the midpoint of the base of the triangle for axial cells. In this case, an integer expresses the pressure in kilobars to the nearest half kilobar, e.g., a 7 represents 7 ± 0.5 kbar; the letters A, B, C, ... are used to denote the pressures 10, 11, 12, ... kbar, respectively. The change in density of the expanding products and the compressed water can be inferred from the change in spacing between the numerals

with time. This is particularly noticeable in the products. Pressures are printed only for every other cell.

Though not shown here, comparison of the experimental reflected and Mach shock configurations and the products/water interfaces from the available shadowgraphs (15,16) (such as Fig. 4.3) with the calculated configurations (such as Fig. 6.2) for $2\ell/a_0 = 5.1$, 5.6, and 6.6 showed good qualitative agreement at corresponding times. This was made by overlaying the shadowgraph enlargements (which are mylar transparencies) onto the corresponding Gould plots. The regions of cavitation are also in reasonable agreement.

Ink tracings of the calculated shock configurations at different times, made from the Gould plots, are shown superposed in Fig. 6.3 for $2\ell/a_0 = 5.625$.

Colebum and Roslund (15) published the experimental values of the shock pressure on the plane of symmetry as a function of R/R_0 for values of $2\ell/a_0$, where $R_0 = 2^{1/3}a_0$ is the radius of a fictitious single pentolite charge of double the mass, i.e., of 450 grams; these are shown in Fig. 6.4. However, use of
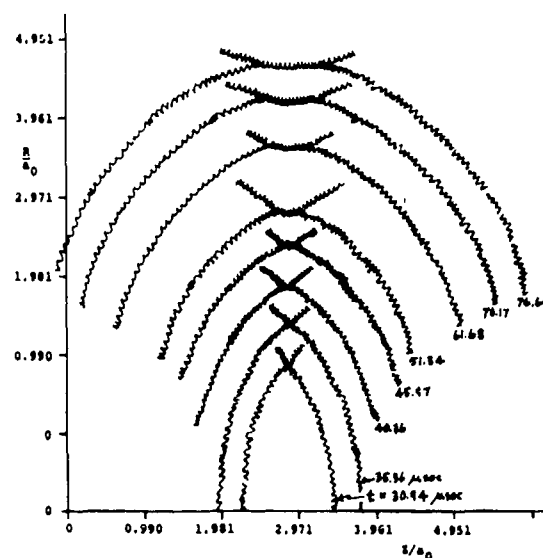
$$R/R_0 = 2^{-4/3}(2\ell/a_0) \tan \beta$$

Fig. 6.3. Reflected shock and Mach stem configurations at different times for $2\ell/a_0 = 5.6225$ with the S-W equation of state.
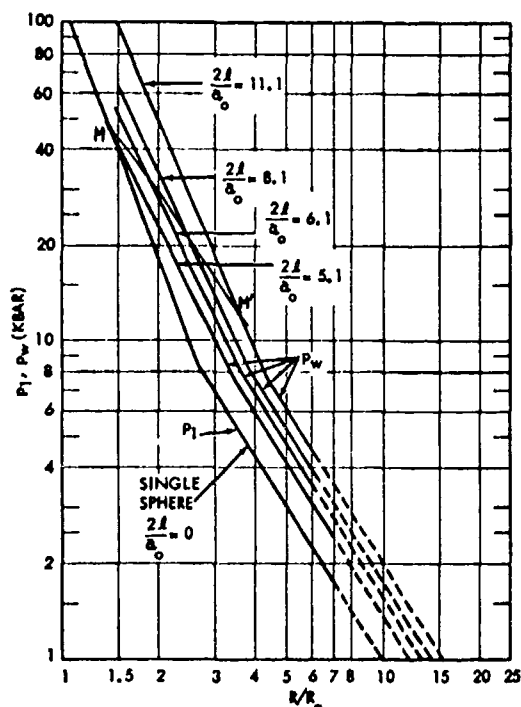
586

Fig. 6.4. Underwater shock wave pressure p_1 versus R/R_0 curves from a single pentolite sphere, mass $2M_1$; and p_W versus R/R_0 from separated twin pentolite spheres, each of mass, M_1. $2\ell/a_0$ is the dimensionless separation distance between the twin spheres (after Ref. 15(a) and (c)).

$$\text{or } R/R_0 = 2^{-1/3} [(r/a_0)^2 - (2\ell/a_0)^2/4]^{1/2}$$

(see Fig. 4.1) and the experimental data in Table 6.1 defines MM', the locus of points at which the Mach stem forms. Thus, the curves below MM' represent Mach stem pressures, p_W; the curves above MM' are fictitious and should be replaced by lower pressure curves corresponding to regular reflection. The latter will be published elsewhere.

Returning to the numerical calculations, it is found that the reflected shock pressure p_2 on the plane of symmetry (see Fig. 4.1) is calculated accurately for regular reflection. At any time t, the calculated one-dimensional pressure distribution is extrapolated in the ln p vs r plane to the point of maximum q, yielding r, $\beta(r)$, and $p_1(r)$. Oblique shock theory yields p_2 (=p_R of Fig. 3.21). This value compares well with that obtained by similarly extrapolating the pressure distribution along the plane of symmetry found from

the numerical calculations. However, the numerical scheme cannot follow the discontinuous increase in pressure (see Fig. 3.21) at the onset of Mach stem formation. This discrepancy is, no doubt, due to the smearing of the shock by the pseudo-viscosity which is much more effective in decreasing (and, therefore, falsifying) the pressure of the decaying Mach stem than the pressure of the decaying one-dimensional spherical shock front. This follows from the fact that the calculations indicate that the pressure gradient just behind the Mach stem is much steeper than behind the spherical shock in accord with Shanes' experimental results (13). As the Mach stem grows with increasing R/R_0, the calculated shock pressures p_W approaches more closely the experimental values. Finer mesh calculations will be used to calculate more accurately the Mach stem and triple point pressure.

Screening Effect of Gas Bubble

Shanes (13) had shown that the reflection of the shock wave from one charge off the product gas bubble of the other had the "screening" effect of delaying the arrival of the shock from the other charge. The experimental shadowgraphs (16) shown in Fig. 4.3 show the rarefaction wave interaction. The shock in the products cannot be observed experimentally. The plots of the numerical solutions given in Fig. 6.2 show that the shock in the expanding products lags behind the shock in the water. The strong rarefaction wave downstream of each reflected shock slows down the reflected shock. While not shown here, the reflected shock in the water diffracts around the expanding bubble. Hence, pressure measurements on the axis of symmetry see a delayed arrival of the shock front from the other charge (i.e., reflected shock).

ACKNOWLEDGMENT

587

REFERENCES

1. W. A. Walker and H. M. Sternberg, "The Chapman-Jouguet Isentrope and the Underwater Shock Wave Performance of Pentolite," p. 27 of Ref. 19.

2. (a) H. Polachek and R. J. Seeger, "Interaction of Shock Waves in Water-like Substances," Bureau of Ordnance, Explosive Report No. 14 (14 Aug. 1944);

   (b) R. J. Seeger and H. Polachek, "On Shock-Wave Phenomena: Waterlike Substances," *J. Appl. Phys.* 22, No. 5 (1951).

3. C. L. Mader and W. R. Gage, "FORTRAN SIN. A One-Dimensional Hydrodynamic Code for Problems Which Include Chemical Reactions, Elastic-Plastic Flow, Spalling, and Phase Transitions," Los Alamos Scientific Laboratory Report LA-3720 (1967).

4. M. L. Wilkins, B. Squier, and B. Halperin, "Equation of State for Detonation Products of PBX 9404 and LX 04-01," in *Tenth Symposium (International) on Combustion* (The Combustion Institute, Pittsburgh, PA, 1965), p. 769.

5. J. von Neumann, "Oblique Reflection of Shocks," Bureau of Ordnance, Navy Dept., Explosives Research Report No. 12 (1943).

6. J. Sternberg, "Triple-Shock-Wave Intersections," *Phys. Fluids* 2, 179 (1959).

7. T. J. Ahrens and P. A. Urtiew, "The Use of Shock Waves in the Vaporization of Metals," Lawrence Livermore Laboratory Report UCRL-51109 (5 Aug. 1971).

8. K. G. Guderley, "Considerations of the Structure of Mixed Subsonic-Supersonic Flow Patterns," Headquarters Air Materiel Command, Wright Field (Dayton, Ohio) Tech. Report F-TR-2168 ND (1947); Guderley, K. G., *The Theory of Transonic Flow* (Pergamon Press, 1962).

9. F. Reines and J. von Neumann, "The Mach Effect and Height of Burst," declassified portion of Chapter 10 of *Blast Wave*, Los Alamos Scientific Laboratory Technical Series, Vol. VII, Part II, edited by H. Bethe, 13 Aug. 1947.

10. P. Libessart, "Spark Photographs of the Mach Effect," R. C. 417, May (1944); D. C. Campbell, "Experiments in the Production and Photography of Intersection Underwater Shock Waves," David Taylor Model Basin Report R-203 (1943), and private communication of 3 Jan. 1944 from David Taylor Model Basin to the Bureau of Ordnance, "Intersection Shock Waves."

11. D. P. MacDougall and G. H. Messerly, "Flash Photography of Underwater Shock-Waves," Underwater Explosives and Explosions No. 15, p. 3-4, Div. 8, NDRC, Interim Report (1943); D. P. MacDougall, G. H. Messerley, and E. M. Boggs, "Note on Mach Reflection in Water," Underwater Explosives and Explosions No. 20, p. 10-11, Div. 8, NDRC, Interim Report (1944).

12. R. W. Spitzer and R. S. Price, "Photographs of Intersecting Shock Waves (Mach Effect)," Underwater Explosives and Explosions No. 16, p. 26-29, Div. 8, NDRC, Interim Report (1943).

13. A. M. Shanes, "Measurements on Pressure Waves in Region of Two Obliquely Intersecting Underwater Shock Waves," Underwater Explosives and Explosions No. 21, p. 52-65, Div. 8, NDRC, Interim Report (1944).

14. R. H. Cole, *Underwater Explosions*, Princeton University Press (Princeton, N.J., 1948).

15. (a) N. L. Coleburn and L. A. Roslund, "Collision of Spherical Shock Waves in Water," Naval Ordnance Laboratory Report NOLTR 68-110 (31 July 1968);

    (b) L. A. Roslund and N. L. Coleburn, "Regular Reflection of Oblique Shock Waves in Water," NOLTR 68-209 (17 Dec 1968);

    (c) N. L. Coleburn and L. A. Roslund, "Interactions of Spherical Shocks in Water," p. 581 of Ref. 20.

16. N. L. Coleburn and L. A. Roslund, private communication.

17. S. J. Jacobs, private communication.

18. In comparison, the HEMP code was used to calculate the two-dimensional and almost all of the one-dimensional flow resulting from a 1-kt explosion in air above an elastic ground by M. L. Wilkins, "Calculation of Surface and Ground Waves from Above-Ground and Underground Explosions," *Astron. Acta.* 17, 399 (1972).

19. Proceedings—Fourth Symposium (International) on Detonation, Office of Naval Research Report ACR-126 (Oct. 1965).

20. Proceedings—Fifth Symposium (International) on Detonation, Office of Naval Research Report ACR-184 (Aug. 1970).

THE PROBLEM OF A STRONG POINT EXPLOSION IN A COMBUSTIBLE MEDIUM

Shmuel Eidelman, Yaakov M. Timnat and Alexander Burcat
Department of Aeronautical Engineering
Technion – Israel Institute of Technology
Haifa, Israel

The problem of a strong point explosion in a combustible medium is solved for three different functions describing the additional energy released by the burning medium. The efficiency of the system in energy related parameters is compared to a standard strong explosion in a noncombustible medium.

INTRODUCTION

The strong point explosion problem was discussed by Sedov (1) and by Taylor (2), who related it to very intense energy sources such as atomic blasts.

The classical solution presented by Sedov (3) was diversified to include additional parameters as reducing the intensity of the initial energy to take into account the counterpressure of the atmosphere (4,5).

Korobeinicov investigated the strong point explosion in a gas with a variable density (6,7), in a moving gas (8), in an electrically conducting gas (7), and together with Levin, he investigated the strong point explosion in a detonating gas (9,10,11). The point explosion with a variable energy was investigated by Dabora (12,13) and by Freeman (14).

A very thorough and systematic investigation of the problems of similarity in blast waves and detonation waves was conducted by Oppenheim and co-workers (15,16,17).

This study deals with the problem of a strong point explosion that occurs in a combustible medium which is ignited by the blast wave. An amount of energy E_b is liberated by the combustible medium. The efficiency of using solely the energy of the point explosion or of a combination of E_0 and E_b is investigated. The influence of the additional energy

E_b on the shock wave parameters and the motion of the gas behind the shock wave, were also studied.

BASIC ASSUMPTIONS

A. The Conservation Equations

The problem starts as a point explosion in a stationary combustible medium. When $t = 0$ at the starting point $r = 0$, a strong explosion releases an amount of energy E_0. The explosion causes a strong shock wave to travel in the combustible medium. Because of the shock wave's strength, the local pressure can be neglected, thus taking $P_1 = 0$.

The shock wave causes combustion to occur in the region where it has passed.

The basic conservation equations for a one dimensional problem with a spheric symmetry are:

$$\frac{\partial \rho}{\partial t} + \rho \frac{\partial V}{\partial r} + V \frac{\partial \rho}{\partial r} + \frac{2\rho V}{r} = 0 \qquad (1)$$

conservation of mass

$$\rho \left(\frac{\partial V}{\partial t} + V \frac{\partial V}{\partial r} \right) + \frac{\partial P}{\partial r} = 0 \qquad (2)$$

conservation of momentum

590

$$\frac{\partial}{\partial t}\left(\rho\epsilon + \rho\frac{V^2}{2}\right) + \frac{\partial}{\partial r}\left[V\left(\rho\epsilon + \frac{\rho V^2}{2}\right)\right]$$

$$+ \frac{\partial(PV)}{\partial r} + \frac{2V}{r}\left(\rho\epsilon + \frac{\rho V^2}{2} + P\right) = \rho\frac{dQ}{dt} \quad (3)$$

conservation of energy

In Eq. (3) the right-hand term describes the rate of heat release in the combustion process. The medium is assumed to be an ideal or a pseudo-ideal gas and therefore $P = \rho RT$.

The internal energy for the combustible mixture will be $\epsilon = P/[(\gamma - 1)\rho]$ + constant.

Equation (3) can be represented in a different form using Eq. (1) and assuming γ = constant:

$$\frac{\partial P}{\partial t} + V\frac{\partial P}{\partial r} + \gamma P\left(\frac{\partial V}{\partial r} + \frac{2V}{r}\right) = \rho(\gamma - 1)\frac{dQ}{dt}. \quad (3a)$$

Equations (1), (2), and (3a), will serve as the conservation equations.

B. The Boundary Conditions

The boundary conditions across the shock wave are:

$$\rho_1(C - V_1) = \rho_2(C - V_2) \quad (4)$$

conservation of mass

$$\rho_1(C - V_1)^2 + P_1 = \rho_2(C - V_2)^2 + P_2 \quad (5)$$

conservation of momentum

$$\frac{1}{2}(C - V_1)^2 + \frac{\gamma P_1}{(\gamma - 1)\rho_1} + Q$$

$$= \frac{1}{2}(C - V_2)^2 + \frac{\gamma P_2}{(\gamma - 1)\rho_2} \quad (6)$$

conservation of energy

Since initially $V_1 = 0$ and $P_1 = 0$ the equations will be simplified to

$$\rho_1 C = \rho_2(C - V_2) \quad (4a)$$

$$\rho_1 C^2 = \rho_2(C - V_2)^2 + P_2 \quad (5a)$$

$$\frac{1}{2}C^2 + Q = \frac{1}{2}(C - V_2)^2 + \frac{\gamma P_2}{(\gamma - 1)\rho_2}. \quad (6a)$$

The energy equation of the boundary can be transformed:

$$Q = \frac{\gamma P_2}{(\gamma - 1)\rho_2} + \frac{V_2^2}{2} - V_2 C \quad (6b)$$

and solving for V_2 one gets

$$V_2 = \frac{C + C\left(1 - \frac{2Q}{C^2}(\gamma^2 - 1)\right)^{1/2}}{(\gamma + 1)} \quad (6c)$$

The negative sign solution of V_2 has no physical meaning since at $Q = 0$, $V_2 = 0$. Thus one can write the following boundary conditions

$$V_2 = \frac{C(1 + K)}{(\gamma + 1)}; \quad \rho_2 = \frac{\rho_1(\gamma + 1)}{\gamma - K};$$

$$P_2 = \frac{\rho_1 C^2(1 + K)}{\gamma + 1} \quad (7)$$

where

$$K = \left(1 - \frac{2Q}{C^2}(\gamma^2 - 1)\right)^{1/2}.$$

SOLUTION OF THE PROBLEM

The parameters defining the problem are γ, r, t, Q, E_0, $P_1 = 0$, ρ_1, $V_1 = 0$. Q can be presented as a function of the time and the distance including a dimensional constant Z:

$$Q = Z\varphi(r, t).$$

Then the new system of parameters defining the flow will be: γ, r, t, Z, E_0, ρ_1. In this parameter system there are three dimensional constants Z, E_0 and ρ_1 with independent dimensions. If the dimension of Z is defined through those of E_0 and ρ_1 the problem will be self-similar (3). In this case in dimensionless

591

coordinates, all dimensionless terms will depend on two parameters only: γ and λ, where

$$\lambda = (\rho_1/E_0)^{1/5} r/t^{2/5}. \qquad (8)$$

It can be shown (18) that for a point explosion with spherical symmetry three of the simplest definitions of Q matching the problem are

$$Q_1 = Z_1/r^3; \quad Q_2 = Z_2/t^{1.2}; \quad Q_3 = Z_3 r/t^{1.6}. \quad (9)$$

These models were chosen because a) they are simple enough, and b) they represent a specific heat release rate which is dependent solely on the distance, on the time and approximately on the gas velocity respectively. The constants Z_1, Z_2, Z_3 will be related to ρ_1 and E which itself is related to E_0 through a dimensionless constant α

$$E_0 = \alpha_i E_i \quad i = 1, 2, 3. \qquad (10)$$

Thus

$$Z_1 = \beta_1 \left(\frac{E_1}{\rho_1}\right) \quad Z_2 = \beta_2 \left(\frac{E_2}{\rho_1}\right)^{2/5} \quad Z_3 = \beta_3 \left(\frac{E_3}{\rho_1}\right)^{1/5}.$$

$$\qquad (9a)$$

The energy equation can therefore be written as

$$\frac{\partial P}{\partial t} + V \frac{\partial P}{\partial r} + \gamma P \left(\frac{\partial V}{\partial r} + \frac{2V}{r}\right) - \rho(\gamma - 1)B_i = 0$$

$$i = 1, 2, 3 \quad (11)$$

where B_i is defined as dQ/dt:

$$B_1 = -3\beta_1 \frac{E_1}{\rho_1} V r^{-4}$$

$$B_2 = -1.2\beta_2 \left(\frac{E_2}{\rho_1}\right)^{2/5} t^{-2.2} \Biggr\} . \quad (12)$$

$$B_3 = -\beta_3 \left(\frac{E_3}{\rho_1}\right)^{1/5} (1, 6rt^{-2.6} - Vt^{-1.6})$$

A. The Differential Equations of Motion in the Self Similar Coordinates System

The subscript 1 has denoted till now the variables and the gasdynamic functions before the shock. The subscript 2 will define the variables and gasdynamic functions after the passage of the shock wave but very close behind it. A set of dimensionless gasdynamic flow functions f, g, h is defined as follows:

$$f = V/V_2; \quad g = \rho/\rho_2; \quad h = P/P_2 \quad (13)$$

f, g, and h depend on the dimensionless variable λ, defined by Eq. (8). The equation of the shock wave motion, $r_2(t)$ is, therefore, found without solving the gas motion equation:

$$r_2(t) = \lambda_2 (E_i t^2/\rho_1)^{1/5} \quad i = 1, 2, 3 \quad (14)$$

where λ_2 is a constant different from zero. Assuming that $\lambda_2 = 1$, λ will change in the interval $0 \leqslant \lambda \leqslant 1$ and will get the value 1 on the shock wave. Therefore, $\lambda = r/r_2$. Thus the equation of motion of the shock wave will be:

$$r_2(t) = (E_i/\rho_1)^{1/5} t^{2/5}. \qquad (14a)$$

By differentiating it one obtains the shock speed

$$C = \frac{dr_2}{dt} = \frac{2}{5}\left(\frac{E_i}{\rho_1}\right)^{1/5} t^{-3/5} = \frac{2}{5}\left(\frac{E_i}{\rho_1}\right)^{1/2} X$$

$$X r_2^{-3/2} = \frac{2}{5} \frac{r_2}{t}. \qquad (15)$$

Using Eqs. (1), (2), and (11), the nondimensional variables f, g, h and the boundary conditions as stated in Eq. (7) and taking into account Eqs. (14a) and (15), one arrives at a set of three first order nonlinear ordinary differential equations (18).

The energy equation will be:

$$[f(1 + K_i) - (\gamma + 1)\lambda]h' + \gamma h$$

$$X\left[f'(1 + K_i) + \frac{2(1 + K_i)}{\lambda} f\right] \qquad (16)$$

$$-3(\gamma + 1)h - L_i \left[\frac{\gamma + 1}{K_i + 1} \lambda - (\gamma + 1)f \right]$$

$$\times h + M_i = 0 \quad i = 1, 2, 3 . \quad (16)$$

<div align="right">Concluded</div>

Consequently the mass and momentum equations will be

$$\left(\frac{1 + K_i}{2} f - \frac{\gamma + 1}{2} \lambda \right) g'$$

$$+ \left[\frac{1 + K_i}{2} f' + f \frac{(1 + K_i)}{\lambda} \right] g$$

$$+ L_i \frac{\gamma + 1}{2(\gamma - K_i)} g(f - \lambda) = 0 \quad i = 1, 2, 3 \quad (17)$$

$$\left[\frac{f(1 + K_i)}{2} - \frac{(\gamma + 1)\lambda}{2} \right] gf' + \frac{(\gamma - K_i)}{2} h'$$

$$- \frac{3}{4} (\gamma + 1)fg + L_i \frac{1}{2}$$

$$\times \left[gf^2 - \frac{\gamma + 1}{K_i + 1} gf\lambda + \frac{h(\gamma - K_i)}{(K_i + 1)} \right] = 0$$

$$i = 1, 2, 3 \quad (18)$$

where h', f' and g' are the derivatives of h, f, and g

$$h' = \frac{dh}{d\lambda}; \quad f' = \frac{df}{d\lambda} \quad \text{and} \quad g' = \frac{dg}{d\lambda} .$$

Also K_i, M_i, and L_i are defined in the following form

$$K_1 = [1 - (25/2)\beta_1 \lambda^{-3}(\gamma^2 - 1)]^{1/2}$$

$$K_2 = [1 - (25/2)\beta_2(\gamma^2 - 1)]^{1/2} \quad \bigg\} \quad (19)$$

$$K_3 = [1 - (25/2)\beta_3 \lambda(\gamma^2 - 1)]^{1/2}$$

$$M_1 = \frac{75}{4} \beta_1 \frac{(\gamma + 1)^2(\gamma - 1)}{(\gamma - K_1)} gf \frac{1}{\lambda^4}$$

$$M_2 = \frac{75}{4} \beta_2 \frac{(\gamma + 1)^3(\gamma - 1)}{(K_2 + 1)(\gamma - K_2)} g$$

$$M_3 = \frac{25\beta_3(\gamma + 1)^2(\gamma - 1)}{(K_3 + 1)(\gamma - K_3)}$$

$$\times \left[\lambda(\gamma + 1) - \frac{f(K_3 + 1)}{4} \right] g$$

$$\Bigg\} \quad (20)$$

$$L_1 = \frac{dK_1}{d\lambda} = \frac{75}{4K_1} \beta_1(\gamma^2 - 1) \frac{1}{\lambda^4}$$

$$L_2 = \frac{dK_2}{d\lambda} = 0 \quad \Bigg\} \quad (21)$$

$$L_3 = \frac{dK_3}{d\lambda} = -\frac{25}{4K_3} \beta_3(\gamma^2 - 1)$$

The boundary conditions of this set are $\lambda = 0$ at the center of symmetry and $f(0) = 0$. On the shock wave $\lambda = 1$; $f(1) = 1$; $g(1) = 1$ and $h(1) = 1$. λ is varied in the range $0 \leqslant \lambda \leqslant 1$.

B. Calculation of the Coefficient α_i

The Eqs. (16) to (18) are not dependent on E_0 but the dimensional variables depend on E_i as expressed in Eqs. (14) and (15).

From the assumption $V_1 = 0$ and $P_1 = 0$ it follows that E_T — the total energy of the gas behind the shock wave equals the explosion energy E_0 and the combustion energy E_b.

Here

$$E_T = E_0 + E_b = 4\pi \int_0^{r_2} \frac{\rho V^2}{2} r^2 dr + 4\pi$$

$$\times \int_0^{r_2} \frac{P}{\gamma - 1} r^2 dr$$

$$E_b = 4\pi \int_0^{r_2} \rho Q r^2 dr \quad (22)$$

E_{bi} is transformed to self similar coordinates using Eqs. (9) and (9a)

$$E_{b1} = 4\pi \int_0^{r_2} \rho\beta_1 \left(\frac{E_1}{\rho_1}\right) \frac{1}{r}\, dr$$

$$= 4\pi(\gamma + 1)\beta_1 E_1 \int_0^1 \frac{g}{(\gamma - K_1)\lambda}\, d\lambda$$

$$E_{b2} = 4\pi \int_0^{r_2} \rho\beta_2 \left(\frac{E_2}{\rho_1}\right)^{2/5} \frac{r^2}{t^{1.2}}\, dr$$

$$= 4\pi(\gamma + 1)\beta_2 E_2 \int_0^1 \frac{g\lambda^2}{(\gamma - K_2)}\, d\lambda$$

$$E_{b3} = 4\pi \int_0^{r_2} \rho\beta_3 \left(\frac{E_3}{\rho_1}\right)^{1/5} \frac{r^3}{t^{1.6}}\, dr$$

$$= 4\pi(\gamma + 1)\beta_3 E_3 \int_0^1 \frac{g\lambda^3}{(\gamma - K_3)}\, d\lambda. \quad (23)$$

E_{bi} will now be related to E_i through another dimensionless coefficient α_{bi} defined by

$$E_{bi} = \alpha_{bi} E_i \qquad i = 1, 2, 3. \quad (24)$$

Transforming the r.h.s. of Eq. (22) into self similar coordinates one gets the following equation for α_i

$$\alpha_i = \frac{16\pi}{25(\gamma + 1)} \int_0^1 \left[\frac{gf^2(1 + K_i)^2}{2(\gamma - K_i)} \right.$$

$$\left. + \frac{h(1 + K_i)}{\gamma - 1} \right] \lambda^2\, d\lambda - \alpha_{bi} \qquad i = 1, 2, 3. \quad (25)$$

The values of α_i can be found after the integration of Eqs. (16) to (18) and after finding the values of f, g, and h.

C. Solution of the Point Explosion Self Similar Problem

In order to solve the system 16 to 18 one first integrates the energy Eq. (16), obtaining (18):

$$h = \frac{\dfrac{\gamma - 1}{\gamma - K_i} \left[D_i - \dfrac{(K_i + 1)^2}{2} gf^2 \right] \left[\lambda - \dfrac{(K_i + 1)}{(\gamma + 1)} f \right]}{(K_i + 1) \left[\lambda - \dfrac{(K_i + 1)}{(\gamma + 1)} \gamma f \right]}$$

$$\text{(26)}$$

where $i = 1, 2, 3$

where D_i is given by

$$D_i = \frac{(\gamma + 1)^2}{C^2} gQ_i = \frac{(1 - K_i^2)(\gamma + 1)g}{2(\gamma - 1)}. \quad (27)$$

Thus the order of the system is reduced from 3 to 2. Now one has to solve a simpler set that consists of Eqs. (17) and (18) and the algebraic Eq. (26). This set has no analytical solution since it contains two nonlinear differential equations with variable coefficients. Therefore one must resort to numerical integration.

D. The Numerical Integration

Equation (18) will be solved for h' and the solution will replace h' in Eq. (16). After solving (16) for f' one gets:

$$f' = \frac{\left\{ \dfrac{3}{2}(\gamma + 1)fg - L_i \left[gf^2 - \dfrac{\gamma + 1}{K_i + 1} gf\lambda + \dfrac{h(\gamma - K_i)}{K_i + 1} \right] \right\} [f(K_i + 1) - (\gamma + 1)\lambda]}{[f(K_i + 1) - (\gamma + 1)\lambda]^2 g - \gamma h(K_i + 1)(\gamma - K_i)}$$

$$- \frac{(\gamma - K_i) \left\{ 3(\gamma + 1)h + L_i h \left[\dfrac{\gamma + 1}{K_i + 1}\lambda - (\gamma + 1)f \right] - \dfrac{2\gamma h(K_i + 1)}{\lambda} f - M_i \right\}}{[f(K_i + 1) - (\gamma + 1)\lambda]^2 g - \gamma h(K_i + 1)(\gamma - K_i)}$$

$$\text{(18a)}$$

where $i = 1, 2, 3$

594

and Eq. (17) will be solved for g'

$$g' = \frac{\left[\dfrac{(K_i + 1)}{2} f' + f \dfrac{(K_i + 1)}{\lambda}\right] g + L_i \dfrac{(\gamma + 1)}{2(\gamma - K_i)} g(f - \lambda)}{\lambda \dfrac{(\gamma + 1)}{2} - \dfrac{(K_i + 1)}{2} f}$$

$$\text{where } i = 1, 2, 3 \qquad (17a)$$

where L_i was defined in Eq. (21), and M_i in Eq. (20). These two equations and Eq. (26) are a set to which Eq. (25) will be added in a differential form in order to be able to compute the coefficient α_i

$$\alpha_i' = \frac{16\pi}{25(\gamma + 1)}\left[\frac{gf^2(K_i + 1)^2}{2(\gamma - K_i)} + \frac{h(K_i + 1)}{\gamma - 1}\right]\lambda^2 - \alpha_{bi}' \qquad (28)$$

Here $\alpha_i' = d\alpha_i/d\lambda$ and $\alpha_{bi}' = d\alpha_{bi}/d\lambda$

$$\left.\begin{aligned}
\alpha_{b1}' &= 4\pi(\gamma + 1)\beta_1 \frac{g}{(\gamma - K_1)\lambda} \\[2mm]
\alpha_{b2}' &= 4\pi(\gamma + 1)\beta_2 \frac{g\lambda^2}{(\gamma - K_2)} \\[2mm]
\alpha_{b3}' &= 4\pi(\gamma + 1)\beta_3 \frac{g\lambda^3}{(\gamma - K_3)}
\end{aligned}\right\} \qquad (29)$$

The differential Eqs. (17a), (18a), and (28) are solved by the Runge-Kuta method. For the solution, double precision was used (on an IBM-370/168) since the size of $g(\lambda)$ declines quickly to zero. At the same time the algebraic Eq. (26) was solved, performing the calculation for the three energy release models.

γ was taken as 1.4 in most calculations, but for special cases (where $\beta_1 = 0.015$, $\beta_2 = 0.04$ and $\beta_3 = 0.03$), it was taken as 1.2, 1.3, 1.5, and 1.6. The value of α_{bi} was also calculated from Eq. (29).

RESULTS

The Results for Model No. 1. $Q_1 = \beta_1(E_1/\rho_1)r^{-3}$

The value of the additional energy liberated by the burning medium is equivalent to 2.5%, and 11% of the total energy liberated for $\beta_1 = 0.0035$ and 0.015 respectively. This model is very sensitive to the additional energy released (18). However, it also shows discontinuities that approach the shock wave with the increase of β_1.

The Results for Model No. 2. $Q_2 = \beta_2(E_2/\rho_1)^{2/5}t^{-1.2}$

These are shown in Figs. 1, 2, and 3 which represent the relative density $g(\lambda)$, gas velocity $f(\lambda)$, and pressure $h(\lambda)$ for different values of β_2. $\beta_2 \doteq 0$ represents the Sedov-Taylor model as a reference. The different values calculated are listed in Table 1.

The values of β_2 could be changed between zero and 0.083. At $\beta_2 > 0.083$, K_2 gets an imaginary value. Negative values of β_2 mean that the energy is dissipated according to the same E_{b2} function.

In Figs. 1, 2, and 3 it can be seen that the release of energy according to Q_2 brings to a big increase in the functions of the density $g(\lambda)$ and the gas velocity $f(\lambda)$.

The increase of $g(\lambda)$ (Fig. 1) is connected with the decrease of ρ_2 when the energy E_{b2} is increased. The functions have the same shape for every β_2. This is

TABLE 1

Values of the Energy Coefficients α_2 and α_{b2} at $\gamma = 1.4$

β_2	0	0.01	0.023	0.04	0.06	0.07	0.072
α_2	0.85	0.78	0.68	0.54	0.37	0.255	0.22
α_{b2}	0.0	0.042	0.097	0.168	0.25	0.293	0.30
E_b as % of E_T	0%	5%	13%	23.5%	40%	53.4%	58%
E_0 as % of E_T	100%	95%	87%	76.5%	60%	46.6%	42%

595
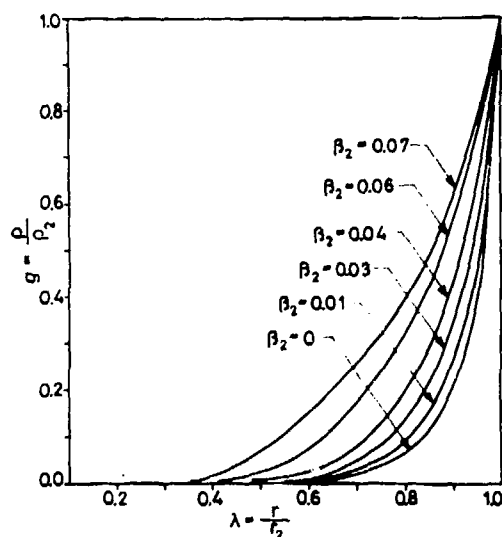
Fig. 1. Graphs of g(λ), the dimensionless density for various $\beta_2 (\gamma = 1.4)$.
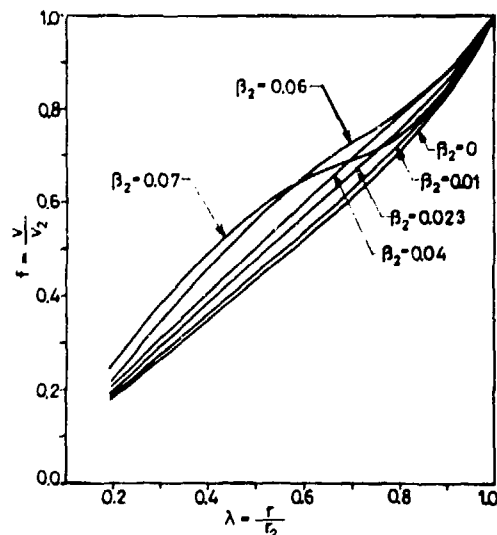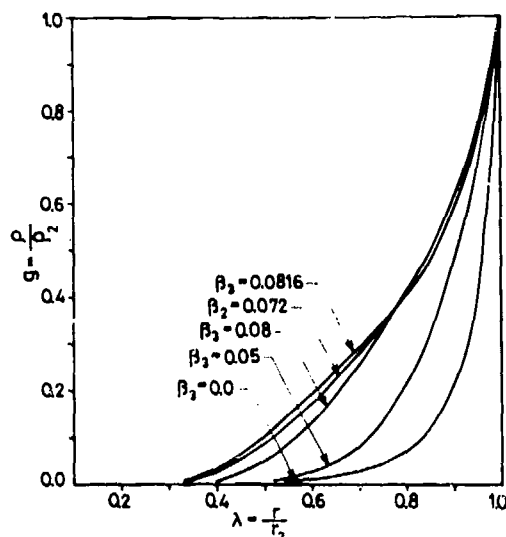

Fig. 2. Graphs of f(λ) the dimensionless gas velocity for various $\beta_2 (\gamma = 1.4)$.

Fig. 3. Graphs of h(λ), the dimensionless pressure for various $\beta_2 (\gamma = 1.4)$.

right also for f(λ) (Fig. 2), up to $\beta_2 = 0.06$. Here the energy starts changing (more so at $\beta_2 = 0.07$) in disfavour of the liberation of additional energy. The heating of the gas on account of the liberation of additional energy is considerable, and this is the cause for the increase of the relative velocity.

The fact that the increase of velocity is favoured in the region $0.5 < \lambda < 0.9$ can be explained by the fact that the volume drops with $\lambda \to 0$ faster than the heat is liberated according to Q_2.
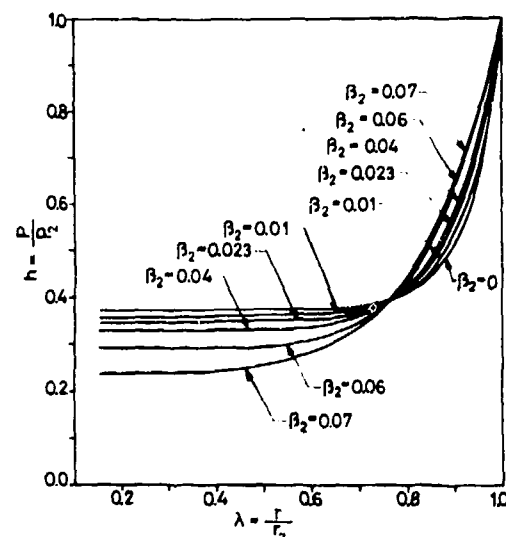
The shape of h(λ) does not change with the increase of β_2. The relative pressure diminishes as β_2 increases and the region of steady pressure is shortened. When the additional energy is increased (β_2 increases) the region where the pressure is high, widens.

The Results for Model No. 3. $Q_3 = \beta_3 (E_3/\rho_1)^{1/5} r/t^{1.6}$

These are presented in Figs. 4, 5, and 6 for h(λ), f(λ), and g(λ). The values of α_3 and α_{b3} are listed in Table 2.

In the three figures it can be seen that the change caused by this model from the standard reference of Sedov-Taylor ($\beta_3 = 0$) is even greater than that caused by Model No. 2. For this purpose in each of the three Figs. 4, 5, and 6, beside the reference line of $\beta = 0$ a comparison line of $\beta_2 = 0.72$ is brought. This value has the same percent of additional energy as $\beta_3 = 0.8$, and therefore both lines are directly comparable. Thus the influence of the Q_i function on the relative parameters h(λ), f(λ) and g(λ) are clearly delineated.

It is known that γ changes during the explosion reaction and that the explosion can occur in gases where γ is different from 1.4. Therefore certain

596
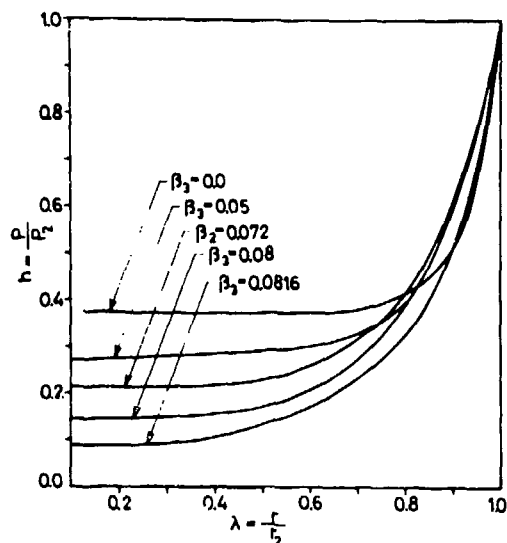
Fig. 4. Graphs of h(λ), the dimensionless pressure for various $\beta_3(\gamma = 1.4)$.

Fig. 6. Graphs of g(λ), the dimensionless density for various $\beta_3(\gamma = 1.4)$.

Fig. 5. Graphs of f(λ), the dimensionless gas velocity for various $\beta_3(\gamma = 1.4)$.

TABLE 2

Values of α_3 and α_{b3} at $\gamma = 1.4$

β_3	0	0.05	0.08	0.0816
α_3	0.85	0.51	0.2	0.13
α_{b3}	0	0.19	0.29	0.29
E_{b3} as % of E_T	0%	27%	59%	70%
E_0 as % of E_T	100%	73%	41%	30%

In general it can be stated that the functions g(λ), h(λ), and f(λ) are more sensitive with the changing of γ but their shape remains unchanged.

DISCUSSION

In order to be able to compare the gasdynamic flow in the Sedov-Taylor model and the one presented here, a problem where the whole energy is caused by the explosion only, is compared with models where the amount of the explosion energy is decreased and the amount of the energy released through combustion is increased so that the sum will be equal to the energy released by the Sedov-Taylor problem.

In Fig. 7 the change of α_{b2} as a function of the radius and different β_2 is shown. For comparison $\alpha_2(\lambda)$ at $\beta_2 = 0.065$ is also presented.

values of β_i were taken for the three models and γ was varied between 1.2 and 1.66.

When integrating for various γ values of the Q_2 model, it was found that α_{b2} depends on β_2 only and does not change with γ. This can probably be explained, because while integrating the function of α_{b2} the result does not include γ. This is not the case with the Q_1 and Q_3 models.

597
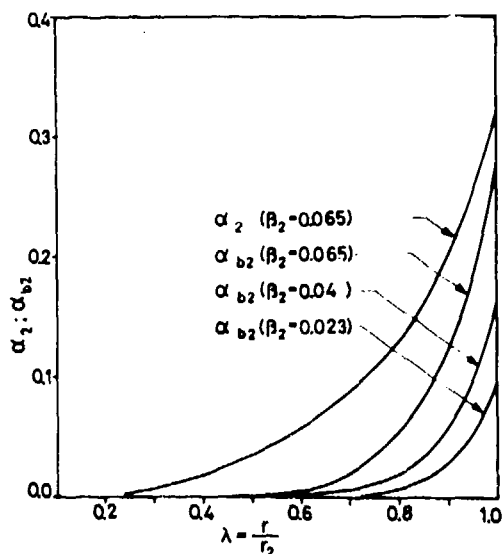
Fig. 7. Graphs of $\alpha_2(\lambda)$, $\alpha_{b2}(\lambda)$ for various $\beta_2(\gamma = 1.4)$.

A look at Fig. 7 reveals that 90% of E_b liberated is concentrated within 15-20% of the shock wave radius and varies with different β_2. It starts immediately after the shock wave (where $\lambda = 1$) and continues inward. For comparison, 90% of the explosion energy expands within 55% of the shock wave radius. This presentation shows that the above model can very well represent explosions in a combustible medium where combustion occurs after the shock wave and continues close to it.

In this work the combustible medium was assumed to be homogeneous. However, if the medium is an aerosol or some other kind of two phase medium, ρ can be represented by some weighted function that will show the equivalent density of the aerosol.

The results obtained can be used to represent the first stages of an explosion caused in a combustible medium by a laser (7,13). They also represent a very good approximation for the first step of the problem treated by Korobeinicov and Levine of the strong point explosion in a detonating gas (9,10,11), since they have calculated only the detonation parameters, disregarding what happens before the detonation starts.

This model has a few advantages over other models presented by Freeman (14) and Dabora (12). The model presented in these cases was $E = Wt^\beta$ where β varies between 0 and 5.

The present model takes into consideration the starting explosion energy E_0. It also enables to change the ratio between E_0 and E_b. And finally the energy spread behind the shock wave is closer to reality where there exists a longer burning period, if the medium contains an aerosol that burns slowly.

In this work we have followed Sedov's (1) example, and plotted relative parameters f, g, and h. However, since by taking a relative parameter one divides V by V_2, ρ by ρ_2 and P by P_2 and since P_2, ρ_2 and V_2 are variables themselves, it is impossible to get from the plots a direct size comparison. In order to be able to do so, one must divide by a constant value such as P_1, ρ_1 and V_1. However, this is impossible with P_1 and V_1 since they are equal to zero. For comparison $g_1 = \rho/\rho_1$ has been plotted for a few values of β_2 and β_3 in Fig. 8. It must be mentioned that $\beta_2 = 0.072$ and $\beta_3 = 0.08$ both give approximately the same percent of additional energy and so do $\beta_3 = 0.045$ and $\beta_2 = 0.04$.
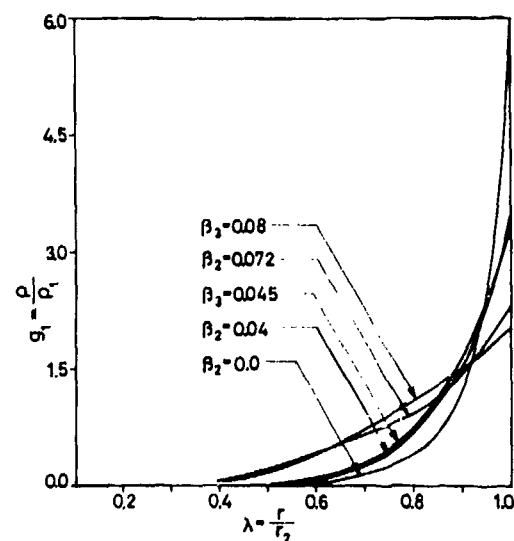
Fig. 8. Graphs of $g_1(\lambda)$, the dimensionless density for various β_2 and $\beta_3(\gamma = 1.4)$.

Calculation of the Energetic Efficiency

The calculation of the efficiency should give an answer to the question whether it is preferable to explode the charge at $t = 0$, or to explode at $t = 0$ only a part of this material and liberate the rest of the energy through the combustion as E_{bi}.

The self-similar solution of the problem is not dependent on a specific E_0. Therefore one must exchange

598

the nondimensional coordinates for the natural coordinates of the problem. For this case one performs the computations for a specific energy of explosion in a medium with a density ρ_1.

The density $\rho_1 = 0.00125$ gr/cc is taken equal to the density of air and E_0 as the energy released in the New Mexico atomic explosion of 1945 (19).

$$E_0 = 7.16 \times 10^{20} \text{ erg} = 7.16 \times 10^{13} \text{ joule}$$

$$= 16.8 \text{ kiloton TNT.}$$

The criterion for efficiency will be the shock wave's velocity, C, and the pressure on the shock wave P_2. C was defined in Eq. (15) and to calculate it, one needs to know E from Eq. (10). Therefore for $\beta = 0$

$$E = \frac{1}{\alpha} E_0 =$$

$$\frac{1}{0.85} E_0 = 1.175 \times 7.16 \times 10^{13} \text{ joule}$$

$$= 8.42 \times 10^{13} \text{ joule}$$

$$C = 2.33 \times 10^2 \times t^{-3/5} \text{ m/sec},$$

and from Eq. (7), if $\beta_2 = 0$

$$K_2 = 1 \quad \text{and} \quad P_2 = 5.57 \times 10^4 \times t^{-6/5} \text{ N/m}^2.$$

Now let us assume that $\beta_2 = 0.072$, i.e., at $t = 0$, 42% of E_T is liberated as E_0 and 58% of E_T is liberated as E_b according to Q_2. (E_T was assumed to be $E_0 + E_b$, i.e., the total energy.)

$$E_2 = \frac{1}{(\alpha + \alpha_{b2})} E_T = 13.8 \times 10^{13} \text{ j}$$

$$C = 2.58 \times 10^2 \times t^{-3/5} \text{ m/sec}$$

$$P_2 = 4.8 \times 10^4 \times t^{-6/5} \text{ N/m}^2.$$

It can be concluded that C has increased by 11% relative to the Sedov-Taylor model. P_2 decreased by 17% and from Eq. (7), ρ_2 decreases two and a half times and V_2 the velocity of the gas behind the shock decreases by 28%.

For the Q_3 model in a comparable way, the results are:

$$E_3 = 14.7 \times 10^{13} \text{ j};$$

$$C = 2.61 \times 10^2 t^{-3/5} \text{ m/sec}$$

and

$$P_2 = 4.26 \times 10^4 t^{-6/5} \text{ N/m}^2.$$

Here E_3 is bigger by 6.5% than E_2; C is bigger by 2%, P_2 decreases by 13% compared to Q_2 or 23.5% compared to Sedov-Taylor. ρ_2 decreases 16% from the Q_2 model while V_2 increases by 12% compared to the Q_2 model. It can therefore be concluded that the models studied are more efficient than the Sedov-Taylor model only in what concerns the shock speed C, while the other parameters V_2, ρ_2 and P_2 show a definite preference for the S.T. model; the Q_2 model being slightly more favorable in the overall performance than Q_3.

The last point to be mentioned in the discussion is the meaningfulness of the model from the standpoint of the possibility of energy release by combustible media. Since we have mentioned that the E_0 energy has to be of the size of an atomic blast, and since the amount of energy liberated by an aerosol in the atmosphere is limited by the amount of oxygen available, one can calculate what is the amount of fuel, and what is the size of the spheric cloud where this fuel has to be spread. Taking TNT as a reference for E_0 at a density of 1.5 it liberates 1010 Kcal/kg (20). Half the size of our bomb will be 8 kt = 8.000.000 kg TNT which will liberate 8.08×10^9 Kcal of heat. Taking pulverized graphite for reference in order to calculate the energy released by a combustible medium that liberates 7840 Kcal/kg, one needs ≈ 1030 tons of pulverized graphite. Since the reaction is $C + O_2 \rightarrow CO_2$ we need approximately 2750 tons of oxygen, i.e., a ball of air of the radius of 138 m.

LIST OF SYMBOLS

B_i	parameter defined in Eq. (12)
C	the shock speed defined in Eq. (15)
D_i	parameter defined in Eq. (27)
E_i	energy quantity related to E_0 through Eq. (10)
E_0	energy of the point explosion
E_b	energy liberated by the combustible media
E_T	total energy equal to $E_0 + E_b$
f	nondimensional gas velocity, Eq. (13)
g	nondimensional gas density, Eq. (13)

599

h   nondimensional pressure, Eq. (13)
K_i parameter defined by Eq. (19)
L_i parameter defined by Eq. (21)
M_i parameter defined by Eq. (20)
P   pressure
Q_i quantity of heat per unit mass liberated by combustion processes
r   radius
t   time
V   gas velocity
Z_i parameter defined by Eq. (9a)
α_i energy parameter defined by Eq. (10) and (25)
α_{bi} combustion parameter defined by Eq. (24)
β_i arbitrary energy parameter defined by Eq. (9a)
γ C_p/C_v
ϵ energy per unit mass
λ dimensionless parameter defined by Eq. (8)
ρ gas density.

Subscripts

0   related to the point explosion
b   related to the combustion
T   total
1   before the shock front
2   behind the shock front   } for P, ρ, and V.

REFERENCES

1. L. I. Sedov, Propagation of Strong Blast Waves, *PMM* **10**, 242 (1946); Le Mouvement d'air en eas d'une forte explosion, *Comptes Rendus (Doklady) Acad. Sci. U.R.S.S.*, **52**, 17 (1946) (French).

2. G. I. Taylor, The Formation of a Blast by a Very Intense Explosion, *Proc. Roy. Soc. A*, **201**, 159 (1950).

3. L. I. Sedov, Similarity and Dimensional Methods in Mechanics, Infosearch., London, 1959.

4. A. Sakurai, On Propagation and Structure of the Blast Wave, *J. Phys. Soc. Japan*, **8**, 662 (1953).

5. D. E. Okhotsimskii, U. L. Kondrasheva, Z. P. Vlasova, and R. K. Kazakova, Calculation of Point Explosion with Counterpressure, Trudy MIAN SSSR, 50, 1957.

6. V. P. Korobeinikov, N. S. Melnikova and E. B. Riazanov, The Theory of Point Explosions, U.S. Dept. of Commerce, 1962.

7. V. P. Koronbeinikov, The Problems of the Point Explosions Theory in Gases, Izd. Nauka, Moskva, 1973.

8. V. P. Korobeinikov, On the Gas Flow Due to Solar Flares, *Solar Phys.*, **7**, 463 (1969).

9. V. P. Korobeinikov and V. A. Levin, Strong Explosion in a Combustible Mixture, *Izv. ANSSSR, Mech. Zhidk. Gaz.*, **4**, 48 (1969). (Eng. Transl. p. 30.)

10. V. P. Korobeinikov, The Problem of Point Explosion in a Detonating Gas, Proc. 1st. Internat. Coll. on Gas Dynamics of Explosions, Brussels, 1967. *Astronaut. Acta*, **14**, 411 (1969).

11. V. A. Levin, Approximate Solution of the Blast Problem in a Combustible Mixture, *Izv. ANSSSR, Mech. Zhidk. Gaz.*, **2**, 122, 1967 (Eng. Transl. p. 80).

12. E. K. Dabora, Variable Energy Blast Waves, *AIAA J.*, **10**, 1384 (1972).

13. M. N. Director and E. K. Dabora, An Experimental Investigation of Variable Energy Blast Waves, Fifth Internat. Coll. on Gas Dynamics of Explosions and Reactive Systems, Bourges 1975, *Acta Astronaut.*, in press.

14. R. A. Freeman, Variable Energy Blast Waves, *Brit. J. Appl. Phys. (J. Phys. D), Ser. 2*, **1**, 1697 (1968).

15. A. K. Oppenheim, E. A. Lundstrom, A. L. Kuhl, and M. M. Kamel, A Systematic Exposition of the Conservation Equations for Blast Waves, *J. Appl. Mech.*, **38**, 783 (1971).

16. A. K. Oppenheim, E. A. Lundstrom, A. L. Kuhl, and M. M. Kamel, A Parametric Study of Self-Similar Blast Waves, *J. Fluid Mech.*, **52**, 657 (1972).

17. A. K. Oppenheim, A. L. Kuhl, and M. M. Kamel, On Self-Similar Blast Waves Headed by the Chapman Jouguet Detonation, *J. Fluid Mech.*, **55**, 257 (1972).

18. S. Eidelman, The Problem of a Strong Point Explosion in a Combustible Two-Phase Medium, M.Sc. Thesis, Technion, Israel Institute of Technology, 1975.

19. K. L. Brode, Review of Nuclear Weapons Effects, *Ann. Rev. of Nuclear Science,* **18**, 153 (1968).

20. J. Taylor, Detonation in Condensed Explosives, Clarendon Press, Oxford, 1952.

PERPENDICULAR EXPLOSIVE DRIVE AND OBLIQUE SHOCKS*

T. Neal
Los Alamos Scientific Laboratory
University of California
Los Alamos, New Mexico 87545

Obliq ie shocks in various materials driven by Composition B-3, 9404, and TNT with the detonation wave perpendicualr to the interface are investigated with flash radio-graphic techniques. The detonation products in the rarefaction behind the detona-tion front expand laterally as the explosive-sample interface bends under shock compression of the sample. With the products described by a polytropic gas equa-tion of state, this expansion is shown to be adequately described in the vicinity of the detonation front by Prandtl-Meyer flow. Some new Hugoniot data for antimony is obtained in the course of the investigation. In some instances of perpendicular drive the compression of the sample is not accomplished strictly by strong shocks. This circumstance is exemplified by baratol driving aluminum, a case where the bulk sound speed exceeds the detonation velocity, and by 9404 driving beryllium, a case where it does not. Some experimental results are presented for both these systems.

INTRODUCTION

A detonating explosive in contact with a metal plate has been the subject of extensive investigations by many shock workers (1, 2). The case where the detonation wave is parallel to the explosive-metal interface has received far more attention than the case where it is oblique. Recently detonation waves at right angles to the interface have been investigated at this laboratory by means of radiographic tech-niques. Perpendicular drive, as it is termed, has been used to determine Hugoniot data, observe phase changes, and drive regular and Mach reflection ex-periments. It is useful in experiments of these types because the waves in the metal plates are driven con-tinally and steadily and radiographs provide a sort of time history. Behind the detonation front the pro-ducts of detonation expand laterally as the metal is compressed. If the compression occurs as a result of

a shock, the metal interface undergoes an abrupt bend where it is intersected by the detonation wave. Viewed from a coordinate system moving at the con-stant velocity of the detonation, the flow pattern is that of an incoming stream of material turning a corner. Flow around a bend in a channel is described by a Prandtl-Meyer expansion if the flow states before and after the bend are constant states. Although the front of the detonation wave can be considered a constant state in this context, the flow behind cannot because of the rarefaction that follows the detona-tion front. The effects of this rarefaction are exhibited in the gradual curvature of the metal-explosive inter-face that occurs behind the abrupt bend due to the shock. In addition, the finite size of experimental assemblies used to investigate perpendicular drive often precludes the flow patterns in the metal being time independent in regions far from the detonation front. Therefore, the first objective of this report will be to investigate the explosives Composition B-3, 9404 and TNT to see if the Prantdl-Meyer ex-pansion can reasonably describe the flow of detona-tion products behind a detonation front followed by

a rarefaction. For the purpose of making this comparison the detonation products will be described by a polytropic gas equation of state. If such a flow model proves adequate, a simple analytical method will henceforward be available for predicting the strength and direction of shocks in materials shock-compressed by perpendicular drive with these explosives. A different material flow pattern occurs in perpendicular drive when the bulk sound speed of the material exceeds the detonation velocity. A shock cannot form in the metal because it tries to run ahead of the detonation, becomes unsupported and hence decays. The case of the explosive baratol driving aluminum is a well known example. Even if the bulk sound speed is less than the detonation velocity, there is no assurance that there is a solution to the flow equations in which the final compression is achieved solely by the leading shock. Beryllium driven by 9404 is an example of a combination in which only part of the compression in the metal is accomplished through a strong shock. Thus, a bulk sound speed smaller than the detonation velocity is a necessary but not sufficient condition for formation of a full-pressure shock in the metal in perpendicular drive. Both the examples mentioned are being investigated, especially with regard to the shocks and pressures transmitted into a second adjacent metal plate. Some experimental results for these flow situations will also be presented.

PERPENDICULAR DRIVE

In order to understand how equation-of-state and flow measurements are obtained from perpendicular drive it is appropriate to consider the fluid dyanmics of the situation depicted in Fig. 1. A detonation wave is proceeding at a right angle with respect to the interface between the explosive and some sample. Not all explosives possess the property that the detonation front remains relatively planar and at right angles to the interface in the immediate vicinity of the interface. The analysis here will be restricted to those that do. The interface has deflected at an angle α as a result of shock compression of the sample. The explosive ahead of the detonation front is, of course, unreacted. Let us assume for the moment that near the interface the region behind the detonation front is a constant state in which the flow streamlines are parallel and steady. The expansion of detonation products into the region previously occupied by the sample can then be described by PM (Prandtl-
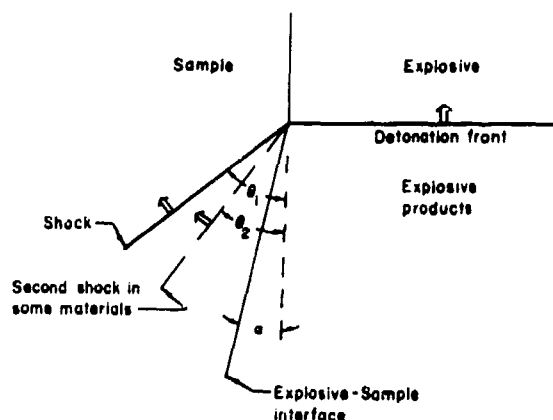
Fig. 1. Schematic of perpendicular drive. The heavy solid lines represent shocks and the small double arrows indicate their direction of propagation.

Meyer) flow around a sharp corner (3). In that case Bernoulli's principle becomes (4)

$$dP = - \rho v^2 C \, d\alpha / \sqrt{v^2 - C^2} \qquad (1)$$

where P is the pressure and ρ is the density of the detonation products. The sound speed C and the velocity along the streamline, v, are related to the pressure and density by

$$C^2 = dP/d\rho \text{ and } v \, dv = - dP/\rho. \quad (2),$$

For many situations explosives have been adequately described by a CJ (Chapman-Jouget) detonation and a γ-law equation of state (5). The pressure and density of the explosive products are then related by

$$P = P_{CJ}(\rho/\rho_{CJ})^\gamma. \qquad (4)$$

The CJ conditions can be expressed as

$$P_{CJ} = \rho_e D^2(\gamma + 1), \rho_{CJ} = \rho_e(\gamma + 1)/\gamma, \text{ and}$$

$$v_{CJ} = C_{CJ} = D\gamma/(\gamma + 1) \qquad (5)$$

where ρ_e is the density of the unreacted explosive and D is the detonation velocity. The model for a PM expansion of a polytropic gas can now be solved using the CJ conditions as initial conditions for the flow.

603

The result is

$$-\frac{d\alpha}{dp} = \frac{\sqrt{\frac{\gamma+1}{\gamma-1}\left(1-p^{(\gamma-1)/\gamma}\right)}}{\left[\gamma p^{(\gamma+1)/(2\gamma)}\left(1+\frac{2}{\gamma-1}\left(1-p^{(\gamma-1)/\gamma}\right)\right)\right]} \quad (6)$$

where p is a dimensionless pressure given by

$$p = P/P_{CJ}. \quad (7)$$

Thus if the value of γ and the detonation velocity are known, the deflection of the explosive-sample interface can be related directly to the pressure at that interface.

Since the detonation velocity is constant, the velocity of the first shock in the sample is given by

$$U_{s1} = D \sin \theta_1. \quad (8)$$

If there is only one shock in the sample the interface deflection and particle velocity behind the shock are related through the expression

$$u_{p1} \cos(\theta_1 - \alpha) = D \sin \alpha. \quad (9)$$

If, in addition to the angle θ, the angle α can be measured, this relationship gives an independent determination of the particle velocity and specifies a state on the Hugoniot. The resulting pressure in the sample is obtained from a Rankine-Hugoniot condition (6) which in this case can be written as

$$P_1 = \rho_0 D^2 \sin^2 \theta_1 [1 - \tan(\theta_1 - \alpha)/\tan \theta_1]. \quad (10)$$

Here ρ_0 refers to the initial density of the sample material. The sample, in this discussion, is assumed to have no strength and behave hydrodynamically. If the Hugoniot relationship for the sample material is well known, the particle velocity can be obtained directly from the shock velocity. For many materials this relationship is linear in the shock velocity-particle velocity representation and can be expressed as

$$U_{s1} = C_0 + S_0 u_{p1} \quad (11)$$

where C_0 and S_0 are constants that depend on the particular material. In that case the angle α can be obtained from the equation

$$\tan(\theta_1 - \alpha) = [\sin \theta_1 (S_0 - 1) + C_0/D]/(S_0 \cos \theta_1). \quad (12)$$

The relationship of interface deflection to shock pressure in the sample is contained in Eqs. (10) and (12) in parametric form with θ_1 acting as the parameter. Since pressure is continuous across the explosive-sample interface, this relationship can be compared with that for the explosive products in Eq. (6) to predict the strength and direction of the shock in the sample when the release isentrope of the explosive products is also known.

In samples that undergo phase transitions upon shock compression a double shock structure may occur (7). The velocity of the second shock in the laboratory frame of reference is

$$U_{\ell2} = D \sin \theta_2. \quad (13)$$

The material in front of the second shock is not at rest. The velocity of the second shock with respect to the material in front of it therefore becomes

$$U_{s2} = U_{\ell2} - u_{p1} \cos(\theta_1 - \theta_2). \quad (14)$$

If the phase transition is completed in a small fraction of the time characteristic for other events Eq. (9) is replaced by

$$u_{p1} \cos(\theta_1 - \alpha) + u_{p2} \cos(\theta_2 - \alpha) = D \sin \alpha \quad (15)$$

which can be used in a like manner. The quantity u_{p2} is the particle velocity associated with the second shock. The final pressure achieved is

$$P_2 = \rho_0 [u_{p1} U_{s1} + u_{p2} U_{s2}/(1 - u_{p1}/U_{s1})]. \quad (15)$$

EXPERIMENTAL METHOD

A flash radiographic technique was employed to observe oblique shocks and interface deflections for various materials. The experimental arrangement was similar to that used by Katz, Doran, and Curran (8) to produce oblique shocks in iron and by Bread and Venable (9) to produce oblique shocks in antimony and bismuth. The explosives Composition B-3, 9404,

TNT and baratol were used in this study. The explosive was in the shape of a rectangular parallelepiped with a width of 10 cm in the case of baratol and 6 cm for the others. The dimension in the direction of the radiographic beam ranged from 3 cm to 10 cm, corresponding to the thickness of the sample that could conveniently be radiographed. These blocks were initiated with a 10-cm-diameter planewave explosive lens. After the detonation had run nine or ten cm the sample was radiographed with the pulsed high-energy radiographic facility of this laboratory. The radiographic technique has been described elsewhere (10). The detonation velocity of the various explosives was measured using either a method in which piezoelectric timing pins are placed along the side of the explosive or a method developed by Hayes (11) which detects an electrical signal when the detonation crosses an explosive-explosive interface. To generate these latter signals some of the explosive blocks were built up out of slabs assembled together. The determination of the detonation velocity was only a minor source of uncertainty in these experiments. The major source of error occurred in the determination of the various angles. A line drawing of the essential features in an actual radiograph is shown in Fig. 2. The line OA is the detonation wave. For all the explosives radiographed the wave was planar, parallel to the reference foil, and perpendicular to the interface. The line OB represents the first shock in the sample and the line OC represents the interface. Both of these lines were slightly curved, corresponding to the decay of the shock as it moved into the sample. All angles were determined in the limit where the lines intersect point O. In analyzing these radiographs the assumption is made that if the radiograph were taken at some different time, the flow pattern in the region of the vertex O would be the same. This assumption has been shown to be valid within the resolution of the radiographs (9,12).

The sample materials used are listed in Table 1. The densities refer to those of the sample used in this investigation. The coefficients for the Hugoniot relationship in Eq. (11) are presented along with the pressure range from which data for the fits were taken (13). Since antimony exhibits a phase change under shock compression, the pressure range for that fit was restricted to a region where no double wave structure is present and the Hugoniot appears linear. The fit for uranium does not include any very low pressure data because those shocks in uranium are not sharply defined. In all but one instance, however,
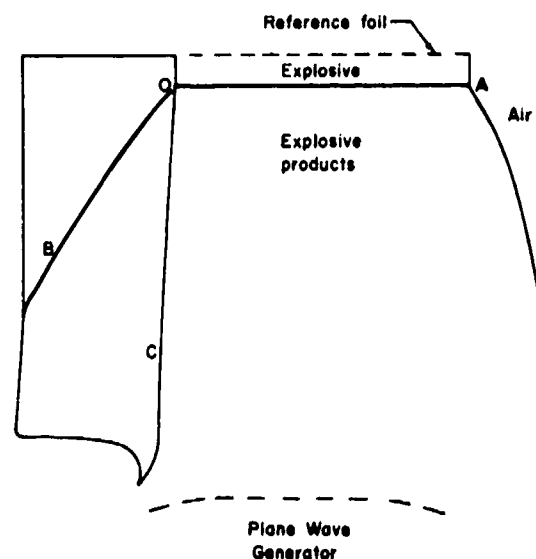
Fig. 2. Line drawing of principal features in a radiograph. The shocks are indicated by heavy solid lines.

the pressure range covers that attained in perpendicular drive by Composition B-3, 9404, and TNT.

COMPOSITION B-3, 9404, and TNT

The explosives Composition B-3, 9404, and TNT were used to generate oblique waves in various samples in order to study the expansion of the explosive products behind the detonation front. The results of the investigation of Composition B-3 are presented in Table 2. The explosive in these experiments had a density of $1.730 \pm .001$ Mg/m^3. The detonation velocity was determined to be $7.915 \pm .01$ km/s. These values agree well with other independent measurements at this laboratory (14). The five different metals that were used as samples are listed in order of increasing interface deflection. The first column lists the measured values of the angle θ along with its standard deviation. The shock velocity, shock pressure, and interface deflection in the immediately succeeding columns were calculated from θ with the use of the reference Hugoniots. Next a value of γ for the explosive products was sought which permitted the PM expansion described by Eq. (6) to match the pressure and deflection of the metal. A weighted average of the values of γ determined by this procedure is given at the bottom of this column. The data for the samples is also presented in Fig. 3 in the

TABLE 1
Reference Hugoniots

	PMMA	Be	Al(2024)	Sb	Cu	Pb	U
ρ_0(Mg/m^3)	1.186	1.85	2.785	6.67	8.93	11.34	18.91
C_0(km/s)	2.586	8.005	5.328	1.572	3.912	2.027	2.503
S_0	1.529	1.119	1.332	1.993	1.500	1.472	1.513
P-range (GPa)	2 < P < 20	0 < P < 89	0 < P < 108	16 < P < 39	0 < P < 158	0 < P < 200	21 < P < 371

TABLE 2
Perpendicular Drive by Composition B-3

	θ (deg)*	U_s(km/s)	P(GPa)	α (deg)	γ	α (deg)*	u_p(km/s)	P(GPa)
U	22.65 ± .37	3.048 ± .047	20.8 ± 2.1	2.45 ± .21	2.76 ± .31	2.49 ± .10	0.366 ± .015	21.1 ± .9
Cu	36.03 ± .14	4.656 ± .016	20.6 ± .5	3.01 ± .06	2.63 ± .08	2.99 ± .17	0.493 ± .027	20.5 ± 1.1
Pb	21.05 ± .18	2.843 ± .023	17.9 ± .7	3.84 ± .10	2.79 ± .11	3.88 ± .11	0.561 ± .016	18.1 ± .5
Al	56.72 ± .16	6.617 ± .012	17.8 ± .2	4.27 ± .03	2.70 ± .03	4.22 ± .20	0.957 ± .041	17.7 ± .8
Sb	23.44 ± .23	3.148 ± .029	16.6 ± .5	5.45 ± .10	2.61 ± .08	5.37 ± .04	0.779 ± .006	16.4 ± .2
			Weighted Mean		2.69 ± .06	*-measured directly		
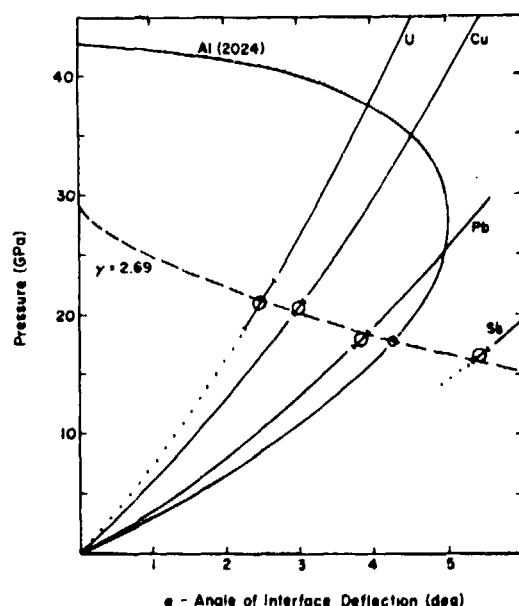
Fig. 3. Perpendicular drive by Composition B-3. The solid lines are the oblique solutions obtained from the reference Hugoniots. The dotted lines cover ranges into which the reference Hugoniots have been extrapolated. The dashed line is the Prandtl-Meyer expansion of detonation products described by a polytropic gas equation.

representation of pressure and angle of interface deflection. The curves for the five different metals are solutions of Eqs. (10) and (12) from the reference Hugoniot. The data, of course, lie on these curves. The behavior of the curve for 2024-aluminum is typical of most materials. The other curves again intersect zero deflection when their shock velocities are equal to the detonation velocity. These pressures are off scale for Fig. 3. The dashed curve describes the PM expansion of the explosive products. The final value of γ yields a CJ pressure of 29.4 ± .5 GPa. This agrees with the pressure determined from planar plate-push techniques (14). The pressure investigated in these oblique expansions, however, were normally in the range of 55-70% of the CJ pressure. These results can also be compared directly with those of Rivard, et al. (12) who investigated the rarefaction behind the detonation front down to pressures of roughly 45% of the CJ pressure and found it could be approximated quite well by a Taylor wave. A fit to their data with a γ-law equation of state produced a CJ pressure of 29.9 ± .4 GPa.

In order to provide a check on our measuring techniques, the interface deflection was also determined from the radiographs. The results for the measured value of the angle α and the subsequent determinations of the particle velocity and shock

pressure are listed in the last three columns of Table 2. The good agreement of these independently determined pressures with those obtained from the measured shock velocity with the aid of the reference Hugoniot indicates a good deal of self-consistency in the measuring methods. The result for antimony was, in fact, used in the determination of the reference Hugoniot since data in that pressure regime is rather scarce.

The next explosive investigated was 9404. Its density was $1.845 \pm .002$ Mg/m^3 and its detonation velocity was $8.80 \pm .01$ km/s. These values are in good agreement with those quoted by Kury, et al. (15). In addition to the five metals used previously, PMMA (polymethyl methacrylate) was included as a sample in order to examine larger interface deflections. The results for 9404 are presented in Table 3. The format, except for the last two experiments, which will be discussed in another section, is the same as for Table 2. The data are also depicted in Fig. 4. The averaged value of γ corresponds to a CJ pressure of $36.3 \pm .4$ GPa. This value of γ is slightly higher than the range 2.83-2.87 reported from expansion methods and the aquarium technique (16). The inclusion of PMMA as a sample permitted the pressure examined in the expansion to be extended from roughly 70% of the CJ pressure down to approximately 30%. The lower pressure PMMA experiment, however, did not seriously alter the final value of γ.

In the series of experiments with 9404 only 2024-aluminum was examined to obtain directly the state

on the Hugoniot. Since the independent pressure measurement correlated well with that obtained from the reference Hugoniot, antimony was also examined to provide an additional state point for use in establishing its reference Hugoniot.

The final explosive whose expansion was investigated was TNT. It had a density of $1.635 \pm .002$ Mg/m^3 and a detonation velocity of $6.90 \pm .01$ km/s, which is again in agreement with measurements by others (17). The results are listed in Table 4 and also
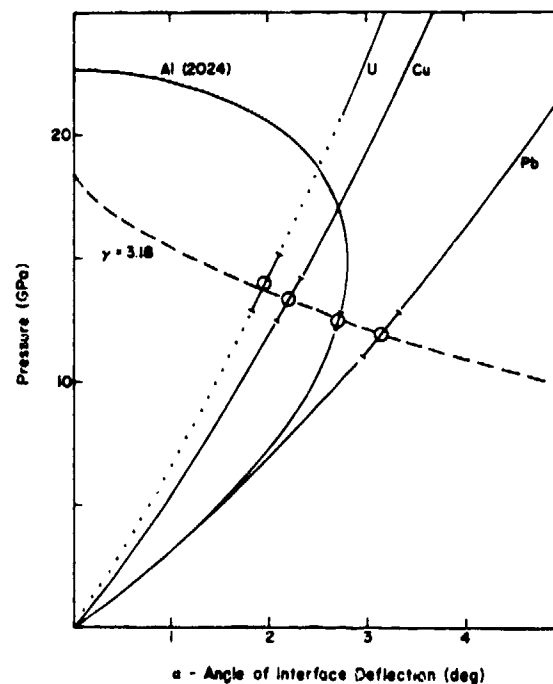

a - Angle of Interface Deflection (deg)
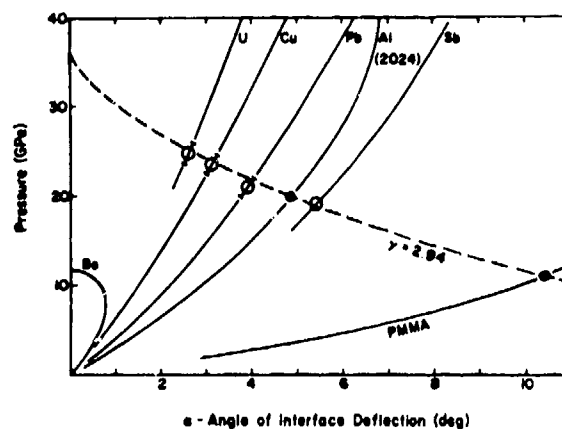
Fig. 4. Perpendicular drive by 9404. The solid lines are oblique shock solutions obtained from the reference Hugoniots. The dashed line is the Prandtl-Meyer expansion of detonation products described by a polytropic gas equation of state.

TABLE 3

Perpendicular Drive by 9404

	θ (deg)*	U_s(km/s)	P(GPa)	α(deg)	γ	α(deg)*	u_p(km/s)	P(GPa)
U	$20.88 \pm .17$	$3.136 \pm .024$	24.8 ± 1.2	$2.59 \pm .10$	$2.99 \pm .15$			
Cu	$32.63 \pm .25$	$4.745 \pm .032$	23.5 ± 1.1	$3.15 \pm .12$	$2.98 \pm .15$			
Pb	$19.58 \pm .24$	$2.949 \pm .035$	20.9 ± 1.0	$3.93 \pm .15$	$3.07 \pm .16$			
Al	$49.97 \pm .08$	$6.738 \pm .008$	$19.9 \pm .1$	$4.87 \pm .02$	$2.95 \pm .02$	$4.82 \pm .31$	$1.048 \pm .062$	19.7 ± 1.2
Sb	$22.03 \pm .18$	$3.301 \pm .026$	$19.1 \pm .4$	$5.42 \pm .08$	$2.91 \pm .07$	$5.57 \pm .18$	$0.891 \pm .027$	$19.7 \pm .6$
PMMA	$37.07 \pm .22$	$5.305 \pm .027$	$11.2 \pm .2$	$10.40 \pm .09$	$2.92 \pm .04$			
				Weighted Mean	$2.94 \pm .04$		*-measured directly	
Al	$48.00 \pm .36$	$6.540 \pm .037$	$16.6 \pm .6$	10 mm Be Insert		$4.56 \pm .31$	0.964 ± 060	17.6 ± 1.1
Sb	$21.78 \pm .15$	$3.265 \pm .021$	$18.5 \pm .4$	3 mm Be Insert		$5.36 \pm .32$	$0.857 \pm .050$	18.7 ± 1.1

presented in Fig. 5. The metal antimony was not included in this investigation because the double wave structure expected under perpendicular drive by TNT complicates the determination of γ. An independent determination of the pressure was again made for 2024-aluminum to confirm there was nothing unusual in the flow near the intersection of the shock and detonation waves. The final value of γ corresponds to a CJ pressure of 18.6 ± .7 GPa which agrees with values of 19-20 GPa found by others (16). The pressure range investigated in the TNT expansion extended over about 65-75% of the CJ pressure. This range is narrower than that covered for the other two explosives.

The results for γ obtained by this technique compare favorably with values determined by methods that do not involve the assumptions associated with a PM expansion. Thus the Prandtl-Meyer expansion provides a useful description of perpendicular drive for the explosives Composition B-3, 9404, and TNT in the immediate vicinity of the intersection of the oblique shock with the detonation wave. This occurs in spite of the fact that the region behind the detonation wave is a rarefaction and not a constant state.

ISENTROPIC COMPRESSION WITH PERPENDICULAR DRIVE

The properties of all the sample materials discussed thus far have permitted full-pressure shock solutions with the explosives used. In order words, in the plane of shock pressure and angle of interface deflection the curve of physically possible solutions obtained from a reference Hugoniot for a material has intersected the curve of physically possible solutions for the PM expansion of the detonation products.

Both these solution curves, of course, come from a model in which the interface undergoes an abrupt bend. There are, however, materials and explosives for which this does not occur. These situations can be divided into two categories. The simplest is that in which the bulk sound speed exceeds the detonation

Fig. 5. Perpendicular drive oy TNT. The solid lines are the oblique shock solutions obtained from the reference Hugoniots. The dotted line covers a pressure range into which the reference Hugoniot has been extrapolated. The dashed line is the Prandtl-Meyer expansion of detonation products described by a polytropic gas equation of state.

TABLE 4

Perpendicular Drive by TNT

	θ (deg)*	U$_s$(km/s)	P(GPa)	α(deg)	γ	α(deg)*	u$_p$(km/s)	P(GPa)
U	24.77 ± .25	2.891 ± .027	14.0 ± 1.1	1.96 ± .14	3.10 ± .28			
Cu	39.82 ± .32	4.419 ± .030	13.3 ± .9	2.22 ± .12	3.16 ± .23			
Al	65.49 ± .45	6.278 ± .022	12.5 ± .3	2.71 ± .02	3.19 ± .09	2.87 ± .13	0.751 ± .033	13.1 ± .6
Pb	22.29 ± .33	2.617 ± .037	11.9 ± .9	3.15 ± .19	3.18 ± .26			
				Weighted Mean	3.18 ± .15		*-measured directly	

velocity. Typical examples are afforded by the baratol-aluminum combination, where the bulk sound speed exceeds the detonation velocity by about 10%, and the TNT-beryllium combination, where it exceeds by about 15%. The former system has been examined by Eden and Wright (18) using streak cameras. In these circumstances compression by a single shock is incompatible with the hydrodynamic flow conditions and such compression is not observed. The other category consists of materials for which there is no full-pressure shock solution even though the bulk sound speed is less than the detonation velocity. An example of this combination discussed below is 9404 and beryllium where the bulk sound speed is 91% of the detonation velocity.

A few radiographic experiments were performed to examine both these effects. The perpendicular drive of beryllium by 9404 will be discussed first. The flow solution for beryllium is indicated in Fig. 4. It does not intersect the PM expansion because a shock velocity in beryllium equal to the detonation velocity produces a shock pressure of only 11.3 GPa, far below the CJ pressure for 9404. A 2024-aluminum sample was placed next to a 10-mm-thick slab of beryllium in order to observe the effect of the pressure pulse transmitted through the beryllium. A line drawing of the principal information content of the radiograph is presented in Fig. 6. An important factor to keep in mind when examining the aluminum in such an experiment is the number of times an acoustic pulse has been able to travel across the beryllium slab by the time the radiograph is taken. The bulk sound speed in beryllium shock-compressed to a pressure of 11.3 GPa can be estimated from the Mie-Grüneisen equation of state (4) to be about 8.8 km/s. Since the detonation has run about 10 cm, acoustic information has been able to cross the beryllium about 10 times. If this number is too small, the material flow in the aluminum may not yet be independent of the time when the radiograph is taken. In the beryllium a density discontinuity is visible. Near the 9404 this shock parallels the detonation front. This would correspond to the shock pressure of 11.3 GPa mentioned previously. The beryllium-explosive interface, though displaced, does not have the abrupt bend characteristic of an oblique shock. Near the aluminum interface the shock appears to have bent and is no longer parallel to the detonation front. A shock is clearly discernible in the aluminum and its interface exhibits a bend and displacement similar to that found when it was in direct

Planewave Lens
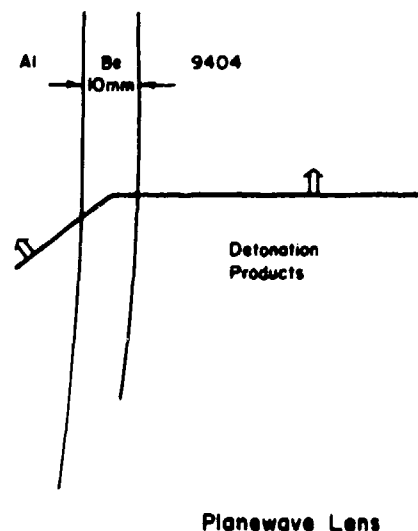
Fig. 6. Line drawing of principal features in a radiograph. The shocks are indicated by heavy solid lines and the small double arrows indicate the direction of propagation.

contact with the 9404. The results for the aluminum are listed at the bottom of Table 3. The pressure in the aluminum is only 83% of that found when the beryllium was not present. Recall, however, that oblique shocks in aluminum are slightly curved and in the absence of the beryllium a similar situation would be observed if the pressure of the shock 1 cm from the interface were compared to the pressure at the interface. This decay in shock pressure arises simply from the fact that the shocks as well as the detonation waves in these systems are followed by rarefactions. Thus the observed decrease across the beryllium is entirely reasonable. The aluminum interface was also inspected to provide an indpendent determination of the shock pressure in the aluminum. This again correlates well with the pressure determined from the reference Hugoniot and confirms the aluminum has been compressed by a single shock. Since pressure is continuous across interfaces the pressure in the beryllium near the aluminum must have achieved at least 16.6 GPa too. In principal it should be possible to treat the beryllium-9404 interface as a flow of explosive products around a gradual bend and confirm this pressure from the expansion of the explosive products. The absence of a sharp bend complicates the determination of the interface angle in the region immediately behind the detonation front but a reasonable estimate is 7.1 ± .5°. As the radius of curvature for a

609

gradual bend approaches zero, the solution for the stream flow approaches that for stream flow around a sharp corner. Since the radius of curvature for the bend in this interface appears smaller than other characteristic lengths in the experiment, the expansion around a sharp corner depicted in Fig. 4 can be used to estimate the pressure in the explosive products. This pressure, which is also the pressure in the beryllium, is 16 ± 1 GPa. No other shocks are discernible in the berylium. Thus behind the shock indicated in Fig. 6 the beryllium has been compressed by some means other than a strong shock. Because of the dynamic nature of this system this latter compression must, like shock compression, be adiabatic. If the process involves several shocks too weak to be discerned individually, the compression would begin to approximate an isentropic process. As such signals become multidudinous and diminish in strength the process tends, in fact, to become strictly isentropic

A second experiment was performed using a 3-mm-slab of beryllium and an antimony sample. A thinner slab of beryllium was chosen to improve assurance that the flow pattern near the interfaces is time independent. The antimony was chosen because it exhibits a sluggish phase transition at 8-9 GPa, just below the shock pressure that appeared to be present in the beryllium. It was hoped that anything too unsuual in the beryllium compression might be manifested as a double shock wave structure in the antimony. These results are also listed in Table 3. The pressure in the antimony was also slightly less than that in the absence of the beryllium. The antimony, in fact, behaved quite normally and the result for its shock compression was used in its reference Hugoniot. It appears from these two experiments that although the compression in the beryllium is not described by a single strong shock, the flow solution becomes pinned near the interface and the material on the other side contains its normal oblique shock.

The case of baratol and aluminum was also briefly investigated. The radiograph of the experiment is presented in Fig. 7. The aluminum contained 0.013-mm-thick tantalum foils to provide radiographic contrast. These foils were initially parallel and all but the top reference foil were spaced 6.36 mm apart. The baratol block was constructed of 25.4 mm slabs. In the radiograph the detonation wave almost coincides with the interface between the last two slabs. The detonation front does not curl back at the
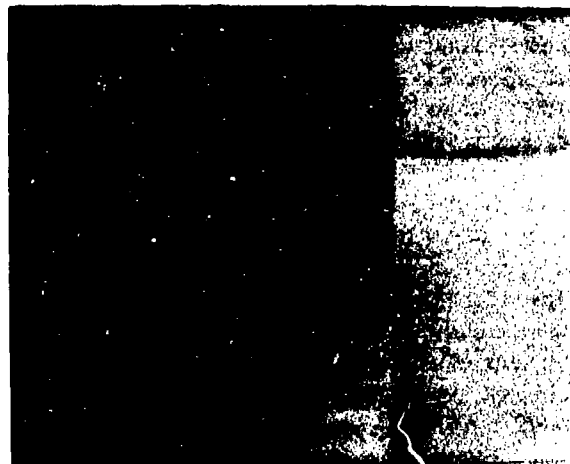
Fig. 7. Radiograph of baratol driving 2024 aluminum. The baratol, on the right, was assembled from slabs. The aluminum contains tantalum foils which initially were equally spaced and parallel to the top reference foiL

aluminum interface as it does with materials whose bulk sound speeds are slower than the detonation velocity. This effect is more easily seen in the work of Eden and Wright. The point of interest here is that no shock is discernible in the aluminum. The foils, however, are displaced and have moved closer together indicating compression. The aluminum-baratol interface has also been displaced. It does not bend sharply at the detonation wave, however, in accordance with the compression not coming from a single shock. A recent investiagtion with antimony on the other side of a thin aluminum slab indicates that the proper shock appears in the antimony. Thus, except for partial shock compression seen in 9404-driven beryllium, the two systems appear similar. The aluminum in Fig. 7 has also been compressed by a process which is approximately or strictly isentropic.

REFERENCES

1. *Proceedings-Fourth Symposium (International) on Detonation* (U. S. Gov. Printing Office, Wash., D.C., 1965).

2. *Proceedings-Fifth Symposium (International) on Detonation* (U. S. Gov. Printing Office, Wash., D. C., 1970).

3. H. M. Sternberg and D. Piacesi, Phys. Fluids 9, 1307-1315 (1966).

4. R. J. Seeger in *Handbook of Physics*, E. U. Condon and H. Odishaw, Eds. (McGraw-Hill, New York, 1967), pp. 314-339.

5. I. C. Skidmore and S. Hart in Ref. 1, pp. 47-51.

6. I. C. Skidmore, Appl. Mat. Res. 4, 131-147 (1965).

7. A. S. Balchan, J. Appl. Phys. 34, 241-245 (1962).

8. S. Katz, D. G. Doran, and D. R. Curran, J. Appl. Phys. 30, 568-576 (1959).

9. B. R. Breed and D. Venable, J. Appl. Phys. 39, 3222-3224 (1968).

10. D. Venable and T. J. Boyd Jr. in Ref. 1, pp. 639-647.

11. B. Hayes, J. Appl. Phys. 38, 507-511 (1967).

12. W. C. Rivard, D. Venable, W. W. Fickett, and W. C. Davis in Ref. 2, pp. 3-11.

13. Shock Wave Physics Group, Los Alamos Scientific Laboratory (work of W. J. Carter, W. E. Deal, J. N. Fritz, S. P. Marsh, R. G. McQueen, M. H. Rice, J. W. Taylor, J. M. Walsh, and F. L. Yarger), personal communication (1972).

14. W. C. Davis and D. Venable in Ref. 2, pp. 13-21.

15. J. W. Kury, H. C. Hornig, E. L. Lee, J. L. McDonnel, D. L. Ornellas, M. Finger, F. M. Strange, and M. L. Wilkins in Ref. 1, pp 3-13.

16. J. K. Rigdon and I. B. Akst in Ref. 2, pp. 59-66.

17. J. B. Ramsay and A. Popolato in Ref. 1, pp. 233-238.

18. G. Eden and P. Wright in Ref. 1, pp. 573-583.

LASER INITIATION OF INSENSITIVE HIGH EXPLOSIVES

L. C. Yang and Vincent J. Menichelli
Jet Propulsion Laboratory
California Institute of Technology
Pasadena, California, USA 91103

Experimental work in three types of laser initiation of insensitive explosives are reviewed. They are: 1) instantaneous detonation caused by a shock wave generated in a thin metallic film from a Q-switched laser pulse, 2) instantaneous detonation by direct interaction between a Q-switched laser pulse and the explosive under study and 3) deflagration to detonation phenomenon in PETN and RDX by free-running laser pulses. The mechanisms and the characteristics of the initiations are discussed.

INTRODUCTION

In this paper, we intend to review the laser initiation of insensitive high explosives. The initiation of pyrotechnics and primary high explosives are well understood and reported elsewhere (1,2). To a large extent, laser initiation mechanisms are similar to conventional initiation techniques. They are heat and shock in origin. However, due to a number of unique features associated with light energy, laser has been demonstrated to be more potent than the conventional methods of initiation. Experimental results have provided information for a general understanding of the initiation phenomena of insensitive high explosive. For practical applications, it is important to understand this phenomenon. Recently, great progress has been made in low-loss fiber optics (3) and in the miniaturization of compact laser systems (4,5). The concept of a laser-fiber optic system to initiate secondary high explosives is now ready for engineering development. A number of military applications are apparent. For the convenience of discussion, the laser characteristics and the laser interaction with materials will be briefly summarized.

Three areas of laser initiation of explosives will be discussed. First, the initiation of several secondary high explosives from a shock generated by a nanosecond-duration Q-switched laser pulse interacting with a thin metallic film. Second, instantaneous detonation by direct interaction of Q-switched laser pulses with the explosives and finally, reliable deflagration to detonation (DDT) in PETN and RDX, initiated by millisecond-duration free-running mode laser pulses. The advantages of using a laser to initiate insensitive explosives and study the DDT phenomena will be discussed.

LASER CHARACTERISTICS AND TERMINOLOGY

Rapid progress has been experienced in the laser field. A number of extremely high powered laser systems of different wavelengths and operational modes have been developed. For explosive initiation studies, less than 10 J of pulsed laser energy is needed. This energy can be easily provided by a xenon flash lamp-pumped ruby crystal laser or a neodymium-glass laser operating at a wavelength of 6943 Å and 1.06 μm respectively. The laser beam (rod) diameter is of the order of 6-15 mm.

The laser energy fluence (J/cm^2) is in general non-homogeneous across the beam and dependent on the

laser optics design. Approximate Gaussian distribution is usually observed (1). Near the lasing threshold, local hot spot emissions are quite common. In order to achieve higher fluences, focusing lenses are used. Lasers have small intrinsic beam divergence, defined as the full angular deviation from the beam axis at the $1/e$ of maximum fluence (6). At the focal plane, the fluence has an approximately Gaussian distribution. Therefore if one defines the beam spot based on the diameter of the $1/e$ fluence contour, the spot diameter is equal to the beam divergence multiplied by the focal length. For a typical 3 to 5 mrad beam divergence, focal lengths larger than 30 cm are needed to allow a spot size compatible to the critical initiation diameters of insensitive high explosives. The average energy fluence can be approximately estimated by dividing the laser energy by the area of spot cross section.

The laser pulse duration is largely dependent on the mode of operation of the laser. For Q-switched operations, the laser power (W) has an approximately Gaussian time profile. The pulse duration defined by the full time width at half intensities (FWHM) can vary from a few nanoseconds up to 100 ns controlled by the switching time and laser cavity length. By adding a mode-locking mechanism to the Q-switch operation picosecond-duration output can be achieved. A rough average laser intensity (W/cm^2) can be estimated by dividing the energy fluence by the pulse duration.

The free-running mode (normal mode) laser energy fluence characteristic is similar to that in the Q-switched mode operation. The output power (of the order of kW) as a function of time shows the emission to be a series of microsecond-long relaxation spikes. The peak laser power is modulated by the flash lamp power. Therefore, the total pulse duration is in the order of the lamp discharge duration, tens of microseconds to a few milliseconds. An approximate laser intensity can be estimated by dividing the energy fluence by the half width of the total pulse duration.

The output energy fluence distribution, beam divergence and pulse duration may vary considerably for a given laser system depending on the output energy. Therefore the laser energy is better controlled by external attenuation of a constant output rather than by varying the high voltage of the flash lamp discharge circuitry. Because of the foregoing uncertainties, one has to be careful when comparing reported laser initiation data.

LASER INTERACTION WITH MATERIALS

Metals absorb light in skin depths on the order of 100 Å or less. Even for the most reflective metals, the small finite absorption under high laser fluence will cause melting and vaporization. The free-running laser has a long duration allowing for effective heat transfer and vaporization. Therefore, it is capable of in-depth heating and damage of metallic surfaces. A Q-switched laser pulse can heat the surface more nearly adiabatically in a thickness on the order of 10^4 Å or less. The high energy density will result in the generation of a highly ionized plasma. High temperatures and shock speeds of the order of 10^5 °K and 10 cm/μs can be easily generated with moderate fluences (7). The damage thresholds are about 0.1 J/cm^2 (4 MW/cm^2) for 25 ns Q-switched laser pulse and 10 J/cm^2 (10 KW/cm^2) for 1 ms free-running mode laser pulse.

A focused Q-switched laser pulse can initiate gas breakdown at room temperature to form a high temperature plasma. The high laser intensity, corresponding to a high electrical field, is capable of accelerating multiphoton absorption produced electrons in the gas causing a cascade breakdown and subsequently high temperatures. This process requires a higher onset laser intensity in the order of 50 GW/cm^2 for air at atmospheric pressure (8). The low gas density allows the laser absorption to take place in a relatively large volume as compared to the case of metal surfaces. Therefore, the resultant shock pressure is lower than that of the latter case for a given energy fluence.

The mechanism of laser induced damage in transparent solid materials appears to be very complicated. It depends upon the physical properties of the material, its purity, and microscopic imperfections. The damage threshold of the surface is much lower than that of the bulk material. This indicates that the imperfections and impurities are more severe on the surface. This threshold is about 100 GW/cm^2 for fused quartz and somewhat lower for optical glasses (9). For the plastic materials such as lucite, due to the low melting temperature and imperfections, the thresholds are about 42 J/cm^2 (1.7 GW/cm^2) for 25 ns Q-switched pulse and 56 J/cm^2 (56 KW/cm^2) for 1 ms free-running mode pulse from a neodymium laser. For powdery plastic materials such as explosives it could be even lower. As in the case of gases, the breakdown is volumetric; therefore the resultant

shocks are lower than that generated on metallic surfaces for a given laser fluence.

Transmission of low power light in transparent materials such as glass, lucite and PETN at ruby and neodymium laser wavelengths is about the same as in the visible regime without significant absorption. However the laser damage thresholds at high power showed a wavelength dependence. For example, the threshold energy fluences (both Q-switched and free-running modes) for lucite by a ruby laser are about a factor of two higher than those by a neodymium laser. Theoretically, this may be due to that the rate of energy acquired from the laser by the electrons is proportional to the square of the laser wavelength (7,8) in a laser-induced electron cascade breakdown. If the material has selective absorptions at the laser wavelengths, the thresholds will be even lower.

In general, the Q-switched laser has higher power and can initiate damages and generate shocks in most materials. The normal mode laser can cause heating of metals and decomposition of plastic materials. This phenomenon results in much lower temperatures and pressures.

SHOCKS GENERATED IN THIN METAL FILMS

In order to utilize a laser generated shock from a metallic surface, it is natural to coat a thin metallic film on the inner surface of the glass window of the explosive container (10). This film is confined between the window and the explosive. The window serves as a part of the confinement of the explosive and the laser pulse entrance port. Under irradiation from a Q-switched laser the film generates a shock wave similar to an exploding foil. Preliminary studies by Anderholm and Skeen and O'Keefe (11,12) have shown that shock pressures on the order of 20 kbars can be generated in confined aluminum films.

Yang (13) has studied the phenomenon in detail with a uniform Q-switched ruby laser beam. The laser pulse was 15 ns in duration, with a maximum energy of 5 J in a circular area 6.35 mm in diameter. The stress waves were studied by using the piezoelectric response of X-cut quartz crystal disks of the same diameter. Thin films made from twenty-six different materials were studied. The thickness of the films ranged from 40 Å up to 1 μm confined between two

glass disks. The main features are summarized as follows:

1. The rise time of the stress pulse is on the order of the total laser pulse duration, 25 ns. The peak stress occurs at the end of the Q-switched laser pulse, then decreases with a fall time on the order of 25 ns to a prolonged lower amplitude stress. For practical purposes, the stress pulse duration can be considered to be twice that of the laser pulse (FWHM).

2. The peak stress increases linearly with the energy fluence to about 22 kbars at 14 J/cm^2.

3. The peak stress is insensitive to the film material.

4. The peak stress is insensitive to the film thickness except for high thermally conductive metals, and in the low fluence regime.

5. The relevant shock generation material thickness in the film is probably on the order of several hundred Angstroms.

6. For the fluence range used in the study, the major part of the laser energy was reflected, transmitted or used for ionization and ablation, little of the energy is converted to the stress energy (proportional to the square of the stress, about 10% at 12 J/cm^2). The temperature of the plasma can be as high as 10^5 °K.

Experimental measurements using larger energy fluences are difficult to make due to the damage threshold of the glass window and the nonlinearity of quartz response under high stress. Focusing of the laser pulse produces a beam spot in the order of mm's in diameter which is difficult to measure because the accuracy of the x-cut crystal requires a minimum crystal diameter to thickness ratio (∼3). Miniature crystals satisfy this condition but will not have sufficient writing time for the measurement. Less accurate measurements indicate that the linear dependence of the peak stress on the energy fluence is probably valid up to 80 kbars (at ∼56 J/cm^2). For fluences beyond this limit, it is felt that the stress should be an increasing function of the fluence, but the exact functional dependence is unknown.

The effect of replacing one confining glass surface by a nonporous plastic surface is easily estimated

from the acoustical impedance of the material. These have been verified by experiments. The peak stress will decrease about 15% with more stress energy being generated in the plastic than in the glass. If porous plastic materials such as the explosives are used as one confining surface, the situation is more complicated. The low impedance of the air will reduce the peak stress. If a large area contact point exists between the explosive grains and the film, the local stress generated in the former may be independent of the presence of air. This condition depends upon the porosity of the explosive and the expansion velocity of the plasma (which is low at low energy fluence near the initiation threshold for a number of explosives).

The laser pulse duration effect on stress generation has not been experimentally studied in detail. At a first glance, the thermal penetration depth is approximately proportional to the square root of the pulse duration. Therefore, for the same amount of Q-switched energy, the shorter the pulse, the larger the stress produced due to the larger energy density in the heated part of the surface. However, since the independence of the stress from the film material and thickness, at high energy fluence, indicated that the heat transfer is not a dominant factor. Other processes, such as the heating and the growth of the confined dense plasma, may have a weak dependence on the pulse duration. Peercy, et al. (14,15) have studied stresses generated by picosecond-duration laser pulses. Their results showed that these short pulses were more effective in stress generation. However, the increase in the peak stress was not large enough to fit the thermal penetration depth estimation. Preliminary experiments in JPL have shown that 15 ns and 25 ns duration laser pulses of the same energy produced about the same peak stresses. The stress generation does not depend upon the laser wavelength. The light absorption characteristics show some differences between 6943 Å and 1.06 μm of wavelengths for different metals. However, the energy required for initial breakdown is very small as compared to that required in the subsequent heating of the plasma. The process in the latter is not very wavelength dependent. Pulsed CO_2 lasers with a wavelength of 10.6 μm can be used to efficiently generate shock waves as well.

THIN FILM SHOCK INITIATION

Yang and Menichelli (16,17) have applied the thin metal film Q-switched laser interaction generated

shock to initiate a number of insensitive high explosives such as PETN, RDX, tetryl and HNS. A Q-switched ruby laser with a duration of 25 ns and a maximum energy of 4 J in a 1.43 cm diameter beam was used. The focused beam spot on a 1000 Å-thick aluminum film deposited on the explosive unit window near the focal point of a 30 cm focal length convergent lens was estimated to have a diameter of 1.5 mm. The explosive columns were 1 to 4 mm in diameter over 20 mm in length. The explosive fixtures had a lucite rod or glass wall view port optics in contact with the explosive columns for smear camera recording of the detonation.

The initiation of coarse particle size ($>100\mu$) explosives appeared to be difficult. High density PETN (1.64 g/cm^3) showed a strong transition phenomenon from about 2 mm/μs to about 5.6 mm/μs in a run distance of 25.4 mm. No detonations were observed for RDX at the maximum laser energy in an explosive column length on the order of 25 mm. For fine milled PETN and RDX (particle size less than 40μ), instantaneous detonations were observed at various densities. No transition from low velocity detonation to high velocity detonation was observed (i.e., zero run distance). The steady-state detonations were either reached at the explosive-thin film interface or transited from a super detonation velocity (several times higher than steady state detonation velocity) which occurred in the first few millimeters of the charge column. Within the experimental resolution, there was a possible time delay in the order of 0.5 μs or less for the detonation originated at the film end of the explosive. This time may be related to the reaction rate of the explosive because it is more prominent at lower laser energies.

Approximate instantaneous detonation thresholds were observed for 1.58 g/cm^3 PETN, 1.18 g/cm^3 RDX and 1.52 g/cm^3 RDX to be 0.63 J, 0.8 J and 2.26 J or 35.6 J/cm^2, 45.3 J/cm^2 and 127.9 J/cm^2 respectively. The 35.6 J/cm^2 of fluence generates about 50 kbars of pressure which is close to the shock sensitivity of PETN at this density and the short (or nil) run distance, as determined in long-duration explosive driven shock initiation experiments (18). It is well known that the threshold shock initiation sensitivity for a given explosive increases with the shock duration. However, for short run distance (<1 mm) initiations the pulse duration has no effect on the required initiation shock strength (19). The threshold shock sensitivity which has a long run-distance and

615

has been defined in small-scale gap tests, is difficult to be observed in the laser shock initiation. The short pulse duration of the laser generated shock presumably decreases this sensitivity to a value very close to the shock strength required for sub-millimeter run distance detonations initiated by long duration shocks (19). So that in laser initiation experiments one normally observes either instantaneous detonation or burning without detonation in an explosive column less than 2.0 cm in length.

The initiation of 1.08 g/cm^3 tetryl also did not show any transition from low velocity detonation to the steady state detonation. Up to 1.5 μs after the laser pulse no activity was observed by the smear camera. Then it appeared to react at a speed 3 to 4 times higher than the steady state detonation speed. The latter state was reached in less than 0.2 μs in a distance of about 5 mm from the initiation end. It is not known whether this was a true superdetonation or because the initiation energy of 3.2 J was below its instantaneous detonation threshold so that a reactive induction period is necessary. This behavior does not fit the run-distance concept by definition. The failure of high density RDX (1.64 g/cm^3), tetryl and low density HNS and diapam to detonate can be understood. The shock initiation strengths for short run distance initiation are well above 100 kbars for these explosives at these densities.

Recently, Wright (20) has studied the initiation of 0.9 g/cm^3 PETN by Q-switched neodymium laser irradiated thin aluminum films. The explosive column was 3.2 mm in diameter and 5.9 mm in length. The beam spot size at the film ranged 1.3 to 2.3 mm in diameter. The detonation propagation time was monitored by a piezoelectric shock arriving detection pin. The observed initiation threshold energy fluence using a 500 Å film ranged from 1 to 3 J/cm^3 depending upon the spot size and using a 2000 Å-thick film was about 11 J/cm^2. The latter corresponds to a shock strength of 17 kbars (13) which is close to the shock strength required to achieve short run distance detonation initiation of PETN near this density (21). The former correspond to 2 to 4 kbars (13) which are close to the threshold shock initiation sensitivity at this density by long pulse shocks. The average detonation speed measured on the order of 4200 m/sec is close to the ideal detonation velocity at this density and with this diameter. It is suspected that this low shock instantaneous detonation is due to the temperature effect. The 500 Å-thick film produces a plasma

which can heat up and ablate the PETN in contact with it. The fast release of the internal energy of the explosive will be effective in accelerating the detonation process. With a thick film, that part of the film behind the plasma and in contact with the explosive is at a lower temperature and serves as a thermal insulator to shield the much hotter plasma from the explosive. Therefore, the origin of the initiation is due to shock rather than to heat in this case. This point of view has been taken by Leopold in the study of EBW initiation of low density PETN (22).

DIRECT INITIATION BY Q-SWITCHED LASER

As discussed previously, the mechanism of the initiation is due to the laser initiated breakdown in the explosive and subsequent heating of the plasma so generated. The phenomenon depends upon the imperfection of the explosive crystals and impurities such as small foreign particles. Therefore, it usually has poor reproducibility. The onset energy fluence for this process is higher than that of the breakdown of a metallic surface. In plastic materials, due to the interaction involving a larger volume of materials, the temperature, energy density of the plasma and the shock so generated are lower than in the cases for metallic surfaces for a given energy fluence. The plasma temperature is at least an order of magnitude lower than in the latter case. Preliminary measurement of stress generated in laser absorptive colored glass irradiated by a Q-switched laser is also about one order of magnitude lower than in the case of thin metallic films for a given energy fluence. A lower stress is expected from the breakdown of plastics.

The significant difference here is that the laser energy is being absorbed in the explosives. The high chemical energy density of the explosive in this case is equal or greater than that provided by laser absorption or stress. Currently the best-fit empirical equation of state for completely reacted secondary high explosive products is that proposed by Jones, Wilkins and Lee (23,24). According to this equation, high pressures exceeding 100 kbars can be developed for completely reacted explosive products under ideal adiabatic and zero volume expansion conditions. In reality, explosives, especially the porous ones have very low acoustical impedance and show large compressibility under high pressure so that the maximum pressure that can be developed in this way is presumably much less than the ideal values.

616

It appears to be reasonable that the reaction rate in the Q-switched laser induced breakdown regime of the explosive can be extremely fast. If one uses the well known exponential dependence of the time delay on the activation energy in an isothermal reaction of the explosive, at a temperature rise on the order of 400 °C, the time delay will be in the nano-seconds regime. Therefore it appears feasible to have a fast release of the chemical energy during the laser pulse irradiation. This view is inconsistent with the critical thermal energy theory (25,26) and the adiabatic compression of porous explosives (18). They predicted that the energy dissipated into heat by the shock are small and the temperature rise is on the order of several hundred degrees. The laser heating can locally heat the explosives beyond that in the detonation front (~ 3000 °K).

While the quantitative understanding of the initiation mechanism in terms of shock strength is not available at this time, there is more independent experimental data in this area than that in the thin film shock initiation. Brish, et al. (27,28) have studied the initiation of low density (1.0 g/cm^3) PETN confined in transparent plastic containers by using an 0.1 μs duration, 0.5 J maximum energy Q-switched neodymium laser. Instantaneous detonation was cited based on the reaction time measured by a photocell technique. Qualitative results on the time delay as a function of energy fluence, threshold initiation energy fluence as a function of explosive density and laser-explosive interaction spot diameter were obtained.

Barbarisi and Kessler (29,30,31) have studied the initiation of thin PETN samples under 9.3×10^7 N/m^2 (13.5 kpsi) of pressure by using a Q-switched ruby laser of 50 ns duration. The laser spot area at the explosive was roughly 1 mm^2. Initiation energy thresholds on the order of 0.02 to 0.03 J were observed. The average detonation velocity observed by a photodiode at a maximum sample thickness of 2.7 mm was on the order of 1250 m/s. It was not known whether this deflagration type transition was due to the small laser spot size or large particle size of the explosive used in their experiment.

Yang and Menichelli (16,17) have studied the initiation of a number of secondary high explosives directly by Q-switched ruby laser. The experimental conditions were identical to those used in their thin film shock initiation experiments. The critical effects

of the explosive particle size were the same as before. Instantaneous detonation was observed in fine milled PETN and RDX at several densities. The detonation features as observed by a smear camera were about the same. The threshold laser energies for high density PETN (1.58 g/cm^3) were about the same in these two cases, i.e., 0.63 J (36.6 J/cm^2). The thin film technique appeared to be slightly more effective in initiating RDX. At 0.8 J of laser energy RDX (1.18 g/cm^3) can be detonated without the film, but there was a time delay of 2 μsec before the appearance of detonation at the window-explosive interface. 1.52 g/cm^3 RDX was successfully instantaneously detonated at higher laser energies. Tetryl detonation could not be initiated at the highest energy of 3.2 J delivered to the explosive without the film. These results indicate that shock strengths up to about 80 kbars (corresponding to the instantaneous detonation of 1.52 g/cm^3 RDX) can be developed in the insensitive high explosives by Q-switched laser energy.

Recently Q-switched laser initiation of PETN was studied by Mavis and Wright (33). A Q-switched neodymium laser was used. The focused (30 cm focal length) beam spot size at the explosive was estimated to be 1.5 mm in diameter. The charge column dimensions were 3.32 mm in diameter and 3 to 5 mm in length. The initiation threshold energy fluences for PETN density of 1.0, 1.2, 1.4 and 1.6 g/cm^3 were observed to be 5, 7, 13 and 15 J/cm^2 respectively. The apparent lower thresholds when compared to Yang and Menichelli's ruby laser results could have been due to a wavelength effect as discussed previously. The detonations were judged to be instantaneous, because the average propagation velocities measured by the shock pin method (about 4,000 m/s for 1.0 g/cm^3 and 7000 m/s for 1.6 g/cm^3) were close to the steady detonation velocities at these densities and charge diameter.

FREE-RUNNING MODE INITIATED DDT PHENOMENA

Low energy (<10 J) free-running mode laser pulses cannot be used to produce high strength shock waves. Therefore, initiation is definitely due to heat and detonation can be achieved only through the DDT process. In the DDT phenomenon, the important parameter, porosity, is well recognized (33,34). Low porosity reduces free volume in the explosive, allowing the rapid pressure build-up. In this sense laser

offers an additional advantage over conventional pyrotechnic igniter materials. The latter have a high theoretical energy density (Kcal/gm); however, the high solid end products and difficulties in achieving a high TMD reduce the pressures which are limited to several kilobars. When they are used to initiate DDT phenomenon, the volume occupied by the reacted materials at low pressure becomes a load to the deflagration of high explosives. Therefore, the DDT process has been decelerated. The use of a laser pulse can achieve the desired heat initiation of high explosives, yet it will not interfere with the conditions for rapid pressure build-up.

After one has achieved the confinement effectiveness, the next important parameter is the volumetric initiation. The common hotwire technique can provide a local high temperature but at the sacrifice of the heating depth. The small ignition depth in high explosives cannot generate enough gas to compensate for the volume expansion due to the compression of unburned high explosives under high gas pressure. The percentage heat loss rate is also larger for a smaller reaction depth. Therefore, the reaction may be rapidly quenched and terminated. Successful volumetric DDT initiation has been demonstrated previously by using electrical discharges in PETN (35) and RDX (36). Laser energy can penetrate the high explosives to heat them in depth much easier and reproducible than this technique. A more favorable initiation condition can thus be achieved. The thermal time constant of a cubic high explosive with volume 1 mm^3 is on the order of 1 sec, for common experimental conditions. If a free-running laser pulse of 1 millisecond duration is used for the heating, the process is very nearly adiabatic.

As it has been previously discussed, insensitive high explosives are capable of producing extremely high pressures under efficient reaction (but not detonated) and ideal confinement. In a laser initiated DDT detonator, the explosive container and the optical window can be designed to withstand very high pressures without significant yield. The weakest confining element is the explosive itself. For practical purposes, the loading pressure of the explosives cannot exceed $6.9 \times 10^8 \text{ N/m}^2$ (100 Kpsi). Therefore, when the pressure build-up reaches this pressure, significant collapse of the explosive will occur. The burning rate of dense high explosive, e.g., HMX at moderate high pressures up to $3.5 \times 10^8 \text{ N/m}^2$ (50 Kpsi) is quite slow (on the order of 10 cm/sec) (37).

The deflagration speed will not reach mm/μs regime until the pressure is approaching the threshold shock sensitivity of the explosive corresponding to the explosive density. Therefore rapid build-up of the pressure to this threshold sensitivity in a finite part of the explosive and follow-up transition to full detonation in the rest part of the explosive is feasible in the laser initiated detonator.

A limited amount of work by Brish, et al. (27,28) and Barbarisi and Kessler (29-31) on free-running laser initiation of PETN demonstrated the initiation but they did not show evidence of achieving detonation.

The first demonstration of reliable DDT (PETN and RDX) from a free running laser were performed at Space Ordnance System Inc. (38). PETN columns about 2.5 mm in diameter and 25 mm in length were loaded under $5.5 \times 10^8 \text{ N/m}^2$ (80 Kpsi) inside a steel body and against a window (glass to metal seal). The glass to metal interface was hermetically sealed and taper shaped to improve pressure stand off. The two ends of the window were approximately 2.5 mm and 2.0 mm in diameter and the window thickness was about 2.1 mm (2). The window was tested to withstand $6.9 \times 10^8 \text{ N/m}^2$ (100 kpsi) hydraulic pressure (the maximum capability of the testing apparatus); therefore much higher transient pressure resistance can be expected. Upon receiving the free-running laser pulse (1.0 ms in duration) the detonator was initiated. Based on the observed deformation of the detonator, a weak detonation started at about the 6 mm position and developed to steady state detonation at about the 20 mm position. With 2 J of focused (2.54 cm focal length) neodymium laser energy through about a 10 m length of conventional high-loss glass fiber optic bundle, DDT can be achieved. This corresponds to an energy sensitivity of the order of 0.05 J or less based upon the known attenuation of the fiber bundle. This energy is close to the recently established shock initiation thermal energy density of 0.06 J/mm^3 for PETN (26,27) if one uses a reasonable assumption that about 1 mm^3 of PETN took part in the laser heating.

RDX detonators constructed in the same way showed the distance to steady state detonation to be longer than 25 mm. A two-column air gap flyer-plate design similar to that in Ref. 36 was used with the exception of replacing the arcing discharge mechanism by the window. Successful full detonation was

achieved for total charge column length on the order of 25 mm. The reaction time for this type detonator using a focused (2.54 cm focal length) ruby or neodymium laser pulse (1.0 ms duration) and through about 0.6 m long fiber optic bundle was measured using photodiodes. The reaction time measured was 560 μs for the 4 J neodymium laser and 240 μs for the 5 J ruby laser. The induction time (i.e., heating time) was not measured but is suspected to be the major part of the total reaction time.

Later, the use of small amount of zirconium powder doping to sensitize the detonators toward laser initiation was qualitatively demonstrated (39).

The mechanism appears reliable both theoretically and experimentally. It is attractive for practical applications because a compact free-running mode laser package is much simpler to design and construct than a compact Q-switched laser package. In applications where detonator response times are not critical, such as in the missile systems, this mechanism can be used reliably.

CLOSING REMARKS

It is apparent that there are many areas in the laser initiation of insensitive high explosives which need to be investigated further. However, based upon the limited available results, the mechanism has exhibited a number of unique features which cannot be achieved by the conventional initiation mechanisms. High shock strengths are produced which can detonate insensitive secondary high explosives loaded at high densities. Initiation of PETN and RDX by Q-switched laser is instantaneous, which will allow a higher degree of simultaneity to be achieved. The initiation thresholds are low which makes it suitable for practical applications. The transmission of laser energy by using fiber optics can be achieved with ease without the inconvenience of electrical circuit parameter interferences associated, for example, with EBW systems. Simultaneous initiation of a large number of detonators can be achieved with a laser pulse energy of the order of 10 J.

Laser initiation can be used as a powerful tool to study the explosive initiation process. Initiation by picosecond-duration shocks generated by mode locking laser techniques appear to be interesting for this type of study, because the stress width induced in the

explosive is on the order of several hundred Angstroms. Free-running laser initiation can be used very effectively in the DDT phenomenon studies. It is worthwhile to mention that currently the laser energy and power available are about 2 to 3 orders of magnitude higher than those mentioned in this paper. Therefore, if the laser is used as a tool for initiation studies its capability is far reaching.

ACKNOWLEDGMENTS

REFERENCES

1. V. J. Menichelli and L. C. Yang, "Sensitivity of Explosives to Laser Energy," JPL TR 32-1474 (April, 1970).

2. L. C. Yang and V. J. Menichelli, "A High Efficiency, Small, Solid State Laser for Pyrotechnic Ignition," JPL Quarterly Technical Review, Vol. 2, No. 4, 29 (1973).

3. "Optical Fiber Technology," Edited by Detlef Gloge, IEEE Press, New York (1976).

4. L. C. Yang, "A Compact Glass Pulser," Laser Focus, pp. 37-39 (July, 1973).

5. L. C. Yang, "Efficiency Q-Switch Design," Laser Focus, pp. 66-76 (October, 1975).

6. H. G. Heard, "Laser Parameters Measurements Handbook," John Wiley & Sons Inc., New York (1968).

7. C. Demichelis, "Laser Interaction with Solids," IEEE J. of Quan. Elec. QE-6, 630 (1970). Also, J. F. Ready, "Effects of High Power Laser Radiation," Academic Press, New York (1971).

8. Yu. P. Raizer, "Breakdown and Heating of Gases Under the Influence of a Laser Beam," Soviet Phys. USPEKHI 8, 650 (1966).

9. D. W. Fradin, "Laser Induced Damage in Solids," Laser Focus, pp. 39-45 (February, 1974).

10. L. C. Yang and V. J. Menichelli, "Optically Detonated Explosive Devices," U.S. Patent No. 3,812,783 (May 28, 1974).

11. N. C. Anderholm, "Laser Generated Stress Waves," Appl. Phys. Lett. 16, 113 (1970).

12. J. D. O'Keefe and C. H. Skeen, "Laser Generated Stress and Impulse Augmentation," Appl. Phys. Lett., 21, 464 (1972).

13. L. C. Yang, "Stress Waves Generated in Thin Metallic Films by a Q-Switched Ruby Laser," J. Appl. Phys., 45, 2601 (1974).

14. P. S. Peercy, E. D. Jones, J. C. Bushnell, and G. W. Gobeli, "Ultra-fast Rise Time Laser Induced Stress Waves," Appl. Phys. Lett., 16, 120 (1970).

15. E. D. Jones, "Ultrafast Laser Induced Stress Waves in Solids," Appl. Phys. Letts., 18, 33 (1971).

16. L. C. Yang and V. J. Menichelli, "Detonation of Insensitive High Explosives by a Q-Switched Ruby Laser," Appl. Phys. Lett. 19, 473 (1971).

17. W. J. Menichelli and L. C. Yang, "Initiation of Insensitive Explosives by Laser Energy," JPL TR 32-1557 (June, 1972). The same paper has been included in the proceedings of the 7th Symposium on Explosives and Pyrotechnics, Franklin Institute, Philadelphia, 1971.

18. D. Stirpe, J. O. Johnson, and J. Wackerle, "Shock Initiation of XTX-8003 and Pressed PETN," J. Appl. Phys., 41, 3884 (1970).

19. B. E. Trott and R. G. Jung, "Effect of Pulse Duration on the Impact Sensitivity of Solid Explosive," 5th Symposium (International) on Detonation, 191 (1970).

20. C. L. Wright, Sandia Laboratories, Livermore, California. Private communication.

21. J. B. Ramsay and A. Popolato, "Analysis of Shock Wave and Initiation Data for Solid Explosives," 4th Symposium (International) on Detonation, 233 (1965).

22. H. S. Leopold, "Effect of Bridgewire Parameters on Explosive Initiation," Exploding Wires, Vol. 3, Edited by W. G. Chace and H. K. Moore, pp. 125-152, Plenum Press, New York (1964).

23. E. L. Lee, H. C. Horning and J. W. Kury, "Adiabatic Expansion of High Explosive Detonation Products," Lawrence Radiation Lab., Report TID-4500, UC-4 (1968).

24. E. L. Lee, M. Finger, and W. Collins, "JWL Equation of State Coefficient for High Explosives," Lawrence Livermore Lab., Report UCID-16189 (1973).

25. R. J. Bauer, "An Analysis of Small Scale Gap Test Sensitivity Data Using Porosity Theory and Nonreactive Shock Hugoniots," NSWC White Oak Lab., TR 75-67 (1975).

26. D. J. Pastine, R. R. Bernecker and R. J. Bauer, "A Theoretical Relation Between Initiating Shock Pressure and Porosity in Secondary Explosives," Proc. 4th International Conference on High Pressure, Kyoto, 1974, pp. 460-465.

27. A. A. Brish, I. A. Galeeve, B. N. Zaitsev, E. A. Sbitnev, and L. V. Tatarinstev, "Laser-Excited Detonation of Condensed Explosives," Fizika Goreniya i Vzryva, Vol. 2, No. 3, pp. 132-133 (1966).

28. Same authors and journal, "Mechanism of Initiation of Condensed Explosives by Laser Radiation," Vol. 5, No. 4, pp. 457-480 (1969).

29. M. J. Barbarisi and E. G. Kessler, "Initiation of Secondary Explosives by Means of Laser Radiation," Picatinny Arsenal, TR 3861 (May 1969).

30. M. J. Barbarisi and E. G. Kessler, "Some Investigations of the Laser Initiation of Explosives," Proceedings of the 6th Symposium on Electroexplosive Devices, Franklin Institute, Philadelphia (1969).

31. E. G. Kessler and M. J. Barbarisi, "The Detonation of Explosives Using Pulsed Laser System as a Stimulus," Picatinny Arsenal, TR 4390 (Oct. 1972).

32. C. Mavis and C. L. Wright of Sandia Laboratories, Livermore, Calif. Private communication through C. L. Wright.

33. R. R. Bernecker and D. Price. Combustion and Flame 22, pp. 111, 119 and 161 (1974).

34. D. Price and R. R. Bernecker, Combustion and Flame 25, 91 (1975).

35. T. J. Tucker and J. E. Kennedy, "Secondary Explosive Spark Detonators," Proceedings of the 7th Symposium on Explosives and Pyrotechnics, Franklin Institute, Philadelphia, 1971.

36. J. Weber, R. H. Stresau and J. Savitt, "A New Secondary Explosives Low-Energy Electrical Detonator," Proceedings of Electrical Initiator Symposium (1960).

37. B. K. Moy, "Burning Rate Study of HMX Propellants at High Pressures," Air Force Armament Lab., AFATL-TR-75-53 (Oct., 1973). Also, R. L. Derr, T. L. Boggs, D. E. Zurn and E. J. Dibble, "The Combustion Characteristics of HMX," 11th JANNAF Combustion Meeting, pp. 231-239 (Sept. 1974).

38. "Observation of Laser Initiation on an all RDX Detonator," Contract N60921-68-M-1198, Naval Ordnance Lab. Final Report, Space Ordnance Systems Inc., Saugus, Calif. (1968).

39. M. E. Anderson, J. E. Means, V. J. Menichelli and L. C. Yang, "Detonator Initiation by a Remotely Located Flash Charge," Proceedings of the 6th Symposium on Electroexplosive Devices, Franklin Institute, Philadelphia (1969).

POSTER SESSION

Chairman: J. W. Kury
            Lawrence Livermore Laboratory

DETERMINATION OF DETONATION PRESSURE USING
A MANGANIN WIRE TECHNIQUE

K. Burrows, D. K. Chilvers, R. Gyton,
B. D. Lambourn, A. A. Wallace
Atomic Weapons Research Establishment, England

A manganin wire pressure gauge technique is described. The technique has been extensively used in shock work on inert solids and is now being applied to the measurement of detonation wave profiles. Two experimental configurations are used -- (a) The gauge assembly is sandwiched between two pieces of explosive and gives a direct measure of detonation pressure, (b) The gauge assembly is sandwiched between two aluminium plates, one in contact with explosive, and the detonation pressure is calculated from the recorded pressure using a mismatch method. The results are analysed using the program RICSHAW. A best fit to the Taylor wave using RICSHAW gives detonation pressures which are greater than the peak measured values by an amount varying from 6 kb for Baratol to 20 kb for HMX/Inert. Best fit values are, Baratol--160 kb, Composition B (pressed)--285 kb and HMX/Inert-- 355 kb.

INTRODUCTION

At the Fifth Symposium, methods (1-7) for determining pressure of explosives were described. However, with the exception of one paper, all the methods measured flow variables other than pressure, and detonation pressure was inferred from the assumed Chapman-Jouguet equations. The one method of measuring pressure directly (4) used a carbon piezo-resistive gauge to determine detonation pressure in very low density explosive systems.

The purpose of this paper is to describe the application of the manganin wire pressure gauge to the measurement of detonation pressure in high density explosives. The manganin gauge has been successfully used for a number of years in equation of state work on inert solid materials (8-12), and reliable data has been obtained at pressures up to about 400 kb.

In the experiments described in this paper two experimental configurations were employed to obtain pressure time profiles of the detonation wave in Baratol, Composition B (Cast and pressed) and HMX/inert.

With a manganin gauge buried inside an explosive, one expects to observe a step rise to a peak pressure followed by a slow decay in pressure due to the Taylor wave following the detonation wave. Apart from possible reaction zone effects, the peak pressure should correspond reasonably well to the detonation pressure and the part of the Taylor wave recorded should give information about the expansion behaviour of the equation of state for the detonation products. However account needs to be taken of the finite thickness of the gauge assembly in interpreting the pressure records. The results of the experiments have therefore been compared with calculations using a 1D unsteady hydrodynamics code RICSHAW (13) which includes a representation of the gauge assembly.

EXPERIMENTAL TECHNIQUE AND RESULTS

Design of Manganin Gauge

The manganin wire (Composition Cu-86%, Mn, Ni-2%) comes from stock held at AWRE which has provided the wire for all manganin gauges used at this

laboratory. The wire is 0.127 mm diameter and for use in the gauge it is flattened to a thickness of 0.03 mm and width 0.40 mm. The gauge is formed by making connection to a 15 mm strip of manganin wire with two copper foil strips 11 mm wide and 0.06 mm thick as illustrated in Fig. 1. The wire strip is soldered to the copper and the junction so formed is 0.09 mm thick. The gauge resistance is low ($\simeq 0.5\Omega$) and this helps to minimise the shunting effects of any possible parallel conduction paths.

The Insulator

In earlier work (8,9) the insulation of the gauge was provided by a loaded epoxy resin and in practice it was found that the minimum reliable thickness of this insulation was about 0.63 mm. In order to increase the time resolution of the gauge the insulation was changed to polytetrafluorethylene (PTFE) sheet, and a range of thicknesses have been tried. All thicknesses (>0.025 mm) have worked in the sense that stress profiles of the correct amplitude and duration have been recorded in inert solids. The useful recording time is normally limited by the wire shorting through the insulation or by the wire circuit being broken. In order to ensure an adequate recording time it has been found that insulation sheets of 0.13 mm thickness are required for measurements in inert solids up to 300 kb. In the present experiments

MANGANIN STRIP
0 03mm THICK,
15mm LONG AND 0 4mm WIDE

COPPER FOILS
0 06mm THICK
11mm WIDE

PTFE (0 13mm)
INSULATION

VOIDS LEFT BY THE GAUGE BETWEEN THE LAYERS
OF INSULATION, FILLED WITH EPOXY RESIN

Fig. 1. Manganin wire measuring station.

where measurements are made directly in explosives the PTFE insulation thickness is substantially increased to allow for the possible effects of a high temperature environment.

It is of interest to note that Champion (14) has reported measurements on the electrical resistivity of PTFE as a function of shock pressure and finds that the resistivity decreases from $10^{16}\Omega$m at atmospheric pressure to 80Ωm at 540 kb. However in samples <1.3 mm thick an anomolous result was obtained in that no measurable decrease in resistivity was observed during shock compression.

The Measuring Station

The layout is shown in Fig. 1. The small quantity of epoxy resin used is outgassed under vacuum then poured over the wire and allowed to set with the assembly clamped between end plates. Considerable care is taken to exclude air from the system between the PTFE sheets and around the wire. The gauge is essentially simple in construction and can be assembled by relatively unskilled labour. The overall thickness of the measuring station is 0.30 mm and the transit time of a shock is approximately 0.05 μs. As already mentioned additional insulation is provided where measurements are made directly in the explosive and here a further PTFE sheet 0.23 mm thick is added to each side of the measuring station (see Fig. 2(a)) giving a total thickness in this case of 0.76 mm and a transit time of 0.13 μs.

Calibration and Measurement

The stress coefficient of resistance for the present gauge system has been well established (8,9,10) with the value 0.00236 kb^{-1} and a standard deviation of $<0.3\%$. This calibration has been carried out at shock pressures up to 300 kb with no departure from a linear dependence of resistance with pressure being observed. The calibration was carried out in experiments where the gauge was sealed in aluminum blocks and, here the velocity of an impacting flying plate and the consequent shock velocity as measured by timing probes were used to calculate the peak stress. Calibration checks are made at regular intervals.

The measuring system uses a pulsed constant current source, tripped by a suitably timed signal from a probe in the explosive, which energises the manganin wire 12 μs before the arrival of the pressure pulse to
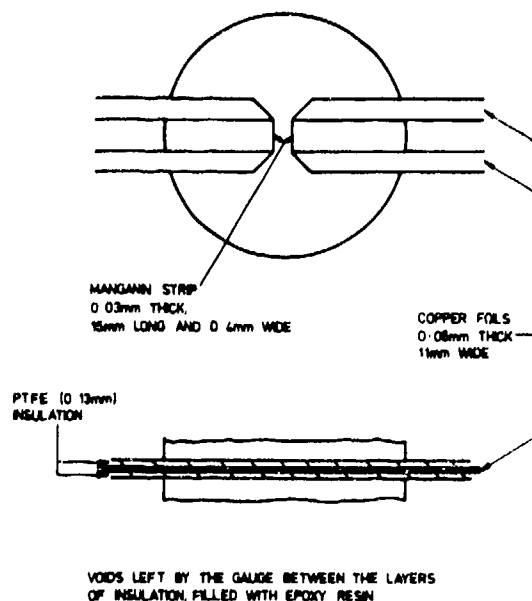
be measured. The voltage across the wire is monitored directly on the plates of a high speed oscilloscope via a 75Ω cable link.

The measured shock pressure is given by $P = 423.2$ $(R/Ro-1)$ kb where R = Resistance of wire under shock loading, and Ro = original wire resistance.

The accuracy with which R/Ro is measured depends on Ro (known to better than 0.3%) and on the measured voltage ratio from the recordings. (In this connection the oscilloscope tube Y deflection linearity is better than 2%.)

R itself may become complicated in time by various effects, etc., which as mentioned earlier put a limit to the available recording times of the gauges.

Experimental Assembly

Two experimental configurations are used and are shown in Figs. 2(a) and (b). In type A the manganin wire measuring station is placed between two cylinders of explosive of 127 mm diameter, and here the wire measures the detonation pressure profile directly, following initial reverberations in the measuring station. In type B a similar explosive charge is used but
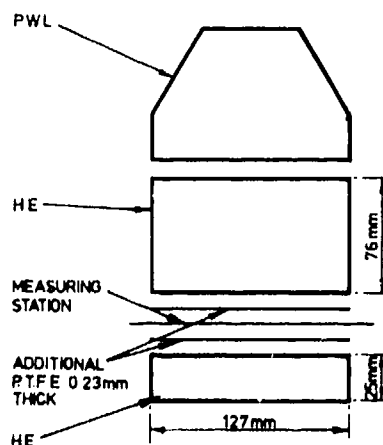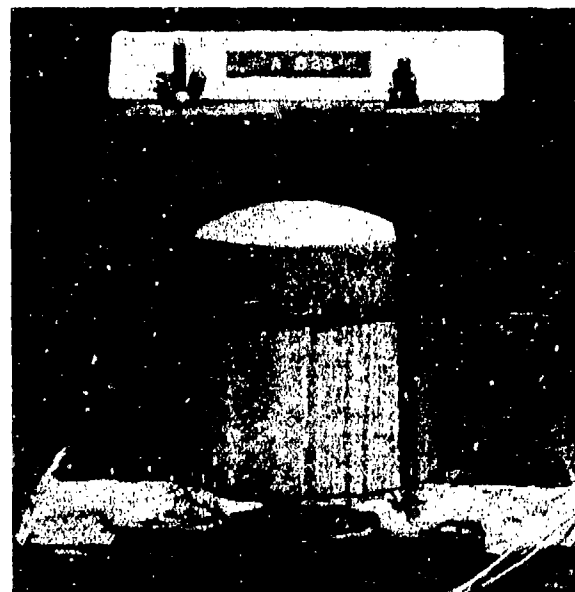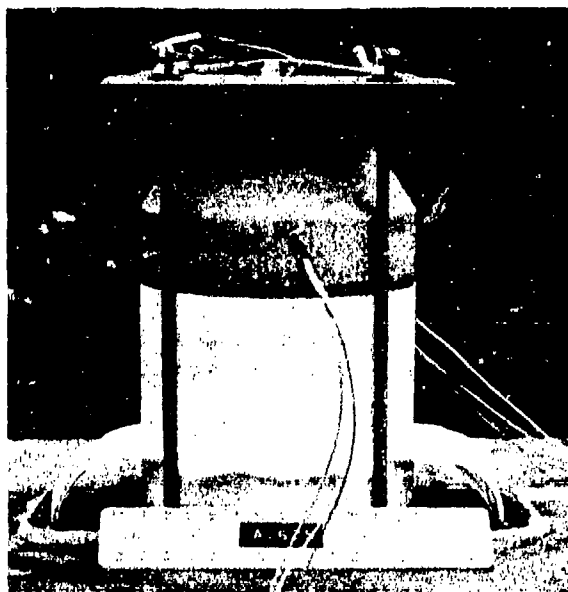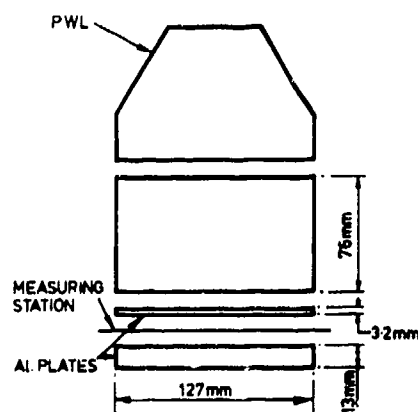
a) TYPE A EXPERIMENTS   b) TYPE B EXPERIMENTS

Fig. 2. Experimental layout.

627

the second cylinder is replaced by an aluminium plate assembly into which the measuring station is located as in Fig. 2(b) and the detonation pressure in the explosive is determined by an impedance mismatch method. In all experiments a plane wave explosive lens is used and the measurement is made essentially in one dimensional conditions.

Experimental Results

Examples of wire recordings are shown in Fig. 3. Here the base line, 1, corresponds to zero volts across the wire, and the voltage level, 2, is due to the pulsed constant current through the wire. The signal in Fig. 3(a) from a type A experiment shows multiple peaks due to reverberations in the gauge assembly. The signal continues for $\simeq 5$ μs before a break is indicated in the wire circuit. Recording from a type B experiment is given in Fig. 3(b) and a single reverberation appears on the front which is the reflection from the PTFE/ aluminium interface. A reflection from the HE/ aluminium is also seen after $\simeq 0.7$ μs, and the reflection of the transmitted shock from the rear surface of the aluminium as a rarefaction wave appears after some 3 μs. Finally the wire circuit becomes short circuited 4.2 μs after initial shock arrival at the wire.

(a) Type A Experiment

(b) Type B Experiment
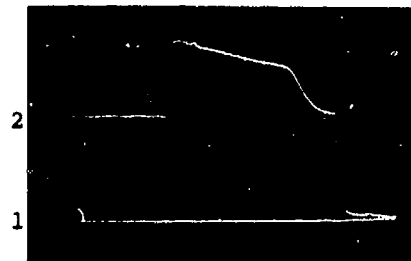
Fig. 3. Typical oscilloscope records of manganin wire response. Time markers at 0.5 μs intervals.

Results have been obtained for Baratol (Cast), Composition B (cast and pressed) and HMX/Inert (pressed) and these are given in Table 1 and Figs. 4(a) → (f).

In all cases the maximum recorded pressure has been measured and this gives the values of P_D kb in Table 1. In type A experiments P_D is given directly from the pressure record. For type B experiments P_D is evaluated by using known P·u data for aluminum and the $\rho_0 D$ line for the explosive. In Table 1 the detonation velocity, D, has been determined from experiments in the present series where time information was available from two or more levels in the explosive.

It can be shown that

$$P_D = \rho_0 D/2 \, (u + p/\rho_0 D)$$

where

u_D = HE particle velocity corresponding to P_D

u = Aluminum particle velocity at measured pressure P (obtained from equation of state data)

It is seen from Table 1 that the values of P_D obtained from both A and B type experiments are in reasonable agreement. If, however P_D is measured in the region immediately following the peak in rounds 639, 621, 625 and 633 (see Figs. 4(e) and 4(g) then the agreement is very good indeed. (These values for P_D are given in parenthesis in Table 1.)

The pressure-time history for Composition B (cast)—round 609 Fig. 4c—is inconsistent with the other results in that the recording time is short, and the peak pressure appears low when compared with the P_D value from round 628 (Table 1). However the peak pressure recorded for 609 is identified, from similar experiments, as the initial shock in the PTFE, and the P_D value given for this round in Table 1 is calculated using the mismatch method. Composition B (cast) is manufactured in controlled temperature moulds and produces a rough detonation front with much microjetting, caused by the presence of very small voids created during manufacture, and early failure of the measuring station in this case is a possibility.

All other explosives, including Composition B (pressed), give consistent results, although, for type B experiments, the HMX/Inert (Fig. 4(h) does not produce the smooth behaviour observed for the other explosives. (The perturbation in the record of Fig. 4(h) at 1.4 μs is due to cross-talk from failure of the neighbouring wire gauge.)

ANALYSIS OF THE EXPERIMENTAL RESULTS

Calculational Method

The results of the experiments are being analysed with a one dimensional unsteady fluid dynamic computer program called RICSHAW (13). RICSHAW integrates the equations of motion using the method of characteristics. It was chosen for use instead of a normal finite difference hydrocode because the fluctuations on the pressure profiles in the latter type of code make the tracing of compression and rarefaction waves difficult. RICSHAW gives not only a smooth

pressure profile between waves but also traces the boundaries of compression and rarefaction waves which are themselves characteristics. A potential disadvantage of RICSHAW, which because the high pressure involved is not regarded as important in these calculations, is that the code has no provision for elastoplastic behaviour. In RICSHAW, all shocks are treated as mathematical discontinuities. When a shock meets an interface or intersects a free surface or another shock, a special interaction subroutine is entered. The interaction calculation solves for the conditions behind the transmitted and reflected waves using a p-u solution. If the reflected wave is a rarefaction, a fan of characteristics is initiated and the edge characteristics of the fan are marked as wave boundaries. The effect of this is that the mesh is fine inside waves where conditions are varying rapidly, but can be coarser between waves where conditions are varying more slowly. Shocks are discarded if they are weaker than a prescribed minimum and may be formed if characteristics cross each other.

TABLE 1

Summary of Results

Explosive		Round Number	Type of Round	Density $(\rho_0$g/cc$)$	Detonation Velocity, D $(mm/\mu s)$	Pressure in Aluminium (kb)	Peak Detonation Pressure P_D (kb)
BARATOL 72% Barium Nitrate 28% TNT		620	A	2.461	5.00		155
		624	A	2.452			152
		626	B	2.443		184	15
COMPOSITION B 59.5% RDX, 39.5% TNT 1% Beaswax	Cast.	609	A	1.670	7.69		254
		628	B	1.672		320	259
	Pressed	639	A	1.699	7.75		276(266)
		640	B	1.707		328	268
HMX/Inert 95/5		621	A	1.778	8.76		334(317)
		625	A	1.775			341(317)
		633	A	1.773			330(314)
		627	B	1.777		359	314
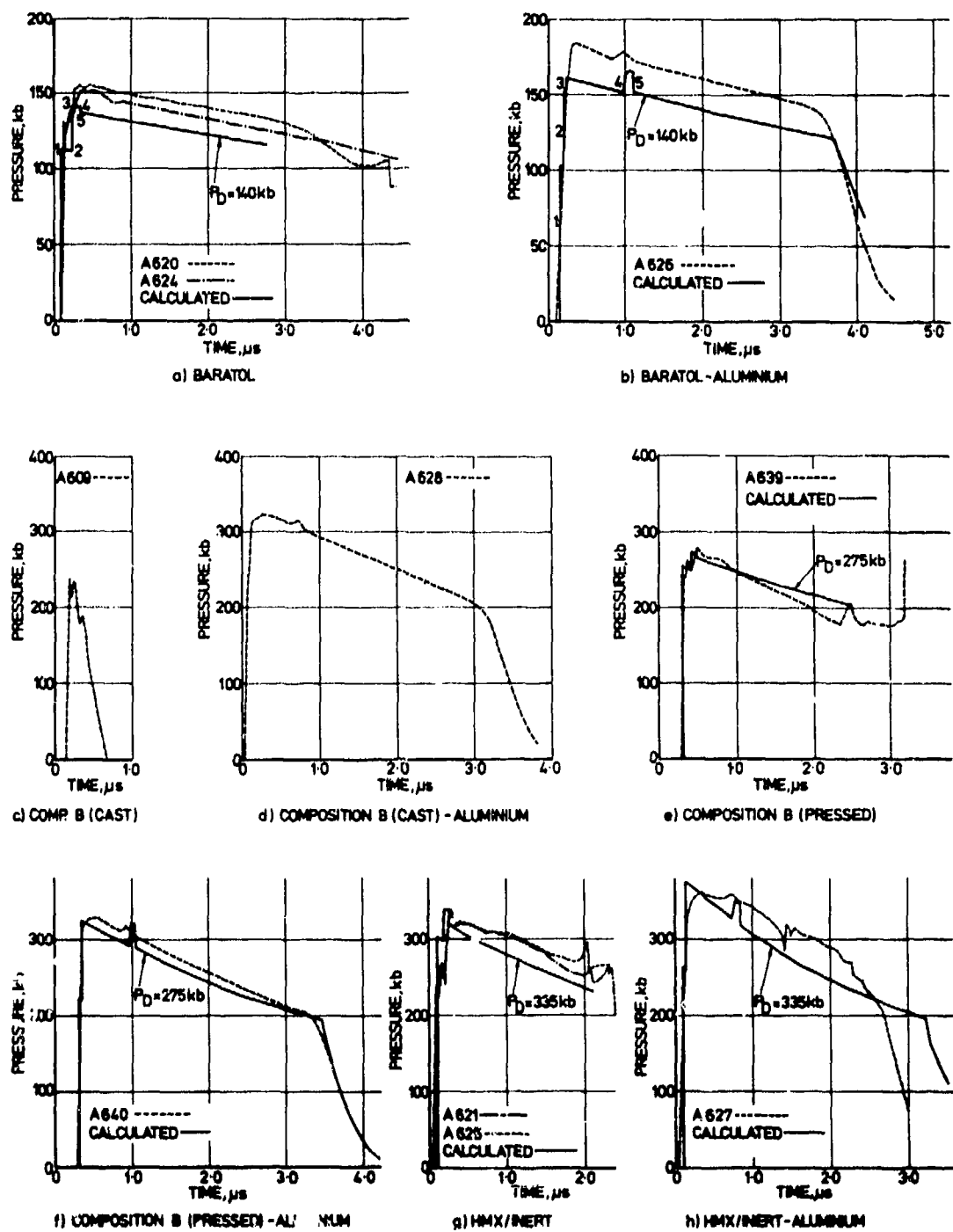
Fig. 4. Comparison of experimental and calculated results.

The reaction zone of a detonation wave is not resolved in RICSHAW. A detonation wave is treated as a jump discontinuity to either a Chapman-Jouguet state or an overdriven state. If an interaction would like to set-up a pressure less than P_D, then the transmitted wave is treated as a Chapman-Jouguet detonation wave followed by a fan of characteristics forming a Taylor wave.

The equations of state parameters assumed for the inert materials and the detonation products of the explosives in the experiments are given in Table 2.

In all the calculations the plane wave lens was represented by 30 mm layer of Baratol which was assumed to be initiated uniformly on its outer surface. In most of the calculations the manganin was not included. Pressure profiles were taken at the Lagrangian mid-plane of the PTFE.

Analysis of Baratol Experiments

The calculations on Baratol assumed an equation of state of perfect gas form. The detonation pressure was taken from Gardner and Wackerle (16) as 140 kb.

Experiments with the Wire Buried in the Explosive

Figure 4(a) shows the comparison between the calculated pressure history and the experimental record. We see that both the calculated peak stress and general level of the calculated pressure are low, though the slope of the main part of the calculated pressure history is in good agreement with the experiment.

The steps on the calculated profile are real effects and may be correlated with events on a wave diagram in Fig. 5(a). The first step (01 in Fig. 4(a)) corresponds to the arrival of the first shock in the PTFE at the wire. The pressure drops ($1 \rightarrow 2$) slightly behind the shock because of the Taylor wave following the detonation wave. When the shock in the PTFE meets the PTFE/Baratol interface a second shock is reflected and this causes the second jump discontinuity ($2 \rightarrow 3$) in the calculated pressure. Again there is a decay of pressure ($3 \rightarrow 4$) behind this shock until the pressure drops suddenly due to the arrival of the rarefaction reflected from the Baratol detonation products, when the 2nd shock reaches the layer of Baratol. Subsequent reverberations of the PTFE are

TABLE 2

Equation of State Data

Perfect Gas (PG) $p = e(\gamma - 1)/v$

JWL $p = ew/v + A(1 - w/k_1 v)\exp(-k_1 v) + B(1 - w/k_2 v)\exp(-k_2 v)$

HE	EOS	ρ_0, g/cc	D mm/μs	P_D kb	γ	A	B	k_1	k_2	w
Baratol	PG	2.61	4.92	140	3.52					
Baratol	PG	2.61	4.92	160	2.96					
Comp.B	PG	1.7	7.86	275	2.82					
HMX/Inert	PG	1.783	8.73	355	2.83					
HMX/Inert	JWL	1.782	8.73	335		9.458	0.0801	8.380	1.605	0.28

Gruneison $W = a + bu$

Material	ρ_o	Γ	a	b						
PTFE	2.16	0.39	0.14	1.97						
Aluminium	2.70	1.57	0.53	1.40						
Manganin	8.46	2.00	0.38	1.72						

631

(a) Baratol/Gauge/Baratol   (b) Baratol/Al/Gauge/Al
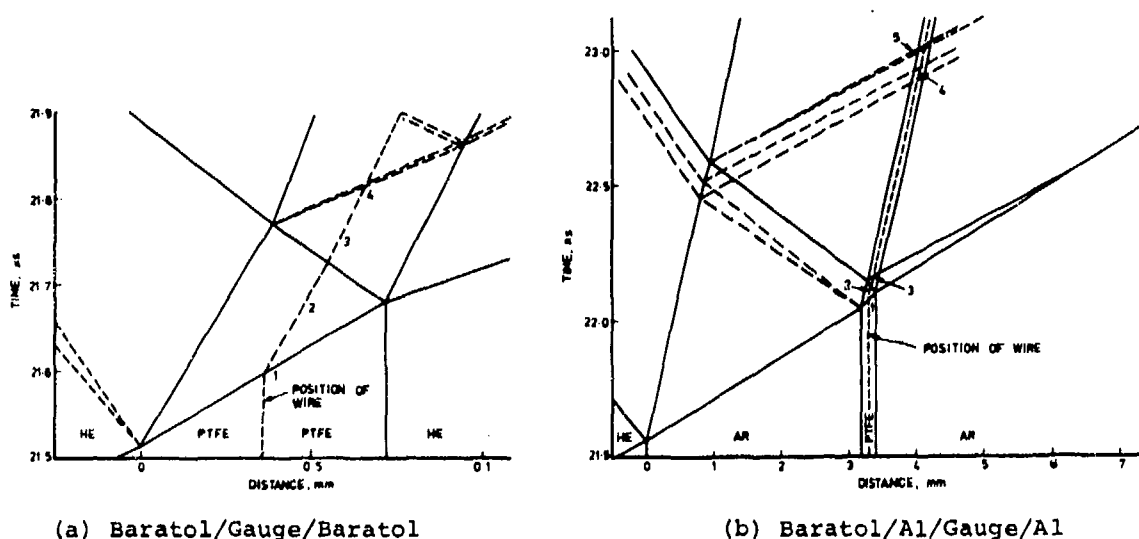
Fig. 5. Wave diagrams.

of negligible magnitude because the PTFE now has an impedance close to that of the Baratol products.

The experimental records show the steps more as a ramp and also have two sharp peaks early in the records. The peaks may have something to do with the finite thickness of the wire and this will be discussed in Section 8, or they might indicate the presence of a von Neuman spike. The ramped nature of the record however suggests that the Baratol is reacting slowly (say over 0.25 μs). Alternatively the ramp might be a combination of the finite thickness of the manganin and a rate dependent behaviour of the PTFE.

Experiments with Wire Buried in Aluminium

Figure 4(b) compares the calculated pressure history with experiment and Fig. 5(b) is the corresponding wave diagram.

In the wave diagram it is seen that a rarefaction is reflected when the shock in the aluminium reaches the PTFE. Steps 1, 2 and 3 in the calculated record correspond to the arrival of the primary shock at the wire and the two shocks of its first reverberation in the PTFE. The reverberation time in the PTFE is much smaller than in the other type of experiment because the PTFE is thinner.

The large blip 4 → 5 on the calculated record is due to the arrival of signals reflected from the aluminium/baratol interface—the rarefaction is reflected as a

compression wave, and the shock reflected into the PTFE from the other slab of aluminium is now reflected as a rarefaction from the detonation products.

Finally the primary shock in the aluminium is reflected at its free surface and causes the pressure in the wire to fall.

The calculated record is again too low, though the slope of the Taylor wave transmitted into the aluminium and the time interval to the arrival of the rarefaction at the free surface are in good agreement.

The experimental record does not show the steps on the rising record and the blip due to waves 4 and 5 is of smaller magnitude and more spread out than the calculated blip.

Calculations with Higher Detonation Pressure

It is clear from Figs. 4(a) and 4(b) that a detonation pressure of 140 kb does not give a good fit to the experiments which indicate a higher detonation pressure for baratol. Taking all three experiments into account, a detonation pressure of 160 ± 2 kb, Figs. 6(a) and 6(b), gives the best fit.

Analysis of Comp.B (Pressed) Experiments

The calculations on pressed Comp.B assumed a perfect gas equation of state with a detonation pressure from Davis and Venable (2) of 275 kb.

632
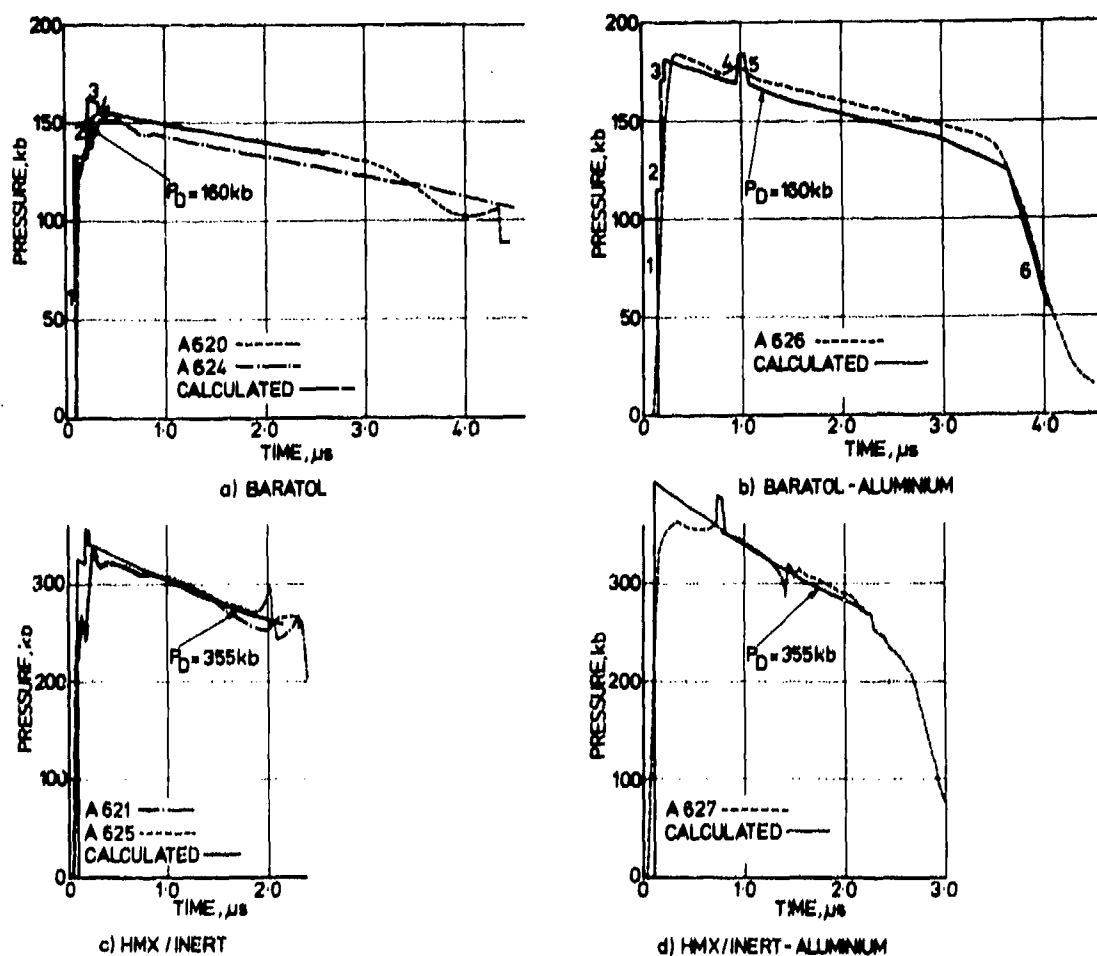
Fig. 6. Best fit calculations to Taylor wave of experimental results.

Experiments with the Wire Buried in the Explosives

Comparing the calculated pressure history with the experimental results Fig. 4(e) shows that the calculated peak stress agrees well with experiment but the calculated Taylor wave is too shallow. The comments on the calculated pressure history given for Baratol apply to these calculations as well; the strength of shocks and rarefactions being the only difference.

Experiments with the Wire Buried in the Aluminium

Figure 4(f) compares the calculated pressure history with experiment, the wave diagram being similar to that of the Baratol/Al Fig. 5(b). The peak stress calculated is approximately correct and the slope of

the Taylor wave is in reasonable agreement with the experimental result.

The calculated rarefaction is approximately 0.1 μs too late and slightly steeper than the experimental results.

In contrast to the Baratol/Al experiments there is a step in the rising record but again the blip, due to the reflection of the gauge signal from the Comp.B/ aluminium interface, is smaller than calculated.

Analysis of HMX/Inert Experiments

The calculations on HMX/Inert assumed a Jones-Wilkins-Lee (JWL) equation of state with a detonation pressure from Allan and Lambourn (14) of

633

335 kb. The various discontinuities in the pressure histories are similar to those of the Composition B.

Experiments with Wire Buried in Explosive

The comparison of calculated pressure history with the experimental results Fig. 4(g) show that the calculated peak stress is in good agreement but the slope of the calculated rarefaction is too low and steep.

Experiments with Wire Buried in Aluminium

Figure 4(h) compares the calculated pressure history with experiment the wave diagram being similar to that of the Baratol/Al Fig. 5(b). The peak stress calculated is too high and again the slope of the rarefaction is too steep.

The calculated rarefaction from the free surface arrives 0.6 µs too late compared with experimental results. However since wire 1 broke at 1.4 µs and good agreement was obtained in the Baratol/Al calculation it is quite probable that wire 2 broke at 2.2 µs.

As with the Baratol/Al experiments there are no steps in the rising record and the blip is smaller than calculated.

Calculations with Different P_D and Perfect Gas EOS

To obtain better agreement in the slope of the rarefaction a perfect gas equation of state was assumed. The slope than agreed tolerably well with experimental results but the calculated Taylor wave was 20 kb too low. Figures 6(c) and 6(d) compare the experimental results with calculation for a Perfect gas EOS

with P_D = 355 kb. The calculated rarefactions agree better with the experimental results than do the original JWL calculations, though the fit is still not as good as for the Baratol results.

DISCUSSION AND CONCLUSIONS

A manganin wire pressure transducer has been used in two types of experiment to determine detonation pressure of explosives. Both types of experiment yield more information than just a detonation pressure, since the pressure history following the peak is a direct measure of the rarefaction (Taylor) wave following the detonation wave, and hence can be interpreted to give the form of the equation of state for pressures below the detonation pressure.

Table 3 compares detonation pressures obtained from the peak pressures recorded in the experiments, values obtained from the calculations which best fit the Taylor wave following the detonation wave, and values in the literature obtained from a variety of other sources.

It will be seen that (1) the pressures determined from the manganin wire experiments are generally within the range of values quoted in the literature. For baratol a value of 140 kb has been quoted by Gardner and Wackerle (16) and the highest figure of 170 kb is referred to by Kineke and West (17). These values however refer to 76/24 baratol not the 72/28 baratol used in the manganin wire experiments. The detonation pressure for cast Comp.B was determined by Allan (18) by measuring free surface velocities of impedance mismatch plates and is referred to by Skidmore and Hart (19). There is no corresponding

TABLE 3

Comparison of Detonation Pressures (kb)

Explosive	From Peak Pressure	Best Fit to Taylor Wave	Range of Values From Other Expts
Baratol (72/28)	154	160	140-170
Comp.B (59.5/39.5/1) Cast	259	280	257
Comp.B (59.5/39.5/1) Pressed	276	285	275-312
HMX/Inert (95/5)	335	355	335

determination for pressed Composition B yet, but the density is similar to that for Composition B-3 whose range of detonation pressure measurements has been reviewed by Davis and Venable (2). Finally the only values for HMX/Inert were determined by Allan and Lambourn (15) again using free surface velocities of mismatch plates. (2) The detonation pressures obtained from using the hydrocode RICSHAW to fit the Taylor wave are greater than those obtained from the peak pressures, by an amount varying from 6 kb for Baratol to 20 kb for HMX/Inert. This point will be discussed further after some comments have been made about the meaning of the records.

In order to try to understand some of the fine structure on the leading edge of some of the pressure histories a calculation has been done with the manganin wire treated as a flat sheet 0.03 mm thick on the HMX/Inert-aluminium experiment. A JWL equation of state was assumed for the HMX/Inert explosive with detonation pressure 335 kb.

Figure 7 is a comparison of the pressure histories on both manganin/PTFE interfaces with the pressure history calculated in the normal way at the mid-plane of the PTFE.

A number of points emerge. (1) Clearly there is a considerable amount of structure on the manganin pressure history, all of which can be related to various shock and rarefaction wave arrivals at the two manganin/PTFE interfaces. (2) The manganin wire ini-
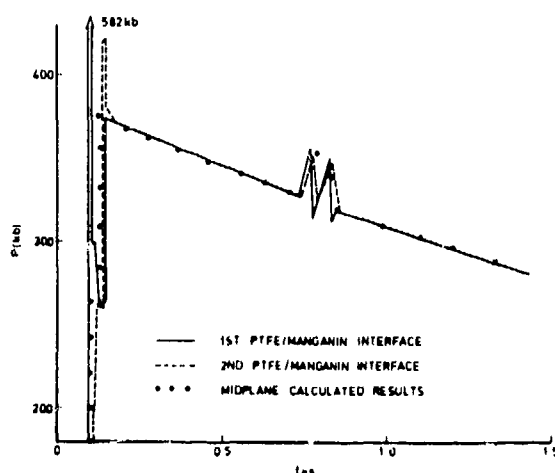
Fig. 7. Comparison of calculated pressure histories at manganin/PTFE interface with assumed history at mid-plane of PTFE.

tially has a very large pressure difference across it—its effective resistance change will be a function of the pressure distribution in the wire and this will of course be affected by side rarefactions in the wire from the potting. (3) After 0.08 μs the reverberations in the wire die out. Thereafter the wire assembly is effectively in equilibrium with the surrounding aluminium until the arrival of the wave reflected from the aluminium-explosive interface forming the blip. (4) The structure of the pressure histories in the blip is in the shape of an M, quite different from the simulation using the mid-plane of the PTFE. The true manganin signal may therefore be much closer to the experimental result which shows the blip as much smaller in amplitude than that previously calculated. (5) Again after the blip the manganin gauge assembly equilibrates to the aluminium.

Thus although the initial behaviour of the gauge assembly on arrival of the first shock is a complicated combination of the waves reverberating in the gauge, the gauge effectively settles down to recording the true pressure history in the aluminium or explosive within a time scale, which is about the reverberation time (a double transit) through the gauge assembly.

Thus until the response of the gauge assembly to known input shock profiles is understood better, it is somewhat difficult to try to interpret the initial structure on the gauge pressure histories.

This is a pity because it is tempting and possibly correct to relate the sharp peak in the pressure histories of the gauge buried in HMX/Inert and Comp.B to a sharp reaction zone and the rather gradual rise of the pressure history for the wire in the baratol to a spread out reaction zone. However, the absence of sharp peaks in the type B experiments suggest that the peaks observed for HMX/Inert and Composition B (pressed) are real and possibly related to the explosive reaction zone.

However the conclusion that the gauge records accurately the regions of slowly varying pressure means that apart from the problem of premature breaking of the wire, considerable confidence can be put in the fact that the slow release of pressure corresponds to the true pressure history in the explosive of aluminium.

If we make the assumption that the Chapman Jouguet condition holds, then the decaying pressure

in the explosive is a Taylor wave. As we have seen, this assumption leads to a measure of detonation pressure, which, because of the uncertainty of the gauge response on the arrival of a sharp shock, may be a better measure than the detonation pressure deduced from the peak recorded pressure.

Taking the comparison of the RICSHAW calculations with the experimental results, we have seen with the HMX/Inert results that the JWL equation of state gives too steep a pressure history but that a perfect gas equation of state agrees satisfactorily for the HMX/Inert and well for baratol. On the other hand a slightly better fit might be obtained for Composition B (pressed) with a JWL equation of state. The reason that the JWL equation of state gives a steeper profile is that as the pressure reduces from the Chapman-Jouguet state, the adiabatic exponent

$$\gamma = \left(\frac{\ln p}{\ln V}\right)_s$$

increases. The present experimental results suggest that γ may remain reasonably constant at least for pressures down to ~75% of Pcj. Perhaps coincidentally, this is in agreement with the modified-Wilkins form of equation of state chosen by Allan and Lambourn to fit the expansion of HMX/Inert to lower pressures.

REFERENCES

1. W. C. Rivard, D. Venable, W. Fickett and W. C. Davis. Proc. 5th Symposium (International) on Detonation. 1970, pp. 3-11.

2. W. C. Davis and D. Venable. Ibid., pp. 13-21.

3. R. L. Jameson and A. Hawkins. Ibid., pp. 23-29.

4. J. L. Austing, A. J. Tulis and C. D. Johnson. Ibid., pp. 47-57.

5. J. K. Rigdon and I. B. Akst. Ibid., pp. 59-66.

6. S. J. Jacobs and D. J. Edwards. Ibid., pp. 413-426.

7. B. Hayes and J. N. Fritz. Ibid., pp. 447-454.

8. P. J. A. Fuller and J. H. Price. Proc. 4th Symposium (International) on Detonation. 1965, pp. 290-294.

9. P. J. A. Fuller and J. H. Price. "Dynamic Pressure Measurements to 300 kilobars with a Resistance Transducer." BRIT J. Appl. Phys. 15, 1964, pp. 751-758.

10. P. J. A. Fuller and J. H. Price. "Dynamic Stress-Strain Release Paths for Aluminium and Magnesium Measured to 200 kilobars." BRIT J. Appl. Phys. (J. PHYS. D), Ser. 2, 2, 1969, pp. 275-286.

11. J. Wackerle, J. O. Johnson and P. M. Halleck. "Projectile-Velocity Measurements and Quartz and Manganin Gauge Determinations in Gas-Gun Experiments," LA-5844, 1975.

12. R. K. Linde, L. Seaman and D. N. Schmidt. "Shock Response of Porous Copper, Iron, Tungsten and Polyurethane." J. Apply Phys. 43, 8, 1972, pp. 3367-3375.

13. B. D. Lambourn and N. E. Hoskin. Proc. 5th Symposium (International) on Detonation. 1970, pp. 501 (Abstract only).

14. A. R. Champion. Effect of Shock Compression on Electrical Resistivity of Three Polymers'. J. Appl. Phys. 43, 5, 1972, pp. 2216-2220.

15. J. W. S. Allan and B. D. Lambourn. Proc. 4th Symposium (International) on Detonation. 1965, pp. 52-66.

16. S. D. Gardner and J. Wackerle. Ibid., pp. 154-155.

17. J. H. Kineke, Jr. and C. E. West, Jr. Proc. 5th Symposium (International) on Detonation. 1970, pp. 533-543.

18. J. W. S. Allan. AWRE Priv. Comm.

19. I. C. Skidmore and S. Hart. Proc. 4th Symposium (International) on Detonation. 1965, pp. 47-51.

MAGNETIC PROBE MEASUREMENTS OF PARTICLE VELOCITY PROFILES

W. C. Davis
Los Alamos Scientific Laboratory
University of California
Los Alamos, New Mexico 87545

The axially-symmetric magnetic probe has been applied to large charges of PBX-9404, Composition B-3, and X-0290 (TATB/KelF 95/5). The technique gives continuous records of particle velocity behind the detonation front, accurate and repeatable to 2%. The results show the time-dependence of the flow by comparison of records from charges of different lengths. Reaction zones are resolved and the departures from the simple model are clearly seen. The data show unexplained differences from the usual interpretation of free-surface velocity measurements.

INTRODUCTION

Particle velocity profiles near the detonation front have been measured in PBX-9404, Composition B-3, and X-0290 plastic bonded TATB, using the axially-symmetric magnetic probe technique. This work is part of an effort to provide accurate values for detonation pressures. The confusion about pressures is well described in what is known as *Kamlet's Complaint*: "Values ranging from 177 to 220 kbar have been quoted as experimental detonation pressures of TNT at 1.63-1.64 g/cm^3, and belief in both extreme values among different knowledgeable detonation hydrodynamicists is encountered by the authors, only recently exposed to the problem. Although values of 341 and 347 kbar for RDX at 1.80 g/cm^3 serve as keystones for most Kistiakowsky-Wilson-type computations in this country, highly respected Russian workers quote 390 kbar for this explosive at 1.80 g/cm^3, and 366 kbar at 1.755 g/cm^3. It seems a fair statement, therefore, that at the present time no single measurement of C-J detonation pressure is universally accepted as being correct to within 5%." (1). A similar observation was made by Davis and Venable (2), who found pressure for Composition B-3 of 268, 275, 292, and 312 kbar from the interpretation of different types of measurements, and all

these measurements were made by them and their coworkers. Many others have commented on the problem of finding trustworthy detonation pressure measurements.

The explanations for these discrepancies are still unknown. Some of the difficulty has certainly been caused by poorly performed experiments, and some by improper interpretation of the experimental results. However, there remain, after casting out suspect data, unreconciled differences.

A promising possibility for the cause of the discrepancies is that the chemical reaction zone in common explosives may be large enough that its effects must be taken into account when analyzing the experiments. The reaction zone affects these in two ways: first, the measurements may sense the pressure in the reaction zone instead of that in the Taylor wave, and the value obtained is not the C-J pressure, but the pressure at some point where reaction is still going on; second, the states and wave profiles depend on the details of the initial conditions of initiation of the explosive, and on how far the detonation wave has run, with the build-up time constant many times the reaction time. Mader and Craig (3) have shown that taking the time dependence into account im-

proves the fit to experimental data, and have proposed an empirical scheme for improving the agreement between numerical computations and experiment. Bdzil and Davis (4) have analyzed a special one-dimensional time-dependent detonation model and compared the behavior of the model with the available experimental results. This effort, and some unpublished extensions by Bdzil, improves the fit of theory to experiment appreciably, but there are still differences (4). There seems to be yet another source of time-dependent effects in the experiments. One possibility is that the metal plates from whose motion the explosive properties are inferred have time-dependent behavior of their own, so that the interpretation as usually made is incorrect.

The experiments described here are intended to provide accurate particle velocity measurements, which do not require interpretation of metal free-surface velocity to obtain the velocities within the explosive. Only some experimental results are given now; the interpretation will need development of more understanding.

EXPERIMENTS

The axially-symmetric magnetic probe has been described by Hayes and Fritz (5) and by Fritz and Morgan (6). A typical arrangement used for the measurements reported here is shown in Fig. 1. The detection dimensions are a compromise which gives adequate signal amplitude combined with insensitivity to variation in foil conductivity, insensitivity to the small unavoidable assembly tolerances, and is small enough that it samples only the small area available for measurement at the end of a charge 200-mm diameter and 200-mm long.

The aluminum foil is moved by the detonation wave, and its interaction with the divergent field of the permanent magnet induces a voltage in the pickup coil. The voltage is recorded on an oscilloscope which has been calibrated so that the deflection distortion can be corrected. The conversion of the voltag. record is a complex procedure, described in Ref. 6, accomplished using a computer code developed by Fritz. The effects of the finite frequency response and resistive losses of the coaxial cable and the single turn coil are corrected by a deconvolution procedure in the code. The finite conductivity of the
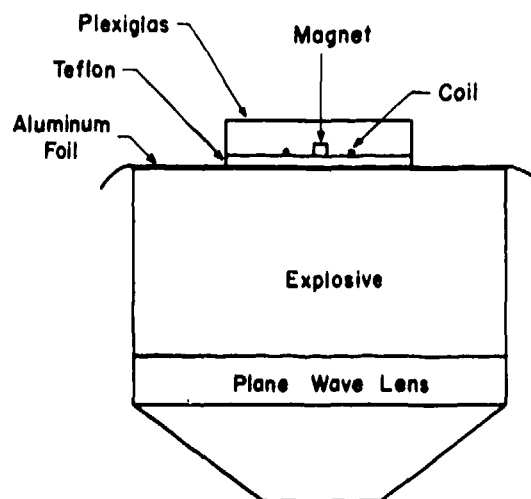
Fig. 1. Diagram of a typical experimental assembly. The initiating lens and the explosive are 203.2-mm diameter. The motion of the aluminum foil (75-μm thick) between the explosive and the Teflon in the non-uniform magnetic field induces a voltage about 150 mV in the single-turn pickup coil. The voltage is recorded during the interval, slightly longer than 1 μs between the time when the foil starts to move and the time when the shock wave in the Teflon (6.35-mm thick) reaches the coil. The voltage record can be unfolded to give foil velocity vs time.

foil, which makes a small correction, is estimated from the shock temperature and the temperature coefficient of conductivity of aluminum.

The charges were assembled with care to hold the necessary tolerances. The explosive was carefully controlled for composition and density. The temperature of the assembly was controlled at 24°C during assembly, storage, and firing; the most temperature sensitive component is the magnet itself, with a coefficient of 0.0019/°C, and it was calibrated at 24°C.

A nine-slit smear-camera trace was taken from the air gap between the Teflon plate and the Plexiglas coil form to check the planarity of the detonation wave. In all cases the departure from plane was less than 40 ns.

The chief contribution to the error in these experiments comes from electrical noise induced in the

unbalanced pickup system by the air shock waves reflecting from the inside of the shot box. These are particularly troublesome for the long lengths of explosives. They were reduced by inserting grounding foils of 20-μm aluminum in the joint of the assembly about 50 mm below the measurement foil. When a strong noise burst arrives just before the signal to be measured, it destroys the base line measurement, and the record is necessarily discarded.

In some earlier experiments we tried to use thin layers of explosive in place of the Teflon shown in Fig. 1. The noise generated by the detonation-electric effect (7) reduced the quality of the records too much, and all the results reported here used Teflon, which has molecular symmetry and produces almost no electrical signal when shocked.

RESULTS

Figure 2 shows the data from a total of 19 shots at five different lengths for PBX-9404. The charges were initiated by a P-80 planewave lens of 203.2 mm diameter, and all the PBX-9404 pieces were also 203.2 mm diameter. The explosive density was 1.84 g/cm^3, and the firing temperature was 24°C. The aluminum foil thickness was 75 μm. The Teflon density was 2.14 g/cm^3, with a spread of about 0.015 g/cm^3 from shot to shot. The curves shown are smoothed averages from the data; the averages are simply fits by eye to the superimposed raw data curves.

Figure 3 shows the data from a total of nine shots with Composition B-3. These charges were made exactly like the PBX-9404 charges described above. The explosive density was 1.73 g/cm^3.

Figure 4 shows the data from a total of eight shots with X-0290, which is a TATB/KelF 95/5 composition with density 1.89 g/cm^3. The charges were initiated with a P-80 planewave lens of 203.2 mm diameter and a booster charge of TNT, density 1.64 g/cm^3, 25.4 mm thick. The booster charge was used to reduce the initiation distance in the TATB to about 1 or 2 mm. The rest of the make-up details were like those for PBX-9404.

The overall error in these data, from both systematic and random sources, is probably less than 2%.
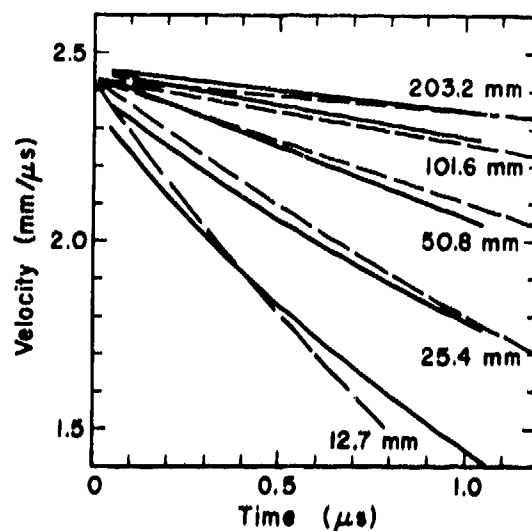
Fig. 2. Plot of velocity vs time for a foil driven by PBX-9404 of five different charge lengths in assemblies like Fig. 1. The faint dashed lines are a comparison calculation for a C-J model with pressure of 35.6 GPa. A change of 1 GPa in the model pressure changes the intercept velocity about 0.05 mm/μs. The data are accurate to about 2%, which is a little less than 0.05 mm/μs.
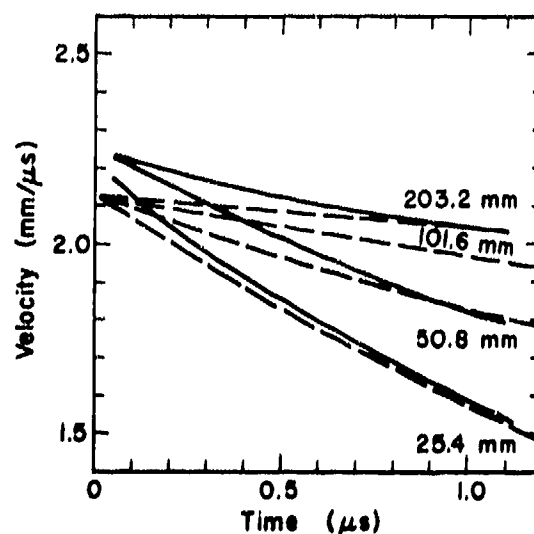
Fig. 3. Plot of velocity vs time for a foil driven by Composition B of four different charge lengths in assemblies like Fig. 1. The comparison calculation pressure is 27.4 GPa. The experimental curves for 101.6- and 203.2-mm lengths are indistinguishable.

Some of the raw data, not smoothed or averaged, are shown in Fig. 5.

DISCUSSION

We are not now prepared to offer any detailed interpretation of these data; we give only a comparison with the simple C-J model. The reverberations in the aluminum foil last about 0.02 µs, and after three reverberations the reverberation amplitude is much less than the experimental uncertainty. Also, the difference between a calculation with the foil and one without is very small after three reverberations. Therefore comparison between experiment and model is made using calculations which have only the C-J model Taylor wave in the explosive impinging upon a Teflon plate, and the velocity used is that of the cells near the interface. In this model the velocity-vs-time curves are similar for all explosive lengths, with that length the only scaling factor.

In Fig. 2 the data for PBX-9404 are compared with a calculation for a C-J explosive with a C-J pressure of 35.6 GPa. The agreement is good, hardly anywhere outside the 2% error limits. One might propose that the lowest curve for 12.7 mm of explosive shows some time-dependent effect, with its slope a little too flat and its intercept velocity a little low indicating that initiation was not quite instantaneous. From these experiments it would seem that PBX-9404 is for practical purposes nearly an ideal explosive, and that the C-J model describes it very well. This result is in disagreement with the results of experiments where the pressure is inferred from the measured free-surface velocity of plates driven by the explosive. The collected free-surface velocity results are presented in Refs. 3 and 4. We do not know how to reconcile the apparent disagreement.

In Fig. 3 the data for Composition B-3 are compared with a calculation for a C-J explosive with a C-J pressure of 27.4 GPa. The disagreement is large, and it is apparent that increasing the C-J pressure, which moves the curves up but does not change the slope appreciably, only changes the point where they cross. The data suggest that there is a resolved reaction zone followed by a time-dependent flow which is approaching the right slope for a Taylor wave in the longest charge. A calculation (made by J. B. Bdzil) using the excellent fit to the free-surface velocity results for Composition B-3 given in Ref. 4, which has
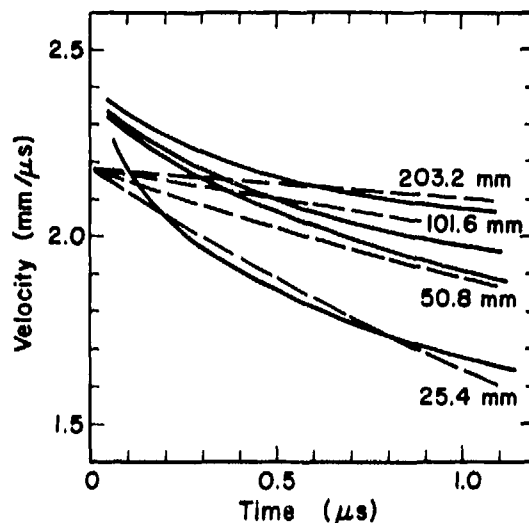
Fig. 4. Plot of velocity vs time for a foil driven by X-0290 (TATB/Kel-F 95/5) of four different lengths, in assemblies like Fig. 1 except that a TNT booster 25.4-mm thick was inserted between the lens and the explosive. The comparison calculation pressure is 29.3 GPa.
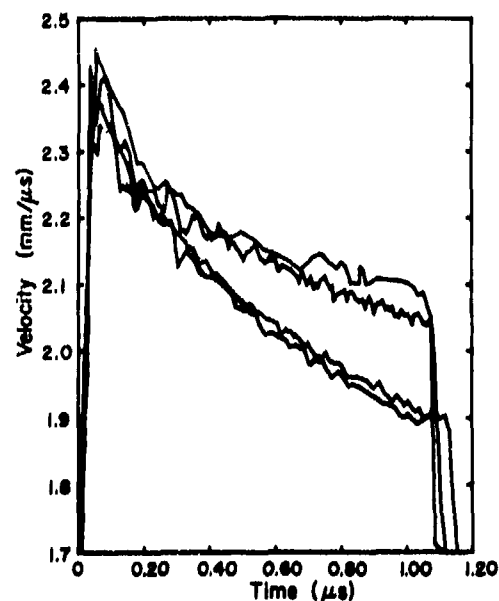
Fig. 5. Computer plot of unsmoothed data for X-0290 shots, two of 203.2-mm length and two of 50.8-mm length. These are of course among the best records, but the others, except for a few which are unreadable because of electrical noise on the baseline trace, are not very different.

640

a resolved reaction zone and time-dependent develop-
ment of the whole reaction zone and, following flow,
is better but still not satisfactory. More work on the
interpretation is clearly necessary.

In Fig. 4 the data for X-0290 (plastic-bonded
TATB/KelF 95/5) are compared with a calculation
for a C-J explosive with a C-J pressure of 29.3 GPa,
with a length equal that of the X-0290 only, exclud-
ing the TNT booster. The fit is not at all satisfactory.

Rather than solving the problem expressed in
Kamlet's complaint, these results just increase the dif-
ficulties. First, they clearly point to a relatively large
reaction zone and appreciable time-dependent flow
region in Composition B and X-0290. Where the
slopes of the experimental curves are steeper than
those of the calculated comparison curves, one can
infer that chemical energy is being released. Second,
they reveal a large and unexplained disagreement with
the free-surface velocity results for PBX-9404 and
Composition B, showing that there is an error in
interpretation for at least one of the sets of experi-
ments.

ACKNOWLEDGEMENTS

REFERENCES

1. M. J. Kamlet and C. Dickenson, J. Chem. Phys.
    48, 43 (1968).

2. W. C. Davis and D. Venable, *Fifth Symposium on
    Detonation*, Office of Naval Research ACR-184,
    1970, p. 13.

3. C. L. Mader and B. G. Craig, "Nonsteady-State
    Detonations in One-Dimensional Plane, Diverg-
    ing, and Converging Geometries," Los Alamos
    Scientific Laboratory Report LA-5865, 1975.

4. J. B. Bdzil and W. C. Davis, "Time-Dependent
    Detonations," Los Alamos Scientific Laboratory
    Report LA-5926-MS, 1975.

5. B. Hayes and J. N. Fritz, *Fifth Symposium on
    Detonation*, Office of Naval Research ACR-184,
    1970, p. 447.

6. J. N. Fritz and J. A. Morgan, Rev. Sci. Inst. **44**,
    215 (1973).

7. B. Hayes, J. Appl. Phys. **38**, 507 (1967).

THE DIAMETER EFFECT IN HIGH-DENSITY HETEROGENEOUS EXPLOSIVES*

A. W. Campbell and Ray Engelke
Los Alamos Scientific Laboratory
University of California
Los Alamos, New Mexico 87545

A phenomenological study of the dependence of steady detonation velocity on charge radius (the "diameter effect") in cylindrical configuration is described. Consideration is mainly given to high-density heterogeneous solid explosives cast or pressed to greater than 94% of theoretical maximum density. The work centers around a new fitting form which fits data for both homogeneous and heterogeneous explosives quite well. Some success is achieved in correlating the parameters of the fit with measured quantities. The effect of joints in rate sticks and of boosting on steady detonation velocity is examined experimentally. A significant joint effect is resolved. Finally, front-curvature measurements on a plastic bonded TATB are used to deduce the reaction-zone length for this explosive. Comparisons are made with zone lengths obtained by other methods.

INTRODUCTION

A study of the dependence of steady-state detonation velocity on charge radius in cylindrical geometry (the "diameter effect") is reported. Emphasis is placed on consideration of solid explosives which are heterogeneous (i.e., cast or pressed from a powder containing many different sizes of microcrystals) and at greater than 94% of theoretical maximum density (TMD). For purposes of comparison, diameter-effect curves of two liquid explosives are also included.

The diameter effect has importance at different levels. For example, it can be used as an engineering tool for gauging the size of system in which an explosive will behave "ideally." On a more basic level, the two-dimensional effects can be used as a probe for studying reaction-zone structure.

The theories of the diameter effect presented to date either have been shown to be incompatible with the experimental data for heterogeneous solid explosives [i.e., those of Eyring et al. (1) and of Jones (2)] or are not expressed in terms of the commonly measured experimental quantities [Wood and Kirkwood (3)]. The treatment given here is phenomenological; i.e., the study is restricted to finding regularities within the data. Such regularities should give hints on the mechanisms which are dominant and should act as a guide and constraint on a basic theoretical treatment. The work in this paper centers around a new fitting form which fits data for both homogeneous and heterogeneous explosives quite well. This form is applied to new data as well as to data taken from the literature.

In the course of obtaining the new experimental data, it was found that joints in small rate sticks perturbed the detonation velocity significantly for the purposes of high precision measurements. These results are discussed. A study was also made of the effect of boosting on the steady-state velocity. No significant effect was observed. Finally measurements of front curvature were made on a plastic-bonded TATB. These measurements, when combined with

the diameter-effect curve and the Wood-Kirkwood (WK) theory, determine a reaction-zone length on the central stream tube as a function of stick radius. The infinite-medium reaction-zone length thus obtained is compared with those from independent measurements.

I. EXPERIMENTAL

Explosives

The explosives for which new data are presented were carefully prepared by casting or pressing following the procedures described by James (4). An exception was XTX-8003, which was composed of PETN n..ixed with a casting resin. This explosive was pressed into grooves cut in polycarbonate slabs and then the resin was allowed to polymerize. For this explosive, the densities of the rate sections were inferred from specimens with the same composition; for all other explosives, densities were obtained by immersion of the pieces used in the rate studies. In the case of Amatex/20, the pieces were sprayed with a thin film of plastic before immersion.

Detonation-Velocity Measurement

Most of the rate measurements were made with the pin technique as described by Campbell et al. (5), except for a few changes of detail. All pieces were measured for length in a temperature-controlled room. The most common piece length was 50 mm, and lengths were measured to about 10^{-2} mm. The pieces were assembled in columns with 50-μm copper magnet wire inserted in the joints as ionization switches. The columns were then clamped as shown in Fig. 1. In order to ensure that joints between rate sections were closed and yet that the sections were not over-compressed, the clamping bolts were passed through carefully machined spacers as shown.

In the case of PBX-9404 at diameters of about 1.3 mm and less, the detonation velocities were measured on individual pieces 12.7 mm long using a smear camera. As the result of carefully determining the image magnification and of dynamically calibrating the camera, the optical rate measurements are thought to be accurate to better than 0.1%.

Shots were temperature controlled to ± 1°C. Detonation velocities were obtained from the pin data by linear least-squares fitting.

II. DIAMETER EFFECT

Figure 2 shows the dependence of the steady-state detonation velocity on the reciprocal of the charge radius for the group of explosives considered. One notes that numerous scales and shapes are present. Except for the liquids (nitromethane and TNT) and for pressed TNT and XTX-8003, all the data necessary to generate these curves were obtained without confinement. The curves for all the solid explosives (except the TATB formulations) show downward concavity. It was shown by Malin et al. (6) using data for Composition B, that this type of curvature is contrary to the theory of Eyring et al. (1) and is not fitted properly by Jones' theory (2). It should be noted that Eyring's theory does fit the data f·. (the homogeneous explosives) liquid nitromethane and liquid TNT quite well. The WK theory (3) cannot be tested against the data because the velocity decrement is expressed in terms of the detonation-wave curvature on the central stream tube rather than in terms of the stick radius.

In view of these failings or inapplicability, it was decided that a phenomenological approach should be made and that the objective of this approach would be to find regularities in the data. Such an approach, if successful, should give hints to, and place constraints on, a correct hydrodynamic theory of the effect. In addition, it would systematize the data and allow accurate velocity interpolations to be made at any desired diameter.

The cornerstone of this treatment is the functional form
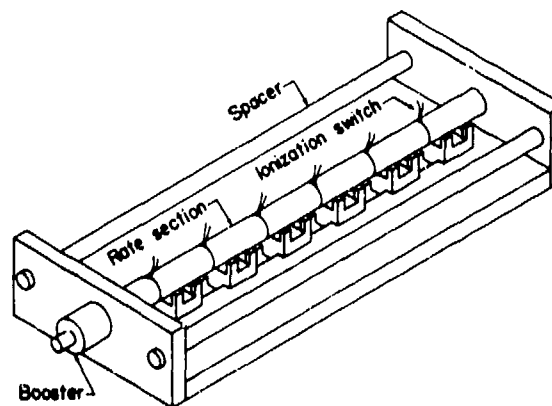
Fig. 1. Schematic of a typical rate-stick assembly.
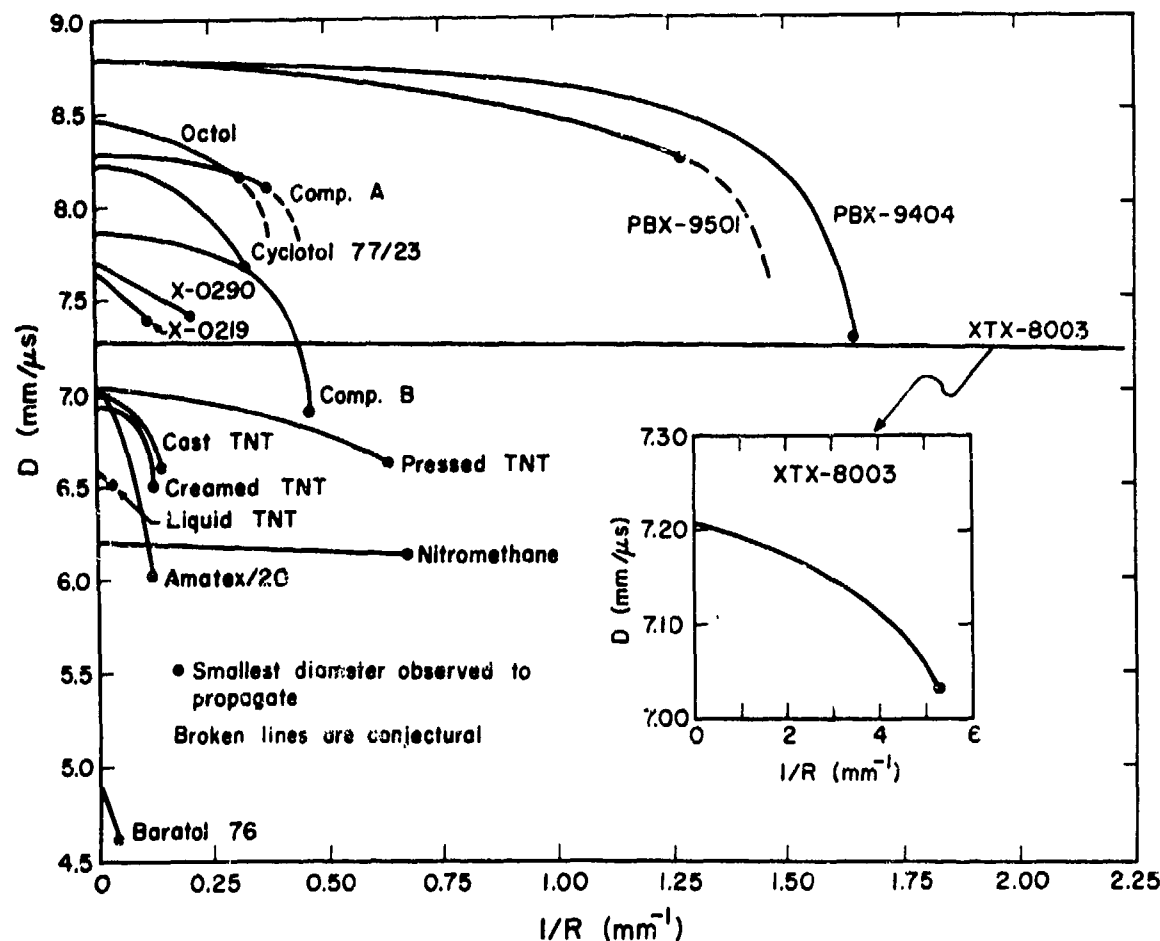
Fig. 2. Composite of diameter-effect curves in the D-vs-1/R plane. Broken lines are conjectural.

$$D(R) = D(\infty)[1 - A/(R - R_c)], \quad (1)$$

where $D(R)$ and $D(\infty)$ are the detonation velocities at charge radius R and in infinite medium, respectively, and A and R_c are length parameters. An alternate form of Eq. (1), which displays the non-Eyring part explicitly is

$$D(R) = D(\infty)\left\{[1 - A/R] - \frac{AR_c}{R(R - R_c)}\right\}. \quad (2)$$

Note that Eqs. (1) and (2) reduce to Eyring's form where $R_c \to 0$. This is a reasonable behavior since a line in the D-vs-1/R plane accurately represents the data at sufficiently large charge diameter. In addition,

as $R \to R_c$, $D(R) \to -\infty$; i.e., there is an asymptote at finite R. At fixed R_c, the parameter A determines how abruptly the downturn in the curve occurs; i.e., the smaller the value of A, the more abrupt the drop. Figure 3 displays this. Since $D(R) \to -\infty$ as $R \to R_c$, the physical region corresponds to values of $R > R_c$ and in particular the failure radius must obey $R_f > R_c$.

Equation (1) was fitted to the available data by the method of least squares. Graphical displays of typical fits are given in Figs. 4 and 5. The results of the fits are given in Table 1. The PBX-9404 result shown in Fig. 4 is typical of high-density heterogeneous explosives. Contrasting behavior is shown by the liquid form of nitromethane (7) and of TNT (8).

644

The liquid TNT data are linear in the D-vs-1/R plane. The fit of the nitromethane data shows slight upward concavity, which is expressed mathematically by R_c having a value less than zero. The TATB formulations are exceptional in the sense that of all the solid explosives treated they are the only ones which show linear diameter-effect curves. There is a hint of upward concavity in the data, but the least-squares analysis shows that R_c is not significantly different from zero.

It should be mentioned that the fit for PBX-9404 is unsatisfactory in that the deviations about the fit are larger than what is believed to be the experimental error in measuring the detonation velocity. It is not known whether this is a shortcoming in the fitting form or is due to some uncontrolled variable in the explosive itself; e.g., particle-size variations (6). The latter explanation cannot be ruled out, because the data for PBX-9404 were accumulated over a long period of time, i.e., approximately 18 years.

Fig. 3. Parametric dependence of the diameter-effect curve. The hashed line represents the approximate position of the maximum observed velocity deficit.
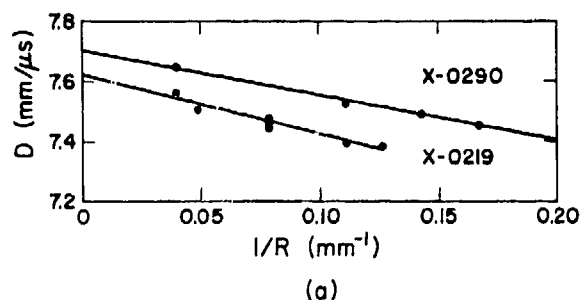
Fig. 5a. Diameter-effect curves for X-0290 ($\rho = 1.895$ g/cm^3) and X-0219 ($\rho = 1.915$ g/cm^3).

Fig. 4. Diameter-effect curve for PBX-9404; $\rho = 1.846$ g/cm^3.
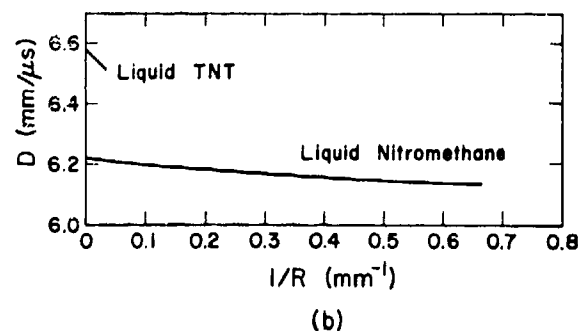
Fig. 5b. Diameter-effect curves for liquid TNT ($\rho = 1.443$ g/cm^3) and liquid nitromethane ($\rho = 1.128$ g/cm^3). The liquid TNT data points all lie within 0.4 m/s of the fit. The liquid nitromethane points all lie within 2 m/s of the fit.

The deviations about the fits of Fig. 5 are of the same size as the experimental error. This is also true of the other fits listed in Table 1.

It is thought that the very different conformation of the curves shown in Figs. 4 and 5 is due to there being two mechanisms supporting wave propagation in heterogeneous solids, i.e., hot spots and homogenous burn; while in homogeneous explosives only homogeneous burn is present. Thus, one can speculate that in heterogeneous explosives at large diameter both mechanisms contribute to driving the wave while at diameters near failure only the hot-spot mechanism sustains wave motion. The lack of a region of sharp drop in the liquid curves is then due to the absence of the hot-spot mechanism.

The quality of the fits obtained with Eq. (1) can be gauged from Fig. 6. In that figure, the fitting form and some typical data points for the various explosives are plotted in a reduced coordinate plane (i.e., $D(R)/D(\infty)$ vs $A/(R - R_c)$). The existence of a plane in which all the data can be plotted near a single curve is suggestive that the processes which control the diameter effect are identical and that the different curves in the D-vs-1/R plane result from variations of the relative effectiveness of the processes.

Another observation that can be made is that the fitting parameter R_c correlates with the experimental failure radius. This correlation is shown in Fig. 7. One sees that except for Amatex/20 and Baratol 76 (not plotted), the linear least-squares fit $R_c = (0.877 \pm 0.054)R_f$ passes close to the data. The Baratol 76 curve is questionable because it is determined by only three points and none of these are very close to the failure diameter. Consequently, the curvature may not be sufficiently well determined for the fit to be useful near failure. Of the other explosives which give data points markedly to the right of the fitting curve, cast TNT, Amatex/20, and Octol may be expected to yield small charges containing critically insensitive regions--cast TNT by variation in the freezing rate, Amatex/20 by segregation of ammonium nitrate, and Octol by virtue of the large-particle-size HMX used. These insensitive regions may have resulted in larger values of R_f.

An attempt was made to correlate A with R_f. This was not as successful. The data scatter badly about

Fig. 6a. *Diameter-effect curve and data points in reduced coordinates over the full range of velocity deficit.*
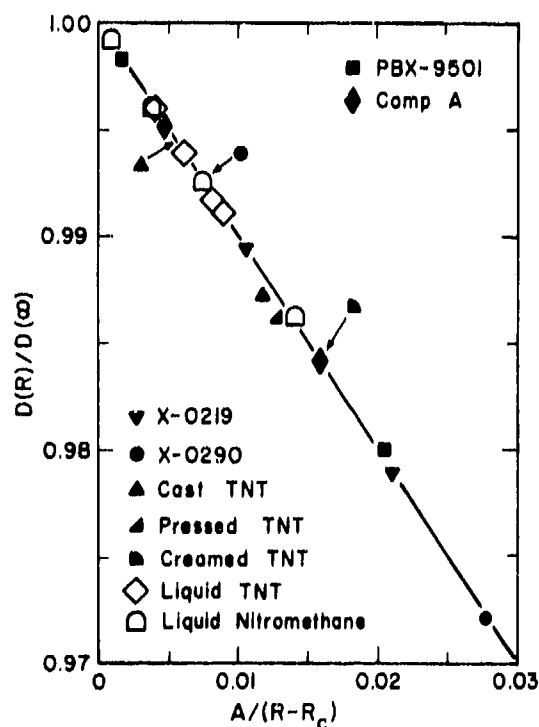
Fig. 6b. *Diameter-effect curve and data points in reduced coordinates over the first 3% of velocity deficit.*

TABLE 1
Diameter-Effect Parameters

Explosive	Data Points* (No./diam)	Density/TMD (g/cm³)	% TMD**	D(∞) ± σ_D (mm/μs)	R_c ± σ_Rc (mm)	(A ± σ_A) × 10² (mm)	Expt. Failure† Radius (mm)	Comment
Liquid Nitromethane	9/5	1.128/1.128	100	6.213 ± 0.001	-0.4 ± 0.1	2.6 ± 0.2	1.42 ± 0.21	Ref. (9). The fit shows slight upward concavity. Shots fired in brass tubes with 3.18-mm thick walls.
Liquid TNT	31/4	1.443/1.443	100	6.574 ± 0.001	0.0	29.1 ± 0.4	31.3 ± 1.3	Ref. (8). R_c fixed at 0.0 gives the smallest variance of fit. Shots fired in pyrex tubes with 2.54-mm thick walls.
XTX-8003	56/4	1.53/1.556	98.3	7.260 ± <0.001	0.111 ± 0.001	0.191 ± 0.001	0.18 ± 0.05	Ref. (10). 80/20 PETN/silicone rubber. Fired in half-cylinder configuration confined in polycarbonate.
Composition A	5/5	1.687/1.704	99.0	8.274 ± 0.003	1.2 ± 0.1	1.39 ± 0.17	< 1.1	Ref. (4). 92/8 RDX/Wax. No sticks that failed were reported.
Composition B	26/12	1.700/1.742	97.6	7.859 ± 0.010	1.94 ± 0.02	2.84 ± 0.19	2.14 ± 0.03	36/63/1 TNT/RDX/Wax
PBX-9404	16/13	1.846/1.865	99.0	8.776 ± 0.012	0.553 ± 0.005	0.89 ± 0.08	0.59 ± 0.01	94/3/3 HMX/NC/CEF
PBX-9501	7/5	1.832/1.855	98.8	8.802 ± 0.006	0.48 ± 0.02	1.9 ± 0.1	< 0.76	Unpublished LASL data. 95/2.5/1.25/1.25 HMX/Batane/BDNPA/BDNPF
Octol	8/6	1.814/1.843	98.4	8.481 ± 0.007	1.34 ± 0.21	6.9 ± 0.9	< 3.2	Ref. (11). 77/23 HMX/TNT
Cyclotol 77/23	8/8	1.740/1.755	99.1	8.210 ± 0.014	2.44 ± 0.12	4.89 ± 0.82	3.0 ± 0.6	77/23 RDX/TNT
Baratol 76	3/3	2.619/2.63	99.6	4.874	4.36	102	21.6 ± 2.5	Unpublished LASL data. 24/76 TNT/Ba(NO₃)₂. Interpolating fit. The curve is not well enough defined near failure to properly test the R_f vs R_c correlation.
Amatex/20	4/4	1.613/1.710	94.3	7.030 ± 0.010	4.4 ± 0.2	59. ± 3.	8.5 ± 0.5	Ref. (12). Composition is nominally 20/40/40 RDX/TNT/AN. The AN median particle size was ~ 0.5 mm.
X-0219	8/6	1.915/1.946	98.4	7.627 ± 0.015	0.0	26.9 ± 2.3	7.5 ± 0.5	Unpublished LASL data. 90/10 TATB/Kel F 800. When R_c is freed a statistically insignificant result R_c = -5. ± 6. mm is obtained. See the nitromethane result.
X-0290	5/5	1.895/1.942	97.6	7.706 ± 0.009	0.0	19.4 ± 0.8	4.5 ± 0.5	Unpublished LASL data. 95/5 TATB/Kel F 800. When R_c is freed a statistically insignificant result R_c = -1.6 ± 0.8 mm is obtained. See the nitromethane result.
Creamed TNT	5/5	1.615/1.654	97.6	6.942 ± 0.028	7.41 ± 0.26	5.67 ± 1.87	7.3 ± 1.0	Ref. (13).
Pressed TNT	>24/8	1.62/1.654	97.9	7.045 ± 0.17	0.57 ± 0.21	6.1 ± 1.3	1.31 ± 0.28	Ref. (14) Confined in cellophane tubes with 0.05-mm thick walls.
Cast TNT	>15/5	1.62/1.654	97.9	6.999 ± 0.011	5.5 ± 0.3	11.3 ± 1.7	7.25 ± 0.25	Ref. (14).

*Number of shots that propagated a steady wave/number of distinct diameters at which observations were made.
**Theoretical maximum density.
†R_f is the average of the radii from two go/no-go shots, or is defined as one-half the difference in the go/no-go radii.

a power law of the form $(A = KR_f^n)$. However, although one cannot quantitatively relate A and R_f, there is a correlation in the sense that a larger value of A tends to correspond to a larger value of R_f.

III. THE JOINT EFFECT

It is necessary to fire very small rate sticks (≈ 1 – mm diam) in order to obtain a complete diameter-effect curve for some of the explosives in Table I. One has the intuitive feeling that the presence of joints and pins in such sticks may significantly perturb the detonation wave trajectory. Such an effect (called the "joint effect") would result in underestimation of detonation velocity and overestimation of failure diameter. These considerations prompted a search for such an effect.

The experimental method was to record with a smear camera the progress of a detonation wave in a rate stick consisting of 4 to 6 cylindrical segments of the same diameter. The explosive was in the form of right-circular cylinders machined to size from singly-

Fig. 7. Correlation between R_f and R_c. The hashed lines correspond to plus or minus one standard deviation of the slope of the line. Where no error bars are indicated they are less than the dot size; where error bars are indicated they are those of Table I. The equation of the straight line is $R_c = (0.877 \pm 0.054) R_f$. An arrow to the left of an entry indicates that no sticks that failed were fired.

pressed billets. The cylinders ranged in length from 25.4 mm to 12.7 mm, and in diameter from 5.01 mm to 1.5 mm. Because PBX-9501 is a rather compliant explosive, the charges having diameters of 1.5 and 2 mm were measured on a contour projector with digital readout.

Each piece was supported at two places and was tied to a cradle with 50-μm copper wire to prevent buckling of the column under pressure. Boostering consisted of a small pellet of PBX-9404 initiated by a detonator which was held in a threaded mount. Good contact was secured at the joints between cylinders by inserting a thin metal shim in one of the joints and tightening the threaded detonator adaptor nut until slight friction was felt upon sliding the shim. The shim was then removed and the nut turned an amount calculated to advance the detonator a distance equal to the thickness of the shim.

The assembled rate stick was mounted before the smear camera with a precision magnification scale and a photographic resolution chart attached to the cradle. To ensure constant magnification along the stick, the whole assembly was arranged perpendicularly to the optic axis by use of a laser beam projected along the camera optical axis and reflected from the magnification scale.

When charge alignment was achieved, photographic resolution was checked on still photographs made on Panatomic-X film. Allowance was made for any deviation between the plane of the magnification scale and the surface of the rate stick by moving the camera axially an appropriate distance. Temperature was controlled to $23° \pm 1°C$.

Before firing the rate stick, the film was lightly fogged by rotating the mirror with the shutter open; a break in the camera slit produced a line indicating the writing direction along the film, and in the analysis of the firing record the writing speed at the location of the record was interpolated from a previous calibration.

Where pin records were taken, the switches were made of silver ribbon 3 mm wide by 10 μm thick. These were inserted in joints between stick segments and held in place with Eastman 910 adhesive.

The experimental space-time trajectories were fitted to the model

648

$$x(t) = \beta + Dt + \delta N, \qquad (3)$$

where N is the segment number on the stick (0, 1, 2, . . .), δ is the spatial joint effect, D is the detonation velocity, t is the time measured from some origin, β is the intercept at N = 0 and t = 0, and x(t) is the position of the detonation at time t. The assumptions of the model are that the detonation velocity is the same in the steady part of each segment and that there is an identical offset (possibly zero) at each joint.

Figure 8 shows the type of behavior to be expected from the model and the experiment if there is a significant joint effect. Figure 9 shows the results for PBX-9501 in terms of the time lag at a joint (i.e., δ/D). One sees that the effect is a strong function of
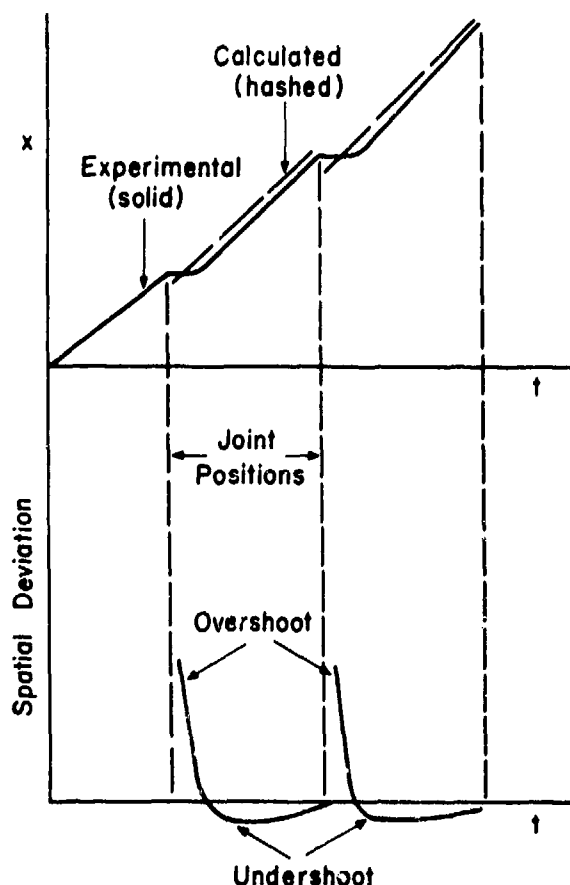
Fig. 8. Schematic of experimental and calculated detonation trajectories are shown in the upper portion. Anticipated deviations of experimental points about the model are shown in the lower portion.

stick diameter for the three sticks fired with clean-butt joints.

Furthermore, the one stick fired with glue and pin foils present in the joints shows a greatly enhanced effect. In this case, the error induced in the pin measurement of velocity due to the joint perturbations was $\approx 0.2\%$ (17 m/s).

One concludes that if one wishes to make highly precise measurements of detonation velocity or of failure diameter this effect must be avoided.

IV. BOOSTER EFFECT

There were indications in the work of Bdzil (15) that the steady-state velocity in a rate stick might be a function of the manner of boosting. If such an effect were present, some of the diameter-effect data would have to be reinterpreted. Since Bdzil's work was concerned with PBX-9404 and since the deviations about the fit were non-random for this explosive, it was decided that an experimental test should be made. This was done by strongly over- and underdriving two very long PBX-9404 rate sticks.
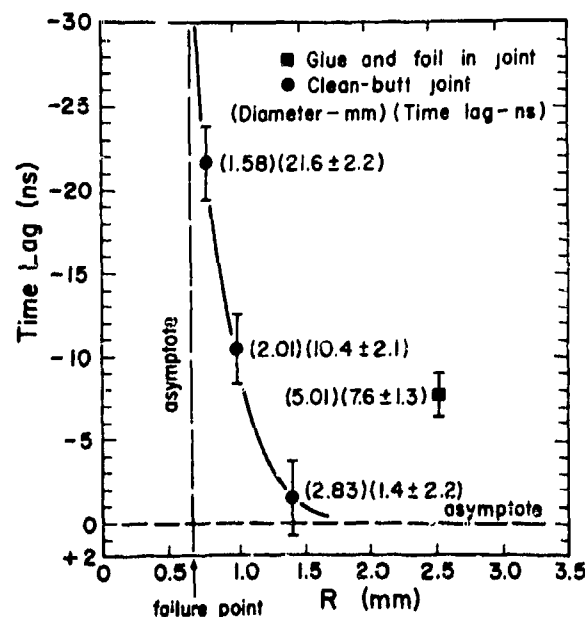
Fig. 9. Joint-effect for PBX-9501 as a function of stick radius and form of the joint. The position of the vertical asymptote is conjectural. The error bars correspond to one standard deviation.

The explosive consisted of 30 carefully machined right-circular cylinders, 25.4 mm diameter by 50.8 mm long, taken from two pressed billets. Density was measured for each piece by immersion in water. The uniformity of the billets was illustrated by the results: 7 pieces had densities of 1.845 g/cm³, 20 pieces 1.846 g/cm³, and 3 pieces 1.847 g/cm³.

These cylinders were randomized between two rate sticks, one of 13 pieces to be overboosted and one of 17 pieces to be underboosted. Underboosting was achieved by use of an Amatex/20 column 25.4 mm in diameter and 152 mm long. (The detonation pressure of Amatex/20 in plane geometry is ≈ 200 kbar.) Overboosting of the shorter stick was obtained by use of the booster diagramed in Fig. 10. (The design of this booster was due to B. G. Craig and produced a pressure of 404 kbar in PBX-9404.)

Wave curvature was measured at the end of each stick by means of a small mirror which was oiled and clamped to the terminal surface. Light from a small shocked-argon light source was reflected into a smear camera so as to produce an extinction record of the arrival of the detonation wave.

Precautions were taken with temperature control, film shrinkage, space resolution, camera writing speed, image magnification, and many other factors.

No large effect on the detonation velocity was observed; the measured velocities were 8.7735 ± 0.0004 and 8.7754 ± 0.0003 mm/μs for the overdriven and underdriven sticks, respectively. Note that the velocity results are not within two standard deviations of each other. The (central) front curvatures were measured and they were significantly different being 337 ± 3 mm (overdriven) and 355 ± 4 mm (underdriven). The larger velocity corresponds to a longer radius of curvature, as it should. It is unexpected that the overdriven stick shows a smaller radius of curvature and a lower detonation velocity.

V. FRONT CURVATURE AND REACTION-ZONE LENGTH IN X-0219

Front-curvature measurements were made on X-0219 (90/10 TATB/KelF 800) at stick diameters of 18, 25.4, and 50.8 mm. It was found that the detonation fronts near the charge axis are quite accurately represented by spherical waves. The three values of front curvature on the stick axis fall close to a straight line in the front-curvature-vs-stick-radius plane. The combination of detonation-velocity and front-curvature measurements allows one to calculate the reaction-zone length on the stick axis as a function of stick radius, if the WK theory (3) is accepted as valid.

In Fig. 11, the radius of curvature (S) is plotted vs the stick radius (R). From the limited amount of
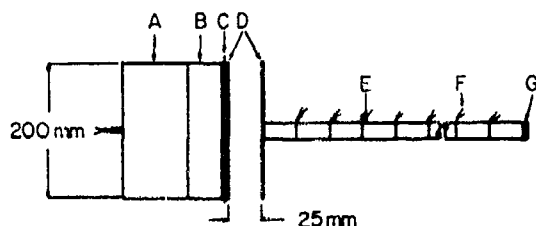
Fig. 10. Diagram of overboosted rate stick assembly.

A. Plane-wave lens
B. 50.8-mm PBX-9404
C. 0.38-mm polyethylene
D. 2.5-mm magnesium
E. Rate sections
F. 0.05-mm copper wire switches
G. Mirror
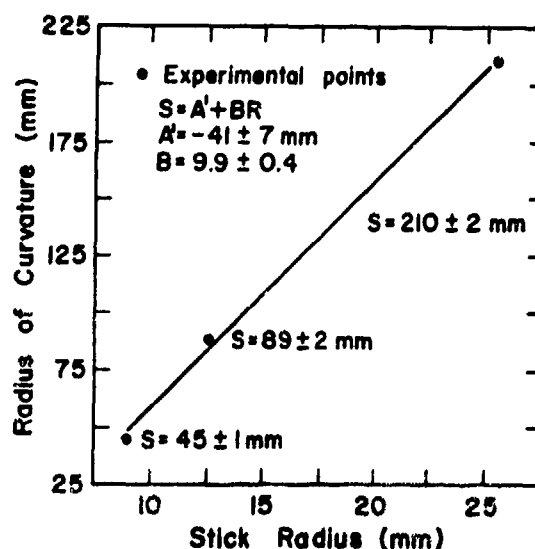
Fig. 11. Central front curvature vs stick radius for X-0219 rate sticks.

available data, one finds an approximately linear relationship between S and R. The curvatures were obtained by fitting a spherical wave model by the method of least squares to the central 50% of the end traces.

The WK relationship for the velocity decrement is

$$D(S) = D(\infty)[1 - \alpha\xi^*(S)/_S], \qquad (4)$$

where $D(S)$ and $D(\infty)$ are the detonation velocities with radii of curvature S and ∞, respectively, α is a constant dependent on the properties of the explosive, and $\xi^*(S)$ is the reaction-zone length on the stick axis.

It should be noted that the WK result has built-in assumptions more appropriate for a homogeneous explosive than for a heterogeneous one. This may be less of a deficiency for X-0219 than for other solid heterogeneous explosives, because TATB formulations exhibit some liquid-like behavior, e.g., linear diameter-effect curves, small velocity deficits before failure, and temperature dependent failure diameter.

Combining the diameter-effect curve, $D(R) = D(\infty)[1 - A/R]$, where $D(\infty) = 7.627 \pm 0.015$ mm/μs and $A = 0.269 \pm 0.023$ mm with the front-curvature relationship $S = A' + BR$, where $A' = -41 \pm 7$ mm and $B = 9.9 \pm 0.4$ gives the form

$$D(S) = D(\infty)\left[1 - \frac{BAS}{S - A'} \, /S\right]. \qquad (5)$$

Comparison of Eq. (5) with Eq. (4) allows one to make the identification

$$\xi^*(S) = \frac{BA}{\alpha} S/(S - A') \qquad (6)$$

or alternately

$$\xi^*(R) = \frac{A}{\alpha}[B + A'/R]. \qquad (7)$$

By use of the experimental values $P_{CJ} = 278$ kbars, $P_{spike} = 364$ kbars, $\rho = 1.915$ g/cm^3, $D = 7.627$ mm/μs, and a γ-law equation of state, one finds that $\alpha \approx 2$. Since A, α, and B are greater than zero and A' is less than zero, Eq. (7) represents a straight line in the the ξ^*-vs-1/R plane with negative slope. This shows

that the axial reaction-zone length (distance from shock to sonic locus) decreases with decreasing charge radius. A decrease in charge radius results in an increase in axial flow divergence and, as a result, the sonic plane moves closer to the shock. The intercept, given by AB/α, is the infinite-medium reaction-zone length and it has the numerical value $\xi^*(\infty) = 1.3$ mm. The result is compared in Table II with reaction-zone lengths obtained by independent means.

One notes that the measurements given in Table 2 break into two classes, i.e., those for zone lengths greater or less than 1 mm. It is felt that the first three entries are superior estimates. Consequently, it is asserted that the reaction-zone is abnormally long in some TATB formulations and of the order of 3mm.

ACKNOWLEDGMENTS

REFERENCES

1. H. Eyring, R. E. Powell, G. H. Duffy, and R. B. Parlin, Chem. Rev. *45*, 69 (1949). Also see R. B. Parlin, C. J. Thorne, and D. W. Robinson, Tech. Rept. No. 1, Institute for the Study of Rate Processes, University of Utah, (1952).

2. H. Jones, Proc. Roy. Soc. (London) *A189*, 415 (1947).

3. W. W. Wood and J. G. Kirkwood, J. Chem. Phys. *22*, 1920 (1954).

4. E. James, Jr., 2nd ONR Symposium on Detonation, p. 1 (1955).

5. A. W. Campbell, M. E. Malin, T. J. Boyd, Jr., and J. A. Hull, 2nd ONR Symposium on Detonation, p. 18 (1955).

TABLE 2

Reaction-Zone Lengths for TATB Formulations

Technique	Reaction-Zone Length (mm)	Formulation (wt %)	Density (g/cm^3)	% TMD	Reference
Wood-Kirkwood theory and axial front curvature measurements	1.3	90/10 TATB/KelF 800	$1.911 \rightarrow 1.915$	$98.20 \rightarrow 98.41$	This paper
Raytrace acoustics and PHERMEX rarefaction-wave experiment	5.	90/5/5 TATB/B^2 wax/Elvax	1.74	99.32	Ref. (16)
Magnetic probe measurement	3.3	95/5 TATB/KelF 800	1.895	97.58	W. C. Davis this symposium
Pushing inert plates of various thicknesses	0.3	90/10 TATB/KelF	1.915	98.41	Ref. (17)
Eyring theory and diameter-effect curve measurements	0.14	90/10 TATB/KelF 800	$1.911 \rightarrow 1.915$	$98.20 \rightarrow 98.41$	This paper

6. M. E. Malin, A. W. Campbell, and C. W. Mautz, 2nd ONR Symposium on Detonation, p. 360 (1955).

7. A. W. Campbell, M. E. Malin, and T. E. Holland, 2nd ONR Symposium on Detonation, p. 336 (1955).

8. E. A. Igel and L. B. Seely, 2nd ONR Symposium on Detonation, p. 320 (1955).

9. M. E. Malin, Los Alamos Scientific Laboratory, unpublished data, 1955.

10. L. E. Hatler, Los Alamos Scientific Laboratory, unpublished data, 1974.

11. C. W. Mautz, Los Alamos Scientific Laboratory, unpublished data, July 1956.

12. A. Popolato, LA-5711-PR, p. 8 (1974). This work was performed with funds provided by the Defense Advanced Research Projects Agency under DARPA Order No. 2502.

13. W. B. Cybulski, W. Payman, and D. W. Woodhead, Proc. Roy. Soc. *197,* 51 (1948).

14. L. N. Stesik and L. N. Akimova, Russ. J. Phys. Chem. (Eng. trans.) *33,* 148 (1959).

15. J. B. Bdzil, Los Alamos Scientific Laboratory, personal communication, April 1974.

16. R. Engelke and W. C. Davis, Bull. Am. Phys. Soc. *18,* 1483 (1973).

17. B. G. Craig, Los Alamos Scientific Laboratory, personal communication, June 1975.

ACCELERATION OF THIN FLYERS BY EXPLODING METAL FOILS: APPLICATION TO INITIATION STUDIES*

R. C. Weingart, R. S. Lee, R. K. Jackson,† and N. L. Parker
Lawrence Livermore Laboratory
University of California
Livermore, California

A simple, inexpensive system for studying initiation properties of explosives has been developed. The system uses electrically exploded metal foils to accelerate plastic flyer plates to velocities in the range 0.5-14 km/s. These flyer plates provide a well-defined stimulus upon impact with a high-explosive specimen. Peak pressures in the range 1-160 GPa and pulse widths in the range 0.005-0.5 μs, can be produced. The wide range of impact pressures and pulse widths permits investigations of explosives over a broad range of shock sensitivities. To demonstrate the capabilities of the system, results of initiation experiments on PETN (1.25-1.77 Mg/m³), TATB (1.80 Mg/m³), PBX-9404 (1.84 Mg/m³), and nitromethane, are reported.

INTRODUCTION

Over the past ten years we have developed at Lawrence Livermore Laboratory a simple, inexpensive facility for studying initiation properties of explosives (1,2). Our system uses electrically exploded metal foils to accelerate plastic flyer plates. These flyer plates provide a well-defined stimulus upon impact with a high-explosive specimen.

Studies of shock initiation require a pressure pulse of known amplitude and duration. Such pressure pulses are usually produced by explosive charges which drive a shock wave through a barrier (gap test) or by flyer-plate-impact experiments. A disadvantage of the gap test is that it produces a rather complex pressure pulse. The flow is divergent and the fall in pressure behind the shock depends on the geometry of the barrier-explosive system. By using a large, plane-wave explosive assembly a well-characterized

pulse may be produced, but such assemblies add considerable cost and complexity to initiation experiments.

Flyer-plate impact produces a pressure pulse that is more easily characterized, but the traditional means of accelerating flyer plates with gas guns or large, plane-wave explosive systems are time-consuming and require the use of expensive facilities. Our "electrical gun" offers the advantages of well-defined pressure pulses, but with experimental convenience and low cost.

ELECTRICALLY ACCELERATED FLYER-PLATE SYSTEM

The use of exploding metal foils to accelerate thin plates to velocities of 4-5 km/s was reported in 1961 by Keller and Penning (3) and Guenther et. al. (4). The design of our system is similar to the systems used by these earlier investigators. We have extended the velocity range to flyer velocities in excess of 14 km/s.

We use a 56 μF, 40 nH capacitor bank system as an energy source. A very convenient foil-flyer laminate is used, shown schematically in Fig. 1, which can be quickly and easily connected to the capacitor bank via a flat-conductor transmission line. Charging voltages vary from 7.5-40 kV and switching is accomplished with a low-inductance detonator switch.

The diagnostics used for our experiments consisted of optical and electrical measurements. The current through the foil was measured with an appropriate current-viewing resistor and voltage across the foil was measured by soldering leads to the transmission line, close to the edges of the foil, and connecting them to a voltage-divider network. Electrical signals were recorded on oscilloscopes. Time resolution was $\sim(10^{-8})$s and signal levels were accurate to about 5%. The streak camera was a Cordin Model 132 with a streaking rate of 20 km/s. Flyer velocity measure-

ments were made using the streak camera and recording flyer impact times at the top and bottom of a step in a plexiglass impact block (step flasher), or with a laser velocity interferometer (VISAR) (5). The VISAR measurements gave the most information, but were more difficult. Most of the calibrations of flyer velocity vs charging voltage or burst current density were made using the step flasher technique. VISAR measurements were used to check the velocity calibrations and to study the details of the flyer acceleration process.

The exploding foil element is aluminum and varies in area from 5.08 × 5.08 cm down to 0.03 × 0.03 cm. Foil thickness varies from 2-51 μm. The flyer plates are usually polyethylene terepthalate (PET) and range in thickness from 0.025-2.5 mm. Flyer diameter is determined by the diameter of the barrel which is clamped onto the foil-flyer laminate. The choice of

To camera

Lucite H.E. holder

H.E. pellet

Barrel

Foil — flyer laminate

Mylar flyer layer

Aluminum bridge foil

0.13 mm copper conductor front and back

0.75 mm Mylar between copper conductors

To camera

Holder	H.E. pellet	Holder
Barrel		Barrel
Foil — flyer laminate		

Flash gives flyer impact time

(Cross section)
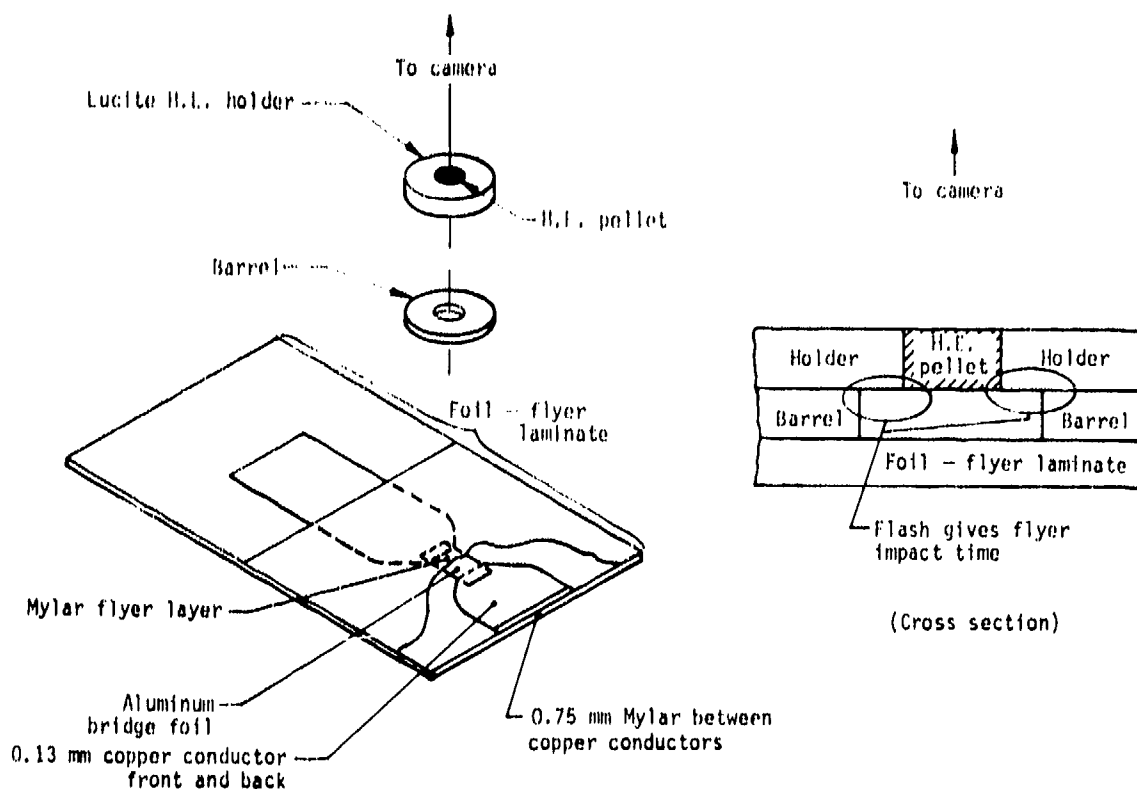
Fig. 1. Schematic diagram of the system used for initiation studies. The foil-flyer laminate is connected to an appropriate capacitor bank and the barrel and HE holder are clamped directly over the foil. When the foil explodes it drives the flyer down the barrel to impact the sample. The cross-sectional view shows how the flash produced by flyer impact can be viewed around the sample.

foil and flyer dimensions depends on the area one wishes to impact and the desired magnitude and duration of the pressure pulse.

The flyer velocity is determined by the selection of barrel length, burst current density, foil thickness, and flyer thickness. Figure 2a shows a laser-interferometer measurement of flyer velocity as a function of time for a 2.54-cm diameter, 0.025-cm thick flyer driven by a 2.54 $\times$ 2.54-cm $\times$ 51 μm foil, with 40 kV charging voltage on the capacitor bank. The arrow indicates the time at which the flyer reached the end of the 5-mm-long barrel. The electrical power expended in the exploding foil was measured simultaneously by monitoring the current and voltage across the foil, and is plotted in Fig. 2b. The electrical power dissipation is sharply peaked at the time the foil explodes (burst time) and the flyer does not show appreciable motion until shortly before burst. Due to the transit time of pressure waves through the 0.25-mm-thick flyer, it appears in the figure as if burst and flyer motion occur simultaneously, but the foil actually begins to expand somewhat earlier. From the early flyer acceleration we estimate an initial pressure behind the flyer of ~5 GPa, which gives an estimated shock transit time through the flyer of ~0.1 μs.

Inspection of Fig. 2a shows that the flyer continues to accelerate as it moves down the barrel. The selection of barrel length defines the range of velocities which can be obtained. Longer barrels increase both the upper and lower limits on the flyer velocity. Maximum barrel length is limited by instabilities which destroy flyer planarity. There is also a minimum feasible barrel length, dictated by two factors. First, to produce a well-defined pulse when the flyer strikes the target, it is necessary that the impact pressure be much greater than the pressure of the metal vapor pushing the flyer. If the barrel length is too short there may still be considerable pressure behind the flyer when it strikes. We can estimate the gas pressure from laser velocity interferometer measurements of the flyer acceleration history. For most of our experiments the residual gas pressure at impact is less than 10% of the impact pressure, so we neglect it. The other effect that puts a lower limit on barrel lengths is that the initial flyer acceleration becomes independent of bank charging voltage at higher charging voltages, as shown in Fig. 3. In some cases it is desirable to sacrifice velocity range in order to attain lower velocities, but one should be aware that for very short barrels (0.5 nm) the flyer velocity may
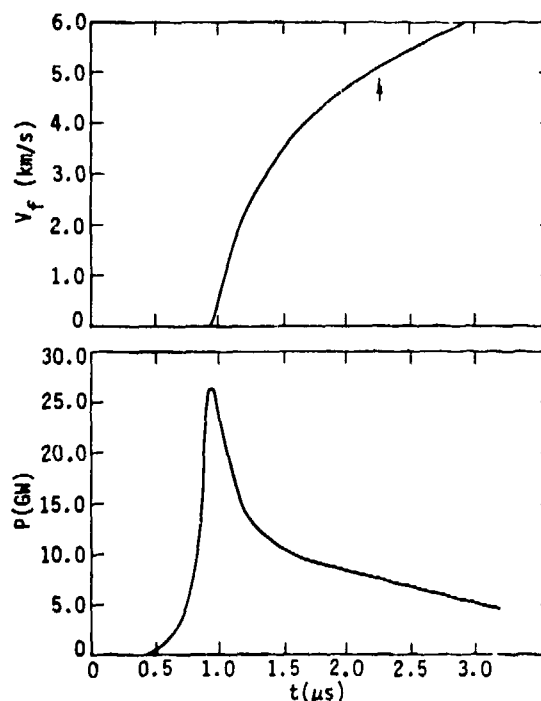
Fig. 2. (a) The upper curve is a laser-interferometer measurement of flyer velocity as a function of time for a 2.54-cm diameter, 0.025-cm thick flyer driven by a 2.54 $\times$ 2.54-cm $\times$ 51-μm foil with 40 kV charging voltage on the capacitor bank. The arrow indicates the time at which the flyer reached the end of the barrel.

(b) The lower curve is the electrical power dissipation in the exploding foil plotted as a function of time. Curves (a) and (b) were measured simultaneously and are plotted on the same time axis. Burst occurs at the peak of the power curve.

not change with charging voltage above a certain voltage.

The barrel diameter was varied over the range 6-40 mm. The width of the exploding foil element was chosen to be greater than or equal to the barrel diameter. If barrels with diameters much greater than the foil width are used, gases jetting around the flyer make it difficult to determine impact time, and adversely affect the characterization of the flyer impact.

The dependence of flyer velocity on flyer mass, foil mass, and burst current density can be described in terms of an electrical analog of the Gurney model

655
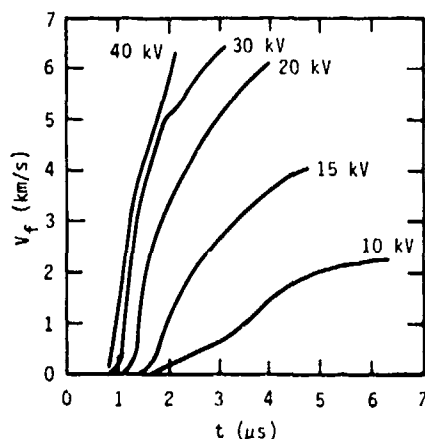
Fig. 3. Laser-velocity-interferometer measurements of velocity-time curves for different capacitor bank charging voltages. Above 20 kV the early acceleration is independent of charging voltage. The 0.025-cm-thick flyers were driven by a 0.95 × 0.95-cm × 51 μm foil.

suggested by Tucker and Stanton (6). The Gurney model (7) predicts the velocity of plates accelerated by a high explosive charge from a characteristic energy E_g that is related to the maximum velocity an explosive material is capable of delivering to a plate. The Gurney model assumes a linear velocity profile in the explosive reaction products and partitions kinetic energy between the plates and the products so as to conserve momentum. For a one-dimensional system, where an explosive sheet of mass C per unit area is backed by a tamper of infinite mass on one side and a plate of mass M per unit area on the other, the final plate velocity is

$$V_g = \sqrt{2E_g}\left(\frac{M}{C} + \frac{1}{3}\right)^{-1/2}. \qquad (1)$$

Tucker and Stanton assumed that the characteristic energy associated with an electrically exploded foil depended only on the burst current density J_B of the foil and wrote the Gurney equation in the form

$$V_g = \sqrt{KJ_B^b}\left(\frac{M}{C} + \frac{1}{3}\right)^{-1/2}, \qquad (2)$$

where the barrel length is assumed to be constant and where K and b are empirically determined constants. By fitting Eq. 2 to some of our data for electrically

accelerated flyer plates, they showed that the Gurney theory was applicable over a wide range of burst current densities. Figure 4 shows a fit to some of our data using Eq. 2. The Gurney theory has been very useful in estimating how the flyer velocity changes with changes in M, C, and J_B. Fitting the Gurney formula to experimental data is also a convenient way to summarize the results of a large number of velocity measurements.

Figure 5 shows a streak camera record of a typical flyer impact on a 1-mm step. Experimental parameters were: 40-kV charging voltage, 51-μm foil thickness, 0.25-mm flyer thickness, 25.4-mm barrel diameter and 5-mm barrel length. The error bars denote the standard deviation of impact times relative to the impact time at the center of the flyer, as determined from 25 individual shots. Over the central 22 mm we estimate the spread in impact times to be $2(10^{-8})$s.
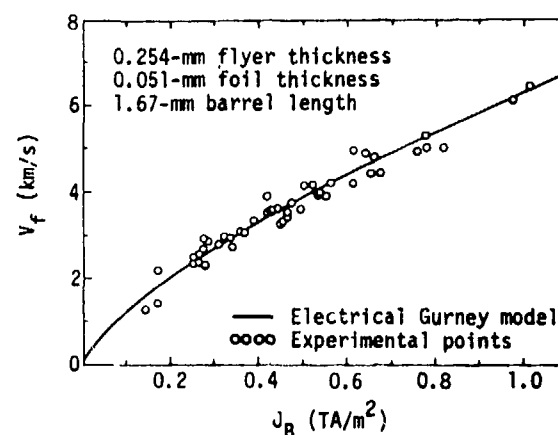
Fig. 4. Flyer velocity vs burst current density.

Fig. 5. Flyer impact on a 1-mm step.

656

INITIATION STUDIES

Figure 1 shows a schematic representation of the system used for initiation studies. The system consists of a foil-flyer laminate connected to an appropriate capacitor bank, a barrel, and a plexiglass (PMMA) holder for the high explosive (HE) sample. The initiation experiments, for the most part, involved impacting the thin flyers on the HE specimens and determining the flyer velocity threshold required for initiation. The transit time of the detonation through the sample was also measured.

Flyer thickness, and diameter are other experimental quantities which were varied. Flyer thickness determines the duration of the pressure pulse introduced into the sample. If the flyer diameter is large enough and the run to detonation is short enough so that edge rarefactions do not reach the center of the shock front before detonation occurs, one-dimensional initiation experiments may be performed. This condition was easily met in nearly all of the tests we report here. By reducing the flyer diameters, critical-initiation-diameter effects may be studied.

The onset of detonation was detected by coating the face of the HE pellet that faces the streak camera with a thin coat of $Al_2(SiF_6)_3$, a porous compound which gives a bright flash when strongly shocked. We recorded the light output for various shock pressures and found that no significant flash was produced for pressures below 20 GPa. A flash, therefore, is indicative of the high pressures associated with detonation. We also could confirm that a detonation had occurred from the transit time of the reactive shock wave through the HE sample. By transit time we mean the time between flyer impact and first detonation light. Flyer impact time was determined from the flash which the flyer produces on impact. For some experiments a flyer 10-mm larger in diameter than the HE sample was used and the flash was observed around the periphery of the sample as in Fig. 1. Flyers are typically flat to within 1 mm of their edge and the edges lag the central portion, so edge effects did not affect the measurement of impact time. For other experiments, two 1-mm diameter holes were drilled through the sample away from the diameter observed by the streak camera. Light pipes were inserted into the holes so that one end was flush with the impact surface of the sample and the other end was twisted back onto the slit line of the camera. The flash pro-

duced when the ends of the light pipes were impacted served to mark the time of impact.

A typical streak camera record of an initiation experiment is shown in Fig. 6. The barrel diameter was

Fig. 6. Typical streak camera record of an initiation experiment. The flyer velocity is well above initiation threshold. The streaking rate was 20 km/s, with time increasing downward. Flyer impact is at time t_i and detonation breakout is at time t_T.

35.6 mm and the sample diameter was 25.4 mm, so the intense light from the exploding foil and the flash at flyer impact could be seen around the periphery of the sample. At flyer impact time t_i the flash was followed immediately by a reduction in light intensity as the shocked plexiglass became opaque. Finally at t_T, the detonation wave broke out of the face of the pellet. The detonation breakout was nearly simultaneous over the face of the pellet, reflecting the simultaneity of flyer impact. The transit time of the detonation was $T = t_T - t_i$. The record shown in Fig. 6 is for a flyer velocity well above the threshold. For flyer velocities near threshold, the detonation breakout was rounded and was often very ragged, as if initiation occurred in isolated regions near the impact surface. The rounding of the detonation near threshold may be attributed to the effect of edge rarefactions. A ragged breakout could result from increased sensitivity near threshold to slight variations in flyer impact or sample homogeneity. When the detonation was ragged or curved, we still defined transit time as the time from flyer impact to the earliest detonation breakout.

The range of flyer velocities available from a given foil-flyer laminate determines the explosives which can be studied. Most of our work has been with a

657

laminate which we used to study TATB, a very insensitive explosive. This laminate, which we designate t] nigh-energy laminate, uses a 51 μm thick Al foil w.ose width and length are equal to the barrel diameter. With 0.25-mm flyer thickness, the high-energy laminate gives flyer velocities in the range 1.5-14 km/s. The barrel length was 5 mm or '.67 mm, depending on the desired velocity range.

We find that the flyer velocities from the high-energy laminate are too high to probe the initiation threshold of the more sensitive explosives. By using a 5.08 × 5.08 cm × 13 μm Al foil and a 51 μn thick flyer, we have produced a laminate which gives flyer velocities in the range 0.5-2 km/s when used with a 0.25 mm long barrel. With this laminate, which we will call the low-energy laminate, we have studied the initiation threshold of 1.25-1.70 Mg/m^3 PETN. It proved to be very difficult to measure flyer velocities below 1 km/s using step-flasher techniques, so the velocity calibration was made using the VISAR. In Fig. 7 we present flyer velocity as a function of burst
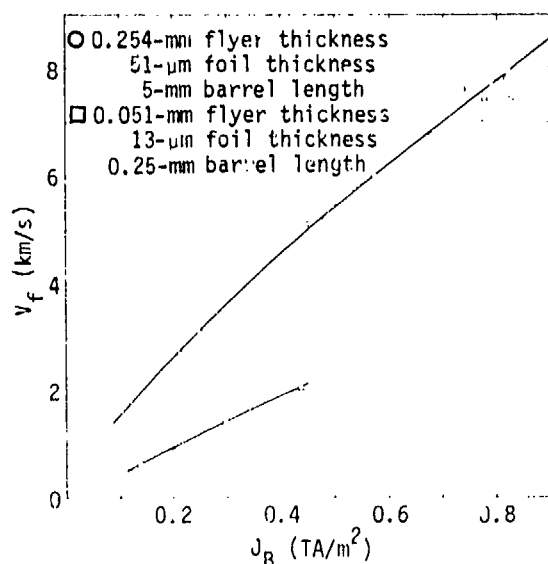
Fig. 7. Flyer velocity calibration curves. The upper curve is for the high-energy laminate with a 5-mm barrel, the lower curve is for the low-energy laminate.

current density for the low-energy laminate and also for the high-energy laminate with a 5-mm barrel length. The calibration curve for the high-energy laminate with a 1.67-mm barrel length was shown earlier in Fig. 4.

In practice, one can calibrate flyer impact velocity against either burst current density or capacitor bank charging voltage. In studying flyer performance the burst current density is more applicable, since one can use the Gurney equation to compare and summarize results for different foil cross sections and flyer thicknesses. Bank charging voltages are more easily and accurately measured, however. For routine initiation experiments we usually measured a voltage threshold for initiation, which we could convert to a velocity threshold through our calibrations. We routinely monitored current on each shot, however, so either a voltage or current calibration could be used. Experimental scatter was about the same using either calibration.

To demonstrate the range of pressure pulses that can be achieved we will consider the impact of the PET flyers on KEL-F fluorocarbon (polychlorotrifluoroethylene). KEL-F is a good shock impedance match to many common high explosives and the Hugoniot equation of state for KEL-F has recently been measured over a wide range of pressures (8). Peak impact pressures, plotted as a function of flyer velocity in Fig. 8, were computed using the Hugoniot data of Table 1. The Hugoniot equation of state of the PET film material (Mylar) used for the flyers has been measured only up to 2.5 GPa (9). Since the
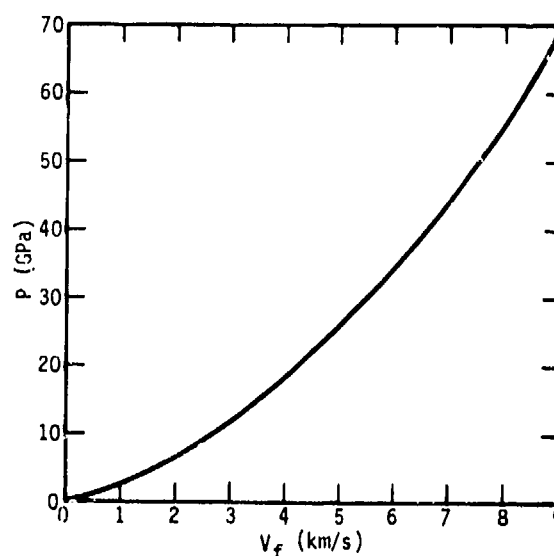
Fig. 8. Peak impact pressure vs flyer velocity for the impact of a PET flyer on a KEL-F target.

658

TABLE 1

Material	Mg/m^3	Equation: Ref. (8)
Polyester	1.4*	$U_s = 2.54 + 1.49\ U_p$ $0.7 < U_p < 2.6$ km/s
	1.4*	$U_s = 2.16 + 1.41\ U_p$ $3.4 < U_p < 5.1$ km/s
Polychlorotri-fluoroethylene (KEL-F fluorocarbon)	2.13	$U_s = 2.05 + 1.66\ U_p$ $0.6 < U_p < 2.9$ km/s
	2.13	$U_s = 2.51 + 1.51\ U_p$ $3.0 < U_p < 4.1$ km/s

*The data quoted in (8) were for a polyester resin of density 1.2 Mg/m^3.

pressure range of interest to us was mostly at higher pressures, we used the Hugoniot equation of state from (8) for clear cast polyester, a material made from the same polymer as the PET film (10). The data for clear cast polyester in (8) was for material of density 1.2 Mg/m^3, and we used these data for the PET film Hugoniot, adjusting the density to 1.4 Mg/m^3.

Using conservation of energy principles and the data of Table 1 we have also computed $P^2\tau$ as a function of flyer velocity, where P is the peak pressure and τ is the pulse duration. In Fig. 9 we show the range of $P^2\tau$ values produced by PET flyer impact on KEL-F. Since some investigators (11) have used a critical value of $P^2\tau$ (or critical energy fluence) as an initiation criterion, the curves of Fig. 9 permit an estimate of the range of explosives which n e studied with the electrically driven flyer plates. Approximate critical values of $P^2\tau$ for varic explosives are indicated on the right hand side of the figure. Figure 9 shows that the more insensitive explosives are more easily studied with the electrically driven flyer plates. For the more sensitive explosives the range of flyer velocities and flyer thicknesses which lie below the initiation threshold becomes very restricted. Threshold velocities for PETN are higher than indicated from Fig. 9 because the curves were calculated for a flyer impacting KEL-F, which is a poor impedance match to the lower density PETN samples.
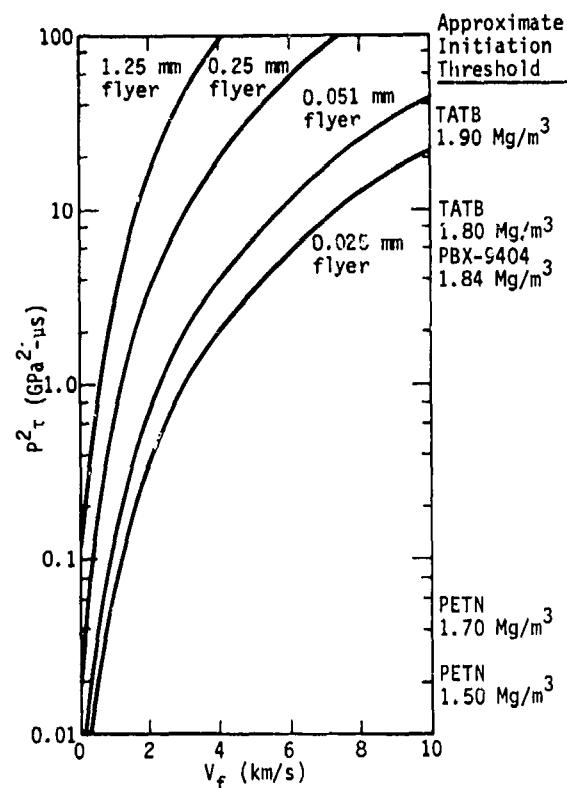
Fig. 9. $P^2\tau$ vs flyer velocity for the impact of a PET flyer on a KEL-F target, where P is the peak pressure and τ is the pulse duration. $P^2\tau$ was calculated using energy conservation principles and the Hugoniot data from (8).

RESULTS AND DISCUSSION OF INITIATION EXPERIMENTS

To demonstrate the versatility of electrically driven flyer plates in initiation studies, we will discuss experiments we have conducted on PETN (pentaerythritol tetranitrate), TATB (1,3,5-triamino; 2,4,6-trinitrobenzene), PBX-9404, and nitromethane.

PETN Initiation

The PETN samples were pressed into 10.2-mm-long, 25.4-mm-diameter cylinders from PETN powder with specific surface of about 6000 cm^2/g. Sample densities were 1.25, 1.50, 1.60, 1.70, and 1.77 Mg/m^3. The 1.77 Mg/m^3 PETN was initiated with 25.4-mm-diameter, 0.05-mm-thick flyers from the

high-energy laminate. These pellets were translucent so no light pipes were necessary. Flyer impact could be viewed directly through the pellet. The lower-density PETN samples were more sensitive, so it was necessary to use 35.5-mm-diameter, 0.05-mm-thick flyers from the low-energy laminate to probe the initiation threshold. Since the flyer diameter was 10 mm larger than the pellet diameter, flyer impact could be viewed around the periphery of the pellet, as was discussed in the previous section.

Figure 10 summarizes the results of our PETN initiation experiments. In Fig. 10 we plot excess transit time, $\Delta t = T-X/D$, as a function of flyer velocity, where T is the measured transit time, X is the pellet thickness, and D is the detonation velocity. If no detonation was observed, we denote the experiment by
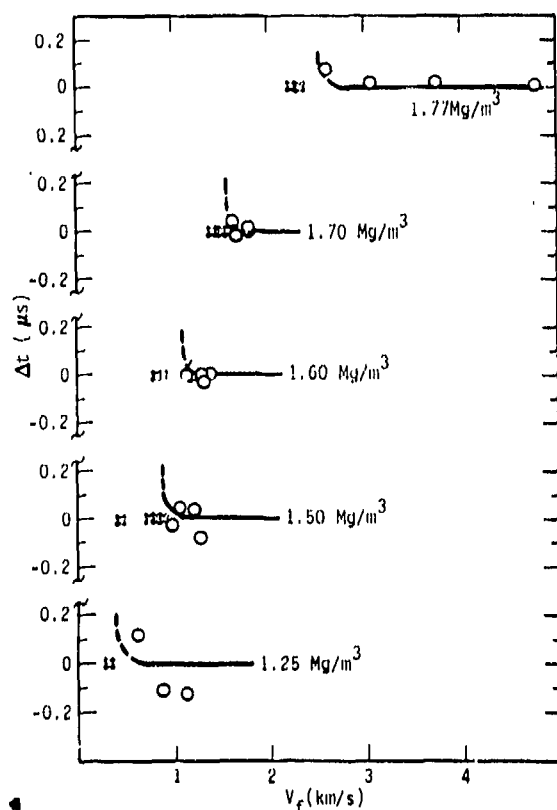
Fig. 10. Results of PETN initiation experiments. Excess transit time is plotted as a function of flyer velocity. If initiation did not occur, the experiment is denoted by an X on the velocity axis at the appropriate velocity.

an X on the velocity axis at the appropriate velocity. Detonation velocities were obtained from the tabulation in (12). The excess transit time remains small, even for flyer impact velocities near the initiation threshold. The initiation behavior appears to be dominated by the rarefaction which catches up to the shock front from the rear. Initiation or failure must occur close to the impact interface. The PETN data together with the TATB data presented below demonstrate the wide range of shock sensitivities which can be studied using electrically driven flyer plates.

TATB Initiation—Flyer Thickness Effects

The initiation of 1.80 Mg/m^3 TATB pellets (B-226 material) (13) was studied using flyer thicknesses of 0.05, 0.13, 0.25, 0.51, and 1.27 mm in conjunction with the high-energy laminate. The pellets were 25.4 mm in diameter and 19.1 mm long. Flyer impact time was detected with light pipes, as described earlier. The initiation threshold was observed to increase with decreasing flyer thickness, as shown in Fig. 11. The excess transit time near threshold increased with increasing flyer thickness. The thicker flyers produce a longer pulse, allowing a longer run distance to detonation and consequently a larger excess transit time.

TATB Initiation—Flyer Diameter Effects

In Fig. 12 we show the initiation threshold for 1.80 Mg/m^3 TATB pellets (B-317-Material) (13) as a function of flyer diameter. The high-energy laminate was used with a flyer thickness of 0.25 mm. The threshold was the same for the 25.4 and 12.7-mm flyers, but increased substantially as the flyer diameter was reduced.

PBX-9404 Initiation—Flyer Velocity Effects

The electrically driven flyers can supply peak pressures far in excess of the detonation pressure of any chemical explosive. In Fig. 13 we show excess transit time as a function of flyer velocity for 1.84 Mg/m^3 PBX-9404. The high-energy laminate with a flyer thickness of 0.25 mm was used. Flyer impact time was detected with light pipes, as described earlier. Near threshold the excess transit time increased as the flyer velocity decreased, as was observed in the TATB experiments. The flyer kinetic energy at initiation threshold was 0.64 MJ/m^2, in agreement with the results of other investigators (11,14).

Fig. 12. Flyer diameter effects. Flyers of 0.25-mm thickness and various diameters were impacted on TATB. Threshold velocity required for initiation is plotted vs flyer diameter.
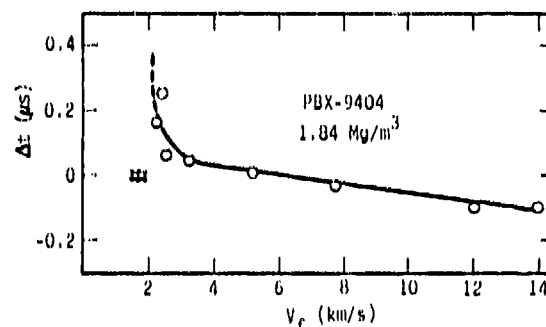
Fig. 13. Flyer velocity effects. Excess transit time vs flyer velocity is plotted for PBX-9404. Flyer thickness was 0.25 mm. Flyer diameters were 25.4 mm except for the 7.7 km/s experiment where a 12.7-mm-diameter flyer was used, and the experiments at 12 km/s and 14 km/s, which employed a 9.5-mm-diameter flyer. Failures are denoted by an X on the velocity axis at the appropriate velocity.

Fig. 11. Flyer thickness effects. Flyers of 25.4-mm diameter and various thicknesses were impacted on TATB. Excess transit time is plotted as a function of flyer velocity. Failures are denoted by an X on the velocity axis at the appropriate velocity.

As the flyer velocity was increased the excess transit time approached zero and then became negative, i.e., the detonation was overdriven. The crossover point occurred when the flyer velocity was about 6 km/s. This corresponds to an impact pressure of 37 GPa, which is very close to the measured Chapman-Jouguet pressure of 9404 (14). At the highest velocity of 14 km/s the peak pressure was 160 GPa and substantial overdrive occurred.

Nitromethane Initiation

Liquid explosives can be easily studied, using electrically driven flyer plates. To study nitromethane (NM) initiation, we used the same experimental configuration as in Fig. 1. The HE holder was made from a polyester material, which is not chemically attacked by the NM, a 13 μm PET film was stretched and bonded across the bottom, and a polyester cover was bonded over the top of the holder. Two small holes were drilled in the cover so that NM could be injected through one hole and air could escape through the other. Since the NM was transparent, flyer impact could be observed directly and detonation arrival was detected by the opaqueing of the cover plate at shock arrival. The high-energy laminate was used, with a 25.4-mm-diameter barrel and a 0.25-mm-thick flyer. Figure 14 shows the initiation of commercial-grade NM where the flyer velocity was 4 km/s, giving a peak pressure of 13 GPa. Impact pressures of 9 GPa initiated the NM, but the initiation was very ragged. We have not performed enough experiments to determine a meaningful initiation threshold.

Fig. 14. Streak camera record of a nitromethane initiation experiment. Flyer velocity was 4 km/s, giving a peak pressure of 13 GPa. Flyer impact is at time t_I and the detonation wave reaches the cover plate at time t_T.

SUMMARY AND CONCLUSIONS

We have developed a simple, inexpensive facility for studying initiation properties of explosives. Our system uses electrically exploded metal foils to accelerate plastic flyer plates to velocities in the range 0.5-14 km/s. These flyer plates provide a well-defined stimulus upon impact with a high-explosive specimen. Peak pressures in the range 1-160 GPa and pulse widths in the range 0.005-0.5 μs can be produced. The wide range of impact pressures and pulse widths permits studies over a broad range of shock sensitivities. To demonstrate the capabilities of the system we report results of initiation experiments on PETN (1.25-1.77 Mg/m^3), TATB (1.80 Mg/m^3), PBX-9404 (1.84 Mg/m^3), and nitromethane.

Our primary use of electrically driven flyer plates has been as a convenient means of ordering HE compositions according to their shock sensitivity. Within the last year we have conducted ~900 initiation experiments with our electrical system, a number that would be difficult to match with any other system capable of one-dimensional initiation studies. By varying the flyer diameter we have also studied some of the two-dimensional aspects of initiation and the propagation of detonation waves.

Some of the unique capabilities of the electrical system will be useful in testing theoretical models of initiation and detonation. The short-pulse, high-pressure capability permits experiments, where for some explosives, the width of the pressure pulse is smaller than the reaction zone width, or where the peak pressure is substantially higher than the detonation pressure. Results of such experiments extend the range over which initiation models can be tested. Electrically driven flyer plates show promise as a standard sensitivity test. The system is relatively inexpensive, experiments can be performed quickly and cost, and the shock stimulus is well characterized.

REFERENCES

1. R. C. Weingart, Rpt. UCRL-5000-69-7, University of California, Lawrence Livermore Laboratory, Livermore, Ca (1969).

2. J. R. Stroud, Rpt. UCRL-5000-70-10, University of California, Lawrence Livermore Laboratory, Livermore, Ca (1970).

3. D. V. Keller and J. R. Penning, Jr. in *Exploding Wires, Vol. 2*, W. G. Chase and H. K. Moore [Eds.] , (Plenum Press, New York 1962), p. 263.

4. A. H. Guenther, D. C. Wunsch and T. D. Soapes in *Exploding Wires, Vol. 2*, W. G. Chase and H. K. Moore [Eds.] , (Plenum Press, New York 1962), p. 279.

5. L. M. Barker and R. E. Hollenbach, J. Appl. Phys. 43, 4669 (1972).

6. T. J. Tucker and P. L. Stanton, Rpt. SAND 750244, Sandia Laboratories, Albuquerque, N.M.

662

7. R. W. Gurney, Rpt. 405, Battelle Memorial Institute, Columbus, Ohio, 1943.

8. W. J. Carter, S. P. Marsh, and R. G. McQueen, Private communication.

9. Frank Davies, Rpt. D2-125304-1, The Boeing Company, Seattle, Wash. 1969.

10. K. J. Mackenzie, Modern Plastics Encyclopedia 52 135 (1975).

11. F. E. Walker and R. J. Wasley, Explosivstoffe, 1, 9 (1969).

12. B. Dobratz, Rpt. UCRL-51319, University of California, Lawrence Livermore Laboratory (1974).

13. R. K. Jackson, *et. al.*, Rpt. UCRL-77611, University of California, Lawrence Livermore Laboratory, (1976), (to be published in Proc. *Sixth Symposium on Detonation*, San Diego, Ca, 1976).

14. L. G. Green, E. J. Nidik, Jr., and F. E. Walker, Rpt. UCRL-51522, University of California, Lawrence Livermore Laboratory (1974).

MULTIPLE-EXPOSURE IMAGE-INTENSIFIER CAMERA

O. G. Winslow, W. C. Davis and W. C. Chiles
Los Alamos Scientific Laboratory
University of California
Los Alamos, New Mexico 87545

An image-intensifier camera with light gain of a few thousand times and exposure pulse times as short as 8 ns has been applied to the study of high explosives. A unique feature is the recording of the self-light of detonating explosive, which appears as a line in the photograph, with up to ten multiple exposures independently spaced in time. The light gain of the intensifier allows recording detonation light with very short exposures even when the light is very weak, too weak for ordinary photography.

Multiple-exposure photography of the self-light of detonation waves has proven a useful technique for the study of detonation phenomena. In solid explosives the light from the detonation emerges from the explosive surface only in a very thin line near the intersection of the wave and the surface, so that a single-exposure photograph records a single narrow line corresponding to that intersection. Multiple exposure records a set of narrow lines corresponding to the intersections at the separate times of exposure. The resulting photograph looks much like a contour map, and can be interpreted easily.

The camera we have used employs a commercial image-intensifier tube purchased from ITT, Electro-Optical Products Division, Tube and Sensor Laboratories, which is about 18-mm diameter, resolves about 20 line pairs/mm over the whole frame, and has a useful light gain of up to about 1000. The image-intensifier tube is a simple proximity-focused diode, with a multi-channel plate introduced between the photocathode and the phosphor. A diagrammatic representation of the tube is shown in Fig. 1. The multi-channel plate consists of a dense array of tiny channels, each about 10-μm internal diameter and 1 mm long, so the aspect ratio is 100. An electron from the photocathode, proximity focused on the multi-channel plate immediately behind the spot
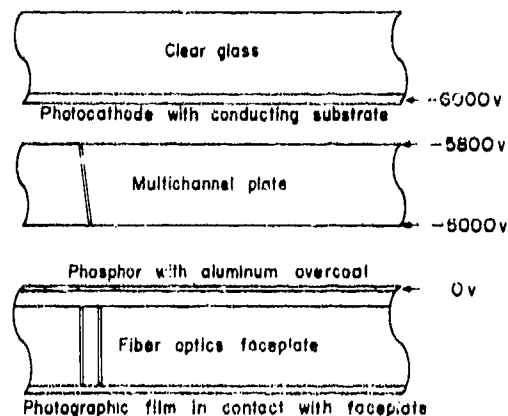
Fig. 1. Image intensifier tube.

where it was produced on the cathode, enters a channel and, because the channel is oriented at an angle to the electron direction, travels through the channel making many reflections at a glancing angle on the channel wall. At each of these reflections secondary electrons are produced, with the number controlled by the voltage applied across the multi-channel plate. The group of electrons emerging from the channel is proximity-focused to a spot on the phosphor behind it, where they are converted to light. Thus the multi-channel plate acts as an imaging light amplifier. The

plate supporting the phosphor is a fiber optics array, so the film is simply pressed against the array, with no other optics needed. The system used only one lens, the objective which images the subject on the photocathode.

The electrical system provides three independent accelerating potentials to the tube: 1) from photocathode to multi-channel plate, which is gated for the exposure time from a back biased condition; 2) across the multi-channel plate, which is varied to adjust the electron gain in the plate for proper exposure; and 3) from multi-channel plate to phosphor, which is held fixed. The gate pulse for potential 1 is derived from a length of coaxial cable; the length of the cable determines the exposure time. The cable is discharged through three avalanche transistors in series to obtain the pulse, which is then fed to the tube. For multiple exposures, a diode mixer is inserted between the pulsers and the tube, so that the pulsers don't interact. The pulse length is about 11 ns/m of cable, and cables from 0.6 m to 60 m are used. An artificial lumped-element cable is used to provide a 30-μs pulse for taking set-up pictures, because dc operation was found to degrade the photocathode, apparently by heating. Potential 2 is used to control the gain of the system for proper exposure, and the gain can be varied more than 100 fold while maintaining even gain over the full picture. With the photocathode back biased, the spontaneous production of light by the multi-channel plate and the phosphor is low enough that there seems to be no need to gate potentials 2 and 3, as the film shows no exposure in the several minutes these potentials are on. A block diagram of the complete system is shown in Fig. 2.
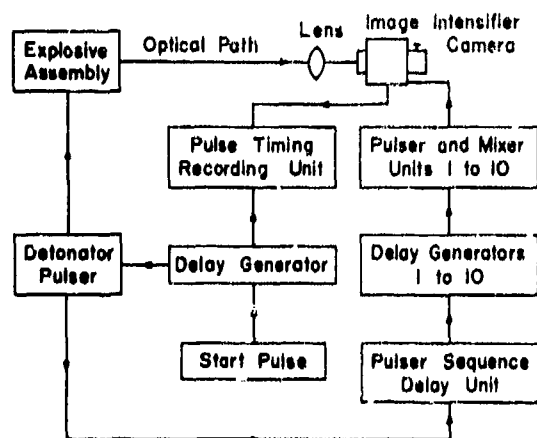
Fig. 2. Block diagram of system.

With its combination of good resolution and high light gain this camera has proven very useful in the single pulse mode, especially because it allows enormous simplification of the lighting for the subject. Ordinary outdoor illumination is adequate for exposures of about 1/2 μs, and small amounts of additional light make possible exposures down to a few ns. Weakly self-luminous objects, such as detonation fronts in diluted liquid explosives, are easy to photograph with short exposures.

The multiple-exposure mode has proven extremely useful for studying the progress of detonation waves while their shape is changing as they run. The light recorded in the self-light produced by the detonation, with the usual brightly luminous air-shock light removed by immersing the explosive in water or another transparent liquid. The detonation front produces light because it is hot, but most of the light is not seen because it is absorbed inside the explosive. Only when the wave is very near a surface can light be seen through the slightly transluscent explosive. The detonation products are also hot and emit light. As they expand, driving a shock wave into the water, they cool rapidly. In most explosives, including high-density TNT, Composition B and PBX-9404, light from the front is brighter than that from the expanding products even right behind the front, and photographs show light through the transluscent explosive ahead of the wave followed by a very sharp cut-off of intensity where the expansion of products begins at the intersection. In the high-density plastic-bonded TATB compositions, however, the light from the front is dim and the explosive is nearly opaque instead of transluscent, so the exposure has to be increased to the point where the light from the expanding products is recorded. Then there is almost no precursor light showing through the explosive ahead of the wave, and there is some light from the products behind it. Thus the intensity-vs-distance profile for TATB compositions seems to be the opposite of that for other explosives. At any rate, either type of explosive gives a narrow line with a sharp leading or trailing edge showing where the wave intersects the surface.

The ability to make multiple, short-duration photographs of the position of a detonation wave has provided a new tool for studying explosive phenomena. Some applications are presented to illustrate the usefulness of this technique. In the first, the relative timing of an electrical "pin switch" signal and the

optical signal from detonating PBX-9404 was measured. Figure 3 shows the results of the experiment.
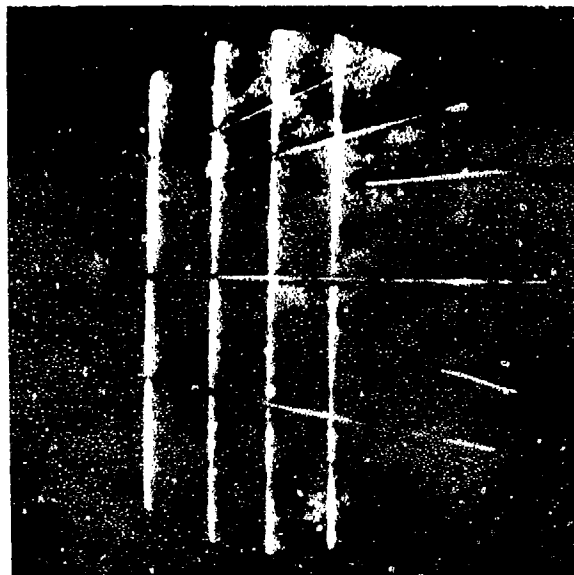
Fig. 3. Multiple-exposure photograph of detonation wave. The bright lines show the intersection of a line detonation in a thin slab of PBX-9404 with the explosive surface. Additional general illumination is provided by exploding bridgewires. The wires running along the surface of the explosive are used to record the time when the high-conductivity wave reached them, and that time was compared with the position of the bright light signal. The field of view is 29-mm diameter. The exposures are 0.4 μs apart, and the black stripe at the right edge is a reference tape for position measurements. Shot B-7826.

To obtain this picture, general illumination from a group of exploding bridgewires in water was used, and the camera was triggered four times at intervals of about 400 ns. The whole assembly was immersed in mineral oil to prevent light from an air shock. The four vertical bright lines in the pictures are the self light of the detonating explosive seen in the four successive exposures. The dark line at the right-hand edge of the pictures is a reference tape used to relate the measured positions of the pins, through the measured magnification, to the positions of the explosive self light. The pins in Fig. 3 are wires about 0.4-mm diameter, lying on the explosive surface, so the end of the contact line at the center of the wire is used as the pin position.

The results of the experiments are: (1) The time between electrical and optical signals for PBX-9404 is zero within 6 ns. (2) The resistance change in the reaction zone of PBX-9404 takes place not more than about 50 μm from the line where the light cuts off. (3) Measurements of edges to about one thousandth of the picture diameter are possible for pictures taken with the 18-mm image-intensifier tube, and local distortion does not seem to be a problem.

Figure 4 shows a corner-turning study of Composition B. The steady detonation wave in a thin slab of explosive meets a larger piece at an angle, as shown in the diagram, Fig. 4a. The 10-exposure photograph,
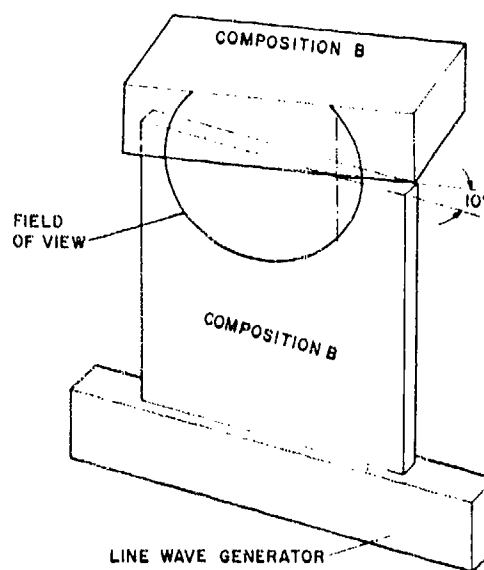
Fig. 4a. Corner turning in Composition B. The line detonation in the thin (~4 mm) slab of explosive intersects the thick piece above at an angle, so the wave can be seen by multiple exposure at several different distances from the intersection.

Fig. 4b, shows how the wave develops in the upper plate. Each bright line shows the intersection of the wave with the surface of the explosive at a known instant of time, and the set of lines can be measured to give the time-dependent trajectories of the detonation wave as it turns the corner. The gap in Figs. 4a and 4b is from a black tape positioned at the intersection of the front surfaces of the two pieces. The field of
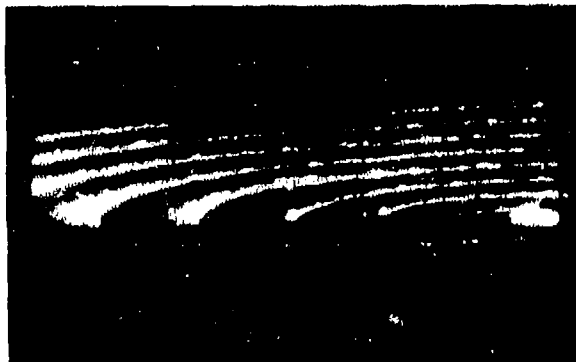
Fig. 4b. Corner turning in Composition B. The photograph shows ten exposures, the first two of which show the line detonation in the thin slab. Shot C-4560.

view is about 70 mm, and the exposures are 0.25 μs apart. The development of lag in the wave at the free lower surface of the top piece can be seen in the fourth to seventh exposures.

ACKNOWLEDGEMENT
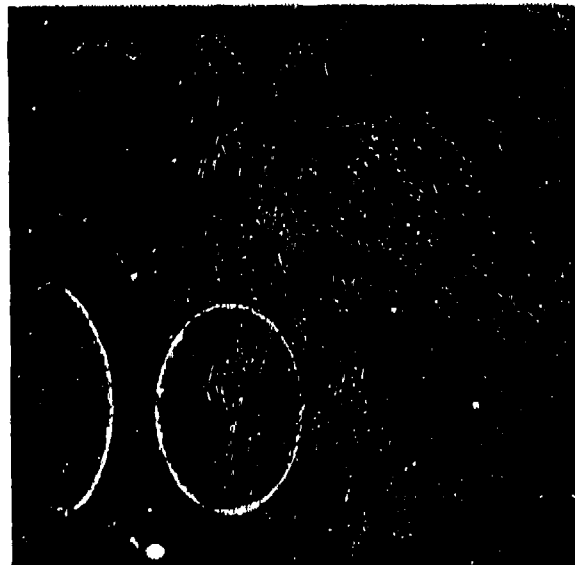
Fig. 5. This figure shows an oblique view of a block of X-0290 (TATB/Kel-F 95-5), which was initiated at a point on the back face. This type of photograph is much easier to interpret than the corresponding smear-camera photograph for asymmetry in the initiating system and for acceleration of the wave as it progresses. Also, this photograph shows the self-light of the explosive, which is too weak to record using a camera without the light gain of the image intensifier.

THE USE OF A DUAL-DELAY-LEG VELOCITY INTERFEROMETER
WITH AUTOMATIC DATA REDUCTION IN A HIGH-EXPLOSIVE FACILITY*

R. A. Lederer, S. A. Sheffield, A. C. Schwarz, and D. B. Hayes
Sandia Laboratories
Albuquerque, New Mexico 87115

A Velocity Interferometer System for Any Reflector (VISAR) has been developed for use in a high-explosive facility. This VISAR has two unique features: (1) a dual delay leg which allows for unambiguous determination of integral fringes associated with shock-wave arrivals, and (2) automatic data acquisition and reduction. The VISAR was tested by measuring the multiwave structure produced by a polymorphic phase change in iron at 13 GPa.

INTRODUCTION

In the past few years, the use of velocity interferometry as a diagnostic tool has become commonplace in shock-wave experimentation where material velocities reach a few millimeters per microsecond. One recently developed instrument for doing this is the Velocity Interferometer System for Any Reflector or VISAR (1, 2). A VISAR senses the motion of a surface by optical analysis of light which has been reflected, and, hence, Doppler-shifted by that moving surface. An ordinary Michelson interferometer can also analyze Doppler-shifted light, but in a different way. A Michelson interferometer produces interference fringes by mixing the Doppler-shifted light with a portion of the virgin light beam. This produces an interference fringe phase angle proportional to the moving surface displacement. In shock experiments, the frequency of such interference fringes is ordinarily much too high to be useful. A VISAR, on the other hand, uses beam splitters and a delay leg to produce interference fringes by mixing light Doppler shifted at time t with light Doppler shifted at time $t - \tau$ where the delay time τ is of the order of a few nanoseconds. The resulting interference fringe phase angle is proportional to the surface velocity. Continuous

records of surface velocity with an accuracy of a few percent may be achieved.

We have developed a VISAR which incorporates state-of-the art technology (1). In addition, two features which greatly enhance its usefulness are: (a) dual delay legs and (b) automatic data acquisition and reduction.

The principle of a dual-delay-leg interferometer is simple; the Doppler-shifted light is split in two upon its return from the moving surface, and a separate VISAR system is built for each half of the beam. The dual-delay-leg circumvents a drawback of a single-delay-leg system. That drawback is the inability of the system to record integral fringes during the burst associated with the discontinuous jump in particle velocity at shock fronts. In the dual-delay-leg system, if the total number of fringes is kept small, and if the two delay times τ do not form a ratio of small whole numbers, then the uncertainty introduced by the loss of integral fringes at discontinuous shock arrivals can be avoided and an accurate, unambiguous measurement can be made of the shock jump magnitude (3), as well as of the following waveform.

Automatic data reduction is accomplished by recording photomultiplier outputs directly on Tektronix R-7912 waveform digitizers which, in turn, are coupled

directly to a PDP-11/40 computer. Data reduction and hard-copy plots of the velocity history are obtained within seconds after an experiment rather than after several hours as is usually required to digitize oscilloscope pictures and to process data by use of an interactive computer.

After describing the specific optical arrangement for our dual-delay-leg interferometer, the results of a single experiment will be described.

OPTICAL LAYOUT

The optical layout of our dual-delay-leg interferometer is shown in Fig. 1. In order to understand the way in which it operates, we will first review the established principles of operation of a single-delay-leg VISAR (1). The Doppler shifted light enters the VISAR at point 2. Since the optical train will use polarized light, it is desirable to remove any remnant of polarization which might have been introduced by either the laser or by the reflecting surface. Such background polarization might cause fluctuations in intensity at later polarizing stages. To accomplish this, the returning beam is passed through a polarization scrambler denoted by point 6. At point 10, a fraction of the beam is extracted and sent to the intensity monitor. The intensity monitor is used to establish variation in peak-to-peak interference pattern amplitudes, allowing an accurate determination of phase angle to within a small fraction of a fringe.

After passing through a spike filter at point 8, the beam is polarized at 45° by the polarizer denoted 9. After being polarized, the beam enters the main beam splitter. We can trace the paths in this VISAR. One-half of the light passes along each path 13-14-18-14 and 13-14-16-14. Along the path 14-16-14, the beam must pass through the etalon denoted 15. The etalon is made from fused quartz and delays the light. The path lengths are chosen so that the light passing along that leg suffers a delay, τ, over and above that experienced by the light passing along the leg 14-18-14. The delay, τ, is related to the etalon length (1).

Notice that the light which traveled along the undelayed leg passed once through a quarter-wave plate. The index of refraction of the quarter-wave plate is different for P than for S polarized light. The quarter-wave plate thickness has been chosen so that a 90°

phase difference is produced between those P and S components of polarization. The recombined beams enter the polarized beam splitter, 24, and the P and S components are recorded separately on photomultipliers called DATA 1 and DATA 2, containing identical information but in a different format: the interference fringes on DATA 1 and DATA 2 are 90° out of phase because of the action of the quarter-wave plate.

A dual-delay-leg interferometer is composed of two separate VISARs, each of which is supplied one-half of the returning Doppler shifted light. As is seen in Fig. 1, the two interleaved VISAR systems are similar in operation, although they are not identical in layout. The entire VISAR system is shown in the photograph of Fig. 2, where the laser and power supplies occupy the lower compartments.

DATA ACQUISITION

One of the most serious drawbacks of a VISAR for routine application is the laborious process of data reduction. It is necessary to calculate the phase angle of an interference fringe history to a small fraction of a cycle in a situation where the intensity, hence peak-to-peak intensity, is varying. We have eliminated the difficulty of reading oscilloscope records by recording all information on Tektronic R-7912 digital recorders. These digital recorders are in turn coupled directly to a PDP-11/40 computer. Data acquisition and reduction are automatically accomplished in seconds, far different from the usual hours required to digitize oscilloscope pictures and proceed by normal methods. Figure 3 shows a flow diagram of the digital interfaces.

Experiment

The intent of our first experiment was to verify the performance of the VISAR. Normally, explosive-driven shocks are subject to considerable variability and therefore are not suitable for calibration purposes. We have overcome this difficulty by tailoring the shock profile by using a plane-wave lens to drive an iron specimen.

At 13 GPa, iron undergoes a polymorphic phase transformation, and the result of that phase change is to produce a multiwave structure. The first large wave which traverses the iron is always at the phase transformation pressure, 13 GPa.

669
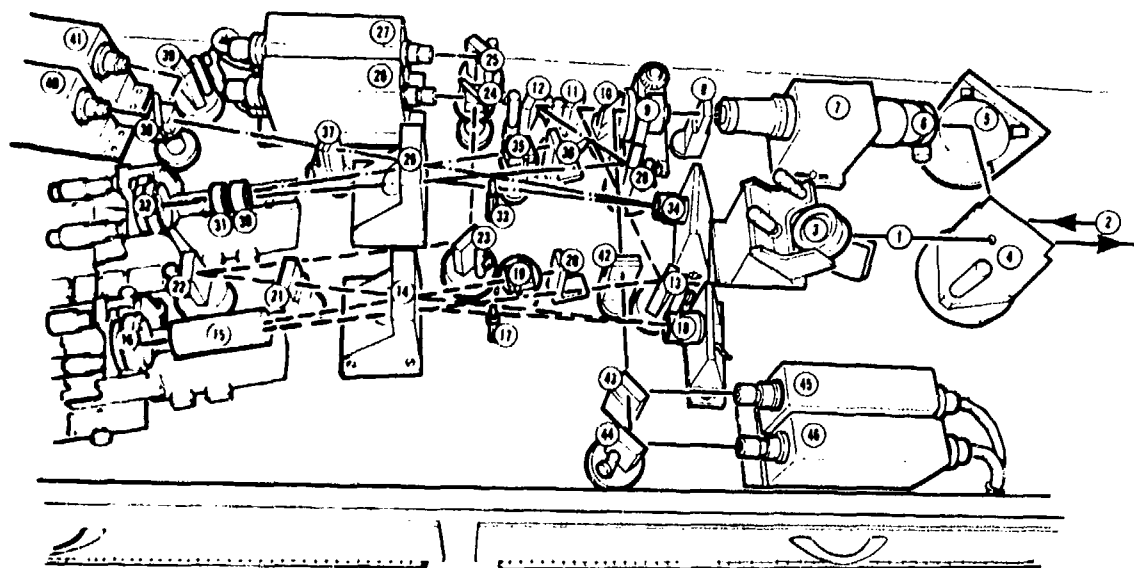
Key to Figure 1

		Delay Leg 1	Delay Leg 2	
1	Laser Beam			
2	Reflected Beam Returning (Spectral)			
3	Adjustable Mirror	13	28	Mirror
4, 5	4″ Mirrors	14	29	Large Beam Splitter
6	Polarization Scrambler	15	30, 31	Etalon
7	Beam Reducing Telescope	16	32	Adjustable Mirror
8	Spike Filter	17	33	1/4 Wave Plate
9	Polarizer	18	34	Translating Mirror
10, 11	Beam Splitter	19	35	Polarized Beam Splitter
12	Mirror	20	36	Fringe Viewing Screen
42	Focusing Lens	21	37	Focusing Lens
43	Beam Splitter	22, 23		Mirror
44	Mirror	24	38	Polarized Beam Splitter
45, 46	Photo Multipliers	25	39	Mirror
		26, 27	40, 41	Photo Multiplier

Fig. 1. Dual-delay-leg VISAR (optical table)

The plane-wave lens and 2.5-mm-thick iron specimen are shown in Fig. 4.

Figure 5 shows the x-t diagram for the waves in iron as they interact with the free surface (5). Inspection of the figure shows that there are many details in the resulting free surface motion. The first arrival is the elastic precursor. When the elastic precursor interacts with the free surface, the reflection proceeds backward and perturbs the oncoming 13-GPa wave. The result is that a new elastic precursor forms and reaches the free surface a short time prior to the arrival of the 13-GPa wave. The final wave to arrive is the loading wave produced by the plane-wave lens. Barker's experimental result, the free surface velocity versus time/specimen thickness, is shown in Fig. 6.

670
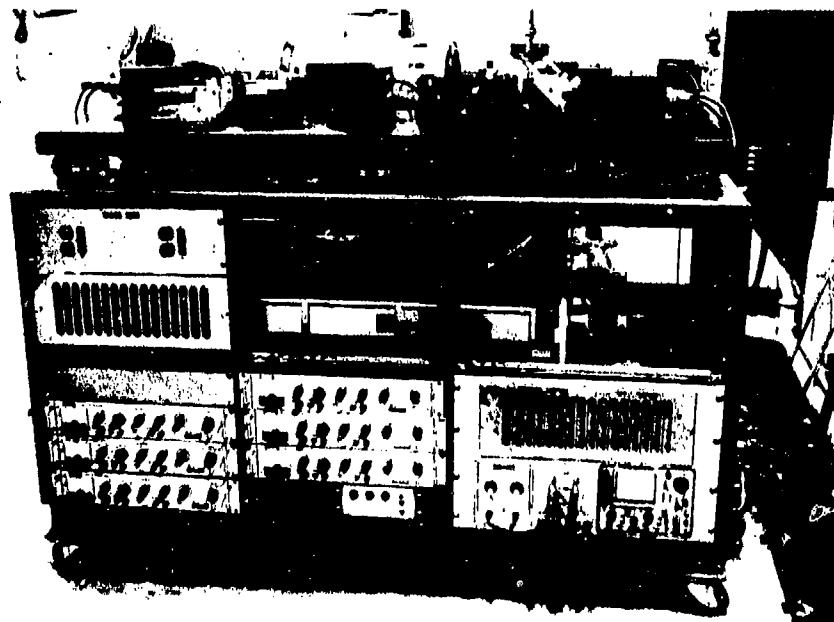
Fig. 2. Dual-delay-leg VISAR
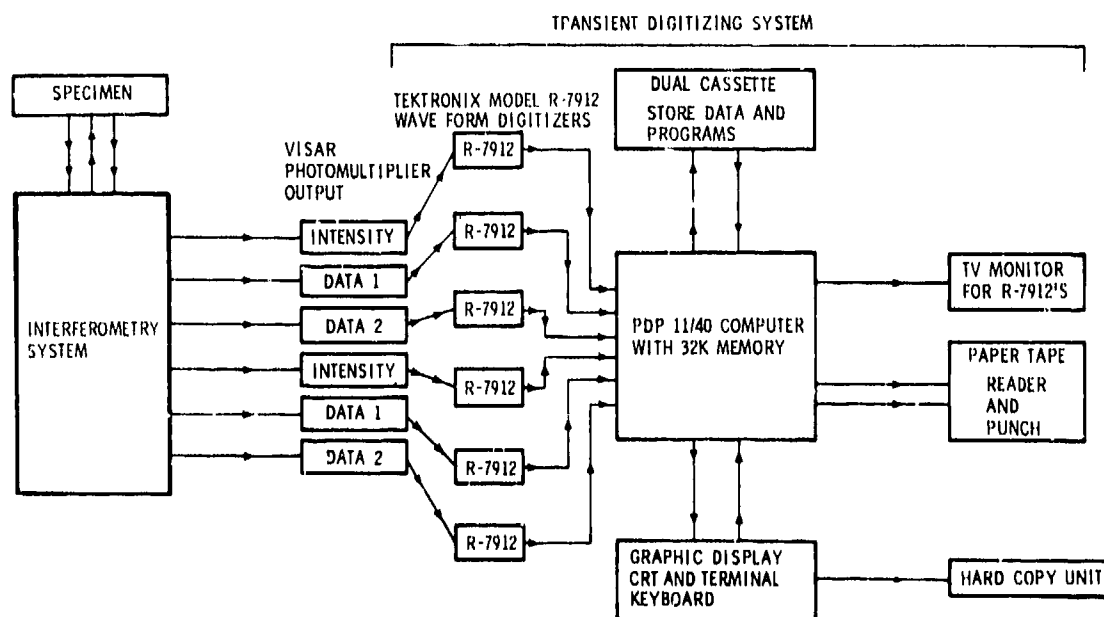
Fig. 3. VISAR instrumentation system

671

Figure 7 shows the six channels of information recorded during our experiment. DATA 1 and DATA 2 from one delay leg contain the same information as DATA 1 and DATA 2 from the second delay leg. As can be seen from Fig. 7, the two records can only be made to coincide if a fringe burst occurred at t = 0.2
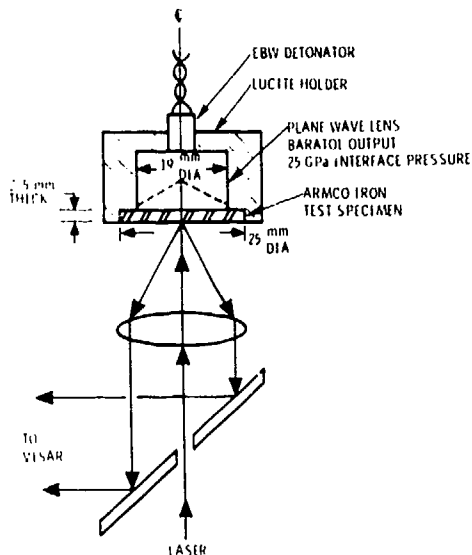
Fig. 4. Test configuration showing the location of the measurement
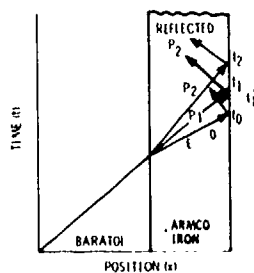
Fig. 5. X-t diagram of stress wave interactions. The elastic (E) wave interactions have been simplified.
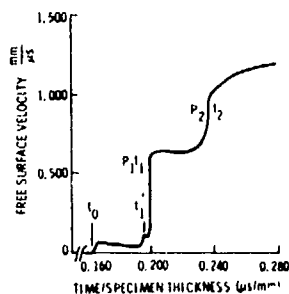
Fig. 6. Free surface velocity history of iron impacted at 25 GPa. Data from Barker[5].

μs and, further, the burst must contain one whole fringe on delay leg 1 and one whole fringe on delay leg 2. The final record is seen to agree with that anticipated from the wave interaction analysis.
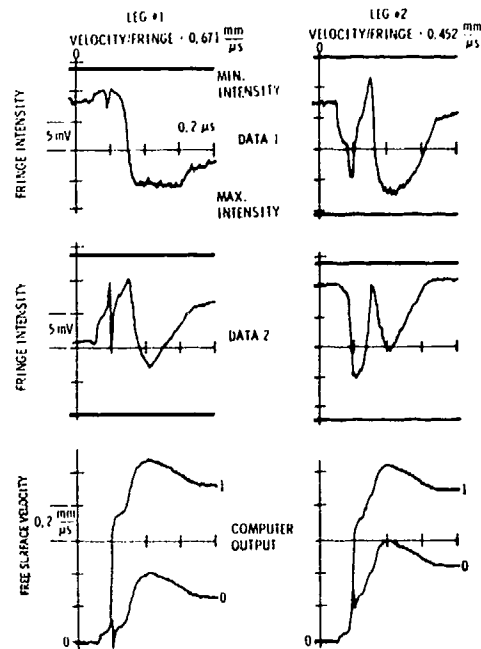
Fig. 7. Raw DATA 1 and DATA 2 and the computer-generated free surface velocity histories are shown for each leg. The history labeled "1" in Leg 1 is nearly identical to that labeled "1" in Leg 2 and corresponds with Barker's data

REFERENCES

1. L. M. Barker and R. E. Hollenbach, J. Appl. Phys. 43, p. 4669, 1972.

2. L. M. Barker and K. W. Schuler, J. Appl. Phys. 45, p. 3692, 1974.

3. J. E. Kennedy and O. B. Crump, to be published.

4. J. R. Asay and L. M. Barker, J. Appl. Phys. 45, p. 2540, 1974.

5. L. M. Barker and R. E. Hollenbach, J. Appl. Phys. 45, 4872, 1974.

WIDE RANGE VELOCITY INTERFEROMETER

B. T. Amery
Ministry of Defence Procurement Executive
Atomic Weapons Research Establishment
Southend-on-Sea Essex England

A Doppler Shift Velocity interferometer has been developed which can measure the velocity of any surface whether it is a specular or diffuse reflector. Two signals in quadrature are provided and these lead to 1% to 2% accuracy in velocity determinations. The instrument may be used over a very wide range of velocities. Examples of foil impact experiments are given on metal and non-metal materials over the velocity range 0.008 mm μsec^{-1} to 0.4 mm μsec^{-1}.

INTRODUCTION

The advent of the laser has enabled interferometry to be used to measure surface and interface velocities in the field of shock wave studies but initial developments in this field have required the specimen to have a small surface tilt during flight and to retain a mirror finish.

This paper describes a velocity interferometer system that provides high contrast fringing signals from any type of surface—specular, diffuse or a mixture of the two. With a diffuse surface the interferometer is also quite insensitive to surface tilt. Moreover there are no strict limitations to the range of velocities over which the instrument may be used other than the space available in the laboratory. It is in this respect that this instrument has an advantage over the VISAR (1).

INTERFEROMETER DEVELOPMENT

Developments in this field by L. M. Barker and R. E. Hollenbach led to the Sandia laser velocity interferometer (2,3). In this arrangement a laser beam is reflected from a specular shocked specimen and the beam is split and recombined after one part has been delayed by a few nanoseconds. At any instant the light reflected from the specimen and having a Doppler shift imparted to it by the surface velocity, is recombined with light that originated from the surface a time τ earlier, where τ is the delay time. The resulting interference fringes are detected using photomultipliers.

Barker and Hollenbach relate the fringe count ΔN_t to the surface velocity U, by

$$U_{(t-\tau/2)} = \frac{\lambda_o}{2\tau} \frac{\Delta N_t}{(1 + \Delta v/v)} \qquad (1)$$

where λ is the laser wavelength, $\Delta v/v$ is an index of refraction correction factor for any "window" material, t is time and $\tau = L/C$ is the delay time of the interferometer with a path-length difference L.

Except when used in measuring very high velocities the interferometer will employ a long path difference which requires the light entering the interferometer being spatially coherent and hence implies a specimen surface that remains specular. If, however, the light illuminating a Michelson interferometer is incoherent, high quality fringes may be obtained if the two end mirrors of the interferometer appear to be coincident from the view of the detector (4). Unfortunately this configuration would detect no motion as a velocity interferometer since the transit

times for the two beams would be equal and τ would equal zero, giving no fringe count (Eq. 1).

The requirement therefore is to modify the interferometer to produce the spatial coincidence of the end mirrors while maintaining their temporal separation. This is achieved by using lenses within the interferometer legs to image the end mirrors M1 and M2 at M1' and M2' so that the two images are coincident and equidistant from the beam-splitter BS.
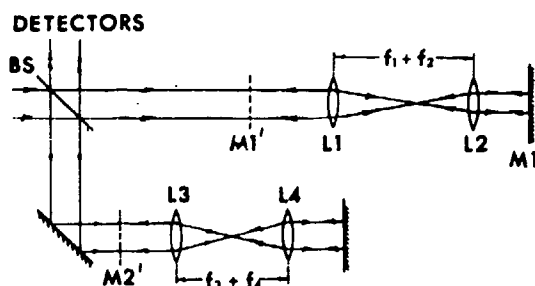
DETECTORS

Fig. 1. Lenses used to produce coincident images of interferometer end mirrors.

A combination of two lenses separated by the sum of their focal lengths is used in each leg and the combinations as a whole are moved to maintain the mirror image positions as the end mirrors are adjusted for different delay leg lengths. A combination of two lenses is used since it is a requirement that each beam exactly reproduces itself at the mirror image position on the way back to the beam splitter. Thus the spatial phase irregularities present in the speckle beam reflected from a diffuse surface are exactly reproduced.

WIDE RANGE VELOCITY INTERFEROMETER

A diagram of the Wide Range Velocity Interferometer as used in conjunction with an electromagnetic foil throwing facility is shown in Fig. 3 and a photograph of the installation in Figs. 4 and 6.

A CRL 1 watt Argon-ion laser producing up to 700 mW single frequency light at 5145Å provides the illumination. The beam is expanded to 3 mm diameter and chopped by a rotating disc shutter to reduce the mean level of light at the photomultipliers. A 2 mm stop S1 limits the beam diameter and mirror M3 steers the light to the specimen which is in the focal

plane of a 50 mm diameter 30 cm focal length lens. This lens receives the diffusely reflected light from the surface and recollimates it. The telescope expands the outgoing 2 mm beam and condenses the return beam to 10 mm diameter for use in the interferometer. In this way the amount of light collected is increased and any intensity fluctuations due to a coarse speckle pattern are reduced.

The beam splitter B3 directs the reflected light into the interferometer and polarizer P, at 45° to the plane o incidence, is used to provide two equal amplitude S and P components. Beam splitter B2 directs one-third of the total light via mirrors M5 and M6 t the intensity monitor photomultiplier. Lenses L5-L7 focus the aperture S2 onto fine ground glass screens to ensure that the photomultiplier photocathodes are evenly illuminated.

Beam splitter B1 directs one beam towards the end mirror M1 and the other via M4 towards M2. The lens combination L1, L2 forms an image of M1 at M1' and the combination L3, L4 forms an image of M2 at M2' such that M1' and M2' appear coincident when viewed from the detectors. The first order $\lambda/8$ wave plate W is arranged to retard the P-light component by a phase angle of 90° on a double transit so that two fringe patterns 90° out of phase are produced. These patterns are separated by a Wollaston prism WP and sensed by the Sine and Cosine photomultipliers.

Since B2 and B1 are not used at normal incidence the reflectivities will not be the same for the P and S light components; however since both components are reflected and transmitted once the combined beams producing the fringe patterns are in the intensity ratio 1:1.096 and high contrast fringes result. Any inequalities produced can be removed by slight rotation of the polarizer P.

ALTERNATIVE FORMS OF INTERFEROMETER

The positions of M1 and M2 required for a particular delay length are set to 0.01 cms by using the vernier scale of the optical bench on which the custom built mountings are carried. To zero the system the coincident positions of M1 and M2, without lenses in the system, is found using white light fringes.

Figure 6 shows the interferometer set for a Fringe Constant of 0.20 mm μsec^{-1} Fringe^{-1}. Each arm of

the interferometer contains two lenses and this is the arrangement used for insensitive settings of the Fringe Constant. When a sensitive setting is required the arrangement shown in Fig. 4 is used. When the Fringe Constant is 0.015 mm μsec^{-1} Fringe^{-1}. M4 returns the light of the beam splitter becoming one end mirror of the interferometer and M2 is reversed to become the other mirror. Lenses L1 and L2 now image M2 via the mirror corner reflector box MB.

OPTICAL COMPONENTS

All the surfaces of the optics in the interferometer are flat to $\lambda/20$ and the spherical surfaces of the lenses are to the same tolerance. The mirrors and beam splitters are dielectric coated, 65 mm in diameter and in addition the beam splitters are wedged to $\frac{1}{2}°$. The mirrors M1, M2 and M3 and beam splitter B3 have tilt adjustments in two orthagonal directions by means of fine screw micrometers.

To maintain high contrast fringes it is a requirement that the residual wave aberration of the lenses used in the interferometer should be less than $\lambda/20$: this prohibits the use of commercial doublets and so a series of zero coma or "crossed" lenses were designed (5). The minimum focal length that could be used (20 cm) was determined by the requirement that over 1 cm aperture the aberration criterion should be met.

For the Corrected Sine Condition Coma to be zero

$$\frac{R_1}{R_2} = \frac{n^2}{n^2 - n - 1} \qquad (2)$$

and

$$f = R_1 \frac{n^2}{n^2 - 1} \qquad (3)$$

where R_1 and R_2 are the lens surface radii, n the refractive index of the glass and f the focal length of the lens.

Each lens is mounted in a tube and adjusted so that its focal point is 10.00 cm beyond a locked locating ring. The tubes then screw into standard couplers or the mirror-box which have locating faces 20.00 cm apart. In this way various lens combinations may be used without the need to refocus the interferometer each time.

Since each lens combination is capable of focusing the end mirrors over a range determined by a lens being either at the mirror or mirror image position a small series of lenses of focal lengths 20 cms-100 cms can give a continuous range of Fringe Constants from 1.168 mm μsec^{-1} Fringe^{-1} to 0.0064 mm μsec^{-1} Fringe^{-1}. The range of leg lengths given by a combination of lenses of focal lengths f_1 and f_2 is

$$\text{Range} = \frac{(f_1 + f_2)^2 (f_1 - f_2)}{f_1 f_2} \qquad (4)$$

RECORDING AND DATA REDUCTION

The fringing signals and intensity monitor are detected by EMI type D254 six stage photomultipliers giving a gain of about 10^4 and recorded on Hewlett-Packard Type 183B oscilloscopes. The rise-time of the combination is 3 nS.

The voltage output from both fringing photomultiplier channels is assumed to be a sinusoidal function of the fringe count ΔN_t at any instant t with a 90° phase difference between the two signals. If $2\alpha_0$ is the peak to peak photomultiplier signal and ϕ is the arbitrary fringe phase before the surface starts to move we have for the P and S light components respectively

$$(\alpha_t)_p = \alpha_0 \left[1 + \text{Sin} (2\pi \Delta N_t + \phi)\right] \qquad (5)$$

and

$$(\alpha_t)_s = \alpha_0 \left[1 + \text{Cos} (2\pi \Delta N_t + \phi)\right] \qquad (6)$$

The mean value of α_t is α_0 and if this is subtracted from the photomultiplier signal we have

$$\frac{(\alpha_t)_p}{(\alpha_t)_s} = \text{Tan} (2\pi \Delta N_t + \phi) \qquad (7)$$

which may be solved for ΔN_t. The mean level α_0 is obtained as a fraction of the intensity monitor signal, being set up with a number of fringes filling the field of the interferometer. It is subtracted from the fringing signals at the recording oscilloscopes which each have two amplifiers whose outputs can be added algebraically.

There are many advantages that arise from recording the fringing signals in the above manner. In particular the interpretation of the records is made unambiguous except, at shock discontinuities, where the frequency response of the system will not allow the signal to be followed. Even here, however, the boundary conditions of the experiment usually allow the uncertainty to be resolved. The data reduction is also simplified.

The photomultiplier signals remain true sine and cosine traces balanced about the zero light position, irrespective of intensity and contrast changes so long as the initial setting-up relationships between the fringing and intensity monitor channels remain unchanged and the photomultiplier outputs are linear. In addition since the signals are in quadrature, an acceleration can be distinguished from a deceleration since in the former case the Cosine trace leads by $90°$ and on a deceleration it lags by $90°$. Ambiguities between fringe turn-rounds occurring at the maxima or minima of the fringe pattern and velocity reversals are also removed. More importantly the insensitivity of the photomultiplier output as a function of the fringe count, which occurs at maxima and minima, is countered since when one signal is at a minimum sensitivity the other is at a maximum. It is this feature which gives the velocity interferometer technique its high accuracy from what appear to be poor quality traces.

The records are reduced by measuring trace coordinates in a digitised trace measuring machine. Immediately after recording the fringing signals two time-marker traces of equal and opposite deflection, either side of the balanced zero light trace position, are put on both records. Co-ordinates on both time-marker traces are also measured. Linear fits in time T
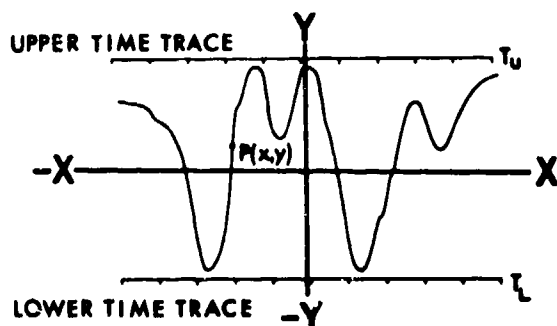
and deflection Y are made in terms of X giving four equations for each record. These equations are used to normalise the two fringing signals, correct for any distortion in the record, and reduce them to a common time scale. The cosine amplitude corresponding to each sine point is calculated by linear interpolation.

At each measured point $P(x,y)$ on both the Sine and Cosine traces the time and amplitude are calculated by substituting x into the linear fit equations to obtain values of T_U, Y_U, T_L, Y_L, thus

$$Y_p = 2000 + \frac{6000}{Y_U - Y_L} (y - Y_L) \qquad (8)$$

$$T_p = T_L + \frac{y - Y_L}{Y_U - Y_L} (T_U - T_L) \qquad (9)$$

RESULTS

The interferometer has been used for about four years over a wide velocity range on various types of specimen to obtain their free surface motion. Three examples are shown in Fig. 5, 7 and 8.

EXPERIMENT 1. Figure 5. PIC ½H Aluminium foil 0.25 mm thick impacted a 5050B Aluminium specimen 1 mm thick at a velocity of 0.41 mm μsec^{-1}. The maximum velocity corresponds to 2.17 fringes which are not quite time resolved. The specimen spalled with a fall-back velocity of 0.193 mm μsec^{-1} and reverberations in the detached layer are clearly seen.

EXPERIMENT 2. Figure 7. Impact as in Experiment 1 on to a 6 mm thick sample of a three dimensional quartz-fibre resin composite. The laser beam was focussed on to an area where the quartz fibres were normal to the surface. The fringes corresponding to the surface acceleration are just resolved but the initial deceleration which was faster is just beyond the resolution of the system.

EXPERIMENT 3. Figure 8. This is a slow strain rate experiment with a drop weight hammer impacting an anvil carrying a specimen of CS Carbon. In this early experiment the $(1 + Sine)$ fringe signal and the intensity monitor are displayed separately and the delay leg was 8.75 m long.

Fig. 2. Record co-ordinates for data reduction.

676

Fig. 3. Schematic of wide range velocity interferometer as used with an electromagnetic foil throwing facility.
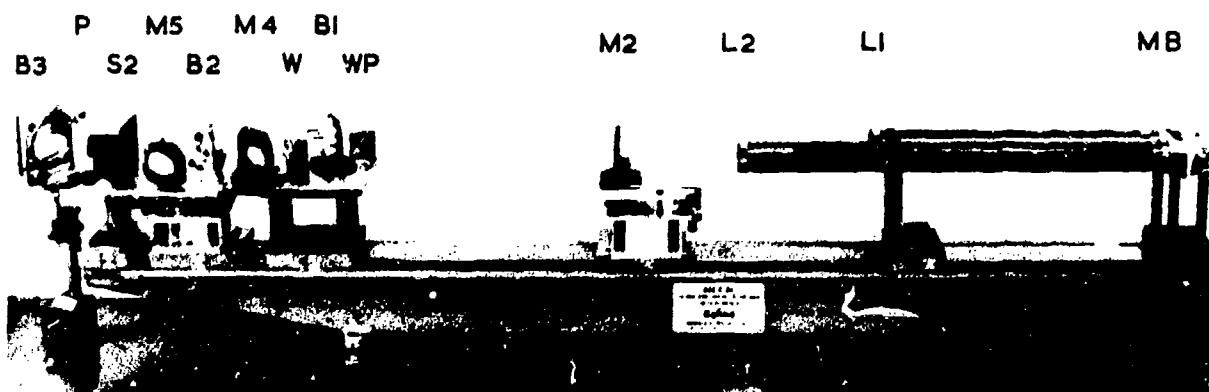
Fig. 4. Interferometer with lens configuration used for high sensitivity settings of the Fringe Constant.
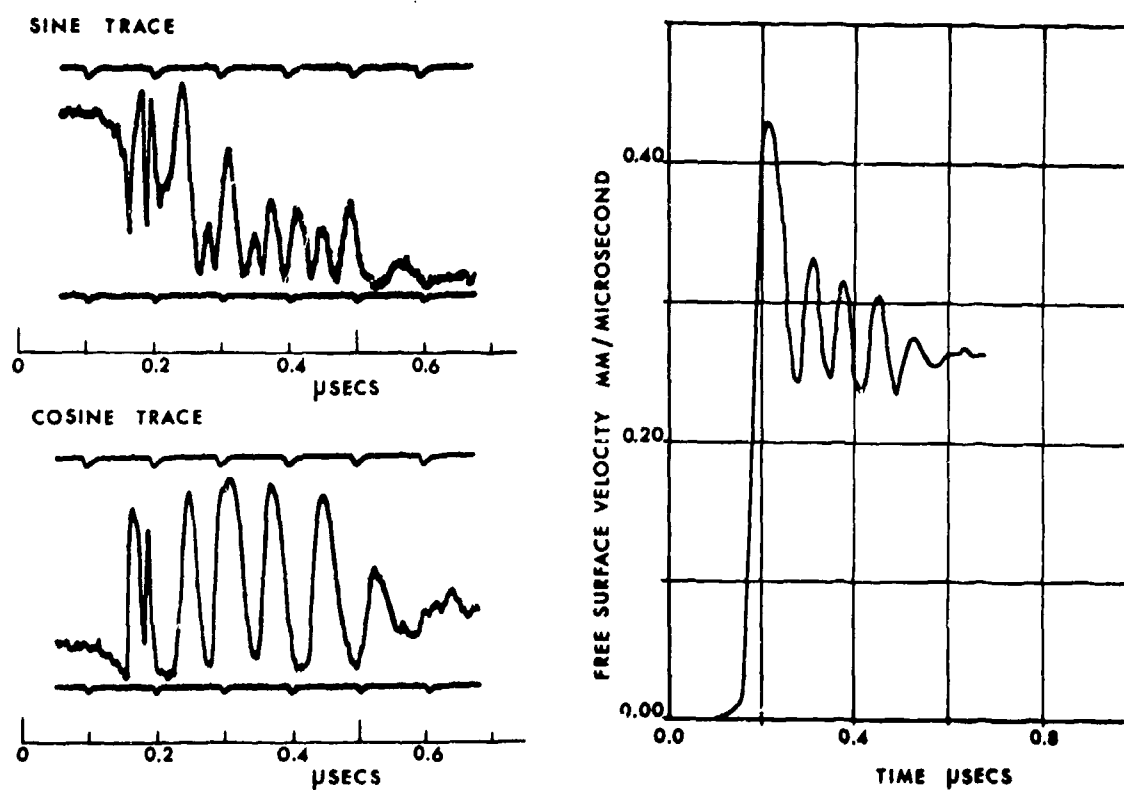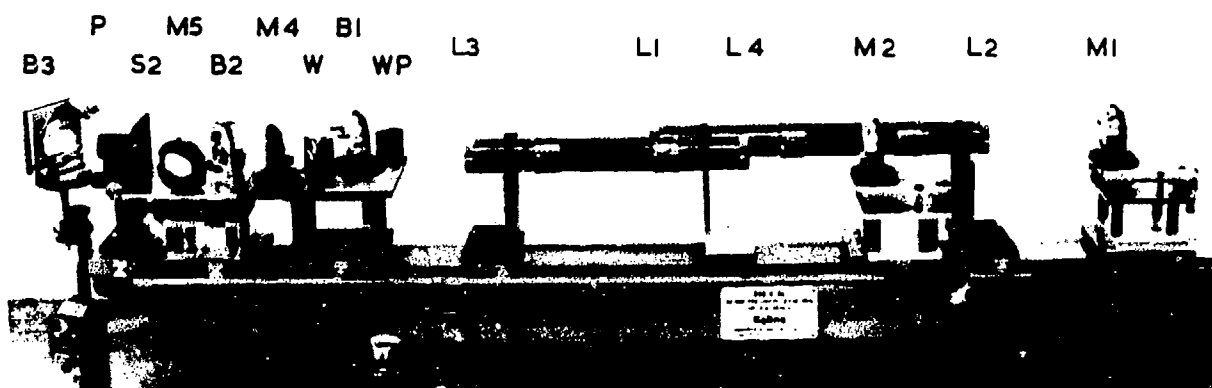

Fig. 5. Records and interpretation of foil impact on 5050B aluminium 1 mm thick. Foil velocity 0.41 mm μsec^{-1}. Fringe Constant 0.20 mm μsec^{-1} $Fringe^{-1}$.

Fig. 6. *Interferometer with lens configuration used with less sensitive settings of the Fringe Constant.*
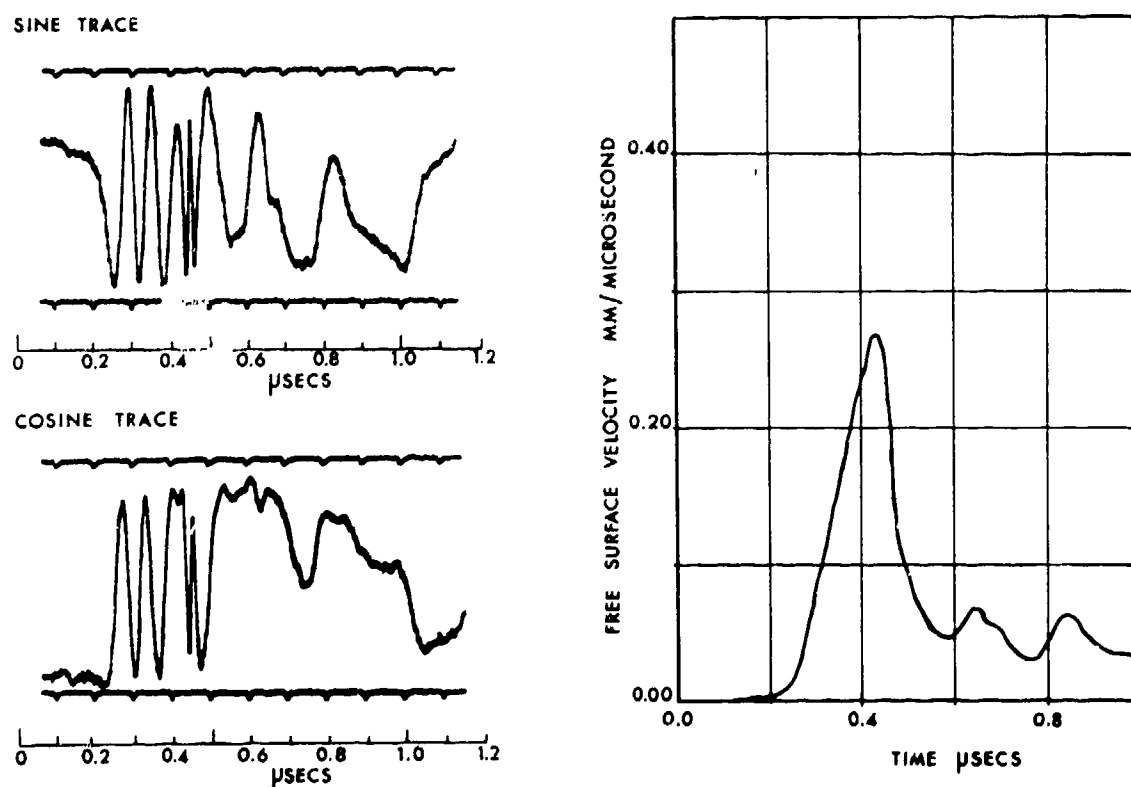
Fig. 7. *Records and interpretation of foil impact on Three Dimensional Quartz-fibre Resin Composite (3DQP) 6 mm thick. Foil impact velocity 0.41 mm μsec^{-1}. Fringe Constant 0.10 mm μsec^{-1} Fringe^{-1}.*
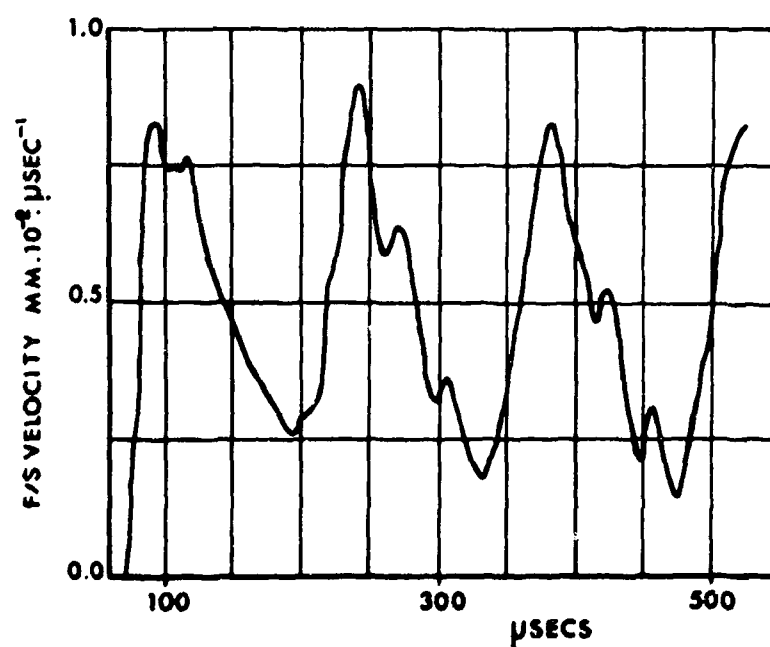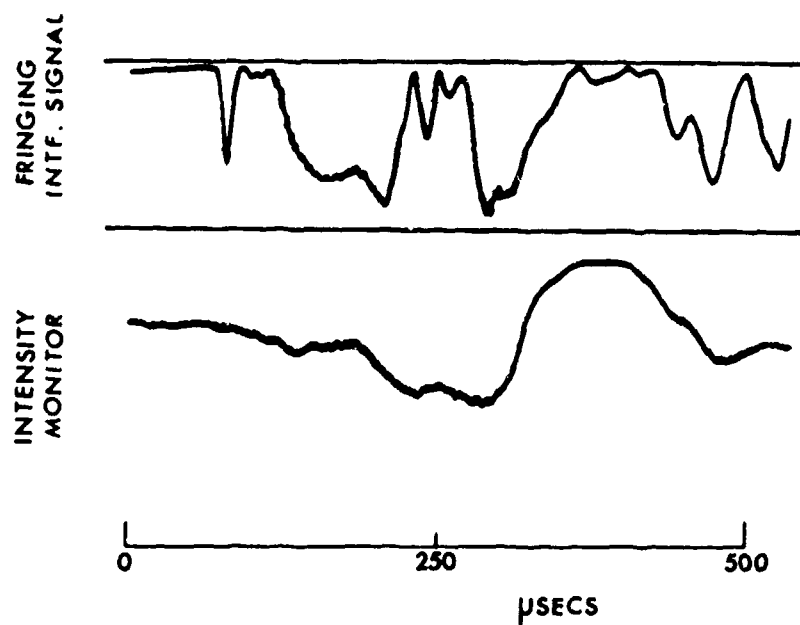
Fig. 8. Records and velocity-time interpretation of low strain rate experiment on CS Carbon. Interferometer Fringe Constant 0.0088 mm μsec⁻¹ Fringe⁻¹.

ACCURACY

There are four main sources of error in deducing a velocity history using the wide range velocity interferometer: specimen tilt, defocussing due to surface translation, photomultiplier noise and non-linearity of the photomultiplier output.

The surface tilt error applies to specular surfaces since it causes the light paths to be different from those originally set, but for Lambertian surfaces the collimating lens remains filled with light and there are no changes. When the surface moves the returned light becomes divergent and this also causes the path through the interferometer to change; this effect is most severe for a diffusely reflecting specimen. Both these effects give rise to errors of about 0.1 - 0.2 fringes.

The statistical noise on the photomultiplier output makes the assumption that the output is a sinusoidal function of the fringe phase not strictly valid. Measurements give a value of less than 0.005 fringes for this error. The linearity of the photomultiplier output is better than 2% over periods of up to 0.5 mS.

CONCLUSIONS

The wide range velocity interferometer described here is capable of measuring the velocity-time history of any surface whether it is a diffuse or specular reflector or a mixture of the two, over a very wide velocity range. An accuracy of 1%-2% is easily ob-tainable. This form of interferometer is particularly insensitive to the tilt of a diffusely reflecting surface.

REFERENCES

1. L. M. Barker and R. E. Hollenbach, "Laser interferometer for measuring high velocities of any reflecting surface," J. Appl. Physics, Vol. 43, No. 11, 4669 (1972).

2. L. M. Barker and R. E. Hollenbach, "Interferometer Technique for Measuring the Dynamic Mechanical Properties of Materials," Rev. Sci. Inst., Vol. 36, No. 11, 1617 (1965).

3. L. M. Barker and R. E. Hollenbach, "Shock Wave Studies of PMMA, Fused Silica and Sapphire," J. Appl. Physics, Vol. 41, No. 10, 4208 (1970).

4. W. H. Steel, "Interferometry," pp. 56, et. seq., Cambridge University Press, Cambridge, 1967.

5. R. J. Bracey, "The Technique of Optical Instrument Design," English Universities Press (1960).

ASSESSMENT METHODS OF THE IMPACT IGNITION
SENSITIVITY OF DIFFICULTLY-DETONABLE EXPLOSIVES

W. H. Andersen and N. A. Louie
Shock Hydrodynamics
North Hollywood California 91602

This paper discusses the assessment of the projectile impact sensitivity of relatively insensitive substances, based on an investigation of small caliber caseless ammunition. Conventional techniques (e.g., Bruceton method of obtaining V_{50}) are not usually applicable. The test evaluation included the use of a photocell monitoring system to temporally resolve the light emitted by the impact reaction. This technique represents a new and novel method of obtaining information regarding energy release by impact. The tests showed that the impact reaction varied widely, depending on conditions. It ranged from no reaction being induced in the fractured propellant, to a partial reaction, to a complete combustive consumption, to a detonative reaction in one case. Interestingly, the sensitivity of this latter propellant was less than that of the others at impact velocities lower than that required to produce the violent reaction. A statistical model is developed to describe projectile impact sensitivity, and a brief discussion presented of ignition induced by spall particle impact.

INTRODUCTION

The measurement of the impact sensitivity of high explosives normally uses high speed photography, pin-switch or witness plate techniques to demonstrate the existence or absence (go or no-go) of a propagating detonation reaction induced in the explosive by the impact. An experimental procedure (e.g., the Bruceton method) that encompasses an impact velocity range sufficient to ensure both 100% and 0% probability of reaction (propagating detonation and non-reaction) is used to establish the impact velocity required for 50% probability of ignition, i.e., the V_{50} of the reaction.

On the other hand many important combustible substances (e.g., various propellants and composite explosives) are relatively insensitive, and their impact ignition occurs only as a low statistical event in the impact velocity range normally available. Moreover

the extent of reaction induced in the substance by the impact can vary over a wide range, and depending on various factors may or may not include propagating detonation. The nature and extent of reaction may depend on various factors including the size, composition and physical form of the material sample, and the geometry and velocity of the projectile. The measurement of the impact sensitivity of these types of materials is more difficult than for conventional explosives, and only limited information is available regarding the evaluation of the impact ignition sensitivity of these types of substances.

This paper concerns itself with the experimental assessment of the impact ignition sensitivity of relatively insensitive combustible substances, based on an investigation of the sensitivity of different kinds of small caliber caseless ammunition to impact by normal and flat nose bullets, and spall particles produced by projectile penetration of steel armor plate. The

various materials exhibited a wide range of reaction behavior, and were investigated using a novel observational technique.

EXPERIMENTAL MEASUREMENTS

Test Ammunition

The tests were conducted on 8 kinds (designated types A through H) of 5.56 mm caseless ammunition rounds (Fig. 1), each of which consisted of a hollow (not shown) cylinder of propellant containing the slug in one end and the primer in the other. Types A, B, C and H consisted of a single sleeve of molded propellant, whereas the other types were dual sleeve with the inner sleeve being made up of single base (SB) propellant. Type A consisted of SB propellant while B was based on HMX in a binder. Type C was the same as B except for containing a different and more energetic primer. Type H employed a different binder and contained a relatively large fraction of HMX. The outer sleeves of the other rounds differed in composition, and some of them contained various fractions of HMX.

Test Apparatus

The sensitivity of the propellant rounds to projectile impact was studied by impacting the rounds side-on at three locations (neck end, body and primer end --see Fig. 1) using a 5.56 mm slug, with both normal (ogive) and flat (sawed-off, Fig. 1) nose ends and
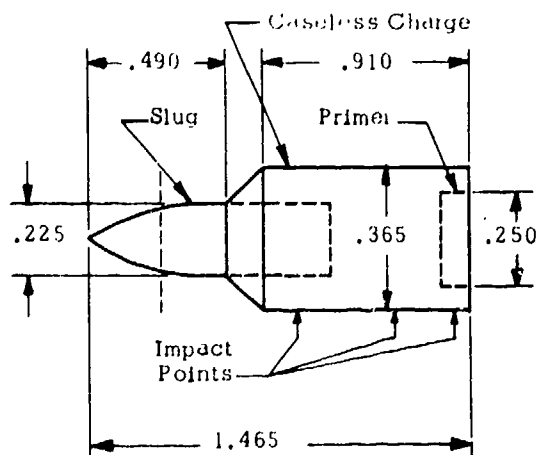
Fig. 1. Diagram of a caseless target round. Dimensions are in inches.

fired at various velocities. Figure 3 shows the test setup used, which consisted of a rigid steel I-beam to which a gun support, gun blast baffles, velocimeter screens (for measuring bullet impact velocity), target box, and a camera and photocell support were bolted to prevent any relative movement. The light-tight steel target box was a one foot cube (painted black inside) with a 6″ diam. safety glass window port on one side, a (lightly covered) bullet entrance hole in front and an exit hole in the back. The test round was supported nose down on a stiff but flexible rubber tube fastened to an adjustable floor support which allowed both side to side and vertical positioning of the round.

The test setup for the spall particle impact tests was essentially the same except for the addition of a (replaceable) sheet of 1/4″ thick steel armor plate to the inside wall of the target box just behind the bullet entrance hole. The penetration of this plate by a .30 caliber armor piercing (AP) bullet produced a cone of spall particles with various sizes. Two test rounds at different locations were used in each test to increase the probability of a particle hit with a round, and the rounds were located at various distances behind the plate and various offset distances from the flight line of the AP slug after its penetration of the armor plate.

Monitoring Systems

The results of the tests were obtained by an open-shutter camera picture of the impact event, by the light emitted during impact and detected by a photocell, and by post inspection of the ammunition fragments remaining in the target box after a test. The camera and photocell were positioned behind the safety glass viewing window, and a light-tight shroud was draped around them in a manner as to exclude any light other than that appearing in the target box. The camera was a Speed Graphic (Polaroid ASA 3000, b/w film) whose lens was set at f/4.5, and whose shutter was left open during a test.

The photocell monitoring system consisted of a TIL67 NPN, Planar Phototransitor in a simple light detector circuit (Fig. 2), which was connected to the input of an oscilloscope set up to make polaroid pictures of the radiant signal produced in the target box during a single sweep. The photocell monitoring system was conceived by one of us (NAL), and represents a useful (as well as rapid and inexpensive)

683

method of obtaining information regarding ignition and energy release by the impact of relatively insensitive materials. It can, for example, distinguish impact flash and the light emitted by very hot (or burning) spall particles from the light emitted by combustive reaction of the material. It can also distinguish transient burning during impact from a self-sustained burning event. The resolution of the event can be controlled by the sweep speed of the oscilloscope on which the phototube output is displayed. By proper calibration the technique could probably be made essentially quantitative in nature, and there are other potential refinements which may further increase the information that can be obtained using this technique.
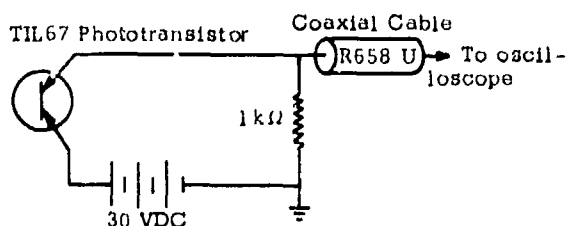
Fig. 2. Photocell circuit used for detecting light emission produced in the impact tests.

EXPERIMENTAL RESULTS

Characteristics of the Bullet Impact Tests

Four general types of bullet impact behavior were observed:

1. *No Burn*—In general, projectile impact on the body or neck of a test round at the lower impact velocities usually produced only a flash during impact, and breakup of the test round occurred without ignition. Higher velocity produced brighter flash. The impact flash appeared clearly on the camera record (Fig. 4a), and the unburned propellant fragments were recoverable after the test. The photocell record appeared as a single or closely-double peak pulse (Fig. 5a), which after reaching the maximum decayed to the no-signal level without any appreciable secondary rise. This behavior of the test round was classified as a No Burn.

2. *Partial Burn*—At higher impact velocities, particularly when flat nosed slugs were used, a partial burning occurred on a low statistical basis when the body or neck of the test round was impacted. When the primer end of the test rounds was impacted, the
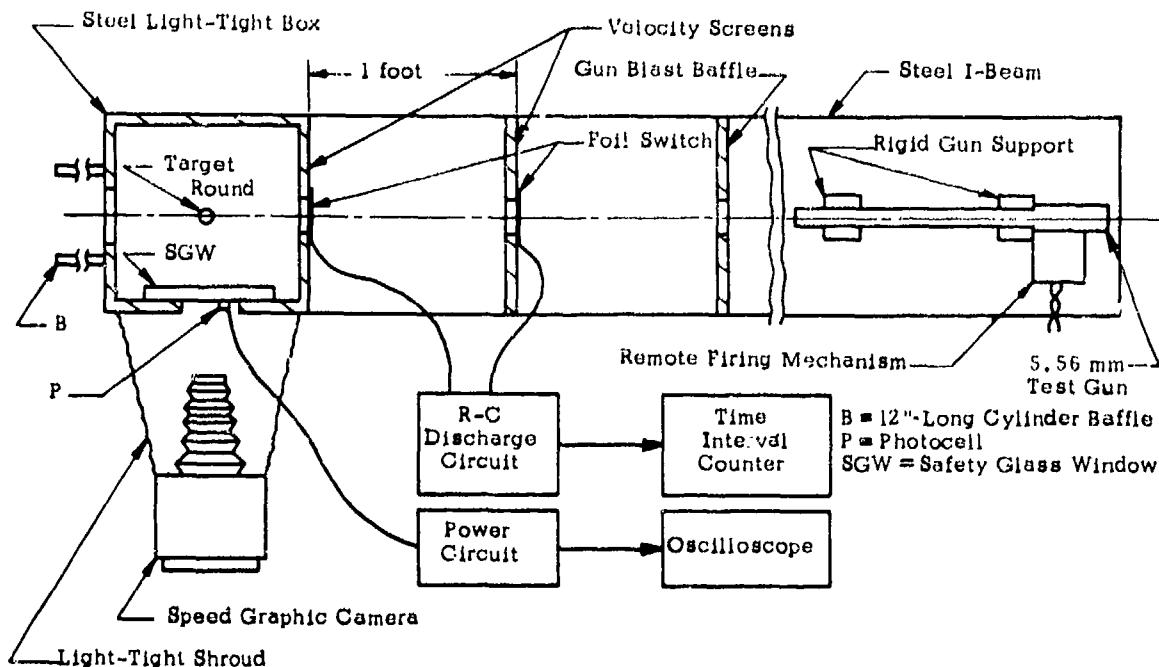
Fig. 3. Experimental configuration for bullet impact tests.

partial burning occurred on a high statistical basis, even at the lower velocities. In these cases, which were classified as a Partial Burn, the camera record (Fig. 4b) showed a multitude of luminous streamers representing the trajectories of burning propellant fragments. The photocell waveform (Fig. 5b) showed the initial impact flash followed by a second broad peak whose amplitude increased with increased extent of burning. This behavior appears to pertain largely to the ignition and burning of material of the test round that interacts directly with the impacting slug. However, although this material ignites quickly at impact there appears to be little spreading of the burning to other parts of the target round not directly at the impact site. This category represents a transition from the No Burn to the Burn states and encompassed a wide degree of reaction behavior, both as to the amount of material consumed and the intensity of the energy released. Many of the partial burns occurred when the impacting slug hit the primer section of the test round, and in these cases little or none of the primer material was found in the test chamber. However, some unburned propellant fragments were always present after the test.

3. *Burn*--At the higher impact velocities, particularly with flat nosed slugs, an essentially complete burning of the test round occurred on a low statistical basis when the body or neck of the round was impacted. For some rounds the complete burning occurred on a high statistical basis when the primer end was struck. In these cases, which were classified

as a Burn, the camera record was white (completely overexposed), and the photocell signal (Fig. 5c) showed a rapid rise to an off-scale position (generally in less than 10 μsec), and did not return during the remainder of the sweep of the oscilloscope. Little or no propellant fragments of the test round were recovered after the test.

4. *Explosion*--The impact of the body or neck of one of the test rounds (type H) in the higher velocity range with a flat nosed slug produced a very violent reaction, which was classified as an Explosion. The specific nature of this reaction was not established, but it was presumably of detonative character since it produced strong blast which fragmented the safety glass viewing window and tore the lid of the steel target box off its hinge. The polaroid photographs in this case were completely overexposed, and the oscillograph reading of the photocell gave a quick rise to a constant level, indicating a sudden rise to a constant light flux. These results were presumably caused by the opening of the light seals on the box as the result of the blast.

Test Results

The overall results of the impact test are summarized in Table 1. In this table the results of the neck impact tests have been included in the body tests, and the impact velocities have been grouped so as to allow the results of all of the tests to be included in the table. In general it was found that the
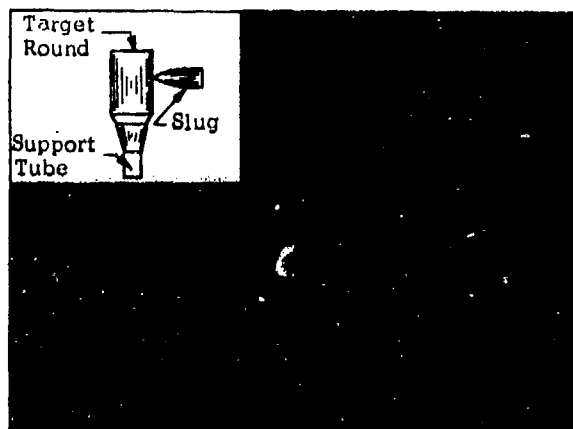

Fig. 4a. Impact flash accompanying a bullet impact test in which the test round experiences no burn.
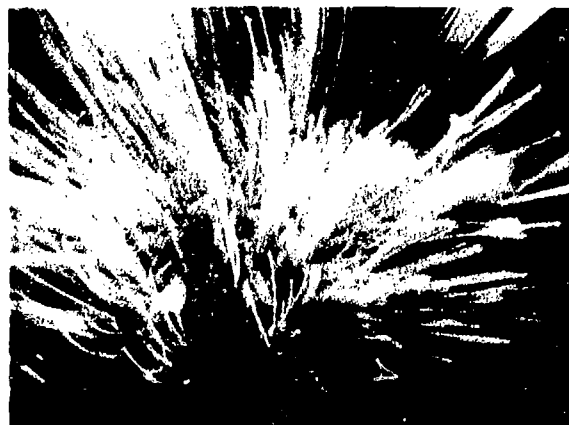

Fig. 4b. Ignited particle trajectories accompanying a bullet impact test in which a partial burn is produced in the test round.

685

only essential difference between the results obtained with both types of slugs was that any impact behavior obtained with an ogive slug was usually obtained at a lower velocity with a flat nosed slug. Impact sensitivity of the rounds increased with increase in impact velocity, as expected. The primer was pronouncedly the most sensitive impact area of the rounds, and the neck area was in general slightly more sensitive than the body. The general sensitivity and reaction violence of the primer end of the rounds appeared to be related (roughly proportional) to the size and weight of the primer material, although the primer composition also affected the results of the type C rounds.

The general sensitivity of the body and neck impacts appeared to be related to the composition of the material. In addition however, the sensitivity of the dual sleeve rounds may have been affected—at least in some cases—by the construction of the rounds. For example, it was found from radiographs of the rounds that the two sleeves were not always in intimate contact with each other, but rather that small cracks or voids were often present at their contact surface which may have (but was not proven to have) sensitized the rounds to impact reaction.

(a) Waveform for flash at bullet impact

(b) Waveform for flash and partial burn at impact
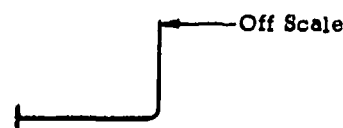
(c) Waveform for burn at bullet impact

Fig. 5. Photocell waveforms from bullet impact tests.

The most interesting round however was type H, which underwent violent explosion at the highest impact velocity with flat nose bullets. Interestingly, the impact ignition sensitivity of this propellant was lower than that of the other propellants at impact velocities lower than that required to produce the violent reaction. This demonstrates that the ignition process is not usually the controlling factor in determining whether an impacted substance undergoes a deflagration to detonation transition.

Sensitivity Analysis

Although the partial burns produced in the impact tests are informative for general comparison purposes, they do not directly provide information regarding impact ignition statistics. A knoweldge of the amount of material burned in these tests would be useful toward this end, and this information could possibly be obtained by weighing the unconsumed material in the partial burn tests and using the results to provide an absolute calibration of the photocell technique. In lieu of this information, a statistical behavior ranging from no reaction to complete reaction was categorized according to certain qualitative characteristics observable from the camera and photocell records of the impact event. A weighting function was used to weight the various categories, and an expression containing this function derived to estimate the probability, $P(V)$, of a Burn reaction for a specified impact velocity, V, from the number of tests at that velocity.

For purposes of the analysis, the test results were divided into six categories in order of increasing amount of burned material, where the category numbers $K = 0,1,2-5$ designate, respectively, impact flash only (no burn), flash plus slight sparking, moderate spark shower, intense spark shower and/or partial ignition, primer burn, and complete burn. The probability, P, of a Burn at a specified velocity, V, is then given by

$$P(V) = \frac{\sum_{i=1}^{N} F(K_i)}{N(F(K))_{max}} \tag{1}$$

where $F(K)$ is a weighting function depending on K, and N is the number of tests $((F)_{max} = F(5))$. Since from physical considerations $F(0) = 0$ ($P = 0$ for $K = 0$), $F(1) =$ a small no. $\simeq 1$, $F(5) \gg F(1)$, and

TABLE 1

Results of the Bullet Impact Tests

Round Type	Bullet Impact Point	Impact Velocity (fps) and Bullet Type						
		4020 Flat	3760 Flat	3250 Ogive	3050 Ogive	2670 Ogive	2060 Ogive	1340 Ogive
A	Body	NB-2	B-1 NB-9	P-1 NB-15	NB-9	NB-5	NB-5	
	Primer		B-3 NB-1	P-10 NB-1			P-1 NB-2	
	Body			Flat NB-4			Flat NB-7	Flat NB-3
	Primer			B-3			P-3	NB-3
B	Body	NB-8	NB-8	NB-4			NB-7	P-1 NB-1
	Primer		B-3	B-2			P-3	NB-2
	Body			Ogive NB-22	NB-9	NB-6	Ogive NB-8	
	Primer			P-9 NB-1			P-2 NB-1	
C	Body	B-1 NB-3	B-1 NB-9	B-1 P-2 NB-15	NB-9	NB-2	NB-5	
	Primer		B-3	B-12			B-3	B-1
	Body			Flat P-1 NB-1			Flat NB-8	NB-3
D	Body	B-12 P-8 NB-6	P-5 NB-5	Ogive B-1 NB-24	B-2 P-2 NB-6			
	Primer			B-10			Ogive B-10	Ogive B-4 P-5 NB-1
E	Body		B-2 P-1 NB-1	B-2 NB-7				
	Primer			P-2	B-2 P-2 NB-2	B-2 P-1 NB-2	P-3	P-4 NB-1

TABLE 1

Results of the Bullet Impact Tests—Continued

Round Type	Bullet Impact Point	Impact Velocity (fps) and Bullet Type						
		4020 Flat	3760 Flat	3250 Ogive	3050 Ogive	2670 Ogive	2060 Ogive	1340 Ogive
F	Body		P-10	P-2 NB-8				
	Primer			P-2	P-3 NB-2	P-2 NB-3	NB-2	NB-5
G	Body		P-8 NB-12	P-1 NB-9				
	Primer			P-2	B-2 P-3	B-1 P-3 NB-1	P-1 NB-1	P-1 NB-4
H	Body		E-4 P-4 NB-4	NB-11				
	Primer			P-2	P-2 NB-3	P-3 NB-2	P-1 NB-1	P-2 NB-3

The number indicates the number of tests; E = Explosion, B = Burn, P = Partial Burn, NB = No Burn.

$F(5)/F(4)$ = total burnable volume of round/volume of igniter, the weighting function was chosen to be of the form $F(K) = AX^K + B$, where $B = -A$, $X = e$, and $A = (e - 1)^{-1}$. This gives $F(K) = 0.6932 (e^K - 1)$. The probability of a total Burn for any impact velocity V is then calculated from N tests at that velocity by

$$P(V) = \frac{\sum_{i=1}^{N} 0.6932(e^{K_i} - 1)}{85.791 \, N} \qquad (2)$$

However since the ignition of a material is determined by an equation of the form of the Arrhenius specific rate constant, and the impact temperature depends on the square of the impact velocity, the variation of burn probability with velocity is also given by a function of the form

$$P(V) = \exp(-E^2/V^2) \qquad (3)$$

where E is a constant which can be evaluated by a least squares fitting using the experimental values obtained from Eq. (2). The impact velocity, V_{50}, for 50% probability of a Burn reaction is then given by

$$V_{50} = E/(\ln 2)^{1/2} = 1.201 \, E \qquad (4)$$

Since bullet impact tests were conducted for impacts into the primer and the body separately, the V_{50}'s obtained apply only to either the primer or to the body (excluding the primer). The overall V_{50} for the entire round is obtained by the solution of the equation

$$R_p \exp(-E_p^2/V_{50}^2) + R_B \exp(-E_B^2/V_{50}^2) = 0.5 \qquad (5)$$

where E_p and E_B are the calculated E parameters for the primer and body, respectively, and

$$R_p = a_p/(a_p + a_B); \quad R_B = a_B/(a_p + a_B) \qquad (6)$$

where a_p and a_B are the side presented areas of the primer and body (excluding the primer), respectively. The V_{50}'s calculated in the preceding manner can serve to differentiate the primer, body, or overall vulnerability of the test rounds.

Figure 6 illustrates the resulting computed overall Burn Probabilities vs Impact Velocity for several of the caseless rounds, and Table 2 shows the computed values of V_{50} for the rounds, including the individual values for the primer and body. In these computations the explosions of the type H round were considered to be Burns.

Spall Particle Impact Tests

The signals obtained by the monitoring systems on the spall particle impact tests differed to some extent from those obtained on the bullet impact tests. To begin with, the hot metal particles produced by the impact and penetration of the steel armor plate by the AP slug emitted luminous paths which generally fogged or overexposed the open shutter camera film to a degree that little information could be obtained

TABLE 2

Estimated Values of V_{50}

Round Type	V_{50}, feet/sec		
	Primer	Body	Combined
H	3360	8600	7100
G	3730	8260	6960
F	4520	7980	6980
E	2520	5000	4280
D	810	3800	3590
C*	< 1430	5730	
A*	2750	5550	
B*	2750	> 4150	

*For the analysis of these early conducted rounds, the number of Partial Burn Tests was distributed into the Burn and No Burn tests according to the ratio of Burns and No Burns obtained in the tests.
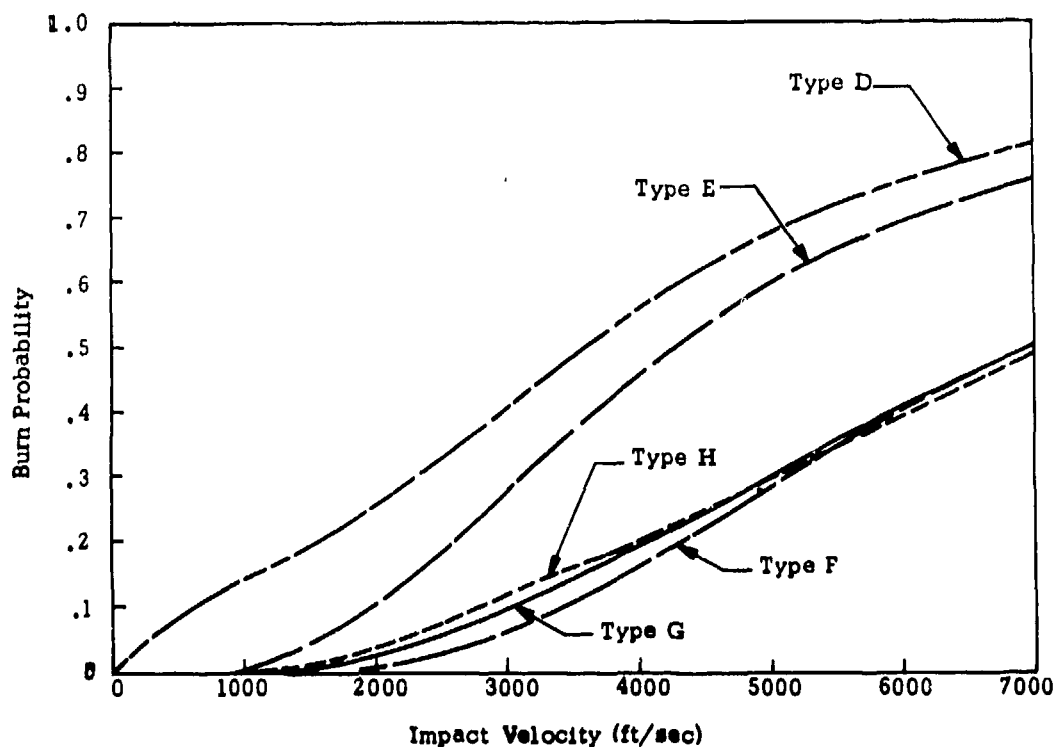
Fig. 6. Estimated burn probabilities versus impact velocity for the various caseless propellant ammunition rounds.

689

from these films. As a matter of fact, this problem provided the impetus for the development of the photocell technique which not only facilitated the interpretation of the spall particle impact data but provided extensive information regarding the details of the bullet impact tests. Whether the light was due to particle combustion or merely glow is not known (glow is most likely), but in any event it was clearly distinguishable from that produced by a Partial or Full Burn reaction induced in the test round by particle impact (Fig. 7).

The metal particles produced by the AP slug penetrating the steel armor plate varied in size. It was determined that the larger particles had the wider cone angles, and these particles were probably largely produced by spallation off the back of the plate in front of the slug. The smaller particles with small cone angles were probably produced by shear action during the passage of the slug through the plate. These particles were probably very hot, and produced the luminous paths detected by the sensors. The test results indicated that these are the most effective particles in producing ignition since the burn probability was greatest at small offset distances. The burn probability can be expressed in terms of the fraction of burns per particle hit. The hits per test depends on the offset distance and the distance to the plate.

ACKNOWLEDGEMENT

(a) Waveform for emission of luminous spall particles

(b) Waveform for spall impacts on test round—no ignition

(c) Waveform for partial burn produced by spall impact

(d) Waveform for total burn produced by spall impact
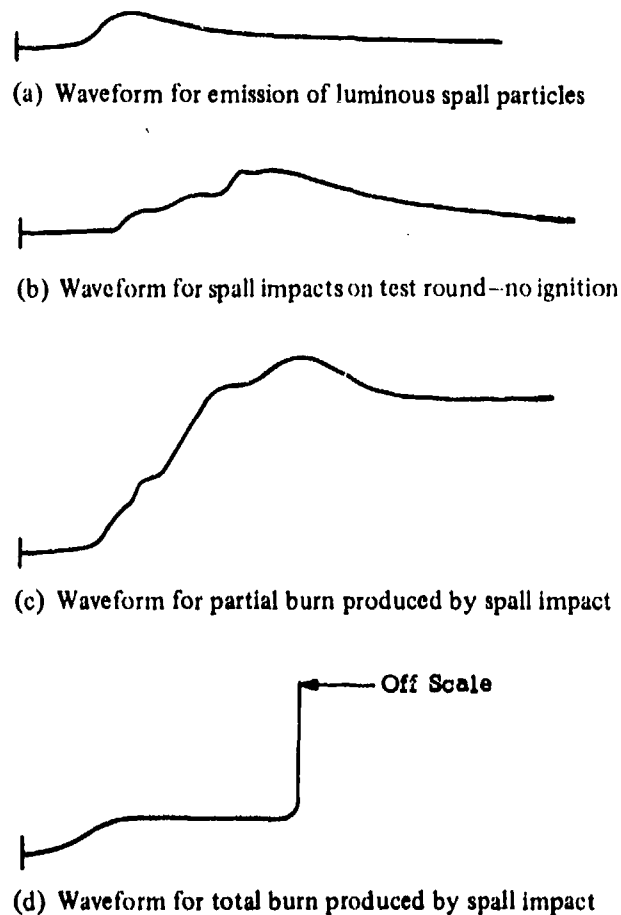
Fig. 7. Photocell waveforms from spall impact tests.

SHAPED CHARGE TEMPERATURE MEASUREMENT

W. G. Von Holle and J. J. Trimble
Detonation & Deflagration Dynamics Laboratory
Ballistic Research Laboratories
Aberdeen Proving Ground, Maryland 21005

In this work, a two-color infrared radiometer with a response time of less than one microsecond was used to measure the residual temperature of shocked copper plates and shaped charge jets in flight. Some explosively driven plates were found to undergo rapid surface contour changes which greatly affected the individual infrared signals, but the radiance ratios provided temperatures consistent with other data.

The interpretation of the infrared signals from shaped charge jets was aided by high speed framing camera results. Jets from the standard rounded-apex liners showed large amounts of debris near the jet, while the jets from especially machined conical liners were free from this. The infrared signals reflected this difference and provided an unambiguous temperature for the jets from pointed liners. The observed jet temperatures from composition B and octol charges were below the melting point of copper indicating that the jets were solid.

INTRODUCTION

A two-band infrared radiometer has been developed as a rapid, non-contact method suitable for the dynamic temperature measurement of complex targets such as shaped charge jets in free flight. A large amount of experimental and theoretical effort has been devoted to shaped charges since their introduction. However, very little experimental work has been done on the estimation of jet temperature because of the great speed and complexity of jets in flight. Accurate jet temperature determination has important consequences in the analysis of the poorly understood jet formation and stretching processes. The design of new shaped charge weapons may benefit most, since the residual jet temperature after the explosive liner collapse process may determine the breakup time and thus the penetration behavior of such jets.

Due to the complexity of the problem, it was divided into two parts. First, a preliminary, less ambitious program was carried out as a check of the system. The two-color technique was applied to the determination of the residual temperature of copper plates driven by various explosives. These results provided some comparison with theory and experiment since the loaded plate problem had been previously studied. The measured shaped charge jet temperatures can be considered with more confidence because many of the troublesome questions encountered have been answered in the preliminary plate study.

THEORY

If one attempts to measure the temperature of an object by the single band or brightness method, the emittance must be known since the output radiation will depend on the emittance as well as the temperature. The object radiance at a detector, W_0, is given as follows:

$$W_0 = \frac{A_s \epsilon_b}{R_s^2} \int_{\lambda_1}^{\lambda_2} W_{\lambda,T}^b \frac{b}{T} \, d\lambda \qquad (1)$$

ϵ_b is the band emittance; $W_{\lambda,T}^b \frac{b}{T}$ is the Planck black-body function. A_s is the area of the source accepted by the detector, and R_s is the distance to the detector. The detector characteristics have been omitted for clarity. The integral is over the wavelength range of the collection optics and detector. W_0 is a sensitive function of the geometrical arrangement and of the surface condition and wavelength through the band emittance, which is a complex and unknown function of many surface variables. However, if the ratio of the outputs of two radiometers with identical geometrical arrangements but different wavelength sensitivities is obtained, this provides a measure of the "color temperature." Since the geometry factors cancel, the "color temperature" approaches the true temperature as the ratio band emittances approaches unity. This ratio also serves to compensate for transient effects in surface conditions which are encountered in shock studies and which will be discussed in detail below. The design of a good two-color radiometer is predicated on the selection of the wavelength bands. They must be close enough together to provide a band emittance ratio near unity but far enough apart to yield adequate sensitivity.

COPPER PLATE RESIDUAL TEMPERA-TURE MEASUREMENT

There is only one reported measurement of the temperature of explosively loaded copper by infrared radiometry. King, Cotgrove and Slate (1) worked at one pressure with a single band, and they found a large discrepancy from the theoretical value calculated by McQueen and Marsh (2). The former authors suggested that the error might have been due to shock-induced emittance and a two-color approach might reduce the error.

In the present study, two identical i. r. line scanners with liquid nitrogen cooled InSb photovoltaic detectors, which have a figure of merit,

$$D^*(500,900,1) = 1.2 \times 10^{11} \frac{\text{cm Hz}^{1/2}}{\text{watt}},$$

were converted to radiometers with 12.7 mm apertures and 3 milliradian fields-of-view. A 4.0 μm cut-

on filter was permanently installed in one radiometer which defined two overlapping bands, 2-5.5 μm and 4-5.5 μm. The response time of the detector-electronics combination was less than 0.5 microseconds. The 0.3 $\times$ 10 $\times$ 10 cm polished copper plates were viewed by the radiometers in an arrangement depicted in Fig. 1. Ambient pressure was in the range of 1 to 10 μm of Hg while a few shots were near 100 μm Hg.
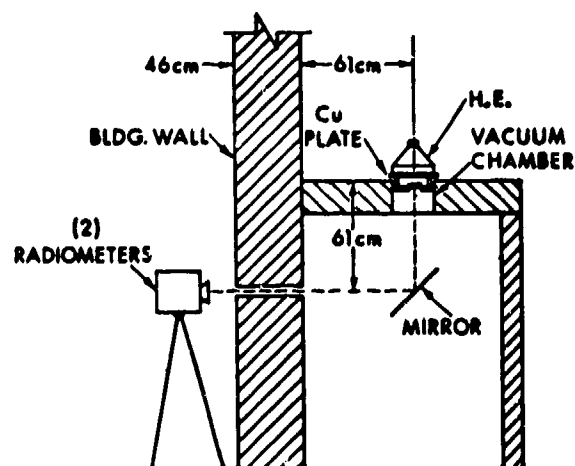
Fig. 1. Experimental arrangement for copper plate range firings.

The radiometers were calibrated with copper plates polished to a mirror surface with 1.0 μm alumina powder and electrically heated in a vacuum. Since they received considerable stress during a shot, the radiometers were calibrated with a blackbody source prior to each shot, which served to correct for any optical misalignment suffered in the previous shot. Fig. 2 shows the results of the copper calibration and a corresponding blackbody calibration. The output ratios are seen to be close over a large temperature range. The copper calibration by electrical heating is unreliable at temperatures above 400° because the heating time is long and the surface may undergo irreversible changes in emittance. The equation in Fig. 2 expresses the output ratio for the copper calibration, assuming all geometrical factors cancel. ϵ_1/ϵ_2 is the ratio of band emittances and $W_{\lambda_1}/W_{\lambda_2}$ is the ratio of blackbody outputs which are modulated by the detector characteristics and integrated over their wavelength ranges. Since ϵ_1/ϵ_2 is close to unity over much of the temperature range, the assumption will be made that any experimental copper
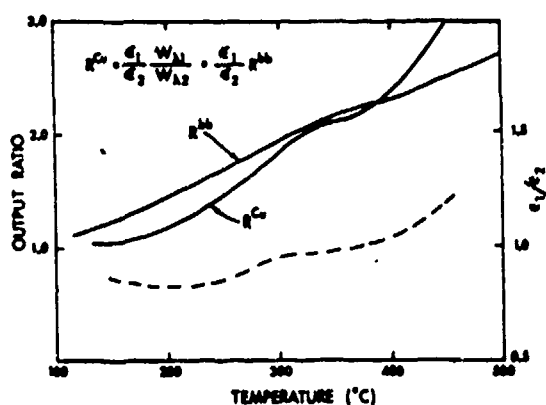
Fig. 2. Radiance ratio for polished copper, heated electrically, R^{Cu}, and the corresponding blackbody ratio, R^{bb}. ϵ_1/ϵ_2 is plotted as the dashed line.

surface, including that which has undergone the shock passage and release wave, is a graybody over this temperature range with the chosen wavelength bands. One may also consider the two ratio curves to define the limits of the actual shocked surface curve. Unfortunately, the uncertainty in the copper ratio is about 20 percent which limits the accuracy of the results. The blackbody ratio is accurate to 5 percent.

Each radiometer output was coupled to a wide band oscilloscope, and the radiance ratios were visually derived from photographs of the traces. Representative traces are shown in Fig. 3. The composition B traces showed a level step at 0.5 μsec after shock arrival, but some octol shots did not level off for several microseconds. Fig. 4 is a plot of derived residual temperature vs. time after shock emergence. A smooth curve was drawn through several averaged points derived from the radiance ratios. The temperatures at 0.5 μsec were assumed to be the residual values; the continued rise with time may be due to shock reverberations and shock heated residual air. Note that the octol plate temperature vs. time behavior is quite different from the individual signal behavior of Fig. 3. It is puzzling why the composition B plate temperature rises faster than the octol even though the individual signals are better behaved.

Table 1 summarizes the copper plate data. The individual radiometer signals are indicated by NF and F; R^{Cu} is the computed ratio, T_A is the temperature derived from the blackbody curve measured prior to that shot, and ΔT_R is the residual temperature, ex-
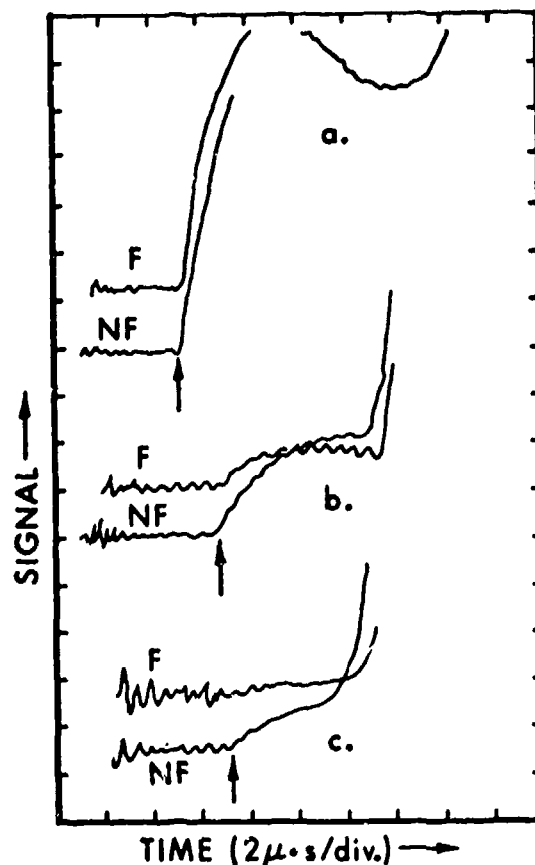
Fig. 3. Typical oscilloscope traces of the radiance signals from explosively loaded copper plates. (a) Cu/Octol; (b) Cu/comp B; (c) Cu/TNT. "F" is the 4-5.5 μm trace at 50mV/div. sensitivity; "NF" is the 2-5.5 μm trace at 100mV/div. The arrows indicate shock arrival.

pressed as an increase above ambient, which was read from the corresponding copper calibration curve.

Table 1 and Fig. 3 indicate that the octol results are basically different than comp B or TNT. The octol signals rise more steeply and exhibit a large round-to-round variation not found in comp B. This different behavior must be due to either surface emittance of temperature differences. Temperatures and ratios are consistent and only slightly above comp B even at later times; therefore, octol loading must induce some transient surface changes which affect the individual signal outputs but which are cancelled by the ratio technique. In support of this contention, framing camera pictures by Boyd Taylor (3) at the Ballistic Research Laboratories show octol-shocked
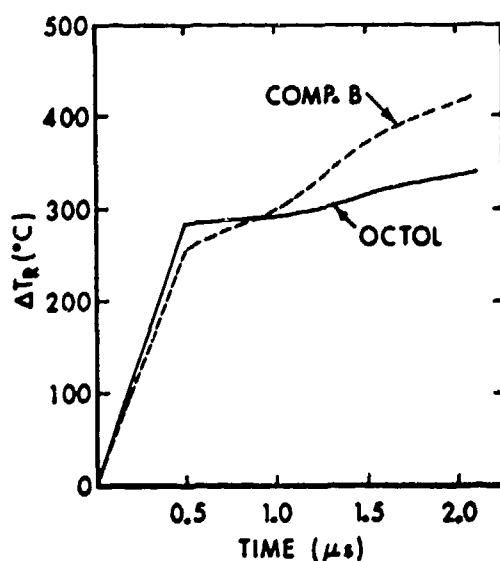
Fig. 4. *Time dependence of temperature for comp B- and octol-shocked copper plates.*

plates considerably more distorted than comp B at all times after shock arrival. These effects are reasonable since octol, which is a mixture of HMX and TNT, has a quite different polycrystalline structure than composition B, which is a mixture of RDX and TNT.

Figure 5 is a graph of residual temperature *vs.* Hugoniot pressure for our results. For comparison it also shows other experimental and theoretical data. Note the agreement with the curve fit of G. Hauver's results (4), which were obtained by fast resistance measurements of shocked copper foils. The TNT results are much too high, but their uncertainty is great due to a low S/N ratio.

The gap between the experimental points and the theoretical curve of McQueen and Marsh is not as easy to explain, but it would be unreasonable for hydrodynamic theory which is meant to describe the bulk material to be valid at the surface.

TABLE 1

Copper Plate Radiometer Data

Explosive Shot No.	NF (mV) (2-5.5 μm Band)	F (mV) (4-5.5 μm Band)	R^{Cu}	T_A	ΔT_R (°C)
TNT					
C21	32.0	23.1	1.39	220	250
C22	36.0	25.0	1.44	168	196
					Ave 223
COMP B					
B12	63.0	42.0	1.50	–	265
B13	50.0	28.0	1.79	210	240
B19	48.0	33.0	1.45	240	264
B23	59.0	34.0	1.74	211	242
					Ave 253
OCTOL					
C10	72	40	1.80	–	340
C11	97	52	1.87	–	330
C17	60	32	1.88	227	253
C18	130	70	1.86	245	265
C20	92	59.0	1.56	260	282
					Ave 294
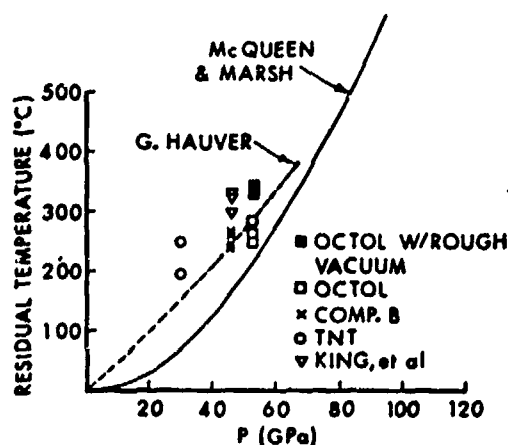
Fig. 5. Plot of experimental and theoretical data vs. the Hugoniot pressures. For the two octol points marked "Rough Vacuum", ambient pressure was near 100 μm; all other experimental points were obtained at less than 10 μm.

The plate work seemed to provide a sound experimental basis for the following shaped charge measurement by demonstrating that the two-color radiometer had the capability to overcome the two main obstacles of the shaped charge problem, namely, speed of response and unknown surface emittance and contour.

SHAPED CHARGE JET TEMPERATURE MEASUREMENTS

The experimental set-up for plate temperature in Fig. 1 was modified for shaped charge vacuum firings by the introduction of a 9 cm inner diameter metal pipe with a 2 X 38 mm diameter sapphire window. The jet was observed through the sapphire window at a point eight cone diameters down range of the 81.3 mm liner. The two radiometers were independently focused through the window on a point in the jet path. The angle formed by the two optical paths with apex at the jet path was 20 degrees. In most cases narrow band-pass filters were used in place of the broad-band filters.

During the course of the program, ambient pressures in the firing chamber were steadily reduced to a level between 1.0 and 0.3 μm of mercury by changing vacuum systems and pipe materials. A 3-inch oil dif-

fusion pump and a stainless steel pipe provided the lowest pressures.

The calibration of the radiometers was extended out to 800°C by induction heating of a copper cylinder. One face of the cylinder was polished, the cylinder was placed in the coils of the r. f. generator, and the whole assembly was sealed in a vacuum chamber fitted with a sapphire window. This calibration method provides better temperature control and more uniform heating than the electrical heating method, especially at the higher temperatures. The result of a calibration with a typical filter combination is presented in Fig. 6. As in the lower temperature calibra-
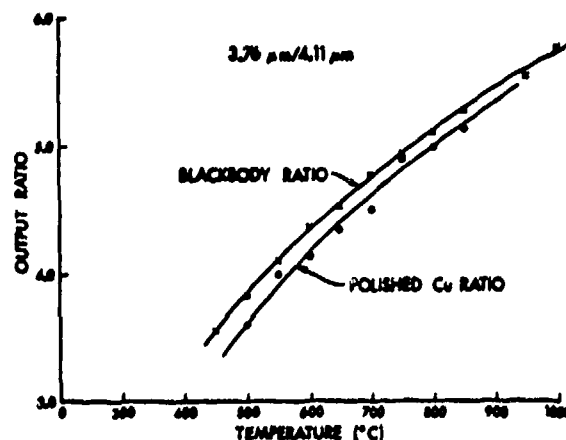
Fig. 6. High temperature calibration curves for a typical narrow-band filter combination.

tion with the broad-band filters, the two curves are in close proximity. However, the position of the copper curve is somewhat more uncertain due to the much smaller radiances entering the ratios.

A photograph of a typical oscilloscope trace for a standard 81.3 mm copper liner with a bare comp B charge fired in the above apparatus is reproduced in Fig. 7. The structure of the radiant intensity signal for about 10 microseconds after signal start and before the large increase in signal was difficult to explain. There is some similarity with all of the experimental records, but in general the intensities and positions of the peaks are random. The steep off-shoot of the signals was assigned at first to detonation products reaching the optical path, but further experiments have proven this interpretation erroneous.

695

In order to explain the complexity of the infrared results, high speed (1.2×10^6 f.p.s.) framing camera coverage of similar shaped charges fired in an evacuated glass tube was obtained. One frame from a standard rounded-apex liner is reproduced in Fig. 3. The results showed a heretofore unreported "prec. ˂or" jet stretching ahead of the jet tip. A large numb r of


Fig. 7. Dual oscilloscope traces of the radiance signals from a typical comp B shaped charge with an 81.3 mm rounded-apex liner. The 5 μsec per division sweeps were triggered by a 62 μsec-delayed pulse from an ionization switch placed at the base of the charge. The upper trace is the 3.94 μm signal at 100mV/div. vertical sensitivity; the lower trace is the 4.11 μm signal at 50mV/div. The traces were off-set for clarity.
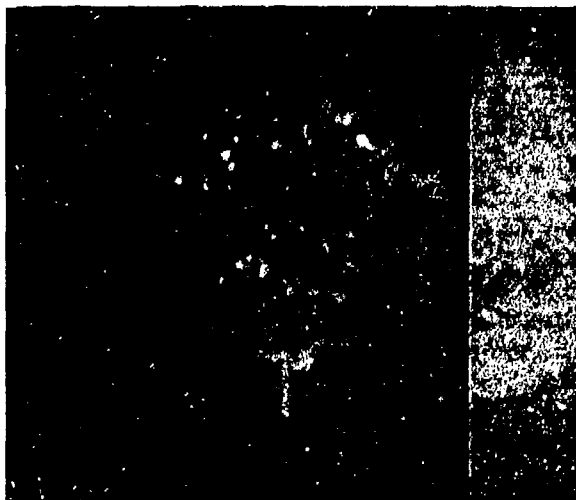
Fig. 8. A copper jet from a 81.3 mm rounded-apex liner at about 8 cone diameters stand-off. The framing rate is 1.2×10^6 f.p.s. Ambient pressure is about 30 milli-Torr. The fiducial marks are 2.54 cm apart. The jet was front and back lighted with argon bombs.

particles were observed near the jet forming a conical cloud. The largest pieces of debris have roughly the same velocity as the jet, and they are smeared out in the photo. There may be a whole spectrum of particle sizes which leads to the appearance of a fog. Aluminum and steel baffles with 1.9 cm centered holes were used in an attempt to clean up the jet tip. They actually made the situation worse by increasing the density of the debris cloud, nearly obscuring the jet altogether.

It has been reported (5) that liners machined to a true conical apex eliminate this cloud of material. Framing camera coverage of a jet from such a liner indicates that this is indeed the case. One frame is reproduced in Fig. 9. The difference between photo-
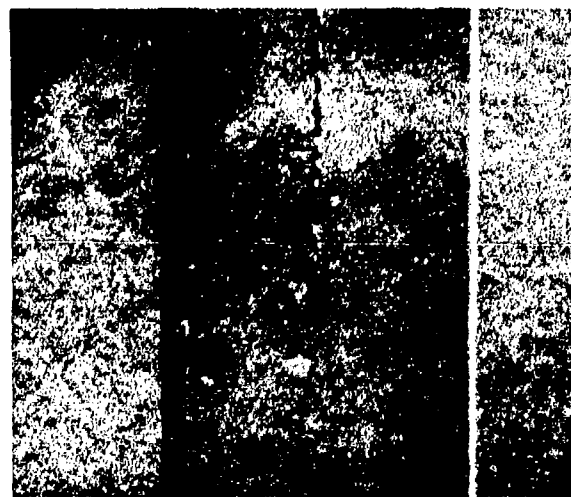
Fig. 9. A copper jet under identical conditions as Fig. 8 except that the liner was a true pointed-apex cone.

graphs of the pointed- and rounded-apex cones is quite marked on the originals; the lack of darkening of the glass tube with the pointed cone of Fig. 9 is further evidence that the jet resulting from this liner configuration is free from foreign material.

The visible pictures lead to an interpretation of the infrared results from rounded cones in which the fog of debris causes the steep signal increase and structure within ten microseconds. Infrared traces from a shot with a pointed cone is shown in Fig. 10. Since the wide bands were used for the radiometers in Fig. 10, the actual signal level is higher, but the framing

696
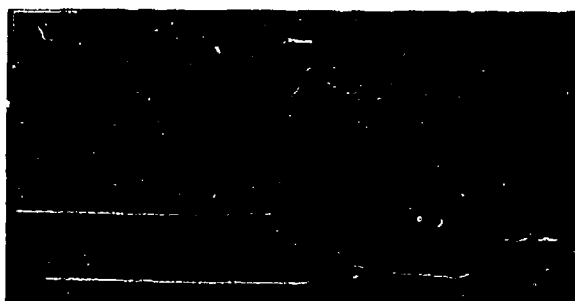
Fig. 10. Dual oscilloscope traces from a pointed-apex liner under similar conditions as in Fig. 7 except that broad-bands were used. The upper trace is the 2-5.5 μm output; the lower one is the 4-5.5 μm signal, both at 500mV/div. sensitivity and 5 μsec/div. sweep rate.

camera results provide the assurance that the observed signals arise from the jet alone. Note that the complex structure of the rounded-cone jet is absent in Fig. 10; the signal trace rapidly increases to its maximum at the jet arrival time.

The difference between the infrared signals from the rounded- and pointed-apex shots is graphically presented in Fig. 11, where the broad-band results of a pointed cone have been reduced to the scale of a rounded-apex shot obtained with narrow bands. The signals of the broad-band shot were adjusted by multiplication by the ratio of experimental blackbody radiances, i.e.,

$$W^{exp}_{3.94} = W^{exp}_{2-5.5} \frac{W^{bb}_{3.94}}{W^{bb}_{2-5.5}}$$

where the superscript "exp" refers to the jet trace value and "bb" the blackbody value. The assumption is that the ratio of band emittances is unity, i.e.,

$$\frac{\epsilon^{3.94 \, \mu m}}{\epsilon^{2-5.5 \, \mu m}} = 1,$$

which is only approximately correct but is good enough for this comparison. The results of Fig. 10 clearly indicate the effect of the debris caused by the rounded cone.

Three out of four i. r. traces from pointed cones resemble Fig. 10, where the abrupt rise is followed by a gradual decline which is followed by a further
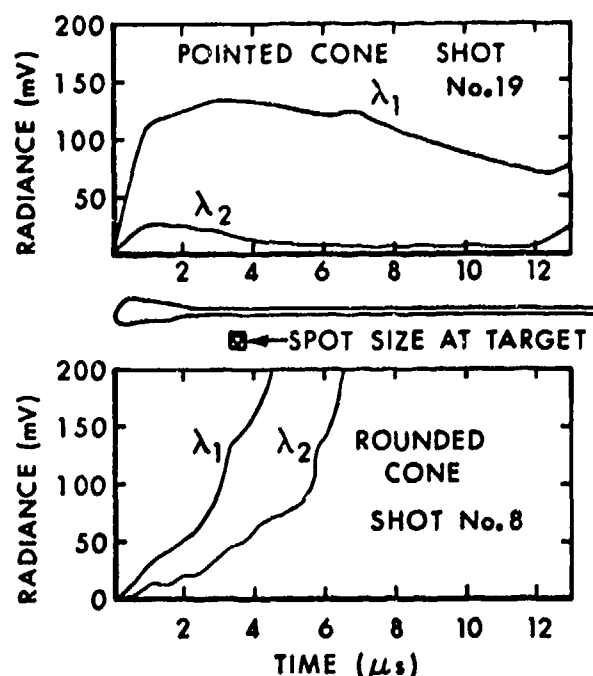
Fig. 11. Comparison of radiance signals from rounded- and pointed-apex liners. For the pointed-liner jet, λ_1 and λ_2 refer to the broad-band signals of Fig. 10, which have been adjusted to the levels expected from the narrow-band filters used for the rounded-apex jet. λ_1 and λ_2 refer to 3.94 μm and 4.11 μm, respectively, for the rounded-apex traces. See text. A scaled drawing of the jet from Fig. 9 (v = 7.7 mm/μsec) is included between the two sets of traces to provide an idea of the time required for traversal of the "spot size", 3 mm, at 1 meter range.

increase after 13 microseconds. The derived temperatures increase with time rapidly after the jet arrival.

Table 2 presents the results of all the successful shaped charge firings including those with rounded cones. The temperatures in all cases were derived from radiances observed within the first microsecond after the signal start. For the rounded cone shots, the thickness of debris near the jet tip is small and may not interfere. Indeed, most traces exhibit shallow signals in the first microsecond.

Shots 13, 14 and 20 were carried out with a different experimental procedure in an attempt to increase the accuracy of the measurements. The beam-splitting arrangement of Fig. 12 was used. In spite of

TABLE 2

Shaped Charge Jet Results

Shot	Wavelength Bands (μm/μm)	Optical Paths S = Separate B.S. = Beam Split	Ambient Pressure (μm)	Temperature (°C)
Comp B				
#1 Rounded Cone	(3.76/4.11)	S	10	400
#2 Rounded Cone	(3.76/4.11)	S	3	410
#3 Rounded Cone	(3.76/4.11)	S	1	395
#7 Rounded Cone	(3.94/4.11)	S	< 1	420
#8 Rounded Cone	(3.94/4.11)	S	< 1	350
#15 Rounded Cone	(3.938/4.274)	S	< 1	413
#16 Rounded Cone	(3.938/4.274)	S	< 1	360
#17 Pointed Cone	(3.938/4.274)	S	< 1	395
#18 Pointed Cone	2-5.5/4.0-5.5	S	< 1	560
#19 Pointed Cone	2-5.5/4.0-5.5	S	2	450
#20 Pointed Cone	2-5.5/4.0-5.5	B.S.	< 1	550
		Comp B Average = 428°C Std. Deviation = 67°C		
OCT				
#5 Rounded Cone	(3.94/4.11)	S	2	540
#6 Rounded Cone	(3.94/4.11)	S	< 1	(> 1000)
#13 Rounded Cone	(3.938/4.274)	B.S.	< 1	555
#14 Rounded Cone	(3.938/4.274)	B.S.	< 1	515
		Octol Average (excluding #6) = 537°C Std. Deviation (excluding #6) = 20°C		
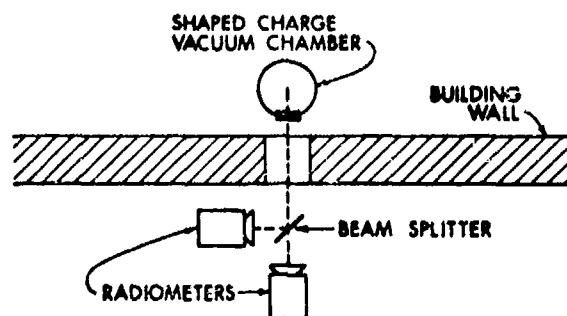
Fig. 12. Schematic of the experimental arrangement used to produce two colinear optical paths.

some uncertainty introduced by the temperature dependence of the reflectivity of the acetate beam splitter, this experiment is designed to rule out gross errors possible in the separate beam arrangement. Proper alignment of the two radiometers resulted in two co-linear beams originating at the same spot on the jet. Unlike the separate beam case, where the two optical paths intersect the target at an angle, any misalignment of the jet could not cause error since both radiometers would be equally affected.

In shot No. 20 the temperature is near the other pointed cone jets and increases with time as in the others. In three pointed-apex liner shots, the derived temperatures exceed 800° after 3 microseconds and go higher beyond that. These data must be considered with caution since the absence of visible interference in the framing camera shots does not preclude the presence of invisible detonation products which may begin to appear at later times. Of course, the sharp increase in signal at the calculated jet arrival time

would argue against any early interference. The i.r. traces show a sharp increase after 13 microseconds which may indicate the arrival of these hot detonation products or interfering jet particles. Unfortunately, the framing camera shot does not extend to the position on the jet corresponding to this time.*

It should be noted that the ambient pressure in the firing tube seemed to have no effect on the observed temperature, at least below 10 milli-Torr.

The octol shaped charges of Table 2 seem to result in higher temperatures than the comp B charges with the same filter combinations. The appearance of the octol oscilloscope records is similar to those of comp B, except peaks are closer together and the signal rises more quickly. Shot #6 seems out of line. A particle of jet may have been positioned off-axis in such a way which influenced one radiometer preferentially. The two beam-spilt octol shots are close to #5. All octol liners used were rounded-apex cones.

The comp B temperatures . rived from the narrow-band filtered signals, most of which were from rounded cones, seem to be lower than those using the broad-band interference filters. This may simply be the result of the interference of the debris. Another explanation may lie in the copper calibration, since the uncertainty in the ratios is high. The difficulty arises from the small emittance of polished copper, which leads to small measured radiances and a correspondingly large percentage effect for any systematic error. Thus the uncertainty of the position of the calibration curves for the narrow band interference filters may be larger than the 20 percent of the broad-band curves. The problem is not as severe in the latter case since radiance signals are much larger. This emittance uncertainty is the limiting accuracy factor for the narrow- and broad-band cases since the random errors are expected to be much less.

CONCLUSIONS

The reliability of the shaped charge temperature measurements is supported by the success of the

residual temperature measurements on copper plates. The ability to compensate for transient emittance changes and to resolve these on a microsecond time scale allows some confidence in the shaped charge results.

Since all measured jet temperatures are well below the melting point of copper, the assertion of a solid jet can be made, at least near the tip. This is supported by other evidence obtained from radiographs of spinning jets (6). The spin rate at which they begin to breakup radially is consistent with an ultimate strength of the copper material of 0.1 GPa. This value is near the yield strength of pure copper.

ACKNOWLEDGMENTS

REFERENCES

1. P. J. King, D. F. Cotgrove, and P. M. B. Slate, Behavior of Dense Media Under High Dynamic Pressures, Gordon and Breach, New York, 1968, pp. 513.

2. R. G. McQueen and S. P. Marsh, "Equation of State for Nineteen Metallic Elements from Shock-Wave Measurements to Two Megabars", *J. of Appl. Phys., 31*, 1253 (1960).

3. Boyd C. Taylor, Unpublished Results.

4. G. E. Hauver, "Residual Temperature Measurements on Shock Compressed Metals," *Bull. Am. Phys. Soc., 20*, 19 (1975). Also BRL Report in Press.

5. E. C. Mutchler, "Transactions of Symposium on Shaped Charges", BRL Report #837, November, 1951.

6. R. Karpp and J. Simon, "An Estimate of the Strength of a Copper Shaped Charge Jet and the Effect of Strength on the Breakup of a Stretching Jet", BRL Report No. 1893, June, 1976.

THE HYDROSTATIC COMPRESSION OF EXPLOSIVES AND DETONATION PRODUCTS TO 10 GPa (100 kbars) AND THEIR CALCULATED SHOCK COMPRESSION: RESULTS FOR PETN, TATB, CO_2 and H_2O

Bart Olinger and Howard Cady
Los Alamos Scientific Laboratory
University of California
Los Alamos, New Mexico 87545

The isothermal linear and volume compressions of PETN, TATB, CO_2, and H_2O are determined from x-ray diffraction patterns taken at hydrostatic pressures up to 10 GPa. From the compressions, the Hugoniots of these materials are calculated assuming that the heat capacity at constant volume and the ratio of the Grüneisen constant to the specific volume both remain constant over the 10 GPa pressure range studied here. The Hugoniots in shock-particle velocity coordinates centered at 0 GPa, $293°K$, are

PETN

$$U_s = 2.320 + 2.61 \ U_p - 0.38 \ U_p^2, U_p < .8 \ \text{km/s}, \rho_o = 1.774 \ \text{g/cm}^3$$

$$U_s = 2.811 + 1.73 \ U_p \qquad , U_p > .8 \ \text{km/s}, \rho_o = 1.774 \ \text{g/cm}^3$$

TATB

$$U_s = 1.43 + 10.13 \ U_p - 11.42 \ U_p^2, U_p < 0.3 \ \text{km/s}, \rho_o = 1.937 \ \text{g/cm}^3$$

$$U_s = 2.90 + 1.68 \ U_p \qquad , U_p > 0.3 \ \text{km/s}, \rho_o = 1.937 \ \text{g/cm}^3$$

CO_2 (solid)

$$U_s = 1.740 + 1.65 \ U_p \qquad , U_p > 0.7 \ \text{km/s}, \rho_o = 1.488 \ \text{g/cm}^3$$

H_2O (ice VII)

$$U_s = 2.872 + 1.69 \ U_p \qquad , U_p > 0.5 \ \text{km/s}, \rho_o = 1.395 \ \text{g/cm}^3$$

INTRODUCTION

Many aspects of dynamic compression of explosives have been investigated to better understand the processes of initiation and detonation propagation. Usually these studies involve a careful definition of the explosive's initial state (i.e., porosity, inert content, grain size) and then a determination of its dynamic properties. If the dynamic properties of the explosive's pure components could be defined, then the investigator and the fabricator both may be able to predict the properties of the aggregate. One such

property is the shock wave compression on Hugoniots centered at theoretical density. Here we describe an experimental method to determine the isothermal compression of explosives and their detonation products. From these data we can then calculate the shock compression with a reasonable assumption about the equation of state.

EXPERIMENTAL

Primarily, the technique provides x-ray powder diffraction patterns of explosives at well-defined pressures. The design of the apparatus was conceived by Jamieson and Lawson (1) and was described in detail by Jamieson (2). Recently, the design was modified by Halleck and Olinger (3) to study low Z materials such as explosives, to produce diffraction patterns of increased resolution, and to include a hydrostatic medium that does not support shear, permitting the study of weakly bonded materials such as explosives.

The principles of the technique are simple. The explosive to be studied and a pressure calibrating material are placed in an annulus that is relatively transparent to x-rays. This annulus is pressed to high uniaxial stress between two tungsten-carbide flats, called Bridgman anvils, and the diffraction patterns are taken of the trapped materials by directing into them an x-ray beam perpendicular to the axis of stress and recording the pattern on a strip of film surrounding the sample and anvils.

In detail, we use two G. E. grade 999 tungsten carbide Bridgman anvils ground from right circular cylinders 12.3 mm in dia and 13.1 mm high. One end of each anvil has a 4.8 mm dia flat bearing surface in its center and a 30° taper ground from the bearing surface to the sides of the cylinder, thus forming a truncated cone. On one bearing surface an annulus of beryllium foil 0.3 mm thick, 3.8 mm dia, with a 0.3 mm dia hole in its center is mounted with a fast-setting epoxy. The center of the annulus is aligned with the center of the bearing surface. After drying, the excess epoxy is removed from the hole and the sides of the annulus. Into the hole is worked a mixture of fine powdered explosive and pressure indicator, either NaF or NaCl. The powders are not packed, but loosely inserted.

The anvil with loaded beryllium annulus is seated on a pedestal that is in turn mounted into the base of

a high pressure frame. The high pressure frame is constructed from two thick steel plates held together by steel tie rods and held parallel by precision machined steel tubes surrounding the rods. On the base of the pedestal is mounted the x-ray camera. The camera is cut from a solid brass cylinder 114.6 mm in dia whose sides and core along the axis have been removed. The top and bottom of the camera on which the film rests are supported by brass pillars through which are mounted the x-ray collimator and exit beam catcher collars. The collimator and beam catcher, when placed in the collars, are directed toward each other along the camera diameter. The x-ray film is mounted over the exit beam collar and is held to the sides of the camera by a light tight steel band under spring tension. An Ni foil is mounted to the camera inside the film radius and serves as a light shield and a x-ray filter for white and $CuK\beta$ x-radiation.

The high pressure frame with pedestal, camera and anvil assembly is mounted before an x-ray port of an x-ray generator for x-ray diffraction work. We use the Norelco generator with fine focus Cu x-ray tubes running at 35 kV and 15 ma. Exposure times are 6 to 8 hrs for zero pressure exposures and 12 to 16 hrs for high pressure exposures. The first several patterns of an experiment are taken at zero pressure. These patterns are compared with others taken of the materials using regular powder cameras or are compared with published diffraction patterns. From this comparison correction factors are calculated for uncentered samples and for x-ray cameras that have circumferences different than the normal 360 mm.

Having carefully marked the position of the anvil on the pedestal, the anvil with annulus and sample is removed and a drop of 4:1 mixture of methanol-ethanol is placed on the annulus. This mixture has been found to remain hydrostatic to pressures slightly higher than 10 GPa [100 kbars] (4). The alcohol is worked into the sample hole with a fine needle; this removes air and, if not done carefully, the sample. As the alcohol drys, more drops are added. The anvil is reset into its former position on the pedestal. A commercial hydraulic ram is mounted through the top plate of the high pressure frame. Attached to the end of its piston is another pedestal on which is mounted the other anvil. Alignment and parallelism of the two anvils are the foremost considerations when the high pressure frame is designed. With the alcohol drop on the annulus replenished, the piston is lowered by

pumping oil into the ram and the anvils are pressed together against the annulus. The usual starting oil pressure for 10 to 25 ton rams is 1000 psi. The oil pressure ranges normally extend to 6000 to 7000 psi for the 10 ton rams and 4000 to 4500 psi for the 25 ton rams. At the maximum pressures of these ranges the pressure in the sample cavity of the annulus is about 10 GPa, the maximum hydrostatic pressure of the alcohol mixture. Also at these maximum ram pressures, the Be annulus extrudes to the extent where good quality diffraction patterns are difficult to obtain. Once the annulus is under stress, the collimator and beam catcher are adjusted to the level of the annulus by shimming the camera on its pedestal seat.

The x-ray films sho·   ·raction lines of the explosive, the pressure indicator at a given ram pressure, and the diffraction lines from the beryllium annulus. The latter forms bands on the film because of the annulus' width. The bands obscure diffraction lines from d-spacings between 2.04 to 1.90 Å and 1.79 to 1.67 Å. An exposure is taken for 12 to 16 hours at a constant ram pressure, then the film is developed and the ram pressure is increased several hundred psi for the next exposure. The procedure followed has been to only increase pressure between exposures. The reason for not decreasing pressure is that there is a chance the relieved stress will induce radial cracks in the annulus.

The pressure in the sample region is deduced from the volume of the pressure indicator. The indicator is a substance that exhibits a simple diffraction pattern and whose compression is well known. The two indicators extensively used are NaCl and NaF. Fritz et al. (5) and Weaver et al. (6) have published isothermal compression equations and tables for NaCl which differ by 2 1/2% in pressure in the vicinity of 10 GPa. The P-V relation for NaCl given by Weaver et al. (6) was calculated from thermodynamic parameters derived near ambient conditions. The values given by Fritz et al. (5) were calculated from P, V values along the Hugoniot. Despite their differences, these two studies are the standards for high pressure, x-ray diffraction work. The other indicator, NaF, though less compressible than NaCl, is the most extensively used by us. The P,V correlation for NaF is derived from two sources. Olinger and Jamieson (7) and Spieglan and Jamieson (8) collected extensive data on the simultaneous compression of NaF and NaCl using high pressure, x-ray diffraction techniques like that

described above. The Fritz et al. (5) NaCl pressure scale was used to correlate the NaF volume with pressure. The other ambient temperature, P,V values for NaF were calculated from Hugoniot data by Carter (9). In that study, the P,V values listed do not exactly correspond to values subsequently calculated by Carter and Fritz (10). Apparently an error occurred in calculations, and the pressures listed by Carter (9) are approximately 2% too high. Using either NaF or NaCl, the pressures are deduced from the volumes calculated from their diffraction patterns at high pressures. The pressures correlated with the relative volumes for both these alkali halides are listed in Table 1.

Once a series of x-ray diffraction patterns for an explosive with pressure indicator have been taken, transforming the patterns to P,V values is straightforward. Neither of the two explosives we have studied, PETN and TATB, has undergone a change in crystal structure up to pressures between 5 and 10 GPa. From extensive x-ray data gathered on these explosives by others, the Miller indices of the diffraction lines of the patterns are well known. The diffraction lines of the pressurized samples are correlated with the ambient diffraction patterns. From

TABLE 1

Relative Volumes of NaCl and NaF as a Function of Pressure at 293°K

Pressure[a] GPa	NaCl[b] V/V_o	NaF[c] V/V_o
0.0	1.00000	1.00000
1.0	0.96268	0.97999
2.0	0.93248	0.96208
3.0	0.90705	0.94588
4.0	0.88506	0.93108
5.0	0.86566	0.91747
6.0	0.84831	0.90488
7.0	0.83259	0.89316
8.0	0.81822	0.88221
9.0	0.80498	0.87193
10.0	0.79270	0.86225
11.0	0.78124	0.85312

[a] 1 GPa = 10 kilobars.

[b] A refinement by J. N. Fritz of the V/V_o listing contained in Ref. (5).

[c] A recalculation by W. J. Carter based on the information contained in Ref. (9).

702

the distance between diffraction line pairs, and the factors determined by the diffraction patterns taken of the explosive-indicator mix at ambient conditions, a d-spacing between molecular planes is calculated. (For background to the powder diffraction technique, see Azaroff and Buerger's book, the Powder Method [11].) From the d-spacings and the Miller indices, the length of the unit cell axes and angles between the axes can be calculated. For any crystal system other than cubic, the assistance of a computer least-squares program is desirable or even essential. From the results of such calculations, the volume of the explosive and the pressure indicator can be calculated.

METHOD OF DATA ANALYSIS

The accumulated crystallographic information about the explosive is presented and analyzed in several ways. The cell edges under pressure are usually represented by least-squares polynomials of the relative cell edge compression. It has been observed (12) that explosives undergo large linear changes in the directions corresponding with weak van der Waals bonding. In PETN all three orthogonal directions have such bonding (12). In TATB, as we shall see, van der Waals bonding occurs in only one direction (also see [13]). The linear compressions may provide important clues about the detonation behavior of an explosive if the explosive is highly oriented, as are some TATB-based materials, or if the explosive contains large crystals of the base explosive.

The volume, too, can be represented by least-squares polynomials, but a more meaningful representation is a form similar to the shock compression Hugoniot

$$U_{st} = c_t + s_t U_{pt} + q U_{pt}^2 \qquad (1)$$

where the t subscript denotes isothermal conditions. Here U_{st} and U_{pt} are obtained from pressure and volume along the isotherm using the analogous Hugoniot conservation relations that apply to shock wave conditions.

$$U_{st} = (P V_o/(1 - V/V_o))^{1/2} \qquad (2)$$

$$U_{pt} = (P V_o (1 - V/V_o))^{1/2} \qquad (3)$$

$$P = U_{st} U_{pt}/V_o \qquad (4)$$

$$V/V_o = (U_{st} - U_{pt})/U_{st} \qquad (5)$$

In the isothermal equation (1) c_t is the isothermal bulk sound speed at zero pressure instead of the adiabatic bulk sound speed. Similarly, the second parameter, s_t, is related to the zero pressure, pressure derivative of the isothermal bulk modulus (B_{ot}') in the same way that the shock second parameter is related to the adiabatic modulus

$$s_t = (B_{ot}' + 1)/4; \quad s = (B_{os}' + 1)/4 \qquad (6)$$

If the adiabatic bulk sound speed, c_s, the volume thermal expansion, α_v, and the heat capacity at constant pressure, C_p, are determined for the explosive of interest, then a refined isothermal compression and a shock compression can be calculated. All of these parameters are readily and routinely determined. The zero pressure bulk sound speed, c_s, is the shock U_s intercept at $U_p = 0$. Both c_t and C_v, the heat capacity at constant volume, are calculated from c_s, C_p, and α_v using the following relations

$$C_v = C_p - \alpha_v^2 T c_t^2 \qquad (7)$$

and

$$c_t = c_s(C_V/C_p)^{1/2} \qquad (8)$$

The calculation is started by assuming $c_t = c_s$ in Eq. (7) and then cycling the results between the two equations until the C_v and c_t values converge. The c_t can be used for the constant in Eq. (1) instead of calculating it from a quadratic fit to the data; this increases the certainty of the other constants.

The shock compression of the explosive is calculated from Eq. (1) in the following manner. The energy change from the initial volume, V_o, to some volume, V_L, at constant temperature T is

$$E_t \{V_L\} - E_t \{V_o\} = \int_{V_o}^{V_L} (T\gamma C_v/V - P_t)dV \qquad (9)$$

The brackets, { }, mean "evaluated at." The subscript, t, again refers to isothermal compression. γ is the Grüneisen constant

$$\gamma = \alpha_v c_s^2/C_p \qquad (10)$$

The assumption made here is that both C_v and γ/V remain constant over all conditions of isothermal and shock compression, as long as the explosive does not transform to another phase. A similar energy change along the Hugoniot of the explosive is

$$E_h \{V_L\} - E_h \{V_o\} = \frac{1}{2} P_h \{V_L\} (V_o - V_L) \quad (11)$$

The subscript, h, refers to shock compression. Finally, the energy cycle is completed by calculating the energy difference between V_L on the isotherm and V_L on the Hugoniot. This difference is calculated from the following thermodynamic relation

$$\partial E/\partial P)_V = V/\gamma \quad (12)$$

Since V/γ is assumed constant,

$$E_h \{V_L\} - E_t \{V_L\} =$$

$$(V/\gamma) [P_h \{V_L\} - P_t \{V_L\}] \quad (13)$$

If we set $E_h \{V_o\} = E_t \{V_o\}$, then combining Eqs. (9), (11) and (13),

$$P_h \{V_L\} =$$

$$\frac{P_t \{V_L\}(V/\gamma) + \int_{V_o}^{V_L} P_t dV - [T(\gamma/V)C_v] (V_L - V_o)}{[(V/\gamma) - 1/2 (V_o - V_L)]} \quad (14)$$

The integral in Eq. (14) is solved by numerical integration

$$\int_{V_o}^{V_L} P_t dV = \sum_{r=1}^{L} \frac{P_{tr} + P_{tr-1}}{2} (V_r - V_{r-1}), \quad (15)$$

where

$$V_r = V_o(U_{str} - U_{ptr})/U_{str} \quad (16)$$

and

$$P_{tr} = (1/V_o)U_{str}U_{ptr}. \quad (17)$$

U_s and U_p are then calculated from $P_h \{V_L\}$ and V_L.

PETN

The study of the compression of PETN was published earlier (12). However, the NaF pressure scale used was the earlier Carter scale (9) and not the revised scale listed in Table 1. In addition, Morris (14) has refined the adiabatic bulk sound speed value (that work appears in this volume). The basic data, V/V_o of PETN correlated with V/V_o of NaF, are listed in the earlier study (12) along with appropriate figures and will not be repeated here. We have listed below the revised isothermal (U_{st}-U_{pt}) compression and the Hugoniot (U_s-U_p) calculated from Eqs. (18) and (19). The thermodynamic properties of PETN are listed in Table 2.

$$U_{st} = 2.233 + 2.737 U_{pt} - 0.511 U_{pt}^2,$$
$$U_{pt} < .8 \text{ km/s}, \rho_o = 1.774 \text{ g/cm}^3 \quad (18)$$

$$U_{st} = 2.759 + 1.695 U_{pt},$$
$$U_{pt} > .8 \text{ km/s}, \rho_o = 1.774 \text{ g/cm}^3 \quad (19)$$

$$U_s = 2.320 + 2.612 U_p - 0.379 U_p^2,$$
$$U_p < .8 \text{ km/s}, \rho_o = 1.774 \text{ g/cm}^3 \quad (20)$$

$$U_s = 2.811 + 1.730 U_p,$$
$$U_p > .8 \text{ km/s}, \rho_o = 1.774 \text{ g/cm}^3 \quad (21)$$

TABLE 2

Thermodynamic Properties of PETN at 293°K, 0 GPa

$\rho_o = 1.774$ g/cm^3	Ref. (12)
$c_s = 2.32$ km/s	Ref. (14)
$c_t = 2.23$ km/s	
$\alpha_v = 2.32 \times 10^{-4}/K°$	Ref. (15)
$C_p = 1.08$ J/gK°	Ref. (16)
$C_v = 1.00$ J/gK°	
$\gamma = 1.15$	

TATB

The symmetry of TATB is much lower than that of PETN (triclinic with 6 parameters to determine as compared to tetragonal with only 2 parameters to determine). [For details on the crystal structure, see Ref. (17)]. The large TATB molecule is flat and shaped like a hexagon in the plane defined by the a and b axes. It is hydrogen bonded to 6 molecules in hexagonal close-packed array. The molecules bonded in this manner form sheets. The resulting symmetry in the a-b plane is nearly hexagonal ($a/b = 0.998$, $\gamma = 119.97°$). The sheets are bonded to one another by weak van der Waals bonds. A point in one sheet is shifted from a position directly over the corresponding point in the sheet beneath it so that the cell edge that connects these points, the c axis, forms an angle of $91.82°$ (β) with the a axis and an angle of $108.59°$ (α) with the b axis. The two assumptions we used to determine the cell parameters from high pressure diffraction patterns are 1) a/b remains constant under pressure and 2) a point on one sheet of molecules remains over the same relative position on the sheet below it. From this assumption the following relations are derived. If c_a is the projection of the c axis on the a axis at zero pressure and c_b is the projection of the c axis on the b axis at zero pressure, then the angles between c and a (β) and c and b (α) at high pressure are

$$\alpha_p = \text{arc cosine } (-c_b \times (b_p/b_o)/c_p) \quad (22)$$

$$\beta_p = \text{arc cosine } (-c_a \times (a_p/a_o)/c_p) \quad (23)$$

$$\gamma_p = \gamma_o \text{ (because of the first assumption)} \quad (24)$$

The subscript, o, in the above expressions denotes zero pressure, and the subscript, p, denotes pressure p.

At low pressures (0.1 to 3.0 GPa) as many as ten diffraction lines were measurable; at high pressure these were reduced to four. The 4θ values measured were used to determine the two independent cell parameter variables, a and c (reduced from 6 to 2 by the above two assumptions). The pressure was indicated by the diffraction pattern of NaF which was mixed with the TATB sample. Table 3 lists the cell parameters and pressures determined from the high pressure patterns. The isothermal compression fits of the two independent variables and the U_{st}-U_{pt} fits are

$$a/a_o = 1 - 4.438 \times 10^{-3} P, \quad 0 < P < 7 \text{ GPa} \quad (25)$$

$$c/c_o = 1 - 4.931 \times 10^{-2} P + 9.495 \times 10^{-3} P^2 - 7.202 \times 10^{-4} P^3, 0 < P < 3 \text{ GPa}$$

TABLE 3

Crystallographic Cell Parameters of TATB

NaF* (V/V_o)	Pressure† (GPa)	a† Å	b‡ Å	c† Å	α‡ (deg)	β‡ (deg)	γ‡ (deg)
1.0000	0.00	9.010§	9.028§	6.812§	108.6§	91.8§	120.0§
0.9965 (09)	0.17 (.05)	9.016 (.009)	9.034	6.807 (.017)	108.6	91.8	120.0
0.9826 (12)	0.87 (.07)	8.986 (.021)	9.004	6.492 (.020)	109.5	91.9	120.0
0.9724 (10)	1.41 (.06)	8.958 (.018)	8.976	6.461 (.014)	109.5	91.9	120.0
0.9597 (09)	2.14 (.08)	8.944 (.009)	8.962	6.376 (.011)	109.8	91.9	120.0
0.9507 (15)	2.69 (.10)	8.877 (.017)	8.895	6.289 (.013)	109.9	91.9	120.0
0.9374 (14)	3.56 (.09)	8.846 (.016)	8.864	6.205 (.012)	110.1	92.0	120.0
0.9029 (11)	6.17 (.10)	8.752 (.018)	8.770	6.039 (.015)	110.4	92.0	120.0
0.8929 (15)	7.02 (.13)	8.678 (.005)	8.695	5.951 (.001)	110.6	92.0	120.0

*Deviation $\times 10^4$ in parenthesis
†Deviation in parenthesis
‡Calculated from a and c
§Ref. (17)

$$c/c_o = 0.9515 - 1.089 \times 10^{-2} P,$$
$$3 < P < 7 \text{ GPa} \tag{26}$$

$$U_{st} = 1.43 + 10.13 \, U_{pt} - 11.45 \, U_{pt}^2,$$
$$U_{pt} < 0.3 \text{ km/s}, \rho_0 = 1.937 \text{ g/cm}^3 \tag{27}$$

$$U_{st} = 2.90 + 1.67 \, U_{pt},$$
$$U_{pt} > 0.3 \text{ km/s}, \rho_0 = 1.937 \text{ g/cm}^3 \tag{28}$$

From the isothermal compression data and thermodynamic parameters listed in Table 4, the shock compression Hugoniots are calculated to be

$$U_s = 1.43 + 10.13 \, U_p - 11.42 \, U_p^2,$$
$$U_p < 0.3 \text{ km/s}, \rho_0 = 1.937 \text{ g/cm}^3 \tag{29}$$

$$U_s = 2.90 + 1.68 \, U_p,$$
$$U_p > 0.3 \text{ km/s}, \rho_0 = 1.937 \text{ g/cm}^3 \tag{30}$$

The U_s-U_p slope, 1.68, claculated for the TATB Hugoniot in the higher U_p region is smaller than found by either Coleburn and Liddard (18), 2.32, or by Craig (18), 2.50, but is of the same magnitude as for many other explosives. For PETN the quadratic fit of the calculated U_s-U_p Hugoniot was necessary to fit the compression data up to 5.5 GPa. As we stated earlier, PETN has van der Waals bonding in all directions. For TATB, however, where van der Waals bonds are in only one direction, the linear fit is adequate for U_s-U_p data above 2.0 GPa. One other item to be noted is that the Grüneisen constant calculated

here (0.20) is considerably smaller than the constant reported in Dorbratz's compendium (18), 1.60. The small Grüneisen constant is due to the small bulk sound speed (1.43 km/s) and small volume thermal expansion (9.9×10^{-5}/K°). Though both may be slightly larger because of porosity effects for the former and accuracy for the latter, the Grüneisen constant is probably no larger than 0.4.

CO$_2$

The work on CO_2 had to be done on the solid form, of course, so that the CO_2 would yield diffraction patterns. The anvil on which was mounted the beryllium annulus containing NaF was cooled by circulating liquid nitrogen around its base. Once cooled, commercial dry ice was scraped on the edge of the annulus, and a small pile of fine CO_2 chips accumulated above the annulus hole. The upper anvil, at room temperature, was lowered onto the pile of CO_2 as quickly as possible, luckily trapping some CO_2 in the hole of the annulus with the NaF. No alcohol was added because the experiment would have been more difficult and there was no proof that CO_2 was not miscible in the alcohol. The specific volumes of CO_2 at 293°K at pressures from 3 to 10 GPa are listed in Table 5.

A Hugoniot for solid CO_2 centered at ambient conditions can be calculated if estimates of the specific volume, V_0, thermal expansion, α_v, and heat capacity, C_p, for these conditions can be made. In 1926

TABLE 4

Thermodynamic Properties of TATB at
293°K, 0 GPa

ρ_0 = 1.937 g/cm^3	Ref. (17)
c_s = 1.43 km/s	Ref. (19)
c_t = 1.43 km/s	
α_v = 9.95 × 10^{-5}/K°	Ref. (20)
C_p = 1.00 J/gK°	Ref. (21)
C_v = 0.99 J/gK°	
γ = 0.20	

TABLE 5

Specific Volume Data for CO$_2$ at
Pressures to 10 GPa, 293°K

V_ρ (cm^3/g)	Pressure (GPa)
0.4965 ± .0007	3.30 ± 0.14
0.4638 ± .0006	5.52 ± 0.12
0.4529 ± .0006	6.68 ± 0.14
0.4462 ± .0006	7.18 ± 0.04
0.4433 ± .0010	7.70 ± 0.12
0.4403 ± .0005	7.89 ± 0.13
0.4357 ± .0007	8.67 ± 0.09
0.4290 ± .0007	9.83 ± 0.07
0.4263 ± .0008	9.99 ± 0.19

Maas and Barnes (22) made a very thorough study of the thermodynamic properties of solid and liquid CO_2. From their solid CO_2 density measurements between 88°K and 186°K (above 186° their measurements deviated suddenly from a linear V-T behavior) and specific heat content measurements between 90°K and 212°K, the values for density and specific heat content were extrapolated to 293°K. The extrapolations were linear for density, quadratic for heat content; α_v and C_p were calculated from the slopes at 293°K. These values are listed in Table 6. Using the V_0 value ($1/\rho_0 = 0.6720$ cm^3/g), a U_{st}, U_{pt} fit to the data in Table 5 is

$$U_{st} = 1.623 + 1.71\ U_{pt},$$
$$U_{pt} > 0.7\ \text{km/s}, \rho_0 = 1.488\ \text{g/cm}^3 \tag{31}$$

Using Eq. (31) and the thermodynamic quantities listed in Table 6, the calculated Hugoniot for solid CO_2 starting at 293°K is

$$U_s = 1.740 + 1.65\ U_p,$$
$$U_p > 0.7\ \text{km/s}, \rho_0 = 1.488\ \text{g/cm}^3 \tag{32}$$

Solid CO_2, like the explosives discussed above, is composed of CO_2 molecules bonded to one another by van der Waals bonds. Therefore, like PETN and TATB, the U_{st}-U_{pt} and U_s-U_p equations are quadratic at low pressures and thus the c_t and c_s are lower than given in Eqs. (31) and (32). The present data does not permit an estimate of the quadratic coefficients, and the fits are only accurate above U_{pt} and U_p values of 0.7 km/s.

H_2O

As with CO_2, the study of H_2O was on a solid form, specifically ice VII, the stable phase of H_2O above 2.5 GPa at 298°K. Data for the compression of ice VII was presented earlier (26) using the experimental technique described here. However, aluminum was used as the pressure indicator, and the pressures correlated with aluminum's relative volumes have been found to be 5% to 4% larger up to 10 GPa (27) than given in that work (26). Therefore, the pressures were revised and the results are presented here. The listings of the relative volumes of aluminum and ice VII are found in the earlier work; the isothermal compression used here for aluminum is

TABLE 6

Thermodynamic Properties of CO_2 (solid) at 293°K, 0 GPa

$\rho_o = 1.488$ g/cm^3	Ref. (23)
$c_s = 1.74$ km/s	
$c_t = 1.62$ km/s	Ref. (24)
$\alpha_v = 5.41 \times 10^{-4}/K°$	Ref. (23)
$C_p = 1.77$ J/gK°	Ref. (25)
$C_v = 1.54$ J/gK°	
$\gamma = 0.93$	

$$U_{st} = 5.290 + 1.388\ U_{pt},$$
$$\rho_0 = 2.701\ \text{g/cm}^3 \tag{33}$$

The ambient specific volume of ice VII is chosen so that the U_{st}-U_{pt} equation (Eq. (1) above) is linear; that volume is 0.717 cm^3/g. The subsequent linear equation for ice VII is

$$U_{st} = 2.872 + 1.685\ U_{pt},$$
$$U_{pt} > 0.5\ \text{km/s}, \rho_0 = 1.395\ \text{g/cm}^3 \tag{34}$$

In order to calculate the Hugoniot of ice VII centered at ambient conditions, assumptions about the specific heat capacity and thermal expansion of ice VII must be made. Normal ice, ice Ih, has a structure only slightly different from the structure of low temperature ice at zero pressure, ice Ic. Their densities, too, are nearly the same. Therefore, we assume that both structures have the same specific heat capacities and thermal expansions. The ice VII structure consists of two interpenetrating but not interconnecting ice Ic frameworks, and thus it is not unreasonable to expect molecular vibrations and relative bond length expansions to be nearly the same between the two structures. Therefore we assume the specific heat capacities and thermal expansions to be the same. Including the isothermal bulk sound speed calculated for Eq. (34) above, the thermodynamic properties of ice VII at ambient conditions are listed in Table 7. Combining these with the isothermal compression, Eq. (34), the ice VII Hugoniot, centered at ambient conditions, is calculated to be

REFERENCES

1. J. C. Jamieson and A. W. Lawson, "X-ray Diffraction Studies in the 100 Kilobar Pressure Range," J. Appl. Phys., Vol. 33, pp. 776-780, 1962.

2. J. C. Jamieson, "The Crystal Structures of High Pressure Modifications of Elements and Certain Compounds, a Progress Report," in Metallurgy at High Pressures, edited by K. A. Gschneidner, Jr., M. T. Hepworth, and N. A. D. Parlee, pp. 201-228, Gordon and Breach, New York, 1964.

3. P. M. Halleck and B. Olinger, "A Method for the Accurate Measurement of Lattice Compression of Low-Z Materials at Pressures up to 12 GPa by X-ray Diffraction," Rev. Sci. Instrum., Vol. 45, pp. 1408-1410, 1974.

4. C. J. Piermarini, S. Block, and J. D. Barnett, "Hydrostatic Limits in Liquids and Solids to 100 Kbar," J. Appl. Phys., Vol. 44, pp. 5377-5382, 1973.

5. J. N. Fritz, S. P. Marsh, W. J. Carter, and R. G. McQueen, "The Hugoniot Equation of State of Sodium Chloride in the Sodium Chloride Structure," Accurate Characterization of the High-Pressure Environment, NBS Special Publication 326, ed. E. C. Lloyd, U. S. Govern. Printing Office, pp. 201-208, 1971.

6. J. S. Weaver, T. Takahashi, and W. A. Bassett, "Calculations of the P-V Relation for Sodium Chloride up to 300 Kilobars at 25°C," Accurate Characterization of the High-Pressure Environment, NBS Special Publication 326, ed. E. C. Lloyd, U. S. Govern. Printing Office, pp. 189-199, 1971.

7. B. Olinger and J. C. Jamieson, "Relative Compression of NaF and NaCl to 130 Kilobars," High Temp.-High Press., Vol. 2, pp. 513-520, 1970.

8. M. Spieglan and J. C. Jamieson, "Relative Compression of NaF and NaCl to 110 Kilobars; a Redetermination," High Temp.-High Press., Vol. 6, pp. 479-481, 1974.

9. W. J. Carter, "Hugoniot Equation of State of Some Alkali Halides," High Temp.-High Press., Vol. 5, pp. 313-318, 1973.

10. W. J. Carter and J. N. Fritz, Private Communication.

11. L. V. Azavoff and M. J. Buerger, The Powder Method, McGraw-Hill, New York, 1958.

12. B. Olinger, P. M. Halleck, and H. H. Cady, "The Isothermal Linear and Volume Compression of Pentaerythritol Tetranitrate (PETN) to 10 GPa (100 kbar) and the Calculated Shock Compression," Jour. Chem. Phys., Vol. 62, pp. 4480-4483, 1975.

13. D. J. Pastine and R. R. Bernecker, P, v, E. T. Equation of State for 1, 3, 5-triamino-2, 4, 6--trinitrobenzene," Jour. Appl. Phys., Vol. 45, pp. 4458-4468, 1974.

14. C. E. Morris, "Adiabatic Elastic Moduli of Single Crystal Pentaerythritol Tetranitrate (PETN)," Sixth Symposium (International) on Detonation, San Diego, 1976.

15. H. H. Cady, "Coefficient of thermal expansion of pentaerythritol tetranitrate and hexahydro-1,3,5 trinitro-s-stiazine (RDX)," Jour. Chem. Eng. Data, Vol. 17, pp. 369-371, 1972.

16. R. Rogers, Los Alamos Scientific Laboratory, Los Alamos, NM, 1974, Private Communication.

17. H. H. Cady and A. C. Larson, "The Crystal Structure of 1,3,5-triamino-2,4,6-trinitrobenzene," Acta Cryst., Vol. 18, pp. 485-496, 1965.

18. B. M. Dobratz, "Properties of Chemical Explosives and Explosive Stimulants," UCRL-51319, Rev. 1, Lawrence Livermore Laboratory, Livermore, California, p. 7-20.

19. B. Olinger, "Sound Speed Measurements on Pressed Samples of Density 1.870 g/cm^3 Treated as Transverse Isotropic," 1976.

20. H. Cady measured the volume thermal expansion of a TATB single crystal. No expansion was detectable parallel to the a-b plane; perpendicular to the a-b plane, the crystal expanded from 1.689 mm to 1.710 mm over a 125°C temperature range.

21. J. Baytos, WX-3, Los Alamos Scientific Laboratory, Los Alamos, NM, 1975, Private Communication.

22. O. Maass and W. H. Barnes, "Some Thermal Constants of Solid and Liquid Carbon Dioxide,"

Royal Soc. Proceedings, Series A, Vol. III, pp. 224-244, 1926.

23. Estimated from linear extrapolation of density versus temperature data of Ref. (21). Higher temperature data which deviates from linear fit was ignored.

24. First component of linear U_{st}, U_{pt} fit, Eq. (33).

25. Determined from quadratic least-squares fit to heat content versus temperature data of Ref. (21). The fit was centered at 25°C.

26. B. Olinger and P. M. Halleck, "Compression and Bonding of Ice VII and an Empirical Linear Expression for the Isothermal Compression of Solids," Jour. Chem. Phys., Vol. 62, pp. 94-99, 1975.

27. B. Olinger, determined from unpublished study of the simultaneous compression of NaCl and Al.

28. ρ_o $(1/V_o)$ adjusted so that $(PV_o/(1 - V/V_o))^{1/2}$, U_{st}, and $(PV_o(1 - V/V_o))^{1/2}$, U_{pt}, were linear.

29. The U_{st} intercept at $U_{pt} = 0$, when U_{st}, U_{pt} were made linear, Ref. (27).

30. B. Kamb, "Overlap Interaction of Water Molecules," Jour. Chem. Phys., Vol. 43, pp. 3917-3924, 1965.

THE EFFECT OF ELEMENTAL COMPOSITION ON THE DETONATION BEHAVIOR OF EXPLOSIVES*

M. Finger, E. Lee, F. H. Helm, B. Hayes, H. Hornig, R. McGuire, and M. Kahara
Lawrence Livermore Laboratory
University of California
Livermore, California 94550

and

M. Guidry
F. J. Seiler Research Laboratory
U. S. Air Force Academy, Colorado

We have determined the effect of chemical composition on explosives performance via a series of experiments on specially formulated explosives. For most of these explosives we have measured detonation pressure, detonation velocity, and isentropic expansion. In some cases we also measured detonation temperature and product composition. Included for comparison are calculated detonation parameters using the BKW and JCZ3 equations of state. The results demonstrate significant differences between the calculational and experimental results for compositions that yield a preponderance of HF and CF_4, H_2O, or predominantly CO and CO_2 as detonation products. The results further indicate not only a need to adjust the equation of state parameters for H_2O and CO_2, and fluorine containing species in the BKW and JCZ3 equations of state, but in all likelihood a need to make changes in the equation of state itself. The data also point to the possible advantages in developing explosives with elemental compositions that are predominantly carbon-oxygen or hydrogen-oxygen in order to achieve particular explosive characteristics.

INTRODUCTION

It is our intent to present a comparison of experimental and predicted detonation performance data so as to indicate clearly the areas in which the calculational model needs improvement. The overall purpose of this work is to improve our ability to predict the detonation behavior of new materials and give better guidance to the direction of explosives development.

The most widely used description of detonation products for predicting the detonation properties of condensed explosives is the BKW (Becker, Kistiakowsky, Wilson) equation of state. This equation of state has been incorporated in thermo-hydro codes such as Fortran-BKW, (1) RUBY, (2) and TIGER (3). There have been many contributions to the development of the current, widely used form of the equation based on a Kistiakowsky and Wilson modification of an equation due to Becker (4,5,6,7,8,9). Cowan and Fickett further modified the equation to its current form (10):

$$P \cdot V/RT = 1 + Xe^{\beta X},$$

where

$$X = \kappa \Sigma n_i \, k_k / V \, (T + \theta)^\alpha$$

Fitting of this equation to detonation data was accomplished by Cowan and Fickett. Later Mader reparameterized BKW to give the set used extensively in the Fortran-BKW Code today (11). Slightly different parameters are incorporated in the RUBY and TIGER codes.

To determine the best BKW parameters one adjusts α, β, κ, and θ and the covolume factors, k_i, of appropriate detonation products to fit the best explosives performance data available. In the early 1960s, the BKW parameters were adjusted to fit experimental Hugoniot data for H_2O, N_2, and CO_2 and five experimental measurements involving two explosives, RDX and TNT. Based on this limited data base, the predictions of relative explosive performance reported by Mader and others have been fairly reliable. However, as we will point out BKW predictions are not accurate on an absolute scale, and where extremes in explosive compositions are investigated, prediction of the relative behavior are also in error.

Several authors have pointed out the shortcomings of BKW as a physically realistic equation of state (12,13,14). The most obvious deficiency is the failure of the equation to calculate finite pressures at high density as the temperature approaches zero (i.e., the equation does not predict a lattice pressure). It has further been observed that the BKW equation of state consistently over-estimates the pressure in the detonation products during isentropic expansion. Fickett (15) developed a calculational program based on the Lennard-Jones (L-J) cell model to calculate detonation products. More recently Jacobs, Cowperthwaite, and Zwisler (14,16) have developed an analytic equation, JCZ3, which possesses most of the features of the L-J model particularly a lattice potential based on the exponential sixth intermolecular potential function. The parameters for the intermolecular potential functions in these equations of state are based on such measurements as molecular scattering and gas compressibility and viscosity. Some adjustments have been made ir JCZ3 based on a very limited set of high explosive measurements (14).

In short, we believe that the current set of parameters used in equations of state or possibly the equations of state themselves, are not very satisfactory. In

this paper we attempt to provide a much broader data base for determining an improved set of parameters for BKW, JCZ3, and/or successors.

To achieve this we have investigated the effect of elemental composition on the detonation performance of explosives by choosing a range of compositions to emphasize one or more important detonation products such as H_2O, HF, N_2, CO, CO_2, and CF_4. We also studied the "independent" effect of these products upon the C-J parameters and energy delivered in isentropic expansion. Reliance on the predicted C-J pressure or detonation velocity alone could be misleading in assessing the relative performance of explosives. We have re-parameterized the BKW constants and covolume factors over a wider base of detonation velocity and pressure measurements to include CNO and HNO explosives. We differentiate in the text between the standard set of TIGER-BKW parameters and the re-parameterized ones by use of the designations BKW and BKWR, respectively. We have carried out a set of calculations to compare the predictions using BKW-TIGER, BKWR-TIGER, and JCZ3-TIGER with the experimental results.

ELEMENTAL COMPOSITIONS

We selected explosives with a wide range of elemental compositions. For the purpose of this paper, we have selected a few of these chemical systems as illustrative of the effect of composition on detonation performance. In Table 1 we list these explosives and their elemental compositions. We have tabulated representative "idealized" detonation products using an arbitrary product priority of N_2, HF, H_2O, H_2, CO, CO_2, and $C_{(s)}$ depending on the system.

CHAPMAN-JOUGET STATE

In Table 2 we have tabulated experimental Chapman-Jouget detonation parameters for each of the chemical systems we have chosen for illustrative purposes. Also included are the calculated C-J parameters based on BKW-TIGER, JCZ3-TIGER, and BKWR-TIGER.

The velocity of detonation is a fundamental and readily measured characteristic property of a high explosive. The detonation velocity of a given explosive, just as other detonation parameters do, depends on

711

its composition, loading density, and geometric factors such as size and confinement of the charge. All the measurements of detonation velocity reported were obtained using an electronic pin switch technique developed by Campbell, et al. (17). The detonation velocities reported for most systems were obtained in 25.4, 50.8, or 101.6 mm diameter charges. Although they are not reported as infinite diameter, plane wave velocities, they are very close to D_∞.

Experimentally, C-J pressures are measured by various indirect hydrodynamic methods. As has been pointed out by Kamlet (18) and Davis (19), these measurements span a range of 10-20%, and their exact interpretation is uncertain. The C-J pressures given in this paper were obtained from front-surface motion measurements. These fall into one class of data which have been shown to be self consistent. Further refinement of these values will not in our view substantially alter the over-all pattern. Recent theoretical studies by Bdzil (20) and more direct measurements using the electromagnetic technique (21,22,23) promise to resolve some of the conflict concerning detonational pressure measurements.

The technique for measuring temperature of the detonation wave is described by Urtiew (24). In short, it is an optical technique, which measures the amount of thermal radiation emitted from a hot radiating surface. Looking through the transparent liquid explosive the photodiode detector measures radiation flux emitted by the oncoming detonation front. The signal is interpreted as a brightness temperature via Planck's radiation law.

As a further test of our current ability to predict C-J parameters we have tabulated the C-J pressure as a function of loading density for two explosives. In Fig. 1, we present the experimental C-J pressures for HMX (actually RDX and HMX are identical up to $\rho = 1.8$). We also plot the calculated C-J pressure vs ρ curves for BKW and JCZ3. TNT is presented similarly in Fig. 2.

The data we present for the C-J state of HCNO explosives fall within the normally expected range of values for condensed explosives. Measurements of other systems were made using the same techniques. It is apparent that the temperature reported by

TABLE 1

Explosives Systems Studied to Determine Effect of Composition on Explosive Performance

| | Name | Composition, wt. % | Formula | Density g/cc | Mole % Products[a] | | | | | | |
					N_2	H_2O	HF	H_2	CO_2	CO	C_s
HCNO	TNT	2,4,6 Trinitrotoluene	$C_7H_5N_3O_6$	1.63	14	22	–	--	0	32	32
	NM	Nitromethane	CH_3NO_2	1.13	16	50	–	--	0	17	17
	HMX	Cyclotetramethylene tetranitramine	$C_4H_8N_8O_8$	1.89	34	33	--	--	0	33	0
	PETN	Pentaerythritoltetranitrate	$C_5H_8N_4O_{12}$	1.77	18	36	--	–	28	18	0
HNO	RX-23-AA	Hydrazine Nitrate/ Hydrazine—79/21	$H_{6.78}N_{3.80}O_{2.49}$	1.421	36	47	–	17	–	–	–
	RX-23-AB	Hydrazine Nitrate/Hydrazine/ H_2O—70/5.9/24.1	$H_{7.10}N_{2.58}O_{3.55}$	1.384	27	73	--	–	–	–	
	RX-23-AC	Hydrazine Nitrate Hydrazine—30/70	$H_{10.31}N_{5.32}O_{0.95}$	1.135	34	12	–	54	–	–	–
CNO	BTF	Benzotrifuroxane	$C_6N_6O_6$	1.859	33	–	–	--	0	67	0
HCNF	1,2-DP	1,2-bis(difluoroamino) propane	$C_3H_6N_2F_4$	1.26	11	–	45	11	--	--	33
HCNOF	FEFO	Bis(2-fluoro-2,2-dinitroethyl) formal	$C_5H_6N_4O_{10}F_2$	1.59	18	18	18	–	28	18	0

[a] Assumes arbitrary formation of products in the order of N_2, HF, H_2O, H_2, CO, CO_2, and C_s.

TABLE 2

Experimental and Calculated Chapman-Jouget Parameters[a]

Explosive	Calculations					
	CJ	EXPT	REF	BKW	JCZ3	BKWR
TNT	D	6.94	(13)	7.30	6.79	7.08
$\rho = 1.63$	P	21.	b	22.3	18.1	19.9
$\Delta H_f = -15$	T	–	–	2562	3501	2698
NM	D	6.37	(13)	6.84	6.11	6.68
$\rho = 1.13$	P	12.5	b	14.4	11.9	13.7
$\Delta H_f = -27.$	T	3300	(24)	2600	3467	2954
HMX	D	9.11	b	9.01	9.11	9.38
$\rho = 1.89$	P	39.	b	39.4	35.6	40.2
$\Delta H_f = +17.9$	T	–	–	2264	3726	3093
PETN	D	8.27	(28)	8.51	8.21	8.71
$\rho = 1.77$	P	33.5	(28)	33.2	28.8	33.7
$\Delta H_f = -128.7$	T	–	–	2631	4237	3445
RX-23-AA	D	8.58	b	8.68	8.11	8.52
$\rho = 1.421$	P	20.9	c	26.3	20.6	24.5
$\Delta H_f = -41.$[d]	T	2900	(24)	1453	2695	2332
RX-23-AB	D	7.48	b	7.92	7.31	7.45
$\rho = 1.384$	P	18.6	c	20.3	15.5	17.6
$\Delta H_f = -140.$[d]	T	4000	(24)	925	1966	1742
RX-23-AC	D	7.87	b	8.41		7.98
$\rho = 1.135$	P	16.9	c	19.8		17.3
$\Delta H_f = +5$[d]	T	2180	(24)	1200		1883
BTF	D	8.48	b	7.82	8.57	8.41
$\rho = 1.859$	P	36.	c	30.9	33.7	34.6
$\Delta H_f = +144.$	T	–	–	3721	5012	4235
1,2 DP	D	5.96	b	6.43	6.79	6.51
$\rho = 1.26$	P	14.	c	17.5	16.5	17.5
$\Delta H_f = -39.3$	T	–	–	3614	4910	3701
FEFO	D	7.50	b	7.30	7.50	7.61
$\rho = 1.59$	P	25.0	c	23.2	22.5	24.6
$\Delta H_f = -178.$	T	–	–	2870	4283	3510

[a]Units: ρ = g/cc; ΔH_f = Kcal/mole; D = Km/sec; P = GPa; T = °K
[b]This work
[c]Estimated from cylinder test data
[d]Per 100 gms of mixture

Urtiew of 4 000 °K for RX-23-AB is unrealistic. A simple estimate based on the calorimetric detonation energy of 1100 cal/g and approximate heat capacities of the detonation products yields a temperature of about 1800 °K. Since the products were limited to N_2 and H_2O (i.e., no Carbon present) in this system and the temperature had to be quite low, there very likely could have been substantial deviations from the black body radiation curve.

DETONATION PRODUCTS

A severe test of our ability to predict explosive performance is the determination of the detonation product composition. Ornellas has attempted the correlation of the product composition as measured in a detonation calorimeter with the values calculated along the insentrope at a freeze-out temperature between 1500 °K–1800 °K (25). He performed these measurements on the same explosive used in this work. Comparisons of HCNO, CNO, and HNO explosives are shown in Tables 3, 4, and 5. The standard BKW parameters yield a calculated product mixture

that is low in both H_2 and CO, and high in solid carbon. This is a result of the low temperatures predicted by BKW. BKWR, which was designed to produce higher temperatures, agrees well with the experimental observations. JCZ3, which also predicts high temperatures, also agrees quite well with experimental observation with the exception of a low prediction on the amount of solid carbon. This is probably a result of using too large a positive value for the heat of formation of carbon.

ISENTROPIC EXPANSION

A hydrodynamic experiment referred to as the cylinder test has been used to obtain isentropic expansion data. The experimental details and data reduction were first given in a paper by Kury, *et al.* (13). It is important to point out that the measurements in most cases have been carried out using several cylinder diameters and charge to mass ratios. The radius-time data were compared to show that the scaled results were indistinguishable. This was done in order to insure that any effects due to the reaction zone in the detonation front would not have significant effects upon the expansion behavior. As we have pointed out in another paper submitted to this symposium, hydrodynamic scaling is often not observed

Fig. 1. HMX C-J pressure dependence on loading density.
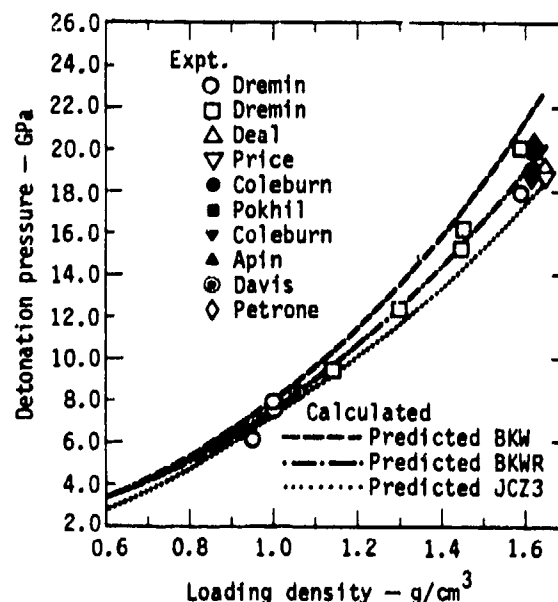
Fig. 2. TNT C-J pressure dependence on loading density.

in commercial composite explosives with significant attendant effects on detonation performance.

Numerical analysis methods were used to convert measurement of distance vs. time from expanding cylinders to detonation product equations of state, more precisely the isentropic expansion curve, $P = P(V)$. These methods have been discussed by Wilkins (26) and Lee (27) in some detail. Briefly, an estimated detonation product equation of state is used in an ap-

propriate 1D or 2D hydrodynamic finite difference calculation to simulate the detonation and subsequent expansion of a particular explosive. A comparison of the calculated and experimental results is made to obtain an improved estimate, i.e., adjustments of equation of state coefficients. If the form chosen for the equation of state is a sufficiently good description of detonation behavior, this process can be repeated until calculational results lie within the experimental error. We have been successful in using

TABLE 3

HMX ($\rho = 1.89$) Detonation Products Experimental vs. Predicted--HCNO System

Species	Expt. mole/Kg	Calculated Detonation Products[a]		
		BKW	JCZ3	BKWR
H_2O	10.74	$12.8 \rightarrow 12.9$	$7.8 \rightarrow 8.3$	$10.4 \rightarrow 11.6$
CO_2	6.48	$6.92 \rightarrow 6.96$	$7.1 \rightarrow 7.5$	$6.4 \rightarrow 6.6$
CO	3.56	0.3	$4.2 \rightarrow 4.7$	$2.5 \rightarrow 3.5$
N_2	12.43	13.42	$12.8 \rightarrow 13.3$	$12.9 \rightarrow 13.1$
NH_3	1.33	0.18	$0.4 \rightarrow 1.4$	$0.9 \rightarrow 1.1$
H_2	1.01	0.02	$1.1 \rightarrow 1.6$	$0.5 \rightarrow 1.0$
CH_4	0.13	$0.1 \rightarrow 0.16$	$1.0 \rightarrow 1.8$	$.02 \rightarrow .28$
$C_{(s)}$	3.28	6.1	$0 \rightarrow 0.9$	$3.0 \rightarrow 4.5$

[a]Data for freeze-out temperature of 1800-1900 °K.

TABLE 4

BTF ($\rho = 1.859$) Detonation Products Experiment vs. Predicted--CNO System

Species	Expt. moles/Kg	Calculated Detonation Products[a]		
		BKW	JCZ3	BKWR
CO_2	6.20	$7.5, \rightarrow 7.8$	$4.5 \rightarrow 5.5$	$5.1 \rightarrow 6.5$
CO	11.23	$8.3 \rightarrow 8.8$	$12.80 \rightarrow 14.7$	$10.9 \rightarrow 13.6$
N_2	11.90	11.90	11.90	11.90
$C_{(s)}$	6.20	$7.5 \rightarrow 7.8$	$45 \rightarrow 5.5$	$5.1 \rightarrow 6.5$

[a]Freeze-out temperature of 1700-2100 °K.

the JWL equation of state in fitting the behavior of a large variety of explosives (27). The form of the JWL equation is:

$$P = A\left(1 - \frac{\omega}{R_1 V}\right)e^{-R_1 V} + B\left(1 - \frac{\omega}{R_2 V}\right)e^{-R_2 V} + \frac{\omega E}{V},$$

where A, B, R_1, R_2, and ω are constants, and V is the relative volume v/v_o. The equation for P as a function of V at constant entropy is:

$$P_s = Ae^{-R_1 V} + Be^{-R_2 V} + CV^{-(\omega+1)}$$

and the energy equation is:

$$E_s = \frac{Ae^{-R_1 V}}{R_1} + \frac{Be^{-R_2 V}}{R_2} + \frac{C}{\omega V^\omega}.$$

In this paper we have used this "experimental" data to compare with the results predicted by equations of state such as BKW or JCZ3 using the chemical equilibrium program code TIGER. In Table 6 we list the JWL coefficients for the explosives cited in this paper. In Figs. 3-8, we graphically present the

TABLE 5

RX-23-AA ($\rho = 1.421$) Detonation Products Experimental vs. Predicted—HNO System

Species	Expt. moles/Kg	Calculated Detonation Products[a]		
		BKW	JCZ3	BKWR
H_2O	24.74	24.74	24.74	24.74
NH_3	4.90	6.24	$4.9 \rightarrow 5.6$	$4.9 \rightarrow 5.4$
N_2	16.41	16.0	$16.3 \rightarrow 16.7$	$16.4 \rightarrow 16.6$
H_2	1.20	0	$0.7 \rightarrow 2.0$	$1.2 \rightarrow 1.9$

[a]Freeze-out temperature of 1500-1800 °K.

TABLE 6

Equation of State Parameters for Explosives Cited

	C-J Parameters				JWL-EOS Coefficients						
	P Mbar	D cm/μsec	E_o Mb·cc/cc	ρ g/cc	Γ	A	B	C	R_1	R_2	ω
TNT	0.210	0.693	0.0600	1.630	2.727	3.738	0.03747	0.00734	4.15	0.90	0.35
NM	0.125	0.628	0.0510	1.128	2.538	2.092	0.05689	0.00770	4.40	1.20	0.30
HMX	0.420	0.911	0.1050	1.891	2.740	7.783	0.07071	0.00643	4.20	1.00	0.30
PETN	0.335	0.830	0.1010	1.770	2.640	6.170	0.16926	0.00699	4.40	1.20	0.25
RX-23-AA	0.280	0.858	0.0630	1.420	2.732	5.086	0.09463	0.00370	4.20	1.20	0.35
RX-23-AB	0.190	0.748	0.0410	1.380	3.064	4.657	0.03661	0.00433	4.40	1.20	0.40
RX-23-AC	0.175	0.787	0.0390	1.130	2.998	4.445	0.08146	0.00350	4.60	1.40	0.40
BTF	0.360	0.848	0.1150	1.859	2.717	8.407	0.14960	0.03137	4.60	1.20	0.30
1,2 DP	0.135	0.596	0.0750	1.260	2.315	1.645	0.08179	0.01321	4.20	1.6	0.25
FEFO	0.250	0.750	0.0800	1.590	2.578	3.824	0.06635	0.01444	4.10	1.20	0.38

comparison of experimental expansion data vs. predicted for HCNO explosives. We show the same detailed comparison of HNO systems in Figs. 9-12 and similarly for CNO explosives in Figs. 13 and 14. HCNF explosives are depicted in Fig. 15 and a HCNOF explosive in Fig. 16. The parameters used in BKW, JCZ3, and BKWR are tabulated in Table 7.

DISCUSSION

We have found in the experimental and calculational data presented above that the current methods for predicting the performance of explosives are not very satisfactory. In an endeavor to improve the BKW calculation, and to avoid the somewhat awkward two parameter set used by Mader (11), we developed a new revised single set of parameters. This new set of BKW parameters we designated BKWR. It has proven successful even when compared with our somewhat limited composition and temperature data. However, because the BKW equation characteristically predicts a relatively gradual decrease in isentropic pressure with increasing volume, BKWR also fails to give an accurate prediction for isentropic expansion. This behavior is attributable to the deficiencies mentioned earlier, particularly the lack of an attractive (i.e., negative) pressure term which is a necessary feature of a lattice type equation of state. Since the JCZ3 parameters in current use predict characteristically low C-J pressures and detonation velocities, it consequently predicts somewhat lower isentropic pressures at $v/v_o > 2$ as shown in Figs.
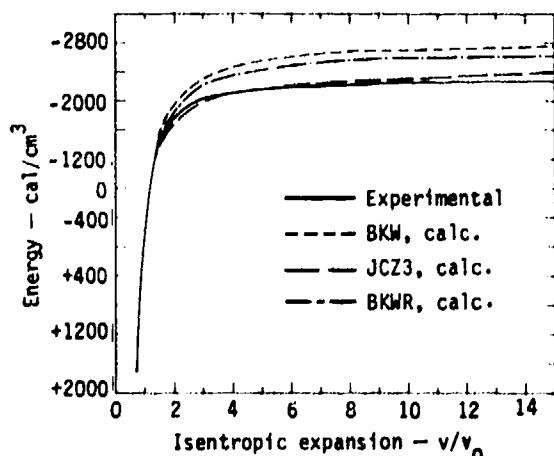
Fig. 3. HMX isentropic expansion.

Fig. 5. TNT isentropic expansion.

Fig. 4. HMX comparison of calculated and experimental isentrope energy.
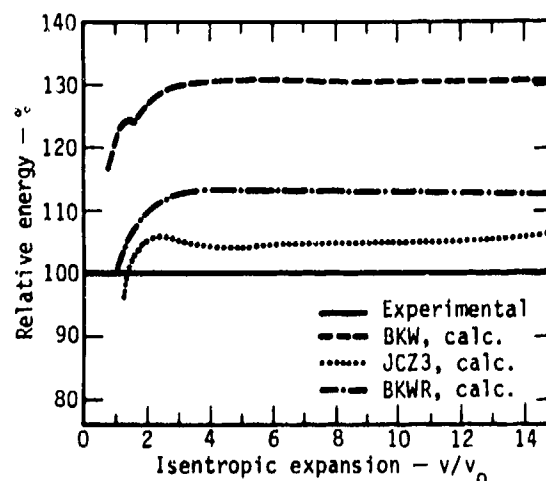
Fig. 6. TNT comparison of calculated and experimental isentrope energy.

717
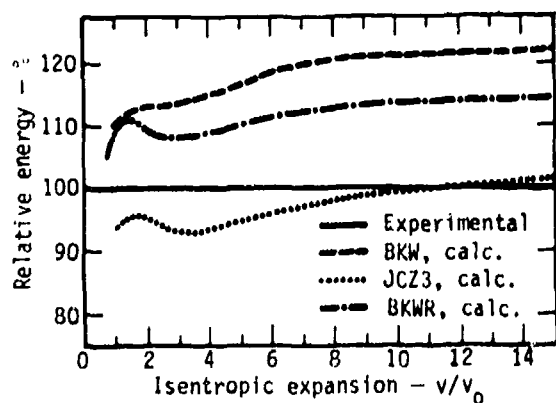
Fig. 7. PETN, ρ = 1.77, comparison of calculated and experimental isentrope energy.
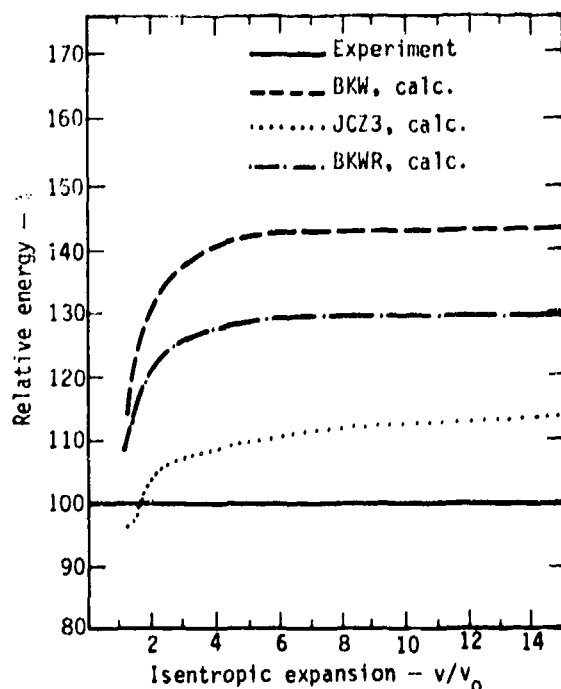
Fig. 8. Nitromethane comparison of calculated and experimental isentrope energy.
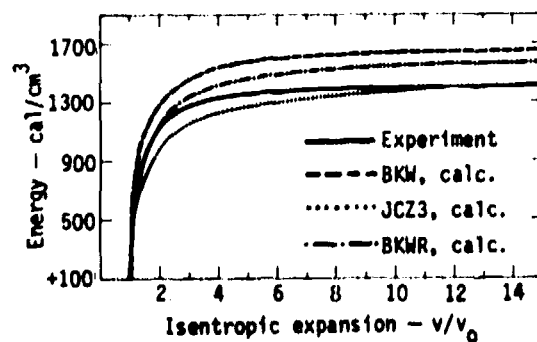
Fig. 9. RX-23-AA, Hydrazine Nitrate/Hydrazine 79/21, isentropic expansion.
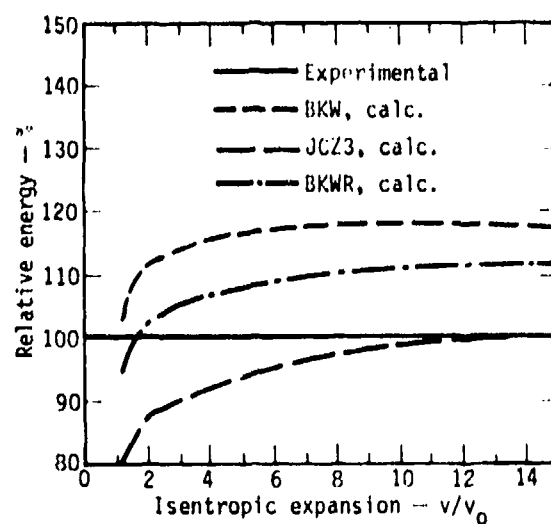
Fig. 10. RX-23-AA comparison of calculated and experimental isentrope energy.
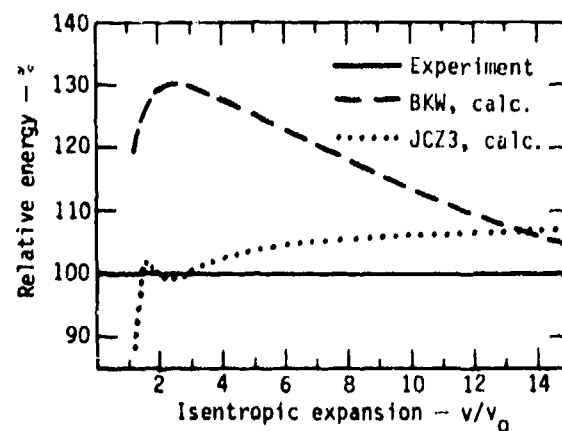
Fig. 11. RX-23-AB, Hydrazine Nitrate/Hydrazine/ H₂O-70/5.9/24.1, comparison of calculated and experimental isentrope energy.

3-16. Were JCZ3 parameters adjusted to predict the correct C-J values it is not certain that it would still succeed in predicting the experimental isentropic expansion. We plan to carry out further studies to answer this question.

We observe in Fig. 17 very interesting energy release patterns for the different elemental composition explosives. This data suggests that selection of explosive composition may be useful in enhancing a particular explosive performance characteristic.

CONCLUSION

We conclude that an equation of state based on intermolecular potentials appears to hold the most promise as a predictive tool for detonation perform-

ance. However, equations of state, such as JCZ3 will require extensive calibration and perhaps modification. We have provided in this paper an enlarged data base for re-parameterizing a suitable equation of state whether it be BKW, JCZ3, or their successor. We also wish to point out that reliance on P_{CJ} or D as a measure of detonation performance in other than HCNO systems may be misleading.

Fig. 14. BTF comparison of calculated and experimental isentrope energy.
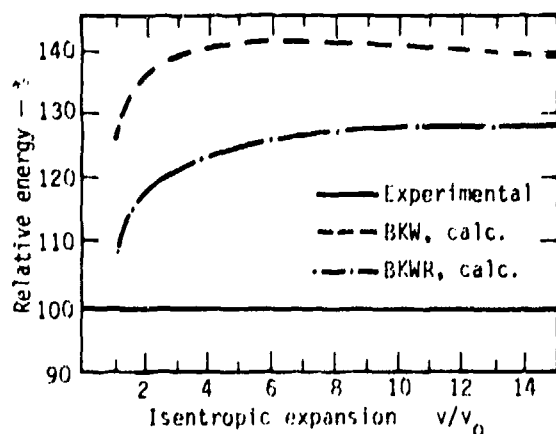
Fig. 12. RX-23-AC, Hydrazine Nitrate/Hydrazine 30/70 comparison of calculated and experimental isentrope energy.
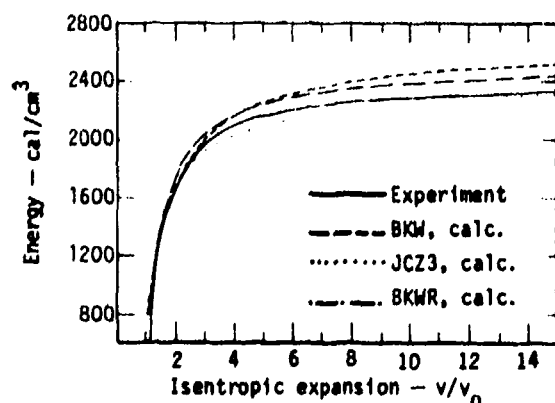
Fig. 13. BTF isentropic expansion.
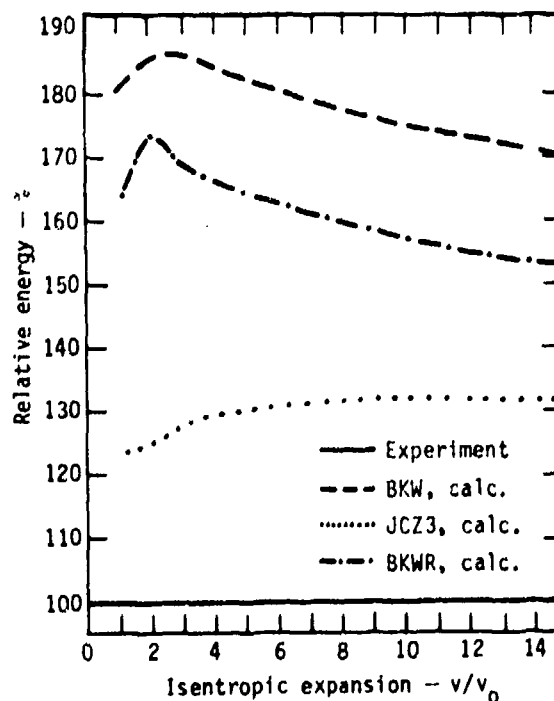
Fig. 15. 1,2-Difluoroaminopropane comparison of calculated and experimental isentrope energy.

We plan to extend our efforts in this area. Not only will it enlarge the data base, but we believe it will point the way to future explosives research. For example, to obtain data for a high-density, CO_2-balanced, hydrogen-free system, we plan experiments on BTF/Hexanitroethane mixtures or similar compositions. There is a great divergence in the predicted behavior of the BTF/HNE system.

		BKW	JCZ3	BKWR
BTF/HNE-$(CNO_2)_x$	D-km/sec	8.58	9.66	9.44
$\rho = 2.05$	P-GPa	40.0	42.8	44.9
	T-$^\circ$K	3826	5351	4631

Thus experimental results on such a system would exert considerable leverage upon the selection of equation of state parameters.

In addition to the judicious selection of explosives systems to give insight into the detonation process, improved experimental techniques are required. Resolution of detonation pressures and temperature discrepancies will be of great importance.

Fig. 16. FEFO comparison of calculated and experimental isentrope energy.
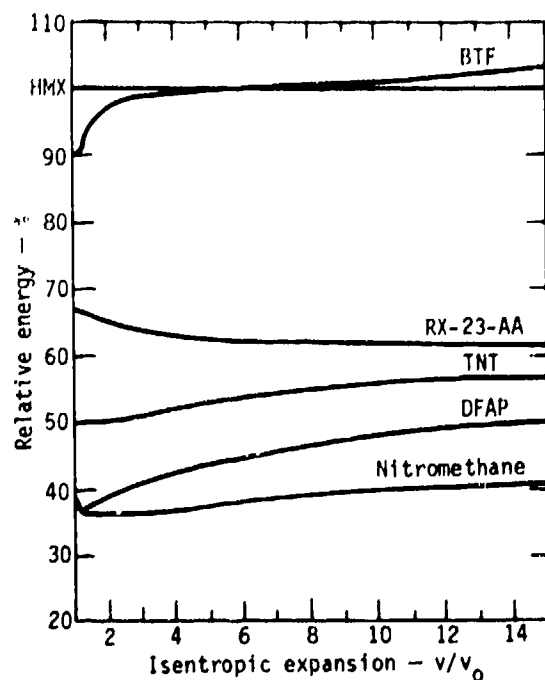
Fig. 17. Comparison of experimental isentropic energy for explosives of differing elemental composition relative to HMX.

TABLE 7

Parameters Used for TIGER Calculations

Constants	EOS		
	BKW	BKWR	JCZ3
α	0.5	0.5	–
β	0.1	0.176	–
K	11.85	11.80	–
θ	400.	1850.	–

Covolumes	BKW	BKWR	r	Σ/k
N_2	380	404	4.05	120.0
CO	390	440	4.05	120.0
CO_2	670	610	4.20	200.0
H_2O	360	270	3.35	138.0
NH_3	476	384	3.35	138.0
CH_4	528	550	4.29	154.0
H_2	180	98	3.34	37.0
NO	386	386	3.97	105.0
O_2	325	325	3.73	132.0
HF	389	389	3.30	100.0
CF_4	1100	1100	5.00	220.0
NF_3	750	750	4.10	200.0
F_2	387	387	3.50	200.0
C ΔH (Kcal/mole)	+15	+12	+15	

REFERENCES

1. C. L. Mader, "FORTRAN BKW: A Code for Computing the Detonation Properties of Explosives," Los Alamos Scientific Laboratory Report No. LA-3704, July 10, 1967.

2. H. B. Levine and R. E. Sharples, "Operator's Manual for RUBY," Lawrence Radiation Laboratory Report No. UCRL-6815, March 20, 1962.

3. W. E. Wiebenson, W. H. Zwisler, L. B. Seely and S. R. Brinkley, Jr., "TIGER Documentation Volume," Stanford Research Institute (prepared for Ballistic Research Laboratory, Aberdeen, Maryland   Contract No. DA-04-200-AMC-3226 (X), Nov. 1968), SRI Publication No. Z106.

4. R. Becker, Z. Physik 4, 393 (1921).

5. R. Becker, Z. Physik 8, 321 (1922) and Z. Technische Physik 3, 249 (1922).

6. G. B. Kistiakowsky and E. B. Wilson, "Report on the Prediction of Detonation Velocities of Solid Explosives," Office of Scientific Research and Development Report OSRD-69 (1941).

7. G. B. Kistiakowsky and E. B. Wilson, "The Hydrodynamic Theory of Detonation and Shock Waves," Office of Scientific Research and Development Report OSRD-114 (1941).

8. S. R. Brinkley, Jr. and E. B. Wilson, Jr., Harvard University, Report on "Revised Method of Predicting the Detonation Velocities in Solid Explosives," to Sept. 12, 1942, OSRD Report No. 905, prepared for National Defense Research Committee of the Office of Scientific Research and Development.

9. J. G. Kirkwood, S. R. Brinkley, Jr., and J. M. Richardson, Cornell University, Progress Report on "The Pressure Wave Produced by an Underwater Explosion: Part V," Report OSRD No. 2022, prepared for National Defense Research Committee of the Office of Scientific Research and Development.

10. R. D. Cowan and W. Fickett, J. Chem. Phys. 24, 932 (1956).

11. C. L. Mader, "Detonation Properties of Condensed Explosives Computed Using the Becker-Kistiakowsky-Wilson Equation-of-State," Los Alamos Scientific Laboratory Report No. LA-2900, June 17, 1963.

12. M. J. Kamlet and S. J. Jacobs, J. Chem. Phys. 48, 23 (1968).

13. J. W. Kury, H. C. Hornig, F. L. Lee, J. L. McDonnel, D. L. Ornellas, M. Finger, F. M. Strange, and M. L. Wilkins, "Metal Acceleration of Chemical Explosives," Fourth Detonation Symposium, ACR-126, p. 137 (1965).

14. S. J. Jacobs, "On the Equation of State For Detonation Products at High Density," Twelfth Symposium on Combustion, p. 501 (1969).

15. W. Fickett, "Detonation Properties of Condensed Explosives Calculated with an Equation of State Based on Intermolecular Potentials," Los Alamos Scientific Laboratory, LA-2712 (1962).

16. Developed by S. J. Jacobs and summarized in "Improvement and Modification to TIGER Code," by M. Cowperthwaithe and W. H. Zwisler, Stanford Research Institute (prepared under Contract N60921-72-C-0013 for Naval Ordnance Laboratory), SRI Project PYU-1377, Jan. 1973.

17. A. W. Campbell, M. E. Malin, T. J. Boyd, Jr. and J. A. Hull, Rev. Sci. Instr. 27, 567 (1956).

18. M. J. Kamlet and C. Dickenson, J. Chem. Phys. 48, 43 (1968).

19. W. C. Davis and D. Venable, "Pressure Measurements for Comp. B," Fifth Symposium on Detonation, ACR-184, p. 13 (1970).

20. J. Bdzil and W. C. Davis, "Time-Dependent Detonations," Los Alamos Scientific Laboratory Report LA 5926-MS (1975).

21. A. N. Dremin and P. F. Pokhil, *Dokl. Akad. Nauk., USSR* **128**, 899 (1959).

22. S. J. Jacobs and D. J. Edwards, "Experimental Study of the Electromagnetic Velocity-Gauge Technique," *Fifth Symposium on Detonation*, ACR-184, p. 413 (1970).

23. W. C. Davis, "Magnetic Probe Measurements of Particle Velocity," *Sixth Symposium on Detonation* (in press).

24. P. A. Urtiew, "Brightness Temperature of Detonation Wave in Liquid Explosives," Aceta Astronautica 3, No.   , pp.   (1976) (in press).

25. D. L. Ornellas, *Combustion and Flame* **23**, 37 (1974).

26. M. L. Wilkins, "The Equation of State of PBX 9404 and LX-04-01," Lawrence Radiation Laboratory, Report UCRL-7797 (1964).

27. E. L. Lee, H. C. Hornig, and J. W. Kury, "Adiabatic Expansion of High Explosive Detonation Products," Lawrence Radiation Laboratory Report, UCRL 50422 (1968).

28. H. C. Hornig, E. L. Lee, and M. Finger, "Equation of State of Detonation Products," *Fifth Detonation Symposium*, ACR-184, p. 503 (1970).

DETONATION CHARACTERISTICS OF LIQUID NITRIC OXIDE

John B. Ramsay and W. C. Chiles
Los Alamos Scientific Laboratory
University of California
Los Alamos, New Mexico 87545

Liquid nitric oxide has been distilled for a number of years to alter the $^{15}N/^{14}N$ ratio. As a result of a small explosion in a distillation unit an investigation has shown that the material is a sensitive explosive. The detonation velocity for the liquid at 115 K is estimated as 5.62 ± 0.07 mm/μs and the detonation pressure as 100 kbar. The failure diameter for the liquid confined in stainless steel is between 4.6 and 3.1 mm. A high pressure reaction, but not a detonation wave, propagates at 0.7 mm.

Nitric oxide (NO) may be considered a "magic liquid" for altering the natural $^{15}N/^{14}N$ ratio by distillation. In 1958 Clusius and Schleich (1) reported that the isotope separation factor for NO was several times higher than for other potential starting compounds. A distillation system was developed by McInteer and Potter (2) for the separation of ^{14}N at greater than 99% purity as the low boiling fraction with 40% ^{15}N collected as the high boiling fraction. This system has been operated at Los Alamos as part of the ICONS project since 1963 with distillation units containing up to 40 kg of NO. An explosion occurred in January 1975 which involved an estimated 50 g of NO in one of the product collection traps. During the subsequent investigation a limited amount of information was found indicating that liquid NO is an extremely sensitive explosive.

The first published paper was by Miller (3) in 1968. With static pressures of 1 and 3 atm on the liquid NO confined in 52-mm diameter stainless steel tubes, high-velocity detonations were obtained. When the static pressure was increased to 23 atm, no detonation was observed. Ribovich, Murphy, and Watson (4) reported on the explosive sensitivities of NO, N_2O, CO, and C_2H_2. They observed high-velocity detonation in liquid NO confined in a 25-mm

diameter, Schedule-40 steel pipe. The booster consisted of a 50 g tetryl charge with a 250-mm long Plexiglas attenuator. With the same booster-attenuator system nitroglycerine propagates in the low-order mode.

Hantel (5) confirmed the sensitivity of liquid NO with a bullet impact test. A violent reaction occurred in a 1.6-mm wall thickness, 76-mm o.d. stainless steel tube, 254-mm long filled to a depth of 100 mm with liquid NO when it was struck by a .30 cal bullet weighing 5.8 g and travelling at 451 m/s (1480 ft/s). In a similar test no reaction occurred with nitromethane.

Several experiments have been performed to estimate the failure diameter and detonation velocity of liquid NO. These experiments provided information on an interesting explosive. Nitric oxide contains neither carbon nor hydrogen, the only significant products of reaction are computed to be N_2 and O_2, (6) and there is no mole change in the reaction. The liquid range for NO is 109.5 to 121.4 K (-163.6 to $-151.7°C$) (7). The compound reacts with air to form NO_2 which is highly toxic. Because of the sensitivity and toxicity all operations with the liquid were performed remotely on the firing mound.

Previous workers transferred the NO from the gas cylinder to the shot tube by freezing the gas as a solid in the tube and then allowing the solid to melt. To reduce the possibility that the presence of solid might affect the results, transfer was accomplished by condensing the liquid above the freezing temperature. A sight glass was placed at a high point in the system to observe the liquid level and to look for gas bubbles. The sight glass was viewed with a remote controlled television camera during the filling operation. The temperature of the shot assembly was controlled by injecting liquid N_2 directly into a bath of isopentane (2-methyl butane) which surrounded the shot tube. The bath liquid was stirred with dry N_2 gas. The temperature for all shots was controlled to 115 ± 1 K over the length of the charge.

FAILURE DIAMETER

The failure diameter of liquid NO was estimated by detonating the liquid in an assembly consisting of stainless steel tubes with the diameter decreasing in steps. Each step was either 10-diameters long or 100 mm, whichever was longer. The booster consisted of an SE-1 detonator, a 12.7-mm long tetryl pellet and a 25-mm diameter X 25-mm long PBX-9404 charge with a 2.5-mm thick stainless steel barrier. In the first shot the inside diameters were 22.1, 18.9, 15.8, 12.6, 9.4, 6.2, 4.6, and 3.1 mm with a 1.65-mm wall thickness and is illustrated in Fig. 1. No fragments were recovered from this assembly. The inside diameters in the second shot were 6.2, 4.6, 3.1, 1.6, 0.71, and 0.25 mm with wall thickness of 1.65, 1.65, 1.65, 0.25, 0.18, and 0.13 mm respectively. The entire length of the 3.1-mm diameter tube was recovered but no fragments of the 4.6-mm diameter tube were found. A view of the 3.1 and 1.6-mm diameter tubes is shown in Fig. 2. The 0.7-mm diameter tube was ruptured in the same fashion as the 1.6-mm diameter tube, while the 0.25-mm diameter tube was not bulged. Detonation also occurred to the top of the liquid in the fill tube (a distance of 600 mm) with an inner diameter of 4.6-mm and a 0.89-mm wall thickness. This indicates that the failure at the transition from 4.6-mm diameter to 3.1 mm was not an effect of the wall thickness. The burst strength of the 1.6-mm diameter tube was estimated to be about 0.6 kbar. These results indicate that the failure diameter of liquid NO confined in stainless steel is about 4.6 mm but that a high pressure reaction can occur at diameters as small as 0.71 mm.
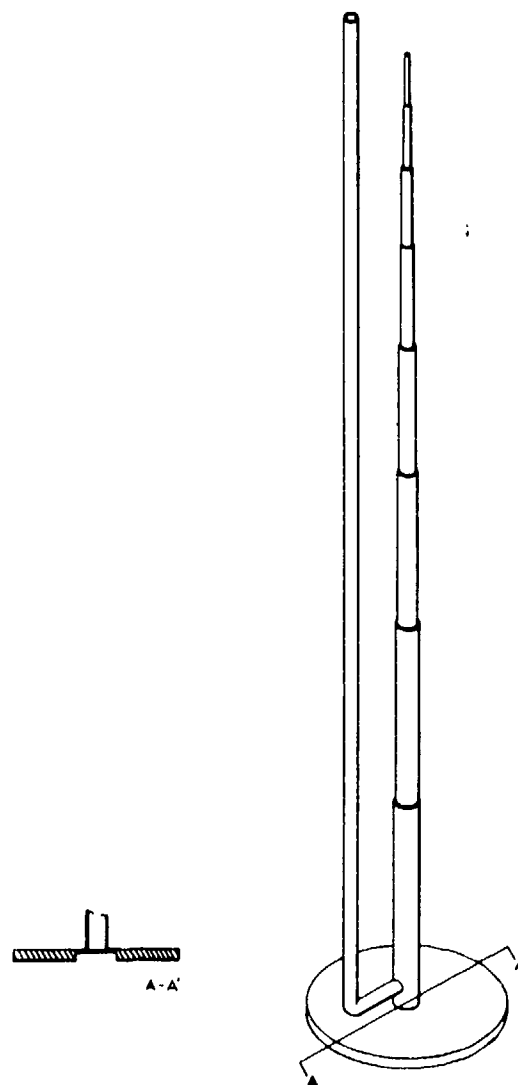
Fig. 1. Shot Assembly for Estimation of Failure Diameter of Liquid Nitric Oxide.

The shot assembly as illustrated was immersed in a bath of isopentane held at 115 K. The fill tube at the side was connected to a cylinder of gaseous NO at a pressure of 20 atm (300 psi) and the liquid condensed in the shot tube. The liquid level was observed through a sight glass mounted above the smallest tube. The booster was mounted in contact with the stainless steel diaphragm and consisted of an SE-1 detonator, a 12-mm long tetryl pellet and a 25-mm diameter X 25-mm long PBX-9404 charge. The length of each segment was either 10 times the diameter or 100 mm whichever was longer.

724
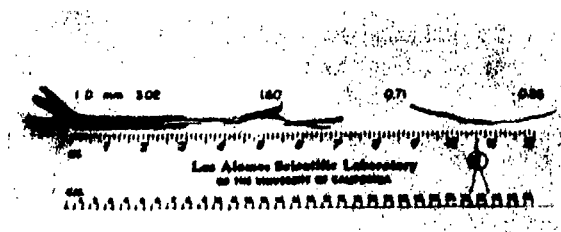
Fig. 2. Fragments Recovered from Liquid NO Test.

Detonation propagated through segments of 6.2- and 4.6-mm diameter and failed at the transition to 3.0-mm diameter. The 1.6- and 0.71-mm diameter tubes show evidence of a high-pressure reaction but have not been fragmented to the extent which would indicate a high-order detonation. No reaction was indicated in the 0.25-mm tube. The initial length of each segment was 100 mm.

DETONATION VELOCITY

The NO was confined in a 25.4-mm o.d., 1.6-mm wall thickness stainless steel tube 305-mm long. The booster consisted of a 25.4-mm long X 25.4-mm diameter PBX-9404 cylinder with a P-16 planewave lens. The booster was separated from the NO by a 2.5-mm stainless steel barrier. The shot assembly is sketched in Fig. 3.

There was some concern that attempting to insert ionization pins directly into the liquid NO might be difficult because of leakage of the sealing glands at the low temperature. An external pin was developed to eliminate the need for the internal pins. A detail is shown in Fig. 3. After brazing six small bosses around the periphery of the tube at each location of a pin the tube was mounted in a lathe and the outer surface of the bosses machined concentric with the tube. Small grooves were cut perpendicular to the
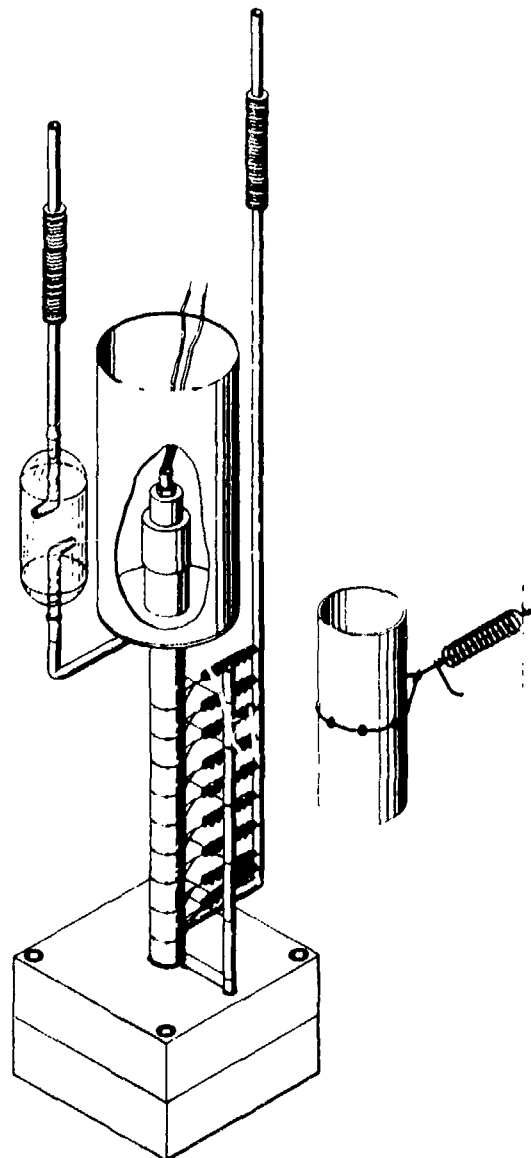
Fig. 3. Shot Assembly for Measuring the Detonation Velocity of Nitric Oxide.

The NO was confined in a 25.4-mm o.d., 1.6-mm wall thickness stainless steel tube 305-mm long. The booster consisted of a 25.4-mm long by 25.4-mm diameter PBX-9404 cylinder and a 40.6-mm diameter planewave lens with a 2.5-mm stainless steel barrier between the explosive and the NO. The booster was isolated from the isopentane bath with foam insulation and a protective stainless steel cylinder. A heavy stainless steel witness plate was used to seal the terminal end of the NO shot vessel.

The contact pin switch is shown in detail. The small bosses were welded in place, machined concentric with the tube and a small groove cut to hold the wire in place. The wire was Formvar-coated copper 0.18-mm diameter which was tied around the tube at the desired locations. The small springs were used to maintain tension on the wires as the shot was cooled. The distance between wires was measured with an optical cathetometer.

tube axis to hold the pin wires. Formvar-coated copper wire 0.18-mm diameter were tied around the tube at each position and held in place with small springs. The distance between the wires was measured with an optical cathetometer.

The data obtained for the detonation velocity are shown in Table 1. The average incremental velocity was 5.62 mm/μs with a standard deviation of 0.09 mm/μs for a single measurement. The range in the incremental velocities was 5.51 to 5.81 mm/μs which is larger than would be expected for an experiment at normal conditions, but does not seem unreasonable for this experiment. The least-squares estimate of velocity was 5.64 mm/μs with a standard deviation of 0.01 mm/μs. It is generally accepted that the least-squares procedure gives the best estimate of the detonation velocity as compared to the average incremental velocity. The most conservative estimate of the standard deviation is the larger of the two computed values. Correcting the least-squares estimate

for the contraction of the stainless steel from 298 K to 115 K and using the standard deviation of the incremental values, the detonation velocity of liquid nitric oxide at 115 K is estimated to be 5.62 mm/μs with 95% confidence limits (7 d.f.) of ± 0.07 mm/μs.

A dent depth of 1.5 mm was obtained in the type 304 stainless steel witness plate but the technique used by Smith (8) to estimate the detonation pressure from the depth of the dent is questionable for this experiment because the charge was cased and the stainless steel did not have the same hardness as the 1018 cold-rolled steel used by Smith. An attempt was made to estimate the detonation pressure of NO from the shock-induced hardness of the witness plate using a technique developed by Zukas (9). However the two-dimensional character of the shock and rarefaction waves in the plate contributed to the hardness. The metallurgical phenomena associated with these waves was unexpected and is not yet understood.

TABLE 1

Detonation Velocity of Liquid Nitric Oxide at 115 K
ρ_0 = 1.294 g/cc*

Pin Position (mm)	Incremental Distance (mm)	Time (μs)	Incremental Time (μs)	Incremental Velocity (mm/μs)
0.00	0.00	0.000	0.000	
25.66	25.66	4.559	4.559	5.628
50.82	25.16	9.130	4.571	5.505
76.29	25.47	13.614	4.484	5.680
101.66	25.37	18.120	4.506	5.630
127.12	25.46	22.502	4.382	5.810
152.16	25.04	26.992	4.490	5.577
177.32	25.16	31.492	4.500	5.590
202.89	25.57	36.093	4.600	5.558
			Average	5.622
			Variance	8.54×10^{-3}
			Standard Deviation	0.092

Least squares Fit
   X(mm) = -0.295 + 5.639t (μs)
      Standard Deviation Intercept = 0.275 mm
      Standard Deviation Slope = 0.012 mm/μs

*G. H. Cheesman, Chem. Soc. J., pp. 889-90, (1932)

COMPUTED RESULTS

During the initial investigation of the liquid NO accident C. Mader (6) computed the detonation properties, which indicated the explosive potential of the material. Since NO contained neither carbon nor hydrogen, calculations using other procedures were made to obtain other numerical estimates of the detonation pressure. The procedures reported by Smith (8) and by Kamlet and Jacobs (11) are based on the average behavior of a large number of CHNO explosives. The BKW (6) and JCZ3 (12) numerical procedures use equation of state parameters for the products to compute an equilibrium composition and the detonation properties. The values obtained by these procedures are presented in Table 2. A density of 1.26 g/cm^3 was used for the JCZ3 computation and the computed values were adjusted to a density of 1.30 g/cm^3 as shown in the table. All numerical procedures gave values in the range 95 to 119 kbar

and it seems reasonable to estimate the detonation pressure of NO at 100 kbar.

CONCLUSIONS

Liquid NO is a sensitive explosive with a detonation velocity of 5.6 ± 0.07 mm/μs and an estimated detonation pressure of 100 kbar. The failure diameter in stainless steel confinement is greater than 3.1 and less than 4.6 mm. In addition, a high pressure reaction can propagate at 0.7 mm diameter. The enthalpy is 720 cal/g relative to N_2 and O_2 products at 298 K.

Any system designed to handle liquid NO should consider the explosive potential of the material. Also the agreement among the various calculational procedures for a material as unique as NO indicates the value of such procedures in assessing the potential hazards of handling exothermic materials.

TABLE 2

Summary of Experimental and Computed Detonation Properties of Liquid NO

	Density (g/cm^3)	Pressure (kbar)	Velocity (mm/μs)	Mole Fraction N_2 in Products
EXPERIMENT				
This paper	1.294	100 ± 15	5.62 ± 0.07	—
Ribovich, et al., Ref. (4)	1.30		5.4	—
Miller, Ref. (3)	1.22		5.1	
CALCULATED				
Smith, Ref. (8)				
$\quad P = 0.2582\rho_0 D^2$	1.29	105	—	
Kamlet, Ref. (11)				
$\quad P = K\rho_0^2\Phi$	1.29	119	5.98	0.50
$\quad D = 1.01 (1 + 1.30\rho_0)\Phi^{1/2}$				

$$\Phi = NM^{1/2}Q^{1/2} = 4.899$$

$N \equiv$ moles gaseous detonation products/g of explosive = 0.033
$M \equiv$ average molecular weight of gaseous products = 30.
$Q \equiv$ cal/g of detonation reaction = 720 cal/g

$K = 15.58$ NM 0.93
14.65 NM > 0.93 (This value was used for the above computations)

	Density (g/cm^3)	Pressure (kbar)	Velocity (mm/μs)	Mole Fraction N_2 in Products
Mader BKW, Ref. (6)	1.30	106	5.61	0.498
Lee JCZ3, Ref. (12)	1.26 (1.30)*	88 (95)	5.38 (5.51)	0.482

*Adjusted for density, $dD/d\rho = 3.2$ (mm/μs)/(g/cm^3), $P = \rho_0 D^2/(\gamma + 1)$

REFERENCES

1. K. Clusius and K. Schleich, Helvitica Chim Acta, 41, p. 1342 (1958).

2. B. B. McInteer and R. M. Potter, I&EC Process Design and Development 4, p. 35 (1965).

3. R. O. Miller, I&EC Process Design and Development, 7, 590-593 (1968).

4. John Ribovich, John Murphy, and R. W. Watson, "Detonation Studies with Nitrous Oxide, Nitric Oxide, Carbon Monoxide and Ethylene," to be published.

5. L. W. Hantel, C. Hannaford, and M. Clancy, unpublished LASL data, 1975.

6. C. L. Mader, private communication.

7. H. L. Johnston and W. F. Giaque, J. Amer. Chem. Soc. 51, pp. 3194-3214 (1929).

8. L. C. Smith, Explosivstoffe, Nr 5, pp. 106-110 and pp. 130-134 (1967).

9. E. G. Zukas, 1966 Westec Conference, March 7, 1967, Los Angeles, California, pp. 1-20 (1967).

10. G. H. Cheesman, Chem. Soc. J., pp. 889-90, (1932).

11. M. J. Kamlet and S. J. Jacobs, J. Chem. Phys. 48, pp. 23-35 (1968).

12. E. Lee, private communication.

CHARACTERIZATION OF COMMERCIAL, COMPOSITE EXPLOSIVES*

M. Finger, F. Helm, E. Lee, R. Boat, H. Cheung
J. Walton, B. Hayes, and L. Penn
Lawrence Livermore Laboratory
University of California
Livermore, California 94550

We have investigated the explosive performance of a number of commercial blasting agents. We have determined EOS detonation parameters for a typical dynamite, aluminized and non-aluminized blasting agents, and ammonium nitrate/fuel oil (ANFO). This investigation also included nitromethane/oxidizer systems including several with aluminum. The time dependent properties in the detonation of several of these explosive materials were investigated. For some explosives we were able to determine the magnitude of charge geometry required in order to neglect the time dependence and to achieve maximum performance. For example, we determined the charge geometry required to achieve maximum detonation performance from ANFO. For some explosives we were able to assign EOS coefficients suitable for specific applications. Some aspects of the time dependent behavior of composite explosives are discussed.

INTRODUCTION

Commercial blasting agents are being used in many research and development programs. These applications include: investigations of controlled blasting for construction; studies of cratering phenomena; blast wave effects on structures; explosive fabrication; and energy and mineral resource recovery projects. Commercial blasting agents (CBAs) are primarily ammonium nitrate based systems. They are attractive for these projects because they are low in cost, safe to handle, easy to load and have unique detonation properties. Since these experimental programs are often closely coupled with theoretical studies aimed toward predictive models, accurate equation-of-state descriptions are required for these CBAs.

COMPOSITE PERFORMANCE

CBAs are also known as slurry blasting agents. In general, these CBAs are multicomponent systems with sensitizers added sometimes and are, therefore, also called composite explosives. To a lesser or greater extent, depending on the particular explosive, fuel and oxidizer are physically separated phases, usually as fine particulates. They, therefore, deviate in their detonation behavior from most homogeneous or "ideal" high explosives since the zone in which the energetic reactions take place is generally much larger than for "ideal" explosives. The CBAs and their "non-ideal" detonation performance characteristics provide low detonation velocity explosives for explosive welding and impedance matching in rock blasting.

This latter application is especially attractive when coupled with a large chemical energy impulse.

Because of the heterogeneous nature of these CBAs, compositional and density variations often plagued our characterization efforts. For example, one manufacturer injected gas to cross-link the binder systems and aerate the explosive to assure initiation. This resulted in the growth of the CBA out of our hydrodynamic test fixtures, and, of course, a considerable density change. Another manufacturer claimed that detonation velocity (D) versus diameter was fairly constant unlike most CBAs. However, in our tests, we observed a significant dependence of D on the charge diameter.

EXPLOSIVES INVESTIGATED

The array of CBAs chosen for performance evaluation involved several criteria, including: reliable, reproducible, and predictable performance; truly representative commercial explosives; and special performance characteristics. For example, this latter property includes the ability to propagate in small diameters for laboratory rock fracture studies, TELEDET; and rheologic properties that allow pouring, POURVEX. In many cases the exact compositions of the explosives evaluated are proprietary. Overall, over 350 CBAs were reviewed in our survey (1). The explosives we evaluated for detonation performance are listed in Table 1. Only generalized descriptions are provided for commercial compositions.

DETONATION PERFORMANCE

We used three kinds of hydrodynamic experiments to evaluate the performance of the commercial blasting agents investigated. These are depicted in Fig. 1. We chose a convenient version of the "sphere" test similar to the one described by Wilkins (2) to emphasize the early expansion history of the detonation products. The cylinder test (3) was used to characterize the isentropic expansion in an intermediate time range. To accurately portray the very late time, large expansion portion of the isentrope, we performed studies on an underwater "sphere" test. In our terminology, the "sphere" test has a hemispherical cap and a cylindrical body as depicted in

Fig. 2. This variation of a truly one-dimensional sphere was required to allow loading of hydro containers with gelled slurry blasting agents. The point of initiation is the center of the hemispherical portion and the radial expansion of the hemisphere is monitored optically. We performed tests in scaled geometries for these composite explosives to qualitatively determine their time dependent detonation behavior. The spherical and cylindrical tests were performed in several scaled sizes in order to assess the effect of delayed combustion typical of these explosives.
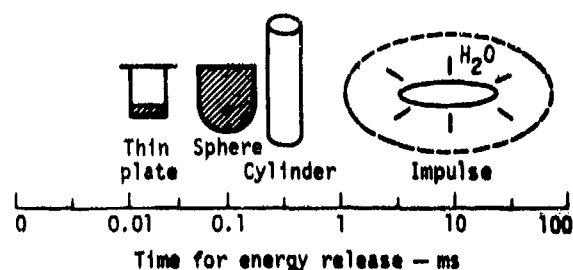
Fig. 1. Explosives performance is determined by hydrodynamic tests chosen to enhance specific regions of isentropic expansion.
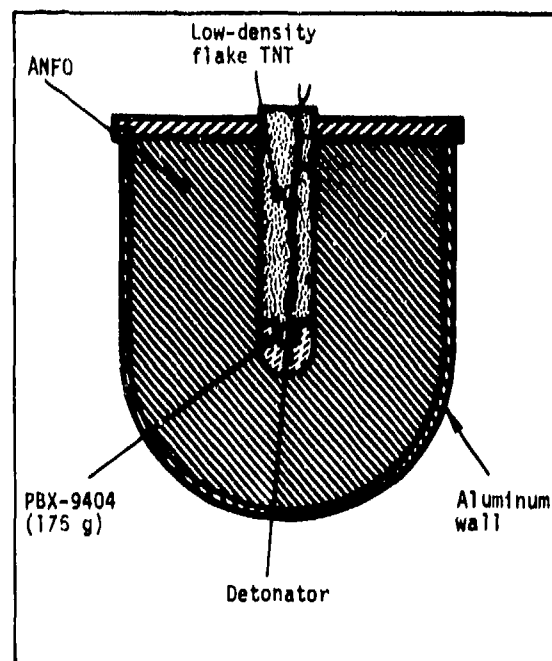
Fig. 2. Sphere and booster assembly for LLL 203- and 406-mm-diameter spherical tests.

TABLE 1

Explosives Systems Studied to Determine Performance of Commercial, Composite Explosives.[a]

Name	Density[b] g/cc	Mfr.	Composition		Sensitizer	Aluminum	H_2O	Carbonaceous Materials
			Ammonium Nitrate	2nd Oxidizer				
ANFO	0.85	Gulf	x					x
DBA 65-T2	1.52	IRECO	x	x	x	x	x	x
POURVEX	1.36	DuPont	x	x	x		x	x
EL-836	1.52	DuPont	x	x	x	x	x	x
UNIGEL	1.28	Hercules	x	x	x			x
TELEDET	1.36	Teledyne	x		x		x	x
AQUANAL	1.43	ATLAS	x			x	x	x
RX-30-AA	1.52	LLL		AP(5μ)-60.8	NM-38.0			Guar 1.2
AB	1.51			AP(200μ)-61.1	NM-37.9			Guar 1.0
AC	1.53			KP(5μ)-47.6	NM-50.8			Guar 1.6
AD	1.53			KP(200μ)-47.1	NM-51.3			Guar 1.6
AE	1.42		AN(9μ)-57.9		NM-40.8			Guar 1.3
AF	1.42		AN(19μ)-57.9		NM-40.8			Guar 1.3
RX-31-AA	1.47		AN(9μ)-28.8		NM-47.0	Aℓ(fine)-22.8		Guar 1.4
AB	1.41		AN(9μ)-43.2		NM-47.0	Aℓ(fine)- 8.3		Guar 1.5

[a]Designations include: AN = ammonium nitrate, AP = ammonium perchlorate, NM = nitromethane and KP = potassium perchlorate.

[b]This represents nominal densities.

NON-ALUMINIZED CBAs

ANFO

In the class of explosives we have designated as non-aluminized CBAs, ANFO, a specially prepared (prilled) ammonium nitrate/fuel oil composite is of special interest. It exhibits remarkable extremes of explosive performance as a function of composition and charge size. Yet it can be made reproducible if formulation parameters are closely controlled. We have made accurate measurements on ANFO detonation performance in a wide range of charge sizes. For these reasons, plus its great importance as a commercial blasting agent, we will dedicate some extra space and treat ANFO as a general example of the class of non-aluminized explosives.

ANFO, the most widely used commercial blasting agent, is comprised of 94 wt% ammonium nitrate and 6 wt% fuel oil. ANFO's detonation performance is influenced by a number of variables. Its detonation velocity increases with increasing density within the density range of interest and application and also increases with greater charge diameters up to about 270 mm, after which ANFO's performance with respect to diameter is "ideal." The detonation velocity and energy are strongly influenced by the fuel-oil percentage. Both of these parameters reach a maximum at 5.8% and then decrease more gradually Above 12%, ANFO will not detonate.

We established the minimum charge size needed for optimum "ideal" ANFO performance by performing 51-, 102-, and 292-mm cylinder tests and by also monitoring the performance with *in situ* gauges of a 109-tonne shot. We also did 203 and 406-mm "sphere" shots in air and a 203-mm "sphere" test under water. Full details are given in Ref. (4). Briefly, we summarize the results in Table 2 in terms of ANFO composition, density, detonation velocity, and detonation pressure. The detonation velocities were obtained using conventional electronic pin-switch techniques (5) and detonation pressure was determined using the axially symmetric magnetic

TABLE 2

ANFO Composition, Density, Detonation Velocity, and Detonation Pressure Results

Test	ANFO Charge kg	Fuel Oil %	Density[b] g/cm³	Detonation Velocity km/s	Detonation Pressure GPa
Metal-acceleration tests					
51 mm cylinder	0.55	5.8	0.80	3.25	—
102 mm cylinder	7	5.2	0.78	3.89	—
292 mm cylinder[a]	104	6.0	0.84	4.56	—
292 mm cylinder	104	5.8	0.82	4.55	5.50
203 mm hemisphere[a]	5	5.2	0.78	—	—
203 mm hemisphere (underwater)	5	5.8	0.87	2.74	—
406 mm hemisphere[a]	40	5.2	0.78	—	—
Pre·Dice Throw field test	109 tonnes	5.8	0.84	4.74	6.14

[a]Test terminated prematurely.

[b]Because of the variation of densities observed, we adjusted detonation parameters to the nominal density of 0.85 g/cc.

probe technique (6). As can be seen in Fig. 3, our measured detonation velocities are in good agreement with published data (7) (8).

The isentropic expansion data is represented in Figs. 4, 6, and 7. In Fig. 4, we show the wall versus radial expansion for 51-, 102-, and 292-mm ANFO cylinder shots. Allowing for a density correction, the 102-mm and 292-mm data are almost identical. Wall motion calculated with a 2D hydrocode and JWL

ANFO parameters from Table 3 is also shown. The 51-mm test showed severe striations in the wall, which are characteristic of a detonation wave propagating near failure (see Fig. 5).

The radial expansion of ANFO "spheres" fired in air and under water is shown in Fig. 6. The two spherical tests in air terminated abruptly. We believe
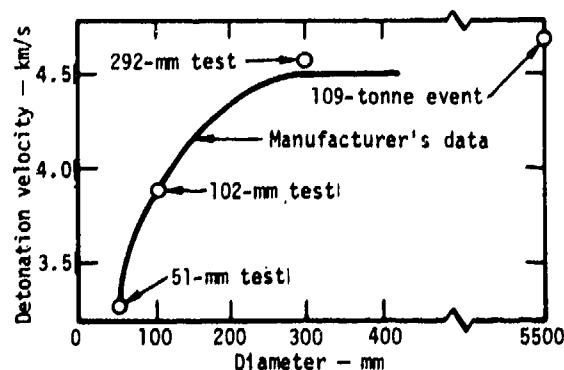
Fig. 3. Detonation velocity data from LLL cylindrical tests and the 109-tonne field tests as a function of charge diameter. These data agree well with manufacturer's information.
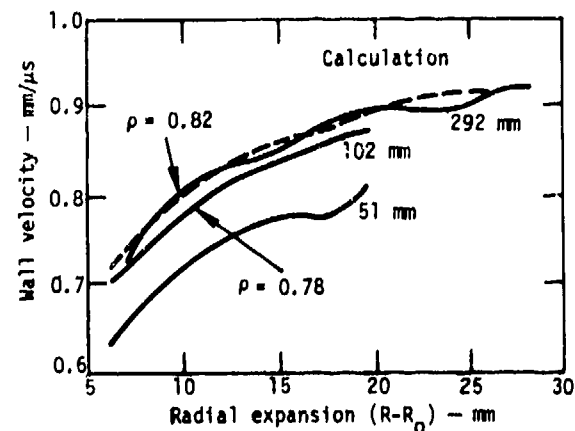
Fig. 4. Cylinder test wall velocity vs radial expansion $(R - R_0)$ scaled to a 25-mm cylinder. If the density (ρ) of the 102-mm and 292-mm charges had been the same, their curves would have been virtually identical.

732

that early breakup of the metal was caused by ANFO's heterogeneous nature. Crushing of the prills and microjetting as the shockwave progressed into the relatively thin aluminum case caused the premature breakup. The underwater spherical test fared much better, providing considerably more data than the air shots. This is due partly to damping of the metal motion in water. The far field pressure data from the underwater test, Fig. 7, are in fair agreement with the response predicted using the EOS described below.

The detonation pressures from the 292-mm-diameter cylindrical test and the 109-tonne field test were in good agreement. We were also able to determine from the magnetic probe data, see Fig. 8, that the ANFO reaction-zone thickness is approximately 4 mm to 6 mm, as compared with 12 mm to

Fig. 5. 51-mm ANFO cylindrical test shows unusual straited failure pattern.
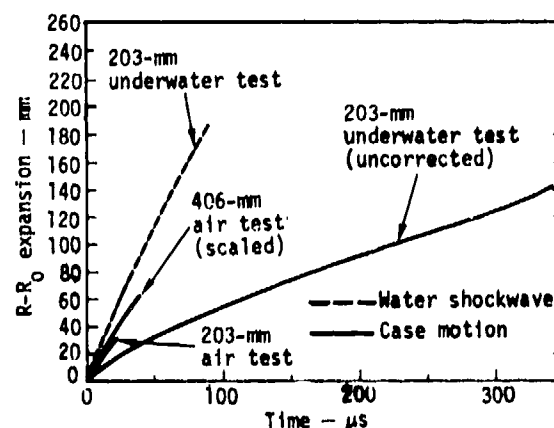
Fig. 6. Hemisphere expansion data for air and underwater tests of ANFO. Because the experiment holds together longer in water, underwater testing can provide valuable far-field (late-time) information not obtainable from air testing.

TABLE 3

Equation of State Parameters For Explosives Cited

	C-J Parameters					JWL-EOS Coefficients					
	P Mbar	D cm/μsec	E_0 Mb·cc/cc	ρ g/cc	Γ	A	B	C	R_1	R_2	ω
ANFO	.060	0.465	.0325	0.850	2.063	0.4760	.00524	.00720	3.5	.9	.31
POURVEX	.130	0.610[b]	.0450	1.360	2.893	3.2207	.07769	.00324	4.7	1.4	.16
EL-836	.135	0.579[a]	.0920	1.520	2.775	2.8123	.02507	.01445	4.5	1.1	.20
DBA-65-T2	.120	0.540[a]	.0800	1.520	2.694	2.1467	.02157	.01295	4.3	1.4	.20
UNIGEL	.120	0.576[a]	.0510	1.262	2.490	1.9070	.07580	.00627	4.4	1.4	.23
TELEDET	.150	0.652	.0410	1.360	2.854	3.0409	.05804	.00347	4.3	1.5	.20
AQUANAL	.055	0.370[a]	.0550	1.430	2.559	0.9123	.00407	.00746	4.4	1.0	.16

[a]These are not D_∞ values. The EOS represents the behavior in the largest charge size tested in this work.
[b]See Fig. 9. Isentropic expansion for 51 and 102 mm POURVEX shots were identical; therefore, detonation velocities were averaged.

16 mm calculated by the detonation velocity versus diameter dependence using Eyrings' curved front theory (9).

OTHER NON-ALUMINIZED CBAs

In Fig. 9, we show the relative isentrope energies determined from cylinder tests for several non-aluminized commercial blasting agents. The materials are compared to nitromethane in all cases, and ANFO is cited again for reference. Detonation velocities determined for each diameter are also cited. The behavior of TELEDET and POURVEX in isentropic expansion is very similar to "ideal" or "high" explosives. However, only Teledet appears to act as an "ideal" explosive in terms of detonation velocity.

ALUMINIZED BLASTING AGENTS

The performance of several aluminized CBAs was measured in cylinder shots. The relative isentropic energy of EL 836, DBA 65T2, and AQUANAL compared to nitromethane is shown in Fig. 10. We can see that scaling laws do not hold for the one system, EL-836, where we have two scaled geometries. Further evaluation of these types of materials in hydrodynamic underwater tests is planned.

Fig. 7. Comparison of calculated and experimental far field shock wave data from 203-mm underwater "sphere" test of ANFO.
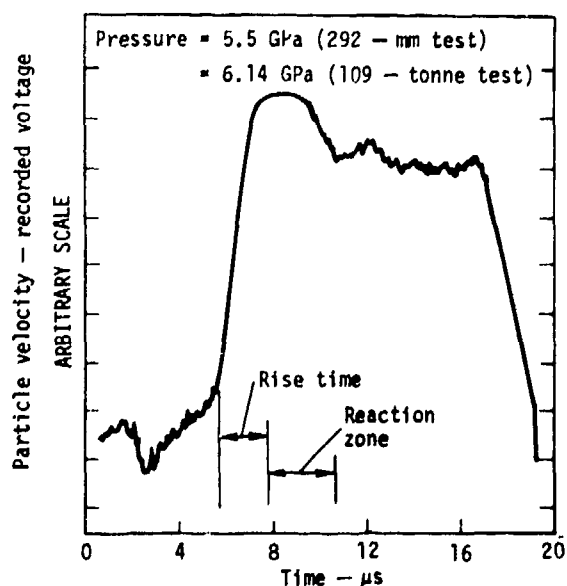
Fig. 8. Magnetic probe record depicting the particle motion of ANFO.
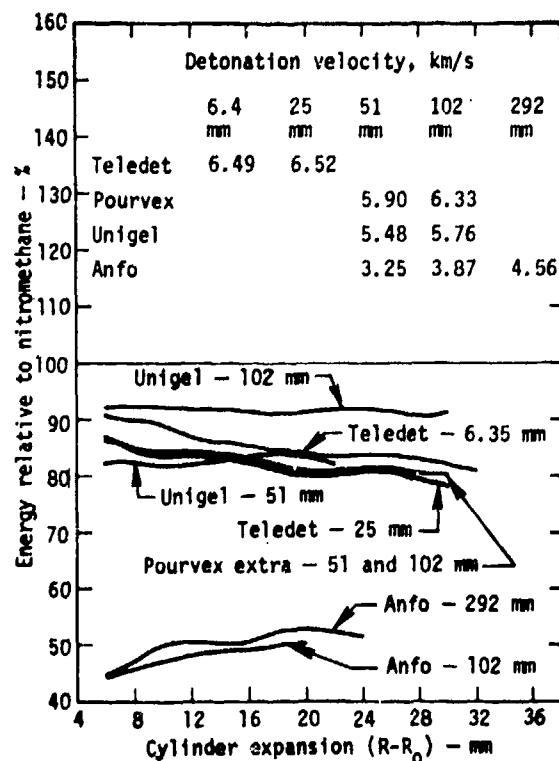
Fig. 9. Relative energy of non-aluminized blasting agents.

734
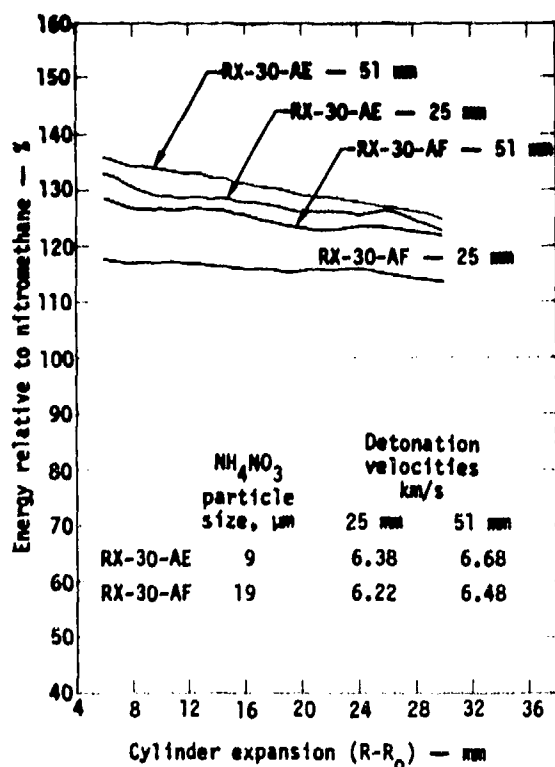
Fig. 10. Relative energy of aluminized blasting agents.

Fig. 11. Relative energy of RX-30-AE and AF.

NITROMETHANE/AMMONIUM NITRATE (AN)

In this section and those below we describe experiments that attempt to provide data of a fundamental nature on the performance of composite explosives. We studied variations in the type and the particle size of the oxidizer. For these experiments we chose a very simple chemical system, a detonable homogeneous, under-oxidized fuel-nitromethane-as the host matrix. We then added oxidizers which have one, two or four excess oxygens available for further reaction with the under-oxidized NM. All systems were stoichiometrically balanced as close as possible to H_2O and CO_2. In the case of fine particle ammonium nitrate (AN) we were only able to balance to H_2O and $CO_{1.5}$. The oxidizers were suspended uniformly in NM with the aid of a gelling agent.

In Fig. 11 we show the effect of AN particle size in terms of isentropic expansion compared to nitromethane. Since the spread in particle diameter of AN was not large (9 μm - 19 μm), the particle size effect

is small. It may also be attributed to the fact that only one excess Oxygen is available.

$$NH_4NO_3 \rightarrow N_2 + 2H_2O + O.$$
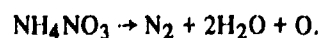
Thus it makes a relatively small contribution to the energetics of the system. Nevertheless, the 9 μm composition shows less charge diameter effect on performance than the 19 μm. This is also shown in the diameter effect on detonation velocity.

NITROMETHANE/AMMONIUM PERCHLORATE (AP)

A large effect due to particle size is seen in the relative isentrope energies depicted in Fig. 12. The 5 μm AP shows essentially no geometry dependence on performance. However, the 200 μm AP shows a considerable charge diameter effect in 25, 51, and 102 mm cylinders compared to nitromethane. We note the effect of charge configuration in Fig. 13. The wall velocity vs sphere expansion for the two

735
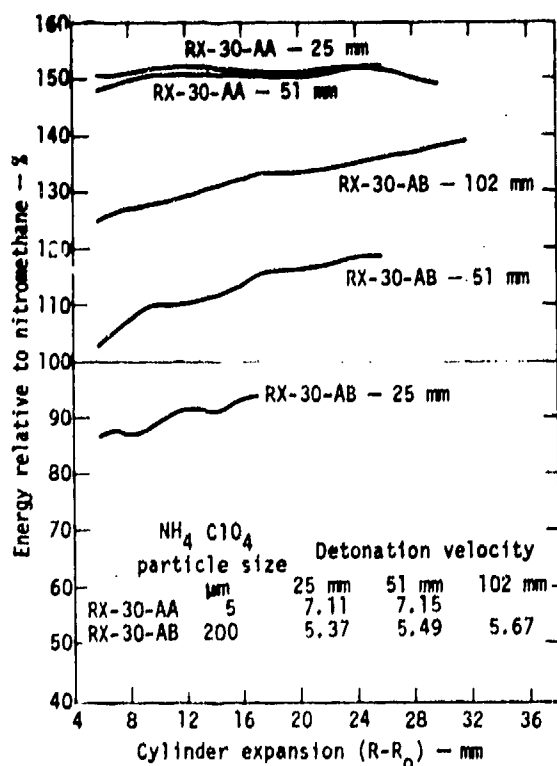
Fig. 12. Relative energy of RX-20-AA and AB.

different particle size AP systems in two scaled "sphere" tests are given. The charge size effect is significant even for the 5 μm AP system. In the sphere test the ratio of mass of explosive to mass of metal confinement is much larger than in the cylinder test. This accentuates the influence of the outer layer of detonation products on the performance.

NITROMETHANE/POTASSIUM PERCHLORATE (KP)

Potassium perchlorate is a non-detonable oxidizer so that its participation in the detonation reaction must be heavily dependent on diffusion. NM/KP relative isentrope energies are shown in Fig. 14 compared to NM and as a function of KP particle size and charge diameter. The KP must decompose and the oxygen diffuse and react with the underoxidized detonation products of NM. Interestingly the 200 μm KP and AP have virtually indistinguishable isentropic expansion in the 25 mm cylinder test. This suggests

Fig. 13. Wall velocities for nitromethane/ammonium perchlorate explosives (RX-30-AA and AB) in sphere tests. ANFO is shown for comparison.
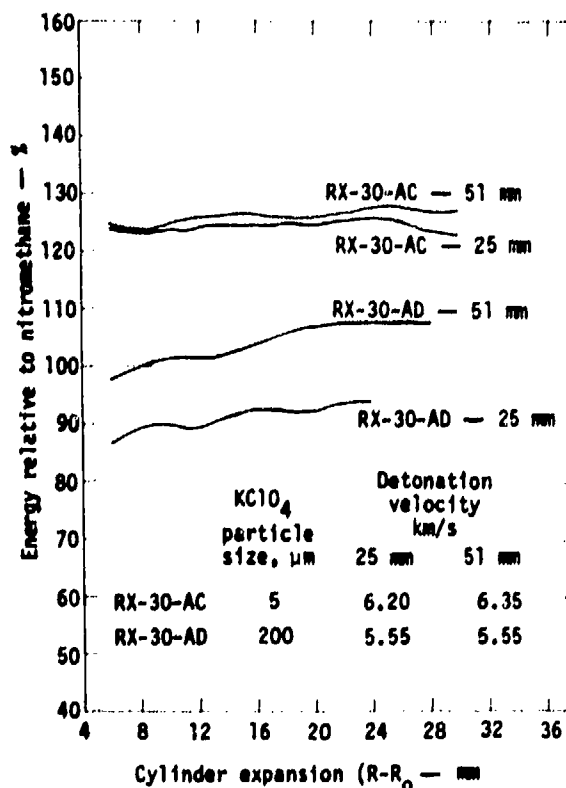
Fig. 14. Relative energy of RX-30-AC and AD.

736

that in this size, AP and KP have decomposed to provide gaseous products but have not contributed energy to the system by reacting with the NM products. Also, the 200 μm KP shows the same detonation velocities in the 25 and 51 mm cylinder tests but a fairly large difference in isentrope energies. In fact, although the 200 μm AP shows some change in detonation velocity with diameter its nominal velocity is about the same value as the 200 μm KP system. The 5 μm KP system in 25 and 51 mm cylinder tests indicate that the KP has fully reacted.

NITROMETHANE/AMMONIUM NITRATE/ALUMINUM

We tested the effect of aluminum in a NM/AN system, choosing a nominal 10. and 25. wt% of Al as representing the extremes of Al concentration. Practical mixing considerations changed this to 8.3 and 22.8%. The relative isentrope energies of these systems are compared to NM in Fig. 15. The non-aluminized NM/AN system is also shown.
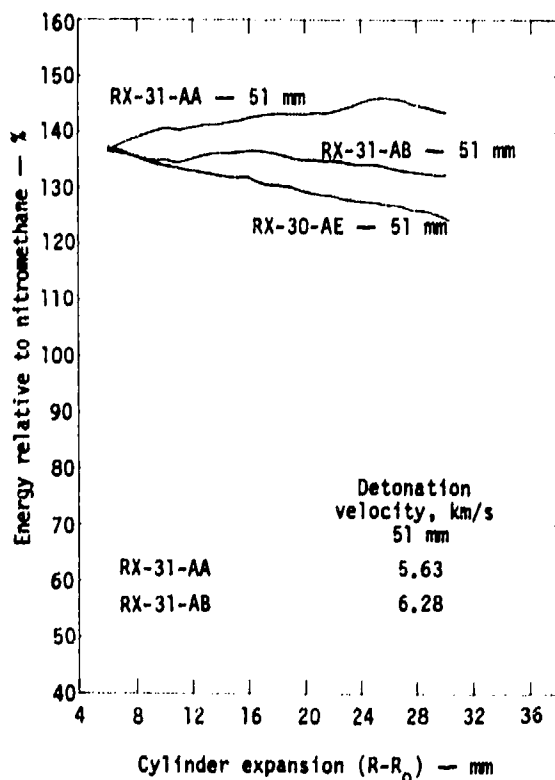
Fig. 15. Relative energy of RX-31-AA and AB.

EQUATION OF STATE

A most simple and useful way of summarizing the detonation performance of an explosive is by means of an equation of state (EOS). It is important to keep in mind the basic limitations on this procedure. Also, for an empirical EOS such as JWL which is used here, some additional experimental quantities are required. Although certain carefully applied compromises are often useful a detonation product EOS can properly be applied only to equilibrium, self-similar flow behind the detonation front. This is equivalent to what we have somewhat loosely referred to as "ideal" behavior and have more precisely described as conforming to scaling laws. The preceding sections have attempted to analyze the degree to which each explosive conformed to these criteria. The experiments were guided by a desire to determine the magnitude of charge diameter above which these criteria are satisfied. We have additionally indicated in our summary of equation of state coefficients, Table 3, where some significant concerns about these criteria still remain.

The most useful function of the detonation product EOS, of course, is to describe the energy output during isentropic expansion. To specify an initial point on the isentropic path, we use the Chapman-Jouget state (i.e., the detonation parameters). To determine the magnitudes for pressure and energy as a function of volume on this isentrope (this primarily determines the equation of state coefficients) we use the cylinder and sphere test data. We have described in earlier papers how the coefficients are evaluated by successive approximation using hydrodynamic computer codes to simulate the expansion experiments.

The quantity, E_o, represents the total available internal energy for a particular isentrope and is, like the detonation velocity and pressure, a detonation parameter. We have estimated the value of E_o by calculating the total chemical energy available and by comparison with experimental results from detonation calorimeter experiments. The detonation calorimetry and the chemical calculations for explosives containing Carbon, Hydrogen, Nitrogen, Oxygen, and Fluorine have been described elsewhere. (10) Explosives containing large amounts of Aluminum present a special problem. The temperature and the energy in the products from the detonation of highly aluminized explosives is considerably higher than for

737

nonaluminized explosives. However, the pressures are generally lower at or near the C-J state. As a result the entropy is higher and a larger fraction of the energy remains in the gas and in the solid particulate aluminum oxide even for large expansions where the pressure has decreased by several decades from the C-J value. The adjustment of the calculated to the "effective" E_o can thus be somewhat greater than for non-aluminized explosives. In this report we have used some empirical rules derived from experience in blasting and in air shock experiments to adjust E_o. We have used an effective energy similar to the available work function, A, described by Cook (11) and the total expansion work, E_{wk}, coined by Noren and Porter (12). Our preliminary experiments in underwater sphere tests were in response to what we view as much needed improvement in the capability for evaluating the behavior of these explosives at large expansions.

SUMMARY AND CONCLUSIONS

The work reported here summarizes our effort thus far in diagnosing some "practical" composite explosive systems and in studying what we believe to be crucial variables in some "exploratory" or model systems. At the outset we believed it was possible to understand and predict the behavior of these formulations based upon the chemical composition and upon the particulate subdivision of "fuel" and "oxidizer." We now recognize two areas where significant additional theoretical and experimental work is needed.

The first is the development of a reaction zone model, in contrast to a C-J model, which will provide a realistic and useful description for blasting explosives utilized in "small" charges, such as small diameter bore holes. Lower pressures and in some cases lower velocities are of great practical use. Our procedures at present for predicting the hydro-dynamic response in such configurations consist of various compromises.

The second need is to develop experimental methods which will yield precise measurements of the expansion of detonation products to large volumes. In many blasting applications the pressure in the explosive products can be effective as long as it exceeds the overburden pressure of the material being moved. Such pressures can be as small as 20

atmospheres. Our present methods of measurement are limited to pressures approximately 1.5 decades higher than this.

ACKNOWLEDGMENT

REFERENCES

1. L. Penn, F. Helm, M. Finger, and E. Lee, "Determination of Equation-of-State Parameters for Four Types of Explosives," Lawrence Livermore Laboratory Report, UCRL-51892 (1975).

2. M. L. Wilkins, "The Equation of State of PBX 9404 and LX-04-01," Lawrence Radiation Laboratory Report, UCRL-7797 (1964).

3. J. W. Kury, H. C. Hornig, E. L. Lee, J. L. McDonnel, D. L. Ornellas, M. Finger, F. M. Strange, and M. L. Wilkins, "Metal Acceleration of Chemical Explosives," *Fourth Detonation Symposium*, ACR-126, p. 137 (1965).

4. F. Helm, M. Finger, B. Hayes, E. Lee, H. Cheung, and J. Walton, "High Explosive Characterization for DICE THROW Event," Lawrence Livermore Laboratory Report, UCRL-52042 (1976).

5. A. W. Campbell, M. F. Malin, T. J. Boyd, and J. A. Hull, *Rev. Sci. Instr.* 27, 567 (1956).

6. B. Hayes and J. N. Fritz, "Measurement of Mass Motion in Detonation Products By An Axially-Symmetric Electromagnetic Technique," *Fifth Detonation Symposium*. ACR 184, p. 447 (1970).

7. *The New Look of Blasting*, Gulf Oil Corporation, Chemical Department, Bulletin BBB 7-67 (1967).

8. *Monsanto Blasting Products ANFO Manual*, Monsanto Company (1972).

9. H. Eyring, R. E. Powell, G. H. Duffey, and R. B. Parlin, *Chem Rev.* **45** 69 (1949).

10. M. Finger, E. Lee, F. H. Helm, B. Hayes, H. Hornig, R. McGuire, E. Kahara, and M. Guidry, "The Effect of Elemental Composition on the Detonation Behavior of Explosives," *Sixth Symposium on Detonation*, (1976).

11. M. A. Cook, *The Science of High Explosives*, Reinhold, N.Y.

12. C. H. Noren and D. D. Porter, "A Comparison of Theoretical Explosive Energy Measured Underwater with Measured Rock Fragmentation," *Advances in Rock Mechanics, Proceedings of Third ISRM Congress*, (1974).

THE EQUATION OF STATE AND SHOCK INITIATION OF HNS II

F. W. Davies, J. E. Shrader, A. B. Simmerschied
Boeing Aerospace Company
Seattle, Washington

and

J. F. Riley
Lockheed Missiles & Space Company, Inc.
Lockheed Palo Alto Research Laboratory, Palo Alto, CA 94304

The Hugoniot and effective Gruneisen parameter of unreacted HNS II and its shock sensitivity to initiation were measured using plate impact and electron beam techniques.

The Hugoniot of HNS II compacted to the indicated densities was found to be

$$U_s = 3.48\, U_p + 1.10 \text{ km/s} \qquad \rho = 1.47\, Mg/m^3 \qquad \sigma < 3.0 \text{ GPa}$$

and

$$U_s = 1.93\, U_p + 1.98 \text{ km/s} \qquad \rho = 1.58\, Mg/m^3 \qquad \sigma < 3.5 \text{ GPa}$$

At stresses below 0.1 GPa, the effective Gruneisen parameter of HNS II was less than 0.1.

The variations in shock sensitivity of HNS II were found to be small over the limited ranges of density and temperature examined. In long pulse (2 μs) experiments, no evidence of reaction was detected for either density at stresses ≤ 1.7 GPa. Above 3.5 GPa, stable detonation was established for propagation distances of $\leq 7.5 \times 10^{-4}$ m.

In short pulse experiments, the initiation thresholds for the two densities were assessed at room temperature and 127°C.

INTRODUCTION

Hexanitrostilbene, HNS, is a secondary explosive being used in many missile and space applications because of its relative stability at elevated temperatures. To assess the response of the explosive to the varied environments of those applications, it is necessary to characterize the equation of state of the explosive and its initiation sensitivity. This study measured these data for two typical compaction densities.

EXPERIMENTAL METHOD

The Hugoniot and the effective Gruneisen parameter of HNS II was measured at room temperature for

two compaction densities. The shock initiation sensitivities of these compactions for two stress wave durations (~ 2 μs and 100 ns) were evaluated for room temperature conditions and, in addition, the short-pulse sensitivities were estimated at 127°C. All tests were conducted under vacuum conditions of approximately 5 Pa.

HUGONIOT MEASUREMENTS

The Hugoniot and long-pulse initiation threshold of HNS II was measured using the gas gun plate impact technique, developed by Davies et al. (1). The method has the advantage of measuring simultaneously both the impact stress profile generated in the explosive and the transmitted stress profiles at various propagation distances. This provides two independent sources of data from which the Hugoniot can be derived as well as several parameters which are sensitive measures of reaction in the explosive.

The test setup is shown in Fig. 1. The HNS is impacted by an aluminum flyer. The HNS II test specimens were pressed in 2024 aluminum alloy cups; pellet densities were 1.47 ± 0.03 Mg/m^3 and 1.58 ± 0.03 Mg/m^3 which are 84 and 91% of theoretical density.

Each piezoresistive gage was laminated between a 0.75-mm-thick disk in front and a 6.3-mm disk in back and bonded with expoxy. The four rear surface gages used Plexiglas disks in the gage assembly to minimize the impedance mismatch with the HNS, while the center gage was laminated between aluminum disks to match the flyer and support disk materials. The transmitted stress gage assemblies were bonded to the exposed HNS surface using an adhesive bond of 3M-3532 urethane cement which was estimated to be less than 0.06-mm thick.

The two methods of determining a point on the Hugoniot which were used in this study are illustrated in Fig. 2. In the first, the stress in the HNS was measured directly using the impact gage, and the particle velocity was calculated using a known aluminum Hugoniot (2) and the measured impact velocity. In the second method, the transit measurements were used to calculate the average shock velocity in the explosive. This velocity then defines the Rayleigh line, which intersects the reflected aluminum Hugoniot at a point on the HNS Hugoniot. The location of the reflected aluminum Hugoniot is defined by the measured impact velocity.
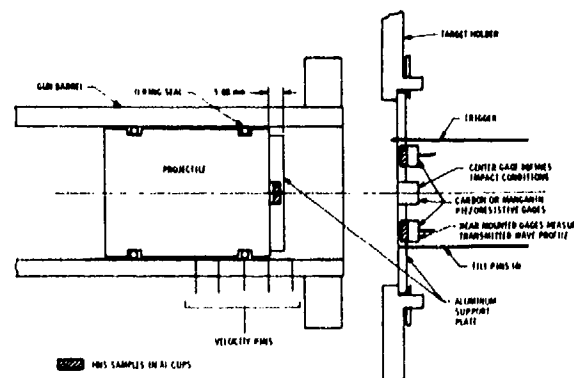
Fig. 1. Gas gun setup.
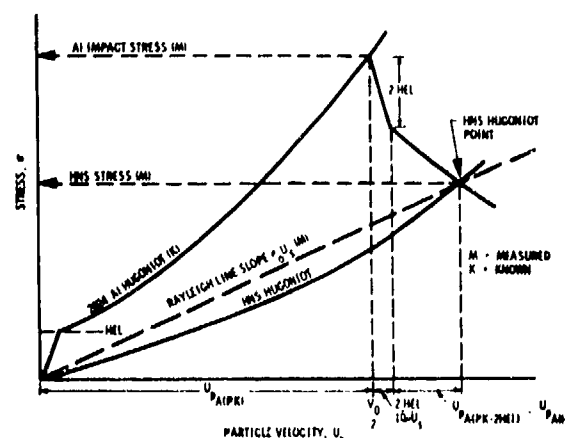
Fig. 2. Hugoniot diagram.

The transmitted stress gages actually measure the stress in the Plexiglass surrounding the gage. The stress in the HNS was calculated using standard impedance matching techniques.

INITIAL THRESHOLD MEASUREMENTS

The shock initiation threshold of HNS II was determined for both 2-μs and 0.1-μs pulse durations. The Hugoniot experiments also provide initiation threshold data. The transmitted stress for each sample thickness was compared to the impact stress and an increase in stress in the sample taken to indicate reaction. To some degree, the rise time of the transmitted stress was used to verify detonation. In addition, the fit of the Hugoniot data point derived from the impact stress data to the Hugoniot determined from the lower stress points is used as a measure reaction. The average shock velocity from transit time

741

measurements was compared to the expected shock velocity and the expected detonation velocity in another test for initiation.

The short-pulse shock sensitivity was also determined by plate impact experiments performed in the Boeing Company's 2.5-in. gas fun. In these tests a single test specimen was impacted by a thin (0.305 mm) aluminum alloy (2024). The target configuration is shown in Fig. 3.

The HNS II pressed into 2024 aluminum cups at two density ranges as in the previous experiment, and then a chrome mirrored 3-mm-thick disk of Lexan polycarbonate was pressed into the cavity behind the HNS with the mirror adjacent to the HNS.

On Heated shots, an aluminum cylinder with an electric heater on the outer surface was bolted to the sample cup and then in turn bonded to the support plate. The temperature was controlled using a thermocouple inserted into a hole in the sample cup.

The impact time was obtained from a coaxial make-circuit pin or a piezo pin flush with the front surface.

It was intended to obtain both shock arrival time and surface velocity of the mirror in contact with the HNS and the rear surface of a thin section of the support plate by using a velocity interferometer. In later shots, this interferometer technique was supplemented by, and then replaced by, a piezoresistive gage on the rear surface of the Lexan disk. The gage was backed up by a second Lexan disk to increase the

duration of the signal. This was necessary because Lexan, which had been chosen for its high-temperature properties, apparently becomes opaque at the stress levels of this test. Shock arrival times were characterized by the sudden absence of light reflected back from the target.

The accuracy of both the transit time and manganin gage data is limited by the uncertainties in the Lexan Hugoniot.

EFFECTIVE GRUNEISEN PARAMETER MEASUREMENT

The Gruneisen parameter of HNS II was measured by determining the velocity response of pellets exposed to an electron beam in the BREL FX-75 machine. Free standing HNS II pellets were bonded to a fused silica blank which was mirrored at the explosive/silica interface, was shown in Fig. 4. The response of this interface to the short time energy deposition was measured by a Michaelson interferometer (displacement) with quadrature encoding which determined direction as well as magnitude of the velocity (3).

The dose in each shot was determined by measuring the temperature rise in a 0.05-mm-thick aluminum foil calorimeter in line with the specimen, as shown in Figs. 4 and 5. The depth dose profile was estimated in separate experiments using a multiple foil calorimeter (4). A 0.9-mm-aluminum filter was used in front
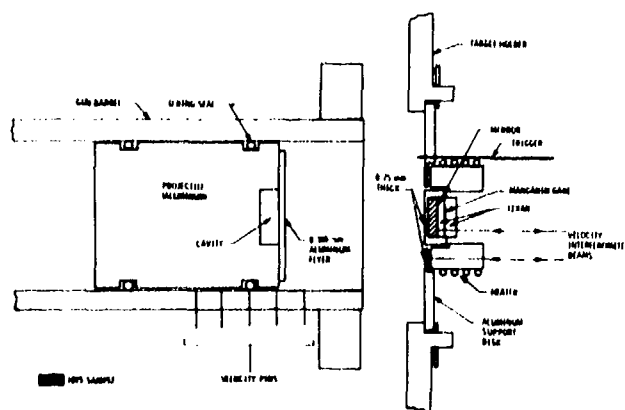
Fig. 3. Short-pulse test setup.
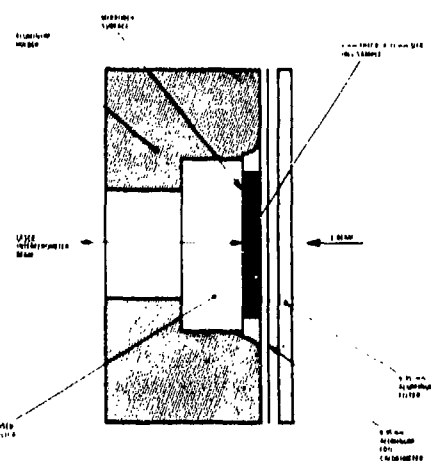
Fig. 4. HNS Gruneisen parameter test setup.

of the test specimen to minimize the dose uncertainty. This and the normalized deposition profile are illustrated in Fig. 5.

Fused silica was chosen as the mounting material because it is not affected optically by doses below 10 cal/g and its Gruneisen is low (~ 0.02), and normally the stresses in the silica can be neglected completely. However, for these experiments, this assumption was not valid. The response of the interface between silica and HNS in this case can be analyzed as a sequence of step waves arriving from each side.

In experiments conducted to check the Gruneisen coefficient of fused silica, a value of 0.021 was obtained, consistent with published data. Using this value and the measured deposition profile (Fig. 5), the Gruneisen of HNS II was given by $\Gamma_{II} = 0.016 - 0.81$ N/E for 1.58 Mg/m^3 HNS and $\Gamma_{II} = 0.011 - 0.74$ N/E for 1.47 Mg/m^3 HNS where N is the number of fringes detected at 514.9×10^{-9} and E is the calorimeter dose.

RESULTS

Equation of State and Shock Initiation Threshold

Typical stress profiles measured in the Hugoniot experiments by the piezoresistive gages are given in Figs. 6 and 7. The wave forms shown in Fig. 6 are representative of those impact velocities which did not result in detonation of the HNS. Both the amplitude and rise time of the transmitted pulses remain constant. The stress profiles shown in Fig. 7 are representative of those shots where detonation of the HNS was observed. In this case, the amplitude and rise time of the transmitted pulse is seen to increase with increasing propagation distance.

Figures 8 and 9 present distance versus transit time plots which illustrate the onset of detonation as a sharp increase in the slope of the curve, and non-detonation reaction as a gradual increase in the slope. The Hugoniot curves in the stress/particle velocity plane are presented in Fig. 10. The results of the two measurement techniques agree well at the lower stress levels for both densities of HNS. The divergence of the stress and transit time data and the steepening of the Hugoniot at the higher stress levels are considered to be indicative of reaction in the explosive.
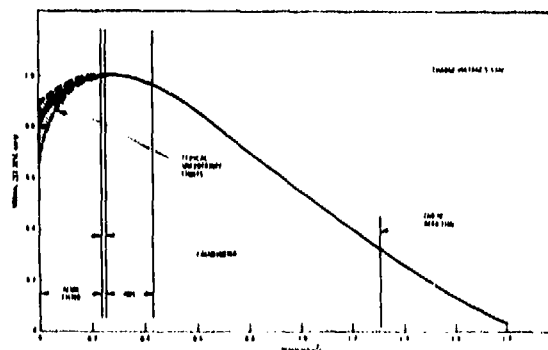
Fig. 5. Normalized depth dose profile for HNS Gruneisen.
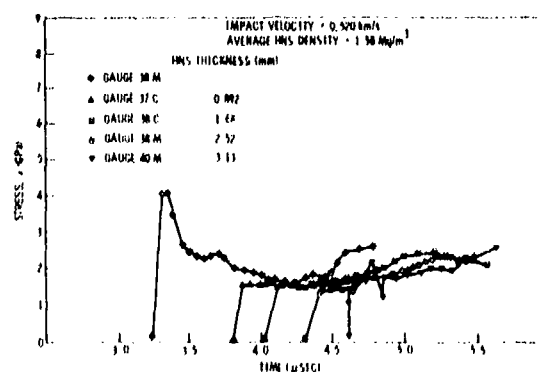
Fig. 6. Shock stress levels, shot 6.
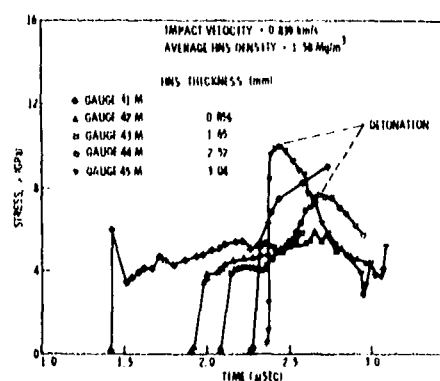
Fig. 7. Shock stress levels, shot 9.

The variation in the Hugoniot as a function of HNS density is observed as a slight change in curvature at low stress levels. This variation shows more clearly in the shock velocity/particle velocity plane

743
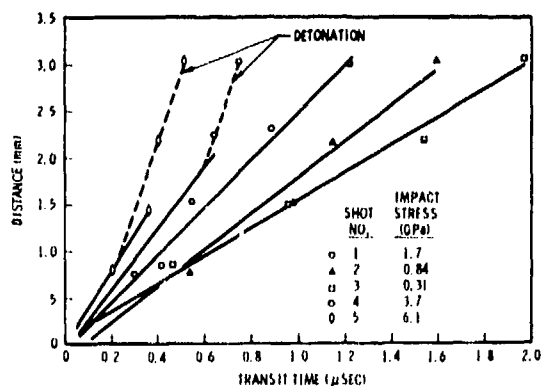
Fig. 8. Shock front progress, low density.
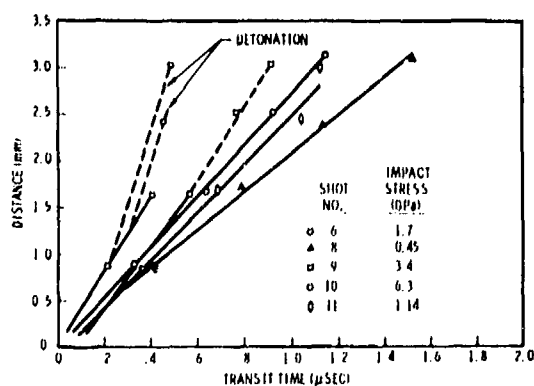
Fig. 9. Shock front progress, high density.

presented in Fig. 11. In this plane, the lower density HNS has a much steeper slope at low stress levels than the higher density HNS.

A linear least squares fitted to the shock velocity/ particle velocity data provides the following relations:

$$U_s = 3.48 \, U_p + 1.10 \text{ km/s}$$

for

$$\rho = 1.47 \text{ Mg/m}^3 \quad \text{and} \quad \sigma < 3.0 \text{ GPa}$$

and

$$U_s = 1.93 \, U_p + 1.98 \text{ km/s}$$

for

$$\rho = 1.58 \text{ Mg/m}^3 \quad \text{and} \quad \sigma < 3.5 \text{ GPa}$$
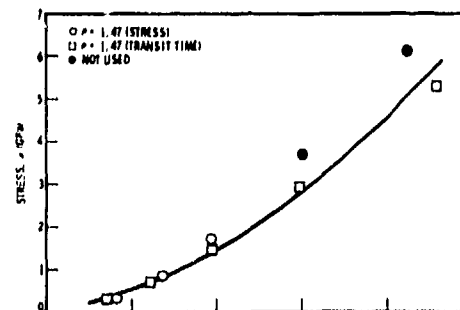
Fig. 10. Hugoniot for HNS II, stress/U_p plane.
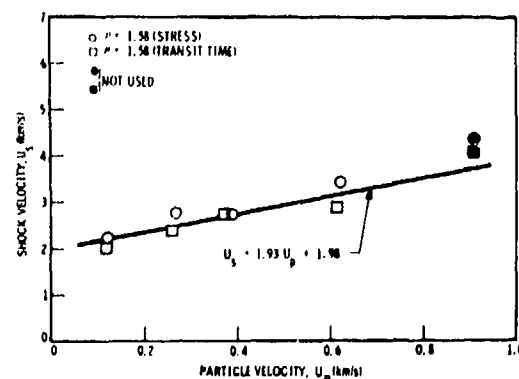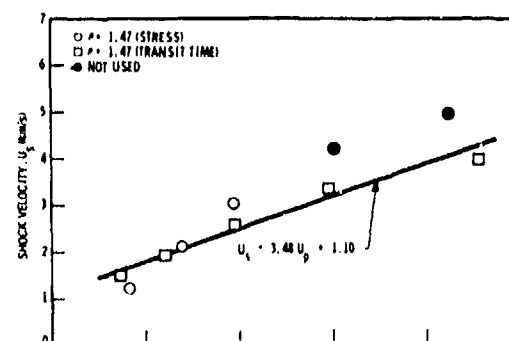
Fig. 11. Hugoniot for HNS II, U_s/U_p plane.

744

Long-Pulse Initiation Threshold

The long-pulse shock initiation threshold for HNS II was determined by examining the variation of the stress profile and its propagation velocity as a function of impact stress and propagation distance. For the low density ($\rho = 1.47$ Mg/m^3) HNS II, the transit time data shown in Fig. 8 and the transmitted stress levels illustrated in Fig. 12 both indicate that the initiation threshold lies between 1.7 and 3.7 GPa. At 1.7 GPa, the initial amplitude of the transmitted stress profile remains constant over the propagation distances examined. Furthermore, the stress profiles show little if any evidence of reaction in the explosive. At 3.7 GPa, reaction occurs within the first millimeter of travel. The maximum shock velocity observed prior to detonation is about 3.9 km/sec which corresponds to a stress of 3.9 GPa. Furthermore, the impact gage data at 3.4 GPa lies well off the Hugoniot derived from the lower stress data. This is interpreted as additional evidence of reaction within the explosive at this stress at early times.

For the high density ($\rho = 1.58$ Mg/m^3) HNS II, similar transit time and stress profile data are shown

in Figs. 9 and 13, respectively. In this case, the initiation threshold is between 1.7 and 3.4 GPa. At 1.7 GPa, the initial amplitude of the transmitted stress profile again remains constant over the propagation distances examined and no evidence of reaction in the explosive is seen in the measured stress profiles. At 3.4 GPa, evidence of reaction is noted after propagation through about 0.75 mm of the explosive. The maximum shock velocity observed prior to detonation is 3.5 km/s which corresponds to a stress of 3.6 GPa. Again, the impact gage data appears to be off the Hugoniot but not as dramatically as with the low-density material.

Short-Pulse Initiation Threshold

The results of the short-pulse initiation threshold experiments are summarized in Fig. 14 for the low density ($\rho = 1.47$ Mg/m^3) HNS at room temperature. Below impact stresses of 3.1 GPa, the measured average shock velocities are less than those derived from the Hugoniot measurements. This is consistent with a nonreactive stress wave being attenuated as it propagates through the porous compaction. Above 4.1 GPa, the measured shock velocity corresponds to the detonation of the HNS.
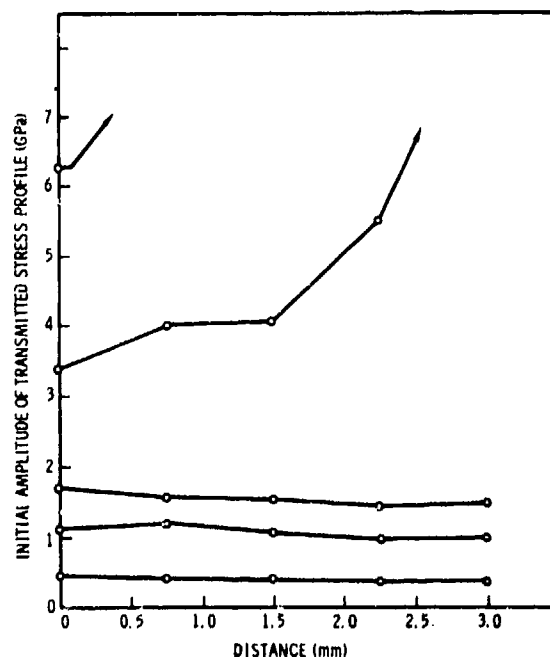

Fig. 12. Variation of stress amplitude with propagation distance for low-density HNS.
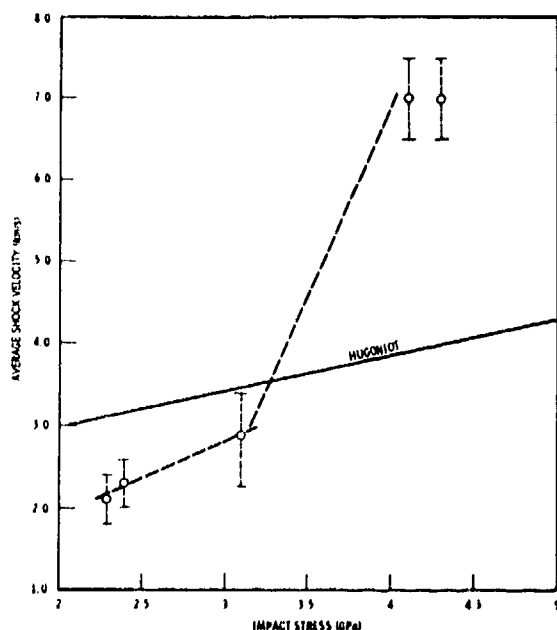

Fig. 13. Variation of stress amplitude with propagation distance for high-density HNS.

745

Fig. 14. Variation of average shock velocity with impact stress (low density).

Fig. 15. Variation of average shock velocity with impact stress for HNS II at 127°C.

At room temperature, similar results were obtained for high density ($\rho = 1.58$ Mg/m^3) HNS. For the impact stresses of 3.2 GPa and below, the measured average shock velocities are less than the corresponding Hugoniot velocities. Above 3.6 GPa, the velocities are greater than the velocities derived from the Hugoniot; however, they are less than the stable detonation velocity and suggest at least partial reaction in the HNS.

The results of the elevated temperature experiments are illustrated in Fig. 15. For the low-density compaction, both the average shock velocity measurements and the manganin gage records indicate that the threshold lies between 3.3 and 3.5 GPa. For the high-density compaction, the threshold lies between 3.6 and 3.8 GPa. The initial stresses in the HNS have been calculated using the room-temperature Hugoniot and consequently are an upper bound. However, the small temperature increment and the off-setting variations in initial density and shock velocity are considered to result in an error of less than 5%.

Gruneisen Parameter

The effective Gruneisen parameter for HNS II was measured for two compaction densities. In general, the magnitude of the displacement of the HNS/fused silica interface was of comparable magnitude but opposite direction to that resulting from the response of fused silica alone. The effective Gruneisen parameter of the 1.58 Mg/m^3 compaction was estimated to be 0.06 while the 1.47 Mg/m^3 compaction was 0.01. The absolute error on these Gruneisen coefficients is estimated to be less than 0.05. These low values and the low shock velocities measured at low stresses consistent with a porous material and consequently the effective Gruneisen parameter can be expected to exhibit a strong energy dependence.

REFERENCES

1. F. W. Davies, A. B. Zimmerschied, F. G. Borgardt and Louis Avrami, "The Hugoniot and Shock Initiation Threshold of Lead Azide," J. Chem. Phys., Vol. 64, No. 6, pp. 2295-2302, 15 March 1976.

2. R. M. Schmidt, F. W. Davies, J. E. Shrader, and K. A. Holsapple, "Spall Behavior of Structural Metals at Elevated Temperature," Boeing Technical Memo 2-5320-0030-233, July 1975.

3. L. M. Barker and R. E. Hollenbach, "Laser Interferometer for Measuring High Velocities of Any Reflecting Surface," J. Appl. Phys., Vol. 43, No. 11, pp. 4669-4675, November 1972.

4. T. J. Bosworth, F. W. Davies, B. M. Lempriere and J. E. Shrader, "Hugoniot Equation of State and Spall Threshold of Tungsten at 5000°F," Boeing Technical Rpt. D2-19729, August 1972.

ACKNOWLEDGMENTS

DISCUSSION

JULIUS ROTH
Portola Valley, California

The Hugoniot data presented in this paper agree rather well with the data I presented at the 5th Deton. Symposium if the data are compared in the P-u plane. Agreement in the U-u plane is less satisfactory, and my results are in better accord with those of Sheffield, Mitchell, and Hayes. Rather more disturbing is that Davis et al. found no indication of any reaction in 1.47 g/cm^3 HNS at or below 17 kbar. Interpolation of our data leads to 50% threshold of 18 kbar for our gap test geometry and I would certainly expect reaction at a considerably lower pressure in plane-wave "long-duration pulse" geometry.

REPLY BY F. DAVIES

The primary measurement reported in this paper and that of Hayes et. al. is stress at the impact face. The primary measurement in Roth's study was shock velocity. The Hugoniot data derived from our impact face measurements compares well with that derived from our transit time measurements at low stresses but deviates when the shock velocity is enhanced by reaction in the explosive. Even though each study used different HNS I would expect agreement at least at low stress.

It is not at all clear that there is any real contradictions in the threshold data for 1.47 Mg/m^3 HNS II when the experiments are compared in detail. We

state in the text that "at 1.7 GPa, the initial amplitude of the transmitted stress profile remains constant over the propagation distances examined (<3 mm) and that the stress profiles show little if any evidence of reaction in the explosive." The ramping of the wave was less than 10 percent. Roth's data was derived from run distances of 12.7 mm. His quoted threshold is derived from a linear interpolation between data at 1.38 Mg/m^3 and 1.57 Mg/m^3. The pulse lengths are not likely to be different by more than a factor of 3 thus both sets of data are in the microsecond regime and little variation in the threshold should be expected. Finally differences between the HNS II examined in this paper and Roth's material (average particle size 15 μ) are more likely to effect the initiation thresholds than the Hugoniot measurements.

THE EQUATION OF STATE AND CHEMICAL KINETICS FOR HEXANITROSTILBENE (HNS) EXPLOSIVE*

S. A. Sheffield, D. E. Mitchell, and D. B. Hayes
Sandia Laboratories
Albuquerque, New Mexico 87115

Plane impact experiments at stresses between 0.3 and 3.5 GPa have been used to determine shock Hugoniots for unreacted hexanitrostilbene (HNS) explosive at five different initial densities ranging from 1.0 to 1.7 Mg/m³. The shock Hugoniot data are used in conjunction with known quasi-static thermodynamic properties to deduce a semiempirical, analytical form for the Helmholtz free energy of the unreacted explosive material. In a limited number of these impact experiments, pressure transients observed at the impact interface have been associated with the onset of chemical decomposition. These transient pressure data have been used to infer the chemical decomposition rate of the shocked material. Initial chemical decomposition rates are observed to vary from 1.3×10^{-2} to $1.1 \times 10^{-1} \mu s^{-1}$ for shock stresses between 0.64 and 1.64 GPa.

INTRODUCTION

Considerable work has been done to determine and calculate equations of state for unreacted porous high explosive materials. By way of example, Erkman and Edwards (1) have developed a method which uses an equation of state of the Mie-Grüneisen form written to include the effect of porosity coupled with an energy jump condition. With this method, Erkman and Edwards successfully calculated P-V-E shock Hugoniots for unreacted porous high explosives. Roth (2) has reported experiments on the shock Hugoniot for porous hexanitrostilbene (HNS) explosive. Those data were obtained from wedge and explosive lens tests. Each of these studies gives a thermodynamically incomplete description of shocked states in the high explosive because they lead to a P-V-E equation of state; neither Erkman's model nor Roth's experiments gives information on shock temperature.

We have performed shock experiments on HNS and have used our results to formulate an equation of state which is thermodynamically complete. Therefore, it is sufficient to calculate shock temperature. The temperature distribution produced by shock compaction of an initially porous high explosive is heterogeneous. Hence, calculations of shock temperature based on thermodynamic equilibrium are not meaningful for accurately describing the shocked solid. However, such an equilibrium equation of state would be useful for describing either hot or cold local regions of the shocked solid which are in thermodynamic equilibrium.

In addition to the equation of state of the unreacted material, a description adequate to study shock initiation requires knowledge of the kinetic laws which govern the chemical decomposition. Kennedy (3) has performed experiments on the explosive PBX-9404 where growth of the pressure at the loading interface is attributed to chemical decomposition. We have used a technique involving those pressure transients to obtain quantitative estimates of the chemical decomposition rate.

Specifically, in this study, plane shock wave experiments have been used to determine the shock Hugoniot of unreacted HNS at a variety of initial densities. These data are used to develop a semi-empirical, thermodynamically complete equation of state. The experiments also provide some information on chemical decomposition rates.

EXPERIMENTAL SHOCK HUGONIOT OF UNREACTED HNS

The plane-wave shock experiments with HNS explosive were conducted on the Sandia light gas gun (4). This gun is operated with either helium or air as a driver gas and can accelerate a 0.25-kg projectile to a terminal velocity as high as 1.5 km/s. Projectile velocity is determined by three charged pins, located at a known spacing near the muzzle of the 24-metre-long barrel. These pins are shorted by the projectile as it exits the barrel and the time of shorting is recorded on time interval counters. Impact velocity is determined by this method to within 0.5 percent. Tilt, the angle of inclination between the colliding surfaces, was not measured during the experiments. However, prealignment of the specimen mounting ring normal to the gun bore was better than 0.5 mrad. However, due to the difficulty in preparing specimens which are extremely porous in nature, tilt was probably as large as 2.2 mrads in some of the experiments on HNS at the lowest density; a result deduced from the risetime of certain quartz-gauge records.

All experiments conducted in this work were constructed in the target quartz-gauge/ projectile quartz-gauge configuration which is also referred to as the front-back method (5). In this technique, an X-cut quartz gauge is mounted to the projectile and records impact stress. A second gauge is affixed to the target and records the transmitted stress wave amplitude. Figure 1 shows the experimental configuration. The impact of the projectile gauge onto the HNS specimen produces a constant stress directly related to the shock properties of the explosive. Under the constant stress loading, output current from the quartz gauge is simply related to input stress up to 3 GPa.

Redundant information is obtained when using the front-back method since three independent shock quantities are measured and only two independent quantities are required to determine a datum

on the shock Hugoniot. These three measured quantities are: 1) impact stress from the quartz gauge, 2) impact particle-velocity from the known projectile velocity and shock stress in the quartz, and 3) shock velocity determined from known specimen thickness and transit time measurements. Agreement among Hugoniot points calculated from the redundant data was better than 6 percent, an estimate of the overall accuracy of the experiments. In addition to the above redundancy, the amplitude of the reshocked state produced at the target gauge by the impedance mismatch between HNS and quartz was measured and is in excellent agreement with calculated values.

Impact data shown in Table 1 were determined using standard data reduction methods for quartz gauges (5). For impacts which produced stresses greater than 2.8 GPa (shots 27, 28, 32), relaxation resulting from electrical conductivity in the gauge produces data which are considered unreliable.
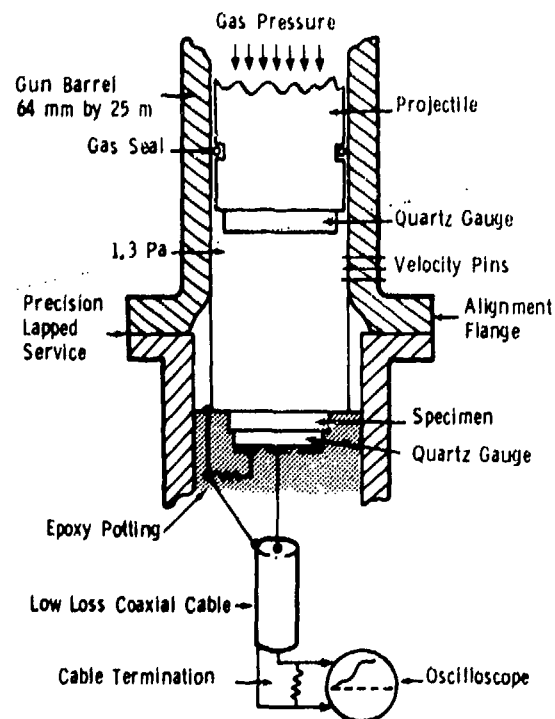

Fig. 1. Experimental configuration, slightly modified from Ref. 5.

749

TABLE 1

Impact Data

Shot No.	Density Mg/m³	Stress GPa		Shock Velocity km/s		Particle Velocity km/s		V(m³/Mg)	Comment
		From Impact Gauge	From Transit Time (1)	From Impact Stress (2)	From Transit Time	From Impact Gauge (3)	From Transit Time		
10	1.01	0.225	–	0.737	–	0.302	–	0.5843	Target data lost
11	1.01	0.644	–	1.244	–	0.517	–	0.5844	Target data lost
12	1.01	1.407	–	1.871	–	0.744	–	0.5863	Target data lost
13	1.01	1.640	3.160	1.892	4.128	0.858	0.758	0.5411	Detonated specimen
20	1.58	0.980	0.980	2.084	2.089	0.297	0.297	0.5427	
21	1.58	1.760	1.770	2.512	2.530	0.443	0.443	0.5213	
23	1.58	0.465	0.495	1.747	< 1.882	0.168	0.166	0.5770	Transit time est.
26	1.58	3.070	4.270	2.969	4.706	0.654	0.575	0.5071	Detonation
28	1.58	> 3.392	5.157	> 2.949	5.334	< 0.727	0.851	< 0.4769	Gauge relax; detonation
18	1.49	1.800	1.97	2.340	2.610	0.518	0.507	–	Detonation
25	1.710	0.617	0.621	2.947	< 2.998	0.122	0.121	0.5606	Lost primary data
17	1.710	1.270	1.31	2.864	2.981	0.259	0.256	0.5319	
19	1.710	1.990	–	3.154	–	0.369	–	0.5162	
15	1.710	2.100	2.03	3.346	3.180	0.367	0.372	0.5206	
16	1.710	2.790	2.74	3.425	3.345	0.476	0.479	0.5034	
27	1.710	> 3.395	4.02	> 2.886	3.639	< 0.687	0.646	< 0.4454	Gauge relaxation
8	1.19*	0.800	1.00	1.470	1.910	0.456	0.443	0.5796	Poor tilt
9	1.20*	0.330	0.33	0.937	0.941	0.291	0.290	0.5755	
29	1.20*	1.250	3.12	1.205	3.516	0.863	0.746	0.3406	Detonation
6	1.18*	1.430	–	1.658	–	0.731	–	0.4738	Target data lost

* HNSII all others were HNSI

(1) $P = \rho_0 U_s V_p (1 + \rho_0 U_s / Z_q)$

(2) $U_s = P V_0 / (1 - P/Z_q)$

(3) $u_p = V_p - P/Z_q$

In those cases where impact gauge data are judged unreliable, measurement of impact velocity and transit time through the specimen are sufficient to infer a datum on the Hugoniot.

Target gauge stress data shown in Table 2 are sparse since detonation occurred within many specimens at the impact stresses and densities chosen, negating information on the properties of the unreacted material. Detonation pressures which are in excess of 10 GPa cause severe quartz-gauge breakdown. Target gauge data from specimens which did not detonate were used to infer additional information on the Hugoniot for the unreacted HNS.

ANALYTICAL EQUATION OF STATE OF UNREACTED HNS

An important result of this work is the development of semiempirical analytical free energy function which describes unreacted HNS explosive. By using a free energy function (6-8), thermodynamic completeness and consistency are guaranteed. The approach is to choose a specific analytical form for the Helmholtz free energy which contains parameters which are unknown. Specific forms for thermodynamic observables are obtained by second order differentiation, and the parameters are adjusted until good agreement is obtained between thermodynamic

TABLE 2

Available Target Gauge Data

Shot No.	Density Mg/m^3	Pressure GPa		V_2 m^3/Mg	Comment
		Measurement	Hugoniot Equation		
20	1.58	1.95	1.79	0.5200	
21	1.58	3.37	3.19	0.4909	
23	1.58	0.84	0.53	0.5353	Backup trace used
25	1.71	0.89	0.79	0.5467	
17	1.71	1.95	2.25	0.5678	
19	1.71	3.17	3.11	0.4890	
15	1.71	3.13	3.21	0.4880	
16	1.71	>4.07	4.99	0.4594	Target gauge relaxation
27	1.71	>6.39	9.85	0.4079	Target gauge relaxation

observables as calculated and as measured. Thermodynamic observables are meant to include quasi-static measurements of specific heat and coefficient of expansion as well as the slope of the Hugoniot curves from the present shock work.

The specific form chosen for the Helmholtz free energy is:

$$F(T, V) = C_v \left[(T - T_0)\left(1 + \frac{\gamma}{V}(V_0 - V)\right) \right.$$

$$+ T \log (T_0/T) \right] + \frac{K_{T_0} V_0}{N(N-1)}$$

$$\left[\left(\frac{V_0}{V}\right)^{N-1} - (N-1)\left(1 - \frac{V}{V_0}\right) - 1 \right], \quad (1)$$

where it is assumed that pressure, entropy, and energy are zero in the reference state. Differentiation of Eq. (1) leads to the following simple forms for the thermodynamic observables:

$$K_T = K_{T_0}\left(\frac{V_0}{V}\right)^N$$

$$C_v = Const.$$

$$\frac{\gamma}{V} = Const. \quad (2)$$

Hence, we have a five-parameter equation of state, completely defining the thermodynamic properties of HNS whenever the parameters V_0, C_v, K_{T_0}, N, and γ/V are specified.

Quasi-static information exists on specific heat and on thermal expansion for unreacted HNS (9). However, no information on the isothermal compressibility is available, hence we must use our shock data. When almost full density HNS is shocked, the P-V states produced lie close to the isentrope. We used such P-V states as an approximation to the isentrope in order to evaluate the initial isentropic bulk modulus, K_{S_0}. Further, the shock data were sufficient to allow estimation of the pressure derivative of the isentropic bulk modulus. Given the crystal density, the specific heat at constant pressure, thermal coefficient of expansion, the isentropic bulk modulus, and pressure derivative of the isentropic bulk modulus all at reference conditions, the five parameters in the equation of state are uniquely determined. The numerical values used in this method are given in Table 3.

Since we have constructed a thermodynamic potential function, thermodynamic completeness is

751

TABLE 3

Parameters for HNS

$$V_0 = 0.575 \text{ cm}^3/\text{g}$$

$$C_v = 1.5 \times 10^{-5} \text{ cm}^2/\mu\text{s}^2/K$$

$$K_{T_0} = 0.146 \text{ Mbar}$$

$$N = 3.465$$

$$\frac{\gamma}{V} = 2.41 \text{ g/cm}^3$$

assured. Thus, we have sufficient information to integrate the well known equations for the Hugoniot,

$$\left.\frac{dP}{dV}\right|_H = \left[\left(\frac{\partial P}{\partial V}\right)_S + \frac{\gamma P}{2V}\right]\bigg/\left[1 - \frac{\gamma}{2V}(\alpha V_0 - V)\right]$$

(3)

$$-\left.\frac{dT}{dV}\right|_H = \left[\frac{\gamma}{V}T + \frac{1}{2C_v}\left(\frac{K_T}{V}(\alpha V_0 - V) + P\right)\right]\bigg/$$

$$\left[1 - \frac{\gamma}{2V}(\alpha V_0 - V)\right]$$

(4)

where αV_0 is the initial specific volume of the specimen. Further discussion of some of the aspects of this work is given in Ref. 11. Figs. 2 and 3 show a comparision between measurements and Hugoniots calculated in this way. Figure 4 shows the temperature-pressure Hugoniot obtained from Eq. (4).

CHEMICAL KINETICS

Experiments performed to obtain the equation of state of the unreacted HNS also yielded some sparse information on chemical kinetics; the pressure at the impact interface was observed to grow. The only experiments which displayed such pressure growth were for initial HNS density of about 1.00 Mg/m^3. Figure 5 shows an example of pressure growth at the impact surface as recorded by the quartz gauge in shot 13. For experiments with initial HNS densities of 1.58 and 1.71 Mg/m^3, impact stesses were such that critical pressures to induce prompt reaction were not delivered. Although shots 26 and
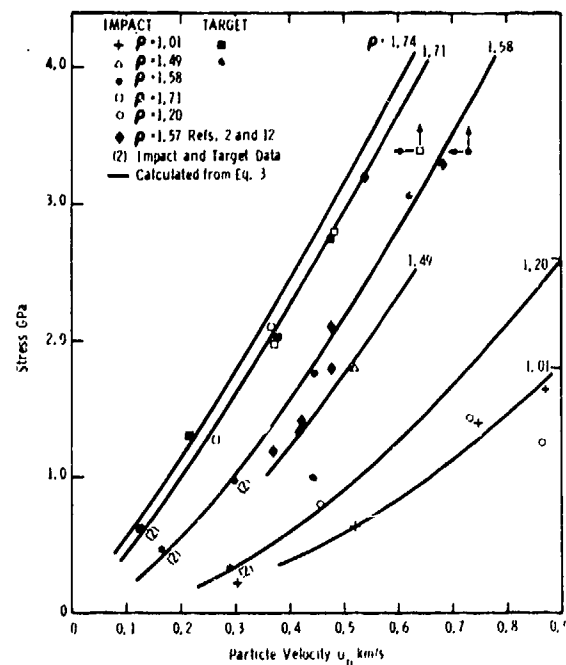
Fig. 2. Stress particle velocity Hugoniot data for various densities.
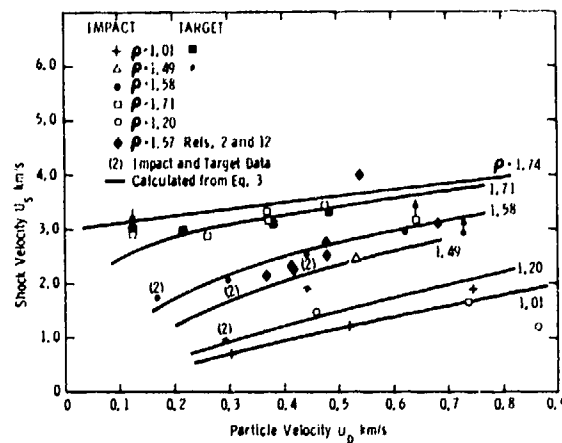
Fig. 3. Shock velocity-particle velocity Hugoniot data for various densities.
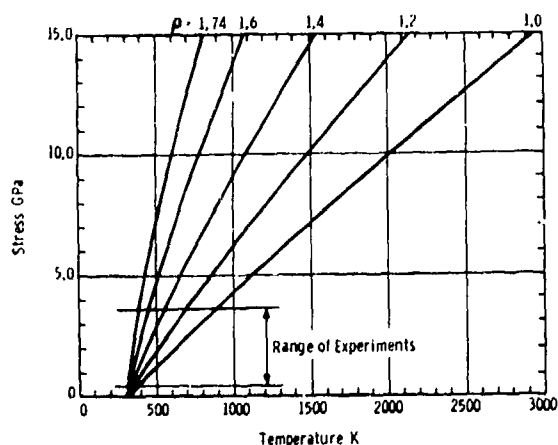
Fig. 4. *Calculated stress-temperature Hugoniots for HNS at various initial densities.*

TABLE 4

Chemical Reaction Rate in Shocked HNS Explosive Initially at 1.0 Mg/m³ Deduced from Pressure Growth Rate at the Impact Interface

Shot No.	Density Mg/m³	Impact Stress GPa	$(\partial P/\partial t)_h$ GPa/μs	$\dot{x}\,\mu s^{-1}$
11	1.01	0.64	0.237	0.0128
12	1.01	1.41	0.770	0.0505
13	1.01	1.64	1.656	0.1134
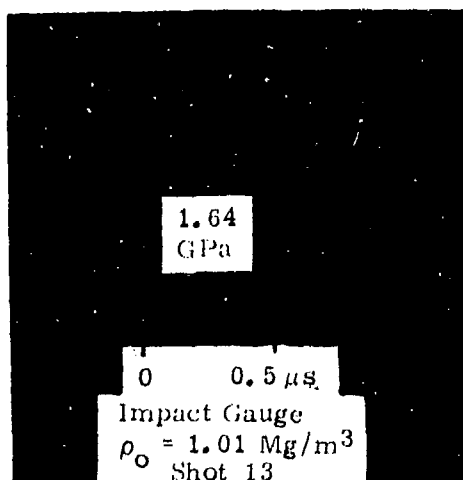
Fig. 5. *Pressure growth at impact interface*
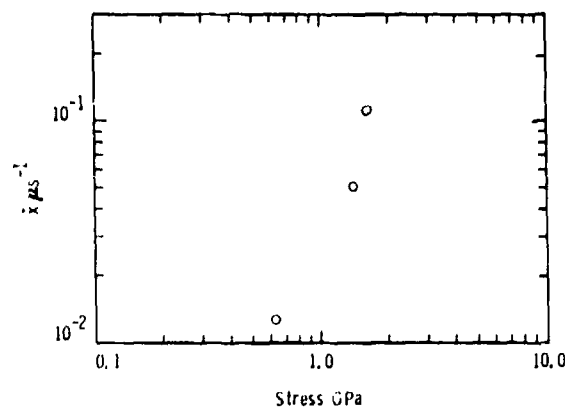
Fig. 6. *Calculated decomposition rate vs. stress for HNS at $\rho_0 = 1.01$ Mg/m³.*

28 at densities of 1.58 Mg/m³ resulted in detonation, as determined from unusually high measured shock velocities, the transient behavior preceding growth to detonation was not evident from the impact gauge records. We attribute this to gauge conductivity at stresses large enough to produce appreciable reaction at these higher densities.

Table 4 shows calculated chemical reaction rate deduced from these three experiments. A complete description of the theory used to calculate decomposition rate from pressure growth rate is given in Ref. 10. Figure 6 shows the calculated decomposi-

SUMMARY

Plane shock wave experiments have been used to determine the Hugoniots for unreacted hexanitrostilbene (HNS) explosive at pressures from 0.3 GPa to 3.5 GPa for densities from 1.00 to 1.71 Mg/m³. A semiempirical thermodynamically complete equation of state was developed using the shock data. That analytical form can be used to calculate shock Hugoniots for unreacted HNS at any density. Furthermore, shock temperature can be calculated.

In certain experiments, the loading pressure produced by the impact of the flyer plate was observed

to grow spontaneously. This growth is attributed to chemical decomposition. The equation of state for the unreacted material and the transient pressure data were combined with theory to give quantitative estimates of the chemical decomposition rates.

REFERENCES

1. J. O. Erkman and O. J. Edwards, "Computed and Experimental Hugoniots for Unreacted Porous High Explosives," NOL Technical Report 74-213, Naval Ordnance Laboratory, White Oak, Maryland, Dec 1975

2. J. Roth, "Shock Sensitivity and Shock Hugoniots of High Density Granular Explosives," Fifth Symposium (International) on Detonation, Pasadena, California, 18-21 Aug 1970

3. J. E. Kennedy, "Pressure Field in a Shock-Compressed High Explosive," Fourteenth Symposium (International) on Combustion, University Park, Pennsylvania, 20-25 Aug 1973

4. S. Thunborg, G. E. Ingram, and R. A. Graham, "Compressed Gas Gun for Controlled Impacts Over a Wide Velocity Range," *Rev. Sci. Inst.* **25**, 1, 1964

5. G. E. Ingram and R. A. Graham, "Quartz Gauge Technique for Impact Experiments," Fifth Symposium (International) on Detonation, Pasadena, California, 18-21 Aug 1970

6. D. B. Hayes, "Polymorphic Phase Transformation Rates in Shock-Loaded Potassium Chloride," *J. Appl. Phys.* **45** 1208, 1974

7. J. N. Johnson, D. B. Hayes, and J. R. Asay, "Equations of State and Shock-Induced Transformations in Solid I - Solid II - Liquid Bismuth," *J. Phys. Chem. Solids,* **35** (501) 1974

8. J. R. Asay and D. B. Hayes, "Shock-Compression and Release Behavior Near Melt States in Aluminum," *J. Appl. Phys.* **46** 4739, 1975

9. B. M. Dobratz (ed.) "Properties of Chemical Explosives and Explosive Simulants," UCRL-51319, Lawrence Livermore Laboratory, Livermore, California, 1974

10. D. B. Hayes, "A $P^n t$ Detonation Criterion From Thermal Explosion Theory," Sixth Symposium (International) on Detonation, Pasadena, California, 1976

11. D. E. Mitchell, S. A. Sheffield, and D. B. Hayes, "The Equation of State of Unreacted HNS Explosive," SAND76-0109, Sandia Laboratories, Albuquerque, New Mexico, May 1976

12. J. Roth and J. H. Blackburn, "The Effect of Initial Temperature on the Shock Sensitivity of Granular Explosives," Stanford Research Institute, First Annual Report, Contract 58-1348, 28 Aug 1967

INITIATION AND DETONATION CHARACTERISTICS OF TATB*

R. K. Jackson,† L. G. Green, R. H. Barlett, W. W. Hofer,
P. E. Kramer,‡ R. S. Lee, E. J. Nidick, Jr., L. L. Shaw, and R. C. Weingart
Lawrence Livermore Laboratory
University of California
Livermore, California 94550

The initiation and detonation characteristics of TATB were investigated using several different experimental techniques. In the crushing impact environment of the Susan Test, TATB formulations were among the least sensitive explosives ever tested. Thin flyer plates accelerated by electrically exploded metal foils or by gas guns were used to study shock sensitivity. In high density TATB the minimum flyer kinetic energy required for initiation decreased with increasing pressure. All compositions investigated were substantially less sensitive to shock than nominal density PBX-9404. Wavefront propagation in TATB compositions of lower-density, lower-binder-percentage and smaller HE particle size was closest to the ideal Huygens propagation. Shock initiation experiments were performed at sample temperatures ranging from -54° to +74°C. At lower temperatures a significant decrease in the divergence of the detonation wave was observed.

INTRODUCTION

TATB (1,3,5-triamino 2,4,6-trinitrobenzene) is a very stable explosive that is remarkably insensitive to severe impact and thermal environments. It is of interest to high explosive safety programs because the probability of ignition or accelerated reactions in an accident situation is low. We have investigated the initiation and detonation characteristics of TATB using several different experimental techniques. These include the Susan Test (1-3) crushing impact experiments; experiments studying initiation and divergence of the detonation wave using thin flyers driven by an electrically exploded metal foil (4); initiation experiments using gas-gun-driven flyers of various thicknesses; and experiments using conventional wedge techniques (5).

The TATB compositions were blended and pressed from different batches of powder having significantly different particle size distributions. Representative particle size distributions for a fine-particle batch and a coarse particle batch are shown in Fig. 1. The majority of experiments used TATB similar to that of B-226 unless otherwise stated. Binder material, when used, was KEL-F-800, polytrifluorochloroethylene.

CRUSHING IMPACT EXPERIMENTS

The Susan Test was used to investigate the response of TATB and TATB/KEL-F formulations of different composition and density to a severe crushing impact environment. In these tests an explosive-loaded projectile was gun fired against an armor plate target at various velocities and the explosive response

noted. Overpressures from thirty-eight experiments were converted to relative energy release and the results plotted against impact velocity in Fig. 2. Individual data points are not shown, since all results fell within the shaded area and differences between individual formulations had no statistical significance. Results with standard explosives are included for reference. TATB and TATB/KEL-F formulations are among the least sensitive explosives ever tested in the Susan Test. The explosive response is hardly discernable from that of a mock explosive. There is no evidence of accelerated burning reactions at the higher impact velocities such as occur with almost all of the commonly used explosives.

FLYER PLATE INITIATION

Over the range of pressures and pulse lengths where the pulse length is important to the initiation process, we distinguish between short-pulse and long-pulse experiments on the basis of the TATB behavior near threshold. For the short-pulse experiments the transit time of the detonation wave through the test specimen is essentially constant, except near failure where the transit time increases drastically over a narrow range of flyer energies. For the short-pulse experiments it was therefore possible to define the critical flyer energy for initiation as a go, no-go condition.

For the longer pulses at lower pressures the transit time varied more gradually near failure so we deter-

mined the critical initiation energy E_c from the empirical equation (6)

$$(X - 1)(Y - E_c) = C,$$

where X is the reduced excess transit time, Y is the flyer-plate kinetic energy and C is a constant.

Short Pulse Initiation

Thin flyer plates (0.25-mm-thick PET polyester film) were used to achieve relatively short pressure pulses (0.04-0.2 μs for the first shock reverberation in the flyer plate) over the range of 1-100 GPa. The flyers were accelerated by electrically exploding a thin (~50 μm) aluminum foil (4). Figure 3 shows the electrical conductor, exploding foil, layer of flyer material, barrel, and lucite-cone HE pellet holder. Aluminum foils varied in size from 3 X 3 mm to 50 X 50 mm and the barrel (and flyer) diameter varied from 3 to 50 mm accordingly. When the foil explodes the flyer layer is sheared by the edge of the inner diameter of the barrel. The flyer is accelerated down the barrel impacting the explosive mounted in the lucite holder.
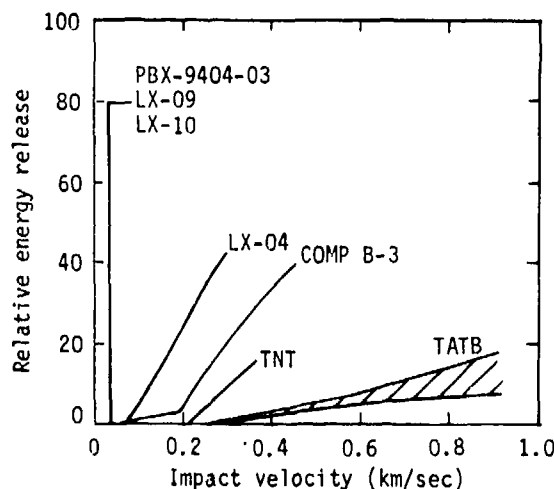

Fig. 2. Summary of Susan test data. All TATB formulations fell within the shaded region. These included neat TATB at densities of 1.70 and 1.84 Mg/m^3; and the following TATB/KEL-F formulations: 95/5 at ρ = 1.81 Mg/m^3, 92.5/7.5 at ρ = 1.80 and 1.90 Mg/m^3 and 90/10 at ρ = 1.92 Mg/m^3. The LX-10 and LX-04 shown for reference are 94.5/5.5 and 85/15 HMX/Viton A respectively.

Fig. 1. Particle-size distributions for two batches of TATB used for many of the experiments reported here.

Flyer velocities could be varied in a controlled manner from 1 km/s to over 10 km/s by changing the charging voltage on the capacitor discharge unit, the foil cross section, or the barrel length (distance of flyer travel before impact). We used a 56-μF capacitor bank capable of being charged to 40 kV. This initiation and diagnostic system is described in (4).

We performed experiments to determine the minimum flyer velocity necessary to initiate various compositions of TATB using several sizes of flyers and various criteria for defining initiation. Some of these data are shown on Table 1. In most of these experiments the flyer travel distance was only 1.7 mm, resulting in very flat flyer impacts—planar to within 20 ns over the center 22 mm of a 25-mm diameter.

We used three criteria for initiation. The first, called "any breakout," considered initiation to be any detonation breakout from the back side of the HE pellet, no matter how narrow or ragged; the second, called "flat breakout," considered initiation to have occurred only when the detonation breakout was simultaneous to within about 50 ns across the pellet. This criterion was used when 25-mm diameter flyers were used on 25-mm diameter explosive pellets. The third criterion, called "diverging detonation," was used when the flyer diameter was significantly less than the diameter of the HE pellet. A "diverging detonation" was one in which the detonation reached the corner (point "B" in Fig. 4) of the 19-mm long pellets. Generally the flyer velocities needed to achieve "flat breakout" were about 0.2 km/s higher than those at which "any breakout" would occur. In the higher density pressings the flyer velocities needed to achieve "diverging detonations" were significantly greater than those required to obtain a nondiverging detonation ("any breakout"). Threshold velocities increased rather sharply with increasing HE density and were somewhat higher when a binder was present.
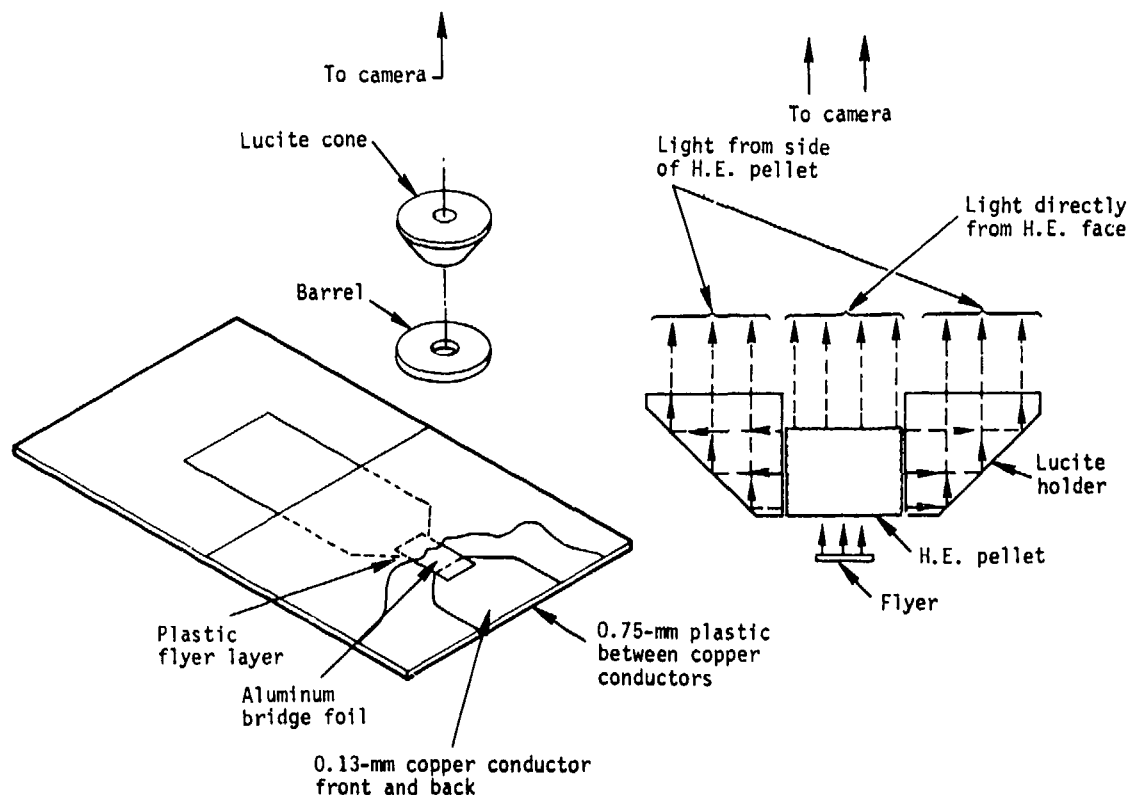

Fig. 3. Experimental system showing the copper conductor and the thin aluminum foil covered with a thin plastic "flyer" layer. The barrel is centered over the foil and the lucite cone HE holder is placed over the barrel. The internal sloping (45°) surface of the HE holder provides a view of the detonation moving up the side of the pellet.

Most of our work used 25-mm-diameter flyers to avoid edge effects and initiation-spot-size effects. We also studied flyer velocity thresholds using 13- and 6-mm-diameter flyers. For some compositions these smaller flyers are very near, or perhaps smaller than, the minimum spot size needed to achieve a sustained detonation. The existence of such a critical initiation spot size is strongly implied by the fact that flyer velocity thresholds do not rise significantly in going from 25- to 13-mm-diameter flyers, but rise dramatically for some compositions in going from 13- to 6-mm-diameter flyers (see Fig. 5). This phenomenon is probably related to the failure diameter of TATB. These data show that to obtain proper detonation performance TATB needs to be initiated over a much larger area than HMX-based explosives.

Using the same experimental method as for TATB, we measured the flyer velocity threshold for PBX-9404 using 25-mm-diameter flyers (4). The results showed that the threshold velocity (~1.9 km/s) of this HE is significantly below that of the most sensitive TATB tested (pure, fine-particle material at a density of 1.70 Mg/m^3). Thus, in terms of thin-flyer initiation, even the lower-density, no-binder compositions of TATB remain very insensitive.

For most of the experiments described thus far we also measured the transit time of the detonation through TATB pellets. The measured transit times of long pellets do not vary significantly (less than for the various compositions and densities tested; there is virtually no difference in transit time at temperature (-54°C) for any composition tested. However, as the flyer velocity is decreased to near threshold conditions (within 0.5 km/s of threshold), the transit time begins to increase (see Fig. 6).

The short pulse experiments are summarized by the data in Table 1. Flyer kinetic energy thresholds,

TABLE 1

"Short" Pulse Initiation Threshold Data from Electrically Accelerated Thin Flyer Experiments

Composition TATB/KEL-F	Blend (See Fig. 1)	Density (Mg/m^3)	Flyer Velocity Threshold—km/s					
			25-mm Flyer Dia.		12.7-mm Flyer Dia.		6.3-mm Flyer Dia.	
			Any Breakout	Flat Breakout	Any Breakout	Diverging Breakout	Any Breakout	Diverging Breakout
90/10	B-226	1.80	3.5-3.8	3.8-4.0				
90/10	B-226	1.70	3.2-3.5	3.5				
92.5/7.5	B-226	1.91	4.2-4.6					
95/5	B-226	1.90	4.2-4.6					
95/5	B-226	1.88	3.8-4.0	>4.0	3.9-4.2	6.7-7.5	9.0-9.2	>10.3
95/5	B-226	1.85	3.5-3.8	3.8-4.0	3.5-3.8	3.9-4.5		
95/5	B-226	1.80	3.2-3.5	3.5-4.0	3.4-3.6	3.5-3.7	6.3-8.2	>10.3
95/5	B-226	1.70	2.8-3.0	3.0-3.2	2.9-3.2	2.9-3.2	9.0-9.4	9.4-10.3
95/5	B-226	1.50	2.8-3.0	3.5-4.0				
100/0	B-226	1.85	3.2-3.5	3.5-4.0			4.2-4.5	5.5-6.3
100/0	B-226	1.80	2.8-3.0	3.0-3.2			4.2-4.8	4.2-4.8
100/0	B-226	1.70	2.4-2.6	2.6-2.8			3.4-3.8	4-5
100/0	B-317	1.85	3.1-3.5	>3.5				
100/0	B-317	1.80	2.7-2.9	2.7-2.9	2.7-3.0	2.7-3.0	3.8-4.2	3.8-4.2
100/0	B-317	1.70	2.4-2.6	2.4-2.6				

neglecting critical diameter effects, vary from 1.0 to 5.1 MJ/m^2. Kinetic energy threshold data for the 92.5/7.5 TATB/KEL-F composition is shown on Fig. 7 together with threshold data using 0.5-mm thick PET flyers and data from gun experiments to be described below.

Long Pulse Initiation

Gun-accelerated flyer plates were used to achieve longer duration (0.2-0.6 μs for the first shock reverberation in the flyer plate) impulses at pressures that ranged from 15 to 20 GPa. Piezo-electric pins are used to determine flyer plate velocity, time of arrival and tilt at the HE front surface, and shock arrival times at the various back surfaces of the HE. The planarity of the flyer plate is maintained by a 200 kg/m^3 carbon foam disk between the front of the projectile and the flyer plate, using a method reported by Wasley et. al. (7). The gun used to propel the flyer plate assembly has a 101-mm-dia. $\times$ 18-m long smooth bore barrel. The velocity capability is 2.0 km/s with a 0.8 kg projectile using 1800 g of cannon powder. Using a 0.8 kg projectile the gun has a 1.7 km/s capability with a double-diaphragm helium breech, while with a Wilson valve breech a 1.0 km/s velocity can be achieved. A reduced pressure of 11 Pa or less is maintained over the test sample before impact to eliminate air-cushion effects.

"Long"-pulse initiation data on 90/10 TATB/ KEL-F at a density of 1.92 Mg/m^3 and 92.5/7.5 TATB/KEL-F at a density of 1.90 Mg/m^3 appears in
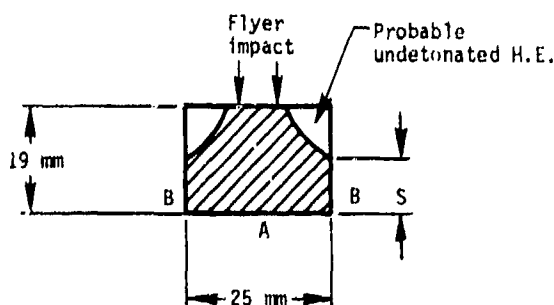
Fig. 4. Side view of a TATB pellet. Two parameters used to quantify the propagation of the detonation front are: the time from detonation breakout at point "A" to breakout at point "B" ("corner delay time"), and the length of the detonation along the side of the pellet ("side burn").

Table 2. For comparison, PBX-9404 at a density of 1.84 Mg/m^3 requires a flyer plate kinetic energy of 0.64 MJ/m^2 which remains relatively constant over the pressure range 4 to 10 GPa (4,6,8). The initiation data on TATB from gun experiments give some indication of a trend toward lower minimum initiation energy with increasing pressure, but when these data are compared with the short pulse, higher pressure data, the trend becomes unmistakable. (See Fig. 7.) The minimum energy required is a factor of three less at the highest pressure measured. This is in contrast to the behavior of PBX-9404 as discussed above, where the line between initiation and failure seems to hold at constant energy over a wide range of pressures.

Sustained Pulse Initiation

Sustained pulse initiation was achieved using gun accelerated flyer plates and conventional wedge shock initiation techniques. The gun experimental system was described above under Long Pulse Initiation. For sustained pulses the flyer plate thickness was typically about 6 mm. The wedge type experiments have been described elsewhere. See, for example (5). In these experiments we investigated the effects of pressure and temperature on various compositions and densities of TATB/KEL-F formulations.
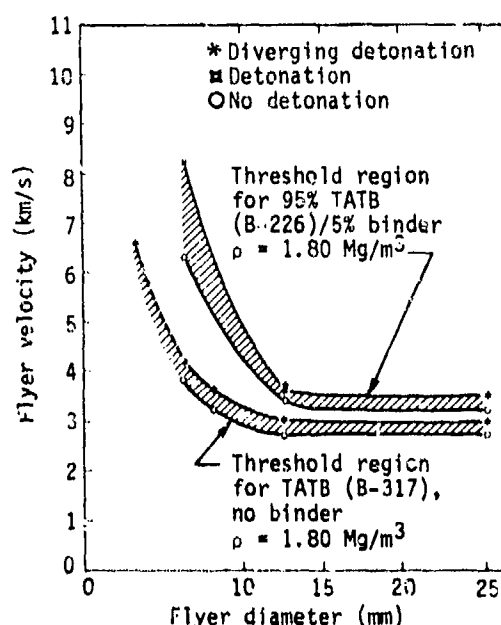

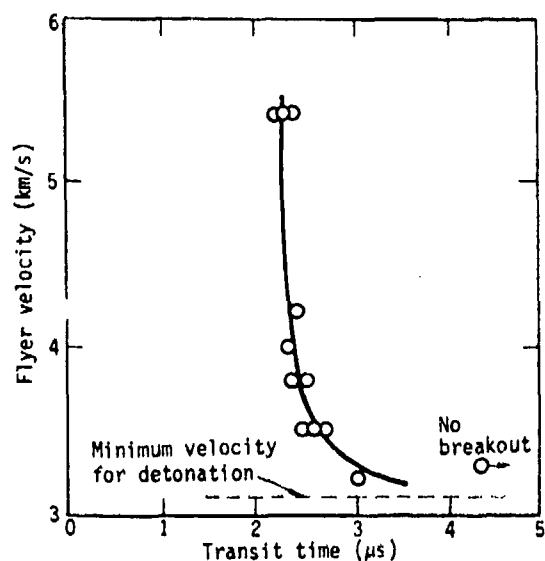*Fig. 5. Flyer velocity threshold regions are shown for two compositions of TATB.*

Fig. 6. Transit time of the detonation through 19-mm long pellets vs flyer velocity for 95% TATB (B-226)/5% KEL-F at a density of 1.80 Mg/m³.
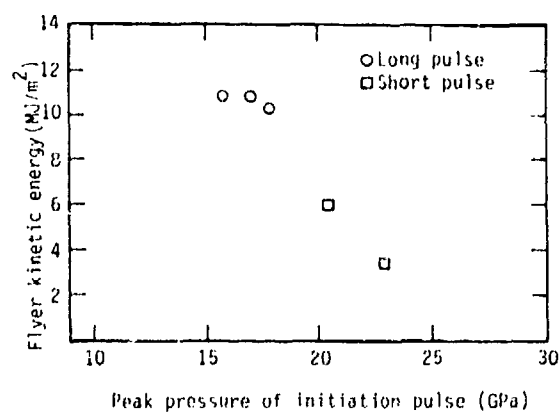

Fig. 7. Threshold flyer kinetic energy is shown for 92.5/7.5 TATB/KEL-F, $\rho = 1.90$ Mg/m³.

TABLE 2

"Long" Pulse Initiation Data from 101-mm Gun Experiments on TATB/KEL-F Formulations

| Composition TATE/KEL-F | Density Mg/m³ | Flyer | | | Pressure into HE GPa | Excess Transit Time (μs) | | Critical Energy MJ/m² |
		Thickness mm	Velocity km/s	Density Mg/m³		Long Pulse	Sustained Pulse (Fig. 8)	
90/10	1.92	0.80 Brass	1.839	8.39	15.3	No det.	0.42	>11.3
90/10	1.92	1.02 Brass	1.873	8.53	15.8	0.52	0.37	13.6
90/10	1.92	0.93 Brass	1.880	8.53	15.9	0.89	0.36	13.6
90/10	1.92	0.66 Brass	1.893	8.53	16.1	No det.	0.35	>10.0
90/10	1.92	0.46 Ta	1.830	16.65	17.6	0.59	0.25	12.3
90/10	1.92	0.44 Ta	1.940	16.65	19.2	0.27	0.18	12.7
92.5/7.5	1.90	0.77 Brass	1.860	8.53	15.6	0.37	0.19	11.0
92.5/7.5	1.90	0.66 Brass	1.977	8.53	17.0	0.37	0.12	10.8
92.5/7.5	1.90	0.66 Brass	2.034	8.53	17.7	0.14	0.10	10.3
92.5/7.5	1.90	0.69 Brass	2.089	8.53	18.5	<0.2	0.08	<12.5

Sustained pulse initiation data on 90/10 TATB/ KEL-F at density 1.92 Mg/m³ and 92.5/7.5 TATB/ KEL-F at densities 1.90 and 1.81 Mg/m³ appear in Table 3. The results of -44°C and +68°C wedge experiments on the 92.5/7.5 formulation (ambient temperature density 1.90 Mg/m³) are also tabulated. The distance to detonation vs initiating pressure is plotted on a log-log scale in Fig. 8. The uncertainty in distance to detonation in the gun experiments is about ±1 mm, while the uncertainty in the wedge experiments is about ±0.2 mm. Pressure measurements for both experimental methods are probably good to a few percent. The nonreactive Hugoniot equation of state used for the 92.5/7.5 formulation at density 1.90 Mg/m³ was

$$U_s = 2.33 + 2.32\, U_p, \text{ all in km/s.}$$

The equation was derived from the gun experiments and wedge experiments described above and from some additional ultrasonic data.

It would appear that density is more important than composition in the detonation buildup of high density TATB/KEL-F formulations. These data are discussed further in the section on temperature effects.

DETONATION WAVE PROPAGATION

One of the most unusual properties of TATB is the behavior of its detonation wave as it travels through the explosive. HMX-based explosives, such as PBX-9404, appear to detonate in all directions from the point of initiation at nearly the same velocity. An example of the propagation of the detonation through a composition of TATB containing 5% KEL-F 800 binder is shown in Fig. 9. The HE adjacent to the area of flyer impact does not detonate at all. It is possible, particularly in higher-density TATB, to detonate a hole directly through fairly long (~40 mm) pellets leaving unreacted HE around the hole (Fig. 9).

The difficulty in obtaining a good, diverging detonation in some compositions of TATB led us to mount the HE pellets inside a Lucite cone (Fig. 3) so that we could view the side as well as the bottom of the pellets. We used two parameters to quantify the divergence of the detonation: corner delay time, the time difference between breakout of the detonation at the center and the corner of the pellet (points A

and B in Fig. 4); and side burn (S), the length of detonation burn observed along either side of the pellet (Fig. 4).

Some of our measurements of these parameters are shown in Figs. 10 thru 13. The effects of density and binder are shown on Figs. 10 and 11. The corner delay time vs density (Fig. 10) is plotted for compositions having 10% KEL-F-800 binder, 5% binder and no binder. The side burn, S, is also shown (Fig. 11) for the same experiments.

Figures 12 and 13 show the effects of particle size and temperature. TATB data from the two particle size distributions shown in Fig. 1 are compared at ambient temperature and at -54°C. The effects of particle size on divergence are significant. For example, the corner delay time for fine-particle TATB initiated by 6.3 mm diameter flyers is 0.56 μs (only 12% longer than the corner delay time at ambient). The coarse particle TATB, however, will not produce a
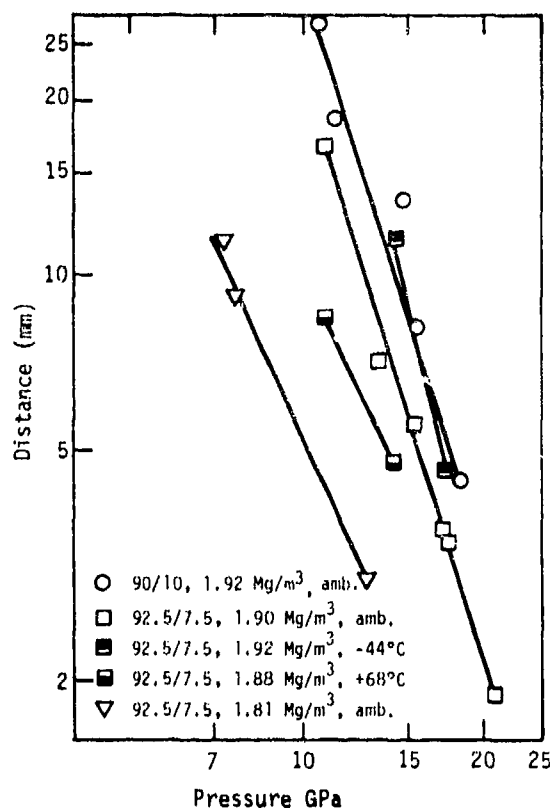
Fig. 8. Sustained pulse initiation data on TATB/ KEL-F formulations at various temperatures.
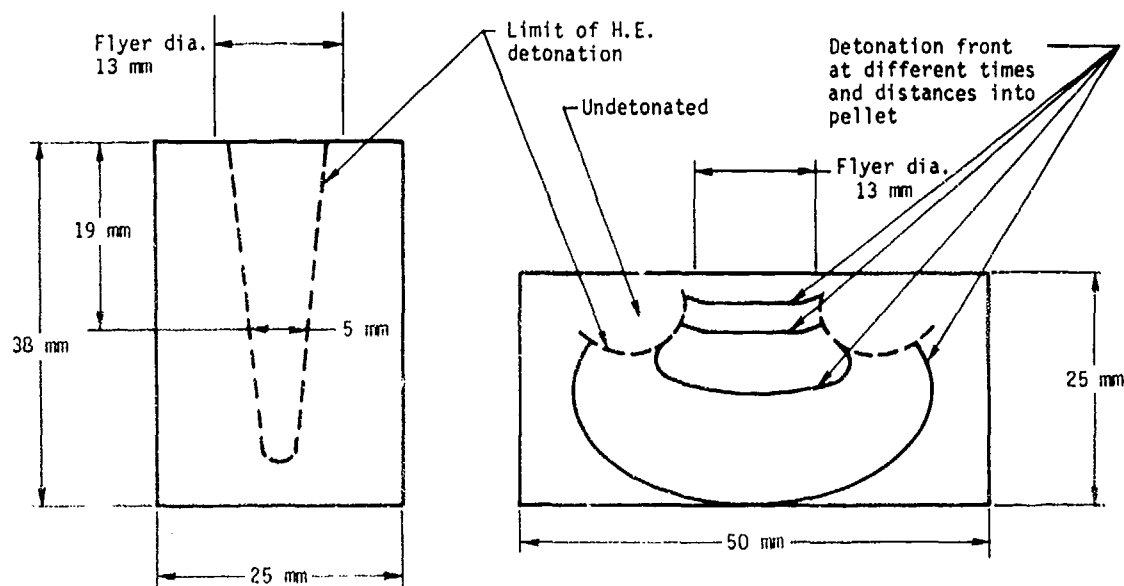
Fig. 9. Propagation of a detonation front in TATB (B-226) containing 5% binder. On the left a flyer having a velocity of 4.2 km/s detonates a hole into pressings of density 1.89 Mg/m^3. No detonation breakout was observed from the 38-mm long pressings. On the right a flyer having a velocity of 5.0 km/s initiates a diverging detonation in pressings of 1.80 Mg/m^3. Both figures represent compilations of a number of experiments using charges of varied sizes and shapes.
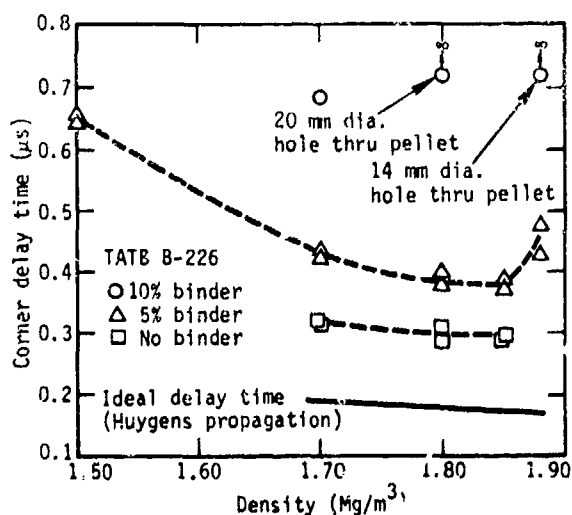

Fig. 10. Corner delay time (see Fig. 4) vs density. The flyer velocity was ~7 km/s.
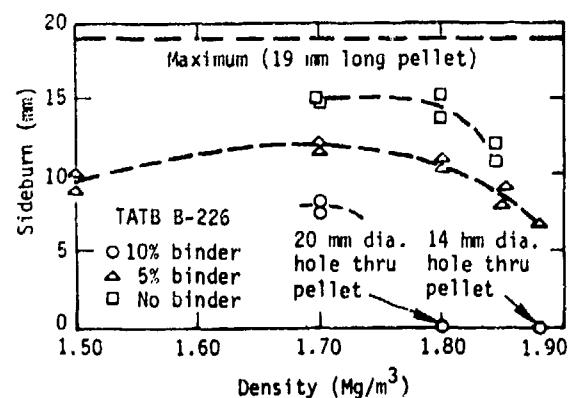
Fig. 11. Side burn (see Fig. 4) vs density for the same experiments shown in Fig. 10.

762

consistently diverging detonation under the same initiation conditions. (Holes were detonated through the pellet as in Fig. 9.)

We have found that the divergence of the detonation wave in TATB is made more ideal, over the ranges indicated, by any of the following changes: decreasing the HE density (1.91-1.70 Mg/m^3); decreasing the amount of binder in the HE (10%-0%); decreasing the particle size of the HE powder (58-18 μm average diameter); increasing the flyer velocity (2.0-10 km/s), increasing the environmental temperature (-54 to +74°C).

The ranges given are those over which our experimental data extend. The divergence seems to improve smoothly over these ranges, and the various parameters can be traded off against one another.

TEMPERATURE EFFECTS

Sustained pulse and short pulse experiments were conducted where the sample temperatures were varied over the range -54°C to +74°C. The sustained-pulse experiments were done on high density (~1.90 Mg/m^3) TATB and the material was observed to have a shorter run to detonation at elevated temperatures and a longer run to detonation at lower temperatures. These data are shown on Fig. 8 and on Table 3. While the change in run to detonation could be attributed to the change in density of the TATB with temperature, this may not be justified based on present understanding of initiation mechanisms. The change in density of the sample is not accompanied by a change in the degree of inhomogeneity since the percent voids will remain about the same. The bulk of the change in distance to detonation at a given initiating pressure is more plausibly explained by a change in the rate of chemical reaction due to the difference in temperatures.

The short pulse experiments were conducted on lower density (~1.80 Mg/m^3) TATB. The propagation of the detonation wave was significantly temperature dependent, as shown in Figs. 12 and 13. For a fixed flyer impact velocity, we observed a pronounced increase in the curvature of the detonation front as the temperature was lowered. The critical initiation energy, however, did not vary with temperature.
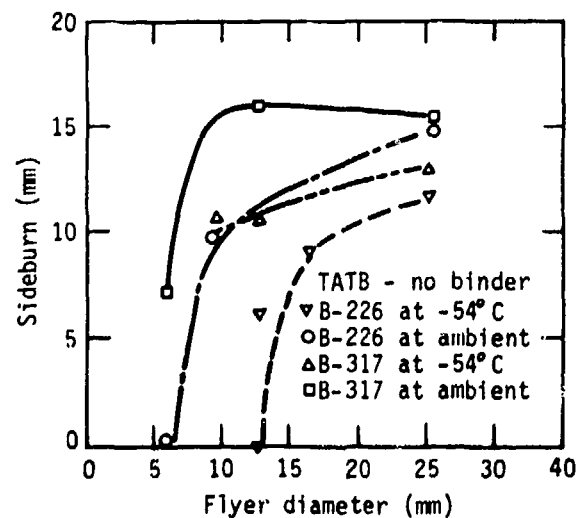

Fig. 12. Corner delay time (see Fig. 4) vs flyer diameter. The flyer velocity was ~6.5 km/s. Blends of TATB having different particle size distributions (see Fig. 1) are compared at both ambient and low (-54°C) temperature.

Fig. 13. Side burn (see Fig. 4) vs flyer diameter for the same experiments shown in Fig. 12.

763

In comparing the short pulse and sustained pulse temperature effects, we note that both the increase in run to detonation and the increase in wave front curvature are consistent with a temperature-dependent reaction rate. We cannot directly compare the critical initiation energy data with the sustained pulse data since the relationship between critical initiation energy and run to detonation has not been established. We also measured transit time of the detonation in the short pulse experiments, but do not have sufficient data to determine whether the transit time near threshold is temperature dependent.

CONCLUSION

Our studies of the detonation properties of TATB have uncovered and characterized many of the un-

expectedly large changes in the divergence of the detonation wave in TATB when various HE parameters are changed. We have also determined the threshold flyer velocities (critical flyer kinetic energy) required to initiate various formulations of TATB and have investigated the transit time of the detonation through pellets of the explosive. While HMX-based explosives (PBX-9404) show a relatively constant minimum initiation energy over a wide range of initiation pressures (4,6,8), the data reported here show that not all explosives follow this pattern.

The characterization of TATB still leaves much room for investigation, particularly in the effects of HE particle size and in the explosive's behavior under differing means of initiation. The relationship between run distance to detonation and critical initiation energy should be investigated. The mechanism(s)

TABLE 3

Sustained Pulse Initiation Data from Wedge and Gun Experiments on TATB/KEL-F Formulations

Composition TATB/KEL-F 800	Density (Mg/m^3)	Experiment		Pressure into HE (GPa)	Excess Transit Time (μs)	Distance to Detonation (mm)
		Temp.	Type			
90/10	1.92	Amb.	Gun	10.6	1.76	27.5
90/10	1.92	Amb.	Gun	11.3	1.12	18.7
90/10	1.92	Amb.	Gun	13.6	0.84	14.7
90/10	1.92	Amb.	Gun	15.6	0.40	8.1
90/10	1.92	Amb.	Gun	16.0	0.32	6.6
90/10	1.92	Amb.	Gun	18.2	0.21	4.5
92.5/7.5	1.90	Amb.	Gun	10.9	0.99	16.7
92.5/7.5	1.90	Amb.	Wedge	13.5	0.32	7.2
92.5/7.5	1.90	Amb.	Gun	15.4	0.24	5.6
92.5/7.5	1.90	Amb.	Wedge	17.3	0.11	3.6
92.5/7.5	1.90	Amb.	Gun	17.5	0.16	3.5
92.5/7.5	1.90	Amb.	Wedge	20.9	0.034	1.9
92.5/7.5	1.81	Amb.	Wedge	7.2	0.97	11.4
92.5/7.5	1.81	Amb.	Wedge	7.6	0.74	9.3
92.5/7.5	1.81	Amb.	Wedge	12.9	0.15	3.0
92.5/7.5	1.92	-44°C	Wedge	14.2	0.50	11.6
92.5/7.5	1.92	-44°C	Wedge	17.6	0.16	4.6
92.5/7.5	1.88	+68°C	Wedge	10.8	0.53	8.5
92.5/7.5	1.88	+68°C	Wedge	14.2	0.28	4.8

governing the propagation of the detonation front for various compositions, initiation pulses, and temperatures should be modeled on a fundamental level. The effects observed in TATB may be indicative of similar effects which may occur on a much smaller scale in other pressed organic explosives. If this is true, TATB-like explosives provide an especially useful tool for studying the general initiation and detonation properties of high explosives.

ACKNOWLEDGMENTS

We would like to acknowledge the support and encouragement of R. L. Wagner and S. Sack; the individual advice and assistance of M. H. Martin; and especially the dedicated efforts of the many LLL technicians who prepared and fired the experiments reported here.

REFERENCES

1. G. D. Dorough, L. G. Green, and D. T. Gray, "The Susan Test for Evaluating the Impact Safety of Explosive Materials," Lawrence Radiation Laboratory Report UCRL-7394 (1965).

2. G. D. Dorough, L. G. Green, "Further Studies on the Ignition of Explosives," in *Proc. Fourth Symposium (Intl.) on Detonation*, October 12-15, 1965, U.S.N.O.L., White Oak, Maryland, ONR Rept. ACR-126 (U.S. Government Printing Office, Washington, D.C., n.d.) pp. 447-486.

3. L. G. Green and A. M. Weston, "Data Analysis of the Reaction Behavior of Explosive Materials Subjected to Susan Test Impacts," Lawrence Radiation Laboratory Report UCRL-13480, July 1970.

4. R. C. Weingart, R. S. Lee, R. K. Jackson, and N. L. Parker, "Acceleration of Thin Flyers by Exploding Metal Foils: Application to Initiation Studies," Lawrence Livermore Laboratory Report UCRL-77610, Rev. 1 (to be published in *Proc. Sixth Symposium on Detonation*, San Diego, CA, 1976.

5. A. W. Campbell, *et al.*, "Shock Initiation of Solid Explosives," Phys. Fluids 4, 511 (1961).

6. L. G. Green, E. J. Nidick, Jr., F. E. Walker, "Critical Shock Initiation Energy of PBX-9404, a New Approach," Lawrence Livermore Laboratory Report UCRL-51522, January 25, 1974.

7. R. J. Wasley, R. H. Valentine, and E. J. Nidick, Jr., "Designing Flyer Plate Gun Experiments to Provide Sharp Compressive Shocks and Soft Recovery Targets," Lawrence Livermore Laboratory Report UCRL-50887, 1970.

8. F. E. Walker and R. J. Wasley, "Critical Energy for Shock Initiation of Heterogeneous Explosives," Explosivstoffe 17, 9 (1969).

COMPUTED AND EXPERIMENTAL HUGONIOTS FOR
UNREACTED POROUS HIGH EXPLOSIVES

John O. Erkman and David J. Edwards
Naval Surface Weapons Center
White Oak Laboratory
Silver Spring, Maryland 20910

A theory of the response of porous, nonreactive materials to shock has been applied to a potential reactive material, porous TNT. The computed Hugoniots which are based on this theory were generated and confirmed by obtaining an experimental Hugoniot for TNT at a density of 0.98 g/cc. The calculated and experimental Hugoniots agree to within 2 kbar over the range 0.35 to 1.72 mm/μsec and 3.6 to 55 kbar in the particle velocity and pressure, respectively. Other experimental data on TNT have been compared with our results. Computer Hugoniots are compared with both experimental and computed results found in the literature for several explosives.

INTRODUCTION

A knowledge of the Hugoniot of unreacted explosives is required to interpret transitional phenomena in explosives and to determine the shock sensitivity of explosives (1). For example, the Naval Surface Weapons Center Large Scale Gap Test (LSGT) (2,3) is used to determine the relative shock sensitivity of explosives. The LSGT is calibrated to give the pressure in the gap material as a function of gap length. But after a determination of the critical gap pressure for initiating detonation, the question still remains: What is the critical pressure transmitted to the test explosive? This question cannot be answered without a knowledge of the Hugoniot of the unreacted explosive.

The usual method employed to obtain the Hugoniot of a material is to perform a series of experiments which measure two of the following variables: shock velocity, particle velocity, pressure, and volume. There are two drawbacks to this approach for porous (granular) explosives. (1) Because porous explosives react very readily, it is difficult to measure any of the above variables for the unreacted state.

(2) Because a new Hugoniot is needed for every density, this approach rapidly becomes expensive. However, computational methods have been developed which yield the Hugoniot of inert, porous materials when the Hugoniot of the nonporous material is known. If these computational methods can be applied to porous explosives, much work and expense can be saved.

In this study, the authors have applied these computational methods to porous TNT for a range of densities from 1.60 to 0.98 g/cc. This method was confirmed by experimentally obtaining the Hugoniot for unreacted TNT at a density of 0.98 g/cc over the range of particle velocities of 0.350-1.720 mm/μsec and of pressures of 3.6-55.0 kbar. The electromagnetic velocity (EMV) gage (4) was used in conjunction with the known Hugoniot data of the attenuator material (PMMA) to obtain the Hugoniot data for unreacted TNT at 0.98 g/cc. The EMV gage follows particle velocity as a function of time. The gage was mounted at the inert/TNT interface and responded to the particle velocity at the interface. In the pressure range (3.6-55.0 kbar) covered in this work, some finite induction period is required before

reaction occurs in the TNT. The EMV gage leads were covered by a thin layer of mica to insulate them from any reacting products.

COMPUTATIONAL MODELS

A computational model which reproduces the response of porous materials to shock has been used by several researchers (5,6,7). It has been usefully applied to a wide variety of materials—metals, graphite, plastics, boron nitride and others—all of which are nonreactive. Successful application of this model to potentially reactive materials, such as porous explosives, has the advantage of expediting the studies of these materials by saving much experimental effort. The model requires a knowledge of the equation of state of the material under study in solid (voidless) form. This is furnished by a curve or relation giving the Hugoniot of the solid and a relation for computing the Gruneisen parameter, $\Gamma(v)$. Because of the lack of data, we have had to assume that the Gruneisen parameter is a constant in our computations.

The relation between the Hugoniots of the solid and porous material is obtained as follows. The Gruneisen equation of state is written as:

$$P_f - P_s = (\Gamma/v)(E_f - E_s) \tag{1}$$

where P, v, and E are the pressure, specific volume, and specific internal energy, respectively, and the subscripts f and s refer to the porous and solid material, respectively. The Rankin-Hugoniot energy equations for both materials are then substituted into Equation (1). Next, the assumption is made that the zero pressure internal energy of the two materials are equal (5,8). This yields

$$P_f = P_s \frac{v_{os} - v - 2v/\Gamma}{v_{of} - v - 2v/\Gamma} \tag{2}$$

where the subscript o refers to the zero pressure state. An expression for P_s is obtained by using the Rankin-Hugoniot momentum and mass flow equations along with a linear shock velocity-particle velocity (U-u) relation and solving for P_s in the momentum equation. This yields

$$P_s = \frac{c_o^2 (v_{os} - v)}{[v_{os} - S(v_{os} - v)]^2} \tag{3}$$

where c_o and S are sound speed and slope of the U-u relation, respectively. (P_o of the momentum equation is negligible compared to F_s and is assumed to be zero.) With the above mentioned approximations, Equations (2,3) will yield the Hugoniot of the porous material.

Dremin, Shvedov, and Avdonin (9) used a more involved method for calculating the Hugoniots of porous materials. The method is described in some detail by Al'tschuler, et al. (10). Zel'dovich and Raizer (11) also describe the method. The method starts with the use of the caloric equation of state

$$P + \frac{dE_c}{dv} = \Gamma(E - E_c)/v \tag{4}$$

where the subscript c refers to the 0°K isotherm. This is the chief difference between this method and the one described above which uses the Hugoniot of the solid as the reference thermodynamic path. Equation (4) is specialized to describe a Hugoniot by replacing E by 0.5 $P(v_o - v)$, the change in energy across a shock. There results

$$v \frac{dE_c}{dv} + E_c = \frac{\Gamma P_H}{2}(v_o - v - 2v/\Gamma). \tag{5}$$

The subscript H means that the pressure is evaluated along the Hugoniot curve. Al'tshuler, et al. show how Equation (5) can be converted into an integral equation which can be solved numerically. The reason for doing this is that E_c is a function of the volume which has, so far, not been specified. In order to solve the equation, the function $P_H(v)$ must be known, usually from experiments. If the variable Γ is also treated as a function of the volume, it also must be specified. Dremin, et al. treated Γ as a constant, as will be done throughout this paper. Once $E_c(v)$ is known, the Hugoniot of the same material in porous form can be obtained from Equation (5). That is,

$$P_H(v_{of},v) = \left(\frac{2v}{\Gamma}\frac{dE_c}{dv} + 2F_c\right)/(v_{of} - v - 2v/\Gamma). \tag{6}$$

As in the derivation of Equation (2), it is assumed here that the surface energy of the porous material can be neglected.

Because $E_c(v)$ is known as a function of v, Equation (6) can also be solved numerically, giving

$P_H(v_{of},v)$ as a function of v for any specified value of v_{of}. This Dremin, Shvedov, and Avdonin (9) have done for RDX (1.0 g/cc), tetryl (0.86 g/cc), PETN (0.82 g/cc), and ammonium nitrate (0.86 g/cc). Their results agree well with their experiment as shown in a later section of this paper. We used the model, Equations (2,3), to compute Hugoniots for the same explosives. These results will be discussed below.

EXPERIMENTAL

The experimental configuration used in this work is shown in Fig. 1. The pentolite booster and polymethyl methacrylate (PMMA) cylinder constitute the pressure-doner and pressure-attenuator parts, respectively, of the NAVSURFWPNCEN Large Scale Gap Test LSGT (2,3). The 50/50 pentolite booster consists of two pellets, 50.8 mm diameter by 25.4 mm long, at a density of 1.56 g/cc. The PMMA cylinder is 50.8 mm diameter and is machined to the desired length, x.

The electromagnetic velocity (EMV) gage (4) consists of a rectangular loop of aluminum foil 0.025 mm thick and 2 mm wide; the effective gage base length used in this work was 1.11 cm. The EMV gage used in this work is in the radial configuration (i.e., the leads come out the side of the charge) because this configuration facilitiates the assembly of the setup. The EMV gage is mounted on the surface of the PMMA cylinder and the TNT is then pressed to the desired density of 0.98 ± 0.03 g/cc. The TNT is a coarse, granular material and has an average particle

Fig. 1. Experimental Arrangement.

size of approximately 400 μ. The experimental assembly is placed in a magnetic field of ~400 gauss generated by a pair of Helmnolt? coils.

The pressure-donor and pressure-attenuator parts of the LSGT were chosen for this work because the LSGT is a calibrated pressure vs distance (P,x) and particle velocity vs distance (u,x) system which can be used with the Helmholtz coils without destroying them. The main drawbacks of this system are: (1) the shock front in the PMMA is curved, and (2) PMMA is a viscoelastic solid. Earlier work with the EMV gage (4) in curved shock fronts showed that the main effect of the curved fronts was to lengthen the rise time of the output signals.

ANALYSIS OF DATA

The EMV gage record yields a particle velocity vs time profile of the shock loaded TNT at the PMMA/TNT interface. The governing equation for this method is

$$u(t) = V(t)/(H\ell'\, 10^{-4}) \qquad (7)$$

where u(t) is the particle velocity as a function of time in mm/μsec, V(t) is the output voltage as a function of time in volts, H is the magnetic field in gauss, and ℓ' is the effective gage base length in mm. For the radial configuration, ℓ' is the distance between the middle of the leads, see Fig. 1.

The u,t data e fitted, for most cases, to a straight line by least squares using the data from the peak recorded value of u to a point 0.5 μsec beyond this value (3). The velocity intercept, u_e, is then assumed to be the particle velocity at the shock front. For the lowest pressure, the u,t curve had a long rise time (500 ns) and did not have a sharp peak. For this record, the peak of the observed curve was used for the shock-induced particle velocity.

The rise time of the u,t profile in the porous TNT is longer than that obtained in a volidless solid by a factor of two or more. This is apparently due to the time-dependent collapse of the pores (12).

Reaction is always a potential problem in the experimental determination of the unreacted Hugoniot of a shock-sensitive material. In this study, the experimental problem created by reaction is that
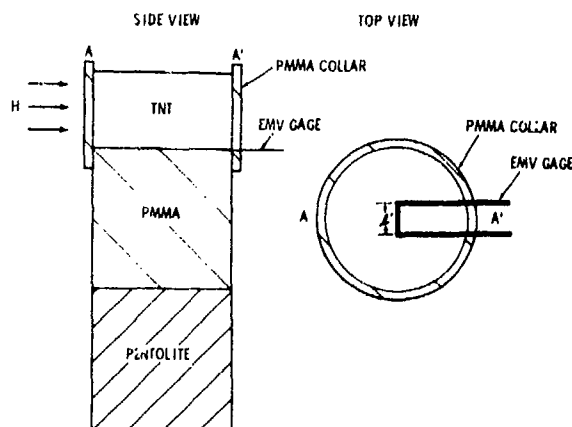
768

explosives become electrically conductive and affect the gage output. The TNT is going to react to some degree during the 0.5 μsec observation time, especially at high pressures. However, even if the TNT starts to react, the initial value of the particle velocity at the interface should lie on the unreacted Hugoniot. The reason for this is the following. The shock emerging from the PMMA is nonreactive. Any reaction which occurs at the interface, where the gage is located, must start at zero reaction and follow some type of rate law. Thus, the initial shock state, and the particle velocity associated with this state, must be on the unreacted Hugoniot. The problem is to obtain this initial value without interference from reaction. To circumvent this problem, it was decided to cover the EMV gage leads with an insulator. A thin (0.0025 cm) layer of mica was used. A shot was fired with two gages at the interface, one with leads covered with mica, the other bare. Figure 2 shows

the resulting u,t profiles. The lower curve is the bare gage result. The t = 0 value of the particle velocity obtained using this curve would not be very reliable. The upper curve is the mica covered gage result and is similar to u,t curves obtained in inerts. Thus, covering the gage leads with an insulator (mica) prevents conductivity from affecting the gage output up to at least 55 kbar which was the highest pressure used in this study.

Several pairs of values of u_e and x were obtained by using attenuators of different length. From these data, and the known Hugoniot of PMMA, the pressure, P_e, at the interface was obtained by impedance matching. From the work of Schuler and Nunziato (13) and Barker and Hollenbach (14), it is inferred that PMMA is a nonlinear, viscoelastic material in the range $7 < P < 40$ kbars. Using the data of (13,14) a correction to P_e was obtained in this range (15). The data were also adjusted to a single density, 0.98 g/cc (15). The resulting data are listed in Table 1.
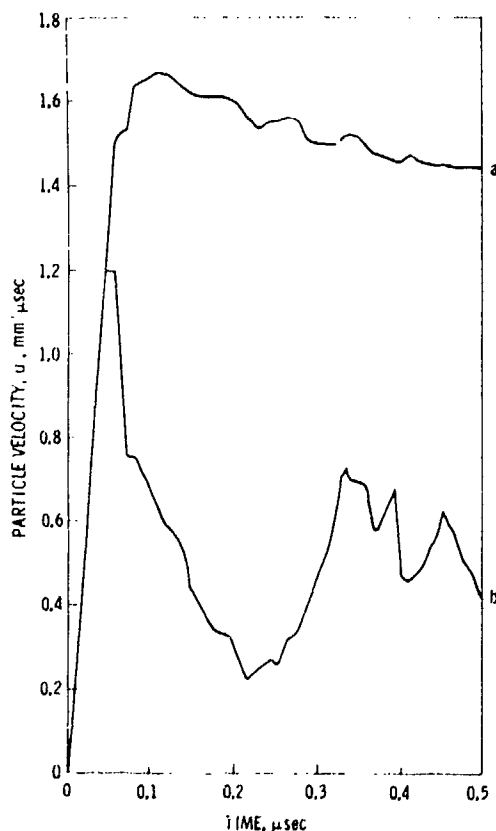
Fig. 2. u,t Profiles from Mica covered (a) and bare (b) EMV gages at PMMA/TNT interface.

TABLE 1

Hugoniot Data for Porous TNT, $\rho_o = 0.98$ g/cc

u_e mm/μsec	P_e Kbar	U mm/μsec	v cc/g	Shot No.
0.350[a]	3.6	1.05	0.680	254
0.435	8.4	1.97	0.795	257
0.440	8.6	1.99	0.795	252
0.680	12.0	1.80	0.635	285A
0.700[b]	11.5	1.68	0.594	251
0.725	10.4	1.46	0.515	253
0.772[m]	13.2	1.74	0.551	336
0.793[m]	12.7	1.63	0.525	333
0.794[m]	12.7	1.63	0.525	332
0.960	17.0	1.80	0.478	293
1.080[m]	23.0	2.17	0.513	335
1.030	26.3	2.60	0.617	290
1.330	40.5	3.11	0.583	316
1.340	40.0	3.06	0.572	291
1.340[m]	40.0	3.05	0.572	327
1.720[m]	55.0	3.26	0.428	330
1.720[m]	55.0	3.26	0.428	331

[a]Peak of u,t curve.
[b]5 mil gage, all others 1 mil.
[m]Mica covered gage leads.

Data on the dynamic compressibility of 1.0 g/cc TNT has been published by two groups of investigators. Vasil'ev, Bolkhovitinov, and Khrisotoforov (16) also employed the EMV gage but the gage was located in the TNT. Their results are plotted in Fig. 3 as open triangles. The results of Table 1 are plotted in Fig. 3 as solid circles for comparison. The errors in pressure of our data were computed using the method described in (15). The error in particle velocity lies within the size of the circles. As is evident from the figure, Vasil'ev's results diverge from ours as the pressure increases. This divergence is due to the fact that their gage is in the TNT and is thus affected by any reaction which has built up. These authors are aware of this because of observed buildup of the detonation velocity. Dremin, Koldunov, and Shvedov (17) have investigaged the buildup of particle velocity and shock veloc'tv in 1.0 g/cc TNT using the EMV gage. Although most of their data were obtained from gages located in the TNT, Dremin, et al report some results where the gage was located at the interface. These interface data, which were obtained from Fig. 2 of (17), are plotted in Fig. 3 as open squares. As is evident from the figure, Dremin's data agree very well with ours.

The shock velocity (U)–particle velocity (u) representation of the Hugoniot for 0.98 g/cc TNT is obtained by using u_e and P_e from Table 1 and the Rankine-Hugoniot momentum equation. The result-

ing shock velocity values are presented in column 3 of Table 1 and plotted as a function of u in Fig. 4.
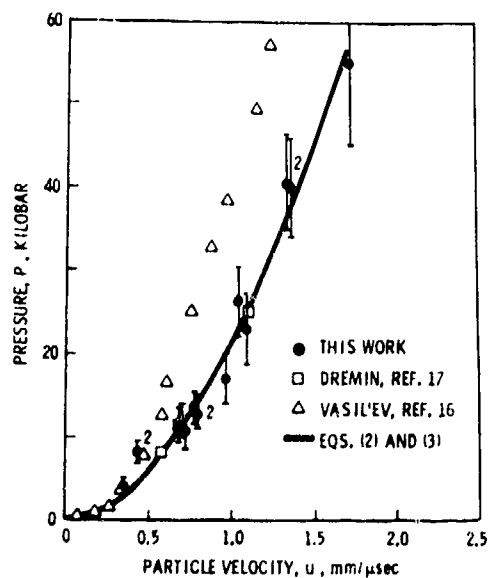
The pressure-volume (P-v) representation of the Hugoniot for 0.98 g/cc TNT is obtained by using the P_e and u_e data of Table 1 and the following equation:

$$v = v_{of} - u_e^2/P_e \qquad (8)$$

where v_{of} is the initial volume of the TNT. The calculated values of the volume are presented in column 4 of Table 1. Figure 5 is the resulting P,v plot. The errors in P and v were obtained using Equations (B7,B8) of (15). The large errors in volume are due to the fact that even small errors in P and u can cause a relatively large error in v.

The experimentally determined Hugoniot for TNT at 0.98 g/cc can now be compared with the results from computational models. The required data for Eqs. (2,3) are: the Hugonoit of the solid material, a value of $\Gamma(v)$ (or Γ_o if $\Gamma(v)$ is not available),
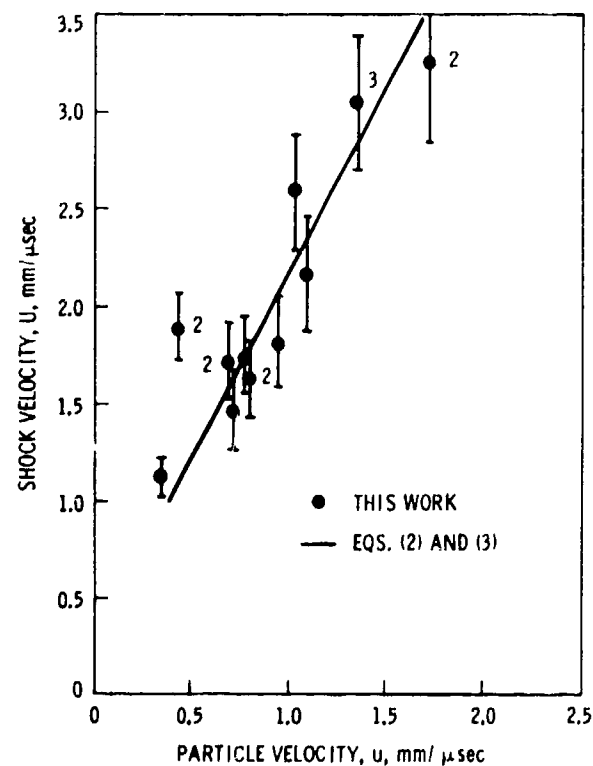

Fig. 3. Comparision of data for porous TNT.

Fig. 4. U,u plot of 0.98 g/cc TNT Hugoniot.

and the specific volume of the solid. The Hugoniot and Γ_o for solid TNT at a density of 1.614 g/cc (18) are

$$U = 2.39 + 2.05 \, u \qquad (9)$$

and

$$\Gamma_o = 0.737 \qquad (10)$$

where U and u are in mm/μsec. The resulting Hugoniot for unreacted TNT at a density of 0.98 g/cc is shown as the solid curve in Fig. 3 (P,u plane). Except for the two pressure points at $\sim$8.5 kbar, the calculated Hugoniot agrees with the experimental data to within the calculated error in pressure and particle velocity. The data at $\sim$8.5 kbar are better explained in the P-v plane and will be discussed below.

The calculated Hugoniot for 0.98 g/cc TNT in the U,u plane is plotted in Fig. 4 as a solid curve. Except for the two data points at u$\sim$0.44 mm/μsec and U$\sim$1.98 mm/μsec, the calculated Hugoniot agrees with the experimental data. As mentioned above, these two data points are more profitably discussed in the P,v plane. The experimental data (omitting the aforementioned data points) were fitted to a straight line by the method of least squares and the resulting equation is

Fig. 5. P,v plot of 0.98 g/cc TNT Hugoniot.

$$U = 0.366 + 1.813 \, u \qquad (11)$$

where U and u are in mm/μsec. The calculated Hugoniot for this density is nearly a straight line. The constants for this straight line were determined by fitting the computed results to a straight line by the method of least squares. The resulting equation is

$$U = 0.307 + 1.848 \, u. \qquad (12)$$

The experimental result is essentially parallel to, but lies 0.059 mm/μsec above the calculated Hugoniot.

In the P,v plane (Fig. 5), the calculated Hugoniot is again plotted as a solid curve. The agreement between the experimental data and the calculated Hugoniot does not seem to be as good as in the P,u and U,u planes. But as was mentioned above, a large error in the value of v can result from small errors in P and u. Taking this fact into account, the agreement is reasonable. The two data points at P$\sim$8.5 kbar and v = 0.795 cc/g of Fig. 5 correspond to the two data points in the P,u and U,u planes which did not agree with the calculated Hugoniot (Figs. 3 and 4). These two data points probably lie on the crushup portion of the Hugoniot. The dashed line in Fig. 5 represents a *possible* crushup path of the Hugoniot. It is an arbitrary straight line originating at v_{of} and ending at the calculated Hugoniot. However, there are too few data available to properly define this portion of the Hugoniot. Another possibility which could explain the position of these two data points is that melting of the TNT may be occurring. This possibility has been investigated but no conclusions about melting could be drawn because buildup to detonation occurred too rapidly and erased any hint of a phase change (15).

Data on five other porous explosives are available in the Russian literature from which the unreacted Hugoniots can be calculated and compared with experimental results. Densities of the porous explosives, the coefficients for the relation $U = c_0 + Su$ for the solid materials, and values of Γ_o for each explosive are given in Table 2.

Data for NB-40 (60% pyroxyline, 40% nitroglycerine) are from Reference (19); the remainder are from (9). Computed and experimental results are shown for NB-40 in Fig. 6 as a plot of shock velocity as a function of particle velocity. The experimental
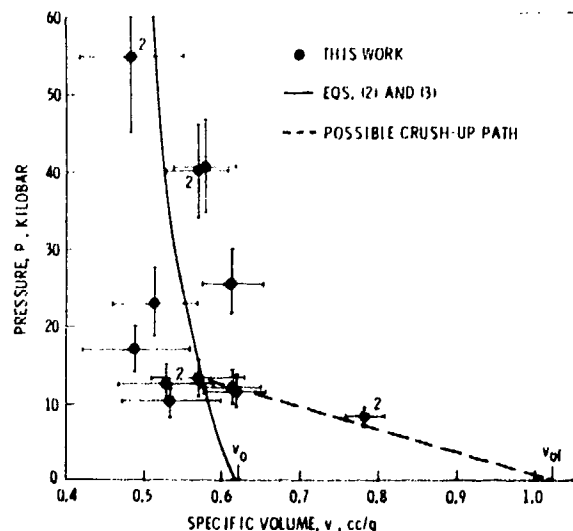
TABLE 2

Parameters for Five Explosives for the Herrmann Model

Explosive	Density g/cc	c_0 mm/μsec	S	Γ_0	Density of Solid g/cc	Ref.
NB-40	1.00	1.70	1.85	1.50	1.63	19
RDX	1.00	2.87	1.61	2.60	1.80	9
Tetryl	0.36	2.17	1.91	1.65	1.73	9
PETN	0.82	2.42	1.91	1.70	1.77	9
AN	0.86	2.20	1.96	0.90	1.73	9
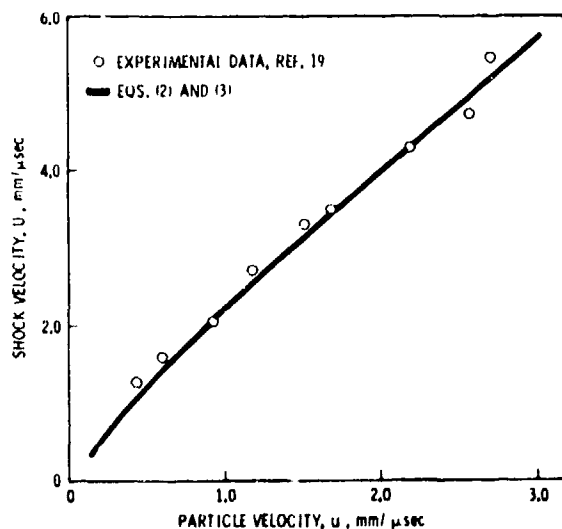
Fig. 6. Comparison of experimental and computed Hugoniots for NB-40 at 1.0 g/cc.

results are closely approximated by the results using Equations (2,3) (solid curve).

For the other four materials listed in Table 2, results are shown in the U,u plots of Figs. 7 through 10. Results shown are (a) the experimental results as reported in (9), (b) results of computations using Equation (6) as given by the same source using the values of Table 2, and (c) results computed with Equations (2,3) also using the values of the parameters given in Table 2. Dremin, et al. (9) reported computed results at 25, 50, 75, 100, and 150 kbar. These data are plotted in Figs. 7 through 10 as points rather than as curves.

For tetryl, PETN, and AN, Dremin, et al. list two values of the shock velocity for each listed particle velocity. They did this because shock velocity was determined by two different methods. Their directly measured values of shock velocity for these three materials have been plotted. Where possible, the value which they obtained by the "reflection technique" (i.e., impedance matching) is also plotted. They explain how the coincidence of the results of these two methods assures them that reaction has not affected their results.

The agreement between experimental data and the two computational methods are summarized in Table 3 for the six explosives for which data exists. (No attempt to adjust any of the parameters in Equations (2,3) was made.)

For AN, the computations in both cases may be in error because of errors in the Hugoniot of the solid AN. This material changes phase under pressure so that the Hugoniot cannot be represented by a single linear relation between shock and particle velocity.

Equations (2,3,9,10) have been used to generate computed unreacted Hugoniots for TNT for densities from 1.60 to 1.00 g/cc, see Figs. 11 and 12. Note that in Fig. 11 the relation for 1.00 g/cc TNT is very nearly linear—this is why Equation (12) can be used. At greater initial densities, the relations tend to become curved for small values of the particle velocity, that is, at low pressures. This is noticeable even for 1.60 g/cc TNT. Because the crushup process has been ignored, a great deal of importance cannot be attached to this curvature. Actually, the TNT U,u curves resemble those published by Herrmann (7) in his Fig. 2 which is for aluminum. In his calculations,
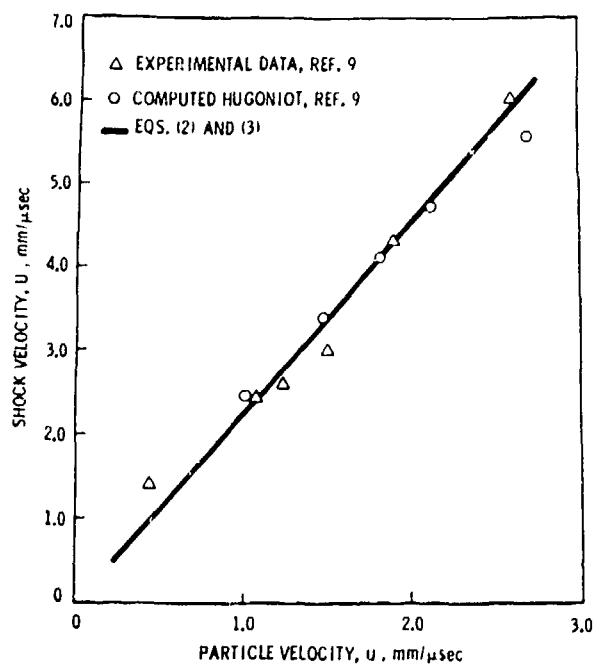
Fig. 7. Comparison of experimental and computed
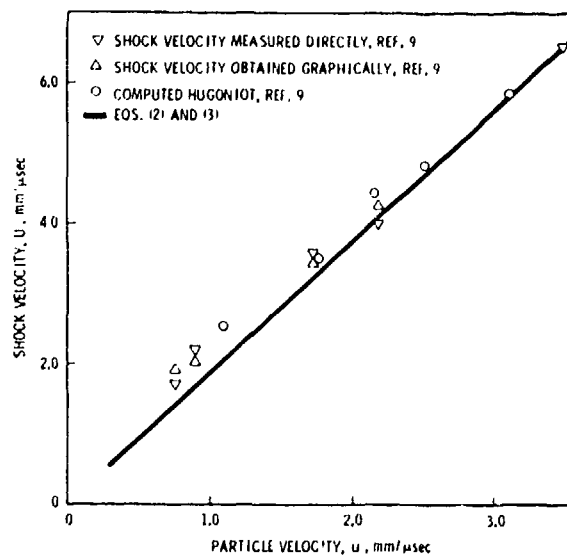Hugoniots for RDX at 1.0 g/cc.

Fig. 9. Comparison of experimental and computed
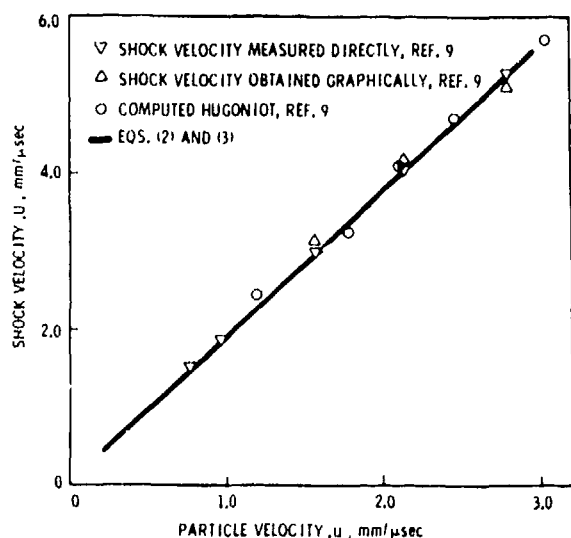Hugoniots for PETN at 0.82 g/cc.

Fig. 8. Comparison of experimental and computed
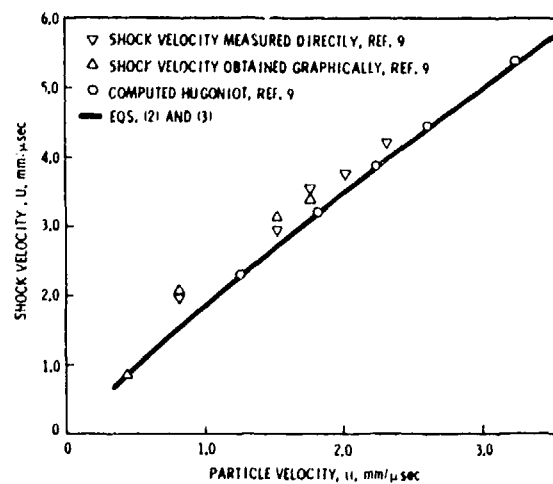Hugoniots for tetryl at 0.86 g/cc.

Fig. 10. Comparison of experimental and computed
Hugoniots for AN at 0.86 g/cc.

TABLE 3

Comparison of Computed and Experimental Results for Six Explosives

Material	Ref.	Density g/cc	Eqs. (2) and (3) vs. Experimental Data	Russian Calc. Eq. (6) vs. Experimental Data
TNT		0.98	good	*
NB	(22)	1.00	good	*
RDX	(9)	1.00	good	good
Tetryl	(9)	0.86	good	good
PETN	(9)	0.82	poor[†]	good
AN	(9)	0.86	poor[†]	poor[†]

*No results reported in Russian literature.
†Calculated shock velocity is low.
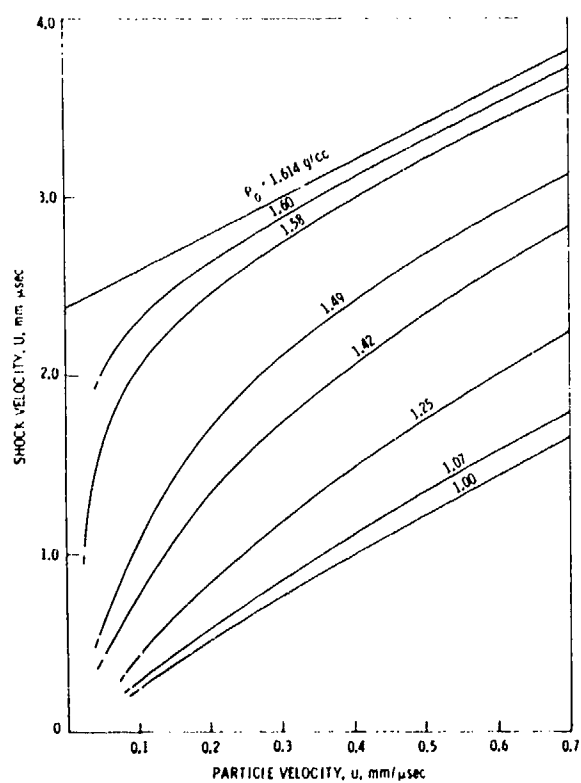
Fig. 11. Shock velocity, U, vs. particle velocity, u, for TNT at different densities.
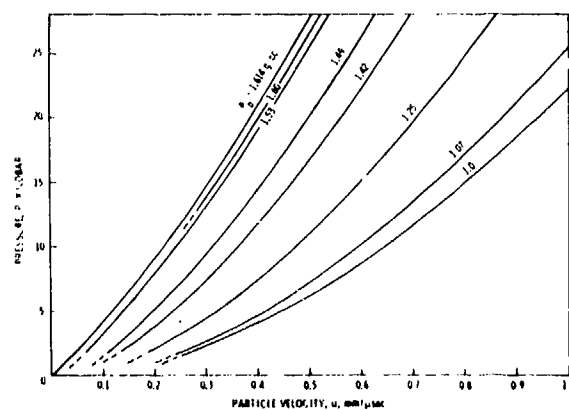
Fig. 12. Pressure vs, particle velocity for TNT at different densities.

he neglected the elastic response of the porous alumi-
num. For iron, the curves become more complex, see
Fig. 6 of (7). In that case, Herrmann tried to account
for the elastic response of the distended iron and the
crushup process. Therefore, more complicated curves
than those shown in Fig. 11 might result if compac-
tion was taken into account.

SUMMARY

The present results show that Hugoniots for por-
ous TNT can be calculated to a good degree of ac-
curacy by using the mathematical model described by
Equations (2,3). Furthermore, this model reproduces
experimental Hugoniots for NB-40 (19), RDX (9),
and tetryl (9) to a good degree of accuracy. For
PETN and AN, this model agrees less well with the
experimental data (9). This failure may be due to
inaccuracies in the experimental data on the low
density forms of each material, or on the values of
the parameters which are used to describe the
Hugoniots of the solid materials, or a combination of
these. Dremin, et al. (9) do not obtain close agree-
ment between calculated and experimental Hugoniots
for AN. This material is hygroscopic which makes it
difficult to keep pure in experimental work. Also, it
undergoes phase changes under pressure. For these
reasons, the Hugoniots of porous AN may be difficult
t model. In the case of PETN, a fairly sensitive
explosive, reaction may have caused errors in the
interp tation of the experimental data, especially
with the porous forms of the explosives. These errors
may exist in spite of the precautions employed by
Dremin, et al. (9).

The successes reported above lead to the conclu-
sion that the model used (Equations 2,3) is adequate
for predicting good approximations for the Hugoniots
of porous explosives. It would be most surprising if
the outcome had been negative. The model, and
variations of the model, have been used successfully
for years to describe the compaction of porous, un-
reacting solids by shock waves. The difficulty in
working with explosives is, of course, their tendency
to react when shocked. This challenges the experi-
mentalist when he tried to acquire Hugoniot data for
explosives in either their solid or porous form.

Otherwise, the degree of success in computing the
Hugoniot for a porous explosive depends on the
same factors as for an inert material. For example,

if the explosive undergoes a phase change under pres-
sure (hydrostatic or by shock), the model cannot be
applied in the form now available to us. If the solid
material does not undergo a phase change under pres-
sure (and the measurements are made before reaction
can proceed to any significant degree in the experi-
ment), the relation between the shock and particle
velocities is apt to be linear. Curvature in the U,u
relation for the solid can be handled by using a power
series which relates the pressure sure to the volumet-
ric strain, $\eta = (v_0 - v)/v_0$ (7).

The Gruneisen parameter of the solid material
must be known. Studies of the same material in
both solid and porous forms gives, in principle, values
of the Gruneisen parameter (17). Our TNT data are
too imprecise and too restricted in range for us to get
any improvement in the value of Γ for TNT. Dremin
(9) and Veretennikov (19), using this method, have
given values of Γ for some explosives to pressures as
great as 200 kbar. This is an extraordinary feat, ex-
perimentally, in view of the rapidity of the onset of
reaction in most of these materials at these higher
pressures.

REFERENCES

1. S. J. Jacobs, *ARS Journal*, **30** (2), 151 (1960).

2. Explosives Hazard Classification Procedures,
   NAVORDINST 8020.3, p. 9.

3. J. O. Erkman, D. J. Edwards, A. R. Clairmont,
   Jr., and D. Price, "Calibration of the NOL Large
   Scale Gag Test; Hugoniot Data for Polymethyl
   Methacrylate," NOLTR 73-15, 4 April 1973.

4. David J. Edwards, John O. Erkman, and Sigmund
   J. Jacobs, "The Electromagnetic Velocity Gage
   and Application to the Measurement of Particle
   Velocity in PMMA," NOLTR 70-79, 20 July
   1970.

5. R. R. Boade, *J. App. Phys.*, **39**, 5693-5702
   (1968).

6. R. Hofmann, D. J. Andrews, and D. E. Maxwell,
   J. App. Phys., **39**, 4555-62 (1968).

7. W. Herrmann, *J. App. Phys.*, **40**, 2490-99 (1969).

8. L. B. Seely, J. H. Blackburn, B. O. Reese. and M. W. Evans, *Comb. and Flame*, 13, 375-91 (1969).

9. A. N. Dremin, K. K. Shvedov and Avdonin, *Comb., Expl. and Shock Waves*, 6 (4), 449-55 (1970).

10. L. V. Al'tschuler, K. K. Krupnikov, B. N. Ledenev, V. I. Zhuchikhin, and M. I. Brazhnik, *Soviet Phys. JETP*, 34 (4), 606-14 (1958).

11. Ya. B. Zel'dovich, Yu. P. Raizer, "Physics of Shock Waves and High Temperature Hydrodynamic Phenomena," Academic Press, New York, 1966.

12. A. Holt, A. Kusubov, M. Carroll, and B. Hord, "Stress-Wave Propagation in Distended Asbestos Phenolic," UCRL-51120, Lawrence Livermore Laboratory, 3 Sep. 1971.

13. K. W. Schuler and J. W. Nunziato, "The Dynamic Mechanical Behavior of Polymethyl Methacrylate," Sixth Inter. Congress of Rheology, Lyon, France, 1972 (preprints).

14. L. M. Barker and R. E. Hollenbach, *J. App. Phys.*, 41 (10), 4208-26 (1970).

15. J. O. Erkman and D. J. Edwards, "Computed and Experimental Hugoniots For Unreacted Porous High Explosives," NOLTR 74-213, 31 December 1974.

16. V. A. Vasil'ev, L. G. Bolkhovitinov, and B. D. Khrostoforov, *Comb., Expl. and Shock Waves*, 3 (4), 371 (1967).

17. A. N. Dremin, S. A. Koldunov, and K. K. Shvedov, *Comb., Expl. and Shock Waves*, 7 (1), 87-92 (1971).

18. N. L. Coleburn and T. P. Liddiard, Jr., "The Unreacted Hugoniot Equation of State of Several Explosives," Preprints, 4th Symp. on Detonation, 1965. (Also see *J. Chem. Phys.*, 44, 1929 (1966)).

19. V. A. Veretennikov, A. N. Dremin, and K. K. Shvedov, *Comb., Expl. and Shock Waves*, (4), 342-45 (1969).

THE INFLUENCE OF INERT CASES ON AIRBLAST: AN EXPERIMENTAL STUDY

William S. Filler
Naval Surface Weapons Center
White Oak Laboratory
Silver Spring, Maryland 20034

The effect of casing mass and fragment size on the airblast from a high explosive
was examined experimentally using piezoelectric pressure gauges and scotchlite
photography. The explosive was an 8 pound sphere of pentolite (50/50, PETN/
TNT). The casings consisted of plaster, which weight as a ratio to the weight of
high explosive (S/X) was 0.5 to 3.7, and plaster bonded iron pellets, 1.2 and 4.4
mm in diameter. Shock wave peak pressure time records were obtained in the range
5 to 29 feet using 12 gauges. Photographs were obtained at nearly 8800 frames/sec.
of the expanding shock and case particles in the range 7 to 25 feet from the charge.
Compared with the peak shock pressure of a bare charge the peak pressure of the
cased charge is strongly depressed at the shorter distances but recovers dramatically
with increasing distance. Trajectories of pellets ahead of the shock are correlated
with precursors recorded on the pressure histories. Particle behavior is shown to
correlate qualitatively with theory for dust laden gas by Gerber and Bartos. It is
proposed that airblast shock pressure variation with distance is strongly influenced
by the effects on the ambient medium of particle kinetic energy dissipation due to
drag during the particles' flight ahead of the shock.

INTRODUCTION

For solid materials that surround or encase a high
explosive there exists a vast literature describing the
break up and flight of the case materials after deto-
nation of the high explosive. In sharp contrast little
consideration has been given to the general influence
of inert case materials on the blast wave itself (1).
Furthermore, while scattered test efforts involving
specific materials and geometries have been con-
ducted, systematic experimental effort is rare. This
paper reports on an experimental study that was
made in which spheres of high explosive encased in
plaster and plaster bonded iron pellets (Fig. 1) were
detonated to determine the effect of the surrounds
on the shock wave in free air. The explosive was
pentolite (50/50, PETN/TNT) 6.5 inches in diameter
and weighed about 8.5 pounds. The plaster casings
varied in thickness from 0.5 to 2.5 inches (Table 1).

The iron pellet cases were 0.5 inches thick and con-
sisted of 1.2 and 4.4 mm pellets closely packed with
the intersticies filled with plaster that acted as a bond.
Measurements were made in a plane 11 feet above
ground and over the range from 5 to 29 feet (about
18 to 107 charge radii) by means of twelve piezo-
electric airblast pressure gauges, Fig. 2. Pressure
histories of the shock wave were recorded. High
speed ($\sim$ 8800 frames/sec.) scotchlite shadowgraphs
also were taken of the expanding shock and case
debris in the range from about 7 to 25 feet, Fig. 2.
A comprehensive description of contemporary airblast
experimental technique may be found in (2).

EXPERIMENTAL METHODS

1. Cased Charge Fabrication

Case specifications relevant to the experiments are
reported in Table 1. Shells containing plaster were

TABLE 1

Test Charge Specifications

Material	Case Density g/cm^3	Case Weight S (lb)	S/X	Pellet P (lb)	P/X	Explosive* Weight X (lb)
Plaster 0.5"	1.65	4.55	.54			8.40
1.0"	1.38	8.77	1.04			8.41
1.5"	1.35	14.64	1.75			8.38
2.5"	1.35	31.41	3.67			8.56
Iron Pellets 1.2 mm (Plaster Bonded)		12.32	1.46	10.62	1.26	8.43
4.4 mm	–	13.97	1.66	12.40	1.47	8.44
Bare Charge Control						8.56

*Pentolite (50/50, PETN/TNT) Spheres
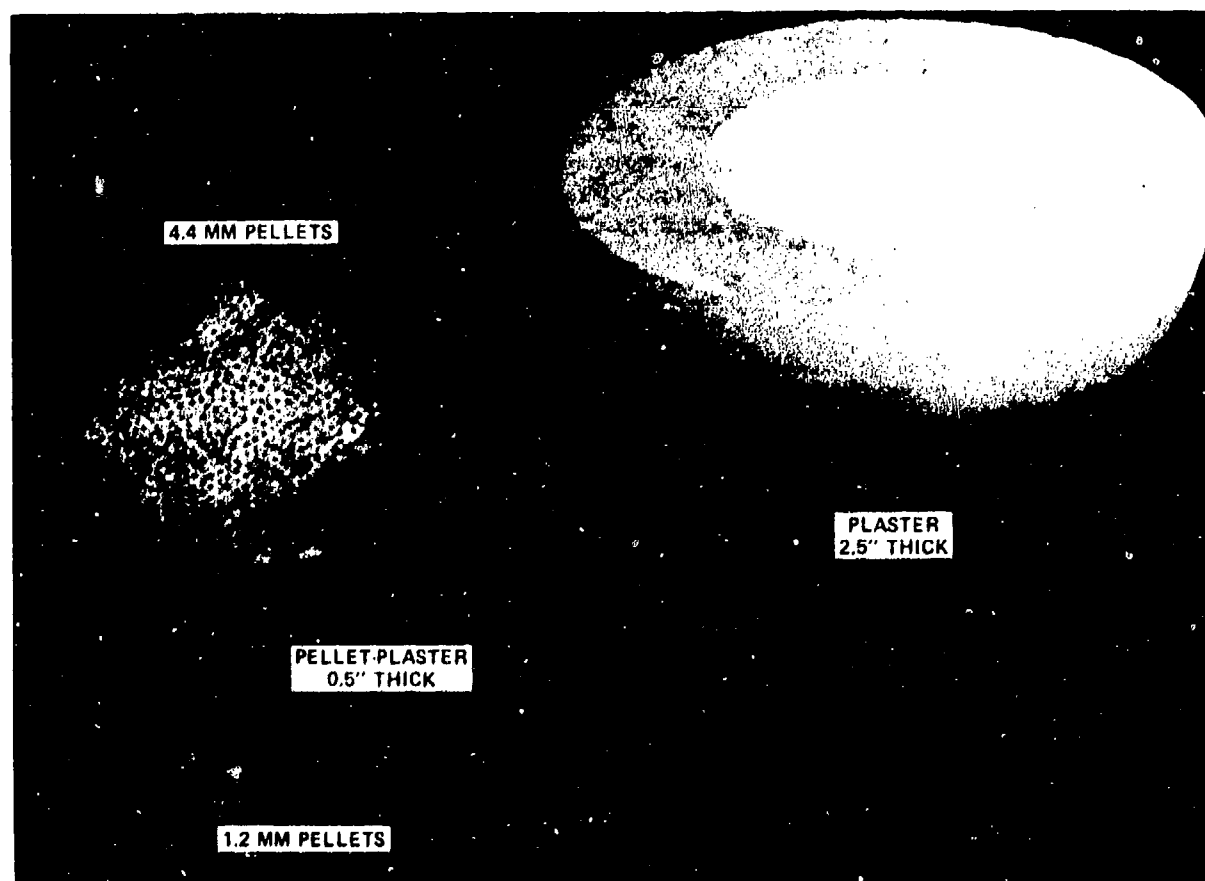
Fig. 1. Materials representative of casings used in experiments.
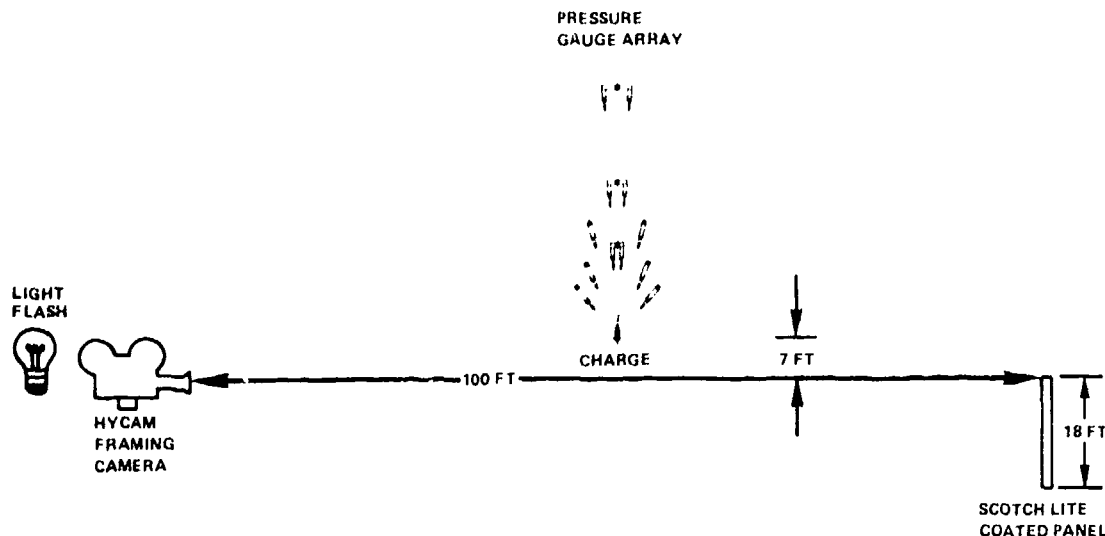
Fig. 2. Field arrangements for airblast measurements.

cast as hem spheres in wood molds, essentially as described [3] for thinner plaster shells. In this program, however, hydrocal, a form of plaster-of-paris specifically intended for casting purposes, was used. In the plaster only series the 1/2-inch shell was made with a weight ratio 3/1, dry plaster to water. However, because of the short setting time it was decided to use a 2/1 ratio for subsequent castings. This caused the change in density indicated in Table 1. The greater water content was an actual necessity for the shells containing metal pellets for they had an accelerating effect perhaps due to surface wetting of the metal pellets.

The metal pellet casings were intended to contain the maximum amount of metal. Perfectly packed spheres should occupy about 3/4 of a given volume. In fact, the large pellet size took up a bit less than 3/5 and the other just 1/2 of the available volume. The large iron pellets were air gun BB shot with a measured diameter of 4.4 ± 1% millimeters. The small iron pellets were supplied from "shot blasting" stock and had an average measured size of 1.2 ± 25% millimeters. Both iron pellet cases when completed had a nominal thickness of 1/2 inch.

Preparation of the charges for field use involved casting the explosive melt directly into the casing hemispheres. After cooling, the hemispheres were paired and bonded with adhesive. For detonator access, a 1/4-inch diameter hole extending from the surface to a point 1/4 inch beyond the center of the charge was cast into the explosive. The bare charges used in the program were cast as monolithic spheres and drilled for detonator access. Pentolite sensitivity is adequate to allow direct initiation with a detonator, in this case an "Engineer's Special."

2. Instrumentation and Field Arrangements

The shock pressure gauge array consisted of two gauges at each of six positions, nominally 5, 7, 9, 12, 17 and 29 feet. The peak shock pressure measurements ranged from 3 to nearly 200 psi. A quartz, piezoelectric, pencil-type gauge, Susquehanna model ST-7, was used at the 5- and 7-foot distances and sometimes at the 9-foot distance. This is a rugged, temperature insensitive, airblast gauge designed for relatively high shock pressures. At other distances the transducers were Atlantic Research LC 33 units with lead zirconate titanate sensing elements. These elements are 1/4 inch long and 1/2 inch in diameter mounted coaxial to and at mid-length along a cylinder of high length-to-diameter ratio. This arrangement minimizes the disturbance to the airflow and its pressure at the sensing element.

A signal generated by a gauge is processed and displayed on an oscilloscope as a spot deflection. Permanent recording is done on 35mm film strips mounted on rotating drums that provide a relatively

779

long time base. A system response check and amplitude calibration are accomplished by means of an integral square step method. A time base calibration signal of one kHz is coupled into the signal channel and appears superimposed on the signal trace at a square step.

The scotchlite technique (4), through highly efficient utilization of source light, makes field shock wave photography practical. It employs a high intensity light flash source that illuminates a panel (18 feet X 12 feet in this case) with a reflective "scotchlite" coating. A high speed framing camera (Hycam in this case) located near but ahead of the light source records the event. As the shock wave passes between the camera and scotchlite panel the light refracts at the shock front and a fairly sharp image of it results. A total time of about 4 milliseconds is recorded as the main shock wave moves from a position about 7 feet from the charge center to about 25 feet away.

Charges were suspended in fishnet material weighing a few grams with the intent of minimizing the amount of combustible extraneous mass in proximity to the charge. A series of bare pentolite charges was fired throughout the program as a control on potential unsuspected instrumentation and environmental variables that might affect comparative results.

3. Record Analysis

In Fig. 3 are shown representative sets of pressure histories from bare, plaster and iron pellet cased charges. They include records from paired gauges at each of the six distances where measurements were made. Bare charge records provide a comparison standard. In contrast with their clean, classical shape several major disturbance patterns are apparent on the cased charge records.

One type of disturbance is the precursor. For the 4.4 mm iron pellet records the precursor appears on the 7-foot record and its duration increases to about 11 msec at 29 feet. If the average main shock front velocity over this range of distances is taken to be about 2000 feet per second, then the percursor duration implies a disturbance moving about twice as fast or about 4000 feet per second. Bow shock waves generated by fragments moving at various supersonic speeds near a gauge would be expected to generate a succession of disturbances not unlike that observed

here. Some main shock wave irregularities could be similarly attributed as it overtakes bow shock remnants in the vicinity of a gauge before equilibrium has occurred. Other main shock wave irregularities are due simply to the fact that the blast wave has not yet stabilized and is in a poor state of organization as it passes the nearest gauges particularly.

This is graphically illustrated in scotchlite photographs, Fig. 4. Here are assembled frames selected at regular intervals. In frame 1 the highly disturbed main shock front is just at the photo's edge. The iron pellets visible through their self-generated bow shocks are just ahead of the main shock. In successive frames the main front distrubances gradually subside as the main shock velocity rapidly decreases from about 2200 to 1300 feet/second, while the iron pellets streak rapidly across the field of view at speeds on the order of 4000 feet/second.

Returning to the pressure gauge records of Fig. 3 representing plaster cased charges, high acceleration of case particles is shown by the early precursor presence at 5 and 7 feet. However, subsequent deceleration due to air drag is apparently so rapid that no precursor or shock wave disturbance is present on gauge records beyond 9 feet. The enlarged records at the bottom of Fig. 3 show more clearly another distinctive feature of the plaster records. The nature of the disturbance, compared with that of the iron pellet case disturbances, has changed here to very short-time pulses that appear as fine vertical lines and persist to great times after the shock front. The fact that these occur throughout the records themselves without significant amplitude attenuation suggests that these pulses may not be due to bow shocks at all, but rather may result from direct solid particle impact on the sensor. This would require particle trajectories to intercept the gauge at some, probably small, angle due perhaps to slight gauge misalignment and/or slight particle trajectory shifts. There is a greater density of these fine disturbances for the heavy plaster case compared with the light.
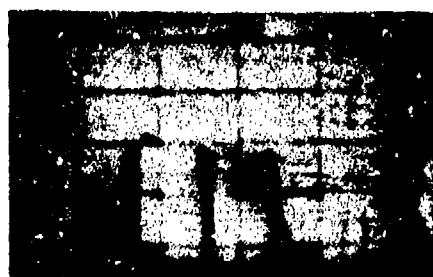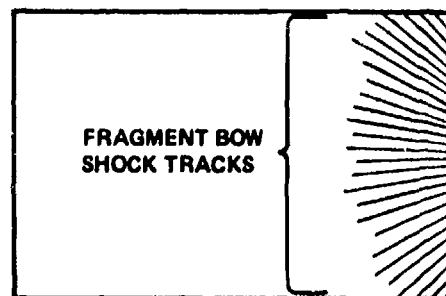
4. Peak Shock Pressure Data

Some of the peak shock pressure versus distance data produced from the puressure-time records is presented in Fig. 5 in conventional log-log plot form. More sensitive and useful curves for comparison purposes are those of Fig. 6. Here, for all case configurations treated in this paper, are smoothed curves
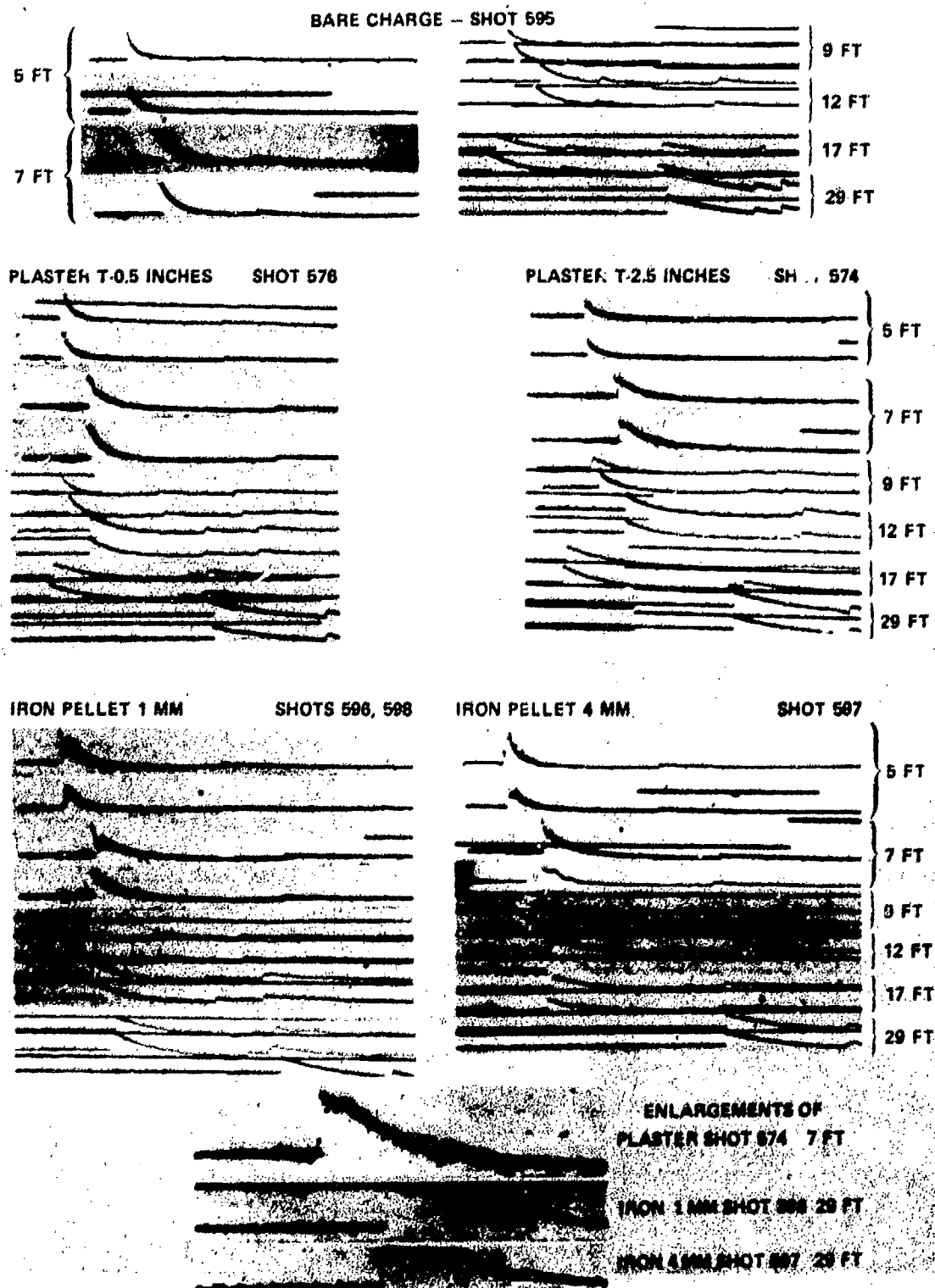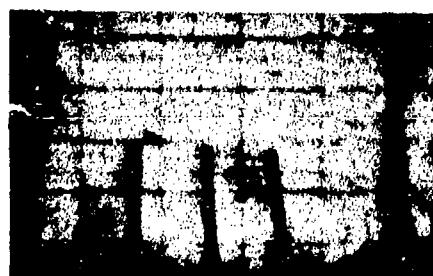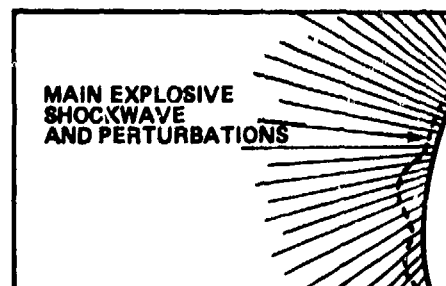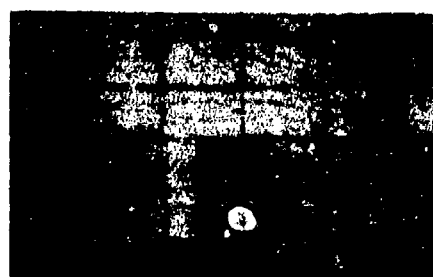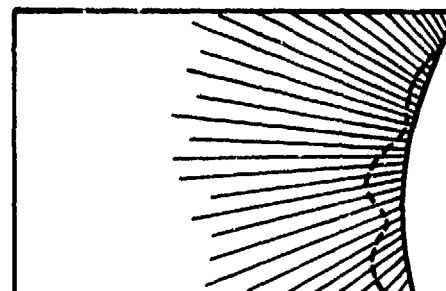
Fig. 3. Shock wave pressure histories.
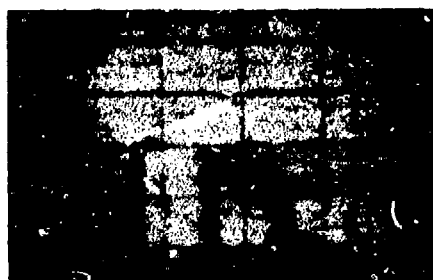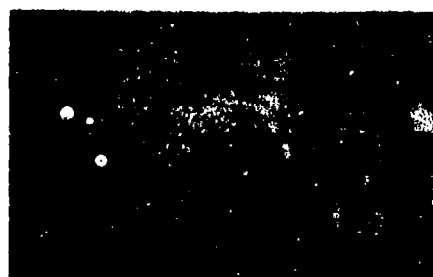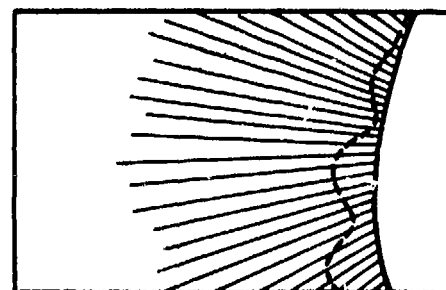
Fig. 4. Scotchlite photos: 4.4 mm iron pellet case
interframe time: 0.113 milliseconds/single frame
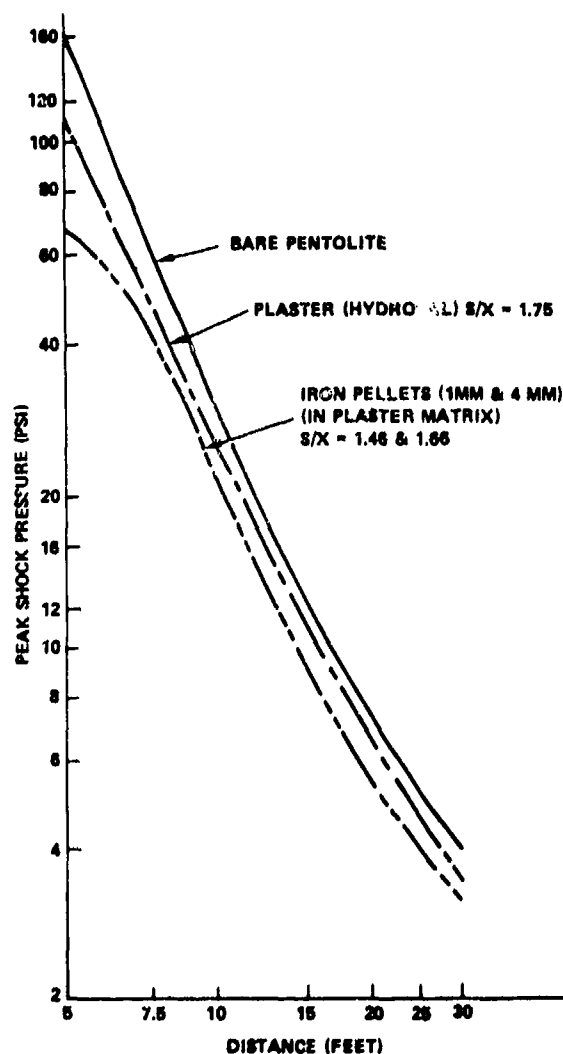
Fig. 5. Peak shock pressure vs distance for 8 lb. pentolite sphere encased in various materials.

Fig. 6. Relative peak shock pressure trends (S/X-case weight/explosive weight)

drawn through data for the ratio of cased charge pressure to bare charge pressure plotted as a function of distance (and pressure level for reference purposes). It is apparent that compared with a bare high explosive charge the relative peak shock pressure of all cased charges is depressed substantially at the shorter distances but recovers dramatically with increasing distances. This pattern is most pronounced for the heaviest plaster case and the cases containing iron pellets, both of which have peak shock pressures that are initially depressed by about 50%. However, the peak pressures for all cased charges recovered at the farthest distances to within 5-20% of the bare charge levels.
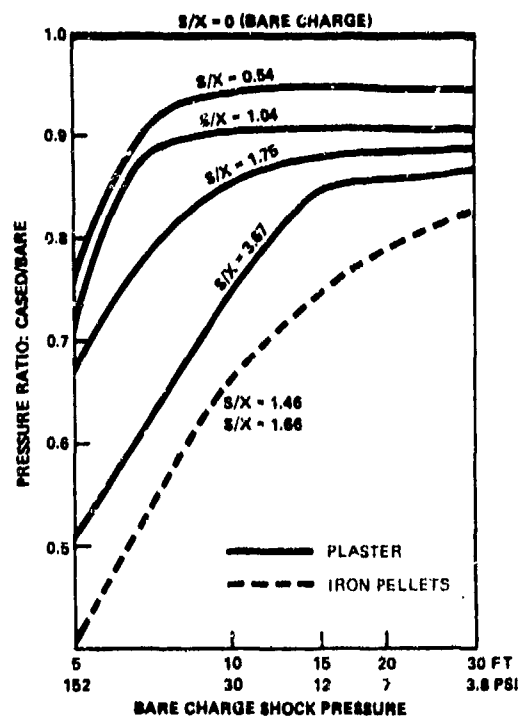
DISCUSSION

Gerber et. al., (5) treat the problem of a Taylor-Sedov blast wave encounter with dust particles. These are considered to have mass, in contrast with earlier treatments. One result of the calculations is to show that particles initially located within a spherical region about the explosion center determined by a theoretically defined critical radius, may move through and ahead of the shock wave. After undergoing high drag forces in the ambient gas ahead of the shock front, a particle that is small enough may in turn be overtaken by the shock. In a final paragraph Gerber et. al., (5) state that these results imply similar behavior on the part of solid particles that are explosion products or unburned matter.

Since (5) deals with individual particles of specific size undergoing acceleration due to aerodynamic drag force, the acceleration phase for a solid case is a very different situation and is understandably not mentioned in (5). Nonetheless, the theoretical description of (5) is relevant to a cased charge configuration if

783

applied to the period after case break up when particles have been formed and projected ahead of the main shock. Regardless of origin, particles of sufficient fineness must then decelerate and be overtaken by the shock. Plaster cased charges subjected to detonation shocks would be expected to produce mainly fine particles. On the other hand the iron pellet particles would be expected for the most part to remain integral although deformed.

In Fig. 3 as discussed in a previous section of this paper disturbances on pressure-time records from plaster cased charges are observed to disappear at an intermediate distance (beyond 9 feet) in the range of measurements; while the iron pellet disturbances persist out to the maximum range of recording. Scotchlite photography gave direct visual confirmation of at least part of this behavior--the 4.4 mm iron pellet projection ahead of the shock over nearly the same region of observation as the pressure gauges. However, this photographic effort was not sensitive enough to show the fine particles of the plaster cases. Even the 1.2 mm iron particles were not visible.

This particle behavior pattern is, in a qualitative sense at least, just what is predicted by (5).

Another aspect of the physical circumstances involved here but not dealt with in (5) is of critical importance to the content of the present paper. This has to do with the changed conditions in the medium ahead of the shock wave that results from the prior passage of high velocity particles that dissipate their energy in that medium by heating and accelerating it. A shock wave that subsequently passes through such a heated moving medium must itself decelerate more slowly with distance than otherwise and thus have greater strength at greater distances than otherwise. The net effect of this is to provide an apparent or effective feedback of energy from leading fragments to following shock wave.

It is felt that the airblast recovery evidenced so graphically in Fig. 5 is due at least in part to the above described process. This pattern is particularly apparent in the way the blast wave recovery occurs over increasing distance as the plaster case relative mass increases. With increased relative case mass lower average particle velocities will result and this in turn

will cause slower dissipation of particle energy ahead of the shock. Yet, remarkably, even with the most massive plaster case--nearly 4 times the charge weight--the airblast pressure is only about 15% below that of the same charge without any case.

The iron pellet case behavior in this regard is similar except for its overall lower pressure level compared with plaster for similar values of S/X. The larger pellet particle size is most likely the cause. Deceleration is a function of particle cross-section area. With increasing size the cross-section area to volume ratio decreases and the kinetic energy of the particle is lost more slowly to the ambient air.

SUMMARY

Airblast piezoelectric pressure gauge and scotchlite photography techniques were employed to observe patterns of behavior of fragments from friable cased high explosive charges. The pressure gauge data shows a remarkable pattern of shock wave pressure recovery with distance (relative to bare charge results). The level to which relative pressure recovers is essentially independent of case mass.

Theory by Gerber et. al., for airblast wave interactions with dust particles is shown to be qualitatively applicable to acceleration and deceleration behavior of fine case fragments apparent on pressure gauge records as well as course iron pellet case fragments observed photographically.

The insensitivity of far field airblast pressure to the presence of inert and massive but friable cases is believed due, at least in part, to an effective energy feedback mechanism. This mechanism is believed related to influences on the medium ahead of the blast wave by precursor fragments as they lose kinetic energy due to drag

REFERENCES

1. F. B. Porzel, "A Unified Theory of Explosions," NOLTR 72-209, Sept. 1972.

2. W. E. Baker, Explosions in Air, University of Texas Press, Austin, Texas, 1973.

3. W. S. Filler, "The Effect of a Case on Airblast Measurements, Part I: Friable Inert Cases," NOLTR 74-62, 9 April 1974.

4. D. Mclanahan, "Shock Wave Photography Using Scotchlite Reflective Sheeting," HAVORD 6760, June 1960.

5. N. Gerber and J. N. Bartos, "Strong Spherical Blast Waves in a Dust-Laden—Gas," AIAA Journal, Vol. 12, No. 1, pp. 120-122, Jan. 1974. Also BRL Rept. 1696, Jan. 1974.

A MULTIPLE LAGRANGE GAGE STUDY OF THE SHOCK INITIATION PROCESS IN CAST TNT*

M. Cowperthwaite and J. T. Rosenberg
Stanford Research Institute
Menlo Park, California 94025

A multiple Lagrange gage study of the shock initiation process in cast TNT was undertaken to determine the mechanism of initiation, the hydrodynamic flow, and the energy-release rate in the initiating wave. The particle-velocity histories recorded at different positions in the explosive combined with the equations of motion and the Rankine-Hugoniot jump conditions show that the flow derivatives and the energy-release rate at the shock front change sign twice in the buildup to detonation. The pressure gradient becomes negative before the particle velocity gradient in the compressive region behind the shock. A particle at the shock front is compressed when the negative pressure gradient created by the overall liberation of energy in the flow exceeds the expansion associated with the local reaction. The negative energy-release rate is taken as evidence for the occurrence of a shock-induced phase change in cast TNT in the 55-kbar region. The gage data also lead to the conclusion that a nonlinear-shock velocity/shock-particle velocity relationship is necessary to describe shocked states in cast TNT.

INTRODUCTION

Multiple Lagrange gage studies (1) of a shocked explosive provide the information required to establish the mechanism of the shock initiation process and to determine the flow and energy-release rate in the initiating wave. The Lagrange gages (2)-(4) record flow histories along particle paths because they are embedded directly in the explosive at different depths and follow the shock-induced flow. These flow histories are combined with the equations of motion to determine other hydrodynamic properties and the associated energy-release rate in the flow.

This paper presents a multiple Lagrange gage study of the shock initiation process in cast TNT. Experimental procedures and gage profiles recorded in cast TNT are presented. Features of the initiating flow deduced from the gage records are discussed to elucidate the mechanism of initiation, and calculations of the flow parameters and the energy-release rate along the shock trajectory are given.

The shock front calculations presented here constitute the first step in calculating the energy release rate in the initiating wave from data recorded by multiple embedded gages.

EXPERIMENTAL PROCEDURES

Three multiple Lagrange gage experiments were performed to investigate the shock initiation process in cast TNT. The driver systems were designed to deliver an initial pressure in the cast TNT of about 55 kbar. A typical driver system contains a P-80 plane wave generator; a 3-inch-thick, 8-inch-diameter Baratol high explosive pad; and an attenuator to

produce an initial pressure in the cast TNT in the 55-kbar region. The attenuators were impedance-mismatch combinations of either PMMA (poly-methylmethacrylate) and high-density glass or PMMA and polystryene foam, and their outputs were checked using a manganin stress gage embedded in PMMA.

A typical TNT target with gages embedded in the explosive at different depths is shown before and after assembly in Figure 1. The first two TNT charge targets for the initiation experiments were essentially built as replicas. Each assembly contained a set of seven Dremin loop particle-velocity gages (5) - (9) and a set of five stress gages. The set of particle-velocity gages includes four primary measurement gages, one time-of-arrival gage, and two baseless gages for investigating explosive conductivity. A new method
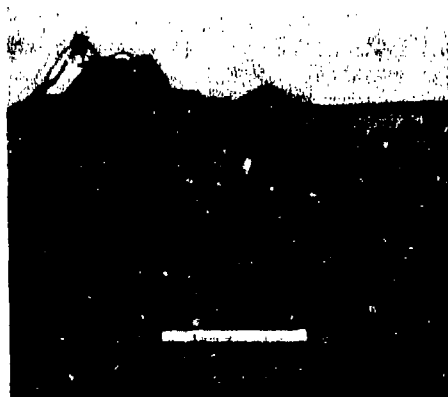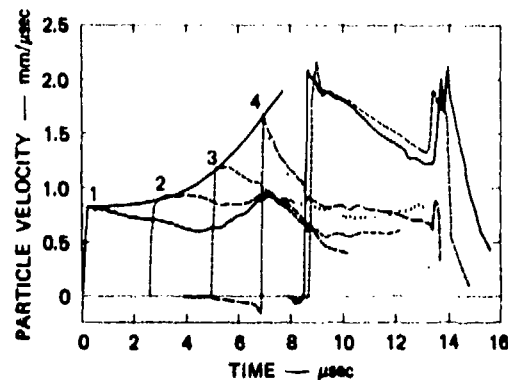

(a) Expanded view showing gages in place before assembly

(b) assembled experiment

Fig. 1. Cast TNT experiment with gages emplaced in explosive at several depths.

Fig. 2. Particle-velocity histories recorded at different Lagrange positions in case TNT in the third initiation experiment.

of embedding the gages between the TNT pads, intended to minimize flow perturbations by the gages, was used in building the third initiation experiment. Additional gages were also incorporated at the top of the charge in an attempt to generate more data in the final stages of initiation. A PMMA block containing two stress gages and one particle-velocity gage was placed on the top of the TNT, and a stress and particle-velocity gage were emplaced at the interface between this PMMA block and the TNT. Figure 2 shows the particle-velocity time profiles generated from the gage records obtained in the third initiation experiment. The first and fifth profiles in Figure 2 give the particle velocities recorded at the external interfaces between PMMA and TNT at the bottom and top of the charge. The second, third, and fourth profiles give the particle velocities recorded at the internal TNT interfaces, and the last profile gives the particle velocity induced in the PMMA at the top of the charge by the reactive wave. Comparison of the particle-velocity records obtained in all three initia-tion experiments showed that the records obtained in the third experiment are superior to those obtained in the first two experiments. The improvement in the records is attributed to the new method of embedding the gages between the pads of TNT. The calculation of the flow and energy-release rate at the shock front was consequently based largely on the particle-velocity records obtained in the third experiment.

THE SHOCK INITIATION PROCESS IN CAST TNT

The sets of particle-velocity profiles obtained in the shock-initiation experiments show the develop-ment of the wave produced in cast TNT by a shock

with an initial peak pressure in the 55-kbar region. The observation that peak particle velocity increases with wave propagation distance shows immediately that the flow is reactive and that the TNT is undergoing initiation of detonation. More detailed, but still qualitative, interpretation of the particle-velocity profiles leads to properties of the particle-velocity fields of these initiating waves. The combination of these properties with the equations of motion yields other properties of the flow that elucidate the mechanism of the shock initiation process in cast TNT. These properties are derived from the cast-TNT particle-velocity data in the remainder of this section. The quantitative calculation of states, flow derivatives, and energy-release rate along the shock trajectory are given in the following section.

Examination of the digitized data used to construct the particle-velocity profiles leads to the conclusion that the impulsive acceleration recorded by a gage entering the flow can be treated as a shock discontinuity governed by the Rankine-Hugoniot jump conditions. The shocked state is chosen as the point on the particle-velocity profile where the time derivative of the particle velocity changes most rapidly. The flow after this point is assumed to be governed by the differential equations expressing the conservation of mass, momentum, and energy.

It is convenient at this point to introduce the notation we will use to describe the shock-induced flow. Let t, h, u, and U denote time, Lagrange distance, particle velocity, and shock velocity; let v, p, and e denote specific volume, pressure, and specific internal energy; and let the subscripts o and s denote the unshocked state and the shocked state at the top of the shock discontinuity. Then states connected by the shock are related by the jump conditions expressing the balance of mass, momentum, and energy across the discontinuity.

$$v_s U = v_0 (U - u_s) \qquad (1)$$

$$v_0 (p_s - p_0) = U u_s \qquad (2)$$

$$e_s - e_o = \frac{1}{2} (p_s + p_o)(v_o - v_s) \qquad (3)$$

The adiabatic flow behind the shock is governed by the corresponding differential equations,

$$\frac{\partial v}{\partial t} = v_o \frac{\partial u}{\partial h} \qquad (4)$$

$$\frac{\partial u}{\partial t} = - v_o \frac{\partial p}{\partial h} \qquad (5)$$

$$\frac{\partial e}{\partial t} = - p \frac{\partial v}{\partial t} \qquad (6)$$

The combination of Eq. (6) with the $e = e(p, v, \lambda)$ equation of state yields a more useful form of the energy equation

$$\frac{\partial p}{\partial t} = - \kappa \frac{p}{v} \frac{\partial v}{\partial t} + \frac{\Gamma}{v} Q \frac{\partial \lambda}{\partial t} \qquad (7)$$

where λ denotes the extent of reaction, Q denotes the heat of the reaction, κ is related to the sound speed c by the identity $c^2 = \kappa p v$, and $\Gamma/v = (\partial p/\partial e)_{v,\lambda}$ is the well-known Grüneisen parameter. It is convenient to rewrite the volumetric energy-release rate, the third term in Eq. (7), as $\dot{P}$, and the specific energy-release rate as $\dot{Q} = \dot{P} v / \Gamma$.

We will now derive properties of the particle-velocity field in the initiating wave. Consider the best set of $(u - t)$ profiles shown in Figure 2 where the shock trajectory is shown schematically as 1234. Examination of these profiles shows that the variation of particle velocity behind the shock depends strongly on the Lagrange coordinate. The particle velocity attains its maximum value at the shock front and decays behind the shock, $\partial u/\partial t < 0$, at the first and the fourth Lagrange gage positions but not at the second and third. At these latter positions the particle velocity behind the shock front first increases, $\partial u/\partial t > 0$, then attains a maximum value, $\partial u/\partial t = 0$, and finally decays, $\partial u/\partial t < 0$. Thus, the sign of the acceleration $(\partial u/\partial t)_s$ at the shock front changes from negative to positive and back from positive to negative as the shock accelerates and the wave builds up to a steady state. Consequently, there must be two points, say U and U', on the shock trajectory where $(\partial u/\partial t)_s = 0$. In Figure 2, these points are located somewhere between the first and second Lagrange gage positions and somewhere between the third and fourth Lagrange positions. The locus of points, where $\partial u/\partial t = 0$, forms a curve in the $(t - h)$ plane, say UU', which intersects the shock trajectory at the points U and U' and divides the flow behind the shock into two regions according to the sign of $\partial u/\partial t$. The flow lying below UU' satisfies the condition $\partial u/\partial t > 0$, and the flow lying above UU' the condition $\partial u/\partial t < 0$.

788

Properties of the pressure field behind the shock in the initiating wave determined by the acceleration follow from the momentum equation, Eq. (5). Since $(\partial p/\partial h) > 0$ when $\partial u/\partial t < 0$, $(\partial p/\partial h) < 0$ when $\partial u/\partial t > 0$, and $\partial p/\partial h = 0$ when $\partial u/\partial t = 0$, it follows from the previous discussions of the $(u - t)$ profiles that the sign of the pressure gradient behind the shock also depends strongly on Lagrange position. To be more specific, the pressure attains a maximum with respect to Lagrange distance in the $(t - h)$ plane along UU', the pressure gradient is negative, $\partial p/\partial h < 0$, in the flow behind the shock lying below UU', but is positive, $\partial p/\partial h > 0$, in the flow behind the shock lying above UU'.

Other properties of the particle-velocity field in the initiating wave follow from the relative positions of the shock trajectory and the $(u - t)$ profiles, and the following equations governing the shock

$$\frac{Du_s}{Dt} = \frac{\partial u}{\partial t_s} + \frac{U}{v_o} \frac{\partial v}{\partial t_s} \qquad (8)$$

$$\left(\frac{Dp}{Du}\right)_s \frac{Du_s}{Dt} = \frac{\partial p}{\partial t_s} - \frac{U}{v_o} \frac{\partial u}{\partial t_s} \qquad (9)$$

$$\left[\left(\frac{Dp}{Du}\right)_s + \frac{U}{v_o}\right] \frac{Du_s}{Dt} = -\left[\left(\frac{\kappa p}{v}\right) - \left(\frac{U-u}{v}\right)^2\right]_s \frac{\partial v}{\partial t_s} + \dot{P}_s \qquad (10)$$

Equation (8) is a combination of the identify $Du_s/Dt = \partial u/\partial t_s + U \partial u/\partial h_s$ and Eq. (4), and Eq. (9) is a combination of the corresponding identify for Dp_s/Dt', Eq. (5), and the equation $Dp_s/Dt = (Dp/Du)_s Du_s/Dt$ relating the pressure and particle velocity along a Hugoniot curve. Equation (10) is a combination of Eqs. (8), (9), and (7). Note that the term in square brackets on the right-hand side of Eq. (10) is positive because $c_s^2 - (U - u)_s^2 > 0$ for a stable shock. It follows from Eq. (8) that the sign of $\partial u/\partial h_s$ and $\partial v/\partial t_s$ at a point on the shock trajectory can be determined by comparing the values of Du_s/Dt and $\partial u/\partial t_s$ at that point. When the shock is accelerating and $Du_s/Dt > 0$ as in the present case, $\partial u/\partial h_s$ and $\partial v/\partial t_s > 0$ where $\partial u/\partial t_s < 0$, but $\partial u/\partial h_s < 0$ and $\partial v/\partial t_s < 0$ where $\partial u/\partial t_s > Du_s/Dt$. Examination of Figure 2 shows that $\partial u/\partial h_s < 0$ and $\partial v/\partial t_s < 0$ at the second and third gage positions where $\partial u/\partial t_s > Du_s/Dt$, but that $\partial u/\partial h_s > 0$ and $\partial v/\partial t_s > 0$ at the

first and fourth gage positions where $\partial u/\partial t_s < Du_s/Dt$. The sign of $\partial u/\partial h_s$ and $\partial v/\partial t_s$ at the shock front therefore changes from positive to negative and back from negative to positive as the shock accelerates and the wave builds up to a steady state. There must be two points, say V and V', on the shock trajectory where $(\partial u/\partial h)_s = (\partial v/\partial t)_s = 0$. The points V and V' must lie between the points U and U' where $\partial u/\partial t_s = 0$ because $\partial u/\partial h_s > 0$ when $\partial u/\partial t_s = 0$. Particles entering the wave below V and above V' on the shock trajectory are compressed to their smallest volume at the shock front, and they then expand $\partial v/\partial t > 0$. But particles entering the wave between V and V' on the shock trajectory are compressed first by the shock and then compressed again behind the shock to their smallest volume before undergoing expansion $\partial v/\partial t > 0$. The locus of points where $\partial v/\partial t = 0$ is a curve in the $(t - h)$ plane that intersects the shock trajectory at V and V' and lies to the right of the curve where $\partial u/\partial t = 0$. This curve, say VV', divides the flow in the $(t - h)$ plane behind the shock into two regions according to the sign of $\partial u/\partial h$. The flow behind the shock below VV' satisfies the condition $\partial u/\partial h < 0$, and the flow above VV' the condition $\partial u/\partial h > 0$.

The other important flow derivative to be considered in the initiation process is $\partial p/\partial t$. At points on the shock trajectory between U and U', $\partial p/\partial t_s > 0$ because $\partial p/\partial h_s < 0$ and $Dp_s/Dt > 0$. There must therefore be a point above U' on the shock trajectory, say P', where $\partial p/\partial t_s = 0$ because $\partial p/\partial t_s < 0$ in the self-sustaining wave. It is not clear whether there is another point on the shock trajectory where $\partial p/\partial t_s = 0$ because $\partial p/\partial h_s > 0$ at the first Lagrange gage position. There will, however, be such a point if initially $\partial p/\partial t_s < 0$. This is the situation in the present case because evaluation of Dp_s/Dt and $U \partial p/\partial h_s$ at the first gage position shows that $\partial p/\partial t_s < 0$ there. This point, say P, on the shock trajectory where $\partial p/\partial t_s = 0$ must lie below the point U where $\partial p/\partial t = 0$ generates a curve in the $(t - h)$ plane to the left of the curve UU' where $\partial p/\partial h = 0$ that divides the flow in the $(t - h)$ plane behind the shock into a region where $\partial p/\partial t > 0$ and a region where $\partial p/\partial t < 0$.

In cast TNT initiated by a shock with an initial pressure in the 55-kbar region, the derivatives of pressure and particle velocity at the shock front change sign twice as the wave builds up to a steady state. The first change in sign occurs in the order $\{\partial p/\partial t_s, \partial p/\partial h_s, \partial u/\partial h_s\}$, and the second change in sign in the reverse

789

order $\{\partial u/\partial h_s, \partial p/\partial h_s, \partial p/\partial t_s\}$. The hydrodynamic properties of the flow deduced from the $(u - t)$ profiles can now be used to consider the energy-release rate in the initiating wave.

It is clear from the way the flow derivatives change sign as the wave develops that the initiation process is governed predominantly by the energy-release rate in the whole wave rather than by the energy-release rate close to the shock front. The shock accelerates when the energy-release rate at the shock front exceeds the hydrodynamic loss associated with the expansion at the shock front. Initially, the shock accelerates and the pressure increases along the shock trajectory but decreases along a particle path, because the energy-release rate is not large enough to compensate for the positive pressure gradient created by the expansion of the wave. As the shock continues to accelerate, however, the energy liberation in the wave opposes the rarefaction and reduces the pressure gradient. This reduction in pressure gradient leads first to the conditions $\partial p/\partial t_s > 0$, then to the conditions $\partial p/\partial h_s < 0$ when $\partial u/\partial t_s > 0$, and finally to the conditions $\partial u/\partial h_s < 0$ and $\partial v/\partial t_s < 0$. When $\partial p/\partial h_s < 0$ and $\partial u/\partial h_s > 0$, the mechanical compression exerted by the negative pressure gradient at the shock front cannot overcome the expansion associated with the local reaction at the shock front. When $\partial p/\partial h_s < 0$ and $\partial u/\partial h_s < 0$, the compression at the shock front created by the overall liberation of chemical energy in the wave more than offsets the expansion associated with the local reaction at the shock front, and particles are compressed at the shock front as they enter the wave. As the shock accelerates, the expansion associated with the reaction at the shock front starts to dominate the flow and the wave becomes rarefactive. This expansion leads first to the conditions $\partial v/\partial t_s > 0$ when $\partial u/\partial h_s > 0$, then $\partial p/\partial h_s > 0$ when the particles are decelerated at the shock front $\partial u/\partial t_s < 0$, and finally back to the conditions $\partial p/\partial t_s < 0$ where the pressure falls along a particle path.

The energy-release rate and flow derivatives are simply related at points on the shock trajectory where one of the flow derivatives is zero. It follows from (8), (9), and (10) that

$$\dot{P}_s = \left(\frac{c}{v}\right)_s^2 v_0 \frac{\partial u}{\partial h_s} \qquad (11)$$

at P and P' where $\partial p/\partial t_s = 0$, that

$$\dot{P}_s = \left[\left(\frac{Dp}{Du}\right)_s U + \left(\frac{c}{v}\right)_s^2 v_0\right]\frac{\partial u}{\partial h_s} \qquad (12)$$

at U and U' where $\partial u/\partial t_s = \partial p/\partial h_s = 0$, and that

$$\dot{P}_s = \left[\left(\frac{Dp}{Du}\right)_s + \frac{U}{v_0}\right]\frac{Du_s}{Dt} \qquad (13)$$

at V and V' where $\partial u/\partial h_s = \partial v/\partial t_s = 0$.

Consider now the flow behind the shock. In the initial and final stages of buildup below P and above P', the pressure falls along a particle path because the energy-release rate cannot overcome the hydrodynamic loss associated with expansion, and $\dot{P} < (c/v)^2 v_0 \partial u/\partial h$. In the intermediate stage, however, the pressure first increases along a particle path $\dot{P} > (c/v)^2 v_0 \partial u/\partial h_s$, attains a maximum where $\dot{P} = (c/v)^2 v_0 \partial u/\partial h$, and then decays $\dot{P} < (c/v)^2 v_0 \partial u/\partial h$.

Thus, interpretation of the particle-velocity histories recorded in a single shock-initiation experiment on cast TNT leads to an understanding of the mechanism of initiation in this explosive. The deduced flow properties of the initiating wave are considered to be realistic because they are based on features of the particle-velocity histories that are obtained in all three initiation experiments.

CALCULATION OF FLOW PARAMETERS AT THE SHOCK FRONT

Calculations of the flow parameters at the front of the initiating wave are based on the $(u - t)$ profiles shown in Figure 2. It is first necessary to construct the Hugoniot curve from the shock arrival times and shock particle velocities recorded by the gages. An analytic $(t - h)$ expression for the shock trajectory was constructed to fit the time-of-arrival data and differentiated to find shock velocity. Shock velocity was then plotted against shock-particle velocity to determine the form of the Hugoniot curve in the U-u plane. Examination of this plot showed that a non-linear $U - u_s$ relationship is required to fit the Hugoniot curve in the region spanned by the gages. The following $U - u_s$ relationship

$$U = 2.343 + 3.150\,u_s - 0.839\,\exp[(u_s - u^*)/\beta_1] \qquad (14)$$

with $u^* = 0.839$ mm/μsec and $\beta_1 = 1.288$ was found to give a good fit to the gage data. A relationship for the dependence of shock-particle velocity on Lagrange position in the initiating wave was then constructed. The following u_s - h relationship

$$u_s = u_i + 0.45 \, \beta \, \ell n \left[(a + e^{h/\beta})/(a + 1) \right] \qquad (15)$$

where u_i denotes the initial shock-particle velocity, $a = 1500$, and the value of the characteristic distance $\beta = 0.18$ was found to give a good fit to the shock-particle velocity in the range $0 \leqslant h \leqslant 3.208$ cm spanned by the first four gages.

Equations (14) and (15), together with the Rankine-Hugoniot jump conditions, allow the calculation of u_s, U, v_s, p_s, Du_s/Dh, DU/Dh, Dp_s/Dh, $(Dp/Dv)_s$ and $(c/v)_s^2$ along the shock trajectory in the domain of the $(t - h)$ plane spanned by the first four gages. Equations (14) and (15) can be used to calculate u_s and U for a given value of h, and then v_s and p_s can be calculated from Eqs. (1) and (2) when the initial density ρ_0 of the explosive is specified. Differentiation of Eqs. (14) and (15) gives expressions for computing Du_s/Dh and DU/Dh, and differentiation of Eq. (2) gives the following expression in terms of those derivatives for computing Dp_s/Dh,

$$\frac{Dp_s}{Dh} = p_s \frac{Du_s}{Dh} \left[\frac{1}{u_s} + \frac{1}{U} \frac{DU}{Du_s} \right] \qquad (16)$$

The corresponding equation for computing the slope of the Hugoniot curve in the $(p - v)$ plane,

$$\left(\frac{Dp}{Dv} \right)_s \left[\frac{DU}{Du_s} \frac{u_s}{U} - 1 \right] = \frac{p}{v_0} \left[\frac{DU}{Du_s} + \frac{U}{u_s} \right] \qquad (17)$$

is obtained by differentiating Eqs. (1) and (2). And the equation for calculating the sound speed $c_s^2 = (\kappa p v)_s$ along the Hugoniot curve

$$\left(\frac{c}{v} \right)_s^2 = - \left(\frac{Dp}{Dv} \right)_s + \frac{\Gamma}{2} \left[\left(\frac{p}{v} \right)_s + \left(\frac{v_0}{v_s} - 1 \right) \left(\frac{Dp}{Dv} \right)_s \right] \qquad (18)$$

is obtained by combining differential forms of the Hugoniot equation Eq. (3) and the $e = e(p, v)$ equation of state of the explosive.

Values of these shock parameters in cast TNT at the first four gage positions are given in Tables 1 and

2 for an initial density of 1.61 gm/cm³. The values of the derivatives in Table 2 are given to five figures for computational purposes, and a value of $\Gamma = 0.68$ was used to compute the sound speed.

The values of $\partial u/\partial t_s$ calculated from the gages records can now be combined with the identities

$$\frac{Du_s}{Dh} = \frac{\partial u}{\partial h_s} + \frac{1}{U} \frac{\partial u}{\partial t_s} \qquad (19)$$

$$\frac{Dp_s}{Dh} = \frac{\partial p}{\partial h_s} + \frac{1}{U} \frac{\partial p}{\partial t_s} \qquad (20)$$

the momentum equation Eq. (5), and the energy equation Eq. (7), to calculate $\partial u/\partial h_s$, $\partial p/\partial t_s$, and the volumetric energy-release rate $\dot{P}_s$ along the shock trajectory in the region spanned by the first four gages. The calculated values of these derivatives at the gage positions are given in Table 3. Plots of the dependence of $\partial u/\partial t_s$, $\partial u/\partial h_s$, and $\partial p/\partial t_s$ on Lagrange distance are shown in Figure 3 and a plot of $\dot{P}_s$ along the shock trajectory is shown in Figure 4.

TABLE 1

Hugoniot Data for Cast TNT

h (cm)	u_s (mm/μsec)	U (mm/μsec)	v_s (cm³/gm)	p_s (kbar	$-(Dp/Dv)_s$ (kbar gm/cm³)
0.000	0.825	4.11	0.496	54.66	1325.69
1.057	0.839	4.15	0.495	56.05	1358.21
2.121	1.196	5.00	0.473	96.30	2219.18
3.208	1.675	6.01	0.448	162.22	2462.53

TABLE 2

Derivatives Along the Shock Path in Cast TNT

h (cm)	Du_s/Dh (μsec)$^{-1}$	DU/Dh (μsec)$^{-1}$	Dp_s/Dh (kbar/mm)	$(c/v)_s^2$ (kbar gm/cm³)
0.000	0.00003	0.00008	0.00299	1249.96
1.057	0.00861	0.02657	0.86592	1279.53
2.121	0.04449	0.10193	5.54552	2051.51
3.208	0.04500	0.08568	6.67061	2262.47

TABLE 3

*Flow Derivatives and Energy-Release Rate Along
the Shock Path in Cast TNT*

h (cm)	$\partial u/\partial t_s$ (mm/μsec^2)	$\partial u/\partial h_s$ (μsec)$^{-1}$	$\partial p/\partial t_s$ (kbar/μsec)	$\dot{P}_s$ (kbar/μsec)
0.000	−0.075	0.018	−4.92	9.15
1.057	0.242	−0.050	19.77	−19.81
2.121	0.121	0.020	37.51	11.70
3.208	−0.804	0.158	−37.70	184.84

MA-310643-2
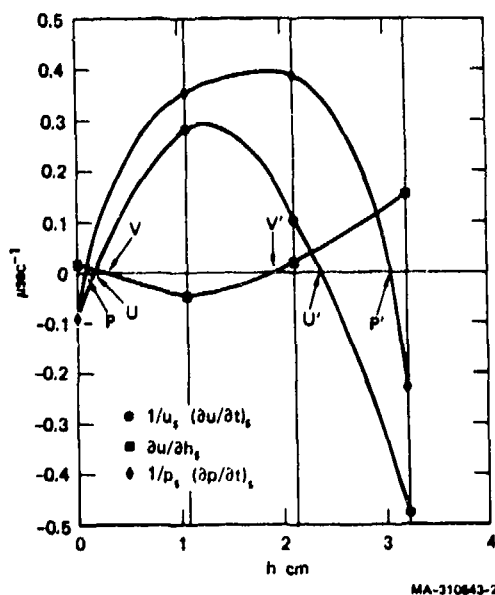
*Fig. 3. Flow derivatives of particle velocity and
pressure at the shock front.*

Figure 3 shows the relative positions of the points
on the shock trajectory considered in the previous
section, where the derivatives $\partial p/\partial t_s$, $\partial u/\partial t_s$, and
$\partial u/\partial h_s$ change signs and become zero as the wave
builds up to detonation. Examination of the plots in
Figure 3 shows that the points P, U, and V where
these derivatives first change sign lie very close
together, but that the points P′, U′, and V′ where
these derivatives change sign again are clearly
separated. Figure 4 shows that the energy-release rate
at the shock front $\dot{P}_s$ changes sign as the wave
develops. The rapid change in $\dot{P}_s$ with shock pressure
is taken in this paper as evidence of a phase change
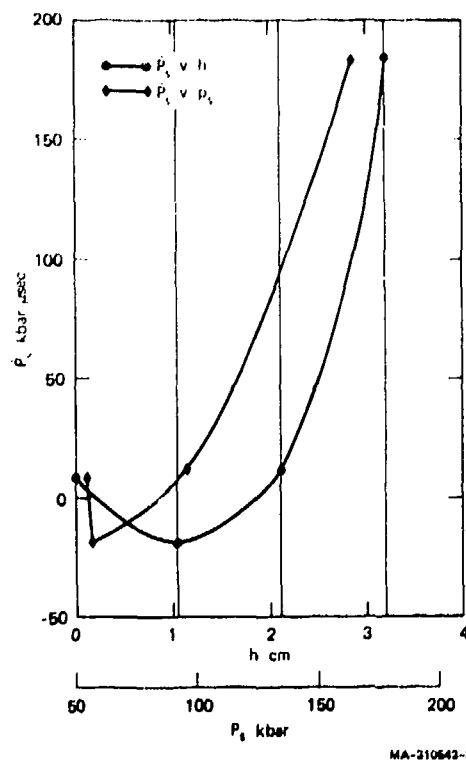in the 55-kbar region in cast TNT. However, the

MA-310643-3

*Fig. 4. Volumetric energy-release rate along the
shock trajectory.*

calculations leading to this conclusion are based on
the assumption that the shock always accelerates, and
an initially decaying shock is compatible with the
shock-arrival times recorded at the first two gage
positions.

CONCLUSIONS

Multiple Lagrange gage studies of explosives pro-
vide the data required to establish mechanisms of
initiation, to calculate the shock properties of
explosives, and to determine the flow properties and
energy-release rates in their initiating waves. The
present Lagrange gage study of cast TNT leads to the
following conclusions:

- Appreciable reaction occurs behind the shock
  in the early stages of initiation because the
  derivatives of pressure and particle velocity at
  the shock front change sign in the order
  $\{\partial p/\partial t_s, \partial p/\partial h_s, \partial u/\partial h_s\}$ as the wave builds up.
  While $\partial p/\partial t_s$ becomes positive, $\partial p/\partial h_s$ and
  $\partial u/\partial h_s$ become negative.

- In the region of the wave where the particle velocity gradient is negative and particles are compressed, the negative pressure gradient created by the overall reaction in the wave exceeds the expansion associated with the local reaction.

- A nonlinear shock-velocity/shock-particle velocity relationship is required to describe the shocked states attained in cast TNT.

- The calculated negative rate of change of energy-release rate at the shock front with increasing pressure is evidence for the occurrence of a shock-induced phase change in cast TNT in the 55-kbar region.

The particle velocity profiles shown in Figure 2 will be used in future work to integrate the equations of motion from the shock front and determine the flow and energy-release rate in the initiating wave behind the shock.

ACKNOWLEDGMENTS

REFERENCES

1. M. Cowperthwaite, "Determination of Energy-Release Rate with the Hydrodynamic Properties of Detonation Waves," p. 1259, 14th Symposium (International) on Combustion, Combustion Institute, 1973

2. William J. Murri and Dennis E. Grady, "Equation of State of Rocks," SRI Project Rept PYU-1883, Apr 1973

3. M. Cowperthwaite and D. C. Erlich, "Investigation of Low-Velocity Detonation Phenomena in Liquid Monopropellants and Explosives," SRI Project Rept. PYU-2382, Feb 1974

4. William J. Murri, "Use of Particle-Velocity Gages to Determine Energy-Release Rates in Explosive Materials," SRI R&D Report, Dec 1974

5. A. N. Dremin and K. K. Shvedov, "The Determination of Chapman-Jouguet Pressure and of the Duration of Reaction in the Detonation Wave of High Explosives," Zh. Prikl, Mekhan. i Teckin. Fiz. (2), pp. 154-159, 1964

6. V. A. Veretennikov, A. N. Dremin, and K. K. Shvedov, "Determination of the Detonation Parameters of Condensed Explosives," Combustion, Explosion and Shock Waves 1, (3), 1, 1965

7. A. N. Dremin, O. K. Rozanov, and I. G. Koba, "Investigation of the Reaction Time for Liquid Explosives Detonated by the Electromagnetic Method," Combustion, Explosion and Shock Waves 1, (3), pp. 52-56, 1965

8. D. J. Edwards, J. O. Erkman, and Donna Price, "The Measurement of Particle Velocity in Pressed Tetryl," NOL Rept 72-83, Aug 1974

9. D. J. Edwards, J. O. Erkman, and Donna Price, "The Measurement of Particle Velocity in Pressed TNT," NOL Rept. 72-82, Aug 1972

LIST OF ATTENDEES *(INCLUDING AUTHORS)*

G. Abrahamson
Stanford Research Institute
333 Ravenswood Avenue
Menlo Park, CA 94025

I. B. Akst
Idos Corporation
P.O. Box 285
Pampa, TX 79065

B. T. Amery
Ministry of Defence
Atomic Weapons Research Establishment
Foulness, Southend-on-Sea
Essex, England

J. T. Amlie
David W. Taylor Naval Ship Research &
    Development Center
Bethesda, MD 20034

A. B. Amster
Naval Sea Systems Command
SE \332
W... .gton, DC 20362

A. B. Anderson
University of California
Los Alamos Scientific Laboratory
P.O. Box 1663
Los Alamos, NM 87545

R. A. Anderson
University of California
Lawrence Livermore Laboratory
P.O. Box 808, L-153
Livermore, CA 94550

W. H. Andersen
Shock Hydrodynamics
4710-16 Vineland Avenue
North Hollywood, CA 91602

E. V. Andreev
Bauman Institute
Iaum 14
Moscow
USSR

E. A. Andrew
Olin Corporation
Winchester-Western Division
Building T189
East Alton, IL 62024

L. Avrami
Picatinny Arsenal
Explosives Division, SARPA-FR-E
Building 407
Dover, NJ 07801

W. H. Bachelder
University of California
Lawrence Livermore Laboratory
P.O. Box 808, L-125
Livermore, CA 94550

C. B. Bangerter
STD Research Corporation
P.O. Box 2007
Granger, UT 84120

L. A. R. Barcellos
Brazilian Naval Commission
4706 Wisconsin Avenue, N.W.
Washington, DC 20016

D. W. Baum
Artec Associates, Inc.
26046 Eden Landing Road
Hayward, CA 94545

J. B. Bdzil
University of California
Los Alamos Scientific Laboratory
Group M-3, MS-960
Los Alamos, NM 87545

R. L. Beauregard
Naval Sea Systems Command
SEA-992E
Navy Department
Washington, DC 20362

M. Beckstead
Hercules, Inc.
P.O. Box 98
Magna, UT 84044

B. M. Belgaumkar
I. A. E. C. (BOM) PVT. LTD. Bhandup.
"Vainatheya," III Floor, No. 1 Flat
192-B-II, S. V. Rd., V. Parle
Bombay-56
India 400 056

M. E. Berger
University of California
Los Alamos Scientific Laboratory, TD-4
P.O. Box 1663 MS-250
Los Alamos, NM 87545

O. R. Bergmann
E. I. du Pont de Nemours & Co., Inc.
Building 336-Polymer Intermediates
    Dept.
Experimental Station Laboratory
Wilmington, DL 19898

N. E. Berkholtz
Stetter Associates, Inc.
3000 Sand Hill Road
Menlo Park, CA 94025

R. R. Bernecker
U.S. Naval Surface Weapons Center
White Oak Laboratory
Silver Spring, MD 20910

E. N. Bjordal
DYNO Industrier A · S
Explosives Division
P.O. Box 1076, 3001
Drammen, Norway

G. Bjarnholt
Swedish Detonic Research Foundation
Box 32058, S-126, 11
Stockholm, Sweden

J. H. Blackburn
Honeywell, Incorporated
600 Second Street North
Hopkins, MN 55343

P. G. Blaine
Council for Scientific & Industrial
    Research
Private Bag X105
Somerset West, South Africa 7130

G. H. Bloom
University of California
Lawrence Livermore Laboratory
P.O. Box 808, L-96
Livermore, CA 94550

J. K. Boettner
Mason & Hanger-Silas Mason Co.,
    Inc.
Pantex Plant
P.O. Box 647
Amarillo, TX 79177

Y. Boldirev
Moscow Auto-Road Institut
Leningradsky Prospect
Moscow
USSR

A. A. Boni
Science Applications, Inc.
1200 Prospect St.
La Jolla, CA 92037

F. G. Borgardt
Lockheed Palo Alto Research Laboratory
3251 Hanover St.
Palo Alto, CA 94304

A. A. Borisov
Institute of Chemical Physics
USSR Academy of Science
Vorobyevskoe chaussee 2b
Moscow 117334 USSR

P. Boulley
Commissariat à l'Energie Atomique
Boîte Postale n° 2
Le Barp 33, France

V. M. Boyle
U.S. Ballistic Research Laboratories
BRL-WMD
Aberdeen Proving Ground
Aberdeen, MD 21005

J. R. Brinkman
Mound Laboratory
Monsanto Research Corporation
P.O. Box 32
Miamisburg, OH 45342

C. G. J. Brochet
Lab. Energetique et Detonique
E. N. S. M. A.
Poitiers, France 86034

P. S. Brown
University of California
Lawrence Livermore Laboratory
P.O. Box 808, L-24
Livermore, CA 94550

A. Burcat
Aeronautical Engineering Department
Technion—Israel Institute of
    Technology
Haifa, Israel 32000

T. J. Burgess
University of California
Lawrence Livermore Laboratory
P.O. Box 808, L-156
Livermore, CA 94550

F. B. Burkdoll
Explosive Technology, Inc.
P.O. Box KK
Fairfield, CA 94533

A. J. Buys
Council for Scientific & Industrial
    Research
Private Bag X105
Somerset West, South Africa 7130

H. H. Cady
University of California
Los Alamos Scientific Laboratory
WX-2, MS-920
P.O. Box 1663
Los Alamos, NM 87545

P. D. Calderon
University of California
Lawrence Livermore Laboratory
P.O. Box 808, L-125
Livermore, CA 94550

A. W. Campbell
University of California
Los Alamos Scientific Laboratory
Group M-3, MS-960
P.O. Box 1663
Los Alamos, NM 87545

W. P. Carvalho
Brazilian Naval Commission
4706 Wisconsin Avenue. N.W.
Washington, DC 20016

R. F. Chaiken
U.S. Bureau of Mines
4800 Forbes Avenue
Pittsburgh, PA 15313

S. K. Chan
Canadian Industries Ltd.
Explosives Research Laboratory
McMasterville, Quebec
Canada J3G 1T9

H. H. Chau
University of California
Lawrence Livermore Laboratory
P.O. Box 808, L-156
Livermore, CA 94550

M. S. Chawla
U.S. Army Ballistic Research Laboratory
Aberdeen Proving Ground
Aberdeen, MD 21009

R. Cheret
C. E. A. "tablissement T
Boîte Postale n° 7
93270 Sevran, France

H. Cheung
University of California
Lawrence Livermore Laboratory
P.O. Box 808, L-402
Livermore, CA 94550

W. C. Chiles
University of California
Los Alamos Scientific Laboratory
Group M-3, MS 960
Los Alamos, NM 87545

T. S. Chou
Mound Laboratory
P.O. Box 32
Miamisburg, OH 45342

S. G. Cochran
University of California
Lawrence Livermore Laboratory
P.O. Box 808, L-24
Livermore, CA 94550

C. S. Coffey
U.S. Naval Surface Weapons Center
White Oak Laboratory
Silver Spring, MD 20910

G. D. Coley
MOD(PE)
Atomic Weapons Research Establish-
    ment
Reading, Berkshire, England

W. Connick
Australian Department of Defence
Materials Research Laboratories
P.O. Box 50, Ascot Vale
Melbourne, Victoria
Australia 03-318-3368

G. R. Cowan
E. I. du Pont de Nemours & Co.
Potomac River Development Lab
Martinsburg, WV 25410

M. Cowperthwaite
Stanford Research Institute
Menlo Park, CA 94025

E. A. Dahout
University of California
Lawrence Livermore Laboratory
P.O. Box 808, L-125
Livermore, CA 94550

F. W. Davies
Boeing Aerospace Company
P.O. Box 3999, Mail Stop 42-37
Seattle, WA 98070

796

W. C. Davis
University of California
Los Alamos Scientific Laboratory
Group M-3, MS 960
P.O. Box 1663
Los Alamos, NM 87545

L. W. Davison
Explosives Physics Division 5131
Sandia Laboratories
KAFB East
P.O. Box 5800
Albuquerque, NM 87115

E. A. Day
Systems, Science & Software
P.O. Box 1620
La Jolla, CA 92038

W. E. Deal, Jr.
University of California
Los Alamos Scientific Laboratory
M-Division, MS-682
P.O. Box 1663
Los Alamos, NM 87545

Y. de Longueville
Société Nahouales des Poudres et
    Explosifs
Centre de Recherches du Bouchet
91 710 Vert-Le-Petit, France

L. De Luca
Politecnico di Milano
32 Piazza L. Da Vinci
Milano, Italy 20133

L. A. Dickinson
U.S. NAVEODFAC
Indian Head, MD 20640

J. Dick
Washington State University
Pullman, WA 99163

R. H. Dinegar
University of California
Los Alamos Scientific Laboratory
Group WX-7, MS 950
P.O. Box 1663
Los Alamos, NM 87545

B. M. Dobratz
University of California
Lawrence Livermore Laboratory
P.O. Box 808, L-401
Livermore, CA 94550

A. B. Donaldson
Sandia Laboratories
P.O. Box 5800
Albuquerque, NM 87115

G. D. Dorough, Jr.
University of California
Lawrence Livermore Laboratory
P.O. Box 808, L-32
Livermore, CA 94550

A. N. Dremin
Institute of Chemical Physics
USSR Academy of Sciences
142432, Chernogolovka, Moscow Region
USSR

R. Duff
Systems, Science & Software
P.O. Box 1620
La Jolla, CA 92038

G. E. Duvall
Department of Physics
Washington State University
Pullman, WA 99163

R. Edelman
R & D Associates
Marina del Rey, CA 90291

D. Edwards
U.S. Naval Surface Weapons Center
White Oak Laboratory
Silver Spring, MD 20910

C. W. Eilo
Hercules, Inc.
910 Market St.
Wilmington, DL 19899

R. Engelke
University of California
Los Alamos Scientific Laboratory
Group M-3, MS 960
P.O. Box 1663
Los Alamos, NM 87545

J. W. Enig
U.S. Naval Surface Weapons Center
White Oak Laboratory
Silver Spring, MD 20910

A. Erez
Ministry of Defense
P.O. Box 2250
Haifa, Israel

L. M. Erickson
University of California
Lawrence Livermore Laboratory
P.O. Box 808, L-24
Livermore, CA 94550

H. D. Fair, Jr.
Energetic Materials Laboratory
Picatinny Arsenal
Dover, NJ 07801

C. Fauquignon
French-German Research Institute
12 Rue de L'Industrie
68301 Saint-Louis, France

K. K. Feng
Department of Energy, Mines & Re-
    sources
CANMET
Mining Research Laboratories
555 Booth Street
Ottawa, Ontario, Canada K1A 0G1

W. S. Filler
U.S. Naval Surface Weapons Center
White Oak Laboratory
Silver Spring, MD 20910

M. Finger
University of California
Lawrence Livermore Laboratory
P.O. Box 808, L-402
Livermore, CA 94550

H. L. Flaugh
University of California MS-933
Los Alamos Scientific Laboratory
P.O. Box 1663
Los Alamos, NM 87545

W. Fleming
Unidynamics/Phoenix, Inc.
P.O. Box 2990
Phoenix, AZ 85062

D. A. Fojt
Naval Weapons Center
China Lake, CA 93555

C. A. Forest
University of California
Los Alamos Scientific Laboratory
P.O. Box 1663, MS-212
Los Alamos, NM 87545

G. R. Fowles
Washington State University
Physics Department
Pullman, WA 99163

H. Freund
Battelle-Institut e.V
Am Roemerhof 35
6000 Frankfurt 90
West Germany

R. B. Frey
U.S. Ballistics Research Laboratory
Attn: AMX-BR-DL
Aberdeen Proving Ground
Aberdeen, MD 21005

J. W. Fronabarger
Unidynamics/Phoenix, Inc.
P.O. Box 2990
Phoenix, AZ 85062

F. J. Fulton
University of California
Lawrence Livermore Laboratory
P.O. Box 808, L-426
Livermore, CA 94550

W. A. Gans
Lockheed Missiles & Space Co., Inc.
Orgn. 83-30
P.O. Box 504
Sunnyvale, CA 94088

S. D. Gardner
University of California
Los Alamos Scientific Laboratory
AWA, MS 100
P.O. Box 1663
Los Alamos, NM 87545

R. L. Geisler
Air Force Rocket Propulsion Laboratory
Attn: MKP
Edwards Air Force Base, CA 93523

M. J. George
University of California
Los Alamos Scientific Laboratory
P.O. Box 1663, Group M-4, MS 940
Los Alamos, NM 87545

A. W. M. Gibb
Defence Research Establishment
   Suffield
Department of National Defence
Ralston, Alberta
Canada T0J 2N0

T. Gibbon
Naschem (PTY) Ltd.
Private Bag X2
Braamfontein 2017
Johannesburg, South Africa 2017

T. R. Gibbs
University of California
Los Alamos Scientific Laboratory
Group M-3, MS 960
P.O. Box 1663
Los Alamos, NM 87545

R. G. Gillis
Embassy of Australia
1601 Massachusetts Ave., N.W.
Washington, DC 20036

M. J. Ginsberg
University of California
Los Alamos Scientific Laboratory
Group WX-7, MS 950
P.O. Box 1663
Los Alamos, NM 87545

C. S. Godfrey
Physics International Co.
2700 Merced Street
San Leandro, CA 94577

J. Goliger
Le Bouchet Research Center/SNPE
Vert-Le-Petit
France 97 710

H. A. Golopol
University of California
Lawrence Livermore Laboratory
P.O. Box 808, L-402
Livermore, CA 94550

T. Gora
Feltman Research Laboratory
Picatinny Arsenal
Dover, NJ 07801

J. E. Gover
Sandia Laboratories
Division 2315
P.O. Box 5800
Albuquerque, NM 87115

H. Gray
David W. Taylor Naval Ship Research &
   Development Center
Bethesda, MD 20084

L. G. Green
University of California
Lawrence Livermore Laboratory
P.O. Box 808, L-402
Livermore, CA 94550

R. C. Green
Aerojet Nuclear Company
550 2nd Street
Idaho Falls, ID 83401

G. A. Greene
Naval Weapons Center
Explosives Technology Branch
Code 4541
China Lake, CA 94555

D. R. Grine
Systems, Science & Software
P.O. Box 1620
La Jolla, CA 92038

H. J. Gryting
Naval Weapons Center
Code 4542 NAVWEPCEN
China Lake, CA 93555

R. P. Guarienti
University of California
Lawrence Livermore Laboratory
P.O. Box 808, L-871
Livermore, CA 94550

R. H. Guay
Naval Plant Rep. Office (NAVPRO)
P.O. Box 504
Sunnyvale, CA 94088

R. M. Guidry
Frank J. Seiler Research Laboratory
FJSRL/NC
USAF Academy, CO 80840

Y. M. Gupta
Stanford Research Institute
333 Ravenswood Avenue
Menlo Park, CA 94025

R. R. Hammond
Naval Undersea Center
Systems Analysis Group, Code 14
San Diego, CA 92132

D. L. Harp
Explosives Technology Branch
Naval Weapons Center
China Lake, CA 93555

J. E. Hay
Department of the Interior
Bureau of Mines, PMSRC
4800 Forbes Avenue
Pittsburgh, PA 15213

B. Hayes
University of California
Lawrence Livermore Laboratory
P.O. Box 808, L-402
Livermore, CA 94550

D. B. Hayes
Sandia Laboratories
P. O. Box 5800
Albuquerque, NM 87115

M. Held
Messerschmitt-Bölkow-Blohm
8898 Schrobenhausen, Postfach 7340
West Germany

F. H. Helm
University of California
Lawrence Livermore Laboratory
P.O. Box 808, L-402
Livermore, CA 94550

798

C. R. Henry
University of California
Lawrence Livermore Laboratory
P.O. Box 808, L-450
Livermore, CA 94550

J. L. Hepworth
Thiokol Corporation
P.O. Box 524
Brigham City, UT 84302

J. Hershkowitz
Feltman Research Laboratory
Explosives Division
Picatinny Arsenal
Dover, NJ 07801

A. N. Hicks
Navel Construction Rese   Establish-
   ment
St. Leonard's Hill
Dunfermline, Fife KY11 5PW
United Kingdom

T. Hikita
The University of Tokyo
Koishikawa 2-4-1, Bunkyo-Ku
Tokyo, Japan 112

G. G. Hill
University of California
Los Alamos Scientific Laboratory
P.O. Box 1663 MS-936
Los Alamos, NM 87545

E. Hirsch
Ministry of Defence of Israel (Rafael)
Palmach St. 6
Kyriat Motzkin, Israel

J. M. Holovka
Sandia Laboratories
P.O. Box 5800
Albuquerque, NM 87115

H. C. Hornig
University of California
Lawrence Livermore Laboratory
P.O. Box 808, L-402
Livermore, CA 94550

P. M. Howe
U.S. Ballistic Research Laboratory
Aberdeen Proving Ground
Aberdeen, MD 21005

J. R. Humphrey
University of California
Lawrence Livermore Laboratory
P.O. Box 808, L-402
Livermore, CA 94550

R. W. Ingham
Teledyne McCormick Selph
3601 Union Road
Hollister, CA 95023

B. L. Iwanciow
Chemical Systems Division
United Technologies
1050 E. Arques Road
Sunnyvale, CA 94088

M. Jackson
Explosives Technology, Inc.
P.O. Box KK
Fairfield, CA 94533

R. K. Jackson
University of California
Lawrence Livermore Laboratory
P.O. Box 808, L-24
Livermore, CA 94550

S. J. Jacobs
U.S. Naval Surface Weapons Center
White Oak Laboratory
Silver Spring, MD 20910

J. J. Jacoby
University of California
Los Alamos Scientific Laboratory
P. O. Box 1663 MS-250
Los Alamos, NM 87545

E. H. Jager
Messerschmitt-Bölkow-Blohm GmbH
Hagenauer Forst
Schrobenhausen
West Germany D-8898

E. James
University of California
Lawrence Livermore Laboratory
P.O. Box 808, L-402
Livermore, CA 94550

R. M. James
Ministry of Defence
Atomic Weapons Research Establishment
Aldermaston, Reading RG7 4 PR
England

R. L. Jameson
U.S. Ballistic Research Laboratories
Aberdeen Proving Ground
Aberdeen, MD 21005

G. J. Jenks
Materials Research Laboratories
P.O. Box 50
Ascot Vale, Victoria
Australia 3032

J. O. Johnson
University of California
Los Alamos Scientific Laboratory
Group WX-7, MS 950
Los Alamos, NM 87545

D. C. Jones
83-01 Propulsion Systems
Lockheed Missiles & Space Co., Inc.
P.O. Box 504
Sunnyvale, CA 94088

H. D. Jones
U.S. Naval Surface Weapons Center
White Oak Laboratory
Silver Spring, MD 20910

T. B. Joyner
Naval Weapons Center
Code 6056
China Lake, CA 93555

M. J. Kamlet
U.S. Naval Surface Weapons Center
White Oak Laboratory
Silver Spring, MD 20901

Y. Kato
Laboratoire d'Energetique et de
   Détonique
E. N. S. M. A.
Universite de Poitiers
rue Guillaume VIII
Poitiers, France 86034

B. W. Kelley, P. E.
Stetter Associates, Inc.
3000 Sand Hill Road
Menlo Park, CA 94025

J. E. Kennedy
Sandia Laboratories
Explosives Physics Division 5131
KAFB East
Albuquerque, NM 87115

N. Kidron
Building Research Station—"Technion"
Israel Institute of Technology
Technion City
Haifa, Israel 32000

K. Kim
Jet Propulsion Laboratory
California Institute of Technology
4800 Oak Grove Drive
Pasadena, CA 91103

C. King
Mound Laboratory
Monsanto Research Corporation
P.O. Box 32
Miamisburg, OH 45342

B. Kirk
McDonnell Douglas Astronautics Co.
Dept. E261, Bldg. 106/3
P.O. Box 516
St. Louis, MO 63166

J. L. Knowles
University of California
Lawrence Livermore Laboratory
P.O. Box 808, L-401
Livermore, CA 94350

R. Knystautas
McGill University
P.O. Box 6070 Station A
Montreal, Quebec, Canada

P. E. Kramer
Mason & Hanger
Silas Mason Co., Inc.
P.O. Box 647
Amarillo, TX 79177

H. Kruger
University of California
Lawrence Livermore Laboratory
P.O. Box 808, L-96
Livermore, CA 94550

M. I. Kuhlman
Potomac River Development Laboratory
E. I. DuPont de Nemours & Company
P.O. Box 863
Martinsburg, WV 25401

M. Kusakabe
National Chemical Laboratory for
    Industry
8th Division
3-4, Nishiyawata 1 chome
Hiratsuka City, Japan

J. W. Kury
University of California
Lawrence Livermore Laboratory
P.O. Box 808, L-401
Livermore, CA 94550

B. D. Lambourn
MOD (PE)
Atomic Weapons Research Establish-
    ment
Aldermaston, Reading
England RG7 4PR

J. Le Boucher
C. E. A.-Etablissement T
Boite Postale n° 7
93270 Sevran, France

E. L. Lee
University of California
Lawrence Livermore Laboratory
P.O. Box 808, L-402
Livermore, CA 94550

R. E. Lee
University of California
Lawrence Livermore Laboratory
P.O. Box 808, L-24
Livermore, CA 94550

D. J. Lewis
Imperial Chemical Industries Ltd.
P.O. Box 7, Winnington
Northwich, Cheshire, England

L. L. Lieptke
Naval Weapons Center
Code 4025
China Lake, CA 93555

C. D. Lind
Naval Weapons Center
Code 4541
China Lake, CA 93555

W. B. Lindquist
University of California
Lawrence Livermore Laboratory
P.O. Box 808, L-153
Livermore, CA 94550

O. Listh
National Defence Research Institute
Box 416, S-172 04
Sundbyberg 4, Sweden

J. J. J. Liebenberg
Naschem (PTY) Ltd.
Private Bag X-2
Braamfontein, Johannesburg 2017
South Africa

N. A. Louie
Shock Hydrodynamics
4716 Vineland Avenue
North Hollywood, CA 91602

D. Ludwig
Messerschmitt-Bölkow-Blohm
8898 Schrobenhausen, Postfach 7340
West Germany

H. J. MacDonald
Reynolds Industries, Inc.
3420 Fostoria Way
San Ramon, CA 94583

O. Machacek
Atlas Powder Corporation
207 North 27th Street
Allentown, PA 18104

C. L. Mader
University of California
Los Alamos Scientific Laboratory
P.O. Box 1662
Group T-14 MS-214
Los Alamos, NM 87545

H. D. Mallory
Naval Weapons Center
Code 6034
China Lake, CA 93555

N. Manson
University of Poitiers
E. N. S. M. A.
rue Guillaume F
Poitiers 86, France

J. J. Marron
Sandia Laboratories
Division 2314
P.O. Box 5800
Albuquerque, NM 87115

E. F. Marshall
University of California
Los Alamos Scientific Laboratory
Group M-4, MS 940
P.O. Box 1663
Los Alamos, NM 87545

W. W. Marshall
U. K. Directorate General Weapons
(Naval) DGW(N)
ASWE
Cosham, Hampshire, England

R. H. Martinson
Lockheed Missiles & Space Co.
3251 Hanover St.
Palo Alto, CA 94304

W. McBride
U.S. Naval Weapons Station
Yorktown, VA 23691

C. B. McCampbell
Sandia Laboratories
Department 2310
P.O. Box 5800
Albuquerque, NM 87115

C. R. McColloch
U. S. Air Force
10 Japonica Lane
Shalimar, FL 32576

J. A. McCrae
Council for Scientific & Industrial
    Research
Private Bag X105
Somerset West, Cape 7130, South Africa

R. R. McGuire
University of California
Lawrence Livermore Laboratory
P.O. Box 808, L-402
Livermore, CA 94550

C. Michaud
C. E. A.–Etablissement T
Boite Postale n° 7
93270 Sevran, France

T. Middleton
A/S Raufoss
Ammunisjor.sfabrikker
Oslo, Norway

R. W. Miller
Office of Naval Research
Power Program
800 N. Quincy Street
Arlington, VA 22217

D. E. Mitchell
Sandia Laboratories
P.O. Box 5800
Albuquerque, NM 87115

K. Miyasaka
Mechanical Engineering
School of Engineering
Osaka University
Yamada-kami
Suita, Osaka 565, Japan

H. J. Mize
University of California
Lawrence Livermore Laboratory
P.O. Box 808, L-810
Livermore, CA 94550

O. Molnar
Council for Scientific & Industrial
    Research
Private Bag X105
Somerset West Cape 7130
South Africa

R. Morales
University of California
Los Alamos Scientific Laboratory
Group WPC-1, MS 634
P.O. Box 1663
Los Alamos, NM 87545

B. Mossinson
Ministry of Defence of Israel
    (Rafael)
Fichman St. 12
Ramot Remez, Haifa, Israel

H. S. Napadensky
ITT Research Institute
10 West 35th Street
Chicago, IL 60616

T. R. Neal
University of California
Los Alamos Scientific Laboratory
Group M-2, MS 942
P.O. Box 1662
Los Alamos, NM 87545

H. Nebel
Bundesamtf, Wehrtechnik und
    Beschaffung
54 Koblenz, Am Rhein ZbisG,
    BWB-WM VI2
54 Koblenz
West Germany 54

W. A. Nelson
University of California
Lawrence Livermore Laboratory
P.O. Box 808, L-80
Livermore, CA 94550

E. Nidick
University of California
Lawrence Livermore Laboratory
P.O. Box 808, L-402
Livermore, CA 94550

P. Nikowitsch
Messerschmitt-Bölkow-Blohm
8898 Schrobenhausen, Postfach 7340
West Germany

B. Olinger
University of California
Los Alamos Scientific Laboratory
Group M-6, MS 970
P.O. Box 1663
Los Alamos, NM 87545

T. S. Olver
Australian Department of Defence
Materials Research Laboratories
P.O. Box 50, Ascot Vale.
Melbourne, Victoria 3032
Australia

A. K. Oppenheim
University of California, Berkeley
Engineering
Berkeley, CA 94720

D. L. Ornellas
University of California
Lawrence Livermore Laboratory
P.O. Box 808, L-402
Livermore, CA 94550

H. D. Owen
Gearhart-Owen Industries, Inc.
P.O. Box 1936
Fort Worth, TX 76101

D. Paisley
Mound Laboratory
Monsanto Research Corporation
P.O. Box 32
Miamisburg, OH 45342

N. L. Parker
University of California
Lawrence Livermore Laboratory
P.O. Box 808, L-24
Livermore, CA 94550

J. L. Parkinson
University of California
Los Alamos Scientific Laboratory
P.O. Box 1663
Group WX-3, MS 933
Los Alamos, NM 87545

Y. Partom
Armament Development Authority
P.O. Box 2250
Haifa, Israel

H. J. Pasman
Technological Laboratory TNO
P.O. Box 45
Ryswyk-2100
Netherlands

M. A. Persechino
Naval Research Laboratory
4555 Overlook, S.W.
Washington, DC 20375

A. Persson
Physics Laboratory, NITRO NOBEL AB
Vinterviken
117 48 Stockholm, Sweden

P. A. Persson
Swedish Detonic Research Foundation
Box 32058
S-126 11
Stockholm, Sweden

D. T. Pilcher
Hercules, Inc.
Computation Department
P.O. Box 98
Magna, UT 84044

J. W. Pitsenberger
Department of the Navy
Strategic Systems Project Office
Washington, DC 20376

A. Popolato
University of California
Los Alamos Scientific Laboratory
Group WX-3, MS 933
Box 1663
Los Alamos, NM 87545

V. A. Popov
Institute Power Energy
19 Lenin Prospect
Moscow, USSR

C. Potthoff
Sandia Laboratories
P.O. Box 969
Livermore, CA 94550

D. Price
U.S. Naval Surface Weapons Center
White Oak Laboratory
Silver Spring, MD 20910

R. L. Rabie
University of California
Los Alamos Scientific Laboratory
Group WX-7, MS 950
P.O. Box 1663
Los Alamos, NM 87545

J. B. Ramsay
University of California
Los Alamos Scientific Laboratory
Group M-3, MS 960
P.O. Box 1663
Los Alamos, NM 87545

A. Rauch
C. E. A.–Etablissement T
Boite Postale n° 7
93270 Sevran, France

R. L. Remillard
University of California
Lawrence Livermore Laboratory
P.O. Box 808, L-24
Livermore, CA 94550

N. O. Rhoton
Mason & Hanger-Silas Mason Co., Inc.
P.O. Box 647
Amarillo, TX 79177

M. H. Rice
Systems, Science & Software
P.O. Box 1620
La Jolla, CA 92038

J. F. Riley
Lockheed Palo Alto Research
    Laboratory
3251 Hanover Street
Palo Alto, CA 94304

Z. W. Ritter
University of California, Berkeley
Department of Mechanical Engineering
Berkeley, CA 94720

H. F. Rizzo
University of California
Lawrence Livermore Laboratory
P.O. Box 808, L-402
Livermore, CA 94550

L. W. Roberts
University of California
Lawrence Livermore Laboratory
P.O. Box 808, L-401
Livermore, CA 94550

R. R. Rollins
University of Missouri-Rolla
1708 Lee Circle
Rolla, MO 65401

J. Romain
E. N. S. M. A.
rue Guillaume 7
86034 Poitiers, France

G. Rosenberg
Washington State University
Department of Physics
Pullman, WA 99163

J. T. Rosenberg
Stanford Research Institute
333 Ravenswood Avenue
Menlo Park, CA 94025

L. A. Roslund
U.S. Naval Surface Weapons Center
White Oak Laboratory
Silver Spring, MD 20910

J. Roth
Consultant
308 Canyon Drive
Portola Valley, CA 94025

L. R. Rothstein
U.S. Naval Weapons Station
Yorktown, VA 23691

J. W. Routh
University of California
Lawrence Livermore Laboratory
P.O. Box 808, L-353
Livermore, CA 94550

L. D. Sadwin
I. M. I.
P.O. Box 7055
Tel Aviv, Israel

L. W. Saffian
U. S. Army
Picatinny Arsenal
SARPA-MT, Bldg. 172
Dover, NJ 07801

J. A. Saint-Cloud
Lab. Energetique et Detonique
E. N. S. M. A.
Poitiers 86034, France

P. K. Salzman
General Dynamics/Pomona Division
P.O. Box 2507
Pomona, CA 91766

M. Schaffer
Science Applications, Inc.
P.O. Box 2351
La Jolla, CA 92038

A. A. Schilperoord
Technological Laboratory TNO
P.O. Box 45
Ryswyk-2100
Netherlands

W. G. Schmacker
Bundesamtf. Wehrtechnik und
    Beschaffung
54 Koblenz, Am Rhein ZbisG,
    BWB-WM VI2
54 Koblenz, West Germany 54

N. A. Schneider
University of California
Lawrence Livermore Laboratory
P.O. Box 808, L-125
Livermore, CA 94550

H. Schubert
Institute für Chemie der Treibund
    Explosivstoffe
Institutsstrasse
7507 Pfinztal-Berghausen
West Germany

A. C. Schwarz
Sandia Laboratories
P.O. Box 5800
Albuquerque, NM 87115

K. J. Schribner
University of California
Lawrence Livermore Laboratory
P.O. Box 808, L-402
Livermore, CA 94550

J. Q. Searcy
Sandia Laboratories
Org. 2515
P.O. Box 5800
Albuquerque, NM 87115

G. E. Seay
University of California
Los Alamos Scientific Laboratory
P.O. Box 1663 MS-950
Los Alamos, NM 87545

R. T. Sedqwick
Systems, Science & Software
P.O. Box 1620
La Jolla, CA 92038

W. L. Seitz
University of California
Los Alamos Scientific Laboratory
P.O. Box 1663 MS-950
Los Alamos, NM 87545

R. Shaw
1162 Quince Avenue
Sunnyvale, CA 94087

G. D. Shock
Naval Explosive Ordnance
   Disposal Facility
Indian Head, MD 20640

H. M. Shuey
Rohm and Haas Company
723-A Arcadia Circle
Huntsville, AL 35801

B. D. Smith
Naval Surface Weapons Center
Dahlgren Laboratory
Code IDG-31
Dahlgren, VA 22448

D. Smith
Hercules Inc.
P.O. Box 98
Magna, UT 84044

L. Smith
General Dynamics/Pomona Division
P.O. Box 2507
Pomona, CA 91766

L. C. Smith
University of California
Los Alamos Scientific Laboratory
Group WX-7, MS 950
P.O. Box 1663
Los Alamos, NM 87545

R. I. Soloukhin
Heat and Mass Transfer Institute
BSSR Academy of Science
15 Podlesnaya
Minsk 220728, USSR

R. L. Spaulding
University of California
Los Alamos Scientific Laboratory
P.O. Box 1663 MS-950
Los Alamos, NM 87545

D. E. Stanfel
University of California
Lawrence Livermore Laboratory
P.O. Box 808, L-80
Livermore, CA 94550

R. L. Steele
Aerojet Solid Propulsion Company
Bldg. 2019, Dept. 4350
P.O. Box 13400
Sacramento, CA 95813

H. M. Sternberg
U.S. Naval Surface Weapons Center
White Oak Laboratory
Silver Spring, MD 20910

V. Stocker
E. I. duPont de Nemours & Co., Inc.
Potomac River Development Lab
P.O. Box 761
Martinsburg, WV 25401

R. A. Strehlow
University of Illinois
105 Transportation Building
Urbana, IL 61801

R. H. Stresau
R. Stresau Laboratory, Inc.
Star RTE
Spooner, WI 54801

J. R. Stroud
University of California
Lawrence Livermore Laboratory
P.O. Box 808, L-125
Livermore, CA 94550

S. Taki
Fukui University
Department of Mechanical Engineering
3-9-1 Bunkyo
Fukui, Japan

C. M. Tarver
Stanford Research Institute
333 Ravenswood Avenue
Menlo Park, CA 94061

B. C. Taylor
U.S. Ballistic Research Laboratory
Attn: DRXBR-WM
Aberdeen Proving Ground
Aberdeen, MD 21005

B. F. Throneburg
Hercules, Inc.
P.O. Box 98
Magna, UT 84044

G. M. Thornley
IRECO Chemicals
Suite 726 Kennecott Bldg.
Salt Lake City, UT 84133

V. M. Titov
Institute of Hydrodynamics
630090 Novosibirsk
Novosibirsk, USSR

E. L. Throckmorton, Jr.
Strategic Systems Projects Office
Department of the Navy
Washington, DC 20376

J. E. Toni
Ministry of Defense
Zufriategui Yuarelo
U. Martelli
Pcia Buenos Aires
Argentina

G. Torti
Snia Viscosa GSR/CSE
Corso Garibaldi 8
00034 Colleferro (Roma)
Italy

A. J. Tulis
IIT Research Institute
10 West 35th Street
Chicago, IL 60616

L. L. Udy
IRECO Chemicals
726 Kennecott Building
Salt Lake City, UT 84133

P. A. Urtiew
University of California
Lawrence Livermore Laboratory
P.O. 808, L-402
Livermore, CA 94550

R. W. Van Dolah
U.S. Bureau of Mines
4800 Forbes Avenue
Pittsburgh, PA 15213

R. E. Varosh
University of California
Lawrence Livermore Laboratory
P.O. Box 808, L-406
Livermore, CA 94550

M. Van Thiel
University of California
Lawrence Livermore Laboratory
P.O. Box 808, L-450
Livermore, CA 94550

P. Veyrie
C. E. A.-Etablissement T
Boîte Postale n° 7
93270 Sevran, France

W. G. Von Holle
U. S. Ballistics Research Laboratories
Aberdeen Proving Ground
Aberdeen, MD 21005

J. D. Wackerle
University of California
Los Alamos Scientific Laboratory
P. O. Box 1663, Group WX-7, MS 950
Los Alamos, NM 87545

F. E. Walker
University of California
Lawrence Livermore Laboratory
P.O. Box 808, L-401
Livermore, CA 94550

R. Walker
Explosive Laboratory
Picatinny Arsenal
Dover, NJ 07801

J. R. Walton
University of California
Lawrence Livermore Laboratory
P.O. Box 808, L-402
Livermore, CA 94550

D. Warne
Science Applications, Inc.
P.O. Box 2351
La Jolla, CA 92038

R. K. Warner
Harry Diamond Laboratories
2800 Powder Mill Road
Adelphi, MD 20783

R. H. Warnes
University of California
Los Alamos Scientific Laboratory
M-4; MS 940
P.O. Box 1663
Los Alamos, NM 87545

T. W. Warren
Mason & Hanger
Silas Mason Co., Inc.
Pantex Plant
P.O. Box 647
Amarillo, TX 79177

R. W. Watson
Department of the Interior
Bureau of Mines, PMSRC
4800 Forbes Avenue
Pittsburgh, PA 15213

R. C. Weingart
University of California
Lawrence Livermore Laboratory
P.O. Box 808, L-24
Livermore, CA 94550

A. B. Wenzel
Southwest Research Institute
8500 Culebra Road
San Antonio, TX 78284

G. T. West
Mason & Hanger-Silas Mason Co., Inc.
P.O. Box 647
Amarillo, TX 79177

J. C. Whitson
Naval Weapons Center
Code 4541
China Lake, CA 93555

A. H. Wiedermann
ITT Research Institute
10 West 35th Street
Chicago, IL 60616

M. L. Wilkins
University of California
Lawrence Livermore Laboratory
P.O. Box 808, L-450
Livermore, CA 94550

R. A. Williams, Jr.
GEAR, Inc.
260 Sheridan Avenue
Palo Alto, CA 94301

B. T. Wolfson
AFOSR (NA)
Bolling Air Force Base (Bldg. 910)
Washington, DC 20332

D. F. Wright
University of California
Lawrence Livermore Laboratory
P.O. Box 808, L-24
Livermore, CA 94550

L. C. Yang
Jet Propulsion Laboratory
4800 Oak Grove Drive
Pasadena, CA 91103

T. T. Yee
Naval Weapons Center
Code 4542
China Lake, CA 93555

M. Yoshida
University of Tokyo
Department of Reaction Chemistry
Faculty of Engineering
Hongo Bunkyo-ku
Tokyo 113, Japan

S. D. Zaharia
Northrop Corporation
Electro-Mechanical Division
500 East Orangethorpe Division
Anaheim, CA 92801

T. A. Zaker
Department of Defense
Explosives Safety Board
1000 Independence Avenue, S.W.
Washington, DC 20314

A. Zehavi
Ministry of Defence of Israel
P.O. Box 2250
Haifa, Israel

L. Zernow
Shock Hydrodynamics Division
Whittaker Corporation
4716 Vineland Avenue
North Hollywood, CA 91602

T. H. Zimmerman
Schlumberger Well Services
P.O. Box 2175
Houston, TX 77001

A. Zin
Ministry of Defence of Israel
P.O. Box 2250
Haifa, Israel

R. Zoret
University of California
Lawrence Livermore Laboratory
P.O. Box 808, L-125
Livermore, CA 94550

AUTHOR INDEX

(D) indicates Discussion

Abouseif, G. E., 502 (D)
Akst, I., 439
Amery, B. T., 673
Andersen, W. H., 682
Antipenko, A. G., 143
Austing, J. L., 183
Avrami, L., 389

Barlett, R. H., 755
Bdzil, J. B., 352
Beckstead, M., 258
Belgaumkar, B. M., 20, (D)
Benhaim, P., 195
Bernecker, R. R., 426
Bjarnholt, G., 510, 540
Boat, R., 729
Borgardt, F. G., 389
Borisov, A. A., 250
Boyle, V., 11
Brochet, C., 124
Burcat, A., 590
Burrows, K., 625

Cady, H. H., 700
Campbell, A. W., 642
Carlson, L. A., 460
Catalano, E., 214
Chaiken, R. F., 344
Chawla, M., 325
Chen, P. J., 379
Cheung, H., 729
Chiles, W. C., 664, 723
Chilvers, D. K., 625
Christensen, L. W., 258
Clairmont, A. R., 426
Coburn, M. D., 460
Coley, G. D., 290
Cowperthwaite, M., 162 (D), 231 (D), 786
Cramer, J. P., 466
Cruysberg, E. E. A., 299

Davies, F. W., 389, 740 (D)
Davis, W. C., 637, 664
de Longueville, Y., 105
de Luca, L., 281
Dietzel, R. W., 455
Dinegar, R. A., 460
Downs, D. S., 390
Dremin, A. N., 29, 143

Eden, G., 477 (D)
Edwards, D. J., 766
Edwards, J. C., 344

Eidelman, S., 590
Ek, S., 272
Elson, R. E., 466
Engelke, R., 642
Enig, J. W., 570
Erkman, J. O., 426, 766
Ermolaev, B. S., 250
Ervin, L. H., 3 (D)

Fair, H. D., 390
Farag, S. A., 502 (D)
Fauquignon, C., 105
Filler, W. S., 777
Finger, M., 710, 729
Freund, H. V., 521 (D)
Frey, R., 11, 325
Fyfe, R. R., 466

Geiger, W., 521 (D)
Goodale, T. C., 231 (D)
Goliger, J., 195
Gora, T., 390
Green, L. G., 755
Groothuizen, Th. M., 299
Guidry, M., 710
Guirguis, R. H., 502 (D)
Gyton, R., 625

Halleck, P. M., 20
Hardesty, D. R., 47
Hay, J. E., 115 (D)
Hayes, B., 710, 729
Hayes, D. B., 76, 668, 748
Held, M., 225
Helm, F., 710, 729
Hershkowitz, J., 439
Hicks, A. N., 551
Hofer, W. W., 755
Holmberg, R., 540
Honica, G., 521 (D)
Hornig, H., 710
Howe, P., 11
Hurwitz, H., 528

Jackson, R. K., 653, 755
Jacobs, S. J., 305
Jacquesson, J., 151
James, R. M., 489
Johnson, J. O., 20

Kahara, M., 710
Kamel, M. M., 502 (D)
Kamlet, M. J., 305, 312
Kato, Y., 124
Kennedy, J. E., 47 (D), 68, 379
Khasainov, B. A., 250
Khrapovskky, V. E., 250
Korothov, A. I., 250
Kot, C. A., 336

Kramer, P. E., 755
Kravtsov, V. V., 36
Kusakabe, M., 133 (D), 450

Lambourn, B. D., 477 (D), 489, 561, 625
Lederer, R. A., 668
Lee, E., 214, 710, 729
Lee, R. S., 653, 755
Leslie, W. B., 455
Listh, O., 204
Louie, N. A., 682
Ludwig, D., 225

Mader, C. L., 405
Mark, P., 390
McQuire, R., 214, 710
Melani, G., 325
Menichelli, V. J., 612
Mitchell, D. E., 748
Moore, P. W. J., 489
Morris, C. E., 396
Moulard, H., 105

Napadensky, H. S., 336
Neal, T. R., 602
Nidick, E. J., 755
Nikowitsch, P., 225
Nunziato, J. W., 47 (D)

Olinger, B., 700
Oppenheim, A. K., 502 (D)
Ornellas, D., 214

Parker, N. L., 653
Pasman, H. J., 299
Pastine, D. J., 305
Penn, L., 729
Persson, G., 414
Persson, P. A., 414
Pilcher, D. T., 258
Price, D., 426

Ramsey, J. B., 723
Riley, J. F., 740 (D)
Romain, J. P., 151
Rosenberg, J. T., 786

Schilperoord, A. A., 371
Schwarz, A. C., 62, 668
Scribner, K., 466
Searcy, J. Q., 62, 455
Shaw, L. L., 755
Shaw, R., 231 (D)
Sheffield, S. A., 668, 748
Siino, K., 450
Shikari, Y. A., 336
Shrader, J., 740 (D)
Shvedov, K. K., 29

805